

CARBON MATERIALS FOR CATALYSIS

CARBON MATERIALS FOR CATALYSIS

Edited by

Philippe Serp
José Luís Figueiredo



WILEY

A JOHN WILEY & SONS, INC., PUBLICATION

Copyright © 2009 by John Wiley & Sons, Inc. All rights reserved.

Published by John Wiley & Sons, Inc., Hoboken, New Jersey.

Published simultaneously in Canada.

No part of this publication may be reproduced, stored in a retrieval system, or transmitted in any form or by any means, electronic, mechanical, photocopying, recording, scanning, or otherwise, except as permitted under Section 107 or 108 of the 1976 United States Copyright Act, without either the prior written permission of the Publisher, or authorization through payment of the appropriate per-copy fee to the Copyright Clearance Center, Inc., 222 Rosewood Drive, Danvers, MA 01923, (978) 750-8400, fax (978) 750-4470, or on the web at www.copyright.com. Requests to the Publisher for permission should be addressed to the Permissions Department, John Wiley & Sons, Inc., 111 River Street, Hoboken, NJ 07030, (201) 748-6011, fax (201) 748-6008, or online at <http://www.wiley.com/go/permission>.

Limit of Liability/Disclaimer of Warranty: While the publisher and author have used their best efforts in preparing this book, they make no representations or warranties with respect to the accuracy or completeness of the contents of this book and specifically disclaim any implied warranties of merchantability or fitness for a particular purpose. No warranty may be created or extended by sales representatives or written sales materials. The advice and strategies contained herein may not be suitable for your situation. You should consult with a professional where appropriate. Neither the publisher nor author shall be liable for any loss of profit or any other commercial damages, including but not limited to special, incidental, consequential, or other damages.

For general information on our other products and services or for technical support, please contact our Customer Care Department within the United States at (800) 762-2974, outside the United States at (317) 572-3993 or fax (317) 572-4002.

Wiley also publishes its books in a variety of electronic formats. Some content that appears in print may not be available in electronic formats. For more information about Wiley products, visit our web site at www.wiley.com.

Library of Congress Cataloging-in-Publication Data:

Serp, Philippe.

Carbon Materials for Catalysis / Philippe Serp, José Luís Figueiredo.

p. cm.

Includes index.

ISBN 978-0-470-17885-0 (cloth)

1. Carbon. 2. Catalysis. I. Figueiredo, José Luís. II. Title.

TP245.C4S47 2009

660'.2995—dc22

2008019014

Printed in the United States of America

10 9 8 7 6 5 4 3 2 1

Contents

Contributors	xv
Preface	xix
1 Physicochemical Properties of Carbon Materials: A Brief Overview	1
<i>Ljubisa R. Radovic</i>	
1.1. Introduction, 1	
1.2. Formation of Carbons, 2	
1.2.1. Gas Phase, 2	
1.2.2. Liquid Phase, 3	
1.2.3. Solid Phase, 4	
1.3. Structure and Properties of Carbons, 5	
1.3.1. Macrostructure, 5	
1.3.2. Microstructure, 8	
1.3.3. Nanostructure, 8	
1.3.4. Bulk Properties, 16	
1.3.5. Surface Properties, 19	
1.4. Reactions of Carbons, 23	
1.4.1. Gas Phase, 23	
1.4.2. Liquid Phase, 25	
1.4.3. Solid Phase, 27	
1.5. Conclusions, 33	
References, 34	
2 Surface Chemistry of Carbon Materials	45
<i>Teresa J. Bandosz</i>	
2.1. Introduction, 45	
2.2. Surface Functionalities, 47	
2.2.1. Oxygen-Containing Functionalities, 48	
2.2.2. Nitrogen-Containing Functionalities, 50	
2.2.3. Hydrogen–Carbon Species, 51	
2.2.4. Sulfur, Phosphorus, and Halogen Functionalities, 51	

2.3.	Surface Modifications, 54
2.3.1.	Oxidation, 54
2.3.2.	Introduction of Nitrogen-Containing Species, 55
2.3.3.	Introduction of Sulfur Functionality, 55
2.3.4.	Halogenization, 56
2.3.5.	Impregnation and Dry Mixing, 56
2.3.6.	Heat Treatment, 56
2.4.	Characterization of Surface Chemistry, 58
2.4.1.	Elemental Analysis, 58
2.4.2.	Titration, 58
2.4.3.	pH of Carbons, Point of Zero Charge, and Isoelectric Point, 61
2.4.4.	Spectroscopic Methods, 63
2.4.5.	Calorimetric Techniques, 72
2.4.6.	Inverse Gas Chromatography, 75
2.4.7.	Temperature-Programmed Desorption, 75
2.4.8.	Characterization of Surface Functionalities by Electrochemical Techniques, 78
2.5.	Role of Surface Chemistry in the Reactive Adsorption on Activated Carbons, 78
2.6.	Role of Carbon Surface Chemistry in Catalysis, 80
	References, 82

3 Molecular Simulations Applied to Adsorption on and Reaction with Carbon 93

Zhonghua (John) Zhu

3.1.	Introduction, 93
3.2.	Molecular Simulation Methods Applied to Carbon Reactions, 94
3.2.1.	Electronic Structure Methods (or Quantum Mechanics Methods), 94
3.2.2.	Molecular Dynamics Simulations, 97
3.2.3.	Monte Carlo Simulations, 98
3.3.	Hydrogen Adsorption on and Reaction with Carbon, 98
3.3.1.	Atomic Hydrogen Adsorption on the Basal Plane of Graphite, 98
3.3.2.	Reactivities of Graphite Edge Sites and Hydrogen Reactions on These Sites, 101
3.3.3.	Hydrogen Storage in Carbon Nanotubes, 104
3.4.	Carbon Reactions with Oxygen-Containing Gases, 105
3.4.1.	Carbon Reactions with Oxygen-Containing Gases and the Unified Mechanism, 106
3.4.2.	Catalyzed Gas–Carbon Reactions, 110

3.4.3. More Specific Studies on NO _x , H ₂ , CO ₂ , and O ₂ –Carbon Reactions, 118	
3.5. Metal–Carbon Interactions, 122	
3.6. Conclusions, 125	
References, 126	
4 Carbon as Catalyst Support	131
<i>Francisco Rodríguez-Reinoso and Antonio Sepúlveda-Escribano</i>	
4.1. Introduction, 131	
4.2. Properties Affecting Carbon’s Role as Catalyst Support, 132	
4.2.1. Surface Area and Porosity, 132	
4.2.2. Surface Chemical Properties, 134	
4.2.3. Inertness, 136	
4.3. Preparation of Carbon-Supported Catalysts, 137	
4.3.1. Impregnation, 137	
4.3.2. Other Methods, 139	
4.4. Applications, 140	
4.4.1. Ammonia Synthesis, 141	
4.4.2. Hydrotreating Reactions, 143	
4.4.3. Hydrogenation Reactions, 147	
4.5. Summary, 150	
References, 150	
5 Preparation of Carbon-Supported Metal Catalysts	157
<i>Johannes H. Bitter and Krijn P. de Jong</i>	
5.1. Introduction, 157	
5.2. Impregnation and Adsorption, 157	
5.2.1. Interaction Between Support and Precursor, 158	
5.2.2. Role of Pore Structure, 164	
5.3. Deposition Precipitation, 165	
5.3.1. Increase in pH, 166	
5.3.2. Change of Valency, 169	
5.3.3. Ligand Removal, 170	
5.4. Emerging Preparation Methods, 171	
5.5. Conclusions, 172	
References, 173	
6 Carbon as Catalyst	177
<i>José Luís Figueiredo and Manuel Fernando R. Pereira</i>	
6.1. Introduction, 177	
6.2. Factors Affecting the Performance of a Carbon Catalyst, 178	

6.2.1.	Nature of the Active Sites,	178
6.2.2.	Concentration of the Active Sites,	179
6.2.3.	Accessibility of the Active Sites,	179
6.3.	Reactions Catalyzed by Carbons,	180
6.3.1.	Oxidative Dehydrogenation,	181
6.3.2.	Dehydration of Alcohols,	186
6.3.3.	SO _x Oxidation,	188
6.3.4.	NO _x Reduction,	190
6.3.5.	H ₂ S Oxidation,	194
6.3.6.	Hydrogen Peroxide Reactions,	196
6.3.7.	Catalytic Ozonation,	198
6.3.8.	Catalytic Wet Air Oxidation,	203
6.3.9.	Other Reactions,	205
6.4.	Conclusions,	207
	References,	208
7	Catalytic Properties of Nitrogen-Containing Carbons	219
	<i>Hanns-Peter Boehm</i>	
7.1.	Introduction,	219
7.2.	Nitrogen Doping of Carbons,	220
7.2.1.	Preparation of Nitrogen-Containing Carbons,	220
7.2.2.	Quantitative Analysis,	227
7.2.3.	Electron Emission Spectrometric Analysis,	227
7.2.4.	Properties of Nitrogen-Containing Carbons,	233
7.3.	Catalysis of Oxidation Reactions with Dioxygen,	238
7.3.1.	Oxidation of Aqueous Sulfurous Acid,	238
7.3.2.	Oxidation of Oxalic Acid,	244
7.3.3.	Oxidation of Sulfur Dioxide,	244
7.3.4.	Oxidation of Iron(II) Ions,	246
7.3.5.	Oxidation of Other Compounds,	247
7.4.	Catalysis of Aging of Carbons,	251
7.5.	Catalysis of Dehydrochlorination Reactions,	254
7.6.	Mechanism of Catalysis by Nitrogen-Containing Carbons,	257
	References,	259
8	Carbon-Anchored Metal Complex Catalysts	267
	<i>Cristina Freire and Ana Rosa Silva</i>	
8.1.	Introduction,	267
8.2.	General Methods for Molecule Immobilization,	268
8.3.	Methods for Immobilization of Transition-Metal Complexes Onto Carbon Materials,	270

8.3.1.	Functionalization of Carbon Materials,	271
8.3.2.	Direct Immobilization of Metal Complexes,	278
8.3.3.	Metal Complex Immobilization via Spacers,	285
8.4.	Application of Coordination Compounds Anchored Onto Carbon Materials in Several Catalytic Reactions,	289
8.4.1.	[M(<i>salen</i>)]-Based Materials,	290
8.4.2.	[M(<i>acac</i>) ₂]-Based Materials,	293
8.4.3.	Metal Phthalocyanine and Porphyrin-Based Materials,	
	294	
8.5.	Application of Carbon-Supported Organometallic Compounds in Hydrogenation and Hydroformylation Catalytic Reactions,	296
8.5.1.	Materials Based on Pd and Rh Amino Complexes,	296
8.5.2.	Materials Based on Rh and Pd Complexes with π-Bonding Ligands (Phosphines and Dienes),	297
8.6.	Carbon-Supported Organometallic Complexes in the Polymerization Reaction of Olefins,	300
8.7.	Conclusions,	301
	References,	302

9 Carbon Nanotubes and Nanofibers in Catalysis 309

Philippe Serp

9.1.	Introduction,	309
9.2.	Catalytic Growth of Carbon Nanofibers and Nanotubes,	312
9.2.1.	Catalytic Carbon Deposition,	312
9.2.2.	Growth Mechanism,	313
9.3.	Why CNTs or CNFs Can Be Suitable for Use in Catalysis,	324
9.3.1.	Structural Features and Electronic Properties,	324
9.3.2.	Adsorption Properties,	328
9.3.3.	Mechanical and Thermal Properties,	330
9.3.4.	Macroscopic Shaping of CNTs and CNFs,	331
9.4.	Preparation of Supported Catalysts on CNTs and CNFs,	333
9.5.	Catalytic Performance of CNT- and CNF-Based Catalysts,	340
9.5.1.	Hydrogenation Reactions,	340
9.5.2.	Reactions Involving CO/H ₂ ,	344
9.5.3.	Polymerization,	345
9.5.4.	Carbon Nanotubes Synthesis by Catalytic Decomposition of Hydrocarbons,	348
9.5.5.	Ammonia Synthesis and Decomposition,	349
9.5.6.	Environmental Catalysis and Oxidation Reactions,	350
9.5.7.	Other Reactions,	351
9.5.8.	Fuel Cell Electrocatalysts,	354
9.5.9.	CNTs for Enzyme Immobilization,	355

9.5.10. CNTs and CNFs as Catalysts,	356
9.6. Conclusions,	356
References,	358
10 Carbon Gels in Catalysis	373
<i>Carlos Moreno-Castilla</i>	
10.1. Introduction,	373
10.2. Carbon Gels: Preparation and Surface Properties,	374
10.3. Metal-Doped Carbon Gels,	376
10.3.1. Dissolving the Metal Precursor in the Initial Mixture,	378
10.3.2. Introducing a Functionalized Moiety,	381
10.3.3. Depositing the Metal Precursor on the Organic or Carbon Gel,	382
10.4. Catalytic Reactions of Metal-Doped Carbon Gels,	383
10.4.1. Environmental Applications,	384
10.4.2. Fuel Cell Applications,	387
10.4.3. C=C Double-Bond Hydrogenation,	389
10.4.4. Skeletal Isomerization of 1-Butene,	391
10.4.5. Hydrodechlorination Reaction,	392
10.4.6. Other Reactions,	392
10.5. Conclusions,	393
References,	395
11 Carbon Monoliths in Catalysis	401
<i>Karen M. de Lathouder, Edwin Crezee, Freek Kapteijn, and Jacob A. Moulijn</i>	
11.1. Introduction,	401
11.2. Carbon,	401
11.3. Monolithic Structures,	402
11.4. Carbon Monoliths,	402
11.5. Carbon Monoliths in Catalysis: An Overview,	404
11.6. Example of Carbon Monoliths as Catalyst Support Material,	405
11.6.1. Carbon Monoliths as Support Material in Biocatalysis,	405
11.6.2. Selective Hydrogenation of D-Glucose over Monolithic Ruthenium Catalysts,	405
11.6.3. Performance of Carbon Monoliths,	406
11.6.4. Morphology and Porosity of Various Carbon Composites,	407
11.6.5. Enzyme Adsorption and Catalyst Performance in the MSR,	413
11.6.6. Performance of Monolithic Ruthenium Catalysts,	416
11.7. Evaluation and Practical Considerations,	420

11.7.1.	Monolithic Biocatalysts, 420	
11.7.2.	Monolithic Ruthenium Catalysts, 421	
11.7.3.	Practical Considerations, 421	
11.8.	Conclusions, 423	
	References, 424	
12	Carbon Materials as Supports for Fuel Cell Electrocatalysts	429
	<i>Frédéric Maillard, Pavel A. Simonov, and Elena R. Savinova</i>	
12.1.	Introduction, 429	
12.2.	Structure and Morphology of Carbon Materials, 433	
12.2.1.	Carbon Blacks, 433	
12.2.2.	Activated Carbons, 434	
12.2.3.	Carbons of the Sibunit Family, 435	
12.2.4.	Ordered Mesoporous Carbons, 436	
12.2.5.	Carbon Aerogels, 436	
12.2.6.	Carbon Nanotubes and Nanofibers, 437	
12.3.	Physicochemical Properties of Carbon Materials Relevant to Fuel Cell Operation, 438	
12.3.1.	Electron Conduction, 438	
12.3.2.	Surface Properties, 440	
12.4.	Preparation of Carbon-Supported Electrocatalysts, 443	
12.4.1.	Methods Based on Impregnation, 444	
12.4.2.	Colloidal Synthesis, 445	
12.4.3.	Electrodeposition, 445	
12.4.4.	Other Methods, 446	
12.5.	Structural Characterization of Carbon-Supported Metal Catalysts, 446	
12.5.1.	Adsorption Studies, 447	
12.5.2.	Transmission Electron Microscopy, 448	
12.5.3.	Xray Diffraction and Xray Absorption Spectroscopy, 449	
12.5.4.	Electrochemical Methods, 450	
12.6.	Influence of Carbon Supports on the Catalytic Layers in PEMFCs, 452	
12.6.1.	Intrinsic Catalytic Activity, 452	
12.6.2.	Macrokinetic Parameters, 456	
12.6.3.	Novel Carbon Materials as Supports for Fuel Cell Electrocatalysts, 462	
12.7.	Corrosion and Stability of Carbon-Supported Catalysts, 464	
12.7.1.	Influence of Microstructure on the Corrosion of Carbon Materials, 464	
12.7.2.	Mechanism of Carbon Corrosion, 466	

12.7.3. Corrosion and Stability of MEAs,	467
12.8. Conclusions,	469
References,	470
13 Carbon Materials in Photocatalysis	481
<i>Joaquim Luís Faria and Wendong Wang</i>	
13.1. Introduction,	481
13.2. Carbon Materials Employed to Modify TiO ₂ in Photocatalysis,	482
13.2.1. Activated Carbon,	482
13.2.2. Carbon Black and Graphite,	483
13.2.3. Carbon Fiber,	483
13.2.4. Carbon Nanotubes,	483
13.2.5. Other Forms of Carbon,	484
13.3. Synthesis and Characterization of Carbon–TiO ₂ Composites,	484
13.3.1. Mechanical Mixture of TiO ₂ and Carbon Materials,	485
13.3.2. TiO ₂ Coated or Loaded on Carbon Materials,	485
13.3.3. Carbon Materials Coated or Deposited on TiO ₂ ,	485
13.3.4. Other Approaches and Concurrent Synthesis of TiO ₂ –Carbon Composites,	486
13.3.5. Methods of Characterization,	486
13.4. Photodegradation on Carbon-Containing Surfaces,	487
13.4.1. Heterogeneous Photocatalysis in the Liquid Phase with Carbon–TiO ₂ Composites,	487
13.4.2. Heterogeneous Photocatalysis in the Gas Phase with Carbon–TiO ₂ Composites,	491
13.5. Role of the Carbon Phase in Heterogeneous Photocatalysis,	492
13.6. Conclusions,	498
References,	499
14 Carbon-Based Sensors	507
<i>Jun Li</i>	
14.1. Introduction,	507
14.1.1. Structure of Various Carbon Allotropes,	507
14.1.2. sp ² Carbon Materials: Graphite, Fullerenes, and Carbon Nanotubes,	509
14.2. Physicochemical Properties of sp ² Carbon Materials Relevant to Carbon Sensors,	510
14.2.1. Electrical and Electronic Properties,	510
14.2.2. Chemical Properties,	515
14.2.3. Electrochemical Properties,	516

14.3.	Carbon-Based Sensors, 517	
14.3.1.	Carbon Materials as Loading Media, 518	
14.3.2.	Carbon Electronic Sensors, 518	
14.3.3.	Carbon Electrochemical Sensors, 523	
14.3.4.	Carbon Composite Sensors, 530	
14.4.	Summary, 530	
	References, 530	
15	Carbon-Supported Catalysts for the Chemical Industry	535
	<i>Venu Arunajatesan, Baoshu Chen, Konrad Möbus, Daniel J. Ostgard, Thomas Tacke, and Dorit Wolf</i>	
15.1.	Introduction, 535	
15.2.	Requirements for Carbon Materials as Catalyst Supports in Industrial Applications, 536	
15.2.1.	Activated Carbon, 536	
15.2.2.	Carbon Black, 540	
15.3.	Industrial Manufacture of Carbon Supports, 544	
15.3.1.	Activated Carbon, 544	
15.3.2.	Carbon Black, 544	
15.4.	Manufacture of Carbon-Supported Catalysts, 545	
15.4.1.	Powder Catalysts, 545	
15.4.2.	Preparation Technology, 547	
15.5.	Reaction Technology, 547	
15.5.1.	Batch Stirred-Tank and Loop Reactors, 548	
15.5.2.	Fixed-Bed Reactors, 550	
15.6.	Industrial Applications, 551	
15.6.1.	Fatty Acid Hydrogenation, 551	
15.6.2.	Selective Nitrobenzene Hydrogenations, 554	
15.6.3.	Reductive Alkylation, 555	
15.6.4.	Toluenediamine, 556	
15.6.5.	Butanediol, 558	
15.6.6.	Purified Terephthalic Acid, 560	
15.7.	Testing and Evaluation of Carbon Catalysts, 561	
15.7.1.	Current Methods for Catalyst Evaluation, 561	
15.7.2.	High-Throughput Testing of Carbon Powder Catalysts, 563	
15.7.3.	Catalyst Profiling, 565	
15.8.	Conclusions, 567	
	References, 568	
Index		573

Contributors

VENU ARUNAJATESAN, Evonik Degussa Corporation, 5150 Gilbertsville Highway, Calvert City, KY, 42029
e-mail: venu.arunajatesan@evonik.com

TERESA J. BANDOSZ, Department of Chemistry, Marshak Science Building J-1024, The City College of New York, The City University of New York, 160 Convent Avenue, New York, NY 10031
e-mail: tbandosz@ccny.cuny.edu

JOHANNES H. BITTER, Department of Inorganic Chemistry, Debye Institute, Utrecht University, Sorbonnelaan 16, 3584 CA Utrecht, The Netherlands
e-mail: j.h.bitter@uu.nl

HANNS-PETER BOEHM, Department of Chemistry and Biochemistry, University of Munich, Butenandtstrasse 5-13, 81377 Munich, Germany
e-mail: hpb@cup.uni-muenchen.de

BAOSHU CHEN, Degussa GmbH, Business Line Catalysts, Rodenbacher Chaussee 4, 63457 Hanau-Wolfgang, Germany
e-mail: baoshu.chen@evonik.com

EDWIN CREZEE, Albemarle Catalysts, Nieuwendammerkade 1-3, P.O. Box 37650, 1030 BE Amsterdam, The Netherlands
e-mail: edwincrezee@yahoo.co.uk

KRIJN P. DE JONG, Department of Inorganic Chemistry, Debye Institute, Utrecht University, Sorbonnelaan 16, 3584 CA Utrecht, The Netherlands
e-mail: k.p.dejong@uu.nl

KAREN M. DE LATHOUDER, Shell Nederland Raffinaderij B.V., Vondelingenweg 601, Postbus 3000, 3190 GA Hoogvliet, Rotterdam, The Netherlands
e-mail: karen.delathouder@shell.com

JOAQUIM LUÍS FARIA, Laboratório de Catálise e Materiais, Departamento de Engenharia Química, Faculdade de Engenharia, Universidade do Porto, Rua Dr. Roberto Frias, 4200-465 Porto, Portugal
e-mail: jlfig@fe.up.pt

JOSÉ LUÍS FIGUEIREDO, Laboratório de Catálise e Materiais, Departamento de Engenharia Química, Faculdade de Engenharia, Universidade do Porto, Rua Dr. Roberto Frias, 4200-465 Porto, Portugal
e-mail: jlfig@fe.up.pt

- CRISTINA FREIRE**, REQUIMTE/Departamento de Química, Faculdade de Ciências, Universidade do Porto, 4169-007 Porto, Portugal
e-mail: acfreire@fc.up.pt
- FREEK KAPTEIJN**, Catalysis Engineering, DelftChemTech, Delft University of Technology, Julianalaan 136, 2628 BL, Delft, The Netherlands
e-mail: f.kapteijn@tudelft.nl
- JUN LI**, Department of Chemistry, Kansas State University, 111 Willard Hall, Manhattan, KS 66506-3701
e-mail: junli@ksu.edu
- FRÉDÉRIC MAILLARD**, Laboratoire d'Electrochimie et de Physico-chimie des Matériaux et des Interfaces, UMR 5631 CNRS/INPG/UJF, 1130, rue de la Piscine, BP75, 38402 Saint Martin d'Hères, France
e-mail: frederic.maillard@lepmi.inpg.fr
- KONRAD MÖBUS**, Evonik Degussa GmbH, Business Line Catalysts, Rodenbacher Chaussee 4, 63457 Hanau-Wolfgang, Germany
e-mail: konrad.moebus@evonik.com
- CARLOS MORENO-CASTILLA**, Inorganic Chemistry Department, Granada University, 18071 Granada, Spain
e-mail: cmoreno@ugr.es
- JACOB A. MOULIJN**, Catalysis Engineering, DelftChemTech, Delft University of Technology, Julianalaan 136, 2628 BL, Delft, The Netherlands
e-mail: J.A.Moulijn@tudelft.nl
- DANIEL J. OSTGARD**, Degussa GmbH, Business Line Catalysts, Rodenbacher Chaussee 4, 63457 Hanau-Wolfgang, Germany
e-mail: dan.ostgard@evonik.com
- MANUEL FERNANDO R. PEREIRA**, Laboratório de Catálise e Materiais, Faculdade de Engenharia, Universidade do Porto, Rua Dr. Roberto Frias, 4200-465 Porto, Portugal
e-mail: fpereira@fe.up.pt
- LJUBISA R. RADOVIC**, Energy and Minerals Engineering, 205 Hosler Building, The Pennsylvania State University, University Park, PA 16802
e-mail: lrr3@psu.edu
- FRANCISCO RODRÍGUEZ-REINOSO**, Universidad de Alicante, Departamento de Química Inorgánica, E-03080 Alicante, Spain
e-mail: reinoso@ua.es
- ELENA R. SAVINOVA**, Laboratoire des Matériaux, Surfaces et Procédés pour la Catalyse, UMR-7515, ECPM, Université Louis Pasteur, 67087 Strasbourg, France
e-mail: elena.savinova@ecpm.u-strasbg.fr
- ANTONIO SEPÚLVEDA-ESCRIBANO**, Universidad de Alicante, Departamento de Química Inorgánica, E-03080 Alicante, Spain
e-mail: asepul@ua.es

PHILIPPE SERP, Laboratoire de Chimie de Coordination, composante ENSIACET, UPR 8241 CNRS 118 Route de Narbonne, Toulouse University, 31077 Toulouse Cedex 4, France
e-mail: Philippe.Serp@ensiacet.fr

ANA ROSA SILVA, REQUIMTE/Departamento de Química, Faculdade de Ciências, Universidade do Porto, 4169-007 Porto, Portugal *Present address:* Unilever R&D, Port Sunlight, UK
e-mail: anarosa.silva@unilever.com

PAVEL A. SIMONOV, Boreskov Institute of Catalysis, Russian Academy of Sciences, Pr. Akademika Lavrentieva 5, 630090 Novosibirsk, Russia
e-mail: spa@catalysis.nsk.su

THOMAS TACKE, Evonik Degussa GmbH, Science to Business Center Bio, Paul-Baumann-Strasse 1, 45764 Marl, Germany
e-mail: thomas.tacke@evonik.com

WENDONG WANG, Department of Chemical Physics, University of Science and Technology of China, Hefei 230026, Anhui, China
e-mail: wangwd@ustc.edu.cn

DORIT WOLF, Evonik Degussa GmbH, Business Line Catalysts, Rodenbacher Chaussee 4, 63457 Hanau-Wolfgang, Germany
e-mail: dorit.wolf@evonik.com

ZHONGHUA (JOHN) ZHU, Division of Chemical Engineering, School of Engineering, University of Queensland, Brisbane 4072, Australia
e-mail: z.zhu@uq.edu.au

Preface

Carbon is a versatile and fascinating material that can be used in a number of technological processes, including high-tech processes. This is due largely to the ability of carbon atoms to bond with each other in various ways to form linear, planar, and tetrahedral bonding arrangements, thus producing materials with a large range of properties. Physicochemical characteristics such as electrical conductivity, surface area and porosity, and surface chemistry may be tuned for specific applications.

Carbon materials such as activated carbons, carbon blacks, graphite, and graphitic materials have been used for decades in heterogeneous catalysis, as either catalysts or catalyst supports. Activated carbon catalysts are used in the synthesis of phosgene from carbon monoxide and chlorine, in the synthesis of thionyl chloride from sulfur dioxide and chlorine, and in the oxidation of *N*-phosphonomethyliminodiacetic acid to produce a biodegradable herbicide, Glyphosate. Activated carbons impregnated with ZnO, CuO, or Fe₂O₃ are designed specifically for the desulfurization of natural gas. The Merox process developed by Universal Oil Products to remove mercaptan sulfur from petroleum fractions involves a catalyst consisting of cobalt phthalocyaninedisulfonate impregnated onto a suitable high-surface-area activated carbon. Furthermore, because of their high thermal stability in reducing atmospheres and their ability to facilitate the preparation of well-dispersed metal particles on surfaces that do not exhibit acid–base properties, carbon materials are used to support precious metals for hydrogenation reactions in the fine-chemicals industry. The recovery and recycling of metals, particularly of noble metals, is simplified with carbons, as these supports can be burned off. These materials offer unparalleled flexibility in tailoring catalyst properties to specific needs.

Compared to the predominant applications of these carbon materials as adsorbents for drinking water, wastewater, and gas purification, as fillers in rubber production, or as refractory materials, however, their use in the catalyst market represents only a moderate share. The potential growth of the market for carbons in catalysis depends on (1) better understanding of the chemistry of carbon surfaces and fine tuning of the microstructure of these materials, which could then be exploited in the design of truly unique catalysts; and (2) improvements in quality control and production methods, to supply constant-quality materials (synthetic carbons). There are additional opportunities to increase the market value of carbon materials in the near future, due to the rapidly advancing development of fuel cells, the use of novel carbon materials, the increasing need for catalytic

materials in very selective reactions, and the identification of some high-volume applications.

Patents appear continuously to meet industrial needs, and the growth of scientific publications dealing with the use of carbon materials in catalysis is exponential. However, the last major review of this field was published over a decade ago (L.R. Radovic and F. Rodríguez-Reinoso, in P.A. Thrower, Ed., *Chemistry and Physics of Carbon*, Vol. 25, Marcel Dekker, New York, 1997, p. 243). In the meantime, new materials, such as carbon nanotubes, nanofibers, aerogels, and xerogels, have become widely available, and our knowledge of the surface chemistry of carbon materials has improved substantially. We are now able to modify in a controlled manner the nature and concentration of functional groups on the surface of carbon materials, which can serve as active sites in catalysis or as anchoring centers for active phases or their precursors. High-performance nanostructured catalysts can thus be prepared. Moreover, analytical tools have been developed for the identification and quantification of surface groups, paving the way for the proper interpretation of kinetic data and providing for useful correlations of catalytic activity. There is clearly a need to establish the state of the art in order to identify the required areas of research, to stimulate more systematic approaches, and to promote further technological developments in the field—and that is the purpose of this book.

The material is organized into 15 chapters written by recognized experts in their fields. It has been decided to cover in depth new and hot topics as well as those that have not yet been the subject of extensive reviews. In the first three chapters the properties of carbon materials relevant to catalysis are discussed, with a special emphasis given to the description of carbon surface features, in particular to surface functional groups and their characterization methods, and to the theoretical investigation of molecular interactions on carbon surfaces. This provides a fundamental background for an understanding of the material covered in subsequent chapters.

The next two chapters provide a comprehensive review of carbon-supported metal catalysts and their preparation methods. The most important applications are discussed, special attention being given to the most innovative.

Chapter 6 provides an extensive review of the uses of carbon as a catalyst, with particular emphasis being placed on cases in which active sites have been properly identified and activity correlations established. The special case of nitrogen-doped carbons and their catalytic activity in oxidation reactions is discussed in Chapter 7, and Chapter 8 covers the heterogenization of homogeneous catalysts by anchoring transition-metal complexes onto the surface of suitable carbon materials.

Two important classes of new carbon materials, carbon nanotubes/nanofibers and carbon aerogels/xerogels/cryogels are reviewed and discussed in the next two chapters. These materials exhibit interesting properties that can be exploited in many applications, particularly in catalysis.

Chapter 11 provides a short review of carbon-based monoliths, their preparation, and applications in various liquid-phase processes, including bioconversions.

Chapters 12 and 13 cover two of the most important novel catalytic applications of carbon materials, electrocatalysis and photocatalysis. In the first case, carbons are used mostly as supports for metal catalysts in fuel cells, while the synergistic effects of carbon-based composite semiconductor materials, such as C-TiO₂, make them particularly effective in photocatalytic degradation reactions.

Chapter 14 addresses the special topic of sensors, in which advantage is taken of the unique properties of nanostructured carbon materials such as nanotubes and fullerenes. Finally, applications of carbon-supported precious metal catalysts are reviewed from an industrial perspective in Chapter 15.

Since this is a multiauthored book, significant differences in style from chapter to chapter are inevitable, but we have tried to avoid overlaps as much as possible. We thank all the authors for their efforts to meet the deadlines and to follow the format defined for the book. We would also like to acknowledge the assistance of Anita Lekhwani at Wiley, whose advice has been most helpful at the various stages of preparation of the manuscript. Finally, we hope that the book will be useful to fellow scientists and practitioners and will stimulate further research and discussion on the development of carbon materials for catalysis.

Toulouse

PHILIPPE SERP

Porto

JOSÉ LUÍS FIGUEIREDO

February 2008

1 Physicochemical Properties of Carbon Materials: A Brief Overview

LJUBISA R. RADOVIC

1.1 INTRODUCTION

To justify the title and the contents of this brief introductory review, it is appropriate to recall the words of Nernst, written more than a century ago (1893) in the Preface to the first edition of his *Theoretical Chemistry from the Standpoint of Avogadro's Rule and Thermodynamics* (<http://books.google.com>): “[T]he development of physical chemistry as a special branch of natural science means—and I would lay particular emphasis on this—not so much the shaping of a new science, but rather the co-operation of two sciences which hitherto have been, on the whole, quite independent of each other.”

Catalytic applications of carbon materials are as old as the discipline of physical chemistry, and probably even older. Over the past century or so, the level of fundamental understanding of these technological applications and this discipline has increased tremendously, of course. Yet, despite (or because?) of this progress, there is a pervasive problem in carbon science and technology: It is an eminently interdisciplinary field, and the danger that “the left hand doesn’t know what the right hand is doing” is considerable. In principle and increasingly in practice, as Nernst himself had anticipated, this problem has also plagued physical chemistry but it has been overcome; it took almost a century for Dirac’s prophecy to be realized, but it has been done. With the discovery of quantum mechanics, chemistry has been essentially reduced to physics. Dirac proclaimed that “the underlying physical laws necessary for the mathematical theory of a large part of physics and the whole of chemistry are thus completely known” [1]. So in the second century of existence of physical chemistry as a discipline, the key question is whether carbon chemists really understand what the carbon physicists are arguing, and vice versa. Here I explore some answers to this question, those that are considered

2 PHYSICOCHEMICAL PROPERTIES OF CARBON MATERIALS: A BRIEF OVERVIEW

to be of greatest relevance to catalytic applications of carbon materials. Knowing that, despite the wonderful opportunities offered by electronic storage and retrieval of information, researchers today continue to struggle to keep up with the literature in their own (increasingly narrow?) field, it is anticipated that the path outlined by Dirac continues to be a difficult one. Yet the obvious rewards to those who succeed in integrating carbon physics and carbon chemistry should be a powerful enough incentive. Much of the evidence of progress in this endeavor, or lack thereof, has accumulated in the 30 volumes [2] of the book series *Chemistry and Physics of Carbon* inaugurated by Philip Walker almost half a century ago, when carbon science was in its infancy. It is true that “the study of carbon has grown to become a specialism” [3] but, as argued below, it is inappropriate to obscure it unduly [3] as not only “a combination of physics and chemistry” but also of “fluid dynamics and chemical engineering, with dashes of astrophysics and geology” [3]. From a historical perspective, the development of carbon science and technology provides several ironic and exemplary twists of fate for chemists and physicists. The most fascinating one is related to the discovery of C₆₀, buckminsterfullerene. Its chemical identification [4] was brought about by the pursuit of an astrophysical issue (the nature of interstellar dust), whereas researchers in a physics department [5] were the first to achieve its chemical separation.

Catalytic behavior of carbon materials depends on their surface properties, but surface properties are to a large extent a consequence of bulk properties. Therefore, after a brief overview of the ways that carbon materials are formed, I discuss their bulk properties briefly before focusing on their physical and chemical surface properties and their chemical (re)activity.

1.2 FORMATION OF CARBONS

All carbon materials, including those used for catalytic applications, are formed in either the gas, liquid, or solid phase; and these conditions to a large extent dictate the variabilities possible in their physicochemical properties. The range of hydrocarbon feedstocks used as carbon precursors is also dictated by these conditions; and seemingly subtle changes often produce profound structural effects. These are discussed briefly below.

1.2.1 Gas Phase

Figure 1.1 summarizes the very wide range of carbon products that can be produced in gas-phase reactions under perhaps surprisingly similar conditions from a very wide variety of carbon-containing gases (e.g., CO, CH₄, C₂H₂, C₃H₆, C₆H₆, natural gas, volatile products of coal or biomass pyrolysis). The relatively disordered (but not amorphous), nongraphitic and nongraphitizable carbon black or soot particles result because nucleation of the carbon precursors occurs during pyrolysis in the gas phase. The much more ordered (quasicrystalline)

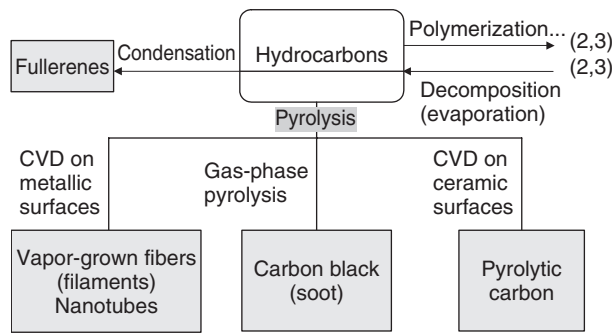


Figure 1.1 Summary of the processes of carbon formation in the gas phase and the resulting carbon macrostructures. (Hydrocarbon polymerization or decomposition can lead to interconversion of gaseous, liquid, or solid carbon precursors; see also Figures 1.2 and 1.3.)

nongraphitic but graphitizable pyrolytic carbon is obtained by virtue of chemical vapor deposition (CVD) of carbon precursors on a relatively inert (e.g., ceramic) substrate; the structure of crystalline graphite (in pyrolytic graphite) is achieved upon simple heat treatment above about 2773 K. On a more reactive metallic surface (most notably, Fe, Co, or Ni), the deposition of carbon precursors typically results in carbon dissolution, intra- and/or suprametal diffusion, and precipitation in the form of nanotubes or filaments (fibers). The novel aspect of this process is the emergence of curvature of sp^2 bonds in the growing graphene layers; its origin remains a debatable and arguably unresolved issue. Whether it is analogous to the curvature induced by formation and entrapment of pentagons and/or heptagons, phenomena responsible for the formation of fullerenes upon condensation of gas(eous fragments), or to some other effect, including the role of the crystallography or morphology of the metal substrate, remains to be verified.

1.2.2 Liquid Phase

Figure 1.2 summarizes the variety of carbon products obtained in liquid-phase reactions using thermoplastic polymers, either the natural (such as bituminous coals) or synthetic ones [such as poly(vinyl chloride), $-CH_2Cl_2-n$]. At the most commonly utilized carbonization conditions, typically above 2273 K in a largely nonreactive medium, the degree of alignment and the mobility of emerging, growing, and coalescing carbon crystallites is considerable, but the consequent relative orientations of the resulting graphene layers are insufficient to achieve the perfect crystalline structure of graphite, and these materials are the nongraphitic but graphitizable cokes. However, their further exposure to higher temperature, typically in excess of 2773 K, results readily in the formation of (synthetic) graphite. If during the carbonization process the intermediate molten phase is

4 PHYSICOCHEMICAL PROPERTIES OF CARBON MATERIALS: A BRIEF OVERVIEW

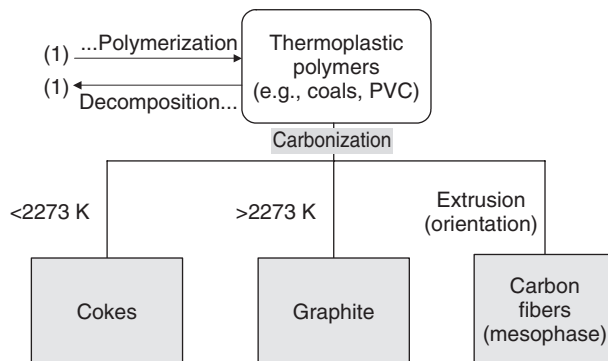


Figure 1.2 Summary of the processes of carbon formation in the liquid phase and the resulting carbon macrostructures.

subjected to extrusion and orientation, highly graphitizable carbon fibers (e.g., from mesophase pitch) can be obtained.

1.2.3 Solid Phase

Figure 1.3 summarizes the carbon formation processes taking place in the solid phase, with thermosetting carbon precursors such as low-rank coals, preoxidized bituminous coals, and wood, or thermosetting polymers such as poly(vinylidene chloride) (PVDC), $-\text{CHCl}_3-n$. (Note how very sensitive the carbonization process is to structural details of the carbon precursor: The absence of one hydrogen atom in the monomer precludes the formation of a molten phase during thermal decomposition of PVDC.) Because there is no plastic phase during the devolatilization process, there is extensive development of porosity in chars,

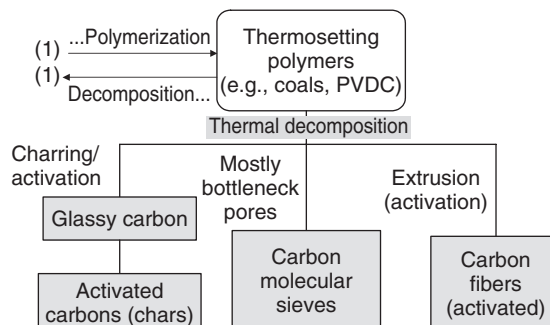


Figure 1.3 Summary of the processes of carbon formation in the solid phase and the resulting carbon macrostructures.

and this can be tailored further by selective gasification to produce activated carbons or molecular sieves, from either carbonized granules or powders or fibers. If the heat-treatment temperature is high, the product remains nongraphitic and nongraphitizable, but it acquires a shiny appearance and its pores become very narrow and essentially impervious to most gases and liquids: It is glassy or glasslike (vitreous) [6] and possesses a low surface area, although its low density (e.g., 1.5 g/cm³) reveals the presence of considerable closed porosity (even to helium at ambient temperature), which can be exposed and developed upon activation (selective gasification) at higher temperatures.

1.3 STRUCTURE AND PROPERTIES OF CARBONS

Both the bulk and the surface properties of carbon materials are dependent on their structure (i.e., on the spatial arrangement of carbon atoms). The structure is in turn dependent on the precursor used and the conditions of formation, as outlined in Section 1.2. Because of the prodigious variety of possible carbon atom arrangements within the seemingly restrictive constraint of sp² hybridization characteristic of graphitelike carbons, it is useful to distinguish between the various levels of structure, and these are discussed in the following sections. The increasingly popular and often abused term *nanostructure* should be the easiest to define unambiguously, at a scale below 10 nm, although of course it is the most difficult one to verify experimentally. Conversely, the boundary between *macrostructure* and *microstructure* is much easier to ascertain experimentally, but it is less straightforward to define it precisely. The latter term is well recognized, especially for polycrystalline materials, although perhaps surprisingly it does not have an International Union of Pure and Applied Chemistry (IUPAC) definition (see www.iupac.org/publications/compendium/index.html): for example, “the structure of a crystal on the scale on which deviations from perfect order become evident” [7] or “the structural features ... (e.g., grain and phase structure) that are subject to observation under a microscope” [8,9]. In practice, this sets the macro/micro boundary in a broad range of about 1 to 100 μm.

In Table 1.1 we summarize the prodigious variety of bulk and surface properties of carbon materials, especially those of greatest relevance for catalytic behavior. Typical values or typical ranges are most often quoted rather than definite values, because these depend on too many factors to discuss here. Specific literature references are also not provided for this reason; not only handbooks [10,11] and the *Chemistry and Physics of Carbon* series [2] were consulted, but representative research or review papers as well as some commercial product brochures were examined.

1.3.1 Macrostructure

The macrostructure level of carbon atom arrangement confers the most readily recognizable features on carbon materials, and it should not allow room for

Table 1.1 Typical Property Values of Principal Carbon Materials^a

Property	Graphite	PC	CF	GLF	AC	CB	Cokes	Chars
True (He) density (g/cm ³)	2.268	>2.0	<2.2	<2.0	<2.0	<2.0	<2.0	<2.0
Particle (Hg) density (g/cm ³)	>2.0	>2.0	—	1.5	1.2–1.6	1.5–2.0	1.5–2.0	1.4–1.8
Packing (bulk) density (g/cm ³)	>1.0	—	1.4–2.2	0.75	0.6–0.8	0.2–0.5	0.7–1.0	0.7–0.9
Spacing between two adjacent basal planes (nm) ^b	0.3354	0.34–0.36	0.34–0.36	>0.344	>0.344	0.35–0.36	0.34–0.36	>0.344
Crystallite height (nm)	>100	>10	>5	<10	<5	1.0–2.5	2.0–100	<5
Crystallite width (nm)	>100	>5	5.0–50	<10	<5	1.0–3.0	2.0–50	<5
Specific heat (kJ/kg/K)	0.8	—	—	—	—	—	—	—
Thermal conductivity (W/m/K)	—	—	—	—	—	—	—	—
Parallel to basal plane (<i>ab</i> -direction)	400	190–390	8–1100	—	—	—	—	10
Perpendicular to basal plane (<i>c</i> -direction)	<80	1.0–3.0	—	—	—	—	—	—
Electrical resistivity (Ω·m × 10 ⁶)	—	—	—	10–10 ²	10 ³ –10 ⁶	ca. 10 ²	10–10 ³	10 ² –10 ³
Parallel to basal plane (<i>ab</i> -direction)	0.4	4.0–5.0	2.0–20	—	—	—	—	—
Perpendicular to basal plane (<i>c</i> -direction)	>40	1000–3000	<10	<1	500–3000	20–2500	<500	<500
BET surface area (m ² /g)	<10	—	—	—	—	—	—	—

^aPC, pyrolytic carbon; CF, carbon fibers; GLF, glasslike fibers; AC, activated carbon (including fibers or cloth); CB, carbon blacks.^bCarbons with spacing greater than 0.344 nm are turbostratic.

Note: If no values are provided, the variability is considered too wide for a meaningful summary.

ambiguity. It is, however, symptomatic of the nomenclature confusion existing even in the peer-reviewed literature that the most authoritative reference regarding these issues [6] has been cited in only 15 subsequent papers (according to the *Science Citation Index*). Earlier versions of the “recommended terminology for the description of carbon as a solid” [12–17] fared even worse. There is no question that an update on the terminology for the various carbon structures is long overdue, especially after the discovery of fullerenes and nanotubes, and also because of the tremendous popularity of nanomaterials. But much of the confusion can be avoided by more careful perusal of the references cited above.

A case in point, of particular relevance to catalytic applications, is what should be a trivial distinction between activated carbon and carbon black (see Figures 1.1 and 1.3). These two materials have very similar micro- and nanostructures (see below), but their macrostructures are very different: The mean particle size of both granular and powdered activated carbons is at least three orders of magnitude larger (e.g., 0.010 to 1 mm vs. 0.010 to 1 μm) than that of carbon blacks, and its porous structure (see Section 1.3.5) is typically much more developed. Yet, especially in the carbon catalysis literature, it is too often found that they are misidentified. Such an oversight should not be dismissed as a terminology detail. It reflects the degree of success in bridging the chemistry–physics gap: If one is attempting to maximize the catalytic behavior of interest (chemistry), a profound understanding of even the subtle differences in nano-, micro-, and macrostructure (physics) is necessary to be able to exploit the structure of the catalyst and thus obtain desirable and optimized properties.

Missing from the accepted terminology [6] (of special relevance to catalytic applications are, for example, activated carbon fibers, glasslike carbon, coke, char, charcoal) are the now common carbon structures such as fullerenes (e.g., C_{60}), single- and multiwalled nanotubes (SWCNTs and MWCNTs), nanofibers (CNFs), and aerogels and xerogels. The world’s fascination with C_{60} and SWCNT stems from their elegant and simple structure at any geometric scale, and there is no ambiguity here. In contrast, the distinctive features of MWCNTs versus CNFs require closer scrutiny of their nanostructure (see Section 1.3.3). Finally, as discussed in detail in Chapter 10, sol–gel processing, which has revolutionized the preparation of inorganic materials (e.g., ceramics, glasses), has also been applied to polymeric materials, whose processing results in at least two distinct carbon macrostructures: (1) xerogels, when conventional (subcritical) solvent evaporation is used, and (2) aerogels, when supercritical drying is employed. For example, in the seminal contribution by Pekala [18], “the covalent crosslinking of [polymer] clusters produce[d] gels which [we]re processed under supercritical conditions to obtain low density, organic aerogels ($<0.1 \text{ g cm}^{-3}$) … similar to the sol–gel processing of silica.” Despite this comparison, many researchers may have the impression that these are relatively recent concepts. However, the *Web of Science* (isiwebofknowledge.com) quickly reveals, for example, that aerogel catalysts were compared to the more conventional aerosol counterparts in the 1930s [19]. The origin of the term *aerogel* is straightforward: The solvent is

replaced by gas (air), thus maintaining the low density of the final product. Xerogel surfaces are somewhat more recent [20], and the origin of the term is just a little bit more mysterious; in Greek, *xero* means “dry.” The macrostructural differences resulting from these polymer-processing variations have important consequences for the porous structure of these materials and thus for their catalytic performance.

1.3.2 Microstructure

We need to explore the equivalent of grain boundaries in carbons as the most recognizable feature of carbon microstructure. In metals and ceramics, the grains are the “individual crystallites in a polycrystalline microstructure” [21], and a grain boundary is a “region of mismatch between two adjacent grains in a polycrystalline microstructure” [21] or “the interface separating two adjoining grains having different crystallographic orientation” [8]. From the definitions of these fundamental concepts, the important practical message is that most carbons are polycrystalline materials, especially those of interest in catalytic applications, because the spaces between the crystallites are the pores accessible for adsorption of gases and liquids as the first step in a catalytic process. This is illustrated in Figure 1.4 using the venerable models of Franklin and Bokros. So the key issue is how to identify and quantify the crystallites in the carbon material of interest, particularly when its structure, especially at the nanoscale (see Section 1.3.3), is not as well defined as in a perfect single crystal of graphite. A typical size of a crystallite in an activated carbon, or a char, or a carbon black, is 2 to 5 nm, as determined from x-ray diffraction. So even a small 20-nm carbon black particle is polycrystalline and may develop extensive porosity, as is the case with channel blacks, whose total surface area can exceed 1000 m²/g, in contrast to furnace blacks [10,11] whose surface area is typically much closer to its geometric (external particle) area of about 200 m²/g [i.e., $6/(20 \times 10^{-9} \text{ m})/(1.5 \times 10^6 \text{ g/m}^3)$, assuming spherical particles].

Perhaps the most difficult fundamental issue that has not yet found a satisfactory answer, precisely because it is at the interface between physics and chemistry, is the supramolecular [22,23] (i.e., supraphene) constitution of the various carbon materials. Notwithstanding the great popularity of the models shown in Figure 1.4, as well as that shown in Figure 1.5 for (glassy) carbon fibers, it is not clear how the graphene edges (crystallites) are connected in three-dimensional space. Which intra- and/or intermolecular forces are responsible for the formation of the microstructure in these materials? For decades this issue has been ignored or essentially “swept under the rug.” In the next section I discuss this admittedly difficult problem.

1.3.3 Nanostructure

The attentive reader will note that a density of 1.5 g/cm³ was used in estimation of the geometric surface area of carbon black, which is a relatively disordered form

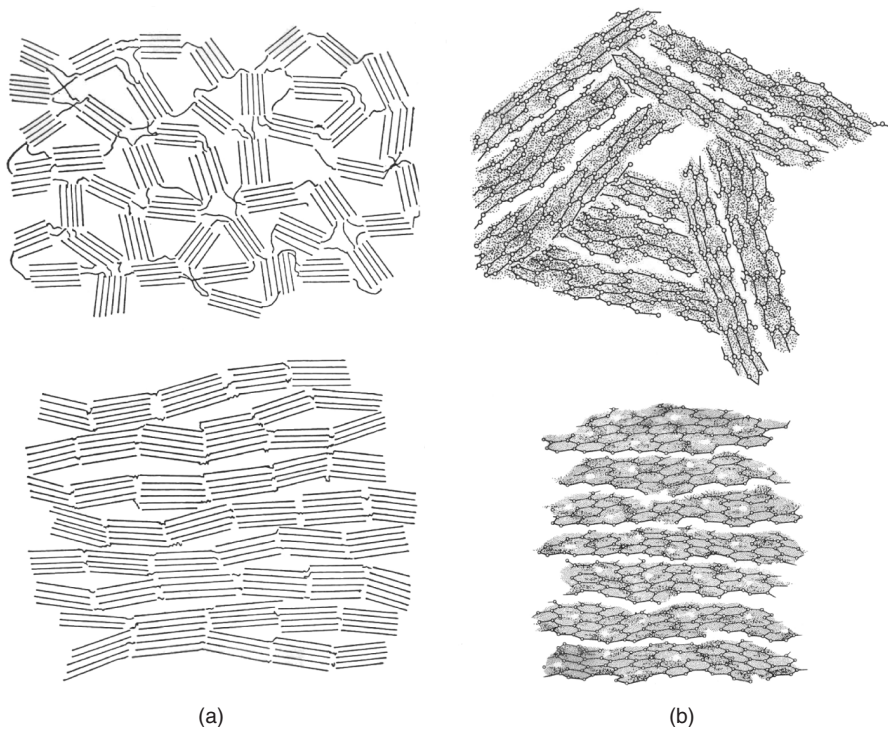


Figure 1.4 Two popular models of carbon microstructure: (a) two-dimensional arrangement of graphene layers in graphitizable (bottom) and nongraphitizable (top) carbons proposed by Franklin [273]; (b) analogous three-dimensional arrangement of graphene layers proposed by Bokros [317].

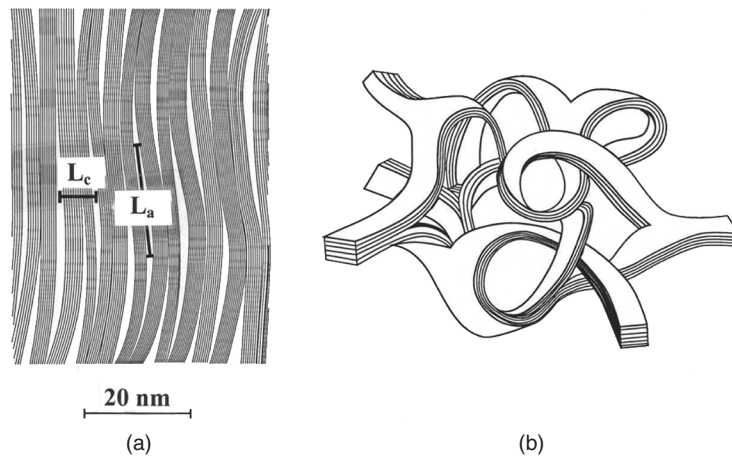


Figure 1.5 (a) Two- and (b) three-dimensional arrangements of graphene layers in carbon fibers proposed by Jenkins and Kawamura [151].

of carbon, certainly in comparison with graphite (whose density is 2.268 g/cm³). Use of the terms *disordered carbon* and *amorphous carbon*, without further explanations, is quite common, but it should be avoided, even though the latter does have a IUPAC definition (albeit a rather vague and complicated one): “carbon material without long-range crystalline order” [6]. The challenge, and the obligation of a responsible researcher, is to qualify this absence of long-range order. The IUPAC description of an amorphous carbon does contain one such important qualification [6]: This definition “is not applicable to carbon materials with two-dimensional structural elements present in all pyrolysis residues of carbon compounds as polycyclic aromatic layers with a nearly ideal interatomic distance of $a = 142$ pm and an extension greater than 1000 pm.” Given this nanoscale clarification, soot, carbon blacks, cokes, chars, carbon filaments, and vapor-grown carbon fibers (see Figures 1.1 to 1.3) are not amorphous carbons. The literature devoted to the preparation of fullerenes and carbon nanotubes suffers notoriously from this ambiguity. In too many instances this product is actually an impurity, whereas the materials dismissed as amorphous carbon impurities are in fact dominant and therefore must be identified more precisely, especially in the context of procedures used for purification of fullerenes and nanotubes [24].

With this background, it should be clear that *nanostructure* is what defines, in classical terminology, the three allotropic modifications of carbon materials: (1) flat sp² hybridization of carbon atoms in graphite, (2) curved sp² hybridization in a fullerene or nanotube, and (3) sp³ hybridization in diamond. Figure 1.1 does include the formation of diamond or diamondlike carbons, but for catalytic applications these materials are not of great interest—at least not yet, despite the advent of the low-pressure CVD process of diamond synthesis [25]—and therefore they are excluded from the discussion that follows as they are from the other chapters in this book.

There is another important concept embodied in the term *nanostructure*; it is of great relevance in catalytic applications. As a consequence of the widespread (and somewhat unfortunate) use of the terms *nanocarbons* and *nанопорозные карбон*, it was discussed by Inagaki and Radovic [26]: “Nanocarbons are carbon materials produced when *either* their size or their structure is controlled at the nanometer scale.” It is therefore true that nanotechnology and nanoscience were born in the wake of the discovery of fullerenes and nanotubes, with enthusiastic support of the media fascinated by their beauty [3,27,28]; but many of the classical (flat sp²-hybridized) carbons are also nanomaterials because “we have learned how to control either their nano-structure or their nano-size, or both” [26]. A case in point is the template approach to preparing porous carbons [29], which affords a versatile and elegant method of controlling both the size and the spatial distribution of nanometer-size pores.

An obvious potential source of confusion at the nanostructure level—and one that is conceptually easy to resolve but where the inappropriate terminology may persist—is the reference to microporous carbons. Now that the qualifier of the scale of porosity of interest has the connotation of exact size (i.e., nanometers) and not simply of being small (i.e., micro), it is more appropriate to refer to this

increasingly large and important group of materials—having the same macro- and microstructure but different nanostructures (e.g., CNTs vs. CNFs vs. activated carbons)—as nanoporous rather than microporous carbons.

An important distinction, which goes to the heart of the (nano)structural differences among carbons, is that between multiwalled carbon nanotubes and vapor-grown carbon fibers (VGCFs). The former are often misidentified and are actually fibers rather than tubes (see Chapter 9), while the latter were recently dubbed carbon nanofilaments or nanofibers (CNFs), presumably in the desire to join the nanotechnology revolution. An entire workshop has been devoted to this topic [30], so clearly all its subtleties cannot be summarized here (see Chapter 9). But the key issue is clear, based on the following quote from the Preface to the aforementioned workshop report [30]: “[After the discovery of carbon nanotubes by Iijima] . . . [t]he scientific community soon learned that researchers who had been producing carbon filaments had been unknowingly growing nanotubes years before Iijima’s publication.” Have they, really? Let’s begin to answer this question by briefly reviewing some definitions. Although not defining VGCF, Fitzer et al. [6] do define filamentous carbon, which is essentially the same material (see Figure 1.1): It is “a carbonaceous deposit from gaseous carbon compounds consisting of filaments grown by the catalytic action of metal particles. . . . Typical filaments consist of a duplex structure, a relatively oxidation-resistant skin surrounding a more easily oxidizable core, with a metal particle located at the growing end of the filament.” The reference for this summary is, appropriately, a pioneering study of Baker and co-workers [31,32] in which the authors were struggling to understand how to suppress the formation of detrimental deposits on catalytic surfaces or on nuclear fuel cladding, and in which they proposed the now well-accepted diffusion–precipitation mechanism of filament growth, as illustrated in Figure 1.6(a). These authors commented on the more or less simultaneous mechanistic proposal for a related structure, reported by Oberlin et al. [33] and reproduced in Figure 1.6(b). They attributed this proposal to Baird et al. [34] and emphasized that its key distinctive feature is that the filament formed “appears to be a tubule” because “diffusion through the particle does not take place to any significant extent; instead, the carbon is entirely that which is transported around the particle.” A fine example of a filament that supports this mechanism was given by Evans and co-workers [35]; indeed, Figure 1.1 in ref. 28 does show clearly a single hollow 0.5- μm filament with a metal tip. In the other seminal paper, Oberlin et al. [33] emphasize this tubular morphology of the hollow fibers, but their interpretation is in terms of conventional flat sp^2 carbon structures: “turbostratic stacks of carbon layers, parallel to the fiber axis and arranged in concentric sheets, like the annual ring structure of a tree” [33]. The VGCFs thus have a flat sp^2 nanostructure, whereas MWCNTs have a curved sp^2 nanostructure. Consequently, before referring to a carbon material as MWCNTs, and especially if the preparation procedure is apparently similar to that well known for VGCFs, it is incumbent on a researcher to show evidence of the existence of a curved sp^2 nanostructure (e.g., using Raman spectroscopy) [36]. The nanostructure of VGCFs is therefore the same as that of,

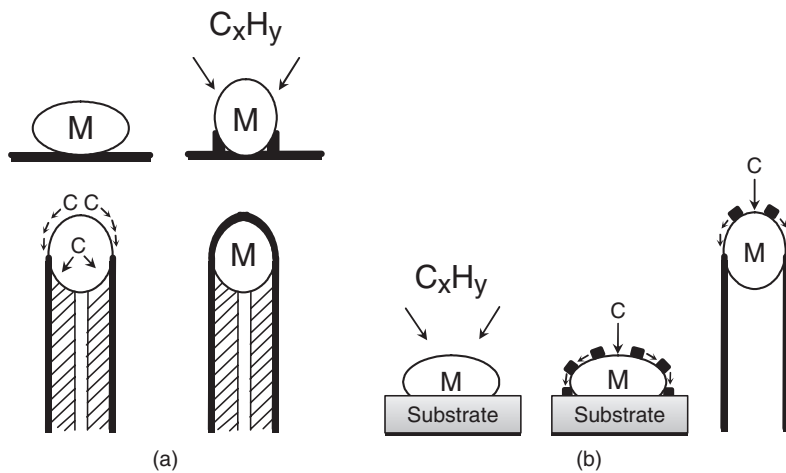


Figure 1.6 Schematic representation of (a) the diffusion–precipitation mechanism of carbon filament growth from the gas phase [32], and (b) the carbon-fiber growth mechanism proposed by Oberlin et al. [33]. Important details regarding the effects of metal particle size and shape on the chemical reactions occurring at the metal–carbon interface, and thus on the nature and size of the filaments or nanotubes produced, have yet to be sorted out.

say, pyrolytic carbon (both are produced in the gas phase; see Figure 1.1) and their differences only become apparent at the microstructure level: In the former, the crystallites are oriented, say, in a herringbone or platelet fashion with respect to the fiber (filament) axis, whereas in the latter they are stacked on top of each other and parallel to a substrate on which the carbon precursor was deposited.

So the key fundamental question here is the following: Which precursor- and/or process-driven factors are responsible for this detour from flat to curved sp^2 structures? In competition with the well-documented tendency of (fused) benzene rings to stack parallel to each other and thus retain planarity and resist curvature, there is an apparently effective mechanism for the elimination of pentagons at graphene edges. It is summarized in Table 1.2 and Figure 1.7 and is discussed in some detail below.

It is tempting to conclude that a monograph devoted to answering an/or clarifying some or all of these questions [30] has fallen short of accomplishing this goal, at least from a chemical perspective. For example, Endo et al. [37] summarized “the differences between carbon nanotubes obtained by chemical vapor deposition and VGCFs” as follows: “(1) The diameter of carbon nanotubes must be below 30 nm, thin enough so that no faceting phenomena may occur during the graphitization process. (2) Graphene layers in nanotubes are aligned along the fiber axis. (3) Nanotubes have no microdomains of amorphous carbon on

Table 1.2 Heats of Reaction Calculated for a Prototypical Process of Conversion of Pentagons to Hexagons at the Edge of a Graphene Layer^a

Reaction (see Figure 1.7)	B3LYP/6-31G(d)	PM3 ^b
1	-44	-43
2	4.5	15
3	30	11
4	55	44
5	-59	-50
6	-63	-48

^aSee Figure 1.7.

^bFrom ref. 61.

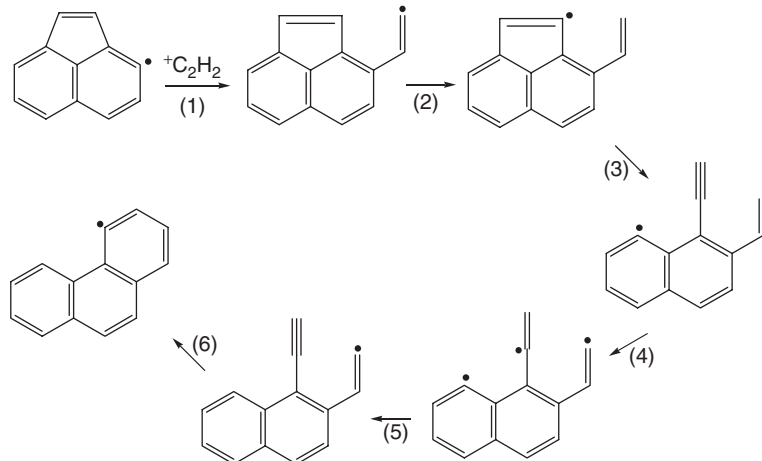


Figure 1.7 One possible mechanism of elimination of pentagons at graphene edges. (From ref. 61.)

their surfaces, as determined by scanning tunneling microscopy. (4) Nanotube tips contain no catalyst particles.” Alas, for a chemical explanation of these presumed physical differences, one must look elsewhere. In a round-table discussion summarized in the same monograph [30], it was concluded that the typical growth conditions of CNTs and VGCFs are remarkably similar except that presumably CNTs can be produced in the absence of a catalyst, although at significantly higher temperatures than VGCFs.

Interestingly, in a valiant attempt to set the various priority records straight, Monthioux and Kuznetsov [38] stated that the early paper by Oberlin et al. [33] “show[s] a nanotube resembling SWCNT” even though its diameter appears to be on the order of 5 nm, as subsequently acknowledged by the

authors themselves. They emphasized the key point that, before the discovery of fullerenes, “nobody from the carbon material[s] community . . . was ready to admit that nanotubes built up using a rolled single graphene could ever exist.” Clearly, a chemistry-oriented discussion of these issues is lacking because the key issue—the driving force for curvature—is not mentioned in these physics-oriented papers.

In the same context, it is also instructive to explore the analogy between carbon blacks or soot and fullerenes. The relevant issues have been controversial [39–42], and the discussion was occasionally very heated [3,28], but the dust appears to have settled [43]. Fullerenes do form under the same conditions as soot (or carbon black), because “both species have common precursors” [43]. But there is no compelling evidence for the dominant, or even substantial, presence of curved sp² nanostructure in soot or carbon black. Ebert [44] has analyzed this issue carefully and has concluded that the “data support a traditional model of soot as polynuclear aromatic compounds rather than as clusters of carbon atoms with minimal edge site density.” He did note that “the proposal of carbon clusters is exciting and that the idea has captured the imagination of many.” Among the many is none other than Donnet [45,46], a leading authority on carbon blacks [47]. An authoritative summary of this exciting episode of carbon physical chemistry research has been offered by Curl in his Nobel award lecture [48]: “[T]he conjecture that soot consists of spiraling spheroidal shells is probably wrong. However, I think it likely that there is some more subtle connection between the curvature introduced by five-membered rings and soot formation. Regardless of its validity, this conjecture has turned out to be extremely valuable because it got the soot community, in some cases somewhat grumpily, thinking about the formation of fullerenes and other carbon morphologies in flames.”

A case—and a surprisingly prolific one [49–56]—has been made that even chars, cokes, and activated carbons have a considerable fraction of curved sp² domains. For example, Shibuya et al. [57] reported that “small but measurable amounts of C₆₀ were found in two samples of charcoal,” presumably “providing the first indication of fullerene formation in the solid state.” Harris has recently analyzed this issue in some detail [54]. He argued that “detailed studies of chars both before and after high-temperature heat treatments have provided evidence that they might contain fullerene-related elements” and that “glassy carbons may have a fullerene-like structure.” If such arguments are to be convincing, however, they should include a rebuttal of the very large body of evidence that supports the overwhelming presence of flat sp² structures in these materials.

Obviously, entrapment of a pentagon or a heptagon by hexagons—but not both contiguously—is a necessary condition for the growth of curved sp² structures, as illustrated in Figure 1.8 for the simplest case of [5]circulene (corannulene) and [7]circulene [58–60]; the presence of pentagon–heptagon pairs, as in a Stone–Wales defect (see Section 1.4.3), retains planarity [Figure 1.8(c)]. So, as mentioned earlier, the interesting question is whether there is a counterbalancing efficient mechanism of pentagon elimination at flat graphene edges. Such

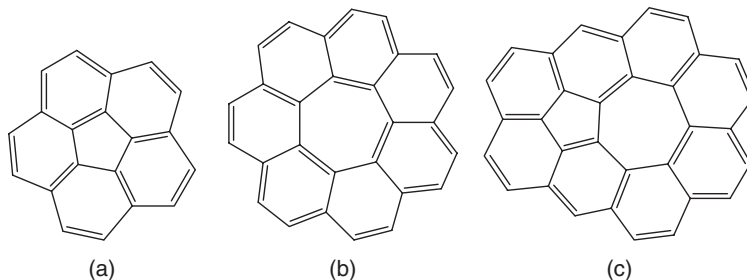


Figure 1.8 Entrapment of (a) pentagons, (b) heptagons, and (c) pentagon–heptagon pairs within a graphene layer.

analysis [61,62] was carried out by Frenklach and co-workers (see Table 1.2 and Figure 1.7). The overall process, whose key intermediate steps involve hydrogen migration, well investigated reactions in the soot formation literature [63], is thermodynamically favorable (Table 1.2): Semiempirical PM3-level quantum chemistry analysis yielded -71 kcal/mol as the enthalpy of the overall reaction $\text{C}_{12}\text{H}_7 + \text{C}_2\text{H}_2 = \text{C}_{14}\text{H}_9$ (Figure 1.7). Our own higher-level density functional theory calculations were in good agreement with such analysis in both qualitative and quantitative terms.

When transition-metal catalyst particles are involved in carbon growth (see Figure 1.6), the mechanistic aspects are much more complex and also more controversial. In a particularly thought-provoking recent contribution, Phillips and co-workers [64] argue that the mechanism according to which “the metal acts as a template for carbon atoms such that as they diffuse to the metal surface they can organize into a low-energy form” is “at best a vague model” because, for example, it does not explain why graphite is “formed several atomic layers from the metal surface.” Indeed, the absence of a detailed discussion on the origin of, or evidence for, curvature—even in presumably mechanistic papers published in reputable journals—is too common and thus puzzling. For example, in a study entitled “Mechanism of carbon nanotube growth by CVD” [65], the authors investigated the “reaction pathways leading to CNT and NTC [nontubular carbon] deposition.” Without any substantive justification, they speculated that “ C_2H_4 decomposed to produce free radicals, which in presence of the iron catalyst formed CNTs” and “[o]nce the catalyst was exhausted, the NTC formation occurred”; such an argument introduces further uncertainty regarding the formation of pyrolytic carbon versus VGCFs. Yet despite the fact that none of the 11 elementary reactions proposed includes or clarifies the formation of pentagons, they presented graphs of production rates for CNTs and NTCs as a function of reaction conditions. As another example, Kataura et al. [66] present “a schematic picture of a growth model” of single-walled carbon nanotubes that is essentially identical to the classical diffusion–precipitation mechanism of VGCF growth (see Figure 1.6). Intriguingly, they do not even mention this fact, nor do they

cite the relevant literature. Even more disturbing is the fact that the recent review by Harris [67] further propagates this citing and conceptual oversight: First, it emphasizes inappropriately the analogy between this model and that of Geohegan et al. [68], and thus fails to place it into the proper context (see Figure 1.6); second, it fails to discuss the reasons for the presumed prevalence of curvature under the relevant carbon growth conditions. As a final example, Gorbunov et al. [69] do discuss the “solid–liquid–solid” growth mechanism of single-wall carbon nanotubes” in the context of catalytic graphitization [70] and VGCF growth [71,33], but they failed to explain exactly how this “catalytic root growth mechanism” becomes also applicable to curved sp² structures and thus becomes “valid for the CVD synthesis of carbon bamboo particles, multi-, and single-wall nanotubes.”

Clearly, the reconciliation of chemical and physical aspects of the nanostructure of carbons will require much additional research effort; the multidisciplinary discussion of their catalytic applications in the chapters that follow is an important step toward the much needed interdisciplinary physicochemical approach.

1.3.4 Bulk Properties

The volumetric or bulk properties of carbon are the ones that best reflect its structure. Here, apart from the typical ranges of values for each of the properties of interest in a given application (see Table 1.1), the key issue is the degree of anisotropy. At the nanometer scale, all sp² carbon materials are intrinsically anisotropic, as is well known. In the direction (*a* and *b* axes) parallel to the basal plane, the dominant chemistry in graphene is that of the very strong aromatic C–C bond; in the direction (*c*-axis) perpendicular to the basal plane, the weak van der Waals or π–π interactions are dominant. Such structural anisotropy often leads to anisotropy of properties, and during manufacture this can often be translated into a key advantage of carbon-based products. Surely a most remarkable example in this regard is the use of pyrolytic carbon as a heat shield in very demanding applications (e.g., for nose cones in rockets and space reentry vehicles): The thermal conductivity anisotropy is at least two orders of magnitude (e.g., 390 W/m/K in the *ab*-direction and 2 W/m/K in the *c*-direction) [11].

The electronic or electrical properties of carbons are a most immediate consequence of their structure. The nanostructure anisotropy, and its degree of replication at the macrostructure level, is responsible for the entire range available here, from good conductors to effective insulators [72].

Thermal properties most often follow the electronic properties quite closely. For example, thermoelectric power (TEP) studies have revealed the unique semiconductor properties of carbons. In a pioneering and largely neglected study [73,74], Walker and Tietjen had already documented the recently rediscovered [75–79] TEP changes in both flat and curved sp² carbons [80]. These can lead to both p- and n-type semiconducting behavior of carbons and thus make possible the fabrication of inter- and intramolecular logic gates, the “basic units of

computers” [81]. More recently, Bar-Ziv and co-workers [82,83] explored the relationship between carbon porosity, its percolation threshold, and thermal conductivity.

Optical properties [84,85] of interest for catalytic applications are particularly those that reveal “contributions of the inter-band transitions of π -electrons” [86] because these can, in principle, shed light on the electron-donating or electron-accepting properties of carbons, which in turn may lead to a new level of understanding of their catalytic properties and behavior [24]. Optical anisotropy has been exploited in microscopy studies that have provided unique insights into the mechanism and the extent of mesophase development [87–91], as well as the contrasting behavior of graphitizing and nongraphitizing carbons [92]. Use of infrared spectroscopy techniques [93,94] has been very useful in elucidating the surface chemical properties of carbons, especially in a qualitative sense (see Chapter 2). The optical properties of particle dispersions [95] have been exploited in the pursuit of an understanding of carbon growth processes in the gas phase [96,97]. Of course, the unique optical properties of fullerenes and carbon nanotubes [36] are not only a very fertile research field but also offer exciting opportunities for practical nanotechnology applications.

Until very recently, interest in the magnetic properties [98–101] has been focused on diamagnetic and paramagnetic susceptibility issues in conjunction with the electronic properties of carbons [102,103]. In fact, in the early development of electron spin resonance as an analytical technique, carbon materials played a very prominent role [104–110]. Interestingly, the pioneering investigations of carbon catalyst supports by Walker, Vannice, and co-workers [111–115] also included a magnetic susceptibility study [116,117], in which “the effective electron mass of the delocalized electrons and the Fermi level were estimated” [116]. Today, however, the intriguing and exciting ferromagnetic properties of carbons [118–126] have taken center stage. Despite the controversy and the retractions [122,123], it appears that some impurity-free carbons are indeed ferromagnetic [121,125,127]. Not surprisingly, the mechanism responsible for this newly discovered phenomenon is uncertain and controversial, and the differences between curved and flat ferromagnetic sp^2 -hybridized carbons need to be clarified in much greater detail. Most explanations offered are based on purely physical arguments [80,128] without due cognizance of chemical constraints [80]. An explanation that arguably bridges the carbon physics–chemistry gap has been proposed recently [80], and it is thought to have important implications for the catalytic behavior of carbons [24]: a carbenelike site at the zigzag edge of a graphene layer has a triplet ground state and its basicity is responsible for unique gas–solid and liquid–solid interactions of carbons (see Section 1.4).

Among the mechanical properties of greatest practical impact on catalysis applications is the attrition and crushing resistance of powdered or granular activated carbons, the most commonly used catalytic carbon materials, versus that of activated carbon fibers (ACFs) or of other, less-surface-active carbons (e.g.,

cokes or high-surface-area graphite). For example, if carbon's surface chemical properties are duly utilized [129–131], it is often not necessary to use carbon adsorbents, catalyst supports, or catalysts that have extremely high surface area but consequently have poor mechanical resistance. Also, fibrous carbons—both the more conventional ACFs and VGCFs, as well as CNTs—offer advantages [132,133] not only in terms of mechanical properties but also better control of transport and other characteristics that can ensure maximum accessibility of catalytically active sites, not only their maximum concentration. Development of monoliths for catalytic applications may offer distinct advantages in this regard [134–136], as discussed in Chapter 11.

Two additional issues are of special relevance here, because of the impact of bulk properties on both surface properties and catalytic behavior: (1) the effect of heteroatom incorporation into the carbon structure; and (2) the x-ray diffraction characterization of carbons in terms of the two-dimensional 10 or the three-dimensional 100 and 101 peaks. The former is discussed in greater detail elsewhere [24]. Incorporation of boron, phosphorus, or nitrogen (see Chapter 7) is of special interest [137,138]. Incorporation of boron produces especially fascinating effects, not only in terms of catalyzed graphitization [139] and modification of electronic properties—the latter currently being the subject of prolific investigations for applications of carbon nanotubes—but it also seems to reveal a macroscopic complementarity principle [140,141]. Simultaneous catalytic and inhibiting effects on carbon oxidation were interpreted “in terms of a balance between three potentially competing effects of substitutional boron: (a) reduced total electron density; (b) decreased contribution of delocalized π electrons to the electron density of the remaining carbon atoms; and (c) σ electron localization on carbon atoms due to the higher electronegativity of carbon with respect to boron” [141].

X-ray diffraction [142–146] continues to be [147–149] the most powerful single tool for characterizing the bulk properties of carbons. However, the interpretation of the diffraction signal at about 40 to $45^{\circ}2\theta$ is too often unnecessarily sloppy, even though it provides a straightforward distinction for graphitic carbons: Unless and until the 10 peak of a turbostratic (i.e., nongraphitizable or not yet graphitized) carbon splits into the 101 and 100 peaks [150,151], this carbon is not graphitic.

A battery of complementary techniques is often necessary (and always desirable) to provide reliable, applications-oriented characterization of the bulk properties of (catalytic) carbon materials. Arguably the most useful ones are transmission electron microscopy (TEM), thermoelectric power (TEP) measurements, electron spin resonance (ESR) spectroscopy coupled with a superconducting quantum interference device (SQUID), and Raman spectroscopy. For example, among the recently reported virtues of Raman spectroscopy is the identification of graphite whiskers [152,153] in three carbonaceous chondrite meteorites (M. Fries and A. Steele, *Science Online*, Feb. 28, 2008), which contain some of the oldest matter in the solar system and has thus generated tremendous interest among astrophysicists.

1.3.5 Surface Properties

Surface properties are at the heart of all catalytic applications and are discussed in more specific terms elsewhere in the book, most notably in Chapters 2, 4, 6, and 15. Here, therefore, only the key aspects of the physics and chemistry of carbon surfaces will be highlighted. More extensive analysis is also offered in several recent reviews [24,94,129,154,155].

Physical Surface Properties This is the most mature topic [156–161]; much is well known and understood, including the origin of porosity and the characterization of pore size distribution (PSD), and yet there are several unresolved issues that have repercussions in catalytic applications. While template-based synthesis of porous carbons [29,162,163] offers the opportunity to obtain zeolite-type regularity of the porous structure, the porosity of most carbons can be tailored over a very wide range, but it is spatially random. In particular, the radial distribution of pores that constitute the well-documented aperture-cavity system in a carbon particle or fiber is largely unknown. Simons and co-workers [164–168] had proposed a tree or river system, which, although not as popular as the random pore models [169,170], has key distinctive features that are worth emphasizing: “The primary difference between the pore tree theory and the random pore model is that the random pore model allows a single small pore to connect two larger pores. This requires that the pore aspect ratio (length to diameter) be of order one hundred. The pore tree theory predicts that all pores possess an aspect ratio of order ten. Hence, small pores may connect to larger pores only on one end and all pores must branch from successively larger pores like a tree or river system.”

Simons’s pioneering efforts anticipated the need for a detailed examination of pore connectivity in carbons. This issue continues to be in need of careful experimental assessment [171–174]. For example, Figure 1.9 reproduces the approach proposed by López-Ramón et al. [174]: “The smaller adsorptive species probes all the pores, and its adsorption isotherm yields the complete PSD. The larger species is excluded from the smaller pores and also from the larger pore that is ‘shielded’ by the smaller pores. So the PSD obtained using the larger species is (i) zero for pores that are smaller than the molecules of that species and (ii) smaller than the PSD for the smaller species above this pore size. The extent to which shielding occurs in a real pore network depends on the connectivity of the network, with the shielding effect being more pronounced for less well connected networks.” This is an increasingly popular subject of computational simulations of varying degree of sophistication [175–179]. Often painstaking evaluation of the degree of pore accessibility using molecular probes of judiciously selected sizes has been useful both at a fundamental level [162,180–193] and for the potential commercialization of carbon molecular sieves [194–210].

Because of the almost ubiquitous presence of very narrow porosity in most catalytically relevant carbon materials, and no doubt because of their complex connectivity, the effective diffusivity in nanopores of particulate carbons is

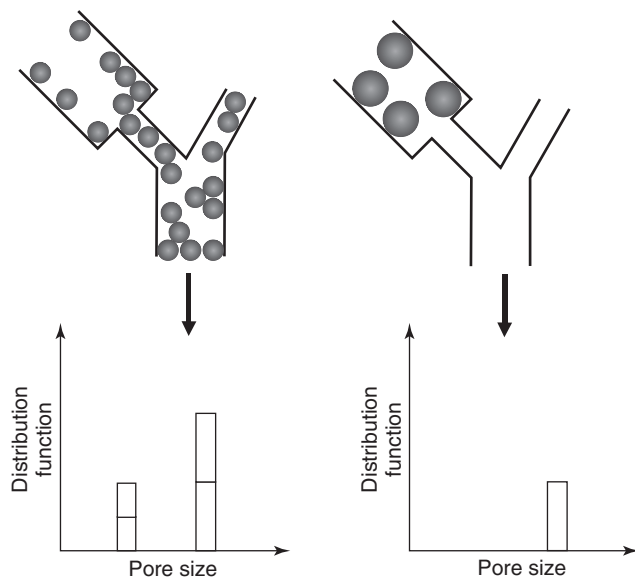


Figure 1.9 Schematic representation of a methodology for experimental assessment of connectivity of pores in carbon materials. (From ref. 174.)

activated and its value often does not exceed $10^{-9} \text{ m}^2/\text{s}$, especially in liquid-phase applications. Therefore, when very fast diffusion toward and/or away from carbon surfaces is a requirement, the advantages of activated carbon fibers—with their typically shorter and more regularly distributed pores—may be a sufficient compensation for their economic disadvantage when compared to powders or granules. As mentioned in Section 1.3.4, the use of monoliths (see Chapter 11) is also of interest.

As a final comment, it should be mentioned that the fractal approach [211,212] to the elucidation of carbon surface physics (including pore size distribution, surface roughness, and transport characteristics), although initially very promising [213–227], does not yet seem to have fulfilled the optimistic expectations. For example, Huang et al. [224] combined TEM with image processing to investigate the micropore structure of two rayon-derived ACFs and concluded, rather prosaically, that the “fractal dimensions obtained were consistent with those obtained by nitrogen adsorption.” More recent studies along the same lines seem to be devoted to the characterization of carbon nanotubes [228,229].

Chemical Surface Properties While a few other porous solids can match most of the physical surface properties of carbon materials (except the very high surface areas, in excess of $2000 \text{ m}^2/\text{g}$), when it comes to surface chemistry the flexibility offered by carbons is rather unique. This is because of their unique proton-,

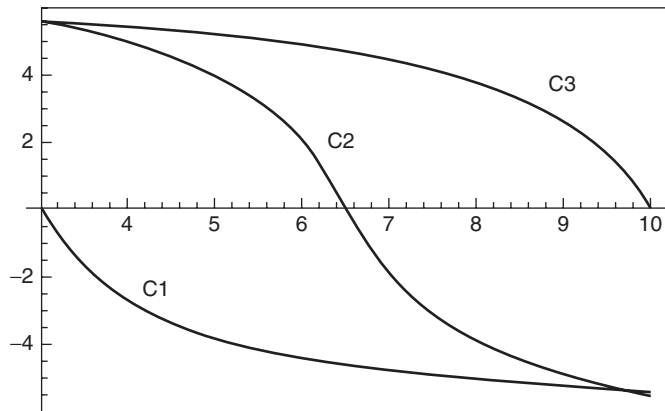


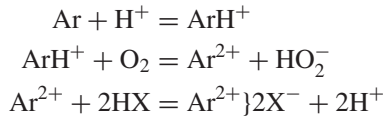
Figure 1.10 Dimensionless surface potential (y-axis) versus pH (x-axis) for three types of carbon materials: C1, acidic carbon [point of zero charge (PZC) = 3]; C2, typical as-received, air-exposed, amphoteric carbon (PZC = 6.5); C3, basic carbon (PZC = 10).

electron-, and oxygen-transfer characteristics, and these are summarized below. A more detailed discussion is provided elsewhere [24].

Figure 1.10 summarizes the remarkable flexibility of carbons when it comes to proton transfer. This is due largely to the presence of surface functional groups at graphene edges. Oxygen-containing groups are ubiquitous, especially in the catalytically most relevant high-surface-area carbon materials, whether introduced deliberately or accidentally (e.g., by simple exposure to ambient atmosphere). Functional groups containing other heteroatoms, such as sulfur or nitrogen, can be introduced as well, the latter being increasingly popular. The presence of hydrogen is most often a residue from the carbonization process, unless it is introduced in conjunction with the other heteroatoms (e.g., as COOH or NH₂ groups). These functionalities are not only responsible for the development of surface charge, but also for much of the “chemical activity” of carbons (especially at low temperatures) because the sp²-hybridized aromatic carbon atoms with a delocalized π-electron system, especially those in the basal plane (i.e., within a graphene sheet), are much less (re)active. In this sense carbons are unique (zwitterionic?) amphoteric solids [230]: Not only can they be acidic (e.g., by virtue of dissociation of carboxyl groups) or basic, but their surface charge (or electrophoretic mobility) versus pH plots are not symmetric. The key parameter here is the point of zero charge, pH_{PZC}, with a net positive surface charge developing at pH < pH_{PZC} and a net negative surface charge developing at pH > pH_{PZC}. For *basic carbons* [i.e., those carbons exhibiting pH_{PZC} > 7 (in the older literature also called *H-carbons*, following the nomenclature introduced by Steenberg [231,232])] it is important to recall that a very concrete proposal was formulated half a century ago by Garten and Weiss [233,234] to “account for the ability of an H-carbon electrode to catalyze the reduction of oxygen [in alkaline solution]

at a sufficient rate for it to operate at reasonable current densities.” It involves quinone functionalities and the olefinic bonds associated with them, which “add on oxygen to form a hydroperoxide or moloxide” and which in turn “accept an electron from the cathode to form the monovalent peroxide anion radical which may remain attached to the carbon by the ability of the quinone to form a semiquinone”; subsequently, the oxygen molecule “accepts a second electron and splits off as the peroxide anion.” The mechanistic discussion of (the inconsistencies of) such a scheme is discussed elsewhere [24]. Here it is worth emphasizing that one portion of the authors’ argument, regarding the quinone–hydroquinone character of activated carbon, carbon black [233] and other carbon materials, has withstood the test of time remarkably well [232].

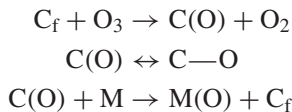
In addition to quinone groups, and to some extent to pyrones, which undoubtedly confer basicity to carbons, the possibility of existence of an oxygen-free, positively charged basic site on the carbon surface was acknowledged in elegant early studies by Rivin [235]:



A zigzag carbene atom is a very promising candidate for this heretofore unidentified site; this is discussed in more detail elsewhere [80].

Figure 1.11 shows a proposed surface chemistry that highlights the electron-transfer possibilities both at graphene edges and within the basal plane. Its main features are (1) the existence of free edge sites, and (2) the notion that the basal plane is not as chemically inert as is often envisaged, due to the presence of (delocalized) unpaired electrons, a common consequence of the presence of an uneven number of C–H bonds in the condensed polyaromatic structure of graphene. A detailed justification for the existence of carbenelike zigzag edge sites and carbynelike armchair edge sites has been provided elsewhere [80]. This proposal is not only theoretically sound and consistent with the key experimental observations in the behavior of carbon surfaces, but also provides a straightforward explanation for ferromagnetism in certain impurity-free carbons.

The following sequence of key reactions illustrates the oxygen-transfer characteristics of carbon surfaces. Use of any oxidizing agent (e.g., O₂, CO₂, H₂O, H₂O₂, NO, N₂O) is analogous to that of ozone, shown here interacting with a free carbon (re)active site:



The second step represents a dynamic equilibrium between stable surface complexes (“spectators”) and reactive surface intermediates [236,237], and the third one is the venerable “spillover” [238–241] from the carbon (e.g., support) surface

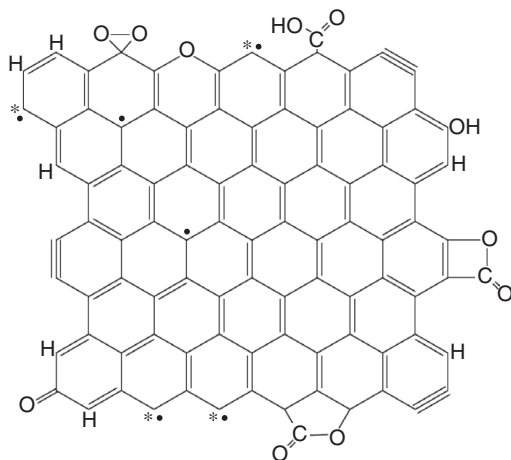


Figure 1.11 Representation of the surface chemical features that exist, to a greater or lesser extent, in the graphene layers of flat sp^2 -hybridized carbon materials, including carbene- and carbyne-type free edge sites; carboxyl-, lactone-, quinone-, pyrone-, and phenolic-type oxygen functionalities; delocalized unpaired π electrons; and nondissociatively adsorbed O_2 on carbene-type sites.

to the surface of an active metal (e.g., catalyst). The implications of this admittedly simplified, but arguably not oversimplified mechanism [242] are explored briefly in Section 1.4.1.

1.4 REACTIONS OF CARBONS

Both the relative inertness and the remarkable affinity of carbon for oxygen are exploited in a very wide variety of carbon reactions—primarily with gases and liquids—a large fraction of these having a direct impact on catalytic applications of carbon materials.

1.4.1 Gas Phase

In the gas phase the topics of principal concern are adsorption and gasification or combustion, both uncatalyzed and catalyzed by adventitious or inherent impurities. The degree of flexibility and the opportunities for tailoring the properties of carbons in the relevant applications—as adsorbent (see Chapter 14), catalyst support (see Chapters 4, 5, 8 to 13, and 15), catalyst (see Chapters 6, 7, and 9), reactant, electrode (see Chapter 14), and electrocatalyst (see Chapter 12)—are truly phenomenal. Some of these are also discussed in Section 1.4.2. Here the focus is on gas-phase physisorption or chemisorption and their impact on the formation of surface intermediates and thus on catalytic surface reactions, as well as

on reactions of carbons with mostly oxidizing gases [242]. Even though carbon can be both a sink and a source for electrons, it is symptomatic that it reacts less readily with reducing gases. The most important example is its interaction with ammonia, for incorporation of basic surface functionalities and for improved catalytic or electrochemical performance [243–249].

Physisorption occurs on the entire carbon surface, and if the adsorbing species has access to all the pores, it titrates the total surface area. Chemisorption of a suitable molecule—most often O₂ [250,251], but also, say, propylene during chemical vapor deposition [252]—titrates the active surface area. Transient kinetics or judiciously (and somewhat painstakingly) executed temperature-programmed desorption techniques are needed to titrate the reactive surface area [236,253–257]. The painstaking part is related to the fact that carbon surfaces are not only heterogeneous [258], but offer a prime (and rather unique) example of induced heterogeneity [259], a well-established concept in heterogeneous catalysis: The affinity of the surface, and thus the number of reactive surface intermediates (or reactive sites), changes as reaction proceeds. In the case of the carbon–oxygen reaction, this can be summarized as a seemingly simple reaction sequence and its corresponding kinetic expression:



$$\text{rate} = \frac{-d[C]}{dt} = k_3[C(O)]^2 + k_4[C(O)] \quad (1.5)$$

Contrary to the case of a conventional heterogeneous (catalytic) reaction, the usefulness of equation (1.5) is limited by the fact that both the rate constants k_3 and k_4 and the reactive site concentration [C(O)] appear to be not only material-dependent but also conversion-dependent. Given these experimental complexities, current research is focusing increasingly on exploring the opportunities offered by computational quantum chemistry (see Chapter 3). A particularly fruitful result of such research is a rather straightforward formulation of the long-puzzling pathway to CO₂, which reconciles the well-known and seemingly contradictory experimental facts that it is a primary reaction product and yet O₂ adsorption is (predominantly?) dissociative. The feasibility of existence of a carbene edge site [80] and of a mobile epoxy-type oxygen on the basal plane [260–264] suggest the mechanism summarized in Figure 1.12. The latter pathway is exactly analogous to the well-known conversion of benzene oxide to oxepin [265].

As mentioned in Section 1.3.4, another intriguing aspect of gas reactions of carbons is the simultaneous inhibiting and catalytic effect of boron additives [141,242]. Its rationalization is another prime example of the need to bridge the physics–chemistry gap. In addition to presenting a diffusion barrier and a

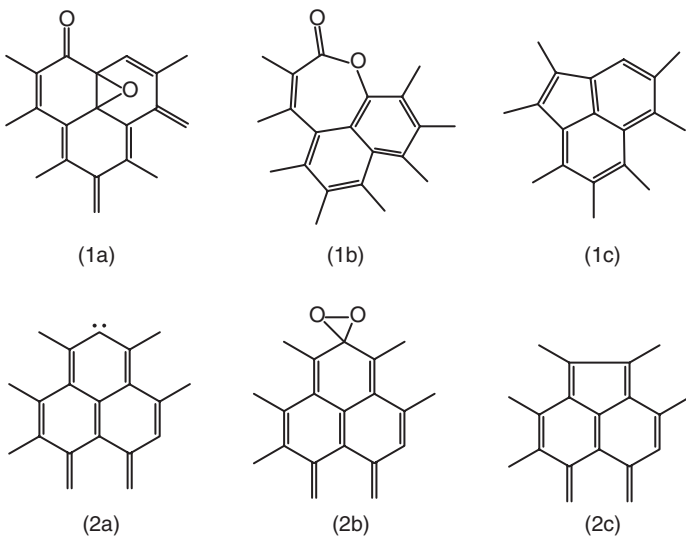


Figure 1.12 Proposed mechanisms for CO₂ formation in the carbon–oxygen reaction: 1a → 1b → 1c, oxygen insertion (dissociative chemisorption) route; 2a → 2b → 2c, nondissociative chemisorption route on the carbene edge sites.

specific site blocking and thus inhibiting effect, there is a simultaneous intrinsic (or electronic) effect whose elucidation is very much aided by a quantum chemical analysis: reduced total electron density, decreased contribution of delocalized π electrons to the electron density in the graphene layer, and σ -electron localization on carbon atoms due to higher electronegativity of carbon relative to boron.

1.4.2 Liquid Phase

In the liquid phase the topics of principal concern are adsorption and proton and/or electron transfer across the electric double layer. Carbon materials are unique in these applications because they are insoluble over the entire practical range of pH, are amphoteric, and can exhibit either acidic or basic properties; this was illustrated in Figure 1.10. Furthermore, because of their more or less extensive delocalized π -electron system in the graphene layer, they can either accept or donate electrons. Such remarkable flexibility offers, on the one hand, a unique opportunity to tailor carbon's properties to specific needs in adsorption, catalysis, and electrocatalysis; but, as argued in detail elsewhere [24], it is also responsible for the persistent lack of fundamental understanding in the increasingly important field of carbon electrochemistry, despite the tremendous amount of research and development focused on carbon-based capacitors, batteries, and fuel cells.

The key factors governing liquid-phase physical adsorption on carbons are well understood [131]. Coulombic adsorbate–adsorbent attraction is important for maximizing the uptake of inorganic cations or anions; conversely, coulombic repulsion by the charged carbon surface is responsible for the reduced adsorption. In this regard, the isoelectric point (or the point of zero charge) of the carbon—which can vary, say, from pH 2 to pH 10—is the key optimization parameter. As another illustration of the need for (and the rewards of) interdisciplinary analysis, this has been a well-recognized concept in carbon colloid physics [266], but until the early 1990s [129,130] it was essentially ignored in the carbon catalysis literature.

For organic solutes, and especially aromatic solutes, the factors controlling adsorbate–adsorbent interactions are decidedly more complex, but they appear to conform to well-established concepts in organic chemistry [131]. In addition to coulombic attraction or repulsion, the strength and the extent of dispersive (van der Waals) attraction depends on the electron density in both the graphene layer and the adsorbing molecule; and this charge density—and thus, for example, the extent of $\pi-\pi$ overlap—depends on the presence of electron-donating or electron-withdrawing substituent groups both on the edges of graphene layers and in the adsorbing molecules.

The nature of the double layer in nanoporous solids in general, as opposed to its characteristics on an open surface or in relatively large pores, as predicted, for example, by the Gouy–Chapman model, is a topic of increasing interest [267,268]. Be that as it may, the principles of the DLVO theory [269] have been shown to apply remarkably well. For example, López-Ramón et al. [270] clarified “the effects of the ionic strength in the adsorption of metal ions on activated carbons. An increase in the ionic strength of the solution reduces the electrostatic interactions, either attractive or repulsive, due to a screening effect of the electrolyte.” This has practical importance because it provides additional flexibility in selecting the appropriate conditions of surface and solution chemistry for maximum uptake of either anions or cations from aqueous solution, which in turn affects the preparation of carbon-supported catalysts [130] and the double-layer development in supercapacitors [24].

The opportunity to develop commercially attractive rechargeable batteries using carbon materials has revived interest in cation intercalation, or insertion. Despite remarkable progress in achieving large storage capacities [271,272], the surface chemical properties responsible for this process remain unclear. This is arguably due to continued uncertainties regarding appropriate methodology to quantitatively titrate, and even clearly identify, the basic sites on carbon surfaces (see Section 1.3.5 and Chapter 2).

Liquid-phase redox reactions on carbon surfaces are particularly interesting because they typically involve both proton and electron transfer (see Chapter 12). Because electron transfer is not as well understood as proton transfer, essential details of the physicochemical principles that govern important applications such as H_2O_2 decomposition and O_2 reduction are still far from being well established [24].

1.4.3 Solid Phase

The multitude of topics of interest in the solid phase all have in common the mobility of atoms that make up the structure of carbon materials. At the nanoscale we can distinguish, at least conceptually, the rearrangement of carbon atoms from that of the heteroatoms (see below). Among the most prominent macroscale phenomena studied to date are high-temperature treatment (HTT), graphitization, and annealing; they have been of interest since the early years of carbon technology development, but especially so since the pioneering studies of Franklin [273]. Their role in catalytic applications cannot be overemphasized because both the number and the density of catalytically (re)active sites depend on the prevalence of these processes in the carbon formation stage. For example, the important study by Smith [274] established variations of up to four orders of magnitude in surface-area-normalized reactivities of carbons at constant temperature; the author hypothesized that such differences were due in part to “the effects of the atomic structure of the carbons.” In a follow-up study, Radovic et al. [251] showed that heat treatment during pyrolysis, even when not causing significant modifications in surface area, produced major reductions in the active-site concentration of carbons.

Here the most relevant topics are of more fundamental nature than those summarized in Sections 1.4.1 and 1.4.2, related primarily to the thermodynamics and kinetics of structural ordering. The first issue of interest in this context is one of semantics although, as is often the case in carbon science, it does embody a fundamental structural concept: carbon graphitizability. As clearly defined by Fitzer et al. [6], although too often ignored in the literature, exposure of chars (i.e., non-graphitizable carbons) to high temperature (e.g., in excess of 2773 K) is merely HTT, whereas such exposure of cokes is indeed graphitization. Heat treatment, which is necessary for structural ordering, is not sufficient for graphitization [6]; the latter process implies that the definite structure of graphite is achieved, and this requires not only exposure to temperatures in excess of 2773 K but also a suitable (graphitizable) precursor and, almost invariably, that the intermediate product passes through a plastic phase (e.g., liquid mesophase). For example, the very much engrained concept of a graphitized carbon black [275–277] makes no sense, because carbon blacks are far from being graphitizable.

One persistently puzzling experimental fact in solid-state transformations of carbons exposed to HTT is the relative growth of crystallite width (L_a) and crystallite height (L_c). It remains essentially unexplored since Franklin’s incisive and influential discussions based on her pioneering x-ray diffraction analyses [273]. These results are reproduced in Figure 1.13. The two groups of carbons are clearly distinguishable: (1) The nongraphitizing or nongraphitizable carbons experienced limited crystallite growth even at temperatures as high as 3273 K [e.g., a Northumberland coal heat-treated to 3273 K achieved a crystallite diameter of only 6.5 nm and a crystallite height of only 3.9 nm (11.6×0.336)]; and (2) The graphitizing or graphitizable carbons have a larger “number of layers per parallel group,” achieved at temperatures as low as 1993 K [e.g., a

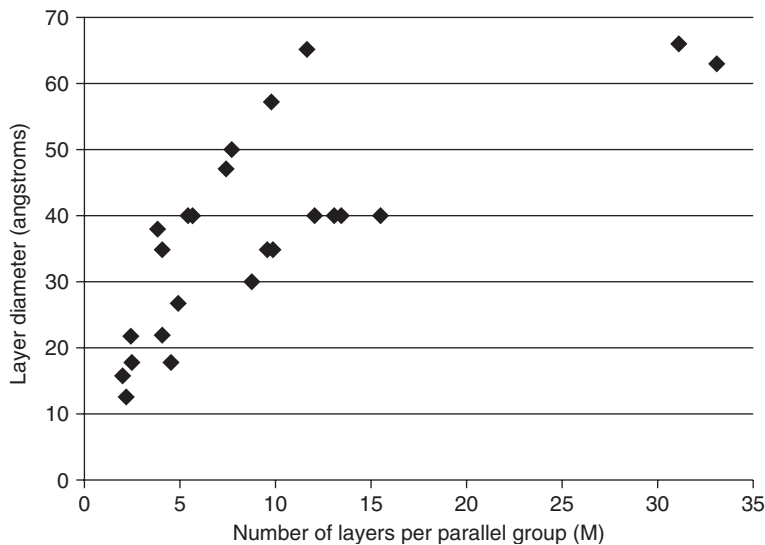


Figure 1.13 Comparison of crystallite growth as a consequence of heat treatment of graphitizable and nongraphitizable carbons. (From ref. 273.)

petroleum coke achieved a crystallite diameter of 6.6 nm and a crystallite height of 10.4 nm (31.0×0.336) when heat-treated to 1993 K]. Franklin noted that, while $L_a < 2.5$ nm and “as long as there remains an appreciable quantity of non-organized carbon,” an increase in temperature caused L_a to increase with little change in L_c ; in contrast, for $L_a > 2.5$ nm, L_c increased much more rapidly than L_a in graphitizable carbons than in nongraphitizable carbons. She argued that crystallite growth does not occur by migration of isolated carbon atoms or small groups of atoms from the smaller to the larger ordered units, either “through the vapour phase” or “by surface migration,” or “by means of an unstable intermediate compound formed by combination of the carbon with a trace of impurity (for example, hydrogen).” Rather, she envisioned the following mechanism, worth quoting in detail because here again there is a potential conflict between the physics and chemistry of carbons: “[I]f a whole migrating layer-plane or group is to join itself to an existing crystallite, there is, a priori, a higher probability of its being fixed on the basal plane than of its becoming attached to the edge-atoms of a layer-plane; for the former, it only requires to be parallel to, and at a fixed distance from, the basal plane, whereas for the latter it must not only lie in the correct plane, but must also adopt the correct orientation. This may, perhaps, explain why, in the graphitizing carbons, the crystallites grow in height more rapidly than in diameter. If, on the other hand, growth occurred through the movement of isolated atoms or small groups, these would tend to be fixed by the unsaturated valencies at the edges of the layers rather than on the basal planes.” The validity of such an argument hinges on Franklin’s

(apparently intuitive) understanding of the term *fixed*; obviously, formation of covalent bonds at graphene edges is required for an increase in crystallite diameter, whereas only $\pi-\pi$ stacking is thought to be sufficient for an increase in crystallite height.

A quantitative but still physics-based treatment of this process has been proposed by Emmerich [278]. A pioneering essay that attempts to bridge the physics–chemistry gap has been published by Oberlin et al. [91]. Related to this issue is the phenomenon of annealing [279–283] in general and nascent site [284–286] deactivation in particular. The former process, although possessing a distinct metallurgical connotation, has been a popular research topic mostly in the coal combustion literature and is distinct from that of HTT or graphitization because its kinetics, not just thermodynamics, is of primary interest. In the classical study of Strickland-Constable [287], the anomalous temperature dependence of the reaction rate at high temperatures forced the author to conclude that “some rather important change in the surface of the graphite occurs [between 1473 and 1873 K]” [287] and that “although the absolute values of the rates may be in need of considerable correction for mass transfer, the curves . . . are in broad outline of a shape determined by chemical factors” [288]. Very recently, Senneca et al. [289] confirmed the well-known trend [251] that thermal annealing [279] produces upon “heat treatment of coal for different times (in the range between 1 s and 30 min) at different temperatures (in the range 1733–2273 K)”: The severity of heat treatment “has a pronounced effect on char combustion rate” and “[c]hars prepared under severe heat treatment conditions show negligible oxygen uptake and strongly reduced combustion rates.” In an earlier study by the same group, Salatino and co-workers [280] compared the time scales for the processes of gasification and annealing and discussed the potential influence of the latter on the determination of kinetic parameters of the former; this, of course, is of special relevance to combustion conditions, whose characteristic time scales are on the order of seconds. Indeed, in the carbon burnout kinetic (CBK) model proposed by Hurt and co-workers [290], whose principal concern is the prediction of behavior at close to 100% carbon consumption (thus being of direct relevance to the performance of pulverized coal boilers), thermal annealing is explicitly described as a first-order process with a distributed activation energy (E_d) of annealing [279] of the different types of sites (N_j):

$$\frac{dN_j}{dt} = -N_j A_d \exp\left(-\frac{E_d}{RT}\right)$$

For example, if about 2% of the carbon active sites remain after 1 second at 1200 K, the thermal annealing submodel of the CBK model predicts that <0.1% remains at 1900 K.

A special case of annealing, distinguishable by its very rapid rate and elusive quantification, is nascent site deactivation (NSD). Figure 1.14 illustrates four possibilities at the molecular level. Upon desorption of CO (e.g., during carbon

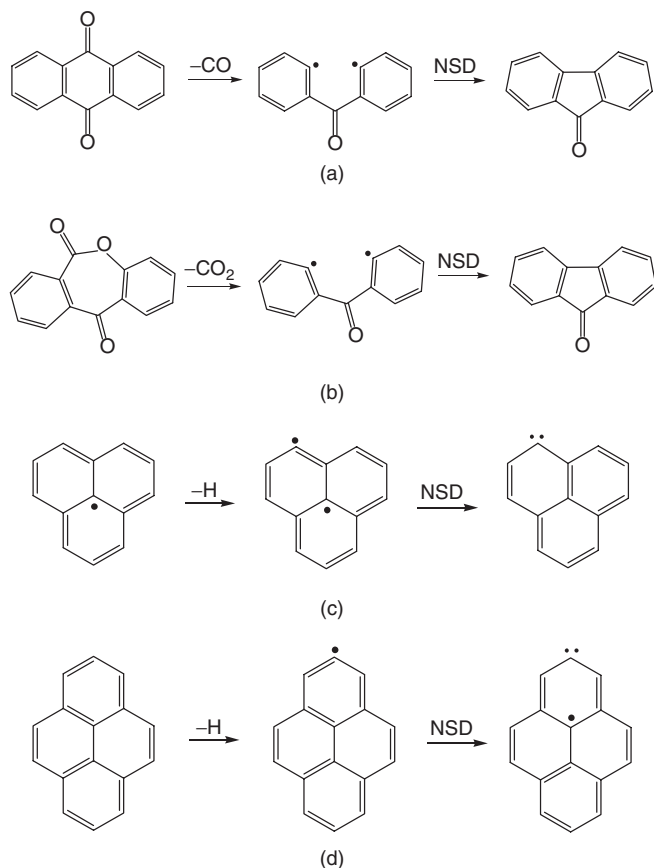


Figure 1.14 Representation of nascent carbon active-site deactivation.

gasification in H_2O , CO_2 , NO , N_2O , or O_2 [Figure 1.14(a)] or CO_2 (e.g., during carbon gasification in O_2 , NO , or N_2O [Figure 1.14(b)]), a triplet structure is formed with two residual radical sites; here the NSD process is its conversion to a singlet by virtue of pentagon formation. Formation of a carbene edge site, by virtue of π -electron localization by a (σ) radical site [Figure 1.14(c,d)], also results in nascent site deactivation; in fact, this process is thought to be a straightforward explanation for the development of positive thermoelectric power and even ferromagnetic behavior of carbons [80]. The most dramatic practical illustration of the NSD process, summarized in Table 1.3, can be found in a path-breaking study by Johnson [291]. If deactivation of nascent sites is prevented upon cleavage of bonds (primarily C–C and C–H) in the carbon precursor, in this case by performing coal pyrolysis in the presence of reactive H_2 gas at high pressure, the entire coal char sample can be converted (hydrogasified) to CH_4 ; in contrast, if such deactivation is allowed to take its course—in this case

Table 1.3 Typical Weight Losses (%) Obtained for Gasification of a Bituminous Coal and Its Parent Char at About 1073 K

Sample	Time (min)			
	0.5	2	4	7
Coal, N ₂ , 35 atm	22	25	25	25
Char, H ₂ , 35 atm	26	27	30	35
Coal, H ₂ , 35 atm	37	45	48	50
Coal, H ₂ , 69 atm	53	58	62	68

Source: Ref. 291, p. 72.

by performing coal pyrolysis in an inert atmosphere (e.g., N₂)—the resulting char undergoes subsequent hydrogasification in H₂ at a much reduced rate. The mechanism of deactivation had remained largely ignored until very recently (as summarized in Figure 1.14); nevertheless, since then it has been invoked successfully, albeit primarily in qualitative terms, in a remarkable variety of surface phenomena.

An incisive and authoritative early analysis was provided by Walker et al. [292] as a possible explanation for the gasification rate-enhancing effects of a presumably inert diluent: Xe > N₂ > Ar > He. The authors argued as follows: “[N]ascent or highly reactive carbon sites are produced continually during carbon gasification... [P]ositive holes are formed in carbons by electrons jumping from the π band to the σ state, forming a spin pair at the edge of the crystallite. Or put another way, sp³–s²p² rehybridization is expected to occur at some carbon atoms located at crystallite edges.... The net effect is to convert a carbon atom having an unpaired electron on it to one having no unpaired electrons. It is suggested that the nascent sites produced by gasification are those with unpaired electrons on them (sp³ sites) and at some rate these sites rehybridize to s²p² sites, which are less reactive towards O₂ and CO₂. Possibly the rate of rehybridization is affected (slowed) by interaction with diluent gases.” Other examples of nascent site interactions are the chemisorption of hydrogen on the surface vacated by desorption of surface oxygen complexes [293], the enhancement of hydrogasification reactivity upon preoxidation of carbons with nitric acid [294], and the enhancement of their reactivity to NO in the presence of O₂ [295,296].

Surface diffusion as a solid-phase process is conceptually similar to those discussed above, except that it involves the movement of heteroatoms rather than carbon atoms. Oxygen and hydrogen are of special interest, because of the widely documented importance of their spillover on the carbon surface. Indeed, the phenomenon of spillover was first observed on the surface of a channel carbon black [238].

In a set of ingenious argon flush experiments with single-crystal natural graphite, Yang and Wong [297] observed that “surfaces with low edge carbon densities continue to ‘burn’ for prolonged periods of time after O₂ is cut off

from the gas phase.” The surface oxygen diffusion coefficient was estimated to be quite small, of the order of 10^{-16} m²/s, with an activation energy of at least 35 kcal/mol. The authors’ interpretation was that the “active sites were fed . . . exclusively on the chemisorbed oxygen from the neighboring ‘nonactive’ sites,” a powerful argument that reinforced the early insight provided by Marsh [298].

Gasification-induced carbon densification (e.g., particle shrinkage) is another intriguing experimental fact [82,83,299–307]. Like annealing, it is a consequence of structural ordering, but here thermally induced diffusion is assisted by chemical removal of the more reactive carbon atoms. Usually it results in carbon structures that are very far from the structure of graphite, despite claims that “[i]n actuality densification is a pseudonym for graphitization” [307], which is especially not true in the case of nongraphitizable soot particles [307]. For example, instead of a uniform bulk density decrease of form coke (surface area, 475 m²/g; true density, 2.07 g/cm³) from 0.87 to 0.52 g/cm³ under chemically controlled conditions of CO₂ gasification [308], Easler et al. [300] reported about 37% densification to 0.71 g/cm³. In the incisive analysis of Hurt et al. [301] it is emphasized that such shrinkage is common to both graphitizable cokes and nongraphitizable chars and soot, and “over a wide range of length scales . . . over six orders of magnitude,” from 30-nm diesel soot particles to 100-μm char particles and even to macroscopic coke samples. A model that assumes particle shrinkage to occur as a consequence of “random complete gasification of a crystallite plane” and thus predicts that an “increase in the number of crystallite planes reduces shrinkage” has been proposed by Bhatia [304]; its predictions highlighted the “importance of detailed characterization at the crystallite level” and confirmed the expectation of Walker [303] that “highly ordered carbons of large crystallite size, high crystallite alignment, and little cross-linking [should] not show significant densification as a result of carbon gasification.” The modeling efforts of Kantorovich, Bar-Ziv, and co-workers [82,302,305,306] resulted in the proposal that restoration of broken joints between carbon microcrystals, as well as new joint formation by virtue of changes in microcrystal position and coalescence of neighboring microcrystals, is responsible for shrinkage; in particular, the phenomena of uniform and nonuniform shrinkage appear to lend themselves to convenient analysis using such an approach.

It is intriguing, however, that not a single one among the studies of gasification-induced densification cites the early insightful paper by Walker et al. [309], which offers a most straightforward explanation for an intimately related effect: Contrary to the intuitive expectation that the average crystallite height (L_c) and especially the average crystallite width (L_a) should decrease monotonically as gasification proceeds and the crystallites are reduced in size due to preferential removal of edge carbon atoms, “gasification to either 45 or 85% weight loss produces an increase in both the L_c and L_a dimensions of the residual carbon . . . [This] increase in average crystallite size . . . can be accounted for by either crystal growth during reaction or the elimination of the small crystallites by reaction.” The authors dismissed the former possibility because “[c]arbon graphitized to

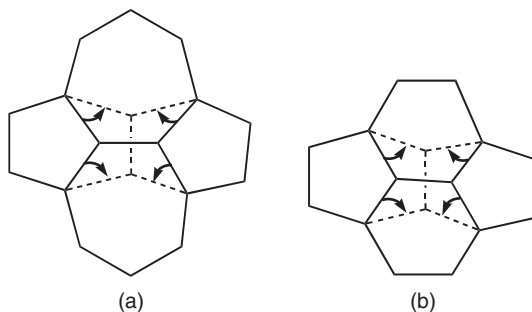


Figure 1.15 Representation of Stone–Wales rearrangements: (a) $5/7 \leftrightarrow 6/6$; (b) $5/6 \leftrightarrow 6/5$.

2773 K would hardly be expected to undergo further crystal growth during gasification at 1373 K. Therefore the latter explanation would seem to be the more logical.” The more recent arguments put forward to explain gasification-induced densification have hardly been more insightful.

A nanoscale solid-phase reaction of great current interest—a decidedly fundamental one but with important practical implications—is the Stone–Wales rearrangement of sp^2 -bonded carbon structures [310] [i.e., the transformation of four hexagons to (or from?) two pentagons and two heptagons by virtue of a 90° rotation of a C–C bond in the interior of a graphene layer]. Related to this issue is the fate of pentagons at graphene edges: If there is an efficient mechanism of their elimination and conversion to hexagons, the growth of flat graphenes will be favored over the emergence of fullerene-like structures, as is of course most often observed in hydrocarbon pyrolysis (see Section 1.3.3). Figure 1.15 shows the Stone–Wales rearrangement of primary interest here, together with the analogous pentagon/hexagon rearrangement, which is presumably important for understanding the fullerene growth mechanism and which, as pointed out by Telling and Heggie [311], was originally analyzed by Dienes [312] in the context of atomic self-diffusion in graphite.

1.5 CONCLUSIONS

Not surprisingly perhaps, a scrutiny of, and reflection upon, the scientific literature on catalytically relevant carbon materials revealed both positive and negative examples of congruence between the physical and chemical approaches used to study the dominant phenomena. The topics discussed in the remaining chapters provide additional case studies. The rewards awaiting those who can bridge this physics–chemistry gap (often quite wide!), and thus understand the physical chemistry of carbons, provide a strong motivation to continue on this increasingly feasible, interdisciplinary research path.

At least one particularly fertile avenue is both obvious and pertinent to the main theme of this essay. In view of the steadily growing cross-fertilization between novel carbons (fullerenes and nanotubes) and the more traditional ones, there is a need to define and carry out critical experimental and theoretical analyses of the evidence in favor, or against, a significant presence of curved sp² nanostructures in soot, carbon blacks, vapor-grown carbon fibers, chars, and cokes. In this sense, recalling the classical microstructure-level discussion of the PAN AM or Brooks-and-Taylor arrangement of graphene layers in (mostly graphitizable) carbon particles or fibers [91,313–316] may be instructive: The chemical driving force to maintain planarity by π–π overlap in the aromatic molecule(s) is in competition with the physical driving force to minimize surface tension. The outcome of this competition determines the quantity and quality of catalytically relevant carbon (re)active sites and is thus a seminal issue whose resolution should now be within reach of the interested readers of this chapter and of this book.

Acknowledgments

Partial support for the research described here was provided by FONDECYT project 1060950, with the assistance of Fernando Vallejos and Braulio Cid. The editors (P.S. and J.L.F.) deserve special recognition for their patience with this author, and for their encouragement, as well as for bringing together an enviable group of topics and authoritative contributions in this pioneering book.

REFERENCES

- [1] P.A.M. Dirac, *Proc. R. Soc. A* 123 (1929) 714.
- [2] L.R. Radovic, Ed., *Chemistry and Physics of Carbon*, Vol. 30, Taylor & Francis (CRC Press), Boca Raton, FL, 2008.
- [3] H. Aldersey-Williams, *The Most Beautiful Molecule: The Discovery of the Buckminsterfullerene*, Wiley, New York, 1995.
- [4] H.W. Kroto, J.R. Heath, S.C. O'Brien, R.F. Curl, R.E. Smalley, *Nature* 318 (1985) 162.
- [5] W. Krätschmer, L.D. Lamb, K. Fostiropoulos, D.R. Huffman, *Nature* 347 (1990) 354.
- [6] E. Fitzer, K.H. Köchling, H.P. Boehm, H. Marsh, *Pure Appl. Chem.* 67 (1995) 473.
- [7] J.I. Gersten, F.W. Smith, *The Physics and Chemistry of Materials*, Wiley, New York, 2001.
- [8] W.D. Callister, Jr., *Materials Science and Engineering: An Introduction*, Wiley, New York, 1991.
- [9] W.D. Callister, Jr., *Fundamentals of Materials Science and Engineering: An Interactive e-Text*, Wiley, New York, 2001.
- [10] C.L. Mantell, *Carbon and Graphite Handbook*, Interscience, New York, 1968.
- [11] H.O. Pierson, *Handbook of Carbon, Diamond and Fullerenes*, Noyes Publications, Park Ridge, NJ, 1993.

- [12] Anon., *Carbon* 20 (1982) 445.
- [13] Anon., *Carbon* 21 (1983) 517.
- [14] K.H. Köchling, B. McEnaney, S. Müller, E. Fitzer, *Carbon* 23 (1985) 601.
- [15] K.H. Köchling, B. McEnaney, S. Müller, E. Fitzer, *Carbon* 24 (1986) 246.
- [16] J.B. Donnet, E. Fitzer, K.H. Köchling, *Carbon* 25 (1987) 449.
- [17] J.B. Donnet, E. Fitzer, K.H. Kochling, *Carbon* 25 (1987) 317.
- [18] R.W. Pekala, *J. Mater. Sci.* 24 (1989) 3221.
- [19] W.E. Gibbs, H. Liander, *Trans. Faraday Soc.* 26 (1930) 656.
- [20] T.W. Boyle, W.J. Gaw, R.A. Ross, *J. Chem. Soc.* (1965) 240.
- [21] J.F. Shackelford, *Introduction to Materials Science for Engineers*, 4th ed., Prentice Hall, Upper Saddle River, NJ, 1996.
- [22] H. Kuhn, H.-D. Försterling, *Principles of Physical Chemistry: Understanding Molecules, Molecular Assemblies, Supramolecular Machines*, Wiley, Chichester, UK, 2000.
- [23] J. Steed, J. Atwood, *Supramolecular Chemistry*, Wiley, Chichester, UK, 2000.
- [24] L.R. Radovic, in F. Béguin, E. Frackowiak, Eds., *Electrochemistry of Carbon Materials*, Taylor & Francis, (CRC Press), Boca Raton, FL, in press.
- [25] S.N. Marinkovic, in L.R. Radovic, Ed., *Chemistry and Physics of Carbon*, Vol. 29, Marcel Dekker: New York, 2004, p. 71.
- [26] M. Inagaki, L.R. Radovic, *Carbon* 40 (2002) 2279.
- [27] M.W. Browne, *The New York Times*, June 22, 1993, p. C11.
- [28] J. Baggott, *Perfect Symmetry: The Accidental Discovery of Buckminsterfullerene*, Oxford University Press, Oxford, UK, 1996.
- [29] F. Su, Z. Zhou, W. Guo, J. Liu, X.N. Tian, X.S. Zhao, in L.R. Radovic, Ed., *Chemistry and Physics of Carbon*, Vol. 30, Taylor & Francis (CRC Press), Boca Raton, FL, 2008. p. 63.
- [30] L.P. Biró, C.A. Bernardo, G.G. Tibbetts, P. Lambin, Eds., *Carbon Filaments and Nanotubes: Common Origins, Differing Applications*, Kluwer Academic, Dordrecht, The Netherlands, 2001.
- [31] R.T.K. Baker, R.J. Waite, *J. Catal.* 37 (1975) 101.
- [32] R.T.K. Baker, P.S. Harris, in P.L. Walker, Jr., P.A. Thrower, Eds., *Chemistry and Physics of Carbon*, Vol. 14, Marcel Dekker: New York, 1978, p. 83.
- [33] A. Oberlin, M. Endo, T. Koyama, *J. Crystal Growth* 32 (1976) 335.
- [34] T. Baird, J.R. Fryer, B. Grant, *Carbon* 12 (1974) 591.
- [35] E.L. Evans, J.M. Thomas, P.A. Thrower, P.L. Walker, *Carbon* 11 (1973) 441.
- [36] M.S. Dresselhaus, G. Dresselhaus, P.C. Eklund, *Science of Fullerenes and Carbon Nanotubes*, Academic Press, San Diego, CA, 1996.
- [37] M. Endo, Y.A. Kim, T. Matusita, T. Hayashi, in L.P. Biró, C.A. Bernardo, G.G. Tibbetts, P. Lambin, Eds., *Carbon Filaments and Nanotubes: Common Origins—Different Applications?* Kluwer Academic, Dordrecht, The Netherlands, 2001, p. 51.
- [38] M. Monthioux, V.L. Kuznetsov, *Carbon* 44 (2006) 1621.
- [39] Q.L. Zhang, S.C. O'Brien, J.R. Heath, Y. Liu, R.F. Curl, H.W. Kroto, R.E. Smalley, *J. Phys. Chem.* 90 (1986) 525.

- [40] M. Frenklach, L.B. Ebert, *J. Phys. Chem.* 92 (1988) 561.
- [41] H. Kroto, *Science* 242 (1988) 1139.
- [42] H. Kroto, *Pure Appl. Chem.* 62 (1990) 407.
- [43] K. Homann, *Angew. Chem.* 37 (1998) 2435.
- [44] L.B. Ebert, *Science* 247 (1990) 1468.
- [45] J.B. Donnet, T.K. Wang, C.C. Wang, M. Monthoux, M.P. Johnson, D.T. Norman, R.W. Wansborough, P. Bertrand, *Kautsch. Gummi Kunstst.* 52 (1999) 340.
- [46] J.B. Donnet, M.P. Johnson, D.T. Norman, T.K. Wang, *Carbon* 38 (2000) 1885.
- [47] J.-B. Donnet, R.C. Bansal, M.-J. Wang, Eds., *Carbon Black*, 2nd ed., Marcel Dekker, New York, 1993.
- [48] R.F. Curl, *Rev. Mod. Phys.* 69 (1997) 691.
- [49] A. Burian, J.C. Dore, *Acta Phys. Pol. A* 98 (2000) 457.
- [50] P.J.F. Harris, A. Burian, S. Duber, *Philos. Mag. Lett.* 80 (2000) 381.
- [51] A. Burian, P. Daniel, S. Duber, J. Dore, *Philos. Mag. B* 81 (2001) 525.
- [52] A. Burian, A. Szczygielska, J. Koloczek, J.C. Dore, V. Honkimaki, S. Duber, *Acta Phys. Pol. A* 101 (2002) 751.
- [53] F. Cataldo, *Carbon* 40 (2002) 157.
- [54] P.J.F. Harris, in L.R. Radovic, Ed., *Chemistry and Physics of Carbon*, Vol. 28, Marcel Dekker, New York, 2003, p. 1.
- [55] P.J.F. Harris, *Philos. Mag.* 84 (2004) 3159.
- [56] P.J.F. Harris, *Crit. Rev. Solid State Mater. Sci.* 30 (2005) 235.
- [57] M. Shibuya, M. Kato, M. Ozawa, P.H. Fang, E. Osawa, *Fullerene Sci. Technol.* 7 (1999) 181.
- [58] K. Yamamoto, T. Harada, M. Nakazaki, T. Naka, Y. Kai, S. Harada, N. Kasai, *J. Am. Chem. Soc.* 105 (1983) 7171.
- [59] K. Yamamoto, *Pure Appl. Chem.* 65 (1993) 157.
- [60] K. Yamamoto, H. Sonobe, H. Matsubara, M. Sato, S. Okamoto, K. Kitaura, *Angew. Chem. Int. Ed.* 35 (1996) 69.
- [61] M. Frenklach, N.W. Moriarty, N. Brown, in *Proceedings of the 27th International Symposium on Combustion*, 1998, p. 1655.
- [62] M. Frenklach, J. Ping, *Carbon* 42 (2004) 1209.
- [63] N.W. Moriarty, N.J. Brown, M. Frenklach, *J. Phys. Chem. A* 103 (1999) 7127.
- [64] J. Phillips, T. Shiina, M. Nemer, K. Lester, *Langmuir* 22 (2006) 9694.
- [65] R. Brukh, S. Mitra, *Chem. Phys. Lett.* 424 (2006) 126.
- [66] H. Kataura, Y. Kumazawa, Y. Maniwa, Y. Ohtsuka, R. Sen, S. Suzuki, Y. Achiba, *Carbon* 38 (2000) 1691.
- [67] P.J.F. Harris, *Carbon* 45 (2007) 229.
- [68] D.B. Geohegan, H. Schitthelm, X. Fan, S.J. Pennycook, A.A. Puretzky, M.A. Guillorn, D.A. Blom, D.C. Joy, *Appl. Phys. Lett.* 78 (2001) 3307.
- [69] A. Gorbunov, O. Jost, W. Pompe, A. Graff, *Carbon* 40 (2002) 113.
- [70] F.J. Derbyshire, A.E.B. Presland, D.L. Trimm, *Carbon* 13 (1975) 111.
- [71] R.T.K. Baker, P.S. Harris, R.B. Thomas, R.J. Waite, *J. Catal.* 30 (1973) 86.
- [72] S. Mrozowski, *Phys. Rev.* 85 (1952) 609.

- [73] J.J. Tietjen, Ph.D. dissertation, The Pennsylvania State University, 1963.
- [74] P.L. Walker, Jr., L.G. Austin, J.J. Tietjen, in P.L. Walker, Jr., Ed., *Chemistry and Physics of Carbon*, Vol. 1, Marcel Dekker, New York, 1965, p. 327.
- [75] J. Hone, I. Ellwood, M. Munro, A. Mizel, M.L. Cohen, A. Zettl, A.G. Rinzler, R.E. Smalley, *Phys. Rev. Lett.* 80 (1998) 1042.
- [76] K. Bradley, S.H. Jhi, P.G. Collins, J. Hone, M.L. Cohen, S.G. Louie, A. Zettl, *Phys. Rev. Lett.* 85 (2000) 4361.
- [77] H.E. Romero, G.U. Sumanasekera, G.D. Mahan, P.C. Eklund, *Phys. Rev. B* 65 (2002) 205410.
- [78] G.U. Sumanasekera, B.K. Pradhan, H.E. Romero, K.W. Adu, P.C. Eklund, *Phys. Rev. Lett.* 89 (2002) 166801.
- [79] J. Vavro, M.C. Llaguno, J.E. Fischer, S. Ramesh, R.K. Saini, L.M. Ericson, V.A. Davis, R.H. Hauge, M. Pasquali, R.E. Smalley, *Phys. Rev. Lett.* 90 (2003) 65503.
- [80] L.R. Radovic, B. Bockrath, *J. Am. Chem. Soc.* 127 (2005) 5917.
- [81] V. Derycke, R. Martel, J. Appenzeller, P. Avouris, *Nano Lett.* 1 (2001) 453.
- [82] I.I. Kantorovich, E. Bar-Ziv, *Combust. Flame* 109 (1997) 521.
- [83] X. Zhang, A. Dukhan, I.I. Kantorovich, E. Bar-Ziv, *Combust. Flame* 113 (1998) 519.
- [84] S. Ergun, in P.L. Walker, Jr., Ed., *Chemistry and Physics of Carbon*, Vol. 3, Marcel Dekker, New York, 1968, p. 45.
- [85] R.A. Forrest, H. Marsh, C. Cornford, B.T. Kelly, in P.A. Thrower, Ed., *Chemistry and Physics of Carbon*, Vol. 19, Marcel Dekker, New York, 1984, p. 211.
- [86] Y.H. Ichikawa, K. Kobayashi, *Carbon* 3 (1966) 401.
- [87] H. Marsh, F. Dachille, J. Melvin, P.L. Walker, Jr., *Carbon* 9 (1971) 159.
- [88] H. Marsh, P.L. Walker, Jr., in P.L. Walker, Jr., P.A. Thrower, Eds., *Chemistry and Physics of Carbon*, Vol. 15, Marcel Dekker, New York, 1979, p. 229.
- [89] A.N. Chuvyrov, Y.A. Lebedev, V.M. Cornilov, *Carbon* 28 (1990) 85.
- [90] S. Bonnamy, *Carbon* 37 (1999) 1691.
- [91] A. Oberlin, S. Bonnamy, P.G. Rouxhet, in L.R. Radovic, Ed., *Chemistry and Physics of Carbon*, Vol. 26, Marcel Dekker, New York, 1999, p. 1.
- [92] J.N. Rouzaud, A. Oberlin, *Carbon* 27 (1989) 517.
- [93] J. Zawadzki, in P.A. Thrower, Ed., *Chemistry and Physics of Carbon*, Vol. 21, Marcel Dekker, New York, 1989, p. 147.
- [94] P. Burg, D. Cagniant, in L.R. Radovic, Ed., *Chemistry and Physics of Carbon*, Vol. 30, Taylor & Francis (CRC Press), Boca Raton, FL, 2008, p. 129.
- [95] B. Michel, T. Henning, C. Jäger, U. Kreibig, *Carbon* 37 (1999) 391.
- [96] D.M. Roessler, *Carbon* 22 (1984) 619.
- [97] I. Llamas-Jansa, C. Jäger, H. Mutschke, T. Henning, *Carbon* 45 (2007) 1542.
- [98] P. Delhaes, in P.L. Walker, Jr., Ed., *Chemistry and Physics of Carbon*, Vol. 7, Marcel Dekker, New York, 1975, p. 193.
- [99] C. Ayache, I.L. Spain, *Carbon* 17 (1979) 277.
- [100] I.L. Spain, *Carbon* 17 (1979) 209.
- [101] Y. Hishiyama, Y. Kaburagi, M. Inagaki, in P.A. Thrower, Ed., *Chemistry and Physics of Carbon*, Vol. 23, Marcel Dekker, New York, 1991, p. 1.

- [102] I.L. Spain, in P.L. Walker, Jr., P.A. Thrower, Eds., *Chemistry and Physics of Carbon*, Vol. 8, 1976, Marcel Dekker, New York, 1973, p. 1.
- [103] M.S. Dresselhaus, G. Dresselhaus, K. Sugihara, I.L. Spain, H.A. Goldberg, *Graphite Fibers and Filaments*, Springer-Verlag, Berlin, 1988.
- [104] J.G. Castle, Jr., *Phys. Rev.* 92 (1953) 1063.
- [105] J.E. Bennett, D.J.E. Ingram, J.G. Tapley, *Def. Cryst. Solids*, (1954) 65.
- [106] J.G. Castle, Jr., *Phys. Rev.* 95 (1954) 846.
- [107] D. Ingram, J. Tapley, R. Jackson, R. Bond, A. Murnaghan, *Nature* 174 (1954) 797.
- [108] J. Bennett, D. Ingram, J. Tapley, *J. Chem. Phys.* 23 (1955) 215.
- [109] G.R. Hennig, B. Smaller, in *Proceedings of the 2nd Carbon Conference*, 1956, p. 113.
- [110] J.G. Castle, Jr., D.C. Wobischall, in *Proceedings of the 3rd Carbon Conference*, 1959, p. 129.
- [111] P.L. Walker, Jr., in *Proceedings of the London Carbon Conference*, Society of the Chemical Industry 1978, p. 427.
- [112] C. Moreno-Castilla, O.P. Mahajan, P.L. Walker, Jr., H.-J. Jung, M.A. Vannice, *Carbon* 18 (1980) 271.
- [113] M.A. Vannice, P.L. Walker, Jr., H.-J. Jung, C. Moreno-Castilla, O.P. Mahajan, in *Proceedings of the International Catalysis Congress*, Tokyo, Japan 1980, paper A31.
- [114] H.-J. Jung, P.L. Walker, Jr., M.A. Vannice, *J. Catal.* 75 (1982) 416.
- [115] K.J. Yoon, P.L. Walker, Jr., L.N. Mulay, M.A. Vannice, *Ind. Eng. Chem. Prod. Res. Dev.* 22 (1983) 519.
- [116] L.N. Mulay, A.V. Prasad Rao, J. Rivera Utrilla, M.A. Vannice, P.L. Walker, Jr., *Carbon* 23 (1985) 493.
- [117] L.N. Mulay, A.V.P. Rao, P.L. Walker, K.J. Yoon, M.A. Vannice, *Carbon* 23 (1985) 501.
- [118] R. Höhne, P. Esquinazi, *Adv. Mater.* 14 (2002) 753.
- [119] T.L. Makarova, K.H. Han, P. Esquinazi, R.R. da Silva, Y. Kopelevich, I.B. Zakhrova, B. Sundqvist, *Carbon* 41 (2003) 1575.
- [120] G.P. Collins, *Sci. Am.* 291 (2004) 26.
- [121] K.H. Han, P. Esquinazi, *J. Appl. Phys.* 96 (2004) 1581.
- [122] T.L. Makarova, B. Sundqvist, R. Höhne, P. Esquinazi, Y. Kopelevich, P. Scharff, V.A. Davydov, L.S. Kashevarova, A.V. Rakhmanina, *Nature* 436 (2005) 1200.
- [123] T.L. Makarova, B. Sundqvist, R. Höhne, P. Esquinazi, Y. Kopelevich, P. Scharff, V. Davydov, L.S. Kashevarova, A.V. Rakhmanina, *Nature* 440 (2006) 707.
- [124] Y. Kopelevich, P. Esquinazi, *J. Low Temp. Phys.* 146 (2007) 629.
- [125] T.L. Makarova, *Diamond Relat. Mater.* 16 (2007) 1841.
- [126] H. Ohldag, T. Tyliszczak, R. Höhne, D. Spemann, P. Esquinazi, M. Ungureanu, T. Butz, *Phys. Rev. Lett.* 98 (2007) 187204.
- [127] K.-H. Han, D. Spemann, P. Esquinazi, R. Höhne, V. Riede, T. Butz, *J. Magn. Magn. Mater.* 272–276 (2004) 1190.
- [128] O.E. Kvyatkovskii, I.B. Zakhrova, A.L. Shelankov, T.L. Makarova, *Fullerenes Nanotubes and Carbon Nanostruct.* 14 (2006) 385.

- [129] C.A. Leon y Leon, L.R. Radovic, in P.A. Thrower, Ed., *Chemistry and Physics of Carbon*, Vol. 24, Marcel Dekker, New York, 1994, p. 213.
- [130] L.R. Radovic, F. Rodríguez-Reinoso, in P.A. Thrower, Ed., *Chemistry and Physics of Carbon*, Vol. 25, Marcel Dekker, New York, 1997, p. 243.
- [131] L.R. Radovic, C. Moreno-Castilla, J. Rivera-Utrilla, in L.R. Radovic, Ed., *Chemistry and Physics of Carbon*, Vol. 27, Marcel Dekker, New York, 2001, p. 227.
- [132] N.M. Rodriguez, M.S. Kim, R.T.K. Baker, *J. Phys. Chem.* 98 (1994) 13108.
- [133] N.M. Rodriguez, A. Chambers, R.T.K. Baker, *Langmuir* 11 (1995) 3862.
- [134] A. Cybulski, J.A. Moulijn, *Catal. Rev. Sci. Eng.* 36 (1994) 179.
- [135] M. Yates, J. Blanco, P. Avila, M. Martin, *Micropor. Mesopor. Mater.* 37 (2000) 201.
- [136] E. Crezee, A. Barendregt, F. Kapteijn, J.A. Moulijn, *Catal. Today* 69 (2001) 283.
- [137] A. Marchand, in P.L. Walker, Jr., Ed., *Chemistry and Physics of Carbon*, Vol. 7, Marcel Dekker, New York, 1971, p. 155.
- [138] S. Marinkovic, in P.A. Thrower, Ed., *Chemistry and Physics of Carbon*, Vol. 19, Marcel Dekker, New York, 1984, p. 1.
- [139] H.N. Murty, D.L. Biederman, E.A. Heintz, *Fuel* 56 (1977) 305.
- [140] L.R. Radovic, M. Karra, K. Skokova, in *Proceedings of the Carbon Conference*, San Diego, CA, 1995, p. 646.
- [141] L.R. Radovic, M. Karra, K. Skokova, P.A. Thrower, *Carbon* 36 (1998) 1841.
- [142] B.E. Warren, *J. Chem. Phys.* 2 (1934) 551.
- [143] J. Biscoe, B.E. Warren, *J. Appl. Phys.* 13 (1942) 364.
- [144] B.E. Warren, *Proceedings of the 1st and 2nd Carbon Conference*, 1956, p. 49.
- [145] S. Ergun, in P.L. Walker, Jr., Ed., *Chemistry and Physics of Carbon*, Vol. 3, Marcel Dekker, New York, 1968, p. 211.
- [146] W. Ruland, in P.L. Walker, Jr., Ed., *Chemistry and Physics of Carbon*, Vol. 4, Marcel Dekker, New York, 1968, p. 1.
- [147] N. Iwashita, C.R. Park, H. Fujimoto, M. Shiraishi, M. Inagaki, *Carbon* 42 (2004) 701.
- [148] N. Iwashita, C.R. Park, H. Fujimoto, M. Shiraishi, M. Inagaki, *Carbon* 42 (2004) 2131.
- [149] Z.Q. Li, C.J. Lu, Z.P. Xia, Y. Zhou, Z. Luo, *Carbon* 45 (2007) 1686.
- [150] E. Fitzer, S. Weisenburger, *Carbon* 12 (1974) 657.
- [151] G.M. Jenkins, K. Kawamura, *Polymeric Carbons: Carbon Fibre, Glass and Char*, Cambridge University Press, Cambridge, UK, 1976.
- [152] R. Bacon, *J. Appl. Phys.* 31 (1960) 283.
- [153] P.H. Tan, S. Dimovski, Y. Gogotsi, *Philos. Trans. R. Soc London A* 362 (2004) 2289.
- [154] H.P. Boehm, in C. Morterra, A. Zecchina, G. Costa, Eds., *Structure and Reactivity of Surfaces*, Elsevier, Amsterdam, 1989, p. 145.
- [155] H.P. Boehm, *Carbon* 32 (1994) 759.
- [156] F. Rodríguez-Reinoso, A. Linares-Solano, in P.A. Thrower, Ed., *Chemistry and Physics of Carbon*, Vol. 21, Marcel Dekker, New York, 1989, p. 1.

- [157] M. Jaroniec, J. Choma, in P.A. Thrower, Ed., *Chemistry and Physics of Carbon*, Vol. 22, Marcel Dekker, New York, 1990.
- [158] T.J. Bandosz, M.J. Biggs, K.E. Gubbins, Y. Hattori, T. Iiyama, K. Kaneko, J. Pikunic, K.T. Thomson, in L.R. Radovic, Ed., *Chemistry and Physics of Carbon*, Vol. 28, Marcel Dekker, New York, 2003, p. 41.
- [159] D. Mowla, D.D. Do, K. Kaneko, in L.R. Radovic, Ed., *Chemistry and Physics of Carbon*, Vol. 28, Marcel Dekker, New York, 2003, p. 229.
- [160] E.J. Bottani, J.M.D. Tascon, in L.R. Radovic, Ed., *Chemistry and Physics of Carbon*, Vol. 29, Marcel Dekker, New York, 2004, p. 209.
- [161] A. Linares-Solano, D. Lozano-Castelló, M.A. Lillo-Ródenas, D. Cazorla-Amorós, in L.R. Radovic, Ed., *Chemistry and Physics of Carbon*, Vol. 30, Taylor & Francis (CRC Press), Boca Raton, FL, 2008, p. 1.
- [162] R. Ryoo, S.H. Joo, S. Jun, *J. Phys. Chem. B* 103 (1999) 7743.
- [163] T. Kyotani, *Carbon* 41 (2003) 1451.
- [164] G.A. Simons, *Combust. Sci. Technol.* 19 (1979) 227.
- [165] G.A. Simons, M.L. Finson, *Combust. Sci. Technol.* 19 (1979) 217.
- [166] G.A. Simons, in *Proceedings of the International Combustion Symposium*, Haifa, Israel, The Combustion Institute, 1982, p. 1067.
- [167] G.A. Simons, *Prog. Energy Combust. Sci.* 9 (1983) 269.
- [168] G.A. Simons, *Combust. Flame* 50 (1983) 275.
- [169] S.K. Bhatia, D.D. Perlmutter, *AIChE J.* 26 (1980) 379.
- [170] G.R. Gavalas, *AIChE J.* 26 (1980) 577.
- [171] N.A. Seaton, *Chem. Eng. Sci.* 46 (1991) 1895.
- [172] H.L. Liu, L. Zhang, N.A. Seaton, *Chem. Eng. Sci.* 47 (1992) 4393.
- [173] B.P. Russell, M.D. LeVan, *Carbon* 32 (1994) 845.
- [174] M.V. López-Ramón, J. Jagiello, T.J. Bandosz, N.A. Seaton, *Langmuir* 13 (1997) 4435.
- [175] S.K. Bhatia, J.S. Gupta, *Rev. Chem. Eng.* 8 (1992) 177.
- [176] P. Rajniak, R.T. Yang, *AIChE J.* 42 (1996) 319.
- [177] B. Coasne, S.K. Jain, K.E. Gubbins, *Mol. Phys.* 104 (2006) 3491.
- [178] Q. Cai, A. Buts, M.J. Biggs, N.A. Seaton, *Langmuir* 23 (2007) 8430.
- [179] T.X. Nguyen, S.K. Bhatia, *J. Phys. Chem. C* 111 (2007) 2212.
- [180] M.M. Dubinin, O. Kadlec, A. Zukal, *Nature* 207 (1965) 75.
- [181] P.L. Walker, M. Shelef, *Carbon* 5 (1967) 7.
- [182] T. Nakahara, M. Hirata, T. Omori, *J. Chem. Eng. Data* 19 (1974) 310.
- [183] S.V. Moore, D.L. Trimm, *Carbon* 15 (1977) 177.
- [184] P.L. Walker, Jr., A. Oya, O.P. Mahajan, *Carbon* 18 (1980) 377.
- [185] G. Horvath, K. Kawazoe, *J. Chem. Eng. Jpn.* 16 (1983) 470.
- [186] M.B. Rao, R.G. Jenkins, W.A. Steele, *Langmuir* 1 (1985) 137.
- [187] D.M. Ruthven, N.S. Raghavan, M.M. Hassan, *Chem. Eng. Sci.* 41 (1986) 1325.
- [188] J.E. Koresh, A. Soffer, *Sep. Sci. Technol.* 22 (1987) 973.
- [189] S.K. Verma, P.L. Walker, Jr., *Carbon* 30 (1992) 837.

- [190] D. Cazorla-Amorós, J. Alcañiz-Monge, M.A. de la Casa-Lillo, A. Linares-Solano, *Langmuir* 14 (1998) 4589.
- [191] Y.S. Bae, J.H. Moon, H. Ahn, C.H. Lee, *Korean J. Chem. Eng.* 21 (2004) 712.
- [192] Y.S. Bae, C.H. Lee, *Carbon* 43 (2005) 95.
- [193] S.W. Rutherford, J.E. Coons, *J. Colloid Interface Sci.* 284 (2005) 432.
- [194] D.L. Trimm, B.J. Cooper, *Chem. Commun.* 1970, 477.
- [195] A. Zlatkis, H.R. Kaufman, D.E. Durbin, *J. Chromatogr. Sci.* 8 (1970) 416.
- [196] J.L. Schmitt, P.L. Walker, Jr., *Carbon* 9 (1971) 791.
- [197] J.L. Schmitt, P.L. Walker, Jr., *Carbon* 10 (1972) 87.
- [198] S.P. Nandi, P.L. Walker, Jr., *Fuel* 54 (1975) 169.
- [199] H. Jüntgen, K. Knoblauch, K. Harder, *Fuel* 60 (1981) 817.
- [200] W.R. Betz, W.R. Supina, *Pure Appl. Chem.* 61 (1989) 2047.
- [201] A. Kapoor, R.T. Yang, *Chem. Eng. Sci.* 44 (1989) 1723.
- [202] G.C. Grunewald, R.S. Drago, *J. Am. Chem. Soc.* 113 (1991) 1636.
- [203] J.L. Schmitt, *Carbon* 29 (1991) 743.
- [204] C.W. Jones, W.J. Koros, *Carbon* 32 (1994) 1419.
- [205] A.I. Shirley, N.O. Lemcoff, *Adsorption* 8 (2002) 147.
- [206] D.Q. Vu, W.J. Koros, S.J. Miller, *Ind. Eng. Chem. Res.* 41 (2002) 367.
- [207] A. Vinu, C. Streb, V. Murugesan, M. Hartmann, *J. Phys. Chem. B* 107 (2003) 8297.
- [208] M. Hartmann, A. Vinu, G. Chandrasekar, *Chem. Mater.* 17 (2005) 829.
- [209] A. Vinu, M. Miyahara, K. Ariga, *J. Phys. Chem. B* 109 (2005) 6436.
- [210] A. Vinu, K.Z. Hossain, G.S. Kumar, K. Ariga, *Carbon* 44 (2006) 530.
- [211] B.B. Mandelbrot, *The Fractal Geometry of Nature*, W.H. Freeman, New York, 1983.
- [212] D. Avnir, Ed., *The Fractal Approach to Heterogeneous Chemistry*, Wiley, Chichester, UK, 1989.
- [213] K. Kaneko, M. Sato, T. Suzuki, Y. Fujiwara, K. Nishikawa, M. Jaroniec, *J. Chem. Soc. Faraday Trans.* 87 (1991) 179.
- [214] M. Sato, T. Supegawa, T. Suzuki, S. Hagiwara, K. Kaneko, *Chem. Phys. Lett.* 181 (1991) 526.
- [215] A. Neimark, *Physica A* 191 (1992) 258.
- [216] R. Tsunoda, *J. Colloid Interface Sci.* 152 (1992) 571.
- [217] F. Ehrburger-Dolle, M. Holz, J. Lahaye, *Pure Appl. Chem.* 65 (1993) 2223.
- [218] M. Jaroniec, R.K. Gilpin, J. Choma, *Carbon* 31 (1993) 325.
- [219] R. Tsunoda, *J. Colloid Interface Sci.* 155 (1993) 259.
- [220] F. Ehrburger-Dolle, *Langmuir* 10 (1994) 2052.
- [221] F. Ehrburger-Dolle, A. Lavanchy, F. Stoeckli, *J. Colloid Interface Sci.* 166 (1994) 451.
- [222] R. Diduszko, A. Swiatkowski, B. Trznadel, *Carbon* 38 (2000) 1153.
- [223] F. Kano, I. Abe, H. Kamaya, I. Ueda, *Surf. Sci.* 467 (2000) 131.
- [224] Z.H. Huang, F.Y. Kang, W.L. Huang, J.B. Yang, K.M. Liang, M.L. Cui, Z.Y. Chen, *J. Colloid Interface Sci.* 249 (2002) 453.

- [225] P. Pfeifer, F. Ehrburger-Dolle, T.P. Rieker, M.T. Gonzalez, W.P. Hoffman, M. Molina-Sabio, F. Rodríguez-Reinoso, P.W. Schmidt, D.J. Voss, *Phys. Rev. Lett.* 88 (2002) 115502.
- [226] C.-H. Kim, S.-I. Pyun, J.-H. Kim, *Electrochim. Acta* 48 (2003) 3455.
- [227] Y.L. Wang, H.W. Zhou, F.L. Yu, B.Y. Shi, H.X. Tang, *Colloids Surf. A* 299 (2007) 224.
- [228] C.H. Sun, F. Li, Z. Ying, C. Liu, H.M. Cheng, *Phys. Rev. B* 69 (2004) 33404.
- [229] C.H. Sun, F. Li, H.M. Cheng, G.Q. Lu, *Carbon* 43 (2005) 1785.
- [230] L.R. Radovic, in J.A. Schwarz, C.I. Contescu, Eds., *Surfaces of Nanoparticles and Porous Materials*, Marcel Dekker, New York, 1999, p. 529.
- [231] B. Steenberg, *Adsorption and Exchange of Ions on Activated Charcoal*, Almqvist & Wiksell, Uppsala, Sweden, 1944.
- [232] B. Epstein, E. Dalle-Molle, J.S. Mattson, *Carbon* 9 (1971) 609.
- [233] V.A. Garten, D.E. Weiss, *Austral. J. Chem.* 8 (1955) 68.
- [234] V.A. Garten, D.E. Weiss, in *Proceedings of the 3rd Carbon Conference*, Buffalo, NY, 1959, Pergamon Press, New York, p. 295.
- [235] D. Rivin, in *Proceedings of the 5th Carbon Conference*, Vol. 2, University Park, PA, 1963, Pergamon Press, New York, p. 199.
- [236] A.A. Lizzio, H. Jiang, L.R. Radovic, *Carbon* 28 (1990) 7.
- [237] L.R. Radovic, *Carbon* 43 (2005) 907.
- [238] A. Robell, E. Ballou, M. Boudart, *J. Phys. Chem.* 68 (1964) 2748.
- [239] S. Asaoka, K. Masamizu, K. Fujimoto, T. Kunugi, *Nippon Kagaku Kaishi* (1976) 388.
- [240] E. Baumgarten, A. Schuck, *Appl. Catal.* 37 (1988) 247.
- [241] J.A. Menéndez, L.R. Radovic, B. Xia, J. Phillips, *J. Phys. Chem.* 100 (1996) 17243.
- [242] L.R. Radovic, in K.H.J. Buschow, R.W. Cahn, M.C. Flemings, B. Ilschner, E.J. Kramer, S. Mahajan, Eds. *Encyclopedia of Materials: Science and Technology*, Pergamon Press, Oxford, UK, 2001, p. 975.
- [243] H.P. Boehm, A.R. de Rincon, T. Stöhr, B. Tereczki, A. Vass, *J. Chim. Phys.* 84 (1987) 1449.
- [244] B. Stöhr, H.P. Boehm, R. Schlögl, *Carbon* 29 (1991) 707.
- [245] K.B. Bota, G.M.K. Abotsi, *Fuel* 73 (1994) 1354.
- [246] R.J.J. Jansen, H. van Bekkum, *Carbon* 32 (1994) 1507.
- [247] Q. Zhu, K. Grant, K.M. Thomas, *Carbon* 33 (1995) 35.
- [248] K. Jurewicz, K. Babel, A. Ziolkowski, H. Wachowska, *Electrochim. Acta* 48 (2003) 1491.
- [249] R. Pietrzak, H. Wachowska, P. Nowicki, K. Babel, *Fuel Process. Technol.* 88 (2007) 409.
- [250] N.R. Laine, F.J. Vastola, P. Walker, Jr., *J. Phys. Chem.* 67 (1963) 2030.
- [251] L.R. Radovic, P.L. Walker, Jr., R.G. Jenkins, *Fuel* 62 (1983) 849.
- [252] W.P. Hoffman, F.J. Vastola, J.P.L. Walker, *Carbon* 23 (1985) 151.
- [253] H. Freund, *Fuel* 65 (1986) 63.
- [254] J.J. Carberry, *J. Catal.* 114 (1988) 277.
- [255] L.R. Radovic, H. Jiang, A.A. Lizzio, *Energy Fuels* 5 (1991) 68.

- [256] L.R. Radovic, A.A. Lizzio, H. Jiang, in J. Lahaye, P. Ehrburger, Eds., *Fundamental Issues in Control of Carbon Gasification Reactivity*, Kluwer Academic, Dordrecht, The Netherlands, 1991, p. 235.
- [257] F. Kapteijn, R. Meijer, J.A. Moulijn, D. Cazorla-Amorós, *Carbon* 32 (1994) 1223.
- [258] J.M. Calo, P. Hall, in J. Lahaye and P. Ehrburger, Eds., *Fundamental Issues in Control of Carbon Gasification Reactivity*, Kluwer Academic, Dordrecht, The Netherlands, 1991, p. 329.
- [259] M. Boudart, *J. Am. Chem. Soc.* 74 (1952) 3556.
- [260] S.G. Chen, R.T. Yang, F. Kapteijn, J.A. Moulijn, *Ind. Eng. Chem. Res.* 32 (1993) 2835.
- [261] K. Skokova, L.R. Radovic, *ACS Preprints* (Division of Fuel Chemistry), New Orleans, LA, 1996, p. 143.
- [262] K. Skokova, L.R. Radovic, *ACS Prepr. Div. Fuel Chem.* 211 (1996) 27.
- [263] K. Skokova, L.R. Radovic, in *Proceedings of the Carbon Conference*, State College, PA, 1997, p. 414.
- [264] N. Chen, R.T. Yang, *Carbon* 36 (1998) 1061.
- [265] C.C. Pye, J.D. Xidos, R.A. Poirier, D.J. Burnell, *J. Phys. Chem. A* 101 (1997) 3371.
- [266] A.C. Lau, D.N. Furlong, T.W. Healy, F. Grieser, *Colloids Surf.* 18 (1986) 93.
- [267] K.L. Yang, S. Yiakoumi, C. Tsouris, *J. Chem. Phys.* 117 (2002) 8499.
- [268] A. Tanimura, A. Kovalenko, F. Hirata, *Chem. Phys. Lett.* 378 (2003) 638.
- [269] J. Lyklema, *Fundamentals of Interface and Colloid Science*, Vol. 1, *Fundamentals*, Academic Press, London, 1995.
- [270] V. López-Ramón, C. Moreno-Castilla, J. Rivera-Utrilla, L.R. Radovic, *Carbon* 41 (2003) 2020.
- [271] E. Frackowiak, F. Béguin, *Carbon* 39 (2001) 937.
- [272] E. Frackowiak, *Phys. Chem. Chem. Phys.* 9 (2007) 1774.
- [273] R.E. Franklin, *Proc. R. Soc. A* 209 (1951) 196.
- [274] I.W. Smith, *Fuel* 57 (1978) 409.
- [275] W.R. Smith, M.H. Polley, *J. Phys. Chem.* 60 (1956) 689.
- [276] G.D. Parfitt, N.H. Picton, *Trans. Faraday Soc.* 64 (1968) 1955.
- [277] G.R. Birkett, D.D. Do, *Mol. Simul.* 32 (2006) 887.
- [278] F.G. Emmerich, *Carbon* 33 (1995) 1709.
- [279] E.M. Suuberg, M. Wojtowicz, J.M. Calo, *Carbon* 27 (1989) 431.
- [280] O. Senneca, P. Russo, P. Salatino, S. Masi, *Carbon* 35 (1997) 141.
- [281] H. Yokomichi, *Vacuum* 74 (2004) 677.
- [282] K.H. Han, *J. Korean Phys. Soc.* 48 (2006) 1427.
- [283] J.M. Jones, D.H. Jones, *Carbon* 45 (2007) 677.
- [284] K. Y. Gomi, Hishinuma, *Fuel* 61 (1982) 77.
- [285] J.M. Ranish, P.L. Walker, Jr., *Carbon* 31 (1993) 135.
- [286] B. Bayarsaikhan, J.-I. Hayashi, T. Shimada, C. Sathe, C.-Z. Li, A. Tsutsumi, T. Chiba, *Fuel* 84 (2005) 1612.
- [287] R.F. Strickland-Constable, *Trans. Faraday Soc.* 40 (1944) 0333.

- [288] J. Nagle, R.F. Strickland-Constable, *Proceedings of the 5th Carbon Conference*, Vol. 1, 1961, p. 154.
- [289] O. Senneca, P. Salatino, D. Menghini, *Proc. Int. Combust. Symp.* 31 (2007) 1889.
- [290] R. Hurt, J.-K. Sun, M. Lunden, *Combust. Flame* 113 (1998) 181.
- [291] J.L. Johnson, *Kinetics of Coal Gasification: A compilation of research*, Wiley, New York, 1979.
- [292] P.L. Walker, Jr., L. Pentz, D.L. Biederman, F.J. Vastola, *Carbon* 15 (1977) 165.
- [293] J.M. Calo, D. Cazorla-Amorós, A. Linares-Solano, M.C. Román-Martínez, C. Salinas-Martínez de Lecea, *Carbon* 35 (1997) 543.
- [294] M.H. Treptau, D.J. Miller, *Carbon* 29 (1991) 531.
- [295] H. Yamashita, H. Yamada, A. Tomita, *Appl. Catal.* 78 (1991) L1.
- [296] H. Yamashita, H. Yamada, T. Kyotani, L.R. Radovic, A. Tomita, *Energy Fuels* 7 (1993) 85.
- [297] R.T. Yang, C. Wong, *J. Chem. Phys.* 75 (1981) 4471.
- [298] H. Marsh, in *Oxygen in the Metal and Gaseous Fuel Industries*, Spec. Publ. 32, Chemical Society, London, 1978, p. 133.
- [299] R.H. Hurt, D.R. Dudek, J.P. Longwell, A.F. Sarofim, *Carbon* 26 (1988) 433.
- [300] T.E. Easler, R.C. Bradt, P.L. Walker, *Fuel* 69 (1990) 124.
- [301] R.H. Hurt, A.F. Sarofim, J.P. Longwell, *Combust. Flame* 95 (1993) 430.
- [302] I.I. Kantorovich, E. Bar-Ziv, *Combust. Flame* 97 (1994) 61.
- [303] P.L. Walker, *Carbon* 34 (1996) 1603.
- [304] S.K. Bhatia, *AICHE J.* 44 (1998) 2478.
- [305] I.I. Kantorovich, E. Bar-Ziv, *Combust. Flame* 113 (1998) 532.
- [306] E. Bar-Ziv, I.I. Kantorovich, *Prog. Energy Combust. Sci.* 27 (2001) 667.
- [307] R.L. Vander Wal, A. Yezerski, N.W. Currier, D.H. Kim, C.M. Wang, *Carbon* 45 (2007) 70.
- [308] P.L. Walker, Jr., F. Rusinko, Jr., L.G. Austin, in D.D. Eley, P.W. Selwood, P.B. Weisz, Eds., *Advances in Catalysis*, Vol. 11, Academic Press, New York, 1959, p. 133.
- [309] P.L. Walker Jr., H.A. McKinstry, J.V. Pustinger, *Ind. Eng. Chem.* 46 (1954) 1651.
- [310] A.J. Stone, D.J. Wales, *Chem. Phys. Lett.* 128 (1986) 501.
- [311] R.H. Telling, M.I. Heggie, *Philos. Mag.* 87 (2007) 4797.
- [312] G.J. Dienes, *J. Appl. Phys.* 23 (1952) 1194.
- [313] J.D. Brooks, G.H. Taylor, *Nature* 206 (1965) 697.
- [314] J.D. Brooks, G.H. Taylor, in P.L. Walker, Jr., Ed., *Chemistry and Physics of Carbon*, Vol. 4, Marcel Dekker, New York, 1968, p. 243.
- [315] M. Inagaki, *Carbon* 35 (1997) 711.
- [316] F. Watanabe, Y. Korai, I. Mochida, Y. Nishimura, *Carbon* 38 (2000) 741.
- [317] J.C. Bokros, in P.L. Walker, Jr., Ed., *Chemistry and Physics of Carbon*, Vol. 5, Marcel Dekker, New York, 1969, p. 1.

2 Surface Chemistry of Carbon Materials

TERESA J. BANDOSZ

2.1 INTRODUCTION

Activated carbons or carbon fibers are the most common materials used as adsorbents and catalysts. They are employed widely in both liquid and gaseous phases. This “universality” is due not only to their high surface area and high volume of pores, but also to the variety of chemical properties of their surfaces. Although for physical adsorption the porous structure is the most important feature, for reactive adsorption and catalysis the chemical environment plays an important role, provided that the structure is developed sufficiently for dispersion of active chemical species and for accommodation of molecules to be adsorbed or to undergo a targeted chemical reaction.

Besides traditional applications of activated carbons and carbon fibers in adsorption and catalysis, modern nanocarbons emerged with promising properties in the electronic industry (e.g., diamond), metallurgy (e.g., graphitic carbon), electrochemistry, catalysis, adsorption, and so on. Examples of these materials include fullerenes and fullerene-like structures, nanotubes, nanohorns, and graphite nanocomposites. Their common features with activated carbons are graphitic-like layers whose arrangements and coordination of carbon atoms determine the type of nanostructure. Just as the layers in activated carbons, these layers can have defects, contain heteroatoms, or foreign species chemically bonded.

When activated carbons and carbon fibers were the carbonaceous materials used most extensively and their applications were limited mainly to adsorption with the requirement to remove pollutants to the levels of micrograms or parts per million, the surface chemistry of carbons was not even taken into account. It was a common belief that if adsorbents were used in excess, their purifying action was sufficient. This approach can be considered as history. Nowadays, when the environmental regulations are stricter and stricter and when sophisticated

electronic instruments require an ultraclean atmosphere, the carbon surface chemistry becomes a factor of paramount importance. This chemistry has a significant influence on the physicochemical properties of the carbons, and hence on the properties desired for the intended application. Moreover, due to carbon surface reactivity under ambient conditions, even leading to dangerous self-ignition, the chemistry has to be monitored continuously to retain stable materials with reliable performance.

An example of the effects of the stability of carbon chemistry is its impact on the electrochemical performance of carbon electrodes, which is altered by the presence of surface groups [1–3]. Now that the use of carbons as supercapacitors for energy storage has begun to attract interest [4–6], some attention has been devoted to the influence of the surface chemistry of these materials on their capacitance. It was found that surface functionality has a tremendous effect on the electrical double-layer properties and the capacity of the latter for energy storage [7–9].

Very straightforward effects of surface chemistry of carbons are seen on the adsorption from solutions of aromatics [10–17], dyes [18], heavy metals [19–24], pharmaceuticals [25–27], polar species such as alcohols [28–30], acids or aldehydes [31,32], and even small-molecule gases [33,34]. In those applications the species present on the carbon surface can enhance the specific interactions or even alter the porosity via blocking of pore entrances for molecules to be adsorbed. Specific interactions include hydrogen bonding, acid–base, and complexation.

The specific interactions are also very important in the field of catalysis, where the carbon surface acts as a support. Here the surface chemistry governs dispersion of the catalyst, its loading, the catalytic activity, or selectivity [35–43]. It is also important for the heterogeneous and multireaction processes, where surface functional groups can influence catalytic interactions, causing agglomeration of species which, further, can act as a solvent (e.g., water, alcohols). They can help in the diffusion or provide an environment for such processes as dissociation [33]. Since on the surface of a porous carbonaceous material reactions occur in a confined nanospace, its dimensions and enhanced dispersive interactions can significantly change the chemical equilibrium [44,45], the yield of chemical reaction and its selectivity, and thus the efficiency of the reactor or catalytic process.

For all of the causes described above, in addition to traditional and relatively simple methods of carbon surface modifications (e.g., oxidation in liquid or gaseous phases), more sophisticated approaches are proposed which employ newly developed techniques such as intercalation [46,47], chemical vapor deposition (CVD) [48,49], and self-assembly of molecules [50].

The most important and at the same time the most abundant heteroatom that affects the use of carbon is oxygen. It is usually either chemisorbed on the surface or arranged in the form of functional groups analogous to those existing in organic chemistry [51–54]. Since those groups increase the reactivity of the otherwise hydrophobic carbon surface, oxidation often opens the door to further

modifications via interactions of specific chemicals with the groups and their reactions on the surface. An example is introduction of nitrogen to the carbon matrix, which is more efficient when the carbons are preoxidized [55–57].

Owing to carbon reactivity, surface chemistry provides unlimited opportunities to face contemporary environmental challenges and high-tech applications. Moreover, chemical modifications open the door to development of new structures, which are important for applications of materials as adsorbents and catalysts [58]. In many cases our imagination may be the only limitation. An important challenge of carbon science in the twenty-first century is the fine tailoring of surface properties toward the desired application, which in fact becomes more and more sophisticated. Thus, many researchers in several technical fields devote their time to controlling carbon surface chemistry in the race toward new technological discoveries.

Although numerous reviews on the characteristics of carbonaceous materials have been published [51–54,59–63], in this chapter we focus on a detailed description of carbon surface chemistry and its importance for catalytic processes and those involving reactive adsorption. Thus, the classification of surface groups is followed by an overview of methods of surface modification and characterization, with a brief description and examples of their role in reactive adsorption and catalysis.

2.2 SURFACE FUNCTIONALITIES

Carbon materials exhibit a high content of sp^2 -hybridized carbon. This arrangement is responsible for a two-dimensional order in the carbon structure. In carbonaceous materials carbon atoms are grouped into layers of fused aromatic rings. The degree of planarity of those layers depends on the degree of graphitization of the carbons. Van der Waals interactions connect graphene layers, which can be either in an ordered structure (e.g., graphite, graphitizable carbons) or in a turbostratic structure with disordered stacking of the layers (e.g., activated carbons, carbon blacks) [64–67]. This arrangement of the graphene layers governs the physicochemical properties of carbons and thus their applications.

Basal and edge carbon atoms are considered as two different sites distinguished in their interactions with other molecules and in their susceptibility to undergoing chemical reactions. The reactivity of the carbon surface is also linked to its disordered fraction, which contains a large number of imperfections and defects (e.g., structural carbon vacancies, nonaromatic rings). These imperfections and defects along the edges of graphene layers are the most active sites, owing to the high densities of unpaired electrons [68]. On them, heteroatoms such as oxygen, hydrogen, nitrogen, and sulfur can be chemisorbed, leading to stable surface compounds [52]. The concentration and distribution of the surface groups present on the carbon depend on the carbon type and the pretreatment applied [69]. Chemical reactivity of the specific groups is also affected by their local environment [70].

Although the analogy to the functional groups classified in organic chemistry exists, the chemical complexity of the carbon surface and the fact that the heteroatoms are located in confined space mean that we cannot expect a full prediction of the behavior of those groups based on well-known organic chemistry reaction mechanisms. All of this implies that the carbon surface should be seen as a unique whole entity for which there is an overall contribution of individual functional groups [52]. The picture of those complex entities cannot be drawn based on a single experimental technique. On the contrary, a combination of theories and results obtained from different techniques is needed to get as accurate a view of the carbon surface as possible.

2.2.1 Oxygen-Containing Functionalities

Oxygen-containing groups are the most common functionalities present on the carbon surface. Oxygen adsorbed on carbon was first investigated in the nineteenth century [71,72], and the findings suggested that while other adsorbed gases could be removed easily, removal of oxygen required strong heating. Increasing temperatures result in an increase in the amount of oxygen adsorbed, with its maximum between 673 and 773 K. One of the first links of the surface oxidation level to the adsorption phenomena was made by Bartell and Miller [73], who reported that charcoals oxidized by air at a low temperature adsorbed basic substances, and on charcoals allowed to cool down before reexposure to air, adsorption of acids occurred. Findings about the presence of oxygen in functional groups were first mentioned by Garten and Weis [74–76], although this matter was later discussed extensively by Boehm [51,63] and Donnet [77].

Oxygen-containing functionalities present on carbonaceous surfaces, similar to those found in many organic compounds, are shown in Figure 2.1. Besides such well-defined functional groups as the carboxylic, phenolic, and ketone, the π -electron density of the carbon basal planes is considered to be chemically active. Generally, oxygen-containing functionalities are considered as acidic or basic. Acidic surface groups are formed when the carbon surface is exposed to oxygen via reactions with oxidizing agents from solutions or gas phase, either at room or high temperatures. Oxidative treatments designed to produce acidic carbon surfaces with different distributions of oxygen-containing acidic groups are described in the literature [53,63,78–82] and are addressed briefly in Section 2.3.1. On the other hand, basic groups are formed when an oxidized surface is reduced by heating in an inert atmosphere at high temperature. The decomposition of acidic groups (e.g., carboxylic acid, lactone, phenol groups) results in active sites at the edges of the graphene layers, which upon cooling in an inert atmosphere and reexposure to air, attract oxygen-forming basic functional groups such as chromene or pyrone [55,83–85].

Since the concept of acidic and basic surface oxides was introduced by Steenberg in 1944 [86], research on carbon chemistry has attracted a lot of attention [51,52,87,88]. Although there is general consensus regarding the types of surface

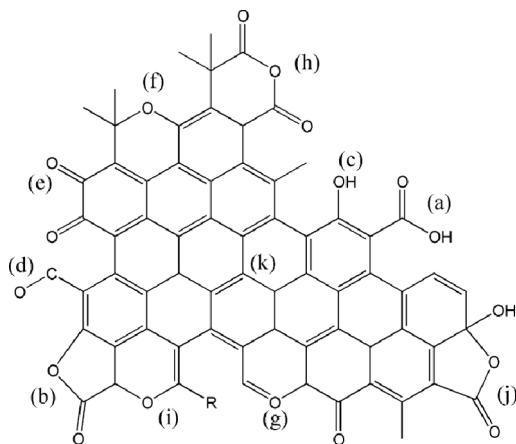


Figure 2.1 Acidic and basic oxygen-containing functionalities of carbon surface: (a) carboxyl groups, (b) lactone, (c) hydroxyl, (d) carbonyl, (e) quinone, (f) ether, (g) pyrone, (h) carboxylic anhydride, (i) chromene, (j) lactol, and (k) π electron density on carbon basal planes.

functionalities that determine the acidic character of a carbon material (e.g., carboxyl groups, anhydrides, hydroxyls, lactones and lactol groups), the nature of carbon basic surfaces remains controversial and open to investigation [87–91]. Generally speaking, oxygen-containing functionalities (e.g., chromene, pyrone, quinones) [71,85,92,93] and nonheteroatomic Lewis base sites, characterized by regions of π -electron density on the carbon basal planes [85,89,91], govern carbon basicity. So far, the strength of both types of sites as bases, and the extent of their contribution to the overall carbon basicity, have not been defined.

The basicity of activated carbon has been discussed extensively by Montes-Morán and co-workers [90]. Using experimental and theoretical results, they suggest that oxygen functional groups, and the existence of pyrone-type structures on the edges of the polyaromatic layers, are the main contributors to overall surface basicity. On the other hand, the basicity of the π -electron density of the basal planes is considered to be weak.

By applying the concept of hard and soft acids and bases to the interpretation of the adsorption of metal ions onto activated carbons, Alffara and co-workers [20] proposed to consider the surface of the basal structural units of carbon as soft centers that might trap soft ions, whereas the oxygen surface groups are proposed to be considered as hard sites that fix hard metal ions. Following this explanation, a given ion may be thought to be adsorbed on the surface of basal planes or by oxygen surface groups. The efficiency of this adsorption can be changed by modifying either the ion hardness or that of carbon materials, leading in other words, to carbon surface modification.

2.2.2 Nitrogen-Containing Functionalities

In contrast to functionalities containing oxygen, nitrogen-containing functionalities are not formed spontaneously on carbon surfaces by contact with air. Usually, the nitrogen content in carbonaceous materials is very small unless it is a constituent of the carbon precursor, as, for example, carbazole, nitrogen-enriched polymers, acridine, or melamine. Another way of introducing nitrogen to the carbon matrix is by treatment with nitrogen-containing reagents (e.g., ammonia, urea, melamine, HCN). So far, the presence of nitrogen has been shown to be the key parameter for the performance of carbon materials as adsorbents [94–99], catalyst supports, and for catalytic activity [100].

The type of nitrogen functionalities present on a carbon surface is a function of the treatment applied. This includes the type of nitrogen-containing precursor, the chemical activity of the carbon surface, and most important, the temperature of heat treatment. The latter determines the type of chemistry, owing to the fact that some nitrogen-containing species are unstable at high temperatures. The various nitrogen-containing functionalities present on carbon surfaces are summarized in Figure 2.2. According to the studies performed, lactams and imide structures are formed primarily by ammoniation, and amide by ammoxidation; the former are transformed to pyrrole and pyridine by heat treatment [101–104].

As in the case of oxygen, nitrogen-containing functionalities determine the acidic or basic character of carbons and thus its surface chemical reactivity or catalytic activity. Treatment of carbonaceous surfaces with nitrogen-containing reagents at low temperatures (below 800 K) lead to the formation of lactams, imides, and amines slightly acidic in nature. On the other hand, treatment at high temperatures results in an increase in quaternary nitrogen (N atoms incorporated

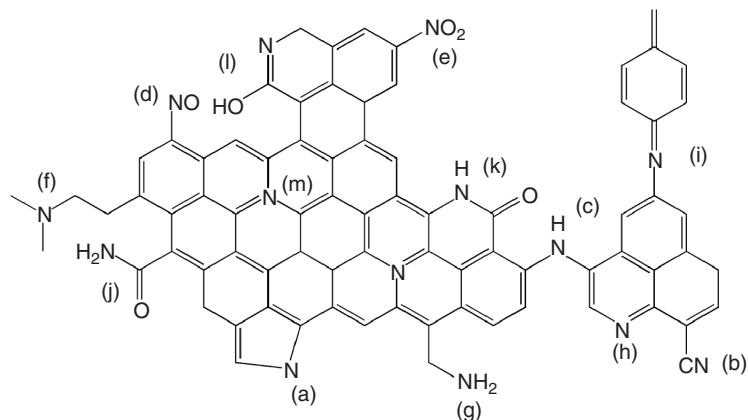


Figure 2.2 Types of nitrogen-containing functionalities on the carbon materials: (a) pyrrole-like group; (b) nitrile; (c) secondary amine; (d) nitro group; (e) nitroso group; (f) tertiary (g) amine; (h) pyridine-like group; (i) imine; (j) amide; (k) lactam; (l) pyridone; (m) quaternary amine.

in the graphitic layer in substitution of C atoms), pyridinic, and pyrrole-type structures [105]. Nitrogen-containing functionalities are responsible for an increase in the surface polarity of carbon [106–108], and for basicity since both pyridine and pyrrole-type structures are considered as basic. Nevertheless, the overall basic–acidic nature is governed by the degree of heterogeneity of nitrogen-containing surface groups created on the surface of carbon materials [98].

2.2.3 Hydrogen–Carbon Species

Hydrogen is present on a carbon surface as chemisorbed water, as surface functionalities (e.g., carboxylic acids, phenolic groups, amines), or is bonded directly to carbon atoms as a part of aromatic or aliphatic structures. The carbon–hydrogen bond is very stable but breaks on heating at about 1273 K. Nevertheless, the complete desorption of hydrogen does not happen at temperatures below 1473 K.

The chemisorption of hydrogen on charcoals does not happen below 473 K [109,110]. Hydrogen is usually attached at the edges of the crystallites [111,112]. Whereas on carbon blacks hydrogen atoms are present at the edges of the graphene layers, in the case of graphite, besides the edge planes of graphite sheets, where strong interactions take place, defects and the space between the basal planes of graphite are also active for the weak chemisorption [113]. There are also studies which report that on charcoals, hydrogen is chemisorbed primarily in the interior of char particles [114,115]. Heat treatment in an inert atmosphere eliminates part of the hydrogen via surface reduction [116,117].

Hydrogen influences the carbon properties; for example, the electrical resistance of carbon black is related to its hydrogen content [112]. Moreover, the presence of hydrogen at the edge sites on carbon blacks inhibits graphitization [118]. The stable carbon–hydrogen bond inspired researchers to develop methods for its functionalization [119,120], which is an important aspect of carbon surface modification.

2.2.4 Sulfur, Phosphorus, and Halogen Functionalities

Sulfur Sulfur is present in carbonaceous materials as elemental sulfur, inorganic species, and organosulfur compounds. Its content varies between 0 and 5%. Carbon–sulfur complexes are extremely stable [121] and are not removed completely from the carbon matrix even at temperatures reaching 1373 K. Only heating in a reducing hydrogen atmosphere is able to remove sulfur completely from the carbon matrix [121].

Carbon surfaces can be modified by reactions with sulfur-containing compounds such as H₂S, CS₂, or SO₂ at various temperatures, which results in the formation of sulfur-containing groups [122,123]. It was found that the maximum sulfur uptake takes place at 873 K and that the amount of sulfur fixed depends on the nature of the carbon [124,125]. The reactivity of various types of carbon materials toward sulfur has been investigated by Boehm and Puri [51,52].

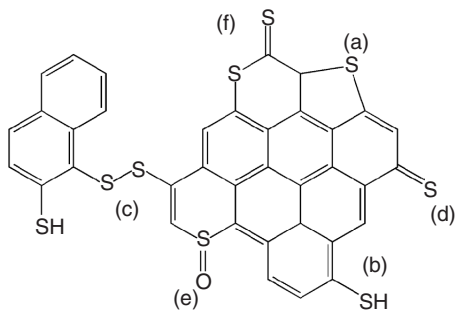


Figure 2.3 Carbon-sulfur surface compounds as described in the literature: (a) sulfide; (b) thiophenol; (c) disulfide; (d) thioquinone; (e) sulfoxide; (f) thiolactone [126,128,129].

The surface complexes [126–129] and their possible configurations are shown in Figure 2.3.

Puri and co-workers [128,129] found that sulfur is introduced to the carbon matrix by interactions with oxygen-containing functional groups or by addition to unsaturated sites. Thus, the substitution reactions with quinone and phenolic groups lead to thioquinone and thiophenol structures, and the addition reactions result in the formation of sulfide and sulfoxide groups. Moreover, Chang showed the evidence of thiolactones in a number of carbonaceous materials after reaction with various sulfur-containing materials [126].

The use of sulfur complexes includes minimizing adsorption of water vapor on charcoals [52] and adsorption of metal ions such as cadmium [130], mercury [131], and lead [132]. Strong bonds between the metals and the carbon–sulfur complexes are also used in the desulfurization of liquid fuels [133–135].

Phosphorus The main role of phosphorus in carbon materials is as an oxidation protector and a fire retardant [136–144]. Its source can be in phosphoric acid, which is used in some technologies of carbon activation [143,144] or in the cross-linking precursor. The phosphorus present in the carbon matrix is stable between 773 and 1273 K. It can be fixed as red phosphorus and/or in chemically bonded forms, such as –C–P–bonds or –C–O–P–bonds [143–145]. During the carbonization process at low temperatures, phosphocarbonaceous species are created. Their content decreases by scission of the P–O–C bonds with an increase in the temperature, due to the growth of aromatic structures [143]. Possible phosphorus-containing functionalities are presented in Figure 2.4.

Halogens Although reactions of halogens with carbon materials to generate carbon–halogen functionalities have so far been investigated less thoroughly than those with oxygen or nitrogen, there are reports showing that treatment of carbon materials with halogen vapors or aqueous solutions of halogens results in the formation of carbon–halogen complexes [146–149]. As for other heteroatoms,

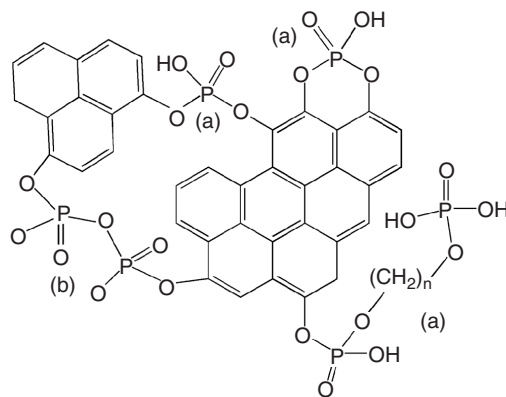


Figure 2.4 Phosphate–carbon complexes as described in the literature: (a) phosphocarbonaceous esters; (b) pyrophosphate species [143].

the amount of halogen introduced to the carbon matrix varies with the nature of the carbon and the temperature of the treatment [150–152]. The reactivity of halogen toward carbon and the stability of the carbon–halogen complex decreases in the order chlorine > bromine > iodine.

As a result of the reaction of chlorine with carbon at high temperatures, a C–Cl bond is formed, with the maximum chlorine uptake between 673 and 773 K. The incorporation of chlorine takes place either by addition at the unsaturated sites formed as a result of removal of oxygen from the edges of the graphene layers, or by substitution of chlorine for hydrogen in aliphatic groups (low temperature) or at the edges of the aromatic platelets (high temperature). Tobias and co-workers [148] suggested three types of chemical reactions of chlorine on carbon surfaces: (1) double-bond saturation, (2) exchange with chemisorbed hydrogen, and (3) dehydrogenation. Although chlorine–carbon complexes are considered stable, they can be removed completely by fusion with sodium hydroxide or by heating at 973 K in a hydrogen atmosphere. This can lead to other modifications, as chlorine can be replaced by cyanide groups after fusion with sodium cyanide or treatment with copper(I) cyanide [152].

Analogous to chlorine, bromine or iodine form stable halogen–carbon complexes, with the maximum amount fixed at about 773 K. The mechanism of bromine incorporation varies depending on the physical form of bromine (vapors or aqueous solution). When bromine is present in aqueous solution, bromine occupies unsaturated sites on the carbon surface, whereas in reaction with vapor, partial substitution for hydrogen also takes place. The former reaction is used as a measure of surface unsaturation [147,153,154]. The driving force for a partial substitution of hydrogen by bromine is inaccessibility of the small pores to the large bromine molecule.

Iodine is also fixed in the unsaturated edges of a carbon surface when it is incorporated from the vapor [155–158]. On the other hand, from its solution,

aqueous or nonaqueous, reversible adsorption takes place [157,158]. The efficiencies of bromine- and iodine-impregnated activated carbons as adsorbents of heavy metals were found to be comparable to that of sulfur-impregnated materials [159–161]. Moreover, they have the advantage of low cost of preparation.

Fluorine–carbon composites were investigated as functional coating materials in a wide variety of applications. Examples include coating materials for construction in low-temperature environments [161], protective coating for computer hard disks [162], automotive components [163], semiconductors in optoelectronic devices [164,165], and biomedical implants [166]. These applications are governed by the exceptional physicochemical, electrical, and mechanical properties of the materials (i.e., hardness, friction, water repellency, chemical inertness, infrared transparency, interfacial and tensile strength), which are also linked to their microstructure. Fluorine-treated carbons are much more polar than as-received carbons; the main challenge lies in the homogeneous distribution of the fluorine–carbon functionalities [161,167–170].

Boron Because of its small size, the boron atom is easily incorporated in the carbon lattice and can be substituted in both sp^2 and sp^3 configurations. A standard CVD process with BCl_3 is used to produce highly boron-doped carbons, which have a hexagonal, graphitelike structure and contain up to 17% boron. That substituted boron atoms in the carbon lattice can accelerate the graphitization and suppress the oxidation of carbon materials [171–174]. Even in a small quantity, they change the electromagnetic properties of graphite [175]. Boron-doped carbon fibers, BC_x , are used as a reinforcement of C–C composites in the aerospace industry or as an alternative to C–C structural materials that oxidizes at temperatures in excess of 673 K [176,177].

2.3 SURFACE MODIFICATIONS

2.3.1 Oxidation

Carbon surface oxidation is in fact the most often used and the most traditional method of carbon surface modification. It can be done in either a gaseous or a liquid phase. In gas-phase oxidation, oxidants such as oxygen, ozone, air, or nitric oxides, are used. Although conditions of oxidation vary, it is usually done in an oven at elevated temperatures between 473 and 623 K, with a continuous flow of the oxidant or exposure to air. Air oxidation is considered to be weak, and its effects depend on the susceptibility of the carbon surface [81,82]. As a result of oxidation, various oxygen-containing groups are formed with a predominant population of weakly acidic groups such as phenols. A variation of gas-phase oxidation, plasma treatment, has been increasing in popularity [178–181]. Air or oxygen is generally used as plasma.

Oxidation from the liquid phase is much more complex and results in more severe changes in the carbon surface chemistry. Here the most common oxidizing

agents are nitric acid, hydrogen peroxide, potassium permanganate, sulfuric acid, and sodium peroxydisulfide. The oxidations are usually carried out in open vessels with oxidants in the entire range of concentrations, depending on the desired effects. Another important factor in this type of oxidation is temperature. The higher the temperature and the stronger the oxidant, the more oxidized the carbon surface is [81]. In some cases, strong oxidation, such as that with nitric acid at its boiling point, can totally destroy the carbon structure, resulting in some type of water-soluble humic substance. It is generally accepted that oxidation with strong oxidants such as nitric acid or sodium peroxydisulfate leads to carbons with a predominant population of surface carboxylic groups [81,82], whereas treatment with hydrogen peroxide increases the population of phenols. In addition to an increase in the oxygen content, the use of nitric acid or nitric oxide as oxidants results in the incorporation of nitrogen, as nitro groups probably attached the carbons at the edges of graphene planes [82].

A significant part of the treatment from both gaseous and liquid phases is washing with water, which removes excess oxidants and water-soluble entities formed as a result of oxidation.

2.3.2 Introduction of Nitrogen-Containing Species

As in the case of oxygen, introduction of nitrogen to a carbon matrix can be done from either a liquid or a gas phase using nitrogen-containing precursors. As a gaseous source of nitrogen, ammonia is generally used at temperatures between 673 and 1273 K [105]. When the modifications are carried out on carbon samples, either preoxidized or not, in the liquid phase such compounds as carbazole, nitrogen-enriched polymers, acridine, melamine or urea are used. The carbons are impregnated with the water or alcohol solutions of the nitrogen-containing compounds and then exposed to heat treatment at temperatures between 673 and 1293 K [55,106,182]. Preoxidation of carbons, especially char with a low degree of carbonization, results in the formation of chemical bonds, usually between a basic nitrogen-containing precursor and a carbon surface, resulting in an increased nitrogen content [55–57]. The chemistry of such carbon is discussed in Chapter 6.

2.3.3 Introduction of Sulfur Functionality

The introduction of sulfur functionalities to a carbon surface is usually done by heating carbons in the presence of elemental sulfur [183] or other sulfur-containing compounds, such as hydrogen sulfide [122,123]. In this way, up to 10% of sulfur can be fixed to the carbon matrix. The temperature of heat treatment varies from 476 to 1273 K. The most common sulfur reactions on the carbon surface are addition to the carbon active sites, substitution of oxygen, and reaction with metals, leading to formation of sulfides. Moreover, a significant amount of CS₂ can be deposited on the surface. Generally, it was proposed that at temperatures below 873 K, addition of H₂S to the active sites of carbons

occur with a significant role of oxygen-containing species. On the other hand, at temperatures higher than 873 K, a direct reaction of H₂S with the carbon surface is predominant.

2.3.4 Halogenization

As mentioned in Section 2.2.4, halogenation can be done from either the gaseous or liquid phases, depending on the type of halogen used. When gases or vapors such as Cl₂ or F₂ are used, the sample is exposed to their flow for various periods of time (at least half an hour) at 473 to 673 K [184–186]. The treatment is sometimes done on a reduced carbon surface [184]. As a result of this, C–X bonds are introduced. For halogenation using iodine or bromine, their vapors are often used. Carbon and halogen are kept in separate containers connected with each other. When the latter is heated at about 373 K, its vapors are adsorbed by carbon in another vessel. Then heat treatment at various temperatures can be carried out.

2.3.5 Impregnation and Dry Mixing

It is well known that the presence of inorganic impurities in activated carbons affects the adsorptive and catalytic behavior [60]. It was pointed out that the ash content or the constitution of activated carbon is one possible cause of catalytic side reactions [187,188] and that it affects the gasification process significantly [189–192]. The pH of basic carbons is reduced greatly after washing with water or diluted HCl, which is accompanied by a drop in the ash content [90]. Thus, it is clear that the effect of the mineral matter has to be taken into account in order to assess the basicity of an adsorbent and catalyst. If so, the reverse technique, the introduction of inorganic matter to the carbon surface, has attracted substantial interest as a method of modification leading to efficient catalysis and adsorbents. An example is Midas carbon, obtained by physical “dry” mixing of microporous carbon with mesoporous inorganic oxides of magnesium and calcium [193].

Carbon is usually impregnated using either excess-solution impregnation [194,195] or incipient wetness impregnation [197–199]. In the former approach, carbon is dispersed in the solution of a catalytic precursor with a predetermined concentration. Sometimes the liquid, which facilitates wetting, is added. Then the slurry is filtered and some amount of the catalyst is adsorbed in the pore system or is ion-exchanged with the groups on the carbon surface. In the incipient impregnation method, a volume of the catalytic solution usually equal to the volume of carbon pores is added very slowly accompanied by vigorous stirring. This technique allows more control of the amount of catalyst dispersed on the surface.

2.3.6 Heat Treatment

The major effect of heat treatment is decomposition of surface functional groups with release of oxides or heteratoms containing gases (e.g., CO, CO₂, NO, NO₂,

H_2S , NH_3), and sometimes, changes in carbon porosity. The latter happens mainly for low-temperature carbonized samples, such as those obtained using phosphoric acid activation [28,29,31,32]. The decomposition of surface groups results in an increase in basicity. Changes in the surface chemical nature upon heat treatment between 773 and 1223 K in a reducing (hydrogen) and an inert (nitrogen) atmosphere were investigated by Menendez and co-workers [84]. Their results suggest that a hydrophobic surface is produced only upon heating in hydrogen at temperatures greater than 1073 K. Moreover, such a surface is stable when exposed to air. It was proposed that H_2 treatment removes surface oxygen, stabilizes some reactive sites by involving them in C–H bonds, and gasifies the most reactive unsaturated carbon atoms from the edges of graphene layers. When the treatment is carried out in an inert atmosphere, the resulting surface, although without oxygen-containing groups, is very susceptible to reoxidation and the formation of new acidic groups. A model of the finding proposed by Menendez and co-workers is presented in Figure 2.5. For details, readers are directed to their work [84].

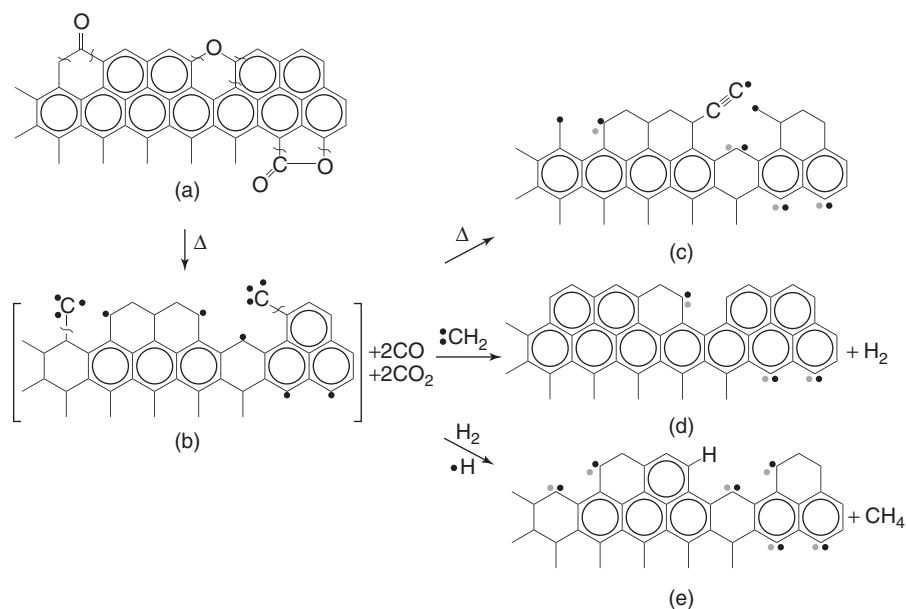


Figure 2.5 Proposed model for stabilization of carbon surfaces upon heat treatment () in N_2 (inert gas) and H_2 . For simplicity and illustrative purposes, only two types of oxygen surface groups (pyrone and lactone) and three other types of active sites are shown. These three types are in order of increasing stability: (1) type I isolated unpaired-electron sites $\text{Ar}-\lambda$ (where Ar represents the aromatic (graphene layer); (2) type II, $\text{Ar}-\text{C}\equiv\text{C}\lambda$; and (3) type II, divalent in-plane σ pair, $\text{Ar}-\lambda\epsilon$ (where ϵ represents a localized π electron). Structures C and D are formed in H_2 . Structure D is much more abundant in H_2 -treated carbons because of the higher concentration of CH_2 radicals. (From ref. 84, with permission. Copyright © 1996 American Chemical Society.)

2.4 CHARACTERIZATION OF SURFACE CHEMISTRY

Those involved in the characterization and application of activated carbons must realize that no single analytical chemistry discipline can successfully explain all surface chemical properties. A broad and comprehensive view can be obtained only when a battery of methods, often based on different physicochemical principles, are used. Owing to space limitations, only a brief review of the techniques is presented in this section. For more information the reader is directed to ref. [54]. Generally speaking, the methods used to characterize carbonaceous material surfaces are referred to as “wet” and “dry” techniques. The former include potentiometric titrations and zeta potential or electrochemical methods; the latter include temperature-programmed desorption (TPD) and spectroscopic methods such as x-ray photoelectron spectroscopy (XPS) and diffuse reflectance infrared spectroscopy (DRIFT).

2.4.1 Elemental Analysis

Determination of the carbon, hydrogen, nitrogen, and sulfur contents of carbon samples is based on their combustion at high temperatures (i.e., 1473 K) in a stream of oxygen. Then the products of combustion (carbon dioxide, water, and sulfur dioxide) are measured and analyzed. The nitrogen present in the sample is reduced to N₂ by copper turnings. In many cases, the oxygen content is calculated indirectly as the difference between 100 and the percentage of other measured components present in the carbon material (C, H, S, N). Usually, depending on the types of modifications used, the carbon content varies from 70 to 98%; hydrogen, 1 to 5%; sulfur, 0 to 5%; and nitrogen, 0 to 5%.

The metal content and the constituents of inorganic matter, which can also be crucial for the performance of carbons, are usually determined using atomic absorption spectroscopy, and the technique used most often is inductively coupled plasma (ICP) atomic spectroscopy. Before the experiments, the samples have to be digested in strong acids.

2.4.2 Titration

Boehm Titration The most popular approach to determining carbon surface chemistry is based on classical analytical chemistry. It was first developed by Boehm [51], who proposed to neutralize the surface functionalities based on their acid strength. Sodium bicarbonate, NaHCO₃ ($pK_a = 6.37$), sodium carbonate, Na₂CO₃ ($pK_a = 10.25$), sodium hydroxide, NaOH ($pK_a = 15.74$), and sodium ethoxide, NaOC₂H₅ ($pK_a = 20.58$) are used as bases. It is assumed that sodium bicarbonate neutralizes carboxylic acids, sodium carbonate neutralizes carboxylic acids and lactones, sodium hydroxide neutralizes carboxylic acids, lactones, and phenols, whereas sodium ethoxide reacts with all oxygen species, even extremely weak acids ($pK_a < 20.58$). In practice, owing to the difficulties in using sodium

ethoxide related to its nonaqueous-media and oxygen-free conditions, Boehm titration is limited to the determination of carboxylic groups, lactones, and phenols [81,200–204]. Sodium salts were chosen as bases because they do not form precipitates after reaction with gaseous CO₂, and their specific interactions with carbon surfaces are minimal [205].

When there are not significant amounts of other heteroatoms, the rough but reliable estimation proposed by Boehm is sufficient to obtain a good correlation with other surface properties tested [93,206]. One deficiency of the method is that classification of all groups as oxygen-containing acids and of all other groups containing nitrogen, sulfur, or phosphorus, can be misinterpreted. This is because the selectivity of Boehm titration is based on the pK_a value. Moreover, the surface heterogeneity of carbonaceous materials makes it extremely difficult to determine accurately the surface functionalities on carbons based only on their acidic and basic properties [53]. Nevertheless, the effects of heat treatment and chemical oxidation on the distribution of surface groups determined from Boehm titration have been discussed widely in the literature [14,16,63,85,207]. Examples of Boehm titration results for carbons with different degrees of surface oxidation are presented in Table 2.1.

When Boehm titration is used to characterize chemically modified carbons, one has to be extremely cautious, since groups containing other atoms can be classified as surface oxide. A safe and still meaningful way of using the Boehm approach is to limit it to the total number of acidic groups, which would include all species neutralized by sodium hydroxide. Examples of this approach are the result obtained for the nitrogen-modified samples presented in Table 2.1 [56]. It is seen that the incorporation of nitrogen in the matrix resulted in an increased amount of the basic groups, at the expense of their acidic properties. On the other hand, annealing of the modified carbons at high temperature resulted in a decrease in the nitrogen content as a consequence of the decomposition of some of the nitrogen functionalities (e.g., amides, free amines) [105]. This is due to the fact that after heating at 1223 K, the majority of nitrogen seemed to be incorporated in the carbon structure as pyridinelike and pyridine-N-oxide functionalities, changing the basic properties of the carbon [104].

Table 2.1 Results of Boehm Titration (mmol/g) for Initial and Urea-Treated Carbons at 623 and 1223 K

Sample	pH	Carboxylic	Lactonic	Phenolic	Acidic	Basic	Total
BAX	6.55	0.255	0.140	0.367	0.763	0.363	1.125
BAXN-450	6.92	—	—	—	0.718	0.563	1.281
BAXN-950	7.1	—	—	—	0.678	0.595	1.272
BPL	7.54	0.000	0.025	0.163	0.188	0.450	0.638
BPLN-950	6.78	—	—	—	0.167	0.507	0.674
BPLN-450	6.99	—	—	—	0.178	0.675	0.853

Source: From ref. 98, with permission. Copyright © 2002 American Chemical Society.

Although some alternatives to Boehm titration have been proposed, such as that by Rivin [61], which combines TPD and titration analyses, the classical Boehm approach is still the most powerful method of first screening for carbon surface chemistry. As seen in Table 2.1, it is usually combined with titration of basic groups using acids. Early studies employed acids of increasing strength [86]. Results indicated an increase in neutralization capacity due to physical adsorption on weakly basic sites, in the order $\text{HCl} < \text{HNO}_3 < \text{HClO}_4$. Nevertheless, the total content of basic groups is generally determined by titration with HCl [74]. Another method of determination of carbonaceous adsorbent surface chemistry is titration in nonaqueous solvents (e.g., toluene) with organic acids or bases (amines) [208].

Potentiometric Titration Direct potentiometric titration has been used to study for years the carbon surface, but until the mid-1990s the curves obtained did not show discrete endpoints useful for meaningful interpretation [200,205,209]. The derivatives obtained in some studies were difficult to characterize due to the many maxima revealed when no well-defined endpoints were present [210]. A first meaningful deconvolution of titration curves with theoretical description of acid-based dissociation on the surface of carbons was proposed in the mid-1990s [211,212]. In this approach it is assumed that the system under study consists of acidic sites characterized by their acidity constants, K_a . It is also assumed that the population of sites can be described by a continuous $\text{p}K_a$ distribution, $f(\text{p}K_a)$. The experimental data can be transformed into a proton-binding isotherm, Q , representing the total amount of protonated sites, which is related to the $\text{p}K_a$ distribution by the following integral equation:

$$Q(\text{pH}) = \int_{-\infty}^{\infty} q(\text{pH}, \text{p}K_a) f(\text{p}K_a) \, d\text{p}K_a \quad (2.1)$$

The first solution of this equation was obtained using the Rudzinski–Jagiello method (RJ approximation) [213], but the distributions obtained showed the presence of peaks associated with various functional groups and the approximation was not able to fully resolve peaks for very heterogeneous surfaces [210,214]. An application of the numerical procedure SAIEUS (solution of adsorption integral equation using splines) [211,212,215], which uses regularization combined with nonnegativity constraints, was a real breakthrough in the interpretation of results. The choice of the degree of regularization or smoothing is based on an analysis of a measure of the effective bias introduced by the regularization and a measure of uncertainty of the solution. SAIEUS was tested using simulated data and experimental titration data of organic standards, and it was demonstrated that this method can resolve completely peaks which are less than 1 $\text{p}K_a$ unit apart [211,212,215]. Comparison of the RJ and SAIEUS methods [211,212] showed the superiority of the latter approach.

Because many heteroatom configurations can result in similar $\text{p}K_a$ values [216,217], in the potentiometric titration approach, which also depends on the

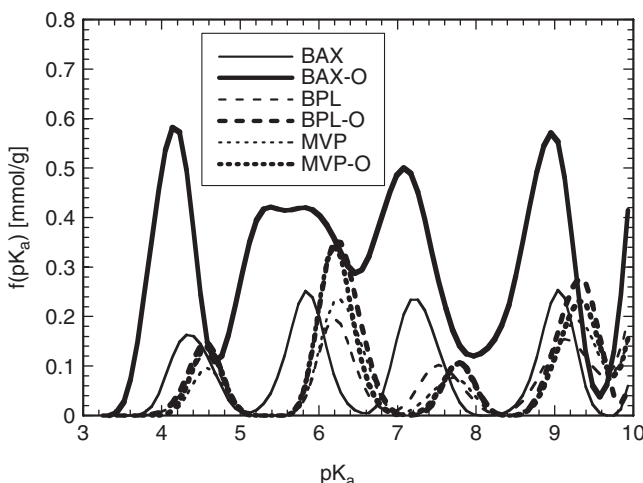


Figure 2.6 Distributions of acidity constant for the initial and oxidized carbons (O). (From ref. 32, with permission from Elsevier.)

unknown activity of the solution, the exact classification of species is impossible. Nevertheless, when the changes in a series of carbons are studied and the content of heteroatoms is known, this method shows clearly the trend in surface functionality and offers a meaningful description of acidic properties of the carbon surfaces, in terms of their proton affinity distribution (Figure 2.6), proving qualitative and quantitative information on the number and strength of the acidic sites [211,212]. Despite this, potentiometric titration also presents some limitations, such as very slow establishment of the ion-exchange equilibria [85].

A quantitative comparison between direct potentiometric titration and the classical Boehm method for characterization of the acidity of activated carbons has been drawn by various researchers [85,215,218]. Although a rather acceptable agreement is generally accomplished for both methods, when applied to a carbon surface where oxygen is the major constituent, some discrepancies exist. Figure 2.7 shows a correlation between the total acidic groups detected on an activated carbon using both Boehm and potentiometric titrations.

2.4.3 pH of Carbons, Point of Zero Charge, and Isoelectric Point

The pH of an aqueous slurry of carbons represents the average chemistry of the carbon surface. Brönsted acidic groups of the carbon surface tend to donate their protons to water molecules, and hence the surface becomes negatively charged while Lewis bases adsorb protons from solution, becoming positively charged. Thus, various surface functionalities are responsible for the amphoteric nature of carbon, the pH in aqueous solution, and its surface charge. To estimate the surface

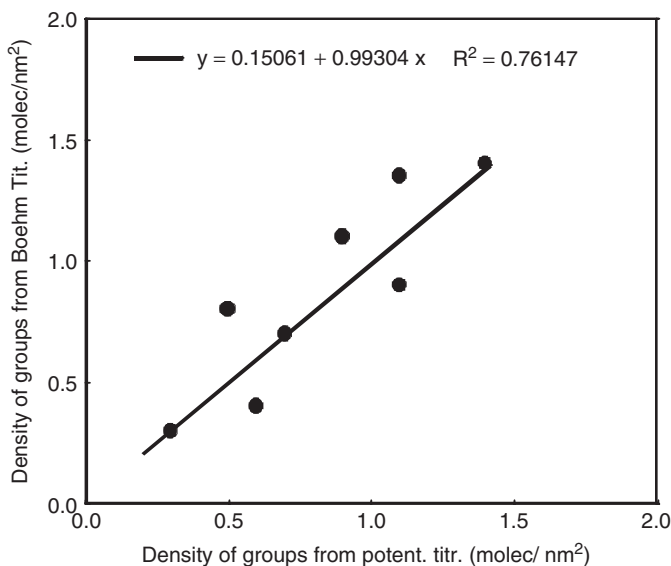


Figure 2.7 Number of acidic groups determined from Boehm titration versus potentiometric titration. (From ref. 82, with permission from Elsevier.)

chemistry of carbons, the standard test of the American Society for Testing and Materials (ASTM) can be used [219,220].

The surface charge of carbons is governed by the nature of the surface groups and the pH. In an electrolyte solution, a charged particle of carbons is surrounded by ions of opposite sign, which alter the dispersive and electrostatic interactions of the carbon surface and the electrolyte [221].

To characterize the electrical state of the carbon surface in solution, the iso-electric point and the point of zero charge are used. The *isoelectric point* (IEP) is defined as the pH where the charge at the slipping-plane pH of the Stern layer is zero. It is obtained when an electric field, a pressure gradient, or the like is used to move the charged particles of colloids in solution in microelectrophoresis, electroosmosis methods, and so on. The *point of zero charge* (PZC) is defined as the pH where the net surface charge resulting from the adsorption of the potential-determining ions, H⁺ and OH⁻, is zero. It can be considered as the pH value below which the surface of carbon particles in solution is, on average, positively charged, the opposite being true for pH < PZC. It is accepted that electrophoretic mobility measurements are only representative of the external surface charges of carbon particles in a solution (the internal surface charges cannot be measured by this method), whereas the PZC varies in response to the net total (external and internal) surface charge of the particles [221–223]. Following this, the PZC–IEP difference can be interpreted as a measure of the surface

Table 2.2 Point of Zero Charge and Isoelectric Point for Activated Carbon Cloth and Various Activated Carbons

Commercial Name	Specific Surface Area (m^2/g)	pH_{PZC}	pH_{IEP}
ACC	1125	7.0	
Ketjenblack	950	9.85	
Darco KB	1500	4.25	
Nuchar WVV	1215	10.4	2.2
Filtrasorb 400	1236	7.45	3.0
Darco HDB	606–650	5.35	
Nuchar SN	1400–1800	2.2–9.0	
Norit C	1085–1380	—	1.4–4.9
Filatrasorb 400	1050–1200	—	7.10
Nuchar 722	—	—	5.70
DARCO	—	—	6.15
Pittsburgh HGR	—	—	6.70
Nuchar C-190-N	890	—	4.75

Source: From ref. 223, with permission from Elsevier.

charge distribution of carbons, with positive values corresponding to more positively charged internal than external particle surfaces (i.e., less acidic external than internal surfaces), and values close to zero corresponding to a more homogeneous distribution of the surface charges [88]. For a detailed interpretation of IEP and PZC on various carbons, the reader is directed to papers by Menendez and co-workers [88–91]. Since the PZC is related to surface acidity [88], it can be considered as an indicator of the oxidation of the carbon surface. Examples of PZC and IEP values obtained for various carbons (oxidation) are collected in Table 2.2.

2.4.4 Spectroscopic Methods

Infrared Spectroscopy Infrared spectroscopy has been one of the most frequently used instrumental analysis methods to characterize qualitatively the surface functionalities in coals [224,225], carbon blacks [226], charcoals [227], activated carbons [80,228–233], activated carbon fibers [234,235], and carbon films [236,237]. Fourier analysis (FTIR) provides an improvement over dispersive IR spectroscopy in signal-to-noise (S/N) ratio, energy throughout, accuracy of the frequency scale, and a capacity for versatile data manipulation.

One of the major sample-handling problems in FTIR analysis of carbonaceous materials is that many of them are effective blackbody absorbers and thus are too opaque for direct transmission analysis in the midinfrared spectral region. Addition of KBr intensifies the signal to obtain transmission infrared spectra. It is time consuming, and grinding conditions and moisture are known to affect the spectrum of the sample [238]. Alternative techniques such as specular reflectance, diffuse reflectance (DRIFT), photoacoustic spectroscopy (FTIR-PAS), and total

internal reflectance (ATR) have become widely used for the characterization of carbon surfaces [80,224,229,232]. Among them, the most common are the diffuse reflectance and photoacoustic methods. While DRIFT shows good sensitivity and high quantitative precision, FTIR-PAS eliminates possible spectral artifacts such as baseline shifts due to light scattering [239].

As in organic chemistry, the assignment of the IR absorption bands and peaks to the different carbon surface functional groups is made by comparison with the absorption bands of specific organic compounds [240]. In the analysis of the spectra, one has to remember that the frequency of the absorption bands is affected by resonance and conjugation effects caused by proximity of several functionalities. The intensity of the bands obtained for the carbon surfaces is affected by the presence of peripheral groups at the edges of the carbon surfaces. The absorption bands and peaks for oxygenated functionalities on the carbon materials are summarized in Table 2.3. Although some discrepancies exist for an assignment of the band 1700 to 1550 cm^{-1} , it is generally accepted that quinone groups are seen at 1550 to 1680 cm^{-1} or 1660 to 1670 cm^{-1} and the band at 1660 cm^{-1} can be assigned either to oxygen surface compounds or to aromatic C=C stretching vibration of the basal planes. Readers can find details of the assignments of FTIR absorption bands in refs. 80, 224–239. Although IR spectroscopy does not provide quantitative information about the carbon surface chemistry, it can identify groups created or destroyed on the carbon surface as a result of various modifications (Figure 2.8).

Table 2.3 Infrared Adsorption Bands on Carbon Surfaces and Their Corresponding Assignments to Oxygenated Functionalities

Group or Functionality	Assignment Region (cm^{-1})		
	1000–1500	1500–2050	2050–3700
C–O stretch of ethers	1000–1300		
Ether bridge between rings	1230–1250		
Cyclic ethers containing COCOC groups	1025–1141		
Alcohols	1049–1276	—	3200–3640
Phenolic groups			
C–O stretch	1000–1220		
O–H bend/stretch	1160–1200	—	2500–3620
Carbonates; carboxyl carbonates	1000–1500	1590–1600	
Aromatic C=C stretching	—	1585–1600	
Quinones	—	1550–1680	
Carboxylic acids	1120–1200	1665–1760	2500–3300
Lactones	1160–1370	1675–1790	
Anhydrides	980–1300	1740–1880	
Ketenes (C=C=O)	—	—	2080–2200
C–H stretch	—	—	2600–3000

Source: From ref. 229, with permission from Elsevier.

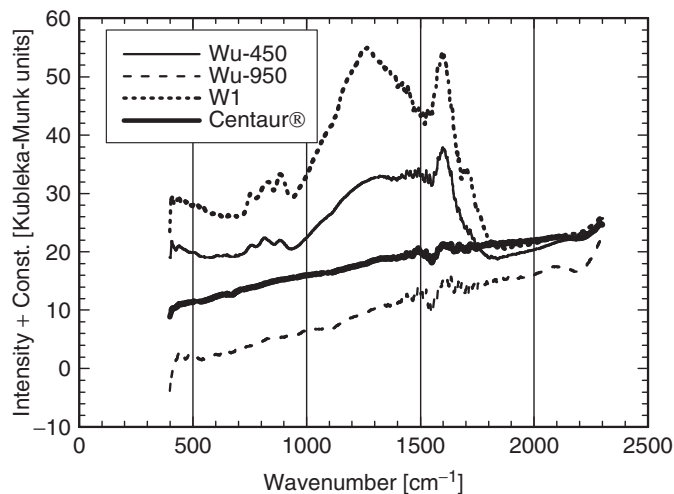


Figure 2.8 FTIR spectra for the initial (W1) and urea-modified samples at various temperatures. (From ref. 33, with permission from Elsevier.)

The FITR technique has been used widely to study changes in the carbon surface upon heating [234,241,242] or upon introduction of nitrogen-containing species [243]. In the former approach a decrease in the intensity of the characteristic DRIFT bands reflects changes in the surface chemistry upon decomposition of the surface functional groups during thermal heating of the carbons.

Although nitrogen-containing groups have also been investigated by FTIR spectroscopy, interpretation of the absorption IR spectra for nitrogen-containing carbons is not very clear [224,244–246], due to the fact that the broad band between 1700 and 1000 cm⁻¹ represents a superposition of several bond contributions involving either oxygen or nitrogen [246]. Salame and Bandosz showed that oxidation of low-carbonization-degree carbon surfaces with HNO₃ solutions leads to formation of nitro groups which were seen as bands at 1530 and 1330 cm⁻¹ [215]. Biniak and co-workers reported that nitric acid treatment of carbon materials results in the formation of pyridine structures and pyridine-N-oxide species at the expense of pyrrolic moieties [105]. An increase in the intensity of the bands at 1330 and 880 cm⁻¹, respectively, characteristic of pyridine, pyridine-N-oxide, or pyridone structures suggested that the ammonia treatment incorporated nitrogen into the carbon aromatic lattice with the formation of pyridinolike structures. The assignment of other nitrogen-containing bonds that can be found on the carbon surface is presented in Table 2.4.

The FTIR method was also used to determine the sulfur compounds present on the surface of activated carbons after H₂S adsorption or oxidation. Using an approach proposed by Dandekar and co-workers [230] in which the spectrum for an initial sample is subtracted from that of a modified sample, Adib and

Table 2.4 Assignments to the Peak Positions in the 1700- to 1000-cm⁻¹ Absorption Band of Hydrogenated Carbon Nitrile Films

Wavenumber (cm ⁻¹)	Assignment
1620–1650	C=C, C=N, NH ₃
~1600	C=N, C=C
1550–1570	Raman G, C=N
1500–1510	C–N, C=N, C=C
1450	sp ³ CH _x
1360–1380	Raman D, CH ₃ , CC, C=N
1300–1350	sp ² carbon, C–N, C=N
1220–1265	C–N (in C ₃ N ₄), CC, C=N
1020–1150	C–N (aliphatic), N–H

Source: From ref. 246, with permission from Elsevier.

co-workers [206] was able to identify oxidized sulfur species chemisorbed on carbons.

In addition to qualitative analysis, a semiquantitative analysis of selected spectral regions can be carried out from the IR absorption bands [234,246]. In this approach the ratio of the aliphatic hydrogen content to aromatic carbon (H_{al}/C_{ar}) provides a measure of the evolution of aliphatic structures, while the methyl-to-methylene ratio (CH₃/CH₂) is considered as an estimation of the length of the aliphatic chains. The ratios are calculated by integration of the peak areas or measurements of the peak intensities, often referred to as an *internal standard*.

X-ray Photoelectron Spectroscopy X-ray photoelectron spectroscopy (XPS), also known as ESCA (electron spectroscopy for chemical analysis), uses x-rays to excite electrons, and then their kinetic energy is measured. X-ray photons of $h\nu$ energy (typically, energy of incident photons ranges from 1 to 2 keV) directed to the sample are absorbed by atoms of the solid, leading to ionization and emission of an inner-shell electron. By absorbing a photon, atoms gain the energy of the photon and release an electron returning to the ground state. The ejected electron retains all the energy from the striking photon, and it can then escape from the atom with a kinetic energy that depends on its binding energy, the incident photon energy, and a correction factor called the *work function*. Consequently, some atoms lack electrons in the internal shells from which photoelectrons have been released. To regain from this ionized state, the atom can emit another photon (fluorescence) or undergo an Auger transition. Since the kinetic energy of the ejected electrons is dependent on their binding energy, different chemical species can be identified. For each and every element, there is a characteristic set of peaks in the photoelectron spectrum at kinetic energies determined by the photon energy and the respective binding energies. Since the intensity of the peaks is related to the concentration of the element within the region sampled, quantitative analysis of the surface composition can be carried out. One has to remember

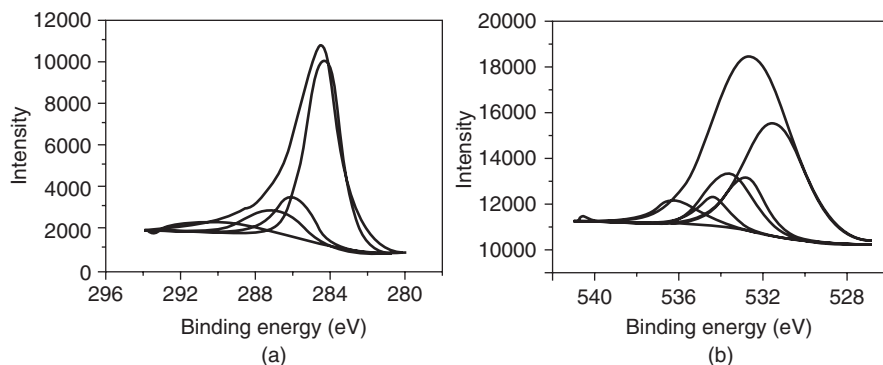


Figure 2.9 High-resolution XPS spectra of carbon nanofiber oxidized in stagnant air at 773 K for 2 hours and fitting curves: (a) C1s peak; (b) O1s peak. (From ref. 244, with permission from Elsevier.)

that quantification in this type of analysis only corresponds to the surface of the materials.

XPS spectroscopy is used to characterize surface functionalities on carbons via employing binding energies of the C1s, N1s, and O1s photoelectrons of surface groups [103,247–253]. For the identification of oxygen-containing functionalities, the C1s signal is measured and groups are assigned based on the differences in their binding energy of carbon atoms, which depends on the number of oxygen atoms to which they are linked. Figure 2.9 shows the patterns for oxidized carbons. Upon oxidation, the C1s region of graphitic carbon splits into various individual peaks, representing the oxide regions, given by two main signals corresponding to keto–enol groups and carboxyl–ester groups. Other assignments to oxygen-containing functional groups upon the binding energies (BEs) involve carbodic carbon ($\text{BE} = 282.6$ to 282.9 eV), graphitic carbon ($\text{BE} = 284.6$ to 285.1 eV), alcohol or ether groups ($\text{BE} = 286.3$ to 287.0 eV), carbonyl groups ($\text{BE} = 287.55$ to 288.1 eV), carboxyl or ester groups ($\text{BE} = 289.33$ to 290.0 eV), and shake-up satellite peaks due to $\pi-\pi$ transitions in aromatic rings ($\text{BE} = 291.2$ to 292.1 eV) [105].

Another application of XPS is the evaluation of the amount of surface oxygen [80,84] or other heteroatoms. This is linked to the fact that the oxygen content determined by XPS roughly reflects the percentage of oxygen on the most external surface [254,255] of the carbon, while the oxygen obtained by chemical analysis represents the total oxygen content.

The identification of nitrogen functionalities by application of the XPS technique is complicated. Nevertheless, this type of analysis has become more and popular [101,103,105,244,250,253]. Jansen and co-workers used the XPS data of the curve fit of N1s spectra to study the chemical state of nitrogen incorporated into carbon [101]. The assignment of the binding energies of the N1 spectrum is presented in Table 2.5.

Table 2.5 Binding Energies and Peak Widths at Half-Height Assigned to Nitrogen-Containing Groups

Functional Group	BE (eV) × Peak Width at Half-Height	BE (eV)
Pyridine	398.7×1.76	398.8
Lactam and imide	399.7×2.5	
Ammine (of esther)	399.7×2.4	
Amide	399.9×2.5	400.2, 399.6, 400.8, 399.6
Alkylamide and amine	399.9×2.7	399.6
Nitrile	400.1×1.7	400.1, 399.4
Pyrrole	400.7×2.5	400.7
Protonated lactam	402.2×2.7	
Alkylammonium	402.4×2.6	401.4
Protonated pyridine	402.6×2.0	401.0
Protonated pyrrole	402.8×2.0	
Protonated amide	403.1×2.7	
Alkyl nitrite	404.1×2.6	404.1

Source: From ref. 101, with permission from Elsevier.

Another application of XPS is carbon chemical environment analysis, based on the chemical shift of the C1s peak in the presence of surface groups or chemisorbed species on carbon. The identification of halogenated species on carbon surfaces has been reported [165,168,256]. In the neighborhood of halogen atoms, due to new contributions at higher binding energies, changes are observed in the C high-resolution spectrum. The results of XPS measurements show incorporation of fluorine as C–F and C–F₂ bonds and the incorporation of chlorine (both dichlorinated and monochlorinated bonds) to carbon black surfaces [165,159,256].

Electron Spin Resonance Spectroscopy When the molecules of a solid exhibit paramagnetism as a result of the presence of unpaired electron spins, transitions can be induced between spin states by applying a magnetic field and then supplying electromagnetic energy, usually in the microwave range of frequencies. The resulting absorption spectra are described as electron spin resonance (ESR) or electron paramagnetic resonance (EPR).

Most carbon materials behave as semiconductors, due to the π electrons and the holes present in the graphene layers, which can act as charge carriers [69]. Since the enhancement of conductivity of carbons at high temperatures is related to structural rearrangements (graphitization), the conductivity of carbons provides valuable information about the carbon surfaces. Due to the fact that the ESR is sensitive to unpaired electrons (delocalized π electrons and free radicals), it can be useful to study the chemical and electrochemical processes that occur on carbon surfaces. Despite this, only a few papers address the use of ESR spectroscopy for the surface characterization of carbon samples [59,257]. The shape

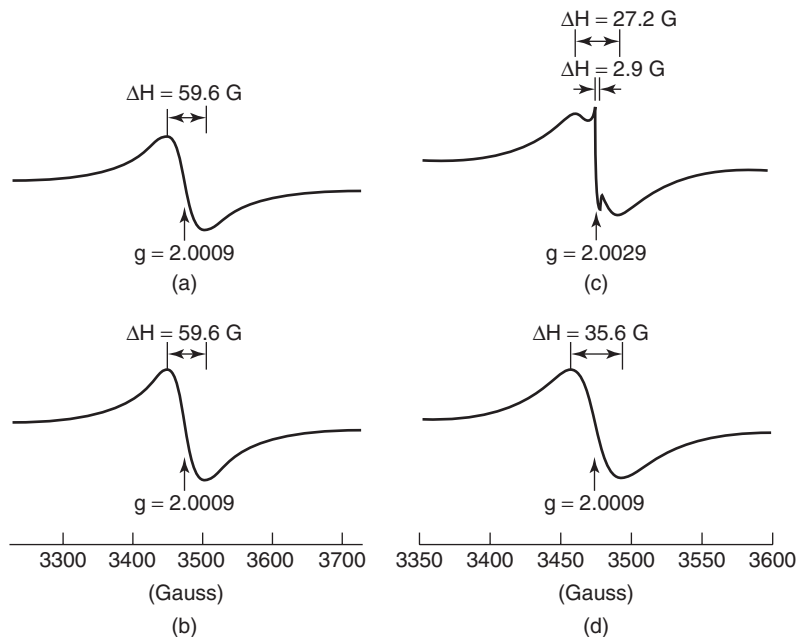


Figure 2.10 ESR spectra of a carbon black: (a) as received; (b) after O₂ exposure at 623 K; (c) after oxidation with nitric acid; (d) after oxidation followed by H₂ exposure at 573 K. (From ref. 257, with permission from Elsevier.)

of the ESR spectrum for carbon materials is affected by chemical, mechanical, and thermal treatments [258]. By means of ESR, it has been suggested that the loss of heteroatoms below 973 K generates stable free radicals on the edges of the carbon surfaces, and their concentration depends on the temperature of treatment [259].

Changes in the ESR spectra of carbon blacks after oxidation treatments are presented in Figure 2.10. While oxygen chemisorbed on a precleaned carbon black surface increased the concentration of both localized spin centers and holes and created higher electrical conductivity, oxidation with HNO₃, increased the number of localized spin centers and decreased the hole concentration. The latter was linked to the formation of surface functional groups on the edges of carbon atoms, which caused an increase in conductivity [257]. A significant number of surface sites generated upon oxidation of the surface of carbon blacks related to the presence of functional groups such as lactones, phenols, and quinones as new bands on the ESR spectrum were observed by Liu and co-workers [257].

Nuclear Magnetic Resonance Nuclear magnetic resonance is a spectroscopic technique based on measurement of absorption of electromagnetic radiation in the frequency region 4 to 900 MHz. Here the nuclei of the atoms are involved

in the absorption process. Although NMR is not often used to study the surface of carbons, its use increased recently due to an improved resolution obtained using magic-angle spinning (MAS). The most promising approach is that based on adsorption of xenon [261–263]. The physical properties of a ^{129}Xe molecule make it extremely suitable as a NMR probe (nuclear spin of $I = 1/2$; no quadrupolar effect, relative sensitivity of nucleus is higher than that of ^{13}C). Moreover, the ^{129}Xe NMR parameters are extremely sensitive to the local environment of atoms [263]. The interpretation of the results is based on an analysis of chemical shift, δ_0 , which is caused by a small difference in the absorption frequency of xenon. This is related to the chemical environment and in the case of carbons, is governed by the chemical nature of their surfaces.

Dependence of the chemical shift on ^{129}Xe NMR spectra on the degree of carbon oxidation was studied by Simonov and co-workers [263]. Since the chemisorbed oxygen can have a significant influence on the state of adsorbed xenon [261,262], the shift on the spectra was analyzed in comparison with the degree of carbon surface oxidation. The results showed a linear correlation between increments of the ^{129}Xe NMR chemical shift and the surface density of oxygen-containing groups (determined using Boehm titration) for chemically modified carbons (Figure 2.11). It was also found that not only oxygen but other heteroatoms, such as chlorine, result in an increased shift.

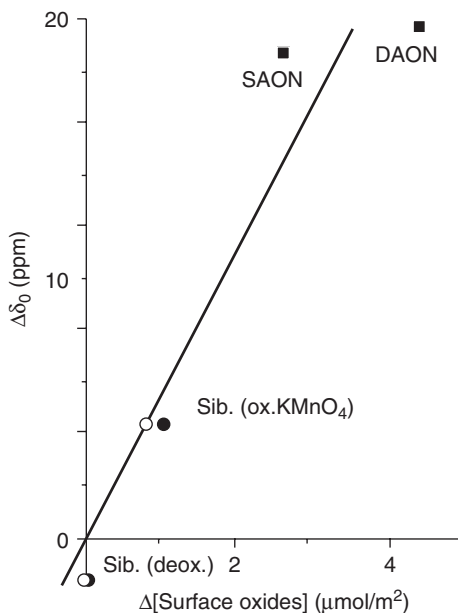


Figure 2.11 Correlation between the increments of the ^{129}Xe NMR chemical shift and the surface density of oxygen-containing groups for chemically modified carbons. (From ref. 263, with permission from Elsevier.)

The results discussed above led to the following quantitative evaluation of the effects of surface groups (SGs) on the chemical shift, δ_0 [263]:

$$\delta_{\text{SG}} = \delta(\text{Xe-SG})\rho_{\text{SG}} \quad (2.2)$$

where δ_{SG} characterizes the effect of the surface functional groups on the ^{129}Xe chemical shift detected, $\delta(\text{Xe-SG})$ is a characteristic of the interaction between adsorbed xenon and the group, and ρ_{SG} is the surface density of groups.

Another NMR approach used to evaluate changes in the surface chemistry of carbons is based on a study of ^{13}C NMR spectral parameters, which by deconvolution of the spectra, can give the aromatic carbon-to-aliphatic carbon ratio in the structure of carbonaceous materials [141,264,265]. Besides ^{13}C , the spectra of ^{31}P [143], ^{11}B [266], and ^{19}F [267] were found to be useful to study the changes in surface chemistry and heteroatom arrangements present on the carbon surface (Figure 2.12). A large chemical shift for ^{31}P allows us to distinguish easily between various phosphorus-containing compounds, and a study of the chemical shift for ^{11}B was found to be useful to evaluate the incorporation of boron atoms

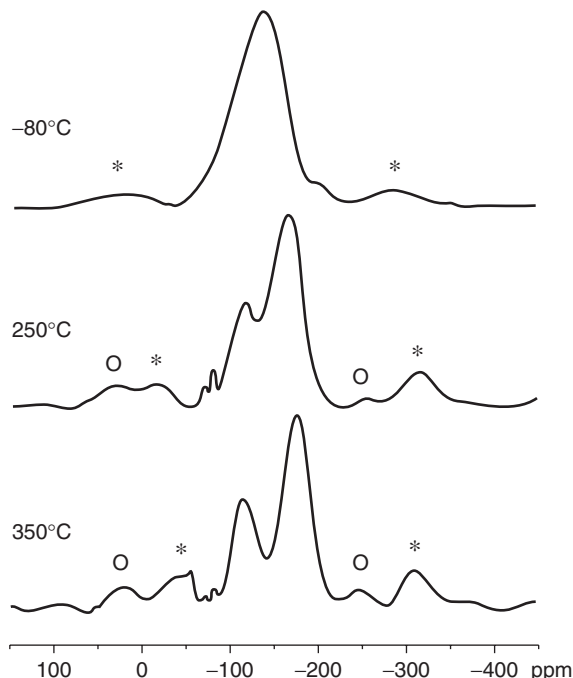


Figure 2.12 ^{19}F NMR spectra of charcoal fluorinated at various temperatures. Asterisks indicate spinning sidebands of CF peak (-144 to -170); circles indicate sidebands of the CF_2 peak (-166 to -1470). (From ref. 267, with permission. Copyright © 1998 American Chemical Society.)

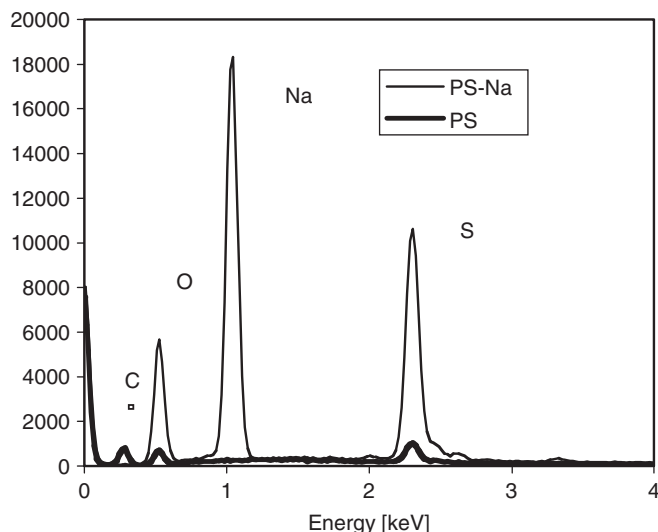


Figure 2.13 EDX spectra for polymer-derived carbons. (From ref. 271, with permission. Copyright © 2006 American Chemical Society.)

in the carbon structure and boron atom environment (boron-to-boron connected configurations or isolated boron atoms) [266].

X-ray Fluorescence and Energy-Dispersive X-ray Analyses In x-ray fluorescence methods the elements in the samples are excited by absorption of the primary beam, and they emit their own characteristic fluorescence x-rays. These methods are widely used for the qualitative and quantitative determination of elements with atomic numbers greater than that of oxygen. In carbon surface science, XRF and EDX are used mainly to determine the inorganic constituents of carbons which either exist there as a result of activation method (e.g., phosphorus in phosphoric acid activated carbon), are present in the precursor [268] (Figure 2.13), or are deposited on the surface as a product of surface reactions [99]. Quantitative determination of the content of elements in carbon using XRF is a difficult task, and a solid matrix requires special calibration procedure and special filters [269].

EDX analyses (EDAX is, in fact, the brand name of the EDX detector produced by EDAX, a division of Ametek) provide valuable information about relative amounts of elements and the location of these elements on the surface [268,270,271].

2.4.5 Calorimetric Techniques

Calorimetric techniques measure the heat that may be generated (an exothermic process), consumed (an endothermic process), or dissipated by a sample.

Such techniques have been used to measure the surface area and to study surface reactivity of both gas–solid and liquid–solid systems. Relevant information concerning the chemical properties of carbon surfaces and their influence on the sorption properties of carbons can be obtained when using the appropriate calorimetric technique. Immersion, flow adsorption, and gas-adsorption calorimetry have been employed for the study of surface chemistry of carbons. Immersion calorimetry provides a direct measurement of the energy involved in the interaction of molecules of the immersion liquid with the surface of the solid, since this energy depends on the chemical nature of the solid surface and the probe molecules (i.e., the specific interaction between the solid and the liquid). When the enthalpies of immersion into liquids with different polarities are compared, a picture of the surface chemistry of the solid is provided. This is especially important for carbonaceous materials, whose surface represents a combination of basal planes and unsaturated sites at the edges of the graphene layers with other heteroatom-based functional groups. The affinity of their surfaces to polar and nonpolar probes is related to their hydrophobic and hydrophilic nature. Thus, calorimetric techniques have been used in the quantification and determination of the nature of the hydrophobic and hydrophilic sites of the carbon surfaces, by measurement of the preferential heats of adsorption on those probes. An example is the enthalpy of immersion of carbonaceous materials into liquids of different polarities, which can be described using surface graphiticity and surface polarity indices [22]. The latter index is an important parameter that allows us to study the changes induced in carbon surfaces by various modifications (oxidation, annealing).

The enthalpy of immersion of carbonaceous materials into water has been correlated with the amount and nature of their surface oxygen functional groups [272–280]. Since the heat of immersion in nonpolar solvents showed less variation than that in water [279], it indicated a partial perturbation of the graphitic structure on the surface by the oxidation process. On the other hand, the heat of immersion in water increased linearly with the surface oxygen level, indicating that the polarity of the carbon black surface increased due to the formation of oxygen functionalities on the surface.

Analysis of the enthalpy of immersion in water can also lead to information about the number of primary adsorption centers of activated carbons and oxygenated surface groups. The relationship between these two quantities was proposed by Stoeckli and co-workers [281]:

$$\Delta H_i (\text{J/g}) = -25.0 (\text{J/mmol H}_2\text{O}) a_0 - 0.6 (\text{J/mmol H}_2\text{O}) (a_s - a_0) \quad (2.3)$$

where ΔH_i , a_0 , and a_s are the enthalpy of immersion, number of primary adsorption centers, and limiting amount adsorbed, respectively. Using this approach, one can analyze the changes in the degree of carbon oxidation [281,282].

The enthalpies of immersion of carbon materials into water were correlated with specific and nonspecific interactions between the liquid and the carbon surface [273,276–279,281]. It was found that the acidic heat values increase rapidly with the total oxygen content (Figure 2.14), while the basic heat values decrease.

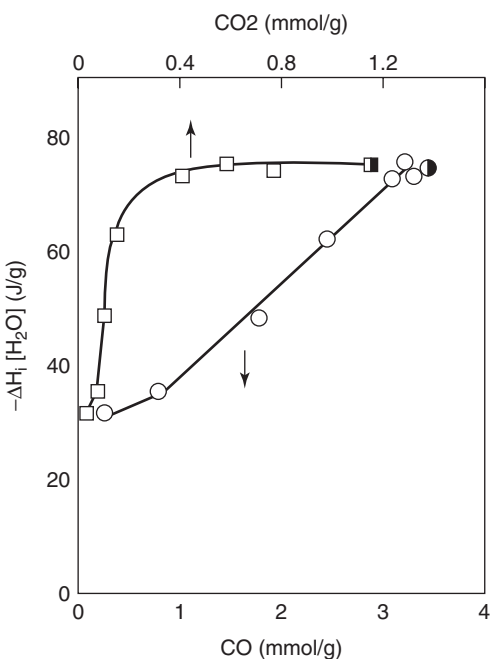


Figure 2.14 Evolution of the enthalpies of immersion in water as a function of CO and CO₂ groups. Half-filled symbols, oxidized carbon H110; open symbols, heat-treated oxidized carbon. (From ref. 272, with permission. Copyright © 1997 American Chemical Society.)

The latter were not affected by the specific structure to which an oxygen atom was incorporated, due to the fact that basic sites are associated with the carbon itself [277]. For carbons with low oxygen contents, the enthalpy of neutralization of basic sites was higher than that for acidic sites, suggesting the coexistence of basic oxygen groups (chromene-, pyrone-, and quinone-type structures, of basic character) with the π -electron-rich regions on the basal planes of the graphitic microcrystals. On the other hand, for a nonpolar liquid such as benzene, the enthalpies of immersion remained unaffected by changes in the content of oxygen functional groups of the carbon surface [275,283].

The surface chemistry of carbon was also evaluated using heats of immersion in alcohols [284–287]. The immersion heats of the carbon blacks into ethanol and *n*-butanol increased linearly with an increase in the content of active hydrogen on the surface. The interactions of the active hydrogen sites with the alcohol molecules were proposed to be electrostatic and hydrogen bonding in type [285]. In the case of water, dissociation–hydration reactions are also involved. The analysis of the heats of adsorption of the homologs of normal alcohol and fatty acid from aqueous solution on activated carbons lead Hukao and co-workers

[284] to conclude the existence of two type of sites with different adsorption energies on the surface of activated carbons.

Despite the fact that when using calorimetry it is only possible to estimate the hydrophobic or hydrophilic character of carbon, useful information about surface chemistry that could be complemented by other techniques is provided.

2.4.6 Inverse Gas Chromatography

Inverse gas chromatography (IGC) is a rapid and reliable method used to evaluate the acid–base character of activated carbon surfaces. This method employs physical adsorption of appropriate molecular probes in a chromatographic (dynamic) experiment [288]. The amounts of solutes injected are very small, and it is assumed that the adsorption is described by Henry's law. From the retention volume the free energy of adsorption, ΔG° , is calculated as follows:

$$\Delta G^\circ = -RT \ln \frac{V_N}{mS} + C \quad (2.4)$$

where R is a gas constant T the temperature in kelvins, V_N represents the retention volume, m and S are the mass and specific surface area of the adsorbent, and C is a constant related to the standard state of gas and adsorbed phases.

When saturated and unsaturated hydrocarbons are used as the probe molecules, the value of the difference in the ΔG_{CH_2} of alkane and alkene is used to study the effect of the π -bond interactions with electron acceptor sites on the surface [203,288–290]. ΔG_{CH_2} is defined as

$$\Delta G_{\text{CH}_2} = \Delta G_N^\circ - \Delta G_{N-1}^\circ \quad (2.5)$$

where N represents the number of carbon atoms in a hydrocarbon molecule. The difference in free energy, called the parameter of specific interactions, ε_π , represents the average number and strength of the acidic centers present on the carbon surface [319,320]. The more positive (the less negative) it is, the more acidic is the surface of the carbon.

$$\varepsilon_\pi = \Delta G_{\text{CH}_2\text{alkane}} - \Delta G_{\text{CH}_2\text{alkene}} \quad (2.6)$$

This approach was used to characterize carbons [203,215,290]. The results showed good correlation with the data obtained using the Boehm titration method (Figure 2.15). The advantage of the IGC approach is that it provides information about acidity in a nonaqueous environment, and the results are obtained in a rapid and reproducible way.

2.4.7 Temperature-Programmed Desorption

Temperature-programmed desorption (TPD) involves heating carbon in a carrier gas at a programmed heating rate to induce thermal desorption of adsorbed species from the surface. The desorbed gaseous products are analyzed by mass and IR

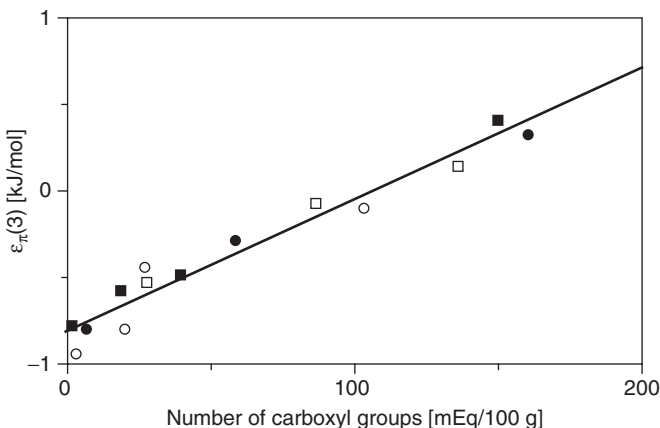


Figure 2.15 Dependence of ϵ_{π} . versus total number of acidic groups for different carbons. (From ref. 81, with permission. Copyright © 1992 American Chemical Society.)

spectroscopy, gas chromatography, or gravimetric analysis. The deconvolution of thermal desorption profiles [241] (concerning the number of peaks and the temperature of desorption) provides information on the types of species desorbed from the carbon surface, from the decomposition of surface functionalities, and on the nature of interactions of the gaseous species and carbon.

While being heated, the surface functionalities chemically bonded to carbons decompose, releasing various gaseous compounds at different temperatures. The dominant gases evolved during thermal desorption are oxides. Generally speaking, oxygen-containing functional groups decompose mostly as CO, CO₂, and H₂O, while nitrogen functionalities also release NO. The amount of oxygen evolved as oxides is usually consistent with the values obtained by ultimate analysis of the carbon materials [241]. TPD peaks are assigned to specific surface groups; however, the peak temperatures may be affected by the texture of the material, the heating rate, and the geometry of the experimental system used [291,292].

Studies of surface chemistry of carbons using TPD are quite common in the literature [291–300]. The important aspect is determination of surface groups based on their decomposition temperature [291,298]. Complexes yielding CO₂ groups decompose at two different temperatures, invoking two types of chemically or energetically different entities. Carboxylic acids are proposed to be predominantly responsible for the low-temperature peak (648 K), and the high-temperature CO₂ evolution (898 K) is attributed to carboxylic anhydrides and lactones. The CO-yielding groups are also represented by two distinct groups of peaks with CO evolution maxima at 898 and 1098 K, corresponding to phenols, ethers, and carbonyls structures. The peak of water release at low temperatures is generally attributed to the removal of physisorbed water. The one at high temperatures is assigned either to the evolution of water hydrogen-bonded to oxygen

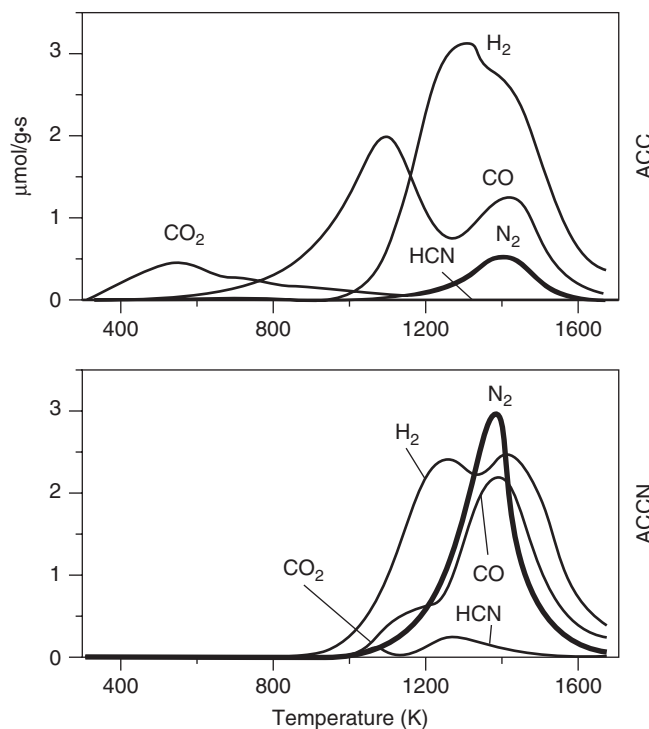


Figure 2.16 TPD profiles from 313 to 1673 L at 30 K/min obtained for the untreated and ammonia treated activated carbon cloth. (From ref. 300, with permission from Elsevier.)

complexes, to condensation of any phenolic groups, or to dehydration reactions of neighboring carboxylic groups to give carboxyl anhydrides [296]. Using TPD measurements, it has also been reported that gas-phase oxidation of activated carbons increases mainly the concentration of hydroxyl and carbonyl surface groups, whereas oxidation in the liquid phase increases especially the concentration of carboxylic acids. Figure 2.16 shows the CO_2 -TPD profiles of several modified activated carbons. The different shapes of the profiles after modification indicate the formation of different functionalities.

When nitrogen-modified carbons are studied [245,291,299,300], the release of NO is from decomposition of nitrogen functional groups in carbon, which react with surface oxygen species. Mangun and co-workers analyzed the TPD profiles for several series of activated carbon fibers treated with ammonia [245]. The data revealed distinct peaks related to decomposition of a nitrogen-containing group. The profiles obtained suggested the presence of pyridine groups, imine-type structures, linear and cyclic amide functionalities, and nitrile groups.

The presence of sulfur-containing functionalities on carbon surfaces was investigated by Terzyk and co-workers [12]. They identified three main groups formed

on a carbon surface modified with fuming sulfuric acid. The first peak, in the range 573 to 613 K, was attributed to a SH group since the products of decomposition of thiol groups can recombine with surface oxygen. The second peak, centered around 633 K, was assigned to sulfonic acids and sulfoxides and/or sulfone, and the third peak, at around 698 K, was assumed to represent surface sulfides (C–S–C). A small peak at around 973 K was linked to the formation of surface sulfides as a result of the decomposition of surface thiols of the carbon [12].

2.4.8 Characterization of Surface Functionalities by Electrochemical Techniques

Linear-sweep voltammetry and polarography are used to describe the surface of carbon materials. Despite the fact that these techniques do not provide comprehensive information about the type of surface groups, good agreement was reported with the conventional techniques used in the identification of surface functionalities [301–303]. Cyclic voltammograms of carbon blacks after heating at high temperatures and oxidation treatments showed clear evidence of the presence of redox couples on their surfaces [304]. After oxidation, an increase was observed in both the anodic and cathodic currents. The evidence of the presence of quinone groups as electrochemically active species on carbon blacks was provided by polarographic analysis [303,305]. An example of changes in the electrochemical behavior of carbons after various treatments is presented in Figure 2.17.

Quantitative as well as qualitative analysis can be done by means of voltammetry and polarography [305,306]. Kinoshita and co-workers attempted to quantify the quinone and hydroquinone groups detected by voltammetry on carbon blacks [304]. Although an excellent agreement with data available from TPD analysis was found, the authors remained skeptical, mentioning that such agreement can be coincidental, owing to the difficulties of linking the amount of surface oxide groups and the cyclic voltammograms results.

2.5 ROLE OF SURFACE CHEMISTRY IN THE REACTIVE ADSORPTION ON ACTIVATED CARBONS

Specific adsorption includes interactions stronger than those of dispersive, van der Waals type. They can be dipole–dipole, hydrogen bonding, acid–base interactions, complexation, or others. To imcompose these interactions, a carbon surface has to be modified by introduction of various oxygen [51,53,69]–, nitrogen [99,103,105]–, sulfur [101,117]–, phosphorus [143,145,146]–, or halogen [147,185,186]–containing groups, or various inorganic impregnates [307]. Although the presence of these species does not necessarily lead to a chemical reaction on the surface, they certainly affect the efficiency of physical adsorption. Examples are adsorption of water or alcohols, which is greatly

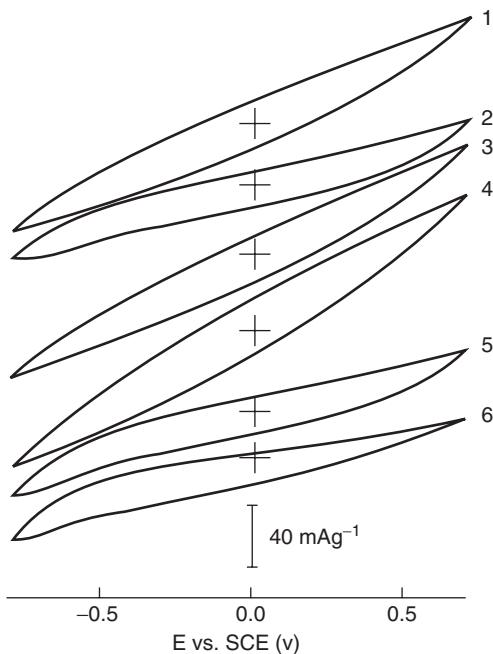


Figure 2.17 Cyclic voltammograms of studied carbon electrodes materials recorded in base ($0.1\text{ M NaNO}_3 + \text{HNO}_3$) solution (pH 1.33). 1, AW (initial sample); 2, HTW (heated at 1173 K); 3, HTA (heated at ammonia at 1173 K); 4, OPA (heated at 1 : 1 oxygen ammonia at 673 K); 5, OWA (oxidized with moist air at 673 K); 6, ONA (oxidized with concentrated nitric acid at 353 K). Sweep rate = 0.003 V/s. (From ref. 302, with permission from Elsevier.)

enhanced by the presence of species on the carbon surface, which otherwise is hydrophobic in its nature [308–310]

Adsorption of small organic molecules containing functional groups is also affected by carbon surface chemistry. The specific studies were done on adsorption of numerous pollutants, such as phenols and their derivatives [16,311–315], carboxylic acids [14,62,63], amines [316–318], alcohols [319–321], and others [322]. In all cases the surface chemistry was established to affect the adsorption process. In the case of phenols, however, some evidence of surface reactions with functional groups was found [16]. It is generally accepted that the presence of functional groups impedes adsorption of phenols, creating obstacles for their favorite positions on the carbon surface. For other polar molecules, functional groups containing either oxygen or nitrogen were found interacting favorably with the adsorbate, depending on its chemistry. Thus, surface basic groups increase the adsorption of organic acids at low relative pressure [23], whereas adsorption of bases such as amines is enhanced by the presence of acids [317].

Another well-known system where surface chemistry was found crucial for removal of pollutants is adsorption of sulfur dioxide. Besides having a certain distribution of pore sizes, carbons for this purpose should be rich in surface basic groups [323–325]. They are able to specifically attract sulfur dioxide molecules and thus increase the total capacity of carbons for their removal.

The surface chemistry of carbon is also crucial in the ink jet industry, where various functional groups are introduced to the surface of carbon blacks to increase adhesion to different types of paper surfaces via the specific interactions mentioned above. It has also been found that carbon surface functional groups containing either oxygen or sulfur are very important for the desulfurization of liquid fuels. On them, thiophenic compounds are specifically adsorbed via hydrogen bonding. Moreover, it was proposed that strong acids on the carbon surface contribute to the formation of carbonium ions, which leads to oligmerization of dibenzothiophene and its deposition in the pore system [134,135]. For this type of desulfurization, transition metals such as copper and cobalt were also found important for the activation of oxygen or π -complexation.

Carbon functional groups were also found to be critical for the removal of ammonia [34]. When water is present in a system, carboxylic groups bound to ammonia as ammonium ions and in a dry environment, ammonia interactions are possible, with involvement of Lewis acidic centers. Moreover, hydrogen-bond interactions play a role in the immobilization of ammonia. Also, metals, when present in the form of chlorides, participate in the removal of this gas by providing acidic centers and taking part in complexation reactions [326]. When oxycations such as Keggin Al_{13} are introduced to the carbon surface, their Brønsted and Lewis acidity attract ammonia significantly and increase the strength of adsorption. An excellent review of the role of impregnants in reactive adsorption of warfare gases is presented elsewhere [307].

Functional groups are also important in the removal of transition metals from various environments [23,24]. They provide sites for cation-exchange reactions, which is the main mechanism by which those metals are retained on carbon surfaces. On the other hand, heavy metal removal is governed by the strong affinity of sulfur to form complexes with those species [130,132,160].

2.6 ROLE OF CARBON SURFACE CHEMISTRY IN CATALYSIS

The catalytic role of carbon surfaces has been discussed in excellent reviews by Leon y Leon and Radovic [53] and by Radovic and Rodriguez-Reinoso [43] and is discussed extensively throughout this book. In this section, examples of the specific catalytic effect of carbon surface functionality are introduced only briefly.

Besides providing high-energy adsorption sites for physical or specific adsorption, carbon, which consists of both small pores and functional groups, is able to catalyze surface reactions. A simple example is oxidation of sulfur dioxide where it was found that basic functional groups present on the surface of carbons

not only provide centers for specific physical adsorption but also contribute to SO₂ oxidation to H₂SO₄ [327,328].

A well-known example of a complex catalytic reaction that takes place on the surface of carbon is the oxidation of hydrogen sulfide [329,330]. When water is present on the carbon surface and the surface has the basic pH required for dissociation of H₂S, oxidation of the HS⁻ ions by active oxygen occurs either to elemental sulfur or sulfuric acid. The latter is formed when the reaction takes place in very small pores, where only sulfur radicals very susceptible for further oxidation to SO₃ are formed. Catalytic oxidation also occurs in the case of methyl mercaptan adsorption [331], where on basic carbon, thiolate ions formed as a result of dissociation are further oxidized to dimethyldisulfide strongly adsorbed in the pore system. In the case of desulfurization, inorganic constituents of carbon such as iron and calcium also play a crucial role. Those elements, present even in small amounts, contribute significantly to the oxidation reactions as catalysts [332,333].

Catalytic oxidation of hydrogen sulfide or methyl mercaptan is also enhanced in the presence of nitrogen-containing functionalities [57]. Besides providing the basic pH needed for effective dissociation of HS⁻, they were proposed to activate oxygen via formation of superoxide ion, which participates in the oxidation of thiolate ions to sulfur and sulfuric acid [95].

Another important catalytic reaction crucial for environmental remediation is reduction of NO_x. When activated carbons are used as removal media, the elimination process includes adsorption combined with either oxidation or reduction, with carbon acting as the reducing agent and perhaps even as a catalyst [332,333]. Oxidation usually leads to the formation of nitric acid, whereas N₂ is the product of NO_x reduction. It was found that surface chemistry affects NO removal performance, and an optimal amount of oxygen-functional groups on the surface of char is needed [334–337].

The production of “glyphosate” herbicide (Round-up), the world’s most successful herbicide, is another example of utilization of the catalytic properties of carbon surfaces [338]. The Monsanto process by which Round-up is produced uses activated carbon as an oxidation catalyst for one of the key synthesis steps. The catalyst is produced by the treatment of activated carbon with ammonia at a high temperature to impart the desired nitrogen functionality. These functionalities are also commercially important for the reduction of chloramine in potable (drinking) water. Since water utilities are increasingly using chloramine rather than chlorine for water disinfection, and standard activated carbon products are not effective for removal of residual chloramine (which, for example, is highly toxic to dialysis patients), a catalytic carbon must be used to reduce its content [339,340].

The main applications of the carbon support include hydrogenation reactions (Pd/C, Pt/C, Pt–Fe/C, Fe–Ru/C, Fe–Co/C, Ni/C/Co/C), oxidation reactions (Sn/C, Ni/C), and environmental automotive catalysis (Cu/C, Cu–Cr/C) [341]. The examples of carbons working as catalyst supports are discussed in the following chapters. The best known examples are whetlerites used for military filters

[307,341], caustics [342], oxidant- or copper-impregnated carbons for desulfurization [343], and transition-metal-impregnated carbons for removal of HCN [344] and reduction of nitric oxides [331,345].

REFERENCES

- [1] D. Lozano-Castelló, D. Cazorla-Amorós, A. Linares-Solano, S. Shiraishi, H. Kurihara, A. Oya, *Carbon* 41 (2003) 1765.
- [2] D. Qu, *J. Power Sources* 109 (2002) 4.
- [3] Y.R. Nian, H. Teng, *J. Electroanal. Chem.* 540 (2003) 119.
- [4] F. Béguin, F. Chevallier, C. Vixb, S. Saadallahb, J.N. Rouzaud, E. Frackowiak, *J. Phys. Chem. Solids* 65 (2004) 211.
- [5] E. Frackowiak, *Fuel* 77 (1998) 571.
- [6] E. Frackowiak, F. Béguin, *Carbon* 39 (2001) 937.
- [7] E. Frackowiak, F. Béguin, *Carbon* 40 (2002) 1775.
- [8] M. Volpe, F. Cleri, *Chem. Phys. Lett.* 371 (2003) 476.
- [9] A. Alfarra, E. Frackowiak, F. Béguin, *Electrochim. Acta* 47 (2002) 1545.
- [10] C. Moreno-Castilla, *Carbon* 42 (2004) 83.
- [11] A.A.M. Daifullah, B.S. Grgis, *Colloids Surf. A* 214 (2003) 181.
- [12] A.P. Terzyk, *J. Colloid Interface Sci.* 268 (2003) 301.
- [13] A.P. Terzyk, *J. Colloid Interface Sci.* 275 (2004) 9.
- [14] Y. El-Sayed, T.J. Bandosz, *J. Colloid Interface Sci.* 273 (2004) 64.
- [15] T. Garcia, R. Murillo, D. Cazorla-Amorós, A.M. Mastral, A. Linares-Solano, *Carbon* 42 (2004) 1683.
- [16] I.I. Salame T.J. Bandosz, *J. Colloid Interface Sci.* 264 (2003) 307.
- [17] N. Adhoum, L. Monser, *Sep. Purif. Technol.* 38 (2004) 233.
- [18] P.C.C. Faria, J.J.M. Orfao, M.F.R. Pereira, *Water Res.* 38 (2004) 2043.
- [19] A.M. Puziy, O.I. Poddubnaya, V.N. Zaitsev, O.P. Konoplytsk, *Appl. Surf. Sci.* 221 (2004) 421.
- [20] A. Alfarra, E. Frackowiak, F. Béguin, *Appl. Surf. Sci.* 228 (2004) 84.
- [21] J.P. Chen, S. Wu, K.H. Chong, *Carbon* 41 (2003) 1979.
- [22] S. Babel, T.A. Kurniawan, *Chemosphere* 54 (2004) 951.
- [23] I. Bautista-Toledo, J. Rivera-Utrilla, M.A. Ferro-Garcia, C. Moreno-Castilla, *Carbon*, 32 (1994) 93.
- [24] L. Monser, N. Adhoum, *Sep. Purif. Technol.* 26 (2002) 137.
- [25] A.P. Terzyk, G. Rychlicki, *Colloids Surf. A* 163 (2000) 135.
- [26] A.P. Terzyk, *Colloids Surf. A* 177 (2001) 23.
- [27] A.P. Terzyk, *J. Colloid Interface Sci.* 272 (2004) 59.
- [28] I. Salame, T.J. Bandosz, *Langmuir* 16 (2000) 5435.
- [29] I. Salame, T.J. Bandosz, *J. Colloid Interface Sci.* 210 (1999) 367.
- [30] J.K. Brennan, T.J. Bandosz, K.T. Thomson, K.E. Gubbins, *Colloids Surf. A* 187–188 (2001) 539.

- [31] Y. Elsayed, T.J. Bandosz, *Phys. Chem. Chem. Phys.* 5 (2003) 4892.
- [32] Y. Elsayed, T.J. Bandosz, *J. Colloid Interface Sci.* 242 (2001) 44.
- [33] T.J. Bandosz, *J. Colloid Interface Sci.* 246 (2002) 1.
- [34] L.-M. Le Leuch, T.J. Bandosz, *Carbon* 45 (2007) 568.
- [35] H.H. Huang, M.C. Lu, J.N. Chen, C.T. Lee, *Chemosphere* 51 (2003) 935.
- [36] G. de la Puente, A. Centeno, A. Gil, P. Grange, *J. Colloid Interface Sci.* 202 (1998) 155.
- [37] M.A. Fraga, M.J. Mendes, E. Jordão, *J. Mol. Catal. A* 179 (2002) 243.
- [38] A. Calafat, J. Laine, A. Lopez-Agudo, J.M. Palacios, *J. Catal.* 162 (1996) 20.
- [39] C. Moreno-Castilla, A.F. Pérez-Cadenas, F.J. Maldonado-Hódar, F. Carrasco-Marín, J.L.G. Fierro, *Carbon*, 41 (2003) 1157.
- [40] H. Teng, Y.F. Hsu, Y.T. Tu, *Appl. Catal. B* 20 (1999) 145.
- [41] C. Aguilar, R. Garcia, G. Soto-Garrido, R. Arriaga, *Appl. Catal. B* 46 (2003) 229.
- [42] S. Biniak, A. Swiatkowski, M. Pakula, in L.R. Radovic, P.A. Thrower, Eds., *Chemistry and Physics of Carbon*, Vol. 27, Marcel Dekker, New York, 2000, p. 125.
- [43] L.R. Radovic, F. Rodríguez-Reinoso, in P.A. Thrower, Ed., *Chemistry and Physics of Carbon*, Vol. 25, Marcel Dekker, New York, 1996, p. 243.
- [44] K. Kaneko, N. Fukuzaki, K. Kakei, T. Suzuki, S. Ozeki, *Langmuir* 5 (1989) 960.
- [45] J. Imai, M. Souma, S. Ozeki, T. Suzuki, K. Kaneko, *J. Phys. Chem.* 95 (1991) 9955.
- [46] X. Yang, Y. Makita, Z.-H. Liu, K. Ooi, *Chem. Mater.* 15 (2003) 1228.
- [47] K. Morishige, T. Hamada, *Langmuir* 21 (2005) 6277.
- [48] W. Wasel, K. Kuwana, P.T.A. Reilly, K. Saito, *Carbon* 45 (2007) 833.
- [49] J.L. Tirado, R. Santamaría, G.F. Ortiz, R. Menéndez, P. Lavela, J.M. Jiménez-Mateos, F.J. Gómez García, A. Concheso, R. Alcántara, *Carbon* 45 (2007) 1396.
- [50] L. Xu, J. Liu, J. Du, Y. Peng, Y. Qian, *Carbon* 43 (2005) 1560.
- [51] H.P. Boehm, in D.D. Eley, H. Pines, P.B. Weisz, Eds., *Advances in Catalysis*, Vol. 16, Academic Press, New York, 1966, p. 179.
- [52] B.R. Puri, in P.L. Walker, Ed., *Chemistry and Physics of Carbon*, Vol. 6, Marcel Dekker, New York, 1970, p. 191.
- [53] C.A. Leon y Leon, L.R. Radovic, in P.A. Thrower, Ed., *Chemistry and Physics of Carbon*, Vol. 24, Marcel Dekker, New York, 1990, p. 212.
- [54] T.J. Bandosz, C.O. Ania, in T.J. Bandosz, Ed. *Activated Carbon Surfaces in Environmental Remediation*, Elsevier, Oxford, UK, 2006, p. 159.
- [55] V.V. Strelko, V.S. Kuts, P.A. Thrower, *Carbon* 38 (2000) 1499.
- [56] Y. Elsayed, T.J. Bandosz, *Langmuir* 21 (2005) 1282.
- [57] A. Bagreev, J.A. Menéndez, I. Dukhno, Y. Tarasenko, T.J. Bandosz, *Carbon* 43 (2005) 208.
- [58] M. Seredych, T.J. Bandosz, *Chem. Eng. J. Environ.* 128 (2007) 59.
- [59] K. Kinoshita, *Carbon: Electrochemical and Physicochemical Properties*, Wiley-Interscience, New York, 1988.
- [60] R.C. Bansal, J.B. Donnet, F. Stoeckli, *Active Carbon*, Marcel Dekker, New York, 1988.
- [61] D. Rivin, *Rubber Chem. Technol.* 44 (1971) 307.

- [62] J.S. Mattson, H.B. Mark, Jr., *Activated Carbon: Surface Chemistry and Adsorption from Solution*, Marcel Dekker, New York, 1971.
- [63] H.P. Boehm, *Carbon* 32 (1999) 759.
- [64] T.J. Bandosz, M.J. Biggs, K.E. Gubbins, Y. Hattori, Y. Liyama, K. Kaneko, J. Pikunic, K.T. Thomson, in L.R. Radovic, P.A. Thrower, Eds., *Chemistry and Physics of Carbon*, Vol. 28, Marcel Dekker, New York, 2001, p. 41.
- [65] G.R. Henning, in P.L. Walker, Ed., *Chemistry and Physics of Carbon*, Vol. 2, Marcel Dekker, New York, 1966, p. 149.
- [66] J.M. Thomas, in P.L. Walker, Ed., *Chemistry and Physics of Carbon*, Vol. 1, Marcel Dekker, New York, 1965, p. 121.
- [67] R.T. Yang, in P.A. Thrower, Ed., *Chemistry and Physics of Carbon*, Vol. 19, Marcel Dekker, New York, 1984, p. 163.
- [68] P.L. Walker, Jr., R.G. Jenkins, *Fuel* 62 (1983) 849.
- [69] C.A. Leon y Leon, Ph.D. dissertation, The Pennsylvania State University, 1993.
- [70] J.D. Roberts, M.C. Caserio, *Basic Principles of Organic Chemistry*, W.A. Benjamin, New York, 1965, p. 507.
- [71] T. De Saussure, *Gilberst Ann.* 47 (1814) 113.
- [72] A. Smith, *Proc. R. Soc. London A* 12 (1863) 424.
- [73] F. Bartell, E. Miller, *J. Am. Chem. Soc.* 44 (1922) 1866.
- [74] V.A. Garten, D.E. Weiss, *Aust. J. Chem.* 10 (1957) 309.
- [75] V.A. Garten, D.E. Weiss, *Rev. Pure Appl. Chem.* 7 (1957) 69.
- [76] V.A. Garten, D.E. Weiss, J.B. Willis, *Aust. J. Chem.* 10 (1957) 295.
- [77] J.P. Donnet, *Carbon* 6 (1968) 181.
- [78] J.S. Noh, J.A. Schwarz, *Carbon* 28 (1990) 675.
- [79] J.M. Solar, F.J. Derbyshire, V.H.J. de Beer, L.R. Radovic, *J. Catal.* 129 (1991) 330.
- [80] C. Moreno-Castilla, M.V. López-Ramón, F. Carrasco-Marín, *Carbon* 38 (2000) 1995.
- [81] T.J. Bandosz, J. Jagiello, J.A. Schwarz, *Anal. Chem.* 64 (1992) 891.
- [82] I. Salame, T.J. Bandosz, *J. Colloid Interface Sci.* 240 (2001) 252.
- [83] J.A. Menéndez, L.R. Radovic, B. Xia, J. Phillips, *J. Phys. Chem.* 100 (1996) 17243.
- [84] J.A. Menéndez, J. Phillips, B. Xia, L.R. Radovic, *Langmuir* 12 (1996) 4404.
- [85] A. Contescu, C. Contescu, K. Putyera, J.A. Schwarz, *Carbon* 35 (1997) 83.
- [86] B. Steenberg, *Adsorption and Exchange of Ions on Activated Charcoal*, Almqvist & Wiksell, Uppsala, Sweden, 1944, p. 59.
- [87] C.A. Leon-Leon, J.M. Solar, V. Calemma, L.R. Radovic, *Carbon* 30 (1992) 797.
- [88] J.A. Menéndez, M.J. Illan-Gomez, C.A. Leon-Leon, L.R. Radovic, *Carbon* 33 (1995) 1655.
- [89] E. Fuente, J.A. Menéndez, D. Suarez, M.A. Montes-Morán, *Langmuir* 19 (2003) 3505.
- [90] M.A. Montes-Morán, D. Suarez, J.A. Menéndez, E. Fuente, *Carbon* 42 (2004) 1219.
- [91] M.A. Montes-Morán, J.A. Menéndez, E. Fuente, D. Suarez, *J. Phys. Chem. B* 102 (1998) 5595.

- [92] E. Papirer, S. Li, J.B. Donnet, *Carbon* 25 (1987) 243.
- [93] H.P. Boehm, M. Voll, *Carbon* 8 (1970) 227.
- [94] R. Matzner, H.P. Boehm, *Carbon* 36 (1998) 1697.
- [95] F. Adib, A. Bagreev, T.J. Bandosz, *Langmuir* 16 (2000) 1980.
- [96] A. Bagreev, S. Bashkova, T.J. Bandosz, *Langmuir* 18 (2002) 1257.
- [97] I. Mochida, Y. Korai, M. Shirahama, S. Kawano, T. Hada, Y. Seo, M. Yoshikawa, A. Yasutake, *Carbon* 38 (2000) 227.
- [98] Y. Elsayed, T.J. Bandosz, *Langmuir* 18 (2002) 3213.
- [99] A. Bagreev, J.A. Menéndez, I. Dukhno, Y. Tarasenko, T.J. Bandosz, *Carbon* 42 (2004) 469.
- [100] A. Stohr, H.P. Boehm, R. Schlögl, *Carbon* 29 (1991) 707.
- [101] R.J.J. Jansen, H. Bekkum, *Carbon* 33 (1995) 1021.
- [102] R.J.J. Jansen, H. Bekkum, *Carbon* 32 (1994) 1507.
- [103] F. Kapteijn, J.A. Moulijn, S. Matzner, H.P. Boehm, *Carbon* 37 (1999) 1143.
- [104] J.R. Pels, Ph.D. dissertation, Delft University of Technology, The Netherlands (1995).
- [105] S. Biniak, G. Szymanski, J. Siedlewski, A. Swiatkowski, *Carbon* 35 (1997) 1799.
- [106] J. Lahaye, G. Nanse, A. Bagreev, V. Strelko, *Carbon* 37 (1999) 585.
- [107] K. Kaneko, T. Suzuki, Y. Fujiwara, K. Nishikawa, in F. Rodríguez-Reinoso et al., Eds., *Characterization of Porous Solids*, Vol. II, Elsevier, Amsterdam, 1991, p. 389.
- [108] Y. Tomastubara, S. Ida, H. Fujitsu, H. Mochida, *Fuel* 63 (1984) 1738.
- [109] R.C. Bansal, F.J. Vastola, P.L. Walker, *Carbon* 12 (1974) 355.
- [110] R.M. Barrer, *J. Chem. Soc.* 2 (1936) 1256.
- [111] P. Redmon, P.L. Walker, *J. Phys. Chem.* 64 (1974) 355.
- [112] M.L. Studebaker, *Rubber Chem. Technol.* 30 (1957) 1401.
- [113] J.P. Redmond, P.L. Walker, *J. Phys. Chem.* 64 (1960) 1093.
- [114] N. Smith, J. Duffield, R.A. Pierottir, J. Mooi, *J. Phys. Chem.* 60 (1956) 495.
- [115] R.C. Bansal, T.L. Dhami, S. Parkash, *Carbon*, 15 (1977) 157.
- [116] R.N. Smith, G. Pierce, C.D. Joel, *J. Phys. Chem.* 58 (1954) 298.
- [117] B.R. Puri, B. Kuar, D.D. Singh, *J. Sci. Ind. Res.* 200 (1961) 366.
- [118] J. Biscoe, B.E. Warren, *J. Appl. Phys.* 13 (1942) 364.
- [119] A.A. Fokin, P.R. Schreiner, *Adv. Synth. Catal.* 345 (2003) 1035.
- [120] T.R. Cundari, S. Vaddadi, *Inorg. Chim. Acta* 357 (2004) 2863.
- [121] B.R. Puri, C.M. Jain, R.S. Hazra, *J. Indian Chem. Soc.* 43 (1966) 554.
- [122] W. Feng, E. Borguet, R.D. Vidic, *Carbon* 44 (2006) 2990.
- [123] W. Feng, E. Borguet, R.D. Vidic, *Carbon* 44 (2006) 2998.
- [124] J.P. Wibaut, *Recl. Trav. Chim.* 38 (1919) 159.
- [125] J.P. Wibaut, *Recl. Trav. Chim.* 41 (1922) 153.
- [126] C.H. Chang, *Carbon* 19 (1081) 175.
- [127] R. Juza, W. Blanze, *Z. Anorg. Allg. Chem.* 210 (1933) 81.
- [128] B.R. Puri, A.K. Balwar, R.S. Hazra, *J. Indian Chem. Soc.* 44 (1967) 975.
- [129] B.R. Puri, C.M. Jain, R.S. Hazra, *J. Indian Chem. Soc.* 43 (1966) 67.

- [130] A. Macías-Garcia, V. Gómez-Serrano, M.F. Alexandre-Franco, C. Valenzuela-Calahorro, *J. Hazard. Mater. B* 103 (2003) 141.
- [131] K.A. Krishnan, T.S. Anirudhan, *J. Hazard. Mater. B* 92 (2002) 161.
- [132] A. Macías-Garcia, C. Valenzuela-Calahorro, A. Espinosa-Mansilla, A. Bernalte-Garcia, V. Gómez-Serrano, *Carbon* 42 (2004) 1755.
- [133] C. Song, *Catal. Today* 86 (2003) 211.
- [134] C.O. Ania, T.J. Bandosz, *Langmuir* 21 (2005) 7752.
- [135] C.O. Ania, T.J. Bandosz, *Carbon* 44 (2006) 2404.
- [136] T. DohI, M. Asano, S. Margari, *Tanso* 57 (1969) 192.
- [137] J.F. Rakiszawski, W.E. Parker, *Carbon* 2 (1964) 53.
- [138] D.W. McKee, C.L. Spiro, E.J. Lamby, *Carbon* 22 (1984) 285.
- [139] M. Molina-Sabio, F. Rodríguez-Reinoso, F. Catarla, M.J. Selles, *Carbon* 33 (1995) 1105.
- [140] M.S. Solum, R.J. Pugmire, M. Jagtoyen, F. Derbyshire, *Carbon* 33 (1995) 1247.
- [141] C. Toles, S. Rimmer, J.C. Hower, *Carbon* 34 (1996) 1419.
- [142] S. Marinkovic, in P.A. Thrower, Ed., *Chemistry and Physics of Carbon*, Vol. 19, Marcel Dekker, New York, 1984, p. 1.
- [143] S. Bourginot, M. Le Bras, R. Delobel, P. Breant, J.M. Tremillon, *Carbon* 33 (1995) 283.
- [144] M. Jagtoyen, F. Derbyshire, *Carbon* 36 (1998) 1085.
- [145] R. Imamura, K. Matsui, S. Takeda, J. Ozaki, A. Oya, *Carbon* 37 (1999) 261.
- [146] D. Rivin, J. Aron, *Carbon* 3 (1965) 358.
- [147] B.R. Puri, S.L. Malhotra, R.C. Basal, *J. Indian Chem. Soc.* 40 (1963) 179.
- [148] H. Tobias, A. Soffer, *Carbon* 23 (1985) 281.
- [149] B.R. Puri, S.S. Tulsi, R.C. Basal, *J. Indian Chem. Soc.* 4 (1966) 7.
- [150] P.H. Emmet, *Chem. Rev.* 43 (1948) 69.
- [151] F.J. Pinchin, *Fuel* 37 (1958) 293.
- [152] H.P. Boehm, U. Hoffmann, A. Clauss, in *Proceedings of the 3rd Conference on Carbon*, Buffalo, NY, 1957, Pergamon Press, New York, 1959, p. 241.
- [153] B.R. Puri, R.C. Bansal, *Carbon* 3 (1966) 533.
- [154] B.R. Puri, N.K. Sandle, O.P. Mahajan, *J. Chem. Soc.* (1963) 4480.
- [155] B.R. Puri, K.C. Kehgal, *Indian J. Chem.* 4 (1966) 206.
- [156] P. Connor, J.B. Lewis, W.J. Thomas, in *Proceedings of the 5th Conference on Carbon*, Penn State University, 1961, Vol. I, Pergamon Press, New York, 1962, p. 120.
- [157] A. Hill, H. Marsh, *Carbon* 6 (1966) 31.
- [158] B.R. Puri, R.C. Bansal, *Carbon* 3 (1965) 227.
- [159] H. Zeng, F. Jin, J. Guo, *Fuel* 83 (2004) 143.
- [160] C.M. Yang, K. Kaneko, *J. Colloid Interface Sci.* 246 (2002) 34.
- [161] M. Futamata, X. Gai, H. Itoh, *Vacuum* 73 (2004) 519.
- [162] T. Robertson, *Thin Solid Film* 383 (2001) 81.
- [163] J. Günther, J. Reschke, *Surf. Coat. Tech.* 60 (1993) 531.

- [164] L. Valentini, V. Salerni, I. Armentano, J.M. Kenny, L. Lozzi, S. Santucci, *J. Non-Cryst. Solids* 321 (2003) 175.
- [165] F.L. Freire, Jr., *J. Non-Cryst. Solids* 304 (2002) 251.
- [166] V. Tainen, *Diamonds Relat. Mater.* 10 (2001) 153.
- [167] A. Lamperti, P.M. Ossi, *Appl. Surf. Sci.* 205 (2003) 113.
- [168] P. Ayala, M.E.H. Maia da Costa, R. Prioli, F.L. Freire, Jr., *Surf. Coat. Tech.* 182 (2004) 335.
- [169] S.J. Park, M.K. Seo, Y.S. Lee, *Carbon* 41 (2003) 723.
- [170] L.G. Jacobsohn, M.E.H. Maia-da-Costa, V.J. Trava-Airoldi, F.L. Freire, Jr., *Diamond Relat. Mater.* 12 (2003) 2037.
- [171] C.E. Lowell, *J. Am. Ceram. Soc.* 50 (1967) 142.
- [172] T. Hagio, M. Nakamizo, K. Kobayashi, *Carbon* 27 (1989) 259.
- [173] M. Inagaki, T. Nakahashi, H. Konno, T. Sogabe, *Carbon* 35 (1997) 657.
- [174] L.E. Jones, P.A. Thrower, *Carbon* 28 (1990) 239.
- [175] Y. Hishiyama, Y. Kaburagi, K. Kobayashi, M. Inagaki, *Report 117-241-AS*, JSPS Committee 117, Tokyo, Japan, 1997.
- [176] C.T. Hach, L.E. Jones, C.E. Crossland, P.A. Thrower, *CAER Report 6*, Center for Applied Energy Research, University of Kentucky, Lexington, KY, 1995.
- [177] S. Seghi, B. Fabio, J. Economy, *Carbon* 42 (2004) 3043.
- [178] L.I. Schukin, M.V. Kornievich, R.S. Vartapetjan, S.I. Bezisko, *Carbon* 40 (2002) 2021.
- [179] Y.-L. Lee, H.-H. Kim, H. Hatori, *Carbon* 42 (2004) 1053.
- [180] M.A. Montes-Morán, A. Martínez-Alonso, J.M.D. Tascon, M.C. Pavia, C.A. Bernardo, *Carbon* 39 (2001) 1057.
- [181] M. Domingo-García, F.J. Lopez-Garzon, M. Perez-Mendoza, *Carbon* 38 (2000) 555.
- [182] N. Inagaki, K. Narushima, H. Hashimoto, K. Tamura, *Carbon* 45, (2007) 797.
- [183] H.E. Blayden, J.W. Patrick, *Carbon* 5 (1967) 533.
- [184] A. F. Pérez-Cadenas, F.J. Maldonado-Hódar, C. Moreno-Castilla, *Carbon* 41 (2003) 473.
- [185] E. Papirer, R. Lacroix, J.-B. Donnet, *Carbon* 33 (1995) 63.
- [186] H. Touhara, F. Okino, *Carbon* 38 (2000) 241.
- [187] H. Chang, B. Li, W. Li, H. Chen, *Fuel* 83 (2004) 679.
- [188] L.Y. Hsu, H. Teng, *Appl. Catal. B* 35 (2001) 21.
- [189] A. Linares-Solano, I. Martin-Gullon, C. Salinas-Martínez de Lecea, B. Serrano-Talavera, *Fuel* 79 (2000) 635.
- [190] C. Sentorun, H. Haykiri-Acma, S. Kucukbayrak, *Thermochim. Acta* 277 (1996) 65.
- [191] H. Haykiri-Acma, A. Ersoy-Mericboyu, S. Kucukbayrak, *Energy Conserv. Manage.* 42 (2001) 11.
- [192] G. Skodras, G.P. Sakellaropoulos, *Fuel Process. Technol.* 77–78 (2002) 151.
- [193] J. Graham, U.S. patent 6,858,192, 2005.
- [194] Z. Bodnar, T. Mallat, S. Szabo, J. Petro, in G. Poncelet, P.A. Jacobs, P. Grange, B. Delmon, Eds., *Preparation of Catalyst*, Vol. V, Elsevier, Amsterdam, 1991, 459.

- [195] C.N. Satterfield, *Heterogeneous Catalysis in Industrial Practice*, 2nd ed., McGraw-Hill, New York, 1991.
- [196] L. Daza, Mendioroz, S. Pajares, J.A., *Carbon* 24 (1986) 33.
- [197] A.J. Bridgewater, R. Burch, P.C.H. Mitchell, *J. Catal.* 78 (1982) 116.
- [198] G.M.K. Abotsi, A.W. Scaroni, F.J. Derbyshire, *Appl. Catal.* 37 (1988) 93.
- [199] B. Scheffer, P. Arnoldy, J.A. Moulijn, *J. Catal.* 112 (1988) 516.
- [200] S. Neffe, *Carbon* 25 (1987) 441.
- [201] Y. Matsumura, S. Hagiwara, H. Takahashi, *Carbon* 14 (1976) 163.
- [202] E. Papirer, E. Guyon, *Carbon* 16 (1978) 127.
- [203] J. Jagiello, T.J. Bandosz, J.A. Schwarz, *Carbon* 30 (1992) 63.
- [204] T.J. Bandosz, J. Jagiello, J.A. Schwarz, A. Krzyzanowski, *Langmuir* 12 (1996) 6480.
- [205] J.W. Hassler, *Activated Carbons*, Chemical Publishing Company, New York, 1963.
- [206] F. Adib, A. Bagreev, T.J. Bandosz, *J. Colloid Interface Sci.* 214 (1999) 407.
- [207] H.P. Boehm, *Carbon*, 40 (2002) 145.
- [208] P.H. Given, L.W. Hill, *Carbon* 7 (1969) 649.
- [209] K. Laszlo, K. Josepovits, E. Tombacz, *Anal. Sci.* 17 (2001) 1741.
- [210] T.J. Bandosz, J. Jagiello, C. Contescu, J.A. Schwarz, *Carbon* 31 (1993) 1193.
- [211] J. Jagiello, T.J. Bandosz, J.A. Schwarz, *Carbon* 32 (1994) 1026.
- [212] J. Jagiello, T.J. Bandosz, K. Putyera, J.A. Schwarz, *J. Colloid Interface Sci.* 172 (1995) 341.
- [213] W. Rudzinski, J. Jagiello, Y. Grillet, *J. Colloid Interface Sci.* 87 (1982) 478.
- [214] I.I. Salame, T.J. Bandosz, *J. Colloid Interface Sci.* 240 (2001) 252.
- [215] J. Jagiello, *Langmuir* 10 (1994) 2778.
- [216] G. Kortum, W. Vogel, K. Andrussow, *Dissociation Constants of Organic Acids in Aqueous Solutions*, Butterworth, London, 1961.
- [217] E.M. Perdue, J.H. Reuter, R.S. Parrish, *Geochim. Cosmochim. Acta* 48 (1984) 1257.
- [218] J. Bakauskas, F.S. Cannon, in *Proceedings of the International Carbon Conference*, Oviedo, Spain, 2003.
- [219] *Standard Test Method for pH of Activated Carbon*, ASTM D3838-80, ASTM International, West Conshohocken, PA, 1999.
- [220] *Standard Test Methods for Carbon Black-pH Value*, ASTM D1512-95, ASTM International, West Conshohocken, PA, 2000.
- [221] C.A. Leon-Leon, A.A. Lizzio, L.R. Radovic, in *Proceedings of the International Carbon Conference*, Paris, 1990.
- [222] M.O. Corapcioglu, C.P. Huang, *Carbon* 25 (1987) 569.
- [223] B.M. Babic, S.K. Milonjic, M.J. Polovina, B.V. Kaludierovic, *Carbon* 37 (1999) 477.
- [224] J.L.G. Cimadevilla, R. Alvarez, J.J. Pis, *Vib. Spectrosc.* 31 (2003) 133.
- [225] I.E. Nosyreva, R. Gruber, D. Cagniant, A. Krzton, J. Pajak, M.D. Stefanova, S. Grishchuk, *Fuel* 75 (1996) 1549.
- [226] F. Rositani, P.L. Antonucci, M. Minutoli, N. Giordano, A. Villari, *Carbon* 25 (1987) 325.

- [227] A. Koch, A. Krzton, G. Finqueneisel, O. Heintz, J.V. Waber, T. Zimny, *Fuel* 77 (1998) 563.
- [228] C. Moreno-Catilla, F. Carrasco-Marfn, A. Mueden, *Carbon* 35 (1997) 1619.
- [229] P.E. Fanning, M.A. Vannice, *Carbon* 31 (1993) 721.
- [230] A. Dandekar, R.T.K. Baker, M.A. Vannice, *Carbon* 36 (1998) 1821.
- [231] B. Buczek, S. Biniak, A. Swiatkowski, *Fuel* 78 (1999) 1443.
- [232] I.I. Salame, T.J. Bandosz, *Ind. Eng. Chem. Res.* 39 (2000) 301.
- [233] F. Adib, A. Bagrrev, T.J. Bandosz, *J. Colloid Interface Sci.* 216 (1999) 360.
- [234] S. Shin, J. Jang, S.H. Yoon, I. Mochida, *Carbon* 35 (1997) 1739.
- [235] J.M. Valente Nabais, P.J.M. Carrott, M.M.L. Ribeiro-Carrott, J.A. Menéndez, *Carbon* 42 (2004) 1315.
- [236] J. Zawadzki, *Carbon* 18 (1980) 281.
- [237] J. Zawadzki, *Carbon* 19 (1981) 19.
- [238] I.A. Breger, J.C. Chandler, *Anal. Chem.* 41 (1969) 506.
- [239] C.Q. Yang, J.R. Simms, *Fuel* 74 (1995) 543.
- [240] G. Socrates, *Infrared Characteristic Group Frequencies*, Wiley, Chichester, UK, 1994.
- [241] J.L. Figueiredo, M.F.R. Pereira, M.M.A. Freitas, J.J.M. Orfão, *Carbon* 37 (1999) 1379.
- [242] M. Benlahsen, M. Therasse, *Carbon* 42 (2004) 2255.
- [243] J. Zawadzki, in P. A. Thrower, Ed., *Chemistry and Physics of Carbon*, Vol. 21, Marcel Dekker, New York, 1989, p. 147.
- [244] J.-H. Zhou, Z.-J. Sui, J. Zhu, P. Li, D. Chen, Y.C. Dai, W.-K. Yuan, *Carbon* 45 (2007) 785.
- [245] C.L. Mangun, K.R. Benak, J. Economy, K.L. Foster, *Carbon* 39 (2001) 1809.
- [246] G. Lazar, I. Lazar, *J. Non-Cryst. Solids* 331 (2003) 70.
- [247] A. Proctor, P.M.A. Sherwood, *Carbon* 21 (1983) 357.
- [248] Y. Nakayama, F. Soeda, A. Ishitani, *Carbon* 28 (1990) 21.
- [249] T. Tahagaki, A. Ishitani, *Carbon* 22 (1984) 43.
- [250] J.R. Pels, F. Kapteijn, J.A. Moulijn, Q. Zhu, K.M. Thomas, *Carbon* 33 (1995) 1641.
- [251] R.H. Bradley, I. Sutherland, E. Sheng, *J. Colloid Interface Sci.* 179 (1996) 561.
- [252] H. Schmiers, J. Friebel, P. Streubel, R. Hese, R. Kopsel, *Carbon* 37 (1999) 1965.
- [253] C. Kozlowski, P.M.A. Sherwood, *Carbon* 24 (1986) 357.
- [254] P.G. Rouxhet, M.J. Genet, in N. Mozes, P.S. Handley, H.J. Busscher, P.G. Rouxhet, Eds., *Microbial Cell Surface Analysis: Structural and Physicochemical Methods*, VCH, New York, 1991, p. 175.
- [255] F. Rodríguez-Reinoso, *Carbon* 36 (1998) 159.
- [256] S.J. Park, M.K. Seo, Y.S. Lee, *Carbon*, 41 (2003) 723.
- [257] C.C. Liu, A.B. Walters, M.A. Vannice, *Carbon* 33 (1995) 1699.
- [258] S. Mrozowski, F. Andrews, in *Proceedings of the 4th Conference on Carbon*, Pergamon Press, New York, 1959, p. 129.
- [259] I.L. Spain, in P.L. Walker, Jr., P.A. Thrower, Eds., *Chemistry and Physics of Carbon*, Vol. 16, Marcel Dekker, New York, 1981, p. 119.

- [260] D.L. Suh, T.J. Park, S.K. Ihm, R. Ryoo, *J. Phys. Chem.* 95 (1991) 3767.
- [261] P.C. Wernett, J.W. Larsen, O. Yamada, H.J. Yue, *Energy Fuels* 4 (1990) 412.
- [262] C. Tsiao, R.E. Botto, *Energy Fuels* 5 (1991) 87.
- [263] P.A. Simonov, S.V. Filimonova, N.G. Kruykova, E.M. Moroz, V.A. Likhobov, T. Kuretzky, H.P. Boehm, *Carbon* 37 (1999) 591.
- [264] J.Z. Hu, M.S. Solum, C.M.V. Taylor, R.J. Pugmire, D.M. Grant, *Energy Fuels* 15 (2001) 14.
- [265] F. Haghseresht, G.Q. Lu, A.K. Whittaker, *Carbon* 37 (1999) 1491.
- [266] T. Shirasaki, A. Derre, M. Menetrier, A. Tressaud, S. Flandrois, *Carbon* 38 (2000) 1461.
- [267] E.W. Hagaman, D.K. Murray, G.D. DelCul, *Energy Fuels* 12 (1998) 399.
- [268] D. Hines, A. Bagreev, T.J. Bandosz, *Langmuir* 20 (2004) 3388.
- [269] A. Bagreev, T.J. Bandosz, unpublished results.
- [270] J.B. Donnet, D. Paulmier, H. Oulanti, T. Le Huu, *Carbon* 42 (2004) 2215.
- [271] C.O. Ania, T.J. Bandosz, *Energy Fuels* 20 (2006) 1076.
- [272] F. Rodríguez-Reinoso, M. Molina-Sabio, M.T. Gonzalez, *Langmuir* 13 (1997) 2345.
- [273] M.V. López-Ramón, F. Stoeckli, C. Moreno-Castilla, F. Carrasco-Marín, *Carbon* 37 (1999) 1215.
- [274] S.S. Barton, M.J.B. Evans, J.A.F. MacDonald, *Langmuir* 20 (1994) 4250.
- [275] M.V. López-Ramón, F. Stoeckli, C. Moreno-Castilla, F. Carrasco-Marín, *Carbon* 38 (2000) 825.
- [276] S.S. Barton, M.J.B. Evans, B.H. Harrison, *J. Colloid Interface Sci.* 45 (1973) 542.
- [277] F. Stoeckli, C. Moreno-Castilla, F. Carrasco-Marín, M.V. López-Ramón, *Carbon* 39 (2001) 2231.
- [278] S.S. Barton, M.J.B. Evans, E. Halliop, J.A.F. MacDonald, *Carbon* 35 (1997) 1361.
- [279] E. Sheng, I. Sutherland, R.H. Bradley, P.K. Freakley, *Mater. Chem. Phys.* 50 (1997) 25.
- [280] R.H. Bradley, R. Daley, F. Le Goff, *Carbon* 40 (2002) 1173.
- [281] H.F. Stoeckli, F. Krahenbuehl, D. Morel, *Carbon* 21 (1983) 589.
- [282] F. Rodríguez-Reinoso, M. Molina-Sabio, M.T. Gonzalez, *Langmuir* 13 (1997) 2354.
- [283] F. Stoeckli, A. Lavanchy, *Carbon* 38 (2000) 475.
- [284] K. Hukao, Y. Takeda, *Carbon* 29 (1991) 173.
- [285] G.J. Yung, J.J. Chessick, F.H. Healey, *J. Phys. Chem.* 60 (1956) 394.
- [286] S. Hagiwara, K. Tsutsumi, H. Takahashi, *Carbon* 19 (1981) 107.
- [287] J.M. Corkill, J.F. Goodman, J.R. Tate, *Trans. Faraday Soc.* 62 (1966) 979.
- [288] J.R. Conder, C.L. Young, *Physicochemical Measurement by Gas Chromatography*, Wiley, New York, 1979.
- [289] M. Sidqi, G. Ligner, J. Jagiello, H. Balard, E. Papirer, *Chromatographia* 28 (1989) 588.
- [290] J. Jagiello, T.J. Bandosz, J.A. Schwarz, *J. Colloid Interface Sci.* 151 (1992) 433.
- [291] Y. Otake, R.G. Jenkins, *Carbon* 31 (1993) 109.
- [292] Q.L. Zhuang, T. Kyotani, A. Tomita, *Energy Fuels* 8 (1994) 714.

- [293] Q.L. Zhuang, T. Kyotani, A. Tomita, *Carbon* 32 (1994) 539.
- [294] U. Zielke, K.J. Huttinger, W.P. Hoffman, *Carbon* 34 (1996) 983.
- [295] B. Marchon, J. Carrazza, H. Heinemann, G.A. Somorjai, *Carbon* 26 (1998) 507.
- [296] S. Haydar, C. Moreno-Castilla, M.A. Ferro-Garcia, F. Carrasco-Marín, J. Rivera-Utrilla, A. Perrard, J.P. Joly, *Carbon* 38 (2000) 1297.
- [297] G.S. Szymanski, Z. Karpinski, S. Biniak, A. Swiatkowski, *Carbon* 40 (2002) 2672.
- [298] E. Papirer, J. Bantzer, L. Sheng, J.B. Donnet, *Carbon* 29 (1991) 69.
- [299] Y.F. Jia, B. Xiao, K.M. Thomas, *Langmuir* 18 (2002) 470.
- [300] J.P. Boudou, *Carbon* 41 (2003) 1955.
- [301] M. Kikuchi, Y. Ikezawa, Takamura, *J. Electroanal. Chem.* 396 (1995) 451.
- [302] A. Swiatkowski, M. Pakula, S. Biniak, M. Walczyk, *Carbon* 42 (2004) 3057.
- [303] I.F. Jones, R.C. Kaye, *J. Electroanal. Chem.* 2 (1969) 213.
- [304] K. Kinoshita, J.A.S. Bett, *Carbon* 11 (1973) 403.
- [305] J.V. Hallum, H.V. Drushel, *J. Phys. Chem.* 62 (1958) 110.
- [306] D. Lowe, J.O. Williams, P.A. Attwood, R.J. Bird, B.D. McNicol, R.T. Short, *J. Chem. Soc. Faraday Trans.* 1 (1979) 2312.
- [307] P. Lodewyckx, in T.J. Bandosz, Ed., *Activated Carbon Surfaces in Environmental Remediation*, Elsevier, Amsterdam, 2006, pp. 475–528.
- [308] J.K. Brennan, T.J. Bandosz, K.T. Thomson, K.E. Gubbins, *Colloids Surf. A* 187–188 (2001) 539.
- [309] V.V. Turov, V.M. Gun'ko, R. Leboda, J. Skubiszewska-Zieba, D. Palijczuk, T.J. Bandosz, Tomaszewski, S. Zietek, *J. Colloid Interface Sci.* 253 (2002) 23.
- [310] M.M. Dubinin, V.V. Serpinsky, *Carbon* 19 (1981) 402.
- [311] C.O. Ania, J.B. Parra, J.J. Pis, *Adv. Sci. Technol.* 22 (2004) 1619.
- [312] C.H. Tessmer, R.D. Vidic, L.J. Uranowski, *J. Environ. Sci. Technol.* 31 (1997) 1872.
- [313] P. Magne, P.L. Walker, Jr., *Carbon* 24 (1986) 101.
- [314] V.L. Snoeyink, H.T. Hai, J.H. Johnson, J.F. Young, *Chemistry of Water Supply: Treatment and Distribution*, Ann Arbor Science, Ann Arbor, MI, 1974.
- [315] T. Karanfil, J.E. Kilduff, *Environ. Sci. Technol.* 33 (1999) 3217.
- [316] M. Perez-Mendoza, M. Domingo-Garcia, M., F. Lopez-Garzon, *Langmuir* 16 (2000) 7012.
- [317] Y. Elsayed, T.J. Bandosz, H. Wullens, P. Lodewyckx, *Ind. Chem. Eng. Res.* 45 (2006) 1441.
- [318] R.M. Dell, R.A. Beebe, *J. Phys. Chem.* 59 (1955) 754.
- [319] H. Naono, M. Hakuman, M. Shimoda, K. Mahai, S. Kondo, *J. Colloid. Interface Sci.* 18 (1996) 230.
- [320] S.S. Barton, M.J.B. Evans, J.A.F. MacDonald, *Carbon* 36 (1998) 969.
- [321] V. Gunko, T.J. Bandosz, *Phys. Chem. Chem. Phys.* 5 (2003) 2096.
- [322] I.I. Salame, T.J. Bandosz, *Mol. Phys.* 100 (2002) 2041.
- [323] P. Davini, *Carbon* 28 (1990) 565.
- [324] J.K. Lee, H.J. Shim, J.C. Lim, G.J. Choi, Y.D. Kim, B.G. Min, D. Park, *Carbon* 35 (1997) 837.
- [325] A. Bagreev, S. Bashkova, T.J. Bandosz, *Langmuir* 18 (2002) 1257.

- [326] C. Petit, Ch. Karwacki, G. Peterson, T.J. Bandosz, *J. Phys. Chem. B* 111 (2007) 12705.
- [327] E. Raymundo-Piñero, D. Cañorla-Amorós, C. Salinas-Martínez de Lecea, A. Linares-Solano, *Carbon* 38 (2000) 335.
- [328] I. Mochida, K. Kuroda, S. Kawano, Y. Matsumura, M. Yoshikawa, E. Grulke, R. Andrews, *Fuel* 76 (1997) 537.
- [329] M. Steijns, P. Mars, *J. Catal.* 35 (1974) 11.
- [330] T.J. Bandosz, in T.J. Bandosz, Ed., *Activated Carbon Surfaces in Environmental Remediation*, Elsevier, Amsterdam, 2006, p. 231.
- [331] S. Bashkova, A. Bagreev, T.J. Bandosz, *Ind. Chem. Eng. Res.* 41 (2002) 4346.
- [332] G. S. Szymanski, T. Grzybek, H. Papp, *Catal. Today* 90 (2004) 51.
- [333] H. Jüntgen, in P. Thrower, Ed., *Chemistry and Physics of Carbon*, Vol. 22, Marcel Dekker, New York, 1989, p. 145.
- [334] M.T. Izquierdo, B. Rubio, *Environ. Sci. Technol.* 32 (1998) 4017.
- [335] B. Xia, J. Phillips, C.K. Chen, *Energy Fuels* 13 (1999) 903.
- [336] Y. Kong, C.Y. Cha, *Energy Fuels* 9 (1995) 971.
- [337] T. Valdes-Solis, G. Marban, A.B. Fuertes, *Appl. Catal. B Environ.* 46 (2003) 261.
- [338] A. Hershman, U.S. patent 3,969,398, 1974.
- [339] F.S. Baker, J.F. Byrne, U.S. patent 6,706,194, 2004.
- [340] F.S. Baker, J.F. Byrne, U.S. patent 6,699,393, 2004.
- [341] L.R. Radovic, C. Sudhakar, in H. Marsh, E.A. Heintz, F. Rodríguez-Reinoso, Eds., *Introduction to Carbon Technologies*, University of Alicante, Alicante, Spain, 1997, p. 103.
- [342] A. Bagreev, T.J. Bandosz, *Ind. Eng. Chem. Res.* 41 (2001) 672.
- [343] D. Nguyen-Tanh, T.J. Bandosz, *Carbon* 43 (2005) 359.
- [344] L.V. Rajakovic, M.R. Ilic, P.B. Jovanic, P.B. Radosevic, *Carbon* 33 (1995) 1433.
- [345] Y.W. Lee, J.W. Park, J.H. Yun, J.H. Lee, D.K. Choi, *Environ. Sci. Technol.* 36 (2002) 4928.

3 Molecular Simulations Applied to Adsorption on and Reaction with Carbon

ZHONGHUA (JOHN) ZHU

3.1 INTRODUCTION

Carbon gasification reactions with various gases have been studied extensively, due to their practical importance as well as scientific merit [1–5]. A large volume of literature has been devoted to the study of mechanisms for the gasification reactions of carbon, mainly through experimental methods, including thermogravimetric techniques, evolved gas analysis, temperature-programmed desorption (TPD), transient kinetics (TK), and scanning electron microscopy (SEM) [6–10]. However, theoretical understanding and prediction of the reaction behavior and mechanism still lag behind. Molecular simulations (MSs) provide a potential method for the complete description of the electronic properties of molecular systems, their structures, their physical and chemical properties, and their reactivities. The computational difficulties encountered in the general case, as well as the magnitude of extraneous information generated by multielectron wave functions, have been overcome by the development of entire conceptual frameworks, new computational methods, and more powerful computational machines. Progress in MS has made it possible to make reliable predictions of molecular structures, relative energies, potential surfaces, vibrational properties, reactivities, and reaction mechanisms [11,12]. An increasing number of MS programs based on different theoretical approaches have become available (e.g., MOPAC, AMPAC, Amber, GAMES, SIESTA, VASP, Gaussian).

In this chapter, the theoretical background and different molecular simulation methods are introduced with stress on electronic structure methods, followed by a comprehensive review of studies on gas–carbon reactions using MS in the last four decades, which include the hydrogen–carbon reactions, carbon reactions with oxygen-containing gases, and metal–carbon interaction.

3.2 MOLECULAR SIMULATION METHODS APPLIED TO CARBON REACTIONS

3.2.1 Electronic Structure Methods (or Quantum Mechanics Methods)

Electronic structure methods or quantum mechanics (QM) methods use the laws of quantum mechanics rather than classical physics as the basis for their computations. QM states that the energy and related properties of a molecule may be obtained by solving the Schrödinger equation: $H\Psi = E\Psi$. For any but the smallest systems, however, exact solutions to the Schrödinger equation are not computationally practical. QM methods are characterized by various mathematical approximations to its solution. There are three classes of QM methods: semiempirical, ab initio, and density functional theory (DFT).

Semiempirical Methods Semiempirical methods use parameters derived from experimental data to simplify the computation. They solve an approximate form of the Schrödinger equation that depends on having appropriate parameters available for the type of chemical system under investigation. Different semiempirical methods are characterized largely by their differing parameter sets.

HMO (Hückel molecular orbital theory) is the simplest quantitative molecular orbital theory. It was developed in the 1930s by Erich Hückel to describe planar hydrocarbons with conjugated π bonds [13]. HMO is based on the idea of $\sigma - \pi$ separation, treating π electrons only. HMO calculations are the only ones that are practical to do without the aid of a computer, giving rather poor energies and orbital functions but faithfully reproducing the symmetry properties of orbitals.

EHT (extended Hückel theory) was developed by Wolfsberg and Helmholz (1952) and used widely by Hoffmann (1963) [13] to provide qualitative insights into chemical bonding, particularly for inorganic compounds. In EHT, all valence orbitals (both π and σ) are included in the molecular orbitals; it is not restricted to the π system. This method, however, still gives poor prediction of molecular properties such as dipole moments and rotational barriers.

PPP (Pariser–Parr–Pople) [14–16] is an SCF (self-consistent field) π -electron theory, assuming $\sigma - \pi$ separability. Only a single ($2p_z$) atom orbital is considered on each atom and the π -electron Hamiltonian includes electron–electron interactions with ZDO (zero differential overlap) approximation. All integrals are determined by semiempirical parameters. The PPP method can only be used to calculate those physical properties for which π electrons are mainly responsible.

CNDO (complete neglect of differential overlap) is an SCF valence-electron theory [16,17]. CNDO ignored most of the integrals used in ab initio calculations and approximated, by simple expressions, those integrals that were retained. CNDO was a significant advance over earlier methods, such as Hückel, which could not represent electron–electron interactions and considered π electrons only. The next stage, **INDO** (intermediate neglect of differential overlap) [16,18], including one-center repulsion integrals between atomic orbitals on the same

atom, is an improvement on the CNDO method. The *NDDO* (neglect of diatomic differential overlap) [16,17] approximation was the first in which the directionality of the atomic orbitals was considered in calculating the repulsion integrals. In this case, three- and four-center integrals in which the overlap occurs between atomic orbitals on the same atom were included.

MINDO (modified intermediate neglect of differential overlap) [16,19] is a modified INDO. *MINDO/3* is the last in a series of three MINDO methods and represents a milestone in the use of calculations in chemistry. Rather than evaluating the one-center repulsion integrals analytically, MINDO/3 uses a set of parameters to approximate them. It was the first easy-to-use program package with automatic geometry optimization to be made available to a wide range of nonspecialist research groups. *MNDO* (modified neglect of diatomic overlap) is not a more sophisticated version of MINDO/3, but rather, an independent method based on the NDDO approximation, and was under development when MINDO/3 was published. The use of NDDO rather than INDO was found necessary to avoid some of the systematic MINDO/3 errors for molecules, such as hydrazines or polyfluoroalkanes, in which lone pair–lone pair repulsions are important.

AM1 (Austin model 1) [20], similar to MNDO, based on NDDO approximation, was to rectify the problem of hydrogen bonding in MNDO. In AM1, each atom was assigned a number of spherical Gaussians that were intended to mimic the correlation effects. The number of parameters from the original seven in MNDO is increased to between 13 and 16 per atom in AM1. *PM3* (parametric method 3) [20] was called MNDO-PM3 to indicate that it was the third parameterization of MNDO, AM1 being the second. PM3 employs a new procedure for optimizing parameters, using first and second derivatives of all calculated values for reference data, to speed the optimization (without the use of chemical intuition). PM3 substantially reduces errors made by MNDO and AM1 in calculating heats of formation, and produces reasonably good results for hydrogen-bonded systems and hypervalent compounds.

Ab Initio Methods Unlike semiempirical methods, ab initio methods use no experimental parameters in their computations. Instead, their computations are based solely on the laws of quantum mechanics (the first principles referred to in the name *ab initio*) and on the values of a small number of physical constants: the speed of light, the masses and charges of electrons and nuclei, and Planck's constant. Semiempirical and ab initio methods differ in the trade-off between computational cost and accuracy of result. Semiempirical calculations are relatively inexpensive and provide reasonable qualitative descriptions of molecular systems and fairly accurate quantitative predictions of energies and structures for systems for which good parameter sets exist. In contrast, ab initio computations provide high-quality quantitative predictions for a broad range of systems. They are not limited to a specific class of system. Early ab initio programs were quite limited in the size of the system they could handle. However, this is not true for modern ab initio programs. Gaussian is the most popular ab initio

molecular orbital calculation package and has been used successfully in many fields [21–23].

Different ab initio methods can be characterized by their treatment of electron–electron interactions, called *electron correlation*. The first practical ab initio method was the HF (Hartree–Fock) method, which treats each electron as if it exists in a uniform field made from the total charge and space occupied by the other electrons. This treatment is only an approximation to the interactions between electrons as point charges in a dynamics system and excludes the contribution of excited electronic configurations. This neglect of electron correlation can lead to significant error in determining thermochemical properties.

This inclusion of electron correlation can be accomplished in several ways. One method has been to use Møller–Plesset (MP) perturbation theory. This theorized that the electron correlation was a perturbation of the wavefunction, so the MP perturbation theory could be applied to the HF wavefunction to include the electron correlation. As more perturbations are made to the system, more electron correlation is included (these methods are denoted MP2, MP3, and MP4). Another method is to calculate the energy of the system when electrons are moved into vacant orbitals. These methods move electrons either one at a time (single), two at a time (double, such as the QCISD method), or three at a time (triple, such as the QCISDT method). These methods calculate energy values more accurately but at greater computational cost.

Density Functional Theory Methods In parallel to the development of ab initio theory, it was theorized that all molecular properties could be described as a function of the electron density [24]. By using mathematical functions, called *functionals*, to describe the electron density, a new theoretical approach, density functional theory (DFT), was developed. In 1965, Kohn and Sham [25] produced a set of equations that demonstrated how to determine a self-consistent density from DFT decomposition of the Schrödinger equation:

$$E_{\text{KS}} = T + V + J + XC \quad (3.1)$$

$$E_{\text{HF}} = T + V + J + K \quad (3.2)$$

where E_{KS} is the Kohn–Sham electronic energy of the Schrödinger equation compared to the Hartree–Fock energy (E_{HF}), T the kinetic energy of the electrons, V the electron–nuclear interaction, J the Coulomb self-interaction of the electron density, K the exchange self-interaction of the electron density, and XC the exchange correlation part of the electron–electron repulsion energy, which is treated as a functional of the electron density.

Developments in DFT in the 1990s have led to nonlocal (gradient-corrected) functionals (e.g., BP86, BLYP) and to “hybrid” functionals (e.g., B3LYP) [23,26]. The nonlocal or gradient-corrected functionals account for the nonuniformity of the overall electron distribution. The hybrid methods use a linear combination of the Hartree–Fock and DFT electron correlation, with parameters adjusted to

provide the best fit with specific experimental data. The dynamic interaction between electrons is theoretically included by these density functional methods, therefore including electron correlation into the calculation directly, which is insufficiently included in HF calculations. This gives these methods the benefit of including electron–electron correlation for a computational expense similar to that of HF, giving DFT methods the major advantage of low computational cost compared to accuracy.

3.2.2 Molecular Dynamics Simulations

Molecular dynamics (MD) simulations predict the movement of atoms and molecules with time under some basic laws of physics. Normally, real molecular systems have a larger number of freedoms, because a huge amount of particles are included. It is impractical to solve the movement equations and find the properties of such complex systems analytically. Assisted by the development of computational technique, MD simulations overcome the problem using numerical methods, and build an interface between laboratory experiments and theory.

MD simulations use different physical principles to simulate actual laboratory conditions [27]. One is the NVE ensemble, in which the number of particles (N), volume (V), and energy (E) are kept unchanged. The kinetic and potential energies of the system can convert to each other with the total energy being conserved, corresponding to an adiabatic process. One is constant-temperature molecular dynamics, where the number of particles (N), volume (V), and the temperature (T) are conserved. In the NVT ensemble, the energy of endothermic and exothermic processes is exchanged with a thermal state. Another is the isothermal–isobaric ensemble, with the number of particles (N), pressure (P), and temperature (T) being conserved. It resembles most closely laboratory conditions with a flask open to ambient pressure and temperature. The replica exchange method used originally to treat the slow dynamics of disordered spin systems is a general ensemble of MD simulations. It tries to overcome the multiple-minima problem by exchanging the temperature of noninteracting replicas of a system running at several parallel temperatures.

MD simulations require the description of the interactions between the particles (potential function, or a force field) of a molecular system [27]. The potential function can be defined on various levels. The most commonly adopted potential functions in chemistry and biology are based on molecular mechanics (MM), with a classical treatment of particle–particle interactions. With well-chosen parameter sets, these potential functions can reproduce structural and conformational changes in systems, except chemical reactions. The analytic forms of the potential functions, which involve low computational cost, make it possible for MD simulations to include a huge number of atoms. When potentials based on quantum mechanics (QM) are adopted, MD simulations can give finer levels of detail, such as chemical reactions and electronic structures, but expensive computational costs are involved simultaneously. As a compromise, hybrid QM/MM approaches are

developed in which the system is partitioned into an electrically important region which requires a QM treatment and a remainder that acts only in a perturbative fashion, thus admitting classical MM description.

3.2.3 Monte Carlo Simulations

Monte Carlo (MC) methods are stochastic techniques that are widely used for simulating the behavior of complex systems [28]. They are distinguished from MD simulations in that they are based on the use of random numbers and probability statistics to handle problems. In MC methods, a large system can be sampled in a number of random configurations, and the data can be used to describe the system as a whole. Instead of determining particle motions by solving movement equations, MC simulation simply imposes random motions on the systems and determines whether or not the altered structure is energetically feasible at the temperature simulated, making the system jump abruptly from conformation to conformation. Therefore, it is much better than MD simulations in estimating average thermodynamic properties. The MC method is also an efficient method of solving physical or mathematical problems that have many variables, and its efficiency relative to other methods increases as the dimension of the problem increases.

3.3 HYDROGEN ADSORPTION ON AND REACTION WITH CARBON

The interaction of hydrogen with carbonaceous surfaces is important in three practical areas: molecular hydrogen formation in space, hydrogen–wall interactions in fusion reactors, and hydrogen storage. In this section, simulation studies on atomic hydrogen adsorption on the basal plane of graphite, hydrogen reaction with the edge sites of graphite, and hydrogen storage in carbon nanotubes are reviewed separately.

3.3.1 Atomic Hydrogen Adsorption on the Basal Plane of Graphite

It is well known that graphite has a multilayer structure and that atomic or molecular hydrogen may adsorb on either basal or edge planes. Early theoretical studies were focused on the basal plane despite the fact that the edge sites are much more active, as is to be shown. Nevertheless, studies on basal plane sites provide good background in terms of fundamental understanding and simulation methods for investigations on edges sites as well as the more recent carbon nanotubes.

Bennett et al. [29] first used extended Hückel theory (EHT) to treat hydrogen chemisorption on graphite. An equi-binding energy surface obtained using a 16-carbon atom representation is shown in Figure 3.1. The maximum binding occurs above a carbon atom. It was emphasised that the absolute values of the

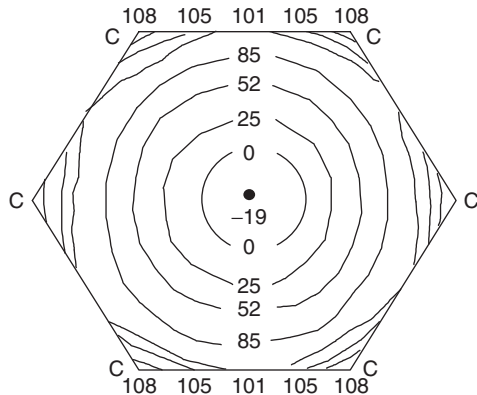


Figure 3.1 Equibinding energy contours (kJ/mol) for atomic hydrogen adsorbed on the model graphite (16 C atoms). Positive energies correspond to binding. (Adapted from ref. 29.)

adsorbate binding energies were determined only crudely by the EHT method. The differences calculated between the energies of various configurations are, however, relatively invariant to various details of the procedure.

CNDO and Hartree–Fock ab initio methods were used by Dovesi et al. [30,31] in calculating the binding energy as a function of the distance of the adsorbed layer from the graphite surface by considering different regular adsorbed phases. CNDO calculations [31] indicated that stable adsorption is possible on the basal plane of graphite. Contrary to CNDO results, no stable phase was found from ab initio calculations [31]. Whereas the study by Chen and Yang [32] using EHT supports the latter, the more recent studies by Yang and Yang [33] and Ferro et al. [34] using more advanced ab initio and DFT methods support the former.

As EHT is not able to deal correctly with electrophilic adsorbates [29,35] and CNDO/2 makes necessary the use of an arbitrary scaling factor in the energies calculated [30], a theoretical study of the dissociative chemisorption of molecular hydrogen on graphite and the recombination of two adsorbed hydrogen atoms to give molecular hydrogen in the gas phase was conducted using the MINDO/3 method, which has been found to avoid these difficulties and gives results comparable to ab initio band structure calculations [36]. Dissociative chemisorption of molecular hydrogen, which involves rotation of a nearly vertical orientation to a nearly horizontal one, was predicted to take place on the basal plane of graphite with a high potential barrier, over 340 kJ/mol. This is probably why molecular hydrogen could not be used as a reactant in the molecular beam experiments of Balooch and Olander [37]. The theoretical activation energies for the recombination step were from 40 to 120 kJ/mol, which are comparable with the experimental results (74 kJ/mol) [37].

To understand the process of migration of atomic hydrogen on the graphite surface, the potential energy surface for interaction of hydrogen with a cluster

model ($C_{10}H_8$) simulating the basal plane of graphite was calculated by using an open-shell RHF version of the MINDO/3 method by Caballol et al. [38]. Results suggested that there existed only an active center, which is coincident with a carbon atom of the model. The migration of chemisorbed hydrogen from one active center to another could take place through a potential barrier of about 8 kJ/mol, with the corresponding saddle point located above the center of a C–C bond. According to this result, migration takes place almost freely, following the C–C bonds, again in agreement with the mechanism suggested by Balooch and Olander [37], but contradictory to the more advanced study to be discussed next.

A further comparative study of atomic hydrogen on the basal plane of graphite was conducted by Barone et al. [39] using both MNDO and ab initio (HF/STO-3G) employing finite cluster models. Their results were in agreement with those of Bennett et al. [29,40] and Caballot et al. [38]: that a hydrogen atom favors a site directly over the carbon atoms of graphite. The hydrogen–graphite interaction was studied more recently in the framework of density functional theory by Jeloaica and Sidis [41], and the same conclusion was drawn.

Ferro et al. [34] investigated hydrogen atom interaction with a graphite surface using the DFT method. Once again, a hydrogen atom favors a site directly over a carbon atom, with an exothermic adsorption energy varying from –18.4 to –74.2 kJ/mol, in agreement with the calculations of Yang and Yang [33]. Ferro et al. also investigated the diffusion and recombination of hydrogen on a graphite surface [42]. For recombination, two reactive pathways are known. In the Eley–Rideal (ER) mechanism, a gas-phase hydrogen atom combines directly with a hydrogen atom adsorbed on the surface to yield desorbed H_2 ; whereas the Langmuir–Hinshelwood (LH) mechanism assumes that two adsorbed hydrogen atoms diffuse on the surface until they meet and recombine. The diffusion–LH recombination pathway was characterized by three activation energies [42]: 125 kJ/mol for an isolated chemisorbed hydrogen atom diffusing on a graphite layer, 46 kJ/mol for diffusion in the vicinity of another hydrogen atom, and 272 kJ/mol for recombination. The desorption–ER recombination pathway is characterized by only one activation energy: 80 kJ/mol on the surface and 413 kJ/mol in the bulk. The diffusion energy is much higher than the value 8 kJ/mol obtained by Caballol et al. [38]. The activation energy for H_2 recombination on graphite during experimental thermal desorption process by Zecho et al. [43] was 57.6 to 91.2 kJ/mol. This indicates that the ER mechanism on the surface may be dominant in H_2 recombination during the thermal desorption. This is consistent with studies by Sha and Jackson [44].

Although lower-level calculations produced varying results, recent advanced ab initio and density functional theory (DFT)–based studies provide more reliable data. All the theoretical investigations noted above were, however, focused on chemisorption on the basal (0001) plane of graphite, and the results can be summarized as follows. Hydrogen atoms prefer adsorption sites directly above carbon atoms of graphite, and a stable phase is available based on the more advanced ab initio or DFT methods. The dissociative chemisorption of molecular hydrogen

on the basal plane is more difficult, with a high potential energy barrier over 340 kJ/mol [36]. The desorption–ER mechanism on the surface may be dominant in H₂ recombination during thermal desorption. The chemisorption and reaction of hydrogen on graphite takes place much more favorably on the edge planes [45–47]. Therefore, from the standpoint of practical use, it is at least equally important to study the edge sites during the investigation of hydrogen–carbon reactions.

3.3.2 Reactivities of Graphite Edge Sites and Hydrogen Reactions on These Sites

Before discussing hydrogen reactions on the edge planes of graphite, it is important to clarify the different classes of edge sites with their different electronic structures, which in turn play a key role in edge site–related reactions. Coulson and colleagues [48] studied the change in electronic energy levels from benzene to graphite using both LCAO (linear combination of atomic orbitals) approximation (introduced by Hückel), and LCBO (linear combination of atomic bond orbitals) approximation (proposed by Coulson et al.). The most interesting features of the change were to be related to the π electrons. Calculations showed that the molecule increases in size and the discrete energies gradually merge into a band. In a follow-up study [49], the electronic structures of the graphite edge sites were first analyzed systematically as shown in Figure 3.2. When the carbon atoms on the edge of a plane aromatic hydrocarbon molecule have their third valence bond attached to a hydrogen atom, their electronic structure is based on a tetravalent state. This is sp² for the δ bonds and π for the delocalized electrons. But if the third valence is not used, the atom may (a) remain as before (zigzag sites), (b) pair with a neighboring edge atom to form a partially triple bond (armchair sites), or (c) revert to a carbenoid. The reactivity difference between zigzag and armchair edge sites of graphite is a critical issue in studying gas–carbon reactions, which can in turn be used as a litmus test for validating the computational chemistry studies. This issue was well addressed by Stein and Brown [50–52], who conducted calculations on hexagonally symmetric molecules using structure-resonance theory to evaluate resonance energies, perturbation molecular orbital theory to obtain electron localization energies, and Hückel molecule orbital theory to derive approximate electron densities in free radicals. The properties near the edge depend on the specific edge structures. The zigzag edge structure is thermodynamically unstable and reactive. π -Electron conjugation on this type of edge site is blocked between edge and interior atoms and is therefore nonaromatic. In contrast, armchair edges lead to highly efficient conjugation between edge and interior atoms. Even in irregular graphitelike molecules, these edge structures can stabilize the part of the molecules to which they are attached. Simple calculations showed that molecules containing these edges are not highly reactive.

Fujita et al. [53,54] investigated the electronic and magnetic properties of a ribbon-shaped nanographite system with zigzag and armchair edges in a magnetic

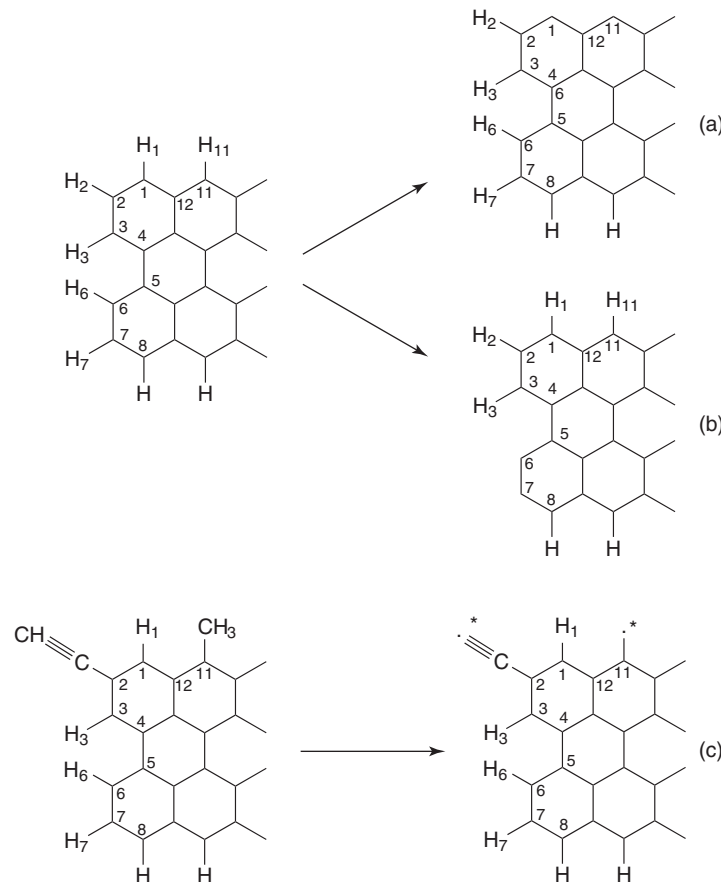


Figure 3.2 Three states of graphite edge sites if the third valence is not used (a) remain as before (zigzag), (b) pair with a neighboring edge atom to form a partially triple bond (armchair), or (c) revert to a carbenoid. (Adapted from ref. 49.)

field using a tight-binding model. They also found that the charge density in the edge site is strongly localized on the zigzag edge sites, but no localized state appears in a graphite system with armchair sites. The study by Klein and Bytautas [55] also emphasized that edge sites with higher concentrations of edge-localized unpaired electrons would be reactive and under many preparatory conditions undergo additional reactions to quench this free valence.

The chemical nature of graphene edges has been revisited by Radovic and Bockrath [56] using DFT methods [B3LYP/6-31G(d)], and the origin of stability and potential for magnetism in carbon materials were investigated. The zigzag sites are carbenelike, with the triplet ground state being most common. The armchair sites are carbynelike, with the singlet ground state being most common.

This proposal is not only consistent with the key electronic properties and surface (re)activity behavior of carbons, but can also explain the recently documented and heretofore puzzling ferromagnetic properties of some impurity-free carbon materials.

The experimental results of Yang and Duan [46] on monolayer etch pit formation further indicated that the chemisorption of hydrogen takes place preferentially on the zigzag plane rather than on the armchair plane. Therefore, Chen and Yang [32] used extended Hückel theory to study the feasibility and relative strengths of chemisorption of hydrogen on three faces of graphite: the (0001) basal plane, the (1010) zigzag face, and the (1121) armchair face. Chemisorption of atomic hydrogen on the zigzag and armchair faces was stable; however, the C–H bond strength on the zigzag face (ca. 370 kJ/mol) was significantly stronger than that on the armchair face (ca. 296 kJ/mol). For the binding of hydrogen on a basal plane, only metastable states exist. More recently, Yang and Yang [33], using UHF/3-21G(D) for geometric optimization and B3LYP/6-31G(D) for energy calculations, obtained the same trend: The relative energies of adsorption (or C–H bond energies) follow the order zigzag edge > armchair edge > basal plane, but the adsorption of hydrogen atoms on the basal plane was found to be stable, contradictory to the result from lower-level method calculations [32].

In a follow-up study, the mechanism of methane formation from the reaction between graphite and hydrogen was investigated by Pan and Yang using the same method (EHT) [57]. The mechanism is shown in Figure 3.3. It was found that the zigzag edge face is more reactive than the armchair face before and after one hydrogen atom is chemisorbed on the surface atom. However, a reversal in the relative reactivity occurs after the second hydrogen addition; the C–C bond on the armchair face becomes weaker and carbon atoms become more reactive for the third hydrogen chemisorption. This is apparently related to the partially triple bond character of armchair sites as suggested by Coulson [49]; that is, the partial triple bond on the armchair sites becomes a very weak single bond after

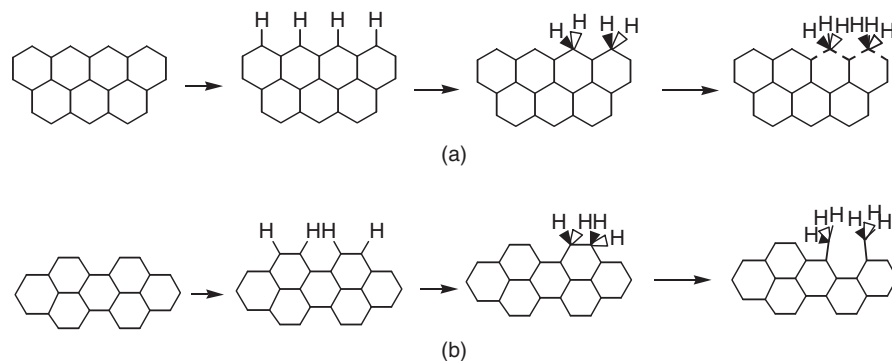


Figure 3.3 Mechanism for methane formation on (a) zigzag and (b) armchair sites. (Adapted from ref. 57.)

the second hydrogen atom adsorption and is thus very active for the following adsorption. Breakage of C–C bonds takes place upon the third hydrogen addition, and this step is the rate-limiting step for CH₄ formation.

The work of Yang et al. [32,57] focused on the edge sites instead of the basal plane of graphite and was thus more practical than previous studies. Hydrogen adsorption, desorption, and the formation of CH₄ were investigated thoroughly, and consistent results were achieved from both theoretical and experimental methods. Their results were also in good agreement with the classic studies of the electronic structure of graphite edge sites and the corresponding reactivity pioneered by Coulson and Stein. On the other hand, studies on hydrogen reaction with the graphite basal plane by other authors provided important information on the theoretical methods and molecular structure. First, to achieve accurate results, a large cluster size is required, but a relatively small single-layer cluster still provides a reliable qualitative trend. Second, various theoretical methods were examined, and semiempirical methods were found to be able to save computational resources and present good semiquantitative results, but the absolute values are poorly determined. In this case, the ab initio method becomes necessary.

3.3.3 Hydrogen Storage in Carbon Nanotubes

Extensive theoretical studies on hydrogen storage in carbon nanotubes have been reported but are not the emphasis of this chapter. We review briefly the relevant theoretical work with the intent to introduce the molecular simulation methods utilized.

Two main approaches, the classical and quantum methods, which focus on physisorption and chemisorption, respectively, have been used to simulate hydrogen storage in carbon nanotubes (CNTs). Darkrim and Levesque predicted that hydrogen adsorption decreases with the increase in diameter of single-walled carbon nanotubes (SWCNTs) by performing a grand canonical Monte Carlo simulation based on the Lennard-Jones potential [58]. They attributed this finding to the fact that a large part of the volume inside or outside the tube is out of the attractive force range of the solid–gas interaction. A study of hydrogen adsorption in neutral [59] and positively and negatively charged [60] SWCNTs was then performed by Johnson et al., using the Silvera–Goldman potential for H₂–H₂ interaction and the Crowell–Brown potential for H₂–tube interaction. It was shown that idealized graphitic nanofibers are preferable to SWCNT arrays for hydrogen storage. The hydrogen storage capacity is sensitive to the charges of the SWCNTs. A 0.1e/C charging of the tubes can increase the adsorption up to 30%. Williams and Eklund [61] used a grand canonical Monte Carlo method to simulate H₂ physisorption in finite-diameter carbon nanotube ropes. Small-diameter ropes were predicted to be preferable for hydrogen storage. These classical approaches are advantageous to deal with large systems and take temperature into account in the simulations. The disadvantage is that they are parameter dependant and cannot describe chemical reactions as the ab initio methods can do [21–23].

Introducing quantum mechanics (QM) into the MD simulations of hydrogen in SWCNTs is also of interest in the mechanism study. The H₂ adsorption in a trigonal two-dimensional lattice of armchair (9,9) SWCNTs was simulated by Cheng et al. [62] using a QM MD simulation embodied in the Vienna ab initio simulation package (VASP). It was found that the potential energy surface near the equilibrium point is relatively flat. The H₂ adsorption inside the pores formed by different tubes (exohedral adsorption) was predicted to be energetically favorable. Ma et al. [63] first used a many-body Tersoff–Brenner potential to simulate low-energy collision of atomic hydrogen on the sidewall of an armchair (5,5) SWCNT. For some selected snapshots of the MD simulations, minimal HF/STO-3G ab initio calculations were performed to provide insights into the chemical bonds and electronic structures. Interestingly, the hydrogen atoms could be adsorbed on the tube sidewall, rebounded, penetrate the sidewall and stay in the tubes as H₂, or even enter the tube from one side and escape from another side, depending on the incident energy. Dubot and Cenedese [64] studied the adsorption of lithium and molecular hydrogen on SWCNTs using semiempirical AM1 simulations. They predicted that Li can adsorb endohedrally and exohedrally on SWCNTs, with the most stable site right above the center of a carbon hexagon. After the Li adsorption, molecular hydrogen can be bonded to the Li atom with a binding energy of 48 kJ/mol; otherwise, it is repelled from the tube wall.

The major obstacle in the ab initio calculations of the hydrogen adsorption in SWCNTs is that a relatively large number of atoms (>200 atoms) are required to model a SWCNT effectively. The problem that arises in such an attempt is how to handle a large system using an accurate enough ab initio method without ending up with a prohibitively large calculation. To solve the problem, two different approaches were adopted. The first is to use an ab initio method with periodic boundary conditions to simulate periodic SWCNTs [65]. In this approach, the entire system is treated with ab initio techniques, but external periodicity forced on the system is obviously unrealistic. The second is to use a hybrid quantum mechanics/molecular mechanics (QM/MM) method, which was used by Froudakis for hydrogen storage in carbon nanotubes with doped alkali metals [66]. They suggested that the charge transfer from alkali metal to tube polarizes the H₂, thus increasing hydrogen adsorption, although the theoretical revisit by Zhu using the DFT method shows that the improvement by alkali metals is negligible at room temperature [67].

3.4 CARBON REACTIONS WITH OXYGEN-CONTAINING GASES

Only a couple of reports appeared on carbon reactions with oxygen or oxygen-containing gases using molecular orbital theory compared to the overwhelming theoretical studies on hydrogen–carbon reactions before the 1990s. Similar to hydrogen–carbon reaction, the early studies of oxygen atom or oxygen-containing gases concerned mainly the adsorption on the basal plane of the graphite substrate.

The molecular simulations on the edge-site reactions with oxygen-containing gases started after the 1990s. This section includes the molecular simulation studies on the noncatalyzed and catalyzed carbon reactions with oxygen-containing gases with focus on the unified mechanism, followed by more specific studies in recent years.

3.4.1 Carbon Reactions with Oxygen-Containing Gases and the Unified Mechanism

As mentioned above, satisfactory results were obtained by Bennett et al. [29] on hydrogen adsorption on the basal plane of graphite using extended Hückel theory (EHT). Calculations based on EHT for electrophilic adsorbates such as C, O, and N were found less encouraging, and thus a more complete self-consistent treatment, CNDO, was used by Bennett et al. [35]. It was found that the strength of binding to the simulated graphite increases in the order H, F, O, N, and C. Although some quantities were not reproduced well by these calculations, consistent results for the sequence of adsorbates were obtained and a simple scaling factor brought the results consistently into agreement with experimental data.

Hayns [68] further investigated the usefulness of the CNDO method for examining chemisorption and diffusion of oxygen and water on a graphite substrate by means of an equipotential contour map. It was shown again that a model substrate containing 16 carbon atoms that has the dangling carbon bonds saturated with hydrogen atoms provides an adequate basis for the calculations and that a larger system having 24 carbon atoms and 12 hydrogen atoms reproduces very well the results from calculations having periodically connected boundary conditions. As will be discussed, similar molecular structures (i.e., a finite single graphite layer with dangling edge sites terminated with hydrogen atoms) are selected in modern ab initio studies.

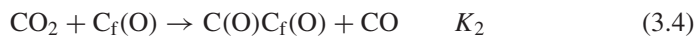
The drawback of these two studies is twofold. First, only the basal plane was discussed; the more active edge plane was not mentioned. Although oxygen can also adsorb effectively on the basal plane, the edge sites are still much more active in reactions and should be the emphasis. Second, previous experiments have shown that oxygen desorption from the carbon surface is the rate-limiting step [10,69–72]. However, only oxygen adsorption was discussed in these two studies, and oxygen desorption was not involved.

In the past five decades there has been a large volume of literature in the study of carbon reactions with oxygen-containing gases, and the central issue is the determination of the active sites on carbon so that the kinetics of carbon can be correlated for different forms of carbon based on the active sites existing on these carbons. Since the groundbreaking work of Laine, Vastola, and Walker [7], this area has been somewhat dormant until recently, when further advances have been made [4–6,8,9,73–76].

There were still several important experimental facts that remain poorly explained regarding the carbon gasification reactions. The kinetic behavior of

the C + CO₂ and C + H₂O reactions are similar and are very different from that of the C + O₂ reactions. The activation energy for the C–O₂ reaction is 208 to 241 kJ/mol, and that for the C–CO₂ and C–H₂O reactions is in the range 333 to 358 kJ/mol [1]. The C–O₂ reaction is also orders of magnitude faster than the other two reactions [1]. It should be pointed out that the absolute values of activation energies for these three reactions may vary from sample to sample, but the relative values always follow the same order (i.e., C–O₂ reactions has an activation energy about 30% lower than the C–CO₂ and C–H₂O reactions). Moreover, TPD results show a CO desorption peak near 950°C for all three gas–carbon reactions and a broad shoulder at the lower temperature near 723 K for the C–O₂ reaction only. Obviously, two or more oxygen-containing intermediates exist for these carbon gasifications, which can desorb below 1273 K. The third fact was that a fast decay (with a small amount of CO desorption) and a slow decay (with more CO desorption) were observed by Kapteijn et al. during TK experiment [77].

The breakthrough turned up later when Yang and colleagues did further molecular orbital theory calculations using the INDO (intermediate neglect of differential overlap) method, which is modified from the CNDO (complete neglect of differential overlap) method [78]. The bond strengths obtained by CNDO or INDO are usually about five times as large as the experimental values [68], but the relative comparisons are reliable. The structures shown in Figure 3.4 were used. The calculations (Table 3.1) showed that the C–C bond energies (for CO desorption from graphite) are lowered by about 30% by the formation of off-plane oxygen on the saturated carbon atoms. These structures (D4 and E4) with off-plane oxygen are formed due to the high net electron charges of the saturated carbon sites. Structures D4 and E4 are abundant in the C–O₂ reaction but not in the C–CO₂ and C–H₂O reactions. This more active form of oxygen complex is a main contributor to the C–O₂ reaction. From the discussion above, a unified mechanism for gasification of carbon by oxygen-containing gases is proposed. Taking CO₂ as an example, the mechanism is expressed as follows:



where K represents an equilibrium constants and k a rate constant. The symbols C_f(O) and C(O)C_f(O) represent the complexes in substrates B4,C4 and D4,E4, respectively (or to be more exact, they represent the two main groups of oxygen-containing structures, i.e., in-plane and off-plane groups). C_f is the edge carbon site with a free sp² electron, and C is the saturated carbon atom. This unified mechanism can account for the key TPD and kinetic results for gas–carbon reactions reported in the literature. In the TPD results, the CO desorption peak at

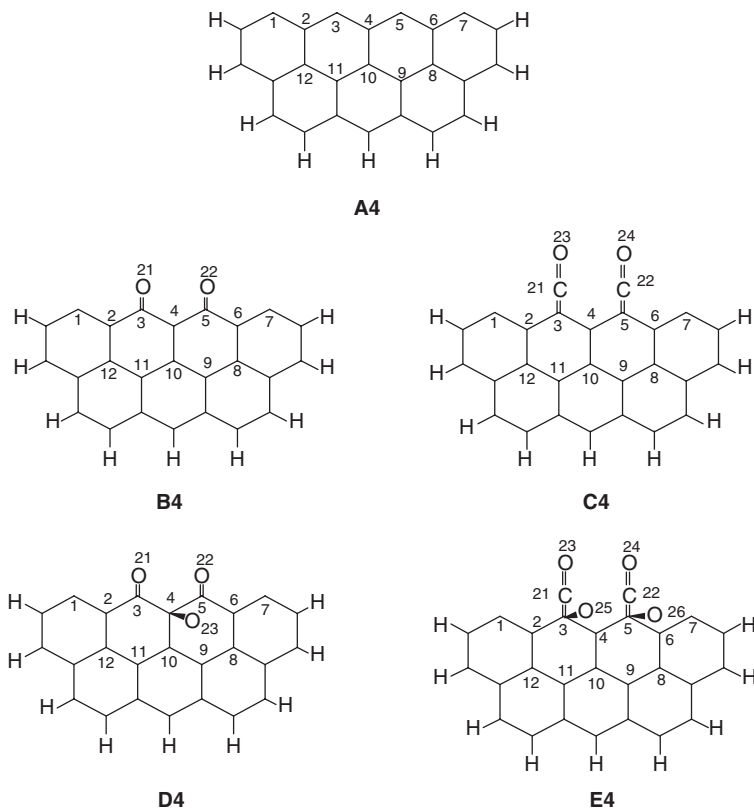


Figure 3.4 Structures of chemisorbed oxygen on graphite. (Adapted from ref. 78.)

Table 3.1 Carbon–Carbon Bond Strength in Various Substrates in Terms of Diatomic Energy (kJ/mol)^a

No.	Model A4	Model B4	Model C4	Model D4	Model E4
C2-3	2373	2115	2057	1738	1677
C3-4	2412	2151	2109	1504	1613
C4-5	2412	2151	2109	1504	1613
C5-6	2373	2115	2057	1738	1677
C3-21	—	2754 (C–O)	2387	3590 (C–O)	1813
C5-22	—	2754 (C–O)	2387	3590 (C–O)	1813
C21-23	—	—	3606 (C–O)	—	3293 (C–O)
C22-24	—	—	3606 (C–O)	—	3293 (C–O)
C3-25	—	—	—	—	1677 (C–O)
C5-26	—	—	—	—	1613 (C–O)
C4-23	—	—	—	1904 (C–O)	—

Source: Ref. 78.

^aSee Figure 3.4.

near 1223 K for all gas–carbon reactions was caused by $C_f(O)$, the broad shoulder at lower temperatures for only the $C+O_2$ reaction, was caused by $C(O)C_f(O)$. Kinetic results show lower activation energies and higher rates for the $C+O_2$ reaction and higher activation energies and lower rates for the $C+CO_2$ and $C+H_2O$ reactions. The reason is still that there is sufficient $C(O)C_f(O)$ in $C+O_2$, while $C_f(O)$ exists mainly in $C+CO_2$ and $C+H_2O$ reactions. The fast decay with a small amount of CO during TK [77] was also caused by $C(O)C_f(O)$.

Nevertheless, the drawbacks of INDO semiempirical methods of Chen et al. [78] are also apparent. First, the C–C bond energies in previous studies using semiempirical molecular orbital theories were on the order of 2293 kJ/mol, which was about four times higher than the experimental value. Second, the proposed mechanism did not take into account the existence of the carbonyl intermediate and the difference between the semiquinone and carbonyl types of intermediate. Another interesting, yet poorly understood experimental observation pertains to the shape of the etch pits on the basal plane of graphite that are created by different gases. The two hydrogen-containing gases (H_2O and H_2) form hexagonal pits, whereas circular pits are formed by the other gases (CO_2 , O_2). Ab initio molecular orbital theories are capable of substantially more accurate energy calculations than are semiempirical theories.

Yang et al. did a systematic ab initio (+ DFT) study on a single layer of graphite to select the model chemistry and molecular structure [79]. The configuration B3LYP/6-31G(d)//HF/3-21D(d) can produce a good balance between computational cost and accuracy, and a single-layer graphite $C_{25}H_9$ is a suitable model for graphite structure and yields parameters in excellent agreement with the experimental data. In a follow-up study [70], ab initio methods were used to calculate all oxygen-containing intermediates, and the molecular structures selected are shown in Figure 3.5. The results were encouraging (Table 3.2). First, the models were well selected and were representative, as the geometric parameters calculated by all different models are in agreement. Second, hydrogen atoms are good terminators for the graphite model boundaries, as the deviations from experimental data for bonds that involved hydrogen were minimal (i.e., 0.2 to 0.4%). Moreover, calculated bond length (C–C, C–H, and C–O) and bond angle (C–C–C, C–C–H, and in-plane C–C–O) were in agreement with the experimental data and were also consistent among the various models.

Comparing the C–C bond energies of models C5 and E5, the bond energies are similar [i.e., 264 kJ/mol vs. 325 kJ/mol at the B3LYP/6-31G(d) calculation level] (Table 3.3). This is the reason that the gasifications of carbon on both the armchair and zigzag edges are of equal ease and why the etched pits for the $C+O_2$ and $C+CO_2$ reactions are circular in shape. The reason for the etch pits formed by the $C+H_2O$ reaction being hexagonal in shape and being bounded by zigzag edges is due to chemisorbed hydrogen atoms on the edge carbon atoms [57,68]. Hydrogen atoms are more likely to adsorb on zigzag sites; hence, the armchair edges are preferentially gasified by oxygen atoms from H_2O . The presence of epoxy oxygen weakens the adjacent C–C bonds by 33% (the

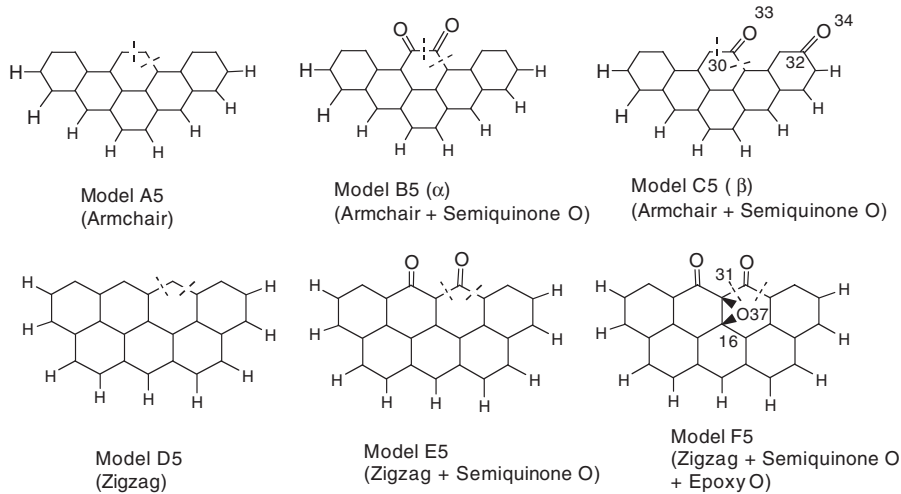


Figure 3.5 Graphite models selected for calculation, including three oxygen intermediates. The dashed lines indicate where C–C bond breakage takes place to free CO. (Adapted from ref. 70.)

last column in Table 3.3). This degree of weakening is nearly the same as the 32% decrease in activation energies (i.e., from 354 kJ/mol for the C + CO₂ and C + H₂O reactions to 241 kJ/mol for the C + O₂ reaction). An improved unified mechanism which takes into account semiquinone (in-plane), carbonyl (in-plane), and epoxy (off-plane) oxygen intermediates was proposed. Two reaction pathways (as Figure 3.6) were deduced from the calculation results, one for C + O₂ reaction and one for the C + CO₂ and C + H₂O reactions. The zigzag edge is used as an example, while the same pathways also apply to the armchair edge.

The importance of Chen and Yang's study [70] is not only because of the more accurate calculations for the unified mechanism, but also because it presents the promising prospect that with relatively small molecular structures and reasonable model chemistry, ab initio methods can provide reliable quantitative or semiquantitative results in the complicated studies of gas–carbon reactions.

3.4.2 Catalyzed Gas–Carbon Reactions

Alkali and alkaline earth oxides are the best catalysts for the gasification reactions of carbon by CO₂ and H₂O, which are the bases of coal gasification processes. Because of its importance, a voluminous literature has been devoted to this area, and much progress has been made during the past over three decades toward an understanding of the mechanism of these catalyzed reactions, possible active intermediates, and phenomena involved in catalyst behaviors [80,81]. Molecular orbital theory calculations were again found to be an effective tool in the investigation of catalyzed gas–carbon reactions.

Table 3.2 Geometric Parameters Calculated for Graphite Models and Oxygen Intermediates at the HF/3-21G(d) Level^a

Bond	BL (Å)	C–C	Armchair			Zigzag			Model F5	Experimental Data
			Model A5	Model B5	Model C5	Model D5	Model E5			
C–H	Average	Average	1.402	1.416	1.413	1.416	1.414	1.424	1.42	
		SigmaN	0.0329	0.0392	0.0321	0.0184	0.0206	0.0348		
		DTED (%)	1.3	0.3	0.5	—	0.3	0.4	0.3	
C–O(IP)	Average	Average	1.072	1.072	1.072	1.073	10.72	1.072	1.07	
		SigmaN	0.0007	0.0006	0.0015	0.0007	0.0009	0.001		
		DTED (%)	0.2	0.2	0.2	0.2	0.2	0.2	0.2	
C–O(OP)	Average	Average	—	1.2302	1.292(C ₃₀ –O ₃₃)	—	1.2759	1.246	1.13(CO)	
		SigmaN	—	—	—	—	—	1.509(C ₁₆ –O ₃₇)	1.43(CH ₃) ₂ O	
		DTED (%)	0.3	0.1	0.4	0.4	0.2	0.1	0.1	
C–C–C	Average	Average	120.38	120.14	120.46	120.53	120.22	120.1	120.1	
		SigmaN	1.4903	1.8818	2.7265	2.3263	2.2751	1.8549		
		DTED (%)	0.3	0.1	0.4	0.4	0.2	0.1	0.1	
C–C–H	Average	Average	119.42	119.57	119.52	119.52	119.51	119.66	119.66	
		SigmaN	1.2764	1.1371	1.1421	0.6752	0.7195	0.8344		
		DTED (%)	0.5	0.4	0.4	0.4	0.4	0.3	0.3	
C–C–C(IP)	Average	Average	—	121.81	121.71	—	121.34	121.29	120(CO)	
		C–C–O(OP)	—	—	—	—	—	59.35(C ₃₁ –C ₁₆ –O ₃₇)	110[(CH ₃) ₂ O]	
DA	Property	Plane	Plane	Plane	Plane	Plane	Plane	Plane	Nonplane	

Source: Ref. 70.

^aSee Figure 3.5. BL, bond length; BA, bond angle; DA, dihedral angle; IP, in-plane oxygen; OP, off-plane oxygen; SigmaN, standard deviation; DTED, deviation to experimental data; plane, 0 or 180° dihedral angle.

Table 3.3 Calculated C–C Bond Energies (kJ/mol) for Gasification^a for Various Models

	Armchair		Zigzag			Weakening of C–CO by Epoxy (%)	
	Model A5	Model B5	Model C5	Model D5	Model E5		
HF/3-21G(d)	Raw data	406	164	263	550	336	224
	Calibrated ^b	495	—	—	—	683	33.4
B3LYP/6-31G(d)	Raw data	402	—	264	425	325	217
	Calibrated ^b	487	—	—	—	527	32.9

Source: Ref. 70.^aIndicated by dashed lines in Figure 3.5.^bCalibrated factors are as follows: 1.21 for C₂₄H₈ and 1.24 for C₂₅H₉ (see Figure 3.5). The experimental C–C bond energy is approximately 709 kJ/mol.

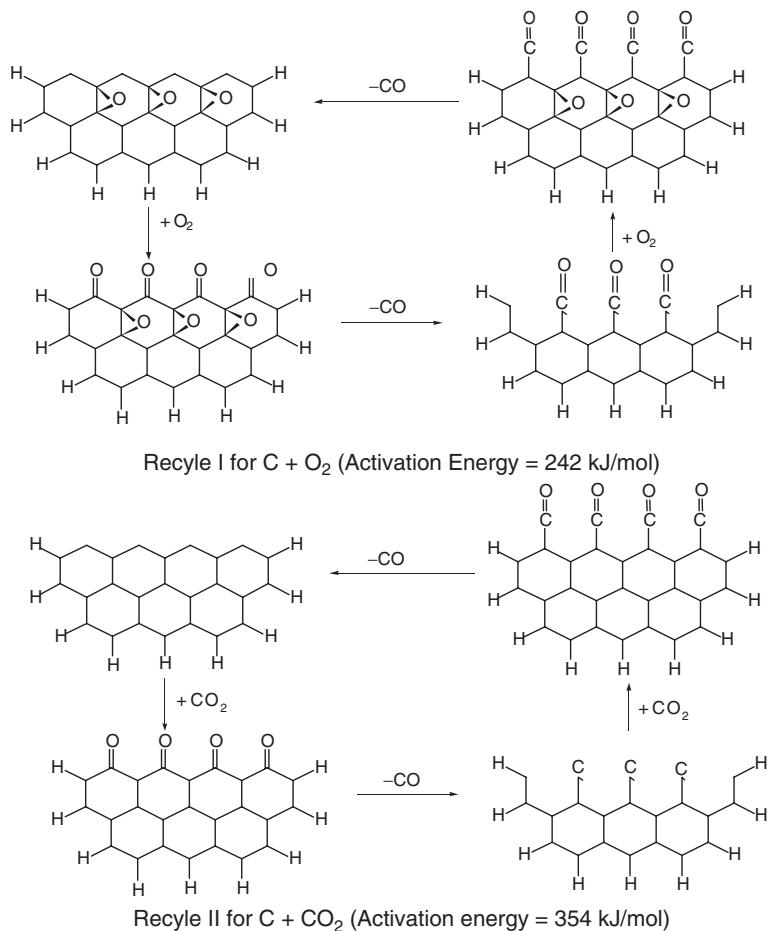


Figure 3.6 Reaction mechanism for O_2 - and CO_2 -carbon reactions. (Adapted from ref. 70.)

The oxygen chemisorption on the basal plane of graphite and the potassium promoter function in the oxidation of graphite were studied by Janiak et al. [82] using the extended Hückel tight-binding procedure. The sticking coefficient of dioxygen on clean graphite is very small. One O_2 molecule strongly adsorbs on top of a potassium atom with no interaction to the graphite layer and can dissociate into oxygen atoms. The favored adsorption sites for the individual species for potassium is above a hexagon (sixfold symmetry site), while oxygen and O_2 more strongly favor a position on top of a carbon atom (O_2 in a bent end-on approach) for the undamaged surface. Surface defects, however, figure prominently in stabilizing the oxygen species and also a potassium atom in the defect area.

More recently, the density function formalism was used to investigate the adsorption of potassium and oxygen on the basal plane of graphite by Lamoen and Persson [83]. Up to three graphite planes were used to represent the graphite, but it was found that the main physics was described correctly by a single graphite layer. For O₂ on potassium-graphite, the barrier for dissociation is much smaller than for O₂ on a clean graphite surface. However, in this study it was shown that the O₂ molecule bonds not on top of the potassium atom (with O–O axis parallel to the graphite surface) as suggested by Janiak et al. [82], but rather, side-on (with O–O axis parallel to the graphite surface, O₂ on one side of potassium and closer to the graphite surface).

Similarly, the studies of Janiak et al. [82] and Lamoen and Persson [83] were concentrated on the basal plane of graphite, although carbon gasification normally occurred on the edge sites. The semiempirical CNDO method was used by Chen and Yang [10] to provide an understanding of the origin of the catalytic activity of C–O–K groups for carbon gasification reactions by H₂O and CO₂. C–O–K groups on zigzag and armchair sites were considered, shown in Figures 3.7 and 3.8, respectively. The net charges of different carbon atoms are given in Tables 3.4 and 3.5, and the bond strengths are shown in Tables 3.6 and 3.7. The results indicated that the chemisorption of oxygen atoms on the edges, for both zigzag and armchair edges, caused positive charges on the carbon atoms. However, when potassium atoms are attached (in the form of C–O–K

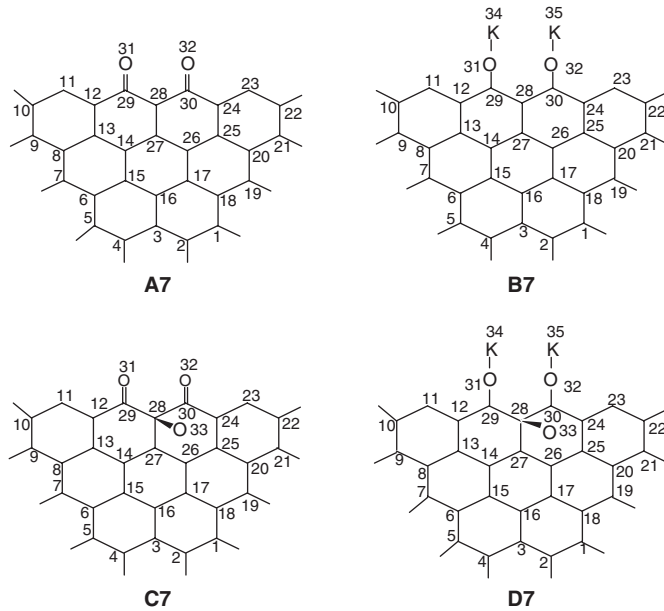


Figure 3.7 Model substrates with a zigzag face on graphite for CNDO molecular orbital calculation. (Adapted from ref. 10.)

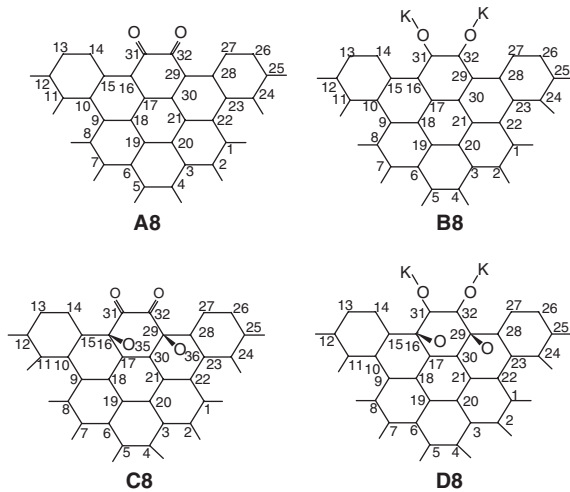


Figure 3.8 Model substrates with an armchair face on graphite for CNDO molecular orbital calculations. (Adapted from ref. 10.)

Table 3.4 Net Charge (Electrons) of Carbon Atoms in Substrates with Zigzag Edges^a

Atom Number	Structure A7	Structure B7	Atom Number	Structure A7	Structure B7
12	0.1579	-0.1548	25	0.2401	-0.0626
13	0.2401	-0.0626	26	0.1359	-0.1605
14	0.1359	-0.1605	27	0.3211	-0.1867
24	0.1579	-0.1548	28	-0.0128	-0.4863

Source: Ref. 10.

^aSee Figure 3.7.

Table 3.5 Net Charge (Electrons) of Carbon Atoms in Substrates with Armchair Edges^a

Atom Number	Structure A8	Structure B8	Atom Number	Structure A8	Structure B8
15	0.1728	-0.0287	21	0.1751	-0.0038
16	0.0558	-0.0813	28	0.1728	-0.0287
17	0.2297	-0.0003	29	0.0558	-0.0813
18	0.1751	-0.0038	30	-0.2297	-0.0003

Source: Ref. 10.

^aSee Figure 3.8.

**Table 3.6 Carbon–Carbon Bond Strengths in Substrates with Zigzag Edges.^a
Expressed by Diatomic Energy (kJ/mol)**

Bond	Structure A7	Structure B7	Structure C7	Structure D7
C28-C29	1978	2265	1668	1660
C28-C30	1978	2265	1668	1660
C12-C29	1750	2197	1727	2123
C24-C30	1750	2197	1727	2123

Source: Ref. 10.

^aSee Figure 3.7.

**Table 3.7 Carbon–Carbon Bond Strengths in Substrates with Armchair Edges.^a
Expressed by Diatomic Energy (kcal/mol)**

Bond	Structure A8	Structure B8	Structure C8	Structure D8
C16-C31	1909	2406	1651	2128
C29-C32	1909	2406	1651	2128
C31-C32	1797	2296	1705	1911

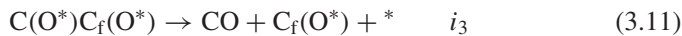
Source: Ref. 10.

^aSee Figure 3.8.

groups), net charges decreased (i.e., electron populations increased). The increase in electron density was more pronounced when C–O–K groups were attached to the zigzag edges. Consequently, carbon atoms with more negative net charges become more favorable for oxygen adsorption, resulting in the formation of more off-plane oxygen. The reaction can thus be catalyzed through the role of the off-plane oxygen as discussed above. The authors claimed that from the bond strengths, they could also explain the well-known observation reported in the literature that the activation energies were not changed in the alkali- and alkaline earth–catalyzed carbon gasification reactions by H₂O and CO₂. In our understanding, however, the CNDO results were not good enough to account for such an important phenomenon, as the C–C bonds calculated remained unchanged on the zigzag faces (Table 3.6) but were strengthened on the armchair faces (Table 3.7) by the C–O–K groups. No experiments have shown that activation energies remain unchanged on the zigzag faces and increase on the armchair faces in the alkali- or alkaline earth–catalyzed gas–carbon reactions.

Chen and Yang also pointed out that [10] diatomic energy in CNDO calculations was not a good representation for bond energy. Therefore, MOPAC, using MNDO approximation methods, was applied [69] and the results were based on bond dissociation energy. On the basis of the off-plane oxygen species, a more comprehensive mechanism for alkali- and alkaline earth–catalyzed gasification reactions of carbon by H₂O and CO₂ was proposed. The mechanism is given by

using CO_2 as the reactant:



where K represents an equilibrium constant and i a rate constant. An asterisk indicates a catalyst cluster, which is a nonstoichiometric compound and could be described as M_xO_y (where M is an alkali or alkaline earth metal atom and x and y are changeable during the gasification reaction). The mechanism proposed (still based on the off-plane oxygen theory) can account for several unresolved experimental observations: TPD and TK (transient kinetics) desorption results of the catalyzed system. Moreover, the relative activities of the alkali and alkaline earth elements can also be explained. The net charge of the edge carbon active site is substantially changed by gaining electron density from the alkali or alkaline earth element. The relative catalytic activities of these elements can be correlated with their abilities to donate electrons and change the net charge of the edge carbon atoms. Unfortunately, the explanation for similar activation energies for the uncatalyzed and catalyzed reactions was still not convincing, as in this study [32]; only zigzag structures were calculated and no results were presented on armchair structures.

As shown in the literature [10,72], the mechanism of the catalytic activity of clusters of the alkali compounds is different from that of C–O–K groups. The latter derives from the ability of the clusters to dissociate CO_2 and H_2O to form oxygen atoms, and the mobility of the dissociated oxygen atoms is facilitated by the clusters. So far, no electronic structure methods have been applied to study the metal cluster–catalyzed gas–carbon reactions.

Ab initio calculations were also performed on model graphite substrate with $-\text{O}$ and $-\text{O}-\text{M}$ groups (where M represents a metal) bonded to the zigzag face by Yang's group [84]. The surface C–C bonds in these structures are substantially weakened by adding $-\text{O}$ or $-\text{M}$ on the active carbon atoms, leading to CO release. It was thought that the extent of weakening in the C–C bond energy by different metals is in general agreement with the order of catalyst activities measured as turnover frequencies (TOFs). The rank order of TOFs by different catalysts is $\text{Cu} > \text{Ba} = \text{K} > \text{Sr} > \text{Ca} > \text{Mg} > \text{Na} > \text{Co} > \text{Fe} \geq \text{Li}$. However, as mentioned above, the experimental observation was that the uncatalyzed and alkali- and alkaline earth–catalyzed gas–carbon reactions have similar activation energies, and no experiments can tell the little difference in the activation energies of these different catalysts. Therefore, the explanation above of the different rank order of TOFs based on the extent of the weakening in the C–C bond energy by different metals is not convincing either.

In the studies noted above, the catalysts were located either above the basal plane or on the edge sites of graphite in the form of $-O-M$. The study of Radovic et al. [85] was very different, in which substitutionally doped boron was investigated. Both inhibiting and catalytic effects were observed in the experiments. The simple Hückel molecular orbital theory and a generalized Hückel theory, the self-consistent-field Pariser–Parr–Pople (SCF-PPP) approach, were used extensively to rationalize the experimental results. It was found that in the presence of substitutional boron, electron density on reactive carbon atoms was reduced and O_2 chemisorption was reduced, thus having an inhibiting effect on carbon oxidation. Nevertheless, the redistribution of electrons that inhibits O_2 chemisorption was thought to be responsible for a catalytic effect on CO and CO_2 desorption. The net effect appears to be a complex balance between the influences of boron content and distribution, carbon nature (e.g., surface area), and reaction conditions. It is very possible that in potassium-catalyzed gas–carbon reactions, some carbon atoms could also be replaced by potassium atoms and a similar mixed catalytic and inhibiting effect could occur, although no reports have appeared regarding the activities of substituted doped potassium. As mentioned above, Wong and Yang [86] did observe the inhibiting effect in K_2CO_3 -loaded graphite reactions with H_2O . Although Chen and Yang attributed the inhibiting effect to the $-O-K$ structure on the armchair sites [10], we think that the substitutional potassium may also play an important role.

3.4.3 More Specific Studies on NO_x , H_2O , CO_2 , and O_2 –Carbon Reactions

The unified mechanism of Yang focused on the formation and desorption of oxygen complexes, a common characteristic shared by carbon reactions with all the oxygen-containing gases. However, different reactions have their own behaviors, such as the formation of N_2 in NO_x –carbon reaction and H_2 formation in H_2O –carbon reaction. The pathway in which these gas molecules adsorb on the surface of carbon are also different, although the oxygen will finally be transferred to the carbon sites. Following Yang’s work, there have appeared many interesting specific studies in recent years.

The different adsorptions of oxygen-containing gases such as CO_2 and SO_2 on the different planes of graphite were studied by Chen and Yang using CNDO [87]. The results show that for CO_2 , the total energy change on the edge plane is six times that on the basal plane. For SO_2 , the change is only slightly stronger on the edge plane. The result is in agreement with the experimental fact that CO_2 has a strong preference for the edge plane, whereas SO_2 adsorbs on both planes with almost equal strength. This is also strong evidence that edge sites are much more active than basal plane sites in gas adsorption.

An attempt was made by Kyotani and Tomita [88] to analyze the reaction of carbon with NO or N_2O using an ab initio method. This method allows simulation of the chemisorption process of these gas molecules on zigzag and armchair edge sites of carbon by calculating the thermodynamics and the orbital bond

data. It was found that NO adsorption with the nitrogen atom down is more thermally favorable than the adsorption with the oxygen atoms down, while the oxygen down mode is more favorable than the nitrogen down mode for N₂O adsorption. Both NO and N₂O are more likely to adsorb in the side-on pathway with the bond axis parallel to the edge line forming the most stable chemisorbed species. The formation of N₂ in an N₂O–carbon reaction is apparently through the breakage of O–NN, but the mechanism for C–NO is more complicated, and possible N₂ formation routes were proposed through the reaction of surface C(N) with another adsorbed NO. However, this study is still far from reality, as the presence of O₂ was not included.

The opposite roles of O₂ in NO– and N₂O–carbon reactions were investigated in our recent study [89]. Previous experimental studies showed that the presence of O₂ greatly enhances NO–carbon reaction, while it depresses N₂O–carbon reactions on carbon surfaces. A popular explanation for the rate increase is that the addition of O₂ results in a large number of reactive carbon–oxygen complexes, and decomposition of these complexes produces many more active sites. The explanation for the latter is that excess O₂ simply blocks the active sites, thus reducing the rate of N₂O–carbon reaction. The contradiction is that O₂ can also occupy active sites in NO–carbon reaction and produce active sites in N₂O–carbon reduction. By using ab initio calculation, Zhu et al. [89] found that these opposite roles of O₂ are caused by the different manners of N₂O and NO adsorption on the carbon surface. In the presence of excess O₂, most of the active sites are occupied by oxygen groups. In the competition for the remaining active sites, NO is more likely to chemisorb in the form of NO₂, and NO chemisorption is more thermodynamically favorable than O₂ chemisorption. By contrast, the presence of excess O₂ makes N₂O chemisorption much less thermally stable either on the consecutive edge sites or on edge sites isolated by semiquinone oxygen. Similarly, in N₂O–carbon reaction with the presence of excess oxygen, the transfer of an oxygen atom of N₂O to the carbon sites is followed by the formation of N₂. From NO–carbon reaction, the –C–ONO–C–group (i.e., NO adsorbed in the form of NO₂ with the presence of excess O₂) can react with another adsorbed NO to form N₂, and the mechanism proposed compares well with the experimental results.

Montoya et al. [90] found that density function theory (DFT) is even better than the Hartree–Fock method in modeling graphite reactions with gases, as the former can effectively overcome spin contamination. In a follow-up study [91], they investigated the reaction of NO with char-bound nitrogen during combustion. DFT method B3LYP/6-31G(d) was used to optimize the geometries of reactants, NO adsorption complexes, and products. Schematic energy profiles for each reaction were obtained to elucidate mechanisms for N₂O evolution. It was found that NO molecule reacted with char-N to release predominantly N₂ and CO to the gas phase. For the model char structures studied, the presence of adsorbed oxygen on the char-containing nitrogen enhances reduction of the NO molecule to N₂, but N₂O can also be released as a minor nitrogen product. The same group also investigated the effect of the local structure of the active sites and

the surface coverage on CO desorption, particularly from carbonyl groups [92]. They also investigated the kinetics of CO desorption from a carbon surface [93]. They found that in the initial stage of the desorption process, the six-membered ring of the carbonaceous model opens slightly to let the CO break away and then closes up to form the five-membered ring. Transition-state theory was used to calculate the thermal rate constant for desorption of CO in the range 873 to 1973 K. The fitted Arrhenius expression for the rate constants calculated is $k(T) = 1.81 \times 10^{17} \exp[-47,682/T(\text{K})](\text{s}^{-1})$, which is within the experimental uncertainty for char gasification. But their kinetic treatment was disputed by Frankcombe and Smith [94].

Carbon gasification with steam to produce H₂ and CO is an important reaction used widely in industry for hydrogen generation. Although the literature is vast, the mechanism for the formation of H₂ is still unclear. In particular, little has been done to investigate the potential of molecular orbital theory to distinguish different mechanism possibilities. In our recent work [95], the DFT method [B3LYP/6-31g(d)//B3LYP/3-21g(d)] was used to demonstrate a favorable energetic pathway as in Figure 3.9, where H₂O is first physically adsorbed on the virgin graphite surface with negligible change in molecular structure. Chemisorption occurs via oxygen approaching the carbon edge site with one hydrogen atom stretching away from the oxygen in the transition state. This is followed by a local minimum state in which the stretching hydrogen is further disconnected from the oxygen atoms, and the remaining OH group is still on the carbon edge site. The disconnected hydrogen then pivots around the OH group to bond with

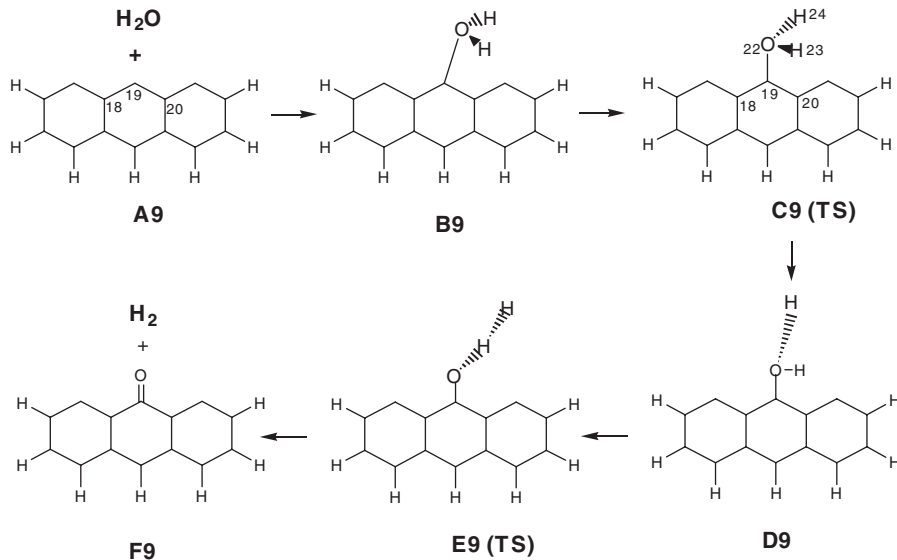


Figure 3.9 Pathway of a H₂O–carbon reaction. (Adapted from ref. 95.)

the hydrogen of the OH group and forms H₂. The oxygen atom remaining on the carbon edge site is subsequently desorbed as CO. The reverse pathway occurs when H₂ reacts with the surface oxygen to produce H₂O. Our mechanism is based upon DFT calculations and in good agreement with all the experimental observations and results. First, it explains that H₂O is first physically adsorbed. This process is slightly exothermic and with negligible change of the molecular structure. The located minimum state of the physical adsorption (model B9) is in agreement with the electronic structure of H₂O being insignificantly perturbed. Second, for the total reaction H₂O + C → H₂ + CO, our calculated ΔH is +146.0 kJ/mol. This is very close to the experimental value (129.0 kJ/mol) [1]. Third, the mechanism is consistent with the reverse reaction [i.e., H₂ + C(O) → H₂O + C] being possible, as demonstrated by other workers [1]. Finally, our study can do further justice to the results by Yang et al. [46,96] regarding inhibition and anisotropy in H₂O–carbon reactions. The hydrogen inhibition is apparently due to the much stronger adsorption of hydrogen on edge sites compared with H₂O. The anisotropy of reaction is due to the different affinities of hydrogen atoms (the hydrogen atoms may come from either H₂O dissociation or product H₂) on zigzag and armchair sites; the C–H bond is stronger on the former than on the latter. Consequently, hexagonal etched pits with zigzag edges were observed [46,96]. For a C–CO₂ reaction, the etched pits are round, due to the absence of hydrogen atoms.

Radovic has also investigated the modes of chemisorption of CO₂ on the zigzag surface, giving particular attention to the nature of bonding at the zigzag edge [97] using DFT methods. In agreement with long-standing experimental evidence, dissociative CO₂ adsorption was found to be particularly favorable; furthermore, dissociation was found to be favored on isolated carbinelike zigzag sites.

The reaction between molecular oxygen and the zigzag and armchair surfaces of two model graphites was studied by Sendt and Haynes [98,99] using the density functional theory at the B3LYP/6-31G(d) level of theory. The chemisorption of O₂ on zigzag sites is barrierless and highly exothermic, releasing 640 to 740 kJ/mol, while two desorption processes were found to have barriers of 420 and 340 kJ/mol, with the possibility of a stable intermediate forming in the latter pathway. For O₂ chemisorption on armchair sites, a small barrier of 18 kJ/mol was found for the chemisorption reaction, which is a 578-kJ/mol exothermic overall, producing a stable quinone. Gasification of carbon occurs as CO, with barriers of 296 and 435 kJ/mol for the first and second CO loss, respectively. The stable quinone can also undergo a rearrangement reaction to form two ketene groups, with a barrier of 260 kJ/mol.

CO desorption has been the focus in all the previous work on carbon reactions with oxygen-containing gases, but CO₂ is also a very important product, especially in the lower-temperature regime. The mechanism for the formation and desorption of CO₂-yielding groups is another important issue that should be investigated thoroughly. A molecular orbital theory calculation that takes CO₂ into account could be a new breakthrough in this area. Such a study would

also shed light on the question of whether CO₂ is a primary product or only a secondary product formed from CO in the gas phase.

The inflection point on Arrhenius plots of NO-and N₂O–carbon is yet to be clarified. For example, the activation energy of NO–carbon reaction increases from 60 to 125 kJ/mol in the lower-temperature range (such as lower than 823 K) to 170 kJ/mol in the higher-temperature range (such as above 823 K) [71]. It was explained by Yang et al. [71] as NO basal-plane C-attack and the formation of deep pits at higher temperatures, but they could not explain why such a breakpoint has not been observed experimentally in an O₂–carbon reaction, and why at the lower-temperature regime, NO_x–carbon reactions have such a low activation energy. We think that the very low activation energy may be caused by the production of CO₂ at the lower-temperature regime. However, before the mechanism for the formation and desorption of CO₂ could be fully clarified, the inflection point is still a problem. This question has proved to be beyond the ability of experiment, and breakthrough could come from molecular simulations.

In addition, no molecular dynamics simulations have been applied to catalyzed or noncatalyzed carbon gasifications. An interesting Monte Carlo simulation of carbon gasification was conducted by Kyotani et al. [100]. A simple Hückel method was applied to calculate the molecular orbitals of a large polynuclear aromatic molecule which was employed as a model crystallite for carbon. A free valence at each carbon atom in model crystallites of varying size and shape was determined, and this value was taken as a measure of reaction probability for the Monte Carlo simulation. This method could simulate the following commonly observed features in actual gasification: (1) Gasification starts at edge carbon atoms; (2) zigzag sites are more reactive than armchair sites, and (3) there is a specific monotonic rate increase with conversion. However, this was still at a very primitive stage and the introduction of ab initio or DFT method (instead of semiempirical methods) accompanied by more powerful computer hardware is necessary for more valuable simulation studies. Various reaction conditions, such as temperature, pressure, and type of gaseous reactant, should be incorporated in the next stage of simulation. The introduction of surface functional groups into the model would also be important, and catalysts should also be taken into account.

3.5 METAL–CARBON INTERACTIONS

Metal nanoclusters exhibit physical, chemical, and electrical properties that differ significantly from those of bulk materials, due to the large fraction of surface atoms and the quantum confinement effect in small clusters, and the potential applications of these nanostructures in areas such as heterogeneous catalysis, sensors, and microelectronics are thus very promising. Metal nanoclusters deposited on substrate are particularly suitable for catalysis applications and are receiving increasing attention. Highly oriented pyrolytic graphite is a widely used

substrate for metal nanoclusters in electrocatalysis, because it is electronically conducting, in addition to being inert and stable. Owing to the influence of the substrate, the properties of substrate-supported metal nanoclusters are different from those of isolated nanoclusters, and strongly dependent not only on the cluster size and surface composition, but also on the surface morphology and nature of metal–substrate interactions. Understanding and developing the heterogeneous catalysis of these clusters require comprehensive studies of their thermal, structural, and dynamic properties.

Advanced techniques of surface and particle characterizations have made it possible to study the properties of supported metal nanoclusters experimentally. Wang et al. [101] studied the *in situ* temperature-induced shape transformation and surface-melting platinum nanoclusters deposited on substrate with transmission electron microscopy (TEM). It was found that the cubic and tetrahedral platinum clusters evolve into spherical shapes, as the temperature is higher than 773 K, while surface and overall melting occur at slightly higher temperatures. The melting temperature depends on the size, shape, and composition of the clusters and in most cases is higher than that of bulk melting, which can be attributed to the larger fraction of surface atoms of nanoclusters. Bardotti et al. conducted experimental investigation of the diffusion of large spherical antimony nanoclusters containing around 2300 atoms deposited on graphite substrate, and obtained the diffusion coefficient of the clusters moving on a graphite substrate, which is $D = D_0 \exp(-E_a/k_B T)$, with $D_0 = 1.6 \times 10^4 \text{ cm}^2/\text{s}$ and $E_a = 67 \pm 0.9 \text{ kJ/mol}$ [102]. Such a surprising value of D_0 suggests that the diffusion cannot be explained by a simple atomic active process and that a new mechanism should be introduced.

In addition to experimental investigations, considerable theoretical effort has been devoted to provide insights into understanding the thermal and dynamical properties of metal nanoclusters deposited on graphite substrate. Molecular dynamics (MD) simulation was commonly employed as a complement of experimental investigations. MD simulations have the advantages of probing picosecond-time-scale dynamics for a small length of scale of nanoclusters, whereas experimental studies are impossible. Accurate potential functions for the metal–metal, metal–carbon, and carbon–carbon interactions are essential for MD simulations. Considering that the thermal and dynamic properties, such as melting and diffusing processes, can only be obtained at the expense of long MD runs and that the nanoclusters under investigation always include thousands of atoms, an *ab initio* method that can only deal with small systems (a few tens of atoms) over a limited time scale (tens of picoseconds at best) is ruled out at present; instead, empirical or semiempirical potential functions of analytic forms and computational convenience are adopted. The interactions between carbon atoms in graphite substrate are always modeled by a simple Lennard-Jones form or a more precise many-body Tersoff potential which takes the covalent features into account. In some special cases, the atoms in graphite are fixed to represent a static substrate. The commonly used potential function for metal–metal interactions is the Sutton–Chen potential, a many-body potential that has been

successful in reproducing the bulk properties of metals [103]. The metal–carbon interactions are represented by the Lennard-Jones potential. This set was shown to give a good balance between accuracy and computational cost, and makes MD calculations practical.

Based on this potential function scheme, Huang and Ballbuena [104] used MD simulation to investigate the structural and dynamic evolution of single platinum nanoclusters of cubic and spherical shape deposited on graphite substrate. Heating and cooling curves calculated between –346 and 1800 K indicated that the melting behavior depends on the shape and size of the clusters. The solid–liquid transition of the cubic nanoclusters containing 256 Pt atoms was predicted to take place at 1000 K, whereas for a cluster with a spherical shape of 260 Pt atoms, the transition temperature is 1020 K. At 700 K (for cubic particles) and 900 K (for spherical particles), the outmost surface layers start to melt and their atoms migrate to the layers closest to the substrate, indicating a temperature-induced wetting phenomenon. Huang et al. [105] also conducted MD simulations to examine the structural and dynamic properties of bimetallic nanoclusters (Cu–Ni and Pt–Au) deposited on graphite substrate. The evolutions of potential energy and heat capacity indicate that bimetallic nanoclusters supported on graphite substrate melt at a much lower temperature than the bulk metal, although their melting temperature is slightly higher than that of isolated nanoclusters of identical size and composition in vacuum, owing to the effect of weak graphite support. One of the elements (Cu in Cu–Ni and Au in Pt–Au) of the bimetallic nanoclusters was found to wet the graphite substrate. The wetting characteristics are dominated by the delicate balance between metal–metal and metal–graphite interactions. The two metals in bimetallic nanoclusters behave differently upon melting. One of the metals (Cu in Cu–Ni and Au in Pt–Au) diffuses toward the cluster interior while the other (Ni in Cu–Ni and Pt in Pt–Au) diffuses slowly to the outer layers, resulting in surface segregation. Similar conclusions have also been drawn by Sankaranarayanan et al. [106] in the MD study of other bimetallic nanoclusters (Pd–Pt, Pd–Rh, and Pd–Cu) deposited on graphite substrate and by Huang and Balbuena [107] for isolated Cu–Ni bimetallic nanoclusters.

The study of the mobility of metal nanoclusters deposited on graphite substrate is another interesting issue, which provides valuable insights into understanding the fabrication of supported catalysts, thin films, and self-organized structures by cluster deposition. Deltour et al. [108] first attempted to interpret the rapid diffusion of metal nanoclusters deposited on a crystalline surface using MD simulations. In their work, metal–metal, metal–substrate, and substrate–substrate interactions are all simply represented by Lennard-Jones forms. The rapid diffusion of substrate-supported nanoclusters was attributed to a Brownian motion induced by the internal vibrations of the clusters and/or the vibrations of the substrate, where the clusters diffuse “as a whole.” Similar results were also obtained by Lewis et al. [109] using MD with more elaborate potential functions. They modeled the Au–Au interactions using an embedded-atom method, while carbon atoms are assumed to interact via Tersoff potential. Their calculations concluded that the diffusion of large gold clusters on graphite substrate can take place at a

pace that is comparable to that for a single adatom, and large islands formed by cluster aggregation are also expected to be mobile.

It is noteworthy that the present MD studies can provide theoretical insights into the thermal and dynamical processes of the metal nanoclusters deposited on graphite substrate, but are unavailable for probing the chemical reactions and catalytic activity of these supported clusters directly, where ab initio method is required, similar to the situation of carbon gasifications. However, these MD results, especially the shape evolution and diffusion behaviors, are essential for growing metal clusters and shape control, which significantly affect the catalytic activity of these metal clusters. It may be a practical way to study the catalytic activity of graphite-supported metal nanoclusters by establishing a model system of medium size representing well the dynamic features of the clusters and suitable for ab initio calculations, on the basis of MD results. Such MD simulations would be very useful for the fundamental understandings of many catalytic reactions involving carbon-supported catalysts.

3.6 CONCLUSIONS

Based on the preceding discussions, the following conclusions may be drawn:

1. Different molecular simulations have been used in the investigations of gas–carbon reactions, which can provide deep insights into the fundamental understandings. Semiempirical methods could provide reliable relative comparison, but the absolute values were crudely determined, thus used primarily in the early theoretical studies. Relatively small single-layer graphite plane also proves to be enough in the qualitative investigation. But for higher accuracy, ab initio (plus DFT) methods and larger molecular structures are necessary.
2. Early theoretical studies on hydrogen–carbon interaction were focused on the basal plane of graphite, but the edge sites of graphite are much more active. The reactivities of the graphite basal or edge sites are closely related to their electronic structures.
3. Yang’s group summarized a unified mechanism based on an off-plane oxygen, which can account for many key kinetic facts of carbon reactions with oxygen-containing gases such as the 30% lower activation energy and the much higher reaction rate of O₂–carbon reactions compared with CO₂–and H₂O–carbon reactions. The different TPD and TK behaviors following O₂–carbon reactions can also be well explained. This unified mechanism can also be broadened to the catalyzed gas–carbon reactions.
4. Following Yang’s work, more recent studies using ab initio and DFT methods on carbon reactions with NO_x, H₂O, CO₂, and O₂ followed. Some issues have proved difficult to solve through experiments, such as the mechanism of N₂ formation in an NO–carbon reaction, the opposite roles of O₂ in NO–and N₂O–carbon reactions, and the formation of H₂ in H₂O–carbon

reactions. But with the aid of molecular simulations, satisfactory explanations have been obtained.

5. There are some important issues yet to be addressed. An explanation of the complicated anisotropic character of the O₂–carbon reaction is still not available. The reason for the similar activation energies of uncatalyzed and alkali metal–catalyzed gas–carbon reactions remains unclear. Due to the limitations of computational loading, simulations by incorporating ab initio or DFT into molecular dynamics is neither available for studying (catalyzed or noncatalyzed) carbon reactions with oxygen-containing gases nor ready for providing insights into the catalytic reactions of carbon-supported metal catalysts. The CO₂ product should be included in future modeling work on gas–carbon reaction, and the mechanism for the inflection point on the Arrhenius plots of NO– and N₂O–carbon is yet to be clarified.

REFERENCES

- [1] P.L. Walker, Jr., F. Rusinko, Jr., L.G. Austin, in *Advances in Catalysis*, Vol. 11, Academic Press, New York, 1959, p. 133.
- [2] S. Ergun, M.R. Mentser, in P.L. Walker, Jr., Ed., *Chemistry and Physics of Carbon*, Vol. 1, Marcel Dekker, New York, 1965, p. 203.
- [3] R.T. Yang, in P.A. Thrower, Ed., *Chemistry and Physics of Carbon*, Vol. 19, Marcel Dekker, New York, 1984, p. 163.
- [4] J.K. Floess, J.P. Longwell, A.F. Sarofim, *Energy Fuels* 2 (1988) 18.
- [5] S.R. Kelemen, H. Freund, *Carbon* 23 (1985) 619.
- [6] J.L. Su, D.D. Perlmutter, *AICHE J.* 31 (1985) 1725.
- [7] N.R. Laine, F.J. Vastola, P.L. Walker, Jr., *J. Phys. Chem.* 67 (1963) 2030.
- [8] K.J. Huttinger, J.S. Nill, *Carbon* 28 (1990) 457.
- [9] L.R. Radovic, H. Jiang, A.A. Lizzio, *Energy Fuels* 5 (1991) 68.
- [10] S.G. Chen, R.T. Yang, *J. Catal.* 141 (1993) 102.
- [11] H.F. Schaefer, *Quantum Chemistry: The Development of Ab Initio Methods in Molecular Electronic Structure Theory*, Oxford University Press, New York, 1984.
- [12] P.S.C. Matthews, *Quantum Chemistry of Atoms and Molecules*, Cambridge University Press, New York, 1986.
- [13] C.A. Coulson, B. O'Leary, R.B. Mallion, *Hückel Theory for Organic Chemists*, Academic Press, London, 1978.
- [14] R. Pariser, R.G. Parr, *J. Chem. Phys.* 21 (1953) 466.
- [15] R. Pariser, R.G. Parr, *J. Chem. Phys.* 21 (1953) 767.
- [16] J.N. Murrell, A.J. Harget, *Semi-empirical Self-Consistent-Field Molecular Orbital Theory*, Wiley-Interscience, London, 1972.
- [17] J.A. Pople, D.P. Santry, G.A. Segal, *J. Chem. Phys.* 43 (1965) S12.
- [18] J.A. Pople, D.L. Beveridge, P.A. Bobosh, *J. Chem. Phys.* 47 (1967) 2026.
- [19] N. Bodor, M.J.S. Dewar, A. Harget, E. Haselbach, *J. Am. Chem. Soc.* 92 (1970) 3854.

- [20] J.J.P. Stewart, in K.B. Liprowits, D.B. Boyd, Eds., *Reviews in Computational Chemistry*, Vol. I, VCH Publisher, New York, 1990, pp. 45–118.
- [21] W.J. Hehre, L. Radom, P.R. Schleyer, J.A. Pople, *Ab Initio Molecular Orbital Theory*, Wiley, 1986.
- [22] T. Clark, *A Handbook of Computational Chemistry: A Practical Guide to Chemical Structure and Energy Calculations*, Wiley, New York, 1985.
- [23] J.B. Foresman, A. Frisch, *Exploring Chemistry with Electronic Structure Methods*, 2nd ed., Gaussian, Pittsburgh, PA, 1996.
- [24] P. Hohenberg, W. Kohn, *Phys. Rev. B* 136 (1964) 864.
- [25] W. Kohn, L.J. Sham, *Phys. Rev. A* 140 (1965) 1133.
- [26] R.G. Parr, W. Yang, *Density Functional Theory of Atoms and Molecules*, Oxford University Press, New York, 1989.
- [27] J.M. Haile, *Molecular Dynamics Simulation: Elementary Methods*, Wiley, New York, 1992.
- [28] D.P. Landau, K. Binder, *A Guide to Monte Carlo Simulations in Statistical Physics*, Cambridge University Press, New York, 2000.
- [29] A.J. Bennett, B. McCarroll, R.P. Messmer, *Surf. Sci.* 24 (1971) 191.
- [30] R. Dovesi, C. Pisani, F. Ricca, C. Roetti, *J. Chem. Phys.* 65 (1976) 3075.
- [31] R. Dovesi, C. Pisani, C. Roetti, *Chem. Phys. Lett.* 81 (1981) 498.
- [32] J.P. Chen, R.T. Yang, *Surf. Sci.* 216 (1989) 481.
- [33] F.H. Yang, R.T. Yang, *Carbon* 40 (2002) 437.
- [34] Y. Ferro, F. Marinelli, A. Allouche, *J. Chem. Phys.* 116 (2002) 8124.
- [35] A.J. Bennett, B. McCarroll, R.P. Messmer, *Phys. Rev. B* 3 (1971) 1397.
- [36] J. Casañas, F. Illas, F. Sanz, J. Virgili, *Surf. Sci.* 133 (1983) 29.
- [37] M. Balooch, D.R. Olander, *J. Chem. Phys.* 63 (1975) 4772.
- [38] R. Caballol, J. Igual, F. Illas, J. Rubio, *Surf. Sci.* 149 (1985) 621.
- [39] V. Barone, F. Lelj, C. Minichino, *Surf. Sci.* 189 (1987) 185.
- [40] R.P. Messmer, A.J. Bennett, *Phys. Rev. B* 6 (1972) 633.
- [41] L. Jeloaica, V. Sidis, *Chem. Phys. Lett.* 300 (1999) 157.
- [42] Y. Ferro, F. Marinelli, A. Allouche, *Chem. Phys. Lett.* 368 (2003) 609.
- [43] T. Zecho, A. Guttler, X.W. Sha, B. Jackson, J. Kuppers, *J. Chem. Phys.* 117 (2002) 8486.
- [44] X. Sha, B. Jackson, *Surf. Sci.* 496 (2002) 318.
- [45] D.L. Biederman, A.J. Miles, F.J. Vastola, P.L. Walker, Jr., *Carbon* 14 (1976) 351.
- [46] R.T. Yang, R.Z. Duan, *Carbon* 23 (1985) 325.
- [47] A. Sen, J.E. Bercaw, *J. Phys. Chem.* 84 (1980) 465.
- [48] C.A. Coulson, L.J. Schaad, L. Burnelle, in *Proceedings of the 3rd Conference on Carbon*, Buffalo, NY, Pergamon Press, New York, 1959, pp. 27–35.
- [49] C.A. Coulson, in *Proceedings of the 4th Conference on Carbon*, Buffalo, NY, American Carbon Society, 1960, p. 215.
- [50] S.E. Stein, R.L. Brown, *Carbon* 23 (1985) 105.
- [51] S.E. Stein, R.L. Brown, *Mol. Struct. Energet.* 2 (1987) 37.
- [52] S.E. Stein, R.L. Brown, *J. Am. Chem. Soc.* 109 (1987) 3721.

- [53] K. Nakada, M. Fujita, G. Dresselhaus, M. Dresselhaus, *Phys. Rev. B* 54 (1996) 17954.
- [54] K. Wakabayashi, M. Fujita, H. Ajiki, M. Sigrist, *Phys. Rev. B* 59 (1999) 8271.
- [55] D.J. Klein, L. Bytautas, *J. Phys. Chem. A* 103 (1999) 5196.
- [56] L.R. Radovic, B. Bockrath, *J. Am. Chem. Soc.* 127 (2005) 5917.
- [57] Z.J. Pan, R.T. Yang, *J. Catal.* 123 (1990) 206.
- [58] F. Darkrim, D. Levesque, *J. Chem. Phys.* 109 (1998) 4981.
- [59] Q. Wang, J.K. Johnson, *J. Chem. Phys.* 110 (1999) 577.
- [60] V.V. Simonyan, P. Diep, J.K. Johnson, *Chem. Phys.* 111 (1999) 9778.
- [61] K.A. Williams, P.C. Eklund, *Chem. Phys. Lett.* 320 (2000) 352.
- [62] H. Cheng, G.P. Pez, A.C. Cooper, *J. Am. Chem. Soc.* 123 (2001) 5845.
- [63] Y. Ma, Y. Xia, M. Zhao, R. Wang, L. Mei, *Phys. Rev. B* 63 (2001) 115422.
- [64] P. Dubot, P. Cenedese, *Phys. Rev. B* 63 (2001) 241402.
- [65] S.M. Lee, Y.H. Lee, *Appl. Phys. Lett.* 76 (2000) 2877.
- [66] G.E. Froudakis, *J. Phys. Condens. Matter* 14 (2002) R453.
- [67] Z.H. Zhu, G.Q. Lu, S. Smith, *Carbon* 42 (2004) 2509.
- [68] M.R. Hayns, *Theor. Chim. Acta (Berl.)* 39 (1975) 61.
- [69] S.G. Chen, R.T. Yang, *Energy Fuels* 11 (1997) 421.
- [70] N. Chen, R.T. Yang, *J. Phys. Chem. A* 102 (1998) 6348.
- [71] N. Chen, R.T. Yang, R.S. Goldman, *J. Catal.* 180 (1998) 245.
- [72] S.G. Chen, R.T. Yang, *J. Catal.* 138 (1992) 12.
- [73] P.L. Walker, Jr., R.L. Taylor, J.M. Ranish, *Carbon* 29 (1991) 411.
- [74] B. Marchon, W.T. Tysoe, J. Carrazza, H. Heinemann, G.A. Somorjai, *J. Phys. Chem.* 92 (1988) 5744.
- [75] A.A. Lizzio, H. Jiang, L.R. Radovic, *Carbon* 28 (1990) 7.
- [76] Z. Zhang, T. Kyotani, A. Tomita, *Energy Fuels* 2 (1988) 679.
- [77] F. Kapteijn, R. Meijer, S.C.V. Eck, J.A. Moulijn, in *Preprints, ACS Symposium, Division of Fuel Chemistry*, New York, 1991, pp. 990–997.
- [78] S.G. Chen, R.T. Yang, F. Kapteijn, J.A. Moulijn, *Ind. Eng. Chem. Res.* 32 (1993) 2835.
- [79] N. Chen, R.T. Yang, *Carbon* 36 (1998) 1061.
- [80] W.Y. Wen, *Catal. Rev. Sci. Eng.* 22 (1980) 1.
- [81] B.J. Wood, K.M. Sancier, *Catal. Rev. Sci. Eng.* 26 (1984) 233.
- [82] C. Janiak, R. Hoffmann, P. Sjövall, B. Kasemo, *Langmuir* 9 (1993) 3427.
- [83] D. Lamoen, B.N.J. Persson, *J. Chem. Phys.* 108 (1998) 3332.
- [84] H. Huang, R.T. Yang, *J. Catal.* 185 (1999) 286.
- [85] L.R. Radovic, M. Karra, K. Skokova, P.A. Thrower, *Carbon* 36 (1998) 1841.
- [86] C. Wong, R.T. Yang, *Ind. Eng. Chem. Fundam.* 23 (1984) 298.
- [87] S.G. Chen, R.T. Yang, *Langmuir* 9 (1993) 3259.
- [88] T. Kyotani, A. Tomita, *J. Phys. Chem. B* 103 (1999) 3434.
- [89] Z.H. Zhu, J. Finnerty, G.Q. Lu, R.T. Yang, *J. Phys. Chem. B* 105 (2001) 821.
- [90] A. Montoya, T.N. Truong, A.F. Sarofim, *J. Phys. Chem. A* 104 (2000) 6108.

- [91] A. Montoya, T.N. Truong, A.F. Sarofim, *J. Phys. Chem. A* 104 (2000) 8409.
- [92] A. Montoya, T.T. Truong, F. Mondràgon, T.N. Truong, *J. Phys. Chem. A* 105 (2001) 6757.
- [93] A. Montoya, F. Mondràgon, T.N. Truong, *J. Phys. Chem. A* 106 (2002) 4236.
- [94] T.J. Frankcombe, S.C. Smith, *Carbon* 42 (2004) 2921.
- [95] Z.H. Zhu, J. Finnerty, G.Q. Lu, M.A. Wilson, R.T. Yang, *Energy Fuels* 16 (2002) 847.
- [96] R.T. Yang, K.L. Yang, *Carbon* 23 (1985) 537.
- [97] L.R. Radovic, *Carbon* 43 (2005) 907
- [98] K. Sendt, B.S. Haynes, *Combust. Flame* 143 (2005) 629.
- [99] K. Sendt, B.S. Haynes, *Proc. Combust. Inst.* 30 (2005) 2141.
- [100] T. Kyotani, K. Ito, A. Tomita, L.R. Radovic, *AICHE J.* 42 (1996) 2303.
- [101] Z.L. Wang, J. M. Petroski, T.C. Green, M.A. El-sayed, *J. Phys. Chem. B* 102 (1998) 6145.
- [102] L. Bardotti, P. Jensen, M. Treilleux, A. Hoareau, B. Cabaud, *Phys. Rev. Lett.* 74 (1995) 4694.
- [103] A.P. Sutton, J. Chen, *Philos. Mag. Lett.* 61 (1990) 139.
- [104] S.P. Huang, P.B. Balbuena, *Mol. Phys.* 100 (2002) 2166.
- [105] S.P. Huang, D.S. Mainardi, P.B. Balbuena, *Surf. Sci.* 545 (2003) 163.
- [106] S.K.R.S. Sankaranarayanan, V.R. Bhethanabotla, B. Joseph, *Phys. Rev. B* 72 (2005) 195404.
- [107] S.P. Huang, P.B. Balbuena, *J. Phys. Chem. B* 106 (2002) 7225.
- [108] P. Deltour, J.L. Barrat, P. Jensen, *Phys. Rev. Lett.* 78 (1997) 4597.
- [109] L.J. Lewis, P. Jensen, N. Combe, J.L. Barrat, *Phys. Rev. B* 61 (2000) 16084.

4 Carbon as Catalyst Support

FRANCISCO RODRÍGUEZ-REINOSO and ANTONIO SEPÚLVEDA-ESCRIBANO

4.1 INTRODUCTION

Porous carbon materials constitute a very flexible set of supports for the preparation of heterogeneous catalysts. Their physical and chemical surface properties can easily be tailored to develop a large surface area to disperse the active phases, the proper pore size distribution to facilitate the diffusion of reactants and products to and from the surface, and the acid–base character needed for obtaining the best performance.

Although carbon-supported catalysts are considered to be the best choice for a great number of reactions, few large-volume processes currently use these systems, and less than 1% of the activated carbon production worldwide is used as catalyst support. This may be due to the lack of reproducibility that sometimes arises with carbon-supported catalysts as a result of the relatively poor knowledge of the properties of these materials that influence their behavior.

Fortunately, the increasing number of scientific publications on this subject is shedding light on this field and helping to better understand the behavior of carbon-supported catalysts. As early as in 1984, Pierre Ehrburger reviewed the advantages of carbon supports for the preparation of highly dispersed metal catalysts [1]. Other recent reviews deal with the role of carbon-supported catalysts in reactions such as hydrodesulfurization of thiophene and Fischer–Tropsch synthesis [2], and with the advantages of carbon materials as support for precious metals [3], pointing out the additional properties required for carbon supports for fuel cell applications. More recently, Rodríguez-Reinoso [4–6] and Radovic et al. [6,7] have reviewed various aspects of the use of carbon materials as catalysts and catalyst supports.

A large variety of carbon materials can and have been used as catalyst supports. The most important are granular and powdered activated carbons and carbon blacks, but there is increasing interest in related materials, such as activated carbon fibers and cloths, nanotubes, and nanofibers [8]. A comprehensive review

of the use of these materials as catalysts and catalyst supports has been published [9]. Although carbon materials cannot be used in reactions that are carried out under certain conditions (hydrogenation at temperatures higher than 700 to 800 K or oxidation above 500 K), they show some advantages over other traditional catalyst supports [4]:

- The carbon surface is resistant to both acidic and basic media.
- The structure is stable at high temperatures.
- The pore structure can be tailored to obtain the pore size distribution needed for a given application.
- Porous carbons can be prepared with a variety of macroscopic shapes (e.g., granules, powder, fibers, cloths, pellets, monoliths, disks).
- The chemical properties of the surface can be modified to control polarity and hydrophobicity.
- The active phase can be recovered easily from spent catalysts by burning away the carbon support.
- Carbon supports are usually cheaper than other conventional catalyst supports.

These properties can be exploited in a great number of catalytic reactions. The *Catalytic Reaction Guide* published by Johnson Matthey gives a list of 69 reactions catalyzed by noble metals. Among them, carbon materials can act as a catalyst support in 50 reactions of industrial interest. The main properties of carbon materials involved in their role as catalyst support, and some of the processes that employ carbon materials as catalyst support, are presented in this chapter.

4.2 PROPERTIES AFFECTING CARBON'S ROLE AS CATALYST SUPPORT

4.2.1 Surface Area and Porosity

High surface area and a well-developed porosity are very important for achieving a high dispersion of the active phase in the catalyst (*dispersion* is the fraction of metal atoms that are on the surface of the support in relation to the total metal loading). Carbon materials, especially activated carbon, exhibit surface areas much higher than those of other conventional catalyst supports (e.g., alumina, silica). However, a great part of this surface area may be contained in narrow micropores, in which case it may not be available to reactants.

Many studies report the effect of porosity and surface area on metal dispersion and catalytic activity. Linares-Solano et al. [10] prepared platinum catalysts supported on a graphitized carbon black (V3G), which was subjected to various degrees of activation in air to increase the surface area. They observed that as the surface area of the parent sample increased from $62 \text{ m}^2/\text{g}$ to $136 \text{ m}^2/\text{g}$,

the platinum dispersion on the carbon support increased from 0.17 to 0.35. In a different system it was also found that the catalytic activity for thiophene hydrodesulfurization (HDS) of molybdenum supported on activated carbons, prepared from the same precursor but with increasing surface area and porosity, increased with surface area up to $1200\text{ m}^2/\text{g}$, remaining constant thereafter [11].

Some authors have found that the shape of pores in activated carbons can play an important role in the catalytic process when it is used as support, in opposition to other solids with pores that are not slit shaped. This is the case for Laine et al. [12,13], who used activated carbons as support for Ni–Mo HDS catalysts. On the basis of their results, these authors suggested that the narrow slit-shaped pores in activated carbon are able to lower the vapor pressure of sulfur to such an extent that they create a driving force for sulfur transfer from the active compound to the micropores, this process forming active vacancies in the metal sulfide. This *sink effect* was not observed in microporous silica, whose pores are not slit shaped.

In some cases, a high surface area of the carbon support may be detrimental if it is confined in narrow micropores that are not accessible to the reactant molecules. This is especially important in processes where large molecules are involved, as in the treatment of petroleum feedstocks and in liquid-phase reactions in which diffusion of reactants and/or products may be hindered by the narrow porosity.

There are also reports indicating that the surface area and porosity of carbons do not affect either the active-phase dispersion or the catalytic activity. A very important factor influencing active-phase dispersion is the precursor used to prepare it. Rodríguez-Reinoso et al. [14] used two different iron precursors (iron nitrate in aqueous solution and iron pentacarbonyl in organic solution) to prepare iron catalysts supported on activated carbons with different pore size distributions. They obtained an increase in iron dispersion with the support surface area for the nitrate series, but a high and unaffected dispersion was found for the pentacarbonyl series. These catalysts were used in the CO hydrogenation reaction, where no important differences in catalytic behavior were found for catalysts in both series.

In a more recent study, Li et al. [15] investigated the catalytic behavior of ruthenium catalysts supported on carbon materials with different porous and graphitic structures in the catalytic ammonia decomposition. They found that the catalytic activity followed the trend Ru/GC (graphitic carbon) > Ru/CNTs (carbon nanotubes) > Ru/CB-S (carbon black) > Ru/CB-C > Ru/CMK-3 (mesoporous carbon) = Ru/AC. It was concluded that the graphitic structure of the carbons was critical to the activity of the ruthenium catalysts, whereas the surface area and porosity were less important.

It seems clear that a large surface area formed by accessible pores is important for obtaining highly dispersed and active catalysts. However, there are other carbon characteristics that have to be taken into account to explain the catalytic behavior of carbon-supported catalysts. One of the most important is the chemical composition of its surface.

4.2.2 Surface Chemical Properties

The carbon surface contains a given number of heteroatoms (O, N, H) in the form of functional groups, similar to the way that heteroatoms appear in organic compounds. The presence of these groups can affect the preparation of carbon-supported catalysts, as they confer the carbon surface acid–base and hydrophilic character.

The first attempt to clarify the influence of surface functional groups on the catalytic behavior of carbon-supported catalysts was made by Derbyshire et al. [16]. Later, Prado-Burguete et al. [17,18] reported some interesting studies on the role of surface oxygen groups in the dispersion and resistance to sintering of Pt/C catalysts. They used a high-surface-area carbon black, which was heat treated in hydrogen at 1223 K to remove most of the oxygen surface functionalities, and then oxidized with hydrogen peroxide solutions. In this way, they prepared a number of supports with similar porosity but different amounts of oxygen surface groups, which were impregnated with H_2PtCl_6 solutions. It was observed that the more acidic groups, created by oxidizing treatment with H_2O_2 , decreased the hydrophobic character of the carbon surface and made the surface more accessible to the aqueous solution of the metal precursor on the impregnation process. Thus, platinum dispersion increased with an increase in oxygen surface groups. On the other hand, the less acidic and more thermally stable surface groups favored interaction between the metal precursor or the metal particle with the carbon surface, thus minimizing the sintering of the platinum particles. Similar results have been obtained in the preparation of K-promoted Ru/C catalysts for ammonia synthesis [19], although in this case the activated carbons were oxidized with HNO_3 . The authors concluded that the presence of oxygen surface groups improved the hydrophilic character of the carbon surface, thus enhancing the dispersion of K and Ru and the catalytic activity.

However, it has to be taken into account that some oxygen groups may not be stable under the heat-treatment conditions (i.e., reduction) to which the catalysts are subjected during the preparation stage to obtain the active phase. If they are acting as anchoring centers for the active phase or for the precursor, their decomposition could lead to sintering of the metal species and a loss of dispersion [20].

But the presence or absence of surface functionalities can also directly affect the catalytic behavior of the active phase. This has been shown clearly in studies related to the use of Pt/C in selective hydrogenation reactions. The catalytic hydrogenation of α,β -unsaturated aldehydes to yield unsaturated alcohol is not an easy task, since the olefinic double bond is preferentially hydrogenated to yield the saturated aldehyde. Monometallic platinum catalysts usually hydrogenate the $\text{C}=\text{C}$ bond with 100% selectivity, and support effects or promotion by other metals or oxides are the most common solution to improving the selectivity for hydrogenation of the carbonyl bond. But the selectivity can also be improved by the use of carbon supports with a relatively high amount of oxygen surface groups if they are removed before the reaction takes place.

In a study on vapor-phase crotonaldehyde (2-butenal) hydrogenation on Pt/C catalysts, Coloma et al. [21] used a demineralized activated carbon prepared from olive stones (AC) that was oxidized with H_2O_2 to introduce oxygen surface functionalities (AC_{ox}) and then heat treated under helium at 773 K to remove the less stable surface groups ($\text{AC}_{\text{ox}}\text{T}$). The carbons were impregnated with a basic aqueous solution of $[\text{Pt}(\text{NH}_3)_4]\text{Cl}_2$ to introduce 1 wt% Pt. The specific activity of these catalysts was high in the reaction described above and followed the order $\text{Pt}/\text{AC} < \text{Pt}/\text{AC}_{\text{ox}}\text{T} < \text{Pt}/\text{AC}_{\text{ox}}$. The degree of selectivity to the unsaturated alcohol (crotyl alcohol) was low for Pt/AC catalyst and much higher for the others, especially for $\text{Pt}/\text{AC}_{\text{ox}}$ catalyst. To understand the origin of this different behavior, the catalytic behavior was determined after reduction at various temperatures (i.e., 623, 723, and 773 K). There was an increase in catalytic activity when increasing the reduction temperature which was much more important for $\text{Pt}/\text{AC}_{\text{ox}}\text{T}$ and $\text{Pt}/\text{AC}_{\text{ox}}$. With regard to selectivity, the increase in the reduction temperature did not affect the selectivity of Pt/AC , but it enhanced the selectivity of the other two catalysts, especially $\text{Pt}/\text{AC}_{\text{ox}}$, for which selectivity to crotyl alcohol reached 60%. The beneficial effect of using preoxidized carbon as support was related to the decomposition–reduction of oxygen surface groups upon the heat treatment in hydrogen to which the catalysts were subjected before the catalytic measurements [21].

Similar results have been reported by other authors. In a very interesting study, Toebe et al. [22] used carbon nanofiber–supported ruthenium catalysts to study the influence of oxygen surface groups on catalytic performance in the liquid-phase hydrogenation of cinnamaldehyde. The carbon nanofibers were oxidized to introduce the oxygen functionalities, and the metal precursor was introduced by homogeneous deposition–precipitation. After reduction, the catalysts were heat-treated in nitrogen at different temperatures to tune the number of oxygen surface groups. They observed by transmission electron microscopy (TEM) a narrow and stable particle size distribution (1 to 2 nm) even after heat treatment at 973 K. The overall specific activity increased by a factor of 22 after treatment at this high temperature, which was related to the decreased number of oxygen surface groups. In this case, the selectivity to the unsaturated alcohol (cinnamyl alcohol) decreased from 48% to 8%, due to the enhanced rate of hydrocinnamaldehyde production when increasing the temperature of the heat treatment. The authors concluded that these results demonstrated the metal–support interaction in this system, which involves the oxygen surface groups that affect the metal activity and selectivity. In a similar study carried out with carbon nanofiber–supported platinum catalysts [23], the authors also found an increase in catalytic activity with increasing thermal treatment temperature, and a linear decrease in hydrogenation activity with an increase in the number of acidic groups on the carbon nanofiber surface. In this way they suggested that the hydrogenation process was favored by the adsorption of cinnamaldehyde on the carbon support after removal of the oxygen-containing surface complexes.

Although less important than oxygen (at least they have been studied to a lesser extent), nitrogen surface groups also play their role. They can be introduced on

the carbon surface by treating the carbon with ammonia in the temperature range 673 to 873 K [24]. The effect of these nitrogen functionalities depends on the system studied. In this way, Derbyshire et al. [16] obtained more active Mo catalysts for HDS by pre-nitriding the carbon support, and Guerrero-Ruiz et al. [25] found the same effect for Fe/C and Ru/C catalysts. Matter and Zhang [26] prepared catalysts for the oxygen reduction reaction by high-temperature pyrolysis of acetonitrile over Vulcan XC-72 carbon and Fe- or Ni-impregnated Vulcan carbon, and observed that the more active catalyst, the iron-loaded catalyst, contained a significantly higher amount of pyridinic nitrogen groups, as determined by x-ray photoelectron spectroscopy (XPS). They proposed the formation of different nanostructures on the carbon surface depending on which support material was used for acetonitrile decomposition. In this way, nitrogen-containing carbon samples with nanostructures resulting in the exposure of more edge planes (in which pyridinic nitrogen is found) would be more active for the oxygen reduction reaction. On the other hand, Wachowski et al. [27] studied the polymerization of styrene with $\text{CpTiCl}_2(\text{OC}_6\text{H}_4\text{Cl}-p)$ catalyst supported on carbon materials with different degrees of coalification and analyzed the effect of the modification of the support by nitrogen on the efficiency of the catalytic system in the polymerization of styrene. It was found that the introduction of nitrogen functionalities on the carbon surface lowered the catalytic activity of these systems.

4.2.3 Inertness

Despite the fact that the presence of heteroatoms on the carbon surface can induce some types of active phase-support interaction, as discussed above, it is clear that this takes place to a lesser extent than in other common catalyst supports, such as oxides (silica, alumina, titania, ceria, etc.). One clear example is provided in work carried out by Milone et al. [28], in which they investigated the influence of the surface area and the nature of the support on product distribution in the hydrogenation of citronellal (3,7-dimethyl-6-octen-1-al) on Ru supported on silica and carbon. It was found that the main products obtained on the Ru/SiO₂ catalyst were the unsaturated cyclic alcohols (isopulegols), which were produced via the isomerization of citronellal on the SiO₂ surface. However, the main reaction products on Ru/C were the open-chain hydrogenated products (i.e., citronellol, 3,5,7dimethyloctanal, and 3,7-dimethyloctanol), and this was attributed to the low activity of the carbon surface toward the isomerization reaction.

The relatively low reactivity or inertness of the carbon surface is also very useful in the preparation of bimetallic catalysts, since the low interaction between the carbon surface and the two metals or metal precursors facilitates their mutual interaction. This is especially interesting when the objective is the formation of bimetallic particles. One clear example is the preparation of bimetallic Pt–Sn catalysts for selective hydrogenations. The catalytic behavior of this system is determined by at least three aspects [29,30] that determine the catalytic activity and the selectivity toward the desired product: (1) the oxidation state of tin in

the catalyst, (2) the possibility of formation of platinum–tin alloy phases, and (3) the extent of tin–support interactions.

In the selective hydrogenation of α,β -unsaturated aldehydes to obtain unsaturated alcohols, hydrogenation of the C=C bond yielding the saturated aldehyde is hindered on bimetallic PtSn catalysts. In this way it is interesting to obtain this phase to a given extent, and this is determined by the easiness of reduction of the tin species, which, in turn, depends on the interaction between the tin precursor and the support. Huidobro et al. [31] prepared bimetallic PtSn catalysts supported on TiO_2 , and studied the chemical surface composition by XPS. They observed that even after reduction under hydrogen at 773 K, the main part of tin (about 78%) was in an oxidized state, limiting the possibility of formation of alloy phases. However, a nearly complete reduction of tin to the metallic state can be achieved by using carbon materials as supports, depending on the preparation method and on the relative amount of tin, as evidenced by Coloma et al. [29,30].

Another interesting example of the exploitation of the relative inertness of the carbon surface is provided by the use of Fe/C catalysts in the hydrogenation of carbon monoxide. In this case, the inertness of the carbon surface facilitates the presence of zero-valent iron in the catalyst [32,33], which is more difficult for other supports, such as alumina, on which the reduction of the oxidized iron species is hindered. Vannice et al. carried out an extensive study of carbon-supported iron catalysts using different carbons and preparation methods and concluded that highly dispersed Fe/C catalysts could be prepared on high-surface-area carbons, due to the weak chemical interactions between oxidized iron precursors and the carbon surface [32–34].

4.3 PREPARATION OF CARBON-SUPPORTED CATALYSTS

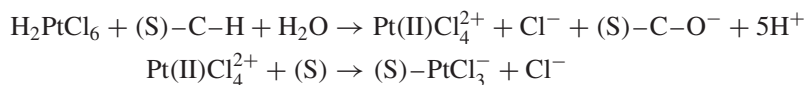
The methods used for the preparation of carbon-supported catalysts are similar to those used with other supports. However, some particularities of carbon materials make it necessary, in some cases, to adapt the preparation recipes to be used with these supports. A fundamental point in obtaining reproducible results is to have a comprehensive knowledge of the characteristics of the support material, primarily with regard to its porous texture and surface chemical properties.

4.3.1 Impregnation

Catalyst preparation by impregnation is carried out by contacting the support with a solution containing the precursors of the active phases. Two different approaches can be followed: incipient-wetness impregnation and excess-solution impregnation. In the former, the carbon support is wetted with a solution of the precursor, drop by drop, in the proper amount to just fill its pores. A slurry is formed with the pore volume filled with the solution, which is finally dried to remove the solvent, leaving the precursor of the active phase deposited on the

pore walls. The second approach consists of the use of a volume of solution much larger than the pore volume of the support. A slurry is formed from which, after a given period of time, the excess solvent is removed by evaporation or the impregnated solid is separated by filtration or decantation. This method does not permit precise control of the amount of catalyst precursor loaded unless a previous study is carried out to determine the adsorption isotherms. Thus, it is likely that some of the catalyst precursor will remain in the liquid phase after filtration.

When the carbon surface is contacted with a solution containing the precursor of the active phase, the latter can interact with the former to different extents, from a very weak interaction to a chemical reaction, passing through electrostatic interactions. Highly dispersed catalysts are generally obtained when strong anchoring centers are available on the carbon surface for the catalyst precursor, or when they are formed upon impregnation. This is what takes place when hexachloroplatinic acid (H_2PtCl_6) is used as a supported platinum precursor. Coloma et al. [35] impregnated several carbon blacks with an aqueous solution of H_2PtCl_6 . Using XPS and temperature-programmed decomposition (TPD) studies they observed that the carbon surface became oxidized upon impregnation with the platinum precursor, whereas platinum was reduced from Pt(IV) in PtCl_6^{2-} species to Pt(II). This study demonstrated that the chemical properties of the carbon were modified upon the impregnation step. Similar results were obtained in other studies [20,29,36]. Van Dam and Van Bekkum [36] proposed a carbon oxidation pathway for this process, by which the reduction of Pt(IV) species is followed by the formation of phenolic surface groups:



where (S) denotes a carbon surface site. In this way, platinum species are anchored to the carbon surface.

Electrostatic interactions between the carbon surface and the active-phase precursors have also to be taken into account in the preparation of carbon-supported catalysts. The presence of oxygen functionalities on the carbon surface, which can be produced upon the activation process (for activated carbons) and/or by subsequent oxidation treatments, renders it amphoteric. This implies that it can be more or less charged, positively or negatively, depending on the pH of the surrounding solution. Preparation variables such as the polarity of the solvent, the pH of the solution, the anionic or cationic nature of the metal precursor, and the isoelectric point (IEP) of the carbon support determine the extent of precursor–support interaction and, in this way, the total uptake and dispersion of the active phase in the final catalyst [17,20,37]. Thus, for carbons containing acidic surface groups and, as a consequence, a low isoelectric point, best results in the preparation of supported catalysts are achieved when a cationic precursor is used in basic media. Under these conditions, the acidic complexes ($-\text{COOH}$, $-\text{OH}$) are deprotonated ($-\text{COO}^-$, $-\text{O}^-$) in such a way that

interaction with a cationic active-phase precursor (e.g., $[\text{Pt}(\text{NH}_3)_4]^{2+}$) is favored. Interaction with an anionic precursor (e.g., molybdate) would be hindered, however, as its negative charge would repel the negative charge of the solid surface.

4.3.2 Other Methods

Several other methods have been employed for the preparation of carbon-supported catalysts, although to a lesser extent than impregnation methods. Nakamura et al. [38] prepared molybdenum catalysts for ethene homologation by physical deposition of gaseous $[\text{Mo}(\text{CO})_6]$. Their supports were commercial activated carbons that were subjected to different treatments to modify their surface. The authors compared these supports with oxidic supports and concluded that the interaction between the metal carbonyl and the carbon supports were weaker. Furthermore, they observed that oxidation of the carbon surface was effective in enhancing the catalytic activity of Mo/C, and they ascribed this effect to the contribution of the surface oxygen groups to the partial oxidation of decomposed $[\text{Mo}(\text{CO})_6]$.

Serp et al. [39] prepared activated carbon-supported platinum catalysts by chemical vapor deposition of organometallic compounds. They contacted carbon rods with a gas mixture containing He, 3% H_2 , and a 10^{-3} molar ratio of $[\text{Pt}(\text{CH}_3)_2(\text{COD})]$ (COD : $\eta^4\text{-1,5-cyclooctadiene}$) for 12 minutes at 383 K and 50 torr. They concluded that preoxidation of the carbon support with HNO_3 was a very important factor in obtaining well-dispersed platinum particles, as the oxygen surface complexes acted as anchoring centers for the platinum precursor.

Precipitation or coprecipitation methods are also often used. Suh et al. [40] analyzed the effect of the oxygen surface functionalities of carbon supports on the properties of Pd/C catalysts prepared by the alkali-assisted precipitation of palladium chloride on carbon supports, followed by liquid-phase reduction of the hydrolyzed salt with a saturated solution of formaldehyde. They observed that the metal dispersion increased with increasing amount of oxygen surface groups. Nitta et al. [41] also used a deposition–precipitation method, with sodium carbonate and cobalt chloride or nitrate, to prepare carbon-supported Co catalysts for the selective hydrogenation of acrolein.

Harada et al. [42] prepared nanosized palladium particles supported on activated carbons using a simple liquid-phase reduction of aqueous Pd complexes with KBH_4 . They found that the addition of appropriate amounts of NaOH into aqueous solutions of Na_2PdCl_4 , followed by reduction with KBH_4 , produced highly dispersed Pd particles (less of 5 nm in diameter), irrespective of the carbon support used. The prepared catalysts were used efficiently in the liquid-phase oxidation of benzyl alcohol to benzaldehyde and in the liquid-phase hydrogenation of cinnamaldehyde to obtain the saturated aldehyde.

Similar methods for the preparation of noble metal nanoparticles on carbon materials are being used extensively for the synthesis of electrocatalysts,

for which high metal loadings are usually needed, although they should be reduced at least by one order of magnitude for practical application in, for example, fuel cell-powered vehicles. Traditional procedures for the preparation of carbon-supported catalysts (i.e., impregnation, precipitation, etc.) usually yield Pt clusters with heterogeneous particle size distributions. A recent publication by Coker et al. [43] describes a new method for the preparation of size-controlled Pt clusters on nanostructured carbon. The process involved the stabilization of the metal clusters in a zeolite host, pore filling of the host with a carbon precursor, pyrolysis, and removal of the host. In this way, they could obtain platinum clusters of very small particle sizes, ranging from 1.3 nm on an essentially microporous carbon to 1.7 nm in a hybrid microporous/mesoporous carbon matrix, with Pt loadings up to 17 wt%.

Carbon-supported bimetallic or even ternary catalysts are of increasing interest in electrocatalytic reactions such as methanol oxidation. In this sense, the preparation routes are of pristine importance in determining the catalytic performance. As an example, it has been shown that $\text{Pt}/\text{Ru}/\text{Ni} = 5:4:1$ nanoparticles have a higher catalytic activity for methanol electrooxidation than does $\text{Pt}/\text{Ru} = 1:1$ [44]. Ni-containing catalysts have been prepared following different methodologies, such as the molecular precursor approach [45,46], the borohydride method [47], the borohydride with freeze drying technique [48], and electrochemical deposition [49]. Martínez-Huerta et al. [50] prepared a series of carbon-supported (Vulcan XR72-R) Pt–Ru–Ni catalysts by different techniques, using H_2PtCl_6 , RuCl_3 , and NiCl_2 as metal precursors. In the *colloidal route*, an aqueous solution of $\text{Na}_2\text{S}_2\text{O}_5$ was added to an aqueous solution of H_2PtCl_6 . After stirring, the pH was set at a value of 5 by Na_2CO_3 addition, and two solutions containing H_2O_2 and RuCl_3 were added. Finally, a NiCl_2 solution was added to the mixture and stirred roughly. At this stage, the desired carbon amount was incorporated and hydrogen was bubbled for 1 hour. The solid was recovered, washed thoroughly with water, and dried at 110°C overnight. The *microemulsion route* involved dissolution of the metal precursors in water. Then the solution was added to a mixture containing isooctane and Tergitol TS-15-S-5. A microemulsion was obtained after vigorous stirring. Hydrazine was added as reducing agent, under stirring, and the mixture was added dropwise to a suspension containing carbon dispersed in isooctane and isopropanol. After stirring overnight, tetrahydrofuran was added dropwise to the mixture and it was settled to decant. The solid recovered was washed with isopropanol–water and dried at 383 K. From the results obtained, it was concluded that the interaction between platinum and nickel, and hence the catalytic performance, was strongly dependent on the preparation route.

4.4 APPLICATIONS

One of the first applications of carbon as a catalyst support was in the hydroprocessing of petroleum feedstocks. In 1934, a U.S. patent showed that

sulfur-containing naphthalene could be converted into tetrahydronaphthalene at 573 K and 50 to 70 atm with a charcoal-supported catalyst containing nickel oxide, molybdenum sulfide, and calcium carbonate [51]. This is still one of the main areas of research and application of carbon materials as catalyst supports. Other interesting fields are hydrogenation reactions, including hydrogenations in fine chemical synthesis, ammonia synthesis and decomposition, environmental catalysis, and in more recent years, electrocatalysis. A complete revision of the use of carbon-supported catalysts in all these fields is out of the scope of this chapter. Consequently, in this section we review some aspects of carbon-supported catalysts in some of these fields, paying special attention to how the physical and chemical properties of porous carbons can be exploited to obtain more active and selective catalysts. The processes taken as representative will be the synthesis of ammonia, hydrotreating reactions, and the hydrogenation of carbon oxides.

4.4.1 Ammonia Synthesis

The early development of catalysts for ammonia synthesis was based on iron catalysts prepared by fusion of magnetite with small amounts of promoters. However, Ozaki et al. [52] showed several years ago that carbon-supported alkali metal-promoted ruthenium catalysts exhibited a 10-fold increase in catalytic activity over conventional iron catalysts under the same conditions. In this way, great effort has been devoted during recent years to the development of a commercially suitable ruthenium-based catalyst, for which carbon support seems to be most promising. The characteristics of the carbon surface, the type of carbon material, and the presence of promoters are the variables that have been studied most extensively.

Kowalczyk et al. [53] reported the preparation of Ru-based catalysts supported on activated carbon subjected to thermal treatment at 2173 K under helium. They compared the performance of this catalyst (9.1 wt% Ru, KOH as promoter) with that of a commercial iron-based catalyst. They also compared catalysts prepared with different metal precursors, RuCl_3 and $[\text{Ru}_3(\text{CO})_{12}]$, supported on activated carbon, both untreated and heat-treated under helium at 2173 K [54]. In all cases, the most active catalyst was that supported on the heat-treated carbon, irrespective of the metal precursor, despite the fact that ruthenium dispersion was similar in the heat-treated and untreated supports. Using transmission electron microscopy they observed that the heat treatment developed some degree of structural ordering in the carbon support, and it was suggested that the higher activity was related to the partial graphitization of the support's structure, which became closer to that of the high-surface-area graphite (HSAG) used in the commercial ruthenium-based catalyst [55].

Thermal treatment of the support at much lower temperatures has also resulted in positive effects on the catalytic performance of Ru in ammonia synthesis. Zhong and Aika [56,57] treated three commercial activated carbons, with different ash contents, at temperatures ranging from 1073 to 1188 K under hydrogen.

Catalysts prepared with raw activated carbons showed different activities, depending on their ash content, but heat-treated carbons showed similar activities. It was concluded that the heat treatment was able to remove acidic impurities which were able to remove electron density from ruthenium and, in this way, decrease its catalytic activity.

A more complete study on the effect of thermal treatments of activated carbon supports was carried out by Zheng et al. [58]. They corroborated previous studies showing that activated carbon treated at high temperature under an inert atmosphere undergoes a more or less pronounced graphitization, the degree of which is determined by the temperature of the process; in addition, the thermal treatment can eliminate impurities and improve the carbon support resistance to methanation under the reaction conditions, although the surface area and porosity of the carbon decrease dramatically. These poor textural properties could be partially recovered by treating the thermally modified carbons in a flowing gas mixture (10% O₂ + 90% N₂) at 723 K for 16 hours. The ruthenium dispersion on the oxidized carbons was significantly higher than on their untreated counterparts. Although this result was ascribed to an enhanced surface area, it has also been shown that oxygen surface groups on the carbon surface can enhance its hydrophilicity and, in this way, can improve the dispersion of both the active metal and the promoters [59].

As mentioned above, the type of carbon material to be used as support for ruthenium and promoters is also a matter of research. The first commercial catalyst for ammonia synthesis using ruthenium as active metal contained high-surface-area graphite as support [55], but other carbon materials have also been studied. Liang et al. [60] compared the catalytic performance of ruthenium catalysts supported on activated carbon, activated carbon fiber, and carbon molecular sieve. They reported that the activated carbon-supported catalyst exhibited the highest level of activity, which was attributed to the high dispersion of the active metal. But the catalyst that used activated carbon fiber as support showed the highest activity level in terms of turnover frequency, and this was explained on the basis of its high purity and its electronic conductivity. Finally, the less active catalyst was that supported on carbon molecular sieve. The conclusion was that carbon supports with high purity, high electronic conductivity, and high surface area favor the activity of Ru-based catalyst in ammonia synthesis.

It has been claimed that carbon-supported ruthenium-based catalysts for ammonia synthesis show some important drawbacks, such as high catalyst cost and methanation of the carbon support under industrial reaction conditions. This has stimulated the research for alternative catalysts, although the use of carbon supports is a common feature. One example of these new catalysts is provided by the work of Hagen et al. [61], who reported very high levels of activity with barium-promoted cobalt catalysts supported on Vulcan XC-72. It was demonstrated that although cobalt had received little attention as a catalyst for ammonia synthesis, promotion with barium and the use of a carbon support resulted in very active catalysts with very low NH₃ inhibition.

4.4.2 Hydrotreating Reactions

Industrial hydrotreating reactions [hydrodesulfurization (HDS) and hydrodenitrogenation (HDN)] are commonly carried out on cobalt–molybdenum and nickel–molybdenum systems supported on γ -alumina. However, a great amount of research has been devoted to the development and application of carbon-supported catalysts since the pioneering work of Stevens and Edmonds [62]. It has been claimed that carbon-supported catalysts have potential advantages, which are based on the textural and surface properties of the carbon supports, leading to a lower propensity to coke formation, weaker metal–support interactions, and higher activity levels per unit mass of catalyst [63]. There are many studies that have used carbon materials in the preparation of both model catalysts and industrial catalysts for hydrotreating reactions [64–66].

Early studies by Breysse et al. [67] and Bridgewater et al. [68], among others [69–74], were devoted to an analysis of the different effects of alumina and activated carbon when acting as supports. On Co–Mo catalysts, Bridgewater et al. [68] observed that the activity of the carbon-supported catalyst was similar to that of the alumina-supported sample, although the butane yield was much higher on the former. The hydrogenation activity of this system has been related to the edge plane of MoS_2 , whereas the desulfurization activity depends on the basal plane [75]. Thus, these authors explained their results on the basis of the epitaxial growth of MoS_2 crystallites, with a high basal-to-edge area ratio, on the alumina support. This phenomenon is favored by the interaction between the metal precursors and the alumina surface, and it has also been evidenced in graphite-supported catalysts [62]. Furthermore, other authors have found that carbon-supported Co–Mo catalysts were more active than their alumina-supported counterparts for both DBT (dibenzothiophene) and 4,6-DMDBT (4,6-dimethyldibenzothiophene) hydrodesulfurization [76]. It seems clear that the weak interaction between the carbon surface and the metal precursors is the origin of the higher activity of these systems, as it facilitates a higher degree of sulfurization and the formation of the more active Co–Mo–S type II structure [77]. More recently, it has been suggested that carbon could stabilize MoS_2 particles, avoiding the sintering of small crystallites and yielding a higher dispersion on the carbon support [78].

Hillerová et al. [71] compared the performance, in parallel HDN of pyridine and HDS of thiophene, of sulfided Ni–Mo catalysts supported on alumina and on a special carbon named Sibunit, which is based on graphitized carbon black and is mainly mesoporous [79]. The carbon-supported catalysts showed a higher resistance to inhibition by pyridine, higher HDN activity, and a higher HDS/HDN activity ratio than that of the commercial alumina-supported catalyst.

Work by Prins, de Beer, and co-workers represents a great contribution to our knowledge of the structure of carbon-supported hydrotreating catalysts as well as of the kinetics and mechanisms of these reactions. These authors first reported that the activity of carbon-supported molybdenum and tungsten catalysts was higher than that of their counterparts supported on alumina or silica [80,81]. They

also compared the catalytic behavior of sulfided Co–Mo, Fe, and Mo catalysts supported on alumina, carbon black composite, and activated carbon [82], and observed that for a given metal, very important differences in activity were found between the carbons and alumina, and even between the carbons themselves, the highest activity being obtained for the activated carbon-supported catalyst. All these effects were explained on the basis of the relatively low interaction between the metal sulfide and the surface of the carbon support, which facilitates sulfurization of the precursor and the dispersion of the active phase [83].

The effects of the textural properties of carbon supports were studied by Farag et al. [76]. They prepared Co–Mo catalysts on two activated carbons with different surface areas, $907\text{ m}^2/\text{g}$ and $3213\text{ m}^2/\text{g}$. They used two different preparation methods, with cobalt and molybdenum acetylacetones as metal precursors. In method I, a successive impregnation method, molybdenum was incorporated first, and the cobalt precursor was added after drying. In method II, Mo was also incorporated first, but the catalyst was sulfurized ($5\% \text{ H}_2\text{S}/\text{H}_2$, 633 K) before impregnation with the cobalt precursor. A final sulfurization step was carried out at the conditions mentioned above, and the catalysts were tested in the hydrodesulfurization of DBT, 4,6-DMDBT, and hydrotreated diesel fuel. The results indicated that the carbon-supported counterparts were more active than the alumina-supported counterparts for the three species compounds. Furthermore, catalyst prepared by method II showed the highest activity. The effect of the porous texture of the support was evident when comparing the relative activities for HDS of the two model compounds. Whereas there were no differences in activity for the HDS of DBT, the activity for the HDS of a much larger molecule such as 4,6-DMDBT was higher for the catalyst whose support was the activated carbon with wider pores.

The effect of the textural properties of the carbon support on the activity of Mo/C catalyst in thiophene HDS was also investigated by Martín-Gullón et al. [84]. They prepared five activated carbons from olive stones, by activation with CO_2 (without the carbonization step) at 1223 K and different periods of time, to cover a burn-off range from 10 to 77%. The BET surface areas of these supports ranged from 532 to $1800\text{ m}^2/\text{g}$. The results showed an important increase in HDS activity with increasing surface area up to about $1000\text{ m}^2/\text{g}$, the activity remaining nearly constant for larger surface areas. These results were explained as a result of a larger dispersion of the active phase favored by increasing the surface area of the support up to an optimal value ($1000\text{ m}^2/\text{g}$). For larger surfaces, sintering of the active phase during the sulfidation stage was predominant. Similar results were found by Vissers et al. [85] for catalysts supported on carbon blacks of different surface area, and by Kouzu et al. [86] using a variety of activated carbons. Lee et al. [87] used a new type of nanoporous carbon, with high surface area and mesoporosity, as support for a Co–Mo–S hydrodesulfurization catalyst. They compared its performance in the HDS of DBT and 4,6-DMDBT with catalysts prepared with other supports. It was found that the overall activity decreased in the order Co–Mo/nanoporous carbon > Co–Mo/activated carbon > Co–Mo/ Al_2O_3 .

The surface area of the activated carbon, which was the largest among the three supports, was significantly lowered after metal loading, but the surface areas of the other two supports were preserved. The specific activity showed a somewhat different trend than the overall activity: Co–Mo/nanoporous carbon \approx Co–Mo/Al₂O₃ > Co–Mo/ activated carbon. The low intrinsic activity of the activated carbon-supported catalysts was attributed to the restricted diffusion of reactants thorough its narrow microporosity. The effect of the presence of oxygen functionalities on the carbon surface on the catalytic performance of carbon-supported Mo, Ni, and Ni–Mo catalyst in the HDS of thiophene was studied by Calafat et al. [88]. They began with a high-purity activated carbon with 917 m²/g, which was subjected to oxidative treatments in order to generate oxygen surface complexes. These treatments affected neither the molybdenum phase obtained nor the catalytic activity of Mo/C, but they were very important for the nickel-containing catalysts. It was assumed that the oxygen groups favored interaction between the carbon surface and the nickel precursor during the impregnation step, this resulting in a high dispersion of the active phase. This high Ni dispersion was also essential for achieving an enhanced Ni–Mo interaction.

It has been mentioned that the interaction between the metal precursors and the carbon surface is very important in achieving highly dispersed and stable active phases. In this sense, the choice of the precursors and the impregnation conditions are of paramount importance, and they should be selected in relation with the surface properties of the carbon supports. Thus, the presence of oxygen surface groups makes the surface more hydrophilic and enhances its wettability. But if these groups have an acidic character, the surface will be negatively charged over a wide range of pH values of the impregnating solution. In this case, impregnation with an anionic precursor such as ammonium heptamolybdate has to be carried out at very low pH values, to render the surface positively charged. But under these conditions, polymerization of molybdenum species takes place and a very low dispersion is obtained. These problems may be avoided by using neutral precursors in less polar solvents. This is the case, for example, for Farag et al. [76] and Sakanishi et al. [89], who used methanolic solutions of cobalt and molybdenum acetylacetones.

Regulations on the sulfur content in fuels are becoming more and more stringent, and conventional HDS processes are not able to remove the desired amounts of sulfur compounds. In this way, deep hydrodesulfurization processes, with more demanding reaction conditions, are being introduced in refineries. However, classical HDS catalysts are not sufficiently active, and there is a need for new catalytic formulations [90,91]. In this sense, one promising candidate for participation in these new formulations is rhenium sulfide, for which activities that are an order of magnitude higher than Mo-based catalysts have been reported [92–94].

Escalona et al. [95] prepared a series of Re-based catalysts supported on activated carbon with different metal loadings (from 0.74 to 11.44 wt% Re₂O₇), which were tested in the simultaneous HDS and HDN of a commercial gas oil. It was observed that an increase in Re loading resulted in a rise in HDS

and HDN activity due to the formation of a monolayer structure of Re and to an increase in surface acidity. However, for Re concentrations higher than 2.47 wt% Re_2O_7 , a decrease in activity was observed, which was related to the loss of BET surface area due to the blocking of microporosity in the activated carbon supports. These authors also studied the effect of nickel addition to alumina- and activated carbon-supported Re catalysts on the simultaneous HDS and HDN of gas oil [96]. The results showed that the incorporation of Ni significantly improved the catalytic performance of rhenium supported on both materials, although the promotion was slightly larger on the carbon-supported catalyst.

Shu and Oyama have recently proposed a new type of hydrotreating catalyst: transition metal phosphides supported on carbon [97], and compared their behavior in the deep HDS of 4,6-DMDBT with that of the silica-supported counterparts and a commercial alumina-supported Ni–Mo sulfide hydrotreating catalyst. The carbon-supported catalysts were prepared by temperature-programmed reduction of the corresponding phosphates, and the activity was studied under simulated industrial conditions of 613 K and 3.1 MPa with a model liquid feed containing 500-ppm sulfur as 4,6-DMDBT, 3000-ppm sulfur as dimethyl disulfide, and 200-ppm nitrogen as quinoline. The $\text{Ni}_2\text{P}/\text{C}$ catalyst showed an excellent performance in HDS and HDN, and it was also the best for sulfur removal from 4,6-DMDBT among the tested catalysts. It was found that the phosphides suffered a partial sulfurization leading to the formation of a phosphor–sulfide layer on top of the Ni_2P phase, whereas the bulk structure of the phosphide was not modified during the reaction. The excellent performance of the carbon-supported catalysts was related to the higher dispersion of the active phase, in comparison to the silica-supported materials, and also to the differences in the strength of interaction with the support.

During the last years, several studies have shown that molybdenum carbides also exhibit high levels of HDS and HDN activities [77,98,99]. In fact, they are considered as potential candidates as catalysts for deep HDS in a second-stage process, in order to remove highly refractory sulfur compounds which do not react in the conventional HDS process. There are many studies dealing with molybdenum carbides supported on different materials, but the use of carbon supports provides some advantages. Thus, the preparation of these systems is much easier on carbon materials, given that one can use the reducing–carburizing character of carbon [100]. The carbon support is impregnated with ammonium heptamolybdate tetrahydrate and then dried. Finally, they are carburized by heating at 973 K under a flow of hydrogen. Following this method, Hynaux et al. prepared molybdenum carbide supported on a mesoporous carbon black composite with a BET surface area of $240 \text{ m}^2/\text{g}$ [101–103]. They first studied the effect of the chemical character of the support surface. To this end they treated the raw carbon support in different ways, in order to modify its surface chemistry: (1) boiling in nitric acid, (2) heating in a stream of wet ammonia, and (3) heating under steam at 1073 K up to 20% burn-off [101]. It was found

that catalysts supported on the carbon with a basic surface showed higher activity levels than those of catalysts supported on the carbon with an acidic surface. In a further work [103], they functionalized the carbon black composite support with nitric acid, under different conditions, in order to introduce surface oxygen groups. It was found that these groups favored anchoring of the metallic precursor complex on the support surface. They also carried out the impregnation step at low pH values. Under these conditions, the carbon surface is positively charged ($\text{pH} <$ isoelectric point) and interaction with the anionic metal precursor (ammonium heptamolybdate) is more favored. The experimental results showed that catalytic activity was increased when dispersion was improved, such that the total DBT disappearance rate was proportional to the number of active sites.

4.4.3 Hydrogenation Reactions

Hydrogenation reactions constitute the most important industrial application of carbon-supported catalysts. Some reactions can only be catalyzed by these systems, as other conventional supports would be destroyed by the severity of the reaction conditions. This is the case for the purification of terephthalic acid, a key compound in the manufacture of polyester [104]. In this process, the by-product 4-carboxybenzaldehyde is converted to 4-carboxytoluene subsequent to the oxidation of *p*-xylene to terephthalic acid, with palladium as catalyst. The difficult reaction conditions, low pH, and relatively high temperatures (about 553 K) are too demanding for oxidic supports such as silica or alumina.

The relative inertness of the carbon surface is of paramount importance when carbon materials are going to be used as supports for hydrogenation catalysts. These systems usually consist of more than one metallic phase (bimetallic systems) and even by metals promoted by metal oxides. The carbon inertness facilitates interaction between the metals and/or between the metals and the promoters, yielding more active and selective catalysts than those supported on other common supports. These aspects will be illustrated by examples of the application of carbon-supported catalysts to the hydrogenation of carbon oxides.

Carbon-supported catalysts have been studied extensively in the hydrogenation of carbon oxides (CO and CO_2) to yield methane and hydrocarbons. Different phases (e.g., metals, metal alloys, carbides) have been prepared by a variety of techniques and precursors. Also, although the early studies used activated carbons as support, more recent studies analyze the possibilities of other carbon materials, such as nanofibers and nanotubes.

Carbon-supported iron catalysts are among the most studied systems. It has been clearly evidenced that carbon inertness favors iron reducibility, in contrast to supports on which the iron precursors are more refractory to reduction. Van-nice et al. showed some years ago that highly dispersed Fe/C catalysts could be prepared on high-surface-area carbons as a consequence of the weak interactions between the iron precursors and the carbon surface [105–107]. These catalysts showed higher selectivity for olefin formation than did silica- and

alumina-supported iron [108], although they strongly deactivated due to the formation of carbon deposits at a H₂/CO ratio of 1 [109], which is most favorable for the synthesis of olefins.

Different iron precursors can be used for the preparation of Fe/C catalysts. Rodríguez-Reinoso et al. [110] compared the catalytic performance of Fe/C catalysts prepared from Fe(NO₃)₃ and from [Fe(CO)₅], using activated carbons with different porous development as supports. It was found that iron dispersion was high and uniform in all catalysts when the metal precursor was iron pentacarbonyl, but in the case of the nitrate, the dispersion was higher for the support with higher surface area. The metal dispersion can also be modified by treatments on the carbon support. It has been reported that when a high-surface-area activated carbon is treated under hydrogen at high temperature (1225 K) to remove surface functionalities, very high iron dispersion is obtained, with a high resistance to sintering. But the opposite is found if the treated support is air exposed before impregnation of the metal precursor. Thus, the presence of acidic oxygen surface groups, formed upon the exposure to air, has a negative effect in this case [111].

The preparation method may have an important effect on the catalytic performance. Van Steen and Prinsloo [112] prepared carbon nanotube-supported iron catalysts by incipient wetness, deposition-precipitation with K₂CO₃, and deposition-precipitation with urea. The incipient wetness method and the deposition-precipitation technique with urea yielded highly dispersed Fe³⁺ species on the carbon nanotubes, but larger Fe₂O₃ crystallites were obtained when K₂CO₃ was used as the precipitating agent. However, although the three catalysts showed similar metal dispersion after the reduction step, their catalytic activities in the Fischer-Tropsch synthesis (CO hydrogenation) differed significantly, with the catalyst prepared by wetness impregnation being the most active. These results were explained on the basis of different crystallite size distribution, which would result in a variation in the amount of the different phases present in the catalysts under reaction conditions. In any case, the selectivity was found to be independent of the preparation method. Similar results were found by Bahome et al. [113], although they also studied the promotion of the carbon nanotube-supported iron catalysts by potassium and/or copper. The Fischer-Tropsch reaction was carried out at 548 K, 8 bar, and a CO/H₂ ratio of 2. The potassium-promoted catalysts gave higher yields of CO₂ and ethylene than those of the unpromoted catalysts, and the lowest methane selectivity. On the other hand, the addition of copper enhanced the catalytic activity but did not have any effect on the product selectivity.

As mentioned above, the addition of promoters, and even the formation of bimetallic particles, can provide carbon-supported iron catalysts with better performances in CO hydrogenation. The method of preparation of these systems is going to determine the final effect, always taking advantage of the relative inertness of the carbon surface. The interaction between the different components of the active phase can be maximized by using mixed-metal carbonyl complexes. Furthermore, use of these precursors allows for the preparation of catalysts with

a variety of relative compositions, which is not easy to achieve by conventional impregnation methods. Martin-Martínez et al. prepared activated carbon-supported iron catalysts promoted by Mn and alkali metal cations. They used mixed metal complexes obtained by the exchange of alkali metal cations with the tetramethylammonium cation in an $N(C_2H_5)_4[Fe_2Mn(CO)_{12}]$ cluster [114]. The highest activity was obtained for the rubidium-containing catalyst, whereas the highest selectivity to olefins (highest olefin-to-paraffin ratio) was obtained with the potassium-promoted catalyst.

Iron–ruthenium bimetallic catalysts have also received considerable attention as interesting catalysts in Fischer–Tropsch synthesis [115,116]. It has been reported that the Fe–Ru alloy system results in catalysts that are more stable than monometallic iron catalysts [117], and that the hydrocarbon product distribution in CO hydrogenation can easily be modified when changing the relative proportions of the two metals [118].

Supported cobalt catalysts also show a high activity level and selectivity in Fischer–Tropsch synthesis [119]. Although oxidic solids have generally been used as support, it is well recognized that their reactivity toward cobalt is a very important drawback of these materials, as very high reduction temperatures are needed to obtain supported metallic cobalt [120]. This problem has been overcome by the use of carbon supports [121,122]. Recent studies deal primarily with the use of carbon nanofibers (CNFs) as support for cobalt. Among them, studies by Bezemer et al. [123–125] are especially interesting, as they cover a wide range of fundamentals which help us to understand the behavior of these systems.

The effect of the preparation procedure was studied by comparing carbon nanofiber-supported cobalt catalysts prepared from a basic solution using ammonia evaporation and conventional deposition from an acidic solution using urea hydrolysis [123]. On CNF from acidic solution, cobalt hydroxyl carbonate precipitated, thanks to low interaction with the carbon surface, and 25-nm metal particles were obtained after reduction at 623 K. On the other hand, a high metal dispersion was obtained when a basic solution was used, which was attributed to the greater interaction between the carbon surface and the cobalt ions in solution under these conditions. After drying, Co_3O_4 crystallites were obtained, which resulted in 8-nm cobalt particles after reduction at 623 K. The carbon-supported catalysts were compared with silica-supported samples prepared by the same procedures, and it was concluded that the use of carbon nanofibers as support combined with the high-pH deposition–precipitation technique gave rise to catalysts with a promising potential in the Fischer–Tropsch reaction.

The effect of Mn as promoter for CNF-supported cobalt catalysts was studied by impregnating a parent 9.5 wt% Co catalyst with different amounts of MnO (ranging from 0.03 to 1.1 wt%) [124]. It was found that manganese hindered cobalt reduction, the cobalt surface remaining more oxidic in character in the presence of Mn. The catalytic performance was affected differently in tests carried out at 1 and 20 bar. At atmospheric pressure, the chain growth probability increased, and the product distribution shifted toward olefinic products

at increasing manganese loadings, this indicating that the promoter moderates the hydrogenating activity of cobalt. When the experiments were carried out at 20 bar, the C_{5+} selectivity first increased at 0.03 wt% MnO before decreasing for higher Mn contents. The results showed that Mn promotion was able to affect both activity and selectivity favorably, depending on promoter concentration and reaction conditions.

A controversial issue related to cobalt catalysts in Fischer–Tropsch synthesis is the structure-sensitive character of this reaction. Iglesia and co-workers [126,127] reported a large increase in activity when the cobalt particle size was decreased from 200 nm to 9 nm, whereas the specific activity [turnover frequency (TOF)] was not influenced by the cobalt particle size. However, other authors have reported that the TOF suddenly decreased for catalysts with cobalt particle sizes smaller than 10 nm [122,128]. Bezemer et al. [125] were the first to investigate the influence of cobalt particle size in the range 2.6 to 27 nm on performance in Fischer–Tropsch synthesis on well-defined catalysts supported on carbon nanofibers. It was found that the TOF for CO hydrogenation was independent of cobalt particle size for catalysts with particles larger than 6 nm (at atmospheric pressure) or 8 nm (at 35 bar). But both the TOF and the C_{5+} selectivity decreased for catalysts with smaller particles. It was proposed that the cobalt particle size effects could be attributed to a structure-sensitivity characteristic of the reaction, together with a CO-induced reconstruction of the cobalt surface.

4.5 SUMMARY

Porous carbons constitute a fascinating kind of material. Different types with distinctive physical forms and properties (i.e., activated carbons, high-surface-area graphites, carbon blacks, activated carbon cloths and fibers, nanofibers, nanotubes, etc.) find a wide range of industrial applications in adsorption and catalysis processes. The main properties of these materials that make them very useful as catalyst supports, as well as some of their applications, have been described. The use of carbon as a catalyst support relies primarily on the relative inertness of its surface, which facilitates the interaction between active phases or between active phases and promoters, thus enhancing the catalytic behavior. This makes porous carbons an excellent choice as catalyst support in a great number of reactions.

REFERENCES

- [1] P. Ehrburger, *Adv. Colloid Interface Sci.* 21 (1984) 275.
- [2] H. Jüntgen, *Fuel* 65 (1986) 1436.
- [3] D.S. Cameron, S.J. Cooper, I.L. Dogson, B. Harrison, J.W. Jenkins, *Catal. Today* 7 (1990) 113.

- [4] F. Rodríguez-Reinoso, in J.W. Patrick, Ed., *Porosity in Carbons: Characterization and Applications*, Edward Arnold, London, 1995.
- [5] F. Rodríguez-Reinoso, *Carbon* 36 (1998) 159.
- [6] L.R. Radovic, F. Rodríguez-Reinoso, in P.A. Thrower, Ed., *Chemistry and Physics of Carbon*, Vol. 25, Marcel Dekker, New York, 1997, p. 243.
- [7] L.R. Radovic, C. Sudhakar, in H. Marsh, A. Heinz, F. Rodríguez-Reinoso, Eds., *Introduction to Carbon Technologies*, University of Alicante, Alicante, Spain, 1997, p. 103.
- [8] C. Pham-Huu, M.-J. Ledoux, *Top. Catal.* 40 (2006) 49.
- [9] P. Serp, M. Corrias, P. Kalck, *Appl. Catal. A* 253 (2003) 337.
- [10] A. Linares-Solano, F. Rodríguez-Reinoso, C. Salinas-Martínez de Lecea, O.P. Mahajan, P.L. Walker, Jr., *Carbon* 20 (1982) 177.
- [11] A. Martín-Guillón, C. Prado-Burguete, F. Rodríguez-Reinoso, *Carbon* 31 (1993) 1099.
- [12] J. Laine, F. Severino, M. Labady, *J. Catal.* 147 (1994) 355.
- [13] J. Laine, M. Labady, F. Severino, S. Yunes, *J. Catal.* 166 (1997) 384.
- [14] F. Rodríguez-Reinoso, C. Salinas-Martínez de Lecea, A. Sepúlveda-Escribano, J.D. López-González, *Catal. Today* 7 (1990) 287.
- [15] L. Li, Z.H. Zhu, Z.F. Yan, G.Q. Lu, L. Rintoul, *Appl. Catal. A* 320 (2007) 166.
- [16] F. Derbyshire, V.H.J. de Beer, G.M.K. Abotsi, A.W. Scaroni, J.M. Solar, D.J. Skrovaneck, *Appl. Catal.* 27 (1986) 117.
- [17] C. Prado-Burguete, A. Linares-Solano, F. Rodríguez-Reinoso, C. Salinas-Martínez de Lecea, *J. Catal.* 115 (1989) 98.
- [18] C. Prado-Burguete, A. Linares-Solano, F. Rodríguez-Reinoso, C. Salinas-Martínez de Lecea, *J. Catal.* 128 (1991) 397.
- [19] W. Han, H. Liu, H. Zhou, *Catal. Commun.* 8 (2007) 351.
- [20] A. Sepúlveda-Escribano, F. Coloma, F. Rodríguez-Reinoso, *Appl. Catal. A* 173 (1998) 247.
- [21] F. Coloma, A. Sepúlveda-Escribano, F. Rodríguez-Reinoso, *Appl. Catal. A* 150 (1997) 165.
- [22] M.L. Toebe, F.F. Prinsloo, J.H. Bitter, A.J. vanPillen K.P. de Jong, *J. Catal.* 214 (2003) 78.
- [23] M.L. Toebe, Y. Zhang, J. Hájek, et al., *J. Catal.* 226 (2004) 215.
- [24] H.P. Boehm, G. Mair, T. Store, A.R. de Rincón, B. Tereczki, *Fuel* 63 (1984) 1061.
- [25] A. Guerrero-Ruiz, I. Rodríguez-Ramos, F. Rodríguez-Reinoso, C. Moreno-Castilla, J.D. López-González, *Carbon* 26 (1988) 417.
- [26] P.H. Matter, L. Zhang, U.S. Ozkan, *J. Catal.* 239 (2006) 83.
- [27] L. Wachowski, W. Skupinski, M. Hofman, *Appl. Catal. A* 303 (2006) 230.
- [28] C. Milone, C. Gangemi, R. Ingoglia, G. Neri, S. Galvagno, *Appl. Catal. A* 184 (1999) 89.
- [29] F. Coloma, A. Sepúlveda-Escribano, J.L.G. Fierro, F. Rodríguez-Reinoso, *Appl. Catal. A* 136 (1996) 231.
- [30] F. Coloma, A. Sepúlveda-Escribano, J.L.G. Fierro, F. Rodríguez-Reinoso, *Appl. Catal. A* 148 (1996) 63.

- [31] A. Huidobro, A. Sepúlveda-Escribano, F. Rodríguez-Reinoso, *J. Catal.* 212 (2002) 94.
- [32] H.J. Jung, P.L. Walker, Jr., M.A. Vannice, *J. Catal.* 75 (1982) 416.
- [33] J.W. Niemanstverdriet, A.M. van der Kraan, W.N. Delgass, M.A. Vannice, *J. Phys. Chem.* 89 (1986) 4832.
- [34] A.A. Chen, M. Kaminsky, G.L. Geoffroy, M.A. Vannice, *J. Phys. Chem.* 90 (1986) 4810.
- [35] F. Coloma, A. Sepúlveda-Escribano, J.L.G. Fierro, F. Rodríguez-Reinoso, *Langmuir* 10 (1994) 750.
- [36] H.E. Van Dam, J. Van Bekkum, *J. Catal.* 131 (1991) 335.
- [37] J.M. Solar, C.A. Leon y Leon, K. Oseko-Asare, L. Radovic, *Carbon* 28 (1990) 369.
- [38] T. Nakamura, M. Yamada, T. Yamaguchi, *Appl. Catal. A* 87 (1992) 69.
- [39] P. Serp, J.-C. Hierso, R. Feurer, et al., *Carbon* 37 (1999) 527.
- [40] D.J. Suh, T.-J. Park, S.-K. Ihm, *Carbon* 31 (1993) 427.
- [41] Y. Nitta, T. Kato, T. Imanaka, *Stud. Surf. Sci. Catal.* 78 (1993) 83.
- [42] T. Harada, S. Ikeda, M. Miyazaki, T. Sakata, H. Mori, M. Matsumura, *J. Mol. Catal. A* 268 (2007) 59.
- [43] E.N. Coker, W.A. Steen, J.T. Miller, A.J. Kropf, J.E. Millar, *Micropor Mesopor. Mater.* 101 (2007) 440.
- [44] J.H. Choi, K.-W. Park, B.-K. Kwon, Y.-E. Sung, *J. Electrochem. Soc.* 150 (2003) A973.
- [45] T.C. Deivaraj, J.Y. Lee, *J. Electrochem. Soc.* 151 (2004) A1832.
- [46] N. Martz, C. Roth, H. Fueß, *J. Appl. Electrochem.* 35 (2005) 85.
- [47] E. Antolini, J.R.C. Salgado, A.M. dos Santos, E.R. Gonzalez, *Electrochem. Solid State Lett.* 8 (2005) A226.
- [48] K.-W. Park, J.-H. Choi, B.-K. Kwon, et al., *J. Phys. Chem. B* 106 (2002) 1869.
- [49] J. Mathiyarasu, A.M. Remona, A. Mani, K.L. Pan, V. Yegnaraman, *J. Solid State Electrochem.* 8 (2004) 968.
- [50] M.V. Martínez-Huerta, S. Rojas, J.L. Gómez de la Fuente, P. Terreros, M.A. Peña, J.L.G. Fierro, *Appl. Catal. B* 69 (2006) 75.
- [51] M. Dunkel, E. Dorrer, W. Breuers, U.S. patent 1,965,956, 1995.
- [52] A. Ozaki, K. Aika, H. Hori, *Bull. Chem. Soc. Jpn.* 44 (1971) 3216.
- [53] Z. Kowalczyk, S. Jodzis, J. Sentek, *Appl. Catal. A* 138 (1996) 83.
- [54] Z. Kowalczyk, J. Sentek, S. Jodzis, et al., *Catal. Lett.* 45 (1997) 65.
- [55] A.I. Foster, G.P. James, J.J. McCarrol, R.S. Tennison, U.S. patent 4,163,775, 1979.
- [56] Z. Zhong, K. Aika, *Chem. Commun.* (1997) 1223.
- [57] Z. Zhong, K. Aika, *J. Catal.* 173 (1998) 535.
- [58] X. Zheng, S. Zhang, J. Xu, K. Wei, *Carbon* 40 (2002) 2597.
- [59] W. Han, H. Liu, H. Zhu, *Catal. Commun.* 8 (2007) 351.
- [60] C. Liang, Z. Wei, Q. Xin, C. Li, *Appl. Catal. A* 208 (2001) 193.
- [61] S. Hagen, R. Barfod, R. Fehrmann, et al., *Chem. Commun.* (2002) 1206.

- [62] G.C. Stevens, T. Edmonds, *Stud. Surf. Sci. Catal.* 3 (1979) 507.
- [63] G.M.K. Abotsi, A.W. Scaroni, *Fuel Process. Technol.* 22 (1989) 107.
- [64] K. Sakanishi, T. Nagamatsu, I. Mochida, D.D. Whitehurst, *J. Mol. Catal.* 155 (2000) 101.
- [65] B. Pawalec, R. Mariscal, J.L.G. Fierro, A. Grennwood, P.T. Vasudevan, *Appl. Catal. A* 206 (2001) 295.
- [66] M. Breysse, P. Afanasiev, C. Geantet, M. Vrinat, *Catal. Today* 86 (2003) 5.
- [67] M. Breysse, B.A. Bennet, D. Chadwick, M. Vrinat, *Bull. Soc. Chim. Belg.* 90 (1981) 1271.
- [68] A.J. Bridgewater, R. Burch, P.C.H. Mitchell, *Appl. Catal.* 4 (1982) 267.
- [69] B.M. Reddy, V.S. Subrahmanyam, *Appl. Catal.* 27 (1986) 1.
- [70] M. Karroua, A. Centeno, H.K. Matralis, P. Grange, B. Delmon, *Appl. Catal.* 51 (1989) L21.
- [71] E. Hillerová, Z. Vit, M. Zdrazil, S.A. Shkuropat, E.N. Bogdanets, A.N. Startsev, *Appl. Catal.* 67 (1991) 231.
- [72] E. Hillerová, M. Zdrazil, *Catal. Lett.* 8 (1991) 215.
- [73] P.M. Boorman, K. Chong, *Appl. Catal. A* 95 (1993) 197.
- [74] V.M. Kogan, N.T. Dung, V.I. Yakerson, *Bull. Soc. Chim. Belg.* 104 (1995) 303.
- [75] D. Chadwick, M. Breysse, *J. Catal.* 71 (1981) 226.
- [76] H. Farag, I. Mochida, K. Sakanishi, *Appl. Catal. A* 194–195 (2000) 147.
- [77] H. Topsoe, B.S. Clausen, F.E. Massoth, Hydrotreating catalysts, in J.R. Anderson, M. Boudart, Eds., *Catalysis Science and Technology*, Vol. 11, Springer-Verlag, Berlin, 1996.
- [78] R.R. Chianelli, T.A. Pecoraro, *J. Catal.* 198 (2001) 9.
- [79] Y.I. Yermakov, V.F. Surovikin, G.V. Plaksin, et al., *React. Kinet. Catal. Lett.* 33 (1987) 435.
- [80] J.C. Duchet, E.M. van Oers, V.H.J. de Beer, R. Prins, *J. Catal.* 80 (1983) 386.
- [81] R. Thomas, E.M. van Oers, V.H.J. de Beer, J. Medema, J.A. Moulijn, *J. Catal.* 76 (1982) 241.
- [82] V.H.J. de Beer, F.J. Derbyshire, C.K. Groor, R. Prins, A.W. Scaroni, J.M. Solar, *Fuel* 63 (1984) 1095.
- [83] B. Scheffer, P. Arnoldy, J.A. Moulijn, *J. Catal.* 112 (1988) 516.
- [84] A. Martín-Gullón, C. Prado-Burguete, F. Rodríguez-Reinoso, *Carbon* 31 (1993) 1099.
- [85] J.P.R. Vissers, T.J. Lensing, V.H.J. de Beer, R. Prins, *Appl. Catal.* 30 (1987) 21.
- [86] M. Kouzu, Y. Kuriki, F. Hamdy, K. Sakanishi, Y. Sugimoto, I. Saito, *Appl. Catal. A* 265 (2004) 61.
- [87] J.J. Lee, S. Han, H. Kim, J.H. Koh, T. Hyeon, S.H. Moon, *Catal. Today* 86 (2003) 141.
- [88] A. Calafat, J. Laine, A. López-Agudo, J.M. Palacios, *J. Catal.* 162 (1996) 20.
- [89] K. Sakanishi, T. Nagamatsu, I. Mochida, D.D. Whitehurst, *J. Mol. Catal. A* 155 (2000) 101.

- [90] I.V. Babich, J.A. Moulijn, *Fuel* 82 (2003) 607.
- [91] C. Song, X. Ma, *Appl. Catal. B* 41 (2003) 207.
- [92] T. Pecoraro, R.R. Chianelli, *J. Catal.* 67 (1981) 430.
- [93] M.J. Ledoux, O. Michiaux, J. Agostini, P. Panissod, *J. Catal.* 102 (1986) 275.
- [94] M. Lacroix, N. Boutarfa, C. Guillard, M. Vrinat, M. Breyssse, *J. Catal.* 120 (1989) 473.
- [95] N. Escalona, M. Yates, P. Ávila, et al., *Appl. Catal. A* 240 (2003) 151.
- [96] N. Escalona, J. Ojeda, J.M. Palacios, et al., *Appl. Catal. A* 319 (2007) 218.
- [97] Y. Shu, S.T. Oyama, *Carbon* 43 (2005) 1517.
- [98] B. Dhandapani, T. St. Clair, S.T. Oyama, *Appl. Catal. A* 168 (1998) 219.
- [99] P. Costa, J.L. Lemberton, C. Potvin, et al., *Catal. Today* 65 (2001) 195.
- [100] D. Mordini, D. Brodzki, G. Djéga-Mariadassou, *J. Solid State Chem.* 141 (1998) 114.
- [101] S. Suppan, J. Trawczynski, J. Kaczmarczyk, G. Djéga-Mariadassou, A. Hynaux, C. Sayag, *Appl. Catal. A* 280 (2005) 209.
- [102] A. Hynaux, C. Sayag, S. Suppan, et al., *Catal. Today*, 119 (2007) 3.
- [103] A. Hynaux, C. Sayag, S. Suppan, et al., *Appl. Catal. B* 72 (2007) 62.
- [104] L.R. Radovic, C. Sudhakar, in H. Marsh, E.A. Heinz, F. Rodríguez-Reinoso, Eds., *Introduction to Carbon Technologies*, University of Alicante, Alicante, Spain, 1997.
- [105] H.-J. Jung, P.L. Walker, Jr., M.A. Vannice, *J. Catal.* 75 (1982) 416.
- [106] J.W. Niemantsverdriet, A.M. van der Kraan, W.N. Delgass, M.A. Vannice, *J. Phys. Chem.* 89 (1986) 4832.
- [107] A.A. Chen, M. Kaminsky, G.L. Geoffroy, M.A. Vannice, *J. Phys. Chem.* 90 (1986) 4810.
- [108] V.K. Jones, L.R. Neubauer, C.H. Bartholomew, *J. Phys. Chem.* 90 (1986) 4832.
- [109] A.P.B. Sommen, F. Stoop, K. van der Wiele, *Appl. Catal.* 14 (1985) 277.
- [110] F. Rodríguez-Reinoso, C. Salinas-Martínez de Lecea, A. Sepúlveda-Escribano, J.D. López-González, *Catal. Today* 7 (1990) 287.
- [111] J.J. Venter, A. Chen, M.A. Vannice, *J. Catal.* 117 (1989) 170.
- [112] E. van Steen, F.F. Prinsloo, *Catal. Today* 71 (2002) 327.
- [113] M.C. Bahome, L.L. Jewell, D. Hildebrandt, D. Glasser, N.J. Coville, *Appl. Catal. A* 287 (2005) 60.
- [114] J.M. Martínez, F. Rodríguez-Reinoso, M.A. Vannice, *Appl. Catal.* 51 (1989) 93.
- [115] K.R. Kannan, G.U. Kulkarni, C.N.R. Rao, *Catal. Lett.* 14 (1992) 149.
- [116] M.C. Bahome, L.L. Jewell, K. Padayachy, et al., *Appl. Catal. A* 328 (2007) 243.
- [117] K. Lázal, W.M. Reiff, W. Mörke, L. Guczi, *J. Catal.* 100 (1986) 118.
- [118] F.J. Berry, L. Liwu, W. Chengyu, T. Renyuan, Z. Su, L. Dongbai, *J. Chem. Soc. Faraday Trans. I* 81 (1985) 2293.
- [119] E. Iglesia, S.L. Soled, J.E. Baumgartner, S.C. Reyes, *Top. Catal.* 2 (1995) 17.
- [120] J.L. Li, G. Jacobs, T. Das, Y.Q. Zhang, B. Davis, *Appl. Catal. A* 236 (2002) 67.
- [121] C. Moreno-Castilla, F. Carrasco-Marín, *J. Chem. Soc. Faraday Trans.* 91 (1995) 3519.
- [122] R.C. Reuel, C.H. Bartholomew, *J. Catal.* 85 (1984) 78.

- [123] G.L. Bezemer, P.B. Radstake, V. Koot, A.J. van Dillen, J.W. Geus, K.P. de Jong, *J. Catal.* 237 (2006) 291.
- [124] G.L. Bezemer, P.B. Radstake, U. Falke, et al., *J. Catal.* 237 (2006) 152.
- [125] G.L. Bezemer, J.H. Bitter, H.P.C.E. Kuipers, et al., *J. Am. Chem. Soc.* 128 (2006) 3956.
- [126] E. Iglesia, S.L. Soled, R.A. Fiato, *J. Catal.* 137 (1992) 212.
- [127] E. Iglesia, *Appl. Catal. A* 161 (1997) 59.
- [128] A. Martínez, C. López, F. Márquez, I. Diaz, *J. Catal.* 220 (2003) 486.

5 Preparation of Carbon-Supported Metal Catalysts

JOHANNES H. BITTER and KRIJN P. DE JONG

5.1 INTRODUCTION

In most catalysts the active phase (e.g., metal, metal oxide, metal sulfide) is deposited on a support in order to keep the active phase stable and highly dispersed during use of the catalyst. As the synthesis of the catalyst is a crucial step that largely affects its performance, fundamental understanding of catalyst synthesis is important. In this chapter we review the literature in which the insight in catalyst synthesis on carbon supports is apparent. The carbon materials included active carbons (ACs), graphite, carbon black (CB), and carbon nanofibers/nanotubes (CNFs/CNTs). First we discuss the most used synthesis techniques: impregnation and adsorption. Next we look at deposition precipitation. Finally, some emerging fields in catalyst synthesis are explored.

5.2 IMPREGNATION AND ADSORPTION

Due to its simplicity, impregnation is used routinely for the preparation of catalysts. Two different modes of impregnation are practiced: wet impregnation and incipient-wetness impregnation. In wet impregnation the support material is brought into contact with a large excess of solution containing the metal precursors; after evaporating the solvent, and after optional calcination (not recommended for carbon) and reduction, the final catalyst is obtained. In general, wet impregnation results in large particles since the majority of the metal precursor is present in the solution outside the pore system of the support. During drying the metal precursors often deposit on the outer surface of the support particles, resulting in large crystals.

To make effective use of the pore structure of the support, incipient-wetness impregnation can be performed in which the metal precursor is dissolved in just

enough solvent to fill the pores of the support. In that case, closer contact is achieved between the metal precursor and the support, which in general results in smaller particles if drying, calcination, and/or reduction are executed carefully. During impregnation, in the first step the metal-precursor ion may adsorb on the support followed by, during drying, nucleation and particle growth. When an excess of solution is used but the drying step mentioned above is replaced by filtering of the excess solution, only the adsorbed ions form the active (precursor) phase. This method is called *ion adsorption*.

After reviewing the literature we conclude that in all three methods—wet impregnation, incipient-wetness impregnation, and ion adsorption—two major factors govern the final dispersion of the active phase: precursor–support interaction and pore structure. These two issues are discussed in the next two subsections. Note that we discuss primarily that literature which adds fundamental insights in the preparation of carbon-supported catalysts.

5.2.1 Interaction Between Support and Precursor

All theory on impregnation and ion adsorption is based on the landmark paper of Brunelle [1]. It was noted that the coulombic interaction between support and active-phase precursor is crucial for obtaining a good distribution of the precursor over the support. Basically, a negatively charged surface [i.e., using a pH of the impregnating solution above the point of zero charge (PZC)] attracts positively charged precursors while positively charged surfaces (i.e., below the PZC) attract negatively charged precursors.

Although different models exist describing the adsorption of ions on carbon supports (see, e.g., ref. 2 and the references therein), the revised physical adsorption (RPA) proposed by Regalbuto et al. [2–4] was able to describe the adsorption of a metal precursor on a given support as a function, in a relatively simple way, of, among others, ionic strength and pH. The model includes only physical adsorption of ions on the support, involving outer-sphere complexes in which the ions retain their hydration shell. The authors state that “the model consists of a non-Nernstian description of the charging of surface hydroxyl groups, a proton balance to account for the shifts in pH caused by the oxide buffering effect, and an adsorption equilibrium constant based solely on the coulombic free energy of adsorption” [3]. Although the model was developed originally for hexachloroplatinic acid on alumina supports, with some modification it was applicable to other supports and metal precursors, including carbon [5]. For carbon supports the model was extended to a dual-site model in which one type of site consists of the oxygen-containing groups and the other type involves the basic π -sites. To demonstrate the strength of the model, Figure 5.1 shows the uptake of H_2PtCl_6 (CPA) and $[Pt(NH_3)_4](NO_3)_2$ over active carbon (AC), graphite (KB), and carbon black (SX). Good agreement between the experimental uptake and the uptake resulting from the model can be observed.

In contrast, others claim the formation of an inner-shell complex during the adsorption of metal–precursor complexes on carbon [7], sometimes even

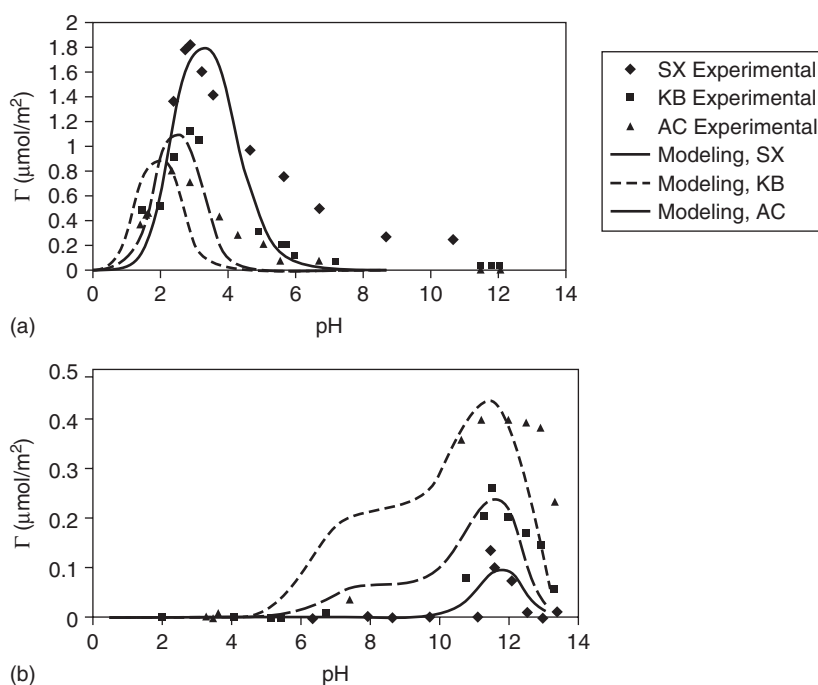


Figure 5.1 Comparison of experimental metal precursor adsorption data using (a) H_2PtCl_6 and (b) $[\text{Pt}(\text{NH}_3)_4]\text{NO}_3_2$ on active carbon (AC), graphite (KC), and carbon black (SX), and the uptake predicted by the RPA model. (From ref. 6, courtesy of J. R. Regalbuto.)

accompanied by a reduction in the metal–precursor complex by the support, as was shown for H_2PtCl_6 on active carbon [8–10]. Irrespective of the model applicable to describe the adsorption properties of a metal precursor during ion adsorption and impregnation, all authors agree on the fact that the surface composition of carbon plays a crucial role in the adsorption of metal ions. Often, oxygen groups are introduced via oxidation (see also Chapters 2 and 3) of the surface of the carbon to enhance the adsorption of the metal in order to obtain high levels of dispersion and metal loading. But the role of basic sites, being either oxygen-containing groups such as chromene and pyrone-like structures [9,11,12] or π -sites [11,13,14], is claimed to be of importance. Next, we give an overview of the existing literature on the role of oxygen groups and basic sites on the dispersion of metals on carbon supports.

Prado-Burguete et al. [15] showed that after impregnating H_2PtCl_6 on a heat-treated carbon black (i.e., without oxygen-containing groups on the surface), the Pt particle size was 5.1 nm. After H_2O_2 oxidation of the heat-treated support, oxygen groups were introduced and after impregnation and reduction, a

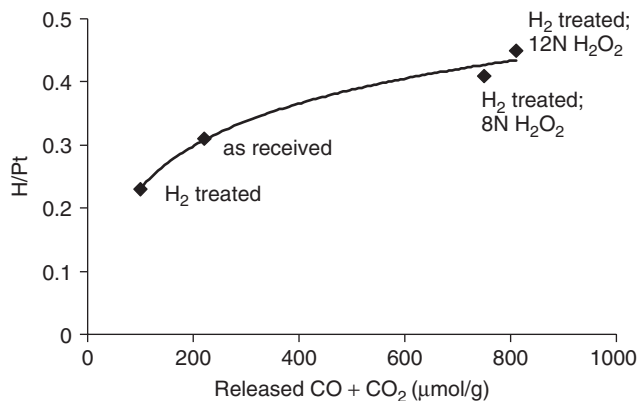


Figure 5.2 Relationship between Pt dispersion of catalysts and amount of oxygen surface complexes (measured as $\mu\text{mol/g}$ of CO_2 and CO evolved) of the supports. The furnace carbon black was used “as received,” after a 12-hour H_2 treatment at 1223 K, after a 12-hour H_2 treatment at 1223 K followed by a 48-hour treatment in 8 N H_2O_2 , and after a 12-hour H_2 treatment at 1223 K followed by 48 hours in 12 N H_2O_2 . (Adapted from ref. 15.)

Pt particle size of 2.4 nm was obtained. The authors attributed this to enhanced interaction of the precursor (H_2PtCl_6) with the oxidized support and increased wettability after oxidation. Figure 5.2 shows the H/Pt ratios from which the Pt particle sizes were calculated, as a function of the amount of oxygen in the support. The latter is expressed as the amount of $\text{CO} + \text{CO}_2$ released during heating. These results are in agreement with Aksaylu et al. [16], who used active carbon and showed that increasing the amount of oxygen groups results in a higher Pt dispersion. Nevertheless, a beneficial role of the increased mesopore area could not be ruled out.

Miguel et al. [8] deposited H_2PtCl_6 on AC with and without oxidative treatment. They observed no influence of oxidation of a peach pit carbon on the Pt dispersion. However, the start material was not submitted to heat treatment, so already contained functional groups on the surface of the carbon. Oxidation increased the amount of oxygen functional groups, but since the metal loading was low (0.85 wt%), the additional oxygen might have had a limited influence.

A beneficial role of oxygen groups was also claimed for other metals. Suh et al. [12] showed that by using the hydrolysis by base of PdCl_2 on both active carbons and carbon black, the Pd dispersion increases with increasing content of surface-oxygen groups. Please note that an extensive overview on the synthesis of supported Pd catalysts was given by Toebe et al. [17 and references therein]. In that review, attention was also paid to the use of carbon as a support.

Zhu et al. [18,19] showed that on untreated active carbon, due to the large number of anchoring sites, 5.7-nm Ru particles could be obtained from RuCl_3 in

water. Removing these groups by heat treatment resulted under the same synthesis conditions in 51-nm particles. Reoxidation of the heat-treated sample in O₂ followed by impregnation with RuCl₃ resulted in 3.8-nm particles. The smallest particles, 2.2 nm, were obtained when the heat-treated sample was subsequently treated in CO₂ followed by HNO₃. The authors speculated that oxidation resulted in increased wetting, while the CO₂ treatment created a higher mesoporous area, which is beneficial for dispersion. In addition, the HNO₃ treatment reduced the ash content, which was also claimed to have a beneficial effect.

Chen et al. [20] showed for silver on activated carbon that increasing the amount of oxygen groups resulted in a bimodal distribution of silver with sizes of 4 to 6 nm and greater than 22 nm. It is, however, essential to have oxygen groups on the surface to obtain the small particles. In our opinion the bimodal distribution might be the result of the high weight loading of silver used in these materials (12 wt%).

The amount of carboxylic acid groups on the surface of the carbon might change during the impregnation procedure, which can be a source for the conflicting results on the role of oxygen groups. Toebe et al. [21] suggested that the number of oxygen groups might change as a function of pH during ion adsorption of [Pt(NH₃)₄](NO₃)₂ on carbon nanofibers. Depending on the pH of the solution, carboxylic anhydride groups, on which metal adsorption is unlikely, can hydrolyze to carboxylic groups, making the site available for adsorption (i.e., increasing the metal loading). The dynamic behavior during the preparation of catalysts was also suggested by others [8,9,22,23], who show that by depositing Pt⁴⁺, reduction to Pt²⁺ takes place with the release of CO and/or CO₂ (i.e., the support reduces the Pt and in turn is oxidized itself). This might increase the amount of oxygen as discussed by Sepúlveda-Escribano et al. [22], who showed that impregnation of acidic solutions of H₂PtCl₆ on carbon black increased the amount of CO₂ and CO that is released from the surface during heating after impregnation compared to before impregnation (Figure 5.3). Oxidation of the support by the acidic solution containing H₂PtCl₆ is claimed to increase the amount of oxygen groups on the carbon surface. The same authors [22] show that [Pt(NH₃)₄]²⁺ strongly adsorbs from basic solutions on the acidic oxygen groups on the surface of carbon.

Others doubt whether metals (precursors) strongly adsorb on oxygen-containing groups. Gurrath et al. [13], using both PdCl₂ or [Pd(NH₃)₄](NO₃)₂ impregnations on active carbon, claim that the oxygen groups might result in a high initial dispersion during metal deposition. However, due to the low thermal stability of the oxygen groups, as was also claimed by van Dam and van Bekkum [9] and by Sepúlveda-Escribano et al. [22], they might decompose during high-temperature treatment such as reduction, which might result in Pd sintering.

Fraga et al. [14] performed ion adsorption using H₂PtCl₆ over activated carbons which differ in their point of zero charge by varying the ratio of acidic oxygen groups over basic π sites. Increasing the amount of oxygen groups on

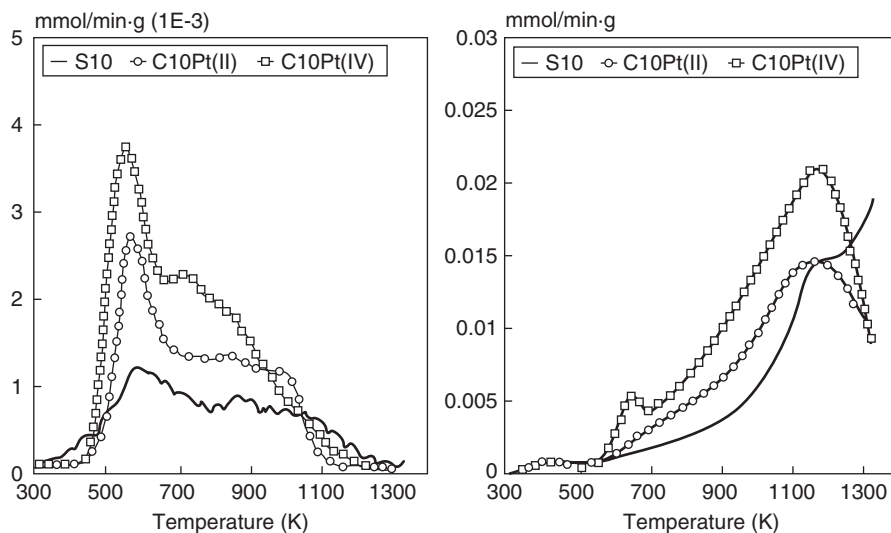


Figure 5.3 Temperature-programmed CO₂ (left panel) and CO (right panel) evolution profiles from the furnace carbon black support after heat treatment at 1273 K (S10) and after [Pt(NH₃)₄]Cl₂ impregnation [C10Pt(II)] or H₂PtCl₆ impregnation [C10Pt(IV)]. (Adapted from ref. 22.)

the support was claimed to result in higher metal loading, due to the better wettability of the support. However, the authors claim that the π sites are responsible for the strong anchoring of Pt.

From the literature reviewed it is clear that the role of oxygen-containing groups on anchoring of metal particles is not unambiguous. Nevertheless, since water is almost exclusively used as solvent, agreement exists on the importance of oxygen functionalities for enhancing the wetting of the carbon surface. Work from our groups on Ni/CNF [24,25] supports that idea. With aqueous solutions of Ni-nitrate, good dispersion could be obtained on oxidized CNFs, while on oxygen-poor CNFs, the Ni dispersion was very low (Figure 5.4). Using ethanol, a less polar solvent compared to water, resulted in high Ni dispersion on both oxidized and oxygen-poor CNFs. Thus, the less polar ethanol was able to wet the hydrophobic unfunctionalized CNFs. However, Ni particles on the oxygen-poor CNFs were not thermally stable, whereas those on functionalized CNF-ox were. Therefore, we concluded that the role of oxygen groups was both to increase the wettability of the support by water and to anchor the Ni particles.

Some care has to be taken not to look at the charge of the support and the metal precursor only. Also, the presence of other ions (i.e., the ionic strength) in the solution plays a crucial role. López-Ramón et al. [26] varied the concentration of ions of the impregnation solution by adding different amounts of NaCl. Figure 5.5

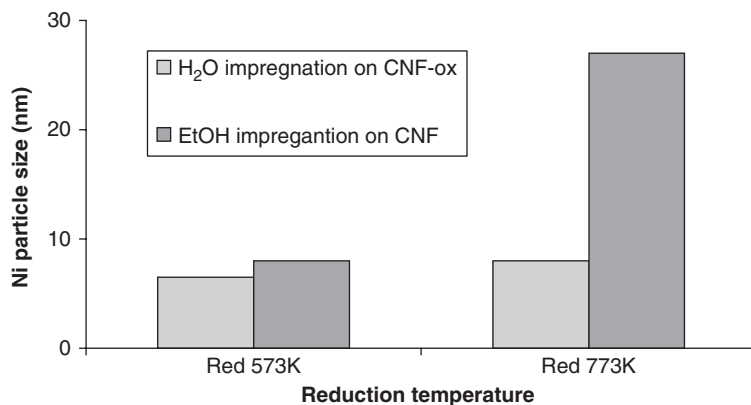


Figure 5.4 Particle sizes of 10 wt% Ni/CNF catalysts prepared by incipient wetness impregnation using aqueous and ethanolic solutions of Ni-nitrate as a function of the reduction temperature.

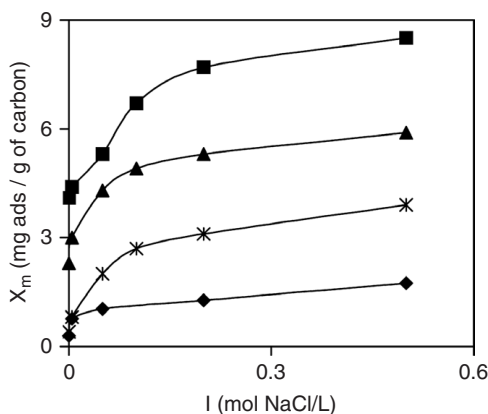


Figure 5.5 Uptake of $[\text{Ni}(\text{CN}_4)^{2-}]$ ions on BV46-S at pH 7 (squares), Ni^{2+} ions on BV46 at pH 6 (triangles), Cr^{3+} ions on BV46 at pH 6 (asterisks), and $[\text{Cr}(\text{C}_2\text{O}_4)^{3-}]$ ions on HS1 at pH 7 (diamonds) as a function of ionic strength. Sample BV46 is an activated carbon from olive stones. Oxidation of this sample with $(\text{NH}_4)_2\text{S}_2\text{O}_8$ yielded sample BV46-S. Sample HS1 was a low-surface-area oxidized active carbon. (From ref. 26, with permission.)

shows that for Ni and Cr salts, the metal loading increases with ionic strength at a given pH. However, this is not a general observation because solutions of higher ionic strength resulted in better screening of the surface charges, therefore modifying interaction of the metal precursor, either attractive or repulsive, with the surface. Thus, the final loading can be higher or lower, depending on the surface charge compared to the charge of the metal precursor.

5.2.2 Role of Pore Structure

As discussed above, oxygen groups play a crucial role in determining the metal loading and dispersion of carbon-supported metal catalysts. Also, the pore structure is claimed to have an influence on the metal dispersion. We give a short overview of the influence of the pore structure on metal loading and distribution, although the field is rather descriptive.

Aksoylu et al. [16] showed that by oxidizing the support in air, next to the introduction of oxygen-containing groups on the carbon surface, the mesopore area increased from $40\text{ m}^2/\text{g}$ to $89\text{ m}^2/\text{g}$ for a Hydraphin (Degussa) support, while a 10% increase, to $44\text{ m}^2/\text{g}$, was observed for HNO_3 oxidation. Since in both oxidized samples the metal dispersion was high, the authors conclude that oxygen groups are the most important factor for obtaining a high level of dispersion, but the role of mesoporous area could not be excluded.

Fuente et al. [27] compared two activated carbons of Norit with similar oxygen content and $\text{p}K_a$ but different pore volumes (i.e., 0.522 mL/g vs. 0.393 mL/g). Loading these supports with either H_2PtCl_6 or $[\text{Pt}(\text{NH}_3)_4]\text{Cl}_2$ resulted in 1 wt% Pt on the high-pore-volume support, with a dispersion of 35% irrespective of the precursor. The low-pore-volume material resulted in metal loading of about 0.7 wt% with a dispersion of 20%; therefore, the authors conclude that high porosity is beneficial for dispersion.

Samant et al. [28] prepared a highly mesoporous carbon by condensing 1,3-dihydroxybenzoic acid with formaldehyde followed by curing and carbonization. On the support obtained, with a mesoporous area of $524\text{ m}^2/\text{g}$, a Pt salt (precursor not mentioned) was impregnated, which resulted, after liquid-phase reduction in sodium formate, in particles of about 1 to 2 nm with 8.5 wt% Pt loading. The authors claim that the high mesoporous area was key to making a highly loaded, highly dispersed Pt catalyst, which is in agreement with results of Zhu et al. [18], who created mesopores in carbon by high-temperature CO_2 treatment. Using this mesoporous carbon, small Ru particles (2.2 nm) were obtained after oxidation of this support with HNO_3 and impregnation of RuCl_3 followed by a reduction step. Similar claims were made by Prado-Burguete et al. [29] for Pt on carbon black. Okhlopkova et al. [30] prepared Pt and Pd catalysts on both meso- and microporous carbon of different origin by impregnating the supports with either a H_2PtCl_6 or a H_2PdCl_4 solution. In general, the Pt catalysts showed a higher dispersion based on CO chemisorption compared to the Pd samples. For a given metal the dispersions decreased with increasing reduction temperature. However, the dispersion did not relate linearly to the catalytic activity in cyclohexene hydrogenation. Therefore, the authors postulate that hampered accessibility of the metal particles in the micropores, which might be partially blocked by other metal particles, is the reason for this discrepancy. In addition, Gurrath et al. [13] observed diffusion limitations in Pd on active carbon catalysts. Due to the narrow micropores, even molecules such as cyclohexene could not reach the metal particles present deep in the pores.

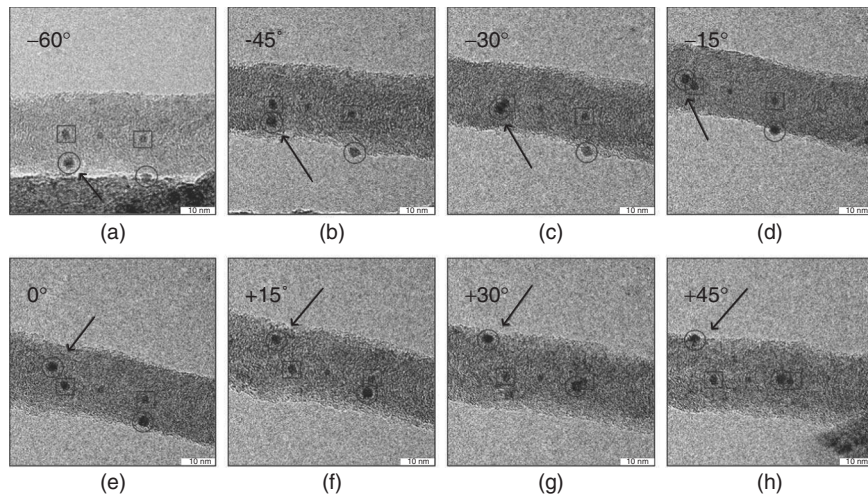


Figure 5.6 TEM tilt series over an angular tilt range with palladium particles on the inside as well as on the outside of the fiber. The tilt axis was chosen parallel to the length of the fiber. Arrows show a particle that appears to have a hemispherical shape when observed from the side. (From ref. 36, with permission.)

In the case of carbon nanotubes it was already known that the hollow inner tube could be filled with a metal [31–35]. However, only recently it was shown by Winter et al. [36] that the inner core of carbon nanofibers, which are supposed to be formed of stacked cups of carbon, was also accessible for metal deposition. The presence of Pd particles in the inner core after ion adsorption of $\text{Pd}(\text{NH}_3)_4^{2+}$ on HNO_3 -treated carbon nanofibers was proven by a transmission electron microscopy (TEM) tilt series (Figure 5.6). Particles in the inner tube maintained their position when the sample was tilted in the microscope, whereas particles on the outside moved during tilting.

5.3 DEPOSITION PRECIPITATION

The deposition of a precursor of an active component from a solution onto a support can be brought about by a chemical reaction rather than by drying or by adsorption. Called *deposition precipitation* (DP), this is done most often in an excess of solution with respect to the pore volume of the support and using the support in the form of a powder. In the suspension, deposition precipitation can be realized in a number of ways:

- Increase of pH (see Section 5.3.1)
- Change of valency of the metal ion (see Section 5.3.2)
- Removal of a stabilizing ligand of the metal ion (see Section 5.3.3)

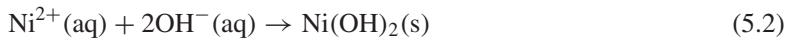
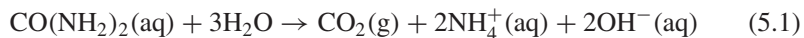
These three fundamentally different methods have also been used with carbon supports and are discussed in detail in separate sections. Among the advantages of DP over other preparation techniques, we mention (1) its reproducibility, (2) the high metal loadings that can be achieved, (3) the high metal dispersions at high metal loadings, and (4) a uniform distribution of the active component over the support.

Deposition precipitation was patented in 1943 and has been studied at length by a number of groups [37]. Geus and co-workers have studied the deposition of a range on nonnoble metals (in particular, Ni, Cu, and Fe) onto silica powders [38, 39]. From their work, optimal conditions to promote nucleation of the respective metal compound onto the support have been obtained. These authors have applied a thermodynamic model of nucleation and growth. Later, Burattin et al. [40–42] studied the molecular details of the process, in particular of nickel hydroxide deposition onto silica. The strong interaction between the hydroxide and the support appeared to be essential to start deposition on its surface and to exclude nucleation in the bulk liquid phase. In fact, in many cases a mixed compound between metal hydroxide and support was formed, providing a thermodynamic driving force for nucleation onto the support. With carbon, however, a strong interaction and mixed compound formation between metal hydroxide and support are not to be expected.

In the early literature of DP with carbon supports, in particular of nickel hydroxide on carbon, nonuniform distribution of metals was observed [43]. With iron on carbon nanotubes, the metal dispersion was quite low [44]. A detailed mechanistic consideration of DP with carbon was needed prior to successful application. This mechanistic study is described for Ni onto carbon nanofibers in the next section.

5.3.1 Increase in pH

The most widely used method of DP comprises an increase in pH brought about by the hydrolysis of urea. For the deposition of nickel from an aqueous solution, the following (simplified) reactions are envisaged:



Please note that equation (5.1) holds for an acidic medium with limited CO₂ solubility. For more elevated pH, bicarbonate and carbonate will be formed and buffering will occur, leading to a maximal pH of about 6. An elegant aspect of the urea method is that the reactant can be added at low temperature and the uniform suspension can be heated to typically 363 K, where hydrolysis of urea takes place uniformly throughout the solution. The urea method is therefore sometimes referred to as homogeneous deposition precipitation (HDP). In the case of noble metals such as palladium or gold, some workers add sodium hydroxide to the suspension to increase the pH. In the latter case, HDP is not fully possible and one should refer to that as DP.

As mentioned in the introduction, the interaction between metal hydroxide and carbon inevitably will be quite subtle. From a study of the DP of nickel hydroxide onto carbon nanofibers, van der Lee et al. [45] concluded that the carboxylic acid groups are key anchoring and nucleation sites on the support surface for the deposition of nickel hydroxide. Surface oxidation of carbon nanofibers typically introduces one COOH group per square nanometer. Nickel ions may adsorb onto these groups. This is what the authors found, as can be inferred from the results shown in Figure 5.7.

With silica, nickel deposition did not occur prior to nucleation inferred from the overshoot in pH at $t = 40$ minutes. With surface-oxidized carbon (CNF–O), deposition already took place at pH 4 and $t = 0$. Nickel ion adsorption is the

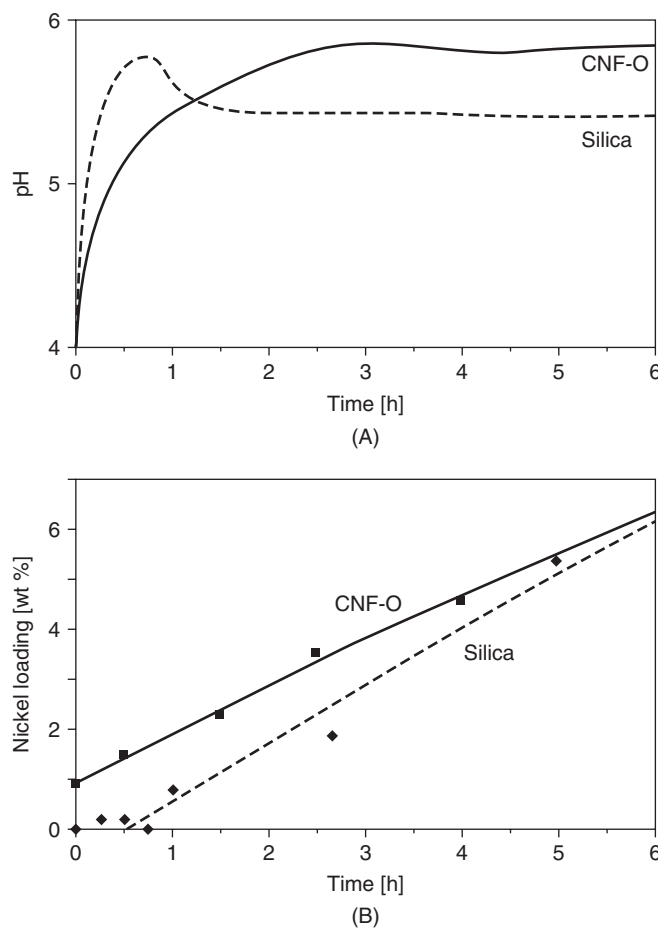


Figure 5.7 Development of pH (A) and nickel loading (B) with silica (dashed lines) and carbon nanofiber support (solid lines) as a function of time

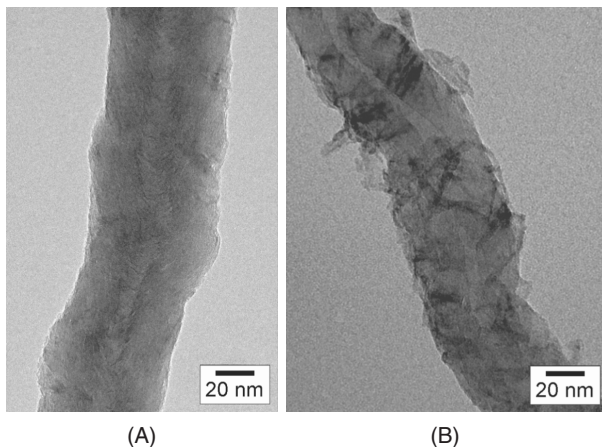


Figure 5.8 Bare carbon nanofiber (A) and one loaded with nickel hydroxide platelets (B).

only process that can explain this phenomenon with CNF–O. Furthermore, with CNF–O the slope of the pH–time curve is much lower than with silica, due to further consumption of hydroxyl ions and related hydrolysis and deposition of nickel species. The smooth nucleation of nickel hydroxide brings about the fact that virtually no overshoot of pH is observed with the carbon support. The interaction of nickel hydroxide platelets with sizes of about $5\text{ nm} \times 30\text{ nm}$ could be inferred from TEM images (Figure 5.8).

After reduction in hydrogen at elevated temperatures, 6- to 8-nm Ni particles were obtained over a wide range of nickel loadings (i.e., 10 to 50 wt%) [46]. In case the carboxylic acid groups were not present on the carbon support, large nickel hydroxide platelets separate from the fibers were observed and poorly dispersed Ni catalysts obtained. For example, phenol-type groups appeared to be insufficient to induce nucleation at the support [45]. The critical role of the (density of) carboxylic acid groups is demonstrated further by a study of the Chen–Holmen group [47, 48]. DP of nickel or copper onto surface-oxidized CNF in their studies led to large metal particles of about 50 nm in both cases. As stated by the authors [47, 48], the difference with the research of Bitter et al. [46] probably involves the time of reflux of the CNF in concentrated nitric acid of 10 minutes versus 2 hours, respectively.

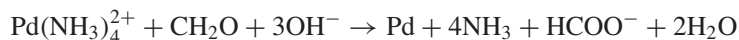
Following extensive research with Ni, one may expect that deposition of Co will be similar. On the contrary, Bezemer et al. [49] have reported that with Co on surface-oxidized CNF, the urea method failed and led to bulk precipitation of needlelike cobalt hydroxycarbonate. For Co, therefore, a different method of DP had to be applied (Section 5.3.3). Successful use of the urea DP method for carbon has also been realized for Ru and for Pt [50]. For Ru, loadings higher than those achieved by ion adsorption have been obtained, whereas with Pt very

similar results for loading and dispersion were achieved. In fact, for platinum, DP could be considered as a gradual ion adsorption process brought about by pH increase due to urea hydrolysis. With noble metals (e.g., Pd, Au, Pt) DP by means of pH increase has been practiced by addition of the metal precursor solution to a suspension of the carbon support in an aqueous solution of, typically, NaOH. Augustine and O'Leary [51] have prepared 1 wt% Pd/MgO with a final Pd dispersion of 40% in this way.

Jin et al. [52] have deposited 5 wt% Pd on activated carbon fibers by alkaline hydrolysis of palladium chloride and obtained metal dispersions of 55 to 77%. Dispersions of 40 to 50% have been reported by Farkas et al. [53], who prepared Pd/C by fast addition of NaOH solution to a suspension of carbon in an aqueous solution of K_2PdCl_4 . More highly loaded Pd and Pt catalysts (10 wt%) have been prepared by dropwise addition of the metal salt solution to the suspension of carbon in Na_2CO_3 solution. In this case [54], a Pt particle size of 10 nm and a Pd particle size of 17 nm were reported. Ion adsorption led to much lower particle sizes. By quick addition of NaOH solution to a suspension of carbon support in $PdCl_2$ solution, Cabiac et al. [55] obtained 5- to 10-nm Pd particles at a loading of about 4 wt%. Clearly, details of support, metal loading, and the method of mixing of reactants all play a vital role in the dispersion and distribution of the metal in the finished catalyst.

5.3.2 Change of Valency

Precipitation can also be brought about by reduction of solvated metal ions to the metal. This method is sometimes referred to as *electroless plating*, but we prefer the term *reduction deposition precipitation* (RDP) for this method. RDP has been explored for the aim of catalysts preparation using oxidic supports by de Jong and Geus [56–58] and by Barbier and co-workers [59–62]. Typically, the support is suspended in a solution of the metal precursor, and a reducing agent such as formaldehyde is added to bring about deposition of the metal as shown for Pd:



By a proper selection of concentrations, temperature, and the support, one can steer the redox reaction to occur exclusively onto the support. Bimetallic catalysts have been prepared advantageously using RDP in which the first metal already present on the support catalyzed the redox reaction to deposit the second metal exclusively onto the first. Barbier and co-workers used hydrogen chemisorption on a noble metal to deposit a nonnoble metal via local chemical reduction [59–62]. With carbon supports, RDP has often been used for deposition of Pd using an organic reductant such as formaldehyde. Typical examples are the work of Hoogenraad et al., Heal and Mkayuala, and Yang et al. [63–65].

Platinum has been deposited onto single-walled nanotubes by reduction of K_2PtCl_4 by ethylene glycol at 393 to 403 K [66]. Gold deposition onto carbon supports has been realized using an aqueous chloride-stabilized gold complex

and formaldehyde as reductant [67–69]. Finally, copper and nickel deposition onto surface-oxidized multiwalled carbon nanotubes sensitized with PdSn has been studied by Ang et al. [70]. Please note that in a number of cases it has been demonstrated that surface oxidation of the carbon support plays an important role in RDP to arrive at selective deposition of the metal onto the support and to realize high dispersions. In a few cases [71,72] it is claimed that the carbon support itself can act as a reducing agent. Metal particles deposited spontaneously from the salt solution on the support without the addition of a reductant. The spontaneous reduction of Pt using highly oriented pyrolytic graphite [71] could be suppressed by an oxidative treatment, using an anodic current, of the surface. The mechanism by which the spontaneous reduction occurs remains unclear.

5.3.3 Ligand Removal

At elevated pH, ligands such ammonia and EDTA can be used to stabilize transition metal ions in water. Removal of these ligands via evaporation or oxidation has been used in the past to bring about deposition onto an oxidic support material [38,39,73,74]. In particular, Lok et al. [73,74] have explored deposition of cobalt onto alumina starting from a cobalt amine complex at elevated pH by removing the ammonia slowly from the solution. Highly loaded and highly dispersed Co/Al₂O₃ active for Fischer–Tropsch synthesis was thus obtained. Bezemer et al. [49] have used the same method to deposit 15 wt% Co onto a CNF support. In Figure 5.9, TEM images of a reduced and passivated sample of Co/CNF are shown that display 8-nm Co particles quite uniformly dispersed over the CNF support.

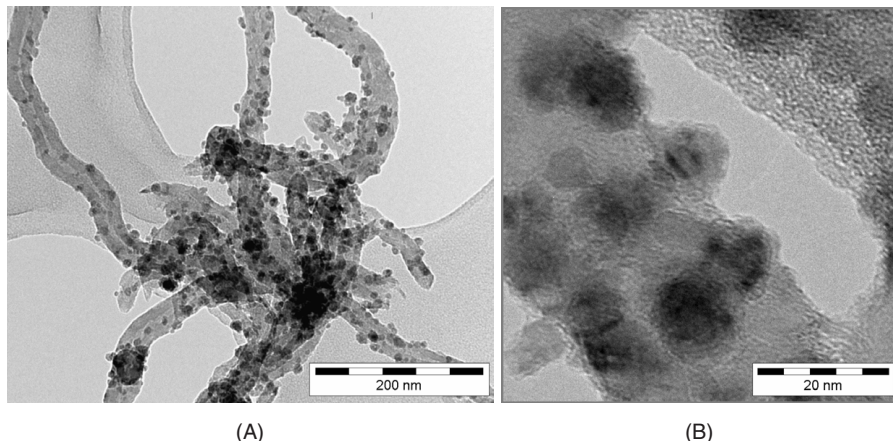


Figure 5.9 TEM images of reduced and passivated Co/CNF at medium (A) and high (B) resolution.

5.4 EMERGING PREPARATION METHODS

Next to the popular adsorption/impregnation and deposition methods, new methods emerged. One of the major drivers, although not the only one, for this is the emerging field of fuel cells. To obtain high charge densities, the electrodes need to contain high amounts of Pt (typically 40 wt% and higher) with a high dispersion. Therefore, we summarize some emerging preparation methods.

Li et al. [75] described the preparation of high-loading Pt/CNT catalyst by two different methods. In the first method, to a slurry of oxidized (HNO_3) CNT, a solution of H_2PtCl_6 was added dropwise. The pH was adjusted to 11, after which the Pt was reduced using formaldehyde at 358 K. This resulted in a catalyst with 10 wt% Pt and a mean particle size of 3.4 nm. Higher dispersions were obtained when the entire procedure was executed in ethylene glycol. The reduction was executed by heating the product mixture to 413 K. In this case, particle loading of 10 wt% was obtained with a mean particle size of 2.6 nm. However, water had a detrimental effect on the particle size; 0% water resulted in particles of 2.0 nm, which increased to 4.5 nm when 70 wt% water was present. The experiment above was performed with 5 wt% water. This method is called *modified polyol synthesis* [76,77]. According to Kim and Park [76], basic groups on the surface of a carbon result in a high level of metal dispersion, while acidic groups result in a low dispersion. Chen et al. [78] developed the polyol method further by performing the drying step by microwave heating. In that way, 20 wt% of spherical Pt particles (3.5 to 4.0 nm) could be prepared (Figure 5.10). The authors claim that this is a fast and energy-efficient way to prepare catalysts and should be applicable to other catalysts that can be prepared by the polyol method.

For direct methanol fuel cells, Pt–Ru bimetallic catalysts seem to be effective. In a number of studies, ultrasonic treatment was claimed to help in obtaining a

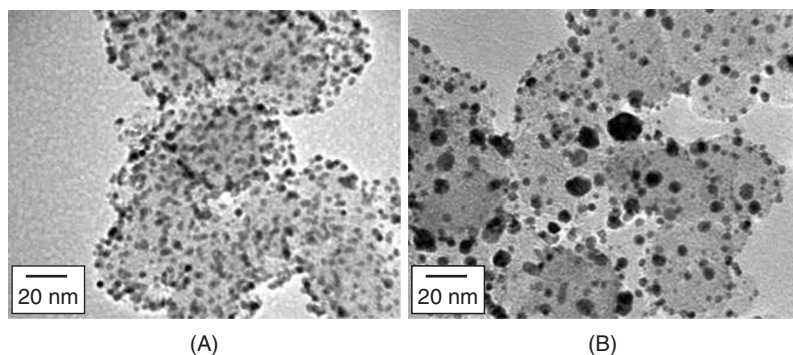


Figure 5.10 TEM images of (A) microwave-synthesized Pt nanoparticles supported on Vulcan carbon XC-72 and (B) commercially available E-TEK Pt/C catalyst (nominal Pt loading 20 wt%). (From ref. 78, with permission.)

high level of metal dispersion. Yang et al. [79] impregnated H_2PtCl_6 and RuCl_3 directly on carbon black. After sonication and drying in different steps, catalysts with 60 wt% total metal loading and 1.5-nm particles were obtained. Nagao et al. [80] compared the preparation of Pt–Ru on carbon black with and without sonication after impregnation. Without sonication, clustered particles of about 5 nm were obtained, while with sonication the particles were not clustered and about 1 to 2 nm. The total metal loading was about 37 wt%.

An elegant way to obtain Pt–Ru mixed metal catalyst was described by Steigerwalt et al. [81], who first prepared an organometallic cluster with one Pt atom and one Ru atom in the cluster. This cluster was impregnated on a carbon nanofiber support, resulting in a metal loading of 42 wt% and a particle size of about 6 nm. In a later publication from the same group [82], a microwave-assisted drying/reduction step was included, resulting in smaller metal particles (2 to 3 nm) with a 1 : 1 Pt–Ru ratio.

Bron et al. [83] used the decomposition of $[\text{Ru}_3(\text{CO})_{12}]$ in the presence of carbon black either refluxing xylene or nonane to prepare Ru-loaded electrode materials (10 wt% turned out to be optimal). In some cases the $[\text{Ru}_3(\text{CO})_{12}]$ -support slurry was added to a solution of elemental selenium in ethanol in order to obtain an Se–Ru-based catalyst. After preparation, small Ru particles, probably containing a Ru core and a Ru–Se shell, of 1 to 2 nm were obtained. After heat treatment at 1173 K, particle sizes increased to 10 to 20 nm; however, some small particles remained.

Chemical vapor deposition on carbon nanofibers/tubes was described by Liang et al. [84]. Oxidized carbon nanofibers were loaded in a fixed-bed reactor, and $[\text{Pd}(\text{allyl})\text{Cp}]$ was sublimed onto the fibers at 353 K. After reduction the final catalyst was obtained. The loading of Pd depended on the number of functional groups introduced by an HNO_3 treatment. Unfunctionalized carbon nanofibers did not show any Pd uptake. Pt loadings of 2 to 4 wt% were typically obtained with Pd particle sizes of 2 to 4 nm.

5.5 CONCLUSIONS

Fundamental understanding of catalyst synthesis is emerging. For carbon-based supports, as for oxidic supports, adsorption and impregnation are the techniques used most often, due to their practical simplicity. However, the fundamental processes at hand during impregnation/adsorption are still complex and not fully understood. Oxygen-containing groups play a crucial role in wetting of carbon supports: however, whether they also function as anchoring sites for metal particles is still a matter of debate. Moreover, it is in many cases difficult to draw unambiguous conclusions since the introduction or removal of oxygen groups can also lead to a difference in the pore structure of the carbon support. The latter might also have an influence on the particle sizes obtained. Micropores in the carbon support might be beneficial for metal dispersion. However, during catalysts these micropores might give rise to diffusion limitations.

Deposition precipitation (DP), developed originally for oxidic supports, has also turned out to be applicable for carbon-based catalysts. The introduction of carboxylic acid groups is crucial here to obtain a high metal dispersion. Apparently, the interaction between metal precursors and oxygen groups is strong enough to induce nucleation during DP and to obtain a well-dispersed catalyst. When bimetallic catalysts are desired, reductive deposition precipitation is very effective. As an alternative for deposition precipitation in which a precipitant (e.g., base) is added to a slurry of metal precursor and support, the selective removal of ligands (e.g., amine ligands) was shown to be very successful for the preparation of Co-based catalysts. Next to these methods the use of methods inspired by colloidal chemistry is popular in the field of fuel cells. These methods result in general in high metal loadings and high dispersions; however, the thermal stability of these catalysts might be too limited to be applicable for high-temperature catalysis.

REFERENCES

- [1] J.P. Brunelle, *Pure Appl. Chem.* 50 (1978) 1211.
- [2] X. Hao, W.A. Spieker, J.R. Regalbuto, *J. Colloid Interface Sci.* 267 (2003) 259.
- [3] J.R. Regalbuto, M. Schrier, X. Hao, et al., *Stud. Surf. Sci. Catal.* 143 (2002) 45.
- [4] W.A. Spieker, J.R. Regalbuto, *Chem. Eng. Sci.* 56 (2001) 3491.
- [5] X. Hao, L. Quach, J. Korah, W.A. Spieker, J.R. Regalbuto, *J. Mol. Catal. A* 219 (2004) 97.
- [6] X. Hao, Ph.D. dissertation, University of Illinois, 2004.
- [7] J.-F Lambert, M. Che, *J. Mol. Catal. A* 162 (2000) 5.
- [8] S.R. Miguel, O.A. Scelza, M.C. Román-Martínez, C. Salinas-Martínez de Lecea, D. Cazorla-Amorós, A. Linares-Solano, *Appl. Catal. A* 170 (1998) 93.
- [9] H.E. van Dam, H. van Bekkum, *J. Catal.* 131 (1991) 335.
- [10] F. Coloma, A. Sepúlveda-Escribano, J.L.G. Fierro, F. Rodríguez-Reinoso, *Langmuir* 10 (1994) 750.
- [11] R.-L Jia, C.-Y. Wang, S.-M Wang, *J. Mater. Sci.* 41 (2006) 6881.
- [12] D.J. Suh, T.-J Park, S.-K Ihm, *Carbon* 31 (1993) 427.
- [13] M. Gurrath, T. Kuretzky, H.P. Boehm, L.B. Okhlopkova, A.S. Lisitsyn, V.A. Likholobov, *Carbon* 38 (2000) 1241.
- [14] M.A. Fraga, E. Jordão, M.J. Mendes, M.M.A. Freitas, J.L. Faria, J.L. Figueiredo, *J. Catal.* 209 (2002) 355.
- [15] C. Prado-Burguete, A. Linares-Solano, , F. Rodríguez-Reinoso C. Salinas-Martínez de Lecea *J. Catal.* 115 (1989) 98.
- [16] E. Aksoylu, M. Madalena, A. Freitas, M. Fernando R. Pereira, J.L. Figueiredo, *Carbon* 39 (2001) 175.
- [17] M.L. Toebe, J.A. Van Dillen K.P. de Jong *J. Mol. Catal. A* 173 (2001) 75.
- [18] H. Zhu, W. Han, H. Liu, *Catal. Lett.* 115 (2007) 13.
- [19] W. Han, H. Liu, H. Zhu, *Catal. Commun.* 8 (2007) 351.

- [20] L. Chen, D. Ma, X. Li, X. Bao, *Catal. Lett.* 111 (2006) 133.
- [21] M.L. Toebees, M.K. van der Lee, L.M. Tang, M.H. Huis in 't Veld, J.H. Bitter, A.J. van Dillen, K.P. de Jong, *J. Phys. Chem. B* 108 (2004) 1161.
- [22] Sepúlveda-Escribano, F. Coloma, F. Rodríguez-Reinoso, *Appl. Catal. A* 173 (1998) 247.
- [23] F. Coloma, A. Sepúlveda-Escribano J.L.G. Fierro, F. Rodríguez-Reinoso *Appl. Catal. A* 150 (1997) 165.
- [24] J.H. Bitter, in D. Yu. Murzin, Ed., *Nanocatalysis*, Research Signpost, Kerala, India, 2006, p. 99.
- [25] J.H. Bitter, M.K. van der Lee, A.G.T. Slotboom, A.J. van Dillen, K.P. deJong *Catal. Lett.* 89 (2003) 139.
- [26] V. López-Ramón C. Moreno-Castilla, J. Rivera-Utrilla, L.R. Radovic, *Carbon* 41 (2002) 2009.
- [27] A.M. Fuente, G. Pulgar, F. González C. Pesquera, C. Blanco, *Appl. Catal. A* 208 (2001) 35.
- [28] P.V. Samant, C.M. Rangel, M.H. Romero, J.B. Fernandes, J.L. Figueiredo, *J. Power Sources* 151 (2005) 79.
- [29] C. Prado-Burguete, A. Linares-Solano, F. Rodríguez-Reinoso C. Salinas-Martínez de Lecea *J. Catal.* 128 (1991) 397.
- [30] L.B. Okhlopkova, A.S. Lisitsyn, V.A. Likholobov, M. Gurrath, H.P. Boehm, *Appl. Catal. A* 204 (2000) 229.
- [31] P.M. Ajayan, S. Iijima, *Nature* 361 (1993) 333.
- [32] P.M. Ajayan, O. Stephan, P. Redlich, C. Colliex, *Nature* 375 (1995) 564.
- [33] P.M. Ajayan, C. Colliex, J.M. Lambert, P. Bernier, L. Barbedette, M. Tence, O. Stephan, *Phys. Rev. Lett.* 72 (1994) 1722.
- [34] R.M. Lago, S.C. Tsang, K.L. Lu, Y.K. Chen, M.L.H. Green, *J. Chem. Soc. Chem. Commun.* 13 (1995) 1355.
- [35] J.-P. Tessonier, L. Pesant, C. Pham-Huu, G. Ehret, M.J. Ledoux, *Stud. Surf. Sci. Catal.* 143 (2002) 697.
- [36] F. Winter, G.L. Bezemer, C. van derSpek J.D. Meeldijk, A.J van Dillen J.W. Geus, K.P. deJong *Carbon* 43 (2005) 327.
- [37] K.P. deJong, *Stud. Surf. Sci. Catal.* 63 (1991) 19.
- [38] L.A.M. Hermans, J.W. Geus, *Stud. Surf. Sci. Catal.* 3 (1979) 113.
- [39] J.W. Geus, A.J. van Dillen, in G. Ert et al., Eds., *Preparation of Solid Catalysts*, Wiley-VCH, Weinheim, Germany, 1999, pp. 460–487.
- [40] P. Burattin, M. Che, C. Louis, *J. Phys. Chem. B* 101 (1997) 7060.
- [41] P. Burattin, M. Che, C. Louis, *J. Phys. Chem. B* 102 (1998) 2722.
- [42] P. Burattin, M. Che, C. Louis, *J. Phys. Chem. B* 103 (1999) 6171.
- [43] T. Wigmans, J. van Doom J.A. Moulijn, *Surf. Sci.* 135 (1983) 532.
- [44] F.F. Prinsloo, D. Hauman, R. Slabbert, in *Proceedings of Carbon'01, International Conference on Carbon*, Lexington, KY, 2001, p. 940.
- [45] M.K. van der Lee, A.J. van Dillen, J.H. Bitter, K.P. de Jong *J. Am. Chem. Soc.* 127 (2005) 13573.
- [46] J.H. Bitter, M.K. van der Lee, A.G.T. Slotboom, A.J. van Dillen, K.P. de Jong *Catal. Lett.* 89 (2003) 139.

- [47] E. Ochoa-Fernández D. Chen Z. Yu, B. Tøtdal M. Rønning A. Holmen, *Catal. Today* 102–103 (2005) 45.
- [48] Kvande, D. Chen, M. Rønning, H.J. Venvik, A. Holmen, *Catal. Today* 100 (2005) 391.
- [49] G.L. Bezemer, P.B. Radstake, V. Koot, A.J. van Dillen, J.W. Geus, K.P. de Jong *J. Catal.* 237 (2006) 291.
- [50] M.L. Toebe, M.K. van der Lee, L.M. Tang, M.H. Huis in 't Veld J.H. Bitter, A.J. van Dillen, K.P. deJong *J. Phys. Chem. B* 108 (2004) 11611.
- [51] R.L. Augustine, S.T. O'Leary *J. Mol. Catal. A* 95 (1995) 277.
- [52] H. Jin, S.-E. Park, J.M. Lee, S.K. Ryu, *Carbon* 34 (1996) 429.
- [53] G. Farkas, L. Hegedus, A. Tungler, T. Mathe, J.L. Figueiredo, M. Freitas, *J. Mol. Catal. A* 153 (2000) 215.
- [54] S.H. Jhung, J.-H. Lee, J.-M. Lee, J.H. Lee, D.-Y. Hong, M.W. Kim, J.-S. Chang, *Bull. Korean Chem. Soc.* 26 (2005) 563.
- [55] A. Cabiac, G. Delahay, R. Durand, P. Trens, D. Plée, A. Medeville, B. Coq, *Appl. Catal. A* 318 (2007) 17.
- [56] K.P. de Jong J.W. Geus, *Appl. Catal.* 4 (1982) 41.
- [57] K.P. de Jong J.W. Geus, *Stud. Surf. Sci. Catal.* 16 (1983) 111.
- [58] K.P. de Jong *Curr. Opin. Solid State Mater. Sci.*, 4 (1999) 55.
- [59] R. Bachir, E. Lafitte, P. Marécot B. Didillon, J. Barbier, *J. Chim. Phys.* 94 (1997) 1906.
- [60] R. Bachir, P. Marécot B. Didillon, J. Barbier, *Appl. Catal. A* 164 (1997) 313.
- [61] C. Micheaud, P. Marécot M. Guérin J. Barbier, *J. Chim. Phys.* 94 (1997) 1897.
- [62] G. Corro, P. Marécot J. Barbier, *Stud. Surf. Sci. Catal.* 111 (1997) 359.
- [63] M.S. Hoogenraad, R.A.G.M.M. van Leeuwarden, G.J.B. van Breda Vriesman, A. Broersma, A.J. van Dillen, J.W. Geus, *Stud. Surf. Sci. Catal.* 91 (1995) 263.
- [64] G.R. Heal, L.L. Mkayula, *Carbon* 26 (1988) 815.
- [65] Y. Yang, Y. Zhou, C. Cha, W.M. Carroll, *Electrochim. Acta* 38 (1993) 2333.
- [66] V. Lordi, N. Yao, J. Wei, *Chem. Mater.* 13 (2001) 733.
- [67] S. Hermans, M. Devillers, *Catal. Lett.* 99 (2005) 55.
- [68] M.D. Hughes, Y.-J. Xu, P. Jenkins, P. McMorn, P. Landon, D. I. Enache, A.F. Carley, G.A. Attard, G.J. Hutchings, F. King, E.H. Stitt, P. Johnston, K. Griffin, C.J. Kiely, *Nature* 437 (2005) 1132.
- [69] G.J. Hutchings, S. Carrettin, P. Landon, J.K. Edwards, D. Enache, D.W. Knight, Y.-J. Xu, A.F. Carley, *Top. Catal.* 38 (2006) 223.
- [70] L.M. Ang, T.S.A. Hor, G.Q. Xu, C.H. Tung, S.P. Zhao, J.L.S. Wang, *Carbon* 38 (2000) 363.
- [71] P. Shen, N. Chi, K.-Y. Chan, D.L. Phillips, *Appl. Surf. Sci.* 172 (2001) 159.
- [72] H.C. Choi, M. Shim, S. Bangsaruntip, H. Dai, *J. Am. Chem. Soc.* 124 (2002) 9058.
- [73] R.L.C. Bonne, C.M. Lok, WO patent 9,604,072, 1996.
- [74] C.M. Lok, *Stud. Surf. Sci. Catal.* 147 (2004) 283.
- [75] W. Li, C. Liang, W. Zhou, J. Qiu, Z. Zhou, G. Sun, Q. Xin, *J. Phys. Chem. B* 107 (2003) 6292.
- [76] S. Kim, S.-J. Park, *Electrochim. Acta* 52 (2007) 3013.

176 PREPARATION OF CARBON-SUPPORTED METAL CATALYSTS

- [77] Z. Zhou, S. Wang, W. Zhou, G. Wang, L. Jiang, W. Li, S. Song, J. Liu, G. Sun, Q. Xin, *Chem. Commun.* 3 (2003) 394.
- [78] W.X. Chen, J.Y. Lee, Z. Liu, *Chem. Commun.* 21 (2002) 2588.
- [79] B. Yang, Q. Lu, Y. Wang, L. Zhuang, J. Lu, P. Liu, *Chem. Mater.* 15 (2003) 3552.
- [80] D. Nagao, Y. Shimazaki, S. Saeki, Y. Kobayashi, M. Konno, *Colloids Surf. A* 302 (2007) 623.
- [81] E.S. Steigerwalt, G.A. Deluga, D.E. Cliffel, C.M. Lukehart, *J. Phys. Chem. B* 105 (2001) 8097.
- [82] D.L. Boxall, G.A. Geluga, E.A. Kenik, W.D. King, C.M. Lukehart, *Chem. Mater.* 13 (2001) 891.
- [83] M. Bron, P. Bogdanoff, S. Fiechter, M. Hilgendorff, J. Radnik, I. Dorbandt, H. Schulenburg, H. Tributsch, *J. Electroanal. Chem.* 517 (2001) 86.
- [84] C. Liang, W. Xia, H. Soltani-Ahmadi, R.A. Fischer, M. Muhler, *Chem. Commun.* 2 (2005) 282.

6 Carbon as Catalyst

JOSÉ LUÍS FIGUEIREDO and MANUEL FERNANDO R. PEREIRA

6.1 INTRODUCTION

In addition to its use as a catalyst support (see Chapter 4), carbon can find applications as a catalyst on its own. Activated carbon catalysts have long been used in the production of phosgene [1,2] and sulfur halides [3]. The corresponding technologies seem to be well established, although the mechanistic details are not known in detail [4]. The only recent publication on this subject concerns the reduction of the by-product carbon tetrachloride using Sibunit (a carbon material developed at the Boreskov Institute of Catalysis) instead of the coconut shell-based activated carbon catalyst [5].

Another important industrial application of carbon catalysts is in flue gas cleaning. The Bergbau-Forschung (now DMT) and Sumitomo processes for simultaneous SO₂/NO_x removal with active coke were developed in the 1980s, and plants have been in operation in Japan and Germany. In these processes, the active carbon acts simultaneously as an adsorbent and as a catalyst in the temperature range 383 to 443 K (i.e., under conditions where the material is stable in the presence of oxygen) [6–11]. Other applications of carbon as a catalyst, in both the liquid and gas phases, have been reported, as indicated in Table 6.1. The literature on this topic is growing quite rapidly; therefore, there is a need to update earlier reviews [7,12–19].

The performance of a catalyst depends on the availability of suitable active sites, capable of chemisorbing the reactants and forming surface intermediates of adequate strength. Oxygen and nitrogen functional groups, which can be incorporated into the carbon materials by a variety of methods, play an important role in this context. The pertinent literature is discussed in this chapter, with particular emphasis on cases in which the active sites have been properly identified and useful activity correlations established.

Table 6.1 Main Reactions Catalyzed by Carbons

Reaction or Process	References
Oxidative dehydrogenation of hydrocarbons	43, 45–51, 53–65, 67–74, 77, 217–223
Dehydration and dehydrogenation of alcohols	77–84, 224, 225
NO_x reduction	6–10, 85, 92, 109, 110, 112–130, 226–231
NO oxidation	131–134
SO_x oxidation	6, 10, 85–108, 232–236
H_2S oxidation	135–149, 237–239
Hydrogen peroxide reactions	150–163
Ozonation	164–171, 173–184, 186–197, 240–244
Catalytic wet air oxidation	198–210, 245–249

6.2 FACTORS AFFECTING THE PERFORMANCE OF A CARBON CATALYST

In heterogeneous catalysis, the reaction occurs at the interface between the catalyst and the gas or liquid phase containing the reactants. Therefore, the activity is expected to increase with the specific surface area of the catalyst. However, activity correlations based on this parameter alone are not adequate. Indeed, the activity of a catalyst is determined by the nature, concentration, and accessibility of its active sites, and all these factors must be taken into consideration. Thus, it is no surprise to find that the most useful correlations are those that have been established by using a specific methodology: namely, when a series of carbon materials of the same nature and origin are produced with very similar textural properties and different amounts of surface functional groups. This approach has become possible because various methods are now available for the identification and quantification of the various types of oxygen and nitrogen functional groups on the surface of carbon materials, as described in Chapter 2.

6.2.1 Nature of the Active Sites

Most of the carbon materials used in catalysis have the graphitic structure (e.g., activated carbons, carbon blacks, activated carbon fibers, carbon aerogels, xerogels). In the absence of defects, the basal planes are not very reactive; we may therefore expect to find active sites essentially at the edges of the graphene layers, where the unsaturated carbon atoms may chemisorb oxygen, water, or compounds such as ammonia, originating on surface groups such as those represented schematically in Figures 2.1 and 2.2. These groups can act as active sites in various reactions, as we will discuss.

Oxygenated functions have been studied most extensively, since they are formed spontaneously by exposure of the carbon material to the atmosphere. The concentration of these groups can be increased further by oxidative treatments, in

either the gas or liquid phase. Thermal treatments at increasing temperatures can then be used to remove selectively some of the groups formed [20–27]. Acidic groups include carboxylic acids and anhydrides, lactones or lactols, and phenols, while carbonyl and ether are neutral or may form basic structures the nature of which is still open to debate, such as quinone, chromene, and pyrone groups. In addition, the π -electron system of the basal planes contributes to the carbon basicity [28–32].

Nitrogen functions are found when a nitrogen-containing precursor is used or as a result of reaction with a nitrogen-containing reagent [31], and were reviewed by Pels et al., Jansen and van Bekkum, and Stanczyk et al. [23,33–35]. A more detailed discussion of this subject is provided in Chapter 7. Pairs of carbonyl groups at the edges of the carbon layers connected by a resonance structure behave as quinones; similarly, pairs of hydroxyl groups behave as hydroquinones [36]. The quinone–hydroquinone system can be involved in redox mechanisms. So, in addition to acid–base catalysis, carbon materials can promote oxidations, such as the oxidative dehydrogenation of hydrocarbons, which we discuss in detail below.

6.2.2 Concentration of the Active Sites

The concentration of active sites depends to a large extent on the microcrystalline structure of the carbon material. Small crystallites can expose more edges; therefore, more surface groups can be formed, while the role of the basal planes and the π electrons will become more important with large crystallites. Thus, the orientation of the graphene layers and the ratio between prismatic and basal plane areas may affect the catalytic performance, and such effects have indeed been reported in the case of carbon nanofibers (see Section 6.3.1).

The concentration of the relevant surface functional groups can be determined by the methods described in Chapter 2. Temperature-programmed desorption (TPD) seems to be the best method to determine the concentration of oxygen groups, especially in the case of porous carbons [21,37–41], and x-ray photoelectron spectroscopy (XPS) is the method used to determine the concentration of nitrogen functions (see Chapter 7).

6.2.3 Accessibility of the Active Sites

High surface areas are normally obtained by using porous materials, and the pore sizes may condition the accessibility of the reactants to the active sites, especially in the case of microporous materials such as activated carbons. Pore diffusion limitations become more important as the pore sizes decrease; in addition, the smaller pores may be more easily blocked (e.g., by coke deposition). Therefore, deactivation and diffusion phenomena will in general affect more strongly the performance of microporous carbons. As a result, there has been a drive to develop mesoporous carbon catalysts (such as aerogels, xerogels, and templated carbons) for some applications, especially in the liquid phase.

Nevertheless, the presence of small micropores (ultra-micropores, i.e., pores smaller than 0.7 nm) may be useful in some cases, due to their ability to retain reaction products in the liquid state; such an example is discussed in Section 6.3.3.

6.3 REACTIONS CATALYZED BY CARBONS

One of the earlier attempts at finding a correlation between the catalytic activity and the chemical properties of the carbon catalyst is that of Manassen and Wallach [42]. They found that polyacrylonitrile pyrolyzed (PPAN) in the presence of oxygen was a strong hydrogen acceptor, being capable of converting 2-propanol into acetone and cyclohexanol into cyclohexanone in the vapor phase at 523 K. In the course of these reactions, PPAN became hydrogenated and lost activity but could be reactivated by air oxidation at 413 K. Similarly, cyclohexene was converted into benzene at 623 K. In contrast to other carbon materials (charcoal, graphite), neither cyclohexane nor hydrogen were formed. Again, the activity could be restored by air treatment. When the process was carried out in the presence of air, PPAN acted as a true dehydrogenation catalyst. It was also capable of promoting double-bond shifts and *cis-trans* isomerizations in olefinic systems. This behavior was explained in terms of the proposed structure of PPAN, consisting of condensed pyridine rings: During dehydrogenation, the condensed aromatic structure is transformed into a hydroaromatic structure, which reverts to the original state upon treatment with oxygen. The hydrogen is retained chemically bound until it is removed by oxygen during the regeneration step. On the other hand, the acidic sites of PPAN were considered responsible for its activity in the dehydration of alcohols [42].

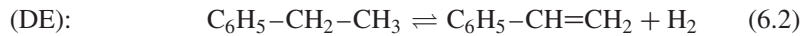
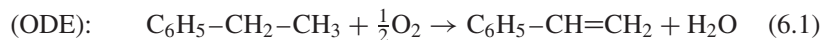
The oxydehydrogenation of cyclohexanol over carbon catalysts provides a fine example of the strong influence of the surface chemistry on product selectivity [43]. Carbon catalysts with surfaces of different chemical nature were investigated. The main products were cyclohexene, cyclohexanone, benzene, and phenol. Dehydration to cyclohexene was found to occur preferentially on the carboxylic acid groups (carbons treated with HNO₃), while the best selectivities to cyclohexanone were obtained on catalysts with high contents in phenol groups (carbons treated with H₂O₂ or oxygen). Carbon treated with N₂O showed high selectivity to phenol, which was explained by the participation of quinone and nitro groups in the oxydehydrogenation mechanism. Unfortunately, the authors were not able to determine precisely the amounts of the different surface groups; thus, no quantitative correlations were established.

Analysis of the pertinent literature shows that the most relevant conclusions regarding the role of surface chemistry in carbon catalysis have been derived following a common methodology whereby a series of catalysts are prepared from the same carbon material by suitable thermal or chemical treatments while keeping the textural properties essentially unchanged. It is then possible to correlate the catalytic properties with the surface chemistry of the carbons. This

methodology has been used with success in a number of cases, as described in the following sections.

6.3.1 Oxidative Dehydrogenation

The oxidative dehydrogenation of ethylbenzene (ODE) is an alternative route to styrene, which is currently produced by dehydrogenation (DE):



The main advantage of the ODE process is that the reaction is complete (therefore, conversions are not limited by equilibrium) and can be carried out at lower temperatures; however, selective catalysts are required to minimize the formation of unwanted carbon oxides [44]. Among others, acid catalysts (such as alumina, zeolites, and metal phosphates) were tested successfully in ODE. One of the peculiar features observed with such systems was the formation of a coke layer, which was found to be the real catalytic surface [45–50]. These results suggested that carbon materials could be used as catalysts for the reaction.

Iwasawa et al. [51] showed that polynatoquinone, a carbonated material, was active in the ODE at low temperatures. Good results were also obtained with PPAN [52]. Alkhazov et al. [53] were the first authors to test activated carbon. They observed that the ODE reaction could be performed at temperatures lower (623 to 673 K) than those normally used with oxide catalysts (723 to 823 K). Several reports on the use of activated carbon as catalyst for ODE appeared subsequently, but the results were interpreted mainly in terms of the textural properties of the catalysts (surface area/pore sizes).

The use of carbon molecular sieves (CMSs) as catalysts for the oxidative dehydrogenation of alkyl aromatics was described in a patent by Lee [54]. Higher conversions and selectivities were reported with molecular sieve carbons with pore sizes in the range 0.5 to 0.7 nm (Carbosieve G from Supelco, and MSC-V from Calgon) than with activated carbon. This work may have triggered subsequent interest for CMS in ODE.

Grunewald and Drago [55] tested various carbon materials in ODE at 623 K, including PPAN, a carbon molecular sieve from Anderson Development Company (AX21, with a nominal surface area higher than 3000 m²/g), and an activated carbon of 800 m²/g. From the results with samples of PPAN of different specific surface areas (between 8 and 50 m²/g), a relationship between surface area and activity was established. However, when activated carbon was used as a catalyst, a proportional increase in styrene production was not observed. An outstanding activity was reported with the carbon molecular sieve AX21 (80% conversion, 90% selectivity). The authors speculated that in addition to the enormous surface area of this material, other factors might play a role, such as surface structure and adsorption capacity.

In a subsequent paper [56], various carbon materials, differing in their texture, were studied. Most of the materials tested were found to be more active than

AX21, a result that quenched the enthusiasm of the earlier report. Coke formation from styrene polymerization was recognized as one of the shortcomings of the reaction, leading to micropore plugging. No direct relationship could be found between the activity and the surface area of the carbon materials, and it was observed that the most active catalysts were those with more mesopores and higher external surface area.

Guerrero-Ruiz and Rodríguez-Ramos [57] used graphite (as a model non-porous carbon material) and activated carbons. Two types of graphite were tested, one with 300 and another with 200 m²/g, but similar activities were obtained. Therefore, it was not possible to correlate the activity with the specific surface area. They also used two activated carbons with the same surface area (about 1000 m²/g) but with different textures, one mainly microporous and the other with larger pores. The activity was high in the beginning, but it decreased with time onstream for the material with smaller pores, while the activity increased slightly at the beginning of the reaction, stabilizing thereafter, in the sample with wider pores. These results were explained in terms of coke deposition, which quickly blocked the small pores. The authors concluded that an adjusted texture, probably with mesopores, could be an important parameter for the catalytic activity of the activated carbons. They also suggested that the selectivity could be related directly to the capacity of the carbon to form surface groups with labile hydrogen.

Similar conclusions concerning the textural requirements of the catalyst were reached by Kane et al. [58], who attributed the differences observed with a range of CMS to the effects of the pore structures on the coupled reaction and diffusion phenomena. They suggested that the pore structure should include substantial amounts of transport pores (meso- and macropores). Pereira et al. [59] used activated carbon fibers obtained from different precursors as catalysts in the ODE. They observed that fibers with an average micropore width lower than 1.2 nm were not good catalysts for this reaction. These reports show that materials with larger pores, consisting mainly of mesopores and macropores, show better performances in the ODE, the smaller micropores quickly being blocked by carbon deposits.

A systematic study of the textural effects was published more recently [60]. Starting with the same material, a Norit-activated carbon, two types of modification were carried out: (1) the catalyst pores were enlarged by gasification; and (2) the pores were narrowed by coke deposition. All the materials were subsequently treated under an inert atmosphere at 1173 K to remove surface functional groups. It was additionally confirmed that all the catalysts exhibited similar amounts of surface groups after reaction. Therefore, the kinetic results obtained could be correlated only with the textural properties of the activated carbons. The following conclusions were reached:

- No direct proportionality was observed between the surface area and activity in the ODE reaction (as shown in Figure 6.1).

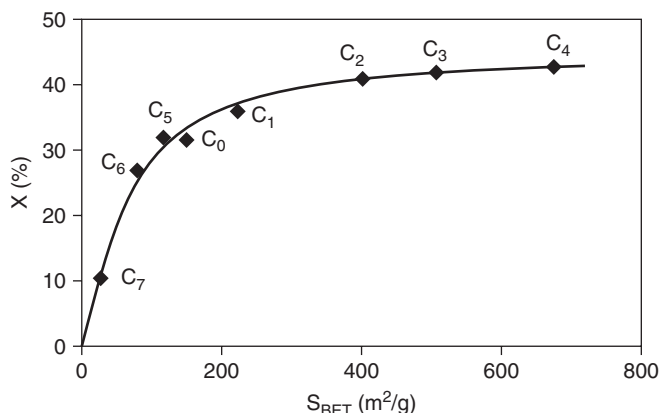


Figure 6.1 Conversion of ethylbenzene versus S_{BET} (measured after reaction). (From ref. 60, with permission.)

- The pores of very small dimensions were quickly blocked, due to coke deposition during the process. Therefore, a wide pore structure is needed.
- Narrowing the pore sizes of the original activated carbons by coke deposition led to lower catalytic activity in the ODE reaction.
- The textural effects were found to be important up to an average pore width of 1.2 nm (sample C_0 in Figure 6.1); for larger pores sizes, the surface chemistry controls the catalyst performance.

Despite apparently promising results, the long-term stability of the catalyst is poor, since the ODE occurs in the presence of oxygen at relatively high temperatures, which affects the physicochemical properties of the activated carbon; in addition, coke is always formed on the catalysts [61].

Systematic studies on the role of surface chemistry in the ODE were reported by Pereira et al. [59,61–63]. In particular, the results obtained support the view that carbonyl and quinone groups on the surface are the active sites for this reaction, in agreement with earlier proposals [51,64].

Starting with the same material (a Norit ROX 0.8 activated carbon), different treatments were used to modify the properties of the carbon catalyst. First, the activated carbon was oxidized with different reactants in either the gas or the liquid phase. The gas-phase treatments proved to be more effective than the liquid-phase oxidations, and the higher activities of the former were explained in terms of the amount of carbonyl or quinone groups on the surface of the catalysts, together with higher surface areas.

Then the performances of the activated carbons oxidized with air to different extents were compared. It was observed that the activity increased with the degree

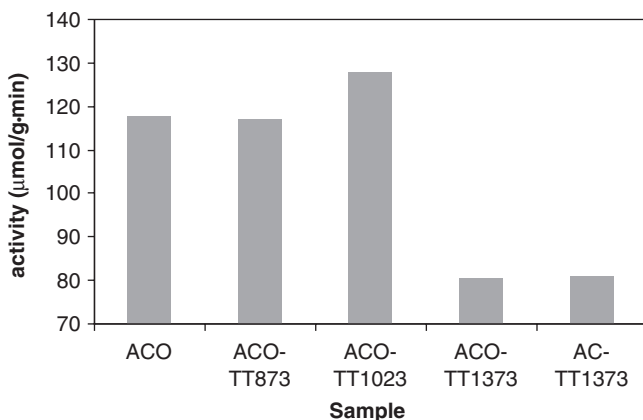


Figure 6.2 Activity in the ODH of ethylbenzene at 623 K obtained on catalysts with different thermal treatments. AC, original activated carbon; ACO, AC oxidized with 5% O₂; ACO-TTX, ACO after thermal treatment at XK. (Adapted from ref. 62.)

of oxidation, while the selectivity to styrene remained approximately constant. The differences were higher at the initial stages of the reaction and became more attenuated as the reaction proceeded, due to coke deposition.

Finally, thermal treatments at increasing temperatures were applied to an oxidized sample in order to remove some of the functional groups selectively while keeping the textural properties unchanged. The performances of the resulting catalysts are shown in Figure 6.2. It was shown that the carbonyl and quinone groups were stable at 1023 K but decomposed at 1373 K. Thus, these experiments confirm that the carbonyl and quinone groups are indeed the active sites for the reaction, since the activity was not changed significantly by thermal treatments up to 1023 K, and dropped abruptly after treatment at 1373 K.

A deconvolution procedure of the TPD spectra [21] was used to estimate the amount of the carbonyl and quinone surface groups of the different oxidized catalysts, and a linear correlation with the catalytic activity for ODE was obtained [62]:

$$a = 3.87 \times 10^{-4}[Q] + 0.71$$

where the activity a is in $\mu\text{mol/g}\cdot\text{s}$ and $[Q]$ is the concentration of carbonyl and quinone groups ($\mu\text{mol/g}$). This correlation is not a straight line through the origin, as active sites are generated on the carbon surface by oxygen present in the reacting mixture.

The experimental results were well described by a kinetic model based on a redox mechanism of the Mars–van Krevelen type, where the quinone surface groups are reduced to hydroquinone by adsorbed ethylbenzene, and reoxidized back to quinone by oxygen [46,63,64], as shown in Figure 6.3. A recent

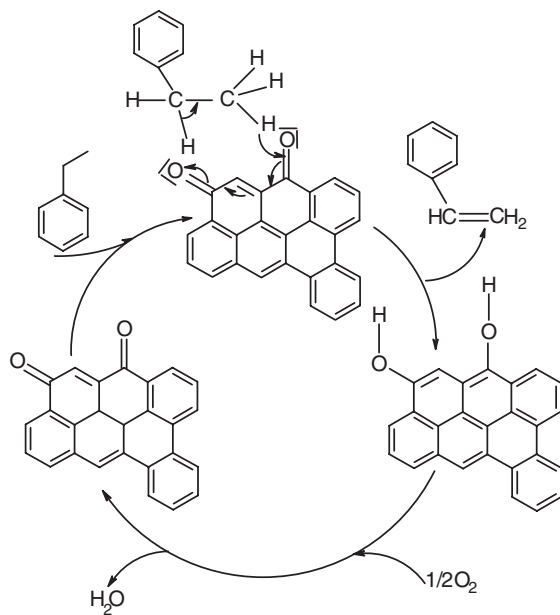


Figure 6.3 Mechanism proposed for the oxidative dehydrogenation of ethylbenzene. (Adapted from ref. 46.)

investigation by quasi-*in situ* XPS confirms that indeed the carbonyl–quinone and hydroxyl groups are involved in this reaction [65].

Recently, the remarkable properties of carbon nanotubes (CNTs) and related structures, such as carbon nanofibers (CNFs) and onionlike carbons, have attracted an increasing interest from the catalysis community [66]. Although these materials are most often used as supports for active phases, some applications as catalysts have been reported, the oxidative dehydrogenation of ethylbenzene to styrene being the most frequently cited example [67–73]. These reports basically confirm the mechanism proposed previously, based on a redox cycle involving the quinone surface groups.

Catalytic tests with CNFs at 673 K revealed that the orientation of the graphene layers has a significant effect on the activity and selectivity, fishbone CNFs exhibiting the best performances. Another parameter that was found to have an effect on the selectivity was the ratio between prismatic and basal plane areas [73]. Nevertheless, the good performances that some of these carbon nanomaterials are claimed to offer must be put into perspective. Indeed, most of the results have been obtained at temperatures in the range 793 to 823 K, and the performances of these new catalysts compared with those of graphites and carbon blacks. However, activated carbons give high styrene yields at 623 K [62], a temperature at which graphite and CNTs show no significant activity. In a recent study, Pereira et al. [74] compared the performance of CNTs with those of graphite and

activated carbon (AC) in the ODE at 723 K. AC gave the highest conversion and selectivity to styrene. Coke deposition occurred on the AC and was negligible on graphite and CNTs. If the specific activity is defined per initial surface area (BET), then CNTs are more active than the AC and graphite samples. This is not a fair comparison, however, since most of the surface area of the AC lies in the micropores, which are not fully accessible to the reactants and which additionally become blocked by coke deposits. When the activity is normalized by the surface area measured at the end of the reaction, the AC still shows the best performance. The main advantage of CNTs over ACs is their higher stability toward oxidation. This is an interesting property, especially if the CNTs are to be used as catalysts or supports for oxidation processes in the liquid phase. However, it is hardly conceivable that these materials will become an alternative to the existing catalysts used for the industrial production of styrene, which give conversions of 60 to 75% and selectivities of 85 to 95% in the temperature range 813 to 923 K [4].

The oxidative dehydrogenation of other substrates has also been studied, such as propane on CNFs [75] and isobutene over ACs [76]. These studies confirm the above-mentioned mechanism involving the quinone–hydroquinone cycle.

6.3.2 Dehydration of Alcohols

The conversion of alcohols on carbon catalysts has been studied most extensively [77–84]. In general, both dehydration and dehydrogenation products are formed simultaneously. With secondary alcohols, the dehydration activity has been found to result from the presence of carboxyl groups, while dehydrogenation depends on the simultaneous presence of Lewis acid and basic sites [80], as shown in Figures 6.4 and 6.5.

By treating the activated carbon catalyst with nitric acid, both dehydration and dehydrogenation were enhanced; however, dehydration was found to occur only on the outer surface, whereas dehydrogenation could also take place within the pores. It was found that there is an optimum concentration of acid groups above which the activity decreases [80]. In a more recent study with carbon catalysts oxidized with nitric acid and subsequently heat treated at different temperatures in the range 423 to 573 K, it has been shown that dehydration is controlled not only by the number and strength of the acid groups, but also by their accessibility [78].

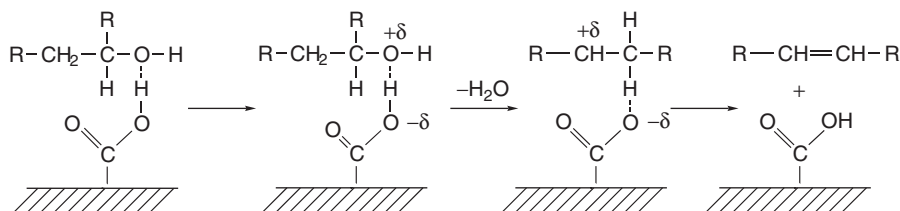


Figure 6.4 Dehydratation mechanism of alcohols. (From ref. 78, with permission.)

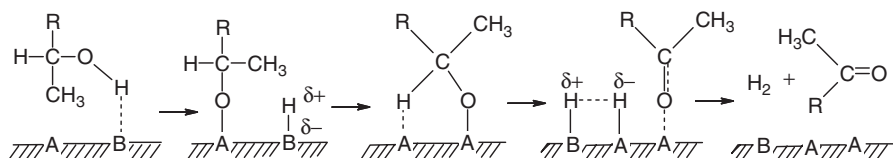


Figure 6.5 Dehydrogenation mechanism of alcohols. (From ref. 80, with permission.)

Similarly, the dehydration of ethanol was found to be catalyzed by the carboxylic acid groups located on the external surface of the carbon particles, the reaction rate increasing with the total surface acidity [83]. The dehydration of methanol to dimethyl ether was studied more recently using activated carbons oxidized with different chemicals [i.e., H_2O_2 , $(\text{NH}_4)_2\text{S}_2\text{O}_8$, and HNO_3] as catalysts. The highest activity was obtained with the catalyst possessing the strongest acid sites. The dehydration activity was found to increase linearly with the H^+ concentration at the point of zero charge:

$$r_{\text{DME}} = (2759 \pm 97)[\text{H}^+]_{\text{PZC}} + (0.53 \pm 0.25)$$

where r_{DME} ($\mu\text{mol/g}\cdot\text{min}$) is the rate of dimethyl ether formation at 453 K. This corresponds to a turnover frequency of 0.138 ± 0.005 per minute [82]. By treating the catalyst at increasing temperatures to decompose the most unstable surface groups (Figure 6.6), these authors also confirmed that the dehydration activity was due to the carboxyl acid groups. Thus, the dehydration activity of

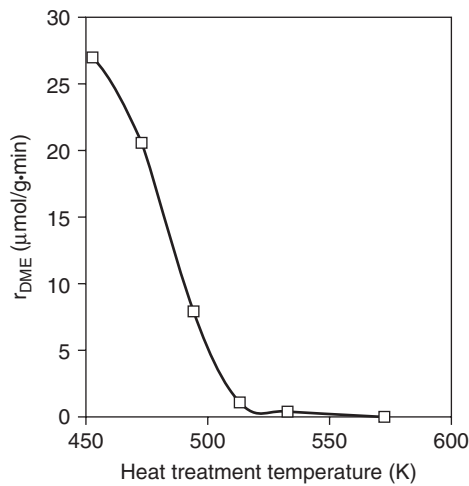
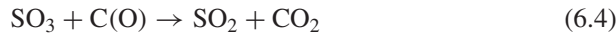


Figure 6.6 Change in catalytic activity with heat treatment temperature. (From ref. 82, with permission.)

the carbon catalyst was correlated with the concentration of the strongest acid groups, located on the external surface of the particles. The oxidative treatments of the carbon catalyst were found to increase both the dehydration activity and selectivity.

6.3.3 SO_x Oxidation

The removal of SO_x and NO_x from gaseous effluents is an important field of application of ACs and activated carbon fibers (ACFs) where technology is already available or under development [10,85]. In these applications the adsorption capacity is combined with the catalytic activity of the carbon materials for oxidation and reduction. Activated carbons are active catalysts for the oxidation of SO₂ into SO₃ and H₂SO₄ in the presence of O₂ and H₂O. The role of surface chemistry in this process has long been recognized, but the results and interpretations of different authors are often contradictory. In most of the earlier studies it was proposed that adsorption and oxidation of SO₂ take place on basic oxygen surface groups [85–92], but Lisovskii et al. [93] reported that the process was improved by treating the carbon with HNO₃ (thereby introducing acid groups). Textural effects may have been overlooked in this case, since the characterization of the ACs was merely based on the BET surface areas. More recently, it was found that higher activity correlated with lower oxygen content [94]. Indeed, most authors observed that heat treatment under inert atmosphere enhanced the desulfurization activity of ACs and ACFs [86,87,95–101]. A correlation between adsorbed SO₂ and evolved CO or CO₂ has frequently been reported, leading to the proposal that the adsorption sites are created by decomposition of the surface oxygen groups. However, such a correlation was not observed in the work of Raymundo-Piñero et al. with carbon materials (ACs and ACFs) covering a wide range of properties and using transient kinetics techniques [100,101]. The SO₂ uptake in the presence of O₂ was determined by its oxidation into SO₃ inside the micropores, and an optimum pore size of about 0.7 nm was identified where the process was favored. It was also proposed that SO₃ was physically adsorbed in the micropores rather than being chemisorbed. The oxidation of SO₂ was explained in terms of a Rideal–Eley mechanism between adsorbed SO₂ and oxygen from the gas phase, the reaction being inhibited by the surface oxygen complexes [101]. Desorption of SO₃ was accompanied by carbon gasification with release of CO and CO₂ according to the following steps:



As a result of these studies, it seems that the higher activity observed upon heat treatment can be attributed to an increase in the surface basicity of the carbon. Another way to increase basicity consists in the introduction of nitrogen atoms

into the carbon material, and this is known to enhance desulfurization activity [85,102]. Stöhr et al. [103] have shown that the catalytic activity of activated carbons in oxidation reactions is enhanced after thermal treatment with ammonia or hydrogen cyanide. The surface chemistry of nitrogen-containing carbons was studied by Pels et al. [34] and by Jansen and van Bekkum [23]. It was shown that the nitrogen functionalities change upon heat treatment, nitrogen atoms being eventually incorporated into the graphene layers as pyridine and pyrrole groups (see Chapter 7).

Recent studies on the use of ammonia-treated activated carbon fibers or cloth for the catalytic removal of SO_2 have shown that the activity increases with the amount of basic nitrogen groups present [104–106]. In particular, it was found that the more basic pyridinic groups are the most active for the catalytic oxidation of SO_2 both into SO_3 and H_2SO_4 [107], and a linear correlation between the activity (normalized by the BET surface area) and the concentration of pyridinic groups was obtained, as shown in Figure 6.7.

The precise mechanism of interaction between SO_2 and these nitrogen groups remains an open issue. In addition, it has been shown that the enhanced catalytic activity of ammonia-treated carbons is not lost upon subsequent heating at high temperatures under nitrogen or hydrogen, a treatment that removes most of the nitrogen. The catalytic activity of these carbons in oxidation reactions was explained in terms of the formation of superoxides, O^{2-} [103]. More recently, the influence of heteroatoms (N, B, P) on the catalytic activity of carbons was interpreted in terms of semiconductor properties [108], a concept discussed in an earlier review [12]. The insertion of nitrogen atoms into the graphite lattice lowers the bandgap, leading to higher electron mobility and lowering the electron workfunction at the carbon–fluid interface. Thus, nitrogen-doped carbons exhibit enhanced catalytic activity in

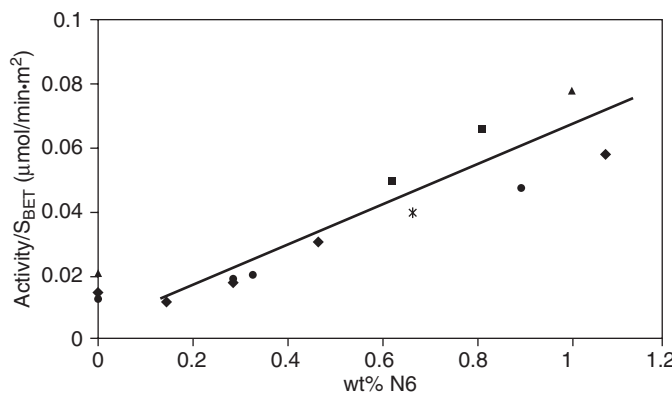


Figure 6.7 Catalytic activity of nitrogen-doped activated carbon powders and fibers for SO_2 oxidation into H_2SO_4 normalized by surface area versus surface pyridinic-like nitrogen percentage. (From ref. 107, with permission.)

electron transfer reactions, in the same way as semiconducting metal oxide catalysts.

The starting point for this approach was the estimation of the bandgap as a function of the position of the nitrogen atoms in a graphene plane. A semiempirical quantum chemical method was used to calculate the donor–acceptor characteristics of various model clusters of pure and nitrogen-containing carbons. The results showed that carbons with pyrrole and pyridine nitrogen-containing groups at the edge of graphene layers have the lowest bandgap, thus the highest catalytic activity. Moreover, it was found that there is an optimum concentration of heteroatoms in a carbon matrix, corresponding to a minimum bandgap and maximum activity [108].

6.3.4 NO_x Reduction

Carbon materials can be used in de-NO_x processes either as adsorbents, reductants, or catalysts. The use of carbon as an adsorbent and/or reducing agent for NO_x has been reviewed [ref. 109 and references therein], and falls outside the scope of the present review. Nevertheless, we discuss briefly some results and conclusions from more recent papers which are relevant in the context of carbon as a catalyst.

The impact of pretreatments on the selectivity of carbon materials for NO_x adsorption and reduction in the presence of oxygen was addressed by Xia et al. [110]. They showed that high-temperature (1223 K) hydrogen-treated carbons adsorb NO at room temperature but not oxygen; on the other hand, N₂-treated carbons strongly adsorb both species. Thus, selectivity for NO adsorption can be induced by hydrogen treatment, and this was explained in terms of the different active surface species generated by this treatment. In particular, it was postulated that the H₂-treated carbon does not contain “dangling carbons” capable of strongly adsorbing oxygen [111]; however, they contain a high concentration of (unsaturated) edge sites (basic sites), capable of NO adsorption at 303 K (oxygen only adsorbing there above about 423 K).

Matzner and Boehm [112] studied the reduction of NO with activated carbons of different nitrogen contents; they observed that the incorporated nitrogen had an enhancing effect on the reduction activity. More recently, Zawadzki et al. [113] studied the interactions of NO₂ and NO/O₂ mixtures with carbons differing in the chemical structure of surface functional groups using *insitu* infrared spectroscopy. The results suggest a complex reaction mechanism in which functional groups containing nitrogen and oxygen are formed on the carbon surface, including C–NO₂, C–ONO, C–NCO, and anhydride structures. The reduction of NO₂ to N₂ without the use of an external reductant can be achieved, significant conversions being obtained at 623 K on both oxidized and nonoxidized carbons. The results show that the effect of carbon surface oxides on the conversion of NO_x is small; however, oxygen facilitates the conversion of NO, which requires the creation of surface C–NO₂ structures.

The commercially available technology to control the emissions of nitrogen oxides from stationary sources is the selective catalytic reduction (SCR) with ammonia, generally with oxide catalysts, in the temperature range 573 to 673 K [114]. The reaction can proceed in either the presence or the absence of oxygen:



Various reports have shown that this reaction can be efficiently catalyzed by carbon materials at temperatures as low as 373 to 473 K [6,115]. It should be noted that in the presence of carbon catalysts, two different mechanisms may be operative in this process: adsorption of NO_x at low temperatures ($T < 423$ K), and reaction at higher temperatures ($T > 423$ K).

Ahmed et al. [116] carried out a detailed study with the objective of identifying the properties of activated carbons that are important for the SCR of NO; they concluded that chemical properties such as surface oxides and mineral matter play a more important role than their physical properties, such as surface area and pore structure. In effect, they found that the catalyst activity correlated directly with the oxygen content of the carbon samples and inversely with their pH. These results indicate that the NO conversion is favored on more acidic carbons. They also reported that NO reduction by ammonia was negligible in the absence of oxygen. Indeed, it has been shown [117] that oxygen enhances the C–NO reaction through the formation of surface oxygen complexes, which are essential for the C–NO reaction to proceed.

Several authors have also reported an increased catalytic activity after treating the carbon material with sulfuric acid [115,118,119]. This effect was ascribed to the formation of (acidic) oxygen functional groups which can be the sites for NH_3 adsorption. A linear correlation between NO conversion and the acidity of the activated carbons was presented by Ku et al. [119]. However, when such sulfuric acid treatment was applied to a PAN-based activated carbon fiber (PAN-ACF), a much higher catalytic activity for the SCR of NO was observed in comparison to the activated carbons [120]. Although the authors could not give a precise explanation for this activity increase, they suggested that it might be due to the presence of residual nitrogen in the PAN-ACF. Other authors reported an increased SCR activity by treating the carbon catalyst in NH_3 at high temperatures [7,121]. The activity was found to increase linearly with a concentration of N between 1 and 3%, leveling off at higher concentrations.

Singoredjo et al. [122] used activated carbons modified with nitrogen- and oxygen-containing compounds in the SCR of NO with NH_3 at 385 to 550 K. Of several additives tested, glucosamine resulted in an outstanding increase in activity, ascribed by the authors to the formation of stable surface oxygen complexes.

None of these earlier reports provided a clear explanation for the role of the incorporated nitrogen; nevertheless, it became clear that the simultaneous presence of oxygen and nitrogen functionalities on the surface of the carbon materials was the key to their high catalytic activity [120,123,124]. Teng et al. [125] studied the SCR of NO using activated carbons with different surface areas

as catalysts. It should be emphasized that these materials were obtained from the same precursor by varying the extent of burn-off in CO_2 , thus ensuring that the chemical properties of the carbons were not changed. They found that the NO conversion increased with the surface area of the carbon catalysts. Under these conditions, the number of sites available for the reduction of NO increases with the specific surface area. However, the conversion normalized by the BET area was found to decrease as the burn-off increased; this clearly demonstrates that the surface is not fully accessible to the reactants. Since the effect observed was similar at all temperatures, the authors concluded that spatial limitations for NO adsorption in the required configuration were probably involved. They also observed that the addition of oxygen increased the NO conversion. It was proposed that the process might be controlled by two consecutive steps: the adsorption of NH_3 on active sites, followed by the addition of NO or NO_2 in the neighborhood of the $\text{C}(\text{NH}_3)$ complexes.

The nature of the active sites was addressed in a subsequent paper [126], where carbons treated with H_2SO_4 and HNO_3 were used as catalysts. It was observed that the concentration of oxygen-containing surface sites significantly affected the course of the reaction before steady state was reached. In the absence of oxygen, the activity was found to increase as a function of the CO_2 evolved in TPD, while it increased with the CO evolved in the presence of oxygen. Therefore, carboxyl groups were thought to be responsible for the reduction of NO in the absence of oxygen, while hydroxyl and carbonyl groups were involved in the presence of oxygen, as shown in Figure 6.8. Thus, the formation of $\text{CO}^-(\text{NH}_4)^+$ and $\text{C}(\text{ONO})$ complexes, and their interactions, were identified as important steps

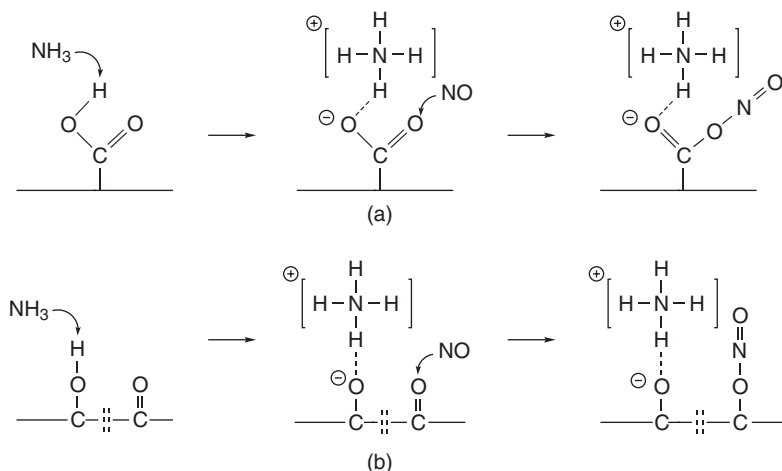


Figure 6.8 Reaction scheme for the formation of surface complexes during NO reduction with NH_3 over carbon catalysts. (From ref. 126, with permission.)

in the SCR of NO, which is basically in agreement with the mechanism originally proposed by Mochida et al. [123].

Muñiz et al. [127] used modified activated carbon fibers for the SCR of NO at low temperatures (<673 K). PAN-ACF showed the highest activity, ascribed to the presence of nitrogen functionalities. They also reported on different pre-treatments to enhance the activity of the fibers; the most effective was oxidation (with nitric acid), followed by reaction with NH₃.

Mochida et al. [128] reported on the very high activity of a pitch-based high-surface-area ACF calcined at 1373 K for the NO–NH₃ reaction at room temperature. The high-temperature treatment (which would remove the surface oxygen functionalities completely) was essential for this high level of activity.

Huang and Teng [129] used phenol–formaldehyde resins impregnated with phenylenediamine to produce porous carbons with different amounts of nitrogen. The catalytic activity of these carbons for the SCR of NO was found to increase upon nitrogen impregnations both at low temperatures (<413 K), where adsorption is the dominant process, and at high temperatures ($T > 413$ K), where reaction occurs. The nature of the nitrogen-containing groups was investigated by XPS; most of the nitrogen was found to be present in pyridine-type groups at the edges of graphene layers (the N5 and N6 groups, with binding energies of 400.3 ± 0.3 and 398.7 ± 0.3 eV, respectively), which are responsible for increasing the basicity. The activity showed a clear correlation with the nitrogen content determined by XPS rather than by elemental analysis, as shown in Figure 6.9. This indicates that the reaction occurs primarily at the external surface of the carbon particles.

More recently, Szymanski et al. [130] reexamined the influence of nitrogen surface functionalities on the SCR of NO_x using samples with different chemical properties, but of the same origin and with similar texture. Ammonia-treated

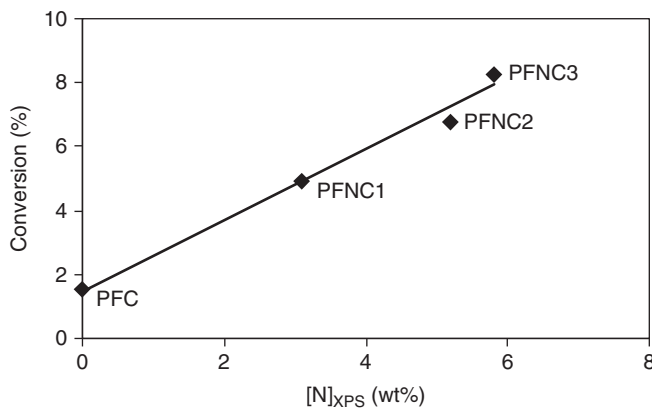


Figure 6.9 NO conversion at 473 K as a function of the nitrogen content of the carbon catalyst determined by XPS. (Data from ref. 129.)

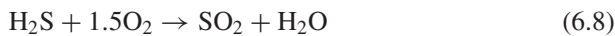
carbons exhibited high activity and selectivity, which was explained by a more facile NO₂ formation, as a result of the easier chemisorption of oxygen and NO. The authors proposed that the catalytic activity is determined not only by the presence of acidic surface oxides (carboxylic and lactonic groups, responsible for NH₃ adsorption), but also by other sites, responsible for NO oxidation to NO₂-like species. The N6 sites were suggested to fulfill this role. Indeed, the extra electrons resulting from the substitution of carbon for nitrogen in the aromatic ring are delocalized and can be transferred to adsorbing species to form reactive surface intermediates, as proposed by Matzner and Boehm [112] and by Stöhr et al. [103]. The work of Strelko et al. [108], already mentioned in relation to the oxidation of SO₂, also provides an adequate interpretation in the present context and highlights the similarities in the reaction mechanisms involved in these two processes when carbon materials are used as catalysts.

The catalytic oxidation of NO to NO₂ is an alternative method for the removal of NO from flue gases. The method is interesting because it can proceed in air at room temperature over appropriate catalysts, and the NO₂ formed can be removed as nitrate in the presence of water or aqueous basic solutions. Carbon materials are efficient catalysts for this reaction [131].

Using pitch-based ACFs, Mochida et al. [132] reported 87% conversion at room temperature in dry air. Lower conversions were obtained in the presence of water vapor. The authors found that heat treatment at 1123 K enhanced the activity of the fibers. Such treatment removes oxygen functional groups from the surface of the ACFs; the vacant sites created as a result of this treatment were thought to be the active sites for the reaction. On the other hand, the hydrophobic surface obtained after the heat treatment helps to decrease the amount of water adsorbed, which decreases NO conversion in humid air. An interesting point noted by Mochida et al. [131] is that PAN- and pitch-based ACFs exhibited the reverse order of activity for the oxidation of SO₂ and NO. Thus, pitch fibers were best for NO oxidation, while PAN fibers were found to be more active for SO₂ oxidation. No explanation was provided by the authors for this finding, which certainly reflects the different surface chemical properties of the two fiber types. A detailed kinetic study of this process was presented in a subsequent paper [133], while Guo et al. [134] compared the performances of different carbon fibers (PAN, pitch) and activated carbons.

6.3.5 H₂S Oxidation

The removal of hydrogen sulfide from industrial off-gases is another process where the adsorptive and catalytic properties of porous carbons can be combined advantageously, particularly when the H₂S concentration is low. Hydrogen sulfide can either be converted into sulfur dioxide or into elemental sulfur:



At low temperatures (i.e., <373 K) activated carbons promote mainly the formation of elemental sulfur. Molten sulfur can be collected by operating above its melting point (392 K). This process has been known since the 1920s. The earlier literature, reviewed by Bansal et al. [15], shows that there are different views concerning the reaction mechanisms involved. Thus, Puri et al. [135] and Cariaso and Walker [136] proposed a Rideal–Eley mechanism between chemisorbed oxygen and hydrogen sulfide in the gas phase, while Steijns et al. [137] suggested a mechanism involving dissociatively adsorbed H₂S and chemisorbed oxygen. The elemental sulfur produced was found to promote further oxidation of H₂S. On the other hand, Hedden et al. [138] proposed that the reaction occurs via intermediate ionic species in a water film formed on the carbon surface, in which both oxygen and hydrogen sulfide dissolve.

The catalytic oxidation of H₂S requires a wide-pore carbon and a large total pore volume, which is needed for retention of the sulfur formed [139]. More recent work suggests that oxygen functional groups on the carbon surface may be involved in the formation of sulfur oxides. It was also reported that carbons with higher nitrogen content were better catalysts [140]. Primavera et al. [141] investigated the effect of water in the low-temperature catalytic oxidation of H₂S in low concentrations over activated carbons. They showed that the presence of water enhanced the reaction rate and the amount of sulfur that could be loaded before regeneration, and explained their results assuming the formation of a liquid layer inside the pores of the carbon, as proposed by Hedden et al. [138]. However, these findings contradict the kinetic data reported by Dalai and Tollefson [142], who did not find any effect of water on the H₂S conversion. Using urea-modified activated carbons, Adib et al. [143] showed that basic nitrogen groups contribute significantly to the oxidation of H₂S to water-soluble sulfur species. The process was assumed to occur by gradual reaction in the water film condensed in the micropores, with formation of sulfuric acid. It was concluded from this work that the important features of the carbon material are small micropores, high microporosity, and highly dispersed basic nitrogen groups built into the carbon matrix. The importance of preadsorbed water and the role of surface chemistry in the process of hydrogen sulfide adsorption and catalytic oxidation on activated carbons were addressed in a subsequent paper [144]. It was found that moderately acidic carbons promote the oxidation of H₂S to sulfur oxides, whereas a high-pH carbon led to the formation of elemental sulfur.

Katoh et al. [145] showed that H₂S, methanethiol, and dimethylsulfide could be removed simultaneously from gaseous streams at room temperature over wet activated carbon fibers, while Dalai et al. [142] reported on the oxidation of methanethiol over an activated carbon. More recently, an activated carbon prepared from a cellulosic precursor by CO₂ activation was found to exhibit outstanding performance in the oxidation of H₂S (1000 ppm) in a hydrogen stream at 423 K: namely, 100% conversion for more than 10 hours, and 100% selectivity to sulfur [146]. The selectivity aspects in the oxidation of H₂S to sulfur were addressed in a paper by Bashkova et al. [147]. These authors reported

that a high volume of micropores and small mesopores, together with a narrow pore size distribution, is desirable for the retention of SO₂, while a high surface reactivity with a significant amount of basic groups was important for the retention of COS.

There have also been attempts to use CNFs and MWCNTs as a catalyst in this process [148,149]. The highest activities and selectivities (toward sulfur) were obtained on CNFs with the graphene layers oriented perpendicularly to the axis (platelet-CNFs) and on MWCNTs. However, the carbon materials were contaminated with remains of the metal catalysts used for their synthesis (Ni, Ni–Cu), which may affect the catalytic properties observed.

6.3.6 Hydrogen Peroxide Reactions

Hydrogen Peroxide Decomposition The decomposition of hydrogen peroxide is one of the oldest reactions known to be catalyzed by carbon materials, the first reports dating from the beginning of the twentieth century. Firth and Watson [150,151] refer a work of Lemoine [152] as the first to observe that AC is an efficient catalyst for hydrogen peroxide decomposition. Two important conclusions were obtained that have been rediscovered in more recent work: The catalytic activity of AC in the decomposition of hydrogen peroxide is not correlated with its textural properties; and the catalytic activity is increased substantially by pre-treating the AC at temperatures in the range 873 to 1173 K [150,151], a treatment that is known to increase the sample basicity. No direct relationship between surface area and catalytic activity was observed, which can be explained by the fact that different ACs studied had both different textural and surface chemical properties, the latter being dominant. King [153] used a similar approach and concluded that the activity toward hydrogen peroxide decomposition was related directly to the basic character of the AC surface. Samples heated to 723 K (with a low level of catalytic activity) were acidic, and those treated at 1123 K (with a high level of catalytic activity) were alkaline. In the same study he noted that after an initial period of high activity, the carbon catalyst was deactivated, presenting thereafter residual activity, as already mentioned by Firth and Watson [150]. In cyclic studies, he observed that the high initial activity could only be obtained if AC was reactivated by heat treatment at 1123 K (and not at 773 K). This result led him to consider the initial high activity of AC toward hydrogen peroxide decomposition not as catalysis, but merely as a reaction between the alkaline surface of carbon and the peroxide, with the formation of acidic surface oxides and molecular oxygen [153]. Later, Smith [154] performed a detailed kinetic study of the hydrogen peroxide decomposition catalyzed by AC, where several aspects of the proposed mechanisms were elucidated: namely, that surface oxides were not required for AC to have catalytic activity since AC samples treated at 1473 K to remove most of the surface oxygen were still very active. Puri and co-workers [155,156] also published a series of studies on the same subject. They concluded that the catalytic activity depends on the surface alkalinity and surface area of the carbon blacks.

The following mechanism was then accepted, taking into consideration the known phenomena with respect to H_2O_2 decomposition [12]:

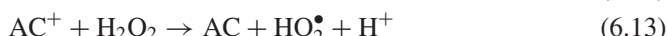
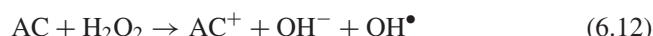


where AC^+ represents the carbon lattice. The surface peroxide formed by reaction (6.10) is regarded as having an increased oxidation potential, which can oxidize another H_2O_2 molecule.

This reaction system was revisited more recently [157–160], but the conclusions obtained were essentially the same as drawn previously except that more sophisticated characterization equipment was used. As an example, Khalil et al. [157] reported that the textural parameters of AC were not important for H_2O_2 decomposition (they had even observed an inverse dependence on surface area) and that the reaction depends on the surface pH of the AC samples.

Oxidation of Organic Contaminants with Hydrogen Peroxide Catalyzed by AC

Recently, there has been renewed interest in the catalytic system $\text{H}_2\text{O}_2/\text{AC}$, due to its potential application in the oxidation of organic contaminants in water and wastewater. The key factor for this application is the formation of free radicals [see reactions (6.12) and (6.13)] which are known to be very strong oxidants in the liquid phase. Carbon materials can act as electron-transfer catalysts, similar to the Haber–Weiss mechanism known from the Fenton reaction, with AC and AC^+ as the reduced and oxidized catalyst states [161]:



The organic compounds studied were 4-chlorophenol [158,159], 2-chlorophenol [160], phenol and hydroquinone [162], textile dyes [162,163], methyl *tert*-butyl ether, trichloroethene, and 2,4,5-trichlorophenol [161]. It was observed that the decomposition of H_2O_2 was significantly lower when the organic compound was present [158–160,161], which was explained by the competitive adsorption of the organic compound on the surface-active sites responsible for the H_2O_2 decomposition.

One of the most interesting works was published by Oliveira et al. [162]. They prepared a series of ACs treated with H_2 at different temperatures and were able to correlate the hydrogen peroxide decomposition rate and the oxidation of organics in water with the reducing sites on the AC surface. The proposed mechanism, which does not correspond exactly to reactions (6.12) and (6.13), is presented in Figure 6.10. According to this mechanism, the reducing sites can promote both H_2O_2 decomposition and the oxidation of organic compounds in aqueous phase by H_2O_2 . These reactions are supposed to follow a radical mechanism,

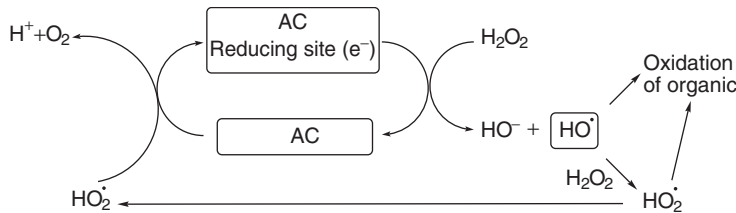


Figure 6.10 Proposed competitive mechanism for H_2O_2 reactions in the presence of activated carbon. (From ref. 162, with permission.)

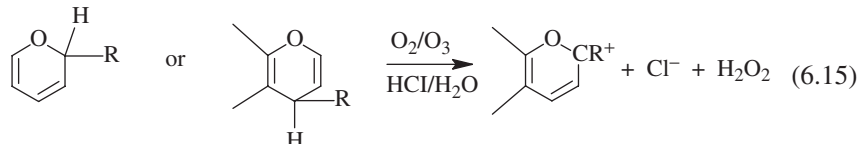
probably initiated by electron transfer from the reducing site to H_2O_2 to produce species such as HO^\bullet and HOO^\bullet .

6.3.7 Catalytic Ozonation

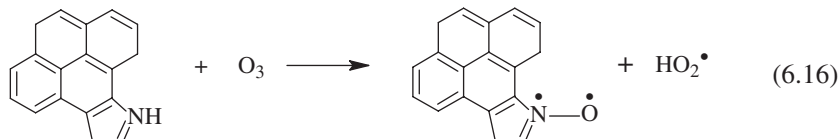
Ozone is one of the most powerful oxidant agents available. It is used widely for drinking water disinfection and for the oxidation of pollutants in industrial wastewaters. Ozone is unstable in water and decomposes into radicals such as HO^\bullet , which are the strongest oxidants in water. To enhance the decomposition of ozone and consequently the efficiency of ozone-based oxidation processes, the combination of ozone with homogeneous or heterogeneous catalysts, with or without metallic phases, has been investigated and recently reviewed [164]. Activated carbon has been mentioned as one of the most attractive alternative catalysts for this process.

Catalytic Decomposition of Ozone in Water Activated carbon by itself was found to be a catalyst for the decomposition of O_3 in water. The pioneering work on this subject was carried out by Jans and Hoigné [165]. They concluded that suspensions of AC and carbon black can initiate the radical chain reactions that proceed in bulk solution and accelerate the transformations of O_3 into highly oxidative species such as hydroxyl radicals (HO^\bullet). This result triggered the use of AC as catalyst for ozone-based advanced oxidation processes (AOPs) since it is “cleaner” (no leaching of metals can occur) and easier to apply than other catalysts. More recently, this subject was revisited by various authors [166–168] and the influence of both chemical and textural features of the activated carbon was evaluated. In these three studies it was concluded that the surface chemical properties controlled ozone decomposition, the most efficient carbons being those with high basicity. Rivera-Utrilla and collaborators [167,169] concluded that O_3 reduction on the AC surface generated OH^- ions and H_2O_2 , which initiate the O_3 decomposition into highly oxidative species [170]. These observations were confirmed by Alvarez et al. [168]. The delocalized π -electron system [reaction (6.14)] and the oxygenated basic surface groups, such as chromene and

pyrone [reaction (6.15)], were the catalytic centers, according to the following reactions [169]:



The same authors [167,171], using basic ACs obtained after treatments with nitrogenating agents, concluded that pyrrolic groups were the nitrogenated active centers for O_3 decomposition. The attack of pyrrolic groups by ozone yields N-oxide-type groups and the hyperoxide radical, which enhances the rate of ozone transformations into OH radicals [172]:



In addition to the influence of the basicity of the AC surface, Faria et al. [166], studying the effect of pH on the catalytic decomposition of ozone, postulated that the electrostatic interactions between activated carbon surface and the solutes involved in the mechanism (such as OH^- ions) may also play a role. When the pH_{PZC} of the activated carbon is higher than the pH of the solution, the surface of the material becomes positively charged, enhancing the attraction of hydroxide ions and, in particular, improving the heterogeneous decomposition of ozone.

Successive experimental runs carried out with the same AC sample in the ozone decomposition showed that the surface chemistry is important only in the first cycles of reaction, due to a slightly progressive oxidation of the surface, which provokes the loss of basic surface groups and an increase of acidic groups, mainly carboxylic acids [166–168]. This led Sánchez-Polo et al. [167] and Alvarez et al. [168] to propose that AC could not be a catalyst for ozone decomposition, but rather, an initiator of the $\text{O}_3/\text{H}_2\text{O}_2$ system. Faria et al. [166] concluded that basic carbons tended to behave as acid ACs upon losing activity, which were shown still to be active catalysts. Nevertheless, Guiza et al. [173] concluded that pre-ozonation of the AC had no effect on its activity, which could indicate that the starting AC used by these authors had already acidic properties.

Concerning the influence of the textural properties in the catalytic decomposition of ozone, it was shown that ACs with large surface areas clearly favored this reaction [166,167,173]. Nevertheless, Alvarez et al. [168] did not find any correlation between the textural properties of ACs and the rate of ozone decomposition. This strange result may be explained by the fact that the ACs tested were from different precursors, which could mask the textural effects. Particularly interesting are the results of Faria et al. [166], who studied the influence

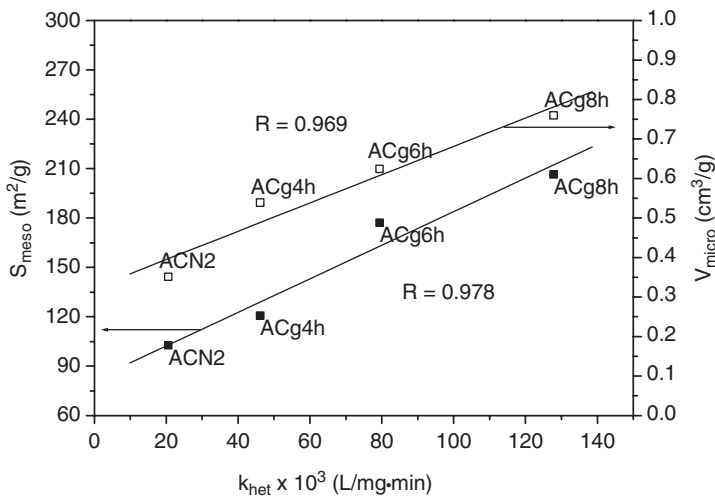


Figure 6.11 Variation of k_{het} with selected activated carbon textural properties. ACN2, the original AC, and ACgxh, where x is the duration (hours) of gasification at 1173 K under CO₂, are the treated samples. (From ref. 166, with permission.)

of a series of modified activated carbons prepared from the same starting material and differing only in their textural properties. A strong correlation between the heterogeneous apparent rate constant (k_{het}) and the activated carbons textural properties was observed, k_{het} increasing significantly with both the mesopore surface area and the micropore volume (see Figure 6.11).

Catalytic Ozonation of Organic Pollutants in Water Catalytic ozonation may be included in the advanced oxidation processes (AOPs), which are based on the formation of HO[•] radicals which are highly reactive toward most organic pollutants. Among these processes, the combination of ozone and activated carbon in a single step was found to be an attractive alternative to the treatment of waters and wastewaters containing organic contaminants: namely, oxalic acid [174,175], oxamic acid [175], gallic acid [176], succinic acid [177], pyruvic acid [178], naphthalenetrisulfonic acid (NTS) [169,171,179–181], phenolic compounds [182–186], nitrobenzene [187], aniline [188], surfactants [189,190], and textile dyes [191–197].

All the works mentioned report significant synergistic effects and enhanced mineralization degrees in the degradation of different organic compounds by the simultaneous use of ozone and activated carbons. Therefore, processes combining these two agents appear to be promising in the removal of a number of aromatic compounds and subsequent oxidation by-products.

One of the most consistent studies was carried out by Rivera-Utrilla and collaborators [169,171,179–181]. They focused their research on the oxidation of

naphthalenetrisulfonic acid, which is a model compound for dye degradation and is characterized by a low reactivity to ozone and low and slow adsorption on AC [180]. It was observed that the catalytic activity was favored both by the basicity of the carbon surface and by a higher macropore volume [169]. They proposed a mechanism where the basal plane electrons and the oxygenated basic groups (chromene and pyrone) were responsible for ozone decomposition in aqueous phase, according to reactions (6.14) and (6.15), by initiating the decomposition of O_3 into highly oxidative species and increasing the NTS ozonation rate [169]. It was also suggested that the reduction in total organic carbon (TOC) was due not only to the catalytic effect, but also to the adsorption of NTS degradation compounds on AC. In a subsequent work [180], a kinetic study was carried out where they showed that the heterogeneous rate constants for NTS ozonation [$(k_{het})_{demi}$] were well correlated with the basicity of ACs, as can be seen in Figure 6.12. ACs used in this study were demineralized to eliminate the possible catalytic role of the mineral matter content.

The same authors [179] observed that using different activated carbon samples preozonated in order to change their surface properties, the catalytic activity decreased as the extent of the pretreatment increased. This result was justified by an increase in the acidic oxygenated surface groups (electron-withdrawing) or by a decrease in the basic oxygenated groups on ACs with ozone pretreatment, which reduced the surface basic character and its reductive properties and therefore decreased the rate of reactions (6.14) and (6.15). In addition, the increase in the surface acidity also lowered the adsorption component of the NTS degradation products. In this study, no correlation was observed between NTS ozonation and AC textural properties. Assuming that the basic groups were the active centers for catalytic ozonation, Rivera-Utrilla and Sanchez-Polo [171] prepared a set of basic ACs with nitrogenated surface groups. It was concluded that the

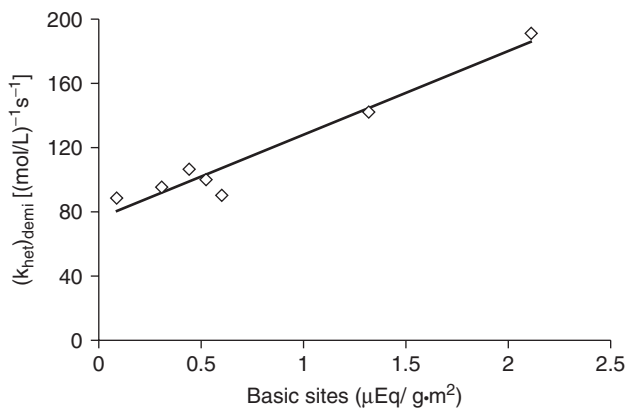
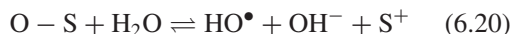
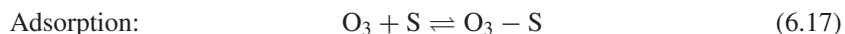


Figure 6.12 Relationship between the heterogeneous rate constant $(k_{het})_{demi}$ and the concentration of basic groups in the demineralized AC. (From ref. 180, with permission.)

catalytic activity of ACs in NTS ozonation increased after their treatment with nitrogenating agents, and pyrrole groups were ascertained as the active centers for this reaction. The high level of activity of pyrrole groups is due to their role in ozone reduction on the AC surface to generate highly reactive radicals in the system, according to reaction (6.16). Nevertheless, this conclusion may be speculative, because the sample with higher activity was that with a larger surface area and meso and macropore volumes, which is expected to exhibit the highest catalytic activity, because the large pores facilitate the access of ozone to the surface-active centers.

In a series of studies of the same type, Beltran and collaborators evaluated the role of ACs in the catalytic ozonation of small organic molecules: oxalic acid [174], gallic acid [176], succinic acid [177], and pyruvic acid [178]. They concluded that the presence of ACs enhances the degradation rate of the organic compound significantly compared to single ozonation and single adsorption, mainly in the total mineralization. The mechanism suggested involves the reaction (in the water phase) between the organic compound and oxidant species, probably hydroxyl radicals resulting from ozone decomposition on the carbon surface. For example, for oxalic acid [174]:



where S is a free active center on AC and B is the oxalic acid. This mechanism was suggested taking into consideration that the presence of radical scavengers inhibits the process, which indicates the presence and action of hydroxyl radicals in the bulk of the liquid phase [174]. Similar results have been obtained by Ma et al. in nitrobenzene degradation [187]. Nevertheless, it is still not clear whether or not these radicals are formed in bulk water, or as adsorbed species, and the catalytic surface reaction cannot be eliminated [175,178].

In terms of the influence of the AC surface properties, they observed that the basicity of the ACs favored the ozonation rate. They found linear correlations between surface reaction rate constants and the pH_{PZC} of the ACs for the ozonation of succinic acid [177]. The advantage of the basic surface groups has also been highlighted for the catalytic ozonation of aniline [188] and different classes of dyes and textile effluents [191].

Another possible advantage of using ozone and AC simultaneously is the possibility of insitu regeneration of the AC, avoiding the costly exsitu treatment of the exhausted AC. This fact was observed experimentally in the catalytic ozonation of textile effluents [194] and phenol [183–185]. Nevertheless, more studies are needed to confirm the real capability of ozone for insitu regeneration of exhausted AC, especially when large molecules such as dyes are adsorbed. The effect of ozone on the surface properties of AC during regeneration should also

be considered, since they will affect the performance of AC both as an adsorbent and as a catalyst.

In conclusion, despite intensive research recently carried out on the ozonation of several organic pollutants in the presence of activated carbon, there are still doubts about the reaction mechanisms. Among the possible mechanisms for the ozonation of organic compounds in the presence of activated carbon, the following seem to be feasible: Activated carbon promotes the decomposition of O_3 into HO^\bullet or other highly active oxygen-radicals, and the oxidation occurs in the homogeneous phase; or activated carbon adsorbs the organic compounds, which then react on the surface both with O_3 and oxygen radicals. Probably, both mechanisms occur simultaneously [175]. Generalizations concerning the mechanisms of catalytic ozonation are difficult [164], as they depend, among other factors, on the nature of the catalyst and of the organic compound to be oxidized.

6.3.8 Catalytic Wet Air Oxidation

Catalytic wet air oxidation (CWAO) is another emerging technology for water and wastewater treatments, which consists in the total oxidation of the polluting species present in the effluent at moderate temperatures and pressures (398 to 493 K, 2 to 50 bar), using oxygen or air as oxidant. The use of carbon materials in CWAO was recently reviewed [198]. AC is used mostly as a catalyst support, but in this section we only summarize the use of AC as a catalyst on its own. Phenol and substituted phenols have been the target compounds most studied in CWAO. In two reports published in 1998, the use of ACs without a metallic phase was compared to other conventional oxidation catalysts [199,200]. In both cases, a higher phenol conversion was observed for the AC, which initiated interest in this system. The major drawback observed initially was the decrease in phenol conversion under typical CWAO conditions (413 K and 9 bar), due to the loss of activated carbon by combustion and reduction of its surface area [199]. Similar conclusions were latter obtained by Santos et al. [201] working at 433 K and 16 bar. To minimize this problem, the oxygen partial pressure was lowered to 2 bar, the loss of AC being negligible under these new conditions, whereas a decrease of only 30% was observed in the conversion [202]. Using three different commercial ACs, the authors concluded that the physical properties and the source of the AC could hardly be related to the conversion of phenol, and postulated that the chemical surface properties should be a key factor with respect to its catalytic activity. Latter, the influence of the AC surface chemistry in the CWAO of phenol was studied by the same authors [198,203]. Starting from two different commercial ACs, they prepared two series of ACs modified by oxidation with HNO_3 , $(NH_4)_2S_2O_8$, and H_2O_2 , and demineralization with HCl. All these treatments led to a pronounced increase in the acidic surface groups (carboxyls, lactones, phenols), but had little impact on phenol conversion. The catalytic behavior of the modified ACs was similar or slightly poorer than that of the original materials, which could be due to the increase in acidity and

the destruction of some basic groups during the surface treatments used. It was concluded that the catalytic activity of AC toward phenol oxidation increases or decreases with an increase in surface basicity or acidity, respectively. In one of the AC series, a good correlation between phenol conversion and the ratio of phenolic to carboxylic and lactone groups was observed. Nevertheless, the authors, without any satisfactory experimental proof, indicated that the quinone groups rather than the phenolic groups were the active centers for the CWAO of phenol [198]. The role of the basic surface groups in generating oxygenated radicals from molecular oxygen in aqueous phase was indicated as the main reason for the varying performance of the modified ACs [203]. The reaction mechanism is not yet fully clarified, and it would have been more interesting if the authors had prepared basic ACs in order to support their conclusions. In a detailed kinetic study, Santos et al. [204] concluded that the oxidation reactions took place almost quantitatively on the catalyst surface, the reaction in the liquid phase being negligible under the reaction conditions used.

The influence of the substituent groups in the oxidation of aromatic compounds was evaluated by different authors [200,205,206]. It was observed that *m*-xylene, *o*-cresol, *o*-chlorophenol, and phenol are readily oxidized, whereas aromatics containing nitrogen and sulfur groups proved to be refractory to CWAO [206]. Under the experimental conditions used, the reactivity sequence was *m*-xylene (99.8%) < *o*-cresol (83%) < *o*-chlorophenol (74%) < phenol (70%) < aniline (15%) < *p*-nitrophenol (9%) < sulfolane (5%) < nitrobenzene (>1%) [198]. This sequence may be explained by taking into consideration that the generally accepted mechanism for liquid-phase oxidation of phenol and substituted phenols by oxygen is an electrophilic reaction that follows a heterogeneous–homogeneous free-radical chain mechanism, where the easiness of the organic compound to form free radicals is a key parameter. The pattern of reactivity follows the reverse order of the chemical oxidation potential [198]. Other possible factors that might affect the CWAO performance, such as adsorption, oxidative coupling reactions, and pore blockage, were additionally studied without giving a satisfactory explanation for the reactivity pattern [206].

In addition to aromatic compounds, CWAO was also studied in the oxidation of ammonia [207] and amines [208] using modified activated carbons. The results for ammonia oxidation are summarized in Figure 6.13. It was observed that the AC samples oxidized with HNO₃ (COX and CHO), where an increase in the amount of carboxylic, lactonic, and anhydride surface groups was observed, presented the highest rate and capacity of adsorption but less activity toward selective ammonia oxidation, probably because of a strong ammonia adsorption. On the other hand, the H₂-treated AC samples (CH and COH), where the acidic groups were removed and basic groups were formed, presented the lowest adsorption capacity and the greatest activity for selective ammonia oxidation. The most outstanding behavior of the latter carbons is that they do not generate total oxidation by-products (nitrites and nitrates), as observed with the other samples. Thus, basic activated carbons present not only the largest conversion to N₂, but also the best selectivity to this product.

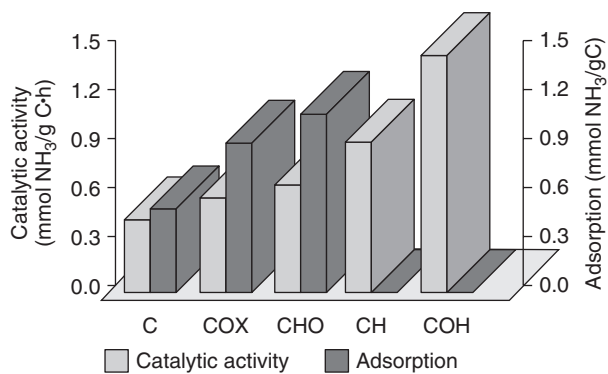


Figure 6.13 Catalytic activity and adsorption capacity of activated carbons in the CWAO process of aqueous ammonia. C, original AC; COX, C oxidized with HNO₃; CH, C treated with H₂ at 673 K; CHO, CH oxidized with HNO₃; COH, COX treated with H₂ at 673 K. (Adapted from ref. 207.)

By deconvolution of the TPD spectra of the AC samples to estimate the amount of each surface group, the authors observed that only the amount of quinone groups followed the same trend as the catalytic activity [207]. Subsequently, the same authors, using the same methodology, observed similar behavior for the CWAO of methyl and dimethyl amines: The ACs with higher catalytic activity were those with lower level of low-temperature decomposing surface groups (carboxylic-like) and important amounts of high-temperature decomposing groups (quinones) [208]. More recently, the use of AC was also shown to be effective in the CWAO of several dye solutions [209]. Other types of carbon materials, such as mesoporous carbon xerogels, are starting to be used as catalysts in the CWAO of aromatic compounds [210].

6.3.9 Other Reactions

Table 6.2 summarizes several other reactions that have been studied using carbon materials as catalysts. So far, their scientific and technical impact is lower than that of the reactions described earlier. Therefore, we will not describe each of them in detail, but just highlight a few examples where the active centers were clearly identified.

Catalytic Oxidation of Fe(II) in Aqueous Media A detailed study of this reaction was carried out recently, where the influence of the AC surface chemistry was assessed [211]. Two situations were considered:

1. Fe²⁺ oxidation without O₂. In this case the proposed mechanism was

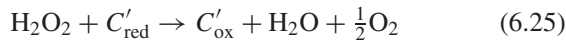
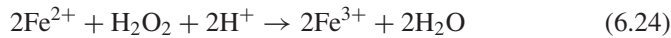
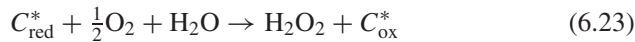


Table 6.2 Other Reactions Catalyzed by Carbons

Reaction or Process	References
Oxidation of Fe(II) in aqueous solution	211, 250–252
Esterification of organic acids	253, 254
Hydrocracking reactions	255–261
Decomposition of dimethyl methylphosphonate	262
Decompositions of hydrazine and hydroxylamine	263, 264
Halogenation and dehalogenation	135, 212–215, 265–270
Selective oxidation	271–279
Oxidation of salts	153
Synthesis of mesoarylporphyrins	280
Oxidative desulfurization	281–283
Knoevenagel condensation	216

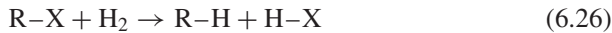
where C'_{ox} represents an oxygen surface group with a redox potential higher than that of the $\text{Fe}^{3+}/\text{Fe}^{2+}$ pair (0.771 V). It was observed that reaction (6.22) occurs only with oxidized activated carbons.

2. Fe^{2+} oxidation in the presence of O_2 . In this case the following reactions may occur:



where C_{red}^* could be quinone or chromene surface groups (redox potential lower than that of the $\text{O}_2/\text{H}_2\text{O}_2$ pair). The hydrogen peroxide generated is then able to oxidize Fe^{2+} directly in solution [reaction (6.24)] or indirectly by reaction (6.25), where oxygen surface groups are regenerated that are able to oxidize $\text{Fe}(\text{II})$ by reaction (6.22).

Hydrodehalogenation Incineration is one of the techniques available for the disposal of halogenated wastes, but incomplete combustion of halogen-containing aromatics can lead to the formation of harmful products such as dioxins. An alternative approach that is receiving increasing attention is hydrodehalogenation:



where X represents halogen. The dehalogenation of chlorinated aromatic compounds can be achieved in the presence of activated carbons at temperatures on the order of 773 K, but rapid deactivation occurs, apparently as a result of coking [212–214]. The role of the surface chemistry of the carbon catalysts was not addressed in any of these papers.

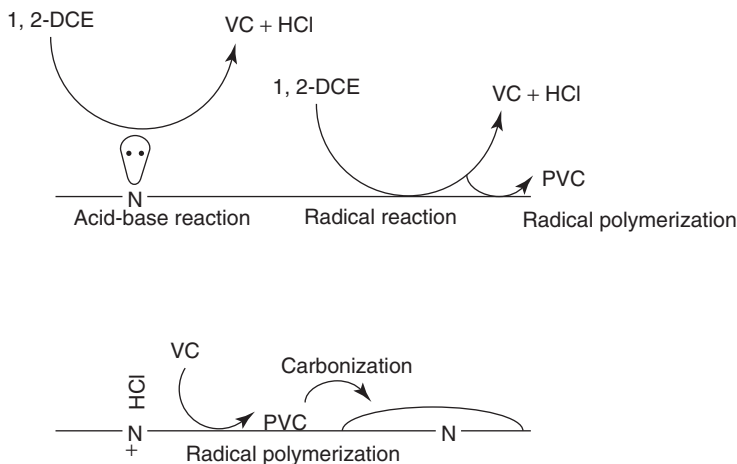


Figure 6.14 Reaction mechanisms proposed for dehydrochlorination and deactivation. (From ref. 215, with permission.)

Another interesting process is the conversion of 1,2-dichloroethane into vinyl chloride, which was shown to be catalyzed by PAN-ACFs at 573 K [215]. The results obtained with a variety of PAN-ACFs suggest that a base-catalyzed reaction occurs on pyridinic nitrogen sites, while a radical reaction is promoted on vacant sites on the ACF surface. The HCl produced deactivates the basic sites, while vinyl chloride polymerization and carbonization leads to coking and deactivation, as shown in Figure 6.14.

Knoevenagel Condensation Van Dommele et al. [216] demonstrated that nitrogen-containing carbon nanotubes (NCNTs) display basic properties and can be used as solid base catalysts. The catalytic activity of the NCNTs was tested in the Knoevenagel condensation of benzaldehyde with ethylcyanoacetate to form ethyl- α -cyanocinnamate, and a strong correlation was obtained between the initial activity and the concentration of pyridinic nitrogen present in the catalyst.

6.4 CONCLUSIONS

The use of carbon as a catalyst was reviewed. It was shown that interesting activity correlations could be obtained by studying the catalytic performance of a series of carbon materials prepared from the same precursor with similar textural properties and different amounts of surface functional groups. The redox couple quinone–hydroquinone was found to be involved in the oxidative dehydrogenation of hydrocarbons, while carboxylic acid groups are the active sites for the dehydration of alcohols. In both cases, thermal treatments at different temperatures were used to identify the nature of the active sites, and correlations

between catalytic activity and the concentration of the corresponding surface groups were established.

Carbon materials have also been used in environmental catalysis for the removal of SO_x , NO_x , and H_2S from gaseous streams. Basic carbons were the most active in these processes, particularly N-doped carbons. Linear correlations between the catalytic activity and the concentration of pyridinic groups were reported in the oxidation of SO_2 and in the selective catalytic reduction of NO with ammonia.

The oxidation of organic compounds in liquid effluents is another environmental application of carbon catalysts, using air, oxygen, ozone, or hydrogen peroxide as oxidants. The reaction mechanisms in the liquid phase are more complex; nevertheless, the following general conclusions can be drawn:

- The reaction mechanisms involve free-radical species.
- Basic carbons are the best catalysts.
- Oxidation of the organic compounds may occur in both the liquid phase (homogeneous reaction) and on the catalyst surface.

From the various processes reviewed in this chapter, it is evident that proper tuning of the surface chemistry of the carbon material can lead to improved catalysts.

Acknowledgments

The authors would like to thank L.R. Radovic for helpful suggestions in the early stages of the preparation of this chapter. J.L.F. also acknowledges FCT grant SFRH/BSAB/500/2005, which financed a sabbatical leave at TU Delft, where a large part of the literature survey for this work was carried out.

REFERENCES

- [1] K.L. Dunlap, in *Kirk-Othmer Encyclopedia of Chemical Technology*, online ed., Wiley, New York, 2001.
- [2] W. Schneider, W. Diller, in *Ullmann's Encyclopedia of Industrial Chemistry*, online ed., Wiley-VCH, Weinheim, Germany, 2002.
- [3] H.-D. Lauss, in *Ullmann's Encyclopedia of Industrial Chemistry*, online ed., Wiley-VCH, Weinheim, Germany, 2002.
- [4] H.F. Rase, *Handbook of Commercial Catalysts: Heterogeneous Catalysts*, CRC Press, Boca Raton, FL, 2000.
- [5] L. Abrams, W.V. Cicha, L.E. Manzer, S. Subramoney, *Stud. Surf. Sci. Catal.* 130 (2000) 455.
- [6] K. Knoblauch, E. Richter, H. Jüntgen, *Fuel* 60 (1981) 832.
- [7] H. Jüntgen, *Erdöl Kohle* 39 (1986) 546.
- [8] E. Richter, K. Knoblauch, H. Jüntgen, *Gas Sep. Purif.* 1 (1987) 35.

- [9] H. Jüntgen, E. Richter, K. Knoblauch, T. Hoang-Phu, *Chem. Eng. Sci.* 43 (1988) 419.
- [10] H. Jüntgen, H. Kühl, in P.A. Thrower, Ed., *Chemistry and Physics of Carbon*, Vol. 21, Marcel Dekker, New York, 1989, p. 145.
- [11] K. Tsuji, I. Shiraishi, *Fuel* 76 (1997) 555.
- [12] R.W. Coughlin, *Ind. Eng. Chem. Prod. Res. Dev.* 8 (1969) 12.
- [13] J.W. Hassler, *Activated Carbon*, Chemical Publishing Company, New York, 1963.
- [14] D.L. Trimm, in C. Kemball, D.A. Dowden, Eds., *Catalysis*, Vol. 4, The Royal Society of Chemistry, London, 1981, p. 210.
- [15] R.C. Bansal, J.B. Donnet, F. Stoeckli, *Active Carbon*, Marcel Dekker, New York, 1988.
- [16] L.R. Radovic, F. Rodríguez-Reinoso, in P.A. Thrower, Ed., *Chemistry and Physics of Carbon*, Vol. 25, Marcel Dekker, New York, 1997, p. 243.
- [17] W. Reimerink, in *Adsorption and Its Applications in Industry and Environmental Protection*, Vol. I, *Applications in Industry*, 1999, p. 751.
- [18] K. Kalra, P. Katyal, K. Singh, *J. Sci. Ind. Res. India* 48 (1989) 186.
- [19] M. Spiro, *Catal. Today* 7 (1990) 167.
- [20] J.S. Noh, J.A. Schwarz, *Carbon* 28 (1990) 675.
- [21] J.L. Figueiredo, M.F.R. Pereira, M.M.A. Freitas, J.J.M. Órfão, *Carbon* 37 (1999) 1379.
- [22] Y. Otake, R.G. Jenkins, *Carbon* 31 (1993) 109.
- [23] R.J.J. Jansen, H. van Bekkum, *Carbon* 32 (1994) 1507.
- [24] P. Vinke, M.v.d. Eijk, M. Verbree, A.F. Voskamp, H. van Bekkum, *Carbon* 32 (1994) 675.
- [25] J.A. Menéndez, J. Phillips, B. Xia, L.R. Radovic, *Langmuir* 12 (1996) 4404.
- [26] C. Moreno-Castilla, F. Carrasco-Marín, F.J. Maldonado-Hódar, J. Rivera-Utrilla, *Carbon* 36 (1998) 145.
- [27] F. Xie, J. Phillips, I.F. Silva, M.C. Palma, J.A. Menéndez, *Carbon* 38 (2000) 691.
- [28] J.B. Donnet, *Carbon* 6 (1968) 161.
- [29] H.P. Boehm, *Carbon* 32 (1994) 759.
- [30] H.P. Boehm, *Carbon* 40 (2002) 145.
- [31] J. Lahaye, *Fuel* 77 (1998) 543.
- [32] E. Fuente, J.A. Menéndez, D. Suárez, M.A. Montes-Morán, *Langmuir* 19 (2003) 3505.
- [33] R.J.J. Jansen, H. van Bekkum, *Carbon* 33 (1995) 1021.
- [34] J.R. Pels, F. Kapteijn, J.A. Moulijn, Q. Zhu, K.M. Thomas, *Carbon* 33 (1995) 1641.
- [35] K. Stanczyk, R. Dziembaj, Z. Piwowarska, S. Witkowski, *Carbon* 33 (1995) 1383.
- [36] H.P. Boehm, H. Knozinger, in J.R. Anderson, Boudart, Eds., *Catalysis: Science and Technology*, Springer-Verlag, Berlin, 1983, p. 39.
- [37] J.L. Figueiredo, M.F.R. Pereira, M.M.A. Freitas, J.J.M. Órfão, *Ind. Eng. Chem. Res.* 46 (2007) 4110.
- [38] G. Barco, A. Maranzana, G. Ghigo, M. Causà, G. Tonachini, *J. Chem. Phys.* 125 (2006).

- [39] H. Muckenhuber, H. Grothe, *Carbon* 44 (2006) 546.
- [40] J.H. Zhou, Z.J. Sui, J. Zhu, P. Li, C. De, Y.C. Dai, W.K. Yuan, *Carbon* 45 (2007) 785.
- [41] J.M. Calo, D. Cazorla-Amorós, A. Linares-Solano, M.C. Román-Martínez, C. Salinas-Martínez de Lecea, *Carbon* 35 (1997) 543.
- [42] J. Manassen, J. Wallach, *J. Am. Chem. Soc.* 87 (1965) 2671.
- [43] I.F. Silva, J. Vital, A.M. Ramos, H. Valente, A.M.B. do Rego, M.J. Reis, *Carbon* 36 (1998) 1159.
- [44] F. Cavani, F. Trifiro, *Appl. Catal. A* 133 (1995) 219.
- [45] T.G. Alkhazov, A.E. Lisovskii, *Kinet. Catal.* 17 (1976) 434.
- [46] G. Emig, H. Hofmann, *J. Catal.* 182 (1983) 15.
- [47] A. Schraut, G. Emig, H.-G. Sockel, *Appl. Catal.* 29 (1987) 311.
- [48] L.E. Cadus, L.A. Arrua, O.F. Gorri, J.B. Rivarola, *Ind. Eng. Chem. Res.* 27 (1988) 2241.
- [49] G.E. Vrieland, P.G. Menon, *Appl. Catal.* 77 (1991) 1.
- [50] A.E. Lisovskii, C. Aharoni, *Catal. Rev. Sci. Eng.* 36 (1994) 25.
- [51] Y. Iwasawa, H. Nobe, S. Ogasawara, *J. Catal.* 31 (1973) 444.
- [52] P.N. Degannes, D.M. Ruthven, *Can. J. Chem. Eng.* 57 (1979) 627.
- [53] T.G. Alkhazov, A.E. Lisovskii, Y.A. Ismailov, A.I. Kozharov, *Kinet. Catal.* 19 (1978) 482.
- [54] C.S. Lee, U.S. patent 4,652,690, 1987, to Mobil Oil Corporation.
- [55] G.C. Grunewald, R.S. Drago, *J. Mol. Catal.* 58 (1990) 227.
- [56] R.S. Drago, K. Jurczyk, *Appl. Catal. A* 112 (1994) 117.
- [57] A. Guerrero-Ruiz, I. Rodríguez-Ramos, *Carbon* 32 (1994) 23.
- [58] M.S. Kane, L.C. Kao, R.K. Mariwala, D.F. Hilscher, H.C. Foley, *Ind. Eng. Chem. Res.* 35 (1996) 3319.
- [59] M.F.R. Pereira, J.J.M. Órfão, J.L. Figueiredo, *Carbon* 40 (2002) 2393.
- [60] M.F.R. Pereira, J.J.M. Órfão, J.L. Figueiredo, *Colloid Surf. A* 241 (2004) 165.
- [61] M.F.R. Pereira, J.J.M. Órfão, J.L. Figueiredo, *Appl. Catal. A* 218 (2001) 307.
- [62] M.F.R. Pereira, J.J.M. Órfão, J.L. Figueiredo, *Appl. Catal. A* 184 (1999) 153.
- [63] M.F.R. Pereira, J.J.M. Órfão, J.L. Figueiredo, *Appl. Catal. A* 196 (2000) 43.
- [64] A. Schraut, G. Emig, H. Hofmann, *J. Catal.* 112 (1988) 221.
- [65] J.A. Maciá-Agulló, D. Cazorla-Amorós, A. Linares-Solano, U. Wild, D.S. Su, R. Schlögl, *Catal. Today* 102–103 (2005) 248.
- [66] P. Serp, M. Corrias, P. Kalck, *Appl. Catal. A* 253 (2003) 337.
- [67] N. Maksimova, G. Mestl, R. Schlögl, in G.F. Froment, K.C. Waugh, Eds., *Studies in Surface Science and Catalysis*, Vol. 133, Elsevier Science, Amsterdam, 2001, p. 383.
- [68] G. Mestl, N.I. Maksimova, N. Keller, V.V. Roddatis, R. Schlögl, *Angew. Chem. Int. Ed.* 40 (2001) 2066.
- [69] N. Keller, N.I. Maksimova, V.V. Roddatis, M. Schur, G. Mestl, Y.V. Butenko, V.L. Kuznetsov, R. Schlögl, *Angew. Chem. Int. Ed.* 41 (2002) 1885.
- [70] D.S. Su, N. Maksimova, J.J. Delgado, N. Keller, G. Mestl, M.J. Ledoux, R. Schlögl, *Catal. Today* 102–103 (2005) 110.

- [71] J.J. Delgado, D.S. Su, G. Rebmann, N. Keller, A. Gajovic, R. Schlögl, *J. Catal.* 244 (2006) 126.
- [72] J.J. Delgado, R. Vieira, G. Rebmann, D.S. Su, N. Keller, M.J. Ledoux, R. Schlögl, *Carbon* 44 (2006) 809.
- [73] T.J. Zhao, W.Z. Sun, X.Y. Gu, M. Ronning, D. Chen, Y.C. Dai, W.K. Yuan, A. Holmen, *Appl. Catal. A* 323 (2007) 135.
- [74] M.F.R. Pereira, J.L. Figueiredo, J.M. Órfão, P. Serp, P. Kalck, Y. Kihn, *Carbon* 42 (2004) 2807.
- [75] Z.J. Sui, J.H. Zhou, Y.C. Dai, W.K. Yuan, *Catal. Today* 106 (2005) 90.
- [76] J.D.D. Velasquez, L.A.C. Suarez, J.L. Figueiredo, *Appl. Catal. A* 311 (2006) 51.
- [77] G.C. Grunewald, R.S. Drago, *J. Am. Chem. Soc.* 113 (1991) 1636.
- [78] G.S. Szymanski, Z. Karpinski, S. Biniak, A. Swiatkowski, *Carbon* 40 (2002) 2627.
- [79] G.S. Szymanski, G. Rychlicki, *Carbon* 29 (1991) 489.
- [80] G.S. Szymanski, G. Rychlicki, *Carbon* 31 (1993) 247.
- [81] G.S. Szymanski, G. Rychlicki, A.P. Terzyk, *Carbon* 32 (1994) 265.
- [82] C. Moreno-Castilla, F. Carrasco-Marín, C. Parejo-Perez, M.V.L. Ramon, *Carbon* 39 (2001) 869.
- [83] F. Carrasco-Marín, A. Mueden, C. Moreno-Castilla, *J. Phys. Chem. B* 102 (1998) 9239.
- [84] J. Zawadzki, M. Wisniewski, J. Weber, O. Heintz, B. Azambre, *Carbon* 39 (2001) 187.
- [85] I. Mochida, Y. Korai, M. Shirahama, S. Kawano, T. Hada, Y. Seo, M. Yoshikawa, A. Yasutake, *Carbon* 38 (2000) 227.
- [86] P. Davini, *Fuel* 68 (1989) 145.
- [87] P. Davini, *Carbon* 28 (1990) 565.
- [88] S. Kisamori, K. Kuroda, S. Kawano, I. Mochida, Y. Matsumura, M. Yoshikawa, *Energy Fuels* 8 (1994) 1337.
- [89] S. Kisamori, I. Mochida, H. Fujitsu, *Langmuir* 10 (1994) 1241.
- [90] J.K. Lee, D.J. Juh, D. Park, *Chem. Eng. Sci.* 49 (1994) 4483.
- [91] S.A. Anurov, *Russ. Chem. Rev.* 65 (1996) 663.
- [92] I. Mochida, K. Kuroda, I. Miyamoto, Y. Korai, S. Kawano, K. Sakanishi, A. Yasutake, M. Yoshikawa, *Energy Fuels* 11 (1997) 272.
- [93] A. Lisovskii, R. Semiat, C. Aharoni, *Carbon* 35 (1997) 1639.
- [94] I. Martín-Gullón, R. Andrews, M. Jagtoyen, F. Derbyshire, *Fuel* 80 (2001) 969.
- [95] M.A. Daley, C.L. Mangun, J.A. DeBarr, S. Riha, A.A. Lizzio, G.L. Donnals, J. Economy, *Carbon* 35 (1997) 411.
- [96] A.A. Lizzio, J.A. DeBarr, *Energy Fuels* 13 (1997) 374.
- [97] L. Ling, K. Li, L. Liu, S. Miyamoto, Y. Korai, S. Kawano, I. Mochida, *Carbon* 37 (1999) 499.
- [98] I. Mochida, S. Miyamoto, K. Kuroda, S. Kawano, K. Sakanishi, Y. Korai, A. Yasutake, M. Yoshikawa, *Energy Fuels* 13 (1999) 374.
- [99] I. Mochida, S. Miyamoto, K. Kuroda, S. Kawano, S. Yatsunami, Y. Korai, A. Yasutake, M. Yoshikawa, *Energy Fuels* 13 (1999) 369.

- [100] E. Raymundo-Piñero, D. Cazorla-Amorós, C. Salinas-Martínez de Lecea, A. Linares-Solano, *Carbon* 38 (2000) 335.
- [101] E. Raymundo-Piñero, D. Cazorla-Amorós, A. Linares-Solano, *Carbon* 39 (2001) 231.
- [102] J. Bimer, P. Satbut, S. Bertozecki, J. Boudou, E. Broniek, T. Siemieniewska, *Fuel* 77 (1998) 519.
- [103] B. Stöhr, H. Boehm, R. Schlögl, *Carbon* 29 (1991) 707.
- [104] K.X. Li, L.C. Ling, C.X. Lu, W.M. Qiao, Z.Y. Liu, L. Liu, I. Mochida, *Carbon* 39 (2001) 1803.
- [105] C.L. Mangun, J.A. DeBarr, J. Economy, *Carbon* 39 (2001) 1689.
- [106] J.P. Boudou, M. Chehimi, E. Broniek, T. Siemieniewska, J. Bimer, *Carbon* 41 (2003) 1999.
- [107] E. Raymundo-Piñero, D. Cazorla-Amorós, A. Linares-Solano, *Carbon* 41 (2003) 1925.
- [108] V.V. Strelko, V.S. Kuts, P.A. Thrower, *Carbon* 38 (2000) 1499.
- [109] M.J. Illán-Gómez, C. Salinas-Martínez de Lecea, A. Linares-Solano, L.R. Radovic, *Energy Fuels* 12 (1998) 1256.
- [110] B. Xia, J. Phillips, C.K. Chen, L.R. Radovic, I.F. Silva, J.A. Menéndez, *Energy Fuels* 13 (1999) 903.
- [111] J.A. Menéndez, J. Phillips, B. Xia, L.R. Radovic, *Langmuir* 12 (1996) 4404.
- [112] S. Matzner, H.P. Boehm, *Carbon* 36 (1998) 1697.
- [113] J. Zawadzki, M. Wisniewski, K. Skowronska, *Carbon* 41 (2003) 235.
- [114] J.N. Armor, *Appl. Catal. B* 1 (1991) 221.
- [115] I. Mochida, M. Ogaki, H. Fujitsu, Y. Komatsubara, S. Ida, *Fuel* 62 (1983) 867.
- [116] S.N. Ahmed, J. Stencel, F. Derbyshire, R. Baldwin, *Fuel Process. Tech.* 34 (1993) 123.
- [117] T. Suzuki, T. Kyotani, A. Tomita, *Ind. Eng. Chem. Res.* 33 (1994) 2840.
- [118] S.N. Ahmed, R. Baldwin, F. Derbyshire, B. McEnaney, J. Stencel, *Fuel* 72 (1993) 287.
- [119] B.J. Ku, J.K. Lee, D. Park, H.-K. Rhee, *Ind. Eng. Chem. Res.* 33 (1994) 2868.
- [120] Y. Komatsubara, S. Ida, H. Fujitsu, I. Mochida, *Fuel* 63 (1984) 1738.
- [121] H. Kühl, E. Richter, K. Knoblauch, H. Jüntgen, in: *Proceedings of the International Carbon Conference, Carbon'86*, Baden-Baden, Germany, 1986, p. 351.
- [122] L. Singoredjo, F. Kapteijn, J.A. Moulijn, J.M. Martín-Martínez, H.P. Boehm, *Carbon* 31 (1993) 213.
- [123] I. Mochida, M. Ogaki, H. Fujitsu, Y. Komatsubara, S. Ida, *Fuel* 64 (1985) 1054.
- [124] H. Fujitsu, I. Mochida, T.V. Verheyen, G.J. Perry, D.J. Allardice, *Fuel* 72 (1993) 109.
- [125] H. Teng, Y.F. Hsu, Y.T. Tu, *Appl. Catal. B* 20 (1999) 145.
- [126] H.S. Teng, Y.T. Tu, Y.C. Lai, C.C. Lin, *Carbon* 39 (2001) 575.
- [127] J. Muñiz, G. Marban, A.B. Fuertes, *Appl. Catal. B* 27 (2000) 27.
- [128] I. Mochida, S. Kawano, N. Shirahama, T. Enjoji, S.H. Moon, K. Sakanishi, Y. Korai, A. Yasutake, M. Yoshikawa, *Fuel* 80 (2001) 2227.
- [129] M.C. Huang, H.S. Teng, *Carbon* 41 (2003) 951.

- [130] G.S. Szymanski, T. Grzybek, H. Papp, *Catal. Today* 90 (2004) 51.
- [131] I. Mochida, S. Kisamori, M. Hironaka, S. Kawano, Y. Matsumura, M. Yoshikawa, *Energy Fuels* 8 (1994) 1341.
- [132] I. Mochida, Y. Kawabuchi, S. Kawano, Y. Matsumura, M. Yoshikawa, *Fuel* 76 (1997) 543.
- [133] I. Mochida, N. Shirahama, S. Kawano, Y. Korai, A. Yasutake, M. Tanoura, S. Fujii, M. Yoshikawa, *Fuel* 79 (2000) 1713.
- [134] Z.C. Guo, Y.S. Xie, I.Y. Hong, J.Y. Kim, *Energy Conserv. Manag.* 42 (2001) 2005.
- [135] B.R. Puri, B. Kumar, K.C. Kalra, *Indian J. Chem.* 9 (1971) 970.
- [136] O.C. Cariaso, P.L. Walker, Jr., *Carbon* 13 (1975) 233.
- [137] M. Steijns, F. Derkx, A. Verloop, P. Mars, *J. Catal.* 42 (1976) 87.
- [138] K. Hedden, L. Hubber, B.R. Rao, *VDI-Bericht* 253, S. 37/42, VDI-Verlag, Dusseldorf, Germany, 1976.
- [139] J. Klein, K.D. Henning, *Fuel* 63 (1984) 1064.
- [140] S.V. Mikhalovsky, Y.P. Zaitsev, *Carbon* 35 (1997) 1367.
- [141] A. Primavera, A. Trovarelli, P. Andreussi, G. Dolcetti, *Appl. Catal. A* 173 (1998) 185.
- [142] A.K. Dalai, E.L. Tollefson, *Can. J. Chem. Eng.* 76 (1998) 902.
- [143] F. Adib, A. Bagreev, T.J. Bandosz, *Langmuir* 16 (2000) 1980.
- [144] A. Bagreev, T.J. Bandosz, *Carbon* 39 (2001) 2303.
- [145] H. Katoh, I. Kuniyoshi, M. Hirai, M. Shoda, *Appl. Catal. B* 6 (1995) 255.
- [146] X. Wu, A.K. Kercher, V. Schwartz, S.H. Overbury, T.R. Armstrong, *Carbon* 43 (2005) 1087.
- [147] S. Bashkova, F.S. Baker, X.X. Wu, T.R. Armstrong, V. Schwartz, *Carbon* 45 (2007) 1354.
- [148] G.G. Kuvshinov, V.V. Shinkarev, A.M. Glushenkov, M.N. Boyko, D.G. Kuvshinov, *China Particul.* 4 (2006).
- [149] V.V. Shinkarev, V. Fenelonov, G.G. Kuvshinov, *Carbon* 41 (2003) 295.
- [150] J. Firth, F. Watson, *J. Chem. Soc.* (1923) 1750.
- [151] J. Firth, F. Watson, *J. Phys. Chem.* 29 (1925) 987.
- [152] G. Lemoine, *Compt. Rend.* 162 (1916) 729.
- [153] A. King, *J. Chem. Soc.* (1936) 1688.
- [154] R. Smith, *Trans. Faraday Soc.* 62 (1966) 2553.
- [155] B. Puri, K. Kalra, *Carbon* 9 (1971) 313.
- [156] B. Puri, L.R. Sharma, D.D. Singh, *J. Indian Chem. Soc.* 35 (1958) 770.
- [157] L.B. Khalil, B.S. Girgis, T.A.M. Tawfik, *J. Chem. Technol. Biotechnol.* 76 (2001) 1132.
- [158] F. Lucking, H. Koser, M. Jank, A. Ritter, *Water Res.* 32 (1998) 2607.
- [159] H.H. Huang, M.C. Lu, J.N. Chen, C.T. Lee, *Chemosphere* 51 (2003) 935.
- [160] H.H. Huang, M.C. Lu, J.N. Chen, C.T. Lee, *J. Environ. Sci. Health A* 38 (2003) 1233.
- [161] A. Georgi, F.-D. Kopinke, *Appl. Catal. B* 58 (2005) 9.
- [162] L.C.A. Oliveira, C.N. Silva, M.I. Yoshida, R.M. Lago, *Carbon* 42 (2004) 2279.

- [163] V.P. Santos, M.F.R. Pereira, P.C.C. Faria, J.J.M. Órfão, *J. Hazard. Mater.* (2008), doi: 10.1016/j.hazmat.2008.05.090.
- [164] B. Kasprzyk-Hordern, M. Ziólek, J. Nawrocki, *Appl. Catal. B* 46 (2003) 639.
- [165] U. Jans, J. Hoigné, *Ozone Sci. Eng.* 20 (1998) 67.
- [166] P.C.C. Faria, J.J.M. Órfão, M.F.R. Pereira, *Ind. Eng. Chem. Res.* 45 (2006) 2715.
- [167] M. Sánchez-Polo, U. von Gunten, J. Rivera-Utrilla, *Water Res.* 39 (2005) 3189.
- [168] P.M. Alvarez, J.F. Garcia-Araya, F.J. Beltran, I. Giraldez, J. Jaramillo, V. Gómez-Serrano, *Carbon* 44 (2006) 3102.
- [169] J. Rivera-Utrilla, M. Sánchez-Polo, *Appl. Catal. B* 39 (2002) 319.
- [170] M.D. Gurol, P.C. Singer, *Environ. Sci. Technol.* 16 (1982) 377.
- [171] J. Rivera-Utrilla, M. Sánchez-Polo, *Langmuir* 20 (2004) 9217.
- [172] J. Staehelin, J. Hoigné, *Environ. Sci. Technol.* 16 (1982) 676.
- [173] M. Guiza, A. Ouederni, A. Ratel, *Ozone Sci. Eng.* 26 (2004) 299.
- [174] F.J. Beltran, F.J. Rivas, L.A. Fernandez, P.M. Alvarez, R. Montero-de-Espinosa, *Ind. Eng. Chem. Res.* 41 (2002) 6510.
- [175] P.C.C. Faria, J.J.M. Órfão, M.F.R. Pereira, *Appl. Catal. B* 79 (2008) 237.
- [176] F.J. Beltran, J.F. Garcia-Araya, I. Giraldez, *Appl. Catal. B* 63 (2006) 249.
- [177] F.J. Beltran, J.F. Garcia-Araya, I. Giraldez, F.J. Masa, *Ind. Eng. Chem. Res.* 45 (2006) 3015.
- [178] F.J. Beltran, B. Acedo, F.J. Rivas, O. Gimeno, *Ozone Sci. Eng.* 27 (2005) 159.
- [179] A. Sánchez-Polo, J. Rivera-Utrilla, *Carbon* 41 (2003) 303.
- [180] M. Sánchez-Polo, R. Leyva-Ramos, J. Rivera-Utrilla, *Carbon* 43 (2005) 962.
- [181] M. Sánchez-Polo, J. Rivera-Utrilla, *Appl. Catal. B* 67 (2006) 113.
- [182] C.A. Zaror, *J. Chem. Technol. Biotechnol.* 70 (1997) 21.
- [183] I. Polaert, A.M. Wilhelm, H. Delmas, *Chem. Eng. Sci.* 57 (2002) 1585.
- [184] S.H. Lin, C.H. Wang, *Ind. Eng. Chem. Res.* 42 (2003) 1648.
- [185] X. Qu, J. Zheng, Y. Zhang, *J. Colloid Interface Sci.* 309 (2007) 429.
- [186] F.J. Beltran, F.J. Rivas, R. Monte-de-Espinosa, *J. Chem. Technol. Biotechnol.* 78 (2003) 1225.
- [187] J. Ma, M.H. Sui, Z.L. Chen, L.N. Wang, *Ozone Sci. Eng.* 26 (2004) 3.
- [188] P.C.C. Faria, J.J.M. Órfão, M.F.R. Pereira, *Chemosphere* 67 (2007) 809.
- [189] J.D. Mendez-Diaz, M. Sánchez-Polo, J. Rivera-Utrilla, I. Bautista-Toledo, M.A. Ferro-Garcia, *Carbon* 43 (2005) 3031.
- [190] J. Rivera-Utrilla, J. Mendez-Diaz, M. Sánchez-Polo, M.A. Ferro-Garcia, I. Bautista-Toledo, *Water Res.* 40 (2006) 1717.
- [191] P.C.C. Faria, J.J.M. Órfão, M.F.R. Pereira, *Water Res.* 39 (2005) 1461.
- [192] I. Arslan-Alaton, *AATCC Rev.* 4 (2004) 21.
- [193] I. Arslan-Alaton, O. Seremet, *J. Environ. Sci. Health A* 39 (2004) 1681.
- [194] S.H. Lin, C.L. Lai, *Water Res.* 34 (2000) 763.
- [195] G. McKay, G. McAleavy, *Chem. Eng. Res. Des.* 66 (1988) 531.
- [196] M.M. Hassan, C.J. Hawkyard, *J. Chem. Technol. Biotechnol.* 81 (2006) 201.
- [197] O. S.G.P. Soares, P.C.C. Faria, J.J.M. Órfão, M.F.R. Pereira, *Sep. Sci. Technol.* 42 (2007) 1477.

- [198] F. Stuber, J. Font, A. Fortuny, C. Bengoa, A. Eftaxias, A. Fabregat, *Top. Catal.* 33 (2005) 3.
- [199] A. Fortuny, J. Font, A. Fabregat, *Appl. Catal. B* 19 (1998) 165.
- [200] V. Tukac, J. Hanika, *J. Chem. Technol. Biotechnol.* 71 (1998) 262.
- [201] A. Santos, P. Yustos, S. Rodriguez, F. Garcia-Ochoa, *Appl. Catal. B* 65 (2006) 269.
- [202] A. Fortuny, C. Miro, J. Font, A. Fabregat, *Catal. Today* 48 (1999) 323.
- [203] M. Santiago, F. Stuber, A. Fortuny, A. Fabregat, J. Font, *Carbon* 43 (2005) 2134.
- [204] A. Santos, P. Yustos, S. Gomis, G. Ruiz, F. Garcia-Ochoa, *Ind. Eng. Chem. Res.* 44 (2005) 3869.
- [205] A. Santos, P. Yustos, S. Gomis, G. Ruiz, F. Garcia-Ochoa, *Chem. Eng. Sci.* 61 (2006) 2457.
- [206] A.E. Suarez-Ojeda, F. Stuber, A. Fortuny, A. Fabregat, J. Carrera, J. Font, *Appl. Catal. B* 58 (2005) 105.
- [207] C. Aguilar, R. Garcia, G. Soto-Garrido, R. Arriagada, *Appl. Catal. B* 46 (2003) 229.
- [208] C. Aguilar, R. Garcia, G. Soto-Garrido, R. Arraigada, *Top. Catal.* 33 (2005) 201.
- [209] A. Santos, P. Yustos, S. Rodriguez, F. Garcia-Ochoa, M. de Gracia, *Ind. Eng. Chem. Res.* 46 (2007) 2423.
- [210] H.T. Gomes, B.F. Machado, A. Ribeiro, I. Moreira, M. Rosário, A.M.T. Silva, J.L. Figueiredo, J.L. Faria, *J. Hazard. Mater.* (2008), doi: 10.1016/j.jhazmat.2008.02.070.
- [211] E. Ahumada, H. Lizama, F. Orellana, C. Suarez, A. Huidobro, A. Sepúlveda-Escribano, F. Rodríguez-Reinoso, *Carbon* 40 (2002) 2827.
- [212] I. W.C.E. Arends, W.R. Ophorst, R. Louw, P. Mulder, *Carbon* 34 (1996) 581.
- [213] D. Santoro, R. Louw, *Carbon* 39 (2001) 2091.
- [214] D. Santoro, V. de Jong, R. Louw, *Chemosphere* 50 (2003) 1255.
- [215] C. Sotowa, Y. Watanabe, S. Yatsunami, Y. Korai, I. Mochida, *Appl. Catal. A* 180 (1999) 317.
- [216] S. van Dommele, K.P. de Jong, J.H. Bitter, *Chem. Commun.* (2006) 4859.
- [217] T.G. Alkhazov, A.E. Lisovskii, T.K. Gulakhmedova, *React. Kinet. Catal. Lett.* 12 (1979) 189.
- [218] R.H. Allen, T.J. Alfrey, L.D. Yats, U.S. patent 3,497,564, 1970, to The Dow Chemical Company.
- [219] P.N. Degannes, D.M. Ruthven, *Can. J. Chem. Eng.* 57 (1979) 627.
- [220] A.E. Lisovskii, A.I. Kozharov, Y.A. Ismailov, T.G. Alkhazov, *Kinet. Catal.* 19 (1979) 760.
- [221] F.J. Maldonado-Hódar, L.M. Madeira, M.F. Portela, *Appl. Catal. A* 178 (1999) 49.
- [222] P. Li, T. Li, J.H. Zhou, Z.J. Sui, Y.C. Dai, W.K. Yuan, D. Chen, *Micropor. Mesopor. Mater.* 95 (2006) 1.
- [223] L. Wang, J. Zhang, D.S. Su, Y. Ji, X. Cao, F.-S. Xiao, *Chem. Mater.* 19 (2007) 2894.
- [224] G.S. Szymanski, G. Rychlicki, *React. Kinet. Catal. Lett.* 43 (1991) 475.
- [225] H. Amano, S. Sato, R. Takahashi, T. Sodesawa, *Phys. Chem. Chem. Phys.* 3 (2001) 873.

- [226] M.J. Illán-Gómez, A. Linares-Solano, L.R. Radovic, C. Salinas-Martínez de Lecea, *Energy Fuels* 10 (1996) 158.
- [227] M.J. Illán-Gómez, A. Linares-Solano, C. Salinas-Martínez de Lecea, J.M. Calo, *Energy Fuels* 7 (1993) 146.
- [228] V.V. Kislykh, A.E. Sidelnikov, *Kinet. Catal.* 16 (1975) 664.
- [229] I. Mochida, M. Ogaki, H. Fujitsu, Y. Komatsubara, S. Ida, *Nippon Kagaku Kaishi* 4 (1985) 680.
- [230] N. Shirahama, S.H. Moon, K.H. Choi, T. Enjoji, S. Kawano, Y. Korai, M. Tanoura, I. Mochida, *Carbon* 40 (2002) 2605.
- [231] J. Zawadzki, M. Wisniewski, *Carbon* 40 (2002) 119.
- [232] S. Biniak, J. Siedlewski, *Przem. Chem.* 65 (1986) 318.
- [233] R.A. Hayden, U.S. patent 5,352,370, 1994, to Calgon Carbon Corporation.
- [234] J.K. Lee, R.R. Hudgins, P.L. Silveston, *Environ. Prog.* 15 (1996) 239.
- [235] E.B.M. Medeiros, M. Petrisans, A. Wehrer, A. Zoulalian, *Chem. Eng. Process.* 40 (2001) 153.
- [236] E. Raymundo-Piñero, D. Cazorla-Amorós, E. Morallon, *J. Chem. Educ.* 76 (1999) 958.
- [237] A. Bagreev, S. Bashkova, D.C. Locke, T.J. Bandosz, *Environ. Sci. Technol.* 35 (2001) 1537.
- [238] A.K. Dalai, A. Majumdar, E.L. Tollefson, *Environ. Sci. Technol.* 33 (1999) 2241.
- [239] T.J. Bandosz, A. Bagreev, F. Adib, A. Turk, *Environ. Sci. Technol.* 34 (2000) 1069.
- [240] F.J. Beltran, J. Rivas, P. Alvarez, R. Montero-de-Espinosa, *Ozone Sci. Eng.* 24 (2002) 227.
- [241] S.H. Lin, C.H. Wang, *Environ. Technol.* 24 (2003) 1031.
- [242] J. Rivera-Utrilla, M. Sánchez-Polo, *Water Resour. Res.* 39 (2003) 1232.
- [243] J. Rivera-Utrilla, M. Sánchez-Polo, M.A. Mondaca, C.A. Zaror, *J. Chem. Technol. Biotechnol.* 77 (2002) 883.
- [244] M. Sánchez-Polo, E. Salhi, J. Rivera-Utrilla, U. von Gunten, *Ozone Sci. Eng.* 28 (2006) 237.
- [245] F. Stuber, I. Polaert, H. Delmas, J. Font, A. Fortuny, A. Fabregat, *J. Chem. Technol. Biotechnol.* 76 (2001) 743.
- [246] G.K. Vasilyeva, V.D. Kreslavski, P.J. Shea, *Chemosphere* 47 (2002) 311.
- [247] T. Nunoura, G. Lee, Y. Matsumura, K. Yamamoto, *Ind. Eng. Chem. Res.* 42 (2003) 3522.
- [248] T. Nunoura, G. Lee, Y. Matsumura, K. Yamamoto, *Ind. Eng. Chem. Res.* 42 (2003) 3718.
- [249] T. Nunoura, G.H. Lee, Y. Matsumura, K. Yamamoto, *Chem. Eng. Sci.* 57 (2002) 3061.
- [250] N.I. Kuznetsova, V.A. Likholobov, M. Gurrath, H.P. Boehm, *Appl. Catal. A* 128 (1995) 41.
- [251] A.M. Posner, *Trans. Faraday Soc.* 49 (1953) 389.
- [252] M.R. Ronnholm, J. Warna, T. Salmi, I. Turunen, M. Luoma, *Ind. Eng. Chem. Res.* 38 (1999) 2607.
- [253] D.M. Nevskaia, R.M. Martin-Aranda, *Catal. Lett.* 87 (2003) 143.

- [254] F. Peng, L. Zhang, H.J. Wang, P. Lv, H. Yu, *Carbon* 43 (2005) 2405.
- [255] M. Farcasiu, C. Smith, *Energy Fuels* 5 (1991) 83.
- [256] M. Farcasiu, C.M. Smith, E.P. Ladner, A.P. Sylwester, in *ACS Preprints, Division of Fuel Chemistry*, 1991, p. 1869.
- [257] M. Farcasiu, S.C. Petrosius, P.A. Eldredge, R.R. Anderson, E.P. Ladner, *Energy Fuels* 8 (1994) 920.
- [258] M. Farcasiu, S.C. Petrosius, E.P. Ladner, *J. Catal.* 146 (1994) 313.
- [259] Z.H. Ni, Z.M. Zong, L.F. Zhang, L.B. Sun, Y. Liu, X.H. Yuan, X.Y. Wei, *Energy Fuels* 17 (2003) 60.
- [260] H. Fukuyama, S. Terai, M. Uchida, J.L. Cano, J. Ancheyta, *Catal. Today* 98 (2004) 207.
- [261] L.B. Sun, Z.M. Zong, J.H. Kou, L.F. Zhang, Z.H. Ni, G.Y. Yu, C. Hong, X.Y. Wei, C.W. Lee, *Energy Fuels* 18 (2004) 1500.
- [262] L.X. Cao, S.L. Suib, X. Tang, S. Satyapal, *J. Catal.* 197 (2001) 236.
- [263] J.W. Larsen, J. Jandzinski, M. Sidovar, J.L. Stuart, *Carbon* 39 (2001) 473.
- [264] J.W. Larsen, M. Freund, K.Y. Kim, M. Sidovar, J.L. Stuart, *Carbon* 38 (2000) 655.
- [265] H.P. Boehm, G. Mair, T. Stoehr, A.R. de Rincon, B. Tereczki, *Fuel* 63 (1984) 1061.
- [266] T.A. Ryan, M.H. Stacey, *Fuel* 63 (1984) 1101.
- [267] G. Nicoll, J. Francisco, *Environ. Sci. Technol.* 33 (1999) 4102.
- [268] J.Y. Gan, N.E. Megonnell, S.R. Yates, *Atmos. Environ.* 35 (2001) 941.
- [269] J.R. Kastner, K.C. Das, Q. Buquoi, N.D. Melear, *Environ. Sci. Technol.* 37 (2003) 2568.
- [270] J.R. Kastner, K.C. Das, N.D. Melear, *J. Hazard. Mater.* 95 (2002) 81.
- [271] C. Pinel, E. Landrivon, H. Lini, P. Gallezot, *J. Catal.* 182 (1999) 515.
- [272] J. Barkauskas, A. Kareiva, *React. Kinet. Catal. Lett.* 53 (1994) 7.
- [273] M. Besson, A. Blackburn, P. Gallezot, O. Kozynchenko, A. Pigamo, S. Tennison, *Top. Catal.* 13 (2000) 253.
- [274] A. Pigamo, M. Besson, B. Blanc, P. Gallezot, A. Blackburn, O. Kozynchenko, S. Tennison, E. Crezee, F. Kapteijn, *Carbon* 40 (2002) 1267.
- [275] M. Besson, P. Gallezot, A. Perrard, C. Pinel, *Catal. Today* 102 (2005) 160.
- [276] F. Gauthard, B. Horvath, P. Gallezot, M. Besson, *Appl. Catal. A* 279 (2005) 187.
- [277] M. Croston, J. Langston, R. Sangoi, K.S.V. Santhanam, *Int. J. Nanosci.* 1 (2002) 277.
- [278] M. Croston, J. Langston, G. Takacs, T.C. Morrill, M. Miri, K.S.V. Santhanam, P. Ajayan, *Int. J. Nanosci.* 1 (2002) 285.
- [279] Z. Kang, E. Wang, B. Mao, Z. Su, L. Gao, L. Niu, H. Shan, L. Xu, *Appl. Catal. A* 299 (2006) 212.
- [280] Y. Vignaud, R. Granet, P. Krausz, *J. Porphyr. Phthalocya.* 10 (2006) 937.
- [281] G. Yu, S. Lu, H. Chen, Z. Zhu, *Carbon* 43 (2005) 2285.
- [282] G.X. Yu, S.X. Lu, H. Chen, Z.N. Zhu, *Energy Fuels* 19 (2005) 447.
- [283] R.V.R.A. Rios, J. Silvestre-Albero, A. Sepúlveda-Escribano, F. Rodríguez-Reinoso, *Colloid Surf. A* 300 (2007) 180.

7 Catalytic Properties of Nitrogen-Containing Carbons

HANNS-PETER BOEHM

7.1 INTRODUCTION

It is an interesting property of carbon materials, in particular those with a high surface area, that they can catalyze oxidation reactions with elementary oxygen (see Chapter 6). It is also possible to oxidize hydrogen or methanol on carbon electrodes in electrochemical cells, while oxygen is reduced to water at the carbon cathode in fuel cells [1,2]. In the course of our studies on surface oxides of carbons [3,4], I learned from researchers working on fuel cells that some activated carbons, such as Anthralur, are very good catalysts for the reduction of dioxygen, whereas other activated carbons and carbon blacks are inferior, and acetylene black is “dead.” It came to my mind immediately that oxygen groups bound to the carbon surface might be involved in the differences in catalytic properties. The surface oxides occur in the form of various functional groups, giving rise to acidic, basic, or neutral behavior in contact with aqueous solutions [3–6]. However, a few experiments showed that such an explanation of the differences observed was too simple. It was a lucky coincidence that we began work at this time with the intention of creating a similar surface chemistry with nitrogen-containing functional groups. This task was not as easy as I thought, but we found that all carbons with incorporated nitrogen showed catalytic activity in oxidation reactions involving dioxygen, and that all carbons described as being catalytically active in fuel cells contained some nitrogen. This was the starting point for our research on catalysis by nitrogen-containing carbons.

Evidently, understanding of the reaction mechanisms and the nature of the catalytically active sites is of considerable importance for possible practical applications. Interest in carbon-catalyzed oxidation reactions and in nitrogen-containing carbons has increased considerably in recent years.

7.2 NITROGEN DOPING OF CARBONS

7.2.1 Preparation of Nitrogen-Containing Carbons

Nitrogen can be chemically bound in or to carbons in several ways. Nitrogen atoms or functional groups containing nitrogen can be bound to edge atoms of the graphene layers analogously to the surface oxides (e.g., in the form of amino or cyano groups). It is also possible, however, that nitrogen atoms are bound substitutionally within the graphene layers or in disordered parts of the carbon structure, containing sp^3 -hybridized carbon atoms. The solubility of nitrogen in well-crystallized graphite is minimal [7], in contrast to the solubility of boron, which is about 1 at%. However, higher nitrogen contents, up to several at%, can be chemically bound in carbons with some structural disorder, such as activated carbons.

Nitrogen can be introduced in carbons essentially in two ways, either by carbonizing nitrogen-containing organic compounds or mixtures of nitrogen-containing precursors with nitrogen-free materials, or by treatment of carbon materials at high temperatures with nitrogen-containing gases which decompose at these temperatures with generation of highly reactive radicals.

Peat is relatively rich in nitrogen, and activated carbons prepared from peat, such as Anthralur, are quite good catalysts. Activated carbons produced from wood or coal also contain small quantities of nitrogen. A logical step is to carbonize nitrogen-containing organic polymers such as poly(acrylonitrile) (PAN) [8,9]. PAN-based carbon fibers always contain some nitrogen and they exhibit catalytic activity. Other polymers used were a polymer prepared from vinylpyridine and about 10% divinylbenzene or a vinylpyridine resin made from monomers containing pyridinic nitrogen and methylpyridinium groups cross-linked with divinylbenzene [10,11]. Nitrogen-containing carbon films were also obtained by carbonization of films of Kevlar, a poly(*p*-phenylene terephthalamide) [12], Nomex, a poly(*m*-phenylene isophthalamide) [13] or Kapton, a polyimide [14] (see Figure 7.1). Melamine-formaldehyde resin is very rich in nitrogen, and chars and carbons produced by pyrolysis retain a high nitrogen content at high temperatures. With commercial melamine foam, 13% N was found after decomposition at 1273 K, and about 5% at 1473 K [15].

A simple way to produce polymers with specific nitrogen functions in controlled concentration is to prepare phenol-formaldehyde resins in which part of the phenol is substituted by aniline (for amine-type nitrogen) or 3-hydroxypyridine (for pyridine-type nitrogen) or tyrosine (for both types of nitrogen) [16–18] (see Figure 7.2). The main advantage of using polymers as carbon precursors is that the added nitrogen is homogeneously distributed.

Another, frequently used method of obtaining nitrogen-doped carbons is to calcine nitrogen-containing molecular organic compounds under inert conditions. Control of the nitrogen content of the resulting carbons can be achieved when the nitrogen compound is mixed with a nitrogen-free organic precursor (e.g., sugar, sucrose) as a cheap commercial product of high purity. Nitrogen was

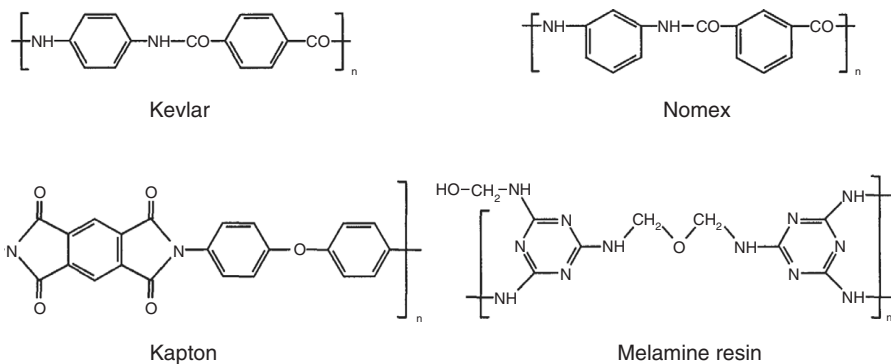


Figure 7.1 Chemical structures of the polymers Kapton, Kevlar, Nomex, and melamine resin.

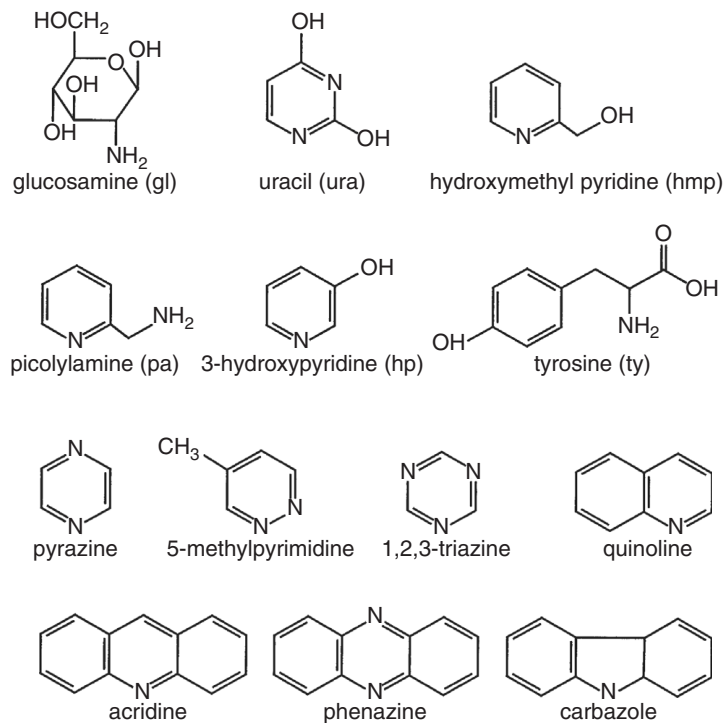


Figure 7.2 Structures of various organic compounds mentioned in this chapter.

introduced in the form of glucosamine hydrochloride, uracil, picolylamine, or hydroxymethylpyridine (see Figure 7.2 for formulas) [19,20]. Sugar has the advantage that it melts to a viscous liquid at relatively low temperatures and that the nitrogen compounds can easily be distributed homogeneously. On further heating, the sugar decomposes to a char (a fume hood is advised because the reaction is quite smelly). The char obtained at 623 to 673 K can be ground to a fine powder. Complete carbonization is achieved by heat treatment at 1273 to 1373 K, followed by activation with steam or CO₂ at 1123 K. The nitrogen content of the carbonized materials depended not only on the quantity of additive, but also on its nature. A relatively larger fraction of the added nitrogen was found in the carbons for smaller quantities of additive [20,21]. Surprisingly, the additive used had an effect on the texture of the carbons; some felt hard and gritty between the fingers, whereas others were soft [20]. The nitrogen-doped carbons had a moderately larger micropore volume than corresponding undoped activated carbons. Mainly narrow micropores are produced in the activation process, especially when CO₂ is used. Similar in principle is the addition of a melamine resin (see Figure 7.1) to a petroleum pitch with a low softening point. This mixture was heated to 623 K and then spun to fibers at about 473 K. After stabilization in air at 573 K for 12 hours, the fibers were carbonized at 1273 K and then activated with CO₂ at 1123 K to prepare nitrogen-containing activated carbon fibers [22].

The carbonization of pure organic compounds such as carbazole, phenazine, acridine (for formulas, see Figure 7.2) has also been studied under 7.5 Mbar argon pressure [23]. Volatile compounds such as benzene, pyridine, pyrazine, quinoline, and phenazine have been calcined at 1073 K in sealed quartz glass tubes [24]. Bent carbon nanotubes and coils with a nitrogen content of about 1% were formed when pyridine, 5-methylpyrimidine, or *s*-triazine (see Figure 7.2) were decomposed on small catalytic cobalt particles at 1123 or 1373 K [25]. Carbon nanotubes with about 2% N were produced in excellent yield and free of other carbon materials by pyrolysis of pyridine vapor at 1373 K in an argon stream with admixed iron pentacarbonyl, [Fe(CO)₅] [26]. In another study, pyrrole vapor has been catalytically decomposed on nickel sheets at 1073 K [27].

Chemical vapor deposition (CVD) has been used to obtain deposits of nitrogen-containing carbon on the surface of other carbon materials. A helium stream with an added aromatic compound such as benzene [28] or pyridine [29] was passed over a commercial activated pitch-based carbon fiber (ACF) with slit-shaped pores. Under the right conditions of flow, concentration, and temperature, the aromatic compounds were decomposed only on the walls of the pores. The aromatic molecules are adsorbed preferentially on the carbon basal planes and rapidly condense to nonvolatile products, and finally, to pyrocarbon layers on the pore walls. This does not happen on the external surface of the ACF because under the flow conditions the residence time of the adsorbed molecules is too short for carbonization to occur. The weight increase was linear with time but terminated abruptly at a value of about 110 mg/g when pyrolysis stopped because the pores had narrowed to a width smaller than the thickness

of a benzene or pyridine molecule (0.37 nm). This deposition was performed at 1073 K for benzene [28], at 998 K for pyridine, and at 973 K for pyrrole [29]. The molecules of these compounds are stable in the gas phase under these conditions. The pore walls were covered by a carbon deposit containing 2.6 or 2.4% nitrogen, respectively. At the end of deposition, a thin slit remained of the original pores which allowed adsorption of small molecules (e.g., CO₂) but excluded molecules larger than 0.37 nm (e.g., methane). Nitrogen and oxygen can be separated on this material by the pressure swing method [29].

A similar procedure was used to introduce nitrogen impurities into the pore walls of ACF by treating them with pyridine in a helium stream at 973 to 1273 K, with the intention of producing hydrophilic sites [30]. The nitrogen content of the samples reached a maximum of 4.4% at a deposition temperature of 1123 K. X-ray photoelectron spectroscopy (XPS) measurements of the fixed nitrogen is discussed in Section 7.2.3. The nitrogen doping of the pore walls had a distinct influence on the adsorption behavior toward water [31]. The adsorption capacity decreased with increasing deposition temperature (1023 K and 1173 K), much more than that for N₂. When carbon was deposited under identical conditions from vapors of pyridine, aniline, or pyrrole on a strongly acidic catalyst for fluid catalytic cracking, the highest nitrogen content was obtained with aniline, which is the most basic of the precursor compounds [32].

An interesting mesoporous nitrogen-doped carbon material was prepared by pyrolysis of acetonitrile on the pore walls of a mesoporous silica template (SBA-15) [33]. The silica was exposed at 1123 to 1273 K to a nitrogen stream saturated with acetonitrile at room temperature. After deposition, the silica matrix was dissolved with hydrofluoric acid. The structure of the remaining carbon was better ordered the higher the deposition temperature was up to 1273 K. At this deposition temperature, well-developed two-dimensional (10) and (11) peaks of turbostratic carbon appeared in x-ray diffraction. The (002) diffraction line was surprisingly sharp for a carbon prepared at 1273 K. The carbon structure was more disordered at higher temperatures. The diffractograms also showed lines at small diffraction angles due to the trigonal packing of carbon rods resulting from the arrangement of the original cylindrical pores in the silica. A carbon rod diameter of 7 nm and a mutual separation of 2.5 to 3 nm was estimated from transmission electron microscopy (TEM). The material prepared at 1273 K showed relatively thin spherical shells in scanning electron microscopy (SEM), indicating that the acetonitrile could penetrate only a short distance into the SBA 15 spheres before it was completely decomposed. The nitrogen content of the deposited carbon was 8 to 9 wt%. These studies were extended to other mesoporous silica templates [34]. While the crystallinity of the carbon increased with increasing deposition temperature up to 1173 K, the mesostructural order decreased when this temperature was exceeded. Such mesoporous carbons might be of interest as catalysts or catalyst supports.

An early and frequently used method for nitrogen doping was the treatment of activated carbons with ammonia at high temperatures (e.g., 873 to 1173 K)

[35–41]. At these temperatures ammonia decomposes, especially in contact with solid surfaces, to H^\bullet , NH_2^\bullet , $\text{NH}^{\bullet\bullet}$, and finally, to H_2 and N_2 . The free radicals attack the carbon surface, as evidenced by mass-spectrometric detection of CH_4 , HCN , and $(\text{CN})_2$ in the gas phase [40]. At the same time, nitrogen species are bound on the carbon surface. The production of CH_4 , HCN , and $(\text{CN})_2$ leads to a loss of carbon (i.e., activation of the carbon materials). The increase in micropore volume becomes significant at 1173 K. Activation with ammonia and its effect on the pore structure of carbons has been described repeatedly in recent years [42–44].

When activated carbons were regenerated with steam, CO_2 , or NH_3 at 873 to 1073 K after adsorption of perchlorate ions, the rate of mass loss was higher with H_2O than with CO_2 or NH_3 as the activating gas. The nitrogen content of an activated carbon doped beforehand by NH_3 treatment at 973 K decreased much more in further gasification with steam than when CO_2 or NH_3 were used as the activating agent [45].

More nitrogen is bound by the carbons when they are heated to reaction temperature and cooled after reaction under ammonia than when the heating and cooling is performed under an inert gas [46–48]. A significant increase in nitrogen content was observed when nitrogen-containing activated carbons from sucrose were treated additionally with NH_3 at 1173 K, but only when the nitrogen content was lower than about 1000 $\mu\text{mol/g}$. The relative increase was higher the smaller the original nitrogen content. At higher nitrogen content, the nitrogen content decreased. [49]. One hour was sufficient for the ammonia treatments; there was not much change at longer times. When the carbons were heated to 1173 K under nitrogen instead, there was a significant decrease in the nitrogen content (by 5.3 to 11.4%) in the case of carbons prepared with glucosamine hydrochloride, whereas with carbons prepared with uracil additions, a small increase of 0.4 to 4.3% was observed [49]. A possible cause for such small increases is discussed below.

Of course, in this preparation of nitrogen-doped carbons, the ammonia can be mixed with water vapor [50] or with oxygen [51]. Ammoniation with ammonia–oxygen mixtures is very effective. It can be performed at quite low temperatures of 473 to 693 K [51–54]. Materials of a low degree of carbonization such as wood chars or lignites are particularly well suited because structural imperfections and aliphatic side chains are preferred sites of attack. Various functional nitrogen groups are formed on the chars' surface (e.g., lactams, imides, amides). At higher temperatures, carbonization proceeds and considerable parts of the nitrogen are converted to species that are part of the aromatic system (see Section 7.2.3). Subsequent activation with steam or CO_2 leads to nitrogen-doped activated carbons.

Nitrogen can also be introduced into carbons by heating with hydrogen cyanide (HCN) [55,56] or cyanogen gas (NC–CN) [47,55]. The quantity introduced is smaller than when NH_3 is used, especially in the case of $(\text{CN})_2$. Otherwise, the results are very similar.

Another way of doping activated carbons is by impregnating them with solutions of nitrogen-containing compounds, drying them, and heating them under

an inert gas to high temperatures. Urea has been used with good success by Rideal and Wright [57] and by other authors more recently [58,59]. A commercial activated carbon, Centaur, is produced in this way [58]. The production of catalytically active carbons by carbonization and oxidation of bituminous coal or a similar material, cooling and impregnation with a solution of urea, melamine, or other nitrogen-containing compounds, and heating to at least 973 K have been described in a series of patents [60,61]. The resulting material can, if necessary, be further activated with water vapor. In a similar reaction, a lignite was heated with urea to 773 K in an autoclave, and finally carbonized at 1073 K and steam-activated at this temperature [62].

An interesting observation was made when activated carbons, prepared from sucrose with an addition of uracil and activated with CO₂ at 1123 K, were subsequently heated to 1173 K under nitrogen. The nitrogen contents increased consistently by 10 to 20 µmol/g [49]. Unexpectedly, a high nitrogen content was also described for an activated carbon, carbonized under nitrogen at 1175 K, and subsequently activated with CO₂ at the same temperature. The nitrogen content was considerably lower when the carbonization step was performed under argon [63]. Experiments were performed in the present author's laboratory for verification using a carbon from phenol-formaldehyde resin [64]. The resin was heat-treated under nitrogen at temperatures up to 1473 K. It had a small nitrogen content originating from nitrogen contamination of the phenol used. The N content of the chars was 19 ± 1 µmol/g after heating to 873 to 1173 K, but increased to 29 µmol/g at 1273 K, 37 µmol/g at 1373 K, and 41 µmol/g at 1473 K. At the same time, the BET surface area increased from 149 m²/g to 220 m²/g, indicating a small degree of porosity.

Reaction of dinitrogen with carbon at such relatively low temperatures was surprising. To check this observation, chars heat-treated at 673, 873, and 1073 K were activated at 683 K with 20% O₂ in Ar to a burn-off of 25 to 32%. The activated materials were submitted to a heat treatment series under either nitrogen or argon. Table 7.1 demonstrates that the nitrogen content increased at high temperatures under nitrogen, but not under argon [64].

Analogous results are shown in Figure 7.3 for an activated carbon from sugar char heated under N₂ or Ar. The carbons activated with oxygen carried large quantities of oxygen complexes on their surface. It is conceivable that nitrogen molecules reacted with the free-radical sites formed in decomposition of the surface oxides and remaining C-H bonds. It seems also possible that HCN was formed, which is known to react at these temperatures with carbon surfaces with incorporation of nitrogen [40,55]. Unfortunately, it was not possible to characterize the bound nitrogen by XPS. These experiments show that nitrogen contamination from gaseous nitrogen is possible at about 1273 K. It is small, however, and will be negligible in most cases.

Finally, a significant increase in surface nitrogen content has been observed when low-modulus PAN-based carbon fibers were anodically oxidized in an aqueous ammonium hydrogen carbonate electrolyte [65].

Table 7.1 Development of Nitrogen Content of Activated Chars from Phenol–Formaldehyde Resin on Heat Treatment (5 Hours) Under N₂ and Ar^a

Sample ^b	Heat Treatment Temperature (K)	Heat Treatment Under N		Heat Treatment Under Ar	
		Surface Area (m ² /g)	N Content (μmol/g)	Surface Area (m ² /g)	N Content (μmol/g)
P-873-act					
	No HT ^c	405	26	405	26
	773	621	13	642	17
	973	673	15	665	13
	1173	669	21	652	16
	1373	621	47	629	16
P-1073-act					
	No HT	701	23	701	23
	773	790	15	808	13
	973	892	20	870	14
	1173	871	37	842	15
	1373	867	90	832	14

^aThe chars were heat-treated at 673 K, 873K, and 1073 K and subsequently activated at 683 K with 20% O₂/Ar to a burn-off of 25 to 32%.

^bP-673-act, phenol resin, carbonized at 673 K, activated.

^cHT, heat treatment.

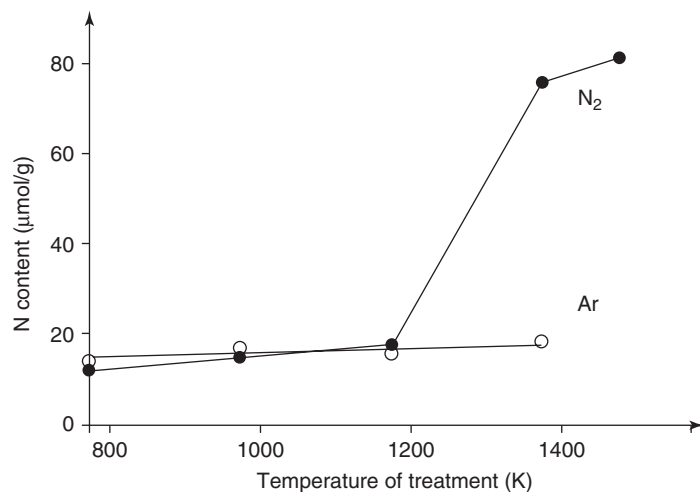


Figure 7.3 Nitrogen uptake of activated carbon on heating under nitrogen. The sample was prepared from a sugar char by carbonization at 1073 K and activation in 10% O₂ in Ar at 863 K, followed by heat treatment under Ar at 773 K. The reference sample was heated analogously under Ar.

7.2.2 Quantitative Analysis

In most publications it is stated without further details that nitrogen content was determined by combustion analysis. The nitrogen content of materials usually varies between 1 and 10%, but in some cases is even higher. Another, uncomplicated way to analyze nitrogen content is by the Kjeldahl method [66]. This analysis is precise and is well suited for low nitrogen content. The carbon samples (30 to 50 mg) were digested with 5 mL of concentrated sulfuric acid with the addition of a commercial catalyst tablet in long-necked flasks heated to near-boiling in a sand bath on a hot plate. The solutions were clear and colorless after heating overnight. They were transferred to the flask of a Kjeldahl distillation apparatus and excess concentrated alkali was added via a dropping funnel. The liberated ammonia was steam-distilled into 10 mL of 0.01 N HCl, and the excess acid was back-titrated with 0.01 N NaOH using a mixture of methyl red and methylene blue as the indicator. For small nitrogen contents, the ammonium chloride solution after distillation was analyzed spectrophotometrically by the indigo blue method [67,68], which is very sensitive and precise.

7.2.3 Electron Emission Spectrometric Analysis

The determination of total nitrogen does not provide information on the nature of its chemical bonding. Unfortunately, chemical methods comparable to those used in the determination of surface oxygen groups failed largely for the characterization of surface nitrogen. However, a spectroscopic method, x-ray photoelectron spectroscopy (XPS; also known as ESCA) can provide valuable information. On irradiation of the samples with monochromatic x-rays (Mg K α or Al K α), electrons of the inner shells of the atoms are excited to leave the atom. Their kinetic energy (E_{kin}) corresponds to the energy of the exciting radiation ($h\nu$) minus the binding energy (E_b) in the atom and a correction for the work function (Φ) of the instrument:

$$E_{kin} = h\nu - E_b - \Phi \quad (7.1)$$

The binding energy can be calculated from the kinetic energy observed. The binding energy of an inner-shell electron is affected by the electron density around the nucleus and thus by the chemical environment. For instance, the electron density is lowered when the atom emitting the electrons is bound to a more electronegative atom, and in consequence, its binding energy (b.e.) is enhanced.

The XPS signals are frequently shifted in their energy by charging of the sample. This can be corrected for by calibrating the energy scale by use of an admixed standard of known b.e. (e.g., vapor-deposited gold). For carbons, usually the main C1s peak at a b.e. of 284.6 eV is taken as an internal standard. The N1s signals are relatively broad, and the differences between the peak positions for differently bonded forms of nitrogen are usually only between <1 and 2 eV and are not much larger than the line widths, resulting in an overlap of the peaks. One has to rely on curve-fitting procedures and a deconvolution to obtain good resolution. The necessary programs are provided by the instrument producers, but

there are often some differences between different laboratories in the assumptions made for line shape and necessary corrections. Thus, the position of a signal is usually defined not better than to ± 0.3 eV. Table 7.2 lists the most often used values of the N1s binding energies of the nitrogen functions in carbon materials [52,69]. They were obtained by comparison with the spectra of model compounds.

The corresponding structures are shown in Figure 7.4. They are frequently abbreviated in the literature [9] as N-6 for pyridine- or acridine-type nitrogen and N-5 for pyrrole-type nitrogen, but this assignment is ambiguous because 2-hydroxypyridine-type nitrogen has a similar binding energy [70]. 2-Hydroxypyridine is the tautomeric form of α -pyridone (see Figure 7.5). The

Table 7.2 Overview of the Literature Data for the N1s Binding Energies of the Various Types of Nitrogen Bound in Carbons

Type of Nitrogen	N1s Binding Energy (eV)				
	Refs. 9 and 15	Ref. 59	Ref. 61	Ref. 60	Ref. 45
N-6	398.7 \pm 0.3	398.3 \pm 0.1	398.9 \pm 0.3	398.5 \pm 0.4	398.2 \pm 0.3
Pyridone	\sim 400.6	\sim 400.4	400.6	400.5	399.6 \pm 0.3
N-5	400.3 \pm 0.3	400.1 \pm 0.1	400.6 \pm 0.3	400.5 \pm 0.3	
N-Q	401.4 \pm 0.5	401.3 \pm 0.1	401.4	401.1 \pm 0.3	400.5
N-oxide		403.1 \pm 0.1	403.2	402.5–403.7	402.1
N-X					403.8
–CN		399.1			
–NH ₂	399.4				

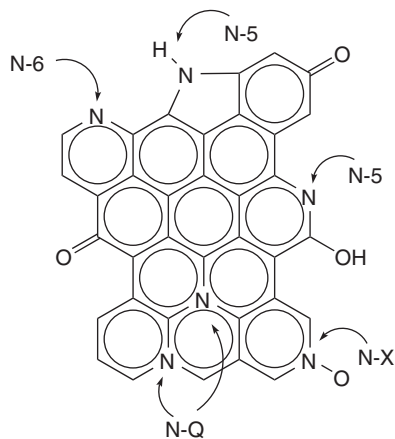


Figure 7.4 Model of a carbon layer with nitrogen atoms bonded differently. (From ref. 16, with permission.)

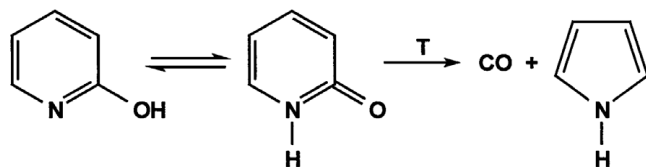


Figure 7.5 Tautomerism of α -pyridone and its thermolysis to pyrrole and CO.

latter assignment is supported by the observation that an N1s signal at about 400.3 to 400.5 eV appears to be stronger in intensity when nitrogen-containing carbons are oxidized with air. More evidence for the existence of pyridone-like structures has come from x-ray near-edge absorption spectroscopy (XANES) data [46,71]. However, an additional explanation for a signal with a b.e. similar to that of pyrrole has been given [72]: In pyrrole, the NH group is part of a ring with aromatic character. However, it is not necessary that this ring be a five-membered ring. The NH group could also be part of a six-membered ring at the edge of an extended graphene layer; the surplus electron of the nitrogen atom will be delocalized in the aromatic system and could be trapped at defects of the layer. The situation is analogous to that assumed for the quaternary nitrogen atoms (see below). The electronic surrounding of the NH group would be similar to that in pyrrole. To keep the commonly used abbreviations, this type of binding will be included in N-5.

The assignment of the various N1s signals were first made in studies of coals, and it was found that a satisfactory deconvolution required signals at 401.4 eV and at still higher binding energies [73,74]. The signal at 401.4 eV was ascribed to quaternary nitrogen atoms (N-Q) (i.e., ammonium ions, R_4N^+). This explanation is quite plausible with coals, but not with carbons, which consist essentially of more or less planar layers. However, it is now generally accepted that in this case the signal is due to nitrogen atoms bound substitutionally within the graphene layers. The extra electrons of the nitrogen atoms must go to higher energy levels (i.e., the conduction band in solids). The nitrogen atoms bound in the layers can also be described as quaternary. Unfortunately, model compounds do not exist for this type of nitrogen bonding. However, the catalytic activity exhibited by nitrogen-containing carbons suggests that electrons bound at high energy levels are available. The quaternary nitrogen atoms can be situated in the interior of the graphene layers or bonded to two edge atoms of a zigzag edge. This position is often called the *valley position* in contrast to the *top position* [9]. It is not known whether nitrogen atoms in the valley and interior positions differ much in their b.e.'s, but this has to be assumed since the calculated charge distribution differs significantly for both types of nitrogen atoms [72].

Other broad signals are often observed in the energy range 403 to 405 eV. Peaks near 403 eV are usually assigned to nitrogen atoms bound as in pyridine-N-oxides. Pyridine-N-oxides are easily formed from pyridine or substituted

pyridines and hydrogen peroxide; they are relatively stable. Signals at 404 to 405 eV are assumed to be generated by nitrogen–oxygen complexes, but not much is known about them. The relative quantity of these oxidized nitrogen species is usually much smaller than that of the other types of nitrogen. The symbols used for them vary in the literature. Pyr-N-O or N-Ox have been used for pyridine-N-oxides and N-X either for the whole broad peak or the signal near 403 eV, sometimes it is differentiated into N-X1 and N-X2. Another nitrogen function, cyanide ($-CN$), is occasionally observed at 399.1 eV [69]. Amino groups, $-NH_2$, at the edges of the graphene layers can be synthesized by first introducing nitro groups, $-NO_2$, with fuming nitric acid under drastic conditions and following reduction with sodium dithionite, $Na_2S_2O_4$ [75]. Amino groups are difficult to detect by XPS because their N1s binding energy, 399.4 eV [9], is between those of pyridine-type nitrogen and cyano groups. The formation of amino groups was proven by the increase in basic surface functions. They are thermally quite unstable. The detection of pyridine-, pyridone-, and pyrrole-type structures by XPS is supported by sharp peaks in Fourier transform IR spectra of ammonia-treated activated carbons [46].

The peak intensities can be used for the determination of the relative concentrations of nitrogen, oxygen, and carbon atoms in the surface layer of the samples. The respective excitation probabilities of the elements are listed in the literature. However, because of the small penetration depth of the photoelectrons, only a surface layer of <5 nm thickness contributes to the signal with the intensity decreasing strongly with the depth. Most of the signal originates in the topmost atom layers. Often, there is a large difference in composition in the surface and in the bulk of carbons.

Another method of studying the distribution of nitrogen functionality is XANES. The signals of the individual functions (the π^* resonances of lowest energy) have similar energies as those in XPS [71]. Several XANES studies [46,71,76–78] have shown as an advantage over XPS that the resolution of the peaks is better, but it is a disadvantage that no peak for quaternary nitrogen can be seen. The signal is probably very broad and hidden under other resonances. Nevertheless, XANES is a good supplement to XPS measurements.

Pyrrole-type nitrogen, N-5, is the most abundant species in coals, especially coals of low rank (i.e., of a relatively low degree of coalification) [74]. Similarly, this species is dominant in chars obtained at relatively low temperatures [69]. The content of pyridine-like nitrogen, N-6, increases with increasing rank of the coal. Significant changes occur in the spectra during heating of the chars to temperatures of 1273 K or higher. The evolution of the types of nitrogen-bonding during pyrolysis has been studied using XPS [9,16,69,70] and XANES [71]. N-5 nitrogen is converted to N-6 at moderate temperatures, and at high temperatures, N-6 signals decrease while N-Q nitrogen increases. An example of these changes is shown in Figure 7.6. Pyridones are often formed during cooling of the samples when some oxygen has access to the samples [71]. The thermal decomposition of pyridone leads to evolution of CO and formation of pyrrole as shown in Figure 7.5 [70].

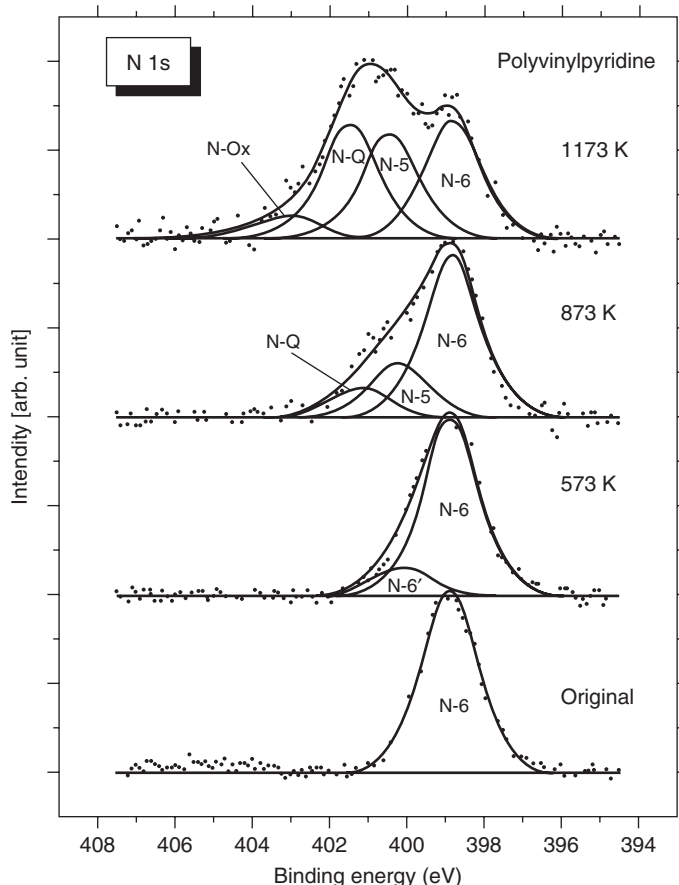


Figure 7.6 Changes in the N1s photoelectron spectra on carbonization of polyvinylpyridine. (From ref. 70, with permission from Elsevier.)

There are important changes in the N1s photoelectron spectra when chars are heated to carbonization temperatures. The charring and carbonization behavior of organic compounds with different nitrogen functionalities has been studied by various researchers using XPS and XANES, with the objective to test whether the individual nitrogen functions are preserved in the carbons. However, transformations occur with increasing heat treatment temperature, and after heat treatment at 1073 K only small or no differences are observed in the spectra, irrespective of the starting functionality [9,69–71]. The nitrogen species on carbons are, in general, thermally more stable than carbon surface oxides. Usually, N-5 nitrogen is converted to N-6 at moderate temperatures, which involves opening the five-membered ring. However, if the N-5 signal is produced by $>\text{NH}$ groups in six-membered rings at the border of the graphene layers (see Section 7.2.3), only

a dehydrogenation would be necessary for this transformation to N-6. A remarkable exception has been observed in the carbonization of poly(vinylcarbazole); N-5 is the main peak up to 1173 K, and only very small quantities of N-5 were developed at 873 K and relatively small quantities of N-6 and N-Q at 1173 K [70]. However, N-5 may increase at moderate temperatures (ca. 573 K) by elimination of CO from pyridones or apparently increase by formation of $>\text{NH}$ groups in the edges of the graphene layers, as discussed above. Thermal decomposition at relatively low temperatures results in only little gas evolution [79], the nitrogen is retained in the carbon in another form. A considerable part of the bound nitrogen is thermally very stable, at least in carbons with a homogeneous distribution of the embedded nitrogen, and even survives heating to 1620 K [80]. In the case of carbons treated with nitrogen-containing gases, only a relatively thin surface layer is doped with nitrogen, and the stability at high temperatures is inferior. At high temperatures, mobile C(N) species of unknown composition are formed which can be either desorbed as gaseous molecules or integrated into the graphene layers as N-6 or N-Q [80]. Up to 40 to 60% of the fixed nitrogen can be bound as N-6 [16], but N-Q increases at the expense of N-6 at temperatures above 1073 K. One reason may be that the graphene layers grow in size at these temperatures, and the increase in the area/circumference ratio favors N-Q over N-6. Clearly, some N-6 nitrogen atoms are lost in the process. Very likely, N-6 functionalities are decomposed at such temperatures with N_2 evolution. From 15 to 40% of the original nitrogen content is retained in the carbons after high-temperature treatment. 42% of the nitrogen remained at 1673 K in a carbon prepared from acridine after thermodesorption. 84% of this was in the form of N-Q, 5% was N-6, and 15% was in an oxidized form, N-X [80]. With PAN-based carbon the ratios were 67% N-Q, 18% N-6, and 15% N-X. In a remarkable case, 91% of the nitrogen introduced was N-Q after heat treatment at 1273 K [30]. Considerably less nitrogen is retained at such high temperatures in the case of carbons into which nitrogen has been introduced by treatment with NH_3 . The reason seems to be that only a relatively thin surface layer is doped with nitrogen. Often, significant quantities of pyridine-N-oxide-like structures (N-Ox) have been observed at 1173 K [69,70]. At higher temperatures these N-Ox structures are likely to decompose with evolution of NO and N_2 [80].

The ratio of the nitrogen species also changes during gasification of the N-doped carbons with oxygen, carbon dioxide, and so on. This is shown in the following example. An activated carbon was prepared by CO_2 activation at 1173 K of a carbonized mixture of sucrose with uracil (carbonization at 1373 K). This activated carbon, with a burn-off of 23% and a nitrogen content of 1275 $\mu\text{mol/g}$, was further activated with CO_2 at 1073 K or with 5% O_2 in He at 853 K to 70 to 75% burn-off levels.

The corresponding N1s XPS spectra are shown in Figure 7.7. There was a decrease in the N-Q content, especially in oxidation with O_2 , while the signals for N-6 and, particularly, N-5 increased. This was confirmed with other activated carbons [16]. The decrease in the N-Q concentration in the carbons can be explained by the decrease in the size of the graphene layers during combustion.

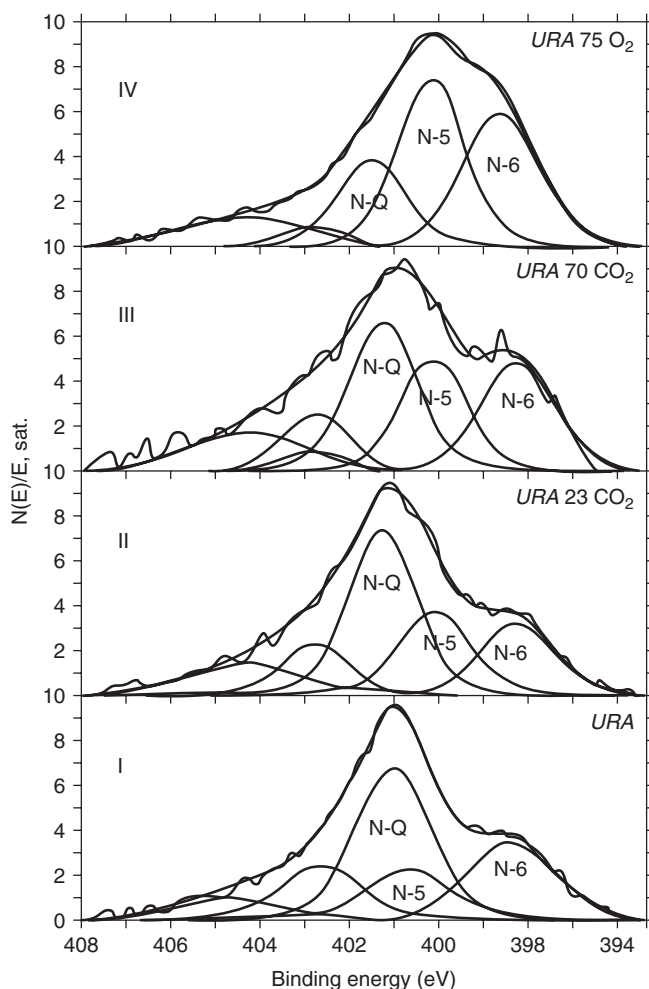


Figure 7.7 Changes in the N1s photoelectron spectra on oxidation of the carbonizate of sugar with addition of uracil: (I) as prepared; (II) after activation with CO_2 at 1123 K to 23% burn-off; (III) after further activation with CO_2 at 1073 K to an additional burn-off of 70%; (IV) sample II after oxidation with 5% O_2/Ar at 853 K to an additional burn-off of 75%. (From ref. 16, with permission from Elsevier.)

Further, it is very likely that N-Q nitrogen atoms near the edge become N-6 when two of the adjoining carbon atoms are removed by gasification.

7.2.4 Properties of Nitrogen-Containing Carbons

Introduction of nitrogen atoms in the structure of carbons will influence many of their properties. Pyridine and pyrrole are Lewis bases, and such structures will

affect the acid–base properties of carbons. After elimination of surface oxides by outgassing at high temperatures (e.g., 1173 K), pure carbons chemisorb some oxygen when they are contacted with air or oxygen at room temperature [5,81]. The same quantity again is taken up in the presence of water, and the suspended carbon exhibits basic properties. These are thought to arise from pyronelike structures at the edges of the graphene layers [6]. Although γ -pyrone is a very weak base, the basicity increases very strongly when the carbonyl group and the ether oxygen of a pyrone are distributed on the edge of an extended graphene layer, due to resonance effects. Theoretical calculations indicate that the basicity can surpass that of acridine [82]. Aqueous acids are adsorbed on such structures, presenting a Langmuir adsorption isotherm. However, the adsorption of hydrochloric acid tends to a saturation value that is a little higher than that of the basic pyrone groups, as estimated from the oxygen uptake [5,81]. This effect can be attributed to the basicity of the π -electron system of the graphene layers. This basicity is very weak, however [82].

There is nearly always some adsorption of hydrochloric acid from dilute solutions on carbons due to basic surface oxides and the basicity of the aromatic π system, even when acidic surface groups are present. However, the HCl adsorption decreases with an increasing content of acidic groups. This is shown in Table 7.3. The reason that the amount of basic sites decrease with increasing concentration of acidic groups is not clear. Possibly, the pyrone-type resonance system is disturbed by other oxygen functions at the edge of the graphene layers. However, the acid adsorption of nitrogen-containing carbons is considerably higher than that of analogously prepared carbons without nitrogen [20,83].

Adsorption isotherms of hydrogen chloride gas have also been determined gravimetrically on ammonia-treated activated carbon fibers as well as on Kymol fabric that was heated and activated under ammonia [43]. The samples were heated in a stream of 5000 ppmv HCl in 1 bar N_2 , corresponding to a partial pressure of about 500 Pa. The Langmuir-type isotherms were reversible and reached nearly saturation at this pressure. The HCl uptakes, calculated from the data in Ref. 43, are in most cases only a little smaller than the total nitrogen contents of the samples in $\mu\text{mol/g}$ (Table 7.4). The nitrogen content of the samples consisted of about 50% N-6, about 35% aromatic amines, and 8 to 15% N-Q. The difference between HCl adsorption and nitrogen content was considerably larger with activated carbon fibers, which are produced by direct activation with ammonia of Kymol [43]. Conceivably, the bound nitrogen is concentrated at or near the surface after the relatively short ammonia treatment of the porous, preactivated carbon, as opposed to the more intense attack in activation with ammonia of the polymer precursor.

Some of the nitrogen functions (e.g., N-6, N-5, N-Ox) are hydrophilic. As for N-Q, increased water vapor adsorption by nitrogen-containing carbon aerogels, compared to similar but N-free material was explained by polarization of the graphene layers near substitutional N-Q atoms that creates hydrophilic adsorption centers [84]. The adsorption isotherms appeared to be superpositions of a type II

Table 7.3 Concentration of Acidic and Basic Sites on Carbons with Various Treatments^a

Sample ^b	Pretreatment ^c	NaOH Uptake (μmol/g)	HCl Uptake (μmol/g)
AC Anthralur STA	Outgassed, 373 K	418	395
	HT, 1173 K	101	452
	O ₂ , 653 K	940	298
	NH ₃ , 1173 K	150	738
AC Norit SCM	Outgassed, 373 K	136	455
	HT, 1173 K	100	490
	O ₂ , 653 K	225	389
AC AR2	Outgassed, 373 K	376	342
	HT, 1173 K	108	499
	H ₂ , 1173 K	11	448
	O ₂ , 653 K	729	233
Carbon black graphite	NH ₃ , 1173 K	107	678
	Outgassed, 373 K	26	35
	HT, 1173 K	20	26
	O ₂ , 653 K	90	43

Source: Data from ref. 83.

^aFrom NaOH and HCl uptake, respectively, from 0.05 N solutions.

^bAC, activated carbon; Anthralur STA, peat activate from Lurgi; Norit STM, peat activate from Allgem. Norit M.I.J.; AR2, AC from Sutcliffe; carbon black graph., Corax 3 from Degussa, graphitized at about 3000 K.

^cOutgassed, vacuum of 10⁻³ Pa at 373 K, 6 hours; HT, heat-treated (under N₂) at 1173 K; O₂, oxidized in an O₂ stream at nominally 653 K (actual temperature somewhat higher), 30 minutes, cooling under nitrogen; NH₃, NH₃ stream at 1173 K, 4 hours, cooling under N₂; H₂, H₂ stream at 1173 K, 4 hours.

Table 7.4 Comparison of HCl Uptake (from the Gas Phase) Near Saturation with the Nitrogen Content of Activated Carbon Fibers Treated with NH₃ at 873 to 1073 K (600 to 800°C)

Sample ^a	Nitrogen Content (μmol/g)	HCl Uptake (μmol/g)
A 10-800-60	4.33	3.21
A 10-800-10	2.90	2.94
A 15-800-60	3.03	2.64
A 15-800-10	2.47	2.24
A 15-700-60	1.73	1.70
A 15-600-60	0.81	1.09

Source: Entries calculated from data in ref. 43.

^aA 10 and A 15 are activated carbon fibers treated with NH₃ at the temperatures (in °C) indicated, for 10 or 60 minutes. The ACFs were produced industrially from Kymol, a phenol-formaldehyde fiber with a surface area of 730 m²/g (A 10) or 1585 m²/g (A 15).

isotherm over a type V isotherm, as has also been observed for diamond powder with a few surface hydroxyl groups [85].

When freshly activated carbons are suspended in water, the slurry has a pH value greater than 7, due to the basic surface oxides (see above). The effect of ammonia treatment was shown by the following experiment. An activated carbon that had been demineralized with hydrochloric acid and washed to neutrality was treated with NH₃ at 773 to 1073 K and cooled under N₂ [44]. The nitrogen content of the samples was 1.61 to 1.63 wt%, corresponding to 1.14 to 1.16 mmol N/g. Whereas the original demineralized carbon produced in aqueous suspension a pH of 8.55 ± 0.03, the pH of the slurries of the NH₃-treated carbons increased with increasing treatment temperature to pH 9.26 to 9.86. The isoelectric point, determined from electrophoretic measurements, was at pH 7.44 to 7.70, compared to a pH value of 6.10 ± 0.02 measured in the aqueous slurry before the NH₃ treatment. The zero points of charge were more on the alkaline side, 9.26 to 9.90 and 8.55, respectively [44]. The smaller difference indicates that a few acidic groups had remained in the pore system; only the external surface of the particles is relevant for electrophoretic measurements (see ref. 6).

It was observed that the gasification of carbons in CO₂ at 1123 to 1173 K is considerably slowed when they contain nitrogen [20,63]. As shown in Table 7.5, the time to reach a burn-off of 21 to 25% increased from 4 to 5 hours to 9 to 19 hours, depending on the doping [20]. An inhibiting effect was also observed in the combustion of nitrogen-containing carbons in 5% O₂ in Ar, at least below 843 to 943 K [20]. This is also demonstrated in Figure 7.8, which shows the thermogravimetric traces for the isothermal combustion at 873 K with 5% O₂ in He of an undoped activated carbon (prepared from sugar) and, superposed, of a corresponding sample doped by addition of uracil to the sugar. A strong oxidation inhibition was also observed by Belz et al. [86] in temperature-programmed

Table 7.5 Time Needed to Reach a Burn-off of Approximately 23% in the Activation of Nitrogen-Containing Carbonized Sucrose (Heat-Treated at 1373 K) with CO₂ at 1123 K

Sample ^a	N Content (μmol/g)	Burn-off (%)	Activation Time (h)
SC	—	22	5.5
N-SC 20 gl	484	25	8.5
N-SC 50 gl	883	25	11.0
N-SC 60 ura	1002	22	13.0
N-SC 80 ura	1047	22	17.5
N-SC 100 pa	854	20	16.0
N-SC 30 hmp	344	21	16.0
N-SC 50 hmp	558	23	17.5

Source: Data from ref. 20.

^aSC, carbon from sucrose; N-SC, nitrogen-doped carbon from sucrose; gl, glucosamine; ura, uracil; pa, picolyamine; hmp, hydroxymethylpyridine. The number is a measure for the amount of additive added per mole of sucrose.

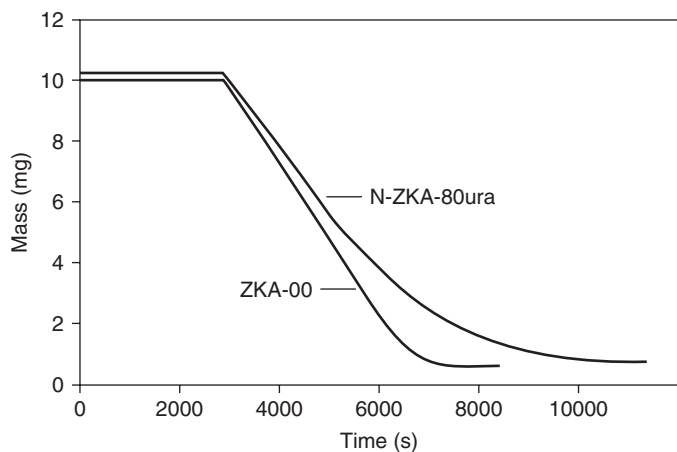


Figure 7.8 Gasification at 873 K with 5% O₂ in He of an undoped activated carbon from sugar char (ZKA-00) and a corresponding sample doped by addition of uracil to the sugar (N-ZKA-80ura). (Adapted from ref. 17.)

oxidation in 20% O₂ in Ar of a nitrogen-containing fullerene black produced in a fullerene generator operated at a relatively high He pressure with N₂ addition.

The nitrogen in carbons is evolved during combustion in the form of N₂ and substantial quantities of NO. Figure 7.9 shows that the rate of NO formation reaches its maximum when most of the carbon is already consumed [20,32,87,88]. Clearly, the nitrogen atoms are retained and enriched on the carbon surface when the edges of the graphene layers recede.

Nitrogen doping of carbons has an effect on their electrical properties. The electrical conductivity of the nitrogen-containing carbons is higher than that of nitrogen-free carbons [24,89], and the bandgap decreases with nitrogen doping of the carbons [90]. A higher electrical conductance than in undoped carbon nanotubes was observed with nanotubes having a coaxial double structure of nitrogen-containing and nitrogen-free multiwalls, despite poorer crystallinity of the nitrogen-doped nanotubes [91]. Studies of the Hall effect showed that nitrogen-containing carbons have n-type semiconducting behavior. The measurements were performed with carbons prepared by carbonization of cellulose in the presence of NH₄Cl and from Kapton [89] or by pyrolysis of 1,2-diaminopropane [92]. A nitrogen-free carbon showed p-conductivity [89].

Oxygen adsorption at 353 K increased with increasing surface area, but also with increasing concentration of negatively charged carriers. The concentration of free electrons decreased during the adsorption process, which took over an hour, resulting in a decrease in the electrical conductivity [89]. The adsorption of O₂ at 378 K on a nitrogen-doped carbon prepared from a demineralized activated carbon (from bituminous coal) increased with increasing temperature

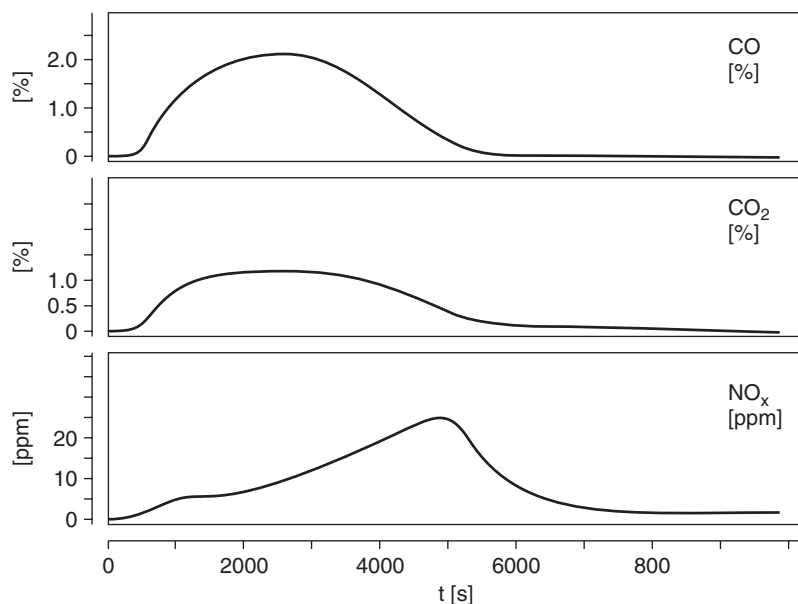


Figure 7.9 Formation profiles for CO, CO₂, and NO in the combustion of activated carbon from phenol-formaldehyde resin with 4-hydroxypyridine addition (260 µmol N/g) in 5% O₂ in He at 853 K. (From ref. 88, with permission from Elsevier.)

of ammonia treatment [93]. Also in this experiment, the adsorption process was slow; saturation was not achieved after 4 hours.

7.3 CATALYSIS OF OXIDATION REACTIONS WITH DIOXYGEN

7.3.1 Oxidation of Aqueous Sulfurous Acid

As mentioned in Section 7.1, it was originally suspected by the author that differences in catalytic activity of activated carbons might be due to different oxygen surface groups on the samples. For a systematic study, an easy test for catalytic activity in oxidation with dioxygen was needed that would be quick to perform and that would not require too-expensive instrumentation. Therefore, the oxidation of dilute aqueous sulfurous acid was chosen as a test reaction. Conversion to sulfuric acid can be monitored easily by the electrical conductivity of the solution. Dilute sulfurous acid in pure water is oxidized by air only very slowly. At a concentration of 10⁻² M, SO₂ is practically completely hydrated and to a large extent dissociated into HSO₃⁻ and H⁺ ions. The pK_a values at 298 K are pK_{a1} = 1.8 and pK_{a2} = 6.91. After oxidation to H₂SO₄, the second proton of the original H₂SO₃ is also dissociated, pK_{a2} = 1.92. At this concentration of 10⁻² M, the degree of dissociation of the first proton of

H_2SO_3 decreases from 0.91 at the beginning of the oxidation to 0.84 near its end, and the extent of the dissociation of the second proton of H_2SO_4 will fall from 0.88 to 0.79. With sufficient precision, one additional H^+ ion is liberated in the oxidation of H_2SO_3 to H_2SO_4 . The increase in H_3O^+ activity in solution can be monitored easily due to the high equivalent conductivity of H_3O^+ . In the experimental setup [17,94], a three-necked flask (500 or 250 mL) was filled with 250 or 100 mL, respectively, of deionized water and thermostated in a water bath. One neck of the flask was used for introduction of the gases, one held a pair of platinized platinum electrodes, and the third neck (open) served as a port for introduction of the catalyst sample. When the temperature was constant, SO_2 from a steel bottle was introduced into the magnetically stirred liquid until the electrical conductivity reached the arbitrarily set value of $5.7 \times 10^{-4} \Omega^{-1} \text{ cm}^{-1}$, corresponding to a H_2SO_3 concentration of 1.65 mmol/L. The concentrations were calibrated by iodometric titration. The solution was saturated with O_2 by bubbling into the solution an O_2 stream of 90 mL/min for 10 minutes. Other partial pressures of O_2 can be adjusted by mixing the gas with N_2 . No SO_2 is blown out of the solution within 2 hours at this low concentration. Spontaneous oxidation of the sulfurous acid is immeasurably slow under these conditions. After starting the recording of the conductivity, a suspension of the catalyst in 3 to 4 mL of the H_2SO_3 solution is transferred into the reaction vessel. A complete wetting of the carbon powder is assured in this way, even when it is hydrophobic. The mass of carbon catalyst was chosen to represent about 100 m^2 of surface area.

Figure 7.10 shows the change of conductivity with time. An initial drop is caused by adsorption of H_2SO_3 on basic surface sites of the carbon. It is followed by a relatively long, almost linear section until the reaction slows, when most of the H_2SO_3 is consumed. The slope of the linear section, expressed in $\mu\text{mol/g}\cdot\text{s}$, is taken as a measure of the catalytic activity. The catalytic activity A comes out as

$$A = fs w^{-1} \quad (7.2)$$

where f is the conversion factor from conductivity to concentration, s the slope of the curve, and w the mass of the catalyst. The maximum rate of conductivity increase after passing the minimum should be used for the determination of reaction rates where the curves are almost linear. The minimum does not appear when the carbon sample is used a second time. The results can also be stated in relation to the surface area of the catalyst, but when this is done, one should keep in mind that BET surface areas of microporous carbons are only apparent surface areas, and that diffusion of reactants in micropores can be very slow. This method of measuring the rate of the catalytic oxidation of sulfurous acid by activated carbons has found its way into the *Journal of Chemical Education* [95].

The order of the catalytic reaction with respect to oxygen pressure was determined by using oxygen–nitrogen mixtures of various O_2/N_2 ratios. Anthralur was chosen as the catalyst because it has an extended mesoporosity, making

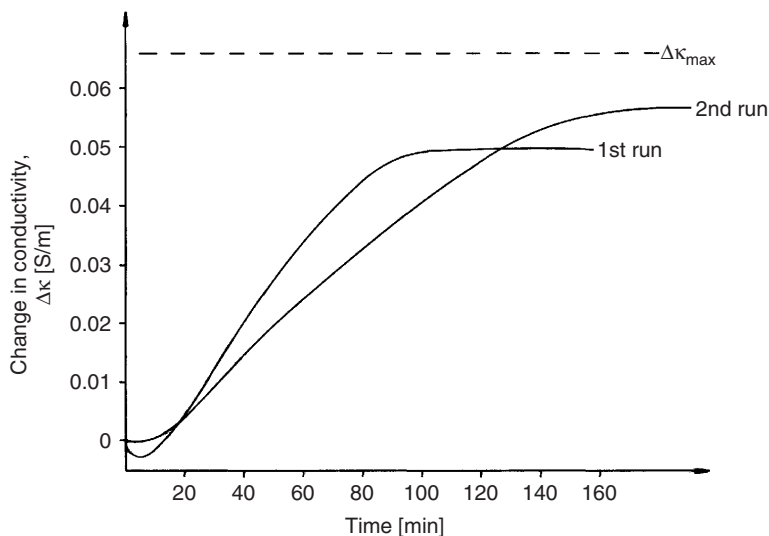


Figure 7.10 Change in conductivity on oxidation of a 1.65×10^{-3} M H_2SO_3 solution. $T = 293$ K. Catalyst: Anthralur, HT 1073 K, $p_{\text{O}_2} = 0.8$ bar. The initial dip due to adsorption of H_2SO_3 is missing in a second run with the same catalyst. (From ref. 37, with permission from Verlag der Zeitschrift für Naturforschung.)

most of the surface easily accessible. The reaction rate was proportional to the square root of the oxygen partial pressure. The reaction order is 0.5, indicating that a dissociation step in the reduction of O_2 is rate determining [37].

The curves for the dependence of the reaction rate on the H_2SO_3 concentration resemble Langmuir adsorption isotherms. Adsorption on the carbon surface is prerequisite to catalytic oxidation. The curves indicated that it might be better to use a higher starting concentration than 2.85 mmol/L, but unfortunately, SO_2 is blown out of the solution by the gas stream at higher concentrations. The decrease in H_2SO_3 concentration during the reaction explains the slightly curved plots of conductivity versus time (see Figure 7.10).

The results in Table 7.6 confirm that the catalytic activity of carbon blacks in the oxidation of sulfurous acid is inferior to that of activated carbons. Carbon blacks that had been extracted with hot xylene to remove adsorbed organic molecules and subsequently heat-treated under Ar at 873 K were catalytically inactive. However, weak catalytic activity was observed after heat treatment of these carbon blacks at 1473 K, with the notable exception of an acetylene black that is free of nitrogen. Catalytic activity was also observed with the as-delivered carbon blacks after heat treatment at 973 to 1073 K.

A 1.85×10^{-3} M solution of H_2SO_3 has a pH of 2.85. The effect of pH on the rate of catalytic oxidation was studied by small additions of H_2SO_4 or HCl using a sample of Anthralur [94]. For pH values 2.5, 2.0, and 1.5, the results

Table 7.6 Change in Catalytic Activity in the Oxidation of H₂SO₃ of Activated Carbons and Carbon Blacks After Oxidation with Oxygen and Subsequent Treatment with Ammonia

Sample	Treatment	Surface Area (m ² /g)	N Content (μmol/g)	Catalytic Activity (μmol/g·s)	Acidic Surface Groups (μmol/g)
Anthralur					
Original	HCl, vac. 573 K ^a	579	710	0.99	500
Sample 1	Air at 723 K	806	580	0.51	2200
Sample 2	NH ₃ at 873 K	812	4310	4.13	670
Eponit					
Original	HCl, vac. 573 K ^a	757	680	0.42	200
Sample 4	Air at 723 K	832	210	0.10	2240
Sample 5	NH ₃ at 873 K	830	3400	1.57	220
Philblack O					
Original	Xylene, vac. 573 K ^b	80	—	0	110
Sample 7	O ₂ at 673 K ^c	381	0	0.037	1100
Sample 8	NH ₃ at 873 K	364	2290	0.193	490
Corax 3					
Original	Xylene, vac. 573 K ^b	89	0.2	0	100
Sample 10	O ₂ at 673 K ^c	301	0	0.036	920
Sample 11	NH ₃ at 873 K	333	1630	0.240	210

Source: Data from ref. 96.

^aExtraction with hot hydrochloric acid, washing to neutrality and outgassing in vacuo at 573 K.

^bExtraction with boiling xylene followed by diethyl ether, outgassing in vacuo at 573 K.

^cOxidized at 673 K with O₂ for 20 minutes only to avoid too much gasification.

agreed with that for pure H₂SO₃ by ±0.03 μmol/g·s. Larger additions could not be used because the electrical conductance became too large to measure relatively small changes. However, an inhibitory effect was observed with nitric acid. The oxidation rate was 1.28 μmol/g·s with pure H₂SO₃, and 0.97 μmol/g·s at pH 2.5, 0.82 μmol/g·s at pH 2.0, and 0.77 μmol/g·s at pH 1.0. This effect seems to be related to the oxidizing properties of HNO₃. Also, KNO₃ and Ca(NO₃)₂ have an inhibiting effect at a concentration as low as 1 mmol/L [94]. Reduced activity was also observed on addition of NaOH to establish a pH of 3.0 or 4.0 [37,94].

Addition of soluble organic compounds had an inhibiting effect, not surprisingly. A strong effect was observed with small amounts of hydroquinone or pyrocatechol (2.7 μmol/L of H₂SO₃ solution), decreasing the oxidation rate to 0.23 μmol/g·s. Of course, one should keep in mind that these compounds are strongly reducing agents.

It was interesting to know how other chemisorbed elements affect the catalytic behavior of carbons. When carbons are heated in oxygen or air to 573 to 673 K, acidic surface oxides are formed [4,5]. In these surface oxides one finds carboxyl groups, lactones or lactols, and hydroxyl groups of phenolic character

(see Chapter 2). A measure for the total quantity of acidic surface groups is neutralization with 0.05 N NaOH. However, these acidic surface groups represent only a fraction of the total oxygen bound to the carbon surface, roughly one-half. Table 7.6 shows that the catalytic activity of two activated carbons and two furnace blacks was reduced considerably after oxidation with air at 723 K. Subsequent treatment with ammonia at 873 K resulted in a decrease in the acidic surface functions and a concurrent large increase in the catalytic activity in H_2SO_3 oxidation.

A further surface treatment was chlorination of a carbon black and an activated carbon with Cl_2 gas at 723 K for 6 hours [96]. Saturation is nearly reached at this reaction time. HCl is evolved in the chlorination of carbon blacks, in most cases in a molar quantity that slightly exceeds the quantity of chlorine fixed in the reaction, suggesting that this is a substitution reaction [97]. The bonding mechanism is less clear in the case of activated carbons. The catalytic activity of the activated carbon Anthralur decreased on chlorination, while a small catalytic activity was established in the case of the carbon black Corax 3 (Table 7.7).

The inhibiting effect increased with increasing Cl content [98]. When the chlorinated carbons were reacted with ammonia at 873 K, almost all of the surface-bound chlorine (in the case of the activated carbon) or all of it (with the carbon black) was removed. [96]. At the same time, nitrogen was bound and the catalytic activity increased drastically [39,40]. It is interesting to note that after

Table 7.7 Inhibiting Effect of Surface Chlorination of an Activated Carbon and a Carbon Black on Their Catalytic Activity in H_2SO_3 Oxidation and Its Restoration by Treatment with NH_3 at 873 K

Sample	Treatment	Surface Area (BET) (m^2/g)	N Content ($\mu\text{mol/g}$)	Cl Content ($\mu\text{mol/g}$)	Catalytic Activity ($\mu\text{mol/g}$)
Anthralur					
Original	HCl, vac. 573 K ^a	579	710	—	0.99
Sample 1	Cl_2 723 K, vac. 573 K ^b	300	740	5360	0.25
Sample 2	NH_3 at 873 K	710	2960	0	3.23
Sample 3	Cl_2 723 K, vac. 573 K	591	2340	3890	1.14
Sample 4	NH_3 at 873 K	750	3900	0	4.43
Corax 3					
Original	Xylene, vac. 573 K ^c	89	0.2	—	0
Sample 6	Cl_2 723 K, vac. 573 K ^b	78	—	2300	0.024
Sample 7	NH_3 at 873 K	87	1120	90	0.139
Sample 8	Cl_2 723 K, vac. 573 K	89	950	2270	0.031
Sample 9	NH_3 at 873 K	109	1610	40	0.279

Source: Data from ref. 96.

^aExtraction with hot hydrochloric acid, washing to neutrality and outgassing in vacuo at 573 K.

^bTreatment in a Cl_2 stream at 723 K, then outgassing in vacuo at 573 K.

^cExtraction with boiling xylene, followed by diethyl ether and outgassing in vacuo at 573 K.

exposure of the ammonia-treated carbons to chlorine, only a surprisingly small fraction of the embedded nitrogen was removed and that the catalytic activity did not decrease to its original low value. These observations were substantiated by measurements with other carbon samples [96]. The impression is that the binding of electronegative elements to the carbon surface results in a decrease in the catalytic activity of nitrogen-containing carbons. The changes in the N1 photoelectron spectrum of the ammonia-treated carbon black Corax 3 after chlorination at 723 K and subsequent repeat treatment with ammonia at 873 K are shown in Figure 7.11. The impression is that mainly N-5 nitrogen is removed by treatment with chlorine, but also, surprisingly, N-Q nitrogen. After the second ammonia treatment, the spectrum is very similar to that after the ammonia treatment of the original carbon black. A similar but not as strong inhibition was found with brominated carbons [96].

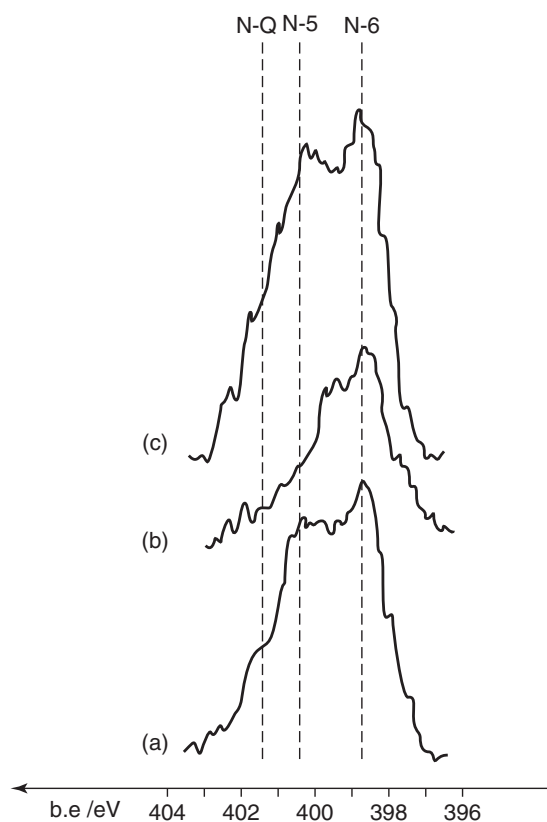
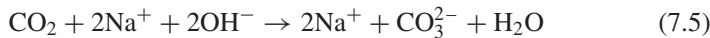


Figure 7.11 Change of the N1s photoelectron spectrum of carbon black Corax 3, chlorinated at 723 K, (a) after treatment with NH_3 at 873 K, (b) after a second chlorination, and (c) after a second NH_3 treatment. (Adapted from ref. 96.)

7.3.2 Oxidation of Oxalic Acid

Catalysis of the oxidation of oxalic acid to carbon dioxide by oxygen (air) has been described by Warburg [99] and studied in detail by Rideal and Wright [57]. The catalytic activity of carbons in this oxidation reaction can also be determined by use of conductometric measurements [94]. In this case, two thermostated vessels, equipped with magnetic stirring, are used in series. In the first one, an O₂ or O₂/N₂ stream (ca. 30 cm³/ min) is bubbled through 100 mL of a 2.05 × 10⁻³ M solution of oxalic acid. After saturation of the solution with oxygen (after 20 to 30 minutes) the catalyst was added (corresponding to about 100 m²/g). The gas was then passed in the second vessel through a sintered-glass frit into 100 mL of a 10⁻² M solution of Ba(OH)₂. The conductivity of this solution was monitored and recorded. It was ascertained by adding acid to a Na₂CO₃ solution that the CO₂ transport to the absorption vessel took no more than 1 minute under these conditions. When the catalytic CO₂ formation was stopped by addition of an inhibitor, the conductivity was constant within a few minutes. One can also absorb the CO₂ in dilute sodium hydroxide, but as reactions (7.4) and (7.5) show, the sensitivity (i.e., the decrease of conductivity) is higher when insoluble BaCO₃ is precipitated. The reactions involved are



It might be mentioned here that this conductometric determination of CO₂ was also used successfully in the author's laboratory for the determination of small quantities of CO in an oxygen-containing gas stream when this was passed over a suitable oxidation catalyst such as Au/TiO₂.

The results confirm earlier reports [98,99]. The reaction rate is dependent on the concentration of oxalic acid. It has a maximum at $c = 2$ mmol/L. A nearly constant reaction rate is established when the pH of the solution is set to pH 2.3 by addition of sulfuric acid. Warburg (cited in ref. 57) found the oxidation rate to be proportional to the square root of oxygen pressure; this was confirmed in ref. 94. The catalytic activity of activated carbons followed the same order as in the oxidation of sulfurous acid [94], and it increased after heat treatment at 973 to 1073 K or NH₃ treatment [39]. Carbon blacks were inactive. Also in this case, KNO₃ had an inhibiting effect, even at a concentration of 1 mEq/L, and more at higher concentrations. Na₂SO₄ had no effect on the oxidation rate.

7.3.3 Oxidation of Sulfur Dioxide

Adsorption of sulfur dioxide and its oxidation to sulfur trioxide or sulfuric acid is an interesting way to remove sulfur dioxide from flue gases (see Chapter 6).

The reactions involved are



The sulfuric acid formed remains in the pores of the activated carbon and blocks access to the reactive surface. It is usually removed by cyclic heat treatment at temperatures above 700 K; SO_2 (in a more concentrated form) and $\text{CO}_2 + \text{CO}$ are released in the reaction.

From the many attempts to elucidate the mechanism of the carbon's catalytic action, several theories have been forwarded to be disproved later. The following facts have crystallized out in time: SO_2 is first adsorbed physically. The adsorption is reversible, and the SO_2 can be desorbed in an inert gas stream [100,101]. Not surprisingly, the quantity of SO_2 that can be physisorbed increases with decreasing temperature at a given partial pressure [102]. Two to three times more SO_2 is adsorbed from a stream of synthetic flue gas in the presence of O_2 than in its absence [100,102]. In TPD experiments, two desorption peaks for SO_2 appear, one for physisorbed SO_2 around 373 K [101,103,104]. Another broad peak is centered at about 535 K. It is caused by reduction of physisorbed but not mobile SO_3 that had been formed in the adsorption step. At the same time, carbon is oxidized to CO_2 and CO and carbon surface oxides are also formed [101]. The quantity of SO_3 increases with time at the expense of physisorbed SO_2 [102]. Much more SO_2 is bound by the carbon in the presence of water in addition to oxygen [100,105] because SO_3 is hydrated to H_2SO_4 , which is hygroscopic and binds additional water. The sulfuric acid is mobile and can fill micropores, freeing the active sites that had been blocked by adsorbed SO_3 . No correlation of SO_2 capacity has been found with pore volume (or BET surface area) [102,105–107], but a correlation was suggested with micropores of <0.7 nm [102,108]. Heat treatment of the carbons enhances the activity for SO_2 adsorption and oxidation. An optimal temperature of 1073 K was found for PAN-based activated carbon fibers (ACFs) [100] and of about 1423 K for pitch-based ACFs [109,110]. The main effect of this treatment seems to be the removal of surface oxides, which block the access of SO_2 to the active sites [102,108,111]. No correlation has been found with the quantity of oxygen bound in the surface oxides [102,105,106]. However, a correlation was suggested with surface oxides that decompose to CO in TPD [105,110]. A role of “free surface sites” created in CO desorption has been ruled out [101,102]. The nature of the active sites and the mechanism of oxidation of SO_2 to SO_3 remained unknown.

Evidence for a role of incorporated nitrogen in the carbon catalysts was presented when Mochida et al. found very high activity in SO_2 conversion by heat-treated ACFs produced from PAN [100,112–115]. Such ACFs have nitrogen contents of 4 to 10%, depending on the heat treatment temperature. A continuous removal of SO_2 from a synthetic flue gas could be achieved by addition of excess H_2O to the flue gas and allowing the more dilute H_2SO_4 to flow down from the vertically aligned catalyst bed [112,113]. It was shown that pitch-based ACFs

become highly active after heat treatment at 1373 K, matching or even surpassing the best PAN-based ACF [109]. The nitrogen content of the pitch-based ACF was 0.2 to 0.7%. Such nitrogen contents also occur in activated carbons from natural precursors. Following these reports, pitch-based ACF or other carbon materials were doped with nitrogen by ammoniation [107,116] or by treatment with $\text{NH}_3\text{--H}_2\text{O}$ mixtures [117].

Many authors correlated the SO_2 adsorption capacity with the basic centers on the carbon surface [107,108,116,118–120]. However, it has been pointed out that more SO_2 was adsorbed than corresponded to the basic centers [102]. This is not surprising since the surface basic sites are quite weak, and SO_2 is not a strong acid. Also, no good correlation of SO_2 conversion per square meter of surface or nitrogen content was found. The correlation was much better with the N-6 content [108]. It was also reported that the SO_2 oxidation capacity increased with increasing N-6 and N-Q contents [118–121].

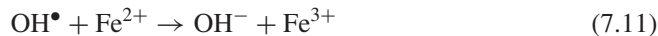
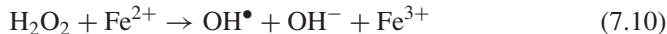
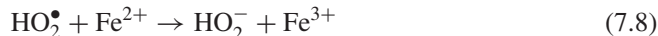
7.3.4 Oxidation of Iron(II) Ions

Lamb and Elder reported in 1931 that ferrous sulfate, FeSO_4 , in acid solution is oxidized by O_2 when wood charcoal was added [122]. The solutions without catalyst are fairly stable over several hours. The authors found that the reaction is first order with respect to O_2 and second order with respect to Fe^{2+} , and they assumed reaction of two Fe^{2+} ions with an adsorbed peroxide species. The first-order reaction with respect to O_2 was confirmed in several reports [47,123–125]. With regard to the reaction order with respect to Fe^{2+} , most authors agree that it is a first-order reaction, too [47,125,126]. In ref. 47, 0.05 M FeSO_4 in 1 M H_2SO_4 (50 mL) was oxidized in the presence of Anthralur Sta with 1 bar O_2 at 398 K. From time to time, 100- μL samples were taken for spectrophotometric determination of Fe^{2+} with 1,10-phenanthroline. An activation energy of 18.5 kJ/mol was found in the temperature range 285 to 303 K, similar to the value of 17 kJ/mol for the oxidation of H_2SO_3 [37], while 29.7 kJ/mol had been found earlier for oxidation of Fe^{2+} [125]. The reaction has a maximum rate at about 323 K, very likely because the solubility of O_2 in the solution decreases with increasing temperature, and diffusion of O_2 molecules to the carbon interface becomes rate determining [47]. The oxidation rate reached a maximum when the Anthralur carbon had been heat-treated at 1223 K, just as in the oxidation of H_2SO_3 . Norit BRX had a lower catalytic activity, and carbon black Corax 3 was inert [47]. An other activated carbon showed increased catalytic activity after treatment in H_2 at 1173 K and in particular after treatment with NH_3 at 1173 K, while its activity decreased after treatment with Cl_2 at 723 K [127].

In a more recent report [128], about a 10^{-3} M FeSO_4 solution was oxidized with 1 bar O_2 over activated carbon from coconut shells. Surprisingly, the oxidation rate was higher when the carbon had been oxidized with 5 M H_2O_2 or 5 M HNO_3 at room temperature. The oxidized carbons also acted as oxidants under N_2 while the original carbon was inactive. However, the final oxidation reached only about 30% of the Fe^{2+} present, when H_2O_2 -oxidized carbon was

used. The activity of the oxidized carbons remained essentially unchanged after heat treatment at 523 and 723 K. The authors concluded that surface quinones and chromenes, which are stable at these temperatures, are responsible for the oxidation. A considerable quantity of H₂O₂ was found in the solution by ultraviolet spectrophotometry when the carbon oxidized with HNO₃ was left standing for 2 hours under O₂ in acidic suspension. This is quite surprising since activated carbons are known to catalyze the decomposition of H₂O₂ (see Chapter 6). The other carbon samples produced only a small absorption at about 190 nm.

A noticeable difference in the oxidation of Fe²⁺ to the other oxidation reactions is that the reaction order with respect to O₂ is 1 and not $\frac{1}{2}$. One might speculate that the Fenton reaction of H₂O₂ with Fe⁺² [reaction (7.10)] might be involved. Posner suggested the following reaction mechanism [125]:



One HO₂[•] radical produces three Fe³⁺ ions in consecutive reactions. If these reactions are fast compared to the production of HO₂[•], its formation would be rate determining. HO₂[•] is formed from O₂⁻ in acidic solutions, and O₂⁻ could arise from transfer of delocalized electrons from the carbon (see Section 7.6).

7.3.5 Oxidation of Other Compounds

Hydrogen sulfide, H₂S, is noxious and malodorous. It is a common contaminant, produced in, for example, the anaerobic fermentation of organic matter in sewage, manure, or biodegradable plant residues. The evolved biogas, consisting mainly of methane and carbon dioxide, can be used as a fuel. It was found about 80 years ago that H₂S can be adsorbed efficiently by activated carbons. Physical adsorption of H₂S is quite limited, but it is oxidized to elemental sulfur when oxygen or air is present, also in small concentrations. Sulfur in microporous carbons is largely insoluble in carbon disulfide, CS₂, because it cannot form S₈ molecules, due to steric hindrance. The sulfur remains in the form of polymeric chains, λ -sulfur [129].

A kinetics reaction order of about 0.5 with respect to O₂ was found in several studies when H₂S was in excess, and of zero order for H₂S/O₂ < 1 [130,131]. The reaction is first order with respect to H₂S. The reaction can be performed at temperatures as low as ambient. The presence of water vapor enhances the breakthrough capacity [132]. At first, only elemental sulfur was found as a reaction product, but later, with some carbons, SO₂ and H₂SO₄ were also observed [130,133]. The formation of H₂SO₄ requires the presence of water vapor; usually, a relative humidity of 80% is used. The selectivity to sulfur oxides increases with increasing reaction temperature. However, H₂SO₄ is obtained exclusively with some carbons, even at room temperature (e.g., with activated carbon fibers [134])

or with the nitrogen-enriched activated carbon Centaur) [135]. The question of the reaction products is of some importance for the regeneration of exhausted catalysts. The capacity of the carbons decreases because of the filling of the pores with the reaction products. Elemental sulfur can be recovered with aqueous ammonium sulfide (NH_4^+HS^-) solution or by hot inert gas at temperatures up to 773 K. H_2SO_4 can be removed by washing with water or by heating until SO_2 is evolved, but both reaction products have to be disposed of. It is a matter of calculation which reaction product provides for a better economy. In most cases, the breakthrough capacities could be restored only in part.

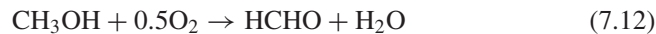
Detailed studies using a variety of activated carbons showed that the retention capacities are the result of a quite complex combination of surface properties [59,136,137]. One important factor is the pore structure. Narrow micropores of widths less than 0.5 nm are ineffective [132,134]. A well-developed system of micropores between 0.5 and 1 nm and small mesopores are essential [59]. Wide mesopores are required as storage volume for the reaction products. Surface acidity is another important point. Formation of sulfuric acid makes the environment in the pores strongly acidic. Suspensions of the exhausted catalysts showed a $pH \leq 2$ [137,138]. The acidic environment prevents dissociation of the very weak acid H_2S , and HS^- ions are apparently preferentially oxidized. Bagreev et al. [138] have estimated that dissociation of H_2S becomes insignificant at a "threshold" pH of about 4.5, below which no oxidation of H_2S occurs. Dissociation of weak acids also depends on their dilution. It is not surprising, therefore, that oxidation of the carbons with HNO_3 or $(\text{NH}_4)_2\text{S}_2\text{O}_8$ also leads to a loss in retention capacity [130].

Unfortunately, no nitrogen contents of the carbons used for H_2S "adsorption" are cited in the literature. The good performance of nitrogen-containing carbons was ascribed to their basic properties [58]. H_2S will dissociate at the basic surface sites, their hydrophilicity would provide for adsorbed water. An adsorbent prepared from bituminous coal with the addition of basic oxides such as CaO and MgO and of iron oxides has a much higher capacity than that of Centaur [136].

Methylmercaptan (CH_3SH) is a gaseous by-product of the sulfate process (Kraft process) for the production of cellulose. Activated carbons can be used for the retention of this malodorous compound, boiling at 279 K. CH_3SH is oxidized by oxygen (air) in the presence of activated carbons to dimethyl disulfide (DMDS) ($\text{CH}_3\text{S}-\text{SCH}_3$), which has a boiling point of 383 K. Because of its low vapor pressure, DMDS is strongly adsorbed in micropores. Methanesulfonic acid ($\text{CH}_3\text{SO}_3\text{H}$) is a further oxidation product. The oxidation is described to be mediated by O_2 and OH radicals [139]. Small quantities of CO_2 and CS_2 are also formed at temperatures above 473 K [140]. A remarkable increase in retention capacity of up to 10 times was found with nitrogen-enriched carbons [141]. With such carbons, methyl methanethiosulfonate [$\text{CH}_3\text{S}(\text{O},\text{S})\text{OCH}_3$] was found as another, minor oxidation product [142]. The breakthrough times, presumably at 393 K, were about 40 minutes for BPL from Calgon and about 150 minutes for an activated carbon produced from a Spanish bituminous coal. No CH_3SH

could be detected, even after 435 minutes [142], when this activated carbon was enriched in nitrogen by impregnation with melamine and heat treatment at 1223 K, as described in ref. 59.

A test used in my laboratory for photocatalytic activity of TiO₂ under ultraviolet (UV) irradiation is the oxidation of methanol to formaldehyde:



which can be determined spectrophotometrically with high sensitivity and precision. This reaction was also used to test the catalytic activity of nitrogen-enriched carbons [143]. Samples of 25, or 50 mg in the case of carbon blacks were suspended in 25 mL of pure methanol in 50-mL Erlenmeyer flasks. Oxygen was introduced and the suspensions were stirred magnetically at constant speed in the dark at 298 K. Every 2 hours a sample of 1 mL was drawn through a filter and diluted in a volumetric flask. Analysis was performed with chromotropic acid following ref. 144 with spectrophotometry at 570 nm. The quantity of HCHO formed increased linearly with time for about 24 hours, and slowed thereafter. The results showed that with the activated carbon Anthralur the rate of oxidation increased from 3 μmol CH₂O/g·h for a sample outgassed at 573 K (710 μmol N/g) to 163 μmol CH₂O/g·h for this carbon treated with NH₃ at 1173 K (2490 μmol N/g), and with furnace black Corax 3 from zero for the outgassed black to 10 μmol CH₂O/g·h for the sample treated with NH₃ at 1173 K (207 μmol N/g) [143].

Cyanide ions (CN⁻) are a very toxic contaminant that must be removed from industrial wastewaters. Oxidation of cyanide to cyanate (OCN⁻) by air on activated carbon catalysts has been suggested as a means of decontamination [145,146]. The effect of nitrogen enrichment on this reaction has been tested [143]. Cyanate can easily be hydrolyzed to NH₃ + CO₂ in acidic solutions. Ammonia can then be isolated from the solution by steam distillation and determined by titrimetric or spectrophotometric analysis as described in Section 7.2.2. Samples of 20 ± 0.1 mg were suspended in 50 mL of 0.01 N KCN solution set, for stabilization, to pH 11 by the addition of 1 mL 1 N NaOH. The suspensions were agitated in polyethylene bottles for 22 hours under oxygen. The samples were then transferred to the distillation apparatus. It turned out that it was essential to use small carbon samples because unreliable results were obtained with larger samples. With Anthralur outgassed at 573 K, the conversion was 43 μmol OCN⁻/g·h, and for this carbon, treated with NH₃ at 1173 K, it was 130 μmol OCN⁻/g·h. The results were zero and 70 μmol OCN⁻/g·h, respectively, for the carbon black Corax 3. These values agree in their order of magnitude with those reported for a pilot plant in ref. 145: 1 to 2 kg CN⁻ per 1000 kg·h, corresponding to 40 to 80 μmol CN⁻/g·h.

It was also shown that the oxidation by O₂ of 0.1 M solutions of SnCl₂ and of arsenite (AsO₃³⁻) in 2 N NaOH to arsenate (AsO₄³⁻) is accelerated in the presence of the peat activate Anthralur [123]. Both Sn²⁺ and AsO₃³⁻ were determined by iodometric titration. The accelerating effect was much larger in the case of the arsenite solution, the tin(II) chloride solution was oxidized relatively fast also

without catalyst. The conversion after 4 hours at room temperature was about 30% without catalyst and 60% with the carbon catalyst. In the case of AsO_3^{3-} , the corresponding values were about 5% and 24%, respectively. No experiments were performed with carbons especially nitrogen enriched.

Not only oxygen but also halogens are activated to a more reactive state on the surface of carbons: in particular, nitrogen-containing carbons. Phosgene (COCl_2) is produced industrially by the reaction of carbon monoxide with chlorine over activated carbon catalysts. In our laboratory, a mixture of Cl_2 and N_2 was first passed over the catalyst in a glass tube at 313 K in order to saturate the carbon surface with chemisorbed Cl [49]. Then Cl_2 and CO in a 45 : 55 ratio were passed over the catalyst in the temperature range 313 to 353 K. The Cl_2 concentration in the gas at the exit of the reactor was measured by UV absorption at 329.5 nm [49]. The catalysts were prepared by carbonization of sucrose with additions of nitrogen-containing compounds, followed by CO_2 activation. The carbons had BET surface areas from about 620 to 870 m^2/g . A Cl_2 conversion of 8.4 $\mu\text{mol/g}\cdot\text{s}$ at 353 K was found with the almost nitrogen-free carbon prepared without any additive. The results for the nitrogen-enriched carbons were 18.3 $\mu\text{mol Cl}_2/\text{g}\cdot\text{s}$ for sample N-SC 35 gl (921 $\mu\text{mol N/g}$), 15.5 $\mu\text{mol Cl}_2/\text{g}\cdot\text{s}$ for N-SC 80 ura (1082 $\mu\text{mol N/g}$), 14.1 $\mu\text{mol Cl}_2/\text{g}\cdot\text{s}$ for carbon N-SC 100 hmp (1285 $\mu\text{mol N/g}$), and 14.1 $\mu\text{mol Cl}_2/\text{g}\cdot\text{s}$ for the activated carbon Anthralur, outgassed at 573 K [49]. The heat of activation was in the range 29 to 33 kJ/mol for the undoped carbon as well as for the doped carbons. The markedly increased activity of the nitrogen-containing samples must be due to a higher preexponential factor (i.e., a higher concentration of active sites).

The synthesis of hydrogen bromide from the elements is also catalyzed by carbons [147]. A few preliminary experiments were performed with carbon black Corax 3. A hydrogen stream saturated with Br_2 at 273 K was passed over the samples at 423 K. At this temperature, thermal dissociation of HBr is negligible, and the conversion is a measure of catalytic activity. The HBr formed was absorbed in water and titrated with standard alkali [96]. The catalytic activity of the carbon black tripled after treatment of the oxidized black with NH_3 at 873 K, and doubled when heat-treated at 1273 K. This behavior agrees very well with that observed in the oxidation reactions described in this section.

7.4 CATALYSIS OF AGING OF CARBONS

It is well known that the adsorption capacities of activated carbons, especially for unpolar compounds, decrease on prolonged storage under ambient conditions [148–150]. This phenomenon, called *aging* of the carbons, is well known in the relevant industries. Puri reported that carbons outgassed at 623 K chemisorbed oxygen from the air under ambient conditions over a six-month period [151]. The presence of moisture was essential; very little oxygen was adsorbed from dry air. The promoting effect of water was confirmed [149]. Aging is faster

under pure oxygen than in air [151]. The retention of $\text{CH}_3^{131}\text{I}$ from exhaust gases of nuclear reactors by activated carbons decreased with an increase of surface oxides after storage for three years [148–150]. It has also been reported that the retention capacity for H_2S (see Section 7.3.5) of activated carbons decreases on aging [152]. Acidic surface functions are formed during aging. The isoelectric point of a carbon black heat-treated at 1773 K shifted from pH 10.5 to pH 5.8 after one year of storage in ambient air [153]. The oxygen chemisorbed during aging comes off mostly in the form of CO_2 during thermodesorption [151]. It was also found that water vapor was slowly, but irreversibly, adsorbed at 423 K on an activated carbon previously oxidized with O_2 at 423 K. At the same time, CO_2 was evolved [154]. The aging process is faster in air than in aqueous suspensions [155].

Aging is a very slow process at ambient temperature, although changes after as few as two days have been reported [156,157]. Therefore, aging at 323 to 353 K has been used for closer studies [83,158]. An activated carbon, Norit SGM, and carbon black Corax 3 were aged either in ambient air at 383 K or in a desiccator over sulfuric acid placed in a drying oven at 353 K (the relative humidity was controlled by the H_2SO_4 concentration). Usually, a relative humidity of 80% was chosen because a further increase has no effect [149]. The formation of acidic surface groups was monitored by acidimetric titration. As shown in Figure 7.12, about a threefold higher level of acidic groups was formed on the activated carbon at the higher humidity, although the temperature was lower. The difference was much smaller with the carbon black. This is probably due to the fact that the carbon black surface contains no micropores in which water vapor can be adsorbed by the micropore filling mechanism. The increase after 31 days of

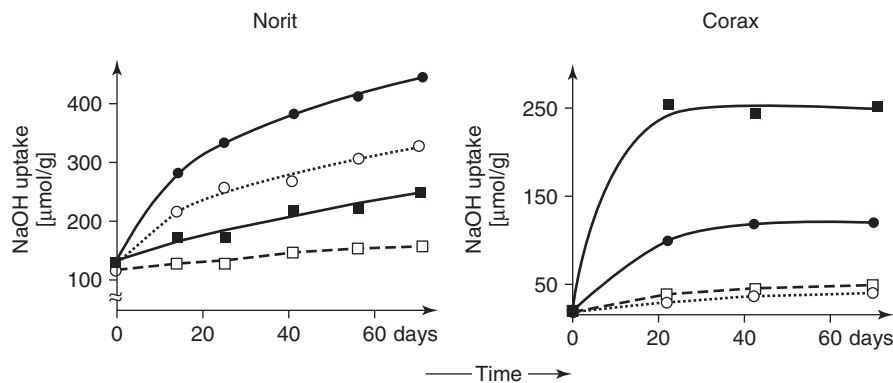


Figure 7.12 Formation of acidic surface groups during aging of an activated carbon (Norit BRX) and a furnace black (Corax 3) (open symbols). Squares: in ambient in air at 383 K; circles: in air of 70% relative humidity at 333 K. The reaction is accelerated by deposition of 200 $\mu\text{mol/g}$ palladium on the carbons (filled symbols). (From ref. 5, with permission from Elsevier.)

acidic groups on the activated carbon determined by reaction with Na_2CO_3 was considerably smaller than that determined by titration with NaOH (14% vs. 32%) [83]. Clearly, more phenolic surface groups were formed than carboxylic groups plus lactones and lactols.

The figure also shows that loading the carbon with finely dispersed palladium has a further accelerating effect on surface oxidation, which is most pronounced with the carbon black. This can be explained by dissociative adsorption of O_2 molecules on the metal surface and oxygen spillover. Platinum had a similar effect. Palladium ($200 \mu\text{mol/g}$) was deposited on the carbons by incipient wetness impregnation followed by H_2 reduction at 523 K; the dispersion was about 25% with Norit and 15% with Corax 3.

The effect on aging of nitrogen-containing activated carbons prepared from sucrose with additives is compared in Table 7.8. One set of samples was filled immediately after preparation into glass ampoules that were sealed after evacuation. Another set was stored in glass vessels with plastic screw-on lids [17,159]. The samples taken from the evacuated ampoules had practically not changed after one year, while those in vessels with a limited access to air exhibited a small-to-large increase in acidic groups and a corresponding decrease of basic surface sites (compare Table 7.8). The third column in Table 7.8 shows that there was a considerable loss in catalytic activity in H_2SO_3 oxidation. The inhibiting effect of surface oxides on the catalytic activity is described in Section 7.3.1. There was also a loss of nitrogen content of 1 to 5.5% during aging of the samples for two years [17], as well as a loss of apparent surface area ranging from a few percent to more than 15% [49]. No correlation of the loss of surface area with the nitrogen content could be seen, however, even in series of similarly prepared activated carbons with increasing nitrogen contents.

Table 7.8 Changes in Catalytic Activity and Acidic and Basic Surface Oxides of Sucrose-Derived Activated Carbons After Storage with Access to Air

Sample ^a	N Content ($\mu\text{mol/g}$)	Catalytic Activity ($\mu\text{mol/g H}_2\text{SO}_3\cdot\text{g}$)		Acidic Surface Sites ^b ($\mu\text{mol/g}$)		Basic Surface Sites ^c ($\mu\text{mol/g}$)	
		Vacuum	Air	Vacuum	Air	Vacuum	Air
N-SCA 00	~20	0	0	90	80	470	440
N-SCA 5 arg	450	2.02	0.76	55	90	560	460
N-SCA 25 ura	960	3.58	1.64	50	160	720	530
N-SCA 75 gl	1170	4.14	4.14	95	95	760	710
N-SCA 100 arg	1250	4.30	4.30	40	75	630	570

Source: Data from ref. 17.

^aN-SCA, nitrogen-doped CO_2 -activated carbon from sucrose; arg, arginine; ura, uracil; gl, glucosamine (hydrochloride). The number is a measure of the quantity of additive added.

^bFrom titration with 0.05 N NaOH .

^cFrom titration with 0.05 N HCl .

We had noticed earlier that the catalytic activity in the oxidation of H_2SO_3 was lower when they were used a second or third time after a first run. At first, it was surmised that this was due to a blocking of micropores by H_2SO_4 or HSO_4^- ions adsorbed on the basic surface sites. The missing dip in the conductivity recordings in the second run (see Figure 7.10) indicates that the basic sites can no longer adsorb HSO_3^- ions. Measurements of the micropore volumes before and after a catalytic run showed that there was indeed a small loss of micropore volume [56,160,161]. However, this effect could explain only a part of the loss in catalytic activity of the carbons, which is mainly due to aging. The catalytic activity could be regenerated in large part by heat treatment at about 1170 K.

An activated carbon prepared from lignite was oxidized with concentrated hydrogen peroxide and then heat-treated under helium at four different temperatures from 673 to 1273 K. The samples so obtained were aged under ambient conditions for two years. The temperature-programmed desorption (TPD) profiles for CO_2 and CO of the aged samples were compared with those measured immediately after oxidation [162]. It was found that the CO_2 evolution curve of the original oxidized carbon was the better restored, in particular at lower temperatures the higher the decomposition temperature had been. Carboxyl groups are decomposed to CO_2 below 673 K. The curve was nearly identical for the sample heat-treated at 1273 K. The CO-evolving groups were restored to a large extent also with the samples heat-treated at the lower temperatures. The results were confirmed by measurement of the acidic surface sites [162].

Clearly, these changes in the surface chemistry of carbons during storage negatively affect the reproducibility of measurements after some time has passed. The samples are not the same as they were a year or two ago. They must be characterized anew if additional measurements are to be done.

Some CO_2 is evolved in the aging reaction. A continuous conversion of carbon to CO_2 could be achieved by treating carbons with oxygen in 0.01 to 0.2 N NaOH at 353 K. An oxygen stream was passed through a suspension of the carbon, and from time to time aliquot samples were taken. After acidifying in a closed vessel, the CO_2 liberated was carried by a gas stream to a conductivity cell filled with a 0.01 M $\text{Ba}(\text{OH})_2$ solution, and the drop in electrical conductivity was measured, taking into account the small carbonate contamination of the NaOH solutions (see Section 7.3.1). The oxidation rate increased with increasing NaOH concentration [40,163]. Some CO was also formed, about 5 to 7% of the quantity of CO_2 [163]. The conversion rate increased markedly after treatment with NH_3 at 1173 K, from zero to 44 μmol $\text{CO}_2/\text{g}\cdot\text{h}$ with activated carbon Eponit and from 10 to 15.5 μmol $\text{CO}_2/\text{g}\cdot\text{h}$ with furnace black Corax 3 [163].

Figure 7.13 demonstrates the accelerating effect of increasing nitrogen content on the activity in aging of activated carbons from phenol-formaldehyde resin, in which part of the phenol was substituted by aniline [164]. The surface area was from 700 to 840 m^2/g . The oxidation rate increased almost linearly with the nitrogen content. Conversion to carbonate proceeds much more slowly at room temperature; reaction times of one to two months were necessary to obtain well-measurable results [163].

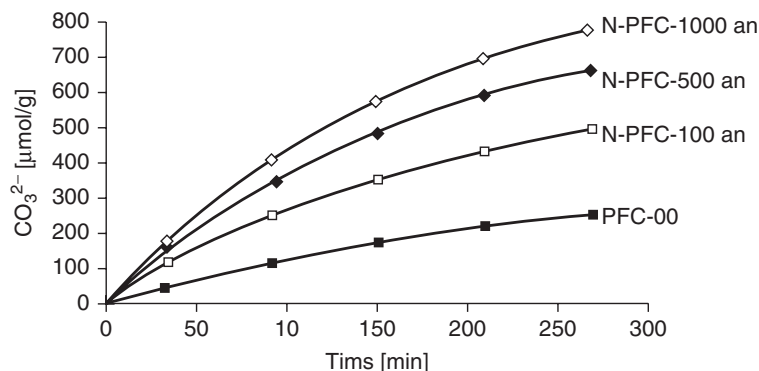


Figure 7.13 Carbonate formation in the reaction with O₂ of nitrogen-containing activated carbons prepared from phenol-formaldehyde resin with the addition of aniline. (Adapted from ref. 164.)

This autoxidation property of carbons leads to a continuous loss of catalyst. When spherical carbon particles of 30 to 100 μm were used in the oxidation with air of aqueous cyclohexanone solutions at 393 K in a trickle-bed reactor, a weak loss of carbon was observed after four weeks, and the originally smooth particles appeared rough and porous in scanning electron microscopy (SEM) [165]. The catalysts used with a nitrogen content of < 1% had been prepared from nitrogen-containing phenol-formaldehyde resin [166]. In this reaction cyclohexanone is oxidized to adipic acid and other dicarboxylic acids. 2-Hydroxycyclohexanone seems to be an intermediate. A carbon loss of several percent was also reported for other wet-air oxidation reactions of pollutants, mainly of phenol [167–169].

7.5 CATALYSIS OF DEHYDROCHLORINATION REACTIONS

Thermal dehydrochlorination of 1,1-dichloroethane at about 820 K is generally used for the production of vinyl chloride. However, the process suffers from heavy coke deposition on the reactor walls, and catalytic reactions operating at lower temperatures were investigated in industry. Carbons were found to catalyze the dehydrochlorination (DHC) of alkyl chlorides to the corresponding alkenes. This reaction had been studied in 1933 for its suitability in the production of vinyl chloride. A list of early patents is given in ref. 170. Formation of 1-butene from 1-*n*-butyl chloride was described by Schwab et al. [171]. However, the activity of the carbon catalysts decreases with time on stream. A considerable mass increase of the catalyst (and decrease of surface area) after reaction has been made responsible for blocking of the active sites [172]. In a later investigation it was suggested that vinyl chloride was polymerized by a radical mechanism with consecutive

thermal decomposition to coke (the PAN-based activated carbon fibers used, PAN-ACF, showed an ESR signal) [173]. Initially, a radical mechanism involving Cl[•] radicals was assumed for DHC reactions because added *n*-hexane or toluene had an inhibiting effect that was ascribed to competition for the Cl[•] radicals [170]. Now, a base-catalyzed mechanism is generally assumed for the DHC reaction (e.g., with pyridine-like N-6 sites) [173]. XPS of the PAN-ACF showed signals of N-Q (higher intensity) and N-6 (see Section 7.2.3). Their intensity, in particular that of the N-6 peak, decreased after reaction. This might be due to a thin overlayer of poly(vinyl chloride) or coke, and the stronger decrease in the N-6 signal was associated with strong binding of HCl on the carbon (strong Cl 2p signals in XPS). After heating to 873 K under nitrogen, the N-6 peak was partly restored but not the catalytic activity [173]. Pitch-based ACF (with a lower nitrogen content) had a much inferior catalytic activity, but became quite active after pyrolytic decomposition of pyridine on the pore walls [174]. A selectivity for vinyl chloride of 99.9% was observed at 633 K. Side products were ethylene, acetylene, and 1,1-dichloroethene (each <0.1%), and butadiene appeared in a yield below 0.01% [175]. The deactivation of the catalyst was slower the lower the reaction temperature, but at the cost of a much reduced catalytic conversion [175]. With PAN-ACF FE-300 the activity was stable at 573 K. Also with activated carbon produced from coal, the highest catalytic activities were found after treatment in hydrogen at 727 K followed by NH₃ at 1173 K or after oxidation with nitric acid followed by NH₃ treatment at 1073 K [176]. The activity increased on stepwise raising of the reaction temperature, but was much lower at a given temperature in the cooling cycle.

The catalytic activity in DHC reactions is usually measured by passing the reactant in an N₂ stream over the catalyst and then through water or NaOH solution and determination of the adsorbed HCl. In the author's and other laboratories the increase in electrical conductivity was measured. The rate of HCl production decreased in the reaction of 1-*n*-butyl chloride at 603 K in the first 2 hours, but became nearly constant for several hours thereafter, and comparison of the activities after different pretreatments of a carbon could be performed when the linear increase of conductivity with time was established [143]. A few results are shown in Table 7.9. The catalytic activity of activated carbons and carbon black also increased in this case after heat treatment under nitrogen, and became quite high after treatment with ammonia at 1173 K. The activity at 603 K increased in the order 1-*n*-butyl chloride < 1-*n*-hexyl chloride < 1-isobutyl chloride < 1,2-dichloroethane. The surface area of the porous carbons had decreased drastically after the reaction.

Analysis of the organic phase condensed in a trap at 203 to 263 K, depending on the reactant, before absorption of the HCl gas, showed the expected olefins and small quantities of the dimer of the alkyl group (i.e., *n*-octane in the case of 1-*n*-butyl chloride, or *n*-dodecane with 1-*n*-hexyl chloride) [40,143,177–179]. The amount of these alkanes corresponded to approximately 10% of that of the olefin formed. No dimer was observed in the production of vinyl chloride and with the other alkyl chlorides when the reaction temperature was relatively

Table 7.9 Dehydrochlorination of Alkyl Chlorides at 603 K

Sample	N Content (μmol/g)	Catalytic Activity (μmol/g·min)	BET Surface Area (m ² /g)	
			Before	After
1-n-Butyl chloride				
Anthralur				
Vac. at 573 K	710	12.5	640	
N ₂ at 1073 K	720	13.6	620	
Eponit				
Vac. at 573 K	680	5.67	760	
NH ₃ at 1173 K ^b	2500	13.0	1140	
Corax 3				
Vac. at 573 K	210	1.1 ^a	83	
NH ₃ at 873 K ^b	1340	1.0	90	
NH ₃ at 1173 K ^b	2280	7.00	500	
1-Isobutyl chloride				
Anthralur				
Vac. at 573 K	710	43.0	640	530
N ₂ at 1223 K	—	51.3	740	660
NH ₃ at 1173 K ^c	1160	68.2	760	680
NH ₃ at 1173 K ^b	2490	83.0	870	720
1-n-Hexyl chloride				
Anthralur				
Vac. at 573 K	710	28.3	640	235
NH ₃ at 1173 K ^b	1160	59.2	760	280
Norit BRX				
Vac. at 573 K	290	56.8	1600	830
Corax 3				
Vac. at 573 K	210	8.17	90	77
1,2-Dichloroethane				
Anthralur				
Vac. at 573 K	710	66.7	695	616
NH ₃ at 1173 K ^b	1160	315	760	685

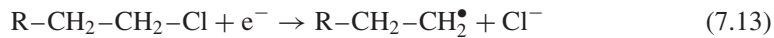
Source: Data from refs. 143 and 178.

^aFrom ref. 177.

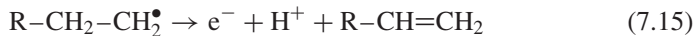
^bCooling to ambient under NH₃.

^cCooling to ambient under N₂.

low. The occurrence of the alkyl dimers can be interpreted as a consequence of electron transfer from the carbons to the alkyl chlorides, followed by elimination of Cl⁻ ions:



It can also be imagined that olefin is produced by elimination of a proton from the alkyl radical and return of the electron to the catalyst:



However, the main route to olefin and hydrogen chloride seems to be a base-catalyzed HCl elimination, but a sequence of reactions (7.13) and (7.14) cannot be ruled out completely. Plots of catalytic activity of carbons prepared from nitrogen-doped phenol formaldehyde resins versus their nitrogen content showed a good correlation whereas no good correlation was found with the concentration of basic surface sites determined by acidimetric titration [180]. Feeding HCl gas into the gas stream together with 1,2-dichloroethane resulted in a strong decrease in the catalytic activity at 573 K, from $6.94 \mu\text{mol/g}\cdot\text{min}$ to $1.50 \mu\text{mol/g}\cdot\text{min}$, using NH₃-treated Anthralur as the catalyst [181]. The quantity of chlorine bound to the carbons was much higher than the concentration of basic surface sites (e.g., $2780 \mu\text{mol/g}$ vs. $742 \mu\text{mol/g}$ basic surface sites for this carbon). It decreased only a little during the catalytic test.

Alkyl bromides react at lower temperatures than chlorides in dehydrohalogenation reactions, but the reactions are complex since brominated precursor molecules appear, indicating that some bromine is formed from the hydrogen bromide [182]. It is worthwhile mentioning that carbons also catalyze hydrogenolysis of C–Hal bonds in monosubstituted benzenes and substituted chlorobenzenes [183,184].

7.6 MECHANISM OF CATALYSIS BY NITROGEN-CONTAINING CARBONS

In the literature, the catalytic activity of nitrogen-containing carbons is often associated with their basic properties (see, e.g., Section 7.3.3). This conclusion seems logical since nitrogen-doping produces enhanced basicity. However, the base strength of the nitrogen groups is not very strong, and one would not expect a strong effect for reactions run at ambient temperature. Other effects, described below, support the theory that electrons are transferred from the catalyst to adsorbed oxygen molecules, producing highly reactive O₂[−] radicals, or HO₂[•] in the presence of water.

O₂[−] radicals are also formed on ultraviolet (UV) irradiation ($\lambda < 366 \text{ nm}$) of TiO₂ in the presence of O₂. In this case, the electrons are excited on irradiation from the valence band, arising mainly from oxygen 2p states, to the conduction band, originating from unoccupied titanium 3d states. Because of mutual electrostatic repulsion, the electrons in the conduction band move to unoccupied surface states, which have a higher energy due to band bending [185,186]. Such electrons can be transferred to adsorbed O₂ molecules, forming superoxide ions, O₂[−], or, in acidic media, HO₂[•] radicals. Both species are aggressive oxidizing agents. Also, H₂O₂ plus singulet oxygen, ¹O₂, can be formed. Uptake of a second electron and a dissociative step, leading to O[−] ions or OH[•] radicals, can be imagined as well.

Thus, UV-irradiated TiO_2 , and similarly ZnO and some other oxides, catalyze oxidation with dioxygen. ESR measurements of ZnO irradiated with UV light in the presence of O_2 showed the existence of O_2^- and O^- . The predominant species below 443 K is O_2^- , and O^- at higher temperatures [187]. The holes, h^+ , in the valence band of the irradiated oxides can react with OH^- ions on the surface, producing OH^\bullet radicals, which are also very reactive.

In the course of studies on surface oxides of carbon in our laboratory, acidic surface groups were characterized by neutralization adsorption of aqueous bases. Very weak acids were determined by adsorption of sodium ethylate, NaOC_2H_5 , from solution in ethanol. In this case, hemiacetals of reactive carbonyl groups are formed [5]. It was observed that on longer standing in contact with carbon and air, the ethylate solutions developed a coloring, from light yellow to orange brown, and even to dark red, depending on the carbon used. The solutions remained colorless under argon or nitrogen, even after one year. It was suspected that the effect was caused by a carbon-catalyzed oxidation of ethanol. The presence of aldehydes was proven by use of the Schiff reagent (fuchsine/sulfurous acid) with an activated carbon Eponit [188]. For further analysis, 2,4-diphenylhydrazones were precipitated in the standard way, isolated, and dried. They were analyzed by thin-layer chromatography on silica gel, using a mixture of 170 parts benzene, 25 parts petroleum ether, and 5 parts ethyl acetate as the mobile phase. The spots were developed with a spray of ethanalamine. At least six different compounds were detected, among them acetaldehyde, glyoxal, and a little ethylene glycol [188]. The same pattern of spots was obtained when an ethanolic NaOC_2H_5 solution was reacted with O_2 in the presence of TiO_2 (Degussa P25) under UV irradiation. In the exclusion of O_2 , only acetaldehyde and ethylene glycol were formed, but no glyoxal. Obviously, glyoxal is a reaction product of ethanol with O_2^- , while acetaldehyde and ethylene glycol are also formed with OH^\bullet radicals [189]. The chromatographic pattern obtained after irradiation of TiO_2 suspended in an acetonitrile-acetone mixture agreed in the number, color, and relative sizes of the spots exactly with that observed when an authentic O_2^- solution in the same solvent mixture was used [189]. This solution was prepared by electrochemical reduction of O_2 . In the exclusion of O_2 , only acetaldehyde and glycol, but no glyoxal, were observed. These observations are good evidence that the oxidizing agent in the O_2 -carbon system is the superoxide ion, O_2^- . The catalyzed decomposition of H_2O_2 is 10 to 100 times faster on nitrogen-containing carbons than on nitrogen-free carbons [190]. This is another indication that free radicals are involved in reactions on such carbon surfaces.

In the dehydrochlorination of alkyl chlorides, dimerization of the alkyl radicals was observed after splitting off of Cl^- ions (Section 7.5). This is also an indication that electrons from the carbon are involved.

The catalyzed oxidation of sulfurous acid, oxalic acid, or SO_2 is inhibited by chemisorbed oxygen or chlorine, two electronegative elements (see Sections 7.3.1 section 7.3.3). The inhibition correlated well with the amount of chemisorbed chlorine on Anthralur or NH_3 -treated Anthralur [98], and the deactivation could be reversed by heat treatment under N_2 or H_2 at 1173 K [96] or with NH_3

(Tables 7.6 and 7.7). Electronegative elements bound to the edge of graphene layers would attract electrons from the delocalized π -electron system and thus reduce their capacity to transfer to adsorbed molecules. This might be an explanation of their catalysis-inhibiting effect.

In many cases the effect of nitrogen doping of carbons on their catalytic properties might be due to two overlapping effects, catalysis by basic surface sites and by electron donation.

Acknowledgments

The dedicated work of many students in my research group, cited in the references with their theses or as co-authors, is gratefully acknowledged.

REFERENCES

- [1] P.S.D. Brito, C.A.C. Sequeira, *J. Power Sources* 52 (1994) 1.
- [2] E. Yeager, *Electrochim. Acta* 29 (1984) 1527.
- [3] H.P. Boehm, E. Diehl, W. Heck, R. Sappok, *Angew. Chem. Int. Ed. Engl.* 3 (1964) 669.
- [4] H.P. Boehm, in D.D. Eley, H. Pines, P.B. Weisz, Eds., *Advances in Catalysis*, Vol. 16, Academic Press, New York, 1966, pp. 179–274.
- [5] H.P. Boehm, *Carbon* 32 (1994) 759.
- [6] H.P. Boehm, *Carbon* 40 (2002) 145.
- [7] A. Marchand, J.V. Zanchetta, *Carbon* 3 (1966) 483.
- [8] E. Fitzer, K. Mueller, W. Schaefer, in P.L. Walker, Jr., Ed., *Chemistry and Physics of Carbon*, Vol. 7, Marcel Dekker, New York, 1971, pp. 237–383, in particular p. 324.
- [9] J.R. Pels, F. Kapteijn, J.A. Moulijn, Q. Zhu, K.M. Thomas, *Carbon* 33 (1995) 1641.
- [10] J. Lahaye, G. Nansé, Ph. Fioux, A. Bagreev, A. Broshniuk, V. Strelko, *Appl. Surf. Sci.* 147 (1999) 153.
- [11] J. Lahaye, G. Nansé, A. Bagreev, V. Strelko, *Carbon* 37 (1999) 585.
- [12] J.J. Freeman, F.G.R. Gimblett, R.A. Hayes, L.M. Amin, K.S.W. Sing, in F. Rodríguez-Reinoso, J. Rouquerol, K.S.W. Sing, K.K. Unger, Eds., *Studies in Surface Science and Catalysis*, Vol. 62, Characterization of Porous Solids II, Elsevier, Amsterdam, 1991, pp. 319–328.
- [13] J.J. Freeman, G.S. Bhatia, F.G.R. Gimblett, A.J. Reynolds, K.S.W. Sing, J.B. Tomlinson, in *Extended Abstracts, 20th Biennial Conference on Carbon*, Santa Barbara, CA, 1991, p. 98.
- [14] H. Konno, T. Nakahashi, M. Inagaki, *Carbon* 35 (1997) 669.
- [15] M. Kodama, J. Yamashita, Y. Soneda, H. Hatori, K. Kamegawa, *Carbon* 45 (2007) 1105.
- [16] F. Kapteijn, J.A. Moulijn, S. Matzner, H.P. Boehm, *Carbon* 37 (1999) 1143.
- [17] S. Matzner, Dr. rer. nat. thesis, University of Munich, Germany, 1996.

- [18] S. Matzner, H.P. Boehm, in *Extended Abstracts, 22nd Biennial Conference on Carbon*, San Diego, CA, 1995, p. 600.
- [19] D. Mang, H.P. Boehm, in *Extended Abstracts, 19th Biennial Conference on Carbon*, University Park, PA, 1989, p. 8.
- [20] D. Mang, H.P. Boehm, K. Stanczyk, H. Marsh, *Carbon* 30 (1992) 391.
- [21] C. Quirós, J. Gómez-García, F.J. Palomares, L. Soriano, E. Elizalde, J.M. Sanz, *Appl. Phys. Lett.* 77 (2000) 803.
- [22] E. Raymundo-Piñero, D. Cazorla-Amorós, A. Linares-Solano, J. Find, U. Wild, R. Schlögl, *Carbon* 40 (2002) 597.
- [23] C.J. Spracklin, K.M. Thomas, H. Marsh, I.A.S. Edwards, in *Extended Abstracts, 20th Biennial Conference on Carbon*, Santa Barbara, CA, 1991, p. 212.
- [24] D.P. Kim, C.L. Lin, T. Mihalisin, P. Heiney, M.M. Labes, *Chem. Mater.* 3 (1991) 686.
- [25] R. Sen, B.C. Satishkumar, A. Govindaraj, K.R. Harikumar, M.K. Renganathan, C.N.R. Rao, *J. Mater. Chem.* 7 (1997) 2335.
- [26] S. Maldonado, S. Morin, K.J. Stevenson, *Carbon* 44 (2006) 1429.
- [27] T. Matsui, M. Yudasaka, R. Kikuchi, Y. Ohki, S. Yoshimura, *Mater. Sci. Eng. B* 29 (1995) 220.
- [28] Y. Kawabuchi, S. Kawano, I. Mochida, *Carbon* 34 (1996) 711.
- [29] Y. Kawabuchi, C. Sotowa, M. Kishino, S. Kawano, D.D. Whitehurst, I. Mochida, *Langmuir* 13 (1997) 2314.
- [30] C.-M. Yang, M. El-Merraoui, H. Seki, K. Kaneko, *Langmuir* 17 (2001) 675.
- [31] C.-M. Yang, K. Kaneko, *Carbon* 39 (2001) 1075.
- [32] I.V. Babich, K. Seshan, L. Lefferts, *Appl. Catal. B* 59 (2005) 205.
- [33] Y. Xia, R. Mokaya, *Adv. Mater.* 16 (2004) 1553.
- [34] Y. Xia, R. Mokaya, *Chem. Mater.* 17 (2005) 1553.
- [35] J. Mrha, *Coll. Czech. Chem. Commun.* 31 (1966) 715.
- [36] H. Böhm, *Wiss. Ber. AEG Telefunken* 43 (1970) 241.
- [37] M. Zuckmantel, R. Kurth, H.P. Boehm, *Z. Naturforsch. B* 34 (1979) 188.
- [38] B. Tereczki, R. Kurth, H.P. Boehm, in *Preprints, Carbon '80, International Carbon Conference*, Baden-Baden, Germany, 1980, p. 218.
- [39] R. Kurth, B. Tereczki, H.P. Boehm, in *Extended Abstracts, 15th Biennial Conference on Carbon*, Philadelphia, PA, 1981, p. 244.
- [40] H.P. Boehm, G. Mair, T. Stöhr, A.R. de Rincón, B. Tereczki, *Fuel* 63 (1984) 1081.
- [41] H.P. Boehm, A.R. de Rincón, T. Stöhr, B. Tereczki, A. Vass, *J. Chim. Phys.* 84 (1987) 1449.
- [42] Y.F. Jia, K.M. Thomas, in *Extended Abstracts, 24th Biennial Conference on Carbon*, Charleston, SC, 1999, p. 476.
- [43] C.L. Mangun, K.R. Benak, J. Economy, K.L. Foster, *Carbon* 39 (2001) 1809.
- [44] W.F. Chen, F.S. Cannon, J.R. Rangel-Mendez, *Carbon* 43 (2005) 573.
- [45] W. Chen, F.S. Cannon, *Carbon* 43 (2005) 2742.
- [46] Y.F. Jia, B. Xiao, K.M. Thomas, *Langmuir* 18 (2002) 470.
- [47] A. Vass, Dr. rer. nat. thesis, University of Munich, Germany, 1989.
- [48] B. Stöhr, Dr. rer. nat. thesis, University of Munich, Germany, 1990.

- [49] D. Mang, Dr. rer. nat. thesis, University of Munich, Germany, 1991.
- [50] K. Li, L. Ling, C. Lu, W. Qiao, Z. Liu, L. Liu, I. Mochida, *Carbon* 39 (2001) 1803.
- [51] J. Zawadzki, M. Vioniewski, *Carbon* 41 (2003) 2257.
- [52] J. Starck, P. Burg, S. Müller, J. Bimer, G. Furdin, P. Fioux, C. Vix-Guterl, D. Begin, P. Faure, B. Azambre, *Carbon* 44 (2006) 2549.
- [53] R.J.J. Jansen, H. van Bekkum, *Carbon* 32 (1994) 1507.
- [54] R.J.J. Jansen, H. van Bekkum, *Carbon* 33 (1995) 1021.
- [55] B. Stöhr, H.P. Boehm, R. Schlögl, *Carbon* 29 (1991) 707.
- [56] H.P. Boehm, A.R. de Rincón, T. Stöhr, B. Tereczki, A. Vass, *J. Chim. Phys.* 84 (1987) 1499.
- [57] E.K. Rideal, W.M. Wright, *J. Chem. Soc. (London)* 127 (1925) 1347.
- [58] F. Adib, A. Bagreev, T.J. Bandosz, *Langmuir* 16 (2000) 1980.
- [59] A. Bagreev, J.A. Menéndez, I. Dukhno, Y. Tarasenko, T.J. Bandosz, *Carbon* 42 (2004) 469.
- [60] R.A. Hayden, U.S. patent 5, 352, 370, 1994.
- [61] R.A. Hayden, U.S. patent 5, 504, 050, 1996.
- [62] P. Burg, P. Fydrych, D. Cagniant, G. Nansé, J. Bimer, A. Jankowska, *Carbon* 40 (2002) 1521.
- [63] L. Singoredjo, F. Kapteijn, J.A. Moulijn, J.-M. Martínez, H.P. Boehm, *Carbon* 31 (1993) 213.
- [64] H. Höpfl, thesis for dipl.-chem. exam, Faculty of Chemistry and Pharmacy, University of Munich, Germany, 1994.
- [65] R.H. Bradley, X. Ling, I. Sutherland, *Carbon* 31 (1993) 1115.
- [66] J. Houben, T. Weyl, *Methoden der Organischen Chemie*, Vol. 4, Georg Thieme Verlag, Stuttgart, Germany, 1953, p. 238
- [67] A.L. Chaney, E.P. Marbach, *Clin. Chem.* 8 (1962) 130.
- [68] M.W. Weatherburn, *Anal. Chem.* 39 (1967) 971.
- [69] K. Stańczyk, K. Dziembaj, Z. Piwowarska, S. Witkowski, *Carbon* 33 (1995) 1383.
- [70] H. Schmiers, J. Friebel, P. Streubel, R. Hesse, R. Köpsel, *Carbon* 37 (1999) 1965.
- [71] Q. Zhu, S.L. Money, A.E. Russell, K.M. Thomas, *Langmuir* 13 (1997) 2149.
- [72] V.V. Strelko, V.S. Kuts, P.A. Thrower, *Carbon* 38 (2000) 1499.
- [73] M.B. Kelly, A.N. Bradley, R.P. Nelson, in *Proceedings of the International Conference on Coal Science*, Newcastle-upon-Tyne, UK, 1991, p. 356
- [74] S.R. Kelemen, M.L. Gorbaty, P.J. Kwiatek, *Energy Fuels* 8 (1994) 896.
- [75] M. Abe, K. Kawashima, K. Kozawa, H. Sakai, K. Kaneko, *Langmuir* 16 (2000) 5059.
- [76] J.M. Ripalda, E. Román, N. Diaz, L. Galin, I. Montero, G. Comelli, A. Baraldi, S. Lizzit, A. Goldoni, G. Paolucci, *Phys. Rev. B* 60 (1999) R3705.
- [77] S. Mitra-Kirtley, O.C. Mullins, J.V. Elp, S.J. George, J. Chen, S.P. Cramer, *J. Am. Chem. Soc.* 115 (1993) 252.
- [78] J.P. Boudou, P. Parent, F. Suárez-García, S. Villar-Rodil, A. Martínez-Alonso, J.M.D. Tascón, *Carbon* 44 (2006) 2452.

- [79] P. Chambrion, T. Suzuki, Z.G. Zhang, T. Kyotani, A. Tomita, *Energy Fuels* 11 (1997) 681.
- [80] B. Xiao, J.P. Boudou, K.M. Thomas, *Langmuir* 21 (2005) 3400.
- [81] M. Voll, H.P. Boehm, *Carbon* 8 (1970) 741.
- [82] M.A. Montes-Morán, D. Suárez, J.A. Menéndez, E. Fuente, *Carbon* 42 (2004) 1219.
- [83] T. Kuretzki, Dr. rer. nat. thesis, University of Munich, 1993.
- [84] T. Matsuoka, H. Hatori, M. Kodama, J. Yamashita, N. Miyajima, *Carbon* 42 (2004) 2346.
- [85] R. Sappok, H.P. Boehm, *Carbon* 6 (1968) 573.
- [86] T. Belz, A. Bauer, J. Find, M. Günter, D. Herein, H. Möckel, N. Pfänder, H. Sauer, G. Schulz, J. Schütze, O. Timpe, U. Wild, R. Schlögl, *Carbon* 36 (1998) 731.
- [87] K.A. Grant, Q. Zhu, K.M. Thomas, *Carbon* 32 (1994) 883.
- [88] S. Matzner, H.P. Boehm, *Carbon* 36 (1998) 1697.
- [89] E. Pollak, G. Salitra, A. Soffer, D. Aurbach, *Carbon* 44 (2006) 3302.
- [90] V. Strelko, in *Extended Abstracts, Eurocarbon '98, International Carbon Conference* Strasbourg, France, 1998, p. 799
- [91] Q. Yang, W. Xu, A. Tomita, T. Kyotani, *Chem. Mater.* 17 (2005) 2940.
- [92] R.D. Gunning, M. Venkatesan, D.H. Grayson, J.M.D. Coey, *Carbon* 44 (2006) 3213.
- [93] W. Chen, F.S. Cannon, J.R. Rangel-Mendez, *Carbon* 43 (2005) 581.
- [94] R. Kurth, Dr. rer. nat. thesis, University of Munich, Germany, 1979.
- [95] E. Raymundo-Piñero, D. Cazorla-Amarós, E. Morallón, *J. Chem. Ed.* 76 (1999) 958.
- [96] B. Tereczki, Dr. rer. nat. thesis, University of Munich, Germany, 1979.
- [97] B.R. Puri, R.C. Bansal, *Carbon* 5 (1967) 189.
- [98] M. Gurrath, H.P. Boehm, in *Proceedings of Carbon'92, International Carbon Conference*, Essen, Germany, 1992, p. 388
- [99] O. Warburg, *Biochem. Z.* 113 (1921) 257.
- [100] I. Mochida, T. Hirayama, S. Kisamori, S. Kawano, H. Fujitsu, *Langmuir* 8 (1992) 2290.
- [101] E. Raymundo-Piñero, D. Cazorla-Amorós, A. Linares-Solano, *Carbon* 39 (2001) 231.
- [102] E. Raymundo-Piñero, D. Cazorla-Amorós, A. Linares-Solano, *Carbon* 38 (2000) 335.
- [103] P. Davini, *Carbon* 28 (1990) 565.
- [104] I. Mochida, S. Miyamoto, K. Kuroda, S. Kawano, K. Sakanishi, Y. Korai, A. Yasutake, M. Yoshikawa, *Energy Fuels* 13 (1999) 374.
- [105] A.A. Lizzio, J.A. De Barr, *Fuel* 75 (1996) 1515.
- [106] P. Davini, *Fuel* 68 (1989) 145.
- [107] J. Muñiz, J.E. Herrero, A.B. Fuentes, *Appl. Catal. B* 18 (1998) 171.
- [108] E. Raymundo-Piñero, D. Cazorla-Amorós, A. Linares-Solano, *Carbon* 41 (2003) 1925.

- [109] I. Mochida, K. Kuroda, S. Miyamoto, C. Sotowa, Y. Korai, S. Kawano, L.K. Sakanishi, A. Yasutake, M. Yoshikawa, *Energy Fuels* 11 (1997) 272.
- [110] I. Mochida, S. Miyamoto, K. Kuroda, S. Kawano, S. Yatsunami, Y. Korai, A. Yasutake, M. Yoshikawa, *Energy Fuels* 13 (1990) 369.
- [111] M.A. Daley, C.L. Mangun, J.A. De Barr, S. Riha, A.A. Lizzio, G.L. Donnals, J. Economy, *Carbon* 35 (1997) 411.
- [112] S. Kisamori, S. Kawano, I. Mochida, *Chem. Lett.* 22 (1993) 1899.
- [113] S. Kisamori, K. Kuroda, S. Kawano, I. Mochida, Y. Matsumura, M. Yoshikawa, *Energy Fuels* 8 (1994) 1337.
- [114] I. Mochida, K. Kuroda, S. Kawano, Y. Matsumura, M. Yoshikawa, *Fuel* 76 (1997) 533.
- [115] I. Mochida, K. Kuroda, S. Kawano, Y. Matsumura, M. Yoshikawa, E. Grulke, R. Andrews, *Fuel* 76 (1997) 537.
- [116] P. Davini, *Carbon* 41 (2003) 277.
- [117] J.P. Boudou, *Carbon* 41 (2003) 1955.
- [118] A. Bagreev, S. Bashkova, T.J. Bandosz, *Langmuir* 18 (2002) 1257.
- [119] C. Moreno-Castilla, F. Carrasco-Marín, E. Utrera-Hidalgo, J. Rivera-Utrilla, *Langmuir* 9 (1993) 1378.
- [120] J.P. Boudou, M. Chehimi, E. Broniek, T. Siemieniewska, J. Bimer, *Carbon* 41 (2003) 1999.
- [121] J. Bimer, P.D. Salbut, S. Berlozecki, J.-P. Boudou, E. Broniek, T. Siemieniewska, *Fuel* 77 (1998) 519.
- [122] A.B. Lamb, L.W. Elder, Jr., *J. Am. Chem. Soc.* 53 (1931) 137.
- [123] G. Drohmann, study for teachers state exam, University of Munich, Germany, 1983.
- [124] G. Thomas, T.R. Ingraham, *Unit Process. Hydromet.* 1 (1965) 67.
- [125] A.M. Posner, *Trans. Faraday Soc.* 49 (1953) 389.
- [126] B.R. Puri, K.C. Kalra, *Indian J. Chem.* 10 (1972) 72.
- [127] N.I. Kuznetsova, V.A. Likhobov, M. Gurrath, H.P. Boehm, *Appl. Catal. A* 128 (1995) 41.
- [128] E. Ahumada, H. Lizama, F. Orellana, C. Suárez, A. Huidobro, A. Sepúlveda-Escribano, F. Rodríguez-Reinoso, *Carbon* 40 (2002) 2827.
- [129] P. Sreeramamurthy, P.G. Menon, *J. Catal.* 37 (1975) 287.
- [130] J. Klein, K.-D. Henning, *Fuel* 63 (1984) 1064.
- [131] K.-D. Henning, J. Klein, H. Jüntgen, in *Extended Abstracts, Carbon '80, International Carbon Conference*, Baden-Baden, Germany, 1980, p. 223.
- [132] F. Adib, A. Bagreev, T.J. Bandosz, *J. Colloid Interface Sci.* 214 (1999) 407.
- [133] S.V. Mikhalovsky, Yu. P. Zaitsev, *Carbon* 35 (1997) 1367.
- [134] J.J. Choi, M. Hirai, M. Shoda, *Appl. Catal. A* 79 (1991) 241.
- [135] T.J. Bandosz, *J. Colloid Interface Sci.* 246 (2002) 1.
- [136] A. Bagreev, T.J. Bandosz, *Ind. Eng. Chem. Res.* 44 (2005) 530.
- [137] F. Adib, A. Bagreev, T.J. Bandosz, *J. Colloid Interface Sci.* 216 (1999) 360.
- [138] A. Bagreev, F. Adib, T.J. Bandosz, *Carbon* 39 (2001) 1897.
- [139] H. Katoh, I. Kuniyoshi, M. Hirai, M. Shoda, *Appl. Catal. B* 6 (1995) 255.

- [140] A.K. Dalai, E.L. Tollefson, A. Yang, E. Sasaoka, *Ind. Eng. Chem. Res.* 36 (1997) 4726.
- [141] S. Bashkova, A. Bagreev, T.J. Bandosz, *Langmuir* 19 (2003) 6115.
- [142] A. Bagreev, J.A. Menedez, I. Dukhno, Y. Tarasenko, T.J. Bandosz, *Carbon* 43 (2005) 208.
- [143] T. Stöhr, Dr. rer. nat. thesis, University of Munich, Germany, 1987.
- [144] M. Kamel, R. Wizinger, *Helv. Chim. Acta* 43 (1960) 594.
- [145] B. Höke, H.A. Wittbold, *Galvanotechnik* 61 (1970) 468.
- [146] B. Höke, H.A. Wittbold, *Wasser Luft Betr.* 13 (1969) 250.
- [147] A. Clauss, H.P. Boehm, U. Hofmann, *Z. Anorg. Allg. Chem.* 290 (1957) 35.
- [148] B.H.M. Billinge, J.B. Docharty, M.J. Bevan, *Carbon* 22 (1984) 83.
- [149] B.H.M. Billinge, M.G. Evans, *J. Chim. Phys.* 81 (1984) 779.
- [150] V. Deitz, *Carbon* 25 (1987) 31.
- [151] B.R. Puri, in *Proceedings of the 5th Biennial Conference on Carbon*, University Park, PA, 1961, Pergamon Press, Oxford, 1962, Vol. 1, p. 165.
- [152] A. Bagreev, H. Rahman, T.J. Bandosz, *Ind. Eng. Chem. Res.* 39 (2000) 3849.
- [153] A.C. Lau, D.N. Furlong, T.W. Healey, F. Grieser, *Colloid Surf.* 18 (1986) 93.
- [154] J.C. Petit, Y. Bahaddi, *Carbon* 31 (1993) 821.
- [155] N.V. Vorob'ev-Desyatovskii, R.I. Ibragimova, S.K. Gordeev, B.P. Nikolaev, *Russ. J. Gen. Chem.* 76 (2006) 946.
- [156] Q.-L. Zhuang, T. Kyotani, A. Tomita, *Carbon* 32 (1994) 539.
- [157] I. Menendez, A.B. Fuertes, *Carbon* 39 (2001) 733.
- [158] T. Kuretzky, H.P. Boehm, in *Extended Abstracts, Carbon '94, International Carbon Conference*, Granada, Spain, 1994, p. 262.
- [159] S. Matzner, T. Kuretzky, H.P. Boehm, in *Extended Abstracts, 23rd Biennial Conference on Carbon*, University Park, PA, 1997, p. 194.
- [160] H.P. Boehm, A. Vass, R. Kollmar, in *Extended Abstracts, 18th Biennial Conference on Carbon*, Worcester, MA, 1987, p. 86
- [161] H.P. Boehm, A. Vass, R. Kollmar, in K.K. Unger, J. Rouquerol, K.S.W. Sing, H. Kral, Eds., *Characterization of Porous Solids*, Elsevier, Amsterdam, 1988, p. 163
- [162] F. Carrasco-Marín, J. Rivera-Utrilla, J.P. Joly, C. Moreno-Castilla, *J. Chem. Soc. Faraday Trans.* 92 (1996) 2779.
- [163] H.P. Boehm, G. Mair, T. Stöhr, in *Extended Abstracts, 17th Biennial Conference on Carbon*, Lexington, KY, 1985, p. 381
- [164] J. Spengler, thesis for dipl.-chem. exam, University of Munich, Germany, 1994.
- [165] M. Besson, P. Gallezot, *Catal. Today* 81 (2003) 547.
- [166] A. Pigamo, M. Besson, B. Blanc, P. Gallezot, A. Blackburn, O. Kozynchenko, S. Tennison, E. Crezee, F. Kapteijn, *Carbon* 40 (2002) 1267.
- [167] A. Fortuny, J. Font, A. Fabregat, *Appl. Catal. B* 19 (1998) 165.
- [168] A. Fortuny, C. Miró, J. Font, J. Fabregat, *Catal. Today* 48 (1999) 323.
- [169] J. Trawczyński, *Carbon* 41 (2003) 1515.
- [170] K. Okamoto, N. Tanaka, K. Adachi, H. Shingu, *Bull. Chem. Soc. Jpn.* 39 (1966) 1522.

- [171] G.-M. Schwab, H. Ulrich, *Kolloid Z. Z. Polym.* 190 (1963) 108.
- [172] J. Zlotnick, J.J. Prinsloo, P.C. van Berge, *J. Catal.* 53 (1978) 106.
- [173] C. Sotowa, Y. Watanabe, S. Yatsunami, Y. Korai, I. Mochida, *Appl. Catal. A* 180 (1999) 317.
- [174] C. Sotowa, Y. Kawabuchi, I. Mochida, *Chem. Lett.* 25 (1996) 967.
- [175] I. Mochida, Y. Yasumoto, Y. Watanabe, H.H. Fujitsu, Y. Kojima, M. Morita, *Chem. Lett.* 23 (1994) 197.
- [176] G.S. Szymański, S. Ziętek, in *Extended Abstracts, Carbon '01, International Conference on Carbon*, Lexington, KY, 2001, p. 571; or CD: Posters, Basic, p. 2.03.
- [177] T. Stöhr, thesis for dipl.-chem. exam, University of Munich, Germany, 1983.
- [178] T. Stöhr, H.P. Boehm, in *Extended Abstracts, Carbon '86, International Carbon Conference*, Baden-Baden, Germany, 1986, p. 354
- [179] G. Mair, thesis for dipl.-chem. exam, University of Munich, Germany, 1982.
- [180] P. Zill, thesis for dipl.-chem. exam, University of Munich, Germany, 1993.
- [181] M. Reiner, thesis for dipl.-chem. exam, University of Munich, Germany, 1993.
- [182] F. Gupta, thesis for dipl.-chem. exam, University of Munich, Germany, 1992.
- [183] I.W.C.E. Arends, W.R. Ophorst, R. Louw, P. Mulder, *Carbon* 34 (1996) 581.
- [184] D. Santoro, R. Louw, *Carbon* 39 (2001) 2091.
- [185] H. Gerischer, A. Heller, *J. Phys. Chem.* 95 (1991) 5261.
- [186] D. Bahnemann, D. Bockelmann, R. Goslich, *Solar Energy Mater.* 24 (1991) 564.
- [187] H. Chon, J. Pajares, *J. Catal.* 14 (1969) 257.
- [188] G. Bewer, Dr. rer. nat. thesis, University of Munich, Germany, 1975.
- [189] R.P. Müller, thesis for dipl.-chem. exam, University of Munich, Germany, 1975.
- [190] S.V. Mikhalovsky, Y u.P. Zaitsev, V.M. Lukianchuk, V.B. Volkov, V.A. Zazhigalov, A.M. Puziy, in *Extended Abstracts, 22nd Biennial Conference on Carbon*, San Diego, CA, 1995, p. 568.

8 Carbon-Anchored Metal Complex Catalysts

CRISTINA FREIRE and ANA ROSA SILVA

8.1 INTRODUCTION

Immobilization of transition-metal complexes with catalytic properties onto solid supports is a theme of intense research [1–10]. Most reports on complex immobilization describe the use of organic polymers and porous inorganic materials, such as zeolites, mesoporous silicas, and clays as metal complex supports. Carbon materials offer advantages over these supports, such as stability, mechanical resistance, high surface area, optimum porosity, and particularly, several types of oxygen superficial groups that may be maximized selectively by thermal and chemical processes, which can be used as building blocks for the covalent attachment of transition-metal complexes. The main objective of immobilization of homogeneous catalysts is to generate heterogeneous catalysts with catalytic properties better than those of homogeneous analogs. The activity and chemo- or enantioselectivities of immobilized systems can be enhanced relative to their free analogs, due to two major key effects: the confinement concept [1–11] and site isolation [4–10].

Improvement in the catalytic properties derived from the confinement concept results from imprisonment of the substrate within the pores of the support, which leads to enhanced interactions between the active catalyst and the substrate [11]. However, this is a two-edged sword, as tight entrapment of the immobilized catalyst molecules can induce lower activity or chemo- and enantioselectivity as a consequence of a compulsory conformation. The lower activities can also be due to reduced or even blocked mass transport in the narrow pores, imposing limits on the effective range of substrates that can be used. On the other hand, the reduced enantioselectivity can be due either to a strong physisorption of the complex on the walls of the support or to a constrained environment that prevents

the chiral complex from taking the special conformation that is required to induce chiral recognition [2,5,6,8].

The improved catalytic activity can also be a consequence of the fact that when metal complexes are attached to a support, the immobilized catalysts can no longer interact with each other as in homogeneous media, preventing the active forms of the catalysts from reacting with each other. This is a phenomenon that is usually observed in homogeneous media and is responsible to a large extent for the deactivation of homogeneous catalysts [1,2,4–8].

This chapter begins with a general description of the several strategies to heterogenize transition-metal complexes onto solid supports, with a special emphasis on those methodologies that have been used for complex grafting onto carbon materials. It will include sections that will focus on the various transition-metal complexes that have been immobilized onto several carbon materials: activated carbons, black carbons, carbons xerogels, and carbon nanotubes; the specific catalytic reactions with these carbon-based systems are also discussed in some detail.

8.2 GENERAL METHODS FOR MOLECULE IMMOBILIZATION

There are several approaches to immobilizing transition-metal complexes on solid supports. One way to present them is to group on the type of interaction between the support and the molecular species to be grafted. In this context, three different groups of support–molecule interactions can be considered [1–10]: (1) covalent bonding, (2) noncovalent interactions (including physical adsorption and electrostatic interactions), and (3) encapsulation. Additionally, for the first two types of immobilization procedures, interaction with the support can occur directly between the support and the molecular species or through bifunctional molecules, previously attached to the support or reacted with the metallic complex, usually termed *spacers* or *linkers*.

Covalent bonding of metallic complexes onto the support is by far the most used strategy to immobilize transition-metal complexes with catalytic properties [1–10]. It can be effected either directly by reaction of the metal complex with the support surface groups or mediated through a spacer previously grafted to the support or reacted with the complex. In the former case the complex can react with the support surface groups through axial coordination at the metal center or throughout the functional groups existing in the ligand coordinated to the metal. On the other hand, the immobilization of metal complexes via spacers involves the selection of a bifunctional molecule that must have reactive groups capable of reacting with both the support surface groups and the complex (via ligand functionalities or metal axial coordination). Selection of the spacer, which ultimately depends on the type of support surface groups, must also consider other aspects, such as its length, flexibility, and degree of surface coverage, which are very important to the design of heterogeneous catalysts with good catalytic performance; for example, in the case of asymmetric catalysis, the point

of attachment of the tether to the ligand should be as far as possible from the stereogenic center in order to minimize the disturbance of the chiral induction [2,6,8,9]. Among the various spacers used, the organosilanes are the most used bifunctional molecules since they have both alkoxy groups, which easily react with surface hydroxyl groups (the majority of the surface groups present in the inorganic supports) and several other reactive groups, such as acid, halide, amine, and mercapto, which can react with an enormous variety of functional groups in the metal complexes, through the ligand, or by metal axial coordination: cyanuric chloride, carbodiimide derivates, and polyamines have also been used as linkers [1–10].

The most important advantage of this method is that molecular species are bonded via chemical bonds and experience almost no leaching from the support, as far as the metal complex ligation and all the bonds are adequately stable in catalytic media. Nevertheless, an important drawback of this method is the large preparative effort, since it involves a multistep procedure that usually includes not only the functionalization of the ligands coordinated to the metal, but also the grafting of spacers onto the support. Furthermore, the covalent bonding of metal complexes, directly or via spacers, can alter, to different extents, the electronic density within the metal, which in turn, can alter the catalytic performance of the catalysts in a way that may be difficult to foresee [3–10].

The other two methodologies for immobilization of metal complexes, *physical adsorption* and *electrostatic interaction*, belong to the group of noncovalent interactions between the support and the metal complex [1–10]. In the former case it includes $\pi-\pi$ interactions, van der Waals and hydrogen bonds, and hydrophobic–hydrophilic interactions between the support and the complex. In the second method, there is an electrostatic interaction between the support and the complex, and consequently, there must be charges of opposite signals between the support and complex. The noncovalent interactions can also occur directly between the support and the complex or via the use of spacers; in the latter case the interaction between the spacer and the complex can be of different in nature, covalent or noncovalent.

The great advantage of noncovalent immobilization methodologies is the easy preparation of these systems compared to covalent bonding, but their sensitivity to solvents is an important weakness which can cause extensive leaching of the active phase by simple manipulation of the experimental conditions in preparation of the immobilized complexes or during catalytic reactions.

Encapsulation implies physical entrapment of the metal complex within the pores of the support, and as a starting point it is supposed that no other interactions between the support and the metal complex exist besides the physical confinement [1,2,4,7,9,12]. Therefore, the encapsulation methodology is that which can better mimic the catalytic behavior of metal complexes in the homogeneous phase. This methodology depends on the respective sizes of the complex and the cavity where the complex should be entrapped. To prevent the leaching of the complex after encapsulation, the size of the complex has to be bigger than the dimensions of the cavity, which is the most important limitation of this method. As in covalent

bonding, this methodology also involves a multistep approach, which can in some cases be lengthy. In general, there are three approaches to encapsulate metal complexes: (1) *in situ* synthesis of the complex, (2) the flexible ligand, and (3) template synthesis; the first two methods are also termed the “ship in a bottle” approaches [4,7,9,12]. In the first two approaches, the support is previously prepared and used as a nanoreactor, since the complex is synthesized within the support cavity/pores. In *in situ synthesis* a molecular complex is used as precursor, and after its adsorption onto the support it is made to react with other reagents to give the desired complex, whereas in *the flexible ligand* approach the metallic salt is previously adsorbed in the support cavity and then complexed by the ligand, which is added to the support in the liquid or gas phase. Finally, in *template synthesis* the metal complex is used as a template in the synthesis of the support itself. Although this approach could be interesting from the point of view of preparative effort, since the complex is prepared by the traditional methods outside the support, it has an important disadvantage, the impossibility of doing the step of support calcination at the usual temperature (500°C) since the complex would decompose. These aspects have pernicious consequences on (1) the purity of the support, as the decomposition of the organic templates used in the synthesis is not complete, and (2) the rigidity and stability of the support, since there is only a partial dehydration of the metal oxides.

8.3 METHODS FOR IMMOBILIZATION OF TRANSITION-METAL COMPLEXES ONTO CARBON MATERIALS

Research on the immobilization of metal complexes using carbon materials is scarce compared with inorganic supports, such as zeolites, silicas, and clay-based materials [1–10]. Nevertheless, carbon materials are unique supports, as they can provide a variety of surface groups at the edges and/or defects of graphene sheets that can be tailored by adequate thermal or chemical treatments, besides the inherent chemical–physical reactivity associated with the graphene sheets themselves, which are hydrophobic, have low polarity, and have a rich π-electron density [13–15]. This can lead to a huge diversity of methods for immobilization of molecular species.

The modification of carbon material surfaces for immobilization of molecular species with catalytic properties had its beginning around 1970 with research work in chemical modification of carbon electrodes, such as graphite, pyrolytic/highly oriented pyrolytic graphites (HOPGs), and glassy carbon, for use in molecular electrocatalysis [16–19]. More recently, the discovery of the new allotropic forms of carbon, fullerenes [20] and carbon nanotubes (CNTs) [21], as well as novel porous carbon materials [22] (including uniform porous carbon materials), has led to an astonishing growth of methods for carbon surface functionalization with a plethora of chemical species, fueled by potentially important applications of all these novel carbon materials in several different areas.

We begin this section with the presentation of several methods for carbon surface derivatization and then describe examples of immobilization of transition-metal complexes onto several carbons materials, excluding fullerenes and those used as electrode materials.

8.3.1 Functionalization of Carbon Materials

Due to the nature of carbon materials, the presentation of representative methods for surface derivatization will follow an approach different from that described in the preceding section, which is based on the spatial target site where physical–chemical modification can take place: (1) immobilization performed at edges and/or ends and defects of graphitic sheets, (2) immobilization onto the graphene sheets, and (3) exclusively for CNTs we present some examples of endohedral encapsulation of metal complexes. For the first two cases, covalent bonding and noncovalent interactions can occur directly between the transition metal complex and carbon supports or via spacers grafted to the carbon surface.

Immobilization Performed at Edges and Defects of Graphitic Sheets Functionalization of the edges or ends and defects of graphitic sheets is probably the oldest and most popular method of anchoring molecular species at carbon material surfaces. It originated in the chemistry of HOPG, glassy carbon, or graphite [16–19], but currently is being applied to all carbon-based materials [23–33]. It is an easily accessible procedure and provides a variety of groups, which allows for direct immobilization of molecular species as well as immobilization via spacers. These groups are mainly oxygen groups that are created as a consequence of oxidation at the most reactive sites of carbons materials, namely, the edges of graphitic planes and their intrinsic defects. The number and type of oxygen functionalities created in a certain material depend on its surface area and method of oxidation [13–15,23–26].

In all carbon materials the total concentration of different oxygen groups, carboxylic acids, anhydrides, carbonyls, and phenols, represented in Figure 2.1, can be increased by oxidation in the gas phase using oxygen, ozone, carbon monoxide, carbon dioxide, and so on, or in the liquid phase using strong acids such as a nitric/sulfuric acid mixture, or other oxidizing agents, such as NaOCl, H₂O₂, KMnO₄/H₂SO₄, K₂Cr₂O₇, or OsO₄ [13–15,23–26].

The most important aspect of carbon surface chemistry, which distinguishes carbon materials from all the other supports, is that the relative amount of the oxygen functional groups can be varied selectively, depending on the oxidant used. For example, liquid-phase oxidation with nitric/sulfuric acid or hydrogen peroxide increases the surface concentration of the acidic groups, in particular the carboxylic acids, whereas gas-phase oxidation using oxygen or nitrous oxide at a high temperature introduces carbonyl and phenol groups, which are more thermally stable [13–15,23–26]. On the other hand, the quantity of phenol surface groups can be maximized by reduction of some of the most oxidized surface groups with lithium aluminum hydride [16–18,36]. In the particular

case of CNTs, these oxidative treatments etch the nanotubes, leaving the tubes open ended, with the ends being decorated with these plethora of oxygenated functionalities; moreover, these functionalities also exist along the sidewalls at intrinsic defect sites, which frequently increase as a result of the oxidative treatments [28–33].

It is the exploitation of the functionalities introduced by oxidative procedures through further chemical reaction that allows immobilization of quite a large number of molecular species onto carbon surfaces. The strategies most frequently used for derivatization of carbon-oxidized surfaces are summarized in Figure 8.1.

The presence of carboxylic acid functionalities provides access to a vast field of amide and ester covalent linkages which usually involve, in the first step, an initial treatment of the oxidized carbon surfaces with thionyl chloride or acetyl chloride [Figure 8.1(a,c)] for activation and then reaction with $-\text{NH}_2$ and $-\text{OH}$ functionalized molecules, respectively [16–18,26–33]. Reaction of the surface carboxylic acid functionalities with amine derivatives can also be mediated by carbodiimide derivatives as EDC [1-ethyl-3-(3-dimethylaminopropyl)carbodiimide] and DCC (N,N' -dicyclohexylcarbodiimide) [Figure 8.1(b)] [16–18,26–33]. In this context, metal complexes with ligands functionalized with $-\text{NH}_2$ and $-\text{OH}$ groups are strong candidates for direct covalent immobilization via the ligand using this route. In parallel, the latter addends can also be used to graft bifunctional spacers with terminal $-\text{NH}_2$ and $-\text{OH}$ functionalities to react with carbon surface groups and other groups that can be further linked to the metal complexes by covalent bond (to the ligand or via metal coordination) or by electrostatic interaction.

The carbon surface phenol groups can also offer several routes for chemical attachment of molecules by formation of ether bonds. Cyanuric chloride (CC) is a spacer that possesses three very reactive chlorine atoms and that can covalently attach to the carbon surface phenol groups with formation of ether bonds [Figure 8.1(d)]. The chlorine atoms that did not react with carbon functionalities may form other covalent bonds with chemical species bearing functional groups of the type hydroxyl/phenol, amines, Grignard reagents, and hydrazines [16–18,34]. The organosilane or siloxane reagents are other type of spacers that can be used to graft to carbon phenol groups [Figure 8.1(e)] through the halides/alkoxy groups leaving the other terminal reactive groups, such as acid, halide, amine, and mercapto, to react with an enormous variety of functional groups in the metal complexes, through the ligand or by metal axial coordination [16–18,35–37].

Finally, the carbon surface oxygen groups can also be used for direct bonding to metal complexes, usually in the form of carboxylate and phenolate groups acting as ligands of their first coordination sphere (covalent bond) or as counter ions for the complex (electrostatic interactions).

Immobilization on Graphene Sheets The graphene sheets have low polarity, behave as hydrophobic surfaces, and are rich in π -electron density [13–16,21,24]. Consequently, these properties can be used to immobilize molecular species by noncovalent interactions [28,31,32,38] and by covalent bonding. In the latter

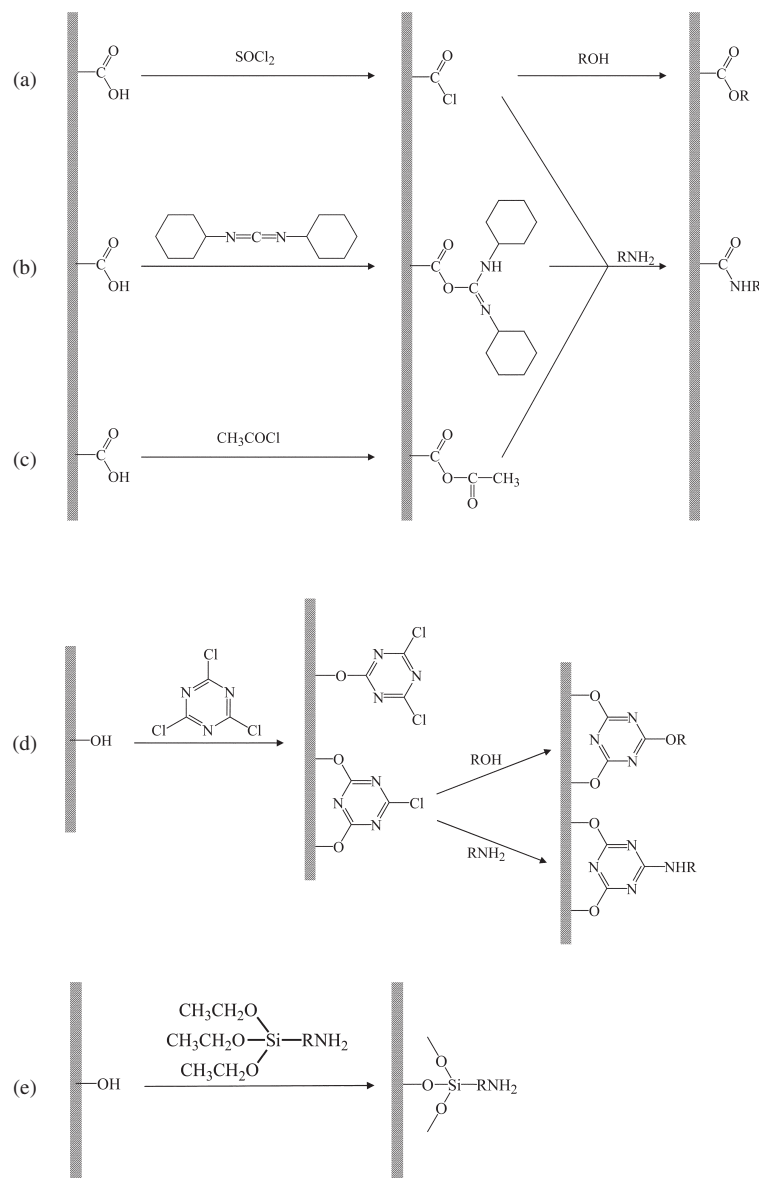


Figure 8.1 Schematic reactions of common functionalization routes for carbon materials upon oxidation: (a–c) derivatization of carboxylic groups; (d, e) derivatization of phenol groups.

case, very reactive addends need to be used, since the graphitic sheets are less chemically reactive than the edge planes and defects. Some of the chemical routes used for covalent attachment of molecular species directly to the graphene sheets also have their origin in the chemistry of HOPG, glassy carbon, or graphite: fluorination [29a,33,39–41] and aryl diazonium–based reactions [28–33,42–47]. Other chemical methods were developed within the chemistry of fullerenes: (1) addition of carbenes, nitrenes, and radicals [28–33,48] and (2) 1,3-dipolar additions [28–33,49]. These methods started to be used extensively in recent years in the functionalization of CNT sidewalls for a diversity of applications [50–53] other than immobilization of metal complexes with catalytic properties. Nevertheless, they are discussed in this section, as we consider them to be promising alternatives to be used in the future for the preparation of novel carbon-based catalysts.

Noncovalent Interactions on Graphene Sheets The noncovalent interactions include $\pi-\pi$ interactions, van der Waals/hydrophobic–hydrophilic, and electrostatic interactions between the carbon surface and the molecular species, and have been used in the functionalization of several carbon surfaces, including activated carbons (ACs); several types of graphites, and CNTs [17,18,28,30,31,38,54–57].

Direct $\pi-\pi$ interactions can occur between the carbon surface and molecules with systems that have large π -electron density. Metal complexes with ligands that have extensive π -delocalization, such as porphyrines, phthalocyanines, and polidentate Schiff base ligands, are thus good candidates to be immobilized by this method, allowing for direct immobilization of metal complexes onto the graphitic sheets of carbon materials [38,54,55,57,58]. Alternatively, there are organic molecules with large aromatic systems that can be used as spacers for complex immobilization. This group includes pyrene, anthracene derivatives, and other polyaromatic organic molecules that form specific $\pi-\pi$ interactions with graphitic sheets [28–31,38,60]. These polyaromatic molecules also have functionalities such as acyl chloride groups, carbodiimide addends, and $-\text{NH}_2/-\text{OH}$ groups that can be coupled with ligand metal complexes by covalent bonds, metal coordination, or charged functionalities that can interact electrostatically with the metal complexes.

Surfactant molecules can also be used as anchors for the immobilization of chemical species by noncovalent interactions [38]. The hydrophobic part of the molecule interacts with the graphene sheets, whereas the hydrophilic head (charged) can interact with the metal complex by electrostatic interactions or covalent bonding. Polyelectrolytes can also act as spacers for charged chemical species, and in this case, strong electrostatic interactions with carbon materials occur [49,53].

A different approach to noncovalent functionalization, which is applied exclusively to CNTs, is polymer wrapping [30,31b,49,52,53]. In this approach CNTs can be wrapped with polymers with different properties by van der Waals or by $\pi-\pi$ interactions. These polymers can also be used as anchors for metal complexes by covalent bonding or by electrostatic interactions.

Covalent Bonding on Graphene Sheets Several chemical approaches can be used to derivatize the graphene sheets; they are summarized in Figure 8.2. As stated before, they involve reactive species and specific experimental conditions, due to the low reactivity of the graphitic aromatic rings.

Fluorination Reaction. Fluorination of the carbon material can be achieved by treatment with elemental gaseous fluorine and/or fluorine-inert gas mixtures leading to the formation of C–F bonds [Figure 8.2(a)]; treatment of carbon materials with fluorine–oxygen mixtures, called oxyfluorination, can also be done [29a,31b,33,39–41]. In that case, additional $>\text{C}=\text{O}$, $-\text{C}(\text{O})\text{F}$, and $-\text{C}(\text{O})\text{OH}$ groups can be inserted into the structure. Because C–F bonds in fluorinated carbon materials are weak, there are many reactions that can be performed at the surface of fluorinated carbon materials, exemplified extensively in CNTs [29a,33]. The sidewall fluorinated CNTs can be further modified by reacting with alkyl magnesium bromides ($\text{R}-\text{Mg}-\text{X}$) in a Grignard synthesis or by reaction with alkyllithium precursors to yield sidewall alkylated CNTs [61]; furthermore, diamines [$(\text{H}_2\text{N}(\text{CH}_2)_n)\text{NH}_2$] or amino alcohols [$\text{HN}(\text{R})(\text{CH}_2)_n\text{OH}$] can displace fluorine to form sidewall aminoalkyl- or hydroxyl-functionalized CNTs, respectively [62]. More recently, fluorinated single-walled CNTs (SWCNTs) have been reacted with diols and glycerol in the presence of alkali metals or alkali hydroxides to give $-\text{OH}$ -terminated moieties on CNT sidewalls [63]. These methods allow the functionalization of CNTs with $-\text{NH}_2$ and $-\text{OH}$ groups that can be used for direct or via spacer attachment of transition-metal complexes.

Aryl Diazonium-Based Chemistry. The modification of carbon surfaces by reactive aryl diazonium salts has currently been widely applied to the sidewall CNT functionalization [Figure 8.2(b)] [28–33]. This reaction proceeds via the aryl radical generated upon one electron reduction of the diazonium salt, and it was first performed using electrochemical reduction [42–47]. Recently, it was shown that diazonium functionalization can also be achieved chemically, and can occur at the sidewalls as well as end-cap functionalization [28–33].

Ozonolysis. Addition of ozone to methanolic dispersions of CNTs led to 1,3-dipolar cyclo-addition reaction to sidewall CNTs following a Criegee mechanism, analogous to the addition of alkenes and fullerenes [Figure 8.2(c)] [29a]. The main purpose of this approach is to generate oxygenated groups, such as carboxylic acids, aldehydes/ketones, or alcohols, through chemical treatment of the primary ozonide intermediate with hydrogen peroxide, dimethyl sulfide, or sodium borohydride, in order to extend the oxygen functionalization to CNT sidewall derivatization.

Addition of Carbenes, Nitrenes, and Radicals. The direct addition of carbenes, nitrenes, and radicals to the unsaturated π -system of the graphene sheets can occur through several reactions [Figure 8.2(d)] [28–33,48]. For example, Chen et al. [64] reported the functionalization of SWCNTs with dichlorocarbene

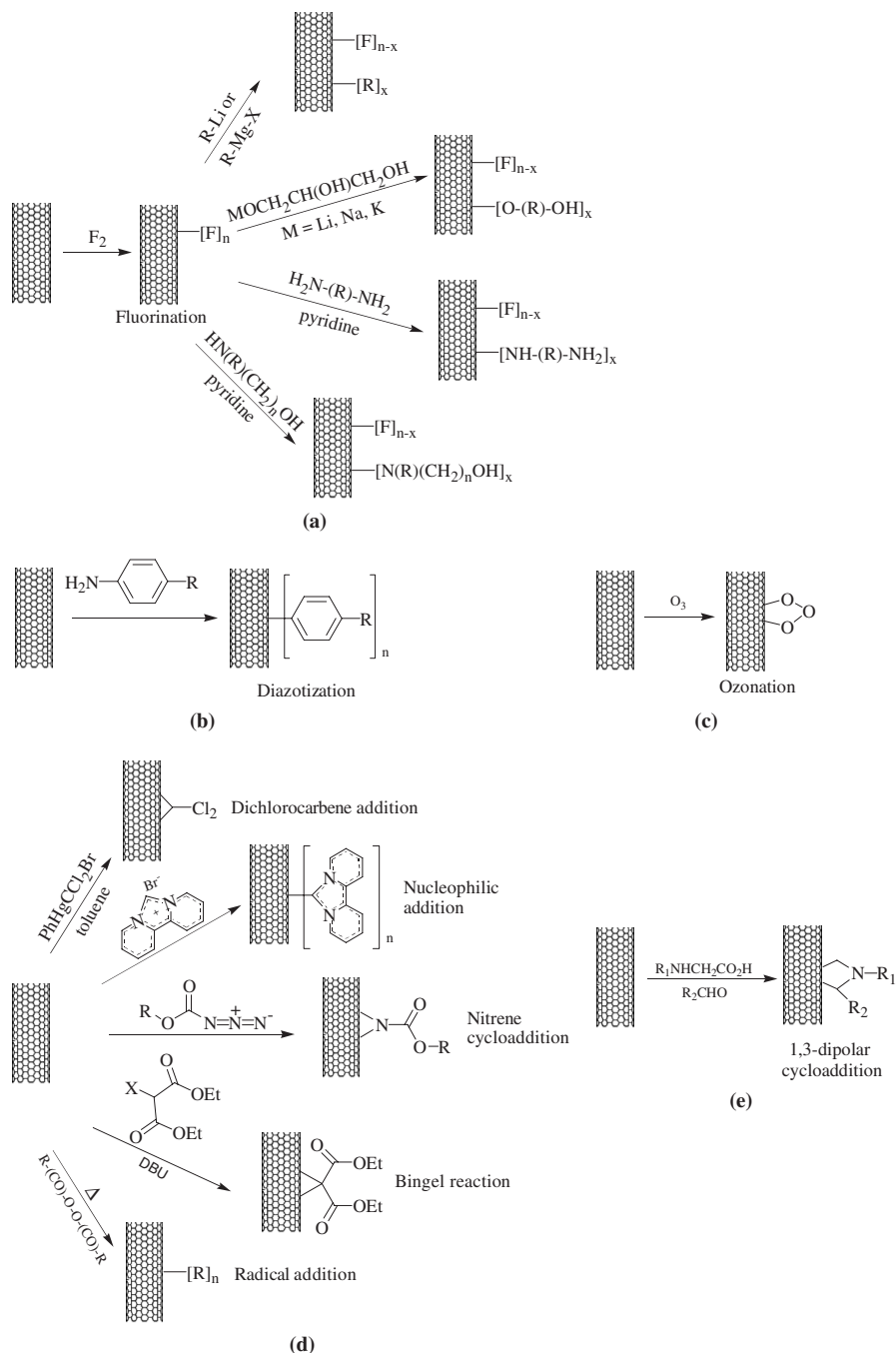


Figure 8.2 Schematic reactions describing derivatization of carbon nanotubes at graphene sheets.

generated from chloroform and later from phenyl(bromodichloromethyl)mercury. Holzinger et al. [48a] reported the functionalization of SWCNTs by three types of addition reactions: the [2 + 1] cyclo-addition of nitrenes in the presence of alkyl azidoformate, the addition of nucleophilic carbenes (dipyridyl imidazolidene), and the addition of perfluorinated alkyl radicals. The sidewall functionalization of SWCNTs via the addition of (*R*)-oxycarbonyl nitrenes, which allows for the covalent binding of a variety of groups, such as alkyl chains, aromatic groups, dendrimers, crown ethers, and oligoethylene glycol units, was also performed by Holzinger et al. [48b]. The presence of chelating donor groups within the addends allowed for the complexation of Cu²⁺ and Cd²⁺.

Another possible pathway to covalent functionalization is provided by the Bingel reaction, which is based historically on the cyclopropanation of fullerenes [20,65] and has more recently been reported for SWCNTs [29a,50,66]. The reaction mechanism was postulated to be a nucleophilic addition of the deprotonated species of diethyl bromomalonate followed by an intramolecular substitution of the halogen in a [2 + 1] cyclo-addition.

A one-step method for derivatization of SWCNTs, which is based on free-radical addition of alkyl groups terminated with a carboxylic acid, was also performed [67]. This method utilizes the organic acyl peroxides of dicarboxylic acids, HOOC(CH₂)_nC(O)OO(O)C-(CH₂)_nCOOH (*n* = 2 or 3), as precursors for the corresponding “functional” radicals.

1,3-Dipolar Addition of Azomethine Ylides. Prato et al. discovered a method of functionalizing SWCNTs using 1,3-dipolar addition of azomethine ylides [Figure 8.2(e)] [31–33,49]. It involves the treatment of graphene sheets with an aldehyde and a nitrogen-substituted glycine derivative, resulting in the formation of substituted pyrrolidine moieties on the carbon surface. The main advantage of this reaction is the easy attachment of pyrrolidine rings substituted with chemical functions to the sidewalls of the CNTs, which can lead to the construction of novel materials with diverse applications [51].

Encapsulation of Metal Complexes The nanostructure of CNTs (typical diameters range from 0.7 to 2.0 nm for SWCNTs) enables the endohedral encapsulation of molecules [14,15,21,31b,38]. It is possible to encapsulate molecules inside the tubes as long as the size of the molecules is smaller than the nanotubes and have enough kinetic energy to enter the open ends of CNTs. Practically, all organic solvents have a surface tension that makes possible the insertion of molecules into the CNT internal diameters.

The majority of the molecules that have been encapsulated in SWCNTs include fullerene-type molecules [38,68]. The non-fullerene-type molecules, based on transition metals, that have been shown to be encapsulated in CNTs are two organometallic complexes, the cobaltocene and ethylcobaltocene and a zinc phenylporphyrin [38,68,69]. The nature of the [CoCp₂]-CNT interaction appeared to be more complex than pure van der Waals forces. The presence

of $[\text{CoCp}_2]$ and $[\text{Co}(\text{CpEt})_2]$ in SWCNTs was probed by ultraviolet-visible absorption spectroscopy, revealing that the oxidation state of Co was changed from +2 to +3 upon their insertion into SWCNTs [69]. It was proposed that in addition to the van der Waals component, the metallocenes were expected to have a major electrostatic contribution to their interactions with SWCNTs. There is also a Rh complex, $[\text{HRh}(\text{CO})(\text{PPh}_3)_3]$, immobilized into ends-opened and ends-unopened CNTs in which the authors claimed, on the basis of catalytic activity of supported complexes, that the Rh complex was located in the hollow channels of CNTs [70].

8.3.2 Direct Immobilization of Metal Complexes

$[\text{M}(\text{salen})]$ complexes (H_2salen is a N_2O_2 tetradeятate Schiff-base ligand derived from salicylaldehyde and diamine derivatives) are one of several examples of transition metal complexes that have been extensively immobilized onto ACs and carbon xerogels (CXs) [57,71–76]. The first studies on the direct immobilization of $[\text{M}(\text{salen})]$ -type complexes onto ACs through covalent anchoring involved Cu(II) complexes with *salen* ligands functionalized with hydroxyl groups [71]. The copper(II) complex, $[\text{Cu}(4\text{-HOsalen})]$, was anchored directly onto an air-oxidized AC, jointly with the unfunctionalized Cu(II) complex, $[\text{Cu}(\text{salen})]$, in order to assess the role of the hydroxyl groups in copper complex anchorage. Data from several techniques [x-ray photoelectron spectroscopy (XPS), nitrogen adsorption at 77 K, temperature-programmed desorption (TPD), thermogravimetry (TG), and electron paramagnetic resonance (EPR)] provided evidence that a Cu(II) complex with a hydroxyl-functionalized *salen* ligand was chemically bound to carbon surface groups by stable chemical bonds formed through the reaction between hydroxyl ligand substituents and surface carbonyl and carboxylic anhydride groups. For the surface carbonyl groups, a direct nucleophilic attack of the hydroxyl originated an ether bond to the complex, and surface carboxylic anhydrides were also subject to a nucleophilic attack from the hydroxyl groups, originating new carboxylic groups and an ester group, as depicted in Figure 8.3. The unfunctionalized complex, $[\text{Cu}(\text{salen})]$, was weakly physically adsorbed onto the AC, since it was leached during Soxhlet extraction purification. The small degree of π -delocalization of the ligand was responsible for the weak π – π interactions between the unfunctionalized complex and AC.

This anchoring method was also used in the immobilization of Mn(III) complexes with other hydroxyl-functionalized *salen* ligands, bearing different diimine bridges: cyclohexanediiimine, $([\text{Mn}(4\text{-HOsalhd})\text{CH}_3\text{COO}], [\text{Mn}(\text{salhd})\text{Cl}])$ [72a], *o*-phenylenediiimine $([\text{Mn}(4\text{-HOsalophen})\text{Cl}])$ [72b], and two phenyl groups $([\text{Mn}(4\text{-HOsaldp})\text{Cl}])$ (Figure 8.4) [57]. For the latter complex, anchoring was also tested on two air-oxidized CXs with different pore textures [73].

The complex $[\text{Mn}(4\text{-OHsalhd})\text{CH}_3\text{COO}]$ [Figure 8.4(a)] was immobilized directly onto untreated and air- or acid-oxidized ACs with adsorption efficiencies of 30, 77, and 62%, respectively, indicating that oxidation of the AC

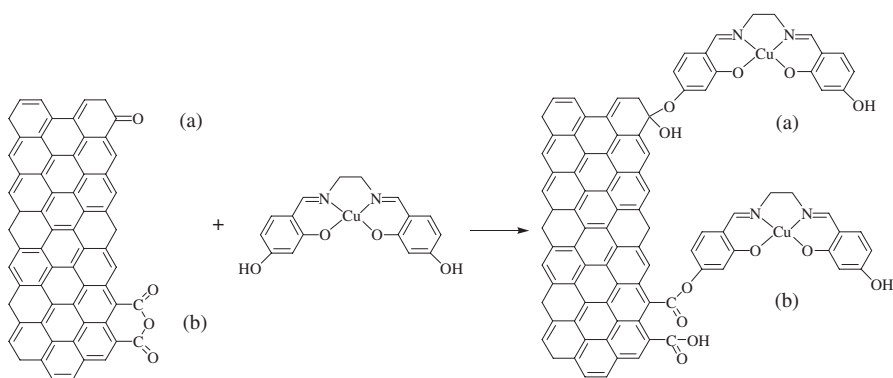


Figure 8.3 Direct immobilization of $[\text{Cu}(4\text{-HOsalen})]$ onto air-oxidized AC. (From ref. 71, with permission. Copyright © 2002 American Chemical Society.)

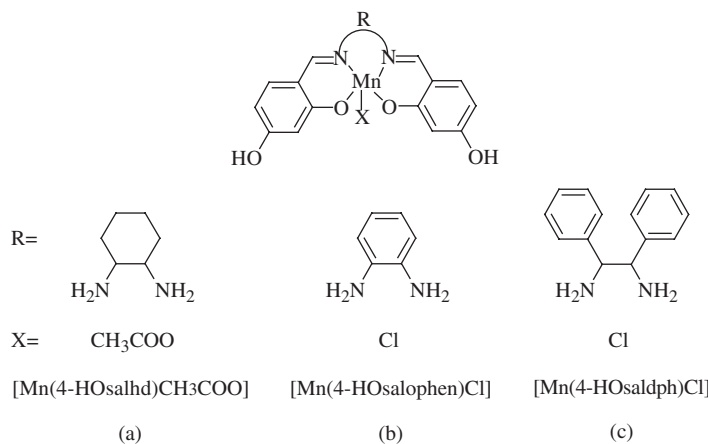


Figure 8.4 Molecular structure of Mn(III) *salen* complexes immobilized onto air-oxidized AC: (a) $[\text{Mn}(4\text{-OHsalhd})\text{CH}_3\text{COO}]$; (b) $[\text{Mn}(4\text{-OHsalophen})\text{Cl}]$; (c) $[\text{Mn}(4\text{-OHsaldph})\text{Cl}]$.

approximately doubled metal complex loading [72a]. The anchoring process for the manganese complex with hydroxyl groups in the aldehyde moieties in both oxidized ACs occurred by the same reaction of the homologous Cu(II), as confirmed by XPS and nitrogen adsorption at 77 K [71]. For unoxidized AC, for which the quantity of accessible oxygen surface groups in the support was very small, the anchoring process occurred mostly by $\pi-\pi$ interactions between the delocalized π -system of the complex and graphitic aromatic rings. As physical adsorption is supposed to be less effective than chemical binding to a carbon surface through ligand functionalities, lower metal complex loadings were obtained. On the other hand, immobilization of the unfunctionalized complex,

[Mn(salhd)Cl] [72a], resulted in low metal complex loadings, even in the presence of an oxygen-rich carbon surface, and therefore it was proposed that the unfunctionalized Mn(III) complex was also immobilized onto the oxidized ACs, not only by $\pi-\pi$ interactions, but also through the acidic groups by ionic exchange.

The complex [Mn(4-OHsalophen)Cl] [Figure 8.4(b)], bearing an aromatic imine bridge, was immobilized onto air-oxidized AC [72b], resulting in a bulk manganese content of 48.8 $\mu\text{mol/g}$ AC, which was quite low compared with 142 $\mu\text{mol/g}$ AC, the value obtained for the analog complex [Mn(4-HOsalhd) CH_3COO]; however, no explanation was given for this behavior.

The complex exhibiting two phenyl rings in the imine bridge [Mn(4-HOsaldph)Cl] [Figure 8.4(c)], which presents a large π -delocalization was also immobilized in untreated and air- or acid-oxidized ACs [57]. The immobilization onto the untreated AC led to relatively higher amounts of [Mn(4-HOsaldph) Cl] compared to immobilization onto the acid-oxidized AC. This result contrasted with what was observed for the immobilization, on the same supports, of the homologous complex that showed lower π -delocalization, [Mn(4-HOsalhd) CH_3COO] [72a]. As no leaching was observed during the purification step of the [Mn(4-HOsaldph)Cl] $@\text{C1}$ material (C1 refers to untreated AC), the authors postulated that $\pi-\pi$ interactions between the extensive delocalized π -system of the complex and graphitic aromatic rings were responsible for immobilization of the complex in untreated AC. For the oxidized AC, although some $\pi-\pi$ interactions could be present, the complex was grafted mainly by covalent anchoring through hydroxyl functionalities of the ligand to carbonyl and carboxylic anhydrides surface groups, as noted earlier [71].

Two air-activated CXs with different textural properties allowed the immobilization of larger amounts of [Mn(4-HOsaldph)Cl] ($\eta\% = 52.2$ to 53.1 and 40.3 to 43.3, respectively) [73] than of unactivated homologous materials ($\eta\% = 6.5$ to 11.9). The results suggested that the as-prepared CXs do not possess a π -system capable of establishing strong $\pi-\pi$ interactions with the extended π -system of the *salen* ligand. This behavior contrasted with that observed in immobilization of the same Mn(III) complex in AC, as noted earlier [57]. Therefore, the surface oxygen groups on the activated CXs also played a key role in the immobilization of the Mn(III) *salen* complex. In this context, it was concluded that the metal complex was immobilized primarily through the reaction between the hydroxyl groups on the aldehyde fragment of the *salen* ligand and carbonyl and carboxylic anhydride groups on the activated surface [71]. Nevertheless, $\pi-\pi$ interactions between the extended ligand and carbon π -systems were not excluded.

Two chiral manganese(III) *salen* catalysts, bearing different chiral diamine bridges (Figure 8.5) [74] were anchored by direct axial coordination of the metal center onto the phenolate groups created by sodium hydroxide treatment of an air-oxidized AC, as confirmed by XPS and TPD: the air activation of these materials introduced mainly phenol and carbonyl–quinone groups that upon reflux with a sodium hydroxide solution were converted into phenolates. This method was also applied to anchoring of the Jacobsen catalyst onto air-oxidized CXs

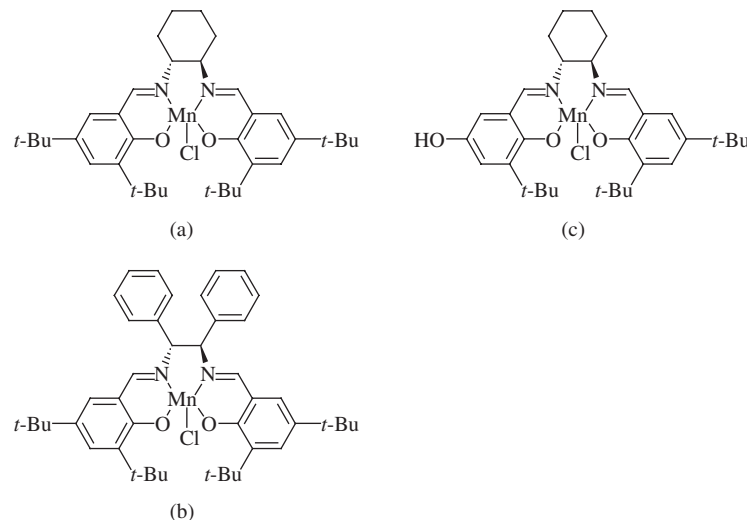


Figure 8.5 Molecular structure of chiral Mn(III) *salen* complexes immobilized onto oxidized AC: (a) Jacobsen catalyst; (b) Katsuki catalyst; (c) modified Jacobsen complex.

with distinct textural properties (different pore radii) [75]. These groups allowed direct axial coordination of the Mn(III) center onto the phenolate groups of the modified CXs. Due to the bulkiness of the chiral complex, material with a larger pore radius anchored more complex.

Two N_2O Schiff-base nickel(II) complexes with pendant amine groups coordinated in the axial positions, $[\text{Ni}(\text{slp})_2]$ and $[\text{Ni}(\text{mslp})_2]$ (H_2slp and H_2mslp are N_2O tridentate Schiff-base ligands derived from aldehyde derivatives and 1,2-diaminoethane), were anchored onto an acid-oxidized AC using a more elaborated procedure involving [76] (1) oxidation of AC with nitric acid, (2) treatment with thionyl chloride in order to convert the carboxylic acid carbon surface functionalities into acyl chloride functionalities, and then (3) reaction between the amine functionalities of the metal complexes with the carbon surface acyl chloride functionalities (Figure 8.6). The data from all the techniques used (XPS, N_2 adsorption at 77 K, TG, and TPD) provided evidence that both nickel(II) complexes were anchored onto the AC via an amide bond formed by the reaction between the acyl chloride carbon surface functionalities and the amine groups of both metal complexes.

Several metalloporphyrins and phthalocyanines and numerous coordination and organometallic complexes of Rh, Ir, and Pd have also been immobilized directly onto micro- and mesoporous carbon materials, as well as onto CNTs.

The Fe(II) and Co(II) phthalocyanines $[\text{FePc}]$ and $[\text{CoPc}]$ were supported by the impregnation method into ACs [54] and for $[\text{FePc}]$ into carbon blacks (CBs) oxidized by different procedures [55]. It was shown [XPS, scanning electron

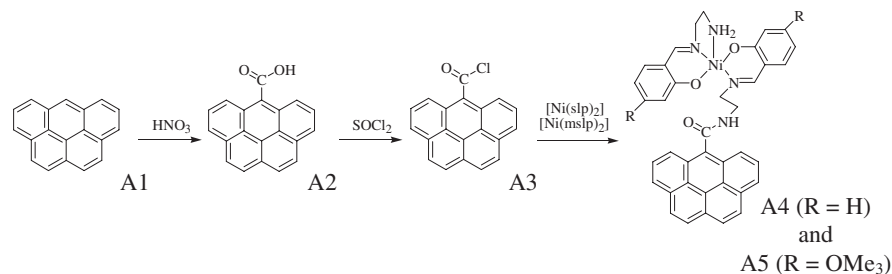


Figure 8.6 Direct anchoring onto AC of an octahedral Ni(II) Schiff-base complex with pendent amine groups coordinated in the axial position. (From ref. 76, with permission from Elsevier.)

microscopy (SEM), and gas adsorption] that complexes adsorbed onto carbons as a monolayer and that the dispersion of metal complexes onto the carbon surface was a consequence of the strong $\pi-\pi$ interaction between the aromatic structure of the carbon surface and the macrocyclic ligand of the complexes.

The palladium and rhodium complexes of the formula $[\text{MCl}_2(\text{NH}_2(\text{CH}_2)_{12}\text{CH}_3)_2]$ were anchored onto several carbon supports with different surface areas and surface chemistry by an incipient wetness technique [56]. According to the results (mainly XPS), the authors concluded that the anchored complexes kept their coordination number and that the immobilization proceeded by hydrophobic interactions between the long aliphatic chain from the ligand and the carbon surface. Several chiral cationic Rh complexes with the formulas $[\text{Rh}(\text{nbd})(\text{diphosphine})](\text{BF}_4)$ ($\text{nbd} = 2,5\text{-norbornadiene}$ and diphosphines = dppb, S-bophoz, skewphos, phanephos, and xylyl-phanephos [77]), $[\text{PdCl}_2(\text{PPh}_3)_2]$, and Wilkinson catalyst $[\text{RhCl}(\text{PPh}_3)_3]$ were immobilized directly onto several carbons with different acid–base properties. [77] Although the authors did not provide direct evidence for the mechanism of immobilization, they proposed that complexes with the general formula $[\text{Rh}(\text{nbd})(\text{diphosphine})](\text{BF}_4)$ were attached to the support via a covalent Rh–O bond. The basic supports showed the highest Rh contents, which was explained by the authors as evidence of the mechanism proposed, since basic carbon would have negatively charged donors on its surface to interact with the cationic species.

The organometallic complex $[\text{Rh}(\mu\text{-Cl})(\text{cod})_2]$ ($\text{cod} = \text{cyclooctadiene}$) was immobilized onto acid-oxidized ACs by two strategies: (1) ion exchange, and (2) addition of diphosphine ligands to increase complex stability and subsequent ion exchange (Figure 8.7) [78]. In method 1, the negatively charged oxygen surface groups substituted for the chloride bridges and this reaction was monitored by the release of HCl. In method 2, diphosphine ligands were added to replace the labile ligand cod, but the immobilization mechanism proceeded in the same way as in method 1. The same complex $[\text{Rh}(\mu\text{-Cl})(\text{cod})_2]$ was also immobilized onto an acid-oxidized AC through covalent bonding between the phosphine ligand and the support [79]. In this case the added diphosphine ligands coordinated to the Rh

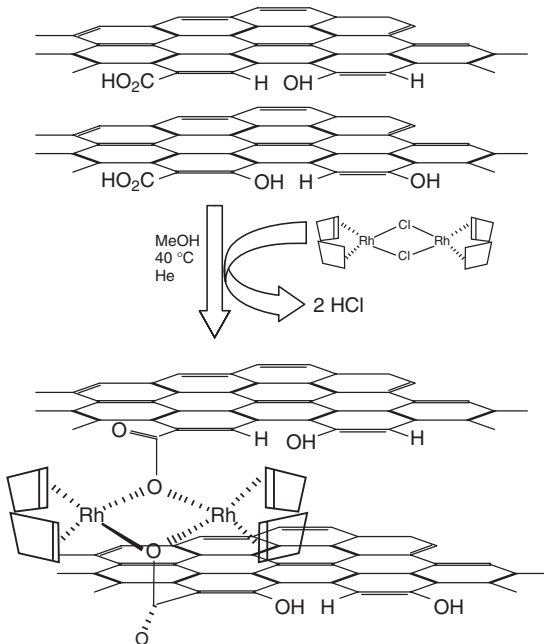


Figure 8.7 Direct immobilization of $[\text{Rh}(\mu\text{-Cl})(\text{cod})]_2$ onto oxidized AC. (From ref. 78b, with permission from Elsevier.)

complex were functionalized with hydroxyl groups that reacted with pre-created acyl chloride groups within the acid-oxidized support by an esterification reaction.

Another Rh complex, $[\text{Rh}(\text{cod})(\text{NH}_2(\text{CH}_2)_2\text{NH}(\text{CH}_2)_3\text{Si}(\text{OCH}_3)_3)]$, was immobilized onto air-oxidized ACs and MWCNTs and characterized by several methods: N_2 adsorption at 77 K, TPD, and XPS [80]. The complex has a diamine functionalized with trimethoxysilane groups that reacted with hydroxyl groups formed within the supports by air oxidation, leading to very stable Si–O–C bonds.

Several heterocyclic polyaromatic molecules, such as porphyrins and phthalocyanines, were immobilized by strong $\pi-\pi$ interactions onto CNTs [30,38,58,81,82]. In some cases the authors detected, using spectroscopic techniques, that the incorporation of metal ions in the phthalocyanine and porphyrin systems weakens their interaction with the nanotube sidewalls. For example, $[\text{Zn}(\text{porphyrin})]$ and $[\text{Cu}(\text{phthalocyanine})]$ showed a weaker binding ability to SWCNTs than that of metal-free molecules [82a]. Similarly, the interactions of THPP [5,10,15,20-tetrakis(hexadecyloxyphenyl)-21H, 23H-porphine] with CNTs were apparently specific to the porphyrin-free base and were hindered upon Zn chelation [82b].

In another study involving porphyrins, acid-oxidized SWCNTs bearing carboxyl groups at the open ends and defect sites were made to react with thionyl chloride and then with aminoporphyrins to yield multiporphyrin-linked SWCNTs

with amido linkage (NT-CONHH₂P) [83a]. Then the sidewalls of functionalized NT-CONHH₂P were derivatized further with aminoporphyrins utilizing an in situ-generated diazonium intermediate to give H₂PNT-CONHH₂P. This study was quite interesting since it demonstrated the possibility of anchoring molecular species, in this case aminoporphyrins, both at the open ends and defects and at CNT sidewalls by different synthetic routes. A porphyrin functionalized with hydroxyl groups, 5-*p*-hydroxyphenyl-10,15,20-tritylporphyrin (por-OH), was also anchored onto oxidized SWCNTs bearing carboxyl groups treated with thionyl chloride [83b].

A ruthenium complex with a bipyridyl ligand functionalized with acyl chloride groups, [Ru(dcbpy)(bpy)₂](PF₆)₂, was grafted onto amino-functionalized MWCNTs through amido bonds (Figure 8.8) [84]. Absorption and emission spectroscopy showed significant changes between starting components and the resulting ruthenium nanotube complex, which was taken by the authors as indicative of successful chemical modification of CNTs.

Wong et al. reported the preparation of nanotubes linked covalently to an Ir organometallic compound. Raw and oxidized CNTs were reacted with Vaska complex, *trans*-[IrCl(CO)(PPh₃)₂] [29b,85]. Based on several techniques (surface and spectroscopic), the authors concluded that the metal complex was coordinated with the nanotubes by two distinctive pathways: with raw nanotubes, the anchoring proceeded through a η^2 -coordination process, whereas with oxidized nanotubes, the reaction occurred by coordination through the oxygen surface atoms, forming a hexacoordinate structure around the Ir atom. The same authors used acid-oxidized CNTs to anchor the Wilkinson complex, [RhCl(PPh₃)₃] [29b,86], and found, as before, that the Rh metal was coordinated to the nanotubes through the created surface oxygen atoms, forming a hexacoordinate structure around the Rh atom.

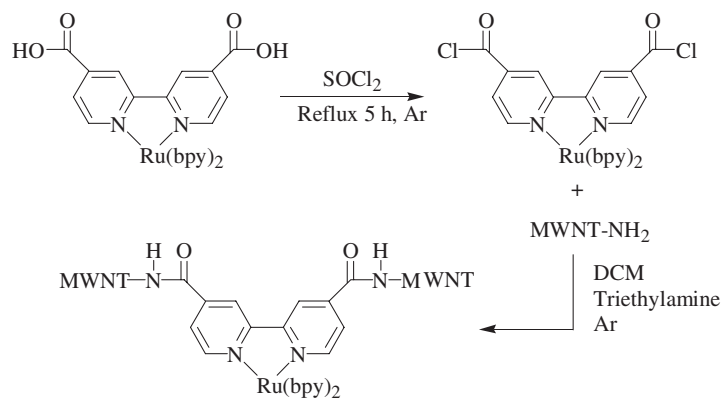


Figure 8.8 Direct immobilization of a Ru complex onto MWCNTs. (From ref. 84, with permission. Copyright © 2002 American Chemical Society.)

A polycationic water-soluble Ru hexamer possessing 12 positive charges was immobilized into oxidized SWCNTs through electrostatic interactions with the carboxylate moieties of the oxidized SWCNTs [87]. The multiple ionic-pair interactions between the positively charged metallohexamer- and carboxylate-modified SWCNTs were evidenced by transmission electron microscopy (TEM) and atomic force microscopy (AFM) images.

Acid-oxidized SWCNTs were also reacted with lanthanide salts containing Eu, La, and Tb [88]. In this study it was found that the lanthanide ions were linked to CNTs through the surface oxygen atoms, forming predominantly ionic arrangements, and thus the oxidized nanotubes acted as primary ligands for these metal ions. The adducts were analyzed using spectroscopic techniques (FTIR, Raman, and photoluminescence) and were characterized structurally by AFM and TEM.

8.3.3 Metal Complex Immobilization via Spacers

Some of the complexes referred in the preceding section were also immobilized onto carbon materials by using spacer molecules. The Ni(II) *salen* complex functionalized with hydroxyl groups, [Ni(4-HOsalen)], was anchored onto an air-oxidized AC using CC as the linking agent and characterized by several methods: SEM, XPS, x-ray diffraction, N₂ adsorption at 77 K, and thermal analysis [89]. Complex anchoring was made in three consecutive steps: (1) air oxidation of AC, (2) attachment of CC to hydroxyl carbon surface functionalities, and then (3) reaction between a metal complex functionalized with hydroxyl groups and carbon-bound CC.

A modified Jacobsen-type catalyst possessing an hydroxyl group on the aldehyde fragment of the *salen* ligand [Figure 8.5(c)] was anchored through the same spacer CC onto two modified ACs [90]: (1) an air-oxidized AC functionalized with 3-aminopropyltriethoxysilane (APTES), and (2) a nitric acid AC treated with thionyl chloride and functionalized with 1,8-diaminoctane. Based on the characterization of the materials by N₂ adsorption at 77 K, TG-IR, and XPS, it was concluded that the complex anchored more effectively in the former material (double-anchoring efficiency) as a result of the different surface areas available (higher for the former material) and as a consequence of the different spatial arrangement of each spacer on the AC surface.

Styryl-functionalized vanadyl(IV) *salen* complexes (nonchiral and chiral versions) were covalently anchored onto mercapto-modified ACs and SWCNTs [91]. The immobilization procedure involved the acid oxidation of the parent ACs and CNTs, reaction of the carboxylic acid groups with thionyl chloride to give the acyl chloride groups, which were finally reacted with the spacer 2-mercaptopethylamine. The mercapto-functionalized SWCNTs and ACs were then linked to the vanadyl complex through a radical chain addition of the mercapto group to the terminal functional C=C group of the complex, initiated by AIBN (2,2'-azobisisobutyronitrile); the modified SWCNTs were more efficient in anchoring the [VO(*salen*)] complex (Figure 8.9).

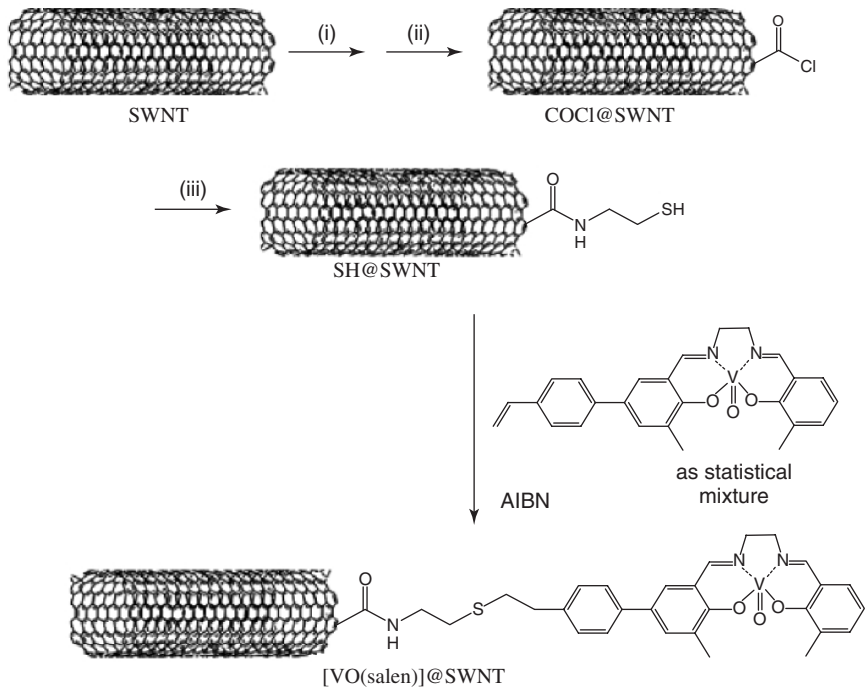


Figure 8.9 Styryl-functionalized vanadyl(IV) Schiff base covalently anchored on mercapto-modified SWCNTs and ACs. (From ref. 91a, with permission from Elsevier.)

Several metal acetylacetones, $[M(\text{acac})_2]$, have been anchored onto amine-functionalized ACs using air- and nitric acid-oxidized ACs as starting supports [92,93]. The acid-oxidized carbons, which possess carboxylic surface groups, were treated with thionyl chloride to give surface acyl chloride groups, which were then reacted with diamines. Subsequent attachment of $[M(\text{acac})_2]$ [$M = \text{Cu}(\text{II})$, $\text{VO}(\text{IV})$, and $\text{Co}(\text{II})$] was achieved by Schiff condensation between the free amine groups of the grafted spacers and the $C=O$ group of the acetylacetone (acac) ligand. The complex $[\text{VO}(\text{acac})_2]$ was also anchored onto an air-oxidized AC in which the phenol surface groups were previously made to react with the spacer APTES; the free amine groups were then used for Schiff condensation with $[\text{VO}(\text{acac})_2]$ [92c].

The Rh complex $[\text{Rh}(\text{cod})(\text{diphosphine})]$, with diphosphine ligands functionalized with hydroxyls groups, was immobilized onto several ACs and carbon cloth with different textural chemistry previously modified with the spacer naphthoic acid; the materials were characterized by gas adsorption, TPD, and TG-DSC [59]. The grafting of the complex onto the modified carbon materials proceeded through the esterification reaction between the phosphine hydroxyl groups and

the acid group of the adsorbed naphtoic acid. It was shown that the presence of oxygen groups on the supports was, in general, not beneficial for the physical adsorption of the anchored molecule, which was immobilized by $\pi-\pi$ interactions.

SWCNTs were modified with several water-soluble pyrene derivatives (1-pyreneacetic acid, 1-pyrenecarboxylic acid, 1-pyrenebutyric acid, and 8-hydroxy-1,3,6-pyrenetrisulfonic acid) bearing negatively charged ionic headgroups, to act as anchors to several pyridium headgroups present in a series of water-soluble metalloporphyrins $[MP]^{8+}$ ($M = Zn$, Co , and Fe) [60a]. Interactions between the metalloporphyrins and SWCNTs proceeded through a combination of associative van der Waals (spacer–CNT) and electrostatic interactions (metalloporphyrins–spacer–CNT), as demonstrated by the combination of spectroscopic and surface techniques.

Using a similar approach, SWCNTs were modified with positively charged pyrene derivatives to act as anchors for porphyrin and metalloporphyrin derivatives with negative charges, $[ZnP]^{8-}$ and $[H_2P]^{8-}$ [60b]. As before, the key step in forming the novel aggregate SWCNT/pyrene $^+$ / $[ZnP]^{8-}$ or SWCNT/pyrene $^+$ / $[H_2P]^{8-}$ consisted of $\pi-\pi$ interactions between CNT and pyrene $^+$ spacers with electrostatic interactions being responsible for the immobilization of $[ZnP]^{8-}$ or $[H_2P]^{8-}$ onto modified SWCNTs (Figure 8.10).

A pyrene derivative was also used as an anchor to immobilize a ruthenium alkylidene complex onto SWCNTs [94]. The immobilization of the Ru complex was performed by two different paths: (1) adsorption of pyrene derivative precursor onto the sidewall of nanotubes by $\pi-\pi$ interactions, followed by cross-metathesis with the ruthenium alkylidene complex, and (2) adsorption onto the sidewall of SWCNTs of the pyrene-substituted ruthenium alkylidene prepared previously.

Using a quite different spacer, a series of SWCNTs were modified using polyamidoamine dendrimers to immobilize tetraphenylporphyrins [95]. The overall procedure involved several different steps, which included, first, a 1,3-dipolar cyclo-addition reaction which led to a pyrrolidine ring functionalized with *N*-*tert*-butoxycarbonyl-protected amine groups, which were then used to build the dendrimers, which reacted with the porphyrins through an amido bond. Similar to other studies, the final materials were characterized by spectroscopic (Raman, UV-vis, and fluorescence), surface (AFM and TEM), and TG techniques.

By using the same type of 1,3-dipolar cyclo-addition of azomethine ylides it was possible to anchor ferrocene (Fc) onto the sidewalls of SWCNTs [96]. Accordingly, a nitrogen-functionalized glycine ($R-NHCH_2COOH$, $R=CH_2CH_2OCH_2CH_2OCH_2CH_2NHCO-Fc$) and paraformaldehyde were refluxed in dimethylformamide in the presence of SWCNTs. From differential scanning calorimetry the extent of functionalization was determined as approximately 1 Fc molecule per 100 carbon atoms of the SWNTs.

Another approach to immobilizing charged porphyrins onto CNTs used polyelectrolytes as spacers [e.g., poly(sodium 4-styrenesulfonate), PSS $^{n-}$]

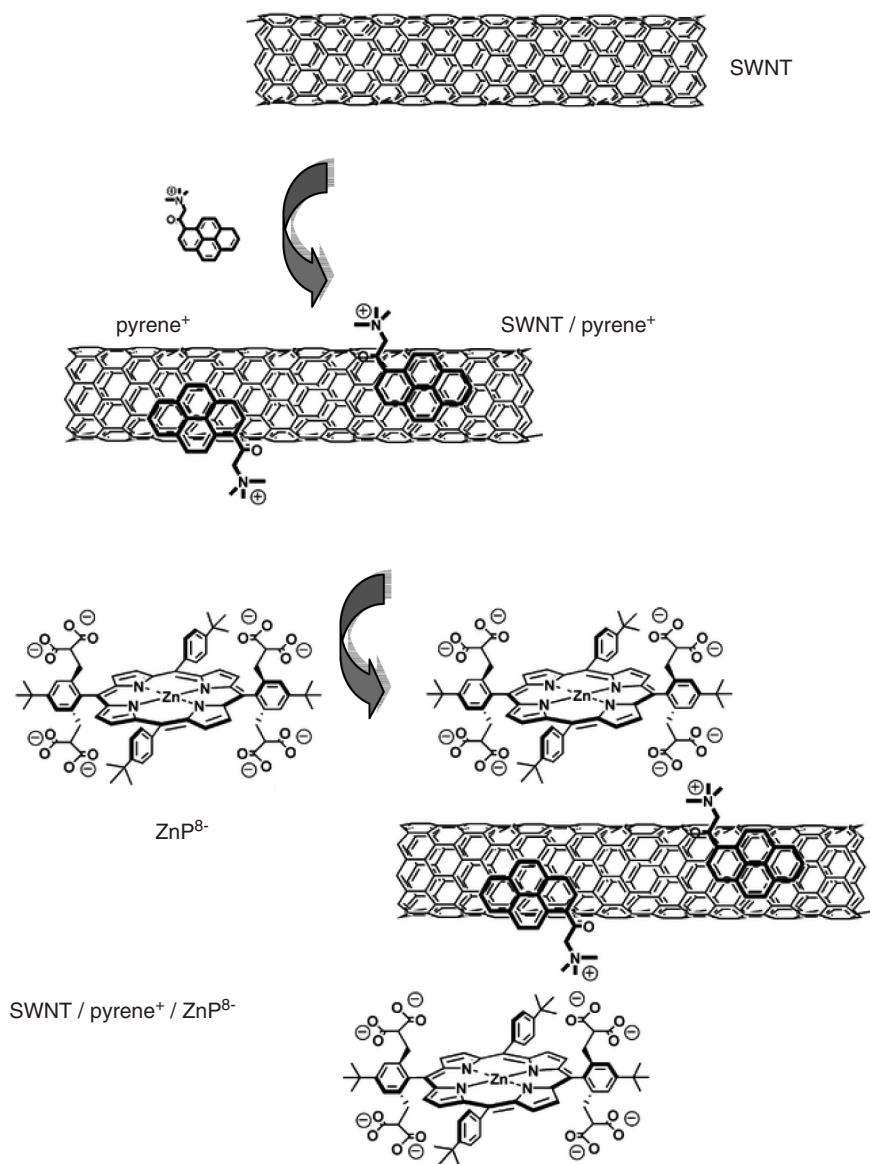


Figure 8.10 Immobilization of a negative Zn porphyrin via pyrene derivative positively charged onto CNTs through a combination of $\pi-\pi$ and electrostatic interactions. (From ref. 60b, with permission. Copyright © 2006 American Chemical Society.)

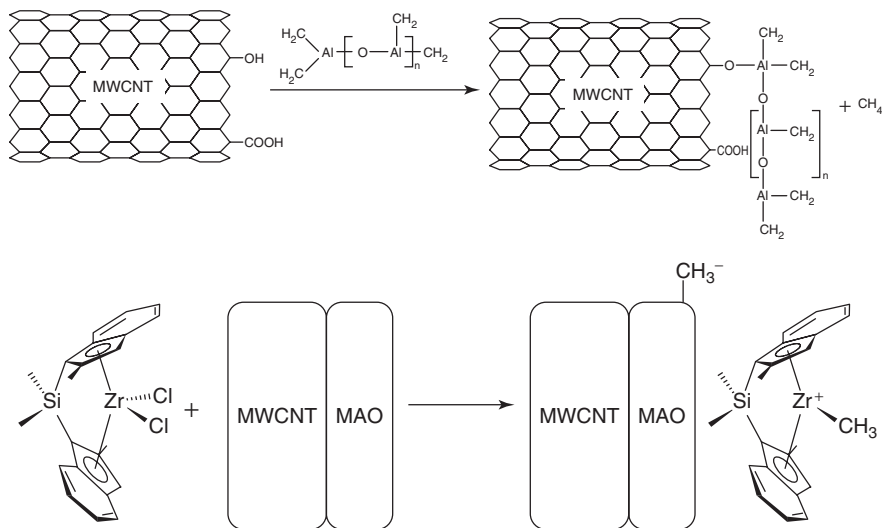


Figure 8.11 Immobilization of a Zr(IV) complex of general formula $[(\pi\text{-ligand})\text{ZrCl}_2]$ onto oxidized CNTs modified with MAO. (From ref. 97d, with permission from Elsevier.)

[38,53]. The polyanion immobilized by noncovalent interactions onto SWCNTs (SWCNT-PSSⁿ⁻) was then able to anchor the octapyridiumporphyrin salt by strong electrostatic interactions. Porphyrins can also be immobilized onto CNTs by polymer wrapping through hydrophobic or $\pi-\pi$ interactions; in one example, poly(methylmethacrylate) with grafted porphyrins was polymerized around the CNTs [38,52].

Finally, several organometallic complexes of Zr(IV) of general formula $[(\pi\text{-ligand})\text{ZrCl}_2]$ exhibiting homogeneous catalytic properties in the polymerization of olefins were immobilized onto oxidized CNT modified with methylaluminoxane (MAO) $[(\text{CH}_3)_2\text{Al}-[\text{O}-\text{Al}(\text{CH}_3)_2]_n]$ [97]. The procedure involved two main steps: (1) oxidized nanotubes bearing surface functional groups such as hydroxyl or carboxyl were reacted with MAO, forming covalent oxygen aluminum bonds; and (2) the grafted MAO was made to react with the metallocene complex. During the last step, the Zr(IV) complexes reacted with MAO-surface-activated CNTs and a methylated cationic complex was formed, $[\text{ZrCp}_2\text{CH}_3]^+$, which was immobilized in the vicinity of the nanotube surface by electrostatic interactions with simultaneously formed MAO counter anions (CH_3^-) fixed at the nanotube surface (Figure 8.11).

8.4 APPLICATION OF COORDINATION COMPOUNDS ANCHORED ONTO CARBON MATERIALS IN SEVERAL CATALYTIC REACTIONS

Some of the transition metal complexes referred in Section 8.3 exhibit catalytic properties in homogeneous media, and their heterogenization onto carbon

materials allowed the preparation of novel carbon-based catalysts with high stability, and consequently, high reusability, making them economically viable in catalytic terms. We begin this section with a description of the catalytic properties of the immobilized coordination compounds, including metal complexes with *salen* and *acac* types of ligands, and porphyrins and phthalocyanines that have been used essentially in oxidation reactions. Subsequently, we describe the catalytic properties of organometallic and other coordination compounds immobilized onto carbon materials that were tested in reduction reactions, including hydrogenation and hydroformylation of alkenes and in the polymerization reaction of olefins.

8.4.1 [M(*salen*)]-Based Materials

The majority of [M(*salen*)]-based complexes immobilized onto carbon materials with catalytic properties refer to Mn(III) complexes that have been shown to behave as highly efficient homogeneous catalysts in the chemoselective [98,99] and enantioselective epoxidation of a large variety of alkenes [99,100]. To date, as noted in Section 8.3, their heterogenization onto carbon materials was carried out with ACs and CXs.

The Mn(III)*salen* complex functionalized with hydroxyl groups on the aldehyde moieties, [Mn(4-HOsalhd)CH₃COO], immobilized directly via a ligand onto a commercial AC and on its air- and acid-oxidized counterparts [72a], was tested in the epoxidation of styrene using iodosylbenzene (PhIO) as an oxidant and acetonitrile as a solvent. The unfunctionalized analog, [Mn(salhd)Cl], immobilized onto the air-oxidized AC, was tested in the same catalytic reaction. All the heterogeneous catalysts showed slightly lower styrene conversion (42%) compared with that of the free complex (56%), but were as chemoselective as their homogeneous counterparts (89%) toward the styrene epoxide (81 to 89%), with the exception of the complex supported onto the acid-oxidized AC, which exhibited the lowest values for styrene conversion (26%) and epoxide selectivity (56%) [72a]. This was a consequence of the acidity of this support, as confirmed by the catalytic experiments done for the three supports. In fact, these experiments showed that all the ACs were not inert in styrene oxidation, although yielding relatively small styrene conversions, with the exception of the acid-oxidized AC, where 0% of styrene epoxide and 27% benzaldehyde were detected. The latter support had the largest amount of surface carboxylic acids, which were practically absent in the other two supports and were responsible for the absence of styrene epoxide since they induced ring opening of the epoxide. With the heterogeneous catalysts, the reaction time increased compared with that of the homogeneous counterparts, which is a general effect that arises upon immobilization of metal complex catalysts in porous matrices and has been attributed to diffusional constraints imposed on substrates and reactants by the porous network of the matrix. Catalyst recycling studies (two cycles) showed that the functionalized Mn(III) complex supported onto the two oxidized ACs kept its catalytic activity (styrene conversion and epoxide selectivity), whereas the same complex supported onto

the untreated AC and the unfunctionalized Mn(III) analog supported onto the air-oxidized AC showed a decrease in styrene epoxide yield from 37 to 25% and 39 to 28%, respectively [72a]. These results indicated that lack of oxygen functionalities on AC or of complex functionalization resulted in deactivation of the Mn(III) *salen*-based heterogeneous catalysts, as a consequence of inefficient active-phase anchoring. Conversely, the combination of support oxidation and suitable complex functionalization led to the establishment of a covalent bond between the functionalized Mn(III) complexes and the carbon surface oxygen groups, and to the efficient site isolation of the complexes; both properties are needed to produce very stable and reusable catalysts.

A similar Mn(III)*salen* complex functionalized with hydroxyl groups but bearing an aromatic imine bridge, [Mn(4-HOsalophen)Cl], and anchored through the ligand onto the surface of an air-oxidized AC was tested in the same catalytic reaction and compared with the corresponding homogeneous catalyst [72b]. The heterogenized catalyst showed a lower styrene conversion (38%) than that of the free complex (70%), but showed higher chemoselectivity toward the styrene epoxide (81%) in relation to its homogeneous counterpart (75%). The catalyst was reused twice and showed slight increases in the substrate conversion to 42% and epoxide selectivity to 77%. Kinetic studies revealed that for the heterogenized catalyst, the epoxide selectivity did not decrease with reaction time, a situation that contrasted with that found for the free catalyst in homogeneous media, for which a decrease in epoxide selectivity with time was observed as a consequence of catalyst deactivation. Sodium hypochlorite was also used in the epoxidation of styrene as oxygen source, but the results were not promising, since it promoted not only the leaching of the active phase, and thus deactivation of the heterogeneous catalyst, but also a decrease in epoxide selectivity.

The Mn(III) complex bearing large π -delocalization, [Mn(4-HOsaldph)Cl] [57], which was immobilized directly through the ligand onto a commercial AC and its air- and acid-oxidized forms (with three different metal loadings), was also screened as a heterogeneous catalyst in the epoxidation of styrene using PhIO as an oxygen source and acetonitrile as a reaction medium. As before, all the heterogeneous catalysts were as chemoselective toward the styrene epoxide (63 to 84%) as were their homogeneous counterparts (70 to 76%), with the exception of the complex supported onto the acid-oxidized AC, which exhibited the lowest styrene epoxide selectivities (2 to 7%), a consequence of its surface acidity. The highest styrene conversions and styrene epoxide yields were obtained again for the complex immobilized onto the air-oxidized AC. Generally, an increase in styrene conversion and styrene epoxide selectivity with the Mn(III) complex loading onto all supports was observed. The heterogeneous catalysts did not lose their styrene epoxide selectivity upon reuse, but generally, a slight decrease in the styrene epoxide yield was observed. Catalyst aging studies done for the complex anchored onto the air-oxidized AC with 1% loading revealed high stability and the same catalytic efficiency for almost two months. To evaluate the effect of particle size on the catalytic reaction parameters (all the catalytic reactions were performed using the catalysts as rodlike pellets with 0.8 mm diameter and

5 mm length), the styrene epoxidation was also carried out using crushed catalyst. The reaction was faster with the crushed catalyst than with the catalyst in the form of pellets, but despite the higher styrene epoxide selectivity obtained with the crushed catalyst, styrene conversion decreased and hence lower styrene epoxide yield was obtained. The faster reaction exhibited by crushed catalyst was attributed not only to the decrease in diffusion constraints inherent to the heterogeneous reactions, but also to the fact that the carbon matrix was active in decomposition of the oxidant (PhIO), resulting in faster depletion of this reagent.

The chiral Mn(III)*salen* catalysts bearing different chiral diamine bridges, denoted as CAT1 and CAT2, anchored by direct axial coordination of the metal center onto the phenolate groups of a modified commercial AC (CoxONa) [74], were active and enantioselective in the epoxidation of styrene and α -methylstyrene in dichloromethane at 273 K using, respectively, *m*-chloroperbenzoic acid (*m*-CPBA)/4-methylmorpholine N-oxide (NMO) and NaOCl as oxidants. The immobilized CAT1 acted as a better heterogeneous catalyst than CAT2 in the asymmetric epoxidation of the alkenes, since it generally showed higher substrate conversion and enantiomeric excess percentage (%ee) values. Nevertheless, turnover number (TON) and turnover frequency (TOF) were lower than those of the corresponding homogeneous phase reactions, a consequence of slow diffusion of the reactants into the AC porous structure, especially when NaOCl was used as an oxidant, a multiphase reaction system. For both catalysts, comparable %ee values to those of the homogeneous phase reactions were found with α -methylstyrene, whereas a decrease in %ee values was found with styrene. Furthermore, catalyst reuse led to no significant loss of catalytic activity and enantioselectivity for epoxidation of α -methylstyrene using NaOCl, whereas a significant loss of enantioselectivity was observed for epoxidation of styrene with the other oxidant. This was attributed to the higher resistance of Mn(III) catalysts under epoxidation conditions when NaOCl was used as an oxidant, compared with *m*-CPBA, for which decomposition of the catalyst has been claimed in other Mn(III)*salen* catalysts heterogenized in solid supports [8]. For both heterogeneous catalysts, no significant metal leaching was observed by ICP-AES after two successive catalytic experiments, showing that the anchoring method was effective against active-phase leaching.

The Jacobsen catalyst (CAT) anchored by the previous methodology onto two air-oxidized CXs with distinct textural properties (denoted as 02CX-16 and 07CX-09) [75] was also tested in the asymmetric epoxidation of styrene, α -methylstyrene, and 6-cyano-2,2-dimethylchromene in dichloromethane at 273 K using several oxygen sources: *m*-CPBA/NMO, NaOCl, or PhIO. The material 02CX-16 had considerably higher mesopore surface area and micropore volume than the sample 07CX-09, but the average pore radius of the latter sample (5.6 nm) was three times larger than the former (1.8 nm). The catalyst CAT@07CX-09 was generally more active than CAT@02CX-16 for all the alkenes tested, which was attributed to the larger pore radius of the material. The highest enantioselectivities were obtained with CAT@02CX-16 for the epoxides of α -methylstyrene and 6-cyano-2,2-dimethylchromene, probably due to confinement effects [75].

Generally, the heterogeneous asymmetric epoxidation reactions showed lower performance levels than those of the corresponding homogeneous phase reactions. With the exception of the epoxidation of α -methylstyrene with NaOCl, where no changes were observed in enantioselectivity or catalytic activity, reuse of both heterogeneous catalysts in the different epoxidation conditions resulted in a loss of enantioselectivity and catalytic activity. Analysis of Mn content after catalyst reuse indicated, however, that there was some leaching of the Mn complex; the epoxidation reactions made with NaOCl as oxygen source led to the highest Mn leaching.

The modified Jacobsen-type catalysts, possessing an hydroxyl group on the aldehyde fragment of the *salen* ligand [Figure 8.5(c)], anchored through CC onto the air-oxidized AC functionalized with APTES and onto an acid AC functionalized with 1,8-diaminoctane, also acted as active and enantioselective heterogeneous catalysts in the epoxidation of α -methylstyrene, using NaOCl as oxidant [90]. Both catalysts showed higher substrate conversions (12 and 24%) than the homogeneous catalyst (10%). The increase in the distance of the Mn(III) *salen* complex to the carbon surface did not have a significant effect on the %ee values (32 and 34%), which were lower than that of the homogeneous catalyst (51%). Nevertheless, the catalyst bearing the shorter amine alkyl chain showed higher catalytic activity, which was attributed by the authors to unique steric effects that prevented hindrance to diffusion of the substrates to the active catalytic sites when this spacer was used. These catalysts were less enantioselective than the Jacobsen catalyst anchored axially onto the AC and CX via phenolate groups [74].

Styryl-functionalized vanadyl(IV) *salen* covalently anchored onto mercapto-modified ACs and SWCNTs showed high catalytic activity in the cyanosilylation of benzaldehyde with substrate conversion of 83 and 93%, respectively [91]. The SWCNTs were shown to be more suitable support for the VO complex relative to the high-surface-area AC, because the latter support exhibited some adventitious activity. The asymmetric version of the reaction was also performed using the chiral vanadyl complex; the SWCNTs also behaved as a better support, as the %ee was 66%, whereas for AC the %ee was 48% [91]. The VO(IV) complex immobilized onto SWCNTs was also tested in the catalytic cyanosilylation of hexanal and 4-fluorobenzaldehyde with high substrate conversions: 97 and 96%, respectively.

8.4.2 [M(acac)₂]-Based Materials

The complexes [M(acac)₂], [M = Cu(II) and Co(II)] anchored onto an AC functionalized with hexanediamine were shown to be efficient catalysts in the oxidation of pinane without leaching of the active phase [93a]. Furthermore, limonene was oxidized by [Co(acac)₂] anchored onto several acid-oxidized carbons modified with diamines (ethylenediamine, tetramethylenediamine, hexamethylenediamine, and dodecamethylenediamine) [93b]. The reaction was carried out in a batch reactor at 333 K in the solvent system acetone: *t*-butanol, with

t-butyl hydroperoxide (TBHP) as oxygen donor. The primary product of limonene oxidation over the carbon-anchored $[\text{Co}(\text{acac})_2]$ was limonene oxide, which, however, polymerized instantly under the experimental conditions used. The catalyst activity expressed as the initial TOF was strongly dependent on both the hydrophilic/hydrophobic balance of the carbon support and the chain length of the spacer. Generally, the initial TOF increased with the hydrophobicity of the carbon support and with the chain length of the spacer. Furthermore, for catalysts bearing the same spacer, selectivity to limonene oxide/polymer was higher for supports with a lower oxygen content; however, its dependence on the spacer length could not be explained. Some of the anchored catalysts kept the activity in three consecutive reusing experiments, and other catalyst samples passed a hot-filtration test successfully, indicating high stability.

The complex $[\text{Cu}(\text{acac})_2]$ anchored onto a triamine-functionalized AC was tested in the aziridination of styrene, using $[[N-(p\text{-tolylsulfonyl})\text{imino}]\text{phenyl}-\text{iodinane}]$ ($\text{PhI} = \text{NTs}$) as a nitrogen source and acetonitrile as a solvent, at room temperature [92b]. The styrene conversion and total TON of the heterogeneous reaction were similar (37% and 7, respectively) to those of the reaction in the homogeneous phase (41% and 8, respectively); nevertheless, the initial activity decreased and the reaction time increased, due to substrate and product diffusion limitations. The heterogeneous catalyst could be reused in further catalytic reactions four times with successive increases in styrene conversion and initial activity and thus TON finally being better than in a homogeneous reaction. No metal complex leaching was observed after the consecutive catalytic reactions.

The homologous complex $[\text{VO}(\text{acac})_2]$ anchored onto two different amine-functionalized oxidized ACs, were tested in the epoxidation of 3-butene-2-ol using TBHP as an oxygen source, and the results were compared with those of the homogeneous phase reaction [92c]. The heterogeneous alkene conversion was similar to that observed in the homogeneous phase, although the rate of oxidation was less than half compared with the homogeneous system. The complex anchored through APTES exhibited higher catalytic efficiency than that anchored by the diamine; upon reuse, both materials showed no significant decrease in their catalytic properties.

8.4.3 Metal Phthalocyanine and Porphyrin-Based Materials

The complex iron(II) phthalocyanine, $[\text{FePc}]$, supported onto activated CBs [55a] by the impregnation method, was used as a heterogeneous catalyst in the oxidation of alkanes, with TBHP as an oxygen source. Carbon black proved to be an appropriate support for $[\text{FePc}]$ complex within the framework of the oxidation of alkanes. The hydrophobicity of the support surface induced the alkane adsorption, leading to a more ideal substrate/oxidant ratio near the active center, which explained the high activity and efficiency reached with the immobilized $[\text{FePc}]$.

Mechanistic insights into the oxidation of alkanes on [FePc]@CB catalysts were obtained on the basis of two reactions: the oxidation of adamantane and the competitive oxidation of cyclohexane and its deuterated analog. The results pointed toward an oxygen rebound mechanism [101] in which an electrophilic oxygen species was responsible for the hydrogen abstraction, forming an alkyl radical and a phthalocyanine/[FeOH]³⁺-stabilized hydroxyl radical. A fast recombination of these two radicals then occurred, leading to the formation of the alcohol, similar to the mechanism path followed by cytochrome P450 in the presence of monooxygen donors.

In another work [55b], [FePc] was impregnated on nonporous CB with different surface hydrophilic/hydrophobic properties, with the objective of evaluating the dependence of the catalytic activity of the new materials in the decomposition of hydrogen peroxide and oxidation of cyclohexane as a function of the support's surface properties. The authors observed that the surface charge and the oxygen content had a prime influence on the catalytic properties of the adsorbed complex: High ionic charges and oxygen content made the surface hydrophilic, leading to high activity of adsorbed [FePc] in the dismutase reaction. However, the reverse relation was observed for the oxidation of alkanes, since the highest cyclohexane conversion to corresponding oxidized products was found with [FePc] immobilized into neutral (hydrophobic) CB.

The same complex [FePc] supported onto AC modified by different chemical and thermal treatments was also used in the oxidation of *cis*-pinane with TBHP at room temperature and atmospheric pressure [54]. The main reaction product was 2-pinane hydroperoxide (77% selectivity at 91% conversion), whose selectivity decreased with increasing complex loading; other products were pinocampheol and verbanol and the respective ketones. As in the studies referred to above, the oxygen content of the support surface played an important role in catalyst activity and selectivity to pinane hydroperoxide. The catalyst bearing a surface with the highest oxygen content exhibited low activity, probably because its high hydrophilicity reduced the access of pinane molecules to the catalyst pore system. Moreover, catalysts presenting surfaces with very low oxygen content also exhibited low catalytic activity, since in this case, the lower hydrophilicity of the carbon surfaces prevented the adsorption of TBHP molecules on their surfaces.

The heterogeneous oxidation of mercaptans (Merox process) in aqueous alkaline (short-chain thiols) and organic media (long-chain thiols) was studied using the cobalt analog complex, [CoPc], immobilized onto ACs with different hydrophobic–hydrophilic properties and compared with the same complex encapsulated in sodium Y zeolite [55c]. In an aqueous phase, zeolite-supported catalysts were less active than those on carbon, which was explained by the ability of carbon to generate free radicals that could initiate the reaction and to adsorb thiols more strongly. However, the opposite occurred in the organic phase, since Y zeolite gave the most active catalyst.

8.5 APPLICATION OF CARBON-SUPPORTED ORGANOMETALLIC COMPOUNDS IN HYDROGENATION AND HYDROFORMYLATION CATALYTIC REACTIONS

8.5.1 Materials Based on Pd and Rh Amino Complexes

The complex $[\text{PdCl}_2(\text{NH}_2(\text{CH}_2)_{12}\text{CH}_3)_2]$ [56a], supported by an incipient wetness technique onto several carbon supports with different surface areas, was tested in the catalytic hydrogenation of cyclohexene to cyclohexane; sulfur resistance studies using tetrahydrothiophene (THT) as a poisoning reagent were also performed. The results showed that supported Pd complexes kept their integrity during the catalytic cycle and exhibited high catalytic activity and THT resistance for the cyclohexene hydrogenation. Some of the materials showed catalytic activity in the presence of THT which was almost twice the value obtained for the free catalyst. The higher sulfur resistance of the carbon-supported catalysts was attributed by the authors to an electronic effect and to retention of the poison molecules on the carbon surface. The authors also concluded that the effect of surface chemistry on catalytic activity was more important than the porosity, but pursued to a deeper study, using the same complex supported in several carbon materials with different characteristics: porosity, specific area, sulfur content, and surface chemistry. These new materials were tested in the same reaction and sulfur-poisoning resistance using THT as the poisoning agent in a concentration of 300 ppm [56b]. They observed that in terms of support porosity, the catalytic activity increased with an increase in supermicropore diameter from 0.7 nm to 2 nm, but no effect was found with regard to the oxygen surface groups and sulfur content of the ACs. Catalyst poisoning by THT was found to be independent of the AC properties and lower than that observed for the free metal complex. This suggested that the poisoning mechanism of the Pd complex by THT was by insertion of the poisoning molecules into the coordination sphere of Pd to form a Pd–S bond. Furthermore, the higher activity and sulfur resistance of the carbon-supported catalysts were due to the nature of the interaction between the complex and the AC through the aliphatic chain of the amine ligands, the apolar AC surface favoring this interaction and decreasing the coordination of the poison. On the other hand, for the three carbon supports, the activity as well as the sulfur resistance followed the same trend as their surface areas and were independent of their granular or pellet shape.

The catalysts *trans*- $[\text{PdCl}_2(\text{NH}_2(\text{CH}_2)_{12}\text{CH}_3)_2]$ and $[\text{RhCl}(\text{NH}_2(\text{CH}_2)_{12}\text{CH}_3)_3]$ supported on a commercial AC and on an almond shell-derived AC were screened in the cyclohexene hydrogenation in three successive catalytic cycles in order to evaluate their stability [56c]. The Rh complex catalyst was more active than the Pd analog, but both catalysts presented a good performance in successive uses. Experimental and modeled results confirmed that these complexes followed a similar reaction mechanism as that observed for homogeneous Wilkinson catalyst, but with different rates. In the case of the Rh complex, the heterogenization made a dramatic change on substrate

conversion since the catalyst supported reached an evident higher conversion for longer reaction times, indicating a positive effect for the carbon support in the catalytic reaction. For the supported Pd catalyst, conversion values were similar to those obtained with the homogeneous analog; for this complex it was postulated that the positive effect of the carbon support on Pd catalyst could only be observed for much longer reaction times. The continuous increase in conversion observed for the supported complexes, instead of the leveling off found with homogeneous catalysts, was attributed to the easy substitution of the outgoing bonded alkane and/or solvent molecules by the amine ligands, which remained adsorbed on the carbon support during the catalytic cycle and, consequently, close to the metal complex.

The same Pd complex, $[\text{PdCl}_2(\text{NH}_2(\text{CH}_2)_{12}\text{CH}_3)_2]$, supported by an incipient-wetness technique onto two microporous ACs (with a large proportion of pore volume in the range of micro- and supermicropores), was tested as a catalyst in the hydrogenation of 1-heptyne [56d]. In all cases 1-heptyne was initially converted to 1-heptene. No substances other than 1-heptyne, 1-heptene, and heptane were detected in the reaction medium. The higher 1-heptyne conversions for supported Pd complex compared with that of the homogeneous analog were attributed to the higher concentration of reactants on the support surface due to their adsorption. For the heterogenized catalysts an important effect of the support porosity was found. The selectivity to 1-heptene, displayed by the Pd complex supported in the AC with narrower pore size distribution and smaller supermicro- and mesoporous contribution, remained constant and very high up to a total conversion of about 92%. In opposition, for the Pd complex supported onto the AC with wider pore size distribution and larger supermicro- and mesoporous contribution, there was a continuous decrease in the selectivity from the beginning of the reaction, and at the final total conversion of 93%, the selectivity decreased markedly to 65%. The authors explained that formation of the planar molecule 1-heptene was favored relatively to heptane only when the active complex was located in a narrow pore; on the contrary, when the porosity of the support allowed for a higher concentration of the product 1-heptene in the neighborhood of the metal complex, the consecutive hydrogenation of 1-heptene to heptane occurred.

8.5.2 Materials Based on Rh and Pd Complexes with π -Bonding Ligands (Phosphines and Dienes)

The $[\text{Rh}(\mu\text{-Cl})(\text{cod})]_2$ complex heterogenized on untreated and oxidized ACs was used as a catalyst for the hydroformylation of 1-octene [78b]. The effects of the surface chemistry of ACs and of the solvents used in reaction media (hexane, acetone, or methanol) on the activity and selectivity to linear products (alcohols and aldehydes) were investigated. The supported complexes showed substrate conversions higher or similar to that of the unsupported analog and exhibited a higher selectivity to linear products. Complex lixiviation depended on the support, the solvent, and the method used to recover the catalyst. Furthermore,

the catalyst prepared with the oxidized AC, anchored by ion exchange and located mostly in the very narrow pores, was more stable and active in further catalytic cycles. The authors also stated that the effect of the solvents was related to polar interactions with the carbon surface, the highest stability being found in hexane. The selectivity of the supported catalyst and the homogeneous analog was influenced by the solvents; in methanol, the catalysts were selective to alcohols.

A similar Rh complex bearing hydroxyl-functionalized diphosphine, [Rh(OH-diphosphine)(cod)], and anchored via covalent bond to oxidized AC using two different synthetic routes, jointly with its homogeneous analog, [Rh(μ -Cl)(cod)]₂, were tested in the catalytic reaction referred to in the preceding paragraph [79]. In the first run, substrate conversion was very high for all the catalysts investigated. However, while the homogeneous catalyst produced only the aldehydes, the heterogenized catalysts produced a noticeable amount of 2-octene. The complex leaching after the fourth catalytic run was in the range 43 to 59%; nevertheless, analysis of the reaction media after each cycle by ³¹P NMR showed that for both immobilized complexes, leaching occurred only during the first cycle. The material prepared by immobilization of the complex synthesized previously was fully active in four consecutive catalytic cycles with conversion to the linear aldehyde that increased with reuse.

Similarly, several Rh complexes of general formula [Rh(diphosphine)(cod)] in the homogeneous phase and upon anchoring by direct axial metal coordination to several ACs were studied in the asymmetric hydrogenation of dimethyl itaconate (DMIT) substrate, which has a prochiral C=C bond [77]. Only the immobilized complexes showed a marked increase in the %ee, which emphasized the influence of the supports during the chiral selection process. Heterogeneous catalytic activity was in all cases remarkable, being very similar to the homogeneous reaction: The activity was in the range 500 to 1000 TON since total conversion was always reached within a few minutes. In a reuse test, one of the anchored catalysts kept its enantioselectivity and activity and no leaching was discernible, showing that the complex was strongly anchored to the support with this simple methodology. Another prochiral substrate, methyl acetamidoacrylate, was also catalytically hydrogenated by these immobilized complexes. In this case, materials denoted as [Rh(cod)(Phanephos)]/Acticarbone 2S and [Rh(cod)(Xylyl-phanephos)]/Acticarbone 2S were the best catalysts obtained, giving conversion values of ee% and 100% values of 97% and 98%, respectively; no metal leaching was detected for either catalysts.

The Pd complex [PdCl₂(PPh₃)₂] immobilized by the same methodology onto the same ACs [77] was tested in a Suzuki reaction using bromoanisole and benzeneboronic acid. Although the complex was immobilized in low loading, it proved to be active in the catalytic reaction, with 65% conversion in a 2-hour reaction time with very low Pd leaching. This result showed that the noncationic catalyst could also be immobilized by metal coordination directly to the support, and this bond was stable under reaction conditions. The catalyst was also tested in a Heck reaction involving the commonly used substrates 4-bromoacetophenone and butyl acrylate [77]. Despite good activity with a nearly total conversion in a

2-hour reaction time, Pd leaching was observed (leaching: 13 ppm Pd); this was probably due to the solvent, dimethylacetamide, and the base, sodium acetate, used.

The Wilkinson catalyst, $[\text{RhCl}(\text{PPh}_3)_3]$, also anchored by direct metal coordination to an AC [77], was tested in 1-hexene hydrogenation, showing good activity (compared with the homogeneous catalyst), with 72% of hexane produced in a 2-hour reaction time and 28% of 2-hexene due to an isomerization side reaction; no complex leaching was observed. This complex was also directly immobilized onto SWCNTs by a Rh metal–oxygen bond and was found to catalyze the hydrogenation of cyclohexene to cyclohexane at room temperature [86].

A similar Rh complex, $[\text{HRh}(\text{CO})(\text{PPh}_3)_3]$, immobilized onto AC and CNTs (ends-opened) by an incipient wetness technique was tested as a catalyst for propene hydroformylation [70]. Activity assay of the catalysts showed that the CNT-supported Rh complex displayed not only high activity for propene conversion but also excellent regioselectivity to the butyraldehyde product. Under the experimental conditions used, the molar ratio of normal to branched aldehydes reached 12 to 13 at a TOF of 0.12 s^{-1} , corresponding to a propene conversion of 32%. To understand the excellent catalytic behavior of the CNT-supported catalyst, an ends-unopened CNT was also used as support and its catalytic properties tested: In this particular case, propene conversion and the *n/i* ratio reached only 17.2% (corresponding to a TOF of 0.06 s^{-1}) and 6.0, respectively. On the basis of this result, the authors concluded that the high propene conversion and excellent regioselectivity demonstrated by ends-opened CNT-supported catalyst was due mainly to the confinement effect induced by the presence of a Rh–phosphine complex in the inner surface of the tubular nanochannels of CNT [70].

Finally, the Rh complex $[\text{Rh}(\text{cod})(\text{NH}_2(\text{CH}_2)_2\text{NH}(\text{CH}_2)_3\text{Si}(\text{OCH}_3)_3]\text{BF}_4$, immobilized onto oxidized ACs and MWCNTs (with an average external diameter of 17 nm and an internal diameter of 8 nm [10]), was tested in the catalytic hydrogenation of cyclohexene; data for an analogous homogeneous complex were included [80]. The immobilized complex showed a catalytic activity higher than in homogeneous conditions, which was explained by electronic modifications induced in the anchored complex by the immobilization procedure and also by the confinement effect caused by the porosity of the supports. For the three catalysts, the oxidation state of rhodium did not change and the coordination sphere was kept during the catalytic cycle. The heterogeneous catalysts could be recycled with no complex leaching, the catalytic activity being clearly higher in the second and following runs, indicating that the Rh complex–support bond was stable under the reaction conditions. The complex anchored onto MWCNTs showed a noticeably higher catalytic activity compared with that of the other supports. The authors suggested that the complex could, at least partially, be anchored in the hollow cavity of the CNTs, as observed in the Rh complex referred to above [70].

8.6 CARBON-SUPPORTED ORGANOMETALLIC COMPLEXES IN THE POLYMERIZATION REACTION OF OLEFINS

An original method for olefin polymerization by active metallocene complexes physicochemically anchored onto a CNT surface, with concomitant coating of CNTs by the in-situ-grown polyolefin chain, has recently been reported. The method is derived from the polymerization-filling technique (PFT) investigated initially in Ziegler–Natta polymerization [102] and developed more recently for metallocene catalysis applied to a broad range of microfillers, such as kaolin, silica, wollastonite, and graphite [103]. Due to the similarity between the chemical structures of graphite and CNTs, this technique has been used tentatively in the polymerization of ethylene and other olefins directly onto the CNT surface.

To date, two types of metallocene complexes have been used in the polymerization of olefins at CNT surfaces by PFT: a ruthenium alkylidene complex anchored by two routes onto SWCNTs via a pyrene derivative spacer [94], and zirconium complexes of general formula $[(R)_2ZrCl_2]$, R being a derivative of cyclopentadienyl or indenyl, anchored onto CNTs modified with MAO [97].

The polymerization of norbornene around SWCNTs by a ruthenium alkylidene complex immobilized onto SWCNTs [94] was achieved using a strategy involving exposure of the nanotubes to solutions of pyrene-functionalized alkylidene complex: homogeneous coatings of variable thickness were obtained in almost all experiments with polymerization times of less than 2 hours. However, reaction times longer than 10 minutes resulted in thinner coatings. This was attributed to two factors: decreasing ability of the pyrenyl spacer to continue to immobilize the polymer onto the SWCNTs effectively, and the solubilization of the polymer, as it grows as the reaction proceeds.

The polymerization of ethylene at the surface of MWCNTs catalyzed directly by the complex $[(Me_5Cp)_2ZrCl_2]$, bis(pentamethyl-5-cyclopentadienyl) zirconium(IV) dichloride, anchored onto nanotubes previously surface-treated with MAO, was compared with that in the homogeneous phase for 1 hour of reaction [97a]. Addition of ethylene to the modified MWCNTs led to the synthesis of polyethylene (PE) exclusively at the surface of the support. After 1 hour of reaction, ethylene consumption for catalyst supported on MWCNTs was 28% higher than that observed in homogeneous ethylene polymerization, showing clearly that the catalytic system onto MWCNTs increased the ethylene polymerization rate significantly. Furthermore, preliminary experiments showed that PE-coated MWCNTs obtained by the PFT technique could be dispersed homogeneously when melt blended in an HDPE matrix, leading to nanocomposites displaying higher tensile properties even with a nanofiller loading as low as 1 wt%.

The same complex anchored now onto MWCNTs functionalized with modified methylaluminoxane (MMAO; MAO where about 3 methyl units per 100 were substituted by longer alkyl chains such as isobutyl for better solubilization)

was used in the in situ polymerization of ethylene [97b]. This polyolefin coating was used for further melt blending with ethylene-*co*-vinyl acetate copolymers, to give high-performance nanocomposites with finely dispersed MWNTs. Other olefins have been polymerized by the same procedure using Zr indenyl analogs. The in-situ copolymerization of ethylene and 2-norbornene was catalyzed by dichloro[rac-ethylenebis(indenyl)]zirconium(IV), rac-[Et(Ind)₂ZrCl₂] immobilized onto MMAO-modified MWCNTs [97c]. The copolymerization reaction allowed for the disruption of native CNT bundles, and the resulting copolymer upon further melt blending with an ethylene–vinyl acetate copolymer (27 wt% vinyl acetate) matrix, gave high-performance polyolefinic nanocomposites. The catalyst rac-[Me₂Si(2-Me-Ind)₂]ZrCl₂ anchored onto MWCNT modified with MAO was also used in the in-situ polymerization of propylene with similar excellent results [97d].

8.7 CONCLUSIONS

Research on the immobilization of catalytically active transition metal complexes onto carbon materials is still a poorly unexploited area compared with that of inorganic materials. The most used immobilization methodologies are based in impregnation methods and derivatization of oxygen functionalities introduced in the edges or ends and defects of graphitic sheets and are focused, basically, in the more traditional materials, such as activated carbons and carbon blacks.

However, research on carbon nanotubes has opened new avenues in the area of materials science and carbon surface derivatization. Their physical and chemical modifications offer excellent opportunities not only in the characterization and understanding of CNT chemistry, but also in highlighting their potential applications. In the context of this chapter, one important application of CNTs is their use as support for homogeneous catalysts; in fact, based on the very few examples published in the literature, this is clearly a very promising area. Furthermore, the potential extrapolation of the CNT derivatization methodologies to more traditional and other recent carbon materials (mesoporous and ordered porous carbon materials) is also one of the major challenges for all researchers who are involved with carbon materials.

Acknowledgments

The authors would like to thank J. L. Figueiredo (Faculty of Engineering, University of Porto, Portugal) for fruitful discussions and stimulating collaboration in the area of carbon materials. The authors are also indebted to Philippe Serp (LCC CNRS UPR 8241, composante ENSIACET, Toulouse University, France) and Clara Pereira (Faculty of Sciences, University of Porto, Portugal) for revising the final version of the manuscript.

REFERENCES

- [1] J. Bird, in A.B. Stiles, Ed., *Catalyst Supports and Supported Catalysts*, Butterworth, Boston, MA, 1987.
- [2] D.E. De Vos, I.F.J. Vankelecom, P.A. Jacobs, Eds., *Chiral Catalyst Immobilisation and Recycling*, Wiley-VCH, Weinheim, Germany, 2000, p. 19.
- [3] J.S. Rafelt, J.H. Clark, *Catal. Today* 57 (2000) 33.
- [4] I.W.C.E. Arends, R.A. Sheldon, *Appl. Catal. A* 212 (2001) 175.
- [5] Q.-H. Fan, Y.-M. Li, A.S.C. Chan, *Chem. Rev.* 102 (2002) 3385.
- [6] C.E. Song, S. Lee, *Chem. Rev.* 102 (2002) 3495.
- [7] D.E. De Vos, M. Dams, B.F. Sels, P.A. Jacobs, *Chem. Rev.* 102 (2002) 3615.
- [8] C. Li, *Catal. Rev.* 46 (2004) 419.
- [9] Q.-H. Xia, H.-Q. Ge, C.-P. Ye, Z.-M. Liu, K.-X. Su, *Chem. Rev.* 105 (2005) 1603.
- [10] J.M. Notestein, A. Katz, *Chem. Eur. J.* 12 (2006) 3954.
- [11] F. Goettmann, C. Sanchez, *J. Mater. Chem.* 17 (2007) 24.
- [12] F. Bedioui, *Coord. Chem. Rev.* 144 (1995) 39.
- [13] H. Marsh, F. Rodríguez Reinoso, *Activated Carbon*, Elsevier, Oxford, 2006.
- [14] L.R. Radovic, Ed., *Chemistry and Physics of Carbon*, Vol. 28, Marcel Dekker, New York, 2003.
- [15] T.D. Burchell, Ed., *Carbon Materials for Advanced Technologies*, Elsevier, New York, 1999.
- [16] C.M. Elliott, R.W. Murray, *Anal. Chem.* 48 (1976) 1247.
- [17] R.W. Murray, *Electroanal. Chem.* 13 (1984) 191.
- [18] H.D. Abrufa, *Coord. Chem. Rev.* 86 (1988) 135.
- [19] K. Kinoshita, *Carbon Electrochemical and Physicochemical Properties*, Wiley, New York, 1988.
- [20] (a) A. Hirsch, M. Brettreich, *Fullerenes: Chemistry and Reactions*, Wiley-VCH, Weinheim, Germany, 2004. (b) K.M. Kadish, R.S. Ruoff, *Fullerenes: Chemistry, Physics, and Technology*, Wiley-VCH, Weinheim, Germany, 2000.
- [21] (a) S. Iijima, *Nature* 354 (1991) 56. (b) S. Reich, C. Thomsen, J. Maultzsch, *Carbon Nanotubes: Basic Concepts and Physical Properties*, Wiley-VCH, Weinheim, Germany, 2004. (c) M.S. Dresselhaus, G. Dresselhaus, P. Avouris, *Carbon Nanotubes: Synthesis, Structure, Properties and Applications*, Springer-Verlag, Berlin, 2001. (d) P.J.F. Harris, *Carbon Nanotubes and Related Structures: New Materials for the Twenty-First Century*, Cambridge University Press, Cambridge, UK, 2001.
- [22] (a) J. Lee, J. Kim, T. Hyeon, *Adv. Mat.* 18 (2006) 2073. (b) J. Lee, S. Han, T. Hyeon, *J. Mater. Chem.* 14 (2004) 478. (c) Y. Wu, B. Yang, B. Zong, H. Sun, Z. Shen, Y. Feng, *J. Mater. Chem.* 14 (2004) 469. (d) R.W. Pekala, *J. Mater. Sci.* 24 (1989) 3221.
- [23] (a) H.-P. Boehm, *High Temp. High Press.* 22 (1990) 275. (b) H.-P. Boehm, E. Diehl, W. Heck, R. Sappok, *Angew. Chem. Int. Ed.* 3 (1964) 669.
- [24] R.C. Bansal, J.-B. Donnet, F. Stoeckli, *Active Carbon*, Marcel Dekker, New York, 1998.
- [25] (a) F. Rodríguez-Reinoso, *Carbon* 36 (1998) 159. (b) F. Rodríguez-Reinoso, U.M. Molina-Sabio, *Adv. Colloid Interface Sci.* 76–77 (1998) 271. (c) J. Ruiz-Martínez,

- E.V. Ramos-Fernández, A. Sepúlveda-Escribano, F. Rodríguez-Reinoso, *Stud. Surf. Sci. Catal.* 160 (2007) 129.
- [26] (a) J.L. Figueiredo, M.F.R. Pereira, M.M.A. Freitas, J.J.M. Órfão, *Carbon* 37 (1999) 1379. (b) J.L. Figueiredo, P. Serp, B. Nysten, J.-P. Issi, *Carbon* 37 (1999) 1809. (c) J.A.C. Alves, C. Freire, B. de Castro, J.L. Figueiredo, *Colloids Surf. A* 189 (2001) 75.
- [27] (a) A. Vinu, K.Z. Hossian, P. Srinivasu, M. Miyahara, S. Anandan, N. Gokulakrishnan, T. Mori, K. Ariga, V.V. Balasubramanian, *J. Mater. Chem.* 17 (2007) 1819. (b) M.J. Lázaro, L. Calvillo, E.G. Bordejé, R. Moliner, R. Juan, C.R. Ruiz, *Micropor. Mesopor. Mater.* 103 (2007) 158. (c) J. Li, M.J. Vergne, E.D. Mowles, W.-H. Zhong, D.M. Hercules, C.M. Lukehart, *Carbon* 43 (2005) 2883.
- [28] A. Hirsch, *Angew. Chem. Int. Ed.* 41 (2002) 1853.
- [29] (a) S. Banerjee, M.G.C. Kahn, S.S. Wong, *Chem. Eur. J.* 9 (2003) 1899. (b) S. Banerjee, T. Hemraj-Benny, S.S. Wong, *Adv. Mat.* 17 (2005) 17.
- [30] D.M. Guldi, G.M.A. Rahman, V. Sgobba, C. Ehli, *Chem. Soc. Rev.* 35 (2006) 471.
- [31] (a) D. Tasis, N. Tagmatarchis, V. Georgakilas, M. Prato, *Chem. Eur. J.* 9 (2003) 4001. (b) D. Tasis, N. Tagmatarchis, A. Bianco, M. Prato, *Chem. Rev.* 106 (2006) 1105.
- [32] S. Niyogi, M.A. Hamon, H. Hu, B. Zhao, P. Bhowmik, R. Sen, M.E. Itkis, R.C. Haddon, *Acc. Chem. Res.* 35 (2002) 1105.
- [33] J.L. Bahr, J.M. Tour, *J. Mater. Chem.* 12 (2002) 1952.
- [34] (a) A.M. Yacynych, T. Kuwana, *Anal. Chem.* 50 (1978) 640. (b) D.C.S. Tse, T. Kuwana, G.P. Royer, *J. Electroanal. Chem.* 98 (1979) 345.
- [35] K.W. Willman, R.D. Rocklin, K.N. Kuo, F.A. Schultz, R.W. Murray, *J. Am. Chem. Soc.* 102 (1980) 7629.
- [36] Y. Matsuo, T. Tabata, T. Fukunaga, T. Fukutsuka, Y. Sugie, *Carbon* 43 (2005) 2875.
- [37] (a) T. Hemraj-Benny, S.S. Wong, *Chem. Mater.* 18 (2006) 4827. (b) M. Aizawa, M.S.P. Shaffer, *Chem. Phys. Lett.* 368 (2003) 121.
- [38] D.A. Britz, A.N. Khlobystov, *Chem. Soc. Rev.* 35 (2006) 637.
- [39] (a) T. Nakajima, N. Watanabe, *Graphite Fluorides and Carbon–Fluorine Compounds*, CRC Press, Boca Raton, FL, 1990. (b) N. Watanabe, T. Nakajima, H. Touhara, *Graphite Fluorides*, 56th Ed., Elsevier, Amsterdam, 1988.
- [40] H. Touhara, F. Okino, *Carbon* 38 (2000) 241.
- [41] Y.-S. Lee, *J. Fluorine Chem.* 128 (2007) 392.
- [42] M. Delamar, R. Hitmi, J. Pinson, J.-M. Savéant, *J. Am. Chem. Soc.* 114 (1992) 5883.
- [43] (a) C.P. Andrieux, F. Gonzales, J.M. Savéant, *J. Am. Chem. Soc.* 119 (1997) 4292. (b) M. Delamar, G. Désarmot, O. Fagebaume, R. Hitmi, J. Pinson, J.-M. Savéant, *Carbon* 35 (1997) 801.
- [44] Y.-C. Liu, R.L. McCreery, *J. Am. Chem. Soc.* 117 (1995) 11254.
- [45] E. Coulon, J. Pinson, J.-D. Bourzat, A. Commerçon, J.P. Pulicani, *Langmuir* 17 (2001) 7102.
- [46] P.R. Marcoux, P. Hapiot, P. Bataila, J. Pinson, *New J. Chem.* 28 (2004) 302.
- [47] (a) J. Liu, M.R.I. Zubiri, B. Vigolo, M. Dossot, Y. Fort, J.-J. Ehrhardt, E. McRae,

- Carbon* 45 (2007) 885. (b) A.T. Masheter, G.G. Wildgoose, A. Crossley, J.H. Jones, R.G. Compton, *J. Mater. Chem.* 17 (2007) 3008.
- [48] (a) M. Holzinger, O. Vostrowsky, A. Hirsch, F. Hennrich, M. Kappes, R. Weiss, F. Jellen, *Angew. Chem. Int. Ed.* 40 (2001) 4002. (b) M. Holzinger, J. Abraham, P. Whelan, R. Graupner, L. Ley, F. Hennrich, M. Kappes, A. Hirsch, *J. Am. Chem. Soc.* 125 (2003) 8566. (c) H. Peng, L.B. Alemany, J.L. Margrave, V.N. Khabashesku, *J. Am. Chem. Soc.* 125 (2003) 15174. (d) H. Sawada, K. Shindo, K. Ueno, K. Hamazaki, *Polym. Adv. Technol.* 16 (2005) 764.
- [49] N. Tagmatarchis, M. Prato, *J. Mater. Chem.* 14 (2004) 437. (b) C. Cioffi, S. Campidelli, F.G. Brunetti, M. Meneghetti, M. Prato, *Chem. Commun.* (2006) 2129. (c) V. Georgakilas, K. Kordatos, M. Prato, D.M. Guldi, M. Holzinger, A. Hirsch, *J. Am. Chem. Soc.* 124 (2002) 760. (d) V. Georgakilas, N. Tagmatarchis, D. Pantarotto, A. Bianco, J.-P. Briand, M. Prato, *Chem. Commun.* (2002) 3050.
- [50] V. Georgakilas, D. Gournis, V. Tzitzios, L. Pasquato, D.M. Guldi, M. Prato, *J. Mater. Chem.* 17 (2007) 2679.
- [51] (a) A. Bianco, K. Kostarelos, C.D. Partidos, M. Prato, *Chem. Commun.* (2005) 571. (b) A. Bianco, M. Prato, *Adv. Mater.* 15 (2003) 1765. (c) M. Prato, K. Kostarelos, A. Bianco, *Acc. Chem. Res.* 41 (2008) 60. (d) D.M. Guldi, G.M.A. Rahman, F. Zerbetto, M. Prato, *Acc. Chem. Res.* 38 (2005) 871.
- [52] (a) Y.-P. Sun, K. Fu, Y. Lin, W. Huang, *Acc. Chem. Res.* 35 (2002) 1096. (b) Y. Lin, M.J. Meziani, Y.-P. Sun, *J. Mater. Chem.* 17 (2007) 1143.
- [53] E. Katz, I. Willner, *Chem. Phys. Chem.* 5 (2004) 1084.
- [54] A. Valente, C. Palma, I.M. Fonseca, A.M. Ramos, J. Vital, *Carbon* 41 (2003) 2793.
- [55] (a) R.F. Parton, P.E. Neys, P.A. Jacobs, R.C. Sosa, P.G. Rouxhet, *J. Catal.* 164 (1996) 341. (b) R.C. Sosa, R.F. Parton, P.E. Neys, O. Lardinois, P.A. Jacobs, P.G. Rouxhet, *J. Mol. Catal. A* 110 (1996) 141. (c) F. Thibault-Starzyk, M.V. Puymbroeck, R.F. Parton, P.A. Jacobs, *J. Mol. Catal. A* 109 (1996) 75.
- [56] (a) P.C. L'Argenti  re, E.A. Cagnola, D.A. Liprandi, M.C. Rom  n-Mart  nez, C.S.-M. de Lecea, *Appl. Catal. A* 172 (1998) 41. (b) J.A. D  az-Au  n  n, M.C. Rom  n-Mart  nez, C.S.-M. de Lecea, P.C. L'Argenti  re, E.A. Cagnola, D.A. Liprandi, M.E. Quiroga, *J. Mol. Catal. A* 153 (2000) 243. (c) M.C. Rom  n-Mart  nez, J.A. D  az-Au  n  n, P.C. L'Argenti  re, C.S.-M. de Lecea, *Catal. Lett.* 77 (2001) 41. (d) P.C. L'Argenti  re, M.E. Quiroga, D.A. Liprandi, E.A. Cagnola, M.C. Rom  n-Mart  nez, J.A. D  az-Au  n  n, C.S.-M. de Lecea, *Catal. Lett.* 87 (2003) 97.
- [57] M. Cardoso, A.R. Silva, B. de Castro, C. Freire, *Appl. Catal. A* 285 (2005) 110.
- [58] (a) X. Wang, Y. Liu, W. Qiu, D. Zhu, *J. Mater. Chem.* 12 (2002) 1636. (b) G.M.A. Rahman, D.M. Guldi, S. Campidelli, M. Prato, *J. Mater. Chem.* 16 (2006) 62. (c) D. Baskaran, J.W. Mays, P. Zhang, M.S. Bratcher, *J. Am. Chem. Soc.* 127 (2005) 6916.
- [59] I. Such-Bas  n  ez, M.C. Rom  n-Mart  nez, C.S.-M. de Lecea, *Carbon* 42 (2004) 1357.
- [60] (a) D.M. Guldi, G.M.A. Rahman, N. Jux, D. Balbinot, U. Hartnagel, N. Tagmatarchis, M. Prato, *J. Am. Chem. Soc.* 127 (2005) 9830. (b) C. Ehli, G.M.A. Rahman, N. Jux, D. Balbinot, D.M. Guldi, F. Paolucci, M. Marcaccio,

- D. Paolucci, M. Melle-Franco, F. Zerbetto, S. Campidelli, M. Prato, *J. Am. Chem. Soc.* 128 (2006) 11222.
- [61] P.J. Boul, J. Liu, E.T. Mickelson, C.B. Huffman, L.M. Ericson, I.W. Chiang, K.A. Smith, D.T. Colbert, J.L. Margrave, R.E. Smalley, *Chem. Phys. Lett.* 310 (1999) 367.
- [62] J.L. Stevens, A.Y. Huang, H. Peng, I.W. Chiang, V.N. Khabashesku, J.L. Margrave, *Nano Lett.* 3 (2003) 331.
- [63] L. Zhang, V.U. Kiny, H. Peng, J. Zhu, R.F.M. Lobo, J.L. Margrave, V.N. Khabashesku, *Chem. Mater.* 16 (2004) 2055.
- [64] (a) Y. Chen, R.C. Haddon, S. Fang, A.M. Rao, P.C. Eklund, W.H. Lee, E.C. Dickey, E.A. Grulke, J.C. Pendergrass, A. Chavan, B.E. Haley, R.E. Smalley, *J. Mater. Res.* 13 (1998) 2423. (b) J. Chen, M.A. Hamon, H. Hu, Y. Chen, A.M. Rao, P.C. Eklund, R.C. Haddon, *Science* 282 (1998) 95.
- [65] (a) C. Bingel, *Chem. Ber.* 126 (1993) 1957. (b) X. Camps, A. Hirsch, *J. Chem. Soc. Perkin Trans. 1* (1997) 1595.
- [66] (a) K.S. Coleman, S.R. Bailey, S. Fogden, M.L.H. Green, *J. Am. Chem. Soc.* 125 (2003) 8722. (b) A.K. Worsley, K.R. Moonosawmy, P. Kruse, *Nano Lett.* 4 (2004) 1541. (c) T. Umeyama, N. Tezuka, M. Fujita, Y. Matano, N. Takeda, K. Murakoshi, K. Yoshida, S. Isoda, H. Imahori, *J. Phys. Chem.* 111 (C 2007) 9734.
- [67] H. Peng, L.B. Alemany, J.L. Margrave, V.N. Khabashesku, *J. Am. Chem. Soc.* 125 (2003) 15175.
- [68] (a) A.N. Klobystov, D.A. Britz, G.A. Briggs, *Acc. Chem. Res.* 38 (2005) 901. (b) D.A. Morgan, J. Sloan, M.L.H. Green, *Chem. Commun.* (2002) 2442.
- [69] L.J. Li, A.N. Klobystov, J.G. Wiltshire, G.A.D. Briggs, R.J. Nicholas, *Nat. Mater.* 4 (2005) 481.
- [70] Y. Zhang, H.-B. Zhang, G.-D. Lin, P. Chen, Y.-Z. Yuan, K.R. Tsai, *Appl. Catal. A* 187 (1999) 213.
- [71] A.R. Silva, M.M.A. Freitas, C. Freire, B. de Castro, J.L. Figueiredo, *Langmuir* 18 (2002) 8017.
- [72] (a) A.R. Silva, J. Vital, J.L. Figueiredo, C. Freire, B. de Castro, *New J. Chem.* 27 (2003) 1511. (b) A.R. Silva, J.L. Figueiredo, C. Freire, B. de Castro, *Micropor. Mesopor. Mater.* 68 (2004) 83.
- [73] N. Mahata, A.R. Silva, M.F.R. Pereira, C. Freire, B. de Castro, J.L. Figueiredo, *J. Colloid Interface Sci.* 311 (2007) 152.
- [74] (a) A.R. Silva, C. Freire, B. de Castro, *Carbon* 42 (2004) 3003. (b) A.R. Silva, V. Budarin, J.H. Clark, B. de Castro, C. Freire, *Carbon* 43 (2005) 2096.
- [75] F. Maia, N. Mahata, A.R. Silva, M.F.R. Pereira, C. Freire, J.L. Figueiredo, *Extended Abstract of the International Conference on Carbon*, Aberdeen, Scotland, 2006.
- [76] A.R. Silva, M. Martins, M.M.A. Freitas, A. Valente, C. Freire, B. de Castro, J.L. Figueiredo, *Micropor. Mesopor. Mater.* 55 (2002) 275.
- [77] C.F.J. Barnard, J. Rouzaud, S.H. Stevenson, *Org. Process Res. Dev.* 9 (2005) 164.
- [78] (a) J.A. Diaz-Auñón, M.C. Román-Martínez, C.S.-M. de Lecea, H. Alper, *Stud. Surf. Sci. Catal.* 143 (2002) 295. (b) J.A. Diaz-Auñón, M.C. Román-Martínez, C.S.-M. de Lecea, *J. Mol. Catal. A* 170 (2001) 81.

- [79] M.C. Román-Martínez, J.A. Díaz-Auñón, C.S.-M. de Lecea, H. Alper, *J. Mol. Catal. A* 213 (2004) 177.
- [80] L. Lemus-Yegres, I. Such-Basáñez, C.S.-M. de Lecea, P. Serp, M.C. Román-Martínez, *Carbon* 44 (2006) 587.
- [81] (a) X. Wang, Y. Liu, W. Qiu, D. Zhu, *J. Mater. Chem.* 12 (2002) 1636.
 (b) T. Hasobe, S. Fukuzumi, P.V. Kamat, *J. Am. Chem. Soc.* 127 (2005) 11884.
- [82] (a) X.B. Wang, Y.Q. Liu, W.F. Qiu, D.B. Zhu, *J. Mater. Chem.* 12 (2002) 1636.
 (b) H. Li, B. Zhou, Y. Lin, L. Gu, W. Wang, K.A.S. Fernando, S. Kumar, L.F. Allard, Y.-P. Sun, *J. Am. Chem. Soc.* 126 (2004) 1014.
- [83] (a) T. Umeyama, M. Fujita, N. Tezuka, N. Kadota, Y. Matano, K. Yoshida, S. Isoda, H. Imahori, *J. Phys. Chem. C* 111 (2007) 11485. (b) D. Baskaran, J.W. Mays, X.P. Zhang, M.S. Bratcher, *J. Am. Chem. Soc.* 127 (2005) 6916.
- [84] F. Frehill, J.G. Vos, S. Benrezzak, A.A. Koós, Z. Kónya, M.G. Rüther, W.J. Blau, A. Fonseca, J.B. Nagy, L.P. Biró, A.I. Minett, M. in het Panhuis, *J. Am. Chem. Soc.* 124 (2002) 13694.
- [85] S. Banerjee, S.S. Wong, *Nano Lett.* 2 (2002) 49.
- [86] S. Banerjee, S.S. Wong, *J. Am. Chem. Soc.* 124 (2002) 8940.
- [87] P. Wang, C.N. Moorefield, S. Li, J. Manríquez, C.D. Shreiner, E. Bustos, A.L. Hartley, L.A. Godínez, G.R. Newkom, *J. Mater. Chem.* 17 (2007) 3023.
- [88] T. Hemraj-Benny, S. Banerjee, S.S. Wong, *Chem. Mater.* 16 (2004) 1855.
- [89] A.R. Silva, C. Freire, B. de Castro, M.M.A. Freitas, J.L. Figueiredo, *Micropor. Mesopor. Mater.* 46 (2001) 211.
- [90] A.R. Silva, V. Budarin, J.H. Clark, C. Freire, B. de Castro, *Carbon* 45 (2007) 1951.
- [91] (a) C. Baleizão, B. Gigante, H. Garcia, A. Corma, *J. Catal.* 221 (2004) 77.
 (b) C. Baleizão, B. Gigante, H. Garcia, A. Corma, *Tetrahedron* 60 (2004) 10461.
- [92] (a) A.R. Silva, M. Martins, M.M.A. Freitas, J.L. Figueiredo, C. Freire, B. de Castro, *Eur. J. Inorg. Chem.* (2004) 2027. (b) A.R. Silva, J.L. Figueiredo, C. Freire, B. de Castro, *Catal. Today* 102–103 (2005) 154. (c) B. Jarrais, A.R. Silva, C. Freire, *Eur. J. Inorg. Chem.* (2005) 4582.
- [93] (a) A. Valente, A.M. Botelho do Rego, M.J. Reis, I.F. Silva, A.M. Ramos, J. Vital, *Appl. Catal. A* 207 (2001) 221. (b) P. Oliveira, A.M. Ramos, I. Fonseca, A. Botelho do Rego, J. Vital, *Catal. Today* 102–103 (2005) 67.
- [94] F.J. Gómez, R.J. Chen, D. Wang, R.M. Waymouth, H. Dai, *Chem. Commun.* (2003) 190.
- [95] S. Campidelli, C. Sooambar, E.L. Diz, C. Ehli, D.M. Guldi, M. Prato, *J. Am. Chem. Soc.* 128 (2006) 12544.
- [96] D.M. Guldi, M. Marcaccio, D. Paolucci, F. Paolucci, N. Tagmatarchis, D. Tasis, E. Vazquez, M. Prato, *Angew. Chem. Int. Ed.* 42 (2003) 4206.
- [97] (a) D. Bonduel, M. Mainil, M. Alexandre, F. Monteverde, P. Dubois, *Chem. Commun.* (2005) 781. (b) S. Peeterbroeck, B. Lepoittevin, E. Pollet, S. Benali, C. Broekaert, M. Alexandre, D. Bonduel, P. Viville, R. Lazzaroni, P. Dubois, *Polym. Eng. Sci.* (2006) 1022. (c) S. Bredeau, L. Boggioni, F. Bertini, I. Tritto,

- F. Monteverde, M. Alexandre, P. Dubois, *Macromol. Rapid Commun.* 28 (2007) 822. (d) A. Funck, W. Kaminsky, *Compos. Sci. Technol.* 67 (2007) 906.
- [98] A.R. Silva, C. Freire, B. de Castro, *New J. Chem.* 28 (2004) 253.
- [99] E.M. McGarrigle, D.G. Gilheany, *Chem. Rev.* 105 (2005) 1563.
- [100] E.N. Jacobsen, M.H. Wu, in A. Pfaltz, E.N. Jacobsen, H. Yamamoto, Eds., *Comprehensive Asymmetric Catalysis*, Springer-Verlag, Berlin, 1999, p. 649.
- [101] (a) J.T. Groves, T.E. Nemo, *J. Am. Chem. Soc.* 105 (1983) 6243. (b) J.T. Groves, R. Quinn, *J. Am. Chem. Soc.* 107 (1985) 5790. (c) R.A. Leising, R.E. Norman, L. Que, Jr., *Inorg. Chem.* 29 (1990) 2553.
- [102] (a) N.S. Enikolopian, U.S.S.R. patent 763,379, 1976. (b) E.G. Howard, U.S. patent 4,097,447, 1978.
- [103] (a) M. Alexandre, E. Martin, P. Dubois, M. Garcia-Marti, R. Jérôme, *Macromol. Rapid Commun.* 21 (2000) 931. (b) M. Alexandre, E. Martin, P. Dubois, M. Garcia-Marti, R. Jérôme, *Chem. Mater.* 13 (2001) 236. (c) M. Alexandre, M. Pluta, P. Dubois, R. Jérôme, *Macromol. Chem. Phys.* 202 (2001) 2239.

9 Carbon Nanotubes and Nanofibers in Catalysis

PHILIPPE SERP

9.1 INTRODUCTION

Carbon nanotubes, carbon or graphite nanofibers, carbon filaments, carbon fibrils, or vapor-grown carbon nanofibers are general terms employed widely to refer to nanofilamentous carbon. Indeed, these structures fulfill the usual nanomaterial definition since they all present a common feature, their diameter being below 100 nm. Basically, these materials can be classified into two categories: tubes, which present a hollow cavity, and fibers, which do not (Figure 9.1). In this chapter we speak of carbon nanotubes (CNTs) having a tubular morphology with one or several concentric graphene layers, and of carbon nanofibers (CNFs) for the other structures. Discussions concerning the discovery of these materials have been reported [1,2]. Filamentous carbons have long been produced, the first reports dating back more than a century [3–5], by the action of a catalyst on the gaseous species originating from the thermal decomposition of hydrocarbons. One of the first pieces of evidence that such carbon materials could consist of nanotubes exhibiting an inner cavity is found in the transmission electron microscope micrographs reported by Hillert and Lange in 1958 [6]. Then the work of Oberlin and Endo [7] and of Wiles and Abrahamson [8] brought a deeper insight on the structure of these materials. The scientific interest in fibrous carbon has been recurrent since then, but a real boost in this research area occurred only in the 1990s, after the publication of two key articles by the Japanese microscopist S. Iijima showing that CNTs, either multiwalled (MWCNTs) [9] or single-walled (SWCNTs) [10], are formed during the synthesis of fullerenes by arc discharge. CNTs have therefore become one of the most active research topics in nanoscience and nanotechnology, owing to exceptional properties that make them suitable for many potential applications such as polymer reinforcements for composites, or breakthrough materials for energy storage, electronics, and catalysis [11].

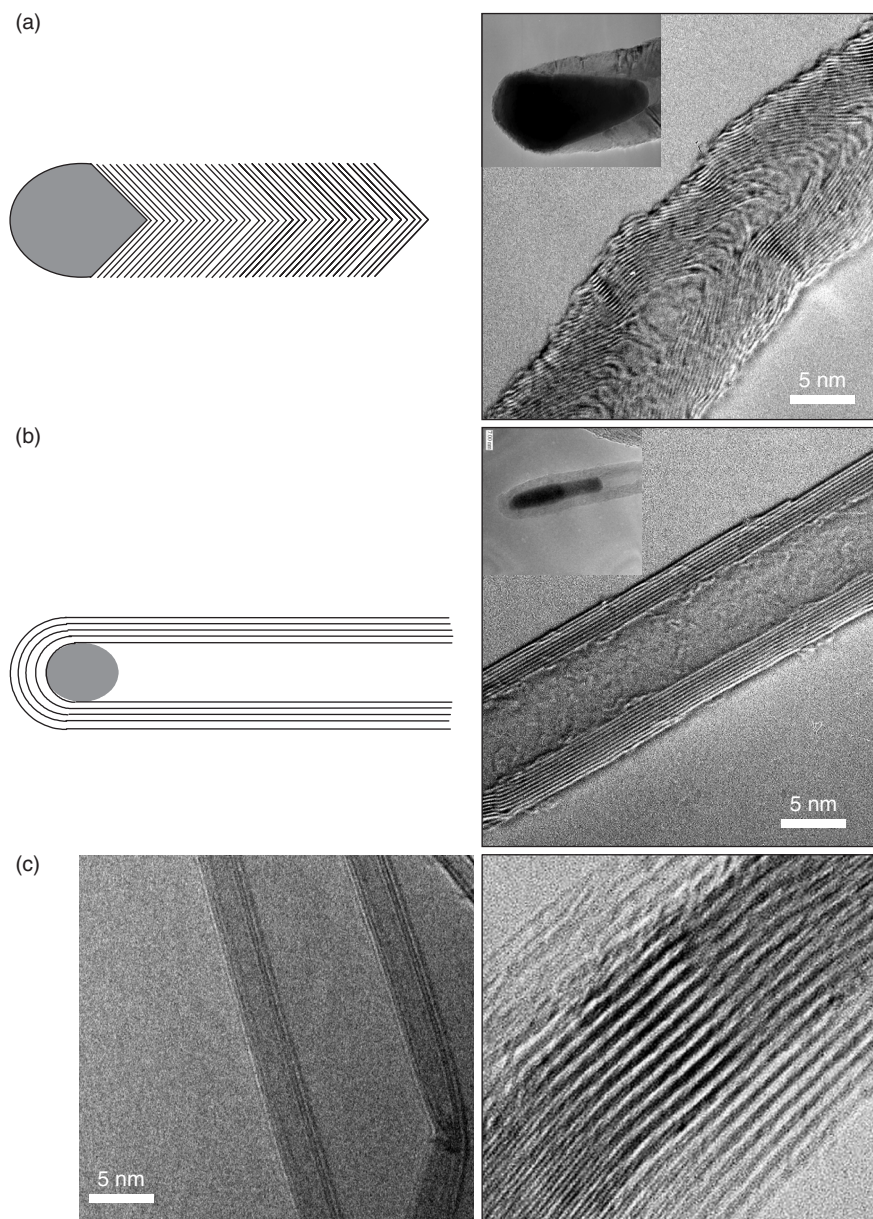


Figure 9.1 Different types of filamentous carbon: (a) CNF; (b) MWCNT; (c) DWCNTs and bundle of SWCNTs.

For decades the catalysis community has worked on the mechanisms of filamentous carbon formation since they were considered only as unwanted by-products and all efforts were focused on how to prevent their formation. Indeed, these filaments were formed by reactions involving conversion of carbon-containing gases, and were identified clearly as one of the reasons of catalyst deactivation and reactor degradation. Such mechanistic studies can be found in comprehensive reviews by Bartholomew [12] and Rodriguez [13]. More recently, also due to the great interest in carbon nanostructures, by both academia and industry, the catalytic formation of CNTs and CNFs received increased attention, and the definition of active and selective (to type of structure, and to diameter and length control) catalysts is nowadays a key point for the development of these materials [14,15]. Indeed, besides the key points about standardization, safety, and impact on environment, which are characteristic of each nanomaterial, the current worldwide CNT and CNF availability is still low, and a middle-term industrial production becomes realistic only if an efficient production process exists. A literature analysis has shown that there is a considerable thrust on patenting in the area of synthesis or of novel processes for the production of CNTs, mainly in the United States and Japan, and to a lesser extent in Europe and Korea [16]. The large-scale synthesis of such materials by catalytic chemical vapor deposition (CCVD) of a carbon-containing gas is the subject of intensive research and appears to be the most promising route, due to the potential cheapness of the material produced, to process flexibility and high-yield productivities. The possibility to produce nitrogen (see Chapter 7) or boron-doped CNTs or CNFs by such a process is also of interest to tune their electron donor–acceptor properties. Hyperion Catalysis International is chronologically one of the first key players on the market. Furthermore, and importantly for industrial production, the use of fluid-bed (FB) technologies is possible [17]. An important fact highlighting the potentiality of this technology is that industrial pilot FB-CCVD reactors are already run for MWCNT and SWCNT manufacture. Thus, Arkema commercializes MWCNTs named Graphistrength, Bayer commercializes MWCNTS named Baytubes, and SouthWest Nanotechnologies produces SWCNTs by the CoMoCAT method, which employs this technology. Up to now, neither precise price estimations nor anticipations are possible, since no market price has yet been fixed, but middle-term scenarios predict a price that could vary between 10 and 50 euros/kg for MWCNTs, and between 50 and 100 euros/kg for SWCNTs.

The first published studies concerning the use of CNTs or CNFs in the field of heterogeneous catalysis date back to 1994 [18,19], and specific activities and selectivities of CNT or CNF-supported catalysts were reported. As a matter of fact, an industrial interest exists in the area of supported catalysts for fluid-phase reactions [20] or for fuel cell electrodes [21]. Since these first reports, numerous studies have brought better knowledge about these carbon nanostructures and opened the way to their application in catalysis. Besides the study of the specific properties of these materials, special attention has been paid to the design of CNT/CNF supports, to the preparation of metal particles on CNTs or CNFs [22],

and to the study of the catalytic properties of these systems [23–28]. The catalytic studies cover (1) the use of CNTs/CNFs as catalysts, mainly for oxidative dehydrogenation reactions; (2) the involvement of CNT/CNF-supported catalysts in liquid-phase reactions for fine chemicals or in gas-phase reaction for CNT growth; (3) electrocatalysis for fuel cells; and (4) the production of specific materials for hydrogen storage or gas sensors. In this chapter we make a survey of the catalytic production of CNTs and CNFs, of the main characteristics of these nanomaterials, of the preparative routes developed to supported catalysts on CNTs or CNFs, and finally, of the catalytic studies conducted on such systems.

9.2 CATALYTIC GROWTH OF CARBON NANOFIBERS AND NANOTUBES

The comprehension of the growth mechanism of CNTs or CNFs is a critical issue, as it contributes to the improvement of manufacturers' catalytic processes. It is important to stress the fact that several of the primary steps in the mechanism of CNT/CNF growth by CCVD were proposed some decades ago by scientists interested in the coking of reforming catalysts, and in the way by which it could be possible to avoid such deactivation mechanism [25].

9.2.1 Catalytic Carbon Deposition

The deactivation of metal-supported catalysts by carbon deposition has been reviewed in comprehensive books [29,30]. It is generally admitted that carbon may (1) chemisorb strongly onto the metal to produce a monolayer, or to be physically adsorbed as multilayers, thus hindering the access of reactants to the metal surface sites; (2) fully encapsulate each metal particle and thereby completely deactivate the catalyst; and (3) plug the micro- and mesopores so that the access of reactants to many crystallites inside the pores is suppressed. Finally, in the worst cases, carbon filaments may build up in the catalyst grain porosity to such an extent that they stress and fracture the support material, ultimately causing disintegration of catalyst pellets and covering the reactor walls [31]. The first studies based on electron microscopy observations, dealing with the structure of these filamentary carbons, date back to the 1950s [32]. Since that time and until the 1990s, no clear difference was revealed between filaments presenting a hollow cavity (CNTs) and CNFs.

Iron, nickel, cobalt, and their alloys are the most studied metals for the catalytic growth of CNFs or CNTs. The readiness of these metals to produce metal–carbon solid solutions and to form metastable carbides in the appropriate reaction temperature range should be an important factor to take into account for the comprehension of their reactivity. The different carbon species formed depending on the temperature range employed in the steam reforming of hydrocarbons on nickel catalysts have been discussed [29] and consist of:

- Encapsulating films that lead to progressive deactivation and are formed at temperatures below 773 K by polymerization of C_nH_m radicals
- CNFs, resulting from carbon diffusion through the metal particles, and formed at temperatures above 723 K (interestingly, CNF formation does not induce catalyst deactivation, thus indicating that the metal nanoparticle is still accessible to reactants)
- Pyrolytic carbon resulting from hydrocarbon thermal decomposition on the particles at temperatures above 873 K, which leads to complete catalyst deactivation by encapsulation

It is important to stress the fact that in a relatively narrow temperature range, a complex series of reactions involving metal particles, hydrocarbons, C_nH_m radicals, and carbon atoms takes place, and a subtle tuning of thermodynamic and kinetic parameters is necessary to direct the reaction toward the desired product. Indeed, the mechanisms involved in the growth of CNTs (both MWCNTs and SWCNTs) or CNFs constitute a very complicated catalysis problem that involves high-temperature reactions on the surface but also in the bulk of the particles as well as at the particle-support interface. The first oriented studies of the mechanisms of filamentous carbon formation concern CNFs, and the relevant models have been widely used to describe the CNTs growth. If this approach seems reasonable in the case of the growth of large-diameter MWCNTs for SWCNTs or few-wall MWCNTs, which are produced from small nanoparticles (≤ 5 nm), the situation might be more complicated. Indeed, decreasing the size of the metal particle to the nanometer scale results in a notable increase in the ratio of surface atoms to internal atoms. The surface atoms are unsaturated electronically and coordinatively, and thus more reactive and mobile. This results in differences in various physical and chemical properties compared to the bulk material. In that case, some size-dependent (scalable or quantum) effects may occur, significantly affecting the growth mechanisms. This is one of the reasons why (1) a unified mechanism that combines the formation of these nanomaterials from a catalyst particle has not yet been proposed, and (2) some aspects of the mechanism remain obscure.

9.2.2 Growth Mechanism

As far as the growth mechanism of CNFs is concerned, pioneering works by Lobo et al. [33] and Baker and co-workers [34] were based on two different techniques, allowing the process to be monitored continuously: a microbalance reactor [33] and controlled-atmosphere electron microscopy [34]. The former technique allowed for detailed kinetic measurements, from which a mechanism was proposed that involved the detachment of metal particles from the support, carbon growing beneath these particles and pushing them away from the surface. Observations of Baker have clearly confirmed this mechanism. These early studies [33–36] mark three important steps after hydrocarbon decomposition

and hydrogen release: (1) carbon dissolution through metal particles; (2) diffusion inside the metal, even though surface diffusion cannot be ruled out; and (3) carbon atoms precipitation at the metal–support interface to form a CNF, resulting in ejection of the particle from the support (Figure 9.2). A detailed analysis of filament growth sequences has provided activation energies for filament growth that show excellent agreement with those for diffusion of carbon through the corresponding metals (Table 9.1) [13,37]. Recent studies have confirmed these results for both CNFs and MWCNTs [17,38,39], so that now it is generally considered that diffusion of carbon in the catalyst particles is the rate-determining step in the mechanism of the growth of filamentous carbon. For iron nanoparticles, the temperature at which the CVD is conducted is also important since phase transitions from may occur α -Fe to γ -Fe, thus modifying the kinetic regimes (see Table 9.1). It is also worth noting that in particular cases, a different rate-determining step could prevail. For example, in the case of acetylene decomposition on Ni, Co, and Fe (1010 K, particles of the same size), the rate of CNF growth is slower on Fe than on Ni and Co [40], although carbon diffusion in metallic Fe is two to three orders of magnitude larger than for Co or Ni (Table 9.1).

Further studies have permitted a better understanding of the mechanism of CNF nucleation and have proposed the involvement of metastable surface metal carbides in this step. Hoogenraad has used magnetic measurements to determine the presence of nonferromagnetic nickel carbide at the beginning of the growth process [41]. Alstrup [42] has proposed that during the growth process the more active and open Ni(110) and Ni(100) faces are exposed to the gaseous phase, whereas carbon precipitation occurs at the (111) face, leading to an epitaxial growth of graphite. Faceting of Ni nanoparticles could explain peculiar morphologies of CNFs; such a faceting, resulting from carburization [43], is shown clearly in Figure 9.1(a).

A model for CNF nucleation and growth on nickel catalysts has been proposed [25] and includes the following six steps:

1. CH_4 decomposes on the nickel catalyst to give C and H atoms; this decomposition occurs preferentially on certain faces.
2. H_2 desorbs, and carbon dissolves and reacts to form surface nickel carbide.
3. Metastable nickel carbide decomposes into metallic nickel and graphitic carbon that surrounds the nickel nanoparticles.
4. Metal particles are squeezed out because the pressure increases dramatically due to the formation of a graphite layer at the metal–support interface, and to the liquidlike behavior of the catalyst particles under these conditions.
5. As soon as the catalyst particles are pushed out, the freed surface is exposed again to the carbon source, and growth proceeds further via carbon dissolution and diffusion through or on the surface of the particle. It has been proposed that the surface structure of the metallic particles directly affects the kinetics of carbon decomposition and the morphology of the carbon deposit at this stage of the growth mechanism.

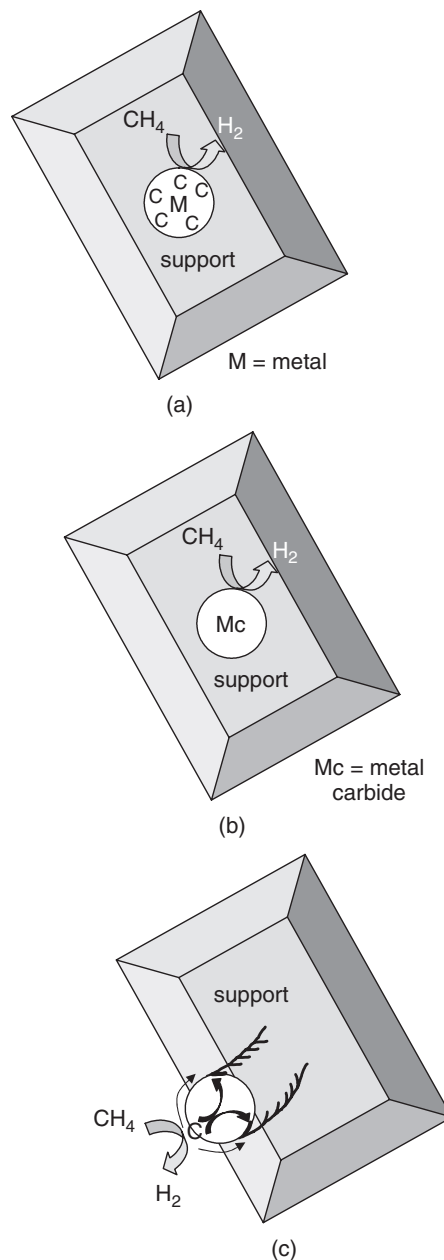


Figure 9.2 Three-step growth mechanism of CNFs: (a) carbon dissolution through metal particles; (b) carbon diffusion inside the metal; (c) carbon atom precipitation and ejection of the particle from the support.

Table 9.1 Physicochemical Properties of the Fe-Co-Ni Triad with Respect to CNT or CNF Growth

Property	Iron	Cobalt	Nickel
Melting point (K)	1809	1768	1726
Metal–carbon eutectic (K)	1427	1597	1601
Vapor pressure of saturation at 1489 K (Pa)	5.5×10^{-3}	4.7×10^{-3}	4×10^{-3}
Carbon solubility at melting point (at%)	20.2	13.9	10.7
Carbon diffusion coefficient D at 873 K (cm^2/s) and temperature dependence ^a	$1-8 \times 10^{-7}$ $D = 3.9 \times 10^{-3}$ $\exp(-80.3/RT)$	5.7×10^{-10} $D = 0.21$ $\exp(-147/RT)$	$2-8 \times 10^{-10}$ $D = 0.1$ $\exp(-138/RT)$
Activation energy for carbon diffusion (kJ/mol)	$142 (\gamma\text{-Fe})$ $67 (\alpha\text{-Fe})$	145	138–145
Metal–carbon bond enthalpy of formation (kJ/mol)	245.2	221.3	191.2
Metal–carbon work of adhesion (J/m^2)	$0.1 (\text{Fe–C})_{\text{solid}}$ $2.2^b (\text{Fe–C})_{\text{melt}}$	$2.1^c (\text{Co–C})_{\text{melt}}$	$0.1 (\text{Ni–C})_{\text{solid}}$ $1.8^d (\text{Ni–C})_{\text{melt}}$

^a $D = D_0 \exp(-E_a/RT)$, activation energy in kJ/mol.

^bFor Fe–C eutectics at 17 at% C.

^cFor Co–C eutectics at 12 at% C.

^dFor Ni–C eutectics at 10 at% C.

- Finally, a steady-state process occurs with either pulsed growth or smooth growth of the straight fiber.

The dissociative chemisorption and decomposition of the reactant gas is the first step in this complex reaction mechanism, and the crystallographic orientation of the metal particles could play a role in gas–solid interaction and metal–carbon bond formation (Table 9.1), thus controlling both catalytic activity and selectivity. The presence of faceted single-crystal particles in filaments formed on Ni, Co, or α -Fe by reaction with methane at 973 K has indeed been evidenced [44]. In general, such nickel particles are usually faceted and induce the formation of CNFs by epitaxial growth. Of course, variations in the chemical nature of the gaseous environment [e.g., the presence of H_2 or of the catalyst (bimetallic or promoted systems)] can exert a dramatic effect on the overall catalytic activity [13], and under given conditions the catalyst particles may undergo surface reconstruction toward unique geometrical shapes that drive CNF formation. If the catalyst does not consist of discrete particles but rather of a thin film, and if the carbon activity of the atmosphere is $a_C > 1$ (in equilibrium with graphite, $a_C = 1$), disintegration of the metal film into a dust of graphite and fine metal particles may occur. This phenomenon, called *metal dusting* in metallurgy, occurs in carburizing atmospheres mostly between 673 and 973 K and is at the origin of

iron and low-alloy steel degradation [45–47]. Metal dusting usually occurs when using syngas or hydrocarbons. The mechanism of metal dusting (Figure 9.3) has been studied for many years. In the case of Ni or Fe, it consists of (1) oversaturation ($a_C > 1$) of the metal by transfer of C atoms [Figure 9.3(a)]; (2) formation of surface carbides that prevent further C ingress [Figure 9.3(b)]; (3) graphite deposition on the cementite layer, at the interface $a_C = 1$ [Figure 9.3(c)]; (4) graphite precipitation $M_3C \rightarrow C + 3M$ onto the M_3C layer, the carbon atoms being incorporated in graphite and the metal atoms diffusing through graphite and agglomerating to nanoparticles [Figure 9.3(d)]; and (5) the catalytic activity

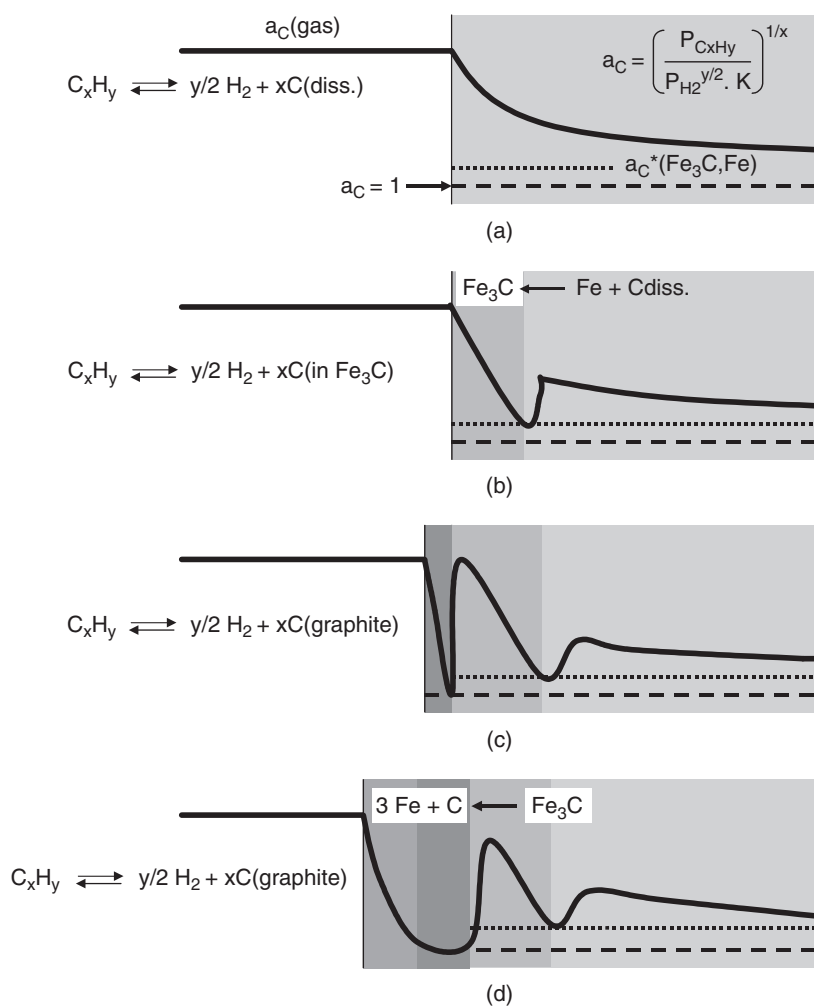


Figure 9.3 Mechanism of metal dusting: (a) oversaturation of the metal; (b) formation of surface carbides; (c) graphite deposition on the cementite layer; (d) graphite precipitation.

of these nanoparticles (< 20 nm) in further carbon deposition (e.g., CNFs or CNTs). This mechanism could explain the growth of CNTs or CNFs on metal films and, although a scale effect should also be taken into account, the production of CNTs of small diameter in the presence of large-diameter particles. If the activation energy of hydrocarbon decomposition on the metal is higher than the activation energy of carbon diffusion through the particle (Table 9.1), the relevant step becomes the rate-determining one.

As for the involvement of metastable metal carbides, several studies have shown by postreaction examination of the catalyst nanoparticles that carbides are indeed present. Yet the possibility of carbide formation during the cooling of the samples cannot be discarded. In the case of iron, several studies have shown the coexistence of iron carbides (Fe_3C , Fe_5C_2) and $\alpha\text{-Fe}$ and also $\gamma\text{-Fe}$ in particles observed after the MWCNT growth reaction [13,48–50]. Although high-purity cementite is not an active catalyst for MWCNT and CNF growth [51], the possible implication of carbides as intermediates in the formation of CNTs and CNFs is attractive. An important limitation in these mechanistic studies is the lack of in situ observations. Rodriguez et al. [52] have used in situ electron diffraction techniques to study the interaction of ethylene at temperatures above 750°C on Cu–Ni-alloyed particles; these particles gave high activities for CNF growth, but no bulk carbides were found during the course of the experiments. Moreover, for butadiene decomposition on iron it has been shown that the activation energy of carbide decomposition (197 kJ/mol) is significantly higher than the activation energy of carbon deposition (96 kJ/mol), the activation energy for carbide formation being equal to 88 kJ/mol [40]. Thus, it has been proposed that in the case of CNTs or CNFs, the carbide cycle mechanism of carbon formation [40] should involve the decomposition of carbidic carbon, defined as surface metal carbides of high activity if compared to bulk carbides, rather than the evolution of such species toward bulk carbides (Figure 9.4).

Depending on the operative conditions (i.e., temperature, carbon source, presence of hydrogen, etc.), the nature of the catalyst, and the metal particle size, one of these two reaction pathways would predominate, thus leading to the formation of different carbon materials. Decomposition of the surface metal carbide species would induce (1) the process of carbon enrichment of a metal particle

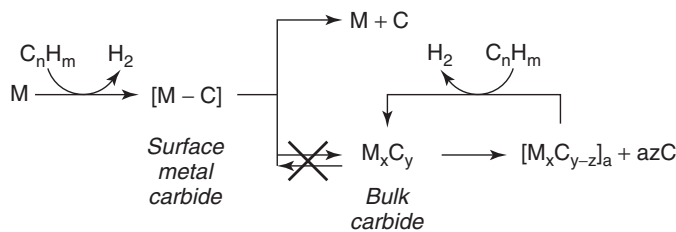


Figure 9.4 Carbide cycle mechanism of carbon formation.

in the solid or liquid state, according to its size; (2) the further formation of a metal–carbon solution at the liquid state, as the saturation of the metal with carbon causes a significant decrease in the melting point [53]; and (3) the precipitation of solid carbon after a high degree of metal particle saturation with carbon is reached. Thus, the analysis of carbon–metal binary-phase diagrams, which can give valuable information about carbon solubility in the solid solution and about the presence or absence of stable carbide phases, could be useful for the prediction of CNT growth mechanism [54].

Following surface metal carbide decomposition at one side of the catalyst particle, a diffusive process is responsible for the transfer of elemental carbon to the opposite side of the particle. This transfer may occur via surface or bulk diffusion, even though internal diffusion is generally assumed to be the dominant pathway in CNT growth [55]. The origin of the driving force for carbon diffusion through the catalyst particle was first presumed to be the temperature gradient [34] that exists between the sites where hydrocarbon decomposition takes place. In that case it was the exothermic acetylene decomposition process and the sites where carbon precipitates (endothermic process). However, hydrocarbons such as methane, whose decomposition is endothermic, also permit the growth of filamentous carbon. An alternative explanation could be the existence of an internal concentration gradient based on supersaturation of the metal phase as the origin of the internal diffusive flux. Indeed, carbon at the front and rear sides of the metal particle is in different states characterized by different chemical potentials. Decomposition of the unstable surface metal carbide species leads to supersaturation of carbon at the frontal regions of the particle, whereas a graphitic phase is formed at the rear sides. The concentrations of saturation of carbon at these sites are in fact different, which makes the gradient required for diffusion [40]. It is worth noting that for small particles, depending on the temperature of reaction and on the metal–carbon eutectic temperature, the catalyst particle responsible for CNT growth may be in the molten state. This is an important point since it would result in higher carbon solubility [56] and a different diffusion rate. For CNF growth on nickel, although the results of Baker et al. support an internal diffusion process, with a nice correlation between the CNF growth activation energy and carbon diffusion activation energy in polycrystalline Ni, recent results based on ab initio DFT calculations suggest that the transport of carbon atoms is mediated by surface or subsurface diffusion, whereas bulk diffusion in single Ni crystals is limited by a very high diffusion barrier [57,58]. These DFT results provide a consistent interpretation of atomic-resolved *in situ* HREM observations of CNF growth from methane on Ni single-crystal particles, on which was suggested an implication of surface Ni step edges in the growth mechanism of graphene layers [59]. It was thus proposed that the metal step edges act as active centers for graphene growth mainly because carbon binds more strongly to such sites than to sites at the close-packed facets on nickel.

As for the carbon diffusion process, the formation of carbon nuclei by carbon precipitation onto the surface of metal particles is a critical step, and the

stability of these nuclei is closely related to their size. Nuclei presenting a radius smaller than the critical value (r_{cr}) are unstable and are prompt to dissolve in the bulk of metal particles, whereas nuclei with radius larger than r_{cr} may continue to grow so that the radii of CNTs or CNFs will become larger than r_{cr} . These nuclei can be viewed as planar round-shaped particles consisting of a fragment of a graphene plane with the boundary carbon atoms chemically bound to the metal surface, the nucleus contacting the metal surface along the boundaries [60–62]. In situ observations have shown that both nucleus stabilization and nanotubes growth involve the dynamic reshaping/deformation of Ni catalyst particles, the latter being ultimately lifted off from the support [62]. A schematic two-dimensional representation of the carbon nucleus on the surface of the metal catalyst particle together with TEM images of carbon nuclei on Ni nanoparticles are shown on Figure 9.5. It has also been shown that the core of the Ni particle remains crystalline all along the carbon nucleus formation. The central moiety of the graphene fragment binds to the supersaturated metal by van der Waals forces [63], and carbon pentagons may exist at the nucleus edges to stabilize its distorted surface [63]. This step should be at the origin of the formation of curved sp^2 carbon. Theoretical calculations have shown that the graphitic network interacts more strongly with Co atoms than with iron atoms, and this difference may reflect the ability to act as a catalyst in the process of formation of SWCNTs [64].

This reaction proceeds via polymerization of C_2 units, leading to the formation of graphene layers by addition of C_n species ($n \geq 2$). A constant and regular feeding of elemental carbon is necessary for the growth of carbon nuclei [65], and it has been proposed that this carbon nucleation step on the metal determines the carbon deposit morphology on the surface [62]. A thermodynamic analysis of carbon nucleation, not taking into account the presence of the support, has shown that the reaction temperature, the degree of metal oversaturation with carbon, and the work of metal adhesion to the graphite surface (Table 9.1) all exert a very pronounced effect on r_{cr} . The effect of the critical size of the nucleus on the morphology of the graphitelike deposit has been discussed [62] and different scenarios of nucleus formation and growth have been proposed:

- When the critical size of the nucleus is large, $r_{\text{cr}} > 10$ to 20 nm, prolonged carbon layers would either encapsulate metal particles or lead to the formation of CNFs characterized by an important contact between metal particles and graphene planes (epitaxial growth in fishbone or Chinese-hat CNFs).
- The formation of small nuclei, $0.35 < r_{\text{cr}} < 1.5$ nm, would favor the formation of SWCNTs.
- When the critical size of the nucleus is intermediate between the limits above, the formation of more or less ordered concentric tubes (MWCNTs) is typical. The inner diameter of the MWCNTs cannot be smaller than the critical size of the carbon nucleus, whereas the external tube diameter usually corresponds to the catalyst particle diameter.

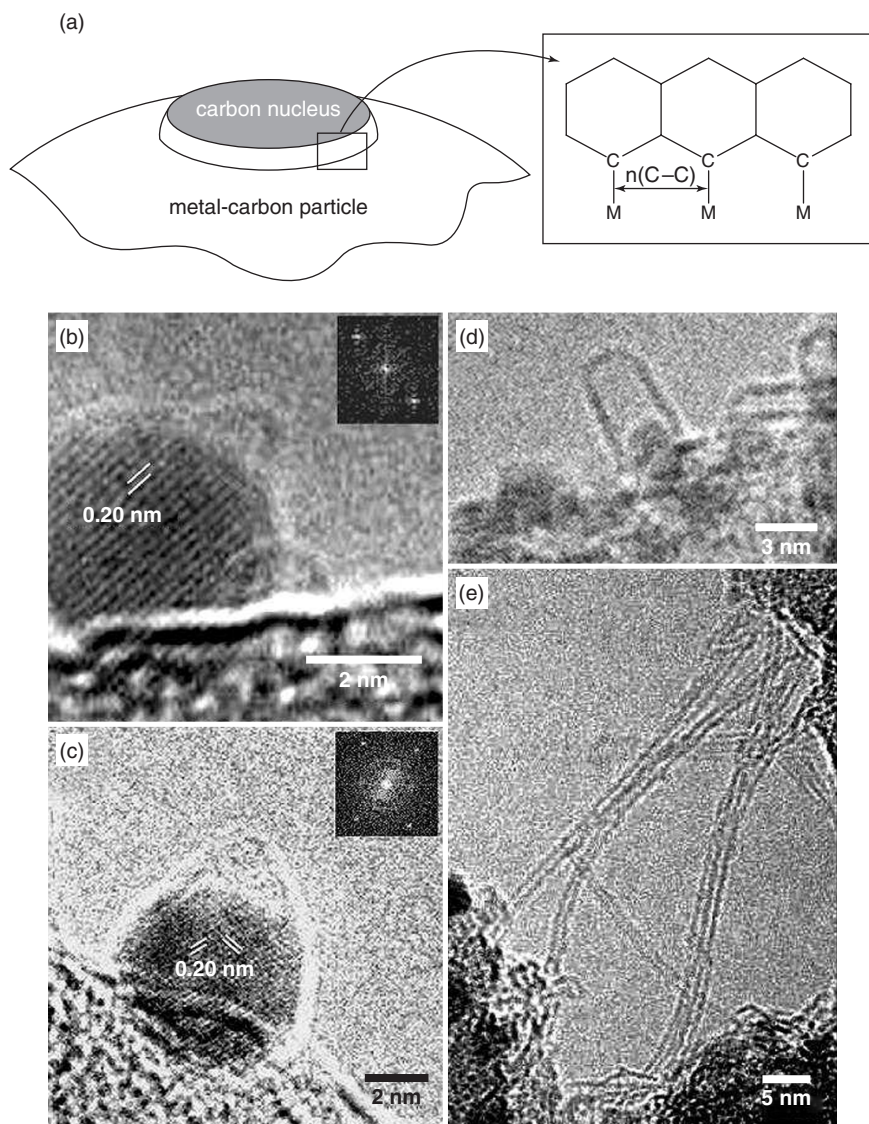


Figure 9.5 Carbon nucleus on the surface of the metal catalyst particle: (a) schematic two-dimensional representation; (b–e) TEM images. [(a) From ref. 60, with permission. Copyright © 2001 American Physical Society. (b–e) From ref. 62, with permission. Copyright © 2007 American Chemical Society.]

Another thermodynamic model, which does not take into account the presence of the support, has also been developed to describe the CNT growth from a droplet of supersaturated carbon melt in a metal catalyst, and the relevant calculations enable the construction of a phase diagram showing that the CNT type depends on the melt supersaturation with carbon and on the droplet radius [63]. SWCNTs appear at high supersaturation, and at low supersaturation the encapsulation of catalyst particles occurs, MWCNTs being formed in the intermediate region. Temperature is also a sensitive parameter determining the size of the nucleus, and an elegant model has been proposed to rationalize the morphology of the filamentous carbon so produced [66]. At low temperatures carbon nucleation is slow and carbon atoms precipitate onto the entire metal–support interface leading to CNFs, whereas at high temperatures the nucleation starts at the metal–support–gas phase before the entire metal–support interface has been covered by carbon atoms, and carbon nanotubes are produced.

Of course, the presence of a support that can stabilize the catalyst particles could have a direct influence on the mechanism of the reaction. Thus, if the metal–support interaction is not very strong and in any case weaker than the metal–carbon interaction, the particle, or a part of a particle if it is in the liquid state, would be released from the support and localized at the nanotube tip. Otherwise, the metal particle would remain anchored onto the support. Thus, one can speak of either a tip or a root-growth mechanism. It is worth mentioning that the presence of nanoparticles in the middle or at the tip of MWCNTs would also be due to a root-growth mechanism, since a part of the molten particle can be lifted off from the support and carried away into the nanotube cavity by capillary forces. Similarly, a particle in the middle of a MWCNT can originate from migration of part of the metal previously located at the tip particle, owing to capillary forces. Generally speaking, CNFs grow from discrete particles located at their tips when supported metal catalysts are used, or by a bi- or multidirectional mode from faceted particles when unsupported metal particles are used [25]. It is also generally accepted that the catalyst composition together with the interaction between the metal and the support are key factors controlling the formation of CNFs of desired structure (i.e., with desired orientation of the graphene layers with respect to the nanofiber axis). For CNTs, both tip and root growth can occur. Under ideal growth conditions, MWCNTs would contain graphene walls parallel to the tube axis and would be straight. In practice, the occurrence of defects (pentagons or heptagons) makes the nanotubes bend during the CVD process, and it is not rare to find the “extreme” case of the production of helical MWCNTs. A nonuniform extrusion of carbon from the particle could provide an explanation for these peculiar structures [67]. Another common digression from ideal growth arises from cyclic changes in carbon supersaturation, close to the value sufficient for the formation of the critical nucleus, which causes the presence of bamboo-shaped compartments with graphene layers perpendicular to the tube walls [68]. Real-time *in situ* TEM observations of bamboolike CNTs from Ni nanoparticles have shown that (1) the shape of the Ni particle changes constantly but remains metallic and crystalline during the growth process, and

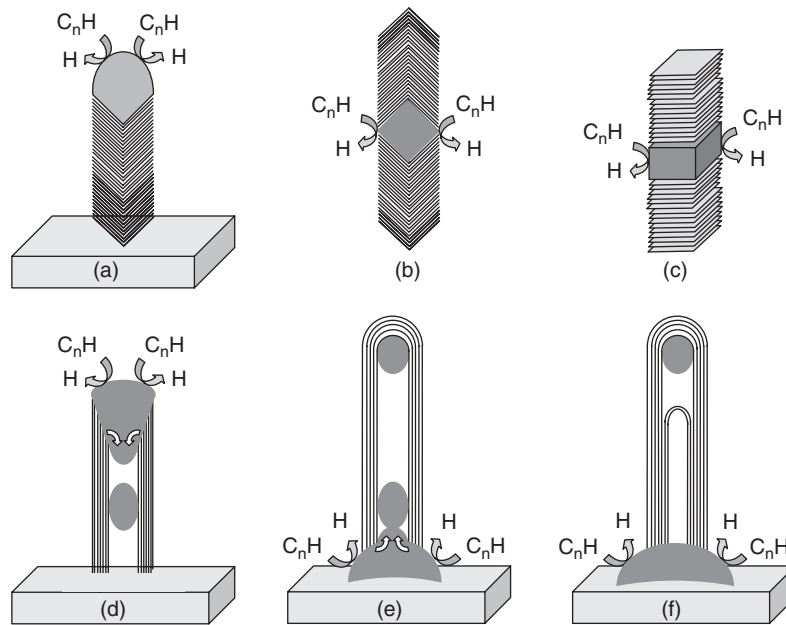


Figure 9.6 Schematic representation of alternative growth routes for CNFs and CNTs: (a) tip growth of fishbone-CNF; (b) bidirectional growth of fishbone-CNF; (c) bidirectional growth of platelet-CNF; (d) tip growth of MWCNT; (e) root growth of MWCNT; (f) formation of compartments in MWCNT from a root growth mechanism.

(2) graphene sheets (bamboo knots) within the nanotube preferentially nucleate on the multistep Ni–graphite edges at the point where the graphene joins the catalyst particle, where it is stabilized by both the graphene walls and the Ni catalyst surface [69]. Figure 9.6 shows a schematic representation of these alternative growth routes.

For SWCNTs the size of the catalyst particle is probably the most important parameter since most studies agree in establishing a correlation between catalyst nanoparticle size and SWCNT diameter. Optimal diameters lie in the range 1 to 5 nm, and at the high temperatures required for CVD growth of SWCNTs, usually between 1073 and 1173 K, the particles would probably be in the liquid state. In addition, a high carbon supply and a low partial pressure of hydrogen are two requirements to grow SWCNTs selectively [70]. Short reaction times are also desirable to avoid diffusion limitations of the carbon source into the SWCNT–catalyst composite materials. Indeed, it has been proposed that at the high temperatures required for this reaction, diffusion limitations from the carbon source to the pores of the catalyst grain would become so important as to make only the most accessible metal nanoparticles (i.e., those at the surface) active for the reaction [15]. Recent experimental and theoretical studies have suggested that

the growth of SWCNTs is initiated at the root of the metal nanoparticle [71,72], and a 12-step qualitative mechanism based on nonclassical effects has been proposed [65] which takes into account energetic and mass transfer phenomena. The first six steps are fast, involving energetic transformations, transitions, and transport. The slower subsequent six steps involve mass transport phenomena and transformations. All of these steps are reversible and cyclic and consist of (1) carbon atomization from a carbon-containing precursor; (2) expansion of the carbon atoms from the atomization site into the reactive carbon–metal solution; (3) hybridization of the carbon atoms present in the solution; (4) confinement of carbon in the reactive solution to avoid any catalyst poisoning; (5) cooling of the reactive solution; (6) energetic relaxation of the reactive solution; (7) carbon nuclei formation; (8) carbon nuclei growth; (9) CNT nucleation; (10) CNT growth; (11) metal nanoparticle formation and reconstruction; and (12) CNT growth termination.

The very last step in filamentous carbon growth has been much less studied than the nucleation itself and at present is still poorly understood. A proposed reason for catalyst deactivation consists of the reconstruction of the surface at the front side of the metal particle, on which hydrocarbon decomposition occurs during the process of carbon deposition [40] that causes particle encapsulation. Another possibility could stem from loss of active metal during the process, due to either (1) particle disintegration (dusting), (2) particle encapsulation inside the tube via capillarity forces, (3) formation of volatile metal carbonyls when CO is used as carbon source [73], or (4) metal sublimation in the case of small nanoparticles at high temperatures.

9.3 WHY CNTs OR CNFs CAN BE SUITABLE FOR USE IN CATALYSIS

The analysis of adsorption, electronic, mechanical, and thermal properties of CNTs and CNFs, with respect to catalytic requirements, is needed to evaluate their stability and to predict how the metallic particles could anchor to the support and how the reagents could interact with these metal-supported catalysts, and to understand what such novel carbon forms could bring to catalysis. The possibility of nanofilamentous carbon shaping and sizing to prevent handling problems is also discussed.

9.3.1 Structural Features and Electronic Properties

Ideally, a SWCNT is made of a single perfect graphene sheet rolled up into a cylinder and closed by two caps (semi-fullerenes). Considering that there are different ways to roll up a section of a two-dimensional graphene sheet, the structure of SWCNTs is characterized by a roll-up vector, also called a helicity vector [11 and Chapter 14]. The diameter of these structures can vary between 0.4 and 2.5 nm and the length between a few micrometers and several millimeters.

Due to the high surface energy of these one-dimensional carbon macromolecules, SWCNTs are commonly arranged in bundles [Figure 9.1(c)]. MWCNTs can be considered as concentric SWCNTs with increasing diameter and coaxially disposed. The number of walls can vary from two (double-wall nanotubes) to several tens, so that the external diameter can reach 100 nm. The concentric walls are regularly spaced by 0.34 nm, which is similar to the intergraphene distance evidenced in turbostratic graphite materials. It is worth noting that residual metallic particles coming from the production process can be found in the inner cavity of MWCNTs [see Figure 9.1(b)]. It is also important to stress the fact that in most of the MWCNTs grown by catalytic CVD, the internal cavity is rarely accessible, due to bamboo-shaped compartments with graphene layers perpendicular to the tube walls [Figure 9.6f], so that relatively few studies deal with the reactivity and confinement effect in the inner cavity of MWCNTs. As already stated, the main difference between CNTs and CNFs consists of the lack of a hollow cavity for the latter. There are three main types of CNFs, which differ in the disposition of the graphene layers: In ribbonlike CNFs (r-CNFs) the graphene layers are parallel to the growth axis, the platelet CNFs (p-CNFs) display graphene layers perpendicular to the growth axis, and herringbone or fishbone CNFs (f-CNFs) have layers stacked obliquely with respect to the growth axis [74]. The diameters of CNFs are generally higher than those presented by nanotubes and can easily reach 500 nm (Table 9.2). Precise control of the CNT and CNF length and/or the inner or outer diameter through appropriate production processes has not yet been achieved. Therefore, there is a problem of standardization for these materials. Finally, it is worth mentioning that it is possible to produce nitrogen-doped MWCNTs with a characteristic bamboolike structure, the introduction of nitrogen altering the physicochemical properties of the nitrogen-doped CNTs compared to conventional CNTs.

The most common characterization techniques for these materials (SWCNTs, MWCNTs, and CNFs) are electron microscopy (SEM and TEM), Raman spectroscopy, thermal analysis (TGA/DTG), and absorption spectroscopy (UV-vis-NIR and IR). A combination of these techniques is highly recommended to distinguish between these materials, to determine the quantity, quality, and properties of the nanotubes in the sample. Indeed, no single technique can give a complete description of a CNT sample. It is also needed to establish a standard for all characterization techniques. Raman spectroscopy is an extremely powerful tool for characterizing SWCNTs and can provide qualitative and quantitative information on their diameter, electronic structure, purity, crystallinity, chirality, and permit us to distinguish metallic and semiconducting. The G-line is a characteristic feature of the graphitic layers and corresponds to the tangential vibration of the carbon sp^2 atoms. The second characteristic mode (D-line) is a typical sign for defective graphitic structures due to finite particle size, curvature defects of the graphene, defects caused by pentagons or heptagons, usually at the closed ends, and graphitic or nanoparticulate-sized carbon material on or near the tubes. Similar to the D mode, D' is a double-resonance Raman feature induced by disorder and defects. Comparison of the ratios of the G and D peaks

Table 9.2 Characteristics of CNTs and CNFs

Property	SWCNTs	MWCNTs	CNFs
Diameter ^a (nm)	0.5–2 (1–1.5)	5–200 (10–40)	10–500 (50–100)
Length	Few μm up to 20 cm	Few to hundreds μm	Few to hundreds μm
d_{002} (Å)	—	3.39–3.48	3.36–3.44
Apparent density (g/cm ³)	0.5–1 (film)	0.02–0.3 ^b	0.3–1.4
S_{BET} (m ² /g)	400–900	150–450	10–250
Porosity (cm ³ /g)	Microporous V_{micro} : 0.15–0.3	Mesoporous V_{meso} : 0.5–2	Mesoporous V_{meso} : 0.2–2
Young's modulus (TPa)	1.05–1.3	0.5–1.2	0.3–0.7
Tensile strength (GPa)	45–150	3–30 to 150 ^c	3–12
Electrical resistivity ($\Omega \cdot \text{cm}$)	6×10^{-4}	0.6–2.10 ⁻⁴	1.5–3
Electrical conductivity (S/cm)	550	80–1000	300
Thermal conductivity ^d (W/K · m)	1000–6000 ^e	300–3000 ^b	800–2000

^aTypical values in parentheses.^bThe lower value is for a powder and the upper one is for short MWCNTs.^cDefect-free MWCNTs.^dAxial thermal conductivity at room temperature.^eFor a single rope of SWCNTs.

intensities gives a measure of the quality of the bulk samples. The position of these two bands may vary slightly from one sample to another and according to the excitation energy. Generally, the G-band is situated at 1587 cm⁻¹ and the D band at around 1300 cm⁻¹; for graphite, the first-order peaks are D, G, and D' at 1350, 1582, and 1615 cm⁻¹ (at 514 nm excitation), respectively [75]. In addition, there is a fourth mode, the radial breathing mode (RBM), where all the carbon atoms are moving in phase in the radial direction, which is very sensitive to the diameter of SWCNTs and DWCNTs. An additional option is the application of Raman microscopy for mapping analysis and depth profiling to view the intensity change in different directions of the sample. A controlled oxidation process (TGA) gives quantitative data on the weight fractions of carbon and metal catalyst in the sample and the temperatures of bulk oxidation events. However, it might be delicate to assign individual oxidation events to specific carbon species due to similar oxidation temperatures, metal-catalyzed oxidation, and exothermic effects. Because of their unique electronic structure, SWCNTs have discrete optical absorptions that do not occur in other graphitic nanocarbons, and UV-vis-NIR absorption spectroscopy can be very useful as a relative purity measurement. Infrared spectroscopy gives valuable information on surface functionalization of CNTs.

Exhaustive studies dealing with the electronic properties of CNTs are available in the literature [76,77]. For CNFs, while r-CNFs are often considered as conductive substrates that can exert electronic perturbations similar to those of graphite [78], few data are available for p- and f-CNFs, but due to the particular orientation of the graphene layers they are expected to be less conductive.

SWCNTs behave as pure quantum wires in which the electrons are confined along the tube axis. Electronic properties are governed primarily by two factors: the tube diameter and the helicity, which are defined according to the way in which the graphene layer is rolled up (armchair, zigzag, or chiral). In particular, armchair SWCNTs display a metal-like conductivity, and zigzag SWCNTs behave as semiconductors. The curvature of the graphene sheets induces strong modifications of the electronic properties; indeed, comparison to graphite shows modification of the π -electron cloud [79]. Rolling up the graphene sheet to form a tube causes rehybridization of carbon orbitals (nonplanar sp^2 configuration), thus leading to modification of the π density in the graphene sheet (Figure 9.7). It is also worth noting that the theoretically predicted electronic properties are often modified by the presence of defects such as pentagons, heptagons, vacancies, or impurities [80]. In addition, production techniques do not currently allow the selective production of only one type of SCWNT, and the final purity of the material obtained after purification steps is often far from satisfactory.

Studies on MWCNT electronic properties have shown that they behave like an ultimate carbon fiber [77]: at high temperature their electrical conductivity can be described by the semiclassical models already used for graphite, while at low temperature they reveal two-dimensional quantum transport features. A reliable prediction of their electronic properties is even more difficult than in the case of SWCNTs, due to the higher complexity of their structure, and experimental measurements on MWCNT resistivity have not given reliable values (Table 9.2), due to different CNT purities and measuring conditions.

In catalysis, the electrical conductivity of CNTs (Table 9.2) as well as the curvature of the surface of these materials and the presence of an inner cavity are expected to affect the metal–support interaction in a different manner if

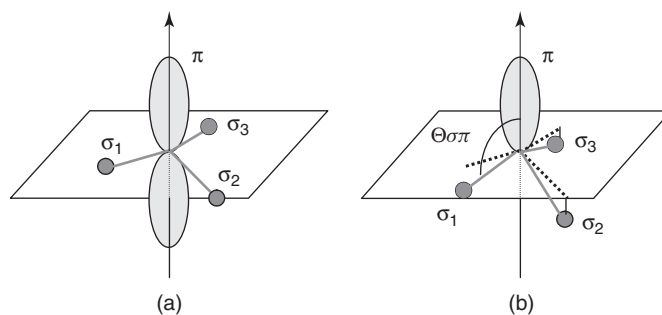


Figure 9.7 Carbon hybridization in (a) graphene and (b) CNT.

compared to activated carbon and graphite. Thus, a theoretical study has showed that the binding sites are related to the support structure: Studies conducted on nickel show that the nature of the most stable anchoring sites varies sensibly passing from graphite to SWCNTs, due to the different curvature of the surfaces where the active species are deposited [81]. Moreover, it has been demonstrated that mechanically bent SWCNTs present kink sites that are chemically more reactive than the others [82]. Such local chemical reactivity can also be present in open-tip CNTs, and stable tip structures can be obtained by putting in contact transition metals with the open ends of SWCNTs [83]. The curvature also affects significantly the values of magnetic moments on the nickel atoms on the nanotube wall, and the charge transfer direction between nickel and carbon can be inverted. Charge transfer, resulting in SWCNT holes doping, has also been evidenced during the room-temperature spontaneous reduction, or galvanic displacement, of gold(III) and platinum(II) ions on the surface of SWCNTs [84]. The metal nanoparticles size depends strongly on metal–CNT/CNF interaction, with stronger interactions giving rise to smaller nanoparticles. Due to their peculiar morphology, p-CNFs and f-CNFs allow for the best dispersions. Of course, strong variations in the interaction energies will be observed according to the metal used. Although strong interactions have been measured for palladium and platinum, such interactions are weaker for gold [85]. The shape of the nanoparticles also depends on these interactions, and it has been proposed that metal nanoparticles grown on CNT surfaces may undergo a bending deformation along the transverse direction to the CNTs because of the nanoparticle–CNT interaction and of the large curvature of small-diameter CNTs [86]. Finally, the presence of relatively well-defined and nanometric inner hollow cavities can also induce differences of reactivity between the convex (external) and concave (internal) surfaces. Thus, it has been proven experimentally that hematite nanoparticles located inside the MWCNT pores are more easily reduced (873 K) by the support than those on the outer surface (1073 K) [87].

9.3.2 Adsorption Properties

The interaction of carbon nanotubes with their environment, and in particular with gases or liquids adsorbed either on their internal or external surfaces, is attracting increasing attention due to the possible influence of such adsorption on the CNT electronic properties (application to chemical sensors) and to the possibility of using these materials for efficient gas storage or for gas separation [11].

Studies concerning nitrogen adsorption on CNTs [88–90] have highlighted the porous nature of these materials. In MWCNTs, pores can be divided mainly into inner hollow cavities of small diameter (narrowly distributed, mainly 3 to 10 nm), external walls, and aggregated pores (widely distributed, 20 to 100 nm) formed by interaction of isolated MWCNTs, the latter being much more important for adsorption issues. Although adsorption among the graphenes (intercalation) has been proposed in the case of hydrogen adsorption in MWCNTs or p-CNFs, it is unlikely that many molecules can do the same, owing to steric effects, on

too-long diffusion paths. Thus, MWCNTs are essentially a mesoporous material that also presents some macroporosity (pores above 50 nm). Chemical activation such as treatments with KOH or NaOH can efficiently give rise to microporosity; indeed, surface areas as high as $1050\text{ m}^2/\text{g}$ have been reported [91]. An efficient one-step treatment based on the solid–solid reaction between NaOH and CNTs has been reported to purify and open MWCNTs simultaneously [92]. Thus, it appears that opening or cutting, and chemical treatments on carbon nanotubes, can considerably affect their surface area and pore structure. CNFs share this behavior with MWCNTs except for the presence of narrower pores due to the presence of inner cavities in MWCNTs. For SWCNTs, N_2 adsorption has clearly evidenced the microporous nature of these materials. Adsorption of gases into a SWCNT bundle can occur inside the tubes, in the interstitial triangular channels among the tubes, on the outer surface of the bundle, or in a groove formed at the contact between adjacent tubes on the outside of the bundle. Most experiments show that the specific surface area of SWCNTs is often larger than that of MWCNTs or CNFs (Table 9.2). Typically, the total surface area of as-grown SWCNTs range from 400 to $900\text{ m}^2/\text{g}$ (mesopore volume, 0.15 to $0.3\text{ cm}^3/\text{g}$), whereas for as-produced MWCNTs, values varying between 150 and $300\text{ m}^2/\text{g}$ are often reported. For CNFs, the surface area can range from 10 to $250\text{ m}^2/\text{g}$, and the mesopore volume varies between 0.5 and $2\text{ cm}^3/\text{g}$ [13].

Model studies have pointed out that the convex surface of CNTs is more reactive than the concave one and that this difference in reactivity increases when the tube diameter decreases [93]. Compared to the highly bent fullerenes, CNTs are only moderately curved and hence are expected to be much less reactive toward dissociative chemisorption. Dissociation of molecules on graphite edge sites, which constitute the major part of the CNF surface and are present at the tip of open-ended CNTs, can indeed occur. Models have also predicted an enhanced reactivity at the kink sites of bent CNTs [94]. In addition, it is worth noting that unavoidable imperfections such as vacancies, Stone–Wales defects, pentagons, heptagons, and dopants are believed to play a key role in tailoring the adsorption properties [95]. The trends observed in the binding energies of gases with different van der Waals radii suggest that the groove sites of SWCNTs are the preferred low coverage adsorption sites, owing to their high binding energies. Furthermore, several studies have shown that at low coverage, the binding energy of the adsorbate on SWCNTs is between 25% and 75% higher than the monolayer binding energy on graphite. The changes observed in binding energy can be related to an increase in the coordination possibilities in binding sites, such as the groove sites in SWCNT bundles [96,97]. For CNFs ($25\text{ m}^2/\text{g}$) and CNTs ($186\text{ m}^2/\text{g}$) it has been shown that the adsorption capacity toward volatile organic compounds is significantly lower than for high-surface-area graphite (100 to $300\text{ m}^2/\text{g}$), the enthalpy of adsorption following the same trend [98].

In summary, it appears that carbon nanotubes present peculiar adsorption properties if compared to graphite or to activated carbon, due mainly to their peculiar

morphology. The role of defects, of the opening and closing of the tubes, of chemical purification, or of the presence of impurities as catalyst particles that can govern the adsorption properties have not yet been examined in detail.

9.3.3 Mechanical and Thermal Properties

CNTs are unique materials because of the particularly strong bonds in the curved graphene sheet that are stronger than in diamond as revealed by the difference in C–C bond length (0.142 and 0.154 nm for graphene and diamond, respectively). This makes CNTs particularly stable toward deformation with a Young's modulus on the order of terapascal [99] and a resistance to traction of 250 GPa [100]. Defective MWCNTs obtained from chemical vapor deposition (CVD) provided a measured range of 3 to 30 GPa [101]. As for their flexural modulus, MWCNTs would exhibit higher values than SWCNTs [102], with flexibility decreasing when the number of walls increases. Concerning CNFs, most authors claim that they present low mechanical strength due to the peculiar arrangement of the graphene layers [103].

Another important feature that ought to be taken into account is the thermal stability under real reaction conditions and the thermal conductivity of these materials. The most common and simplest method to study the resistance of a carbonaceous material toward heating in air is by thermogravimetric analysis (TGA). CNTs or CNFs are more stable than activated carbon (AC) toward oxidation but more reactive than graphite. However, the concentration of surface defects and the presence of residual metal on or inside the nanotubes, which can catalyze carbon gasification, could lower the temperature at which the maximum gasification rate is observed. This makes an objective comparison of these materials difficult. It is generally accepted, however, that amorphous carbon burns first, followed by SWCNTs, and then by MWCNTs, even if TGA is unfortunately not able to separate the different oxidation steps clearly in most cases. High resistance toward air oxidation is often reported for CNFs [98,104] and should be related to the purity of the material.

Finally, thermal control of nanocatalysts becomes increasingly important as the size of the system diminishes. Therefore, for exothermic reactions the thermal conductivity of CNTs or CNFs should play a critical role in controlling the performance of the catalyst. Despite the importance of thermal management, there has been little progress, due mainly to technical difficulties, in measuring the thermal conductivity of individual CNTs. The thermal conductivities of graphite measured along the basal plane range from 940 to 2000 W/K·m, and those perpendicular to the basal plane are two or three orders of magnitude lower. For CNTs, similar behavior is very likely to be observed for their axial and transverse conductivities. Although experimental data and theoretical predictions are scattered by one order of magnitude (Table 9.2), probably depending on CNT type and size, most studies on CNT thermal conductivity agree that values are very high, comparable to those of diamond and to in-plane graphite sheets and that the thermal conductivity is significantly improved for CNT–polymer composites. Although the CNTs present

in catalyst pellets exhibit defects and are aggregated, so that the thermal conductivity of these densely packed CNTs decreases significantly compared to that of single tubes, it is still much higher than that of other supports used in catalysis, and this property should be taken into account when exploring specific catalytic reactions.

9.3.4 Macroscopic Shaping of CNTs and CNFs

Pure CNTs or CNFs can be obtained after postsynthesis purification steps such as removal of the catalyst and of undesired carbon forms. At this stage, one can speak of a “fluffy powder” with low bulk density and low mechanical strength, and so far, CNTs and CNFs have found applications as catalyst supports in the form of powders. Scanning electron micrographs of purified MWCNT powders are shown in Figure 9.8. The use of such powders unfortunately gives some problems linked to their hazardous handling and large-scale use, especially in fixed- or fluidized-bed catalytic reactors. In addition, their low density results in a low catalyst mass/reactor volume ratio and in a difficult fluidization process, and the small size of the aggregates can cause an uncontrolled pressure drop along the catalyst beds. For slurry-phase operation, filtration problems might also be encountered if the granulometry of the powder is not convenient. Different approaches have been employed in order to solve these problems. The first consists of the pelletization of CNTs or CNFs [105], and rigid porous CNT granules have been produced by direct extrusion of functionalized CNTs or by extrusion with addition of a binder. CNT powders and extrudates present similar specific surface area and mesoporous volume. CNT aerogels with significant mechanical strength but reduced conductivity have been produced from CNTs–surfactant–poly(vinyl alcohol) mixtures [106]. The second approach consists of preparing aggregates with controlled particle sizes (0.6 to 0.8 mm), high bulk density (0.5 to 0.9 g/cm³), and high mechanical strength (crushing strength 1.25 MPa) from supported catalysts [103,107,108]. This preparation has been made successfully using highly active high-loading Ni/SiO₂ catalysts, mostly for CNF growth. The macroscopic particles so obtained consist of submillimetric granules characterized by dense CNF networks. At the end of the CVD growth process, the granules can be purified by removal of the Ni/SiO₂ catalyst [108]. The use of structured supports for the growth of CNTs or CNFs has also been explored to prepare structured and resistant catalyst supports [109]. Graphite felt [110–112], carbon cloth [110,113], carbon fiber fabrics [114], woven glass [115] or silica microfibers [116], Ni foams [117–119], and cordierite monoliths wash-coated with alumina [120,121] have been used to prepare CNT- or CNF-containing composites (Figure 9.9). On graphite felts, a high-surface-area (200 m²/g) mesoporous (0.4 cm³/g) composite with good mechanical strength and an apparent density of 0.4 g/cm³ has been prepared [111]. Interestingly, self-supported MWCNT macroscopic objects have been produced by confinement synthesis [122]. Finally, CNT buckypapers, which consist of self-supporting entangled assemblies of CNTs, can be

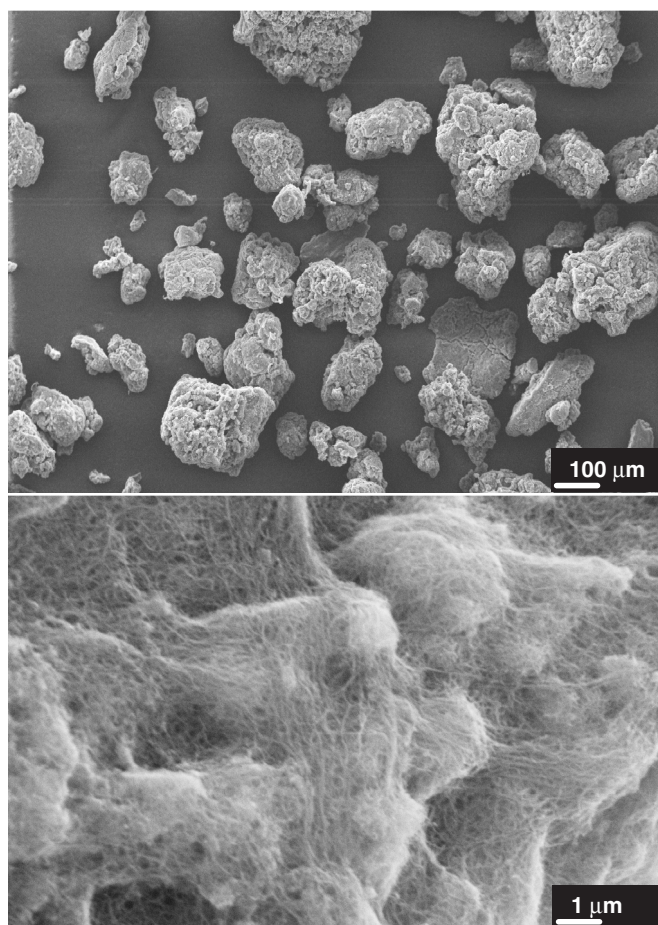


Figure 9.8 SEM micrographs of purified MWCNT powders.

prepared by careful filtration and drying of CNT suspensions [123]. This material presents interesting mechanical properties, thermal conductivity, and gas permeability [123].

To conclude, it appears that the aforementioned properties and the possibility of macroscopic shaping make CNTs and CNFs attractive competitive catalyst supports when compared with activated carbons. Indeed, resistance to abrasion, thermal and dimensional stabilities, and specific adsorption properties are important factors controlling the final activity and reproducibility of the catalytic system. In particular, CNTs and CNFs could replace activated carbons in liquid-phase reactions since the properties of the latter cannot be easily controlled, and since their microporosity has often slowed down catalyst development.

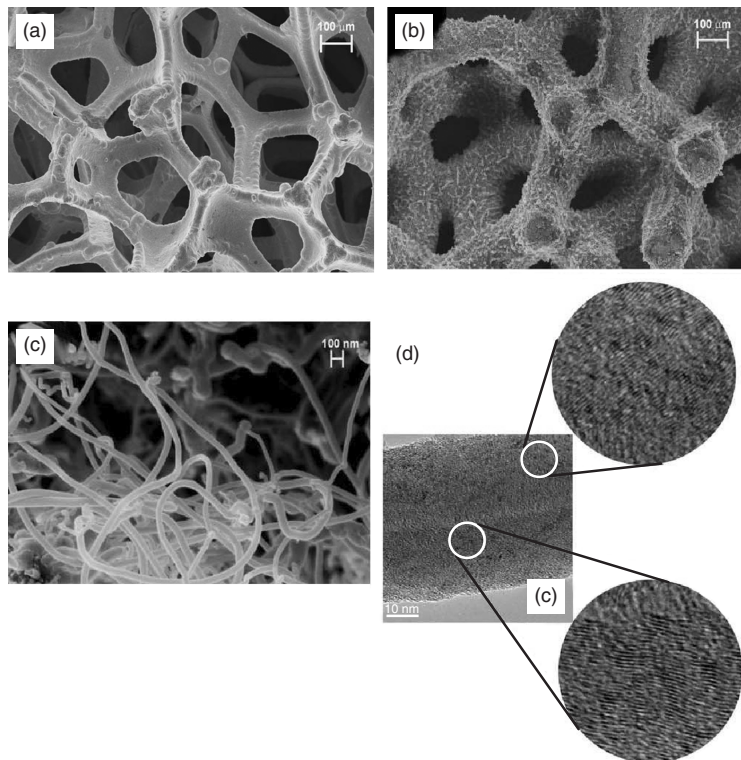


Figure 9.9 SEM micrographs of (a) as-received Ni foam, (b) CNFs–Ni foam loaded with 25 wt% CNF synthesized at 723 K (c) SEM details of the CNF layer, and (d) HREM of a single fiber (scale bar 10 nm). (From ref. 117, with permission. Copyright © 2005 Royal Society of Chemistry.)

9.4 PREPARATION OF SUPPORTED CATALYSTS ON CNTs AND CNFs

As particles supported on nanocarbons could find applications other than in catalysis, a plethora of materials have been deposited on CNTs or CNFs, and many methods have been developed to attain such deposition. Although not exhaustive, Figure 9.10 lists the elements that have been deposited on CNTs or CNFs. Due to possible application in catalysis for the fine chemical industry [124], the deposition of precious metals such as Pd and Pt has been extensively studied. In addition, the potential of CNTs and CNFs as supports for fuel cell electrocatalysts [125] is the reason for the increasing amount of research on Pt and Pt–Ru systems. Besides mono-, bi-, or trimetallic particles, oxides (TiO_2 [126], SiO_2 [127], CeO_2 [128], MgO [129], ZrO_2 [130], ZnO [131], SnO_2 [132], Al_2O_3 [133], MnO_2 [134], Cu_2O [135]), semimetals (Sn [136]), nitrides (Fe_2N , TiN

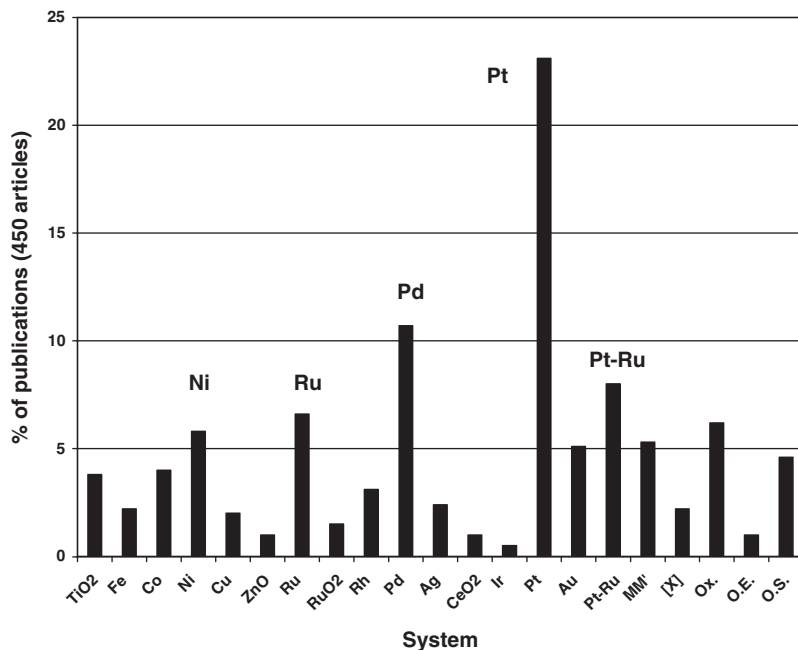


Figure 9.10 Elements that have been deposited on CNTs or CNFs. MM'; bimetallic systems; [x] molecular complexes; Ox., oxides; O.E., other elements; O.S., other systems.

[137]), phosphides (NiP [138]), sulfides (MoS₂ [139], Cu₂S [140], ZnS [141], CdS [142]), selenides and tellurides (CdSe [143], CdTe [144]), and hydrides (MgH₂ [145], NaAlH₄ [146]) have been deposited on CNTs or CNFs.

From a general point of view, both experimental and theoretical results conclude that to attain a high dispersion of the metallic phase, surface activation or functionalization (meaning the creation of active groups on the surface of CNTs or CNFs) is essential. Indeed, as-produced CNTs do not possess a large quantity of functional groups on their surface, and only surface defects such as vacancies, dangling bonds at open ends, Stone–Wales defects, and rehybridization defects can be considered as anchoring sites for metals [147]. The result is poor dispersion of the metallic phase and the impossibility of reaching high metal loadings [26]. The broad spectrum of CNT and CNF applications has permitted the development of reliable methods for their chemical and electrochemical functionalization [148], and today, chemical reactions on these materials receive increasing attention. Without going into detail, the most common methods used for metal particle anchoring are acid oxidation [149], gas-phase (air [149] or CO₂ [150]) oxidation, oxidation by common oxidizing agents (hydrogen peroxide [149], permanganate [151], osmium tetroxide [152], ozone [153]), the use of polymeric additives [154], and physical methods such as ball-milling [155,156].

or sonication [157]. Besides introducing anchoring sites for particles, these treatments can also modify the behavior of CNTs and CNFs toward wetting, and the capability of the precursor to get reduced on the support. Thus, HNO_3 -oxidized CNTs become hydrophilic, whereas untreated CNTs are hydrophobic. This is important for their use as supports in liquid-phase reactions since it is possible to design them so as to obtain a support with optimal wetting properties according to the reaction medium employed. Worthy of further note is the fact that the presence of oxygenated groups could inhibit the easy reduction of the metal on the support. In summary, the CNT or CNF surface chemistry and structural features depend strongly on the treatment chosen.

The HNO_3 or $\text{HNO}_3/\text{H}_2\text{SO}_4$ treatments are the most widely used for nanoparticle anchoring, and it has been shown that surface oxygen functionalities, mostly carboxylic and anhydride carboxylic groups, are introduced at defect sites on the outer and possibly inner walls of CNTs or CNFs [149,158–160]. In refluxing acids, the oxidation proceeds via carbonyl and other oxide groups to carboxylic or anhydride groups. The $\text{HNO}_3/\text{H}_2\text{SO}_4$ treatment creates the higher density of carboxylic groups on the surface [149,161]. A concentration of 1 to 1.4 oxygen-containing surface groups per square nanometer has been measured by chemical titration in the case of oxidized CNFs [103]. A prolonged reflux induces the opening of MWCNT tips, damages the walls, and slightly increases the specific surface area. For SWCNTs, careful and slow oxidation in diluted nitric acid is needed to create surface oxygenated groups, mostly carboxylic acid functions, and to minimize bulk damage to the material. X-ray photoelectron spectroscopy (XPS) analyses have demonstrated that H_2SO_4 treatment can lead to the formation of sulfur-containing species on the surface of MWCNTs [162] and SWCNTs [163,164]. The sonication of mixtures of MWCNTs in $\text{HNO}_3/\text{H}_2\text{SO}_4$ at 333 K permits a homogeneous treatment of the material with 6% atomic oxygen on the surface [157]. In this case, carbonyl, ester, and phenol groups have been detected by infrared spectroscopy, with only few carboxylic groups [165]. A prolonged sonication can lead to fragmentation of the tubes and cause mechanical damage to their surface. Yet the introduction of a large number of functionalities can significantly reduce the mechanical and electronic properties of CNTs, and an alternative method to strong acid treatments employs nitrogen-doped CNTs that present substitutional and pyridinic nitrogen sites [166]. Interestingly, $-\text{SO}_3\text{H}$ sulfonic groups, which can be of interest for proton conduction in fuel cell electrocatalysts, have been introduced on a CNT surface by treatment in fuming sulfuric acid [167]. Depending on CNT quality, these drastic liquid-phase oxidation treatments can generate contaminating debris, which can be removed by CO_2 oxidation [168] or base treatment [169]. The latter treatment, if performed with NaOH , will introduce sodium carboxylate or alcoolate functionalities.

Besides the classical nitric acid treatments, other oxidative agents have been used to prepare functionalized CNTs. Rao et al. [170] have compared the effects of concentrated nitric acid, aqua regia, $\text{HF}-\text{BF}_3$, aqueous OsO_4 , and KMnO_4 (acid/alkali) solutions on MWCNT structures [170]. Indeed, all these oxidants

open the nanotubes, but the essential structural features are still present at the end of the treatment. The advantage of HF–BF₃ superacid and OsO₄ is that reactions can be conducted at room temperature. In the case of osmylation, theoretical calculations have predicted the formation of osmate ester adducts via complexation on the CNT walls via a base-catalyzed cyclo-addition reaction [171]. The concentration of the surface acid groups after 24 hours of treatment under reflux has been measured to be 2.5×10^{20} sites per gram of MWCNTs for HNO₃, 6.7×10^{20} for H₂SO₄, 7.6×10^{20} for aqua regia, and 8 to 10×10^{20} for KMnO₄ (acid/alkali) solution. The localized etching of a CNT surface by iron-catalyzed steam gasification is an effective way to increase the surface roughness and the number of surface defect [172].

Among the different methods proposed to cut nanotubes, ball-milling [155,173,174] is the most popular. The ball-milling treatment allows segmentation of CNTs to shorter tubes, obeying a second-order exponential length-decrease rule [174]. Segmented CNTs present typical length distributions ranging between 200 and 800 nm. Detailed HREM observations on segmented CNTs and on their tips have shown a high percentage of carbon nanotubes that have partially or completely collapsed openings [173]. These results point to the limitations of this method to produce small-diameter, open-ended CNTs.

Several chemical methods, such as incipient wetness impregnation (IWI), ion exchange, chemical vapor deposition, organometallic grafting, impregnation with colloidal solutions, and deposition precipitation, but also electrochemical techniques, have been used to prepare CNT- or CNF-supported catalysts (see Table 9.3) [175,176]. By observation of the dispersion of the metallic phase on these supports, better results are obtained using f-CNF, followed by MWCNTs and then SWCNTs. This order is due on one side to the peculiar orientation of the graphene layers in CNFs, which provide many potential sites for metal anchoring, and on the other to the difficulty in getting a good dispersion of SWCNTs in the medium, since they tend to be arranged in bundles. In Table 9.3 one can see that high dispersions are often obtained with Ru and Pt, whereas Ni, Co, and to a lesser extent Pd give rise to larger particles, pointing to differences in metal–support interactions.

Incipient-wetness impregnation methods involve impregnation of the oxidized CNTs or CNFs with the solution of a metal salt or organometallic complex, followed by drying and reduction to give metal particles bonded to the carbon functionalized surface. The reduction is carried out by either H₂ or sodium borohydride. This method is the most commonly employed, owing to its simplicity, cost, and ease of scaling-up. Generally speaking, this method leads to well-dispersed catalysts and enables high loadings. The use of organometallic precursors is preferred when very small particle sizes are needed [177], and the use of supercritical CO₂ provides a green alternative to organic solvents [178]. When high dispersions and high loadings are targeted, deposition by precipitation or the use of colloidal solutions are often more effective [179]. As for the latter approach, different strategies have been adopted to stabilize the nanoparticles: (1) specific CNT surface functionalization such as creation of thiol groups improves

Table 9.3 Representative Examples of Metals or Oxides Supported on CNFs or CNFs

System	Preparation Method	S_{BET}^a (m ² /g)	Loading (%w/w)	Mean Particle Size (nm)	Ref.
RuO ₂ /f-CNF	Impregnation on oxidized f-CNFs	184	9	1.35	188
Ru/CNF	Homogeneous deposition precipitation on oxidized CNFs	(177) (140)	5 4	~2	189
	Impregnation on oxidized CNFs	157 (192)	5	2.9	190
Ru/MWCNT	IWI	170 (224)	4.8	1.6	191
	IWI on oxidized MWCNTs	170 (224)	4.8	4.2	192
Pd/CNF	Impregnation on oxidized CNFs	(100)	10	3–5	193
	Impregnation on oxidized CNFs	74	8	13	194
Pd/MWCNT	Impregnation on oxidized CNTs	—	20	3–5	195
Pd/SWCNT	Colloidal Pd solution on functionalized SWCNTs	—	5.7	5	196
PdPt/MWCNT	Wet impregnation	126 (140)	0.8Pt–0.7Pd	7.8	197
Pt/MWCNT	Impregnation	87	2	6	198
	Impregnation on oxidized MWCNTs	(400)	3	<2	199
Pt/f-CNF	Homogeneous deposition precipitation on oxidized CNFs	(177)	3.6	~1.5	200
	Impregnation	180	4	2.5	201
Pt/SWCNT	Colloidal Pt solution on functionalized SWCNTs	—	30	2–3	202
PtRu/MWCNT	Impregnation on oxidized MWCNTs	—	25Pt–25Ru	~3	203
	IWI on oxidized p-CNFs	(100)	25Pt–25Ru	2–3	204
Ni/p-CNF	Deposition precipitation on oxidized f-CNFs	(120)	5	6.4	205
Ni/f-CNF	Sol-gel	(150)	20	8	206
TiO ₂ /MWCNT	CVD on oxidized MWCNTs	124 (170)	90	7.7	207
Co/MWCNT	Deposition precipitation on oxidized CNFs	(140)	5.8	7	208
Co/CNF	IWI on oxidized CNFs	(180)	15	8	209
	Impregnation on oxidized CNFs	(161)	13	~8	210
Rh/MWCNT	Impregnation on oxidized MWCNTs	138 (137)	5	3–4	211
	Impregnation from organometallic on oxidized MWCNTs	140 (180)	1	5–10	212
Rh/f-CNF	IWI on oxidized f-CNFs	(200)	1	2–3	213
		212 (215)	4	19	214

^aValues in parentheses are the S_{BET} 's of the supports.

nano particle anchoring [180]; (2) the use of surfactants stabilizes the colloids and permits high dispersions and high loadings [181]; and (3) the use of polymer additives improves CNT dispersibility [182].

Chemical vapor deposition is a recognized method for the preparation of well-dispersed catalysts [183], and it has been explored for CNT- and CNF-based catalyst preparation [184–186]. However, this method has two important limitations: (1) if it is conducted by two successive steps, it only affords low loadings [184,185]; and (2) it is difficult to scale-up since deposition must be carried out in a fluidized bed, and CNTs and CNFs are difficult to fluidize without external activation such as vibration.

Electrodeposition is a process by which metal particles are produced by the reduction of a metal salt solution at a cathode. The electrodeposition method has limitations due to difficulties in controlling the metal loading because of the concurrent reduction of protons and in reaching small particle sizes [125,187].

Supported homogeneous catalysts have been prepared by surface organometallic grafting of various compounds. Two approaches can be adopted: (1) the surface reaction between a complex and the functionalized CNT/CNF surface, which is the most common method; or (2) the synthesis of a complex between a metal salt and modified CNTs/CNFs as the ligand. The first approach has been adopted to anchor different species onto CNTs or CNFs, such as $[\text{IrCl}(\text{CO})(\text{PPh}_3)_2]$ [215], $[\text{RhCl}(\text{PPh}_3)_3]$ [216], $[\text{HRh}(\text{CO})(\text{PPh}_3)_3]$ [217], $[\text{Rh}(\text{COD})(\text{NH}_2(\text{CH}_2)_2\text{NH}(\text{CH}_2)_3\text{Si}(\text{OCH}_3)_3)]$ [218], an octaaminobisphthalocyanine erbium complex $[\text{OAErPc}_2]$ [219], $[\text{Ru}=\text{CHPh}(\text{Cl})_2(\text{Pcy}_3)_2]$ [220], $[\text{ruthenium}(4,4'\text{-dicarboxy}-2,2'\text{-bipyridine})(2,2'\text{-bipyridyl})_2](\text{PF}_6)_2$ [221], a vanadyl salen complex [222], zirconium-based metallocenes [223–225], and nickel metallacboranes [226]. Grafting of the metal complex may occur via oxidative addition of a $-\text{OH}$ or $-\text{COOH}$ group [215], with η^2 coordination by the $\text{C}=\text{C}$ bonds of the CNTs [215] or via surface reaction between a group on the functionalized CNT surface (amino group or thiol) and a ligand present on the metal complex [219,221,222,226]. In the latter case there is no direct bond between the metal and the CNT surface. The functionalization of CNTs or CNFs with transition-metal complexes may also be of help to improve their solubility [216]. The second approach was used to attain the immobilization of a rhodium complex on $\text{HNO}_3/\text{H}_2\text{SO}_4$ -treated f-CNF [227–231]. The coordination chemistry of CNTs is still in its infancy, and additional studies must be conducted for the in-depth characterization of the grafted moieties. Prior theoretical works studying the interaction of CNTs with transition metal complexes have appeared for $[\text{IrBr}(\text{CO})(\text{PPh}_3)_2]$ [228], $[\text{M}(\eta^5\text{-C}_5\text{H}_5)_2]$ ($\text{M} = \text{Fe}, \text{Co}$) [229], and $[\text{M}(\text{C}_{16}\text{H}_{10})(\text{PH}_3)_2]$ ($\text{M} = \text{Pt}, \text{Ni}$) [230].

To conclude, it appears well established that different effective synthetic routes are at the disposal of chemists to prepare supported metal catalysts with high dispersions on CNTs or CNFs (Figure 9.11). As in the case of graphite [231,232], it seems that some metals, such as ruthenium, interact more strongly than others with the graphene layers of CNTs or with the surface of CNFs. From the literature reports on group VIII metal dispersions, it seems that the work of metal adhesion

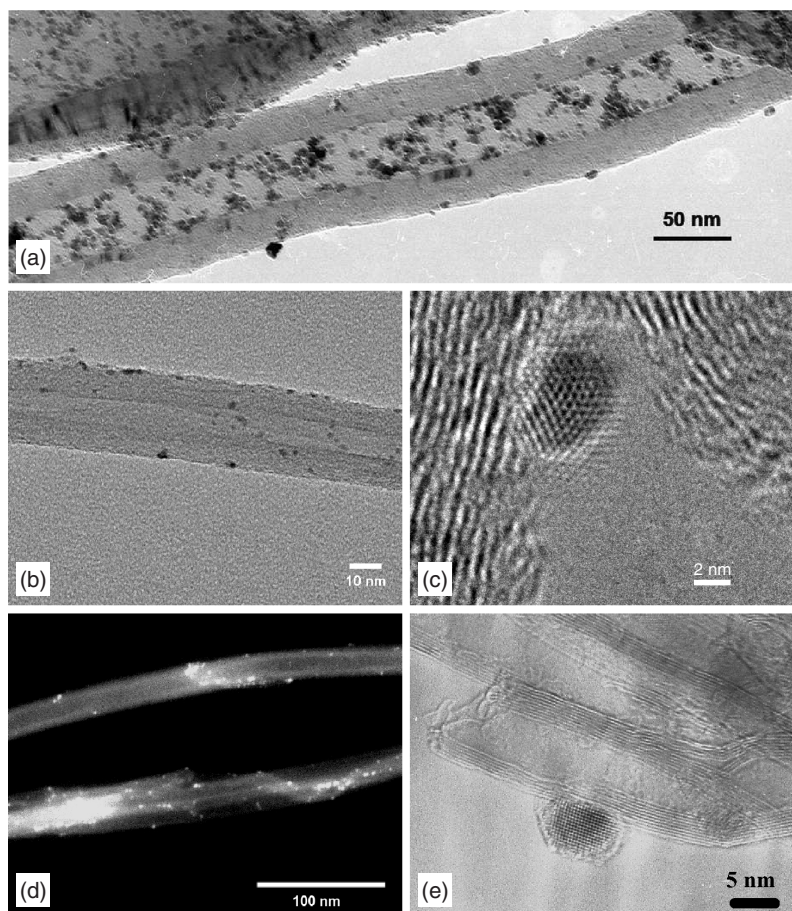


Figure 9.11 MWCNT-based catalysts: (a) TEM micrograph of Pt nanoparticles inside MWCNT; (b) STEM micrograph of Pt–Ru/MWCNT; (c) HREM micrograph of Pt–Ru/MWCNT; (d) STEM-HAADF2 micrograph of Pt–Ru/MWCNT; (e) TEM micrograph of TiO_2 –MWCNT composite catalyst.

follows the order $\text{Ru} > \text{Rh} > \text{Pd} \geq \text{Pt}$. Even though oxidative surface treatments on the supports seemingly improve the dispersion of the metallic phase, it is important to stress that better knowledge of the concentration and distribution of the attached functional moieties will help to understand the dependence of CNT and CNF reactivity on their structure. For the case of nitric acid oxidation [233], which produces mainly carboxylic groups, a simple acid–base titration can be used to determine the concentration of the acidic sites [151,160,234]. Owing to their specific structure, CNTs and CNFs can be considered as tunable and polyfunctional ligands for metal coordination (Figure 9.12).

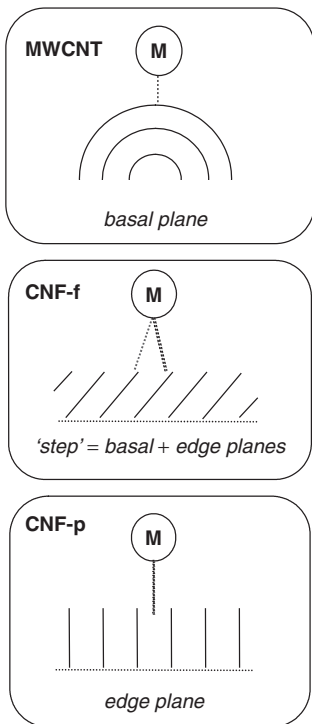


Figure 9.12 CNTs and CNFs as structured and polyfunctional macromolecular ligand.

9.5 CATALYTIC PERFORMANCE OF CNT- AND CNF-BASED CATALYSTS

Owing to the advantageous properties of CNTs and CNFs as supports, several studies have been carried out on different catalytic reactions. In particular, much attention has been dedicated to liquid-phase reactions with MCWNT- and CNF-supported catalysts; indeed, their high external surface and their mesoporosity would result in a significant decrease in mass-transfer limitations compared with activated carbon. It is worth noting that as for fullerenes [28], few studies on SWCNT-supported catalytic systems have been reported, due either to their microporosity or to the fact that it is still very difficult to obtain the large amounts of pure material required to conduct catalytic studies. In this section we present the results obtained for each type of reaction and, when possible, we will try to rationalize these results by comparison with other carbonaceous supports.

9.5.1 Hydrogenation Reactions

One of the most studied catalytic reactions is hydrogenation in both the liquid and gas phases, and two types of reactions have been considered: alkenes

hydrogenation and α,β -unsaturated aldehydes-selective hydrogenation. Several studies report that for liquid-phase hydrogenation, the use of CNT or CNF supports possessing large mesoporosity provided better catalytic activities than did microporous activated carbon, for which mass-transfer limitations are in operation.

Baker's research team has conducted several studies on ethylene, but-1-ene, and buta-1,3-diene hydrogenation on nickel catalysts supported on different types of CNFs (r-CNFs, p-CNFs, or spiral-like CNFs), γ -alumina, and activated carbon (AC) [235–237]. The authors state that the nickel crystallite activity and selectivity can undergo important modifications by interactions with the support; indeed, it was found that the catalyst supported on CNFs yields higher conversion values than those observed employing γ -alumina and AC, even though the metallic particle size is larger (6.4 to 8.1 nm on CNFs, 5.5 nm on AC, and 1.4 nm on Al_2O_3). These results point to the fact that catalytic hydrogenation might be extremely sensitive to the nature of the metal–support interaction. HREM studies have been performed to get a deeper insight on metallic particle morphology: On CNF supports, the crystallites deposited were found to adopt very thin hexagonal structures, and the relevant growth pathways are generally believed to be followed in situations in which strong metal–support interactions are present to cause spreading of the metal onto the support surface. By contrast, a globular particle geometry prevails when nickel is supported on $\gamma\text{-Al}_2\text{O}_3$, providing a somewhat weaker metal–support interaction. Pt/f-CNF catalysts were also reported to be about 1.2 times more active than Pt/AC or Pt/ Al_2O_3 for hydrogenation of toluene [238], the CNF support allowing high Pt dispersion and higher concentration of Pt(0).

Rhodium nanoparticles (1.1 to 2.2 nm) supported on oxidized f-CNFs were used in the hydrogenation of cyclohexene [239]. These catalysts turned out to be extremely active even under low hydrogen pressures at low metal loadings (1% w/w) and low cyclohexene concentrations (1% v/v). The authors claimed that the activity is almost independent of nanoparticle size and that other factors, such as the possible clustering of the support material in the liquid phase and the presence of oxygen-containing species on the support surface, are responsible for the results observed. Unfortunately, no comparison with other activated carbon–supported catalysts was provided. Ruthenium nanoparticles (2 to 4 nm) on CNFs (p-CNF or f-CNF) and MWCNTs showed excellent catalytic activity for arene hydrogenation, and for toluene hydrogenation on a 1.7% w/w Ru/p-CNF, the sum of the turnover numbers for five repeated runs was over 180,000 [240]. A 5% w/w platinum catalyst deposited on CNTs ($100 \text{ m}^2/\text{g}$) was found to be significantly more active than a commercial or homemade 5% Pt/AC and a 5% Pt/graphite for the hydrogenation of *trans*-stilbene and *trans*- β -methylstyrene [241]. A rhodium complex grafted onto MWCNTs was also reported to be very active in cyclohexene hydrogenation [218,242]. Such a catalyst is more active than that supported on activated carbon, and interestingly, the turnover frequency (TOF) increases dramatically after recycling. Pd/CNT catalysts were found to be active in cyclooctene [243] and benzene [244] hydrogenation, and for the latter

a catalyst having Pd nanoparticles in the inner cavity of the tubes is more active than a Pd/AC system. If deposited on CNFs, palladium is also active for phenol hydrogenation [245], and whereas Pd/AC favored partial hydrogenation to cyclohexanone, Pd/CNF affords complete hydrogenation to the alcohol. Rh/CNF catalysts are also active for this reaction in scCO₂, with high selectivity to cyclohexanone [246]. Bimetallic RhPd [247] and PtPd [197] systems supported on MWCNTs are active in the hydrogenation of aromatics and polyaromatics. Irrespective of the reactant molecule, such PtPd catalysts show higher TOF values than those of the corresponding oxide-supported systems [197]. Nitrobenzene has been hydrogenated to aniline at ambient temperature and under atmospheric pressure on 3 wt% Pt/CNT (170 m²/g) presenting 3-nm Pt nanoparticles; good activity was observed [248]. Different hydrogenation mechanisms have been proposed on the basis of the nature of the organic intermediates observed. Due to higher dispersion, the catalysts were more active than their counterparts on activated carbon [249]. For *p*-chloronitrobenzene hydrogenation, the use of bimetallic PtM/CNT catalysts (M = Mn, Fe, Co, and Ni) permits higher activity than monometallic Pt catalyst as well as higher selectivities to *p*-chloroaniline [250]. Interestingly, it has been reported that hydrogenated Pd/CNTs (H₂, 1 hour, 773 K) can effectively reduce NO at 573 K [251]. The hydrogenated CNTs act as a reducing agent that provides both hydrogen and carbon in NO reduction, and surface adspecies such as OH, NO, NO₂, and NO₃ are detected on the catalyst. Thus, an important factor to take into consideration in hydrogenation reactions is the ability of CNTs and CNFs to take up a significant amount of H₂, especially when CNTs or CNFs are used in association with Pd and/or Pt. Indeed, the spillover of physisorbed hydrogen from the metal nanoparticles enhances hydrogen storage compared with pristine CNTs (see Section 9.5.7). The selective partial hydrogenation of acetylene to ethylene was reported on NiB/CNT catalysts [252]. The activation of CNTs with NH₃ (particle size 9 nm) provides better dispersions than does treatment with HNO₃ (particle size 16 nm). The use of CNT-NH₃, which favors high dispersion, results in acceleration of the hydrogenation rate and an increase in the selectivity to ethylene. The selective hydrogenation of cyclohexadiene to cyclohexene over a homogeneous Rh catalyst immobilized in an ionic liquid phase supported on CNFs was used as a test reaction to demonstrate the feasibility of the ionic liquid-phase catalysis approach on a nanostructured carbon support [253]. Palladium catalysts supported on MWCNTs, f-CNFs, and r-CNFs have been compared in the selective hydrogenation of 1,3-butadiene [254]. CNF supports, in particular r-CNFs, make it possible to obtain highly dispersed Pd particles (3 nm), and the strong interaction between Pd and the graphene-edge sites of these supports stabilizes oxidation state +2 of the metal via electron transfer from the metal to the support. The overall activity and selectivity of these catalysts decrease when the fraction of Pd²⁺ increases, and the best results have been obtained on MWCNTs. Finally, cinchona-modified Pt/SWCNT catalysts were found to be efficient for the asymmetric hydrogenation of ethyl pyruvate [255].

The hydrogenation of α,β -unsaturated substrates on CNF- or CNT-supported catalysts has been the subject of several studies. Although the C=C bond is

easier to hydrogenate than the carbonyl group, unsaturated alcohol is often the desired product. Gas-phase hydrogenation of crotonaldehyde to crotyl alcohol was conducted on 5% w/w Ni catalysts supported on p-CNFs, r-CNFs, and γ -alumina [256]. Even though the mean particle size differs greatly according to the support used, from a narrow distribution centered at 1.4 nm for γ -Al₂O₃ to a broad distribution centered at 7 nm for CNFs, the higher activity and selectivity to crotyl alcohol were obtained on the CNF-supported catalysts. Possible reasons for these differences are (1) different Ni crystallographic face exposure according to the support; and (2) the possibility of charge transfer. High activity and selectivity were also obtained with 2 wt% Pt/MWCNT (87 m²/g) catalysts in the selective hydrogenation of citral [198]. Although it presents lower dispersion (6 nm) than Pt systems deposited on high-surface-area graphite (305 m²/g, Pt 3.4 nm) or carbon black (135 m²/g, Pt 1.8 nm), the Pt/MWCNT system is more selective toward the formation of unsaturated alcohol at isoconversion. A Pt-supported catalyst on purified SWCNTs has been found to be active and selective in the hydrogenation of prenol (3-methyl-2-butenal) to prenol (3-methyl-2-butanol) [257].

The selective hydrogenation of cinnamaldehyde has been studied on a variety of supported catalysts, including monometallic Pd [196,258–261], Pt [199,200,262], Ru [18,189], and bimetallic Pt–Co [263,264], Pt–Ni [265], Pt–Ru [266], and Pd–Ru [267] systems. In general, the catalytic systems obtained by deposition on CNTs or CNFs are more active than their counterparts on AC or oxides, and few systems are selective toward unsaturated alcohol. Palladium systems are very active in the selective hydrogenation of C=C bonds. On f-CNFs (50 m²/g), Pd catalysts (4 nm) are more active than commercial Pd/AC (900 m²/g) catalysts [258,259]. Similar results were obtained when Pd was deposited on the surface and into the cavity of large-diameter MWCNTs (20 m²/g) and on the surface of aligned MWCNTs attached to the surface of a structured silica reactor [260,261]. As for SWCNTs, it is worth noting that a commercial Pd/AC catalyst (Pd particle size 14.5 nm) is more active than Pd/SWCNT (Pd particle size 5.6 nm) [196]. Higher selectivity to cinnamyl alcohol has been obtained on Pt catalysts (10 to 60%). On MWCNTs, it has been observed that high selectivity to cinnamyl alcohol can be reached if Pt nanoparticles are located in the inner cavities of large-diameter CNTs (CNT inner diameter 60 to 100 nm, Pt 5 nm), while lower values have been determined with Pt on the outer surface of small-diameter tubes (CNT inner diameter < 10 nm, Pt < 2 nm) [199]. However, the Pt particle size was not the same in these two samples, and that might also affect selectivity [268]. A marked support effect on activity and selectivity has been reported for Pt/CNFs [200,262]. Whereas Pt/CNFs (177 m²/g, Pt < 2 nm) containing a significant amount of oxygenated groups show only moderate activity and selectivity in C=C bond hydrogenation (20 to 30%), in the same catalysts heated to remove the oxygen-containing groups, the activity increased by a factor of 25 and the selectivity to hydrocinnamaldehyde increased by 40 to 70%. This important finding highlights the importance of substrate adsorption onto the support in mechanisms of hydrogenation [262]. The possible role of hydrogen storage on

these supports has not yet been addressed. Different results have been obtained with ruthenium [18,189]. On unpurified MWCNTs ($27\text{ m}^2/\text{g}$) generated by arc discharge evaporation of graphite, a high level of activity compared to Ru/ Al_2O_3 (Ru 3.5 nm) has been obtained, together with exceptionally high selectivity to cinnamyl alcohol (90%) [18]. More recent results on purified MWCNTs (Ru < 2 nm) [264] or CNFs (Ru < 2 nm) [189] report selectivity ranging between 30 and 50%. For Ru/CNF, the crucial role of cinnamaldehyde adsorption on the support has been reported, with CNFs with low amounts of oxygen-containing groups showing increased activity and higher selectivity to hydrocinnamaldehyde (73%). Bimetallic Pt-based systems permit better control of selectivity. Pt–Ni/MWCNT ($135\text{ m}^2/\text{g}$, particles 2 to 5 nm) is more selective than Pt/MWCNTs to hydrocinnamaldehyde formation, showing values of 25% and 88%, respectively [265]. The use of Pt–Co/MWCNT [264] or Pd–Ru/SWCNT [267] permits orientation of selectivity toward cinnamyl alcohol formation of about 90% and 57%, respectively. Finally, the use of Pt–Ru/MWCNT ($175\text{ m}^2/\text{g}$, particles 2 nm) leads to activities higher than with Pt–Ru/AC and selectivity to cinnamyl alcohol of over 90% after heating the catalysts to remove the oxygen-containing groups [266]. This result confirms the importance of the surface chemistry of the support with regard to the final performance of the catalysts.

9.5.2 Reactions Involving CO/H₂

Although ACs are not often employed as supports for these reactions, CNFs and CNTs have been investigated for Fischer–Tropsch reactions [210,269–274], methanol [275,276] or higher alcohol [277,278] synthesis, and hydroformylation [208,214,217]. Copper-promoted Fe/MWCNT catalysts prepared by incipient wetness impregnation are active in Fischer–Tropsch syntheses at 493 K, and an olefin (C₂ to C₁₀) content of 40 to 60 mol% in the hydrocarbon fraction was obtained [269]. Compared to Fe/AC catalysts, Fe/MWCNT systems ($S_{\text{BET}} = 20\text{ m}^2/\text{g}$) lead to lower selectivity to methane, and to high selectivity to olefins [272]. Fe/MWCNT catalysts are more active than Co/MWCNT, and with regard to selectivity to C₅₊ products, Fe/MWCNT shows selectivity values of 40 to 45%, compared to 10 to 20% for Co/MWCNT [273]. A pronounced influence of metal particle size on both activity and selectivity to C₅₊ has been demonstrated in the case of Co/CNF [210]. The turnover frequency at 483 K and under 35 bar decreases from 23×10^{-3} to 1.4×10^{-3} , and selectivity to C₅₊ decreases from 85% to 51% when the Co particle size is lowered from 16 nm to 2.6 nm. The addition of small amounts of a MnO promoter to Co/CNF catalysts also improves the selectivity to C₅₊ products [270,271]. A novel structured catalyst, based on aligned MWCNT arrays in a microchannel reactor, has been used for Fischer–Tropsch reactions [274]. The catalyst, CoRe/ Al_2O_3 , was deposited on the MWCNT material by dipcoating. When integrated into a microchannel reactor, this microstructured catalyst exhibited an enhancement in Fischer–Tropsch reaction activity four times greater than the values observed with a similar system

without CNT arrays. This system also permits us to operate at higher temperatures without selectivity runaway favoring methane formation. Such results can be rationalized by considering the increased mass and heat transfer (minimization of local hot spots) due to the use of MWCNTs.

MWCNTs ($140\text{ m}^2/\text{g}$) have been used as promoters to improve the catalytic activity of Cu–ZnO–Al₂O₃ catalysts for methanol synthesis using H₂/CO/CO₂ mixtures [275]. This catalyst, containing 10 to 15% MWCNTs, is prepared by coprecipitation and permits a significant increase in the methanol formation rate compared to unpromoted systems. The action of CNTs as promoters could arise from (1) a dispersing role of MWCNTs, allowing a significant increase in Cu specific surface area; and (2) the efficiency of MWCNTs to act as a hydrogen reservoir, favoring CO/CO₂ hydrogenation reactions. Rh–ZnO/MWCNT systems are also active and selective for methanol synthesis under 100 bar and at 523 K [276]. f-CNFs ($140\text{ m}^2/\text{g}$) have been used as supports for bimetallic Co–Cu catalysts, and the resulting material affords high selectivity toward the formation of higher alcohols, in particular butanol from H₂/CO/CO₂ mixtures under 50 bar and at 523 to 583 K [277]. Also in this case it has been proposed that a high concentration of reversibly adsorbed hydrogen species on the CNT-promoted catalyst favors surface hydrogenation reactions. For CO hydrogenation to oxygenates on Rh–Ce–Mn/SiO₂ catalysts, improved CO conversion has been observed by addition of 5 to 15% CNTs during impregnation of the catalyst [278].

Rhodium-supported catalysts on f-CNFs, p-CNFs, or r-CNFs have been used to study the hydroformylation of ethylene, and they have also been compared to a Rh/SiO₂ system [214]. Although silica has a higher specific surface area and Rh particles are smaller on it, it has been found that CNF-supported catalysts exhibit higher selectivity and similar catalytic activity. It has been proposed that the hexagonal shape of the rhodium crystallites, as evidenced on CNFs, is responsible for the better results obtained. The highest selectivity was reached on the r-CNF support. The complex [HRh(CO)(PPh₃)₃] has been grafted onto MCWNTs and f-CNFs, and the catalytic activity in the hydroformylation of propene has been compared to that of similar systems prepared on activated carbon, carbon molecular sieves, and silica [217]. Higher conversions and higher regioselectivity toward *n*-butylaldehyde have been reported for CNT- and CNF-supported systems. The authors propose that the rhodium complex can be accommodated into the oxidized channels because of their size and that extensive capillary condensation of *n*-butylaldehyde is prevented compared to the other supports. No information has been provided about possible leaching of the complex from the support into the solution. Finally, good activity and regioselectivity was obtained on Co/MWCNT in oct-1-ene hydroformylation under 50 bar and at 403 K [208].

9.5.3 Polymerization

Both SWCNTs and MWCNTs are very robust along their longitudinal axis and possess excellent thermal and electrical conductivities, and hence could be used as

fillers in polymer-based advanced composites [11]. However, the homogeneous dispersion of CNTs is a difficult task due mainly to their poor solubility. Three different approaches have been adopted to produce polymer-functionalized CNTs: (1) a noncovalent functionalization method by which polymers are produced by ring-opening metathesis polymerization (ROMP) [279–281]; (2) a covalent functionalization performed by first grafting polymerization initiators onto the tubes through covalent bonds and then exposing these CNT-based macroinitiators to the monomer, the polymer being obtained by atom-transfer radical polymerization (ATRP) [282–286]; and (3) olefin polymerization via anchored metallocene catalysts [287–290].

Noncovalent poly(norbornene) coatings [5 to 20 nm, Figure 9.13(a)] have been obtained on SWCNTs by functionalization of the tubes with a ruthenium-based olefin metathesis catalyst followed by the ROMP of norbornene [279,280]. The polynorbornene-functionalized CNTs present a slightly improved solubility in organic solvents [280]. Coatings (ca. 10 nm) of hyperbranched polymers have been obtained on MWCNTs [Figure 9.13(b)] via cationic ring-opening polymerization of 3-ethyl-3-(hydroxymethyl)oxetane with a $\text{BF}_3\text{Et}_2\text{O}$ catalyst [281], and material so prepared exhibits relatively good dispersibility in polar solvents. ATRP of *n*-butyl methacrylate [282] or methyl methacrylate, *tert*-butyl acrylate [283], and styrene [284] has been conducted on SWCNTs via a multistep procedure that includes nitric acid SWCNT functionalization, grafting of a bromide-containing initiator onto the SWCNT surface, and polymerization. Except for the CNTs functionalized with poly(methyl methacrylate), which are insoluble, the other functionalized CNTs show good solubility in organic solvents. On MWCNTs, a similar procedure was followed to obtain poly(methyl methacrylate) [285] and polystyrene-*block*-poly(acrylic acid) [286] coatings; the latter measured thickness ranges from 4 to 8 nm.

Polyethylene–MWCNT composites have been produced by polymerization of ethylene on $[\text{ZrCl}_2\text{Cp}_2]\text{-MAO}/\text{MWCNT}$ [287] and $[\text{ZrCl}_2\text{Cp}_2^*]\text{-MAO}/\text{MWCNT}$ [288] ($\text{Cp} = \eta^5\text{-C}_5\text{H}_5$; $\text{Cp}^* = \eta^5\text{-C}_5\text{Me}_5$). The methylaluminoxane (MAO) is introduced either during the catalytic tests [280] or during the catalyst-grafting procedure [288]. Once $[\text{ZrCl}_2\text{Cp}_2]$ is adsorbed on MWCNTs, the molecular mass of polyethylene increased significantly compared to homogeneous catalytic systems, rising from 300,000 to 1,000,000 [287]. It has been proposed that MWCNTs play a key role as bulky ligand in increasing the molecular mass. When $[\text{ZrCl}_2\text{Cp}_2^*]$ is supported on MWCNTs, ethylene consumption is about 30% higher than for ethylene polymerization with homogeneous systems [288]. A similar result has been obtained in the case of nickel catalysts on SWCNTs [289]. Thus, supporting the catalytic system on MWCNTs clearly increases the polymerization rate of ethylene. Syndiotactic polypropylene–MWCNT composites have been prepared by propylene polymerization on zirconocene–MAO catalysts [290]. Pretreatment of MWCNTs with MAO is necessary to attain satisfactory homogeneity in the polymer matrix. The rate constant of crystallization of pure syndiotactic polypropylene was multiplied more than tenfold in the presence of MWCNTs. Finally, homogeneous surface coating of MWCNTs was achieved by

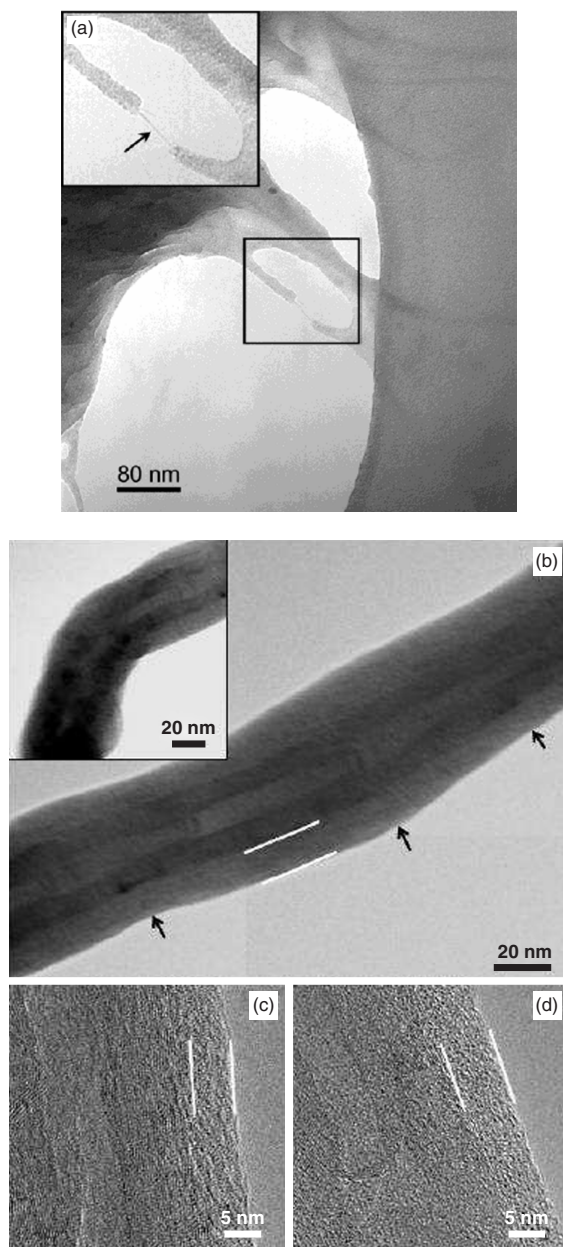


Figure 9.13 TEM images of “polymerized nanotubes”: (a) SWCNT [the inset is a blow-up of the region within the box, showing a single nanotube bridging the gap between two polymer regions (arrow)]; (b–d) MWCNT, where the core–shell structure of the one-dimensional nanohybrids is clearly observed. [(a) From ref. 280, with permission. Copyright © 2004 American Chemical Society. (b–d) From ref. 281, with permission. Copyright © 2004 American Chemical Society.]

ethylene–norbornene copolymerization using a highly active zirconium metallocene grafted on the MWCNT surface [225].

9.5.4 Carbon Nanotubes Synthesis by Catalytic Decomposition of Hydrocarbons

A crucial problem connected to carbon nanotube synthesis on supported catalysts on an industrial scale is the purification step required to remove the support and possibly the catalyst from the final material. To avoid this costly operation, the use of CNT- or CNF-supported catalysts to produce CNTs or CNFs has been investigated. Although most catalytic systems are based on nickel supported on CNFs (see Table 9.4), the use of MWCNTs [305,306] or SWCNTs [307] as supports has also been reported. Nickel, iron [304,308–310], and bimetallic Fe–Mo [305] and Ni–Pd [295] catalysts have been used. Compared to the starting CNTs or CNFs, the hybrid materials produced present higher specific surface area [297,308] or improved field emission characteristics [309].

In these reactions, catalyst deactivation by carbon deposition constitutes a critical issue. Ni/CNF systems have been found to be more active and to be deactivated more slowly than Ni/Y–zeolite [299], Ni/ZrO₂, Ni/Al₂O₃, and Ni/MgO [291], but less active and less stable than Ni/SiO₂ and Ni/TiO₂ [291]. In the case of iron-supported catalysts, the overall performance of CNF supports is higher than that of the corresponding SiO₂ supports [304]. The use of 10 to 50-nm Ni nanoparticles on CNFs affords optimum composition. The formation of larger-diameter Ni particles that are deactivated faster can be avoided by

Table 9.4 Representative Examples of the Use of CNTs or CNFs as Support for Further CNFs and CNTs Growth

Catalyst ^a	C Source/ Gas Phase	T (K)	Activity (g _C /g _M · h)	Product	Ref.
5%Ni/CNF	CH ₄ /pure CH ₄	773	32	CNF	291
15%Ni/CNF (151)	CH ₄ /pure CH ₄	848	13	CNF	292
15%Ni/CNF (115)	CH ₄ /pure CH ₄	823	17.5	CNF	293
40%Ni/CNF (77)	CH ₄ /pure CH ₄	803	50–80	CNF	294
18%Ni18%Pd/CNF (77)	CH ₄ /pure CH ₄	823	39	CNF	295
20%Ni/CNF (10)	C ₂ H ₆ /C ₂ H ₆ –H ₂	923	17.5	CNF	296
0.5%Ni/CNF	C ₂ H ₄ /C ₂ H ₄ –He	673	253	CNF	297
20%Ni/CNF (136)	C ₂ H ₄ /C ₂ H ₄ –H ₂	823	50	CNF	298
4.2%Ni/CNF	C ₂ H ₂ /C ₂ H ₄ –H ₂	973	420	CNF	299
5.6%Ni/CNF (138)	C ₂ H ₂ /C ₂ H ₄ –H ₂	973	392	CNF	300
10%Ni/CNF (360)	C ₂ H ₂ /C ₂ H ₄ –H ₂ – thiophene	1073	320	Nanocoils	301
35%Ni/MWCNT (140)	C ₃ H ₆ /C ₃ H ₆ –H ₂	973	68	MWCNT	302
5%Fe/p-CNF (60–80)	CO–H ₂ /CO–H ₂	833	18	f-CNF	303

^aValues in parentheses are the specific surface areas of the supports.

nitric acid treatment of the CNF support [301]. Use of a bimetallic Pd–Ni system does also permit stabilization of the catalyst [295], and Os–Pd systems show good selectivity toward MWCNTs [303]. Finally, if the goal of the reaction is to produce CO-free hydrogen and not solid carbon, regeneration of the catalyst is possible using He/O₂ mixtures at 673 K [298]. As far as catalyst activity is concerned, it appears that the choice of carbon source has a marked influence, the best performances being obtained with acetylene, followed by ethylene and methane (Table 9.4). Interestingly, the use of low-loading catalysts yields a high activity level when starting with ethylene [298].

9.5.5 Ammonia Synthesis and Decomposition

The use of ruthenium/carbon catalysts for ammonia synthesis could constitute an alternative method to replace conventional iron-based systems that operate under high pressure and at high temperature. However, extensive studies have shown that Ru/AC deactivation occurs upon prolonged reaction, owing to metal sintering, metal leaching, and methanation of the support. Hence, the use of CNFs or CNTs, both intrinsically more stable than activated carbon, has been investigated [311–316]. Ru–K/MWCNT catalysts have been found to be significantly more active than other Ru systems supported on C₆₀ [311] or low-surface-area graphite [312]. Promising activities have also been reported when using Ru–K/MgO–CNT catalysts [313]. Similarly, highly dispersed Ru/CNF and Ru–Ba/CNF catalysts are 25% more active than the corresponding systems prepared on activated carbon [314,315]. Interestingly, the methanation reaction on Ru/CNF catalysts is greatly inhibited if compared to Ru/AC catalysts [316]; the high level of graphitization of the support is probably the reason for the resistance toward the methanation reaction, even at high temperatures.

The catalytic decomposition of ammonia to generate CO-free hydrogen for fuel cells is receiving increasing attention since this process is more economical than using methanol as a H₂ source. Also in this case, ruthenium is the metal of choice, and the possibility of using MWCNTs to support the metal has been investigated [317–323]. The catalytic activities follow the order Ru/MWCNT > Ru/MgO > Ru/TiO₂ > Ru/Al₂O₃ > Ru/ZrO₂ > Ru/AC [321]. A high level of catalytic activity for ammonia decomposition has been attained using highly dispersed catalysts (Ru nanoparticles around 2 nm) deposited on basic conductive MWCNT supports (224 m²/g). The most effective promoter for this reaction is KOH, the activities observed being in the order Ru–K > Ru–Na > Ru–Li > Ru–Ce > Ru–Ba > Ru–La > Ru–Ca > Ru [319]. Use of a conductive support permits electron transfer from promoter and/or support to Ru, a process that would facilitate the recombinative desorption of nitrogen atoms [321], which is the rate-determining step in the reaction [318]. The performance of decomposition catalysts can be improved by eliminating the electron-withdrawing groups that originate from precursor of active component, support, or promoter [321]. Finally, the influence of the porous graphitic structure of carbon supports on the performance of Ru catalysts has been examined, the relevant activities following

the order Ru/graphitic carbon ($92\text{ m}^2/\text{g}$) > Ru/MWCNT ($157\text{ m}^2/\text{g}$) > Ru/carbon black ($768\text{ m}^2/\text{g}$) > Ru/AC ($1080\text{ m}^2/\text{g}$) [323]. These data point to the importance of the graphitic structure of carbons (conductive support), which favors electron transfer between the metal and the support.

9.5.6 Environmental Catalysis and Oxidation Reactions

The high surface area and electrical conductivity of MWCNTs could be of interest for improving the activity of TiO_2 photocatalysts. The resulting composites have been used for phenol [207,324,325], acetone [326], azo dye [327] or NO_x [328,329] photodegradation, photocatalytic H_2 generation from water/alcohol mixtures [330], and CO_2 reduction with water [331]. TiO_2 –MWCNT composites have been prepared either by sol–gel [207,331], ultrasonic irradiation [326], or hydrothermal methods [331]. These studies showed that the presence of MWCNTs in the composite makes it possible (1) to obtain materials having a higher surface area than that of the initial TiO_2 powders; (2) to prevent the agglomeration of TiO_2 particles, and (3) to obtain a strong interface interaction that favors adsorption [327] and electron transfer. In these reactions, MWCNTs could be considered as photosensitizers that promote the transport of electron–hole pairs along the tubes, thus decreasing the recombination rate of electron–hole pairs and improving the photocatalytic activity of TiO_2 via the formation of larger amounts of radicals. It has also been shown that an optimal amount of CNTs to incorporate in the composite, generally between 10 and 20% [207,326], is needed to obtain good improvement in the catalyst efficiency. Above this critical amount the photocatalytic activity decreases, due to the increased absorbing and scattering of photons by the carbon support in the photoreactive system.

MWCNTs have been used as supports for Pt [161,332,333], Ru [161,334], and Cu [161] in the catalytic wet air oxidation of aniline or phenol [335] at 473 K. Under these conditions no stability problem was noted for the support, but the use of high-surface-area activated carbon supports makes possible better performances, except for Ru/AC catalysts [334]. Interestingly, the clear superiority of RuO_2 /f-CNFs over activated carbon- or alumina-supported Ru systems has been reported for the aerobic oxidation of alcohols to aldehydes or ketones at 353 K [336]. In both cases, the ruthenium-based catalysts on MWCNTs [331] or f-CNFs [336] presented very high metal dispersions. If the oxidation reaction is conducted at a high temperature, as in the case of CO oxidation at 523 K [337,338], a Co/CNT catalyst provides better conversion than Co/AC, due to the thermal stability of nanotubes [337], but a Pt/CNT catalyst gives lower conversions than Pt/ Al_2O_3 , presumably because of the very small Pt particle size obtained on the nanotube support [338]. CNTs have also been used to support well-dispersed Cu–Zn crystallites for the partial oxidation of methanol at 533 K to produce hydrogen [339] and to immobilize a ruthenium complex for direct cyclohexene oxidation [340]. A system using immobilized complex showed a higher level of activity than that of homogeneous catalysts. Carbon nanotubes–vanadium oxide

nanorod composites were active for the partial oxidation of *n*-butane to maleic anhydride [341]. NiS₂ nanoparticles encapsulated inside MWCNTs were active for the oxidation of hydrogen sulfide into elemental sulfur at 333 K, and better resistance to solid sulfur deposition was reported than with the classical silicon carbide catalyst [342].

9.5.7 Other Reactions

The peculiarities of CNT- or CNF-based catalysts have prompted scientists to explore their possible use as supports in a large variety of reactions (Table 9.5) on which their properties (surface area, porosity, electronic or thermal conductivity, surface chemistry) could exert a significant impact compared to traditional carbon or oxide supports.

The ability of CNFs or CNTs to store significant amounts of hydrogen could indeed have some consequences on catalytic reactions involving surface hydrogen. Furthermore, it has been demonstrated that an enhancement of hydrogen storage capability on metal/CNTs does occur via spillover from noble metal nanoparticles [363–367], the spilled hydrogen occupying physisorption binding sites on the external walls of CNTs [367]. Even though such behavior of noble metal-supported CNTs or CNFs has not been taken into account to rationalize the high activity levels of metal-supported CNT catalysts in hydrogenation reactions, it can explain the good performance of Pt/CNF [343,201] and Rh/CNF [368] catalysts in *n*-hexane skeletal and methylcyclopentane reactions, respectively. Thus, back-migration of hydrogen retained by the support to create hydrogen-rich active sites on the metal surface would significantly affect activity and selectivity. A similar effect has been observed in thiophene HDS on Co–Mo sulfide catalysts supported on MWCNTs [350].

CNTs and CNFs can also be considered as potential dispersing agents, improving the dispersion of oxide active phases. The positive dispersing effect of CNTs or CNFs on some catalytic phases has also been reported for various reactions, including the water–gas shift reaction on Cu–Ce–Zr/CNF [351,352], MIBK synthesis on hydrotalcites supported on CNFs [353], methanol steam reforming [369], dimethoxymethane catalytic reforming [370] on Cu–ZnO/MWCNT, and photocatalysis on TiO₂–CNT composites [207]. In general, it seems that the preparation method used for the composite can affect the catalytic activity, and physical mixtures of CNTs and the active phase are less efficient than are samples prepared by wet chemistry [358,207].

The specific metal–support interaction existing for CNTs or CNFs has been demonstrated in several studies. A strong interaction between the H₃PW₁₂O₄₀ heteropolyacid and the surface groups of MWCNTs was reported for the esterification of *n*-butanol with acetic acid [371]. For olefin skeletal isomerization on WO₃/MWCNT [344], it was shown that on CNTs, by contrast to oxide supports such as alumina and zirconia, the formation of metallic tungsten is inhibited, thus pointing to the absence of an observable deactivation phenomenon. For dibenzotriphene HDS, TPR data have shown that the active species on Co and

Table 9.5 Representative Examples of the Use of CNTs or CNFs as Support in Catalysis

Reaction	Catalyst	Comments	Refs.
Skeletal <i>n</i> -hexane reaction	Pt/CNF	5%Pt/CNF ($D = 20\%$) is more active at lower temperature than a commercial 6%Pt/SiO ₂ (EUROPT-1, $D = 60\%$). Both activity and isomer formation are better on Pt/f-CNF than on Pt/p-CNF.	201,343
C ₆ olefin skeletal isomerization	WO ₃ /MWCNT	17%WO ₃ /MWCNT catalyst is significantly more active and much more stable than a commercial 25%WO ₃ /ZrO ₂ catalyst.	344
Cyclohexanol	Co/MWCNT	15%Co/MWCNT presents higher activity and selectivity to cyclohexanone than a 15%Co/C*, and HNO ₃ -treated MWCNTs	345,346
Isopropanol	Pt/MWCNT	Low-loading Pt/MWCNT present higher TOFs than their counterparts on activated carbon or graphite flakes.	347
Dehydrogenation Cyclohexane	Pt/MWCNT	0.25%Pt/f-CNF presents same activity and selectivity as commercial 1%Pt/Al ₂ O ₃ .	348
Hydrodechlorination of chlorobenzene	Pd/CNF	Initial activity: Pd/CNF ≈ Pd/C* > Pd/graphite. Catalyst stability: Pd/CNF ≈ Pd/graphite > Pd/C*.	194
	Ni/SiO ₂ -CNF	Activity of Ni/SiO ₂ -CNF was maintained by long reaction times on stream, to ultimately exceed the level of dechlorination achieved with Ni/SiO ₂ .	349
Hydrodesulfurization	Co-Mo/MWCNT	7%Co ₁ Mo ₃ /MWCNT is significantly more active than a 7%Co ₁ Mo ₃ /C* for thiophene hydrodesulfurization.	350
	Ni-Mo/CNF	Ni-Mo/CNF catalyst exhibits higher HDS activity for diesel fuel than that of a conventional Ni-Mo/Al ₂ O ₃ catalyst.	351

Water–gas shift reaction	Cu–Ce–Zr/CNF	13% of the Cu–Ce–Zr mixed oxides can be replaced by CNF without a decrease in the overall activity and stability of the catalyst.	352
MIBK synthesis	Hydrotalcites/CNF	Specific activity of supported hydrotalcites is found to be four times higher than that of unsupported catalysts.	353
Dimethyl oxalate synthesis	Pd/CNF	Significant improvement in catalytic activity compared to Pd/Al ₂ O ₃ , 30%Ir/f-CNF presents far better performances than a commercial Ir/Al ₂ O ₃ catalyst (Shell 405).	354
Hydrazine decomposition	Ir/f–CNF	Catalytic performances of a supported catalyst are found to be better than those of an unsupported catalyst.	355,356
Ammonium perchlorate decomposition	Cu/MWCNT	VO ₆ complex grafted on SWCNT presents better performances than on activated carbon, but higher enantiomeric excess is obtained on silica.	357
Cyanosilylation of aldehydes	VOsalen/SWCNT	High catalytic activity.	222,358
Tandem coupling cyclization	Pd/CNT	Enhanced catalytic activity in the presence of SWCNT.	359
Epoxidation of cyclohexene	[Mo]/SWCNT	Both activity and selectivity increase with the concentration of acid sites on CNFs.	360
Dehydrogenation of hydroxymatairesinol	Pd/CNF	Good catalytic activity; the larger the CNT diameter, the higher the activity.	361
Selective catalytic reduction of NO with NH ₃	V ₂ O ₅ /CNT		362

Mo oxides deposited on MWCNTs can be reduced at lower temperatures than with the active species present on Co–Mo/Al₂O₃, and that the CNT support favors the reduction of active phases [372]. Moreover, besides the high levels of dispersion attainable on CNTs or CNFs [348,355], especially after oxidation of the supports [346], these materials often constitute a very good compromise between activated carbon and graphite in terms of surface area, porosity, and crystalline structure, as shown by enhanced catalytic activity and catalyst stability. This was demonstrated in the case of catalytic hydrodechlorination on Pd catalysts [194,349].

The high thermal conductivity of these supports could also contribute to better catalyst activity and stability than those with insulating oxide supports because of rapid temperature homogenization throughout the entire reaction volume and the absence of hot spots that could damage the catalyst. This peculiarity of MWCNTs has been used advantageously for hydrazine decomposition over Ir catalysts [356,357] and for the construction of a microcombustor based on Pt/MWCNT, providing the heat needed in a methanol steam reforming system [373].

Finally, the influence of oxygen-containing groups, which contribute to CNT or CNF surface acidity, on the activity and selectivity of the final catalyst was demonstrated in the case of hydrogenolysis on Pd/CNF [374]. For hydroxymatairesinol hydrogenolysis, the higher the support acidity, the higher the activity and selectivity.

9.5.8 Fuel Cell Electrocatalysts

The field to which the specific features of CNTs and CNFs could bring the most significant advancements is perhaps that of fuel cell electrocatalysis [125,187]. The main uses of CNTs or CNFs as catalyst support for anode or cathode catalysis in direct methanol fuel cells (DMFCs) or proton-exchange membrane fuel cells (PEMFCs) are covered in Chapter 12. In this section we summarize the main advantages linked to the use of nanotubes or nanofibers for these applications.

The structure and properties of the carbon support, which constitutes the electrode material, have a direct impact on the performance of fuel cells. This material must present (1) a high electronic conductivity value; (2) a high level of mesoporosity, to attain high metal dispersion; (3) a suitable morphology to optimize and stabilize the three-phase boundary reactive sites; and (4) good hydrophobicity for water removal and mass-transport improvement. In comparison with the more widely used Vulcan XC-72R carbon black support, which has an electronic conductivity of 4 S/cm and a specific surface area of 240 m²/g with a significant number of micropores, CNTs and CNFs have significantly higher electronic conductivities and present higher mesoporous volumes for comparable or higher surface areas.

More than a hundred articles have been published on the use of CNTs or CNFs as catalyst supports for DMFC and PEMFC. The most studied reaction is methanol oxidation (anode catalyst), followed by oxygen reduction (cathode catalyst) and to a lesser extent, hydrogen oxidation (anode catalyst). Platinum is

the most used metal, followed by Pt–Ru systems. Other Pt-containing bimetallic (Pt–WO₃ [375,376], Pt–Nb–PO_x [377], Pt–Fe [378], Pt–Sn [379]) and trimetallic (Pt–Ru–Ir [380]) systems have also been reported. Surprisingly, only a few studies have been conducted on the use of cheaper metals, such as Pd [193,381–385], Ag [386], Au [387], Co [388], and MnO₄ [389]. All kinds of CNTs and CNFs have been used for these reactions, including f-CNFs, p-CNFs, r-CNFs [390,391], MWCNTs, SWCNTs, DWCNTs [392], and nitrogen-doped CNTs [393]. In most of these works, high dispersions of the metallic phase have been obtained [125,187].

Although it is not possible to compare all these studies, mainly because of the different origins of the CNT and CNF samples (pointing to the crucial importance of CNT and CNF standardization), the general tendency observed is that catalysts prepared on CNTs or CNFs are more active and in some cases present better resistance to poisoning [394] than do those prepared on conventional carbon supports such as Vulcan XC-72. In some cases it is possible to obtain similar or better performances with significant reductions of Pt loadings [395,396]. Compared to the commonly used carbon black support, the increase in power density of a single stack is generally between 20 and 40%, even if 70% [392], 100% [397], or even higher values [398,399] have been reported. Only a few studies concern systematic comparison of the different types of CNTs and CNFs. If we consider the electronic conductivity and specific surface area of the supports, we would expect the following order: SWCNTs > DWCNTs > MWCNTs > CNFs. In general, and this result could be rationalized on the basis of the electronic conductivity of the support, the activity of metal-supported MWCNT systems is superior to that of CNF-based catalysts. For DWCNTs, which present a higher specific surface area than MWCNTs [392], better performances have been reported. For SWCNTs, contrasting results have been reported, and further work is needed to shed light on the potentiality of these materials.

The advances made by the use of CNTs and CNFs as supports for fuel cell applications are generally attributed to (1) the possibility of reaching high metal dispersion and high electroactive surface area values; for Vulcan XC-72R the catalyst particles can sink into the microporosity, thus reducing the number of three-phase boundary active sites; (2) the peculiar three-dimensional mesoporous network formed by these materials, which provides improved mass transport; and (3) their excellent conducting properties, which improve electron transfer.

9.5.9 CNTs for Enzyme Immobilization

The use of nanomaterials for enzyme immobilization may offer some advantages regarding enzyme stabilization, control of the pore size to protein molecule dimensions, multiple sites for interaction, and reduced mass-transfer limitations [400]. Although CNTs have been used mainly for biosensors [401], where their electrical and electrochemical properties are of particular interest, recent studies have evaluated the possibility of using CNTs as support for biocatalysts.

Enzymes have been immobilized via either noncovalent [402] or covalent [403] sidewall functionalization. Covalent functionnalization of MWCNTs by lipase gives a biocomposite that exhibit remarkable solubility in organic solvents [403]. It is worth noting that physical adsorption of enzymes onto CNTs may induce secondary structural perturbations as a result of protein interaction with the CNT surface, and that substantial perturbation can induce either nearly complete loss [404] or significant increase [405] in catalytic activity. Furthermore, strong interaction between the noncovalently anchored enzyme and the CNT surface results in leaching-stable biocatalytic materials [406,407]. CNT-based biocatalysts have been employed successfully for *p*-cresol oxidation with hydrogen peroxide [404], transesterification [405], and hydrolysis [406]. Recent work has also emphasized biocatalysis with CNTs for enzyme-based biofuel cells [408], and encouraging results have been reported on the use of enzyme–CNT composites for electrocatalytic reduction (cathode) of oxygen [409] or electrocatalytic oxidation (anode) of ethanol [410].

9.5.10 CNTs and CNFs as Catalysts

As for most carbonaceous materials, in addition to their use as supports, CNTs or CNFs have been used as catalysts for some specific reactions, including methane decomposition to produce CO- and CO₂-free hydrogen [411], oxidative dehydrogenation of ethylbenzene to styrene [412–417] and of propane to propene [418], de-NO_x reactions [212,419], selective oxidation of H₂S [420,421], oxidation of aniline [422] and *p*-toluidine [423], catalytic wet air oxidation of phenol [424], esterification [425], and hydroxylation [426]. Nitrogen-doped CNTs have also been used as solid basic catalysts for Knoevenagel condensation [427]. The results obtained in these studies are discussed in detail in Chapter 6. Finally, the possibility of hydrogen generation via splitting of H₂O confined in SWCNTs by the use of a camera flash has been reported [428,429]. In this reaction, the camera flash induces an ultra-photothermal effect that makes it possible to reach high temperatures and causes the dissociation of water molecules into H₂ and O₂.

In summary, CNTs or CNFs offer some advantages as catalysts, due to (1) the possibility of building up macrostructured catalysts [387] that can satisfy the demands on pressure drop and mechanical strength; (2) the possibility of tuning catalyst morphology (e.g., CNTs, f-CNF, r-CNF) [417], surface chemistry [416,425], and composition [426], leading to better catalytic activity and/or selectivity; (3) their high surface area and mesoporosity, which can directly influence their activity as catalysts [419]; and (4) their good thermal stability in oxidizing atmospheres compared to that of activated carbons [420].

9.6 CONCLUSIONS

Even though large-scale industrial production of nanotubes or nanofibers is not now under way, the current synthesis processes for MCWNTs and CNFs permit

us to predict that this goal will be attained shortly. Although the production processes are more and more controlled, it is still very difficult to maintain homogeneity in all the features (i.e., structure, purity, etc.) of these materials, so that precise comparison between different samples of different origin can hardly be made. Progress on that matter should arise from a better understanding of the growth processes of CNTs and CNFs and from the control of catalyst synthesis and high-temperature activation. Additionally, the crucial aspects concerning standardization and toxicity of CNTs and CNFs should be addressed.

Concerning the preparation of supported catalysts, several methods have been used successfully, and the role of surface pretreatments, as in the case of activated carbon, as well as the influence of the structure (CNT or CNF) on the final metal dispersion has been demonstrated clearly [430,431]. A great variety of metals have been supported on CNTs and CNFs, and recent results suggest that enzymes can also be immobilized on CNTs and CNFs for enzymatic catalysis [432,433]. The possibility of shaping these nanomaterials offers some interesting perspectives, including for the design of structured microreactors [434]. Experimental as well as theoretical work would be necessary to have a better understanding of charge transfer phenomena and strength of metal–support interaction in catalytic systems involving CNTs and CNFs.

Catalytic studies conducted on CNT- or CNF-based systems have shown encouraging results in terms of activity and selectivity. In particular, high selectivity has been obtained on catalytic systems displaying different metal–support interaction and/or charge transfer phenomena than those evidenced on other supports, such as activated carbon or alumina. High activity values arise from the mesoporous nature of this support, which avoids mass transfer limitations. For electrocatalysis, which constitutes an important field of application, the combination of specific support morphology and electrical conductivity often allows us to reach high electrocatalytic activity.

Carbon nanotubes and nanofibers constitute a new family of support offering a good compromise between the advantages of activated carbon and high-surface-area graphite. The main advantages offered by CNT or CNF supports are: (1) the high purity of the material helps to avoid self-poisoning; (2) the mesoporous nature of these supports can be of interest for liquid-phase reactions, thus limiting the mass transfer; (3) the high thermal conductivity allows us to limit hot spots that can damage the catalyst; (4) their well-defined and tunable structure is advantageous; (5) their rich surface chemistry offers numerous perspectives for adsorption and dispersion of the active phase; and (6) specific metal–support interactions, due to the high electrical conductivity of the support and to the tunable orientation of the graphene layers, exist that can directly affect catalytic activity and selectivity.

Acknowledgments

I wish to express my particular thanks to my very active co-workers: Massimiliano Corrias, Aurore Morançais, Emmanuel Lamouroux, Régis Philippe, and

Filomena Gonçalves for their work, which has contributed significantly to this chapter.

REFERENCES

- [1] H.P. Boehm, *Carbon* 35 (1997) 581.
- [2] M. Monthoux, V.L. Kuznetsov, *Carbon* 44 (2006) 1621.
- [3] T.V. Hughes, C.R. Chambers, U.S. patent 405,480, 1889.
- [4] P. Schützenberger, L. Schützenberger, *C.R. Acad. Sci. Paris* 111 (1890) 774.
- [5] C. Pelabon, H. Pelabon, *C.R. Acad. Sci. Paris* 137 (1903) 706.
- [6] M. Hillert, N. Lange, *Zeitschr. Kristallogr.* 111 (1958) 24.
- [7] A. Oberlin, M. Endo, *J. Cryst. Growth* 32 (1976) 335.
- [8] P.G. Wiles, J. Abrahamson, *Carbon* 16 (1978) 341.
- [9] S. Iijima, *Nature* 354 (1991) 56.
- [10] S. Iijima, T. Ichihashi, *Nature* 363 (1993) 603.
- [11] M. Monthoux, P. Serp, E. Flahaut, C. Laurent, A. Peigney, M. Razafinimanana, W. Bacsa, J.-M. Broto, in B. Bhushan, Ed., *Springer Handbook of Nanotechnology*, 2nd rev. extend. Ed., Springer-Verlag, Heidelberg, Germany, 2007, pp. 43–112.
- [12] C.H. Bartholomew, *Catal. Rev. Sci. Eng.* 16 (1982) 67.
- [13] N.M. Rodriguez, *J. Mater. Sci.* 8 (1993) 3233.
- [14] A.C. Dupuis, *Prog. Mater. Sci.* 50 (2005) 929.
- [15] E. Lamouroux, P. Serp, P. Kalck, *Catal. Rev. Sci. Eng.* 49 (2007) 341.
- [16] V.K. Gupta, N.B. Pangannaya, *World Patent Inform.* 22 (2000) 185.
- [17] R. Philippe, A. Morançais, M. Corriás, B. Caussat, Y. Kihn, P. Kalck, D. Plee, P. Gaillard, D. Bernard, P. Serp, *Chem. Vapor Depos.* 13 (2007) 447.
- [18] J.M. Planeix, N. Coustel, B. Coq, V. Brotons, P.S. Kumbhar, R. Dutartre, P. Geneste, P. Bernier, P.M. Ajayan, *J. Am. Chem. Soc.* 116 (1994) 7935.
- [19] N.M. Rodriguez, M.S. Kim, R.T.K. Baker, *J. Phys. Chem.* 98 (1994) 108.
- [20] D. Moy, R. Hoch, WO 93/24214, to Hyperion Catalysis International Inc.
- [21] R.T.K. Baker, N.M. Rodriguez, U.S. patent 6,485,858,2000, to Catalytic Materials.
- [22] G.G. Wildgoose, C.E. Banks, R.G. Compton, *Small* 2 (2006) 182.
- [23] B. Coq, J.M. Planeix, V. Brotons, *Appl. Catal. A* 173 (1998) 175.
- [24] K.P. de Jong, *Curr. Opin. Solid State Mater. Sci.* 4 (1999) 55.
- [25] K.P. de Jong, J.W. Geus, *Catal. Rev. Sci. Eng.* 42 (2000) 481.
- [26] P. Serp, M. Corriás, P. Kalck, *Appl. Catal. A* 173 (2003) 337.
- [27] H.B. Zhang, G.D. Lin, Y.Z. Yuan, *Curr. Top. Catal.* 4 (2005) 1.
- [28] N.F. Goldshleger, *Fullerene Sci. Technol.* 9 (2001) 255.
- [29] R.J. Farrauto, C.H. Bartholomew, in *Fundamentals of Industrial Catalytic Processes*, Chapman and Hall, 1997.
- [30] J.L. Figueiredo, in *Progress in Catalyst Deactivation*, NATO Advanced Study Institute Series E, No. 54, M. Nijhoff, Boston, 1982.
- [31] G.F. Froment, *Rev. Chem. Eng.* 6 (1990) 293.

- [32] J.E. Hofer, E. Sterling, J.T. McCartney, *J. Phys. Chem.* 59 (1955) 1153, and references therein.
- [33] L.S. Lobo, D.L. Trimm, J.L. Figueiredo, in J.W. Hightower, Ed., *Proceedings of the 5th International Congress on Catalysis* Miami Beach, FL, 1972, Vol. 2, North-Holland, Amsterdam, 1973, p. 1125.
- [34] R.T.K. Baker, M.A. Barber, R.J. Waite, P.S. Harris, F.S. Feates, *J. Catal.* 26 (1972) 51.
- [35] D.L. Trimm, *Catal. Rev. Sci. Eng.* 16 (1977) 155.
- [36] R.T.K. Baker, P.S. Harris, in *Chemistry and Physics of Carbon*, Marcel Dekker, New York, 1978.
- [37] R.T.K. Baker, P.S. Harris, R.B. Thomas, R.J. Waite, *J. Catal.* 30 (1973) 86.
- [38] K. Liu, K. Jiang, C. Feng, Z. Chen, S. Fan, *Carbon* 43 (2005) 2850.
- [39] K.E. Kim, K.J. Kim, W.S. Jung, S.Y. Bae, J. Park, J. Choi, *Chem. Phys. Lett.* 401 (2005) 459.
- [40] V.V. Chesnokov, R.A. Buyanov, *Russ. Chem. Rev.* 69 (2000) 623.
- [41] M.S. Hoogegeeraad, Ph.D. dissertation, Utrecht University, The Netherlands, 1995.
- [42] I. Alstrup, *J. Catal.* 109 (1988) 241.
- [43] J. Rostrup-Nielsen, D.L. Trimm, *J. Catal.* 48 (1977) 155.
- [44] R.T. Yang, J.P. Chen, *J. Catal.* 115 (1989) 52.
- [45] H.J. Grabke, *Mater. Corros.* 49 (1998) 303.
- [46] P. Szakalos, *Mater. Corros.* 54 (2003) 752.
- [47] Z. Zeng, K. Natesan, *Chem. Mater.* 17 (2005) 3794.
- [48] C. Prados, P. Crespo, J.M. Gonzalez, A. Hernando, J.F. Marco, R. Gancedo, N. Grobert, M. Terrones, H.W. Kroto, *Phys. Rev. B* 65 (2002) 113405.
- [49] H. Kim, W. Sigmund, *Carbon* 43 (2005) 1743.
- [50] H. Kim, W. Sigmund, *J. Cryst. Growth* 276 (2005) 594.
- [51] R.T.K. Baker, J.R. Alonso, J.A. Dumesic, D.J.C. Yates, *J. Catal.* 77 (1982) 74.
- [52] N.M. Rodriguez, M.S. Kim, R.T.K. Baker, *J. Catal.* 140 (1993) 16.
- [53] A.R. Harutyunyan, T. Tokune, E. Mora, *Appl. Phys. Lett.* 86 (2005) 153113.
- [54] C.P. Deck, K. Vecchio, *Carbon* 44 (2006) 267.
- [55] M.J. Height, J.B. Howard, J.W. Tester, J.B. Vander Sande, *J. Phys. Chem. B* 109 (2005) 12337.
- [56] A. Moisala, A.G. Nasibulin, E.I. Kauppinen, *J. Phys. Condens. Matter* 15 (2003) S3011.
- [57] F. Abild-Pedersen, J.K. Nørskov, J.R. Rostrup-Nielsen, J. Sehested, S. Helveg, *Phys. Rev. B* 73 (2006) 115419.
- [58] Y.A. Zhu, Y.C. Dai, D. Chen, W.K. Yuan, *Surf. Sci.* 601 (2007) 1319.
- [59] S. Helveg, C. López-Cartes, J. Sehested, P.L. Hansen, B.S. Clausen, J.R. Rostrup-Nielsen, F. Abild-Pedersen, J.K. Nørskov, *Nature* 427 (2004) 426.
- [60] V.L. Kuznetsov, A.N. Usoltseva, A.L. Chuvilin, E.D. Obraztsova, J.M. Bonard, *Phys. Rev. B* 64 (2001) 235401.
- [61] V.L. Kuznetsov, A.N. Usoltseva, Y.V. Butenko, *Kinet. Catal.* 44 (2003) 726.

- [62] S. Hofmann, R. Sharma, C. Ducati, G. Du, C. Mattevi, C. Cepek, M. Cantoro, S. Pisana, A. Parvez, F. Cervantes-Sodi, A.C. Ferrari, R. Dunin-Borkowski, S. Lizzit, L. Petaccia, A. Goldoni, J. Robertson, *Nano Lett.* 7 (2007) 602.
- [63] N.I. Alekseev, *Tech. Phys.* 49 (2004) 1166.
- [64] Y. Shibuta, S. Maruyama, *Comput. Mater. Sci.* 39 (2007) 842.
- [65] R.B. Little, *J. Clust. Sci.* 14 (2003) 135.
- [66] J.W. Snoeck, G.F. Froment, M. Fowles, *J. Catal.* 169 (1997) 240.
- [67] S. Amelinckx, X.B. Zhang, D. Bernaerts, X.F. Zhang, V. Ivanov, J.B. Nagy, *Science* 265 (1994) 635.
- [68] V.L. Kuznetsov, in S. Guceri, Ed., *Nanoengineered Nanofibrous Materials: Proceedings of the Nato ASI on Nanoengineered and Nanofibrous Materials*, Kluwer Academic, Dordrecht, The Netherlands, 2004, p. 19.
- [69] M. Lin, J.P.Y. Tan, C. Boothroyd, K.P. Loh, E.S. Tok, Y.L. Foo, *Nano Lett.* 7 (2007) 2234.
- [70] K.B.K. Teo, C. Singh, M. Chhowalla, W.I. Milne, in H.S. Nalwa, Ed., *Encyclopedia of Nanotechnology*, Vol. 1, American Scientific Publishers, Valencia, CA, 2003, p. 665.
- [71] J.Y. Raty, F. Gygi, G. Galli, *Phys. Rev. Lett.* 95 (2005) 096103.
- [72] T. Iwasaki, G. Zhong, T. Aikawa, T. Yoshida, H. Kawarada, *J. Phys. Chem. B* 109 (2005) 19556.
- [73] S.H. Lee, E. Ruckenstein, *J. Catal.* 107 (1987) 23.
- [74] Y.A. Zhu, Z.J. Sui, T.J. Zhao, Y.C. Dai, Z.M. Cheng, W.K. Yuan, *Carbon* 43 (2005) 1694.
- [75] K. Behler, S. Osswald, H. Ye, S. Dimovski, Y. Gogotsi, *J. Nanopart. Res.* 8 (2006) 615.
- [76] J.E. Fischer, A.T. Johnson, *Curr. Opin. Solid State Mater. Sci.* 4 (1999) 28.
- [77] J.P. Issi, J.C. Charlier, in K. Tanaka, T. Yamabe, K. Fukui, Ed., *The Science and Technology of Carbon Nanotubes*, Elsevier, Amsterdam, 1999, p. 107.
- [78] C.A. Bessel, K. Laubernds, N.M. Rodriguez, R.T.K. Baker, *J. Phys. Chem.* 105 (2001) 1115.
- [79] T. Dumitrica, C.M. Landis, B.I. Yakobson, *Chem. Phys. Lett.* 360 (2002) 182.
- [80] J.C. Charlier, *Acc. Chem. Res.* 35 (2002) 1063.
- [81] M. Menon, A.N. Andriotis, G.E. Froudakis, *Chem. Phys. Lett.* 320 (2000) 425.
- [82] S. Park, D. Srivastava, K. Cho, *Nano Lett.* 3 (2003) 1273.
- [83] G. Mpourmpakis, G.E. Froudakis, A.N. Andriotis, M.E. Menon, *Appl. Phys. Lett.* 87 (2005) 193105.
- [84] H.C. Choi, M. Shim, S. Bangsaruntip, H. Dai, *J. Am. Chem. Soc.* 124 (2002) 9059.
- [85] A. Maiti, A. Ricca, *Chem. Phys. Lett.* 395 (2004) 7.
- [86] J. Zhong, G.M. Stocks, *Appl. Phys. Lett.* 87 (2005) 133105.
- [87] W. Chen, X. Pan, M.G. Willinger, D.S. Su, X. Bao, *J. Am. Chem. Soc.* 129 (2007) 7421.
- [88] Q.H. Yang, P.X. Hou, S. Bai, M.Z. Wang, H.M. Cheng, *Chem. Phys. Lett.* 345 (2001) 18.
- [89] S. Inoue, N. Ichikuni, T. Suzuki, T. Uematsu, K. Kaneko, *J. Phys. Chem.* 102 (1998) 4689.

- [90] M. Eswaramoorthy, R. Sen, C.N.R. Rao, *Chem. Phys. Lett.* 304 (1999) 207.
- [91] E. Raymundo-Piñero, P. Azaïs, T. Cacciaguerra, D. Cazorla-Amorós, A. Linares-Solano, F. Béguin, *Carbon* 43 (2005) 786.
- [92] E. Raymundo-Piñero, T. Cacciaguerra, P. Simon, F. Béguin, *Chem. Phys. Lett.* 412 (2005) 184.
- [93] Z. Chen, W. Thiel, A. Hirsch, *ChemPhysChem* 1 (2003) 93.
- [94] S. Park, D. Srivastava, K. Cho, *Nano Lett.* 3 (2003) 1273.
- [95] X. Lu, Z. Chen, P. Schleyer, *J. Am. Chem. Soc.* 127 (2005) 20.
- [96] H. Ulbricht, G. Moos, T. Hertel, *Phys. Rev. B* 66 (2002) 075404-1.
- [97] H. Ulbricht, G. Kriebel, G. Moos, T. Hertel, *Chem. Phys. Lett.* 363 (2002) 252.
- [98] E. Díaz, S. Ordóñez, A. Vega, *J. Colloid Interface Sci.* 305 (2007) 7.
- [99] R. Pagani, *C&EN* 1 (1999) 31.
- [100] M.M.J. Treacy, T.W. Ebbesen, J.M. Gibson, *Nature* 381 (1996) 678.
- [101] R.P. Gao, Z.L. Wang, Z.G. Bai, W.A. de Heer, L.M. Dai, M. Gao, *Phys. Rev. Lett.* 85 (2000) 622.
- [102] M.F. Yu, O. Lourie, M.J. Dyer, K. Moloni, T.F. Keley, R.S. Ruoff, *Science* 287 (2000) 637.
- [103] J.H. Bitter, in D.Y. Murzin, Ed., *Nanocatalysis*, Research Signpost, Kerala, India, 2006, p. 99.
- [104] C. Park, R.T.K. Baker, *J. Phys. Chem. B* 103 (1999) 2453.
- [105] D. Moy, C.M. Niu, H. Tennent, U.S. patent to Hyperion Catalysis, WO 97/43116.
- [106] B. Mateusz, B. Bryning, D.E. Milkie, M.F. Islam, L.A. Hough, J.M. Kikkawa, A.G. Yodh, *Adv. Mater.* 19 (2007) 661.
- [107] G.G. Kuvshinov, Y.I. Mogilnykh, D.G. Kuvshinov, D.Y. Yermakov, M.A. Yermakova, A.N. Salanov, N.A. Rudina, *Carbon* 37 (1999) 1239.
- [108] M.K. van der Lee, A.J. van Dillen, J.W. Geus, K.P. de Jong, J.H. Bitter, *Carbon* 44 (2006) 629.
- [109] J.K. Chinthaginjala, K. Seshan, L. Lefferts, *Ind. Eng. Chem. Res.* 46 (2007) 3968.
- [110] M.J. Ledoux, C. Pham-Huu, *Catal. Today* 102–103 (2005) 2.
- [111] C. Pham-Huu, R. Viera, B. Louis, A. Carvalho, J. Amadou, T. Dintzer, M.J. Ledoux, *J. Catal.* 204 (2006) 194.
- [112] P. Li, T. Li, J.H. Zhou, Z.J. Sui, Y.C. Dai, W.K. Yuan, D. Chen, *Micropor. Mesopor. Mater.* 95 (2006) 1.
- [113] C.C. Chen, C.F. Chen, C.H. Hsu, I.H. Li, *Diamond Relat. Mater.* 14 (2005) 770.
- [114] S.S. Tzeng, K.H. Hung, T.H. Ko, *Carbon* 44 (2006) 859.
- [115] N. Keller, G. Rebmann, E. Barraud, O. Zahraa, V. Keller, *Catal. Today* 101 (2005) 323.
- [116] R.Z. Ismagilov, V.N. Shikina, N.V. Kruchinin, A.N. Rudina, A.V. Ushakov, T.N. Vasenin, J.H. Veringa, *Catal. Today* 102–103 (2005) 85.
- [117] N.A. Jarrah, F. Li, J.G. Van Ommen, L. Lefferts, *J. Mater. Chem.* 15 (2005) 1946.
- [118] N. Jarrah, J.G. van Ommen, L. Lefferts, *J. Catal.* 239 (2006) 460.
- [119] P. Tribollet, L.K. Minsker, *Catal. Today* 102–103 (2005) 15.
- [120] N. Jarrah, J.G. Van Ommen, L. Lefferts, *Catal. Today* 79–80 (2003) 29.
- [121] E. García-Bordejé, I. Kvande, D. Chen, M. Ronning, *Adv. Mater.* 18 (2006) 1589.

- [122] C. Pham-Huu, M.J. Ledoux, *Top. Catal.* 40 (2006) 49.
- [123] R. Smajda, A. Kukovecz, Z. Kónya, I. Kiricsi, *Carbon* 45 (2007) 1176.
- [124] E. Auer, A. Freund, J. Pietsch, T. Tacke, *Appl. Catal. A* 173 (1998) 259.
- [125] K. Lee, J. Zhang, H. Wang, D.P. Wilkinson, *J. Appl. Electrochem.* 36 (2006) 507.
- [126] T. Sainsbury, D. Fitzmaurice, *Chem. Mater.* 16 (2004) 3780.
- [127] M. Bottini, A. Magrini, M.I. Dawson, A. Bergamaschi, T. Mustelin, *Carbon* 44 (2006) 1301.
- [128] Z.C. Di, J. Ding, X.J. Peng, Y.H. Li, Z.K. Luan, J. Liang, *Chemosphere* 62 (2006) 861.
- [129] S.F. Yin, B.Q. Xu, S.J. Wang, C.F. Ng, C.T. Au, *Catal. Lett.* 96 (2004) 113.
- [130] Z. Sun, X. Zhang, N. Na, Z. Liu, B. Han, G. An, *J. Phys. Chem. B* 110 (2006) 13410.
- [131] S. Ravindran, G.T.S. Andavan, C. Ozkan, *Nanotechnology* 17 (2006) 723.
- [132] J. Xie, V.K. Varadan, *Mater. Chem. Phys.* 91 (2005) 274.
- [133] D.B. Farmer, R.G. Gordon, *Nano Lett.* 6 (2004) 699.
- [134] X. Huang, C. Pan, X. Huang, *Mater. Lett.* 61 (2007) 934.
- [135] Y. Yu, L.L. Ma, W.Y. Huang, J.L. Li, P.K. Wong, J.C. Yu, *J. Solid State Chem.* 178 (2005) 1488.
- [136] L. Qiu, V.G. Pol, Y. Wei, A. Gedanken, *New J. Chem.* 28 (2004) 1056.
- [137] L. Jiang, L. Gao, *J. Mater. Chem.* 15 (2005) 260.
- [138] F. Wang, S. Arai, K.C. Park, K. Takeuchi, Y.J. Kim, M. Endo, *Carbon* 44 (2006) 1307.
- [139] L. Ma, W.X. Chen, Z.D. Xu, J.B. Xia, X. Li, *Nanotechnology* 17 (2006) 571.
- [140] H. Lee, S.W. Yoon, E.J. Kim, J. Park, *Nano Lett.* 7 (2007) 778.
- [141] J. Du, L. Fu, Z. Liu, B. Han, Z. Li, Y. Liu, Z. Sun, D. Zhu, *J. Phys. Chem. B* 109 (2005) 12772.
- [142] C. Li, Y. Tang, K. Yao, F. Zhou, Q. Ma, H. Lin, M. Tao, J. Liang, *Carbon* 44 (2006) 2021.
- [143] Q. Li, B. Sun, I.A. Kinloch, D. Zhi, H. Sirringhaus, A.H. Windle, *Chem. Mater.* 18 (2006) 164.
- [144] S. Banerjee, S.S. Wong, *J. Am. Chem. Soc.* 125 (2003) 10342.
- [145] Y. Luo, P. Wang, L.P. Ma, H.M. Cheng, *Scr. Mater.* 56 (2007) 765.
- [146] C.P. Baldé, B.P.C. Hereijgers, J.H. Bitter, K.P. de Jong, *Angew. Chem. Int. Ed.* 45 (2006) 3501.
- [147] S.H. Yang, W.H. Shin, J.W. Lee, S.Y. Kim, S.I. Woo, J.K. Kang, *J. Phys. Chem. B* 110 (2005) 13941.
- [148] D. Tasis, N. Tagmatarchis, A. Bianco, M. Prato, *Chem. Rev.* 106 (2006) 1105.
- [149] T.G. Ros, A.G. van Dillen, J.W. Geus, D.C. Koningsberger, *Chem. Eur. J.* 5 (2002) 1151.
- [150] N. Zhao, C. He, Z. Jiang, J. Li, Y. Li, *Mater. Lett.* 61 (2007) 681.
- [151] B.C. Satishkumar, A. Govindaraj, G. Mofokeng, G.N. Subbanna, C.N.R. Rao, *J. Phys. B* 29 (1996) 4925.
- [152] S. Banerjee, S.S. Wong, *J. Am. Chem. Soc.* 126 (2004) 2073.

- [153] S. Agrawal, M.S. Raghuveer, H. Li, G. Ramanath, *Appl. Phys. Lett.* 90 (2007) 193104.
- [154] W. Li, C. Gao, H. Qian, J. Ren, D. Yan, *J. Mater. Chem.* 16 (2006) 1852.
- [155] G. Maurin, I. Stepanek, P. Bernier, J.F. Colomer, J.B. Nagy, F. Henn, *Carbon* 39 (2001) 1273.
- [156] N. Pierard, A. Fonseca, Z. Kónya, I. Willem, G. van Tendeloo, J.B. Nagy, *Chem. Phys. Lett.* 335 (2001) 1.
- [157] Y. Xing, L. Li, C.C. Chusuei, R.V. Hull, *Langmuir* 21 (2005) 4185.
- [158] A. Kusnetzova, I. Popova, J.T. Yates, M.J. Bronikowski, C.D. Huffman, J. Liu, R.E. Smalley, H.H. Hwu, J.G. Chen, *J. Am. Chem. Soc.* 123 (2001) 10699.
- [159] T. Kyotani, S. Nakazaki, W.H. Xu, A. Tomita, *Carbon* 39 (2001) 771.
- [160] M.L. Toebe, J.M.P. van Heeswijk, J.H. Bitter, A.J. van Dillen, K.P. de Jong, *Carbon* 42 (2004) 307.
- [161] G. Ovejero, J.L. Sotelo, M.D. Romero, A. Rodriguez, M.A. Ocaña, G. Rodriguez, J. Garcia, *Ind. Eng. Chem. Res.* 45 (2006) 2206.
- [162] Z. Liu, X. Lin, J.Y. Lee, W. Zhang, M. Han, L.M. Gan, *Langmuir* 18 (2002) 4054.
- [163] J.L. Hudson, M.J. Casavant, J.M. Tour, *J. Am. Chem. Soc.* 126 (2004) 11158.
- [164] J.J. Stephenson, J.L. Hudson, S. Azad, J.M. Tour, *Chem. Mater.* 18 (2006) 374.
- [165] R.V. Hull, L. Li, Y. Xing, C.C. Chusuei, *Chem. Mater.* 18 (2006) 1780.
- [166] A. Zamudio, A.L. Elfas, J.A. Rodríguez-Manzo, F. Lopez-Urías, G. Rodríguez-Gattorno, F. Lupo, M. Rühle, D.J. Smith, H. Terrones, D. Diaz, M. Terrones, *Small* 2 (2006) 346.
- [167] F. Barroso-Bujans, J.L.G. Fierro, S. Rojas, S. Sánchez-Cortes, M. Arroyo, M.A. López-Manchado, *Carbon* 45 (2007) 1669.
- [168] S. Delpeux, K. Szostak, E. Frakowiak, F. Béguin, *Chem. Phys. Lett.* 400 (2005) 374.
- [169] R. Verdejo, S. Lamoriniere, B. Cottam, A. Bismarck, M. Shaffer, *Chem. Commun.* 2007 513.
- [170] B.C. Satishkumar, A. Govindaraj, G. Mofokeng, G.N. Subbanna, C.N.R. Rao, *J. Phys. B* 29 (1996) 4925.
- [171] X. Lu, F. Tian, Y. Feng, X. Xu, N. Wang, Q. Zhang, *Nano Lett.* 2 (2002) 1325.
- [172] W. Xia, V. Hagen, S.S. Kundu, Y. Wang, C. Somsen, G. Eggeler, G. Sun, G. Grundmeier, M. Stratmann, M. Muhler, *Adv. Mater.* 19 (2007) 3648.
- [173] Z. Kónya, J. Zhu, K. Niesz, D. Mehn, I. Kiricsi, *Carbon* 42 (2004) 2001.
- [174] A. Kukovecz, T. Kanyó, Z. Kónya, I. Kiricsi, *Carbon* 43 (2005) 994.
- [175] R. Bacsa, P. Serp, in M. Monthoux, Ed., *Carbon Metatubes*, Wiley, Weinheim, Germany, 2009, in preparation.
- [176] V. Georgakilas, D. Gournis, V. Tzitzios, L. Pasquato, D.M. Guldi, M. Prato, *J. Mater. Chem.* 17 (2007) 2679.
- [177] S. Hermans, J. Sloan, D.S. Shepard, B.F.G. Johnson, M.L.H. Green, *Chem. Commun.* (2002) 276.
- [178] X. Li, I.M. Hsing, *Electrochem. Acta* 51 (2006) 5250.
- [179] G. An, P. Yu, L. Mao, Z. Sun, Z. Liu, S. Miao, Z. Miao, K. Ding, *Carbon* 45 (2007) 536.

- [180] R. Zanella, E.V. Basiuk, P. Santiago, V.A. Basiuk, E. Mireles, I. Puente-Lee, J.M. Saniger, *J. Phys. Chem. B* 109 (2005) 16290.
- [181] Y. Wang, X. Xu, Z. Tian, Y. Zong, H. Cheng, C. Lin, *Chem. Eur. J.* 12 (2006) 2542.
- [182] W. Li, C. Gao, H. Qian, J. Ren, D. Yan, *J. Mater. Chem.* 16 (2006) 1852.
- [183] P. Serp, P. Kalck, R. Feurer, *Chem. Rev.* 102 (2002) 3085.
- [184] W. Xia, O.F.K. Schlüter, C. Liang, M.W.E. van den Berg, M. Guraya, M. Muhler, *Catal. Today* 102–103 (2005) 34.
- [185] C. Liang, W. Xia, H. Soltani-Ahmadi, O.F.K. Schlüter, R.A. Fischer, M. Muhler, *Chem. Commun.* (2005) 282.
- [186] J.D. Kim, B.S. Kang, T.W. Noh, J.G. Yoon, S.I. Baik, Y.W. Kim, *J. Electrochem. Soc.* 152 (2005) D23.
- [187] H. Liu, C. Song, L. Zhang, J. Zhang, H. Wang, D.P. Wilkinson, *J. Power Source* 155 (2006) 95.
- [188] X. Fu, H. Yu, F. Peng, H. Wang, Y. Qian, *Appl. Catal. A* 321 (2007) 190.
- [189] M.L. Toebes, F.F. Prinsloo, J.H. Bitter, A.J. van Dillen, K.P. de Jong, *J. Catal.* 214 (2003) 78.
- [190] W.Z. Li, C. Liang, Z. Feng, P. Ying, D. Wang, C. Li, *J. Mol. Catal. A* 211 (2004) 103.
- [191] L. Li, Z.H. Zhu, Z.F. Yan, G.Q. Lu, L. Rintoul, *Appl. Catal. A* 320 (2007) 166.
- [192] S.J. Wang, S.F. Yin, L. Li, B.Q. Xu, C.F. Ng, C.T. Au, *Appl. Catal. B* 52 (2004) 287.
- [193] W. Yang, S. Yang, J. Guo, G. Sun, Q. Xin, *Carbon* 45 (2007) 397.
- [194] C. Amorim, G. Yuan, P.M. Patterson, M.A. Keane, *J. Catal.* 234 (2005) 268.
- [195] R.B. Rakhi, A. Leela Mohana Reddy, M.M. Shajumon, K. Sethupathi, S. Ramaprabhu, *J. Nanopart. Res.* 10 (2008) 179.
- [196] A. Corma, H. Garcia, A. Leyva, *J. Mol. Catal. A* 230 (2005) 97.
- [197] B. Pawelec, V. La Parola, R.M. Navarro, S. Murcia-Mascarós, J.L.G. Fierro, *Carbon* 44 (2006) 84.
- [198] E. Asedegbega-Nieto, A. Guerrero-Ruiz, I. Rodríguez-Ramos, *Carbon* 44 (2006) 804.
- [199] H. Ma, L. Wang, L. Chen, C. Dong, W. Yu, T. Huang, Y. Qian, *Catal. Commun.* 8 (2007) 452.
- [200] M.L. Toebes, Y. Zhang, J. Hájek, T.A. Nijhuis, J.H. Bitter, A.J. van Dillen, D.Y. Murzin, D.C. Koninsberger, K.P. de Jong, *J. Catal.* 226 (2004) 215.
- [201] R.T.K. Baker, N. Rodriguez, A. Mastalir, U. Wild, R. Schlögl, A. Wootsch, Z. Paál, *J. Phys. Chem. B* 108 (2004) 14348.
- [202] A. Kongkanand, K. Vinodgopal, S. Kuwabata, P.V. Kamat, *J. Phys. Chem. B* 110 (2006) 16185.
- [203] J. Prabhuram, T.S. Zhao, Z.K. Tang, R. Chen, Z.X. Liang, *J. Phys. Chem. B* 110 (2006) 5245.
- [204] W. Li, X. Wang, Z. Chen, M. Waje, Y. Yan, *J. Phys. Chem. B* 110 (2006) 15353.
- [205] Z. Park, R.T.K. Baker, *J. Phys. Chem. B* 102 (1998) 5168.
- [206] M.K. van der Lee, A.J. van Dillen, J.H. Bitter, K.P. de Jong, *J. Am. Chem. Soc.* 127 (2005) 13573.

- [207] W. Wang, P. Serp, P. Kalck, J.L. Faria, *Appl. Catal. B* 56 (2005) 305.
- [208] H. Zhang, J. Qiu, C. Liang, Z. Li, X. Wang, Y. Wang, Z. Feng, C. Li, *Catal. Lett.* 101 (2005) 211.
- [209] G. Leendert Bezemer, P.B. Radstake, V. Koot, A.J. van Dillen, J.W. Geus, K.P. de Jong, *J. Catal.* 237 (2006) 291.
- [210] G. Leendert Bezemer, J.H. Bitter, H.P.C.E. Kuipers, H. Oosterbeek, J.E. Holewijn, X. Xu, F. Kaptjein, A.J. van Dillen, K.P. de Jong, *J. Am. Chem. Soc.* 128 (2006) 3956.
- [211] F. Winter, G. Leendert Bezemer, C. van der Spek, J.D. Meeldijk, A.J. van Dillen, J.W. Geus, K.P. de Jong, *Carbon* 43 (2006) 327.
- [212] J.Z. Luo, L.Z. Gao, Y.L. Leung, C.T. Au, *Catal. Lett.* 66 (2000) 91.
- [213] R. Giordano, P. Serp, P. Kalck, Y. Kihn, J. Schreiber, C. Marhic, J.L. Duvail, *Eur. J. Inorg. Chem.* (2003) 610.
- [214] R. Gao, C.D. Tan, R.T.K. Baker, *Catal. Today* 65 (2001) 19.
- [215] S. Banerjee, S.S. Wong, *Nano Lett.* 2 (2002) 49.
- [216] S. Banerjee, S.S. Wong, *J. Am. Chem. Soc.* 124 (2002) 8940.
- [217] Y. Zhang, H.B. Zhang, G.D. Lin, P. Chen, Y.Z. Yuan, K.R. Tsai, *Appl. Catal. A* 187 (1999) 213.
- [218] L. Lemus-Yegres, I. Such-Basáñez, C. Salinas-Martínez de Lecea, P. Serp, M.C. Román-Martínez, *Carbon* 44 (2006) 605.
- [219] H.B. Xu, H.Z. Chen, M.M. Shi, R. Bai, M. Wang, *Mater. Chem. Phys.* 94 (2005) 342.
- [220] Y. Liu, A. Adronov, *Macromolecules* 37 (2004) 4755.
- [221] F. Frehill, J.G. Vos, S. Benrezzak, A.A. Koós, Z. Kónya, M.G. Ruther, W.J. Blau, A. Fonseca, J.B. Nagy, L.P. Biró, A.I. Minett, M. in het Panhuis, *J. Am. Chem. Soc.* 124 (2002) 13694.
- [222] C. Baleizão, B. Gigante, H. Garcia, A. Corma, *J. Catal.* 221 (2004) 77.
- [223] S. Park, S.W. Yoon, K.B. Lee, D.J. Kim, Y.H. Jung, Y. Do, H.J. Paik, I.S. Choi, *Macromol. Rapid Commun.* 27 (2006) 47.
- [224] K. Wiemann, W. Kaminski, F.H. Gojny, K. Schulte, *Macromol. Chem. Phys.* 206 (2005) 1472.
- [225] S. Bredeau, L. Boggioni, F. Bertini, I. Tritto, F. Monteverde, M. Alexandre, P. Dubois, *Macromol. Rapid Commun.* 28 (2007) 822.
- [226] Z. Yinghuai, S.L.P. Sia, K. Carpenter, F. Kooli, R.A. Kemp, *J. Phys. Chem. Solids* 67 (2006) 1218.
- [227] T.G. Ros, A.J. van Dillen, G.W. Geus, D.C. Koningsberger, *Chem. Eur. J.* 8 (2002) 2868.
- [228] F. Mercuri, A. Sgamelloti, *J. Phys. Chem. B* 110 (2006) 15291.
- [229] E.L. Sceats, J.C. Green, *J. Chem. Phys.* 125 (2006) 154704-1.
- [230] F. Nunzi, F. Mercuri, A. Sgamelloti, *J. Phys. Chem. B* 106 (2002) 10622.
- [231] Y.V. Naidich, V.M. Perevertailo, O.B. Loginova, *Izv. Akad. Nauk. SSSR. Met.* 4 (1979) 37.
- [232] Y. Okamoto, *Chem. Phys. Lett.* 407 (2005) 354.
- [233] I.D. Rosca, F. Watari, M. Uo, T. Akasaka, *Carbon* 43 (2005) 3124.

- [234] H. Hu, P. Bhomwmik, B. Zhao, M.A. Hamon, M.E. Itkis, R.C. Haddon, *Chem. Phys. Lett.* 345 (2001) 25.
- [235] C. Park, R.T.K. Baker, *J. Phys. Chem. B* 103 (1999) 2453.
- [236] A. Chambers, T. Nemes, N.M. Rodriguez, R.T.K. Baker, *J. Phys. Chem. B* 102 (1998) 2251.
- [237] C. Park, R.T.K. Baker, *J. Phys. Chem. B* 102 (1998) 5168.
- [238] M. Zhou, G. Lin, H. Zhang, *Chin. J. Catal.* 28 (2007) 210.
- [239] T.G. Ros, D.E. Keller, A.J. van Dillen, J.W. Geus, D.C. Koningsberger, *J. Catal.* 211 (2002) 85.
- [240] M. Takasaki, Y. Motoyama, K. Higashi, S.H. Yoon, I. Mochida, H. Nagashima, *Chem. Asian J.* 2 (2007) 1524.
- [241] T. Onoe, S. Iwamoto, M. Inoue, *Catal. Commun.* 8 (2007) 701.
- [242] L.J. Lemus-Yegres, M.C. Román-Martínez, I. Such-Basáñez, C. Salinas-Martínez de Lecea, *Micropor. Mesopor. Mater.* 109 (2008) 305.
- [243] W. Xia, O.F.K. Schüller, C. Liang, M.W.E. van den Berg, M. Guraya, M. Muhler, *Catal. Today* 102–103 (2005) 34.
- [244] A.M. Zhang, J.L. Dong, Q.H. Xu, H.K. Rhee, X.L. Li, *Catal. Today* 93–95 (2004) 347.
- [245] C. Park, M.A. Keane, *J. Colloid Interface Sci.* 266 (2003) 183.
- [246] H. Wang, F. Zhao, S.I. Fujita, M. Arai, *Catal. Commun.* 9 (2008) 362.
- [247] B. Yoon, C.M. Wai, *J. Am. Chem. Soc.* 127 (2005) 17174.
- [248] C.H. Li, Z.X. Yu, K.F. Yao, S.F. Ji, J. Liang, *J. Mol. Catal. A* 226 (2005) 101.
- [249] Y. Zhao, C.H. Li, Z.X. Yu, K.F. Yao, S.F. Ji, J. Liang, *Mater. Chem. Phys.* 103 (2007) 225.
- [250] X.X. Han, Q. Chen, R.X. Zhou, *J. Mol. Catal. A* 277 (2007) 210.
- [251] S.J. Wang, W.X. Zhu, D.W. Liao, C.F. Ng, C.T. Au, *Catal. Today* 93–95 (2004) 711.
- [252] C.Y. Hu, F.Y. Li, L. Hua, R.B. Zhang, *J. Serb. Chem. Soc.* 71 (2006) 1153.
- [253] M. Ruta, I. Yuranov, P.J. Dyson, G. Laurenczy, L. Kiwi-Minsker, *J. Catal.* 247 (2007) 269.
- [254] V.V. Chesnokov, I.P. Prosvirin, N.A. Zaitseva, V.I. Zaikovskii, V.V. Molchanov, *Kinet. Catal.* 43 (2002) 838.
- [255] L. Xing, F. Du, J.J. Liang, Y.S. Chen, Q.L. Zhou, *J. Mol. Catal. A* 276 (2007) 191.
- [256] F. Salman, C. Park, R.T.K. Baker, *Catal. Today* 53 (1999) 385.
- [257] V. Lordi, N. Yao, J. Wei, *Chem. Mater.* 13 (2001) 733.
- [258] C. Pham-Huu, N. Keller, L.J. Charbonniere, R. Ziessel, M.J. Ledoux, *Chem. Commun.* (2000) 1871.
- [259] C. Pham-Huu, N. Keller, G. Ehret, L.J. Charbonniere, R. Ziessel, M.J. Ledoux, *J. Mol. Catal. A* 170 (2001) 155.
- [260] J.P. Tessonnier, L. Pesant, G. Ehret, M.J. Ledoux, C. Pham-Huu, *Appl. Catal. A* 288 (2005) 203.
- [261] I. Janowska, G. Winé, M.J. Ledoux, C. Pham-Huu, *J. Mol. Catal.* 267 (2007) 92.
- [262] M.L. Toebe, T.A. Nijhuis, J. Hajek, J.H. Bitter, A.J. van Dillen, D.Y. Murzin, K.P. de Jong, *Chem. Eng. Sci.* 60 (2005) 5682.

- [263] V. Brotons, B. Coq, J.M. Planeix, *J. Mol. Catal. A* 116 (1997) 397.
- [264] Y. Li, Z.G. Li, R.X. Zhou, *J. Mol. Catal. A* 279 (2008) 140.
- [265] Y. Li, G.H. Lai, R.X. Zhou, *Appl. Surf. Sci.* 253 (2007) 4978.
- [266] H. Vu, F. Gonçalves, R. Philippe, E. Lamouroux, M. Corrias, Y. Kihn, D. Plee, P. Kalck, P. Serp, *J. Catal.* 240 (2006) 18.
- [267] J. Qiu, H. Zhang, X. Wang, H. Han, C. Liang, C. Li, *React. Kinet. Catal. Lett.* 88 (2006) 269.
- [268] P. Gallezot, D. Richard, *Catal. Rev. Sci. Eng.* 40 (1998) 81.
- [269] E. van Steen, F.F. Prinsloo, *Catal. Today* 71 (2002) 327.
- [270] G. Leendert Bezemer, U. Falke, A.J. van Dillen, K.P. de Jong, *Chem. Commun.* (2005) 731.
- [271] G. Leendert Bezemer, P.B. Radstake, U. Falke, H. Oosterbeek, H.P.C.E. Kuipers, A.J. van Dillen, K.P. de Jong, *J. Catal.* 237 (2006) 152.
- [272] M.C. Bahome, L.L. Jewell, D. Hildebrandt, D. Glasser, N.J. Coville, *Appl. Catal. A* 287 (2005) 60.
- [273] L. Guczi, G. Stefler, O. Geszti, Z. Koppány, Z. Kónya, É. Molnár, M. Urbán, I. Kiricsi, *J. Catal.* 244 (2006) 24.
- [274] Y.H. Chin, J. Hu, C. Cao, Y. Gao, Y. Wang, *Catal. Today* 110 (2005) 47.
- [275] X. Dong, H.B. Zhang, G.D. Lin, Y.Z. Yuan, K.R. Tsai, *Catal. Lett.* 85 (2003) 237.
- [276] J. Wang, H.B. Chen, H. He, Y. Cai, J.D. Lin, J. Yi, H.B. Zhang, D.W. Liao, *Chin. Chem. Lett.* 13 (2002) 1217.
- [277] H.B. Zhang, X. Dong, G.D. Lin, X.L. Liang, H.Y. Li, *Chem. Commun.* (2005) 5094.
- [278] L. Huang, W. Chu, J. Hong, S. Luo, *Chin. J. Catal.* 27 (2006) 596.
- [279] F.J. Gomez, R.J. Chen, D. Wang, R.M. Waymouth, H. Dai, *Chem. Commun.* (2003) 190.
- [280] Y. Liu, A. Adronov, *Macromolecules* 37 (2004) 4755.
- [281] Y. Xu, C. Gao, H. Kong, D. Yan, Y.Z. Jin, P.C.P. Watts, *Macromolecules* 37 (2004) 8846.
- [282] S. Qin, D. Qin, W.T. Ford, D.E. Resasco, J.E. Herrera, *J. Am. Chem. Soc.* 126 (2004) 170.
- [283] Z. Yao, N. Braidy, G.A. Botton, A. Adronov, *J. Am. Chem. Soc.* 125 (2003) 16015.
- [284] S. Qin, D. Qin, W.T. Ford, D.E. Resasco, J.E. Herrera, *Macromolecules* 37 (2004) 752.
- [285] H. Kong, C. Gao, D. Yan, *J. Mater. Chem.* 14 (2004) 1401.
- [286] H. Kong, C. Gao, D. Yan, *J. Am. Chem. Soc.* 126 (2004) 412.
- [287] S. Park, S.W. Yoon, K.B. Lee, D.J. Kim, Y.H. Jung, Y. Do, Y.J. Paik, I.S. Choi, *Macromol. Rapid Commun.* 27 (2006) 47.
- [288] D. Bonduel, M. Mainil, M. Alexandre, F. Monteverde, P. Dubois, *Chem. Commun.* (2005) 781.
- [289] Z. Yinghuai, S.L.P. Sia, K. Carpenter, F. Kooli, R.A. Kemp, *J. Phys. Chem. Solids* 67 (2006) 1218.
- [290] K. Wiemann, W. Kaminsky, F.H. Gojny, K. Schulte, *Macromol. Chem. Phys.* 206 (2005) 1472.

- [291] K. Otsuka, S. Takenaka, *Catal. Surv. Asia* 8 (2004) 77.
- [292] T.V. Reshetenko, L.B. Avdeeva, Z.R. Ismagilov, A.L. Chuvilin, V.B. Fenelonov, *Catal. Today* 102–103 (2005) 115.
- [293] S.K. Shaikhutdinov, L.B. Avdeeva, B.N. Novgorodov, V.I. Zaikovskii, D.I. Kochubey, *Catal. Lett.* 47 (1997) 35.
- [294] K. Otsuka, H. Ogihara, S. Takenaka, *Carbon* 41 (2003) 223.
- [295] S. Takenaka, Y. Shigeta, E. Tanabe, K. Otsuka, *J. Catal.* 220 (2003) 468.
- [296] C. Pham-Huu, N. Keller, V.V. Raddatis, G. Mestl, R. Schlögl, M.J. Ledoux, *Phys. Chem. Chem. Phys.* 4 (2002) 514.
- [297] P.G. Savva, G.G. Olympiou, C.N. Costa, V.A. Ryzhkov, A.M. Efstathiou, *Catal. Today* 102–103 (2005) 78.
- [298] A. Romero, A. Garrido, A. Nieto-Márquez, A.R. de la Osa, A. de Lucas, J.L. Valverde, *Appl. Catal. A* 319 (2007) 246.
- [299] H. Liu, G. Cheng, R. Zheng, Y. Zhao, *J. Mol. Catal. A* 225 (2005) 233.
- [300] H. Liu, G. Cheng, R. Zheng, Y. Zhao, C. Liang, *J. Mol. Catal. A* 230 (2005) 17.
- [301] Y. Liu, Z. Shen, *Carbon* 43 (2005) 1574.
- [302] C.H. Li, K.F. Yao, J. Liang, *Carbon* 41 (2003) 858.
- [303] K.F. Yung, W.T. Wong, *J. Clust. Sci.* 18 (2007) 51.
- [304] O.C. Carneiro, P.E. Anderson, N.M. Rodriguez, R.T.K. Baker, *J. Phys. Chem. B* 108 (2004) 13307.
- [305] W. Qian, T. Liu, F. Wei, Z. Wang, H. Yu, *Carbon* 41 (2003) 846.
- [306] H. Yu, Z. Li, G. Luo, F. Wei, *Diamond Relat. Mater.* 15 (2006) 1447.
- [307] K. Hernadi, L. Thiên-Nga, E. Ljubović, L. Forró, *Chem. Phys. Lett.* 367 (2003) 475.
- [308] W. Xia, D. Su, A. Birkner, L. Ruppel, Y. Wang, C. Wöll, J. Qian, C. Liang, G. Marginean, W. Brandl, M. Muhler, *Chem. Mater.* 17 (2005) 5737.
- [309] H.J. Kim, I.T. Han, Y.J. Park, J.M. Kim, J.B. Park, B.K. Kim, N.S. Lee, *Chem. Phys. Lett.* 396 (2004) 6.
- [310] W. Xia, X. Chen, S. Kundu, X. Wang, G. Grundmeier, Y. Wang, M. Bron, W. Schuhmann, M. Muhler, *Surf. Sci. Technol.* 201 (2007) 9232.
- [311] Y. Cai, J.D. Lin, H.B. Chen, H.B. Zhang, G.D. Lin, D.W. Liao, *Chin. Chem. Lett.* 11 (2000) 373.
- [312] H.B. Chen, J.D. Lin, Y. Cai, X.Y. Wang, J. Yi, J. Wang, G. Wei, Y.Z. Lin, D.W. Liao, *Appl. Surf. Sci.* 180 (2001) 328.
- [313] Q.C. Xu, J.D. Lin, J. Li, X.Z. Fu, Y. Liang, D.W. Liao, *Catal. Commun.* 8 (2007) 1881.
- [314] C. Liang, Z. Li, J. Qiu, C. Li, *J. Catal.* 211 (2002) 278.
- [315] Z. Li, C. Liang, Z. Feng, P. Ying, D. Wang, C. Li, *J. Mol. Catal. A* 211 (2004) 103.
- [316] S.F. Yin, B.Q. Xu, S.J. Wang, C.F. Ng, C.T. Au, *Catal. Lett.* 96 (2004) 113.
- [317] S.F. Yin, B.Q. Xu, W.X. Zhu, C.F. Ng, X.P. Zhou, C.T. Au, *Catal. Today*, 93–95 (2004) 27.
- [318] W. Xia, D. Su, A. Birkner, L. Ruppel, Y. Wang, C. Wöll, J. Qian, C. Liang, G. Marginean, W. Brandl, M. Muhler, *Chem. Mater.* 17 (2005) 5737.

- [319] S.J. Wang, S.F. Yin, L. Li, B.Q. Xu, C.F. Ng, C.T. Au, *Appl. Catal. B* 52 (2004) 287.
- [320] S.F. Yin, B.Q. Xu, C.F. Ng, C.T. Au, *Appl. Catal. B* 48 (2004) 237.
- [321] S.F. Yin, B.Q. Xu, X.P. Zhou, C.T. Au, *Appl. Catal. A* 277 (2004) 1.
- [322] S.F. Yin, Q.H. Zhang, B.Q. Xu, W.X. Zhu, C.F. Ng, X.P. Zhou, C.T. Au, *J. Catal.* 224 (2004) 384.
- [323] L. Li, Z.H. Zhu, Z.F. Yan, G.Q. Lu, L. Rintoul, *Appl. Catal. A* 320 (2007) 166.
- [324] W. Wang, P. Serp, P. Kalck, J.L. Faria, *J. Mol. Catal.* 235 (2005) 194.
- [325] Z. Kulesius, E. Valatka, *Pol. J. Chem.* 80 (2006) 335.
- [326] Y. Yu, J.C. Yu, J.G. Yu, Y.C. Kwok, Y.K. Che, J.C. Zhao, L. Ding, W.K. Ge, P.K. Wong, *Appl. Catal. A* 289 (2005) 186.
- [327] Y. Yu, J.C. Yu, C.Y. Chan, Y.K. Che, J.C. Zhao, L. Ding, W.K. Ge, P.K. Wong, *Appl. Catal. B* 61 (2005) 1.
- [328] C.-Y. Yen, Y.-F. Lin, C.-H. Hung, Y.-H. Tseng, C.-C.M. Ma, M.-C. Chang, H. Shao, *Nanotechnology* 19 (2008) 045604.
- [329] C.-S. Kuo, Y.-S. Tseng, H.-Y. Lin, C.-H. Huang, C.-H. Shen, Y.-Y. Li, S.I. Shah, C.-P. Huang, *Nanotechnology* 18 (2007) 465607.
- [330] B. Ahmmad, Y. Kusumoto, S. Somekawa, M. Ikeda, *Catal. Commun.* 9 (2008) 1410.
- [331] X.H. Xia, Z.J. Jia, Y. Yu, Y. Liang, Z. Wang, L.L. Ma, *Carbon* 45 (2007) 717.
- [332] H.T. Gomes, P.V. Samant, P. Serp, P. Kalck, J.L. Figueiredo, J.L. Faria, *Appl. Catal. B* 54 (2004) 175.
- [333] J. Garcia, H.T. Gomes, P. Serp, P. Kalck, J.L. Figueiredo, J.L. Faria, *Catal. Today* 102–103 (2005) 101.
- [334] J. Garcia, H.T. Gomes, P. Serp, P. Kalck, J.L. Figueiredo, J.L. Faria, *Carbon* 44 (2006) 2384.
- [335] G. Ovejero, J.L. Sotelo, A. Rodriguez, C. Diaz, R. Sanz, J. Garcia, *Ind. Eng. Chem. Res.* 46 (2007) 6449.
- [336] X. Fu, H. Yu, F. Peng, H. Wang, Y. Qian, *Appl. Catal. A* 321 (2007) 190.
- [337] C.Y. Lu, M.Y. Wey, *Fuel* 86 (2007) 1153.
- [338] K.H. Choi, N. Kunisada, S.H. Yoon, Y. Korai, I. Mochida, in *Proceedings of the International Symposium on Carbon*, 2003 p. 7.
- [339] I. Eswaramoorthi, V. Sundaramurthy, A.K. Dalai, *Appl. Catal. A* 313 (2006) 22.
- [340] X.W. Chen, Z. Zhu, M. Hävecker, D.S. Su, R. Schlögl, *Mater. Res. Bull.* 42 (2007) 354.
- [341] C.B. Li, W.X. Pan, W.K. Wong, J.L. Li, X.Q. Qiu, X.P. Chen, *J. Mol. Catal.* 193 (2003) 71.
- [342] R.T.K. Baker, K. Laubernds, A. Wootsch, Z. Paál, *J. Catal.* 193 (2000) 165.
- [343] B. Pietruszka, F. Di Gregorio, N. Keller, V. Keller, *Catal. Today* 102–103 (2005) 94.
- [344] Z.J. Liu, Z. Xu, Z.Y. Yuan, D. Lu, W. Chen, W. Zhou, *Catal. Lett.* 72 (2001) 203.
- [345] Z.J. Liu, Z.Y. Yuan, W. Zhou, L.M. Peng, Z. Xu, *Phys. Chem. Chem. Phys.* 3 (2001) 2518.

- [346] K. Niesz, A. Siska, I. Vesselényi, K. Hernadi, D. Méhn, G. Galbács, Z. Kónya, I. Kiricsi, *Catal. Today* 76 (2002) 3.
- [347] Y. Wang, N. Shah, G.P. Huffman, *Energy Fuels* 18 (2004) 1429.
- [348] M.A. Keane, P.M. Patterson, *Catal. Lett.* 99 (2005) 33.
- [349] J.M. Nhut, P. Nguyen, C. Pham-Huu, N. Keller, M.J. Ledoux, *Catal. Today* 91–92 (2004) 91.
- [350] K. Dong, X. Ma, H. Zhang, G. Lin, *J. Nat. Gas Chem.* 15 (2006) 28.
- [351] N. Kunisada, K.H. Choi, A. Tanaka, S.H. Yoon, Y. Korai, I. Mochida, in *Proceedings of the International Symposium on Carbon*, 2003, p. 7.
- [352] F. Huber, Z. Yu, J.C. Walmsley, D. Chen, H.J. Venvik, A. Holmen, *Appl. Catal. B* 71 (2007) 7.
- [353] F. Winter, V. Koot, A.J. van Dillen, J.W. Geus, K.P. de Jong, *J. Catal.* 236 (2005) 91.
- [354] T.J. Zhao, D. Chen, Y.C. Dai, W.K. Yuan, A. Holmen, *Ind. Eng. Chem. Res.* 43 (2004) 4595.
- [355] R. Viera, C. Pham-Huu, N. Keller, M.J. Ledoux, *Chem. Commun.* (2002) 954.
- [356] R. Viera, D. Bastos-Netto, M.J. Ledoux, C. Pham-Huu, *Appl. Catal. A* 279 (2005) 35.
- [357] C. Ping, F. Li, Z. Jian, J. Wei, *Propell. Explos. Pyrotech.* 31 (2006) 452.
- [358] C. Baleizão, B. Gigante, H. Garcia, A. Corma, *Tetrahedron* 60 (2004) 10461.
- [359] L. Zhou, H.F. Jiang, *Tetrahedron Lett.* 48 (2007) 8449.
- [360] M. Salavati-Niasari, M. Bazarganipour, *J. Mol. Catal. A* 278 (2007) 173.
- [361] H. Markus, A.J. Plomp, T. Sandberg, V. Nieminen, J.H. Bitter, D.Y. Murzin, *J. Mol. Catal. A* 274 (2007) 42.
- [362] B. Huang, R. Huang, D. Jin, D. Ye, *Catal. Today* 126 (2007) 279.
- [363] E. Yoo, L. Gao, T. Komatsu, N. Yagai, K. Arai, T. Yamazaki, K. Matsuishi, T. Matsumodo, J. Nakamura, *J. Phys. Chem. B* 108 (2004) 18903.
- [364] N. Hammer, I. Kvande, X. Xu, V. Gunnarson, B. Tøtdal, D. Chen, M. Rønning, *Catal. Today* 123 (2007) 245.
- [365] R. Zacharia, S.U. Rather, S.W. Hwang, K.S. Nahm, *Chem. Phys. Lett.* 434 (2007) 286.
- [366] S.C. Mu, H.L. Tang, S.H. Qian, M. Pan, R.Z. Yuan, *Carbon* 44 (2006) 762.
- [367] R. Zacharia, K.Y. Kim, A.K.M. Fazle Kibria, K.S. Nahm, *Chem. Phys. Lett.* 412 (2005) 369.
- [368] Z. Paál, D. Teschner, N.M. Rodriguez, R.T.K. Baker, L. Tóth, U. Wild, R. Schlögl, *Catal. Today* 102–103 (2005) 254.
- [369] H.M. Yang, P.H. Liao, *Appl. Catal. A* 317 (2007) 226.
- [370] Y. Fu, J. Shen, *J. Catal.* 248 (2007) 101.
- [371] M.N. Timofeeva, M.M. Matrosova, G.N. Il'inich, T.V. Reshetenko, L.B. Avdeeva, R.I. Kvon, A.L. Chuvalin, A.A. Budneva, E.A. Paukshtis, V.A. Likholobov, *Kinet. Catal.* 44 (2003) 778.
- [372] H. Shang, C. Liu, Y. Xu, J. Qiu, F. Wie, *Fuel Process. Tech.* 88 (2007) 117.
- [373] D.E. Park, T.K. Kim, S. Kwon, E. Yoon, *Proc. MEMS* 2006 (2006) 942.

- [374] H. Markus, A.J. Plomp, P. Mäki-Arvela, J.H. Bitter, D.M. Murzin, *Catal. Lett.* 113 (2007) 141.
- [375] B. Rajesh, K. Ravindranathan Thampi, J.M. Bonard, N. Xanthopoulos, H.J. Mathieu, B. Viswanathan, *J. Phys. Chem.* 107 (2003) 2701.
- [376] B. Rajesh, V. Karthik, S. Karthikeyan, K. Ravindranathan Thampi, J.M. Bonard, B. Viswanathan, *Fuel* 81 (2002) 2177.
- [377] J.-S. Huang, X.-G. Zhang, J.-M. Luo, J.-Y. Sun, W.-J. Yang, *J. Solid State Electrochem.* 12 (2008) 113.
- [378] W. Li, C. Liang, J. Qiu, H. Li, W. Zhou, G. Sun, Q. Xin, *React. Kinet. Catal. Lett.* 82 (2004) 235.
- [379] X. Zhao, W. Li, L. Jiang, W. Zhou, Q. Xin, B. Yi, G. Sun, *Carbon* 42 (2004) 3251.
- [380] S. Liao, K.A. Holmes, H. Tsapralis, V.I. Birss, *J. Am. Chem. Soc.* 128 (2006) 3504.
- [381] D.J. Guo, H.L. Li, *J. Colloid Interface Sci.* 286 (2005) 274.
- [382] Y. Li, X. Cui, X. Ye, *Electrochem. Commun.* 7 (2005) 267.
- [383] G.Y. Gao, D.J. Guo, H.L. Li, *J. Power Sources* 162 (2006) 1094.
- [384] M. Krishna Kumar, S. Ramaprabhu, *Int. J. Hydrogen Energy* 32 (2007) 2518.
- [385] S. Yang, X. Zhang, H. Mi, X. Ye, *J. Power Sources* 175 (2008) 26.
- [386] D.J. Guo, H.L. Li, *Carbon* 43 (2005) 1259.
- [387] P. Santhosh, A. Gopalan, K.P. Lee, *J. Catal.* 238 (2006) 177.
- [388] A.L.M. Reddy, N. Rajalakshmi, S. Ramaprabhu, *Carbon* 46 (2008) 2.
- [389] Y.G. Wang, L. Feng, F. Li, H.M. Xiong, Y.Y. Xia, *Chem. Mater.* 19 (2007) 2095.
- [390] C.A. Bessel, K. Laubernds, N.M. Rodriguez, R.T.K. Baker, *J. Phys. Chem.* 105 (2001) 1115.
- [391] M. Tsuji, M. Kubokawa, R. Yano, N. Miyamae, T. Tsuji, M.S. Jun, S. Hong, S. Lim, S.H. Yoon, I. Mochida, *Langmuir* 23 (2007) 387.
- [392] W. Li, X. Wang, Z. Chen, M. Waje, Y. Yan, *J. Phys. Chem. B* 110 (2006) 15353.
- [393] T. Maiyalagan, B. Viswanathan, U.V. Varadaraju, *Electrochem. Commun.* 7 (2005) 905.
- [394] L. Li, G. Wu, B.-Q. Xu, *Carbon* 44 (2006) 2973.
- [395] J.-H. Wee, K.-Y. Lee, S.H. Kim, *J. Power Sources* 165 (2007) 667.
- [396] J.M. Tang, K. Jensen, M. Waje, W. Li, P. Larsen, K. Pauley, Z. Chen, P. Ramesh, M.E. Itkis, Y. Yan, R.C. Haddon, *J. Phys. Chem. C* 111 (2007) 17901.
- [397] Y. Xing, *J. Phys. Chem. B* 108 (2004) 19255.
- [398] J.M. Liu, H. Meng, J.I. Li, S.J. Liao, J.H. Bu, *Fuel Cells* 5 (2007) 402.
- [399] Y.L. Hsin, K.C. Hwang, C.T. Yeh, *J. Am. Chem. Soc.* 129 (2007) 9999.
- [400] J. Kim, J.W. Grate, P. Wang, *Chem. Eng. Sci.* 61 (2006) 1017.
- [401] K. Balasubramanian, M. Burghard, *Anal. Bioanal. Chem.* 385 (2006) 452.
- [402] R.J. Chen, Y. Zhang, D. Wang, H. Dai, *J. Am. Chem. Soc.* 123 (2001) 3838.
- [403] Q. Shi, D. Yang, Y. Su, J. Li, Z. Jiang, Y. Jiang, W. Yuan, *J. Nanoparticle Res.* 9 (2007) 1205.
- [404] S.S. Karajanagi, A.A. Vertegel, R.S. Kane, J.S. Dordick, *Langmuir* 20 (2004) 11594.

- [405] S. Shah, K. Solanki, M.N. Gupta, *Chem. Central J.* 1(30) (2007) 1.
- [406] J.M. Gómez, M.D. Romero, T.M. Fernández, *Catal. Lett.* 101 (2005) 275.
- [407] K. Rege, N.R. Raravikar, D.Y. Kim, L.S. Schadler, P.M. Ajayan, J.S. Dordick, *Nano Lett.* 3 (2003) 829.
- [408] J. Kim, H. Jia, P. Wang, *Biotechnol. Adv.* 24 (2006) 296.
- [409] Y. Liu, L. Huang, S. Dong, *Biosens. Bioelectron.* 23 (2007) 35.
- [410] Y.M. Yan, O. Yehezkel, I. Willner, *Chem. Eur. J.* 13 (2007) 10168.
- [411] N. Muradov, *Catal. Commun.* 2 (2001) 89.
- [412] G. Mestl, N.I. Maksimova, N. Keller, V.V. Roddatis, R. Schlögl, *Angew. Chem. Int. Ed.* 40 (2001) 2066.
- [413] D.S. Su, N. Maksimova, J.J. Delgado, N. Keller, G. Mestl, M.J. Ledoux, R. Schlögl, *Catal. Today* 102–103 (2005) 110.
- [414] J.J. Delgado, R. Viera, G. Rebmann, D.S. Su, N. Keller, M.J. Ledoux, R. Schlögl, *Carbon* 44 (2006) 809.
- [415] M.F.R. Pereira, J.L. Figueiredo, J.J.M. Órfão, P. Serp, P. Kalck, Y. Kihn, *Carbon* 42 (2004) 2807.
- [416] P. Li, T. Li, J.H. Zhou, Z.J. Sui, Y.C. Dai, W.K. Yuan, D. Chen, *Micropor. Mesopor. Mater.* 95 (2006) 1.
- [417] T.J. Zhao, W.Z. Sun, X.Y. Gu, M. Rønning, D. Chen, Y.C. Dai, D.K. Yuan, A. Holmen, *Appl. Catal. A* 323 (2007) 135.
- [418] Z.J. Sui, J.H. Zhou, Y.C. Dai, W.K. Yuan, *Catal. Today* 106 (2005) 90.
- [419] H. Ogihara, S. Takenaka, I. Yamanaka, K. Otsuka, *Carbon* 42 (2004) 1609.
- [420] V.V. Shinkarev, V.B. Fenelonov, G.G. Kuvshinov, *Carbon* 41 (2003) 295.
- [421] G.G. Kuvshinov, V.V. Shinkarev, A.M. Glushenkov, M.N. Boyko, D.G. Kuvshinov, *China Particulol.* 4 (2006) 70.
- [422] M. Croston, J. Langston, R. Sangoi, K.S.V. Santhanam, *Int. J. Nanosci.* 1 (2002) 277.
- [423] M. Croston, J. Langston, G. Takacs, T.C. Morrill, M. Miri, K.S.V. Santhanam, P. Ajayan, *Int. J. Nanosci.* 1 (2002) 285.
- [424] S. Yang, W. Zhu, X. Li, J. Wang, Y. Zhou, *Catal. Commun.* 8 (2007) 2059.
- [425] F. Peng, L. Zhang, H. Wang, P. Lv, H. Yu, *Carbon* 43 (2005) 2405.
- [426] Z. Kang, E. Wang, B. Mao, Z. Su, L. Gao, L. Niu, H. Shan, L. Xu, *Appl. Catal. A* 299 (2006) 212.
- [427] S. van Dommelle, K.P. de Jong, J.H. Bitter, *Chem. Commun.* (2006) 4859.
- [428] D.Z. Guo, G.M. Zhang, Z.X. Zhang, Z.Q. Xue, Z.N. Gu, *J. Phys. Chem. B* 110 (2006) 1571.
- [429] C. Srinivasan, *Curr. Sci.* 90 (2006) 756.
- [430] Z. Yu, Ø. Borg, D. Chen, E. Rytter, A. Holmen, *Top. Catal.* 45 (2007) 69.
- [431] J. Lu, *Carbon*, 45 (2007) 1599.
- [432] J.M. Gómez, M.D. Romero, T.M. Fernández, *Catal. Lett.* 101 (2005) 275.
- [433] Y. Liu, L. Huang, S. Dong, *Biosens. Bioelectron.* 23 (2007) 35.
- [434] N. Ishigami, H. Ago, Y. Motoyama, M. Takasaki, M. Shinagawa, K. Takahashi, T. Ikuta, M. Tsuji, *Chem. Commun.* (2007) 1626.

10 Carbon Gels in Catalysis

CARLOS MORENO-CASTILLA

10.1 INTRODUCTION

Carbon gels are novel porous carbon materials that have received considerable attention in the literature since their introduction in 1989 by Pekala [1,2]. They can be obtained by carbonization of organic gels, which are prepared from the sol–gel polycondensation of certain organic monomers (e.g., resorcinol, formaldehyde) [1–11]. Sol–gel processing is a versatile method for synthesizing solid materials carried out in a liquid solution and at low temperatures, generally below 373 K. Sol–gel synthesis was used originally in the preparation of inorganic solids, and the physics and chemistry of the process have been detailed in several reviews and books [9,10,12–14]. The potential advantages of sol–gel processing include the purity, homogeneity, and controlled porosity of the materials obtained.

Carbon gels can be in the form of monoliths, beads, powders, or thin films [2,3,8,11,15–21], and their unique properties make them promising materials for use in adsorption and catalysis. These properties include a well-developed and controlled micro- and mesoporosity and a large surface area. Carbon gels have a network structure of interconnected nano-size primary particles. With regard to their pore structure, micropores are developed in the primary particles, whereas mesopores and macropores are produced in the interparticle structure initially occupied by the solvent. It is therefore possible to control the concentration of micropores and mesopores independently, which is one of the advantages of carbon gels as porous carbon materials. These concentrations depend on the nature of the original ingredients, the curing and drying methods of the organic gel, and the carbonization conditions. Because the structure and texture of carbon aerogels can be designed and controlled at the nanometer scale, they were recently classified as nanostructured carbons [22].

An important feature of these materials is that metal-doped monolithic carbon gels can readily be prepared (see below). These are emergent materials in the field of heterogeneous catalysis, and their use will grow in the near future, due

to the versatility of their shape and pore texture. In this chapter we present an overview of the preparation and characteristics of these materials and their use in the catalytic reactions studied to date.

10.2 CARBON GELS: PREPARATION AND SURFACE PROPERTIES

Carbon gels are obtained by the carbonization of organic gels, which are synthesized by a sol–gel procedure from the polycondensation of different organic monomers. The most widely studied organic gels are those prepared from resorcinol (R) and formaldehyde (F) mixtures dissolved in water (W) in the presence of either a basic or an acid catalyst (C). Other organic gels have been prepared by replacing resorcinol with 2,4-dihydroxybenzoic acid [23–26], melamine [3,27,28], or cresol [28–30]. Al-Muhtaseb and Ritter [11] published a comprehensive review of the influence of synthesis conditions on the final properties of RF organic and carbon gels.

Three main stages can be distinguished in the preparation of carbon gels. The first stage includes preparation of the sol mixture, its gelation, and subsequent curing of the gel; the second stage comprises drying of the wet gel; and the third is carbonization of the dried gel and sometimes activation of the carbonized derivative. In the first stage, R and F are mixed at the appropriate molar ratio. Variation in this molar ratio has a profound effect on the properties of the gel. The solvent can be either W or an organic solvent (S). Sodium carbonate is the most commonly employed alkaline catalyst (C) for the polymerization reaction of resorcinol with formaldehyde, although acidic catalysts have also been used.

By changing the R/C molar ratio, the microstructure of the polymerized gels and therefore of the final carbon gels can be varied. A low R/C ratio results in polymeric gels, whereas high R/C ratios give rise to colloidal gels. The main reactions between R and F include an addition reaction of F to the 2-, 4-, and/or 6- position on the aromatic ring of R, which is catalyzed by bases generating more reactive R anions. This gives rise to hydroxymethyl derivatives, which then undergo a condensation reaction to form methylene and methylene ether bridged compounds. This reaction is catalyzed in acid media. The condensation products form clusters that give rise to colloidal primary particles that cross-link with each other to produce the wet gel, or *hydrogel*.

To obtain gel in a monolithic shape, the colloidal solution is poured into a mold of the desired shape before the gelation and curing step. The molds are usually sealed before being heated to minimize solvent evaporation. The curing period allows cross-linking of the polymer clusters formed previously, giving the final solid shape of the gel. The most important factors controlling the properties of the organic gel in this stage are the concentrations of catalyst and reactants (R and F) and the initial pH.

The second stage in the preparation of carbon gels is drying of the wet gel to remove the solvent trapped in its gel structure. The volume occupied by the solvent will essentially constitute the meso- and/or macropore network of the

dried organic gel. The different methods used to remove the solvent can have a profound effect on the textural properties of the organic gel and hence on those of the final carbon gel.

Three main methods have been developed to dry the hydrogel: subcritical drying, supercritical drying, and freeze-drying. Conventional evaporation of the solvent under subcritical and sometimes atmospheric pressure leads to a collapse of the pore structure due to changes in surface tension of the solvent on formation of the vapor–liquid interface. This collapse results in a large shrinkage of the gel, giving a dense polymer called a *xerogel*. In some cases, solvent exchange is used before subcritical drying, to reduce the capillary forces responsible for pore texture collapse. Thus, water is exchanged with a solvent of lower surface tension, such as acetone or cyclohexane [31].

Subcritical drying can sometimes yield porous xerogels when the gel structure is strong enough to withstand capillary pressures [11,31], although it is not possible to produce carbon xerogels with both small pores and high pore volumes [31]. This is a simpler, quicker, and less expensive method to dry wet organic gels and may be adequate in some cases.

To avoid formation of the liquid–vapor meniscus that appears during subcritical drying and is responsible for pore texture collapse, two additional methods were developed: supercritical drying and freeze-drying. Supercritical drying is the best method for preserving the original pore texture of wet gels. Supercritically dried organic gels are designated *aerogels*, and monoliths can be obtained very easily. Aerogels have higher surface areas and pore volumes than those of the corresponding xerogels.

The solvent of the wet gel (usually, water) is first exchanged with another organic solvent, such as methanol, ethanol, or acetone. The latter solvent is further exchanged with liquid CO₂ ($T_c = 304$ K and $P_c = 7.4$ MPa). Once transformed in a supercritical fluid (e.g., at 313 K and 9 MPa), with null surface tension, it can be evacuated from the pore texture of the gel without pore collapse.

Freezing-drying methods give rise to *cryogels*. In this case, the solvent is frozen and then removed by sublimation, avoiding a vapor–liquid interface [10,11]. When hydrogels are frozen, micro-sized ice crystals ranging from several micrometers to a hundred micrometers form within them; in addition, the aqueous solvent expands on freezing. Both phenomena may destroy the pore network of the gel or result in the formation of large macropores [11]. However, Nishihara and co-workers [16] recently reported that cryogel honeycomb microstructures can be formed if the growth of ice microcrystals is controlled. But in general, freeze-drying of hydrogels leads to broken samples, and it is relatively difficult to obtain monoliths. Water in a hydrogel is sometimes exchanged with another solvent that shows lower density changes upon freezing (e.g., *t*-butanol). However, solvent exchange does not always resolve the problem of sample breakage [31].

The third preparation stage of carbon gels is carbonization of the dried gel by heating in flowing N₂ or Ar at a temperature of 773 to 2773 K. During carbonization, the gel loses oxygen and hydrogen functionalities and there is carbon

enrichment, yielding a highly pure carbon structure. At low carbonization temperatures, the macropore volume decreases and the mesopore volume increases, due to shrinkage of the material, whereas the micropore volume and surface area are enlarged, due to the evolution of gases during carbonization. At higher carbonization temperatures, all of these parameters tend to decrease. Partial graphitization of different areas of the carbon gel takes place at very high carbonization temperatures (≥ 2273 K). Finally, the gel can be activated by its gasification with steam or CO_2 at 1073 to 1173 K for varying time periods. This treatment increases the surface area, pore volume, and pore width. Thus, activated carbon aerogels with BET surface areas between 1460 and 3200 m^2/g were recently prepared [32], although the preparation method was not reported by the authors.

In conclusion, the surface area, pore volume, and pore size distribution of resorcinol–formaldehyde carbon gels are tunable surface properties related to the synthesizing and processing conditions, and a wide spectrum of materials with unique properties can be produced. The surface properties of some carbon gels obtained under different synthesis and processing conditions are listed in Table 10.1 as an example.

On the other hand, the mechanical properties of monolithic carbon gels are of importance when they are to be used as adsorbents and catalyst supports in fixed-bed reactors, since they must resist the weight of the bed and the stress produced by its vibrations or movements. A few studies have been published on the mechanical properties of resorcinol–formaldehyde carbon gels under compression [7,36,37]. The compressive stress–strain curves of carbon aerogels are typical of brittle materials. The elastic modulus and compressive strength depend largely on the network connectivity and therefore on the bulk density, which in turn depends on the porosity, mainly the meso- and macroporosity. These mechanical properties show a power-law density dependence with an exponent close to 2, which is typical of open-cell foams.

Carbon aerogels of varying densities were prepared under different synthesis conditions [35]. For instance, when *para*-toluenesulfonic acid was used as catalyst, a carbon aerogel with a bulk density of 1.04 g/cm^3 was obtained, and its elastic modulus and compressive strength were 1108 and 24 MPa [38]. However, when K_2CO_3 was used as a catalyst, the resulting carbon aerogel had a density of 0.38 g/cm^3 , and its elastic modulus and compressive strength were 166 and 5 MPa, respectively. The surface area and porosity of these two samples are shown in Table 10.1 (rows 13 and 14). These data demonstrate the variability of the mechanical properties of these materials.

10.3 METAL-DOPED CARBON GELS

One area of major interest in carbon gel research is the incorporation of metal species into the carbon framework, taking advantage of the pore texture of these gels to achieve good dispersion and stability of the metal nanoparticles in the

Table 10.1 Surface Properties of Carbon Gels Obtained Under Varying Synthesis and Processing Conditions^a

R/F	C	R/C	S	R/S	Drying	Pyrolysis (K)	Activation ^b	S_{BET} (m^2/g)	V_{micro} (cm^3/g)	V_{meso} (cm^3/g)	V_{macro} (cm^3/g)	ρ_{B}^c (g/cm^3)	Ref.	
0.50	Na_2CO_3	100	Water	0.20	Freeze	1273	NA	1280	—	0.36	—	—	16	
0.50	Na_2CO_3	1000	Water	0.086	Sup. CO_2	1323	NA	500	0.22	—	2.3 ^d	0.38	31	
					Freeze			740	0.31	—	2.6	0.36		
					Vacuum			615	0.26	—	1.3	0.54		
					Sup. CO_2			535	0.23	—	0.5	0.95		
					Freeze			275	0.12	—	0.5	1.02		
					Vacuum			<40	<0.01	—	<0.1	1.26		
0.25	K_2CO_3	50	Water	0.037	Sup. CO_2	1073	NA	690	0.27	0.42	—	—	33	
		1000						720	0.28	0.19	—	—		
0.5	Na_2CO_3	200	Water	?	Sup. CO_2	1323	NA	961	0.15	7.72 ^e	—	0.19	34	
					Acetone	?		620	0.10	0.93	—	0.65		
0.5	Na_2CO_3	800	Water	0.08	Sup. CO_2	1173	NA	934	0.39	1.30	0.00	0.48	35	
								873	0.34	0.00	1.67	0.38		
								751	0.28	0.33	0.00	1.04		
	K_2CO_3							CO ₂ 22%BO	1296	0.53	0.33	0.00	0.87	

Source: Reproduced with permission from Elsevier.

^aR/F, R/C, and R/S are given as molar ratios.

^bNA, not applicable.

^cBulk density.

^dThese values for samples from ref. 31 are total pore volumes.

^eThese values for samples from ref. 34 are pore volumes filled with liquid N₂ when the relative pressure tends to 1.

^f*para*-Toluenesulfonic acid.

porosity of the carbonaceous matrix. Carbon gels that are doped with metals or metallic compounds can be used as catalysts in different reactions. In addition, these materials have sometimes been prepared in order to modify the structure, conductivity, and adsorption behavior of the carbon gel.

Three main strategies have been used to introduce metal species into the carbon framework:

1. Dissolving the metal precursor in the initial resorcinol–formaldehyde mixture
2. Introducing a functionalized moiety with binding sites for the metal ions into the initial mixture or in the organic gel
3. Depositing the metal precursor on the organic or the carbon gel by different methods

A large variety of metal-containing carbon gels have already been prepared and characterized, including Na-, K-, Mg-, Zr-, Cr-, Mo-, W-, Mn-, Fe-, Ru-, Co-, Ni-, Pd-, Pt-, Cu-, Ag-, Ce-, and Eu-containing carbon aerogels and xerogels. The objective of these studies was to characterize these materials for their use as supported catalysts, electrodes for electrical double-layer capacitors, and adsorbents in aqueous solutions.

10.3.1 Dissolving the Metal Precursor in the Initial Mixture

Ce- and Zr-doped carbon aerogels were obtained by dissolving their nitrates in an R/F mixture at different pHs [39,40] and carbonized at 1323 K. Introduction of the metal salts produced changes in the initial pH and therefore in the chemistry of the process. Some of the textural characteristics of these samples are compiled in Table 10.2. Their surface area ranged from 87 to 800 m²/g, the micropore volume from 0.03 to 0.20 cm³/g, and the micropore size from 0.65 to 0.90 nm [40]. Synthesis of Zr-doped carbon aerogels resulted in microporous materials, whereas doping with Ce only yielded a material with very low microporosity.

These results indicate that not only the initial pH of the solution but also the nature of the dopant metal affected the sol–gel chemistry and therefore the structure of the solid. Transmission electron microscopy (TEM) observations

Table 10.2 Textural Characteristics of Ce- and Zr-Doped Carbon Aerogels^a

Sample	Solution pH	Ce (%)	Zr (%)	W ₀ (cm ³ /g)	S _{total} (m ² /g)	L ₀ (nm)
nCACZ	7	0.22	0.14	0.17	800	0.65
aCACZ	3	0.25	0.16	0.17	500	0.70
CAZ	3	—	0.16	0.20	596	0.69
CAC	4	0.31	—	0.03	87	0.91

Source: Adapted from ref. 40, with permission from John Wiley & Sons.

^aW₀, micropore volume; L₀, mean micropore width.

showed nanosized particles of the metals that were homogeneously distributed, despite the high-temperature treatment of 1323 K. Authors suggested that dopant elements were anchored to the carbon structure, preventing their migration and growth. Pt-, Pd-, and Ag-containing carbon aerogels were prepared using an R/F molar ratio of 0.5, replacing the Na_2CO_3 catalyst in the initial mixture with $[\text{Pt}(\text{NH}_3)_4]\text{Cl}_2$, PdCl_2 , or $\text{AgOOC}-\text{CH}_3$ [8]. Aerogels thus obtained were pyrolyzed at 1273 K in N_2 flow and then steam-activated at 1173 K for 25 minutes. Some of the results obtained are compiled in Table 10.3, showing the large meso- and macropore volumes of the steam-activated Pt-containing aerogel. These textural characteristics were produced by the presence of a very small amount of Pt in the carbon aerogel matrix. The large increase in meso- and macropore volumes, V_2 and V_3 , respectively, of this sample was due in part to the high degree of activation, since Pt acted as a gasification catalyst during the activation step. In contrast, the steam-activated Pd-containing carbon aerogel was essentially microporous (W_0) and had the highest nitrogen surface area of the three samples.

In other Pt-doped monolithic carbon aerogels, prepared by adding the Pt precursor to the initial R/F mixture [41], the Pt particle size determined by H_2 chemisorption was much higher than that determined by high-resolution transmission electron microscopy (HRTEM). This indicates that some Pt particles were encapsulated by the carbon matrix and were consequently inaccessible to H_2 . This can be the main problem of this preparation method when the metal-doped carbon gel is to be used as catalyst, because part of the metal will not be accessible to the reactant molecules.

The physicochemical surface properties of Cr-, Fe-, Co-, Ni-, and Cu-doped monolithic organic aerogels and their carbonized and steam-activated derivatives were also studied [42–44]. These samples were prepared by adding chromium nitrate or metal acetates to an initial mixture with an R/F molar ratio of 0.5 and an R/W molar ratio of 0.13. The amount of metal added was that required to yield 1 wt% of the metal in the initial solution.

The surface morphology and pore texture of these metal-doped organic aerogels depended on the nature of the metal used, essentially because of

Table 10.3 Textural Characteristics of Steam-Activated Metal-Doped Carbon Aerogels and the Blank NC-S^a

Sample	Burn-off (%)	S_{BET} (m^2/g)	W_0 (cm^3/g)	L_0 (nm)	V_2 (cm^3/g)	V_3 (cm^3/g)
NC-S	25	1085	0.38	1.29	0.04	0.98
(N-Pt)C-S	60	699	0.35	1.26	0.82	2.98
(N-Pd)C-S	31	1302	0.42	1.36	0.00	0.03

Source: Adapted from ref. 8, with permission from Elsevier.

^a W_0 , micropore volume from the Dubinin–Radushkevich equation applied to CO_2 adsorption at 77 K; L_0 , mean micropore width from CO_2 adsorption at 77 K; V_2 , pores with diameter between 3.7 and 50 nm; V_3 , pores with diameter wider than 50 nm.

its effect on the initial solution pH, which influenced the chemistry of the aerogel-producing process [43]. The surface morphology of these aerogels was composed of fused microbead particles as detected by scanning electron microscopy. The size of these particles was strongly influenced by the pH that the metallic salt gave to the initial solution. Thus, the largest aerogel particles were obtained at the lowest pH. X-ray photoelectron spectroscopy (XPS) showed that some of the metal ions in the Fe- and Co-doped organic aerogels were chelated by the phenolic functionalities of the organic matrix.

These metal-doped organic aerogels were carbonized at temperatures between 773 and 2073 K [42]. The weight loss of these aerogels increased with pyrolysis temperatures, but the release of volatile matter occurred largely at 773 K. So when the organic aerogels were carbonized at these temperatures, there was an increase in the BET surface area, due to the evolution of gases from the organic matrix, which develops the microporosity. This parameter decreased when the pyrolysis temperature was increased. Heat treatments also produced variations in the meso and macroporosity of the metal-doped carbon aerogels.

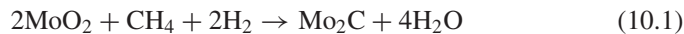
The structure and morphology of Cr-, Fe-, Co-, and Ni-doped monolithic carbon aerogels heat-treated at various temperatures up to 2073 K were studied by HRTEM [42]. Carbon nanoribbons appeared in all metal-containing carbon aerogels heat-treated at 1273 K. Specific regions containing graphitic particles with very well defined 002 lattice fringes and crystallinity appeared when samples were heat-treated at 1673 and 2073 K. These results indicate that carbon atoms in carbon aerogel can grow into a highly ordered solid by the catalytic action of metal nanoparticles. However, disordered and poorly crystallized regions were also observed. HRTEM of these samples also showed that the metallic phase was well dispersed at the nanometer scale.

Job and co-workers [45] prepared Ni-, Fe- Mn-, Pt-, Cu-, and Pd-doped carbon xerogels by dissolving their corresponding metal acetates in the R/F mixture. When necessary, a complexing agent (e.g., hydroxyethylendiamine, diethylene-triaminepentaacetic acid) was added to the initial R/F solution to render the metal cation soluble and to keep the metal dissolved during gelation. After drying, the xerogels were carbonized at 1073 K. The article describes mainly results obtained with Ni, Fe, and Pd. Metal contents ranged between 6 and 7 wt% for Ni, 4.5 and 5.8 wt% for Fe, and 5.55 and 7.50 wt% for Pd. In general, the complexant agent diminished the microporosity, and the metal precursor diminished the mesoporosity. Ni, Fe, and Pd were in a metallic state after drying and required no reduction treatment. As a result, large metal particles (20 nm in diameter) dispersed on texture-tailored carbon xerogels could be observed by TEM.

Some transition-metal carbides such as tungsten and molybdenum carbides have been proposed as new active catalysts for hydrotreating processes [46]. The formation of these carbides on W- and Mo-doped carbon aerogels has also been studied [47–49]. A W-doped carbon aerogel was prepared by adding ammonium tungstate to the initial RF mixture, supercritically dried and carbonized at 773 and 1273 K in an N₂ atmosphere. Heat treatment at 1273 K gave rise to the formation of WC and a Magnelli intermediate phase that probably acted as WC

precursor. Therefore, the organic matrix can reduce and carburize the tungsten oxide phase at 1273 K.

A Mo-doped organic aerogel was prepared similarly by adding ammonium heptamolybdate to the initial RF mixture [49], followed by supercritical drying and carbonization at 1273 K in an N₂ atmosphere. Mo(VI) was reduced to Mo(IV) during this process, as detected by XPS. Additionally, the Mo-doped organic and carbon aerogels were both heat-treated in H₂/Ar flow up to 1073 K. As a result, molybdenum oxide was partially reduced and carburized, giving rise to β-Mo₂C as detected by XPS. The presence of H₂ in the gas phase was necessary to produce the carbide phase [46,50], according to



Carburization of the Mo-doped organic aerogel yielded a higher percentage of carbide phase with better dispersion than that of carburization of the Mo-doped carbon aerogel.

10.3.2 Introducing a Functionalized Moiety

Cu-doped monolithic organic aerogels were prepared by sol–gel polymerization of a resorcinol derivative containing an ion-exchange moiety with binding sites for metal ions with the aim of determining their structure [23,24] and electrochemical [26] and transport properties [25]. Thus, the potassium salt of 2,4-dihydroxybenzoic acid was used instead of resorcinol; once the hydrogel was obtained, K⁺ ions were exchanged with Cu²⁺ ions, dried supercritically, and carbonized at 1323 K.

XPS study of the Cu-doped organic aerogel showed that both carboxyl and hydroxyl groups of the polymer repeat unit were involved in the chelation of Cu ions. After carbonization, the Cu-doped carbon aerogel contained 0.5 wt% K and 9.2 wt% Cu and had a BET surface area of around 700 m²/g, a total pore volume of 2.16 cm³/g, and a mean pore diameter of 14.8 nm. Spherical Cu particles 10 to 50 nm in diameter were formed during carbonization of the aerogel and were well dispersed in the carbon matrix. No Cu–carbon bonds were detected in this network after carbonization.

Baumann and co-workers [51] also used the method described above to prepare Co- and Ni-doped carbon aerogels. They found that Ni and Co nanoparticles around 4 nm in diameter were generated during the carbonization process at about 673 and 723 K, respectively. Their size increased with higher carbonization temperature. Carbon frameworks of metal-doped carbon aerogels obtained below 873 K consisted of interconnected carbon particles of 15 to 30 nm. When the samples were pyrolyzed at 1323 K, growth of graphitic nanoribbons with different curvatures was observed in both metal-doped carbon aerogels. These aerogels, with around a 9 wt% metal loading, retained the overall open cell structures of metal-free carbon aerogels and exhibited high surface areas (around 1000 m²/g) and pore volumes in the micro- and mesopore range (around 4 cm³/g).

Vallribera and co-workers used the approach described above to prepare Ni-, Pd-, and Eu-doped carbon aerogels [52,53]. The Ni- and Pd-doped carbon aerogels were carbonized at 1323 K. The surface area of these samples was 570 and 400 m²/g, the Ni and Pd content was 19 and around 40 wt%, and their mean particle size varied between aggregates and around 30 nm, respectively. The Eu-carbon aerogel was obtained from the corresponding organic aerogel by carbonizing at 1323 K. Its surface area and Eu content were around 500 m²/g and 27 wt%, respectively.

Using the same method, Cotet and co-workers [54] prepared high-content Fe-, Co-, Ni-, Cu-, and Pd-doped carbon aerogels. The metal content of these samples was around 20 wt%, except in the case of the Pd-containing sample, where it was as high as 46 wt%. Mean crystallite size ranged from 12 to 40 nm and the surface areas from 370 to 450 m²/g. The presence of some graphitic nanoribbons was detected in some of the prepared samples, as reported previously by other authors [42,51,55].

A different approach was followed to prepare Pt-doped carbon aerogels [56]. In this case the strategy was to immobilize Pt catalysts on sulfur-functionalized carbon aerogels to mimic the thiophene-modified precious metal binding that occurs with Vulcan carbon. For this purpose, RF gels were generated and reacted with 3-thiophenecarboxaldehyde before aerogel processing. Heterocyclic sulfur was retained after carbonization of this C-S aerogel. The sulfurized carbon aerogel was able to adsorb pre-formed colloidal Pt particles (average diameter of 2.4 nm) spontaneously from an aqueous solution, whereas the sulfur-free carbon aerogel exhibited minimal Pt particle uptake. The Pt-doped C-S aerogel showed oxygen reduction activity similar to that of Pt-modified Vulcan carbon.

10.3.3 Depositing the Metal Precursor on the Organic or Carbon Gel

Several methods have been used to deposit the metal precursor on the organic or carbon gel. These methods include incipient wetness, adsorption, sputtering, sublimation, and supercritical deposition. Pajonk and co-workers [57] described a method to synthesize Pt-doped carbon aerogels by impregnation of the carbon aerogel obtained with an acetone solution of hexachloroplatinic acid. Glora and co-workers [58] deposited Pt on carbon aerogels by sputtering. Pt layers with a loading of about 0.3 mg/cm² were obtained. Pt particle sizes were about 15 and 20 nm.

Erkey and co-workers [59–61] prepared Pt- and Ru-doped carbon aerogels using a supercritical deposition method. This involved dissolution of an organometallic precursor in a supercritical fluid and the exposure of a solid substrate to this solution. After impregnation of the support with the metal precursor, it was converted to the metal form by different methods. Dimethyl(1,5-cyclooctadiene) platinum(II) was used as a precursor for Pt [59,60], and two different Ru complexes, trisacetylacetone Ru(III) and Ru(cod)(tmhd)₂, were used for Ru [61]. Monolithic organic and carbon aerogels

impregnated with the Pt complex were heated in an N₂ flow at 573 to 1273 K to obtain Pt-doped carbon aerogels. High Pt loadings, ranging from 10 to 40 wt% and mean crystallite sizes of between 1.6 and 3.5 nm (depending on the metal loading), were achieved. Pt particle sizes obtained from H₂ and CO chemisorption were consistent with those measured with TEM, showing the accessibility of the surface of Pt crystallites.

The same authors reported the effect of different reduction methods on Pt dispersion and particle size distribution [60]. The metal particle size and Pt loading ranges were 1 to 6 nm and 10 to 73 wt%, respectively. Differences in the mechanism of particle formation and growth during chemical and thermal reduction were found, attributable to the varying chemistry of these processes.

Ru-doped carbon aerogels were obtained by thermally reducing the supercritically impregnated carbon aerogel in an N₂ atmosphere at 573 to 1273 K. Uniformly dispersed Ru particles were obtained, with average sizes of 1.7 to 3.8 nm. Particle sizes determined by H₂ chemisorption agreed fairly well with those obtained from TEM measurements, indicating the accessibility of the metal particles.

Miller and Dunn [62] prepared Ru-containing carbon aerogels by impregnating the carbon aerogel with [Ru(acac)₃] using a sublimation method. Samples with > 60% Ru were obtained by multiple impregnation. After impregnation, they were heated at 593 K under Ar flow to decompose the precursor. HRTEM showed a Ru particle size of 2 to 3 nm. Electron diffraction patterns indicated that the metal particles were amorphous. The authors reported that the Ru particles remained isolated and neither ripened nor aggregated, even at high metal loading, despite repeated heating at 573 K. However, the metal particles migrated to the external surface of the carbon aerogel above 773 K. The BET surface area of the samples decreased with higher metal loading, due to blocking of the microporosity by the metal particles. The authors suggested that the nucleation sites for Ru nanoparticles were the carbon aerogel micropores, which also served to anchor the particles to the surface.

Ag-doped carbon xerogels were prepared by immersion of the organic xerogels in AgNO₃ aqueous solution [63]. After drying, the samples were heated to 573 to 1173 K in N₂. Metal content ranged from 1 to 23 wt%, and samples were used as antibacterial agents. Ag particle size or dispersion was not given in this study, but the authors indicated that the distribution and size of Ag particles depended on silver content, immersion time in the precursor solution, and carbonization temperature.

10.4 CATALYTIC REACTIONS OF METAL-DOPED CARBON GELS

To date, metal-doped carbon aerogels and xerogels have been used as catalysts in different reaction types, which can be grouped into environmental and fuel cell applications, C=C double-bond hydrogenation, skeletal isomerization, hydrodechlorination, and other reactions, including synthesis of methyl

tert-butyl ether, Knoevenagel condensation, Mizoroki–Heck coupling reaction, and Michael addition.

10.4.1 Environmental Applications

Environmental applications of metal-doped carbon gels can be divided between reactions carried out in the gas and aqueous phases. The former group includes volatile organic compound (VOC) oxidation (e.g., toluene and xylene oxidation) and NO reduction. The latter group includes the catalytic wet air oxidation (CWAO) of aniline solutions and advanced oxidation processes (AOPs) (e.g., catalytic ozonation and photooxidation of pollutants).

Reactions in the Gas Phase VOCs are major air pollutants, and catalytic combustion is one of the most important technologies for eliminating low concentrations of VOCs in effluent systems [64]. Platinum metal is the most active catalyst for hydrocarbon combustion and is widely used supported on Al₂O₃ and other oxides. It is important for this combustion to take place at low temperatures. However, the water vapor produced during combustion under these conditions can be adsorbed on the oxide support due to its hydrophilicity, which can negatively affect the catalytic activity of the metal. This activity can also be affected by humidity in the feeding stream. Hydrophobicity of carbon materials could overcome this problem, and activated carbons have been proposed as supports in VOC combustion [65,66].

Similarly, Pt catalysts supported on carbon aerogels were used in the combustion reaction of toluene, *o*-xylene, and *m*-xylene [41,67]. Carbon aerogels were obtained by carbonization of an organic aerogel at 773 and 1273 K. Both samples were mesoporous, and their microporosity was equally accessible to N₂ and CO₂ at 77 and 273 K, respectively. Pt was deposited on both carbon aerogels by an incipient wetness technique using an aqueous solution of [Pt(NH₃)₄]Cl₂. The supported catalysts thus obtained were pretreated in different atmospheres to obtain different mean Pt particle sizes.

Catalytic activities in VOC combustion were evaluated by conversion versus temperature or light-off curves. These curves for toluene combustion are depicted in Figure 10.1 as an example. They were very steep and shifted to lower temperatures with increasing Pt particle size. Complete toluene oxidation was reached in the range between 433 and 503 K, which in some cases was lower than the temperature of around 473 K reported for some Pt/Al₂O₃ catalysts [68]. The activity of these catalysts was similar to that of a similar Pt catalyst supported on hydrophobic solids [69], although the Pt content was 3 wt% in the latter case, higher than the Pt content of the Pt-doped carbon aerogels.

Similarly, larger Pt particles were more active than smaller ones in xylene combustion. The shift to lower temperatures of light-off curves with increasing Pt particle size, in the particle size range studied, suggests that toluene and xylene combustion was a Pt-structure-sensitive reaction, as occurs with benzene combustion on Pt/Al₂O₃ [70]. In the case of xylene combustion, the catalysts

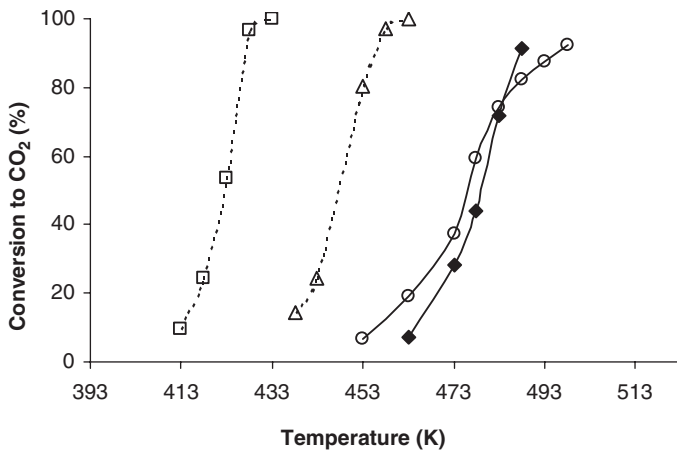
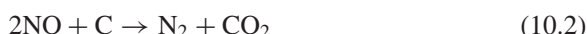


Figure 10.1 Light-off curves for catalysts: squares, A500-Pt/H₂ (6.8 nm); triangles, A1000-Pt/H₂ (5.7 nm); circles, A500-Pt/He (3.9 nm); diamonds, A1000-Pt/He (1.9 nm). Platinum particle sizes are in parentheses. (From ref. 41, with permission from Elsevier.)

supported were activated during consecutive runs and with time onstream, due to the increase in Pt particle size during reaction. Oscillations in the apparent conversion into CO₂ occurred with some catalysts or with *m*-xylene, due to coke formation and accumulation. It was demonstrated that the smaller Pt particles formed strong Pt–O bonds in xylene combustion, explaining their low combustion activity compared with that of larger particles.

On the other hand, carbon materials can be used as reducing agents, as catalysts or supports for catalysts, and as adsorbents for the removal of nitrogen oxides [71]. Thus, Cu- and Co-doped carbon xerogels were used by Liu and co-workers [72] as catalysts for NO reduction. Carbon in these xerogels acted both as a support for the metal and as a reducing agent for NO. The metal–carbon xerogels were prepared by adding the metal precursor to the initial mixture. Samples were carbonized at 1173 K in N₂. For comparison purposes, supported catalysts were also prepared by impregnation of a blank carbon xerogel.

NO conversion to N₂ at 773 K was about 90% over the Cu-doped carbon xerogel obtained by dissolving Cu nitrate in the initial RF mixture, and this rate was maintained for 1000 minutes onstream. Conversely, NO conversion over the same catalyst prepared by impregnation was about 85% and decreased gradually with time onstream. CO₂ formation was also observed, together with NO reduction:

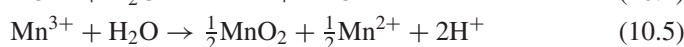
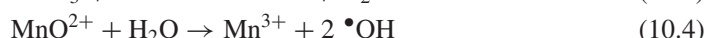


The carbon xerogel with no metal reached about 10% NO conversion, which indicates the catalytic effect of the metal. Co-doped carbon xerogels showed the same behavior as that of Cu-doped carbon xerogels.

Reactions in the Aqueous Phase The CWAO of aniline solutions has been studied using Pt catalysts supported on carbon xerogel, multiwalled carbon nanotube, and activated carbon [73]. Catalysts were prepared by incipient wetness impregnation with hexachloroplatinic acid to yield 1 wt% Pt. A large percentage of mesopores contributed to the surface area of the carbon xerogel (around 70% of 724 m²/g). Complete removal of aniline was obtained at 473 K with all catalysts after 2 hours. Pt supported on carbon xerogel and activated carbon were more selective to CO₂ formation. Activity and selectivity to CO₂ were related to the mesoporous character of the supports and to their concentration of surface oxygen complexes. These characteristics facilitated aniline adsorption on the support and subsequent reaction at the Pt active sites. A higher mesoporous area, as on the carbon xerogel, allowed easier diffusion rates than those for a microporous area. In addition, the basicity of aniline favored its adsorption on acidic supports.

AOPs have been developed [74–76] to increase the degree of transformation of persistent organic micropollutants by oxidation with hydroxyl radicals, OH, the second strongest oxidant after fluorine (2.8 V vs. standard hydrogen electrodes). Many oxidation processes are in current use (e.g., ozonation, photocatalysis, and photo-Fenton). Ozone treatment of drinking waters is limited by chemical kinetics and by the generation of degradation products [77,78]. Further development of O₃ treatment was achieved by adding supported transition metal catalysts to the system, which enhances the transformation of O₃ into •OH radicals [79,80]. Thus, the efficiency of Co-, Mn-, and Ti-doped organic aerogels for the transformation of O₃ into •OH radicals has been investigated [81]. These authors used the term *metal-doped carbon aerogels* both in the title and throughout the text, although they were not in fact carbon aerogels because the organic aerogels were not carbonized, with the exception of that with Mn. The model compound chosen for the study was sodium *para*-chlorobenzoate (pCBA).

The Mn-doped organic aerogel enhanced ozone transformation into •OH radicals, whereas Co- and Ti-doped organic aerogels were not active in this process. The mechanism operating with the Mn-doped organic aerogel was based on oxidation–reduction reactions on Mn surface-active sites:



In this process, oxidation of Mn(II) to Mn(III) and Mn(IV) resulted in the transformation of O₃ into •OH radicals. This capacity decreased with longer exposure, due to irreversible oxidation of Mn(II) to higher oxidation states. The pCBA oxidation rate increased in the presence of Mn-doped activated carbon aerogel compared to the Mn-doped organic aerogel, which the authors attributed mainly to the increase in surface basicity. The efficiency of the Mn-doped activated carbon aerogel to transform O₃ into •OH radicals was greater than that

Table 10.4 Surface Characteristics and Rate Constant (*k*) of NTS Photodegradation in the Presence of Metal-Doped Organic and Carbon Aerogels^a

Sample	<i>S</i> _{BET} (m ² /g)	<i>W</i> ₀ (cm ³ /g)	Metal Content (%)	<i>k</i> × 10 ⁴ (s ⁻¹)
A	500	0.071	—	6
A-Co(II)-15	562	0.073	14	6
A-Ti(IV)-15	550	0.071	15	6
A-Mn(II)-15	554	0.075	16	10
A-Mn(II)-50	593	0.101	7	9
A-Mn(II)-200	646	0.114	2	8
A-Mn(II)-15C	880	0.250	17	10
TiO ₂	—	—	—	50

Source: Adapted from ref. 82, with permission from Elsevier.

^aMedium-pressure lamp, [NTS]₀ = 25 μM, photocatalyst dose = 10 mg/L, pH 7, *T* = 298 K.

of other commercial activated carbons or H₂O₂ in the ozonation of water from Lake Zurich (Switzerland).

The same samples as those used in the ozonation process in aqueous solution were used by some of the foregoing authors [82] in the photooxidation of naphthalenesulfonic acid (NTS). Data in Table 10.4 show that Ti- and Co-doped organic aerogels were not active in the photooxidation of NTS. However, the Mn-doped organic aerogel increased the contaminant elimination rate, enhancing the generation of highly oxidant species in the medium. The photocatalytic activity of these materials increased with a higher surface concentration of Mn(II). The Mn-doped activated carbon aerogel [A-Mn(II)-15C] had a more developed BET surface area and microporosity, but its photocatalytic activity was not enhanced. The photodegradation of NTS was less efficient with Mn-doped organic aerogel than with TiO₂.

10.4.2 Fuel Cell Applications

Carbon aerogels and xerogels have been used as supports for Pt and Pt-based electrocatalysts for proton-exchange membrane fuel cells (PEMFCs), also known as polymer–electrolyte fuel cells [56,58,83–90]. These fuel cells are convenient and environmentally acceptable power sources for portable and stationary devices and electric vehicle applications [91]. These PEMFC systems can use H₂ or methanol as fuel. This last type of fuel cell is sometimes called a DMFC (direct methanol fuel cell).

Pt-doped carbon aerogels have been used successfully in the preparation of cathode catalyst layers for oxygen reduction reaction (ORR) in PEMFC systems [83–86]. Thus, different Pt-doped carbon aerogels with a Pt content of around 20 wt% were prepared by impregnation [83]. Results obtained with these Pt catalysts were compared with others supported on carbon blacks Vulcan XC-72 and BP2000, which are commonly used as electrocatalysts. The accessibility of the electrolyte to Pt surface atoms was lower than expected for high-surface-area

supports. Thus, about 50% of the Pt surface was electrochemically active for catalyst supported on Vulcan XC-72, whereas less than 25% was electrochemically active when carbon aerogels were used as supports. This was probably because some Pt nanoparticles were buried in pores and were partially wetted by the liquid electrolyte.

The specific activity of the Pt catalyst supported on the surface-treated carbon aerogel was between two and three times higher than the catalysts supported on the carbon blacks, demonstrating that oxygenated species introduced during the air treatment can enhance the catalytic ORR [83]. Smirnova and co-workers [84] also tested Pt catalysts supported on carbon aerogels as cathodic catalysts in PEMFC at ambient pressure. The catalysts showed relatively high open-circuit voltages and larger electrochemical surface areas, greater than those of commercial catalysts. Catalyst loading ranged from 0.06 to 0.6 mg/cm². An increase in pore size of the aerogel support from 16 to 20 nm gave rise to an increase in the cell's performance and maximum power density. Pt particles within the porosity of carbon aerogels had a low tendency to agglomeration and sintering during cell operation. The Pt-doped carbon aerogel with a Pt loading of 0.1 mg/cm² showed high power densities of up to 0.8 mW/cm² under fuel cell operation conditions in air and at ambient pressure.

The effect of carbon aerogel pore texture and method of preparation of the supported Pt catalysts on their activity has recently been reported [85]. Two different Pt precursors were used: H₂[PtCl₆] and [Pt(NH₃)₄](OH)₂. For a given Pt precursor, the pore texture of carbon aerogels used had no influence in Pt surface area and ORR activity. The best ORR specific activity was obtained with catalysts prepared with H₂[PtCl₆]. By contrast, the activity of catalysts prepared from [Pt(NH₃)₄](OH)₂ was low, despite the fact that the Pt dispersion value reached was the highest. These authors [85] indicate that this is probably due to the particle size effect on ORR activity, with a smaller Pt particle size showing a lower activity.

The influence of the mesopore size of carbon aerogels on ORR using Pt-doped carbon aerogels has also been reported by other authors [86]. They found practically no influence of pore texture on Pt dispersion. However, they indicate that the ORR activity increased when the mean mesopore size increased, reaching the best ORR performance for a mesopore size of 18.5 nm. Pt-based catalysts have also been used as anodic catalysts in DMFC systems, since Pt is able to activate the C–H bond cleavage in the temperature range of fuel cell operation (298 to 403 K). Thus, different Pt, Pt–Ni, and Pt–Ru catalysts supported on carbon xerogels have been used as catalysts in DMFC systems [87–90].

A Pt-doped carbon xerogel containing 10 wt% Pt was prepared by an incipient wetness technique [88]. The mean particle size was around 2 nm. The activity of the catalyst for methanol electrooxidation was higher in alkaline than in acid solution. In addition, the Pt surface slowly developed more favorable sites during cycling in alkaline solution. Pt supported on carbon xerogel showed better performance in the methanol electrooxidation than another Pt catalyst supported on Vulcan XC-72R with the same metal content. The large mesoporous surface

area of the carbon xerogel significantly increased the metal dispersion, favoring methanol electrooxidation.

Another carbon xerogel was used as support for Pt and Pt–Ni catalysts used in methanol electrooxidation in an alkaline medium [87]. The performance of Pt–Ni was shown to be superior to that of Pt-supported catalysts by electrocatalytic tests. Different shapes in the cyclic voltammograms of these catalysts indicated different electrooxidation mechanisms.

Pt and Pt–Ru catalysts supported on a carbon xerogel, an activated carbon xerogel, and multiwalled carbon nanotubes were also used as electrocatalysts in methanol electrooxidation [89]. The activity in the xerogel-supported catalysts was higher than in a carbon nanotube–supported catalyst. A marked increase in activity was observed for a Pt–Ru catalyst supported on the activated carbon xerogel. However, this effect was not so pronounced for the monometallic catalyst. The authors explained this behavior in terms of the metal oxidation state shown by XPS. The activated carbon xerogel helped to maintain the metal in a metallic state, as required for methanol electrooxidation, and this effect was negligible in the monometallic Pt catalyst.

Finally, the use of Pt–Ru catalysts supported on a carbon aerogel as an anode for DMFC has been reported by Du and co-workers [90]. The total metal loading was fixed to 20 wt%, and the Pt/Ru atomic ratio varied from 3:1 to 1:1. Metal particles were dispersed on the support uniformly, with a mean size of 3 nm. These authors found that with much less metal loading on the carbon aerogel, the membrane electrode assemblies had the same power density as that of commercial catalysts. This was attributed to the mesopore texture of the carbon aerogel, which facilitated methanol transportation in the electrode.

10.4.3 C=C Double-Bond Hydrogenation

Hydrogenation reactions studied have been those of benzene [92], cynamaldehyde [93], and the enantioselective hydrogenation of isophorone and 2-benzylidene-1-benzosuberone [94].

Pt-doped carbon xerogels for benzene hydrogenation reactions were obtained by impregnation with an aqueous solution of $H_2[PtCl_6]$ to yield a metal loading of 1 wt%. Three carbon xerogels were used as supports: two micro-mesoporous xerogels (mean mesopore size of 10 and 40 nm, respectively) and one micro-macroporous xerogel (mean macropore size of 70 nm). Pt dispersion was close to 100% in the xerogel with large mesopores (40 nm). For the other supports, blocking of the micropores by Pt particles was detected, and the particles within these micropores were not fully accessible. According to the authors, the high dispersion obtained with these xerogels can be attributed to two parameters: the texture and surface chemistry.

Benzene hydrogenation is a structure-insensitive reaction [95] (i.e., the reaction rate is directly proportional to the accessible Pt surface atoms). Thus, Figure 10.2 shows that there was a linear relationship between the reaction rate and Pt dispersion. The apparent reaction rates per Pt mass unit obtained with

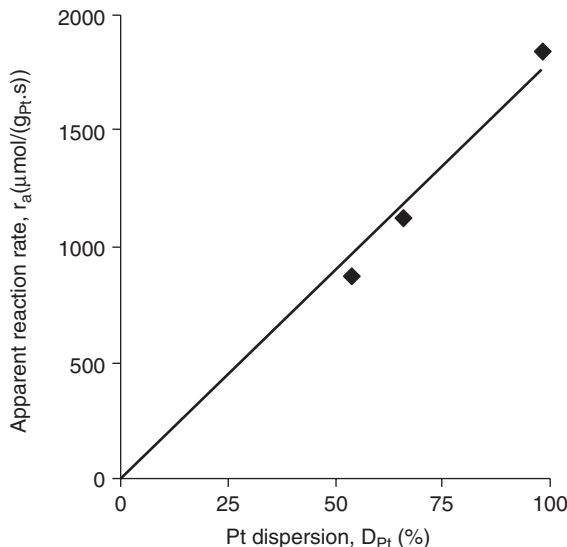


Figure 10.2 Relationship between the apparent reaction rate for benzene hydrogenation at 393 K and Pt dispersion. (From ref. 92, with permission from Elsevier.)

these catalysts were very high compared with other rates reported in the literature [96].

The hydrogenation reaction of cinnamaldehyde on Pt and Pt–Sn catalysts supported on mesoporous xerogels was recently studied [93]. Supported catalysts were prepared by impregnation with hexachloroplatinic acid as precursor and by stepwise impregnation with tin chloride and the Pt precursor above. Pt(0) and Pt(II) were detected in the monomer and bimetallic catalysts, and only oxidized tin was found in the bimetallic catalysts. The reaction products were cinnamylalcohol, hydrocinnamaldehyde, and hydrocinnamylalcohol. No other reaction products were detected. As expected, the bimetallic catalysts were superior to the monometallic catalysts, especially for catalysts prepared on a carbon xerogel activated with O₂ to an 18% burn-off. The higher selectivity of the bimetallic catalyst for unsaturated cinnamylalcohol was due to the promoting effect of Sn. The preferential hydrogenation of the C=O bond was explained by “head-on” reactant approaches to Pt active sites. This is favored on mesoporous supports such as carbon xerogels. However, in microporous activated carbons, the reactant can only enter the slit-shaped micropores sideways, favoring hydrogenation of the C=C bond.

Sipos and co-workers studied enantioselective hydrogenation of isophorone and 2-benzylidene-1-benzosuberone using Pd catalysts supported on mesoporous carbon xerogels [94]. Enantioselective hydrogenation reactions can be strongly affected by the type of support and catalyst [97,98]. A carbon xerogel and its

activated derivative were used as supports. The Pd precursor was deposited on both carbon xerogels and reduced under different conditions to yield 10 wt% Pd loading. The average Pd particle size ranged from 50 to 500 nm, depending on reduction conditions. In both enantioselective hydrogenation reactions studied, Pd-doped carbon xerogels showed higher enantiomeric excesses compared with those of the more dispersed Pd/carbon Selcat commercial catalyst. The enantiodifferentiating ability of Pd-doped carbon xerogels was close to that of Pd supported on titania, but was not competitive with Pd black.

10.4.4 Skeletal Isomerization of 1-Butene

Skeletal isomerization of 1-butene to obtain isobutene is of great practical importance. It is known [99,100], that this reaction, as with other conversion reactions of hydrocarbons, requires materials with proper pore structure and surface acidity. Chromium, molybdenum, and tungsten oxide-doped monolithic carbon aerogels were studied as catalysts in the skeletal isomerization reaction of 1-butene [47]. These materials were prepared by dissolving the metal precursors in the initial R/F mixture and carbonizing at both 773 and 1273 K. All samples obtained had no mesopores or negligible mesoporosity. However, they had a large macropore volume, which increased from the chromium to the tungsten oxide-doped carbon aerogel. The BET surface area increased in the same direction, from 400 to 530 m²/g, and from 400 to 610 m²/g for samples heat-treated at 773 and 1273 K, respectively. The acid–base character of these catalysts was determined by measuring the catalytic activity for isopropanol decomposition. Results obtained with catalysts at 773 K are compiled in Table 10.5. Their activity to obtain propene, or their acidity, increased considerably from chromium- to tungsten-doped carbon aerogel. The activity of catalyst AW773 to obtain propene was higher than that obtained with other tungsten oxide catalysts supported on activated carbons [101] when compared per unit of tungsten oxide content.

Catalytic performance of samples in the isomerization of 1-butene was studied at temperatures ranging from 323 to 698 K. A tungsten oxide-containing carbon aerogel was much more active than those containing chromium or molybdenum oxide. The greater catalytic activity of tungsten oxide was due to the high acidity of this oxide. A loss of activity was observed when this catalyst was obtained at 1273 K (AW1273). The activity of the tungsten oxide-containing carbon aerogel

Table 10.5 Activity of Catalysts ($\mu\text{mol/g}_{\text{cat}} \cdot \text{s}$) to Decompose Isopropanol in Propene and Acetone

Catalyst	r_{propene}	r_{acetone}
ACr773	6.0×10^{-4}	3.5×10^{-2}
AMo773	5.2×10^{-2}	2.9×10^{-2}
AW773	2.7×10^{-1}	5.5×10^{-3}

Source: Adapted from ref. 47, with permission from Elsevier.

in the isomerization of 1-butene was also greater than that of similar catalysts supported on activated carbons [102].

Isobutene and *trans*-2-butene were the main reaction products. Neither C₃–C₅ nor C₂–C₆ by-products were observed among the reaction products, as in the case of small-pore zeolites, suggesting that the reaction followed a monomolecular mechanism and that there was no dimerization, probably due to an effect of the carbon aerogel porosity.

10.4.5 Hydrodechlorination Reaction

Pd–Ag bimetallic catalysts supported on carbon xerogels have been used in the hydrodechlorination reaction of 1,2-dichloroethane [103,104]. Pd and Ag were deposited by co-impregnation using a solution of palladium and silver nitrates. Metal particle size ranged from 2 to 5 nm in Pd catalysts but had a wider distribution (4 to 20 nm) in Ag catalysts. Bimetallic Pd–Ag catalysts showed small particle alloys of 3 to 4 nm. The bulk Ag content in this alloy was limited to about 50 wt%, which fixed the minimum Pd surface content of the alloy at about 10 wt%. Pd catalysts produced mainly ethane, whereas bimetallic Pd–Ag catalysts were selective for the production of ethylene. The ethylene selectivity increased with silver fraction at the alloy surface.

Hydrodechlorination of 1,2-dichloroethane into ethylene on the Pd–Ag bimetallic catalysts above supported on carbon xerogels was chosen as a test reaction to study mass transfer in carbon xerogel-supported catalysts [104]. Results showed that diffusional limitations could be avoided by choosing the appropriate pore size range. Thus, there were diffusional limitations for carbon xerogels with pores smaller than 10 nm, regardless of the reaction temperature, as soon as the pellet size was larger than 0.25 mm. However, for carbon xerogels with a pore size range of 60 to 90 nm, 1,2-dichloroethane conversion, ethylene selectivity, and reaction rate were independent of pellet size up to about 4 mm (at 623 K) and 7 mm (at 573 K). These results indicate that the pore texture of carbon xerogels can be adapted to the reaction in question. This is an advantage over activated carbons, which are generally microporous solids with low meso- and macroporosity, inducing diffusional limitations and diminishing catalyst performance [104].

10.4.6 Other Reactions

Mukai and co-workers [105] used Keggin-type heteropolyacids immobilized in the network structure of resorcinol–formaldehyde carbon gels as catalysts for the synthesis of methyl *tert*-butyl ether from methyl alcohol and *tert*-butyl alcohol. Large amounts of 12-tungstophosphoric and 12-molybdophosphoric acids were immobilized into the support by two methods, pore shrinkage and the ship-in-the-bottle method, which are essentially impregnation methods. The authors reported that these catalysts showed activity in the reaction studied and could be of practical utility as solid acid catalysts in various reactions.

Rojas-Cervantes and co-workers [106] prepared basic Na-, K-, Mg-, and Zr-doped carbon xerogels. The catalysts were prepared by adding the metal precursors to the initial R/F mixture. The basic character of the catalysts was determined by the Knoevenagel condensation of benzaldehyde with different methylenic compounds. The catalytic activity found by the authors was significantly higher than that observed for impregnation-prepared alkaline carbons. The Zr-doped carbon xerogel was the most selective catalyst in promoting the Knoevenagel reaction for all methylenic compounds tested. The activity of the catalysts was determined by the basic character of the M-carbon catalysts, whereas the textural characteristics of samples appeared to exert no influence.

Pd-doped organic and carbon aerogels containing between 20 and 40 wt% Pd were demonstrated to be good catalysts in the Mizoroki–Heck reaction of iodobenzene with styrene and 3-butene-2-one in liquid phase to yield *trans*-1,2-diphenylethylene and *trans*-4-phenyl-3-butene-2-one, respectively [52]. Finally, Eu-doped organic and carbon aerogels were active as catalysts in two Michael addition reactions: the reaction of ethyl 2-oxocyclopentanecarboxylate with 2-butenone and with cyclopentenone. Moreover, these catalysts could be recovered and reused [53].

10.5 CONCLUSIONS

Carbon gels can be obtained from the carbonization of organic gels, which are prepared by sol–gel polycondensation of certain organic monomers, and the most widely studied have been resorcinol–formaldehyde mixtures in water as solvent. These materials are obtained with high purity, homogeneity, and controlled porosity due to the sol–gel synthesis used. With regard to their pore structure, micropores are developed into the primary particles of the gel, whereas meso- and macropores are produced in the interparticle structure occupied initially by the solvent. It is therefore possible to control the concentration of micropores and mesopores independently, which is one of the advantages of carbon gels as porous carbon materials.

Hence, carbon gels with well-developed and controlled micro- and mesoporosity, a narrow mesopore size distribution, and a large surface area can be designed by selection of different ingredients from the original recipe and of the conditions of the three main stages of their preparation. All of this makes carbon gels promising materials for application in adsorption and catalysis. A further advantage of these materials is that carbon gels can be produced in the form of monoliths, beads, powders, or thin films.

Carbon gels are denominated as carbon aerogels, xerogels, or cryogels, depending on the method used to dry the wet organic gel. An important feature of these carbon gels is that metal-doped carbon gels can readily be prepared. These are emergent materials in the field of heterogeneous catalysis, and their use will probably increase in the near future, due to the versatility of their shape and pore texture.

Metal-doped carbon gels for use in catalysis have been prepared by three main strategies. The first is the addition of a soluble metal precursor in the initial mixture. The second is the introduction into the initial mixture or organic gel of a functionalized moiety that has binding sites for the metal. The third strategy is to deposit the metal precursor on the organic or carbon gel by one of various methods, including incipient wetness, adsorption, sputtering, sublimation, and supercritical deposition.

When the metal precursor is added to the initial resorcinol-formaldehyde mixture, it is more difficult to control the pore texture, surface area, and density of the carbon matrix because the metal precursor strongly influences the solution pH, sol-gel chemistry, and pyrolysis of the organic gel, since metals present a different activity at each preparation stage. On the other hand, during the gelification process, some metals can be chelated by functional groups of the organic matrix, favoring good dispersion in the final solid. However, the main problem for this preparation method is that some of the metal particles can sometimes be encapsulated by the carbon matrix, reducing the accessibility of reactant molecules to the metal particles.

The metallic and organic phases can also interact during the carbonization of metal-doped organic gels, which is highly dependent on the nature of the metallic phase present. Thus, some metals, such as Cr, Fe, Co, and Ni, can catalyze the partial graphitization of various carbon areas. In addition, the organic phase influences the nature and properties of the metallic phase. Thus, the organic matrix can progressively reduce or even carburize the metal precursors to an extent that depends on the metal present and the temperature and atmosphere of the treatment. In addition, the organic matrix can to a certain degree modify the acid-base character when the metallic phase is a metal oxide.

According to published results, all three methods for preparing metal-doped carbon gels produce a homogeneous distribution of the metals throughout the material in the form of nano-sized particles. Nevertheless, the smallest metal particle size or highest dispersion can be better achieved by deposition of the metal precursor on the carbon gel, the mesoporosity of the support playing an important role in this case. Thus, a nearly atomic dispersion has been reported in some Pt catalysts supported on either carbon aerogels or xerogels.

In some cases, metal distribution was maintained at the nanometer scale even after high-temperature treatments. This suggests that metal particles were anchored to the carbon structure, preventing their migration and growth. Thus, micro- and mesopores can act as anchorage points for the metal particles, because many of these materials have narrow pore size distributions.

Metal-doped carbon gels have been used as catalysts in several reactions, including the removal of pollutants in either gas or aqueous phase, ORR and methanol electrooxidation for fuel cell applications, C=C double-bond hydrogenations, skeletal isomerization and hydrodechlorination reactions, and other organic syntheses. The activity and/or selectivity of metal-doped carbon gels was better than that of other, more widely used supported catalysts in many of the

reactions studied to date. This has been attributed to the particular pore texture of the carbon gels used and, in some cases, to their surface chemistry.

In fuel cell applications, however, the presence of small micropores can reduce the accessibility of the liquid electrolyte to the metal particles placed within them. This may be avoided by developing carbon gels with the appropriate mesoporous network. Hence, the pore texture of carbon gels can be adapted to the reaction under question, and this is possible because of the pore texture flexibility of carbon gels, which can be tailored by controlling all the steps in carbon gel synthesis. This is an advantage over activated carbons, which are generally microporous solids with low meso- and macroporosity, which induces diffusional limitations and diminishes catalyst performance.

REFERENCES

- [1] R.W. Pekala, U.S. patent 4,873,218, 1989.
- [2] R.W. Pekala, *J. Mater. Sci.* 24 (1989) 3221.
- [3] R.W. Pekala, C.T. Alviso, F.M. Kong, S.S. Hulsey, *J. Non-Cryst. Solids* 145 (1992) 90.
- [4] G.A.M. Reynolds, A.W.P. Fung, Z.H. Wang, M.S. Dresselhaus, R.W. Pekala, *J. Non-Cryst. Solids* 188 (1995) 27.
- [5] R.W. Pekala, J.C. Farmer, C.T. Alviso, T.D. Tran, S.T. Mayer, J.M. Miller, B. Dunn, *J. Non-Cryst. Solids* 225 (1998) 74.
- [6] G. Reichenauer, A. Emmerling, J. Fricke, R.W. Pekala, *J. Non-Cryst. Solids* 225 (1998) 210.
- [7] R.W. Pekala, C.T. Alviso, J.D. LeMay, *J. Non-Cryst. Solids* 125 (1990) 67.
- [8] F.J. Maldonado-Hódar, M.A. Ferro-García, J. Rivera-Utrilla, C. Moreno-Castilla, *Carbon* 37 (1999) 1199.
- [9] G.M. Pajonk, *Catal. Today* 35 (1997) 319.
- [10] A.C. Pierre, G.M. Pajonk, *Chem. Rev.* 102 (2002) 4243.
- [11] S. Al-Muhtaseb, J.A. Ritter, *Adv. Mater.* 15 (2003) 101.
- [12] J. Livage, C. Sánchez, *J. Non-Cryst. Solids* 145 (1992) 11.
- [13] R.D. González, T. López, R. Gómez, *Catal. Today* 35 (1997) 293.
- [14] A.C. Pierre, *Introduction to Sol-Gel Processing*, Kluwer, Boston, 1998.
- [15] T. Yamamoto, T. Sugimoto, T. Suzuki, S.R. Mukai, H. Tamon, *Carbon* 40 (2002) 1345.
- [16] H. Nishihara, S.R. Mukai, H. Tamon, *Carbon* 42 (2004) 899.
- [17] T. Horikawa, J. Hayashi, K. Muroyama, *Carbon* 42 (2004) 169.
- [18] T. Horikawa, Y. Ono, J. Hayashi, K. Muroyama, *Carbon* 42 (2004) 2683.
- [19] S. Jun, W. Jue, Z. Jiwei, G. Yanzhi, W. Guangming, Z. Bin, N. Xingyuan, *J. Sol-Gel Sci. Technol.* 31 (2004) 209.
- [20] N. Liu, S. Zhang, R. Fu, M.S. Dresselhaus, G. Dresselhaus, *Carbon* 44 (2006) 2430.
- [21] B. Friedel, S. Greulich-Weber, *Small* 2 (2006) 859.

- [22] M. Inagaki, K. Kaneko, T. Nishizawa, *Carbon* 42 (2004) 1401.
- [23] R. Fu, N. Yoshizawa, M.S. Dresselhaus, G. Dresselhaus, J. Satcher, T.F. Baumann, *Langmuir* 18 (2002) 10100.
- [24] T.F. Baumann, A.F. Glenn, J. Satcher, *Langmuir* 18 (2002) 7073.
- [25] R. Fu, Y.M. Lin, O. Rabin, G. Dresselhaus, M.S. Dresselhaus, J. Satcher, T.F. Baumann, *J. Non-Cryst. Solids* 317 (2003) 247.
- [26] N. Yoshizawa, H. Hatori, Y. Soneda, Y. Hanzawa, K. Kaneko, M.S. Dresselhaus, *J. Non-Cryst. Solids* 330 (2003) 99.
- [27] M.H. Nguyen, L.H. Dao, *J. Non-Cryst. Solids* 225 (1998) 51.
- [28] R. Zhang, Y. Lu, L. Zhan, X. Liang, G. Wu, L. Ling, *Carbon* 41 (2003) 1660.
- [29] W. Li, S. Guo, *Carbon* 38 (2000) 1520.
- [30] W.C. Li, A.H. Lu, S.C. Guo, *Carbon* 39 (2001) 1989.
- [31] N. Job, A. Thery, R. Pirard, J. Marien, L. Kocon, J.N. Rouzaud, F. Béguin, J.P. Pirard, *Carbon* 43 (2005) 2481.
- [32] H. Kabbour, T.F. Baumann, J.H. Satcher, Jr., A. Saulnier, C.C. Ahn, *Chem. Mater.* 18 (2006) 6085.
- [33] T. Horikawa, J. Hayashi, K. Muroyama, *Carbon* 42 (2004) 1625.
- [34] S. Berthon-Fabry, D. Langohr, P. Achard, D. Charrier, D. Djurado, F. Ehrburger-Dolle, *J. Non-Cryst. Solids* 350 (2004) 136.
- [35] D. Fairén-Jiménez, F. Carrasco-Marin, C. Moreno-Castilla, *Carbon* 44 (2006) 2301.
- [36] R. Saliger, V. Bock, R. Petricevic, T. Tillotson, S. Geis, J. Fricke, *J. Non-Cryst. Solids* 211 (1997) 144.
- [37] J. Gross, G.W. Scherer, C.T. Alviso, R.W. Pekala, *J. Non-Cryst. Solids* 211 (1997) 132.
- [38] D. Fairén Jiménez, Ph.D. dissertation, University of Granada, Spain, 2006.
- [39] E. Bekyarova, K. Kaneko, *Langmuir* 15 (1999) 7119.
- [40] E. Bekyarova, K. Kaneko, *Adv. Mater.* 12 (2000) 1625.
- [41] F.J. Maldonado-Hódar, C. Moreno-Castilla, A.F. Pérez-Cadenas, *Appl. Catal. B* 54 (2004) 217.
- [42] F.J. Maldonado-Hódar, C. Moreno-Castilla, J. Rivera-Utrilla, Y. Hanzawa, Y. Yamada, *Langmuir* 16 (2000) 4367.
- [43] C. Moreno-Castilla, F.J. Maldonado-Hódar, A.F. Pérez-Cadenas, *Langmuir* 19 (2003) 5650.
- [44] F.J. Maldonado-Hódar, C. Moreno-Castilla, A.F. Pérez-Cadenas, *Micropor. Mesopor. Mater.* 69 (2004) 119.
- [45] N. Job, R. Pirard, J. Marien, J.P. Pirard, *Carbon* 42 (2004) 3217.
- [46] C. Sayag, M. Benkhaled, S. Suppan, J. Trawczynski, G. Djega-Mariadassou, *Appl. Catal. A* 275 (2004) 15.
- [47] C. Moreno-Castilla, F.J. Maldonado-Hódar, J. Rivera-Utrilla, E. Rodríguez-Castellón, *Appl. Catal. A* 183 (1999) 345.
- [48] F.J. Maldonado-Hódar, A.F. Pérez-Cadenas, C. Moreno-Castilla, *Carbon* 41 (2003) 1291.

- [49] A.F. Pérez-Cadenas, F.J. Maldonado-Hódar, C. Moreno-Castilla, *Langmuir* 21 (2005) 10850.
- [50] D. Mordenti, D. Brodzki, G. Djega-Mariadassou, *J. Solid State Chem.* 141 (1998) 114.
- [51] R. Fu, T.F. Baumann, S. Cronin, G. Dresselhaus, M.S. Dresselhaus, J. Satcher, *Langmuir* 21 (2005) 2647.
- [52] S. Martínez, A. Vallribera, C.L. Cotet, M. Popovici, L. Martin, A. Roig, M. Moreno-Mañas, E. Molins, *New J. Chem.* 29 (2005) 1342.
- [53] S. Martínez, L. Martin, E. Molins, M. Moreno-Mañas, A. Roig, A. Vallribera, *Monatsh. Chem.* 137 (2006) 627.
- [54] L.C. Cotet, M. Gich, A. Roig, I.C. Popescu, V. Cosoveanu, E. Molins, V. Danciu, *J. Non-Cryst. Solids* 352 (2006) 2772.
- [55] R. Fu, M.S. Dresselhaus, G. Dresselhaus, B. Zheng, J. Liu, J. Satcher, T.F. Baumann, *J. Non-Cryst. Solids* 318 (2003) 223.
- [56] W.S. Baker, J.W. Long, R.M. Stroud, D.R. Rolison, *J. Non-Cryst. Solids* 350 (2004) 80.
- [57] G.M. Pajonk, A.V. Rao, N. Pinto, F. Ehrburger-Dolle, M. Bellido-Gil, *Stud. Surf. Sci. Catal.* 118 (1998) 167.
- [58] M. Glora, M. Wiener, R. Petricevic, H. Probstle, J. Fricke, *J. Non-Cryst. Solids* 285 (2001) 283.
- [59] C.D. Saquing, T.T. Cheng, M. Aindow, C. Erkey, *J. Phys. Chem. B* 108 (2004) 7716.
- [60] C.D. Saquing, D. Kang, M. Aindow, C. Erkey, *Micropor. Mesopor. Mater.* 80 (2005) 11.
- [61] Y. Zhang, D. Kang, M. Aindow, C. Erkey, *J. Phys. Chem. B* 109 (2005) 2617.
- [62] J.M. Miller, B. Dunn, *Langmuir* 15 (1999) 799.
- [63] S. Zhang, R. Fu, D. Wu, W. Xu, Q. Ye, Z. Chen, *Carbon* 42 (2004) 3209.
- [64] J.J. Spivey, *Ind. Eng. Chem. Res.* 26 (1987) 2165.
- [65] M. Zhang, B. Zhou, K.T. Chuang, *Appl. Catal. B* 13 (1997) 123.
- [66] J.C.S. Wu, Z.A. Lin, F.M. Tsai, J.W. Pan, *Catal. Today* 63 (2000) 419.
- [67] M.N. Padilla-Serrano, F.J. Maldonado-Hódar, C. Moreno-Castilla, *Appl. Catal. B* 61 (2005) 253.
- [68] J.C.S. Wu, Z.A. Lin, F.M. Tsai, J.W. Pan, *Catal. Today* 63 (2000) 419.
- [69] J.C.S. Wu, T.Y. Chang, *Catal. Today* 44 (1998) 111.
- [70] T.F. Garetto, C.R. Apesteguía, *Appl. Catal. B* 32 (2001) 83.
- [71] F. Derbyshire, M. Jagtoyen, R. Andrews, A. Rao, I. Martín-Gullón, E. Grulke, in L.R. Radovic, Ed., *Chemistry and Physics of Carbon*, Vol. 27, Marcel Dekker, New York, 2001, p. 1.
- [72] Z. Liu, A. Wang, X. Wang, T. Zhang, *Carbon* 44 (2006) 2345.
- [73] H.T. Gomes, P.V. Samant, P. Serp, P. Kalck, J.L. Figueiredo, J.L. Faria, *Appl. Catal. B* 54 (2004) 175.
- [74] O. Legrini, E. Oliveros, A.M. Braun, *Chem. Rev.* 93 (1993) 671.
- [75] R. Andreozzi, V. Caprio, A. Insola, R. Martota, *Catal. Today* 53 (1999) 51.

- [76] S. Esplugas, J. Jiménez, S. Contreras, E. Pascual, M. Rodríguez, *Water Res.* 36 (2002) 1034.
- [77] C.A. Zaror, *J. Chem. Technol. Biotechnol.* 70 (1997) 21.
- [78] J. Rivera-Utrilla, M. Sánchez-Polo, *Appl. Catal. B* 39 (2002) 319.
- [79] R. Andreozzi, A. Insola, V. Caprio, M.G. D'Amore, *Water Res.* 26 (1992) 917.
- [80] M. Sánchez-Polo, J. Rivera-Utrilla, *J. Chem. Technol. Biotechnol.* 79 (2004) 902.
- [81] M. Sánchez-Polo, J. Rivera-Utrilla, U. von Gunten, *Water Res.* 40 (2006) 3375.
- [82] M. Sánchez-Polo, J. Rivera-Utrilla, *Appl. Catal. B* 69 (2006) 93.
- [83] J. Marie, S. Berthon-Fabry, P. Achard, M. Chatenet, A. Pradourat, E. Chainet, *J. Non-Cryst. Solids* 350 (2004) 88.
- [84] A. Smirnova, X. Dong, H. Hara, A. Vasiliev, N. Sammes, *Int. J. Hydrogen Energy* 30 (2005) 149.
- [85] J. Marie, S. Berthon-Fabry, M. Chatenet, E. Chainet, R. Pirard, N. Cornet, P. Achard, *J. Appl. Electrochem.* 37 (2007) 147.
- [86] H. Du, L. Gan, B. Li, P. Wu, Y. Qiu, F. Kang, R. Fu, Y. Zeng, *J. Phys. Chem. C* 111 (2007) 2040.
- [87] P.V. Samant, J.B. Fernandes, C.M. Rangel, J.L. Figueiredo, *Catal. Today* 102–103 (2005) 173.
- [88] P.V. Samant, C.M. Rangel, M.H. Romero, J.B. Fernandes, J.L. Figueiredo, *J. Power Sources* 151 (2005) 79.
- [89] J.L. Figueiredo, M.F.R. Pereira, P. Serp, P. Kalck, P.V. Samant, J.B. Fernandes, *Carbon* 44 (2006) 2516.
- [90] H. Du, B. Li, F. Kang, R. Fu, Y. Zeng, *Carbon* 45 (2007) 429.
- [91] S.M. Haile, *Acta Mater.* 51 (2003) 5981.
- [92] N. Job, M.F.R. Pereira, S. Lambert, A. Cabiac, G. Delahay, J.F. Colomer, J. Marien, J.L. Figueiredo, J.P. Pirard, *J. Catal.* 240 (2006) 160.
- [93] P.V. Samant, M.F.R. Pereira, J.L. Figueiredo, *Catal. Today* 102 (2005) 183.
- [94] E. Sipos, G. Fogassy, A. Tungler, P.V. Samant, J.L. Figueiredo, *J. Mol. Catal. A* 212 (2004) 245.
- [95] A.E. Aksoylu, M. Madalena, A. Freitas, J.L. Figueiredo, *Appl. Catal. A* 192 (2000) 175.
- [96] A.E. Aksoylu, J.L. Faria, M.F.R. Pereira, J.L. Figueiredo, P. Serp, J.C. Hierso, R. Feurer, Y. Kihn, P. Kalck, *Appl. Catal. A* 243 (2003) 357.
- [97] A. Baiker, *J. Mol. Catal. A* 163 (2000) 205.
- [98] T. Tamai, A. Tungler, T. Máthé, J. Petró, R.A. Sheld, G. Tóth, *J. Mol. Catal.* 102 (1995) 41.
- [99] J. Houzvicka, O. Diefenbach, V. Ponec, *J. Catal.* 164 (1996) 288.
- [100] J. Houzvicka, S. Hansildaar, V. Ponec, *J. Catal.* 167 (1997) 273.
- [101] A.F. Pérez-Cadenas, C. Moreno-Castilla, F.J. Maldonado-Hódar, J.L.G. Fierro, *J. Catal.* 217 (2003) 30.
- [102] M.A. Álvarez-Merino, F. Carrasco-Marín, C. Moreno-Castilla, *J. Catal.* 192 (2000) 374.

- [103] N. Job, B. Heinrichs, F. Ferauche, F. Noville, J. Marien, J.P. Pirard, *Catal. Today* 102 (2005) 234.
- [104] N. Job, B. Heinrichs, J.P. Pirard, J.F. Colomer, B. Vertruyen, J. Marien, *AIChE J.* 52 (2006) 2663.
- [105] S.R. Mukai, T. Sugiyama, H. Tamon, *Appl. Catal. A* 256 (2003) 99.
- [106] M.L. Rojas-Cervantes, L. Alonso, J. Díaz-Terán, A.J. López-Peinado, R.M. Martín-Aranda, V. Gómez-Serrano, *Carbon* 42 (2004) 1575.

11 Carbon Monoliths in Catalysis

KAREN M. DE LATHOUDER, EDWIN CREZEE,
FREEK KAPTEIJN, and JACOB A. MOULIJN

11.1 INTRODUCTION

Recently, there has been a growing interest in the use of monolithic structures for (bio)chemical conversion and adsorption processes. A very versatile type of monolith is based on carbon. The combined properties of carbon and monolithic structures create a support with great potential. In this chapter we describe recent developments in the field of carbon-based monolithic structures with respect to preparation, support properties, and application in catalytic processes. Furthermore, two examples are used to demonstrate the approach and possible pitfalls when using carbon (coated) monoliths in catalysis.

11.2 CARBON

Carbon materials are well known in adsorption and catalytic processes, due to their stability in acidic and basic media. Hence, these materials have a wide range of applications in different areas, such as pollutant removal (active carbon), gas separation (molecular sieves), or chemical reaction (catalysts and catalyst supports). Nevertheless, only a few large-volume catalytic processes currently use carbon-supported catalysts (refs. 1 and 2, and Chapter 15). Problems regarding mechanical properties, reproducibility, and quality control in large-scale production processes of carbons limit the physical form to granules or extrudates. The use of these structures in trickle-bed reactors is associated with potential channeling, high-pressure drops, and decreased catalyst efficiency. These problems can be overcome by using structured carbon–ceramic composite materials. Macrostructured supports such as honeycomb monoliths are very suitable for applying thin-coat layers of various materials.

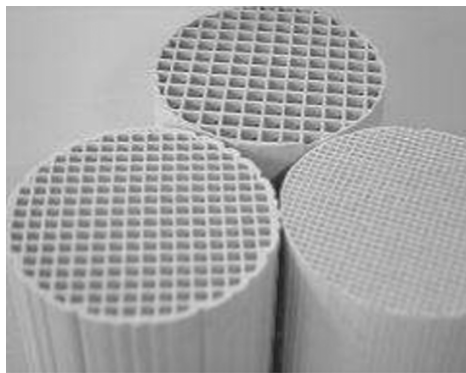


Figure 11.1 Ceramic monoliths of various cell densities.

Table 11.1 Geometric Characteristics of Generally Used Monoliths

Cell Density cpsi	Geometric Surface Area (m ² /m ³)	Void Fraction	Channel Diameter (mm)	Wall Thickness (μm)
200	31	0.72	1.80	270
400	62	0.76	1.27	165
600	93	0.80	1.04	112
1100	170	0.84	0.77	64

11.3 MONOLITHIC STRUCTURES

Monoliths are structured supports and are characterized by long parallel channels separated by thin walls (Figure 11.1). Monoliths offer a low-pressure drop over a reactor, resistance to plugging, high mechanical strength, low axial dispersion, and high mass-transfer rates, due to their high void fraction and large geometric surface area (Table 11.1). Monoliths are widely applied in catalytic off-gas treatment such as automotive exhaust gas purification [3] and de-NO_x-ing of power plant emissions [4].

11.4 CARBON MONOLITHS

Carbon-based monoliths can be of the integral or coated type [5,6]. For practical applications, several requirements are set to monolithic structures. For a coated type of monolithic support, the mechanical properties are adopted from the ceramic or metallic monoliths. It is, however, important that the coating adhere well to the monolith to prevent flaking and subsequent loss of active

material. The geometric surface area and void fraction of the monolith are generally drastically reduced by applying a thicker carbon coating; this can affect the diffusion distances inside the catalytic layer and hence the selectivity.

Integral-type monolithic structures have to provide the mechanical properties themselves. This is an ongoing challenge, considering the mechanical properties of activated carbon [7] compared to ceramic structures. It is therefore important to determine the strength of the integral structures since breakdown of the monolith can lead to expensive reconstruction of the reactor. The geometric properties of integral monoliths are set during manufacturing.

Integral carbon monoliths are prepared by extrusion of the carbon precursor, mixed with various additives. The function of the additive (in general, organic or inorganic powders or cellulose fibers) is to make the resin extrudable. Carbon-coated monoliths can be produced by various methods [5]:

- *Melting*. A ceramic structure is heated with a pitch carbon in an inert atmosphere, resulting in melting of the pitch and penetration of the pores of the monolith structure with the carbonized pitch.
- *Dipcoating*. A liquid polymer (solution) is introduced into the monolith channels by dipcoating, and converted into carbon by heating in an inert atmosphere.
- *CVD method*. Chemical vapor deposition of hydrocarbons or catalytic growth from the gas phase is performed on a ceramic or metallic monolith.

Using the melting or dipcoating method, the carbon coating is anchored to the structure by penetration into the porous network, so that a continuous and interlocked network is formed upon carbonization. CVD-based coating is usually more sensitive to flaking. The melting method has the advantage that only a single preparation step is needed, but it has the risk of maldistribution of the carbon throughout the monolith. The CVD method requires a high-surface-area support because the carbon formed usually does not itself show any porosity. Local variance of process parameters can cause a difference in the degree of coverage of the channels in the longitudinal direction.

The most widely applied preparation method is dipping the supports in a polymeric solution. To remove excess polymer efficiently from the channels, low-viscosity polymer solutions are preferred as carbon precursors. The most straightforward method is the dipcoating method [6]: The honeycombs are dipped in a precursor solution and then dried and/or cured. Subsequently, the precursor is carbonized and, if needed, activated. Many different carbon precursors have been used, such as saccharides [1,8], polyfurfuryl alcohol (PFA) [5,9], and phenolic [10] or furanic [11] resins.

Another method that is becoming increasingly important is the application of carbon on a ceramic surface, as is the growth of carbon filaments over deposited metal particles (the CVD method) [12–14]. Carbon nanofibers (CNFs) have long been known as a nuisance that often emerges during catalytic conversion of

carbon-containing gases [15]. These graphitic materials (see Chapter 9) are chemically similar to fullerenes and carbon nanotubes and have a large potential for a range of applications in catalyst support materials [16–18]. In the CVD method, monolith structures are washcoated and impregnated with metal catalyst, and subsequently heated in a gas flow with carbon precursor to establish growth of CNFs.

11.5 CARBON MONOLITHS IN CATALYSIS: AN OVERVIEW

In catalytic applications, monoliths can provide better control of the contact time of reactants and products with the catalyst. This leads to a potential increase in selectivity. Together with the advantages over conventional trickle-bed reactors (pressure-drop surface area, short diffusion lengths), this makes the monolith reactor very suitable for use in consecutive reaction schemes, such as selective oxidation or hydrogenation. Literature dealing with carbon monolith structures is not yet extensive, however, and a limited number of applications have been reported, as shown in Table 11.2.

Table 11.2 Applications of Carbon-Based Monoliths in Catalysis

Type	Reaction	Conditions	Monolith	Refs.
G/L	Pt-catalyzed selective oxidation of cyclohexanol to adipic acid	413 K, 5.0 MPa	Coated	19, 20
	Pt/Ir-catalyzed selective hydrogenation of cinnamaldehyde to cinnamyl alcohol	303 K, 5 MPa	Coated	21, 22
	Pd-catalyzed selective hydrogenation of fatty acid methyl esters	373 K, 2.0 MPa	Coated	23
	Ru-catalyzed hydrogenation of D-glucose to D-sorbitol	373–403 K, 4.0 MPa	Coated	24
L	Lipase-catalyzed acylation of <i>n</i> -butanol with vinyl acetate	283–323 K, 0.1 MPa	Coated/ CVD	13, 25
G	Selective catalytic reduction: $6\text{NO} + 4\text{NH}_3 \xrightarrow{\text{Mn/CFe/C}} 5\text{N}_2 + 6\text{H}_2\text{O}$ $2\text{SO}_2 + \text{O}_2 \xrightarrow{\text{V}_2\text{O}_5/\text{C}} 2\text{SO}_3$	353–473 K, 0.1 MPa	Integral	26–30
	Pd/Pt-catalyzed low-temperature combustion of xylenes	393–453 K, 0.1 MPa	Coated	31

In this chapter two different catalytic systems with carbon monoliths as the support matrix are discussed in terms of preparation and performance. The main difference between these systems is the effect of the carbon monolith on selectivity. Finally, some practical considerations of the use of different carbon monoliths are discussed.

11.6 EXAMPLE OF CARBON MONOLITHS AS CATALYST SUPPORT MATERIAL

11.6.1 Carbon Monoliths as Support Material in Biocatalysis

Enzymes are an attractive tool in asymmetric catalysis and efficiently complement traditional chemical methods [32,33]. The use of biocatalysts makes it possible to carry out chemical transformations without the need for laborious protection and deprotection steps [34]. Immobilized enzymes are preferred over free enzymes in solution, due to the possibility of repeated use, higher resistance to denaturing effects, and easy separation. The use of a structured support material could be an interesting alternative for conventional particulate enzyme carriers. When optimizing the use of immobilized enzymes, the immobilization method chosen is a very important factor to consider [35]. In this study, a reaction in an organic medium is considered; most enzymes do not readily dissolve in organic media, and the enzyme will not detach from the support. This makes physical adsorption a very suitable technique to prepare a biocatalyst for use in an organic medium [36]. In this example, lipase is immobilized on different carbon monoliths and applied in a transesterification reaction in toluene. The biocatalysts are compared in terms of carrier preparation, enzyme immobilization, and performance. A commercially available immobilized lipase is used as a comparison. A convenient tool to compare monolithic biocatalysts is the monolithic stirrer reactor (MSR), consisting of two monoliths that have the catalyst immobilized on the wall of their channels. These monoliths work as stirrer blades that can easily be removed from the reaction medium, thereby eliminating the need for a filtration step after reaction [37].

11.6.2 Selective Hydrogenation of D-Glucose Over Monolithic Ruthenium Catalysts

Catalytic hydrogenation of D-glucose to D-sorbitol is an industrially important reaction, as the product D-sorbitol is a versatile chemical intermediate. Approximately 60% of the D-sorbitol produced is utilized in processed foods, confections, toothpaste, and other personal care products as humectants, stabilizers, softeners, emulsifiers, and bodying agents [38]. Current D-glucose hydrogenation technology involves either batch stirred-tank reactors or continuous bubble columns [39]. The catalysts used are generally various types of supported nickel or promoted Raney-type nickel catalysts. Because these types of catalysts are subject to severe leaching by the aqueous reaction medium, substantial nickel losses and product

cleanup are inevitable [40]. Ruthenium appears as a new promising catalyst studied both supported on carrier [41] and in the form of a homogeneous phosphine complex [42]. Carbon is the obvious choice of support material, since it does not leach in the acidic and chelating reaction medium. Furthermore, activated carbon has a high surface area, enabling high metal dispersions to be obtained, and the precious metal can be recovered easily from the catalyst by burning off the carbon support. The higher costs of ruthenium is reduced by (1) much lower metal content, due to the superior activity of Ru/C; (2) minor downtime of the plant, due to the prolonged lifetime of the catalyst; (3) omission of the ion-exchange step, since Ru/C does not leach; and (4) ease of handling. In contrast to Raney-type nickel, ruthenium catalysts are not pyrophoric, which facilitates reactor loading and catalyst filtration. Conventional trickle-bed reactors have the disadvantage that local overheating side reactions (e.g., isomerization, caramelization) can occur, deactivating the catalyst. Accompanied by the severe internal diffusion limitations of hydrogen caused by the use of highly concentrated D-glucose solutions (up to 50 wt%), the low solubility of hydrogen, and the high reactivity, the monolithic reactor provides an interesting alternative.

In this study, the influence of dispersion and distribution of the active phase (ruthenium) and the accessibility and performance of the carbon-based monolithic structures have been evaluated in the hydrogenation of D-glucose. Special attention has been paid to the stability of the catalysts in successive hydrogenation runs. Especially, fixed-bed catalysts (e.g., monoliths) require a maintained activity for long periods of time for successful application in industry. The performance of the monolithic reactor has been compared with slurry-phase operation.

11.6.3 Performance of Carbon Monoliths

Different carbon monoliths were prepared from a sucrose coating [8,43], a polyfurfuryl coating [9], a furan coating [44] via the dipcoating method, and from methane [14,35] via the CVD method over deposited Ni. Ruthenium was loaded on furan-based monoliths by impregnation from $[\text{RuCl}_5 \cdot \text{H}_2\text{O}]^{2-}$ in diluted hydrochloric acid, and lipase was loaded on the other monoliths by physical adsorption from a phosphate buffer (pH 7).

Catalytic tests with the lipase-monolithic catalysts were performed in a monolithic stirrer reactor consisting of a glass vessel equipped with a stirrer motor ($V = 2.5 \text{ dm}^3$). 1-Butanol and vinyl acetate concentrations were 0.6 M and 1 M, respectively. Activity tests with immobilized lipase (*Candida antarctica*) were performed at varying stirrer rates and temperatures. Carbon monoliths (Westvaco integral carbon monoliths, with a loading of 30 wt% of microporous activated carbon, wall thickness 0.3 mm) were used as a reference material.

Ru-catalyzed hydrogenation of aqueous solutions of D-glucose (0.56 mol/dm³) was performed in a screw impeller stirred reactor (SISR) of 300-cm³ capacity, suited for testing monolithic and slurry catalysts [45]. The catalysts were first reduced under flowing hydrogen at 1 K/min from room temperature to 413 K, maintained at this temperature for 3 hours, and subsequently cooled under

nitrogen (sample marked as Ru/MC). For comparison, two Ru/C slurry catalysts from Engelhard [Ru/C(1) and (2)] have been included. The reactor is operated semibatchwise with respect to hydrogen. The catalysts have been screened in the temperature range 373 to 403 K at a constant total pressure of 4.0 MPa. The temperature, total pressure, and hydrogen consumption were recorded during reaction. The starting pH of the reactant solution was about 6. To study the stability of the catalysts, several consecutive hydrogenation runs were performed. The Ru catalysts marked as “spent” have been used in the hydrogenation of D-glucose.

11.6.4 Morphology and Porosity of Various Carbon Composites

Characterization of the Monolithic Biocatalysts Depending on the preparation method, the properties of the carbon–ceramic composites could be varied. Scanning electron microscopic (SEM) images of the various carriers are shown in Figure 11.2. As shown in Figure 11.2(a), the sucrose-derived coating seems to consist of dense layers that form a three-dimensional network of carbon with an apparently hexagonal structure. The mainly microporous PFA coating [Figure 11.2(b)] forms a very dense layer, covering the cordierite surface completely. Figure 11.2(c) shows the CNF coating cover the surface completely with a uniform layer of fibers up to 1 μm in length. The textural properties of the 200-cpsi carbon–ceramic composites are displayed in Table 11.3, complemented with the integral carbon monolith. Y_{carrier} represents the mean carbon content in wt%. For comparison, the S_{BET} of unsupported carbons prepared in the same manner as the supported carbons was 430, 350, and 70 m^2/g for the sucrose-derived carbon, the PFA-derived carbon, and CNFs, respectively. The carriers were prepared as supports for the globular α/β protein lipase, with approximate dimensions of $4.0 \times 4.0 \times 5.0$ nm and relative mass of 33 kDa. The pore size of the carriers must be substantially larger than 5 nm for adequate enzyme adsorption inside the pores.

The sucrose-based carriers have a moderate carbon yield, which can be increased by concentrating the precursor or performing two subsequent coating

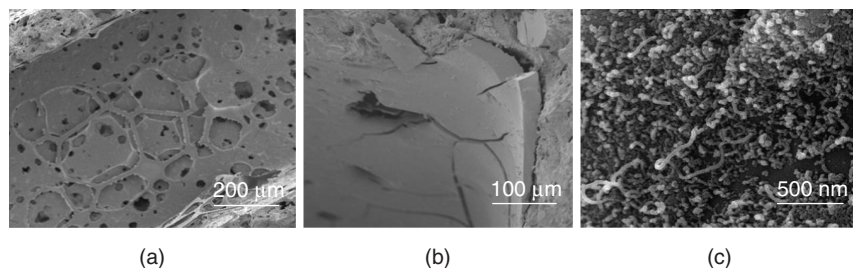


Figure 11.2 SEM micrographs of carbon–ceramic composites: (a) C-SUC; (b) C-PFA; (c) C-CNF.

Table 11.3 Textural Properties of 200-cpsi Carbon-Coated Monoliths

Carbon/Support	Y_{carrier} (wt%)	S_{BET} (m ² /g)	S_{BET} (m ² /g _{carbon})	Pore Diameter (nm)	Pore Volume (cm ³ /g)
C	—	<0.3	—	—	<0.001
C-SUC	3.9	17	420	11	0.21
C-PFA	12	0 ^a	8	<1	0 ^a
C-CNF	3.5	27	128	8	0.05
I-A1	33.2	460	1095	NA ^b	0.22

^aVery narrow pores; equilibrium was not reached during N₂ adsorption.

^bNA, not available.

steps. The average pore diameter is around 10 to 12 nm; therefore, this carrier type appears to be suitable for lipase adsorption. The microporous PFA carriers have a high carbon content, a result of the high viscosity of the polymer precursor employed. For this carrier, both cell density and the preparation process (number of samples, dip time) can affect the yield to a considerable extent. The surface area that was determined from N₂ adsorption isotherms approached zero, but an estimation from the CO₂ adsorption isotherm reveals a large (narrow) microporous surface area. With a pore diameter below 1 nm, these carriers are not expected to be effective for lipase adsorption.

The loading of the CNFs on monoliths is around 3 to 4 wt%, the moderate surface area of the fibers, combined with the open, networklike structure of the fibers and the large total pore volume is expected to lead to a high lipase adsorption capacity. But in the preparation, there is always a risk of cracking or deforming the support [Figure 11.3(a,c)] as a result of excessive CNF growth. This can be prevented by controlling temperature, gas rates, and growth time. Too little CNF formation, however, leads to a partially covered monolith [Figure 11.3(b)]. Optimal growth conditions have to be determined by trial and error.

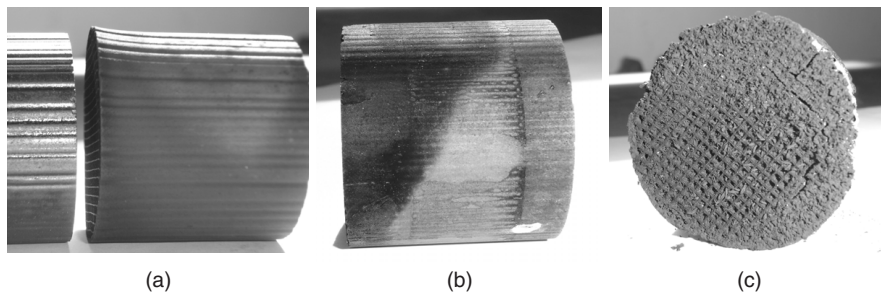


Figure 11.3 Cordierite monoliths after CNF growth: (a) deformed; (b) partly covered; (c) completely filled.

Ruthenium Surface Area and Particle Size Hydrogen chemisorption has been applied to determine the ruthenium surface area and average particle size for both fresh Ru catalysts and those after use in the hydrogenation of D-glucose. As can be noted from Table 11.4, the Ru/C slurry catalysts based on activated carbon possess relatively high ruthenium surface areas. The active ruthenium surface area of catalyst Ru/MC, however, was only $0.12 \text{ m}^2/\text{g}_{\text{sample}}$. This corresponds to an average Ru particle size of 18 nm and a dispersion of 7%. Figure 11.4 shows a representative transmission electron microscopic (TEM) image of the latter catalyst. The ruthenium particles appear as dark dots on the surface of the carbon. The image shows that the Ru distribution was rather inhomogeneous. Some areas contained small Ru particles of about 1 nm (like those observed in the case of the slurry catalyst prepared in a similar way [24]), while other areas contained clusters of small or large Ru particles, resulting in low dispersion.

Table 11.4 Ruthenium Surface Area and Average Particle Size of Fresh and Spent Ru Catalysts

Catalyst	Ru (wt%)	Fresh		Spent	
		S_{Ru} ($\text{m}^2/\text{g}_{\text{cat}}$)	d (nm)	S_{Ru} ($\text{m}^2/\text{g}_{\text{cat}}$)	d (nm)
Ru/MC	0.4	0.12	18		
Ru/C(1)	4.9	6.1	4.0	5.9	4.1
Ru/C(2)	3.5	3.1	5.5		

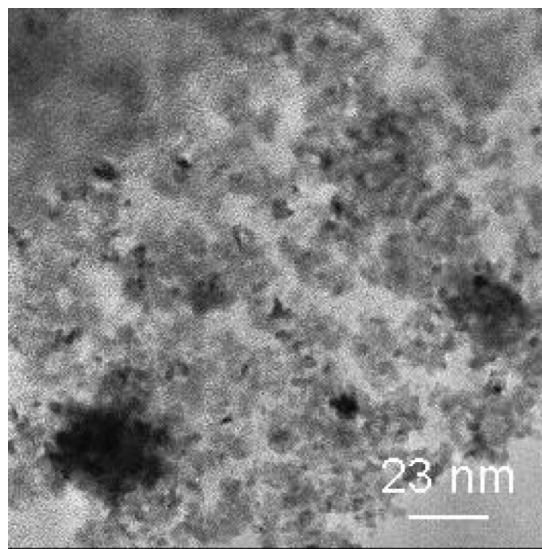


Figure 11.4 TEM image of ruthenium on a carbon-supported monolithic catalyst.

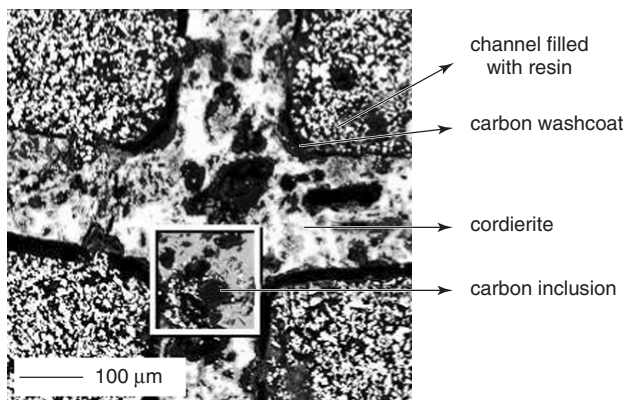


Figure 11.5 Backscattered SEM image of the catalyst Ru/MC. The white box indicates the area shown in Figure 11.7.

Figure 11.5 shows the backscattered electron image of a cross section of a carbon-coated monolithic ruthenium catalyst. It can be seen that the application of the carbon washcoat hardly affected the geometric surface properties of the monolithic support. More detailed information about the carbon distribution was obtained by EPMA analysis. Figure 11.6(a) shows that the carbon is situated primarily within the macroporous structure of the cordierite with only a thin layer on the external surface of the monolith channels. The red spots indicate places where a relatively high amount of carbon is located. In the case of square cells, there is some carbon accumulation in the corners of the channels. The distribution of the Ru species on the carbon-coated monolithic catalyst is shown in Figure 11.6(b). Ruthenium is not only present in the pores of the carbon washcoat layer, but throughout the entire matrix. The bright spots indicate places where a relatively high amount of ruthenium is present. To be able to discriminate whether the Ru species are preferentially located on the carbon inclusions or on the walls of the bare cordierite, the magnification was increased from $150\times$ to $350\times$. EPMA maps of the area indicated by the white box in Figure 11.5 for ruthenium, carbon, and aluminum (the Al K α emission image is not shown) were measured. These show that the Ru species are located at the accessible carbon surface, (i.e., in the pores of the outer washcoat layer and on the edges of the carbon inclusions in the walls) (Figure 11.7). No ruthenium was detected inside the carbon inclusions, indicating that these inclusions were nonporous or not accessible to the impregnation liquid. No correlation was found between the Ru map and the corresponding Al map. Due to the resolution of the EPMA probe (about 1 μm), no information could be acquired concerning the metal particle size in the ruthenium domains.

Principally, two types of strong adsorption sites are present on the carbon carrier for the ruthenium complex: namely, C=C structures in the carbon basal

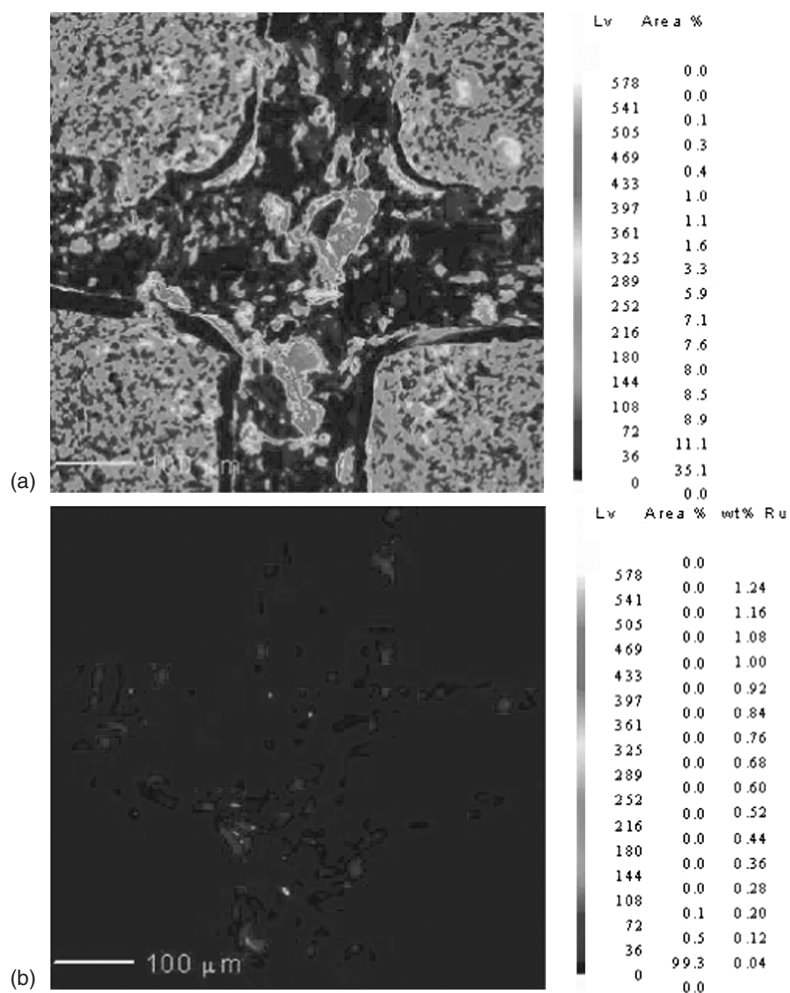


Figure 11.6 EPMA map at an intersection of the catalyst Ru/MC (magnification 150 \times): (a) C K α emission image of the catalyst structure; (b) Ru L α emission image. The relative intensity of the elements corresponds with the level (Lv) indicated in the legend, accompanied by a specific color.

planes (π -complexation) and oxygen-containing functional groups to which the precursor can be anchored. Both types of coordination would take place at the edges of the carbon basal plane structures [46]. The carbon-coated monolithic support contains a relatively low amount of basal plane edges. As a consequence, part of the ruthenium precursor cannot be immobilized by means of strong adsorption, but only through weak physisorption forces. Accordingly, immobilization of this part of the ruthenium is to be effected by crystallization. Hence, the stage

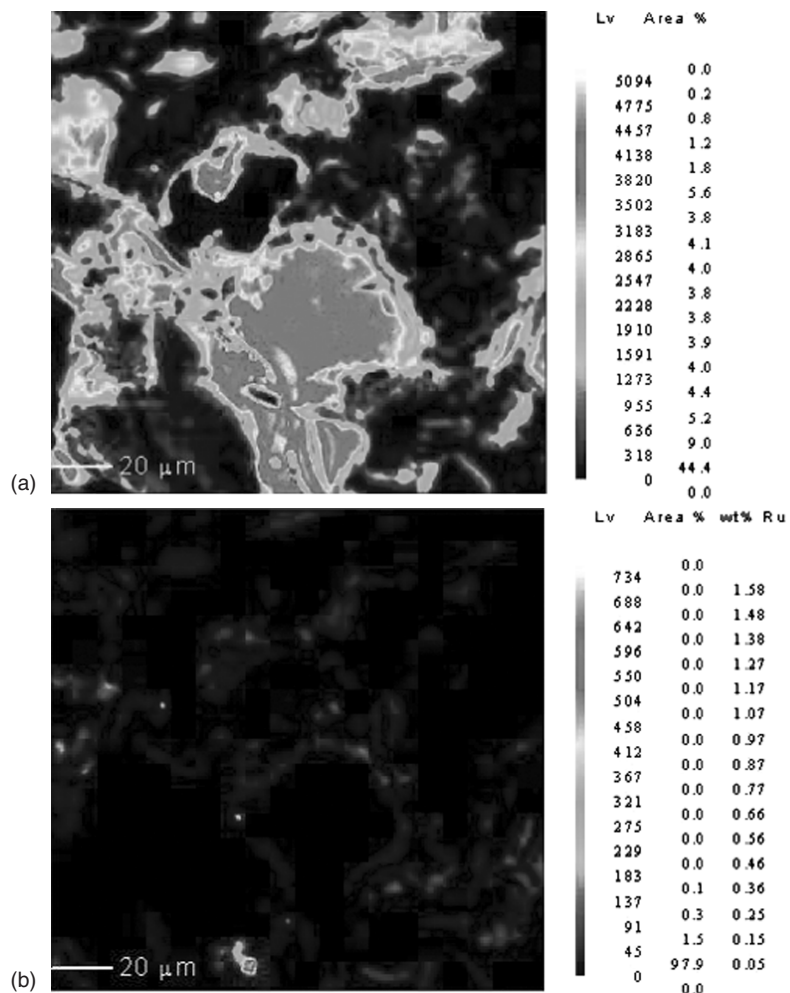


Figure 11.7 EPMA map on the Ru/MC catalyst (magnification 350×): (a) C K α emission image of the catalyst structure; (b) Ru L α emission image.

of drying in which crystallization proceeds is of great importance for the distribution of active precursor within the final catalyst [47,48]. The broad pore size distribution of the carbon-coated monolith can severely affect migration of the metal during drying. Because after washing the micropores preferably remain filled with impregnation liquid due to capillary forces (it is believed that the impregnation liquid in these micropores is only diluted upon washing), and the liquid evaporates from both small and large pores, a net migration of the liquid from the wide meso- and macropores to these narrow pores will occur upon static drying. This migration will result in clusters of particles of the active precursor

at the pore mouth openings. Thus, after primary crystallization, growth of the nuclei will prevail over the formation of new nuclei, resulting in the low dispersion observed for the monolithic ruthenium catalysts. This macroscopic transport of active-phase precursor upon drying has been demonstrated for the deposition of nickel on alumina-washcoated monoliths [48].

11.6.5 Enzyme Adsorption and Catalyst Performance in the MSR

The results of lipase adsorption on the carbon-coated monoliths and subsequent application in the MSR are given in Table 11.5. The 200-cpsi integral carbon monolith, I-A1, is also included. The activity per monolith volume for the CNF composites is relatively high, due to the high enzyme loading inside the open network of fibers. The I-A1 carrier has a high enzyme adsorption capacity but shows decreased activity per monolith volume. Integral carbon monoliths are suitable as a support material for this lipase, but the activity is much lower than for carbon–ceramic composites. For the latter, the activity observed corresponds to the amount of protein that was adsorbed. The activity per gram of enzyme (Table 11.5) is constant around a value of about $0.9 \text{ mmol/s} \cdot \text{g}_{\text{protein}}$ for all types of carbon and cell densities. For the I-A1 monoliths, this value is significantly lower. This could indicate the presence of internal diffusion limitations. This is discussed below. If a lipase content of 20% in the crude protein powder is assumed, a turnover frequency (TOF) value of 175 s^{-1} is found. After each run, the monolithic stirrer was replaced by a normal stirrer, and fresh reactants were added to check if any enzyme had desorbed. No activity could be detected. As expected, the lipase does not desorb from the support under the reaction conditions chosen.

It is interesting to compare the catalyst effectiveness that is reported here with conventional catalyst systems. The characteristic diffusion length (L) for cordierite monoliths is on the order of a tenth of a millimeter in the worst case (wall thickness), which is comparable to the diffusion lengths in the smaller beads ($L = d_p/6$) [49–52].

Table 11.5 Results of Lipase Adsorption and Activity Tests for 200-cpsi Monoliths

Carrier Type	Enzymatic Activity at 150 rpm, 300 K									
	Protein ^a (mg/monolith)		mol/m ³ _{monolith} · s				mmol/s · g _{protein}		Φ	
	200 cpsi	400 cpsi	200 cpsi	400 cpsi	200 cpsi	400 cpsi	200 cpsi	400 cpsi	200 cpsi	400 cpsi
C-SUC	75	113	0.98	1.4	0.95	0.93	0.02	0.02		
C-PFA	81	122	0.94	1.4	0.84	0.86	—	—		
C-CNF	380	400	4.4	5.2	0.84	0.94	0.05	0.05		
I-A1	330	—	1.5	—	0.32	—	1.31	—		

^aLipase content in the lyophilized powder is around 20 wt%.

Internal Diffusion Limitations To rule out possible internal diffusion limitations under these conditions, the Wheeler–Weisz modulus,

$$\Phi \left(F = \frac{n+1}{2} \frac{r_{v,\text{obs}} L^2}{D_{\text{eff}} C_b} < 0.15 \right)$$

was estimated, assuming first-order kinetics. For the microporous PFA layer, all lipase is assumed to be deposited on the outer surface; no internal diffusion problems exist for these catalysts.

Using the reaction rate observed (in mol/s · m³_{catalyst}) in experiments performed at 150 rpm, the Wheeler–Weisz modulus was calculated for all monoliths by estimating the layer thickness (L) from the carbon yield. D_{eff} inside the carbon layers was estimated to be 1 to 3×10^{-10} m²/s inside the various carbons. The values for Φ are presented in Table 11.5. For I-A1, consisting mainly of macroporous carbon, it is likely that internal diffusion limitations are present inside the carbon walls (where the lipase is located). This was also indicated by the decreased activity per gram of enzyme for these monoliths (Table 11.5). For ceramic monoliths, all adsorbed enzyme is used effectively (a constant turnover frequency for all carbon types), as confirmed by the low values for Φ .

For C-SUC, 2 g of carbon per pair of monoliths has a volume of 1 mL ($\rho \approx 2000$ kg/m³). This gives a layer thickness L of 2 μm and yields a Φ value of 0.02, well below the threshold value for the onset of internal diffusion limitations. For CNF, the density of the carbon fibers is significantly lower than for the solid carbon coatings. A layer thickness of 10 μm is assumed (from SEM, see Figure 11.8), which yields a total carbon volume of around 10 cm³ for a pair of monoliths. This gives a Φ value of 0.05, also indicating that no severe internal diffusion limitation exists in the CNF coating.

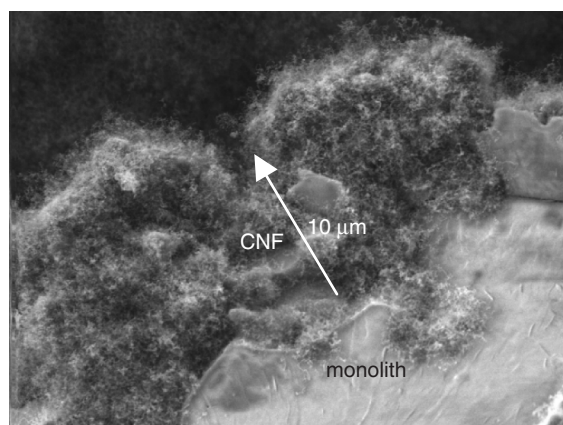


Figure 11.8 Estimation of L for C-CNF.

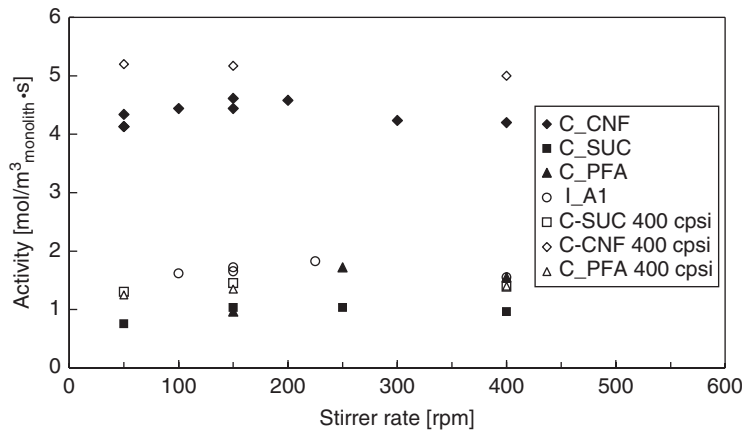


Figure 11.9 Effect of stirrer rate on the initial reaction rate at 300 K in the acylation of butanol with vinyl acetate with different 200- and 400-cpsi monoliths. $V_L = 3$ L, $C_{\text{but}} = 0.6$ M, $C_{\text{VA}} = 1$ M.

External Mass-Transfer Limitations To investigate any external mass-transfer limitations present in the system, the stirrer rate was varied between 50 and 400 rpm. The initial reaction rate for the various carrier materials and cell densities is plotted as a function of stirrer speed in Figure 11.9. For these monolithic biocatalysts, no profound influence of stirrer rate on the reaction rate observed could be detected. Apparently no external mass-transfer limitations are present in the system even at higher cell densities. At these high stirrer rates, the contact time is too short for a mass-transfer boundary layer to develop to the channel axis. Moreover, it can be expected that under these conditions, the velocity profile along the monolith length also has not developed completely. In the following paragraphs, the mass-transfer rates in the MSR are estimated and the effect of cell density is discussed.

Mass Transfer in the MSR Mass transfer can be quantified by calculating the Sherwood number, Sh, using the relation

$$\text{Sh} = \text{Sh}_\infty \left(1 + C \frac{d_{\text{ch}}}{L_m} \text{Re} \cdot \text{Sc} \right)^{0.45} = \text{Sh}_\infty \left(1 + C \frac{1}{Gz} \right)^{0.45}$$

with $Gz = \frac{L_m}{\text{Sc} \cdot \text{Re} \cdot d_{\text{ch}}}$

To apply this relation, Gz must be smaller than 0.03. Under the present conditions, $Gz = 10^{-6}$, indicating that the boundary layer for mass transfer is in development. As a result, the Sherwood number is orders of magnitude higher than the lower limit of 2.96. At a stirrer speed of 150 rpm, liquid velocity (v_L) in the monolith channels is around 0.5 m/s [53]. With an estimated Sc of 1350

and Re of 1150, Sh becomes 180; the liquid–solid mass-transfer coefficient of the system at 150 rpm was estimated to be 5×10^{-5} m/s, using the definition of the Sherwood number, $Sh = k_s d_{ch}/D$ [52].

Effect of Cell Density Based on the larger geometric surface area at higher cell density, theoretically more carrier can be deposited, resulting in a higher enzyme loading per monolith. Therefore, the activity observed is also expected to increase proportionally (factor 1.5) with the available surface area. However, this increase was not found to be proportional with the change in available surface. This is probably caused by the higher velocity in the channels compared to the 200-cpsi samples (cleaning of the smaller 400-cpsi channels was done at the same air pressure as the 200-cpsi monoliths) during the coating step, removing a higher percentage of carbon precursor from the channel walls. In general, an increase in carrier loading by a factor 1.1 to 1.2 was observed. This implies that the layer thickness L for internal diffusion will decrease, while the total catalyst volume will increase. Therefore, Φ will hardly be affected. Values for Φ of the 400-cpsi monoliths at 150 rpm are given in Table 11.5. The reaction rates observed for the 400-cpsi monoliths at different stirrer speeds are presented in Figure 11.9. The enzyme loading generally increases with available surface area; only for the CNF composite is the increase not proportional. The reason for this is unknown. Apparently, the higher enzyme loading does not lead to a change in regime toward mass-transfer-limited operation, even at lower stirrer rates. For 400 cpsi, the channel velocity at 150 rpm decreases to 0.3 m/s [53], which gives $Sh = 105$ and a slightly decreased mass-transfer coefficient $k_s = 4.8 \times 10^{-5}$.

Comparison with Free Lipase and Novozyme To evaluate the catalyst performance, free lipase and a commercial immobilized lipase (Novozyme) were also tested. The results of the activity per gram of protein are plotted in Figure 11.10. The specific activity of immobilized lipase is lower than that of the free enzyme. It is known that the residual activity of an enzyme usually decreases significantly. A decrease in the rate observed can usually be ascribed to conformational changes, steric effects, or denaturation. For the monolithic biocatalysts, the immobilized activity was found to be 30 to 35%, and for Novozyme around 80% in the first run. Deactivation of the commercial sample in consecutive runs is probably due to the instability observed for the support matrix under reaction conditions [54,55]. The deactivation proved to be irreversible. Since no stability tests were performed with Novozyme catalyst, it is not known if the deactivation is caused by leaching.

11.6.6 Performance Monolithic Ruthenium Catalysts

All ruthenium catalysts showed a high selectivity to D-sorbitol (>98%). The main by-product at total conversion was D-mannitol (maximum 2%), formed because a fraction of D-glucose isomerized into D-fructose, which was subsequently hydrogenated into D-sorbitol and D-mannitol. The catalytic hydrogenation

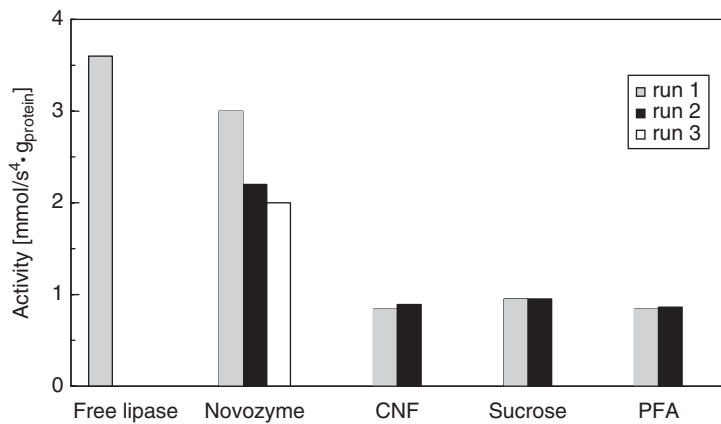


Figure 11.10 Initial reaction rate of free lipase, Novozyme, and 200-cpsi monoliths in the acylation of butanol with vinyl acetate in organic medium in various reactor systems at 300 K.

of D-glucose can usually be described by Langmuir–Hinshelwood kinetics with a transition from zero-order dependency in D-glucose at high concentrations to first-order behavior at low concentrations [56]. At the D-glucose concentrations (0.56 mol/dm^3) used in this study, the reaction can be described by a first-order dependency in D-glucose for all catalysts. The activity of the catalysts can therefore be expressed by the pseudo-first-order reaction rate constant ($\text{kg}_{\text{cat}} \cdot \text{s}$) $^{-1}$ and is given in Table 11.6. To correct the activity data for the dispersion of the Ru catalysts, the results have been expressed in $(\text{m}_\text{Ru}^2 \cdot \text{h})^{-1}$. A much lower activity is observed for the monolithic catalyst Ru/MC than for the Engelhard slurry catalysts, which is caused by an inhomogeneous ruthenium distribution with low dispersion of the monolithic catalyst. Due to the macroporosity of the cordierite, a significant amount of ruthenium is present on the surface of the carbon inclusions located deep inside the cordierite walls, making the diffusion path of the

Table 11.6 Pseudo-First-Order Rate Constants and Intrinsic Activity of the Catalysts Applied

Catalyst	S_{Ru} ($\text{m}^2/\text{g}_{\text{cat}}$)	$k_{\text{kg}_{\text{cat}}}^a$ [($\text{kg}_{\text{cat}} \cdot \text{s}$) $^{-1}$]	$k_{\text{m}^2 \text{Ru}}$ [($\text{m}_\text{Ru}^2 \cdot \text{h}$) $^{-1}$]	η	$k_{\text{kg}_{\text{cat}}}/\eta$ ($\text{kg}_{\text{cat}} \cdot \text{s}$) $^{-1}$
Ru/MC	0.12	0.05	1.4	0.65	0.07
Ru/C(1)	6.1	1.76	1.0	0.93	1.90
Ru/C(2)	3.1	1.14	1.3	0.93	1.22

^a kg_{cat} , the total mass of the catalyst (including support).

reactants to the active ruthenium sites considerably larger than the average carbon coating thickness [57]. As a consequence, the internal effectiveness factor η , calculated from the Wheeler–Weisz criterion [58] assuming an effective diffusivity of $0.1D$ and a characteristic diffusion length L of $15\text{ }\mu\text{m}$, amounts to 0.65 for Ru/MC (Table 11.6). The intrinsic activity, the observed rate constant divided by the internal effectiveness factor, was calculated in order to eliminate the effect of internal diffusion limitations. From a plot of $k_{\text{kg cat}}/\eta$ versus S_{Ru} , it can be concluded that the intrinsic activity is proportional to the metal surface area and independent of the type of carbon support [24].

Stability of the Monolithic Ru Catalyst To meet the stability challenge, the catalysts should be resistant to metal sintering and poisoning. The most crucial point, however, is to avoid metal and support leaching in the acidic and chelating medium [59]. Metal leaching is highly undesirable, because of (1) the resulting metal impurities in the product, which renders product purification necessary, and (2) loss of active catalyst sites. The stability of the catalysts against leaching was investigated for the monolithic catalyst Ru/MC. After each hydrogenation run, the amount of dissolved metal ions present in the reaction mixture was determined by ICP-OES. No leaching of ruthenium was observed, but minor amounts of Si, Mg, and Al were present in the reaction mixture (Table 11.7). These ions originate from the monolithic substrate cordierite, and indicate that the coverage of carbon was not complete. If the coverage of carbon had been complete, leaching of the cordierite should have been negligible. The activity of both types of catalysts during several hydrogenation runs is displayed in Table 11.8.

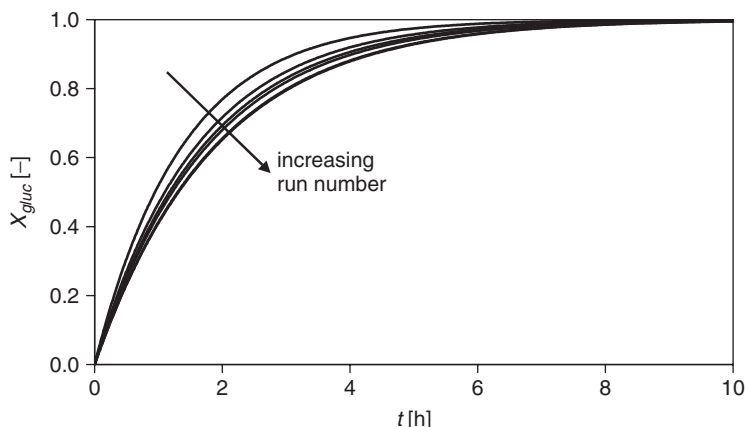
The relative activity can be expressed as the ratio between the reaction rate constant for a particular run and the rate constant of the first run. The activity of Ru/MC in successive recycle runs is shown in Figure 11.11. After rapid deactivation during the first two hydrogenation runs, a steady decrease in activity during subsequent runs is observed. Since the ruthenium particle size and specific surface area of catalyst Ru/C(1) remained constant during several hydrogenation runs, ruthenium agglomeration, as observed by Arena [40] for Ru/Al₂O₃ catalysts, is not occurring. Apparently, the Ru catalysts are deactivated by surface poisoning. At the temperature of the reaction (393 K), carbon formation on the spent catalysts seems unlikely, but the formation of carbohydrate decomposition products is probable. These strongly adsorbed species could be cracking products of D-glucose or D-sorbitol, or other products formed in side reactions

Table 11.7 Amounts of Leached Metal Ions from Catalyst Ru/MC After Several Hydrogenation Runs (mg/dm³)

Run	Al	Mg	Si	Ru
1	2.64	2.29	14.3	<0.02
2	2.03	1.31	4.30	<0.02
6	1.42	1.08	3.53	<0.02

Table 11.8 Stability of Ru/MC During Various Hydrogenation Runs

Run	k_{glucose} [(kg _{cat} · s) ⁻¹]	Rel. Activity (%)
1	0.047	100
2	0.038	80
3	0.040	86
4	0.036	78
5	0.034	73
6	0.034	72
12 (regenerated)	0.037	79

**Figure 11.11** Conversion of D-glucose versus time in six consecutive hydrogenation runs for Ru/MC.

(e.g., polymerization) [60]. Small amounts of gluconic acid, formed by a Cannizzaro type of reaction [61], were identified in the reaction mixture by HPLC. Since it is known that carboxylic acids are strongly bond to ruthenium, this product could well account for the deactivation. Kusserow et al. [62] detected no gluconic acid in the reaction mixture. The authors assigned the deactivation of the ruthenium catalyst to poisoning by metals leached out from the reactor material, which is not applicable here. The rapid initial decrease in activity is probably connected to a structural physical modification of part of the active sites of ruthenium (e.g., recrystallization).

In the case of product inhibition, it is expected that the ruthenium surface area of the spent catalysts, as measured by hydrogen chemisorption, declined due to blocking of the active sites. However, no evidence for this assumption was found (Table 11.4), since the spent catalysts possessed ruthenium surface areas

similar to those of fresh catalysts. It is therefore believed that during pretreatment (evacuation at 393 K) of the sample prior to hydrogen chemisorption, the organic fragments were removed from the catalyst surface. To check this hypothesis, the pretreatment step (reduction and evacuation at 393 K) was mimicked *in situ* in the reactor for the monolithic catalyst Ru/MC, which had been tested in 11 hydrogenation runs. From Table 11.8 it can be seen that after this pretreatment, the relative catalytic activity was restored to about 80% of its original activity and therefore similar to the one obtained after run 2 (after the initial deactivation). If it is supposed that catalyst Ru/MC further deactivated after run 6 with about 2% per run, this would imply that by incorporating the evacuation step, the activity had been increased by about 17% as compared to run 6.

Heinen et al. [63] tested the stability of Ru/C catalysts in the hydrogenation of D-fructose at 345 K and 0.1 MPa. The authors showed that upon reuse of the catalyst after washing with cold water, the activity dropped considerably. However, after refluxing in water for a night, the filtered and dried catalyst regained its original activity. These results also support the interpretation that catalyst deactivation is caused by the presence of strongly adsorbed species on the catalyst surface during reaction. The ^1H NMR spectrum of the filtrate showed that besides D-fructose, D-mannitol, and D-sorbitol, a mixture of other polyhydroxy compounds was present. However, the concentrations were too low to identify these species by means of ^{13}C NMR.

Gallezot et al. [59] studied the stability of carbon-supported ruthenium catalysts in a trickle-bed reactor. A weak deactivation was observed for the catalyst prepared by ion exchange with $\text{Ru}(\text{NH}_3)_6\text{Cl}_3$ (3.7% for 312 hours on stream), while an even smaller deactivation occurred for the catalyst prepared by anionic adsorption with $\text{RuCl}_3 \cdot \text{H}_2\text{O}$. These activity losses in time are less than reported in this study; however, the authors performed the hydrogenation of D-glucose at 373 K and 8 MPa. The lower reaction temperature of 373 K diminished the occurrence of harmful side reactions, thereby preventing catalyst poisoning. The higher hydrogen pressure applied (8 MPa) is possibly also advantageous for the stability of the catalysts with respect to poisoning. Furthermore, the use of concentrated D-glucose solutions (40 wt%) probably caused severe external and internal mass-transfer limitations, resulting in low catalyst effectiveness factors, thereby masking possible catalyst deactivation.

11.7 EVALUATION AND PRACTICAL CONSIDERATIONS

11.7.1 Monolithic Biocatalysts

Several monolithic enzyme biocatalysts were prepared and characterized with carbon coatings consisting of carbonized sucrose, carbonized polyfurfuryl alcohol, and carbon nanofibers. The coated carbon monoliths were also compared with an integral (composite) carbon monolith. A lipase from *Candida antarctica* was adsorbed on the monolithic supports. Adsorption on carbon coatings can be very effective, depending on the carbon microstructure. For a high lipase loading,

mesoporous (I-A1) or open (CNF) carbon structures are preferred. For all prepared biocatalysts, satisfactory immobilization and activity in the acylation of 1-butanol with vinyl acetate was observed. The CNF-based catalysts performed best, showing the highest activity per volume of catalyst. For 400-cpsi cordierite monoliths, the initial rate is high at $5.2 \text{ mol/s} \cdot \text{m}^3_{\text{monolith}}$. The integral carbon monoliths also have a high enzyme loading, but suffer from internal mass transfer limitations. No enzyme leaching was detected from the prepared monolithic biocatalysts. The carbon-based catalysts were found to be stable for several weeks, without a significant loss of activity.

Residual activity of the immobilized enzyme was 30 to 35% of the free enzyme activity. Compared to a commercially available immobilized lipase (Novozyme), the immobilized activity of the monolithic catalysts is slightly lower, but the Novozyme shows significant deactivation in consecutive tests. The applied reactor configuration (MSR) can be operated without any mass-transport limitations, fully utilizing all adsorbed enzyme on the monolith. Increasing the cell density of the monoliths leads to higher lipase loading and hence a higher observed reaction rate. Due to the lower channel velocity at higher cell density, the mass-transfer coefficient decreased slightly.

11.7.2 Monolithic Ruthenium Catalysts

The carbon-coated monolithic supports based on furan resin possessed a broad pore size distribution and a low amount of strong adsorption sites. After impregnation with $[\text{RuCl}_5 \cdot \text{H}_2\text{O}]^{2-}$, macroscopic redistribution of ruthenium occurred during drying of the monoliths due to capillary forces, resulting in low dispersions. Furthermore, part of the ruthenium was located deep in the cordierite walls, eventuating in a low utilization of the catalysts. The monolithic Ru catalyst therefore showed a low activity in the three-phase hydrogenation of D-glucose. In the absence of mass-transport limitations, the D-glucose hydrogenation rate was proportional to the ruthenium surface area of the catalysts. None of the catalysts showed leaching of ruthenium in the acidic and chelating reaction mixture. During successive hydrogenation experiments for the monolithic catalyst Ru/MC, two types of catalyst deactivation were observed: (1) a rapid initial deactivation of 20 to 30%, which is probably related to a structural physical modification of the active sites (e.g., recrystallization), and (2) slow deactivation, caused by strongly adsorbed species on the catalyst surface. These strongly adsorbed species could be cracking products of D-glucose or D-sorbitol, or other products formed in a side reaction (e.g., polymerization). Part of the catalytic activity can be recovered by treatment of the catalyst in vacuum, thereby removing the adsorbed products.

11.7.3 Practical Considerations

When carbon monoliths are to be used in a heterogeneous system, there are some important considerations to make. If the kinetics of the reaction are not

affected by possible internal diffusion limitations, and a high overall rate is the objective, a high catalyst loading on the channel wall is recommended. This was shown in a lipase-catalyzed system, where high enzyme loading was preferred and selectivity was not altered. Use of the integral carbon monolith led to an increase in production rate compared to the similar sucrose/PFA monoliths. The enzyme was not, however, used efficiently in this system. Efficient use of all lipase could only be accomplished by using the very open CNF-monolith system.

If, however, the selectivity of a reaction is influenced by the presence of a “thick” support layer on the channel walls, the use of a different type of monolith support than the classical carbon-coated monolith is recommended. This was shown in the ruthenium-catalyzed reaction. EPMA analyses showed that ruthenium species are present both in the pores of the outer carbon washcoat layer and on the surface of the carbon inclusions located inside the monolith walls. No ruthenium was found in the empty macropores of the cordierite, since (1) there is no strong interaction between the precursor and the cordierite, and (2) after impregnation and washing, the macropores are emptied first upon drying, due to the capillary forces. The presence of active phase in the walls of the monolithic substrate is undesired, since it makes the diffusion path of the reactants to the active ruthenium sites longer. To prevent deposition of ruthenium in the wall, (1) substrates with nonporous walls can be used or (2) the cordierite monolithic substrates can be modified with $\alpha\text{-Al}_2\text{O}_3$, blocking the macroporosity of the cordierite and rounding the channel cross section to enable a more uniform thickness of the carbon coating layer [64]. Alternatively, integral carbon monoliths can be employed with very thin walls having a characteristic diffusion length similar to the activated carbon slurry catalysts. The latter type of monoliths is produced by Mast Carbon Technology, UK, from phenolic resin precursor using a binderless process that allows independent control of the cell–pore structure [7].

Another elegant solution for problems associated with increasing the loading and distribution of a catalyst is the use of ACM (mullite) monoliths [35,65], having highly porous (interconnected) channel walls. These monoliths can be applied in both situations; when kinetics are less important, a high catalyst loading can be achieved to fill up the porous channel wall. When internal diffusion limitations must be prevented (a thin, uniform catalyst layer is required), a very thin film of carrier material can be applied that covers the separate micrograins of the ACM channel walls. In this way the surface area can be increased dramatically.

The decision as to which monolith type to use is therefore dependent on the type of application, but commercial availability and carbon type should also be evaluated. Cordierite and Mast monoliths are commercially available, whereas ACM is not. When cordierite is used in combination with CNFs, possible cracking of the support can occur. For ACM monoliths, the open structure allows high carrier loading and prevents cracking upon the growth of CNF. For integral carbon monoliths in combination with biocatalysts, the pore size and chemistry of the carbon must be tuned to match the properties of the biocatalyst.

11.8 CONCLUSIONS

Carbon-based monoliths form a special class of materials that combine the favorable properties of carbon as a support material and of monolithic structures. Due to the chemical stability and the adjustable porosity of carbon, in combination with the high void fraction and large geometric surface area of the monoliths, carbon monoliths are very versatile catalyst support materials. The current state of the art is either a carbon-coated monolith, or a complete carbon monolith can be prepared. New ceramic materials, such as mullite, greatly improve the properties of the carbon-coated monolith. Also, improved extrusion techniques can be used to minimize the wall thickness of integral carbon monoliths. This can greatly enhance mass-transfer properties in integral systems. The choice between coated type and integral carbon monolith is directed by the final application in terms of the amount of support material needed, wall thickness, process conditions, and intrinsic kinetics. Further improvements could be directed toward improving the mechanical strength of the integral structures, degree of coverage for the coated monoliths, and the texture of the carbon.

Because the application of carbon-based monoliths forms an emerging field in (bio)chemical engineering, new applications and process developments can be expected in the future. One might think of applications of monolith–CNF combinations in water–air filter systems [66], carbon precursors with tailored porous texture for production of integral/coated monoliths, ultrathin coatings on ACM monoliths for higher mass-transfer rates, and carbon monoliths in adsorption processes or as high-surface-area electrodes.

In this chapter, practical implications of the use of different carbon monoliths were illustrated in two different examples. Integral and carbon-coated monoliths were used as carriers for immobilizing a lipase from *Candida antarctica* by physical adsorption. The CNF–monolith combination was shown to be a very good support for lipase. No leaching of enzyme was detected during activity tests. 400-cpsi CNF-coated monoliths have the highest enzyme loading and therefore the highest volumetric activity (i.e., $5.2 \text{ mol/s} \cdot \text{m}^3_{\text{monolith}}$). For carbon-coated monoliths, internal and external mass-transport limitations were absent, and all immobilized enzyme is used effectively. The activity of the immobilized enzyme is 30 to 35% of that of the free enzyme. Compared to a commercial particulate biocatalyst, the initial activity is somewhat lower, but the monolithic biocatalyst shows enhanced stability.

Monolith-based ruthenium catalysts have shown to be very promising in the three-phase hydrogenation of D-glucose. No leaching of ruthenium in the acidic and chelating reaction mixture was detected. During successive hydrogenation experiments, two types of catalyst deactivation were observed: (1) a rapid initial deactivation of 20 to 30%, which is probably related to a structural physical modification of the active sites (e.g., recrystallization), and (2) a slow deactivation, caused by strongly adsorbed species on the catalyst surface. These strongly adsorbed species could be cracking products of D-glucose or D-sorbitol,

or other products formed in side reactions (e.g., D-gluconic acid). Part of the catalytic activity can be recovered by treatment of the catalyst in vacuum, thereby removing the adsorbed products. A more appropriate, industrially relevant method was described by Heinen et al. [63], who showed that after refluxing in hot water, the spent catalyst regained its original activity. It should be noted that in the present study, model feeds have been used with research-grade purity (>99%). Industrial feeds may contain small amounts of polysaccharides and inorganic sulfur and nitrogen compounds that can irreversibly block the active sites of the catalysts. By reason of resistance against poisoning, the ruthenium crystallites should preferably be located in the inner parts of the carbon washcoat (eggwhite metal distribution).

In general, the properties of the carbon (pore size, chemistry) can be tuned to optimize catalyst loading. Especially in the case of biocatalysts, the chemistry of the enzyme has a considerable effect on the final loading. The conversion observed per monolith volume increases with monolith cell density, due to a higher enzyme loading. Integral carbon monoliths can be a good alternative to increase the enzyme loading, but there is a risk of inefficient catalyst use due to mass-transport problems inside the relatively thick wall. Similar carbon monoliths with very thin walls are expected to be a better option. Another way to improve the catalyst loading is to use ACM monoliths with a porous channel wall. The monolithic stirrer reactor is an efficient lab tool for comparing monolithic catalysts in the absence of external diffusion limitations.

For successful application of carbon-coated monolithic catalysts, the deposition of active phase in the walls of a monolithic substrate should be prevented. To prevent deposition of ruthenium in the wall (1) substrates with nonporous walls can be used, or (2) the cordierite monolithic substrates can be modified with $\alpha\text{-Al}_2\text{O}_3$, blocking the macroporosity of the cordierite and rounding the channel cross section to enable a more uniform thickness of the carbon coating layer. Alternatively, ACM monoliths or integral carbon monoliths with very thin walls having a characteristic diffusion length similar to the activated carbon slurry catalysts can be employed.

REFERENCES

- [1] L.R. Radovic, C. Sudhakar, in H. Marsh, E.A. Heintz, F. Rodríguez-Reinoso, Eds., *Introduction to Carbon Technologies*, Universidad de Alicante, Secretariado de Publicaciones, Alicante, Spain, 1997, p. 103.
- [2] F. Rodríguez-Reinoso, *Carbon* 36 (1998) 159.
- [3] M.V. Twigg, A.J.J. Wilkins, in A. Cybulski, J.A. Moulijn, Eds., *Structured Catalyst and Reactors*, Marcel Dekker, New York, 1998, pp. 91–120.
- [4] A. Beretta, E. Tronconi, G. Groppi, P. Forzatti, in A. Cybulski, J.A. Moulijn, Eds., *Structured Catalyst and Reactors*, Marcel Dekker, New York, 1998, pp. 121–148.
- [5] Th. Vergunst, M.J.G. Linders, F. Kapteijn, J.A. Moulijn, *Catal. Rev.* 43 (2001) 291.

- [6] K.P. Gadkaree, *Carbon* 36 (1998) 981.
- [7] S.R. Tennison, *Appl. Catal. A* 173 (1998) 289.
- [8] T. Valdés-Solís, G. Marbán, A.B. Fuertes, *Micropor. Mesopor. Mater.* 43 (2001) 113.
- [9] Th. Vergunst, F. Kapteijn, J.A. Moulijn, *Stud. Surf. Sci. Catal.* 118 (1998) 175.
- [10] E.M. DeLiso, K.P. Gadkaree, J.F. Mach, K.P. Streicher, U.S. patent 5,451,444, 1995.
- [11] K.P. Gadkaree, U.S. patent 5,487,917, 1996.
- [12] N. Jarrah, J.G. van Ommen, L. Lefferts, *Catal. Today* 79–80 (2003) 29.
- [13] K.M. de Lathouder, T.Marques Flo', F. Kapteijn, J.A. Moulijn, *Catal. Today* 105 (2005) 443.
- [14] G.A. Kovalenko, E.V. Kuznetsova, Yu.I. Mogilnykh, I.S. Andreeva, D.G. Kuvshinov, N.A. Rudina, *Carbon* 39 (2001) 1033.
- [15] K.P. de Jong, J.W. Geus, *Catal. Rev.* 42(4) (2000) 481.
- [16] J.H. Bitter, M.K. van der Lee, A.G.T. Slotboom, A.J. van Dillen, K.P. de Jong, *Catal. Lett.* 89(1–2) (2003) 139.
- [17] H.C. Foley, *Micropor. Mater.* 4 (1995) 407.
- [18] N.M. Rodriguez, A. Chambers, R.T.K. Baker, *Langmuir* 11 (1995) 3862.
- [19] F. Kapteijn, J.J. Heiszwalff, T.A. Nijhuis, J.A. Moulijn, *CatTech* 3 (1999) 24.
- [20] E. Crezee, E. Barendrecht, F. Kapteijn, J.A. Moulijn, *Catal. Today* 69 (2001) 283.
- [21] Th. Vergunst, Ph.D. dissertation, Delft University of Technology, The Netherlands, 1999.
- [22] Th. Vergunst, F. Kapteijn, J.A. Moulijn, *Catal. Today* 66 (2001) 381.
- [23] A.F. Perez, M.M.P. Zieverink, F. Kapteijn, J.A. Moulijn, *Carbon* 44 (2006) 173.
- [24] E. Crezee, Ph.D. dissertation, Delft University of Technology, The Netherlands, 2003.
- [25] K.M. de Lathouder, J.J.W. Bakker, M.T. Kreutzer, S.A. Wallin, F. Kapteijn, J.A. Moulijn, *Chem. Eng. Res. Des.* 84 (2006) 390.
- [26] Y. Wang, Z. Liu, L. Zhan, Z. Huang, Q. Liu, J. Ma, *Chem. Eng. Sci.* 59 (2004) 5283.
- [27] T. Valdes-Solis, G. Marban, A.B. Fuertes, *Appl. Catal. B* 46 (2003) 261.
- [28] T. Valdes-Solis, G. Marban, A.B. Fuertes, *Ind. Eng. Chem. Res.* 43 (2004) 2349.
- [29] E. García-Bordejé, M.J. Lazaro, R. Moliner, P.M. Alvarez, V. Gomez-Serrano, J.L.G. Fierro, *Carbon* 44 (2006) 407.
- [30] E. García-Bordejé, J.L. Pinilla, M.J. Lazaro, R. Moliner, *Appl. Catal. B* 66 (2006) 281.
- [31] A.F. Pérez-Cadenas, F. Kapteijn, J.A. Moulijn, F.J. Maldonado-Hódar, F. Carrasco-Marín, C. Moreno-Castilla, *Carbon* 44 (2006) 2463.
- [32] A. Schmid, J.S. Dordick, B. Hauer, A. Kiener, M. Wubbolts, B. Witholt, *Nature* 409 (2001) 258.
- [33] H.E. Schoemaker, D. Mink, M.G. Wubbolts, *Science* 299 (2003) 1694.
- [34] V. Gotor, *J. Biotechnol.* 96 (2002) 35.

- [35] K.M. de Lathouder, Ph.D. dissertation, Delft University of Technology, The Netherlands, 2006.
- [36] R.J. Barros, E. Wehtje, P. Adlercreutz, *J. Mol. Catal. B* 11 (2001) 841.
- [37] I. Hoek, T.A. Nijhuis, A.I. Stankiewicz, J.A. Moulijn, *Chem. Eng. Sci.* 59 (2004) 4975.
- [38] S. Marash, H. Jansekar, N. Takei, Sorbitol CEH report, <http://ceh.sric.sri.com/Public/Reports/693.1000/>, 1999.
- [39] V. Tukac, *Collect. Czech. Chem. Commun.* 62 (1997) 1423.
- [40] B.J. Arena, *Appl. Catal. A* 87 (1992) 219.
- [41] K. Van Gorp, E. Boerman, C.V. Cavenaghi, P.H. Berben, *Catal. Today* 52 (1999) 349.
- [42] A.W. Heinen, G. Papadogianakis, R.A. Sheldon, J.A. Peters, H. van Bekkum, *J. Mol. Catal. A* 142 (1999) 17.
- [43] G.A. Kovalenko, O.V. Komova, A.V. Simakov, V.V. Khomov, N.A. Rudina, *J. Mol. Catal. A* 182–183 (2002) 73.
- [44] E. García-Bordejé, F. Kapteijn, J.A. Moulijn, *Carbon* 40 (2002) 1079.
- [45] R.J. Berger, E.H. Stitt, G.B. Marin, F. Kapteijn, J.A. Moulijn, *CatTech* 4 (2001) 2.
- [46] H.E. van Dam, H. van Bekkum, *J. Catal.* 131 (1991) 335.
- [47] P.J. van den Brink, Ph.D. dissertation, University of Utrecht, The Netherlands, 1992.
- [48] Th. Vergunst, F. Kapteijn, J.A. Moulijn, *Appl. Catal. A* 213 (2001) 179.
- [49] T. Zhang, L. Yang, Z. Zhu, *Enzyme Microb. Tech.* 36 (2005) 203.
- [50] R.J. Barros, E. Wehtje, P. Adlercreutz, *Biotechnol. Bioeng.* 59 (1997) 364.
- [51] F. Shiraishi, K. Kawakami, S. Kono, A. Tamura, S. Tsuruta, K. Kusunoki, *Biotechnol. Bioeng.* 33 (1989) 1413.
- [52] R.K. Shah, A.L. London, in *Advances in Heat Transfer*, Vol. 1, Suppl. 1, Academic Press, New York, 1978.
- [53] H.P. Kritzinger, B.C. Deelder, C.R. Kleijn, J.J. Derksen, H.E.A. van den Akker in *Proceedings of ASME, Fluids Engineering Division*, FEDSM2002-31360, 2002.
- [54] Z. Koszorz, N. Nemestothy, Z. Ziobrowski, K. Belafi-Bako, R. Krupiczka, *Desalination* 162 (2004) 307.
- [55] D. Ganapati, D. Yadav, K. Manjula Devi, *Biochem. Eng. J.* 10 (2002) 93.
- [56] E. Crezee, B.W. Hoffer, R.J. Berger, M. Makkee, F. Kapteijn, J.A. Moulijn, *Appl. Catal. A* 251 (2003) 1.
- [57] E. Crezee, P.J. Kooyman, J. Kiersch, W.G. Sloof, G. Mul, F. Kapteijn, J.A. Moulijn, *Catal. Lett.* 90 (2003) 181.
- [58] F. Kapteijn, G.B. Marin, J.A. Moulijn, in R.A. van Santen, P.W.N.M. van Leeuwen, J.A. Moulijn, B.A. Averill, Eds., *Catalysis: An Integrated Approach*, Elsevier, Amsterdam, 1999, p. 375.
- [59] P. Gallezot, N. Nicolaus, G. Flèche, P. Fuertes, A. Perrard, *J. Catal.* 180 (1998) 51.
- [60] P. Gallezot, P.J. Cerino, B. Blanc, G. Flèche, P. Fuertes, *J. Catal.* 146 (1994) 93.
- [61] G. de Wit, J.J. de Vlieger, A.C. Kock-Van Dalen, R. Heus, R. Laroy, A.J. van Hengstum, A.P.G. Kieboom, H. van Bekkum, *Carbohydr. Res.* 91 (1981) 125.

- [62] B. Kusserow, S. Schimpf, P. Claus, *Adv. Synth. Catal.* 345 (2003) 289.
- [63] A.W. Heinen, J.A. Peters, H. van Bekkum, *Carbohydr. Res.* 328 (2000) 449.
- [64] A.G. Pérez-Cadenas, M.M.P. Zieverink, F. Kapteijn, J.A. Moulijn, *Catal. Today* 105 (2005) 623.
- [65] K.M. de Lathouder, J. Bakker, M.T. Kreutzer, F. Kapteijn, J.A. Moulijn, S.A. Wallin, *Chem. Eng. Sci.* 59 (2004) 5027.
- [66] S.J. Park, D.G. Lee, in *Abstracts of the European Aerosol Conference*, 2005, p. 18.

12 Carbon Materials as Supports for Fuel Cell Electrocatalysts

FRÉDÉRIC MAILLARD, PAVEL A. SIMONOV, and ELENA R. SAVINOVA

12.1 INTRODUCTION

Polymer electrolyte membrane fuel cells (PEMFCs) have recently attracted much attention as promising power sources for small stationary, mobile, and portable applications [1]. A fuel cell is a device converting chemical energy of a fuel (e.g., hydrogen) into electrical energy. If dihydrogen and dioxygen molecules are brought into direct contact, they interact spontaneously, producing water [reaction (12.1)], because of the negative value of the Gibbs energy of reaction ΔG , which for liquid water equals 237.1 kJ/mol at 298.15 K [2]. If the reaction is carried out at constant pressure, the heat liberated, $-\Delta H$, equals 285.8 kJ/mol [2]. Alternatively, the reaction may be carried out in a fuel cell, with dihydrogen and dioxygen fed into two separate compartments: the anode and the cathode, respectively. Dihydrogen is ionized at the anode to produce protons and electrons [reaction (12.1a)]. These flow to the cathode: the electrons through the external electric circuit, the protons through a proton-conducting membrane, separating the anode and the cathode compartments. At the cathode they interact with dioxygen, producing water [reaction (12.1b)]. This allows transformation of the Gibbs energy of reaction into electrical energy.



Other fuels (e.g., methanol, ethanol, or other organic molecules), which can be oxidized under moderate conditions of PEMFCs (≤ 373 K at ambient pressure), may be utilized in the place of dihydrogen. A fuel cell where methanol is oxidized at the anode is called a direct methanol fuel cell (DMFC).

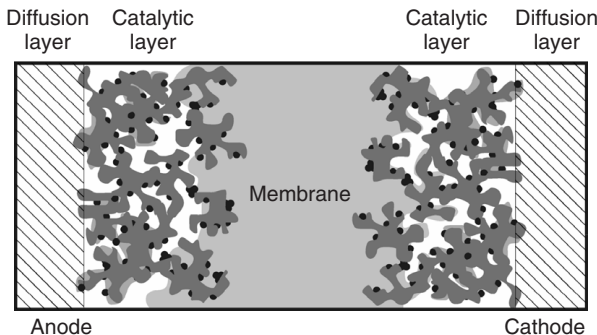


Figure 12.1 Schematic representation of a membrane–electrode assembly of a PEMFC. Platinum particles and carbon agglomerates are colored in black and dark gray, respectively.

The heart of a fuel cell is the membrane electrode assembly (MEA; Figure 12.1). This is a multilayer sandwich composed of *catalytic layers* (CLs), where electrochemical reactions occur; *gas-diffusion layers* (GDLs), providing access of the fuel and the oxidant to the CLs; and a *proton exchange membrane* (PEM) such as Nafion. The structure and composition of the MEAs have undergone decisive changes during the past 20 to 30 years. The CLs of the state-of-the-art fuel cells are multicomponent media comprising a catalyst, accelerating the rates of electrochemical reactions; an ionomer, providing a flow of protons through the MEA; and gas- and liquid-filled pores, providing access of the reagents to, and products from, the catalyst surface. Practically, preparation of the CLs is performed by brushing or spraying the “catalyst ink” (suspension of the catalyst particles in water and/or organic solvent with addition of ionomer, e.g., Nafion) either onto diffusion media (carbon paper or carbon cloth, also referred to as substrates), resulting in a *catalyst-coated substrate*, or directly onto PEM, resulting in a *catalyst-coated membrane* [3].

The maximum equilibrium voltage ΔE_{eq} between the electrodes in a fuel cell is determined by the Gibbs energy of the overall reaction and the number of electrons n transferred in the cell reaction:

$$\Delta E_{\text{eq}} = E_{\text{cathode}} - E_{\text{anode}} = -nF\Delta G \quad (12.2)$$

where F is the Faraday constant. This maximum voltage requires that equilibrium be established at both electrodes. In reality the cell voltage is given by

$$\Delta E_{\text{cell}} = \Delta E_{\text{eq}} - |\eta_{\text{cathode}}| - |\eta_{\text{anode}}| - \Delta E_{\text{ohmic}} \quad (12.3)$$

Here η_{cathode} and η_{anode} stand for overpotentials at the cathode and anode, respectively. In a fuel cell fed with pure dihydrogen, η_{anode} is small, due to the fast kinetics of the hydrogen oxidation reaction (12.1a) on Pt catalysts, and is often neglected [4]. An overpotential may be separated into the reaction overpotential

η_k and the concentration overpotential η_{conc} . The former is the consequence of the sluggish reaction kinetics, while the latter arises from the mass-transport limitations in the CL. ΔE_{ohmic} comprises the following contributions: (1) the contact resistance between the flow-field plates, (2) the membrane resistance, and (3) the resistance of the CLs and GDLs. Figure 12.2 represents the polarization curve, which is the main characteristic of a fuel cell.

Since the electrochemical fuel cell efficiency is given by the ratio between ΔE_{cell} and ΔE_{eq} , equation (12.3) and Figure 12.2 provide guidance on which contributions must be minimized to improve the fuel cell efficiency. At low current densities the difference between the actual cell voltage and the thermodynamic equilibrium value is dominated by the cathode overpotential (η_{ORR}), due to the sluggish kinetics of the oxygen reduction reaction (12.1b). At high current densities, mass transport of dioxygen in the cathode CL and in the GDL provides a significant contribution to the overall losses. The concentration overpotential η_{conc} depends strongly on the architecture of the catalytic layers and the porosities of catalytic supports utilized. Ohmic losses in the membrane, CLs, and bipolar plates may also limit the cell performance significantly and thus have to be controlled.

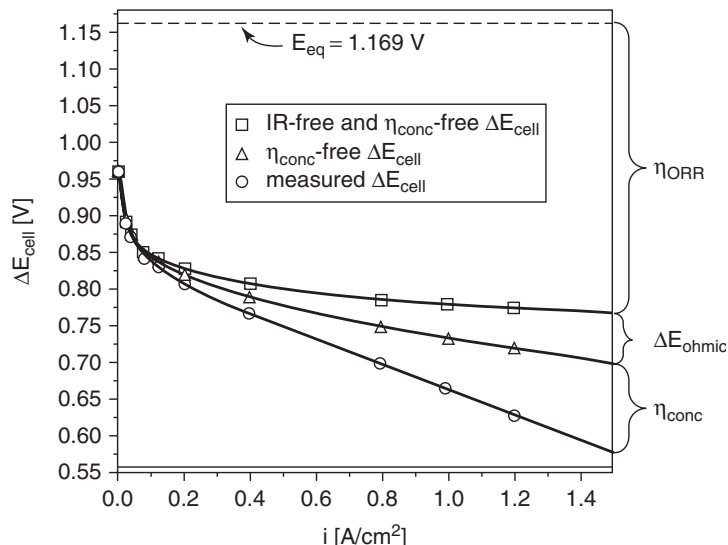


Figure 12.2 Current–voltage characteristic obtained in a 50-cm² dihydrogen/air fuel cell at 353 K at a total pressure of 150 kPa. The anode and cathode layers consist of about 50 wt% Pt/C [0.4/0.4 mg_{Pt}/cm² (anode/cathode)] and ionomer (ca. 900 EW; ionomer/carbon ratio = 0.8 : 1). Circles, experimental data; triangles, mass-transport-free ΔE_{cell} ; squares, mass-transport-free and ohmically corrected ΔE_{cell} . The current density is referred to the geometric surface area of the MEA. (From ref. 4, with permission from Elsevier.)

The CLs of the early PEMFCs were prepared from the noble metal blacks and thus contained very high metal loadings per geometric MEA area. Later, it became apparent that precious metals in these CLs were not utilized efficiently and the new generation of PEMFCs emerged, based on carbon-supported precious-metal catalysts (usually Pt or Pt-based alloy). The MEA preparation techniques have undergone continuous evolution since the early days of PEMFCs. For a historical overview, the reader is referred to refs. 1 and 5. In this chapter we focus on carbon materials as supports for PEMFCs and DMFCs.

For a fuel cell to operate efficiently, carbon materials must satisfy the following requirements:

- Provide high dispersion of metal nanoparticles and protect them from agglomeration
- Be chemically inert and pure in order that impurities do not inhibit electrochemical reactions
- Have high electron conductance to minimize ohmic losses associated with the electron transport
- Possess adequate porosity to ensure efficient mass transport of reactants to, and products from, the CLs
- Be compatible with proton-conducting polymers so that composites containing a catalyst and a proton conductor provide efficient proton transport through the CLs
- Provide optimum water management
- Be corrosion resistant

The right choice of a carbon support greatly affects cell performance and durability. The purpose of this chapter is to analyze how structure and properties of carbon materials influence the performance of supported noble metal catalysts in the CLs of the PEMFCs. The review chapter is organized as follows. In Section 12.2 we give an overview of carbon materials utilized for the preparation of the catalytic layers of PEMFC. We describe traditional as well as novel carbon materials, in particular carbon nanotubes and nanofibers and mesoporous carbons. In Section 12.3 we analyze properties of carbon materials essential for fuel cell performance and how these are related to the structural and substructural characteristics of carbon materials. Sections 12.4 and 12.5 are devoted to the preparation and characterization of carbon-supported electrocatalysts and CLs. In Section 12.6 we analyze how carbon supports may influence fuel cell performance. Section 12.7 is devoted to the corrosion and stability of carbon materials and carbon-supported catalysts. In Section 12.8 we provide conclusions and an outlook. Due to obvious space constraints, it was not possible to give a comprehensive treatment of all published data, so rather, we present a selective review and provide references as to where an interested reader may find more detailed information.

12.2 STRUCTURE AND MORPHOLOGY OF CARBON MATERIALS

The two allotropes of carbon with well-defined properties are diamond (sp^3) and graphite (sp^2), the first being an insulator (although semiconducting forms of diamond are known as well) and thus of marginal value for fuel cells, and the latter being an electron conductor. Of interest for PEMFC applications are numerous hybrid forms, comprising sp^3 -, sp^2 -, and sp^1 -type carbon atoms. In this section we review briefly the structure and morphology of conventional carbon materials (carbon blacks and activated carbons), which nowadays are utilized widely for MEA preparation, and present some information concerning novel carbon materials, which have recently shown promise for PEMFCs. For more details, the reader is referred to Chapters 1 and 8.

12.2.1 Carbon Blacks

The most widely utilized as supports for PEMFCs are carbon soots or blacks. The term *carbon black* refers to a group of industrial products obtained by pyrolysis or incomplete combustion of various carbon-containing compounds. Depending on the type of stock material and the production method, they are classified as furnace, channel, thermal, and lamp blacks [6,7]. Details of the preparation methods are given in Chapter 1 and in refs. 6, 8, and 9. According to the present understanding, the structure of carbon blacks may be described as follows. Graphene clusters are arranged into round primary particles (Figure 12.4) of average size ranging from 10 to 400 nm [10], depending on the type of soot. High-resolution transmission electron microscopy (TEM) indicates that the degree of graphene layer ordering is high at the surface but decreases toward the particle interior [6]. Primary particles may be interconnected via intergrowing and overlapping graphite layers into primary aggregates of various sizes and shapes. As the shape changes from spheroidal to ellipsoidal, linear, and eventually branched, the packing density of primary particles in the aggregates decreases, while the contribution of the empty voids increases, resulting in an increase in the absorptive capacity of carbon blacks for liquids. In this context an important characteristic related to the aggregate shape is dibutyl phthalate (DBP) absorption, which varies between 30 and 400 cm³ per 100 g of carbon black. High and low DBP absorption values are characteristic of high structure and low structure, respectively. Ramified dendritelike aggregates are between 100 and 800 nm [10] and are not disintegrated upon catalyst ink and MEA preparation. These aggregates are usually assembled into loosely bound three-dimensional superstructures—agglomerates, of size between 1 and 100 μ m. Depending on the stock material and synthetic procedure, BET surface areas A_{BET} of carbon blacks range from 10 to 1500 m²/g. Until recently, the most widely used in PEMFC development have been acetylene black, Vulcan XC-72, and Ketjenblack [8,11]. Their distinctive feature is their fairly high degree of ordering, stipulating high electron conductivity. The textural and substructural characteristics of carbon blacks are summarized

Table 12.1 Structural and Morphological Properties of Some Carbon Blacks Utilized in PEMFCs

	Property	Acetylene Black	Vulcan XC-72	Ketjen-black DJ-600	Black Pearls 2000
Textural characteristics	BET surface area (m^2/g)	64	252	1300	1500
	Area of mesopores (m^2/g)	64	177	1230	1020
	Total pore volume (cm^3/g)	0.20	0.63	2.68	2.56
	Micropore volume (cm^3/g)	0.00	0.037	0.029	0.208
	Average pore diameter (nm)	14.4	15.9	9.45	20.6
Substructural parameters ^a	L_a (nm)	3.0	1.6	2.1	1.4
	L_c (nm)	4.1	2.0	1.4	1.1
	d_{002} (nm)	0.348	0.363	0.356	0.374
	I_{002}/I_{10}	10	4.8	2.4	2.1
	Weight proportion of quasi-graphite domains	0.96	0.76	0.83	0.33
Morphology ^b	Primary particle diameter (nm)	42	20–30	35–40	10–15
	Projection area of aggregates (μm^2)	0.52	0.14		
	Anisometry of aggregates	2.02	2.0		
	DBP absorption (cm^3/g)	2.62	1.93	3.50	3.30

^a L_a , average in-plane diameter; L_c , crystallite size in the direction perpendicular to graphene layers; I_{002} and I_{10} , integral intensities of (002) and (10) reflections; d_{002} , interlayer spacing.

^b Adapted from Table 2.6 of ref. 8, with permission from John Wiley & Sons.

in Table 12.1, which shows that carbon materials selected for PEMFC applications have high structural factors, large aggregate sizes, and anisometry factors. The fact that carbon blacks with large volumes of mesopores with $d > 10$ nm and elongated aggregates of submicrometer size proved to be suitable for the catalytic layers of PEMFCs suggests that other mesoporous carbons may also be applicable [12]. Indeed, successful utilization of carbon nanofibers (CNFs) and nanotubes (CNTs) [13–15], carbon microspheres [16], and carbons of the Sibunit family [17,18] supports this conclusion.

12.2.2 Activated Carbons

The term *active* or *activated carbon* refers to carbon materials manufactured by high-temperature (773 to 1273 K) pyrolysis of various vegetative residues (i.e.,

wood chips, peat, coal, nutshells and pits, etc.) as well as pitch and polymer substances, followed by activation to create desirable porous structure of the target materials [19]. During the activation by steam, CO₂, or air at temperatures up to 1173 K, the most reactive amorphous components are burned off. Another approach, *chemical activation*, consists of heat treatment in the presence of alkali (NaOH), inorganic acids (H₂SO₄, H₃PO₄), or salts (ZnCl₂, K₂S) in an inert atmosphere at 873 to 1073 K. The advantage of chemical activation is the more uniform pore structure of the target activated carbon materials. The crystalline structure is influenced largely by the content of aromatic compounds in the stock material. For materials originating from plants, it depends on the ratio between the lignin and the pulp. Activated carbons produced from pulp have amorphous structure, are very brittle, and are difficult to graphitize. Lignin, contrary to pulp, melts during carbonization, thus leading to materials with a higher degree of structural order and stiffness.

Activated carbons possess high BET surface areas (400 to 2500 m²/g) and micropore volumes (up to 1.2 cm³/g), which makes them particularly attractive adsorbents. They are also used as supports for heterogeneous catalysts and sometimes, electrocatalysts [20]. In a number of patents it was claimed that addition of either activated carbons or activated carbon-supported Pt to the CLs composed of carbon black-supported catalysts improves cell performance [21].

12.2.3 Carbons of the Sibunit Family

Sibunit carbons are patented [22] composite materials based on carbon blacks and pyrolytic carbon. They are obtained by pyrolysis of hydrocarbons (usually, a propane–butane mixture, although methane or other hydrocarbons may be used as well) at 1120 to 1220 K onto a template (usually, carbon black), followed by steam activation in a fluidized bed at 973 to 1120 K. At the first stage, *solidification*, hydrocarbons are pyrolyzed, filling the voids of the template with pyrolytic carbon. At the *activation* stage the porous structure of Sibunit materials is formed gradually, while carbon black particles, which are more prone to oxidation compared to pyrolytic carbon, are burned off. Sibunit carbons are mesoporous materials whose pore morphology is determined by the size of the carbon black particles. The information on their preparation and properties may be found in refs. 23 and 24. According to their physicochemical properties, Sibunit carbons are similar to graphite and are characterized by high mechanical stiffness (up to 300 kg/cm²), electron conductivity (ca. 10 S/cm), thermal and chemical stability, very low ash content (below 0.3 wt%), and concentration of surface functional groups. They possess high crystallinity: $L_a - L_c$, ranging from 3.8 to 4.5 nm, d_{002} from 0.348 to 0.352 nm, and I_{002}/I_{10} from 5.0 to 7.5. At the same time, they may have high surface areas (up to 500 m²/g) and pore volume (up to 1.0 cm³/g). Notably, micropore volume in Sibunit carbons does not exceed 0.1 cm³/g. The technology of Sibunit production allows one to vary textural characteristics, adsorption properties, and mechanical stiffness widely by varying the type of template, the degree of solidification, and the degree of activation.

The range of Sibunit carbons is extended by materials obtained through two-step pyrolytic carbon deposition, and high-temperature post-treatments, resulting in an increase in the graphitization degree. Sibunit carbons are utilized as catalysts for phosgene synthesis and liquid-phase oxidation of sulfur-containing substances, and as supports for heterogeneous catalysis. Recently, Sibunit carbons have also shown promise as supports for fuel cell electrocatalysts [17,18].

12.2.4 Ordered Mesoporous Carbons

Ordered mesoporous carbons are synthesized either by nanocasting ordered mesoporous silica or zeolite templates, or directly by templating triblock copolymer structure-directing species [25,26]. The resulting materials have uniform mesoporous structure of periodically arranged interconnected mesopores. Synthesis strategies for ordered mesoporous carbons have recently been reviewed by Chang et al. [25]. In brief, they are as follows. A carbon precursor is infiltrated into the pores of a suitable ordered silica template, polymerized, and then pyrolyzed in an inert atmosphere to produce silica–carbon composite. Then the silica template is dissolved in HF, leading to the desired material. The advantages are widely tunable pore size in the range several nanometers to several micrometers achieved by choosing the size of silica template, and three-dimensional ordered uniform structure composed of interconnected voids. For example, Chai et al. [26] reported preparation of ordered uniform porous carbon frameworks with pore sizes in the range 10 to about 1000 nm synthesized using removable colloidal silica crystalline templates by carbonization of phenol and formaldehyde as a carbon precursor. The resulting ordered mesoporous carbons have BET surface areas ranging from 400 to 1000 m²/g and pore volume from 0.7 to 3.8 cm³/g. Their structure is strongly affected by the nature of the carbon precursor and the conditions applied during the polymerization and the pyrolysis steps. Along with mesopores, whose size is determined by the size of silica template particles, ordered mesoporous carbons may comprise a significant number of micropores within the carbon frameworks. For example, carbons described by Chai et al. [26] comprised a large fraction of micropores, whose contribution to the overall surface area amounted to about 25%. These micropores were nearly fully blocked when Pt–Ru particles were supported on these carbon materials. The pore wall structure of mesoporous carbons may be either amorphous or graphitic, depending on the preparation conditions. Su et al. [27], using hydrogen-form zeolite Y as the template, obtained materials with an amorphous carbon core and a graphitic carbon shell. Graphitic structure is believed to be advantageous for fuel cell durability.

12.2.5 Carbon Aerogels

Carbon aerogels were first synthesized by Pekala in 1989 through pyrolysis of organic aerogels [28,29]. They display three-dimensional random close-packed monolithic structure [30,31] of slightly overlapping carbon spheres (3 to 30 nm)

with small interstitial pores (<50 nm) [32] connected to each other by covalent bonds. This structure imparts unique physical properties, such as high conductivity (1 to 15 S/cm) [28,33], high mesoporosity concomitant with a small degree of microporosity [34,35], and high surface area. The structure (tortuosity, pore volume, pore size distribution, specific surface area) and physical properties (density, conductivity) may be adjusted by varying experimentally controllable parameters (e.g., precursor materials and their ratio, process parameters during sol–gel polymerization and during pyrolysis) [36,37]. For more details on carbon aerogel preparation and properties, see Chapter 9. Whereas carbon blacks are usually arranged into aggregates connected through van der Waals bonds, and are thus subject to (1) electronic insulation by the proton-conducting polymer Nafion, which needs to percolate into the CL, and (2) mass transport hindrance in the random carbon porous layers [38,39], it is believed that the monolithic and tunable structure of carbon aerogels should enable better control of the CL morphology.

12.2.6 Carbon Nanotubes and Nanofibers

The possibility of forming carbon filaments from the thermal decomposition of gaseous hydrocarbons was first mentioned in 1889 [40] in a U.S. patent that proposed the use of such filaments in the light bulbs. Other early reports consist of two papers presented at the French Academy of Sciences [41,42]. However, it was not before the invention of the transmission electron microscope that these structures were imaged with the nanometer resolution. The history of the invention of CNTs has recently been reviewed by Monthioux and Kuznetsov [43]. Although the credit of discovering carbon is often given to the Japanese scientist Sumio Iijima, who discovered them in the insoluble material of arc-burned graphite rods, formation of carbon nanotubes and the respective TEM images were documented 40 years earlier by Russian scientists Radushkevich and Lukyanovich [44]. Since those times a variety of morphologies have been reported in the literature: single- and multiwalled carbon nanotubes (SWCNTs and MWCNTs), as well as CNFs with herringbone, platelet, ribbon, and other structures. CNFs obtained by catalytic pyrolysis of hydrocarbons on the surfaces of oxide-supported transition metals are often addressed as catalytic filamentous carbons. These are very attractive, since varying the type of catalyst and its particle size, allows one to tune the morphology and the nanostructure of the target materials. Catalytic CNFs are mesoporous materials with an average pore diameter of 5 to 50 nm, pore volume of 0.2 to 0.8 cm³/g, BET surface area of 70 to 300 m²/g, and a very low ash content of 0.2 to 1 wt%. From traditional carbon materials utilized in fuel cell electrocatalysis, they are distinguished by the high extent of structural order. Typical x-ray diffraction parameters are as follows: $L_a - L_c = 6$ to 7 nm, $d_{002} = 0.340$ to 0.345 nm, and $I_{002}/I_{10} = 5$ to 7. These depend, however, very much on the type of graphene layer packing. For further details, the reader is referred to Chapter 8. CNFs possess a high stiffness value of 70 to 120 kg/cm², while their electron conductivity differs depending on the nanostructure (see Section 12.3.1). The wide variability of the structures of CNFs and CNTs, their mesoporosity,

and their high degree of structural ordering make them very attractive as supports for fuel cell catalysts. Some of them are mentioned in Section 12.6.3.

12.3 PHYSICOCHEMICAL PROPERTIES OF CARBON MATERIALS RELEVANT TO FUEL CELL OPERATION

12.3.1 Electron Conduction

The electrical conductivity of ordered graphite is anisotropic, with the conductivity in the direction parallel to graphene layers strongly exceeding the conductivity in the perpendicular direction. For example, Kinoshita [8] provides the values of 2.5×10^4 and 1.0×10^2 S/cm in the direction perpendicular and parallel to the *c*-axis, respectively. The electronic conductance of compressed carbon powders depends on the intrinsic conductivity of carbon particles, the resistance of their contacts, and the volume density of the latter. The intrinsic conductivity is higher for carbon particles with more perfect structure [7,8,45–48]; that is, it increases with the size of graphitelike crystallites and decreases with the density of structural defects and with the internal porosity of carbon particles. Heat treatment at temperatures greater than 2700 K stipulates graphitization and subsequent increase of the intrinsic conductivity. In the fuel cell-related literature the intrinsic conductivities of carbon materials are often compared, which are not directly relevant to the electric conductance of the CLs, since the overall resistance of compact carbon powders is dominated by the *contact resistance*. The latter depends on the surface chemistry of carbon particles: their size, shape, and the external pressure. An increase in the concentration of oxygen-containing surface functionalities results in an increase in the work function and a concomitant increase in the resistance of compacted carbon powders [8,48–50].

The conductance of compacted carbon materials has been described by the percolation theory [51] and more recently by the effective media theory [52]. It was shown that above the percolation threshold the conductivity σ of the compact carbon powder comprising gas-filled voids may be described as

$$\sigma = \sigma_h \left(\frac{\Phi - \Phi_c}{1 - \Phi_c} \right)^{t'} \quad (12.4)$$

where σ_h is the intrinsic conductivity of carbon material, Φ its volume fraction, Φ_c the percolation threshold, and t' is an exponent related to the percolation threshold and to the shape of the grains. For more details the reader is referred to the original publication [52]. Figure 12.3 represents the conductivities of various carbon powders as a function of Φ . For graphite materials (1 and 2 in Figure 12.3) the conductivity is high even at low volume fractions. For carbon black* and pinewood activated carbon, the conductivity is low even at very high volume fractions. For powders with a high degree of anisometry [e.g., for the

*Unfortunately, the authors of ref. 52 did not specify the type of carbon black.

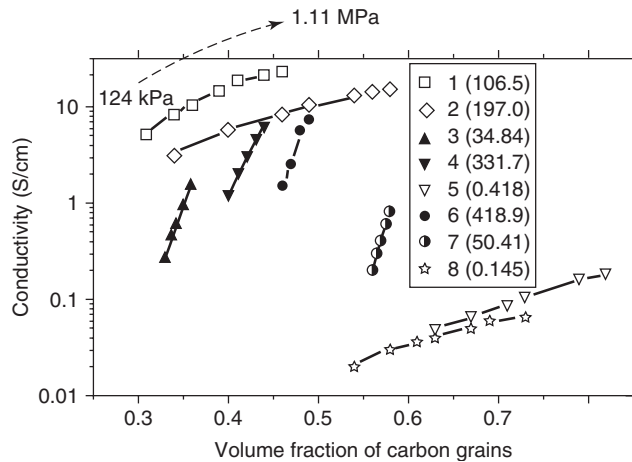


Figure 12.3 Conductivities of various carbonaceous powders as a function of the volume fractions of their grains. Symbols show the experimental data for 1, artificial graphite; 2, natural graphite; 3, coconut shell activated carbon; 4, needle coke; 5, pinewood activated carbon; 6, isotropic coke; 7, anthracite activated at 50% burn-off; 8, carbon black. The intrinsic σ_h conductivity values in S/cm derived from equation (12.4) are given in parentheses. Lines correspond to the values calculated using equation (12.4). (Adapted from ref. 52, with permission from Elsevier.)

ellipsoids of the coconut shell activated carbon (3) and for needle coke (4)], the conductivity at low volume fractions falls very much below their intrinsic conductivities but rises abruptly even at modest compressions. Since for successful PEMFC operation high electrical conductivities of the CLs must be achieved at sufficiently high pore volumes, the development of optimum support materials requires that the dependence of their conductivities on the pressure and volume fraction be considered. Conductivities of compacts of carbon blacks pertinent to PEMFCs are represented in Table 12.2. Note that Vulcan XC-72 shows relatively high conductivity at $\Phi = 0.3$.

The conductivity of carbon black/polymer composites is a function of a number of parameters, including:

- The volume fraction of carbon material (the percolation threshold) [53]
- Its structure, in particular the particle size [54], aggregate morphology, and size [55–57]
- The chemical nature and physicochemical properties of the polymer (e.g., viscosity, surface tension) [58]
- Mixing and finishing conditions [53]

For CNTs and CNFs the conductivity values depend very much on their substructural characteristics. Single-walled CNTs may be either metallic or semiconducting, depending on the tube diameter and helicity [59]. For multiwalled

Table 12.2 Electrical Conductivity and Textural Characteristics of Some Carbon Blacks at Volume Fraction $\Phi = 0.3$

Carbon Black	A_{BET} (m ² /g)	V_{mi} (cm ³ /g)	V_{DBP} (cm ³ /g)	$\sigma_{\Phi=0.3}$ (S/cm)
Thermal black	13	—	0.39	0 ^a
Furnace black	99	0.003	1.15	2.0
Conductex SC	190	0.03	1.15	2.5
Printex L	150	0.04	1.16	3.3
Printex L6	190	0.04	1.20	3.3
Conductex 975	250	0.05	1.70	4.7
Vulcan XC-72	245	0.06	1.78	4.5
Black Pearls 2000	1635	0.59	3.30	2.2 ^a
Printex XE-2	1300	0.03	4.00	12.3 ^a

Source: Ref. 50, with permission from Elsevier.

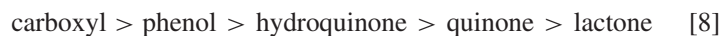
^aExtrapolated value.

CNTs and CNFs, high electrical conductivity values, close to that for graphite, have been reported. Tibbetts et al. [60] review the conductivity measurements of vapor-grown CNF–polymer composites. The electrical conductivity reported reaches about 7 S/cm at 15 vol% of carbon.

12.3.2 Surface Properties

Oxygen Functionalities We now focus on the surface chemical properties of carbon blacks of interest for PEMFC. The reader is referred to Chapter 2 for more details. Carbon blacks always contain a certain fraction of elements different from carbon, which depends on the raw material used for their elaboration. Apart from carbon, the two major constituents of carbon blacks are hydrogen and oxygen [61]. Hydrogen atoms arise from carboxyl or phenol groups and from water chemisorbed on the surface of carbon materials. Decomposition of these groups occurs between 1273 and 1473 K, and the last traces of hydrogen are eliminated by heat treatment at 1873 K [8]. Since graphene sheets are relatively chemically inert, other foreign elements, and in particular oxygen-containing groups, are located predominantly at their edges. Special consideration is given to oxygen-containing groups because they strongly affect the physicochemical properties of carbon supports. Surface oxygen-containing groups may possess acidic, neutral, or basic properties [8,62]. Acidic surface properties are achieved through oxidizing treatment, such as heat treatment in ozone, oxygen-containing atmosphere, or liquid oxidants. Acidic properties arise from the presence of carboxyl, anhydride, lactone or lactol, and hydroxyl groups of phenolic character. Their acidity is also affected by their chemical environment (i.e., the size, charge, electronegativity, and inductive/mesomer character of other substituents). On the other hand, the origin of surface basicity is still under discussion. Groups inducing surface basicity are believed to be oxygen functional groups such as chromene [63], lactone, or pyrone [8,62,64–70]. Other

authors assume that surface basic sites are associated with the carbon itself (π -electron-rich regions within the basal planes) and are of Lewis type [71,72]. In the end, neutral surface groups are formed by the irreversible adsorption of oxygen at unsaturated sites of the carbon support ($>\text{C}=\text{C}<$) and of carbonyl complexes with acidic–basic character, *complex ketones*, as defined by Antonucci et al. [73]. The acidity of surface groups decreases in the range



The reader is referred to refs. [8,61,62,75], and 76 for more details concerning the acidic–basic character of surface groups, their nature, and their titration.

Another important characteristic of carbon materials is the work function, which is related to their nanostructure and their surface chemistry [77], but is not considered in this chapter. The reader is referred to Chapter 1 and ref. 8 for more details.

Double-Layer Capacitance The capacitance of the electrochemical double layer between the basal plane of highly oriented pyrolytic graphite (HOPG) and aqueous electrolytes was studied by Randin and Yeager [78,79]. Capacitance–potential curves exhibited a minimum of approximately 2 to 4 $\mu\text{F}/\text{cm}^2$ around 0.0 V versus SHE (standard hydrogen electrode) independent of pH for the entire pH range (0 to 14) and only slightly dependent on the concentration of the electrolyte. The value of the capacitance minimum was proposed to be a measure of the density of defects at the HOPG basal plane [80]. Modestov et al. [81] performed measurements for the basal and edge planes of HOPG. For the basal plane the capacitance minimum was $1.4 \mu\text{F}/\text{cm}^2$. In contrast to the basal plane electrode, for the edge plane the capacitance versus the electrode potential curve exhibited a maximum, which shifted with the pH of the solution, and was more than an order of magnitude higher than the capacitance for the basal plane. The capacitance of the edge plane was shown to be dominated by pseudocapacitance ascribed to the redox transformations of surface oxygen-containing functional groups.

Double-layer properties of porous carbon materials have been widely investigated in relation to the development of the electrochemical capacitors. For detailed information the reader should consult specialized literature. For porous carbons materials, the double-layer capacitance depends on their specific surface area [82,83], pore structure (notably, the pore size distribution) [84–87], and their crystalline structure and surface chemistry [83,88,89]. Shi [84] measured the dc capacitance of various carbons in a KOH electrolyte and noticed that the overall capacitance may reasonably be described as a sum of the capacitance of micro- and mesopores. Assuming that the electrical double layer propagates into micropores accessible for N_2 adsorption, the author estimated the differential double-layer capacitance per unit of micropore surface area as 15 to $20 \mu\text{F}/\text{cm}^2$. Lower values were reported by Vilinskaya

et al. [87] (4 to 4.5 $\mu\text{F}/\text{cm}^2$ in 0.01 N H_2SO_4) and Gryglewicz et al. [86] (9.8 $\mu\text{F}/\text{cm}^2$ in 1 M H_2SO_4). The double-layer capacitance per unit of the external surface area has been found to depend strongly on the pore structure and on the surface morphology, and the differences between carbon materials may exceed an order of magnitude. It should be noted, however, that penetration of the electrical double layer into micro- and mesopores depends on the pore diameter and on the Debye length (the effective thickness of the diffuse electrical double layer) as demonstrated by, for example, Vilinskaya et al. [87]). Strong correlation between the double-layer capacitance and the amount of surface oxygen-containing complexes, which during temperature-programmed desorption desorb as CO , has been observed [88,89]. Meanwhile, for carboxylic groups (which are usually desorbed as CO_2), no correlation has been observed [90].

Wettability The wettability of carbon materials and carbon-supported electrocatalysts is the key factor influencing the utilization factor and water management within the CLs of PEMFCs (see Section 12.6). The three-phase boundary that is established in a PEMFC porous electrode depends on the wetting properties of carbon materials, on the quantity of the binder [polytetrafluoroethylene (PTFE)], and/or on the ionomer (Nafion) in the CL, as well as their intermixing. The contact angle θ provides a convenient measure of the wettability of carbon materials. The larger the contact angle, the more difficult it is to wet a carbon material by a particular liquid. The macroscopic theory of the capillary flow dynamics was introduced by Washburn in 1921 and forms the basis for measuring the contact angle of water in carbon materials [91]. The Washburn relationship predicts a \sqrt{t} dependence for the rise of the fluid meniscus $l(t)$ in the capillary with time t :

$$l(t)^2 = \frac{\gamma r \cos \theta}{2\eta} t \quad (12.5)$$

where γ is the surface tension of the liquid, r the capillary radius, θ the contact angle between the liquid and the capillary wall, and η the liquid viscosity. The Washburn equation was later demonstrated to be suitable for measuring the contact angle of many different carbon black materials [92]. It has recently been demonstrated that some amendments are required for the application of the Washburn equation to nanoscopic materials [93].

Carbon materials are usually poorly wetted by water unless a surfactant is present. For example, the contact angle of pure water with graphitized Vulcan samples varies between 78 and 83° [94], in agreement with the contact angle reported for Ceylon graphite (ca. 85°) [95]. The addition of a small quantity of PTFE to carbon blacks increases their hydrophobicity [8]. The surface structure and surface chemistry of carbon materials strongly affect their wetting properties. Studebaker et al. [92] established the empirical relationship

$$\cos \theta_{\text{H}_2\text{O}} = (0.037 \times \text{at \% O}) - (0.185 \times \text{at \% H}) + 0.285 \quad (12.6)$$

This indicates that $\cos \theta_{\text{H}_2\text{O}}$ increases with the increase in oxygen content and decreases with the decrease in hydrogen content. This relationship was confirmed by the results of Kinoshita et al. [94] on the electrochemical treatment of carbon blacks. Hydrophilic carbons provide high catalyst utilization factors, whereas hydrophobic carbons (or graphitized carbons) allow easy water removal, avoid flooding of the CLs, and ensure better resistance to corrosion [8,96,97].

12.4 PREPARATION OF CARBON-SUPPORTED ELECTROCATALYSTS

The preparation of carbon-supported noble metal catalysts has been reviewed widely in the literature (see, e.g., refs. 70 and [98–100] and references therein), it is also the subject of Chapter 4 and thus will be reviewed only briefly in this chapter, with the aim of drawing out features characteristic of fuel cell electrocatalysts. The CLs of PEMFCs must be relatively thin, to minimize ohmic losses caused by proton transport, and mass transport losses of reactants and product water (see Section 12.6.2). This, along with the sluggish oxygen reduction kinetics at the cathode, implies utilization of catalysts that contain a high percentage of precious metals, ranging from 20 to 80 wt%, in contrast to conventional heterogeneous catalysts, usually containing below 1 to 5 wt% of the active component. On the other hand, a high dispersion of the metal nanoparticles (nanoscale size distribution) and uniform distribution over carbon support are required for PEMFC electrocatalysts. This implies major consequences regarding the elaboration techniques used for catalyst preparation. For example, catalyst preparation methods based on ion exchange are usually not used for the elaboration of fuel cell electrocatalysts, since they result in low metal contents. Methods utilized for the preparation of carbon-supported metal catalysts may be divided into two groups: those based on deposition from the gas phase or vacuum, and those based on metal deposition from the liquid phase. Metal deposition from the gas phase is well adapted to flat surfaces but less useful for porous substrates such as carbon blacks, because metal precursors often cannot penetrate the pores of carbon particles. There have, however, been some successful examples [101,102] of CL preparation by metal sputtering directly onto the gas-diffusion layers, consisting of carbon paper, carbon black, and PTFE. Metal sputtering allows ultrathin CLs, which often show a high performance level at low metal loadings. For example, Alvisi et al. [102] reported that the mass activity of Pt sputter deposited on the gas diffusion electrode at very low loadings ($<0.02 \text{ mg/cm}^2$) in the methanol oxidation increased about 14 times compared to conventional Pt/C commercial catalysts. Unfortunately, for measuring the catalytic activity, the authors used cyclic voltammetry, which provides information hardly transferable to the fuel cell operation. Sputtering was used in a number of references to support Pt on CNTs [103] and CNFs [104]. A method based on co-sputtering of carbon and Pt has been proposed at the Paul Scherer Institute [105]. However, until now, methods based on metal deposition from the liquid phase are prevailing and are

reviewed briefly below. For more information the reader is referred to review articles [70,99,100,106,107].

12.4.1 Methods Based on Impregnation

Since the target metal contents in PEMFC catalysts exceed the sorption capacity of carbon materials, the preparation methods are aimed at the increase in the amount of deposited metal above the sorption capacity. Formerly, electrocatalysts have been prepared by the impregnation of carbon materials with precursor complexes [e.g., H_2PtCl_6 , $(\text{NH}_3)_2\text{Pt}(\text{NO}_2)_2$, RuCl_3 , $\text{RuNO}(\text{NO}_3)_x$] followed by the solvent evaporation, drying, calcination, and sample reduction (e.g., in the hydrogen stream). The metal dispersion, particle size distribution, and localization of the metal particles in the carbon grains of catalysts thus prepared depend on the solubility of precursor complexes, drying conditions, pore structure, and the surface properties of the carbon material [108]. The strong influence of carbon porosity on metal dispersion limits the range of carbon materials suitable within this synthetic approach. Another limitation of this method is concerned with the localization of highly dispersed metal phase in the narrow pores of carbon material, while coarsely dispersed metal particles are formed on the outer surface of carbon grains. To reduce the contribution of the coarsely dispersed phase, multiple impregnation steps may be applied [109].

Most widespread at present are methods based on *impregnation-reduction* of the active components onto a carbon surface under the action of (1) strong reductants ($\text{Na}_2\text{S}_2\text{O}_4$, N_2H_4 , HCOOH , NaBH_4), (2) an alkali agent followed by reduction, or (3) alkali and a reducing agent simultaneously (e.g., $\text{NaOH} + \text{H}_2\text{CO}$, $\text{NaOH} + \text{ethylene glycol}$, $\text{Na}_2\text{CO}_3 + \text{NaOOCH}$). Dispersion of the target catalysts is strongly influenced by the temperature, solution pH, and the nature and concentration of the reductant [110–115]. The samples obtained within this method contain metal nanoparticles with an average particle size of 2 to 10 nm. The mechanism of their formation is not yet fully understood. Thus, it is not really clear whether the deposition process is chemical (*in situ* generation of colloidal particles followed by their adsorption), electrochemical, or mixed in nature. In both the impregnation and impregnation-deposition methods, the surface properties of carbon materials are of primary importance for obtaining the desired metal dispersion and particle size distribution, since structural defects and functional groups on the carbon surface usually act as nucleation centers for metal deposition [116,117].

The presence of micropores in carbon materials usually facilitates metal dispersion, which does not, however, translate into an increase in the catalytic activity. This may be explained by the blockage of metal nanoparticles in micropores, which are not accessible to reagents [98]. As a consequence, PEMFC specifications require that carbon materials used in PEMFCs comprise a high contribution level of mesopores, but no micropores. The ratio of the surface area of mesopores (the external surface area) to the overall pore area may be characterized by the $A_{\text{CTAB}}/A_{\text{BET}}$ ratio, where A_{CTAB} is the surface area measured using cetyltrimethylammonium bromide. It has been shown that carbon blacks with a $A_{\text{CTAB}}/A_{\text{BET}}$

ratio close to 1 are advantageous for PEMFCs, since they make possible high levels of dispersion of active metal components in mesopores without noble metal crystallites penetrating micropores and thus being inaccessible for electrochemical reactions [118].

12.4.2 Colloidal Synthesis

In this technique, a metal precursor is reduced chemically or electrochemically. A surfactant adsorbing at the metal–solution interface limits the growth of metal nanoparticles and allows preparation of well-dispersed colloidal solutions, with a minimized fraction of agglomerated particles [119]. The preparation of carbon-supported metal nanoparticles usually proceeds by controlled adsorption of the colloidal solution onto the carbon support [120–128], which occurs through weak electrostatic interactions between colloidal particles and a carbon surface. Metal particles are preferentially adsorbed in the pores, whose diameter is commensurable with their size, since the interaction of the particles with the pore walls is stronger than the interaction with plane surfaces. The adsorption step is usually followed by the thermal and/or oxidative treatment required for the surfactant degradation [120–128]. If the surfactant is a polymer or an organic compound, removal of the protective shell is the key step affecting the electrocatalytic activity of target materials. Severe treatment conditions may lead to particle agglomeration, whereas mild treatment conditions lead to the incomplete removal of surfactant, which may be detrimental for electrocatalytic performance [128]. To our knowledge, the first attempt to prepare PEMFC electrocatalysts by a colloidal route was made by Watanabe et al. [129]. The authors suggested a method based on co-deposition of fine metallic oxide particles, followed by reduction with hydrogen. At the same time, Meguro et al. [130] demonstrated that Pt colloids with nearly monodisperse size distribution centered around 3 nm could be obtained via reduction of hexachloroplatinic acid by formaldehyde in the presence of trioctylmethylammonium salt. This opened new frontiers for the preparation of Pt group metallic colloids for PEM fuel cells. Substantial progress in colloid-based preparation methods has been made by the group of Boennemann et al. [131–133]. An elegant approach by Reetz et al. [134,135] used an electrochemical route to drive metal deposition. The metal of choice is electrooxidized at the anode and reduced electrochemically at the cathode, the electrolyte (tetraalkylammonium salt) playing the role of surfactant. The size of colloidal particles can be controlled accurately by playing with the current density [134,135].

12.4.3 Electrodeposition

Metal nanoparticles can also be deposited directly onto the carbon support by classical electrochemical techniques from a solution containing metal species [136–145]. The nature of the electrolyte and the current–potential program used are crucial parameters which allow us to tune the mean particle size and the size

distribution of metal particles. Pulse electrochemical deposition has proven useful for independent control of the nucleation and growth steps [138]. Electrochemical deposition was used successfully on the basal plane of HOPG [136–139], glassy carbon [146,147], and carbon black particles [140–144]. On the other hand, *in situ* Pt electrochemical deposition was first reported by Kuwana in a polymer film formed previously on glassy carbon [148]. Pt particles exhibited high activity for the hydrogen oxidation and oxygen reduction reactions. Later, Antoine and Durand [140] adapted this technique and provided evidence that metal precursors may be directly deposited in a CL with a metal mass fraction as high as 40 wt%. This approach guarantees good ionic and electronic percolations of the CL [140] and implies high catalyst utilization factors [140,145]. Three major drawbacks of the technique are (1) the presence of unreduced platinum, (2) the presence of counter ions (usually, chlorides) that may poison the electrocatalytic activity of metal nanoparticles, and (3) the hydrogen evolution reaction, which competes with Pt deposition and contributes to a pronounced loss of the faradaic yield, if the deposition is performed at low electrode potentials.

12.4.4 Other Methods

Recently it was proposed that PEMFC electrocatalysts may also be prepared by water-in-oil microemulsions. These are optically transparent, isotropic, and thermodynamically stable dispersions of two nonmiscible liquids. The method of particle preparation consists of mixing two microemulsions carrying appropriate reactants (metal salt + reducing agent), to obtain the desired particles. The reaction takes place during the collision of water droplets, and the size of the particles is controlled by the size of the droplets. Readers are referred to the early work of Boutonnet et al. [149], the review paper of Capek [150] and refs. [128,151], and 152 for fuel cell applications. The carbonyl route has the ability to control the stoichiometry between bimetallic nanoparticles, but also the particle size. The reader is referred to review papers for more details [106,107]. Other methods, including sonochemical and radiation–chemical, have been used successfully for the preparation of fuel cell catalysts (see, e.g., review articles 100 and 153).

12.5 STRUCTURAL CHARACTERIZATION OF CARBON-SUPPORTED METAL CATALYSTS

Various approaches have been described in the literature for the characterization of carbon-supported metal catalysts. The catalysts are usually analyzed before and after (postmortem) their electrochemical operation with conventional *ex situ* techniques such as x-ray diffraction (XRD), transmission electron microscopy (TEM), scanning electron microscopy (SEM), energy-dispersive x-ray analysis (EDX), x-ray photoelectron spectroscopy (XPS), and x-ray absorption spectroscopy (XAS). Although *ex situ* analysis provides an important starting point in catalyst characterization, one must keep in mind that significant morphological changes may occur under the operational conditions. It is thus vitally important

to be armed with appropriate *in situ* methods to access the composition, structure, and morphology of catalysts under the operational conditions. In this section we describe briefly approaches utilized for the characterization of carbon-based fuel cell electrocatalysts, with an emphasis on *in situ* characterization.

12.5.1 Adsorption Studies

Gas-phase chemisorption studies are useful both for the characterization of carbon support porosity (e.g., low-temperature nitrogen adsorption) and for determination of the surface area of the active component (chemisorption of reactive gases such as H₂ and CO). It is useful to compare specific surface areas and pore volumes of carbon supports before and after metal deposition in order to verify whether the latter influences the support porosity. As shown, for example, by Park et al. [154], this influence may be quite remarkable. To evaluate the effect of the pore size and distribution of carbon supports on the catalyst performance, the authors used activated carbons with different volumes of micropores as supports for Pt–Ru anodes for air-breathed DMFC. Support samples with different porosities were obtained through reactivation with NaOH at different temperatures. The authors determined the sample porosity using low-temperature nitrogen adsorption before and after metal deposition, the weight percentage of the metal being 60 wt% for all the samples employed. The corresponding values are represented in Table 12.3. Unfortunately, for the metal-containing samples, Park et al. [154] did not specify whether the pore area and volume are referred to the mass of the specimen or to the mass of carbon. Nevertheless, the table demonstrates a strong decrease in carbon porosity after metal deposition, especially remarkable for micropores. This may be explained by the blockage of micropores by metal particles noted above. It is noteworthy that the total volume of 60 wt% Pt–Ru particles estimated assuming a metal density of 17 g/cm³ amounts to 0.088 cm³ per gram of carbon. This volume is considerably lower than the volume of

Table 12.3 BET Surface Areas (A_{BET}), and Micropore (V_{mi}) and Mesopore (V_{meso}) Volumes of Virgin and Metal-Supported Activated Carbon Specimens

Sample ^a	A_{BET} (m ² /g)		V_{mi} (cm ³ /g)		V_{meso} (cm ³ /g)		$d_{\text{Pt-Ru}}$ (nm)	
	Virgin	After Metal	Virgin	After Metal	Virgin	After Metal		
PtRu/AC	1313	358	0.537	0.068	0.710	0.248	1.5	
PtRu/AC&973	1720	447	0.634	0.070	0.708	0.251	1.7	
PtRu/AC&1073	2204	699	0.700	0.071	1.254	0.495	2.1	
PtRu/AC&1173	1121	449	0.334	0.020	0.930	0.457	1.8	
PtRu/AC&1273	251	90	0.081	0.006	0.378	0.168	2.1	

Source: Data from ref. 154, with permission from Elsevier.

^aThe activation temperature in kelvin is denoted in the sample abbreviations. AC, activated carbon.

micropores blocked. Metal particles may be stabilized at the pore openings, making them inaccessible for the adsorbates. To a large extent, micropore blockage levels off the difference between the activated carbons, which may explain the marginal difference between the sample performance in the DMFC [154]. The authors explain their finding by assuming that the major part of metal particles is accessible for the electrochemical reaction. This conclusion does not, however, seem to be in agreement with the low current and power densities reported in the article. Rather, the experimental data suggest low metal utilization factors.

12.5.2 Transmission Electron Microscopy

TEM provides important information on both the active component and the carbon support. The primary goal of TEM characterization is to visualize the structure and morphology of specimens and to determine the shape, mean particle size, and particle size distribution of both metal and carbon particles. However, an analytical electron microscope offers additional possibilities by analyzing the x-ray spectrum or energy-loss spectrum of the electrons transmitted. Figure 12.4, showing TEM images of some fuel cell catalysts, illustrates the round particles of Vulcan XC-72 carbon black (a,b), hollow particles of highly activated Sibunit carbon (c), and particular morphology of high-surface-area Ketjenblack (d). A specific surface area of carbon supports exerts a major influence on the

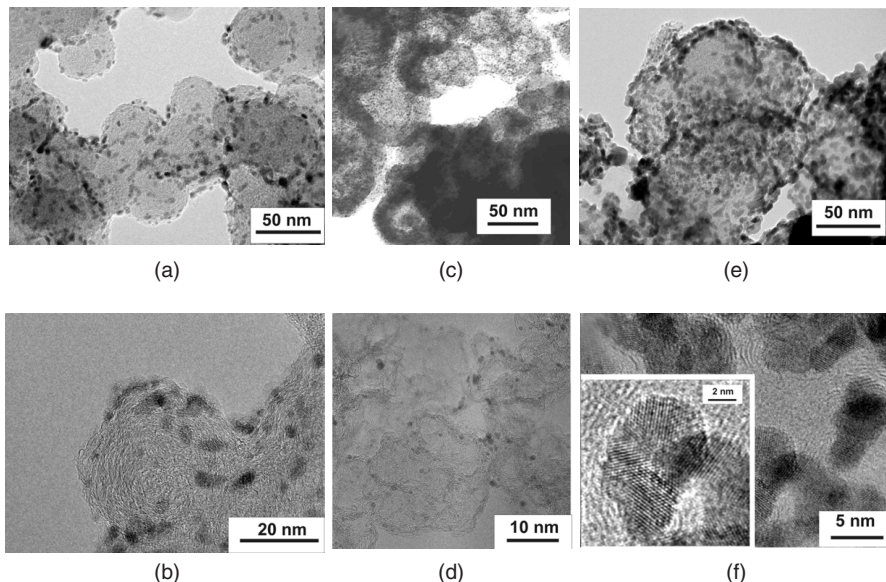


Figure 12.4 TEM images of carbon-supported metal catalysts: (a,b) 20 wt% Ru/Vulcan XC-72; (c) 20 wt% Pt–Ru(1 : 1)/Sibunit ($A_{\text{BET}} = 415 \text{ m}^2/\text{g}$); (d) 70 wt% Pt–Ru(1 : 1)/Ketjenblack; (e,f) 50 wt% Pt–Ru(1 : 1)/Sibunit ($A_{\text{BET}} = 72 \text{ m}^2/\text{g}$). Insert in part (f) shows the Fourier filtered image.

dispersion of metal nanoparticles. It has been widely established that other conditions being equal, an increase in A_{BET} results in more metal particle dispersion and less agglomeration. This explains why high-surface-area carbon supports are often utilized for the preparation of fuel cell catalysts, despite the fact that their pore size distributions may not be advantageous in providing efficient mass transport to the active sites where electrochemical reactions occur. Figure 12.4 illustrates the influence of the morphology and specific surface area of carbon supports and the metal percentage on the dispersion of supported metal particles. Finely dispersed metal particles are observed for 20 wt% Ru supported on Vulcan XC-72 (a,b); 20 wt% Pt–Ru supported on high surface area Sibunit (c), and 70 wt% Pt–Ru supported on Ketjenblack (d). On the contrary, high metal loadings (50 wt% Pt–Ru) on low-surface-area Sibunit carbon ($A_{\text{BET}} = 72 \text{ m}^2/\text{g}$) with a low degree of activation (e,f) result in highly coalesced metal particles. As discussed in Section 12.6.1, this has major and sometimes positive consequences for electrocatalysis.

12.5.3 X-ray Diffraction and X-ray Absorption Spectroscopy

X-ray diffraction analysis is used routinely by every catalyst manufacturer to determine the phase composition of the catalysts produced and the size of coherently scattering domains, and hardly needs a detailed description. An aspect that we would like to emphasize concerns the influence of the environment on the oxidation state of carbon-supported metal nanoparticles. Quite often, authors try to correlate electrochemical performance with the phase composition of as-prepared samples. It has, however, been demonstrated convincingly in a number of publications by both x-ray diffraction [155] and x-ray absorption spectroscopy [156] that as-prepared fuel cell catalysts and samples stored under ambient conditions are often in the form of metal oxides but are reduced under the conditions of PEMFC or DMFC operation. The most dramatic changes are observed for samples with high metal dispersions, while larger particles are affected only marginally [17]. One should keep in mind, however, that the extent of the particle oxidation depends critically on the preparation procedure.

To tackle the problem outlined above and obtain information on the structure and composition of fuel cell catalysts under relevant conditions, a number of authors have proposed *in situ* XRD or XAS cells where samples were (1) subjected to a controlled gas atmosphere (H_2 , CO , etc.) at specified temperatures [17,157–160], (2) characterized in model electrochemical cells filled with liquid electrolytes [160–164], or (3) studied in operating PEMFCs and DMFCs [165–169]. Both XRD [17] and XAS [158] measurements confirm that Pt and Ru oxides are reduced upon heating at 373 to 423 K in a hydrogen atmosphere. On the contrary, Roth et al. [158] have shown that in a CO atmosphere, ruthenium oxides remain relatively stable, their susceptibility to reduction depending on the Pt-to-Ru site distribution. It has been suggested that Pt in contact with Ru acts as a catalyst for the reduction of ruthenium oxides and strengthens the Ru–CO bond, favoring it over Ru–O. Reduction also occurs in electrochemical cells

in the potential region of the underpotentially deposited hydrogen (see below), established either by the electrode polarization [165] or by the interaction with dihydrogen. Methanol exposure also results in the reduction of Pt and Ru oxides, leading to an increase in the catalytic activity of Pt–Ru catalysts in the methanol oxidation reaction. The influence of the electrode potential on the oxidation state of metal catalysts has been monitored by x-ray absorption near-edge spectroscopy XANES (white line intensity) [156,169] and by extended x-ray absorption fine-structure EXAFS spectroscopy (variation in M-O and M-M average coordination numbers) [165].

XAS and XRD are both useful in accessing the particle size ripening resulting from fuel cell operation [170]. Moreover, in the case of highly dispersed metal particles, *in situ* XAS allows monitoring adsorbates on their surfaces. For more information the reader is referred to the review article by Russell and Rose [171] and to the references cited in this section. Except for providing important parameters concerned with the structure, morphology, and composition of metal particles, XAS has also been used to characterize functional groups and heteroatoms in carbon materials [172,173] as well as the interaction of metal particles with the carbon support [160].

The list of spectroscopic methods used in *in situ* characterization of supported metal particles is expanding continuously, new cell designs being proposed to improve the sensitivity and the signal-to-noise ratio and to provide real-time monitoring of fuel cell catalysts.

12.5.4 Electrochemical Methods

Electrochemical methods are widely used to provide relevant information on catalyst structure, composition, and purity. For example, cyclic voltammetry is a simple but very useful technique that is used widely to (1) measure specific surface areas of supported metal nanoparticles; (2) provide information about their surface crystallography, composition, and purity; and (3) characterize the surface functionalities present on the surface of carbon supports. The cyclic voltamogram of Pt particles supported on Sibunit carbon is represented in Figure 12.5. The cyclic voltammogram of Figure 12.5 shows three characteristic potential regions: the hydrogen adsorption–desorption potential (H_{UPD}) region $0.05 < E < 0.35$ V followed by the double-layer region $0.35 < E < 0.75$ V (on the anodic scan), and the oxygen adsorption–desorption region for potentials greater than 0.75 V vs. RHE (reversible hydrogen potential). The features observed in the cyclic voltammogram of Pt catalysts are characteristic of their surface crystallography and their cleanliness. In relation to the first point, strongly bound hydrogen (ca. 0.25 to 0.28 V vs. RHE) is usually attributed to the processes on Pt(111) and Pt(100) facets, while weakly bound hydrogen (ca. 0.13 to 0.15 V vs. RHE) is assigned to Pt(110) sites [174,175]. Poisoning of metal nanoparticles by impurities arising either from the carbon support or from the preparation procedure attenuates the features associated with the hydrogen and oxygen adsorption–desorption and translates into a loss of catalytic activity.

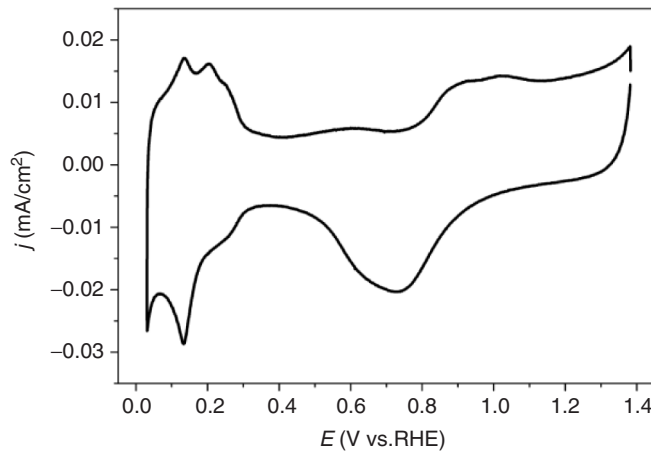


Figure 12.5 Cyclic voltammogram of 7.5 wt% Pt (2.7 nm) supported on Sibunit carbon ($A_{\text{BET}} = 72.3 \text{ m}^2/\text{g}$) at room temperature in 0.1 M H₂SO₄, sweep rate 10 mV/s.

On the other hand, comparison of the electrocatalytic activities of different samples requires determination of the real surface area of metal nanoparticles. This can be achieved by integrating the charge associated with the hydrogen desorption features assuming 210 $\mu\text{C}/\text{cm}^2$ per square centimeter of Pt. Another possibility consists in integrating the charge associated with the electrooxidation of the CO monolayer (CO_{ads} stripping) adsorbed at the electrode surface. CO stripping voltammograms are very useful for the characterization of carbon-supported Pt nanoparticles, since they may be considered as fingerprints of the particle size distribution and make it possible to control the presence or absence of noble metal particle agglomerates [147,176]. Indeed, the position of the CO_{ads} (electro)oxidation peak depends heavily on the mean particle size. It is shifted toward negative potentials when increasing the mean particle up to about 3.5 to 4 nm, where its position is close to that observed for smooth polycrystalline Pt foil [147,176]. Moreover, the presence of Pt agglomerates in Pt/C electrocatalysts brings about an additional peak in a CO_{ads} stripping voltammogram, which is shifted 100 mV negative versus CO oxidation on Pt particles 3.3 nm in size [147,177].

With bimetallic electrocatalysts such as PtRu/C, the hydrogen adsorption–desorption features are strongly attenuated and less resolved compared to those for Pt/C electrodes, making determination of the catalyst surface area by integration of H_{UPD} impossible. On the other hand, Dinh et al. [155] proposed that the position of the CO_{ads} stripping peak may be used as an in situ probe of sample surface composition for unsupported Pt–Ru catalysts in a fuel cell environment. However, Gavrilov et al. [178] and Maillard et al. [179] have demonstrated that along with the composition of Pt–Ru/C catalysts, the position of the CO stripping peak is strongly affected by the metal structure and by the presence of structural defects (see Section 12.6.1).

12.6 INFLUENCE OF CARBON SUPPORTS ON THE CATALYTIC LAYERS IN PEMFCs

The critical components in PEMFCs are the CLs, where the electrochemical reactions take place that transform oxygen molecules into water at the cathode and hydrogen molecules into protons at the anode. Optimization of the CLs is a multiparameter problem, since they must meet numerous requirements simultaneously, ensuring optimum rates of electrocatalytic reactions as well as providing pathways for electrons, protons, reagents, and products. The strongest constraints are imposed on the cathode, where water molecules produced electrochemically must be transferred to the gas phase and removed from the catalytic layer to avoid its flooding. The latter leads to a drastic decrease in cell performance.

Catalytic layers of state-of-the-art PEMFCs usually contain a random mixture of carbon-supported metal particles and proton-conducting polymer (e.g., Nafion). Some manufacturers also add polytetrafluoroethylene (PTFE), to enhance the hydrophobicity of the cathodic CLs and thus avoid flooding. Much effort has been directed to optimization of the structure and composition of the catalytic layers, aimed at increasing the electrochemical efficiency and power density (see the *Handbook of Fuel Cells* [1] and the review articles in refs. 180 and 181). Galvanostatic or (less often) potentiostatic polarization measurements and electrochemical impedance spectroscopy (EIS) are used to provide diagnostic criteria on cell performance (see refs. 182 and 183 and references therein). The advantage of electrochemical impedance spectroscopy is its ability to distinguish, in the frequency domain, individual contributions to cell losses: (1) interfacial charge transfer resistance, (2) ohmic losses, and (3) the mass-transport resistances in the catalyst layer and backing diffusion layer. The electrochemically active surface area (EASA) can be estimated either from the double-layer capacitance value or, more reliably, from the hydrogen desorption charge using cyclic voltammetry (see Section 12.5).

Carbon supports strongly affect fuel cell performance. They may influence the intrinsic catalytic activity and catalyst utilization, but also affect mass transport and ohmic losses. This makes analyses of the role of carbon materials rather complicated. Although numerous studies have been devoted to the carbon support improvement, only a few have attempted to establish relationships between the substructural characteristics of carbon support materials and cell performance. The influence of carbon supports on the intrinsic catalytic activity is the subject of Section 12.6.1. In Section 12.6.2 we consider the influence of support on macrokinetic parameters such as the catalyst utilization, mass transport, and ohmic losses. In Section 12.6.3 we review briefly recent data obtained upon utilization of novel carbon materials as supports for fuel cell electrocatalysts.

12.6.1 Intrinsic Catalytic Activity

Dependence of the intrinsic catalytic activity of metal nanoparticles on the support material may have various origins. First, the support structure and morphology

may influence metal dispersion and nanostructure. Second, the catalytic activity may be affected by metal–support interactions, and finally, but not least important, impurities present in technical carbons may poison metal particles, decreasing their activity.

Metal Dispersion Specific surface area, pore size distribution and surface properties strongly influence the structure and morphology of the active component: that is, metal particle size, size distribution, nanostructure, alloying degree, and so on (see Figure 12.4). Meanwhile, fuel cell reactions are known to be size sensitive. “Negative” particle size effects, with the specific catalytic activity per unit metal surface area decreasing with decreases in particle size, have been observed for Pt/C in the oxygen reduction reaction [8,184–187] and in methanol [188–190] and carbon monoxide [147,176,191,192] oxidation. “Positive” particle size effects, with the specific activity increasing with reductions in particle size, have been reported for the hydrogen [193] and formic acid [189,194] oxidation reactions. Particle size effects have also been reported for bimetallic Pt–Ru particles [195]. In fact, a significant portion of the published results concerned with the influence of carbon on the electrochemical performance of supported fuel cell catalysts may be explained by invoking the influence of particle size and structure on the intrinsic catalytic activity stipulated by the support. To level off the negative particle size effect for the oxygen reduction and methanol oxidation reaction, manufacturers nowadays produce fuel cell electrocatalysts with about 3-nm particles. Other conditions being equal, at this particle size the mass activities of Pt/C in the oxygen reduction reaction, and Pt/C and Pt–Ru/C in the methanol oxidation reaction, reach maximum values.

High metal contents in fuel cell electrocatalysts favor metal coalescence, which is most significant for carbon supports with low surface areas. In the literature, the negative consequences of particle size coalescence are usually highlighted: namely, those concerned with a decrease in the specific surface area. We would like to stress, however, that for some catalytic and electrocatalytic reactions, particle coalescence may bring about major positive consequences. Particle coalescence results in the formation of nanocrystalline (or nanostructured) materials composed of nanometer-sized crystallites interconnected via grain boundaries. Such metal structures have been recognized for their specific properties, differentiating them from single crystals, coarse-grained materials, or nanometer-sized supported single-grained particles [196]. Gavrilov et al. [178] have demonstrated that nanocrystalline Pt–Ru/C catalysts formed on low (ca. 70 m²/g)-surface-area carbon support of the Sibunit family at high metal-on-carbon loadings [Figure 12.4(e,f)] show highly enhanced specific catalytic activities in the methanol and in the CO monolayer oxidation reactions, which increase with the degree of particle coalescence (Figure 12.6). Similar observations were made by Maillard et al. for Pt/C [147] and Pt–Ru/C [179]. Using high-resolution transmission electron microscopy, x-ray diffraction, or energy-dispersive x-ray analysis as the ex situ characterization tools, and cyclic voltammetry as an in situ tool, Gavrilov et al. [178] have proven that this activity

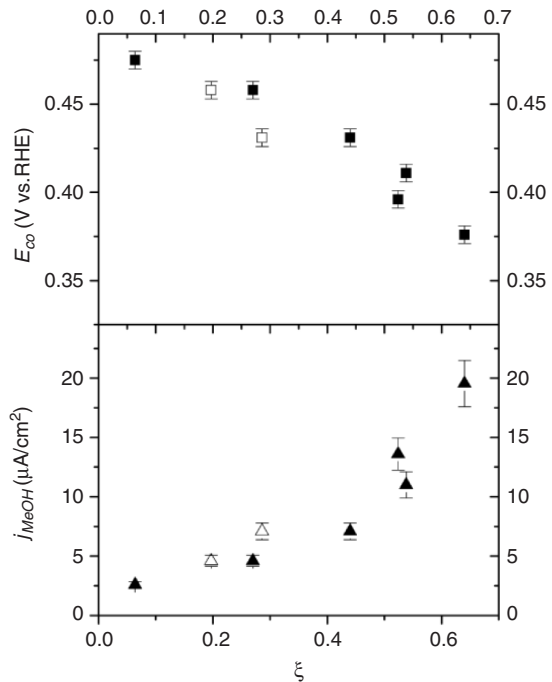


Figure 12.6 Influence of the metal coalescence factor $\xi = 1 - A_{\text{chem}}/A_{\text{calc}}$ in PtRu/Sibunit catalysts on the CO stripping peak (top) and the specific current for 0.1 M methanol oxidation at 0.4 V after 1800 seconds (bottom). A_{chem} is the specific surface area of Pt–Ru particles determined with CO chemisorption, and A_{calc} is the specific surface area calculated either from the results of XRD (filled symbols) or from TEM (open symbols). The measurements were performed in 0.1 M H_2SO_4 at 323 K, BET surface area of Sibunit carbon $72 \text{ m}^2/\text{g}$. (From ref. 178, with permission from the Royal Society of Chemistry.)

enhancement is indeed related to the structural rather than compositional changes in Pt–Ru/C catalysts. It has been proposed that active sites in nanostructured metal particles are located at the emergence of grain boundaries at the surface. Multigrained faulted structures with long-lived defects (grain boundaries and dislocations) have been proposed as a promising approach for preparing highly active catalysts for practical applications (e.g., at the anodes of DMFCs) [178].

Metal–Support Interaction Although in a number of publications metal–support interactions have been invoked to explain the differences in electrocatalytic activities of metal nanoparticles grown on various carbon materials, the evidence is usually vague. What, in fact, is usually observed is the strong interaction of some surface functionalities or fragments with the catalyst precursors, affecting the dispersion of the resulting catalysts, with the consequences described above.

Recently, Wang et al. [197] performed density functional (dft) calculations of free Pt₅₅ and Ru₅₅ and graphite-supported Pt₃₇ and Pt₆Ru₃₁ clusters. The adsorption energies were calculated for monometallic Pt and bimetallic Pt–Ru clusters to a graphite surface. Ru binds much more strongly to the graphite surface, with the adsorption energy for the mixed cluster 5.7 eV higher than that for Pt. Interaction of metal clusters with graphite surface induces buckling for both graphene sheets and metal layers, but relaxes toward the surface of truncated cuboctahedral clusters. The adsorption distance for the Pt₃₇ cluster supported on the graphite surface is 2.34 Å, while for Pt₆Ru₃₁ it is shorter, 2.10 Å, due to stronger Ru–carbon interaction. The interaction with support has been shown to strongly influence bond disorder in the adsorbed clusters. According to the dft calculations of Okamoto [198], introduction of a carbon vacancy affects the adsorption energy of Pt₁₃ and Au₁₃ on graphene sheets. According to Ocamoto [198], CO and H chemisorption energies become smaller on the metal clusters adsorbed on graphene than on clusters without carbon support.

Some authors have suggested that oxygen-containing groups on the carbon surface may influence the intrinsic catalytic activity of supported metal particles. Thus, Shukla et al. [199] supported Pt on Ketjenblack (BET surface area 900 m²/g) using different preparation procedures, resulting in a variation in the concentration of acid–base functional groups on the carbon surface. Ex situ XPS analysis of Pt/C samples revealed that the degree of Pt oxidation increased with the concentration of surface functional groups. The authors established higher electrocatalytic activities for the electrodes with low concentrations of surface functional groups (pHZPC values between 6 and 7). The phenomenon observed was attributed to metal–support interactions through carbon functional groups. This interpretation is not unambiguous, however, since the particle size of the catalysts studied varied in the wide range 3.7 to 17.8 nm. The large discrepancy between Pt surface areas estimated from XRD and from voltammetry also raises doubts. The influence of heteroatoms on the catalytic activity has been addressed, for example, by Roy et al. [200], who reported on the enhanced electrocatalytic activities of Pt nanoparticles supported on nitrogen functionalized carbons toward the methanol oxidation and oxygen reduction reactions.

Influence of Impurities Technical carbon materials may comprise significant amounts of impurities, particularly sulfur. The effect of poisoning of Vulcan support by sulfur was addressed by Swider and Rolison [201,202]. The authors reported that Pt nanoparticles were fully poisoned by sulfur in the Vulcan support when heated in dry atmosphere up to 528 K [202]. Since Pt catalyzes the oxidation of sulfur to sulfate upon heating in the presence of water, such treatment has been recommended for increasing the electrochemically accessible surface area of PEMFC electrocatalysts [202]. Roy et al. [200,203] also reported on the decrease in catalytic activity in the methanol oxidation reaction through sulfur poisoning. However, according to Roy et al., the presence of sulfur may lead to enhanced catalytic activity in the oxygen reduction reaction. These differences may be

explained by the different oxidation states of sulfur in the potential interval of anode and cathode operation.

12.6.2 Macrokinetic Parameters

Catalytic layer performance involves several transport processes that should be balanced in an optimized electrode: the ionic conductivity, the electronic conductivity, and the reactant diffusion. Because fuel cell electrodes are multiphase structures, increasing the transport facility of one process by increasing its phase volume usually decreases the transport facility of the other processes. Optimization involves searching for the correct ratio of materials in the composite layer [204]. The modeling analysis shows that the largest loss in a CL is the proton resistance in the active layer. Diffusion into the agglomerates is the largest diffusion loss in the cell. The electron resistance of CLs is usually not considered, assuming that ohmic losses in the proton conductor exceed greatly those in the electron conducting carbon-supported catalyst. This assumption is based on the comparison of typical conductivity values of carbon materials and Nafion. For a survey of proton conductivities of Nafion membranes, the reader is referred to the paper by Slade et al. [205]. For example, for Nafion 117 membrane immersed in liquid water at 363 K, the proton conductivity amounts to 0.19 S/cm. The conductivity decreases if the membrane is in contact with water vapor and in particular at low relative humidity, when proton migration may become a limiting factor. The assumption on the negligible losses due to the electron resistance may not be valid for poorly ordered carbon materials, which electron conductivity may drop significantly below the corresponding value of highly oriented graphite.

The influence of the metal loading (and thus the catalytic layer thickness) on cell performance has been studied in a number of publications. It has been demonstrated that the current increases with the increased platinum loading up to a point where either mass or proton transfer become limiting (see, e.g., refs. [204,206], and 207). Thus, an increase in CL layer thickness does not translate to an increase in the cell power density, due to the decrease in catalyst utilization at high thicknesses. This drop is particularly strong at high currents. Thus, much effort has been directed to producing thinner catalytic layers. To achieve high power densities while keeping the CL thin, high metal loadings per geometric surface area of MEA are usually employed. If the oxygen diffusion is limited, the active region of the CL may be confined to a narrow region close to the GDL. If the proton conductivity is the limiting factor, the active part of the CL may be confined to a narrow region near the membrane side associated with a higher effective overpotential [208].

Several studies have concentrated on the influence on cell performance of the Nafion content [209,210]. Both experiments [209–211] as well as modeling [207,212] suggest that increasing the Nafion content decreases ohmic losses by improving proton conductivity. The electronic resistance does not increase significantly even at high Nafion loadings, while mass transport losses increase strongly, which may be explained by decreased gas diffusivity in the Nafion film [210,211].

The highest electronic resistances were observed at low Nafion loadings, indicating that the ionomer played a significant role as a binder [211]. Meanwhile, kinetic losses pass through a minimum correlated with the electrochemically active surface area of the catalyst estimated from cyclic voltammograms [209]: The higher the electrochemically active surface area, the lower the kinetic losses. This volcano type of curve reflects the optimum in the metal utilization factor u . Below, we try to understand how carbon properties may influence these characteristics.

Utilization Factor It was formerly widely accepted that only surface sites located at the three-phase boundary (i.e., at the interface between metal catalysts, proton-conducting electrolyte, and gas-filled pores) are electrochemically active. Farhat [213] considered a statistical model of a catalytic layer, consisting of the catalyst and electrolyte particles and gas voids, and estimated a maximum catalyst utilization factor of 22%. More advanced models were proposed by Eikerling and Kornyshev [206,207]. For a low percolation threshold of 0.1, they predicted a maximum catalyst utilization of about 65%. Recently, however, Debe [214] at 3M suggested ultrathin (ca. 200 nm) CLs based on vertically aligned nanostructured organic whiskers, covered with a continuous layer of Pt, which do not contain proton-conducting polymer but nevertheless show close to 100% utilization of Pt surface atoms. Proton conduction in these layers occurs in water-filled voids. Wang et al. [215] performed a modeling study which confirmed that efficient proton penetration could indeed occur at distances below about 100 nm. This suggests that metal particles that are not in direct contact with the proton-conducting ionomer also participate in electrochemical reactions. An important question is how to determine the catalyst utilization factor experimentally. A simple, yet instructive way is to compare the electrochemically active surface area (EASA) measured from H_{UPD} charge in the MEA in the presence of solid polymer electrolyte (EASA_{MEA}) with the EASA of the same catalyst but immersed in liquid electrolyte (EASA_{LE}) (e.g., H₂SO₄ or HClO₄):

$$u = 100\% \times \frac{\text{EASA}_{\text{MEA}}}{\text{EASA}_{\text{LE}}} \quad (12.7)$$

According to Gasteiger et al. [4], u may be close to 100% for the catalytic layers of optimized structure and composition. An interesting observation has been made by Paulus et al. [216], who performed comparative studies on supported Pt/C and unsupported Pt black commercial electrodes, as well as on model microstructured Pt electrodes supported on glassy carbon with defined geometry. The samples were brought into contact with a polymer electrolyte membrane (PEM) but were not impregnated with ionomer solution, thus ensuring that only a part of the Pt was in contact with the PEM. The authors were able to show that for Pt black as well as for Pt/GC samples, comprising contiguous Pt film, up to 90% Pt utilization factors may be obtained even if the significant part of the metal is not in direct contact with the PEM. It should be noted, however, that u depends on the sweep rate, suggesting that some slow processes associated with proton

transport in thin water film are involved. To the contrary, for Pt/C electrodes, only particles in direct contact contributed to the cyclic voltammograms, resulting in rather low utilization factors. Thus, proton conduction is believed to occur in a network of hydrogen-bonded water molecules adsorbed on a Pt surface.

It should be noted that high utilization factors measured with cyclic voltammetry by no means warrant the assumption that under dynamic conditions of fuel cell operation the CLs deliver the same current as they would without mass transport and ohmic constraints. To account for the latter, Gloaguen et al. [185] employed the effectiveness factor: the ratio of the actual reaction rate to the rate expected in the absence of mass and ionic transport limitations. The effectiveness factor is a function of the total catalyst area, the exchange current density, the overpotential, the diffusion coefficient D , the concentration of electroactive species C_0 , the thickness of the CL, and the proton conductivity of the electrolyte, and drops sharply below 100% with increased exchange current density and decreased the product DC_0 .

The discussion above suggests that Nafion distribution in the CLs may have a significant influence on cell performance. The latter must depend on the carbon support porosity and surface properties. Watanabe et al. [217] suggested designating as primary, mesopores between the primary particles within carbon agglomerates, with larger meso- and macropores between carbon agglomerates designated as secondary. Uchida et al. [39] studied the distribution of proton-conducting ionomer in the pores of carbon supports. Based on the mercury porosimetry study of MEAs prepared from an experimental high-surface-area acetylene black ($835 \text{ m}^2/\text{g}$) and various amounts of Flemion perfluorosulfonated ionomer dispersed in butyl acetate, they concluded that ionomer molecules occupied 0.04- to $1.00\text{-}\mu\text{m}$ secondary pores and did not penetrate 0.02- to $0.04\text{-}\mu\text{m}$ primary pores. The authors suggested that about 40-nm colloidal particles of Flemion (the particle size distribution of Flemion in butyl acetate was determined with an Ar laser) could not penetrate pores with diameter below 40 nm. Therefore, metal nanoparticles residing in carbon pores below 40 nm in diameter have no access to ionomer and thus do not contribute to the electrochemical activity [39,218]. The authors observed a decrease in the internal resistance of the electrode, which translated into improved PEMFC performance, with an increase in the specific volume of the pores larger than 40 nm in diameter, and a decrease in the specific volume of pores below 8 nm, which, as they assumed, did not contain perfluorosulfonated ionomer.

Concepts on the structural organization of CLs formulated by Uchida [39,218] dominated fuel cell-related publications for a number of years, and schematic representations of CLs always showed carbon agglomerates wrapped in a thick Nafion layer residing in macropores. This view may not be exactly correct, however. Indeed, according to an investigation by Xie et al. [219], ionomer molecules do penetrate mesopores in carbon materials. Using mercury porosimetry, they observed a continuous decrease in the volume of primary pores (which they identified as pores less than about 17 nm in diameter) within agglomerates of Vulcan XC-72-supported catalysts with increased Nafion content. Cherstiouk

et al. [220] utilized low-temperature N₂ adsorption and discovered that if the catalyst ink is prepared in an isopropanol–water mixture, at low Nafion contents Nafion molecules preferentially occupy the volume of micropores, but at higher contents, also fill mesopores. The results of this work suggest that the interaction of Nafion ionomer with carbon materials, being of crucial importance for the development of efficient catalytic layers for PEMFCs, is not yet fully understood and deserves further investigation.

As suggested by Uchida et al., solvents used for ink preparation strongly affect the state of ionomer molecules, and may thus influence their distribution in CLs [39,221]. Depending on the dielectric constant ϵ of the solvent, perfluorosulfonate molecules form either a solution (at $\epsilon > 10$), reversed micelles ($3 < \epsilon < 10$), or a precipitate ($\epsilon < 3$). The influence on cell performance of the dielectric constant of the solvent used for ink preparation was confirmed by Fernandez et al. [222].

Another reason, which affects the utilization factor, is the structure of the carbon particles themselves. Rao et al. [17] have demonstrated that the catalyst utilization factor may vary significantly depending on the porosity of carbon materials. They have prepared a series of Pt–Ru (1 : 1) catalysts supported on carbon materials from the Sibunit family with grossly different BET surface areas, ranging from 20 to 400 m²/g, which were utilized as the anode catalysts in liquid-fed DMFC. To be able to distinguish between the influence on cell performance of the metal dispersion and the carbon support porosity, the metal dispersion was kept constant and close to 0.3. It was demonstrated that the catalyst utilization factor reached 100% for low-surface-area supports but dropped down to 10% for the high-surface-area Sibunit carbon. As a result, in methanol electrooxidation, both the mass activity ($A_{\text{g}_{\text{Pt}-\text{Ru}}^{-1}}$) and specific activity ($A_{\text{m}_{\text{Pt}-\text{Ru}}^{-2}}$) increased with a decrease in carbon specific surface area [17]. Comparison of the low-surface-area (20- to 70-m²/g) Sibunit carbons to Vulcan XC-72 demonstrated about three-fold activity enhancement. The observed superiority of mesoporous carbons of Sibunit family was ascribed to the lack of Nafion penetration in pores smaller than 20 nm.

It is worth noting that the remarkable effect described for the carbon support porosity on the metal utilization factor and hence on the specific electrocatalytic activity in methanol electrooxidation was only observed when the catalysts were incorporated in MEAs and measured in a single cell. The measurements performed for thin catalytic layers in a conventional electrochemical cell with liquid electrolyte provided similar specific catalytic activities for Pt–Ru/C samples with similar metal dispersions but different BET surface areas of carbon supports [223]. The conclusions drawn from measurements performed in liquid electrolytes are thus not always directly transferable to PEM fuel cells, where catalytic particles are in contact with a solid electrolyte. Discrepancies between the measurements performed with liquid and solid electrolytes may arise from (1) different utilization factors (higher utilization factors are usually expected in the former case), (2) different solubilities and diffusion coefficients, and (3) different electrode structures. Thus, to access the influence of carbon support porosity

on macrokinetic parameters and on catalyst performance under PEMFC relevant conditions, measurements must be performed with solid rather than liquid electrolytes, with the catalysts incorporated within MEAs.

Mass-Transport Losses The influence of carbon porosity on mass-transport losses has been invoked by Antoine [224] to explain the decrease in current densities for the oxygen reduction reaction with increases in the specific surface areas of carbon supports. The authors supported Pt nanoparticles on carbons with BET surface areas ranging from 254 (Vulcan) to 929 m²/g (Ketjenblack), 1000 m²/g (Printex Xe2), and 1475 m²/g (Black Pearls). Pt nanoparticles were prepared by radiolytic deposition (reduction of Pt metal precursor by radical species produced by radiolysis) and had the same mean particle size regardless of the support. Recently, Marie et al. [225] used Pt nanoparticles supported onto carbon aerogels with high pore volumes and surface areas, differentiated by their pore size distributions. The metal weight percentage and metal dispersion were kept identical. The authors claimed that carbon aerogels with smaller pores provided more porous catalytic layers because of the lower Nafion penetration into the pores. As a consequence, the O₂ mass-transport losses were minimized, and higher PEMFC performances were observed at high current densities [226]. An opposite result was obtained in half-cell configuration, for which the catalytic layers were partially flooded by liquid electrolyte, thus lowering the oxygen diffusion rate [227].

Kaiser et al. [18] compared Pt catalysts prepared on the basis of carbon supports from the Sibunit family with various degrees of activation, and BET surface areas ranging from 22 to 415 m²/g with the conventional 20 wt% Pt catalyst supported on Vulcan XC-72. Full cell tests revealed the strong influence of the type of carbon support on both the total and the mass-related currents (Figure 12.7). The highest mass specific currents at 0.85 V are achieved for 30 wt% Pt/Sibunit 20P and 40 wt% Pt/Sibunit 619P with BET surface areas of carbon supports of 292 and 415 m²/g, correspondingly. These exceed the activities of Vulcan XC-72-supported 20 wt% Pt catalyst by a factor of 4 in the oxygen and 6 in the air feed. The increased mass specific activities cannot be ascribed to the influence of the carbon support on the metal dispersion, which was purposely kept constant and equal to about 0.3. Analysis of the I–U curves revealed that the improved cell performance was related to the improved mass transport in the cathode layers. The mass transport overvoltages were found to be strongly dependent on the specific surface area and on the texture of the support. This work proves that utilization of novel carbon materials may lead to major improvements in PEMFC performance and allow preparation of the catalytic layers with significantly lower noble metal contents compared to conventional materials.

Water Management A problem that must not be forgotten, although it is not discussed here in detail, is water management in the CLs. This issue is, in fact,

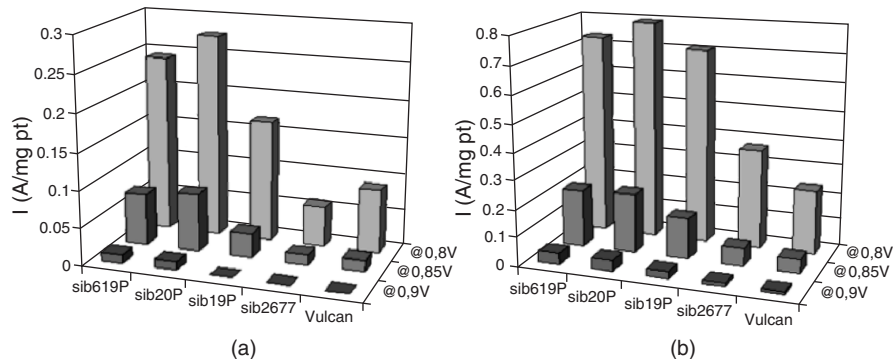


Figure 12.7 Comparison of mass-specific, IR-corrected activities for Pt cathode catalysts prepared on the basis of various carbon materials at different cell voltages for air (a) and oxygen (b) fed PEMFC. $T_{\text{cell}} = 333$ K, anode: H_2 feed, $\text{Pt/C}, 0.4 \text{ mg}_{\text{Pt}}/\text{cm}^2$, dew point 333 K; cathode: $\text{Pt/C}, 0.6 \text{ mg}_{\text{C}}/\text{cm}^2$, dew point 328 K, ambient pressure on both sides. Abbreviated Sibunit sample designations contain the experimental batch numbers. BET surface areas of carbon supports amount to 415, 292, 72.3, 21.9, and 210 for Sib619, Sib20P, Sib19P, Sib2677, and Vulcan, respectively. (From ref. 18, with permission from Springer.)

of primary importance for the efficient performance of a PEMFC. At the cathode side, a danger of flooding exists due both to the production of water but also to the electroosmotic drag of water molecules from the anode side accompanying proton transport. As a consequence of flooding, the mass transport of oxygen molecules is hindered drastically. On the contrary, on the anode side, there is a danger of the electrode overdrying, which may result in the poor proton transport and in a decrease in catalyst utilization. Under equilibrium conditions, filling of (cylindrical) pores with a liquid is governed by the Young–Laplace equation:

$$p^g - p^l = \frac{2\gamma \cos \theta}{r} \quad (12.8)$$

where p^g and p^l stand for the pressure in the gas and liquid phases, respectively, r is the pore radius, γ is the surface tension of liquid water, and θ is the contact angle. From equation (12.8) it is clear that the pore structure and wetting properties must have a dramatic influence on the water balance in the catalytic layers. Unfortunately, in the published literature the water balance is considered primarily for the gas diffusion layers and flow fields, rather than for the catalytic layers. Eikerling [228] has proposed a novel model that links the spatial distributions of processes with water-handling capabilities and current–voltage performance in the CL. The model explicitly considers the porous structure and wetting properties of carbon-supported catalysts. We hope that more interest will be shown by both theoreticians and experimentalists in the important issue of water management in CLs.

12.6.3 Novel Carbon Materials as Supports for Fuel Cell Electrocatalysts

In Sections 12.6.1 and 12.6.2 we have shown that other conditions being equal, variations in carbon support material results in drastic changes in cell performance. Thus, significant effort has recently been put into the design and testing of novel carbon supports as well as into the development of novel strategies for CL preparation. Studies performed by Rao et al. [17] and Kaiser et al. [18] have shown that utilization of mesoporous carbons of the Sibunit family with tunable pore size allows us to augment catalyst utilization significantly [17] and decrease the mass transport losses [18]. It is also important to note that ranking of carbon supports is very different for the anode of a DMFC and the cathode of a PEMFC.

Ordered mesoporous carbons with tunable pore size were recently used as supports for PEMFC and DMFCs. For example, Chai et al. [26] tested these as supports for a Pt–Ru (1 : 1 at%) alloy catalyst to study their effect on the anodic performance of the catalyst in a DMFC. Use of the ordered uniform porous carbons resulted in much improved catalytic activity for methanol oxidation. Among the porous carbons studied in this work, one with a pore diameter of about 25 nm showed the highest performance. The authors attributed the better activity of the ordered mesoporous carbon-supported catalysts to “their high surface areas, large pore volumes, and three-dimensionally interconnected uniform pore structures, which allow a higher degree of dispersion of the catalysts and efficient diffusion of reagents.” It should be noted, however, that neither the catalyst utilization factors, nor the mass transport and ohmic losses were analyzed, which renders the foregoing conclusion unjustified. Superior electrocatalytic activities of the ordered mesoporous carbon-supported anode and cathode catalysts compared to Vulcan XC-supported commercial catalysts have been reported by other authors (see ref. [25] and references therein). On the contrary, Wikander et al. [229] compared Pt particles supported on Vulcan XC-72 and on ordered mesoporous carbon with a BET surface area of 1380 m²/g and total pore volume of 1.6 cm³/g (average pore diameter around 3.5 nm). The latter showed higher ohmic losses and poorer performance at the cathode of a PEMFC.

Recently, utilization of CNFs and CNTs in the CLs of PEMFCs and DMFCs has become an active research area. Numerous studies have focused on the stabilization of Pt and PtRu particles on the surface of CNTs and CNFs (see the review articles [153 and 230] and references therein). Adhesion of Pt to the basal plane of graphite is weak; thus various approaches have been proposed to activate CNTs, including oxidation, grafting with various functional groups [153], and “wrapping” with a polymer [231], in order to stabilize highly dispersed Pt on their surfaces. Pt and Pt–Ru particles supported on CNTs and CNFs were tested in the oxygen reduction reaction and in the methanol oxidation reaction.

In numerous publications, authors claim higher activity of CNF- and CNT-supported catalysts for fuel cell applications, which they attribute to (1) higher electron conductivity, (2) higher particle dispersion, (3) facilitated mass transport, and (4) improved water management. Unfortunately, the conclusions on the origin of the catalytic activity enhancement often lack experimental

grounds. Due to obvious space constraints, only some representative publications concerned with the fuel cell applications of CNFs and CNTs are analyzed in this chapter.

Methanol oxidation on CNF- and CNT-supported Pt–Ru particles in liquid electrolytes has been studied using cyclic voltammetry, chronoamperometry [13,231–237], and electrochemical impedance spectroscopy [236]. Rotating disk electrode and linear potential sweep voltammetry in liquid electrolytes were used to study the oxygen reduction reaction on Pt supported on CNTs and CNFs (see, e.g., refs. [231 and 238]). The samples were compared to commercial E-Tek catalysts, and in some publications up to four fold mass activity enhancements [13] were observed. As noted above, when catalysts are tested in liquid electrolytes using a thin-film approach,* the current is usually determined by the electrochemical kinetics and experiences little, if any, effect of the mass transport and ohmic limitations that come into play in MEAs of fuel cells. Thus, the differences between the catalytic activities of Pt and Pt–Ru catalysts supported on conventional carbon supports, on the one hand, and on CNTs and CNFs, on the other, are likely to originate from different metal dispersion and/or nanostructure. It is interesting to note that as one can deduce from TEM images [13], Pt catalyst supported on platelet CNFs, which showed about fourfold higher activity in methanol oxidation compared to that of 25 wt% Pt/Vulcan-XC-72, contained metal particles with a high degree of coalescence, which were suggested to be very active in CO and methanol electrooxidation [147,177–179] although this fact was not discussed by the authors.

It is more informative to compare the activities of CNT- and CNF-supported catalysts incorporated in MEAs and tested in PEMFCs [239] or DMFCs [234,235,240]. For example, Chien and Jeng [234] tested Pt–Ru supported on multiwalled CNT in a DMFC and reported about 35 to 39% higher power densities than for Pt–Ru supported on conventional carbon supports. Yoo et al. [241] studied the support effect of CNTs on the performance of CO-tolerant electrocatalysts for PEFC using CNTs with and without defect-generating pretreatments, carbon black, and fishbone-type CNTs. PtRu supported on defect-free CNTs revealed very high CO tolerance during $H_2 + 100$ ppm CO oxidation in a half-cell. The catalytic activity was maintained under the 100-ppm CO level with good reproducibility. On the other hand, the hydrogen oxidation current on Pt–Ru supported on defective CNTs, Pt–Ru/fishbone-type CNTs and Pt–Ru/Vulcan XC-72 decreased largely with increasing CO concentration up to 100 ppm. This is a very interesting result. It would be helpful to clarify whether the CO tolerance is indeed determined by the properties of carbon materials (as suggested by the authors), or by the particle size and nanostructure of Pt–Ru particles, which depend on the defect density of carbon supports. Unfortunately, the authors did not analyze whether the structure of Pt particles was influenced by the support material. On the other hand, the improvements in catalyst utilization and mass transport in the CLs are the likely reasons for the tenfold

*About 1 μm catalyst film is deposited on a solid support by drop-casting.

enhancement in the current of the methanol oxidation observed upon the addition of less than 2 wt% of single-walled CNTs to catalytic layers consisting of carbon black-supported Pt catalyst [242]. Further systematic studies will be needed to understand the influence of the structural and textural characteristics of CNTs and CNFs on the performance of the fuel cell catalysts. It is desirable to keep the metal dispersion unchanged in order to understand whether mass transport and ohmic losses are influenced by the characteristics of CNTs and CNFs.

Novel approaches to the design of catalytic layers are being pursued in a number of research centers worldwide. The group of Dodelet [243,244] has introduced a very interesting approach to growing carbon nanotubes on fuel cell backings. The nanotubes were obtained at 1073 K by ohmic heating of a carbon paper support [243]. The multiwalled CNTs are typically up to 20 μm in length and between 30 and 50 nm in diameter. This approach leads to perfect connectivity between the CLs and the GDLs. However, in order to improve catalyst utilization and decrease mass transport and ohmic losses, it would be desirable to obtain three-dimensional ordered catalytic layers.

Approaches to the production of structurally ordered catalytic layers have recently been described in the literature. Caillard et al. [245] reported on improved platinum utilization by creating an open support structure based on aligned CNFs attached to a carbon-loaded cloth gas diffusion layer. The nickel catalyst used to initiate CNF growth, the CNFs themselves, and the 5-nm Pt nanoaggregates were deposited sequentially in the same low-pressure plasma reactor. This oriented catalyst structure was incorporated into a MEA and tested with and without CNFs and on carbon paper or GDL. The performance of fuel cells based on CNFs and a GDL was better over the entire range of operating current. Sun et al. [103] described the structure and electrochemical properties of arrayed nitrogen-containing CNT composites grown directly on Si substrates. The CNT arrays were grown by microwave-plasma-enhanced chemical vapor deposition first and then acted as the template and support for Pt dispersion in the following sputtering process. AuBuchon et al. [246] reported synthesis of a novel multi-branched CNT structure by dc plasma-enhanced chemical vapor deposition. The structure consists of aligned CNTs that have branches of smaller diameter growing aligned along a direction perpendicular to the original CNT. It is shown that the branching induced a large increase in the surface area and total nanotube length and can be beneficial in supporting very fine Pt nanoparticles for fuel cell and other catalytic applications.

12.7 CORROSION AND STABILITY OF CARBON-SUPPORTED CATALYSTS

12.7.1 Influence of Microstructure on the Corrosion of Carbon Materials

Carbon is thermodynamically unstable at operating conditions of a PEMFC cathode because the equilibrium potential of its electrooxidation to carbon dioxide is $E_{\text{C}/\text{CO}_2}^0 = 0.207$ V versus RHE at 298 K [8,247]. In 1970s–1980s, corrosion

of various carbon materials was studied extensively in hot (up to 483 K) concentrated phosphoric acid in relation to the development of phosphoric acid fuel cells (PAFCs). An outstanding review of the relevant publications is provided in Kinoshita's treatise [8]. In the last decade, when the interest in PEMFCs arose, studies on carbon corrosion in sulfuric acid were initiated.

The corrosion current in 85 to 99% H₃PO₄ decays with time and obeys the following dependence [248,249]:

$$i(t) = kt^{-n} \quad (12.9)$$

Both the constant k and the exponent n depend on the time and on the type of carbon material [249,250]. Usually, n is close to 0.5. However, physical understanding of the phenomenological equation (12.9) is still missing. Other conditions being equal, the corrosion current normalized to the unit mass of carbon material increases with increasing electrode potential, temperature [251], and water concentration [252]. Specific corrosion rates depend on the nanotexture and are considerably lower for the basal plane than for heterogeneous surfaces with a significant contribution from the edge planes. It is well known from catalysis that the chemical reactivity of carbon blacks is a function of surface microstructure and crystallinity [8]. The susceptibility of carbon materials to corrosion increases with increasing A_{BET} [249,253] and d_{002} [250,253,254]. It should be noted, however, that A_{BET} and d_{002} are not independent since they both increase with a decrease in the size of graphitelike crystals.

Electrochemical degradation of carbon materials is slowed significantly by carbon graphitization. Thus, the rate of electrochemical corrosion (A/g) of Vulcan XC-72, graphitized at 2973 K, decreased by a factor of 10 compared to pristine material, while its BET surface area decreased only by a factor of 3 [251]. In both a PAFC and a PEMFC environment, graphitized carbons are also reported to have lower oxidation rates than nongraphitized carbons [8,248,255,256]. This is explained by considering that electrochemical corrosion takes place at the edge planes of graphite, whereas the basal planes are relatively inert. Therefore, a pronounced difference exists between the corrosion rates of materials such as Pt/CNTs; which are rolls-up of graphene sheets and present long-range order, and Pt supported on the carbon blacks; which have turbostratic structure and are composed of a mixture of graphite crystallites and amorphous carbon [257–259].

Simonov et al. [260] attempted to find common ground in the literature data and suggested a correlation dependence of the corrosion rate on substructural characteristics of carbon materials determined from x-ray analysis. This is represented in Figure 12.8, which shows that specific corrosion rate increases with the substructural parameter, defined as $(I_{002}/I_{10}) \times d_{002}/L_c$ (these are defined in Section 12.2). This empirical parameter approaches zero for highly ordered carbon materials, since I_{002} , I_{10} , and d_{002} are constant and L_c is large but increases for amorphous carbons.

According to Figure 12.8, we expect that carbon materials with $L_c \geq 3$ nm will possess higher corrosion resistance than that of conventional carbon materials

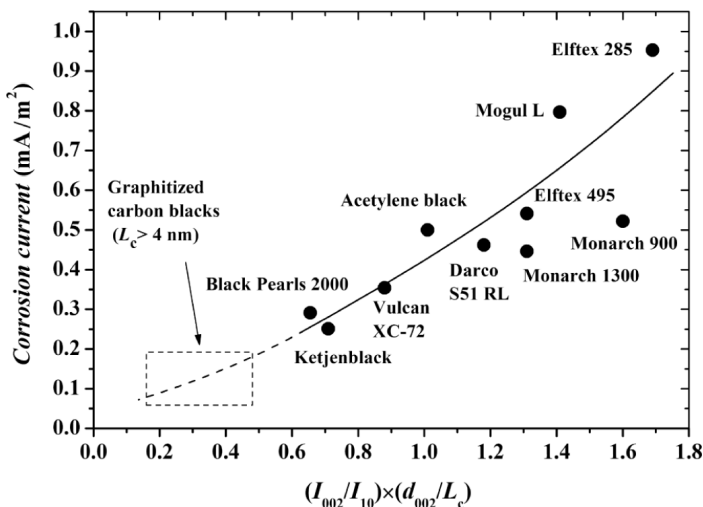


Figure 12.8 Influence of substructural parameters of carbon materials on specific corrosion currents measured after 100 minutes at 1.0 V at 443 K in 85% H₃PO₄ [260]. (Experimental data are replotted from refs. 8 and 249, with permission from John Wiley & Sons and from Elsevier, respectively.)

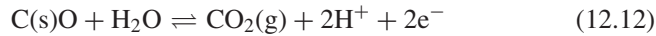
such as Vulcan XC-72, Black Pearls 200, and Ketjenblack. For example, for filamentous carbons, $L_c \sim 6$ nm, whereas for carbons of the Sibunit family, $L_c \sim 3$ nm.

12.7.2 Mechanism of Carbon Corrosion

In one of the first publications devoted to the mechanism of carbon corrosion, Kinoshita and Bett [248] described the electrochemical oxidation of high-surface-area (1000 m²/g) carbon black in concentrated H₃PO₄ and suggested simultaneous occurrence of two anodic processes: formation of the surface oxide (called “graphite oxide”) and the evolution of CO₂, which they believed occurred independently. The rates of both anode processes decaying with time, the faradaic efficiency of CO₂ evolution increased along with the surface coverage with graphite oxide. Stonehart [254] examined corrosion of a variety of carbon materials with specific surface areas ranging from 50 to 1500 m²/g and reported that at extended (above 1000 minutes) times, corrosion currents attained steady-state values. He ascribed this to preferential oxidation and subsequent removal of disordered carbon at short corrosion times.

The mechanism of carbon corrosion is still not fully established. It has been suggested to proceed via the sequence of an electrochemical step followed by a chemical step: namely, an electron transfer step followed by hydrolysis of the resulting C(s)⁺ surface sites, finally yielding CO₂. The latter either escapes from

the cell or is solvated to H_2CO_3 in the cathode water exhaust [8,261]:



The formation of carbon surface oxides, phenols, quinones, lactones, and carboxylic acids upon the electrooxidation of carbon has been detected by physical methods such as infrared spectroscopy [262], ellipsometry [263], x-ray photoelectron spectroscopy [262,264,265], thermal desorption, and electrochemistry (see refs. [8, 96, 248, and 261] and references therein). Cyclic voltammograms of oxidized carbons exhibit increased charge in the potential interval from 0.4 to 0.8 V versus RHE [255,259,266], which is ascribed to quinone–hydroquinone groups [8]:



Kangasniemi et al. [261] reported a decrease in carbon hydrophobicity upon aging, which accelerates carbon corrosion and has major consequences on the long-term performance of electrodes. Similarly, an increase in the interfacial double-layer capacitance for aged MEAs points toward a more hydrophilic surface or an increase in the carbon support roughness [266,267]. It is now well established that Pt nanoparticles catalyze the oxidation of carbon materials [97,256,268–271]. Willsau and Heitbaum [271] explored the corrosion of Norit carbon in 0.5 M H_2SO_4 and found that Pt enhances the reaction rate. In an H_3PO_4 environment, Passalacqua et al. [269] reported that the metal nanoparticles are corroded at high electrode potentials, whereas at low electrode potentials they (electro)catalyze the corrosion of carbon. Later, Tomantschger et al. [272] and Siroma et al. [270] confirmed this finding for Vulcan XC-72 and HOPG.

12.7.3 Corrosion and Stability of MEAs

In PEMFCs, carbon materials are exposed to conditions that favor their corrosion. These are the positive values of the electrode potential, the acidic environment ($\text{pH} < 1$), the presence of water, dioxygen, and elevated temperature (333 to 363 K), but also the presence of electrocatalysts such as metal nanoparticles. Since the electrode potential, water content, and Pt mass fraction are higher at the cathode of a PEMFC, this may explain why stronger degradation of the carbon support is usually reported at this electrode [266]. The rate of corrosion of carbon in PEMFCs has been reported to increase with an increase in the relative humidity [97,255,256], but Borup et al. [273] arrived at the controversial conclusion that the rate of carbon corrosion increases with decreasing relative humidity.

Corrosion of carbon materials in PEMFCs is believed to proceed via two different routes: electrochemical (as described above) and chemical, due to the

interaction of carbon with strong oxidants, including radical species: for example, OH[•] or HO₂[•]. These species result from the decomposition of H₂O₂, the latter being formed at the anode as a consequence of the O₂ crossover [274–276], by reaction with metal ion impurities such as Fe²⁺ and Cu²⁺ present in the PEM as traces (Fenton's reactions) [275,276], or by Pt²⁺ and Pt⁴⁺ ions produced by the electrochemical corrosion of Pt nanoparticles [266,277]. OH[•] species have also been detected at the cathode side by the electron paramagnetic resonance (EPR) spectrometer via spin trapping [278], although the H₂O₂ production at the cathode is believed to be smaller than at the anode [274]. Radical species are extremely corrosive for the carbon | electrocatalyst | recast ionomer interface [256,266,270,279–281]. As a result of the catalytic layer corrosion, Pt nanoparticles electrically disconnected from the carbon support were detected after fuel cell operation [170,266,277,282–284]. On the other hand, the gradual loss of the carbon support also induces agglomeration of Pt nanoparticles [266,282,284–286], and both phenomena result in a decrease in the electrochemical active surface area and in cell performance [170,266,273,277,282,284,286,287]. Although the kinetics of carbon corrosion is rather slow, pronounced corrosion of carbon support has been observed over time [8,96,97,248,256,261]. It has recently been proposed that the crossover of dioxygen to the anode [288], the nonuniform distribution of dihydrogen along the anode [289], and the unprotected starts and stops of a fuel cell [290] are also largely responsible for the accelerated degradation of the active layers. For example, we show in Figure 12.9 a field emission gun–scanning electron microscopy (FEG-SEM) micrograph of the thin cross section of a MEA

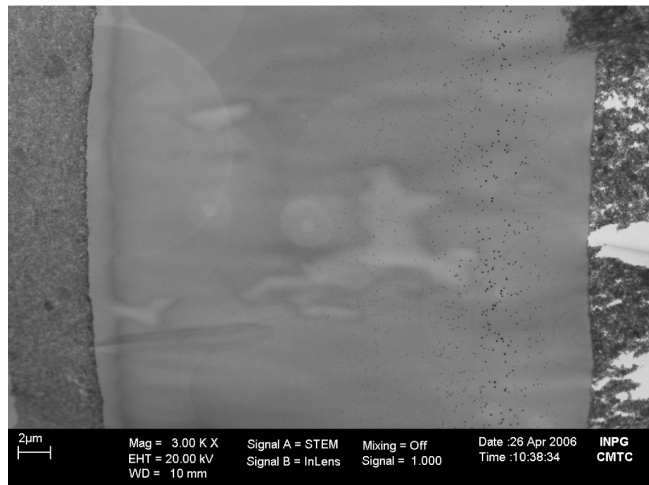


Figure 12.9 Cross-sectional field emission gun–scanning electron microscopy image of a used membrane electrode assembly. The anode is on the left-hand side, the cathode on the right-hand side. (Adapted from ref. 266, with permission from the Electrochemical Society.)

after 529 hours of operation on site. This operation was interrupted by start–stop periods with the overall duration of 63.5 hours [266]. Degradation of the cathode structure after the operation can clearly be seen, notably a decrease in the cathode thickness from 16–25 μm to 9–14 μm and the presence of holes in the cathode active layer [266,277,284]. The presence of platinum nanoparticles inside the membrane was ascribed to their corrosion [266]. These changes were also observed and confirmed by other research groups under similar real or simulated PEMFC conditions [97,256,261,267,282,290,291].

12.8 CONCLUSIONS

During the last decades, impressive advances have been achieved in the research and development of catalytic layers for PEMFCs. The decisive breakthrough was the change from noble metal blacks to carbon-supported noble metal nanoparticles in the 1980s, which has resulted in higher metal dispersions and better size distributions of noble metal nanoparticles, higher utilization factors (and thus higher PEMFC performances), and lower metal loadings per unit MEA surface area. The last two parameters are extremely important for the commercialization of PEMFCs, since they drive the price of a kilowatt produced by this technology. Nowadays, stacks and MEAs represent around 50 and 25% of the global fuel cell system cost, respectively. Therefore, a significant cost reduction is targeted by increasing the MEA performance (i.e., increasing the power density per MEA geometric area) and lifetime (i.e., decreasing the maintenance costs). Carbon supports undoubtedly play a great role in achieving this goal.

Years ago, carbon materials were considered (electro)chemically inert (i.e., as having no significant influence on the intrinsic electrocatalytic activity of metal nanoparticles). In this chapter we tried to provide the reader with the experimental evidence that carbon support plays an important role in catalytic layer performance. First, carbon supports determine the metal dispersion, particle size distribution, structure for monometallic particles, and the alloying degree for bimetallic nanoparticles. Since most PEMFC reactions are structure sensitive, carbon supports thus indirectly influence reaction kinetics in the CLs. Second, the interaction of carbon materials with metal nanoparticles is still a poorly explored domain, but there exists experimental and theoretical evidence that it may influence the adsorption energies and thus the intrinsic catalytic activities of metal particles. We also emphasized the role of oxygen-containing groups formed on a carbon surface. Third, optimization of the CL performance involves a complex interplay between the ionic conductivity, electronic conductivity, and reactant diffusion. Hence, carbon supports must possess adequate porosity to ensure efficient mass transport of reactants to the metal nanoparticles. Also, the distribution of proton-conducting ionomer (usually, Nafion) in the optimized electrodes has a tremendous influence on cell performance. The former depends on the porous structure but also on the physicochemical properties of the carbon support [274].

Finally, we addressed the complex problem of carbon corrosion, which is particularly relevant for PEMFC durability and thus commercialization of PEMFC technology. Carbon supports with an ordered crystalline structure, such as graphitized carbons, CNTs, and CNFs, as well as pyrolytic carbons of the Sibunit family hold out hope for the development of CLs with higher durability. More systematic studies are required to unveil the complex influence of the structure and morphology of carbon supports on the performance of the CLs and eventually, to develop a new generation of structurally ordered tailored materials for PEMFC applications with enhanced catalytic activities, low noble metal contents, and high durabilities.

Acknowledgments

The authors gratefully acknowledge the contribution to Section 12.2.5 by M. Chatenet. We would like to thank V. Zaikovskii for the TEM images, M. Neergat for the preparation of Pt–Ru/Ketjenblack catalyst; V. Fenelonov for the adsorption measurements; S. Pronkin, J. Kaiser, and P. Ruvinskiy for providing some of the figures; and A. Romanenko for helpful discussions. F.M. acknowledges financial support from ANR within the Carbocell and MDM projects, E.R.S. financial support from ANR within the Nano-Spa project; and E.R.S and P.A.S. from the EU within the FCANODE project and RFBR under grant 06-03-32737.

REFERENCES

- [1] W. Vielstich, A. Lamm, H.A. Gasteiger, Eds., *Handbook of Fuel Cells: Fundamentals, Technology and Applications*, Wiley, Chichester, UK, 2003.
- [2] D.R. Lide, Ed., *CRC Handbook of Chemistry and Physics*, CRC Press, Boca Raton, FL., 2003–2004.
- [3] P. Costanaga, S. Srinivasan, *J. Power Sources* 102 (2001) 242.
- [4] H.A. Gasteiger, S.S. Kocha, B. Sompalli, F.T. Wagner, *Appl. Catal. B* 56 (2005) 9.
- [5] C. Stone, A.E. Morrison, *Solid State Ionics* 152–153 (2002) 1.
- [6] J.B. Donnet, R.C. Bansal, M.J. Wang, Eds., *Carbon Black*, Marcel Dekker, New York, 1993.
- [7] J.-B. Donnet, A. Voet, *Carbon Black: Physics, Chemistry and Elastomer Reinforcement*, Marcel Dekker, New York, 1976.
- [8] K. Kinoshita, *Carbon: Electrochemical and Physicochemical Properties*, Wiley, New York, 1988.
- [9] J.I. Kroschwitz, M.H. Grant, Eds., *Encyclopedia of Chemical Technology*, Wiley, New York, 1992, p. 4.
- [10] H.P. Boehm, *Z. Anorg. Allg. Chem.* 297 (1958) 315.
- [11] A.S. Arico, S. Srinivasan, V. Antonucci, *Fuel Cells* 1 (2001) 133.
- [12] P.A. Simonov, E.M. Moroz, V.A. Likholobov, M. Pieruccini, P.L. Antonucci, N. Giordano, in *Proceedings of the 2nd Conference on the Modern Trends in Chemical Kinetics and Catalysis*, Novosibirsk, Russia, 1994, Vol. II(2), pp. 363–364.

- [13] C.A. Bessel, K. Laubernds, N.M. Rodriguez, R.T.K. Baker, *J. Phys. Chem. B* 105 (2001) 1115.
- [14] E.S. Steigerwalt, G.A. Deluga, D.E. Cliffel, C.M. Lukehart, *J. Phys. Chem. B* 105 (2001) 8097.
- [15] E.S. Steigerwalt, G.A. Deluga, C.M. Lukehart, *J. Phys. Chem. B* 106 (2002) 760.
- [16] Y.C. Liu, X.P. Qiu, Y.Q. Huang, W.T. Zhu, *Carbon* 40 (2002) 2375.
- [17] V. Rao, P.A. Simonov, E.R. Savinova, G.V. Plaksin, S.V. Cherepanova, G.N. Kryukova, U. Stimming, *J. Power Sources* 145 (2005) 178.
- [18] J. Kaiser, P.A. Simonov, V.I. Zaikovskii, C. Hartnig, L. Jörissen, E.R. Savinova, *J. Appl. Electrochem.* 37 (2007) 1429.
- [19] E. Auer, A. Freund, J. Pietsch, T. Tacke, *Appl. Catal. A* 173 (1998) 259.
- [20] J. Maruyama, I. Abe, *Electrochim. Acta* 48 (2003) 1443.
- [21] A. Blanchart, Fuel Cell Electrode, U.S. patent 4,447,505, 1984.
- [22] V.F. Surovkin, G.V. Plaksin, V.A. Semikolenov, V.A. Likholobov, I.J. Tiunova, Porous Carbonaceous Material, U.S. patent 4,978,649, 1990.
- [23] Y.I. Yermakov, V.F. Surovkin, G.V. Plaksin, V.A. Semikolenov, V.A. Likholobov, A.L. Chuvinilin, S.V. Bogdanov, *React. Kinet. Catal. Lett.* 33 (1987) 435.
- [24] E.M. Moroz, S.V. Bogdanov, V.A. Likholobov, *React. Kinet. Catal. Lett.* 47 (1992) 311.
- [25] H. Chang, S. Joo, C. Pak, *J. Mater. Chem.* 17 (2007) 3078.
- [26] G.S. Chai, S.B. Yoon, J.S. Yu, J.H. Choi, Y.E. Sung, *J. Phys. Chem. B* 108 (2004) 7074.
- [27] F.N. Su, H.J. Zeng, Y.J. Yu, L. Lv, J.Y. Lee, X.S. Zhao, *Carbon* 43 (2005) 2368.
- [28] R.W. Pekala, *J. Mater. Sci.* 24 (1989) 3221.
- [29] R.W. Pekala, F.M. Kong, *Polym. Prepr.* 30 (1) (1989) 221.
- [30] S. Gavalda, K.E. Gubbins, Y. Hanzawa, K. Kaneko, K.T. Thomson, *Langmuir* 18 (2002) 2141.
- [31] S. Gavalda, K. Kaneko, K.T. Thomson, K.E. Gubbins, *Colloids Surf. A* 187–188 (2001) 531.
- [32] C.D. Saquing, D. Kang, M. Aindow, C. Erkey, *Micropor. Mesopor. Mater.* 80 (2005) 11.
- [33] X. Lu, O. Nilsson, J. Fricke, R. Pekala, *J. Appl. Phys.* 73 (1993) 581.
- [34] Y. Hanzawa, K. Kaneko, N. Yoshizawa, R.W. Pekala, M.S. Dresselhaus, *Adsorption* 4 (1998) 187.
- [35] H. Tamon, H. Ishizaka, M. Mikami, M. Okazaki, *Carbon* 35 (1997) 791.
- [36] J. Gross, C.T. Alviso, R.W. Pekala, *Mater. Res. Soc. Symp. Proc.* 431 (1996) 123.
- [37] G.A.M. Reynolds, A.W.P. Fung, Z.H. Wang, M.S. Dresselhaus, R.W. Pekala, *J. Non-Cryst. Solids* 188 (1995) 27.
- [38] M. Uchida, Y. Aoyama, M. Tanabe, N. Yanagihara, N. Eda, A. Ohta, *J. Electrochem. Soc.* 142 (1995) 2572.
- [39] M. Uchida, Y. Fukuoka, Y. Sugawara, N. Eda, A. Ohta, *J. Electrochem. Soc.* 143 (1996) 2245.
- [40] T. Hughes, C. Chambers, U.S. patent 405,480, 1889.
- [41] P. Schuetzenberger, L. Schuetzenberger, *C.R. Acad. Sci. Paris* 111 (1890) 774.

- [42] C. Pelabon, H. Pelabon, *C.R. Acad. Sci. Paris* 137 (1903) 706.
- [43] M. Monthoux, V.L. Kuznetsov, *Carbon* 44 (2006) 1621.
- [44] L. Radushkevich, V. Lukyanovich, *Zh. Fiz. Khim.* 26 (1952) 88.
- [45] R.O. Grisdate, *J. Appl. Phys.* 24 (1953) 1288.
- [46] P.L. Walker Jr., F. Rusinko Jr., J.F. Rakiszawski, L.M. Liggett, in *Proceedings of the 3rd Carbon Conference*, Pergamon Press, New York, 1959, p. 643.
- [47] LL. Spain, in P.L. Walker, P.A. Thrower, Eds., *Chemistry and Physics of Carbon*, Vol.16, Marcel Dekker, New York, 1981, p. 1.
- [48] P. Delhaes, F. Carmona, in P.L. Walker, P.A. Thrower, Eds., *Chemistry and Physics of Carbon*, Vol. 17, Marcel Dekker, New York, 1981, p. 89.
- [49] S. Mrozovski, in *Proceedings of the 3rd Carbon Conference*, Pergamon Press, New York, 1959, p. 495.
- [50] D. Pantea, H. Darmstadt, S. Kaliaguine, C. Roy, *Appl. Surf. Sci.* 217 (2003) 181.
- [51] F. Ehrburger-Dolle, J. Lahaye, S. Misono, *Carbon* 32 (1994) 1363.
- [52] A. Celzard, J.F. Mareche, F. Payot, G. Furdin, *Carbon* 40 (2002) 2801.
- [53] N. Probst, in J.B. Donnet, R.C. Bansal, M.J. Wang, Eds., *Carbon Black*, 2nd ed., Marcel Dekker, New York, 1993, p. 271.
- [54] W.D. Shaeffer, W.M. Smith, *Ind. Eng. Chem.* 47 (1955) 1286.
- [55] W.F. Verhelst, K.G. Wolthuis, A. Voet, P. Ehrburger, J.-B. Donnet, *Rubber Chem. Technol.* 50 (1977) 735.
- [56] A.I. Medalia, *Rubber Chem. Technol.* 45 (1972) 1171.
- [57] J. Janzen, *J. Appl. Phys.* 46 (1975) 966.
- [58] K. Miyasaka, K. Watanabe, E. Jojima, H. Aida, M. Sumita, K. Ichikawa, *J. Mater. Sci.* 17 (1982) 1610.
- [59] R. Saito, *Appl. Phys. Lett.* 60 (1992) 2204.
- [60] G.G. Tibbetts, M.L. Lake, K.L. Strong, B.P. Rice, *Compos. Sci. Technol.* 67 (2007) 1709.
- [61] F. Rodríguez-Reinoso, *Carbon* 36 (1998) 159.
- [62] H.P. Boehm, *Carbon* 32 (1994) 759.
- [63] V.A. Garten, D.E. Weiss, *Aust. J. Chem.* 10 (1957) 309.
- [64] H.P. Boehm, M. Voll, *Carbon* 8 (1970) 227.
- [65] M. Voll, H.P. Boehm, *Carbon* 8 (1970) 741.
- [66] M. Voll, H.P. Boehm, *Carbon* 9 (1971) 481.
- [67] M. Voll, H.P. Boehm, *Carbon* 9 (1971) 473.
- [68] A.S. Arico, V. Antonucci, M. Minutoli, N. Giordano, *Carbon* 27 (1989) 337.
- [69] A.S. Arico, V. Antonucci, L. Pino, P.L. Antonucci, N. Giordano, *Carbon* 28 (1990) 599.
- [70] E. Antolini, *J. Mater. Sci.* 38 (2003) 2995.
- [71] C.A. Leon y Leon, J.M. Solar, V. Calemma, L.R. Radovic, *Carbon* 30 (1992) 797.
- [72] S.S. Barton, M.J.B. Evans, E. Halliop, J.A.F. MacDonald, *Carbon* 35 (1997) 1361.
- [73] P.L. Antonucci, V. Alderucci, N. Giordano, D.L. Cocke, H. Kim, *J. Appl. Electrochem.* 24 (1994) 58.
- [74] C. Prado-Burguete, A. Linares-Solano, F. Rodríguez-Reinoso, C. Salinas-Marting de Lecea, *J. Catal.* 115 (1989) 98.

- [75] H.P. Boehm, *Carbon* 40 (2002) 145.
- [76] A. Contescu, C. Contescu, K. Putyera, J.A. Schwarz, *Carbon* 35 (1997) 83.
- [77] T.J. Fabish, D.E. Schleifer, *Carbon* 22 (1984) 19.
- [78] J.-P. Randin, E. Yeager, *J. Electroanal. Chem.* 36 (1972) 257.
- [79] J.-P. Randin, E. Yeager, *J. Electroanal. Chem.* 54 (1974) 93.
- [80] M.T. McDermott, K. Kneten, R.C. McCreery, *J. Phys. Chem.* 96 (1992) 3124.
- [81] A.D. Modestov, J. Gun, O. Lev, *J. Electroanal. Chem.* 476 (1999) 118.
- [82] T. Morimoto, K. Hiratsuka, Y. Sanada, K. Kurihara, *J. Power Sources* 60 (1996) 239.
- [83] D. Lozano-Castelló, D. Cazorla-Amorós, A. Linares-Solano, S. Shiraishi, H. Kurihara, A. Oya, *Carbon* 41 (2003) 1765.
- [84] H. Shi, *Electrochim. Acta* 41 (1996) 1633.
- [85] E. Raymundo-Piñero, K. Kierzek, J. Machnikowski, F. Béguin, *Carbon* 44 (2006) 2498.
- [86] G. Gryglewicz, J. Machnikowski, E. Lorenc-Grabowska, G. Lota, E. Frackowiak, *Electrochim. Acta* 50 (2005) 1197.
- [87] V.S. Vilinskaya, A.A. Korobanov, R.K. Burshtein, A.V. Gerasimova, *Russ. Chem. Bull.* 27 (1978) 865.
- [88] M.J. Bleda-Martinez, J.A. Macia-Agullo, D. Lozano-Castello, E. Morallon, D. Cazorla-Amorós, A. Linares-Solano, *Carbon* 43 (2005) 2677.
- [89] M.J. Bleda-Martinez, D. Lozano-Castello, E. Morallon, D. Cazorla-Amorós, A. Linares-Solano, *Carbon* 44 (2006) 2642.
- [90] A. Yoshida, I. Tanahashi, A. Nishino, *Carbon* 28 (1990) 611.
- [91] E.W. Washburn, *Phys. Rev.* 17 (1921) 273.
- [92] M.L. Studebaker, C.W. Snow, *J. Phys. Chem.* 59 (1955) 973.
- [93] D.I. Dimitrov, A. Milchev, K. Binder, *Phys. Rev. Lett.* 99 (2007), Article No. 054501.
- [94] K. Kinoshita, J.A.S. Bett, *Carbon* 13 (1975) 405.
- [95] F.M. Fowkes, W.D. Harkins, *J. Am. Chem. Soc.* 62 (1940) 3377.
- [96] K. Kinoshita, in S. Sarangapani, J.R. Akridge, B. Schumm, Eds., *Proceedings of the Conference on the Electrochemistry of Carbon*, Electrochemical Society, Cleveland, OH, 1983, p. 273.
- [97] D.A. Stevens, J.R. Dahn, *Carbon* 43 (2005) 179.
- [98] P.A. Simonov, V.A. Likhlobov, in A. Wieckowski, E.R. Savinova, C.G. Vayenas, Eds., *Catalysis and Electrocatalysis at Nanoparticle Surfaces*, Marcel Dekker, New York, 2003, p. 409.
- [99] E. Antolini, *Mater. Chem. Phys.* 78 (2003) 563.
- [100] H.S. Liu, C.J. Song, L. Zhang, J.J. Zhang, H.J. Wang, D.P. Wilkinson, *J. Power Sources* 155 (2006) 95.
- [101] S. Hirano, F. Fujikawa, *Denki Kagaku* 64 (1996) 737.
- [102] M. Alvisi, G. Galtieri, L. Giorgi, R. Giorgi, E. Serra, M.A. Signore, *Surf. Coat. Technol.* 200 (2005) 1325.
- [103] C.L. Sun, L.C. Chen, M.C. Su, L.S. Hong, O. Chyan, C.Y. Hsu, K.H. Chen, T.F. Chang, L. Chang, *Chem. Mater.* 17 (2005) 3749.

- [104] A. Caillard, C. Charles, R. Boswell, P. Brault, *Nanotechnology* 18 (2007).
- [105] L. Gubler, N. Beck, S.A. Gursel, F. Hajbolouri, D. Kramer, A. Reiner, B. Steiger, G.G. Scherer, A. Wokaun, B. Rajesh, K.R. Thampi, *Chimia* 58 (2004) 826.
- [106] N. Alonso-Vante, *Fuel Cells* 6 (2006) 182.
- [107] L. Zhang, J.J. Zhang, D.P. Wilkinson, H.J. Wang, *J. Power Sources* 156 (2006) 171.
- [108] J.W. Geus, J.A.R. van Veen, in R.A. van Santen, P.W.N.M. van Leeuwen, B.A. Averill, J.A. Moulijn, Eds., *Catalysis: An Integrated Approach*, Elsevier, Amsterdam, 1999, p. 459.
- [109] A.V. Neimark, V.B. Fenelonov, L.I. Kheifets, *React. Kinet. Catal. Lett.* 5 (1976) 67.
- [110] J. Zhang, X. Wang, C. Wu, H. Wang, B. Yi, H. Zhang, *React. Kinet. Catal. Lett.* 83 (2004) 229.
- [111] J.L. Gómez de la Fuente, S. Rojas, M.V. Martínez-Huerta, P. Terreros, M.A. Peña, J.L.G. Fierro, *Carbon* 44 (2006) 1919.
- [112] A. Guha, W. Lu, T.A. Zawodzinski, Jr., D.A. Schiraldi, *Carbon* 45 (2007) 1506.
- [113] H. Kim, J.-N. Park, W.-H. Lee, *Catal. Today* 87 (2003) 237.
- [114] K.I. Han, J.S. Lee, S.O. Park, S.W. Lee, Y.W. Park, H. Kim, *Electrochim. Acta* 50 (2004) 791.
- [115] Y. Liang, H. Zhang, H. Zhong, X. Zhu, Z. Tian, D. Xu, B. Yi, *J. Catal.* 238 (2006) 468.
- [116] Z. Zhou, W. Zhou, S. Wang, G. Wang, L. Jiang, G. Li, H., Q. Xin, *Catal. Today* 93–95 (2004) 523.
- [117] Z.-B. Wang, G.-P. Yin, P.-F. Shi, *Carbon* 44 (2006) 133.
- [118] P. Albers, E. Auer, W. Behl, K. Vogel, C. Vogler, U.S. patent 66,89,505, 2004.
- [119] H. Boennemann, R. Richards, in A. Wieckowski, E.R. Savinova, in C.G. Vayenas, Ed., *Catalysis and Electrocatalysis at Nanoparticle Surfaces*, Marcel Dekker, New York, 2003, p. 343.
- [120] R.G. Freeman, K.C. Grabar, K.J. Allison, R.M. Bright, J.A. Davis, A.P. Guthrie, M.B. Hommer, M.A. Jackson, P.C. Smith, D.G. Walter, M.J. Natan, *Science* 267 (1995) 1629.
- [121] K.C. Grabar, K.J. Allison, B.E. Baker, R.M. Bright, K.R. Brown, R.G. Freeman, A.P. Fox, C.D. Keating, M.D. Musick, M.J. Natan, *Langmuir* 12 (1996) 2353.
- [122] K.C. Grabar, R. Griffith Freeman, M.B. Hommer, M.J. Natan, *Anal. Chem.* 67 (1995) 735.
- [123] K.C. Grabar, P.C. Smith, M.D. Musick, J.A. Davis, D.G. Walter, M.A. Jackson, A.P. Guthrie, M.J. Natan, *J. Am. Chem. Soc.* 118 (1996) 1148.
- [124] L. Dubau, F. Hahn, C. Coutanceau, J.M. Léger, C. Lamy, *J. Electroanal. Chem.* 554 (2003) 407.
- [125] L. Dubau, C. Coutanceau, E. Garnier, J.M. Léger, C. Lamy, *J. Appl. Electrochem.* 33 (2003) 419.
- [126] T.J. Schmidt, M. Noeske, H.A. Gasteiger, R.J. Behm, P. Britz, H. Boennemann, *J. Electrochem. Soc.* 145 (1998) 925.

- [127] H. Boennemann, R. Brinkmann, P. Britz, U. Endruschat, R. Mortel, U.A. Paulus, G.J. Feldmeyer, T.J. Schmidt, H.A. Gasteiger, R.J. Behm, *J. New Mater. Electrochem. Syst.* 3 (2000) 199.
- [128] S. Brimaud, C. Coutanceau, E. Garnier, J.M. Léger, F. Gérard, S. Pronier, M. Leoni, *J. Electroanal. Chem.* 602 (2007) 226.
- [129] M. Watanabe, M. Uchida, S. Motoo, *J. Electroanal. Chem.* 229 (1987) 395.
- [130] K. Meguro, M. Torizuka, K. Esumi, *Bull. Chem. Soc. Jpn.* 61 (1988) 341.
- [131] H. Boennemann, G. Braun, W. Brijoux, R. Brinkmann, A.S. Tilling, K. Seevogel, K. Siepen, *J. Org. Chem.* 520 (1996) 143.
- [132] H. Boennemann, W. Brijoux, R. Brinkmann, R. Fretzen, T. Joussen, R. Koppler, B. Korall, P. Neiteler, J. Richter, *J. Mol. Catal.* 86 (1994) 129.
- [133] H. Boennemann, R. Brinkmann, P. Neiteler, *Appl. Organomet. Chem.* 8 (1994) 361.
- [134] M.T. Reetz, W. Helbig, *J. Am. Chem. Soc.* 116 (1994) 7401.
- [135] M.T. Reetz, S.A. Quaiser, *Angew. Chem. Int. Ed.* 34 (1995) 2240.
- [136] J.L. Zubimendi, L. Vazquez, P. Ocon, J.M. Vara, W.E. Triaca, R.C. Salvarezza, A.J. Arvia, *J. Phys. Chem.* 97 (1993) 5095.
- [137] J.L. Zubimendi, G. Andreasen, W.E. Triaca, *Electrochim. Acta* 40 (1995) 1305.
- [138] J.V. Zoval, J. Lee, S. Gorer, R.M. Penner, *J. Phys. Chem. B* 102 (1998) 1166.
- [139] J.V. Zoval, R.M. Stiger, P.R. Biernacki, R.M. Penner, *J. Phys. Chem.* 100 (1996) 837.
- [140] O. Antoine, R. Durand, *Electrochem. Solid-State Lett.* 4 (2001) A55.
- [141] S. Adora, J.-P. Simon, Y. Soldo-Olivier, R. Faure, E. Chaînet, R. Durand, *ChemPhysChem* 5 (2004) 1178.
- [142] S. Adora, J.-P. Simon, Y. Soldo-Olivier, R. Faure, R. Durand, E. Chaînet, *J. Cryst. Growth* 275 (2005) e2207.
- [143] S. Adora, Y. Soldo-Olivier, R. Faure, R. Durand, E. Dartige, F. Baudet, *J. Phys. Chem. B* 105 (2001) 10489.
- [144] C. Coutanceau, A.F. Rakotondrainibe, A. Lima, E. Garnier, S. Pronier, J.M. Léger, C. Lamy, *J. Appl. Electrochem.* 34 (2004) 61.
- [145] M. Mastragostino, A. Missiroli, F. Soavi, *J. Electrochem. Soc.* 151 (2004) A1919.
- [146] O.V. Cherstiouk, P.A. Simonov, E.R. Savinova, *Electrochim. Acta* 48 (2003) 3851.
- [147] F. Maillard, S. Schreier, M. Hanzlik, E.R. Savinova, S. Weinkauf, U. Stimming, *Phys. Chem. Chem. Phys.* 7 (2005) 385.
- [148] W.-H. Kao, T. Kuwana, *J. Am. Chem. Soc.* 106 (1984) 473.
- [149] M. Boutonnet, J. Kizling, P. Stenius, *Colloids Surf.* 5 (1982) 209.
- [150] I. Capek, *Adv. Colloid Int. Sci.* 110 (2004) 49.
- [151] J. Solla-Gullon, V. Montiel, A. Aldaz, J. Clavilier, *J. Electrochem. Soc.* 150 (2003) E104.
- [152] J. Solla-Gullon, F.J. Vidal-Iglesias, V. Montiel, A. Aldaz, *Electrochim. Acta* 49 (2004) 5079.
- [153] K. Lee, J.J. Zhang, H.J. Wang, D.P. Wilkinson, *J. Appl. Electrochem.* 36 (2006) 507.
- [154] G.-G. Park, T.-H. Yang, Y.-G. Yoon, W.-Y. Lee, C.-S. Kim, *Int. J. Hydrogen Energy* 28 (2003) 645.

- [155] H.N. Dinh, X.M. Ren, F.H. Garzon, P. Zelenay, S. Gottesfeld, *J. Electroanal. Chem.* 491 (2000) 222.
- [156] W.E. O'Grady, P.L. Hagans, K.I. Pandya, D.L. Maricle, *Langmuir* 17 (2001) 3047.
- [157] F. Dassenoy, W. Vogel, N. Alonso-Vante, *J. Phys. Chem. B* 106 (2002) 12152.
- [158] C. Roth, N. Benker, M. Mazurek, F. Scheiba, H. Fuess, *Appl. Catal. A* 319 (2007) 81.
- [159] M.S. Nashner, A.I. Frenkel, D.L. Adler, J.R. Shapley, R.G. Nuzzo, *J. Am. Chem. Soc.* 119 (1997) 7760.
- [160] R.A. Lampitt, L.P.L. Carrette, M.P. Hogarth, A.E. Russell, *J. Electroanal. Chem.* 460 (1999) 80.
- [161] D. Aberdam, R. Durand, R. Faure, F. Gloaguen, J.L. Hazemann, E. Herrero, A. Kabbabi, O. Ulrich, *J. Electroanal. Chem.* 398 (1995) 43.
- [162] S. Mukerjee, S. Srinivasan, M.P. Soriaga, J. McBreen, *J. Phys. Chem.* 99 (1995) 4577.
- [163] S. Mukerjee, J. McBreen, *J. Electroanal. Chem.* 448 (1998) 163.
- [164] I.V. Malakhov, S.G. Nikitenko, E.R. Savinova, D.I. Kochubey, N. Alonso-Vante, *J. Phys. Chem. B* 106 (2002) 1670.
- [165] P.G. Allen, S.D. Conradson, M.S. Wilson, S. Gottesfeld, I.D. Raistrick, J. Valerio, M. Lovato, *J. Electroanal. Chem.* 384 (1995) 99.
- [166] R. Viswanathan, R. Liu, E.S. Smotkin, *Rev. Sci. Instrum.* 73 (2002) 2124.
- [167] R.J.K. Wiltshire, C.R. King, A. Rose, P.P. Wells, M.P. Hogarth, D. Thompsett, A.E. Russell, *Electrochim. Acta* 50 (2005) 5208.
- [168] A.E. Russell, S. Maniguet, R.J. Mathew, J. Yao, M.A. Roberts, D. Thompsett, *J. Power Sources* 96 (2001) 226.
- [169] C. Roth, N. Martz, T. Buhrmester, J. Scherer, H. Fuess, *Phys. Chem. Chem. Phys.* 4 (2002) 3555.
- [170] M.S. Wilson, F.H. Garzon, K.E. Sickafus, S. Gottesfeld, *J. Electrochem. Soc.* 140 (1993) 2872.
- [171] A.E. Russell, A. Rose, *Chem. Rev.* 104 (2004) 4613.
- [172] Q. Zhu, S.L. Money, A.E. Russell, K.M. Thomas, *Langmuir* 13 (1997) 2149.
- [173] J.A. Turner, K.M. Thomas, A.E. Russell, *Carbon* 35 (1997) 983.
- [174] J. Clavilier, R. Faure, G. Guinet, R. Durand, *J. Electroanal. Chem.* 107 (1980) 205.
- [175] N.M. Markovic, P.N. Ross, *Surf. Sci. Rep.* 45 (2002) 121.
- [176] F. Maillard, M. Eikerling, O.V. Cherstiouk, S. Schreier, E. Savinova, U. Stimming, *Faraday Discuss.* 125 (2004) 357.
- [177] O.V. Cherstiouk, P.A. Simonov, V.I. Zaikovskii, E.R. Savinova, *J. Electroanal. Chem.* 554 (2003) 241.
- [178] A.N. Gavrilov, E.R. Savinova, P.A. Simonov, V.I. Zaikovskii, S.V.T. Cherepanova, G.A., V.N. Parmon, *Phys. Chem. Chem. Phys.* 40 (2007) 5476.
- [179] F. Maillard, A. Bonnefont, M. Chatenet, L. Guétaz, B. Doisneau-Cottignies, H. Roussel, U. Stimming, *Electrochim. Acta* 53 (2007) 811.
- [180] P. Costamagna, S. Srinivasan, *J. Power Sources* 102 (2001) 242.
- [181] P. Costamagna, S. Srinivasan, *J. Power Sources* 102 (2001) 253.

- [182] X. Yuan, J.C. Suna, M. Blanco, H. Wang, J. Zhang, D.P. Wilkinson, *J. Power Sources* 161 (2006) 920.
- [183] X. Yuan, J.C. Sun, H. Wang, J. Zhang, *J. Power Sources* 161 (2006) 929.
- [184] L.J. Bregoli, *Electrochim. Acta* 23 (1978) 489.
- [185] F. Gloaguen, F. Andolfatto, R. Durand, P. Ozil, *J. Appl. Electrochem.* 24 (1994) 863.
- [186] A. Kabbabi, F. Gloaguen, F. Andolfatto, R. Durand, *J. Electroanal. Chem.* 373 (1994) 251.
- [187] P.M. Sattler, P.N. Ross, *Ultramicroscopy* 20 (1986) 21.
- [188] P.A. Attwood, B.D. McNicol, R.T. Short, *J. Appl. Electrochem.* 10 (1980) 213.
- [189] K. Yahikozawa, Y. Fujii, Y. Matsuda, K. Nishimura, Y. Takasu, *Electrochim. Acta* 36 (1991) 973.
- [190] T. Frelink, W. Visscher, J.A.R. Vanveen, *J. Electroanal. Chem.* 382 (1995) 65.
- [191] F. Maillard, E.R. Savinova, U. Stimming, *J. Electroanal. Chem.* 599 (2007) 221.
- [192] M. Arenz, K.J.J. Mayrhofer, V. Stamenkovic, B.B. Blizanac, T. Tomoyuki, P.N. Ross, N.M. Markovic, *J. Am. Chem. Soc.* 127 (2005) 6819.
- [193] O. Antoine, Y. Bultel, R. Durand, P. Ozil, *Electrochim. Acta* 43 (1998) 3681.
- [194] S. Park, Y. Xie, M.J. Weaver, *Langmuir* 18 (2002) 5792.
- [195] Y. Takasu, H. Itaya, T. Iwazaki, R. Miyoshi, T. Ohnuma, W. Sugimoto, Y. Murakami, *Chem. Commun.* (2001) 341.
- [196] H. Gleiter, *Nanostruct. Mater.* 1 (1992) 1.
- [197] L.L. Wang, S.V. Khare, V. Chirita, D.D. Johnson, A.A. Rockett, A.I. Frenkel, N.H. Mack, R.G. Nuzzo, *J. Am. Chem. Soc.* 128 (2006) 131.
- [198] Y. Okamoto, *Chem. Phys. Lett.* 420 (2006) 382.
- [199] A.K. Shukla, M.K. Ravikumar, A. Roy, S.R. Barman, D.D. Sarma, A.S. Arico, V. Antonucci, L. Pino, N. Giordano, *J. Electrochem. Soc.* 141 (1994) 1517.
- [200] S.C. Roy, A.W. Harding, A.E. Russell, K.M. Thomas, *J. Electrochem. Soc.* 144 (1997) 2323.
- [201] K.E. Swider, D.R. Rolison, *J. Electrochem. Soc.* 143 (1996) 813.
- [202] K.E. Swider, D.R. Rolison, *Electrochem. Solid-State Lett.* 3 (2000) 4.
- [203] S.C. Roy, P.A. Christensen, A. Hamnett, K.M. Thomas, V. Trapp, *J. Electrochem. Soc.* 143 (1996) 3073.
- [204] C.C. Boyer, R.G. Anthony, A.J. Appleby, *J. Appl. Electrochem.* 30 (2000) 777.
- [205] S. Slade, S.A. Campbell, T.R. Ralph, F.C. Walsh, *J. Electrochem. Soc.* 149 (2002) A1556.
- [206] M. Eikerling, A.A. Kornyshev, *J. Electroanal. Chem.* 453 (1998) 89.
- [207] M. Eikerling, A.A. Kornyshev, *J. Electroanal. Chem.* 475 (1999) 107.
- [208] Q. Wang, D. Song, T. Navessin, S. Holdcroft, Z. Liu, *Electrochim. Acta* 50 (2004) 725.
- [209] E. Antolini, L. Giorgi, A. Pozio, E. Passalacqua, *J. Power Sources* 77 (1999) 136.
- [210] J.M. Song, S.Y. Cha, W.M. Lee, *J. Power Sources* 94 (2001) 78.
- [211] G.C. Li, P.G. Pickup, *J. Electrochem. Soc.* 150 (2003) C745.
- [212] M. Eikerling, A. Kornyshev, A. Kulikovsky, *Fuel Cell Rev.* 1 (2005) 15.
- [213] Z.N. Farhat, *J. Power Sources* 138 (2004) 68.

- [214] M.K. Debe, in W. Vielstich, A. Lamm, H. Gasteiger, Eds., *Handbook of Fuel Cells: Fundamentals, Technology, and Applications*, Wiley, Hoboken, NJ, 2003, p. 576.
- [215] Q. Wang, M. Eikerling, D. Song, Z. Liu, *J. Electroanal. Chem.* 573 (2004) 61.
- [216] U.A. Paulus, V. Veziridis, B. Schnyder, M. Kuhnke, G.G. Scherer, A. Wokaun, *J. Electroanal. Chem.* 541 (2003) 77.
- [217] M. Watanabe, M. Tomikawa, S. Motoo, *J. Electroanal. Chem.* 182 (1985) 193.
- [218] M. Uchida, Y. Fukuoka, Y. Sugawara, H. Ohara, A. Ohta, *J. Electrochem. Soc.* 145 (1998) 3708.
- [219] J. Xie, K.L. More, T.A. Zawodzinski, W.H. Smith, *J. Electrochem. Soc.* 151 (2004) A1841.
- [220] O.V. Cherstiouk, P.V. Simonov, V.B. Fenelonov, E.R. Savinova (in preparation).
- [221] M. Uchida, Y. Aoyama, N. Eda, A. Ohta, *J. Electrochem. Soc.* 142 (1995) 463.
- [222] R. Fernandez, P. Ferreira-Aparicio, L. Daza, *J. Power Sources* 151 (2005) 18.
- [223] V. Rao, U. Stimming, personal communication.
- [224] O. Antoine, Ph.D. dissertation, Institut National Polytechnique de Grenoble, France, 1998.
- [225] J. Marie, S. Berthon-Fabry, M. Chatenet, E. Chainet, R. Pirard, N. Cornet, P. Achard, *J. Appl. Electrochem.* 37 (2007) 147.
- [226] J. Marie, S. Berthon-Fabry, M. Chatenet, P. Achard (submitted).
- [227] J. Marie, S. Berthon-Fabry, S. Achard, M. Chatenet, E. Chainet, R. Pirard, N. Cornet, *ECS Trans.* 1 (2006) 509.
- [228] M. Eikerling, *J. Electrochem. Soc.* 153 (2006) E58.
- [229] K. Wikander, H. Ekstroem, A.E.C. Palmqvist, A.H. Lundblad, K., L. G., *Fuel Cells* 6 (2006) 21.
- [230] P. Serp, M. Corrias, P. Kalck, *Appl. Catal. A* 253 (2003) 337.
- [231] A. Kongkanand, K. Vinodgopal, S. Kuwabata, P.V. Kamat, *J. Phys. Chem. B* 110 (2006) 16185.
- [232] Y.H. Lin, X.L. Cui, C.H. Yen, C.M. Wai, *Langmuir* 21 (2005) 11474.
- [233] J.S. Ye, H.F. Cui, Y. Wen, W.D. Zhang, G.Q. Xu, F.S. Sheu, *Microchim. Acta* 152 (2006) 267.
- [234] C.C. Chien, K.T. Jeng, *Mater. Chem. Phys.* 99 (2006) 80.
- [235] J. Prabhuram, T.S. Zhao, Z.K. Tang, R. Chen, Z.X. Liang, *J. Phys. Chem. B* 110 (2006) 5245.
- [236] A.L. Ocampo, M. Miranda-Hernandez, J. Morgado, J.A. Montoya, P.J. Sebastian, *J. Power Sources* 160 (2006) 915.
- [237] Y.J. Gu, W.T. Wong, *Langmuir* 22 (2006) 11447.
- [238] Y.Y. Shao, G.P. Yin, H.H. Wang, Y.Z. Gao, P.F. Shi, *J. Power Sources* 161 (2006) 47.
- [239] A.M. Kannan, V.P. Veedu, L. Munukutla, M.N. Ghasemi-Nejhad, *Electrochem. Solid-State Lett.* 10 (2007) B47.
- [240] K.T. Jeng, C.C. Chien, N.Y. Hsu, W.M. Huang, S.D. Chiou, S.H. Lin, *J. Power Sources* 164 (2007) 33.
- [241] E. Yoo, T. Okada, T. Kizuka, J. Nakamura, *Electrochemistry* 75 (2007) 146.

- [242] J. Narayananamoorthy, S. Durairaj, Y. Song, Y. Xu, J. Choi, *Appl. Phys. Lett.* 90 (2007), Article No. 063112.
- [243] X. Sun, B. Stansfield, J.P. Dodelet, S. Desilets, *Chem. Phys. Lett.* 363 (2002) 415.
- [244] X. Sun, R. Li, B. Stansfield, J.P. Dodelet, S. Desilets, *Chem. Phys. Lett.* 394 (2004) 266.
- [245] A. Caillard, C. Charles, R. Boswell, P. Brault, C. Coutanceau, *Appl. Phys. Lett.* 90 (2007).
- [246] J.F. AuBuchon, L.H. Chen, C. Daraio, S.H. Jin, *Nano Lett.* 6 (2006) 324.
- [247] M. Pourbaix, *Atlas of Electrochemical Equilibria in Aqueous Solutions*, National Association of Corrosion Engineers, Houston, TX, 1979, p. 453.
- [248] K. Kinoshita, J. Bett, *Carbon* 11 (1973) 237.
- [249] P.L. Antonucci, F. Romeo, O. Minutoli, E. Alderucci, N. Giordano, *Carbon* 26 (1988) 197.
- [250] P.L. Antonucci, L. Pino, N. Giordano, L. Pinna, *Mater. Chem. Phys.* 21 (1989) 495.
- [251] K. Kinoshita, in *Proceedings of the Workshop on the Electrochemistry of Carbon*, Electrochemical Society, Pennington, NJ, 1984, p. 273.
- [252] P. Stonehart, J.P. MacDonald, *Energy Citations Database*, Report No. EPRI-EM-1664, Stability of Acid Fuel Cell Cathode Materials, 1981.
- [253] H. Binder, A. Kohling, K. Richter, G. Sandstede, *Electrochim. Acta* 9 (1964) 255.
- [254] P. Stonehart, *Carbon* 22 (1984) 423.
- [255] D.A. Stevens, M.T. Hicks, G.M. Haugen, J.R. Dahn, *J. Electrochem. Soc.* 152 (2005) A2309.
- [256] L.M. Roen, C.H. Paik, T.D. Jarvi, *Electrochem. Solid-State Lett.* 7 (2004) A19.
- [257] Y.Y. Shao, G.P. Yin, Y.Z. Gao, P.F. Shi, *J. Electrochem. Soc.* 153 (2006) A1093.
- [258] Y. Shao, G. Yin, J. Zhang, Y. Gao, *Electrochim. Acta* 51 (2006) 5853.
- [259] L. Liang, X. Yangchuan, *J. Electrochem. Soc.* 153 (2006) A1823.
- [260] P.A. Simonov, A.V. Romanenko, V.A. Likholobov, in *Proceedings of the 2nd All-Russian Seminar on Fuel Cells and Fuel Cell Power Plants*, Novosibirsk, Russia, 2003, p. 102.
- [261] K.H. Kangasniemi, D.A. Condit, T.D. Jarvi, *J. Electrochem. Soc.* 151 (2004) E125.
- [262] M.G. Sullivan, B. Schnyder, M. Bartsch, D. Alliata, C. Barbero, R. Imhof, R. Kotz, *J. Electrochem. Soc.* 147 (2000) 2636.
- [263] L.J. Kepley, A.J. Bard, *Anal. Chem.* 60 (1988) 1459.
- [264] G.E. Cabaniss, A.A. Diamantis, W.R. Murphy, R.W. Linton, T.J. Meyer, *J. Am. Chem. Soc.* 107 (1985) 1845.
- [265] K.M. Sundberg, W.H. Smyrl, L. Atanasoska, R. Atanasoski, *J. Electrochem. Soc.* 136 (1989) 434.
- [266] E. Guilminot, A. Corcella, F. Charlot, F. Maillard, M. Chatenet, *J. Electrochem. Soc.* 154 (2007) B96.
- [267] T. Yoda, H. Uchida, M. Watanabe, *Electrochim. Acta* 52 (2007) 5997.
- [268] K. Kinoshita, J.A.S. Bett, *Carbon* 12 (1974) 525.
- [269] E. Passalacqua, P.L. Antonucci, M. Vivaldi, A. Patti, V. Antonucci, N. Giordano, K. Kinoshita, *Electrochim. Acta* 37 (1992) 2725.

- [270] Z. Siroma, K. Ishii, K. Yasuda, Y. Miyazaki, M. Inaba, A. Tasaka, *Electrochem. Commun.* 7 (2005) 1153.
- [271] J. Willsau, J. Heitbaum, *J. Electroanal. Chem.* 161 (1984) 93.
- [272] K. Tomantschger, R. Findlay, M. Hanson, K. Kordesch, S. Srinivasan, *J. Power Sources* 39 (1992) 21.
- [273] R.L. Borup, J.R. Davey, F.H. Garzon, D.L. Wood, M.A. Inbody, *J. Power Sources* 163 (2006) 76.
- [274] O. Antoine, R. Durand, *J. Appl. Electrochem.* 30 (2000) 839.
- [275] J. Healy, C. Hayden, T. Xie, K. Olson, R. Waldo, A. Brundage, H. Gasteiger, J. Abbott, *Fuel Cells* 5 (2005) 302.
- [276] M. Inaba, T. Kinumoto, M. Kiriake, R. Umebayashi, A. Tasaka, Z. Ogumi, *Electrochim. Acta* 51 (2006) 5746.
- [277] M. Chatenet, E. Guilminot, C. Iojoiu, J.-Y. Sanchez, E. Rossinot, F. Maillard, *ECS Trans.* 11 (2007) 1203.
- [278] A. Panchenko, H. Dilger, J. Kerres, M. Hein, A. Ullrich, T. Kaz, E. Roduner, *Phys. Chem. Chem. Phys.* 6 (2004) 2891.
- [279] M. Inaba, H. Yamada, J. Tokunaga, A. Tasaka, *Electrochem. Solid-State Lett.* 7 (2004) A474.
- [280] D.E. Curtin, R.D. Lousenberg, T.J. Henry, P.C. Tangeman, M.E. Tisack, *J. Power Sources* 131 (2004) 41.
- [281] E. Endoh, S. Terazono, H. Widjaja, Y. Takimoto, *Electrochem. Solid-State Lett.* 7 (2004) A209.
- [282] P.J. Ferreira, G.J. la O', Y. Shao-Horn, D. Morgan, R. Makharia, S. Kocha, H.A. Gasteiger, *J. Electrochem. Soc.* 152 (2005) A2256.
- [283] J.R. Yu, T. Matsuura, Y. Yoshikawa, M.N. Islam, M. Hori, *Phys. Chem. Chem. Phys.* 7 (2005) 373.
- [284] E. Guilminot, A. Corcella, C. Iojoiu, G. Berthomé, F. Maillard, M. Chatenet, J.-Y. Sanchez, *J. Electrochem. Soc.* 154 (2007) B1106.
- [285] J. Xie, D.L. Wood, K.L. More, P. Atanassov, R.L. Borup, *J. Electrochem. Soc.* 152 (2005) A1011.
- [286] J. Xie, D.L. Wood, D.M. Wayne, T.A. Zawodzinski, P. Atanassov, R.L. Borup, *J. Electrochem. Soc.* 152 (2005) A104.
- [287] Z. Xie, T. Navessin, K. Shi, R. Chow, Q.P. Wang, D.T. Song, B. Andreus, M. Eikerling, Z.S. Liu, S. Holdcroft, *J. Electrochem. Soc.* 152 (2005) A1171.
- [288] C.A. Reiser, L. Bregoli, T.W. Patterson, J.S. Yi, J.D.L. Yang, M.L. Perry, T.D. Jarvi, *Electrochem. Solid-State Lett.* 8 (2005) A273.
- [289] J.P. Meyers, R.M. Darling, *J. Electrochem. Soc.* 153 (2006) A1432.
- [290] H. Tang, Z. Qi, M. Ramani, J.F. Elter, *J. Power Sources* 158 (2006) 1306.
- [291] M. Cai, M.S. Ruthkosky, B. Merzougui, S. Swathirajan, M.P. Balogh, S.H. Oh, *J. Power Sources* 160 (2006) 977.

13 Carbon Materials in Photocatalysis

JOAQUIM LUÍS FARIA and WENDONG WANG

13.1 INTRODUCTION

Heterogeneous photocatalysis is widely recognized as an effective technology for treating waters containing some refractory organic compounds. The degradation of organics is normally accomplished in the presence of titanium dioxide (TiO_2), the most popular photocatalyst, due mainly to its strong oxidizing power, high chemical stability, and relative inexpensiveness [1].

In photocatalytic reactions, TiO_2 is generally suspended in the liquid phase using slurry reactors. From a fundamental point of view, analysis of the heterogeneous photocatalytic process in such systems requires the determination of all physical parameters governing the kinetics: the mass of catalyst, the wavelength and radiant flux of irradiating source, the quantum yields or turnover numbers of the photocatalytic process, the initial concentration of reactants, and the influence of oxygen pressure and temperature [2]. From a practical point of view, filtration of TiO_2 fine particles and effective absorption of ultraviolet–visible (UV-vis) radiation are the usual shortcomings of the process. As a first approach to facilitating the use of TiO_2 as a photocatalyst, immobilization on a suitable substrate is desired. Therefore, a great deal of effort has been taken to increase the photoefficiency by dispersing TiO_2 over high-surface-area materials. Due to their unique pore structure, adsorption capacity, acidity, and electronic properties, carbon-based materials of different origins can be used for this purpose, for use in either the liquid or gas phase. It was also found that by introducing materials derived from carbon in a TiO_2 matrix, a beneficial effect in the photocatalytic activity of the TiO_2 can be obtained, in addition to the dispersion induced.

In this chapter we list the different carbon materials used to modify TiO_2 , aiming at producing more efficient photocatalysts. After that we describe the synthesis procedures currently used to produce the composite catalysts containing

carbon and TiO_2 phases. Applications of photocatalysis with special incidence in the photodegradation of organic pollutants, in either the liquid or gas phase, are described in subsequent sections. The role of carbon and its interaction with the TiO_2 phase in the composite catalyst concerning the mechanisms involved in heterogeneous photocatalysis are discussed in the final section.

13.2 CARBON MATERIALS EMPLOYED TO MODIFY TiO_2 IN PHOTOCATALYSIS

Carbon materials, with various forms and properties, have been recognized to play an increasingly important role in heterogeneous catalysis processes as an adsorbent, catalyst support, or even a catalyst on its own. Conventional carbon forms, including activated carbon, carbon black, and graphite, as well as graphitized materials, have long been used in heterogeneous catalysis [3], especially as supports for precious metal–loaded catalysts [4], due to their specific characteristics of stability in both acid or basic media, tunable texture and surface chemistry, and easy recovery of precious metals for economic use. Recently, new carbon forms, such as carbon nanotubes (CNTs) and graphite nanofibers or nanofilaments, were found to be very attractive and competitive in catalytic processes, due to the combination of their electronic, adsorption, mechanical, and thermal properties (for a representative review, see ref. 5). In addition to these, some other carbon forms (e.g., fullerenes, pyrolytic carbon, coke, polymer-derived carbon, and those derived from other physicochemical processes) are also valuable in catalytic processes either as supports, adsorbents, or as catalysts themselves. Most of these have been combined with TiO_2 to increase efficiency in the heterogeneous photocatalytic process.

13.2.1 Activated Carbon

Since the early attempts to modify TiO_2 with carbon materials in which activated carbon (AC) was used as support or adsorbent in applications of photocatalytic decomposition of organic amides in dilute aqueous solution [6] and removal of low-concentration pollutants from air [7], a number of research groups continued their investigations on the AC– TiO_2 system during the past decade. Yoneyama and co-workers have studied the effect of AC content [8] and compared AC with different inert adsorbent supports (including zeolites, alumina, silica, etc.) [9–12]. Herrmann, Matos, and co-workers examined the synergy effects between TiO_2 and AC of different origins on the photocatalytic degradation of model pollutants [13–20]. Araña, Colón, et al. demonstrated TiO_2 activation by using AC [21–24] and the preparation of TiO_2/C samples with active carbon as additive [25–27]. Faria and co-workers focused on the photodegradation of different azo dyes by using TiO_2 –AC composite catalysts [28–30]. Tryba et al. prepared TiO_2 -mounted AC for the photocatalytic removal of phenol [31,32]. Lu et al. investigated the photocatalytic oxidation of propoxur insecticide with TiO_2 supported on AC [33,34]. Ao et al. identified the combined effect of AC and TiO_2

for the photodegradation of pollutants at typical indoor air levels [35,36]. Lee et al. employed TiO₂-coated granular AC for the removal of toxic microcystin-LR from water [37,38]. Li et al. observed a higher efficiency for photodegradation of Rhodamine B and methyl orange over TiO₂-coated AC [39–42]. Zhang et al. [43–46] and Ding et al. [47] applied the chemical vapor deposition method to the preparation of TiO₂ coated on AC. Liu et al. combined AC and TiO₂ from the point view of AC regeneration [48–50]. More examples on the use of TiO₂ and an AC system with respect to the preparation procedure [51,52], and descriptions of the photodegradation behavior in the liquid phase [53–76] and gaseous phase [77,78] are to be found in the recent literature.

13.2.2 Carbon Black and Graphite

Except for recent applications in fuel cell catalysts, neither carbon black (CB) nor graphite is commonly used as a catalyst support [4]. In the case of photocatalysis, examples of the use of TiO₂ and CB or a graphite system, are much less frequent than examples of activated carbon. Yoneyama and co-workers compared CB with other adsorbents as a support for TiO₂ applied to the photodecomposition of propyzamide and bromoform [79,80]. Rincon et al. employed nanometric CB to sensitize sol–gel-derived TiO₂ in comparison with physical mixtures [81,82]. Li et al. [83] and Yu et al. [84] examined the photocatalytic activity and stability over CB-modified nanosized TiO₂ films. There are several research studies dealing with TiO₂-exfoliated graphite composite photocatalyst [85–87] and the preparation of TiO₂/graphitized carbon [88].

13.2.3 Carbon Fiber

Most of the works concerning the TiO₂ and carbon fiber (CF) system are carried out by using activated carbon fiber (ACF), normally in the form of felt or cloth with high surface area and uniform microporous texture. Yamashita and co-workers designed a TiO₂/ACF system by an ionized cluster beam method [89–91]. Yuan et al. immobilized TiO₂ on ACF in application to photocatalytic removal of methylene blue and phenol [92–94]. More researches on the CF-modified TiO₂ for photocatalysis have been realized over TiO₂/carbon molecular sieve fibers [95], helical TiO₂/carbon microcoils [96,97], TiO₂/ACF [98–101] and TiO₂ with other carbon fibers [72,102,103].

13.2.4 Carbon Nanotubes

Carbon nanotubes, generally in the form of multiwalled carbon nanotubes (MWCNTs) and single-walled carbon nanotubes (SWCNTs), may exhibit specific adsorption and electronic properties in comparison with activated carbon, due primarily to their peculiar morphology, the role of defects, the probability of opening or closing of the tubes, and so on [5], which are believed to induce cooperative or synergistic interactions between metal or metal oxide

and carbon phases. A few investigations have been devoted to the synthesis and characterization of TiO_2 –SWCNT [104–110] and TiO_2 –MWCNT [111–124] nanoscale heterostructures. In the case of the TiO_2 and CNT system applied to photocatalysis, enhancements on photocatalytic degradation were reported early by Wang et al. [125] and Yu et al. [126,127] respectively.

13.2.5 Other Forms of Carbon

In addition to those forms of carbon materials mentioned above that are ready or commercially available prior to being introduced into the TiO_2 matrix, there are plenty of works dealing with the introduction of amorphous carbon, or carbon doping, into TiO_2 . This is normally accomplished by (1) carbonizing different carbonaceous species deposited on the surface of TiO_2 ; (2) pyrolyzing precursors containing Ti and carbon; or (3) heating or combusting Ti/TiO_2 in a carbonaceous gas atmosphere. Carbon materials can be derived from the carbonization of resorcinol–formaldehyde polymers [128–131], cellulose [87,132–134], poly(vinyl alcohol) or poly(ethylene terephthalate) [133–144], *n*-hexane [145–147], sucrose [148,149], glucose [150], citric acid [151], poly(divirylbenzene) [152], and commercial Sephadex G-100 beads [153]. Carbon materials have been introduced into TiO_2 by combustion of Ti metal in a natural gas flame [154], thermal acetylene treatment [155], heat treatment of the hydrolysis product from Ti precursors and tetrabutylammonium hydroxide [156–159], oxidation of TiC [160–163], calcination of thiourea and urea with TiO_2 [164–166], spray pyrolysis of Ti and carbonaceous precursors [167–169], dc reactive sputtering on a Ti target in $\text{Ar}/\text{N}_2/\text{CO}_2$ ambient [170], ion-assisted electron-beam evaporation [171], carbothermal reduction of TiO_2 [172], and a microemulsion–hydrothermal process [173]. Carbon-modified TiO_2 photocatalysts have also been fabricated by carbonizing TiO_2 –woody composites [174,175], low-temperature treatment of titanium alkoxide or TiO_2 with various alcohols [176–181], heating Ti precursors in the vapor of cyclohexane [182] or ethanol [183–185], combustion of Ti precursors and various fuels [186–188], and pyrolysis of titanium oxyacetyl acetonate [189].

13.3 SYNTHESIS AND CHARACTERIZATION OF CARBON– TiO_2 COMPOSITES

The photocatalytic processes efficiencies of TiO_2 are determined largely by its microstructure and physicochemical properties, such as surface area, particle size, pore volume and pore size distribution, crystal structure and crystallinity, phase composition, surface hydroxyl groups, and bandgap energy, among others, which have strong effects on its adsorption ability and recombination probability of the active photocatalysts during the photocatalytic processes. In the case of carbon-modified TiO_2 photocatalysts, the synergy effects between TiO_2 and carbon depend not only on the different carbon materials employed to modify

TiO₂, but also on the different approaches used to introduce carbon materials into TiO₂–carbon composites. These approaches may be described in detail in terms of the following subcategories, based on the origin of TiO₂ and carbon, as well as the way they are combined in the composites.

13.3.1 Mechanical Mixture of TiO₂ and Carbon Materials

One of the simplest and somewhat effective approaches may be implemented by mechanic mixing of TiO₂ with carbon materials. Both components in the TiO₂ and carbon system are already in their final forms prior to being put together. In this case, TiO₂ and different carbon materials may be mechanically mixed before applying to photoreactions [7,13–20,28,29,60,66–68,82,126], or they are both dispersed in a liquid medium with or without some additives to facilitate the mixing process [21–24,33–36,48,74,76,85,86,92–94,99,105,119,120,122,190,191].

13.3.2 TiO₂ Coated or Loaded on Carbon Materials

To achieve more homogeneous TiO₂ particles over carbon materials, the latter may be immersed in solutions containing the titanium soluble precursors, aged, and then subjected to various heat treatments to produce TiO₂ coated or loaded on carbon materials. TiO₂–carbon composites have been prepared in such a way by various techniques. The sol–gel process [6,8–12,25–27,30,37–41,50,55,63,69–75,77–84,97,103,110,111,116,117,123,125,192–196], generally with alkoxide precursors, is one of the most widely adopted, which may provide a versatile synthetic route with modifiable operation conditions and variables, and thus can be adjusted to produce TiO₂ with tailored morphological features. Other techniques involve mainly controlled hydrolysis of titanium precursors [10,31,32,42,59,61,64,88,95,101,104,107,112–115,118,127,152], improved hydrothermal or solvothermal processes [49,65,131,196,197], chemical vapor deposition (CVD) [43–47,52,96,97,108,124] or a vapor-phase method [100,121], the ionized cluster beam (ICB) method [89–91], liquid-phase deposition or impregnation [51,102,153], and TiO₂ coating on a functionalized CNT surface [106,109].

13.3.3 Carbon Materials Coated or Deposited on TiO₂

As an alternative way, carbon has been loaded on TiO₂ particles. This can be put in practice through the introduction of carbonaceous precursors on the TiO₂ particles formed, and subsequent carbonization to produce TiO₂–carbon composites. The carbon materials, derived from various carbonaceous precursors, have been practically introduced by means of thermal treatment in *n*-hexane, ethanol, or cyclohexane vapor [145–147,182–185] and carbonization of a mixture of TiO₂ with poly(vinyl alcohol), poly(ethylene terephthalate), cellulose, sucrose, or citric acid [87,132–144,148,149,151]. A chemical vapor deposition method was also used to prepare MWCNTs deposited on TiO₂ [198].

13.3.4 Other Approaches and Concurrent Synthesis of TiO₂–Carbon Composites

Apart from the approaches above using formed TiO₂ and/or carbon materials, TiO₂–carbon composites have been synthesized by the heat treatment of precursors containing both Ti and carbon phases. This may result in obtaining the TiO₂ and carbon materials concurrently or chemically modified TiO₂ with carbon, which may feature more homogeneous dispersion and intimate contact between these two phases. Various methods have been attempted to prepare carbon-doped TiO₂, such as combustion [154,186–188] or spray pyrolysis [168,169] of Ti precursors with carbonaceous materials, oxidation of TiC [160–163], hydrolysis of TiCl₄ in the presence of tetrabutylammonium hydroxide followed by calcination [156–158], hydrothermal method [150], and supersonic cluster beam deposition possess [172]. Other carbon-containing TiO₂ composites were obtained from polymerization of a mixture of resorcinol, formaldehyde, and tetrabutyl orthotitanate [128,129], heat treatment of the sol–gel product from titanium alkoxide [176–180], and single-step pyrolysis of titanium oxyacetyl acetonate [189]. Additionally, carbon and nitrogen (or sulfur, iron) co-doped TiO₂ were also synthesized [159,164–167,170,173,181].

13.3.5 Methods of Characterization

The BET surface area and pore size distribution of samples can be obtained from N₂ adsorption–desorption isotherm measurements. The surface area of TiO₂ derived from the sol–gel process depends strongly on the temperature of the final heat treatment. At midtemperature around 673 K, the samples feature a relatively high surface area (about 100 m²/g) and a mesoporous pore texture; high temperature (more than 873 K) may result in a macroporous or even nonporous solid with a rather low surface area [26,30]. Mechanically mixing TiO₂ and carbon hardly induces any changes in the surface area and pore texture of the materials. In the case of TiO₂ loaded on carbon by the sol–gel method, the experimentally determined surface area may be greater or smaller than estimated theoretically (in proportion to the carbon and TiO₂ contents), depending on the nature of the carbon phase [30,194]. However, composites of carbon materials coated on TiO₂ exhibit a much smaller area than neat TiO₂ [138,139].

The composition of TiO₂ crystalline phase in carbon–TiO₂ composites can be analyzed by powder x-ray diffraction (XRD). TiO₂ crystallite size can be estimated from XRD patterns using Scherrer's equation. The low-temperature sol–gel route leads mainly to the formation of TiO₂ anatase, while increasing the calcination temperature leads to an increase in formation of TiO₂ rutile phase. The introduction of carbon materials into the TiO₂ matrix may slow down crystallite growth and suppress the phase transformation from anatase to rutile [25,27,30,40,125,127].

UV-vis spectra of carbon–TiO₂ composites produces strong changes in photoavailability beyond the spectral region of the neat TiO₂ absorbance [23,30,94,125,138,152,176,189], also observed in the case of carbon-doped

TiO_2 with a rather low carbon content [154–158]. This may be indicative of an increment of TiO_2 surface electric charge in the composites, related directly to the presence of the carbon phase.

Scanning electron microscopy (SEM) and transmission electron microscopy (TEM) are used to study the morphology and microstructure of carbon– TiO_2 composites. In the case of CNT– TiO_2 composites, observations on CNT embedded in TiO_2 matrix [111,115] and fine coating of TiO_2 on a CNT surface [107,112–114,116,117] are reported.

Infrared spectroscopy can be used to get an insight on the surface binding within carbon– TiO_2 composites. The infrared spectra of carbon– TiO_2 composites show evidence for chemical interaction between surface hydroxyl groups of TiO_2 particles to the carbon phase and between the surface oxygen-rich groups of carbon material to the metal via the formation of some insipient binding [18,23,84,106,113,119,181].

X-ray photoelectron spectroscopy (XPS) is used to probe the chemical environment of the elements in the near-surface range of carbon– TiO_2 composites. Titanium cations in the composites can be found in oxidation state IV, as in stoichiometric TiO_2 [100,123,129,150,172,188,193]. The XPS data support the formation of surface oxygen groups, with different carbon valences, on the surface of the carbon phase [100,116–118,123,129,150,159,181,188,193].

In addition, there are some other characterization techniques that can be used to examine the carbon– TiO_2 composites, including Raman spectroscopy [40,123], atomic force microscopy (AFM) [106,123], thermogravimetric and differential thermal analysis (TGA-DTA) [26,125], determination of pH_{PZC} [19,29], and electron paramagnetic resonance (EPR) [126,127].

In heterogeneous photocatalysis experiments, especially in reactions dealing with water detoxification and gaseous pollutant removal, the disappearance of target chemicals, the degree of mineralization of total organic carbon (TOC), and the reaction intermediates can be detected by spectroscopic optical methods (UV-vis and IR), TOC measurements, and chromatographic analysis.

13.4 PHOTODEGRADATION ON CARBON-CONTAINING SURFACES

The composites described in the preceding sections are normally thought to be environmentally friendly catalysts, due especially to their nature and composition. Their main application is in one area of great actuality, which is the development of water and air treatment systems based on heterogeneous photocatalysis.

13.4.1 Heterogeneous Photocatalysis in the Liquid Phase with Carbon– TiO_2 Composites

In early reports, AC as a support for TiO_2 in photocatalytic degradation reactions attracted the attention of some groups in relation with the photomineralization of a herbicide (propyzamide) in dilute aqueous solution [6]. In this work the

high adsorption capacity of the AC support was found to be responsible for concentrating the organic molecule around the supported TiO₂, thus leading to a high photocatalytic degradation rate. The photodecomposition of propyzamide in aqueous solution was also investigated using TiO₂–carbon black composite films [79]. It was found that the photodecomposition rate was influenced largely by the content of carbon black in the photocatalyst film. Several works were then developed with different model compounds within the same line of research [8,10,12,79,80]. In all these pioneering works, the most striking feature observed was that conversion of the organic pollutant was drastically enhanced by inclusion of the carbon phase up to an optimal value, beyond which the photocatalytic activity showed a decreasing tendency. The increase in photodecomposition was rationalized in terms of the increase in adsorbability of the pollutant for the carbon–TiO₂ material. Not surprisingly, most of these works appeared at the same time as the most cited text by Rodriguez-Reinoso on the role of carbon materials in heterogeneous catalysis [3].

Since then, materials containing TiO₂ and carbon phases have been referred for the photocatalytic degradation of aqueous solutions of several model molecules followed, including phenol and phenol derivatives [13,15,17–20,22,26,27,31,32,48–50,52,60,68,69,72,74,75,93,99,115,125,138,140,145,147,158,166,176,183,184,187–189,193,194], other molecules of humic acids class [53], phenoxyacetic acids [85,86], insecticides or pesticides [16,33,34,147,150], and dyes, especially those used in the textile industry [28,29,42,63,68,76,81,82,85,105,122,126,137,148,184,185], just to cite a few representative examples.

The advantages or beneficial effects introduced by the carbon phase are often described in terms of a synergy factor (*R*) defined by Matos et al. [14]. This factor has been used by many authors, as the ratio between the apparent first-order rate constants measured for the composite catalyst containing both phases and just for bare TiO₂:

$$R = \frac{k_{\text{app}}(\text{TiO}_2 + \text{C})}{k_{\text{app}}(\text{TiO}_2)} \quad (13.1)$$

Although it can reasonably be well quantified within a certain set of experiments, this factor is very difficult to use as an independent standard to compare the results in different works of photocatalytic degradation performances (of carbon-modified TiO₂). The main issue relates to the way that the kinetic parameters are obtained.

The rate of photoconversion in a heterogeneous process is normally expressed in terms of a limited number of variables that should include the concentrations of the species present, the reactor volume, and the amount of catalyst irradiated in this particular volume. In the case of the immersion well-stirred photochemical reactor, currently used in photocatalytic experiments, the rate (*r*) expression for photoconversion is given by [199]

$$r = \frac{V}{W_{\text{irr}}} \frac{dC}{dt} \quad (13.2)$$

with V the reaction volume, W_{irr} the unit weight of irradiated catalyst, and C the instantaneous concentration at a given time t . Several assumptions are enclosed in this simple expression. First, it assumes that W_{irr} is known. However, care should be taken, since the same weight of catalyst does not mean the same number of illuminated active sites, in particular in the case of biphasic materials with a variable interface. Sometimes this can be replaced by a more meaningful external area of irradiated catalyst (A_{irr}). Second, it is assumed that the illuminated section of the reactor is uniform and a quasiconstant reaction rate can be assumed. This will require the absence of mass-transfer limitations, uniform light scattering, therefore good fluid circulation and effective mixing, which can barely be inferred in many of the published reports. In addition, the irradiated volume (V_{irr}) is not necessarily identical to the reaction volume. Consequently, the conversion observed for a given organic substrate, such as phenol (the most used model compound), in a specific reactor geometry depends on the weight (or area) of catalyst irradiated and volume of mixture illuminated. The kinetic parameters should then be subjected to corrections if they are meant to be used in comparative studies. Different from true rate constants (k), the rate constant derived from equation (13.2) can be expressed in terms of apparent rate constants (k_{app}) defined according to the referred parameters [199]:

$$k_{app} = k'_{app} \frac{V_{irr}}{V} = k''_{app} \frac{A_{irr}}{V} = k \frac{W_{irr}}{V} \quad (13.3)$$

Used properly, these parameters can give a good account on the synergy induced by the carbon phase present in the catalyst.

It can be shown that different synergy factors are obtained for different AC, suggesting that the properties of the carbon phase may play a significant role on the photoefficiency of TiO_2 . Four different carbons were used in the photocatalytic degradation of a commercial azo dye [28]: a chemically activated granular carbon (Norit C GRAN) with high adsorptive capacity and a BET surface area of $1400\text{ m}^2/\text{g}$ (AC1); a steam-activated granular carbon (Norit GAC 1240 Plus) with good adsorption properties and a BET surface area of $1000\text{ m}^2/\text{g}$ (AC2); another steam-activated extruded carbon (Norit ROX 0.8) with a BET surface area of $1100\text{ m}^2/\text{g}$ (AC3); and finally, a sample named as AC4 resulting from AC3 oxidation with a 10 M solution of H_2O_2 at room temperature with a BET area of $908\text{ m}^2/\text{g}$. The kinetics of dye degradation followed an apparent first-order rate; thus, it is reasonable to evaluate the efficiency of the process based on this kinetic parameter. The extent of the effect observed is quantified in terms of the synergy factor [as defined by equation (13.1)] and depends clearly on the type of AC used (Figure 13.1).

Comparing the various carbon phases, the more pronounced effect ($R = 2.0$) was observed for AC1, which corresponds to a carbon with a very open structure, hence being especially effective to adsorb heavier and large organic molecules. The degree in which adsorption may contribute to the synergy can be evaluated by determining the corresponding adsorption equilibrium constant, defined by the ratio between the adsorption and desorption rate constants ($K = k_{ads}/k_{des}$).

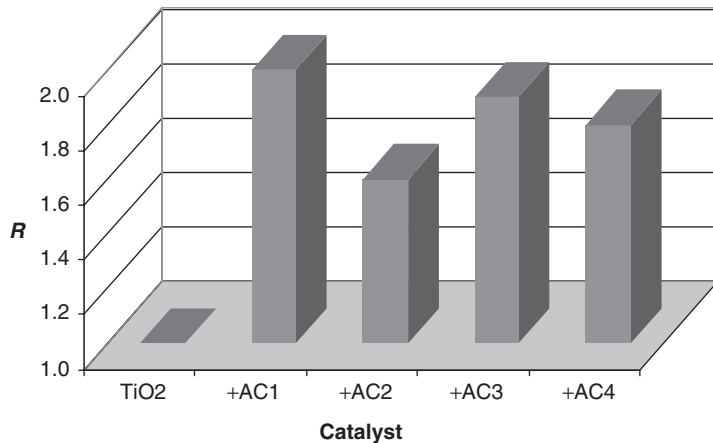


Figure 13.1 Synergy factor in photocatalytic experiments using composite TiO₂ + AC catalysts for the degradation of an azo dye. (For the meaning of the carbon phase, AC1–4, see the text.) (From ref. 28.)

If the rate of degradation is identified with the true rate constant (k) of the Langmuir–Hinshelwood kinetic model, the determination of K is straightforward:

$$r = k\theta = \frac{kKC}{1 + KC} \quad (13.4)$$

In this expression, θ is the fractional surface coverage defined by the Langmuir isotherm expression. The model assumes that a fast adsorption equilibrium is established [equation (13.5)] and the rate-controlling step is the desorption of the adsorbed products [equation (13.6)]:



In photochemical experiments, this very simple approach may be compromised if desorption of the reactants is fast, in that reactant adsorption–desorption equilibrium is not established during the reaction [then equation (13.5) does not hold]. In addition, active center reactivity is continuous because of continuous illumination; thus, no equilibrium is established. This may lead to the derivation of a pseudo-steady-state kinetic model [200,201] with a rate expression slightly different from equation (13.4), the discussion of which is, however, out the scope of this work.

Documenting the beneficial effects of AC on the photocatalytic activity of TiO₂ and recognizing CNTs as an attractive and competitive catalyst support [5] prompted a series of experiments using biphasic materials composed of CNT

and TiO_2 . A first attempt was successful in coating CNT with TiO_2 and alumina by a simple colloidal processing method, but failed to demonstrate the cooperative effect of CNT-coated TiO_2 [115]. The materials showed the same photoactivity as that of TiO_2 , the only advantage being in their separation from solution and subsequent reuse. Composites containing CNTs are now believed to provide many applications and exhibit synergistic effects between the metal oxide and the carbon phase. Efficient degradation of phenol and azo dyes, paralleled by effective TOC abatement of the corresponding aqueous solutions, is now well documented in the presence of TiO_2 -MWCNT materials [126,193–195]. Using ultrasonic irradiation, composites of TiO_2 -CNT with different molar ratios proved to be efficient in the degradation of acetone [127]. The content of CNTs is related directly to the efficiency to a certain extent. An excessive amount of CNT blocks TiO_2 's absorbing capacity above a given threshold, thus defining an optimal ratio of TiO_2 to CNTs.

Also reported are other liquid-phase photodegradation reactions over TiO_2 -MWCNT concerning humic substances [190], copper sulfophthalocyanine [197], and over TiO_2 -SWCNT in relation with the photo-oxidation of methanol in sulfuric acid as supporting electrolyte [191].

13.4.2 Heterogeneous Photocatalysis in the Gas Phase with Carbon- TiO_2 Composites

The number of heterogeneous photocatalysis works in the gas phase with carbon-modified semiconductor materials is much lower than in the liquid phase, probably due to the experimental constraints involved. Following the initial works in the liquid phase, the first reports on the use of activated carbon as a support for TiO_2 started to appear. One of the first was on the oxidation of nitric oxide (NO) to nitric acid (HNO_3) and nitrogen dioxide NO_2 under ultraviolet light illumination [7]. During the process, AC adsorbed efficiently the NO_2 formed. The AC- TiO_2 mixture proved to be an excellent photo-assisted catalyst for the removal of low-concentration (sub-ppm) NO_x from air. Although the catalytic activity decreased with the reaction time, the catalyst was very efficiently recovered by simple washing with water.

Another pioneering work concerning the photocatalytic decomposition of propionaldehyde in the gas phase used several kinds of supports for TiO_2 , including activated carbon [9]. This work was very important from the standpoint of establishing the dependency of the photocatalytic activity on the nature of inert supports used. It was clearly demonstrated that when the adsorption constant was low, the decomposition rate was determined by the amount of adsorbed substrate; while when the adsorption constant was very high, there was plenty of adsorbed substrate on the support, which was not transferred efficiently to loaded TiO_2 .

Heterogeneous photocatalysis for the control of organic volatile compounds in the indoor and outdoor environment is also an active area of research [202]. At the present time, contributions using metal oxide modified with carbon composites are still scarce. A sheet material with TiO_2 photocatalyst supported on

activated carbon fiber for a compact deodorization system was reported [98]. In this system, malodorants were collected on the TiO₂/ACF sheet by adsorption and then decomposed by photocatalysis.

Other recent reports include photocatalytic disinfection [203], photocatalytic H₂ evolution from water [198], and photocatalytic reduction of CO₂ with H₂O [196]. A list of representative examples of carbon–TiO₂ composite photocatalysts and their applications to photodegradation reactions is given in Table 13.1.

13.5 ROLE OF THE CARBON PHASE IN HETEROGENEOUS PHOTOCATALYSIS

In early works, the observed synergistic effect was ascribed to the preferential adsorption of the organic molecule on AC, followed by surface transfer to TiO₂ [13,14]. The adsorption equilibrium constant of aromatics such as phenol on AC is more than one order of magnitude greater than in bare TiO₂. After accumulation of the organic over the carbon phase, the driving force for surface diffusion is the gradient on surface concentration between the two phases. To achieve effective transfer, there must be a close contact interface between the two solid phases. In such a way, the organic is transferred from the AC to the TiO₂ and then undergoes immediate photocatalytic degradation, which originates the synergistic effect.

Of course, when irradiation takes place at wavelengths shorter than the absorption edge of the TiO₂ ($\lambda < 400$ nm, $E_G = 3.02$ eV), it is impossible to quantify the effect on exciting the carbon phase. This is because below that threshold both phases compete for photon absorption. However, when the light used is in the range $\lambda > 400$ nm, photodegradation can arise only from a photosensitized process [176]. In this case, two major pathways can be considered: (1) the carbon phase acts as a photosensitizer without the contribution of TiO₂; and (2) the carbon phase is excited and transfers an electron to the conduction band of the TiO₂, triggering the conventional semiconductor photocatalysis (for recent reviews on the subject, see [204,205]). The experiments described [176] were carried out using a coke-containing TiO₂ catalyst in which the carbon phase can be considered to be rather isotropic; therefore, photosensitization is expected to be rather inefficient.

When functionalized CNT are used as a carbon phase in the composite catalysts, photosensitization is expected to contribute to enhance the photoactivity more efficiently. The photodegradation of phenol in aqueous suspension in the presence of a MWCNT–TiO₂ composite catalyst under visible light was found to follow a pseudo-first-order kinetics, and a synergy factor of 1.8 was measured [194]. In this case, the synergistic effect of MWCNT on the activity of the composite catalysts was explained in terms of its action mainly as a photosensitizer and partially as an adsorbent. An additional role as dispersing agent preventing TiO₂ from agglomeration was also accounted. Since the gradual increase in the amount of MWCNT in the composite catalysts does not provide a significant increase in their adsorption capacities (measured in terms of the adsorption

Table 13.1 Summary of Representative Examples of Carbon–TiO₂ Composite Photocatalysts and Their Applications to Photodegradation Reactions

Type of Catalyst	Materials and Preparation Procedure	Photocatalytic Reaction Tested	Summary of Results and Comments on Activity	Ref.
AC–TiO ₂	TiO ₂ loaded on AC by adding AC to TiO ₂ colloid from Ti tetraisopropoxide	Photodegradation of propyzamide in aqueous solution under the illumination of a xenon lamp	The use of AC as a support for TiO ₂ photocatalysts resulted in a high photodegradation rate, due to high adsorptive activity of the AC.	6
Mechanical mixing of TiO ₂ P-25 and AC		Photodegradation of phenol in aqueous solution under UV light	Addition of AC to TiO ₂ could induce a substantial synergy effect, explained by adsorption of phenol on AC followed by mass transfer to photoactive TiO ₂ .	13
Mechanical mixing of TiO ₂ P-25 and various AC with further treatments		Photodegradation of the Solophenyl Green BLE 155% dyestuff in aqueous solution under UV light	The presence of AC enhanced the photoefficiency of TiO ₂ . The mechanism of degradation was discussed in terms of TiO ₂ photosensitization by AC.	28
TiO ₂ loaded on AC by a modified sol–gel method from titanium alkoxide with AC as additive		Photodegradation of Chromotrope 2R dyestuff in aqueous solution under UV light	The composites exhibited higher activities than TiO ₂ P-25. The adsorption equilibrium and reaction rate constants were determined by a modified L–H model.	30

(continued overleaf)

Table 13.1 (Continued)

Type of Catalyst	Materials and Preparation Procedure	Photocatalytic Reaction Tested	Summary of Results and Comments on Activity	Ref.
CB-TiO ₂	CB-TiO ₂ composites obtained by the sol-gel route or a mechanical mixture from TiCl ₄ or commercial anatase and carbon black	Photodegradation of methyl violet (MV-8) in aqueous solution under UV light	The presence of CB as an adsorbent agent enhanced the adsorption abilities of photocatalysts. The sol-gel composite outperformed the mixture or TiO ₂ alone.	82
Graphite-TiO ₂	TiO ₂ P25-coated exfoliated graphite particles using methyl silicate binder	Photodegradation of rhodamine B dye and chlorophenoxyacetic acids in aqueous solution under a xenon lamp	A type of buoyant TiO ₂ -coated photocatalysts based on highly porous exfoliated graphite, exhibited 50 to 95% of the activity of supported photocatalyst film.	85
ACF-TiO ₂	TiO ₂ -coated ACF prepared by adsorption of TiCl ₄ vapor over ACF: a molecular adsorption-desorption method	Photodegradation of methyl blue (MB) in aqueous solution under UV light	The composite, combining photoactivity of TiO ₂ and adsorptive property of ACF, showed high reactivity in photodegradation of highly concentrated MB solution.	100
MWCNT-TiO ₂	TiO ₂ loaded on MWCNT by a modified sol-gel method from Ti tetrakisopropoxide with MWCNT as additive.	Photodegradation of phenol in aqueous solution under UV light	Synergistic effect was observed for the composite catalysts, which may be explained in terms of a strong interphase interaction between MWCNT and TiO ₂ .	125

Mechanical mixing of TiO_2 P-25 and MWCNT with various ratios	Photodegradation of PR-MX5B, PY-HE4R, and PR-HE3B azo dyes in aqueous solution under UV light	MWCNT can better improve the adsorption capacity, as well as the photocatalytic activity, of P-25 through the strong interaction between P-25 and MWCNT.	126
SWCNT– TiO_2	Composite prepared by mixing sol–gel-derived TiO_2 with SWCNT and an aqueous sodium dodecyl sulfate solution	Photo-oxidation of methanol in sulfuric acid under UV light with a composite as the supporting electrolyte	191
Carbon– TiO_2	Coke-containing TiO_2 obtained by low-temperature treatment of the gel from different Ti alkoxides	Photocatalytic degradation of 4-chlorophenol in an aqueous solution under visible light	176
Chemically modified carbon-doped TiO_2 prepared by controlled combustion of Ti metal in a natural gas flame	Photochemical water splitting under xenon lamp illumination using carbon– TiO_2 photoelectrodes	The carbon-doped TiO_2 had a much lower bandgap energy than rutile and performed water splitting with a total conversion efficiency of 11%.	154

(continued overleaf)

Table 13.1 (Continued)

Type of Catalyst	Materials and Preparation Procedure	Photocatalytic Reaction Tested	Summary of Results and Comments on Activity	Ref.
Carbon-TiO ₂ prepared by hydrolysis of TiCl ₄ with tetrabutylammonium hydroxide followed by calcination	Photodegradation of liquid-phase 4-chlorophenol and remazol red; of gas-phase CH ₃ CHO, CO, and C ₆ H ₆	The superior photocatalytic activities of carbon-doped materials was demonstrated by photodegradation tests under visible light and diffuse indoor daylight.	156	
A thin layer of carbon coating TiO ₂ obtained by mixing TiO ₂ with PVA carbon precursor and heating	Photodegradation of phenol in aqueous solution under UV light	Carbon-coated TiO ₂ increased phenol adsorption but hindered degradation process by weakening the energy of UV rays and diffusion of phenol to TiO ₂ surface.	138	

equilibrium constant), the synergistic effect cannot be due merely to MWCNT acting as an adsorbent.

Considering the semiconductive properties of MWCNT upon light absorption, transfer of the photo-induced electron (e^-) into the conduction band of the TiO_2 particles occurs (Figure 13.2). This electron transfer between the carbon phase and the metal oxide phase was observed experimentally by measuring the enhanced photocurrent in some other systems [104,105,176]. Simultaneously, a positive charged hole (h^+) might be formed by an electron migrating from the TiO_2 valence band to MWCNT.

The role played by MWCNTs is to provide electrons into the TiO_2 conduction band under visible light irradiation and to trigger the formation of very reactive radicals such as the superoxide radical ion $\text{O}_2^{\bullet-}$. Back electron transfer from adsorbed OH^- closes the electrocatalytic cycle and provides a source for the hydroxyl radical HO^\bullet , which is responsible for the degradation of the organic molecules (Figure 13.2).

Besides the electron transfer processes described, it should be stressed that the inclusion of MWCNTs in the TiO_2 matrix leads to a broader absorption of the catalyst toward the visible part of the spectrum [194]. If the absorption of low-energy photons is efficiently converted in charge separation at the

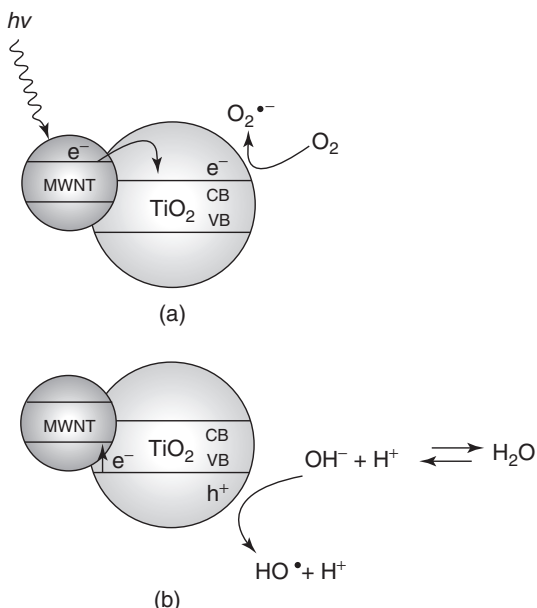
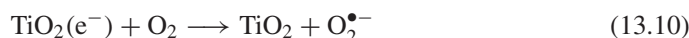
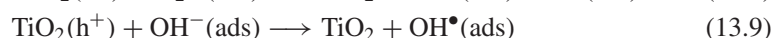
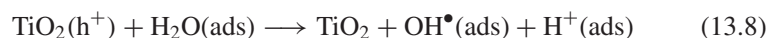
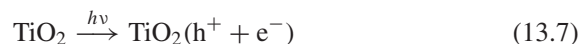


Figure 13.2 (a) MWCNT acting as photosensitizer in the composite catalyst in the process of electron injection into the conduction band of TiO_2 semiconductor; (b) electron back transfer to MWCNT following electron trapping by a hole in the valence band of TiO_2 . (From ref. 194, with permission.)

semiconductor phase (e^-/h^+ formation process, which initiates the photocatalytic mechanism), this will lead to an increase in the relative photonic efficiency of heterogeneous photocatalysis.

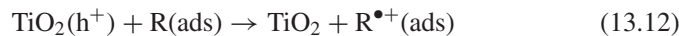
The reaction mechanism of photocatalytic degradation is believed not to be changed by the introduction of the carbon phase [17,18], thus proceeding by the electron transfer from the water solvent molecules (H_2O and OH^-) to the positively charged holes (h^+) forming the very oxidizing nonselective HO^\bullet radical on the surface of the catalyst [equations (13.7) to (13.9)]. Molecular oxygen, which must be present, is adsorbed on the surface of the catalyst and acts as an electron acceptor, forming the superoxide radical anion $O_2^{\bullet-}$ [equation (13.10)].



In the presence of an organic molecule, the HO^\bullet radical generated reacts by adduct formation, which then breaks down into several intermediates until, eventually, total mineralization:



If the organic reactant is able to compete with adsorbed oxygen and water molecules for the active sites of the photocatalyst, direct electron transfer to an active hole is also conceivable, as the first step of an oxidative degradation:



This overall process is commonly accepted [204,205] and can be described by a set of sequential and concurrent multielectron transfers. It should be noticed that the process was found to be pH dependent, not only because of equation (13.9) but also due to sensitivity of the solid–liquid interface to this parameter [206]. Finally, it should be inferred that the role of oxygen [206] can be more complex than suggested by equation (13.10) because many oxidizing chemical species can be generated from reaction of the $O_2^{\bullet-}$ radical anion with the water solvent or other intermediates.

13.6 CONCLUSIONS

Carbon phases can be used to support TiO_2 efficiently for application in heterogeneous photocatalytic processes. Besides facilitating the recovery and reuse of the photocatalysts, there is a significant increase in the photocatalytic activity, which can be measured in terms of a synergy factor. Particularly in the case of CNTs, this effect results from strong interphase interaction and can be rationalized in terms of the support acting as photosensitizer, adsorbent, and to a certain

extent as a dispersing agent. An additional advantage of these systems over conventional TiO₂ catalysts relates to the possible exploitation of wavelengths of the solar spectrum, as a result of broadening the absorption of the composite carbon–TiO₂ catalyst.

REFERENCES

- [1] A. Fujishima, T.N. Rao, D.A. Tryk, *J. Photochem. Photobiol. C* 1 (2000) 1.
- [2] M. Salaices, B. Serrano, H.I. de Lasa, *Chem. Eng. J.* 90 (2002) 219.
- [3] F. Rodríguez-Reinoso, *Carbon* 36 (1998) 159.
- [4] E. Auer, A. Freund, J. Pietsch, T. Tacke, *Appl. Catal. A* 173 (1998) 259.
- [5] P. Serp, M. Corriás, P. Kalck, *Appl. Catal. A* 253 (2003) 337.
- [6] H. Uchida, S. Itoh, H. Yoneyama, *Chem. Lett.* 22 (1993) 1995.
- [7] T. Ibusuki, K. Takeuchi, *J. Mol. Catal.* 88 (1994) 93.
- [8] T. Torimoto, Y. Okawa, N. Takeda, H. Yoneyama, *J. Photochem. Photobiol. A* 103 (1997) 153.
- [9] N. Takeda, T. Torimoto, S. Sampath, S. Kuwabata, H. Yoneyama, *J. Phys. Chem.* 99 (1995) 9986.
- [10] T. Torimoto, S. Ito, S. Kuwabata, H. Yoneyama, *Environ. Sci. Technol.* 30 (1996) 1275.
- [11] N. Takeda, M. Ohtani, T. Torimoto, S. Kuwabata, H. Yoneyama, *J. Phys. Chem. B* 101 (1997) 2644.
- [12] H. Yoneyama, T. Torimoto, *Catal. Today* 58 (2000) 133.
- [13] J. Matos, J. Laine, J.M. Herrmann, *Appl. Catal. B* 18 (1998) 281.
- [14] J. Matos, J. Laine, J.M. Herrmann, *Carbon* 37 (1999) 1870.
- [15] J.M. Herrmann, J. Matos, J. Disdier, C. Guillard, J. Laine, S. Malato, J. Blanco, *Catal. Today* 54 (1999) 255.
- [16] J.M. Herrmann, C. Guillard, *C.R. Acad. Sci. Ser. IIC* 3 (2000) 417.
- [17] J. Matos, J. Laine, J.M. Herrmann, *J. Catal.* 200 (2001) 10.
- [18] J. Matos, J. Laine, J.M. Herrmann, D. Uzcategui, J.L. Brito, *Appl. Catal. B* 70 (2007) 461.
- [19] T. Cordero, J.M. Chovelon, C. Duchamp, C. Ferronato, J. Matos, *Appl. Catal. B* 73 (2007) 227.
- [20] T. Cordero, C. Duchamp, J.-M. Chovelon, C. Ferronato, J. Matos, *J. Photochem. Photobiol. A* 191 (2007) 122.
- [21] J. Arana, J.A.H. Melian, J.M.D. Rodriguez, O.G. Diaz, A. Viera, J.P. Pena, P.M.M. Sosa, V.E. Jimenez, *Catal. Today* 76 (2002) 279.
- [22] J. Arana, J.M. Dona-Rodriguez, E.T. Rendon, C.G.I. Cabo, O. Gonzalez-Diaz, J.A. Herrera-Melian, J. Perez-Pena, G. Colon, J.A. Navio, *Appl. Catal. B* 44 (2003) 153.
- [23] J. Arana, J.M. Dona-Rodriguez, E.T. Rendon, C.G.I. Cabo, O. Gonzalez-Diaz, J.A. Herrera-Melian, J. Perez-Pena, G. Colon, J.A. Navio, *Appl. Catal. B* 44 (2003) 161.

- [24] J. Arana, J.M. Dona-Rodriguez, C.G.I. Cabo, O. Gonzalez-Diaz, J.A. Herrera-Melian, J. Perez-Pena, *Appl. Catal. B* 53 (2004) 221.
- [25] G. Colon, M.C. Hidalgo, J.A. Navio, *Catal. Today* 76 (2002) 91.
- [26] G. Colon, M.C. Hidalgo, M. Macias, J.A. Navio, J.M. Dona, *Appl. Catal. B* 43 (2003) 163.
- [27] G. Colon, M.C. Hidalgo, M. Macias, J.A. Navio, *Appl. Catal. A* 259 (2004) 235.
- [28] C.G. Silva, J.L. Faria, *J. Photochem. Photobiol. A* 155 (2003) 133.
- [29] C.G. Silva, W.D. Wang, J.L. Faria, *J. Photochem. Photobiol. A* 181 (2006) 314.
- [30] W.D. Wang, C.G. Silva, J.L. Faria, *Appl. Catal. B* 70 (2007) 470.
- [31] B. Tryba, A.W. Morawski, M. Inagaki, *Appl. Catal. B* 46 (2003) 203.
- [32] B. Tryba, A.W. Morawski, M. Inagaki, *Appl. Catal. B* 41 (2003) 427.
- [33] M.C. Lu, *J. Environ. Sci. Health B* 34 (1999) 207.
- [34] M.C. Lu, J.N. Chen, K.T. Chang, *Chemosphere* 38 (1999) 617.
- [35] C.H. Ao, S.C. Lee, *Appl. Catal. B* 44 (2003) 191.
- [36] C.H. Ao, S.C. Lee, *J. Photochem. Photobiol. A* 161 (2004) 131.
- [37] D.K. Lee, S.C. Kim, I.C. Cho, S.J. Kim, S.W. Kim, *Sep. Purif. Technol.* 34 (2004) 59.
- [38] D.K. Lee, S.C. Kim, S.J. Kim, I.S. Chung, S.W. Kim, *Chem. Eng. J.* 102 (2004) 93.
- [39] Y.J. Li, X.D. Li, J.W. Li, J. Yin, *Trans. Nonfer. Met. Soc. China* 14 (2004) 1232.
- [40] Y.J. Li, X.D. Li, J.W. Li, J. Yin, *Mater. Lett.* 59 (2005) 2659.
- [41] Y.J. Li, X.D. Li, J.W. Li, J. Yin, *Catal. Commun.* 6 (2005) 650.
- [42] Y.J. Li, X.D. Li, J.W. Li, J. Yin, *Water Res.* 40 (2006) 1119.
- [43] X.W. Zhang, M.H. Zhou, L. Lei, *Carbon* 43 (2005) 1700.
- [44] X.W. Zhang, M.H. Zhou, L.C. Lei, *Mater. Res. Bull.* 40 (2005) 1899.
- [45] X.W. Zhang, M.H. Zhou, L.C. Lei, *Mater. Chem. Phys.* 91 (2005) 73.
- [46] X.W. Zhang, M.H. Zhou, L.C. Lei, *Carbon* 44 (2006) 325.
- [47] Z. Ding, X.J. Hu, P.L. Yue, G.Q. Lu, P.F. Greenfield, *Catal. Today* 68 (2001) 173.
- [48] S.X. Liu, C.L. Sun, S.R. Zhang, *Chin. J. Catal.* 24 (2003) 355.
- [49] S.X. Liu, X.Y. Chen, X. Chen, C.L. Sun, *Chin. Chem. Lett.* 17 (2006) 529.
- [50] S.X. Liu, C.L. Sun, *J. Environ. Sci.* 18 (2006) 557.
- [51] J. Przepiorski, N. Yoshizawa, Y. Yamada, *J. Mater. Sci.* 36 (2001) 4249.
- [52] A.H. El-Sheikh, A.P. Newman, H. Al-Daffaee, S. Phull, N. Cresswell, S. York, *Surf. Coat. Technol.* 187 (2004) 284.
- [53] M. Bekbolet, F. Cecen, G. Ozkosemen, *Water Sci. Technol.* 34 (1996) 65.
- [54] J.B. Liu, J.C. Crittenden, D.W. Hand, D.L. Perram, *J. Environ. Eng. ASCE* 122 (1996) 707.
- [55] Y. Horie, M. Taya, S. Tone, *J. Chem. Eng. Jpn.* 31 (1998) 922.
- [56] M. Harada, M. Honda, H. Yamashita, M. Anpo, *Res. Chem. Intermed.* 25 (1999) 757.
- [57] K.M. Leonard, D. Setiono, *Adv. Environ. Res.* 3 (1999) U8.
- [58] M. Sheintuch, Y.I. Matatov-Meytal, *Catal. Today* 53 (1999) 73.
- [59] X.P. Li, F. Yin, Y. Lin, J.B. Zhang, X.R. Xiao, *Chin. Chem. Lett.* 12 (2001) 549.

- [60] S. Malato, J. Blanco, P. Fernandez-Ibanez, J. Caceres, *J. Sol. Energy Eng. Trans. ASME* 123 (2001) 138.
- [61] H. Tamai, N. Katsu, K. Ono, H. Yasuda, *J. Mater. Sci.* 37 (2002) 3175.
- [62] L.K. Zeng, M.H. Luo, L.H. Huang, H. Wang, X.S. Cheng, M. Zhang, *Rare Met. Mater. Eng.* 31 (2002) 458.
- [63] X.J. Huang, G. Ye, W. Liu, L.C. Wang, N.C. Cai, J.H. Liu, *Chin. J. Chem. Phys.* 16 (2003) 390.
- [64] C. Lu, P. Yang, Y.K. Du, N.P. Hua, H.Y. Song, *Chin. J. Catal.* 24 (2003) 248.
- [65] M. Toyoda, Y. Nanbu, T. Kito, M. Hirano, M. Inagaki, *Desalination* 159 (2003) 273.
- [66] S. Qourzal, A. Assabbane, Y. Ait-Ichou, *J. Photochem. Photobiol. A* 163 (2004) 317.
- [67] F.S. Zhang, J.O. Nriagu, H. Itoh, *J. Photochem. Photobiol. A* 167 (2004) 223.
- [68] Y. Gao, H.T. Liu, *Mater. Chem. Phys.* 92 (2005) 604.
- [69] E. Carpio, P. Zuniga, S. Ponce, J. Solis, J. Rodriguez, W. Estrada, *J. Mol. Catal. A* 228 (2005) 293.
- [70] A. Avraham-Shinman, Y. Paz, *Isr. J. Chem.* 46 (2006) 33.
- [71] T.A. Egerton, M. Janus, A.W. Morawski, *Chemosphere* 63 (2006) 1203.
- [72] Z. Kulesius, E. Valatka, *Pol. J. Chem.* 80 (2006) 335.
- [73] Y.P. Wang, L.J. Wang, P.Y. Peng, *J. Environ. Sci.* 18 (2006) 562.
- [74] M. Kubo, H. Fukuda, X.J. Chua, T. Yonemoto, *Ind. Eng. Chem. Res.* 46 (2007) 699.
- [75] Y.Z. Liu, S.G. Yang, J. Hong, C. Sun, *J. Hazard. Mater.* 142 (2007) 208.
- [76] A.K. Subramani, K. Byrappa, S. Ananda, K.M.L. Rai, C. Ranganathaiah, M. Yoshimura, *Bull. Mater. Sci.* 30 (2007) 37.
- [77] B. Huang, S. Saka, *J. Wood Sci.* 49 (2003) 79.
- [78] M. Nazir, J. Takasaki, H. Kumazawa, *Chem. Eng. Commun.* 190 (2003) 322.
- [79] N. Takeda, N. Iwata, T. Torimoto, H. Yoneyama, *J. Catal.* 177 (1998) 240.
- [80] H. Yoneyama, H. Kanemoto, N. Takeda, S. Torimoto, *Z. Phys. Chem./Int. J. Res. Phys. Chem. Chem. Phys.* 213 (1999) 43.
- [81] M.E. Rincon, M.E. Trujillo-Camacho, A.K. Cuentas-Gallegos, *Catal. Today* 107–108 (2005) 606.
- [82] M.E. Rincon, M.E. Trujillo-Camacho, A.K. Cuentas-Gallegos, N. Casillas, *Appl. Catal. B* 69 (2006) 65.
- [83] L.S. Li, W.P. Zhu, P.Y. Zhang, Z.Y. Chen, W.Y. Han, *Water Res.* 37 (2003) 3646.
- [84] G. Yu, Z.Y. Chen, Z.L. Zhang, P.Y. Zhang, Z.P. Jiang, *Catal. Today* 90 (2004) 305.
- [85] A. Modestov, V. Glezer, I. Marjasin, O. Lev, *J. Phys. Chem. B* 101 (1997) 4623.
- [86] K. Ramanathan, D. Avnir, A. Modestov, O. Lev, *Chem. Mater.* 9 (1997) 2533.
- [87] T. Tsumura, N. Kojitani, H. Umemura, M. Toyoda, M. Inagaki, *Appl. Surf. Sci.* 196 (2002) 429.
- [88] Z.B. Lei, Y. Xiao, L.Q. Dang, W.S. You, G.S. Hu, J. Zhang, *Chem. Mater.* 19 (2007) 477.

- [89] M. Harada, A. Tanii, H. Yamashita, M. Anpo, *Z. Phys. Chem./Int. J. Res. Phys. Chem. Chem. Phys.* 213 (1999) 59.
- [90] H. Yamashita, M. Harada, A. Tanii, M. Honda, M. Takeuchi, Y. Ichihashi, M. Anpo, N. Iwamoto, N. Itoh, T. Hirao, *Catal. Today* 63 (2000) 63.
- [91] H. Yamashita, M. Harada, A. Tanii, J. Misaka, H. Nakao, M. Anpo, *Mol. Cryst. Liquid Cryst.* 388 (2002) 453.
- [92] R.S. Yuan, R.B. Guan, W.Z. Shen, J.T. Zheng, *J. Colloid Interface Sci.* 282 (2005) 87.
- [93] R.S. Yuan, J.T. Zheng, R.B. Guan, Y.H. Liu, *New Carbon Mater.* 20 (2005) 45.
- [94] R.S. Yuan, J.T. Zheng, R.B. Guan, Y.C. Zhao, *Colloid Surf. A* 254 (2005) 131.
- [95] T. Reztsova, C.H. Chang, J. Koresh, H. Idriss, *J. Catal.* 185 (1999) 223.
- [96] S. Motojima, T. Suzuki, Y. Hishikawa, X.Q. Chen, *Jpn. J. Appl. Phys. Pt. 2* 42 (2003) L938.
- [97] S. Motojima, T. Suzuki, Y. Noda, A. Hiraga, S. Yang, X. Chen, H. Iwanaga, T. Hashishin, Y. Hishikawa, *J. Mater. Sci.* 39 (2004) 2663.
- [98] M. Nozawa, K. Tanigawa, M. Hosomi, T. Chikusa, E. Kawada, *Water Sci. Technol.* 44 (2001) 127.
- [99] C.M. Fan, Y.Q. Min, X.G. Hao, Y.P. Sun, X.J. Li, F.B. Li, *Trans. Nonfer. Met. Soc. China* 13 (2003) 452.
- [100] P.F. Fu, Y. Luan, X.G. Dai, *J. Mol. Catal. A* 221 (2004) 81.
- [101] B.Y. Jia, L.Y. Duan, C.L. Ma, C.M. Wang, *Chin. J. Chem.* 25 (2007) 553.
- [102] B. Herbig, P. Lobmann, *J. Photochem. Photobiol. A* 163 (2004) 359.
- [103] N. Keller, G. Rebmann, E. Barraud, O. Zahraa, V. Keller, *Catal. Today* 101 (2005) 323.
- [104] S. Banerjee, S.S. Wong, *Nano Lett.* 2 (2002) 195.
- [105] K.H. Jung, J.S. Hong, R. Vittal, K.J. Kim, *Chem. Lett.* 31 (2002) 864.
- [106] X.H. Li, J.L. Niu, J. Zhang, H.L. Li, Z.F. Liu, *J. Phys. Chem. B* 107 (2003) 2453.
- [107] J. Sun, M. Iwasa, L. Gao, Q.H. Zhang, *Carbon* 42 (2004) 895.
- [108] S. Orlanducci, V. Sessa, M.L. Terranova, G.A. Battiston, S. Battiston, R. Gerbasi, *Carbon* 44 (2006) 2839.
- [109] M.J. Pender, L.A. Sowards, J.D. Hartgerink, M.O. Stone, R.R. Naik, *Nano Lett.* 6 (2006) 40.
- [110] M.E. Rincon, M.E. Trujillo-Camacho, M. Miranda-Hernandez, A.K. Cuentas-Gallegos, G. Oromo, *J. Nanosci. Nanotechnol.* 7 (2007) 1596.
- [111] P. Vincent, A. Brioude, C. Journet, S. Rabaste, S.T. Purcell, J. Le Brusq, J.C. Plenet, *J. Non-Cryst. Solids* 311 (2002) 130.
- [112] K. Hernadi, E. Ljubovic, J.W. Seo, L. Forro, *Acta Mater.* 51 (2003) 1447.
- [113] Q. Huang, L. Gao, *J. Mater. Chem.* 13 (2003) 1517.
- [114] S.W. Lee, W.M. Sigmund, *Chem. Commun.* (2003) 780.
- [115] J. Sun, L. Gao, *Carbon* 41 (2003) 1063.
- [116] A. Jitianu, T. Cacciaguerra, R. Benoit, S. Delpeux, F. Béguin, S. Bonnamy, *Carbon* 42 (2004) 1147.
- [117] A. Jitianu, T. Cacciaguerra, M.H. Berger, R. Benoit, F. Béguin, S. Bonnamy, *J. Non-Cryst. Solids* 345–346 (2004) 596.

- [118] L. Chen, B.L. Zhang, M.Z. Qu, Z.L. Yu, *Powder Technol.* 154 (2005) 70.
- [119] W. Feng, Y.Y. Feng, Z.G. Wu, A. Fujii, M. Ozaki, K. Yoshino, *J. Phys. Condens. Matter* 17 (2005) 4361.
- [120] S. Kedem, J. Schmidt, Y. Paz, Y. Cohen, *Langmuir* 21 (2005) 5600.
- [121] W.G. Fan, L. Gao, J. Sun, *J. Am. Ceram. Soc.* 89 (2006) 731.
- [122] S.L. Kim, S.R. Jang, R. Vittal, J. Lee, K.J. Kim, *J. Appl. Electrochem.* 36 (2006) 1433.
- [123] X.B. Yan, B.K. Tay, Y. Yang, *J. Phys. Chem. B* 110 (2006) 25844.
- [124] H.T. Yu, H.M. Zhao, X. Quan, S. Chen, *Chin. Sci. Bull.* 51 (2006) 2294.
- [125] W.D. Wang, P. Serp, P. Kalck, J.L. Faria, *Appl. Catal. B* 56 (2005) 305.
- [126] Y. Yu, J.C. Yu, C.Y. Chan, Y.K. Che, J.C. Zhao, L. Ding, W.K. Ge, P.K. Wong, *Appl. Catal. B* 61 (2005) 1.
- [127] Y. Yu, J.C. Yu, J.G. Yu, Y.C. Kwok, Y.K. Che, J.C. Zhao, L. Ding, W.K. Ge, P.K. Wong, *Appl. Catal. A* 289 (2005) 186.
- [128] F.J. Maldonado-Hódar, C. Moreno-Castilla, J. Rivera-Utrilla, *Appl. Catal. A* 203 (2000) 151.
- [129] C. Moreno-Castilla, F.J. Maldonado-Hódar, F. Carrasco-Marin, E. Rodriguez-Castellon, *Langmuir* 18 (2002) 2295.
- [130] P.V. Samant, F. Gonçalves, M.M.A. Freitas, M.F.R. Pereira, J.L. Figueiredo, *Carbon* 42 (2004) 1321.
- [131] Z.Y. Wang, N.S. Ergang, M.A. Al-Daous, A. Stein, *Chem. Mater.* 17 (2005) 6805.
- [132] S. Nagaoka, Y. Hamasaki, S. Ishihara, M. Nagata, K. Iio, C. Nagasawa, H. Ihara, *J. Mol. Catal. A* 177 (2002) 255.
- [133] M. Inagaki, S. Kobayashi, F. Kojin, N. Tanaka, T. Morishita, B. Tryba, *Carbon* 42 (2004) 3153.
- [134] M. Inagaki, F. Kojin, B. Tryba, M. Toyoda, *Carbon* 43 (2005) 1652.
- [135] T. Tsumura, N. Kojitani, I. Izumi, N. Iwashita, M. Toyoda, M. Inagaki, *J. Mater. Chem.* 12 (2002) 1391.
- [136] M. Inagaki, Y. Hirose, T. Matsunaga, T. Tsumura, M. Toyoda, *Carbon* 41 (2003) 2619.
- [137] B. Tryba, A.W. Morawski, T. Tsumura, M. Toyoda, M. Inagaki, *J. Photochem. Photobiol. A* 167 (2004) 127.
- [138] B. Tryba, T. Tsumura, M. Janus, A.W. Morawski, M. Inagaki, *Appl. Catal. B* 50 (2004) 177.
- [139] M. Toyoda, Y. Yoshikawa, T. Tsumura, M. Inagaki, *J. Photochem. Photobiol. A* 171 (2005) 167.
- [140] B. Tryba, M. Toyoda, A.W. Morawski, M. Inagaki, *Chemosphere* 60 (2005) 477.
- [141] M. Inagaki, M. Nonaka, F. Kojin, T. Tsumura, M. Toyoda, *Environ. Technol.* 27 (2006) 521.
- [142] T. Matsunaga, M. Inagaki, *Appl. Catal. B* 64 (2006) 9.
- [143] M. Toyoda, T. Yano, T. Tomoki, Y. Amao, M. Inagaki, *J. Adv. Oxid. Technol.* 9 (2006) 49.
- [144] S. Mozia, M. Toyoda, M. Inagaki, B. Tryba, A.W. Morawski, *J. Hazard. Mater.* 140 (2007) 369.

- [145] M. Janus, B. Tryba, M. Inagaki, A.W. Morawski, *Appl. Catal. B* 52 (2004) 61.
- [146] C.S. Enache, J. Schoonman, R.V. de Krol, *Appl. Surf. Sci.* 252 (2006) 6342.
- [147] A.W. Morawski, M. Janus, B. Tryba, M. Inagaki, K. Kalucki, *C.R. Chim.* 9 (2006) 800.
- [148] L. Lin, W. Lin, Y.X. Zhu, B.Y. Zhao, Y.C. Xie, Y. He, Y.F. Zhu, *J. Mol. Catal. A* 236 (2005) 46.
- [149] L. Lin, Y. Zhou, Y.X. Zhu, Y.C. Xie, *Chin. J. Catal.* 27 (2006) 45.
- [150] W.J. Ren, Z.H. Ai, F.L. Jia, L.Z. Zhang, X.X. Fan, Z.G. Zou, *Appl. Catal. B* 69 (2007) 138.
- [151] J. Moskon, R. Dominko, M. Gaberscek, R. Cerc-Korosec, J. Jamnik, *J. Electrochem. Soc.* 153 (2006) A1805.
- [152] L.X. Zhang, P. Liu, Z.X. Su, *J. Mol. Catal. A* 248 (2006) 189.
- [153] D.Y. Zhang, D. Yang, H.J. Zhang, C.H. Lu, L.M. Qi, *Chem. Mater.* 18 (2006) 3477.
- [154] S.U.M. Khan, M. Al-Shahry, W.B. Ingler, *Science* 297 (2002) 2243.
- [155] R. Hahn, A. Ghicov, J. Salonen, V.P. Lehto, P. Schmuki, *Nanotechnology* 18 (2007) 105604.
- [156] S. Sakthivel, H. Kisch, *Angew. Chem. Int. Ed.* 42 (2003) 4908.
- [157] B. Neumann, P. Bogdanoff, H. Tributsch, S. Sakthivel, H. Kisch, *J. Phys. Chem. B* 109 (2005) 16579.
- [158] C. Xu, R. Killmeyer, M.L. Gray, S.U.M. Khan, *Appl. Catal. B* 64 (2006) 312.
- [159] D.M. Chen, Z.Y. Jiang, J.Q. Geng, Q. Wang, D. Yang, *Ind. Eng. Chem. Res.* 46 (2007) 2741.
- [160] H. Irie, Y. Watanabe, K. Hashimoto, *Chem. Lett.* 32 (2003) 772.
- [161] Y. Choi, T. Umebayashi, M. Yoshikawa, *J. Mater. Sci.* 39 (2004) 1837.
- [162] Y. Nakano, T. Morikawa, T. Ohwaki, Y. Taga, *Appl. Phys. Lett.* 87 (2005) 052111.
- [163] M. Shen, Z.Y. Wu, H. Huang, Y.K. Du, Z.G. Zou, P. Yang, *Mater. Lett.* 60 (2006) 693.
- [164] T. Ohno, T. Tsubota, M. Toyofuku, R. Inaba, *Catal. Lett.* 98 (2004) 255.
- [165] T. Tachikawa, S. Tojo, K. Kawai, M. Endo, M. Fujitsuka, T. Ohno, K. Nishijima, Z. Miyamoto, T. Majima, *J. Phys. Chem. B* 108 (2004) 19299.
- [166] H.Q. Sun, Y. Bai, Y.P. Cheng, W.Q. Jin, N.P. Xu, *Ind. Eng. Chem. Res.* 45 (2006) 4971.
- [167] C.S. Enache, J. Schoonman, R. van de Krol, *J. Electroceram.* 13 (2004) 177.
- [168] C.K. Xu, R. Killmeyer, M.L. Gray, S.U.M. Khan, *Electrochim. Commun.* 8 (2006) 1650.
- [169] C.K. Xu, S.U.M. Khan, *Electrochim. Solid-State Lett.* 10 (2007) B56.
- [170] D. Noguchi, Y. Kawamata, T. Nagatomo, *J. Electrochim. Soc.* 152 (2005) D124.
- [171] S.W. Hsu, T.S. Yang, T.K. Chen, M.S. Wong, *Thin Solid Films* 515 (2007) 3521.
- [172] E. Barborini, A.M. Conti, I. Kholmanov, P. Pisari, A. Podesta, P. Milani, C. Cepek, O. Sakho, R. Macovez, M. Sancrotti, *Adv. Mater.* 17 (2005) 1842.
- [173] Y. Cong, F. Chen, J.L. Zhang, M. Anpo, *Chem. Lett.* 35 (2006) 800.

- [174] M. Doi, S. Saka, H. Miyafuji, D.A.I. Goring, *Mater. Sci. Res. Int.* 6 (2000) 15.
- [175] H. Tokoro, S. Saka, *Mater. Sci. Res. Int.* 7 (2001) 132.
- [176] C. Lettmann, K. Hildenbrand, H. Kisch, W. Macyk, W.F. Maier, *Appl. Catal. B* 32 (2001) 215.
- [177] J. Tang, Y.Y. Wu, E.W. McFarland, G.D. Stucky, *Chem. Commun.* (2004) 1670.
- [178] Z.Y. Jiang, C.Q. Lu, H. Wu, *Ind. Eng. Chem. Res.* 44 (2005) 4165.
- [179] P.W. Chou, S. Treschev, P.H. Chung, C.L. Cheng, Y.H. Tseng, Y.J. Chen, M.S. Wong, *Appl. Phys. Lett.* 89 (2006) 131919.
- [180] Y.H. Tseng, C.S. Kuo, C.H. Huang, Y.Y. Li, P.W. Chou, C.L. Cheng, M.S. Wong, *Nanotechnology* 17 (2006) 2490.
- [181] J. Yang, H.Z. Bai, X.C. Tan, J.S. Lian, *Appl. Surf. Sci.* 253 (2006) 1988.
- [182] Y.Z. Li, D.S. Hwang, N.H. Lee, S.J. Kim, *Chem. Phys. Lett.* 404 (2005) 25.
- [183] M. Janus, M. Inagaki, B. Tryba, M. Toyoda, A.W. Morawski, *Appl. Catal. B* 63 (2006) 272.
- [184] M. Janus, M. Inagaki, B. Tryba, M. Toyoda, A.W. Morawski, *J. Adv. Oxid. Technol.* 9 (2006) 43.
- [185] M. Janus, A.W. Morawski, *Appl. Catal. B* 75 (2007) 118.
- [186] H.K. Kammler, S.E. Pratsinis, *J. Mater. Res.* 18 (2003) 2670.
- [187] K. Nagaveni, M.S. Hegde, N. Ravishankar, G.N. Subbanna, G. Madras, *Langmuir* 20 (2004) 2900.
- [188] Y. Cheng, H. Sun, W. Jin, N. Xu, *Chem. Eng. J.* 128 (2007) 127.
- [189] S. Shammugam, A. Gabashvili, D.S. Jacob, J.C. Yu, A. Gedanken, *Chem. Mater.* 18 (2006) 2275.
- [190] Z.P. Zhu, Y. Zhou, H.W. Yu, T. Nomura, B. Fugetsu, *Chem. Lett.* 35 (2006) 890.
- [191] C. Dechakiatkrai, J. Chen, C. Lynam, S. Phanichphant, G.G. Wallace, *J. Electrochem. Soc.* 154 (2007) A407.
- [192] C.G. Silva, W.D. Wang, P. Selvam, S. Dapurkar, J.L. Faria, *Study Surf. Sci. Catal.* 162 (2006) 151.
- [193] W. Wang, P. Serp, P. Kalck, C.G. Silva, J.L. Faria, *Mater. Res. Bull.* (in press, corrected proof, 2007).
- [194] W.D. Wang, P. Serp, P. Kalck, J.L. Faria, *J. Mol. Catal. A* 235 (2005) 194.
- [195] Y. Luo, J. Liu, X. Xia, X. Li, T. Fang, S. Li, Q. Ren, J. Li, Z. Jia, *Mater. Lett.* 61 (2007) 2467.
- [196] X.H. Xia, Z.H. Jia, Y. Yu, Y. Liang, Z. Wang, L.L. Ma, *Carbon* 45 (2007) 717.
- [197] S.Z. Kang, Z.Y. Cui, J. Min, Fuller, *Nanotube Carbon Nanostruct.* 15 (2007) 81.
- [198] Y. Ou, J.D. Lin, S.M. Fang, D.W. Liao, *Chem. Phys. Lett.* 429 (2006) 199.
- [199] H. Lasa, B. Serrano, M. Salaices, *Photocatalytic Reaction Engineering*, Springer, New York, 2005.
- [200] D.F. Ollis, *Top. Catal.* 35 (2005) 217.
- [201] D.F. Ollis, *J. Phys. Chem. B* 109 (2005) 2439.
- [202] W.A. Jacoby, D.M. Blake, J.A. Fennell, J.E. Boulter, L.M. Vargo, M.C. George, S.K. Dolberg, *J. Air Waste Manage. Assoc.* 46 (1996) 891.

506 CARBON MATERIALS IN PHOTOCATALYSIS

- [203] V. Krishna, S. Pumprueg, S.H. Lee, J. Zhao, W. Sigmund, B. Koopman, B.M. Moudgil, *Process Saf. Environ. Protect.* 83 (2005) 393.
- [204] M.R. Hoffmann, S.T. Martin, W.Y. Choi, D.W. Bahnemann, *Chem. Rev.* 95 (1995) 69.
- [205] A. Mills, S. LeHunte, *J. Photochem. Photobiol. A* 108 (1997) 1.
- [206] A.L. Linsebigler, G.Q. Lu, J.T. Yates, *Chem. Rev.* 95 (1995) 735.

14 Carbon-Based Sensors

JUN LI

14.1 INTRODUCTION

Carbon materials have been used widely in the development of sensors and actuators, particularly for electrical or electrochemical biosensors. These applications critically rely on the unique chemical and electrical properties of specific carbon materials [1,2]. It is quite common that similar carbon materials present drastically different properties in the literature. The goal of this chapter is to describe the atomic structures of each carbon material and correlate these structures with their properties so that discrepancies in the literature can be understood. Readers can then optimize the material properties for specific sensing applications by tuning carbon structures. This is particularly important for graphitic carbon materials, which present inherent highly anisotropic properties.

14.1.1 Structure of Various Carbon Allotropes

There are three common allotropes of carbon, as shown in Figure 14.1: amorphous carbon, diamond, and graphite [1]. Among them, diamond consists of sp^3 carbon atoms to form tetrahedral bonding with four neighboring atoms, while graphite is composed of sp^2 carbon atoms bonded trigonally with three neighboring carbon atoms in planar hexagonal rings. Amorphous carbon is essentially graphite but not in a crystalline macrostructure. Instead, it appears as ultrafine powders, which are the main constituent of substances such as charcoal, soot, and activated carbon. There are a few exotic allotropes, including lonsdaleite and aggregated diamond nanorods, which can be categorized as derivatives of sp^3 carbon materials. Recently, a family of sp^2 derivatives (as shown in Figure 14.2), including fullerenes (C_{60} , C_{70} , C_{540} etc.), nanotubes, nanofibers, nanoionions, and nanohorns have attracted extensive research interests due to their intriguing nanostructures [3]. The majority of sensing studies are based on the sp^2 carbon materials, due to their conducting electronic properties.

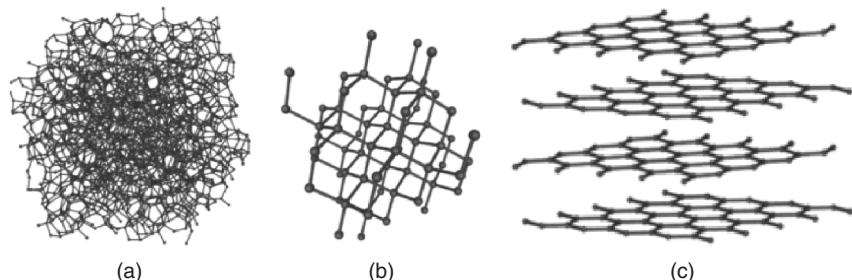


Figure 14.1 Three common allotropes of carbon: (a) amorphous carbon; (b) diamond; (c) graphite.

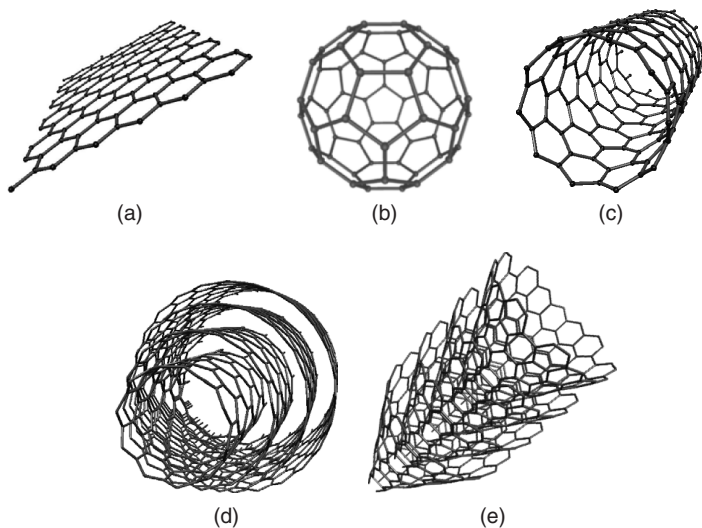


Figure 14.2 Some representative sp^2 carbon materials: (a) graphite; (b) C_{60} ; (c) single-walled carbon nanotubes; (d) multiwalled carbon nanotube; (e) carbon nanofibers grown by plasma-enhanced chemical vapor deposition.

Sensing mechanisms using carbon materials can be summarized into four categories. Each category uses a specific property of carbon materials. It is summarized here briefly so that readers can link these applications with their intrinsic structures, to be discussed later. First, carbon materials are used as loading media. This mechanism requires a large surface-to-volume ratio to enhance the gas adsorption. The smaller the carbon material dimension, the larger the surface-to-volume ratio is. Any nanomaterials may be used for this purpose. The reason to choose carbon for a particular application is due primarily to

other requirements, such as conductivity, chemical stability, weight, and cost. Historically, carbon black and activated carbon, which consist of ultrafine sp^2 powder, have been used widely as catalyst support and sensing media [1]. Carbon nanonions and nanohorns have properties similar to those of conventional carbon ultrafine powders [4,5]. Recent development in carbon nanotubes (CNTs) and nanofibers (CNFs) indicate that the fiberlike materials are more attractive due to both the large surface-to-volume ratio and the long-range electron transfer capability [3]. Second, carbon materials are used as transducers whose electronic properties change upon the adsorption of other chemicals. The most representative example is the single-walled CNT (SWCNT) field-effect-transistor chemical sensor [6]. Other resistive or thermoelectric sensors based on CNT networks or thin films are also based on this mechanism. This type of application requires semiconducting carbon materials. So far, only CNTs have been demonstrated. Third, carbon materials are used as electrodes for electrochemical sensors. The intrinsic properties of carbon materials do not change in these applications. Instead, the electrical signals associated with electrochemical reactions at the electrode surface are transduced through carbon materials. High performance does require a high conductivity. Fourth, in carbon composite sensors, carbon materials are used to connect other sensing materials. Carbon black and CNT mixed in polymer matrix have been employed successfully as sensor materials.

14.1.2 sp^2 Carbon Materials: Graphite, Fullerenes, and Carbon Nanotubes

Essentially all sp^2 carbon materials can be explained with the graphite structure, differentiated only in how they are organized into specific configurations, as shown in Figure 14.2. Graphite consists of planar atomic sheets (i.e., graphenes) within which carbon atoms form a two-dimensional network of six-membered conjugate rings with a C–C bond length of 1.42 Å. There is a very limited interaction between neighboring sheets, so they are loosely bonded with each other by a distance of 3.35 Å [Figure 14.1(c)]. This is the reason that graphite powder is a good lubricant. Fullerenes can be considered as a single graphite sheet folded into a hollow sphere. C_{60} is the best example, forming a perfect soccer ball structure [Figure 14.2(b)] [7]. However, besides the 20 benzenelike hexagons, C_{60} also consists of 12 pentagons. These hexagons and pentagons are uniformly organized such that all atoms in C_{60} are equivalent. Each carbon atom forms two single C–C bonds at the hexagon–pentagon edge with a bond length of 1.46 Å and one C=C double bond at the hexagon–hexagon edge with a bond length of 1.40 Å. Other types of fullerenes vary in the number of hexagons and pentagons as the carbon atom number changes. Due to the high curvature at the surface, fullerenes are much more reactive than defect-free planar graphite sheets. Thus, they can be functionalized with proper functional groups. Nanonions [4] and nanohorns [5] are special types of fullerenes that are composed of multiple shells. They may consist of broken C–C bonds and form more accessible open structures.

Carbon nanotubes (CNTs) are seamless cylindrical graphitic nanofibers made of sp^2 carbon atoms. A carbon nanotube may consist of a single graphitic sheet [single-walled carbon nanotubes (SWCNTs) [8] as shown in Figure 14.2(c)] or multiple concentric graphitic sheets [multiwalled carbon nanotubes (MWCNTs) [9] as shown in Figure 14.2(d)]. CNTs typically present a high-aspect ratio, varying in diameter from 0.7 to 200 nm and in length from tens of nanometers to millimeters. In some samples, fullerene-like caps may be present at the tip of CNTs. Pentagons may also form at the sidewall of CNTs if a CNT is bent or presents a kink [10]. Carbon nanofibers (CNFs) refer to the samples grown by catalytic chemical vapor deposition (CVD) or plasma-enhanced chemical vapor deposition (PECVD), which present a stack of conical graphitic layers [Figure 14.2(e)] [11] or bamboo-like structures [12,13]. They can be considered as a defective form of CNT, due to the hollow cylindrical structure, which is fundamentally different from solid microcarbon or nanocarbon filaments (CFs) produced by conventional methods based on high-temperature pyrolysis of polymer fibers [1]. The tilt angle between the graphitic sheet and the axis in CNFs varies between 5 and 35 degrees, depending on the sample quality. Extensive efforts are being made in reducing the tilt angle so that the CNF approaches the MWCNT structure.

14.2 PHYSICOCHEMICAL PROPERTIES OF sp^2 CARBON MATERIALS RELEVANT TO CARBON SENSORS

The sp^3 carbon materials are generally not electrically conductive (except properly doped diamonds) and thus are not of much interest for sensor applications. Amorphous carbon may be used as a catalyst support or adsorbent materials for some applications relevant to sensors and actuators [1]. Particulate sp^2 carbon materials such as fullerenes, nanoonions, and nanohorns are used as loading materials for the storage of hydrogen [14] and methane [15], drug delivery [16,17], and biomolecular immobilization in sensors [18–20]. These applications do not utilize the intrinsic physical properties of the materials and thus will not be the focus of this chapter. Instead, the main focus is on fibers and crystalline sp^2 carbon materials (i.e., micro-CFs or nano-CFs, graphite, CNTs, and CNFs), which have more interesting electrical and electronic properties for sensing.

14.2.1 Electrical and Electronic Properties

Conventional carbon materials such as carbon black, active carbon, CFs, glassy carbon, graphite powder, and pyrolytic graphite can all be broken down into microscopic graphite crystals, differentiated only in the crystal dimensions [2]. As shown in Figure 14.3, the most critical dimensions are the intraplanar microcrystallite size (L_a) along the a -axis (i.e., the plane of the hexagonal lattice) and the interplanar microcrystallite size (L_c) along the c -axis, which is perpendicular to the graphitic plane.

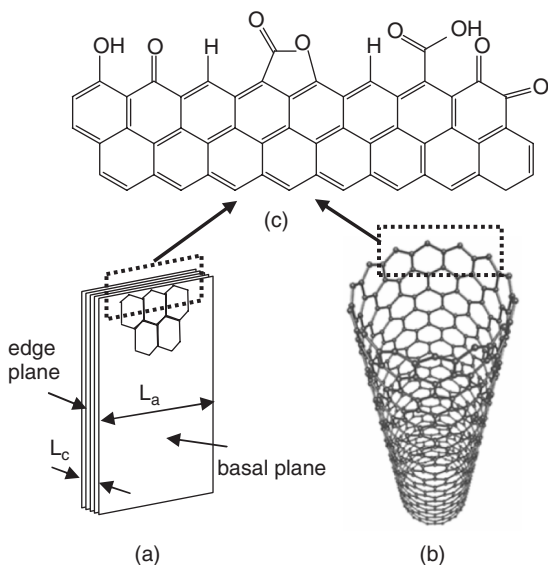


Figure 14.3 Crystalline structure and chemical groups at the broken edge of (a) graphite and (b) carbon nanotubes.

The model graphite crystal [i.e., the highly ordered pyrolytic graphite (HOPG)] is known for its extremely anisotropic feature in electrical, mechanical, and thermal properties associated with its atomic structure [2]. The electrical conductivity of a HOPG is much higher within the graphitic layer (i.e., along the a -axis) than in the direction normal to the graphitic layers (i.e., along the c -axis). Table 14.1 summarizes the electrical resistivity, thermal conductivity, thermal expansion coefficient, and Young's modulus along both directions. Clearly, all of these parameters present high c/a (or a/c) ratios. While the exact ratio may vary over orders of magnitude depending on the sample preparation conditions, the high c/a (or a/c) ratio is essentially universal for all planar pyrolytic graphite structures as well as for tube- and fiber-like sp^2 carbon materials.

Table 14.1 Anisotropic Properties of HOPG

Property	c -Axis	a -Axis	c/a Ratio
Resistivity ($\Omega \cdot \text{cm}$)	1.7×10^{-1}	4.1×10^{-5}	~ 3800
Thermal conductivity ($\text{W}/\text{m} \cdot \text{K}$)	10	2400	0.004
Thermal expansion (10^{-6}K^{-1})	27	-0.5	-54
Young's modulus (TPa)	0.03	1.03	0.03

It has been predicted theoretically [21] and demonstrated experimentally [22] that one or a few layers of atomically flat graphene exhibits two-dimensional semimetal properties with a small overlap (ca. 0.04 eV) between the valence and conductance bands at six symmetric points in the corner of the Brillouin zone, as shown in Figure 14.4. Thus, a nonzero density of states is found at the Fermi level, although the Fermi surface consists of only isolated points. This is attributed to the delocalization of electrons in the graphene plane and results in high in-plane conductivity. Across the plane, there is little interaction, and thus it shows very small conductivity.

In SWCNTs, the wavevector in the circumferential direction is quantized as lines in the plane of the graphene band structure [21,23–25]. Each line gives a one-dimensional energy band by slicing the two-dimensional graphene band structure as shown in Figure 14.5. When some lines pass through the Fermi points, it leads to crossing bands at the SWCNT Fermi level and thus to a metallic character. If none of the lines intersects with the graphene Fermi points, the SWCNT is semiconducting, with a bandgap determined by the two lines that come closest to the Fermi points. Therefore, the electronic structure of the SWCNT depends on how the graphene is rolled. This unique property presents many new opportunities for future electronics.

Generally, the electronic properties of an isolated defect-free SWCNT are dependent on the helicity (or chirality) of the CNT structure (i.e., the circumferential wavevector discussed above). The helicity is defined as the vector \mathbf{C} , along which a graphene sheet is rolled up into a seamless hollow cylinder. The vector \mathbf{C} can be expressed in terms of two integers (m, n) corresponding to the

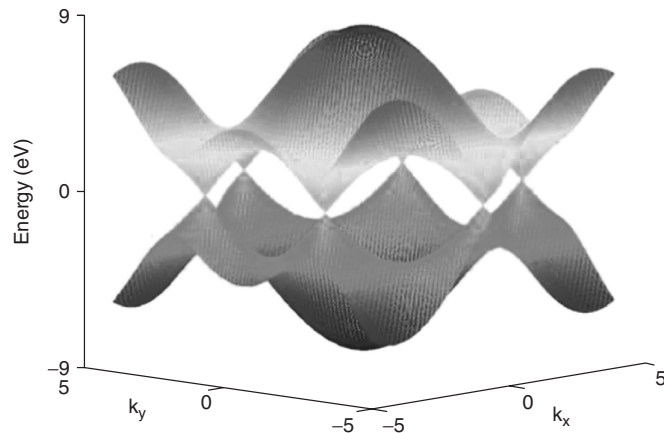


Figure 14.4 Band structure of graphene. The conductance band touches the valence band at the K and K' points. (Adapted with permission from ref. 21. Copyright © 2006 Institute of Physics.)

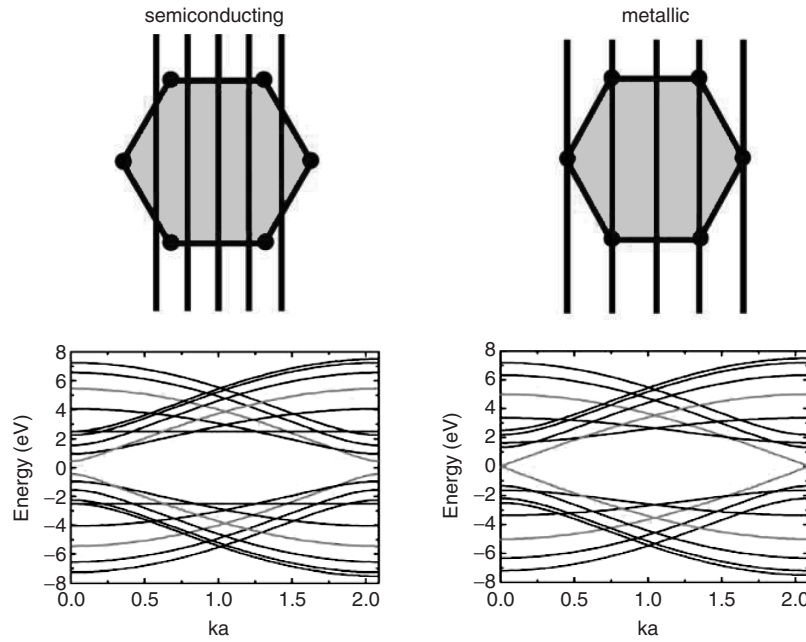


Figure 14.5 Allowed wavevector lines leading to semiconducting and metallic CNTs and examples of band structures for semiconducting and metallic zigzag CNTs. (Adapted with permission from ref. 21 Copyright © 2006 Institute of Physics.)

two primary lattice vectors a_1 and a_2 of the hexagonal graphite structure:

$$\mathbf{C} = ma_1 + na_2 \quad (14.1)$$

As the vector \mathbf{C} wraps around the circumference of the SWCNT, its two endpoints are superimposed exactly. Hence, the notation (m,n) carries the information of both the helicity and the size of the SWCNT. It is known that a defect-free SWCNT presents semiconducting properties if

$$|m - n|/3 \neq \text{integer} \quad (14.2)$$

and it presents metallic properties if

$$|m - n|/3 = \text{integer} \quad (14.3)$$

In the present production technology, the helicity of SWCNTs is essentially random during the growth process. As a result, statistically two-thirds of any given batch of SWCNTs are semiconducting and one-third of them are metallic [25]. The bandgap for a semiconducting tube is given by

$$E_g = \frac{2d_{cc}\gamma}{D} \quad (14.4)$$

where d_{cc} is the C–C bond length of the graphene (0.142 nm), γ the nearest-neighbor hopping parameter (2.5 to 3.2 eV), and D is the diameter of the SWCNT [26].

In MWCNTs, being comprised of parallel concentric SWCNTs, each graphene shell may present electrical properties similar to those of an isolated SWCNT with the same helical structure. The helicity of each shell is random during growth, and there is little coupling to neighboring shells [27]. Most electrical studies only make contact with the outermost shell of MWCNTs [27,28], but a careful end-contact configuration may be implemented to obtain multichannel parallel conductors [29]. Since the bandgap of a SWCNT is proportional to about $1/D$, it decreases as the tube diameter increases. Most MWCNTs are larger than 5 nm in diameter. Thus, they typically have a vanishing bandgap at 300 K and are metallic in nature, which is similar to a nanoscale HOPG cylinder.

Since the first demonstration of a room-temperature transistor based on a single SWCNT [30], CNTs have been studied widely for applications in nanoelectronics and sensors. Native CNTs in air are p-type semiconductors, due to electron withdrawal by oxygen adsorption. Methods have been developed to dope native CNTs with alkaline metal [31] or polymers [32] to modulate them from p-type to n-type properties. Modulation of an electronic property of a semiconducting SWCNT by the adsorption of chemicals on its surface is the basis for using CNTs as electronic sensors. The semiconducting SWCNT shows p-type behavior in the air, due to the strong oxygen adsorption, which withdraws electrons from the CNT. Theoretical calculation indicates that there is about 0.25e withdrawn by each oxygen molecule upon adsorption on a SWCNT [33,34]. Ammonia, on the other hand, is an electron donor, which may produce n-type SWCNT. But in an ambient environment, the oxygen adsorption is much stronger than other gases, such as N₂, CO₂, and H₂O [33,34]. As a result, a semiconducting SWCNT always shows p-type behavior unless it is doped with alkaline metal [31] or amine-containing polymers [32] and are carefully encapsulated to avoid oxygen access.

The naturally produced CNTs are a mixture of metallic and semiconducting CNTs. Still lacking is a good method of separating them during growth or post-production. Sensor application relies on picking out single semiconducting CNTs to make a FET transistor, or using very low density networks in which metallic CNTs do not connect with each other from one side of the metal contact to the other side. It is also possible to apply a current before a sensing application to burn out the metallic ones. The CNT–polymer composite method, on the other hand, uses CNTs as conductors and thus is not affected by the problem of CNT mixtures.

CNFs, on the other hand, are nearly 100% metallic wires with linear I – V properties [35,36]. PECVD-grown CNFs are of particular interest since they can be grown deterministically on a solid substrate at desired locations with well-controlled vertical alignment [12,35,37]. A temperature-dependent study over a range of 4 to 300 K revealed that the electron transport along the CNF consists of the mixture of graphite *a*- and *c*-axis transport mechanisms [36]. At room

temperature, the intrinsic resistance of the CNF is dominated by electron hopping between graphitic layers, similar to graphite *c*-axis transport. High-resolution electron microscopy analysis indicates that this is particularly dominant at the base of the CNF, where graphitic layers are primarily parallel to the surface of the bottom metal contact [38,39]. Even though there is space to improve both the intrinsic conductivity and the contact interface, they appear to be sufficient for the applications as conductive wires or electrodes for sensing applications.

A more defective form of sp^2 carbon fibers, carbon nanotubules (CNTbs), grown by pyrolytic deposition of carbon into anodized aluminum oxide (AAO) nanochannels, are also used as nanoelectrode arrays for electrochemical sensors. Small graphitic crystallites are deposited on the inner surface of the nanochannels. Since the crystallites do not extend very long (less than micrometers) and are structurally discontinued, the resistance is orders of magnitude higher than CNFs [40]. The advantage is that a uniform regular array can be fabricated by tuning the conditions for AAO preparation.

14.2.2 Chemical Properties

Since all carbon atoms form strong conjugate bonds with their neighbors, the basal plane of defect-free graphite is chemically inert. The edge of the crystalline planes, however, presents broken C–C bonds that form various oxides. As shown in Figure 14.3(c), the possible oxygen-containing functional groups include phenol, carbonyl, lactone, carboxylic acid, *o*-quinone, and *p*-quinone. Historically, many methods have been investigated to prepare the surface with desired functional groups, including mechanical polishing, heat treatment, chemical and electrochemical reaction, laser ablation, and plasma etching [2]. The results are reasonably well understood with the model HOPG samples, but are not consistent with most other carbon materials. This is due to the fact that it lacks the control of either crystalline quality or how they are organized. The highly anisotropic properties of graphite make the results extremely sensitive to the microstructure of the materials. For many biosensor applications, the carbon surface needs to be functionalized with biomolecules. A carboxylic acid group is a favored choice, due to the ease in forming amide conjugation, with the primary amine groups in many biomolecules using carbodiimide chemistry. Besides covalent binding, intercalation of small ions and molecules between graphitic layers are also well recognized and utilized in batteries. Functionalization to the basal plane relies primarily on creating sp^3 defects or π -stacking of planar conjugate moieties on the graphene surface.

For CNTs, the broken end is similar to a graphite edge, while the sidewall is like the graphite basal plane. This is advantageous for selectively functionalizing the tip and the sidewall with different chemical schemes. Due to their conical stacking nature, CNFs have more broken graphite edges exposed at the sidewall, resulting in more active sites. Due to the high curvature, fullerenes are much more reactive than basal graphene and thus attractive for attaching biomolecules in drug delivery applications.

14.2.3 Electrochemical Properties

The electrochemical properties are determined by a combination of the highly anisotropic electrical properties and chemical activities. HOPG has been used as a model system to explain two extreme electrochemical behaviors. The electron transfer rate constant k^0 for the basal plane as characterized by the redox reaction of an $\text{Fe}(\text{CN})_6^{3/-4}$ pair is below 10^{-7} cm/s, more than five orders of magnitude lower than that of 0.06 to 0.1 cm/s on an edge plane [2]. This is evidently seen in the small current and large redox peak separation ($\Delta E_p > 0.7$ V) in Figure 14.6(a) compared to those with the edge plane in Figure 14.6(b). By changing the electrical connection from the parallel end contact to side clamping, the electrochemical activity decreased dramatically, although the measurement

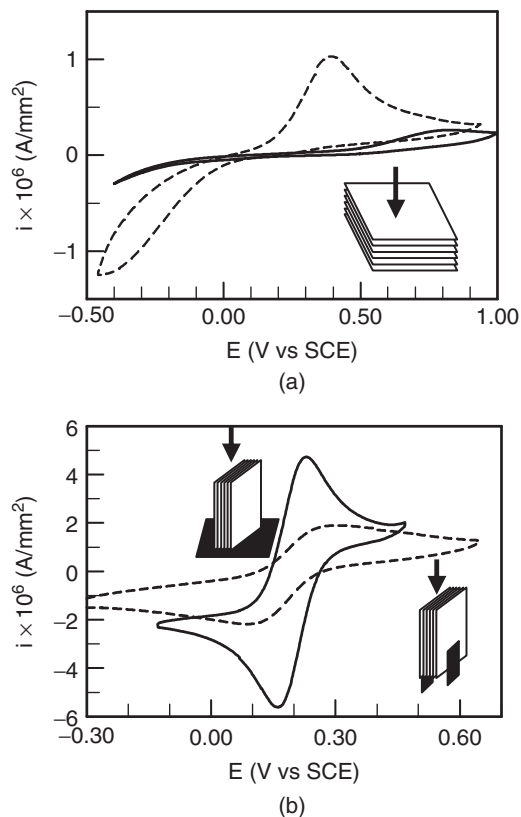


Figure 14.6 Cyclic voltammetry in 1.0 mM $\text{K}_4[\text{Fe}(\text{CN})_6]$ and 1.0 M KCl at a scan rate of 20 mV/s with (a) HOPG basal planes (continuous line, a sample exposed in the air for several days; dashed line, a freshly cleaved sample) and (b) HOPG edge planes (continuous line, end-connected; dashed line, side-connected). (Adapted with permission from ref. 43. Copyright © 2004 Royal Society of Chemistry.)

was done on the same edge plane. Clearly, the high resistance across graphitic layers is one of the most important factors affecting electrochemical activity. In general, a graphite edge-plane electrode has high electrochemical activity and good stability compared to a Pt electrode.

Interestingly, the specific capacitance of basal plane HOPG is anomalously low, with a value of 1.9 to 3.0 $\mu\text{F}/\text{cm}^2$, which is consistent with its low chemical activity. The capacitance of the edge plane, however, is very high, at least 60 $\mu\text{F}/\text{cm}^2$, comparable to Pt electrodes [2]. An open-end MWCNT presents an edge-plane-like structure at the tip and a basal-plane-like structure at the sidewall, which is a perfect wiring material to catch electrochemical signal at the tip and transport it to an electronic circuit connected at the other end, with minimum noise interference (mostly associated with capacitance) along the course. On the other hand, after proper treatment, CNFs and other highly defective CNTs may present a large active surface area that is suitable for adsorbent, supercapacitor, or energy storage [41–43].

14.3 CARBON-BASED SENSORS

Carbon materials have been used extensively in various sensors for centuries [1,2]. It is beyond the scope of this chapter to provide a comprehensive review. Instead, it is focused here to give a quick overview of the general sensing mechanisms of various carbon materials, which will lead to the most recent development in CNT-based nanosensors. These sensors are strongly dependent on the intrinsic electronic, structural, and chemical properties and present many new opportunities for future technologies. Table 14.2 summarizes some of the gas sensing studies to show the flexibility of various carbon materials for sensor development. Clearly, the performance is not simply defined by what materials to use, but also by how they are organized and what sensing mechanism to use.

Table 14.2 Examples of Carbon Electronic Gas Sensors

Material and Device	Gases Detected	Sensitivity	Ref.
SWCNT field-effect transistor (FET)	NO_2	~2 ppm	6
SWCNT FET	NH_3	~0.1%	6
CNT films on resonator	NH_3	~100 ppm	44
SWCNT network FET	Dimethyl methylphosphonate	Sub-ppb	45
PEI-coated multiple-SWCNT FET	NO_2	<1 ppb	46
Nafion-coated multiple-SWCNT FET	NH_3	<100 ppm	46
SWCNT network resistor	NO_2	44 ppb	47
SWCNT network resistor	Nitrotoluene	262 ppb	47
Carbon black/polymer composite	Dimethyl methylphosphonate	~9–46 ppb	48
CNF film	NO_2	10 ppb	49

14.3.1 Carbon Materials as Loading Media

Historically, carbon particles such as carbon black, activated carbon, and graphite powder present large surface-to-volume ratios and abundant active surface functional groups. They are used widely as catalyst supports, storage media, and electrocatalysts in batteries and fuel cells. These material properties are characterized by large BET surface areas, about 20 to 300 m²/g for carbon black and 450 to 1000 m²/g for active carbons [1]. For sensing applications, such porous materials can be used as adsorbents to concentrate molecules on the sensor surface. Fullerenes and nanohorns are just smaller carbon particles. For adsorption, they show properties similar to those of conventional particles. Carbon fiber materials, on the other hand, present unique advantages, due to higher electrical conductivity and the ability to form networks. In SWCNTs, every carbon atom is exposed at the outer surface, which ideally should give the highest BET surface area. The pristine SWCNT samples, however, form long, crystalline SWCNT bundles in which SWCNTs are hexagonally packed due to the strong van der Waals interaction at the sidewall [50]. This reduces the accessible surface area for larger molecules [51]. Extensive efforts have been made to separate the SWCNTs from the bundle, cut them into short, micrometer-long segments, suspend them in solutions, and purify them from the mixture of metal catalysts and other carbon particles. Most of these efforts use strong acid treatments [52], which also create abundant active functional sites. The BET surface area has been reported to increase from about 600 m²/g for raw SWCNTs to about 1600 m²/g for purified samples [53]. Inspired by the high-BET surface, extensive efforts have been made to use CNT as a bulk material for hydrogen storage [54–56]. However, the results vary from about 1% to 14% (in weight), due to the errors in estimating the impurities in the material. It is generally accepted that pure, undoped CNTs will not achieve the goal of 6 wt% hydrogen storage (on a materials basis) at close to room temperature. But alkaline metal-doped SWCNTs are still under investigation [56].

Besides being used as adsorbent for gas molecules, both SWCNTs and MWCNTs can be cast as a random network or a porous thin film on metal electrodes [57–59] or used as a three-dimensional scaffold [41,42] for biosensors. CNTs serve both as large immobilization matrices and as mediators to improve the electron transfer between the active enzyme site and the electrochemical transducer. Various enzymes, such as glucose oxidase and flavin adenine dinucleotide (FAD) can adsorb onto the CNT surface spontaneously and maintain their substrate-specific enzyme activity over prolonged times [57]. Recently, cells have been grown on CNT scaffolds which provide a three-dimensional permeable environment, simulating the natural extracellular matrix in a tissue [60–62].

14.3.2 Carbon Electronic Sensors

The dependence of electronic properties on chemical environment was first reported by Kong et al. based on a study of a single SWCNT field-effect transistor (FET) [6], as shown in Figure 14.7(a). It was demonstrated that the

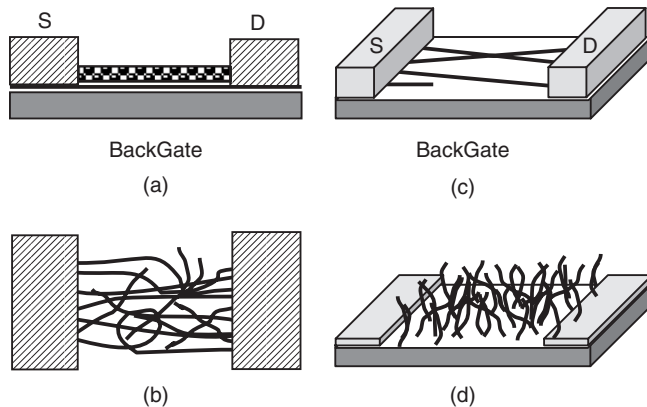


Figure 14.7 Four representative configurations of carbon nanotube sensors: (a) field-effect transistor with a single single-walled carbon nanotube conduction channel; (b) carbon nanotube film resistive sensor; (c) carbon nanotube network field-effect transistor; (d) entangled vertical carbon nanotube film as a resistive sensor.

conductance of a single semiconducting SWCNT decreased about 100-fold after exposure to NH_3 (0.1 to 1% in Ar or air) for about 10 minutes. On the other hand, exposure to NO_2 molecules (2 to 200 ppm in Ar) increased the conductance of the SWCNT FET by about 1000 times when it was initially depleted by a back-gate voltage (V_g) of +4 V. The sensitivity [i.e., the ratio between the resistance after and before gas exposure ($R_{\text{after}}/R_{\text{before}}$)] was found to be significantly better than that of other room-temperature-operated gas sensors based on conventional materials. Since the SWCNT is a hole-doped semiconductor, the adsorption of electron-donating NH_3 molecules causes the hole depletion and reduced conductance, while NO_2 exposure results in enriched hole carriers and enhanced conductance. The chemical nature of the gas molecules is indicated in the $I-V_g$ curve, which is characteristically shifted by -4 V after exposure to NH_3 and shifted by +4 V after exposure to NO_2 . The same group also demonstrated that a large array of FETs consisting of multiple SWCNTs that bridge metal electrodes can be fabricated for gas sensors [46]. Polymer functionalization is used to impart high sensitivity and selectivity for different gas molecules. Polyethylenimine (PEI) coating affords n-type CNT FET for detecting NO_2 below 1 ppb while being insensitive to NH_3 . Coating Nafion, on the other hand, blocks NO_2 and allows for selective sensing of NH_3 .

Collins et al. [63] and Sumannasekera et al. [64] later reported that electrical resistance R and thermoelectric power (TEP) of SWCNT bundles and thin films are sensitive to gas adsorption [Figure 14.7(b)]. The film conductance is changed dramatically upon exposure to O_2 , NO_2 , and NH_3 gases, presumably due to charge transfer from the adsorbates on semiconducting tubes [6,63]. The TEP of SWCNT bundles was also found sensitive to inert gas such as N_2 and

He, due to collision with the CNT walls [64]. Theoretically, it has been shown that O₂ adsorption has a significant effect on the electronic properties of small semiconducting nanotubes [33]. Zhao et al. studied the electronic properties of three types of SWCNTs—semiconducting zigzag (10,0) and (17,0) tubes and metallic armchair (5,5) tubes—upon the adsorption of O₂, NO₂, NH₃, CO₂, CO, H₂O, N₂, H₂, and He with first-principles methods [34]. It was found that O₂ and NO₂ are electron acceptors (−0.06 to −0.14e per molecule) with relatively larger adsorption energy (ca. 0.30 to 1.0 eV), while all other gas molecules are electron donors with negligible charge transfer (ca. 0.01 to 0.035e per molecule) and weak binding (<0.15 eV). Generally, all the gas molecules studied are weakly physisorbed on CNT surfaces. Charge fluctuation of even the weakly bonded molecules was found to have a pronounced effect on the transport properties of metallic SWCNT [64].

Following these CNT electronic gas sensor studies, many other methods have been explored focusing on the reduction of fabrication cost. Snow et al. demonstrated that a low-density random network of SWCNTs can be fabricated into p-type thin-film transistors [Figure 14.7(c)] with a field-effect mobility of about 10 cm²/Vs and an on-to-off ratio of about 10⁵ [65]. They demonstrated that such thin-film transistors can detect dimethyl methylphosphonate (DMMP), a simulant for the nerve agent sarin, at sub-ppb levels [45]. SWCNT network transistors have also been transferred to polymer substrates to form flexible electronic gas sensors [66]. Other resistive sensors based on random SWCNT network [47] or MWCNT films [41] have also been reported. Besides the cost, CNT network and thin-film sensors increase the statistical reliability by averaging out the response at many adsorption sites. This is particularly important when gas concentration is extremely small.

Valentini et al. [49] demonstrated that the three-dimensional hairlike CNFs can be used as resistive gas sensors for NO₂ detection as well. A vertically aligned film with individual CNFs heavily entangled with each other is deposited between two Pt interdigital electrodes by PECVD. Because of the large diameter and abundant defects of these CNFs, the dopant effect due to the charge transfer between CNF and the NO₂ adsorbates should be small. The adsorbed NO₂ molecules may intercalate between the contact points of neighboring CNFs to contribute to the resistance change.

The success of FET-based CNT gas sensors quickly attracted interest for use in biosensing applications, particularly since biomolecules such as DNA and proteins are heavily charged under normal conditions. SWCNT FETs are expected to be more sensitive than chemisorbed gas molecules to the binding of such charged species. However, the wet chemical environment with the presence of various ions and other biomolecules makes it much more complicated than gas environments. Studies demonstrated that proteins in the solution tend to adsorb irreversibly onto the bare CNT surface and induce significant change in FET characteristics [67,68]. Thus, extensive efforts have been made to passivate CNT with various polymers, such as PEI, poly(ethylene glycol) (PEG), Nafion, or Tween 20 [67,69,70]. It is commonly accepted that a polymer or surfactant

coating is necessary to reduce the nonspecific adsorption of biomolecules. It also serves as a linker for immobilizing probe molecules, so that only specific targets can bind onto the CNT FET device. However, the coating also shields the CNT and separates the targets farther away from CNT, the conduction FET channel. This is expected to decrease the detection sensitivity. In the meantime, it increases the device complexity and causes intensive debates in the sensing mechanisms. Questions remaining to be answered include (1) whether the conductance change is due to the modulation to the channel or CNT–metal contact barrier, and (2) whether the adsorbate induces charge transfer to the CNT or forms scattering potentials.

Using a normal back-gated FET device illustrated in Figure 14.8(a), Star et al. [69] found that the SWCNT FET was obscured by the ions in the buffer. To get around with this problem, the SWCNT FET after incubation was washed and dried before characterization in ambient environment [69]. The device was indeed effective for specific streptavidin binding through biotin molecules that were attached to the polymer layer for specific molecular recognition. As shown in Figure 14.9, the SWCNT FET device coated with PEI/PEG polymer alone changes from p-type [Figure 14.9b] to n-type [Figure 14.9(c)] device characteristics, probably due to the electron-donating properties of the NH_2 groups of the polymer. The attachment of biotin molecules through covalent binding to

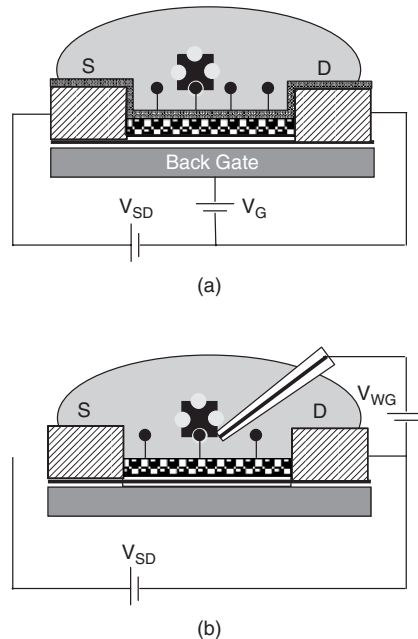


Figure 14.8 Two configurations of field-effect transistor biosensors: (a) with a back gate; (b) with a water gate.

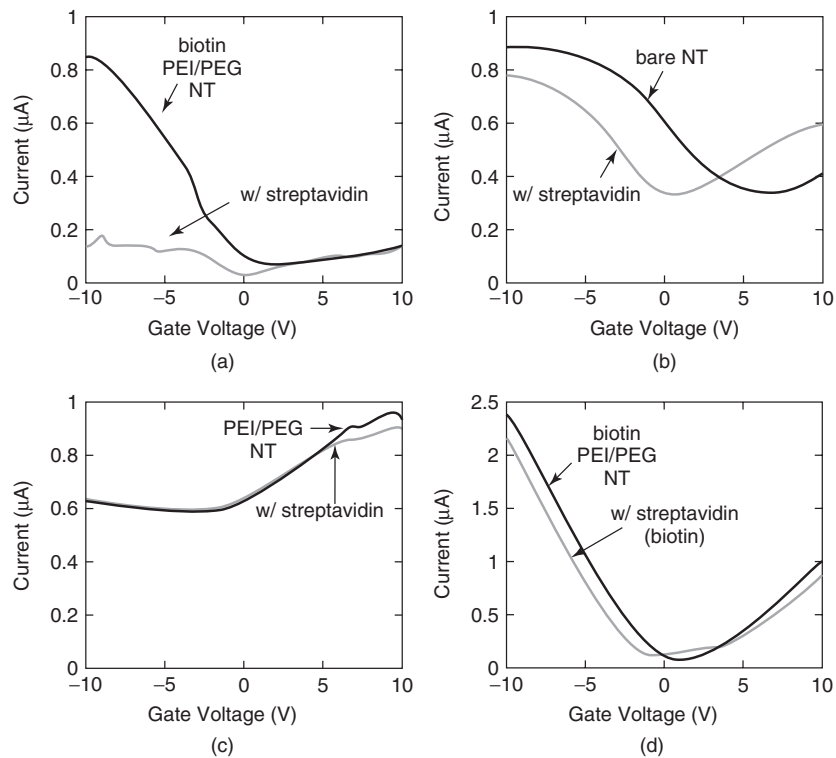


Figure 14.9 Change of the device characteristic $I_{SD}(V_G)$ upon exposure to streptavidin: (a) the biotinylated, polymer-coated CNT FET in the absence (black) and in the presence of streptavidin (gray), (b) the bare CNT FET device before (black) and after nonspecific streptavidin binding (gray), (c) the polymer-coated CNT FET device in the absence (black) and presence (gray) of streptavidin, and (d) the biotinylated, polymer-coated CNT FET device in the absence (black) and presence (gray) of streptavidin that was preincubated with biotin. (Adapted with permission from ref. 69. Copyright © 2003 American Chemical Society.)

the primary NH_2 group reduced the overall electron-donating function of PEI and converted the device back to p-type characteristics [Figure 14.9(a)]. Finally, the specific binding of streptavidin with biotin was found to remove the gating effect almost totally and cause a dramatic decrease in source-drain current at negative gate voltages. Nonspecific binding was observed in devices without the polymer coating, while no binding was found for the device coated with polymer alone. The exposure to streptavidin pretreated with excess biotin shows no change in the characteristic of the biotinylated polymer-coated devices. This study indicates that the nonspecific binding of streptavidin directly on bare CNT alters the conduction mainly by charge transfer [indicated by the shift in gate

voltage in Figure 14.9(b)], while the specific binding of streptavidin on biotinylated polymer coating induces scattering potential [as indicated by the suppression in the current without a shift in V_G in Figure 14.9(a)]. Using a similar off-line device characterization after drying in the air, this group demonstrated the detection of DNA hybridization using CNT network FETs [71].

In another configuration as shown in Figure 14.6(b), Rosenblatt et al [72] demonstrated an water-gated SWCNT FET. The FET device was submerged in a water solution containing 10 mM NaCl. A water gate voltage V_{WG} was applied to the droplet through a silver wire. Such electrolyte gated SWCNT FET showed p-type characteristics with high device mobilities and transconductances. Chen et al. [67] adapted this configuration and demonstrated the real-time detection of proteins such as streptavidin and IgG in buffer solution following specific binding. However, Chen et al. [70] and Tang et al. [73] found that the sensing mechanism may rely more on the modulation of metal contacts by controlling carefully the location that protein ligands and DNA probes were immobilized. It is well known that SWCNT FETs operate as unconventional Schottky barrier (SB) transistors, in which switching occurs primarily by modulation of the contact resistance rather than the channel conductance [74]. The SB effect will dominate especially when the isoelectric point (pI) of a protein is close to the pH of the reaction media [70]. It is needed to point out that all studies on SWCNT FETs in buffer solution use very low ionic strength, such as 10 mM NaCl [72] and 10 mM PBS [67]. Such salt concentrations are more than 10 times lower than those of physiology buffers. Experiments are needed to explore the measurements under the more practical physiological buffers to confirm whether the high ionic concentration will obscure the response. This is critical for further biosensor applications, particularly for the study of real-life processes.

Besides semiconducting SWCNTs, properly doped diamonds can also be used as the channel material for fabricating FETs for biosensing as demonstrated by Song et al. [75]. DNA probes are immobilized directly on the aminated surface of a p-type polycrystalline diamond film which serves as the conduction channel between the source and drain electrodes. Since a diamond surface is chemically stable and presents a wide potential window, it permits direct contact of biomolecules with the channel surface, eliminating the needs of a polymer coating (in CNT FETs) or dielectric encapsulation (in Si-FETs). As a result, diamond FET is potentially a much more sensitive and faster biosensor, which can operate in solution. Hybridization with complementary and 3-mer mismatched DNA targets in 10 pM can be discriminated in cyclically repeated hybridization and denature experiments.

14.3.3 Carbon Electrochemical Sensors

Carbon electrodes have been used widely in many electrochemical sensors, due to their chemical stability, flexibility for chemical functionalization, and wide potential window. The electrochemical activity of a carbon electrode depends critically on the pretreatment and the crystalline structure. References 1 and 2

are recommended for descriptions of conventional carbon electrodes. Here we focus on the new opportunities provided by carbon nanostructures (mainly CNTs and CNFs).

It is known that the performance of an electrode with respect to temporal and spatial resolution and sensitivity scales inversely with the electrode radius. For an inlaid fiber electrode, the exposed end can be approximated as a disk-shaped electrode. As the electrode diameter is smaller than that of the diffusion layer thickness, electrochemical properties become fundamentally different from a conventional macroelectrode. In cyclic voltammetry (CV) measurements, the magnitude of the peak current of the redox signal is the sum of two terms: linear diffusion as described in the Cottrell equation, and nonlinear radial diffusion [76]:

$$i_{l,\text{peak}} = 0.446nFAC_0\sqrt{\frac{nFD_0v}{RT}} + nFAC_0\frac{D_0}{r} \quad (14.5)$$

where $i_{l,\text{peak}}$ is the peak of the diffusion-limited electrical current, n the number of electrons involved in the reaction with one electroactive species, F the Faraday constant, A the surface area of the electrode, C_0 the electroactive species concentration, D_0 the diffusion coefficient, v the scan rate in V/s, and r the radius of the electrode. Both terms are proportional to the concentration of the species present in the solution. The first term is proportional to the electrode surface area and shows a well-defined peak at the characteristic electropotential, whereas the second term is proportional to the electrode radius and represents a sigmoidal steady-state current due to a constant flux of analytes to the surface. The ratio of the second term to the first is proportional to $1/r$. So the radial diffusion dominates the measured peak current if the electrode size is less than 25 μm , commonly referred to as an *ultramicroelectrode* (UME) [77]. The radial diffusion mechanism also applies on CNT and CNF nanoelectrodes (NEs) which are 10 to 100 nm in radius.

On the other hand, the noise (i.e., the background current due to the capacitive charging and discharging current at the electrode–electrolyte interface) is proportional to the surface area (A) of the electrode, as given by

$$i_n = C_d^0 A \frac{dE}{dt} \quad (14.6)$$

where C_d^0 is the specific capacitance at the interface, and dE/dt (i.e., v) is the sweeping rate of the electropotential (E).

In the UME-to-NE regime, the magnitude of the current decreases, but the signal-to-noise ratio is improved as the electrode size decreases, according to

$$\frac{i_{l,\text{peak}}}{i_n} \propto \frac{nFC_0D_0}{r} \quad (14.7)$$

Clearly, the signal-to-noise ratio will be improved 1000-fold if the electrode radius is reduced from 25 μm to 25 nm.

The response time of an electrode is also a function of the electrode dimension. The cell time constant can be described as [76]

$$\tau = R_u C_d = \frac{r C_d^0}{4\kappa} \quad (14.8)$$

where κ is the conductivity of the electrolyte. The electrode can respond 1000 times faster when the size is reduced from micrometers to nanometers, so that fast electrochemical techniques can be applied. The electrochemical signal is defined by the total number of electrons that can be transferred between the electroactive species and the electrode. For high-sensitivity analytical applications, this number is limited. By employing fast electrochemical techniques, the same amount of electrons can be transferred to the measuring circuit in a much shorter time, generating a much larger current that can easily be differentiated from the background noise.

For many practical applications, hundreds to thousands of UMEs or NEs need to be connected in parallel to a common micro or macro contact [78]. With sufficient spacing between neighbors, each UME or NE is capacitively, resistively, and diffusively independent and behaves similar to a single UME or NE. The collective signal from such microelectrode arrays (MEAs) or nanoelectrode arrays (NEAs) is therefore many orders of magnitude larger and can be measured easily with a simple system.

Li et al. [37,79,80] have developed a method to fabricate such inlaid NEAs using microfabrication techniques as shown in Figure 14.10. The processing procedure for fabricating CNF nanoelectrode arrays consists of metal film deposition, catalyst deposition, PECVD CNF growth, tetraethoxysilane (TEOS) CVD, and planarization using chemical mechanical polishing (CMP) or plasma etching. The TEOS CVD process is known for its ability to deposit a conformal SiO_2 layer into small trenches or holes down to a few nanometers, ensuring that the surface of the CNF and its underlying contact is fully insulated. The tip of the CNF is exposed by the planarization and etching process, which removes the excess SiO_2 on top of the samples. All these processes are compatible with microfabrication techniques and thus are amenable to mass production. By combining various lithography techniques, the CNT/CNF site can be defined precisely on top of the microcontact pads. Either well-defined single-CNT/CNF arrays or microbundles can be achieved using nanolithography and microlithography, as shown in Figure 14.11. Tu et al. [81] demonstrated slightly different processing with similar effectiveness using spin-coated epoxy rather than TEOS CVD.

Figure 14.12 shows the CV measurements in 1 mM $\text{K}_4\text{Fe}(\text{CN})_6$ and 1.0 M KCl with a high-density CNF NEA of about 2×10^9 electrodes/cm² and a low-density CNF NEA of about 7×10^7 electrodes/cm², respectively. Clearly, the high-density NEA shows a CV feature similar to that of a conventional macroelectrode with a pair of redox waves, indicating that overlapping of the diffusion layers from neighboring NEs results in linear diffusion. In contrast, the low-density NEA shows a sigmoidal shape similar to that of a single NE with

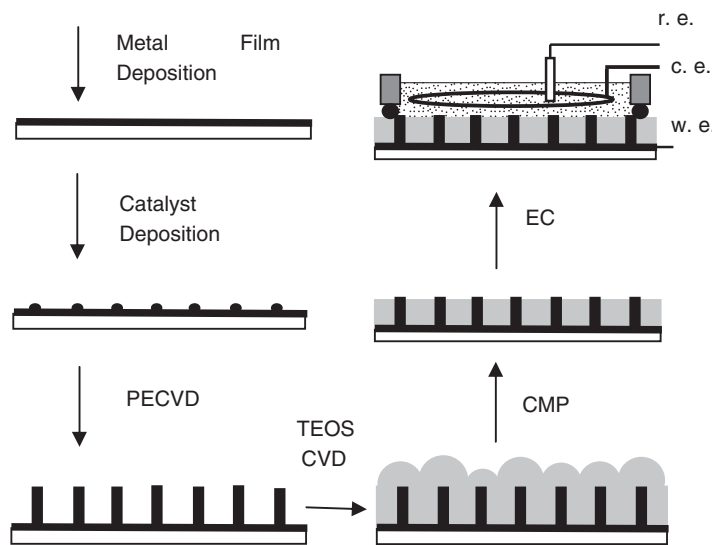


Figure 14.10 Processing procedure for fabricating CNF nanoelectrode arrays with metal film deposition, catalyst deposition, plasma-enhanced chemical vapor deposition (PECVD), tetraethoxysilane (TEOS) chemical vapor deposition (CVD), chemical mechanical polishing (CMP), and the setup for electrochemical (EC) characterization. (Adapted with permission from ref. 43. Copyright © 2004 Royal Society of Chemistry.)

radial diffusion. The average spacing needs to be at least six times the diameter of each NE to show the sigmoidal shape.

With the diameter approaching the size of biomolecules, nanoelectrodes can be used efficiently for biosensors. The exposed tip with broken graphitic structure facilitates selective covalent attachment of probe molecules. Figure 14.13 shows one example for the ultrasensitive detection of DNA hybridization using inlaid CNF NEAs [79]. An oligonucleotide probe with 18 bases is attached covalently to the open CNF end through amide bonds facilitated with carbodiimide reagents. This DNA sequence is related to the wild-type allele (Arg1443stop) of a cancer-related BRCA1 gene. It is estimated that there are about 100 probe molecules functionalized to a single CNF about 100 nm in diameter. Amplified DNA products by a polymer chain reaction (PCR) (i.e., PCR amplicons) of about 300 bases are hybridized with probe oligos. $\text{Ru}(\text{bpy})_3^{2+}$ mediators are introduced to facilitate an amplified guanine oxidation mechanism as illustrated in Figure 14.13(b). The mediators can efficiently transfer electrons from the guanine bases to the electrode even when they are not in direct contact. This mechanism can utilize all the inherent guanine bases within the hemispherical diffusion layer of $\text{Ru}(\text{bpy})_3^{2+}$ mediators, generating a well-defined oxidation peak around 1.04 V, as shown in Figure 14.13(c). Interestingly, guanine oxidation is irreversible. As a result, the first scan (gray line) is clearly higher than the second (black dotted line)

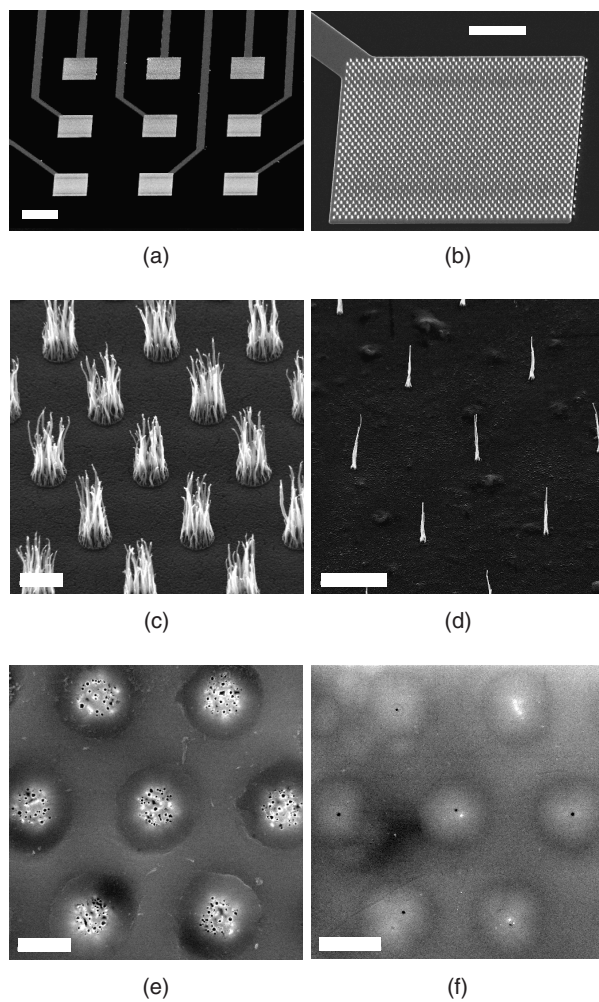


Figure 14.11 SEM images of (a) a 3×3 electrode array, (b) array of CNF bundles on one of the electrode pads, (c, d) array of CNFs at UV lithography and e-beam patterned Ni spots, respectively, (e, f) the surface of polished CNF array electrodes grown on 2- μm and 200-nm spots, respectively. (a–d) 45° perspective views; (e–f) top views. The scale bars are 200, 50, 2, 5, 2, and 2 μm , respectively. (Adapted with permission ref. 37. Copyright © 2003 American Chemical Society.)

and the third (black line) scans, while the latter two are nearly superimposed on each other. The guanine oxidation occurs only in the first scan. Subtracting the second scan from the first gives a clear peak [Figure 14.13(d)], while subtracting the third from the second gives a nearly flat background with only small amounts of active guanine residues.

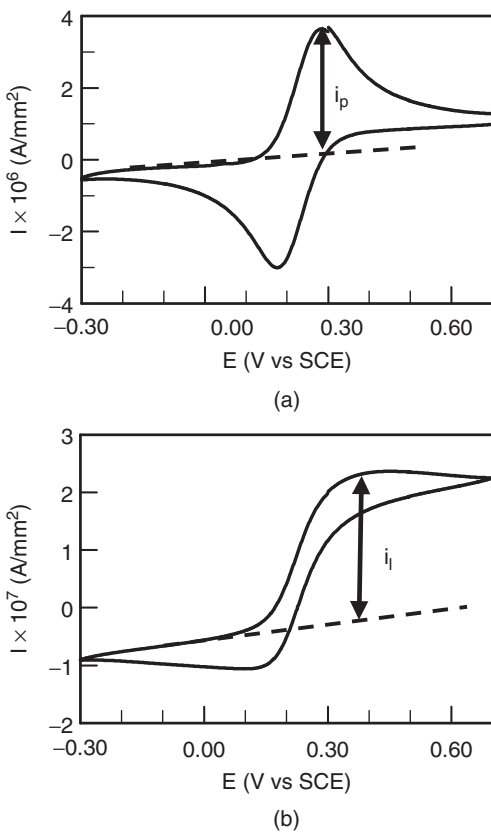


Figure 14.12 CV measurements in 1 mM $\text{K}_4\text{Fe}(\text{CN})_6$ and 1.0 M KCl with (a) the high-density CNF NEA (with ca. 2×10^9 electrodes/ cm^2) and (b) the low-density one (with ca. 7×10^7 electrodes/ cm^2). The scan rate is 20 mV/s. (Adapted with permission from ref. 37. Copyright © 2003 American Chemical Society.)

In similar experiments, Lin et al. [82] covalently attached glucose oxidase (GOx) to the exposed CNT end in a NEA and demonstrated that a linear amperometric response can be obtained from 0.08 to 30 mM of glucose. Both the linear range and detection limit surpass other studies. The same group also demonstrated that the inlaid CNF NEA can be used for heavy metal ion detection. Trace Cd(II) and Pb(II) were deposited onto a bismuth-coated CNF NEA and then measured with stripping voltammetry. The detection limit was as low as 0.04 $\mu\text{g/L}$ (40 ppt) [83,84].

In a series of studies, Gooding et al. [85,86] investigated the possibility of direct-wiring redox molecules with the electrode surface through shortened SWCNTs. They suspected that the SWCNTs may plug into redox enzymes such as GOx, where the redox active center is deeply buried within the protein, and thus

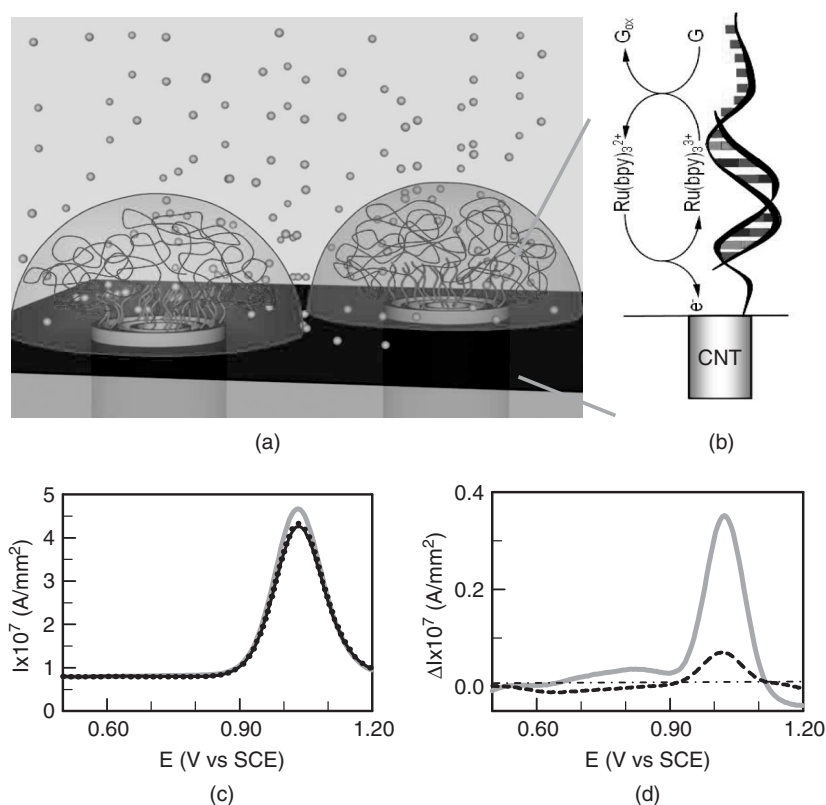


Figure 14.13 Mechanism for detecting DNA hybridization using a CNF nanoelectrode array. (a) The long single-stranded DNA PCR amplicon is hybridized to the short oligonucleotide probes, which are functionalized at the very end of the CNF. Ru(bpy)₃²⁺ mediators are used to transfer electrons from the guanine groups to the CNF nanoelectrode for all target molecules within the hemispherical diffusion layer of the nanoelectrodes. (b) Schematic mechanism for the guanine oxidation amplified with Ru(bpy)₃²⁺ mediators. (c) Three consecutive ac voltammetry measurements (first, gray line; second, black dotted line; third, black line). (d) Differential curves between the first and second scans ($\Delta I_{1,2} = I_1 - I_2$) (gray line) and that between the second and third scans ($\Delta I_{2,3} = I_2 - I_3$) (black dashed line) of a CNF nanoelectrode array functionalized with BRCA1 probes and hybridized with the specific PCR amplicon. (Adapted with permission from ref. 79. Copyright © 2003 IOP.)

enable otherwise impossible direct electron transfer [86]. They modified the gold surface with a self-assembled monolayer of cysteamine and then attached the shortened SWCNT through the amide bond facilitated by carbodiimide. Native GOx and its redox active center, flavin adenine dinucleotide (FAD), were attached covalently to the top end of the SWCNTs. The enzyme was then reconstituted

with FAD [87]. These experiments consistently indicate that SWCNTs improve the efficiency in accessing the redox active center of enzymes.

14.3.4 Carbon Composite Sensors

In previous sections, carbon materials serve either as sensing materials or as transducers. Many studies also use carbon–polymer composites, where carbon materials serve as both support and transducer. The polymer-coated FET discussed above is one example. Arrays of carbon black/organic polymer composite have also been demonstrated in many studies as chemiresistive vapor detectors [48,88]. The sorption of vapor molecules in the polymer matrix changes the resistance and thus can be related to the vapor concentration. Hundreds of compositionally different detector pixels can be fabricated to differentiate slightly different vapors and interference background using a principal component analysis algorithm. Wei et al. [89] demonstrated a similar concept using an aligned CNT film in polymer composites. A film of entangled MWCNT towers produced by pyrolysis of iron(II) phthalocyanine on quartz was covered partially with a polymer coating along the tube length by depositing a droplet of polymer solution such as poly(vinyl acetate) (PVAc) and polyisoprene (PI). The composite film was then peeled off and inverted as a free-standing film. The MWCNT towers partially embedded in the polymer matrix showed reversible changes from 10% to 200%. Interestingly, the sensitivities to different chemical vapors were completely reversed in PVAc relative to those in PI matrices. Such a composite CNT film can also be used as a resistive sensor for polymer swelling due to temperature changes or optical absorption.

14.4 SUMMARY

In summary, carbon materials have a unique structure and unique physical properties. The optimization of these materials for sensing applications depends on how to organize them into the proper configurations. The recent development of one-dimensional nanostructures such as CNTs and CNFs opens up new opportunities that one can electrically wire biomolecules with electronic circuits at molecular levels. Further development in this field is expected to offer highly multiplex and miniaturized sensor arrays with unprecedented sensitivities.

REFERENCES

- [1] K. Kinoshita, *Carbon: Electrochemical and Physicochemical Properties*, Wiley, New York, 1988.
- [2] R.L. McCreery, in A.J. Bard, Ed., *Electroanalytical Chemistry*, Marcel Dekker, New York, p. 221.
- [3] M. Endo, S. Iijima, M.S. Dresselhaus, *Carbon Nanotubes*, Elsevier, New York, 1996.

- [4] N. Sano, H. Wang, I. Alexandrou, M. Chhowalla, K.B.K. Teo, G.A.J. Amaratunga, *J. Appl. Phys.* 92 (2002) 2783.
- [5] K. Murata, K. Kaneko, F. Kokai, K. Takahashi, M. Yudasaka, S. Iijima, *Chem. Phys. Lett.* 331 (2000) 14.
- [6] J. Kong, N.R. Franklin, C.W. Zhou, M.G. Chapline, S. Peng, K.J. Cho, H.J. Dai, *Science* 287 (2000) 622.
- [7] H. Aldersey-Williams, *The Most Beautiful Molecule: The Discovery of the Buckyball*, Wiley, New York, 1995.
- [8] S. Iijima, T. Ichihashi, *Nature* 363 (1993) 603.
- [9] S. Iijima, *Nature* 354 (1991) 56.
- [10] J. Han, M. Anantram, R. Jaffe, J. Kong, H. Dai, *Phys. Rev. B* 57 (1998) 14983.
- [11] B.A. Cruden, A.M. Cassell, Q. Ye, M. Meyyappan, *J. Appl. Phys.* 94 (2003) 4070.
- [12] Z.F. Ren, Z.P. Huang, D.Z. Wang, J.G. Wen, J.W. Xu, J.H. Wang, L.E. Calvet, J. Chen, J.F. Klemic, M.A. Reed, *Appl. Phys. Lett.* 75 (1999) 1086.
- [13] Z.F. Ren, Z.P. Huang, J.W. Xu, J.H. Wang, P. Bush, M.P. Siegal, P.N. Provencio, *Science* 282 (1998) 1105.
- [14] K. Murata, K. Kaneko, H. Kanoh, D. Kasuya, K. Takahashi, F. Kokai, M. Yudasaka, S. Iijima, *J. Phys. Chem. B* 106 (2002) 11132.
- [15] E. Bekyarova, K. Murata, M. Yudasaka, D. Kasuya, S. Iijima, H. Tanaka, H. Kahoh, K. Kaneko, *J. Phys. Chem. B* 107 (2003) 4681.
- [16] K. Ajima, M. Yudasaka, T. Murakami, A. Maigne, K. Shiba, S. Iijima, *Mol. Pharm.* 2 (2005) 475.
- [17] X. Fan, J. Tan, G. Zhang, F. Zhang, *Nanotechnology* 18 (2007) 195103.
- [18] N. Sano, F. Ohtsuki, *J. Electrostat.* 65 (2007) 263.
- [19] J.-S. Shih, Y.-C. Chao, M.-F. Sung, G.-J. Gau, C.-S. Chiou, *Sensors Actuators B* 76 (2001) 347.
- [20] H.-W. Chang, J.-S. Shih, *Sensors Actuators B* 121 (2007) 522.
- [21] M.P. Anantram, F. Leonard, *Rep. Prog. Phys.* 69 (2006) 507.
- [22] K.S. Novoselov, A.K. Geim, S.V. Morozov, D. Jiang, Y. Zhang, S.V. Dubonos, I.V. Grigorieva, A.A. Firsov, *Science* 306 (2004) 666.
- [23] M.I. Katsnelson, *Mater. Today* 10 (2007) 20.
- [24] C.T. White, J.W. Mintmire, *J. Phys. Chem. B* 109 (2005) 52.
- [25] T.W. Odom, J.L. Huang, P. Kim, C.M. Lieber, *J. Phys. Chem. B* 104 (2000) 2794.
- [26] M. Meyyappan, Ed., *Carbon Nanotubes Science and Applications*, CRC Press, Boca Raton, FL, 2004.
- [27] P.C. Collins, M.S. Arnold, P. Avouris, *Science* 292 (2001) 706.
- [28] S. Frank, P. Poncharal, Z.L. Wang, W.A. de Heer, *Science* 280 (1998) 1744.
- [29] P.J. de Pablo, E. Graugnard, B. Walsh, R.P. Andres, S. Datta, R. Reifenberger, *Appl. Phys. Lett.* 74 (1999) 323.
- [30] S.J. Tans, A.R.M. Verschueren, C. Dekker, *Nature* 393 (1998) 49.
- [31] C.W. Zhou, J. Kong, E. Yenilmez, H.J. Dai, *Science* 290 (2000) 1552.
- [32] M. Shim, A. Javey, N.W.S. Kam, H.J. Dai, *J. Am. Chem. Soc.* 123 (2001) 11512.
- [33] S.-H. Jhi, S.G. Louie, M.L. Cohen, *Phys. Rev. Lett.* 85 (2000) 1710.
- [34] J. Zhao, A. Buldum, J. Han, J.P. Lu, *Nanotechnology* 13 (2002) 195.

- [35] J. Li, Q. Ye, A. Cassell, H.T. Ng, R. Stevens, J. Han, M. Meyyappan, *Appl. Phys. Lett.* 82 (2003) 2491.
- [36] Q. Ngo, A.M. Cassell, A.J. Austin, J. Li, S. Krishnan, M. Meyyappan, C.Y. Yang, *IEEE Electron Device Lett.* 27 (2006) 221.
- [37] J. Li, H.T. Ng, A. Cassell, W. Fan, H. Chen, Q. Ye, J. Koehne, J. Han, M. Meyyappan, *Nano Lett.* 3 (2003) 597.
- [38] H.T. Cui, X.J. Yang, M.L. Simpson, D.H. Lowndes, M. Varela, *Appl. Phys. Lett.* 84 (2004) 4077.
- [39] Y. Ominami, Q. Ngo, A.J. Austin, H. Yoong, C.Y. Yang, A.M. Cassell, B.A. Cruden, J. Li, M. Meyyappan, *Appl. Phys. Lett.* 87 (2005) 233105.
- [40] J. Li, C. Papadopolous, J.M. Xu, M. Moskovits, *Appl. Phys. Lett.* 75 (1999) 367.
- [41] H.T. Ng, A. Fang, J. Li, S.F.Y. Li, *J. Nanosci. Nanotechnol.* 1 (2001) 375.
- [42] J. Li, A. Cassell, L. Delzeit, J. Han, M. Meyyappan, *J. Phys. Chem. B* 106 (2002) 9299.
- [43] J. Koehne, J. Li, A.M. Cassell, H. Chen, Q. Ye, H.T. Ng, J. Han, M. Meyyappan, *J. Mater. Chem.* 14 (2004) 676.
- [44] S. Chopra, A. Pham, J. Gaillard, A. Parker, A.M. Rao, *Appl. Phys. Lett.* 80 (2002) 4632.
- [45] J.P. Novak, E.S. Snow, E.J. Houser, D. Park, J.L. Stepnowski, R.A. McGill, *Appl. Phys. Lett.* 83 (2003) 4026.
- [46] P. Qi, O. Vermesh, M. Grecu, A. Javey, Q. Wang, H. Dai, S. Peng, K.J. Cho, *Nano Lett.* 3 (2003) 347.
- [47] J. Li, Y. Lu, Q. Ye, M. Cinke, J. Han, M. Meyyappan, *Nano Lett.* 3 (2003) 929.
- [48] A.R. Hopkins, N.S. Lewis, *Anal. Chem.* 73 (2001) 884.
- [49] L. Valentini, I. Armentano, J.M. Kenny, C. Cantalini, L. Lozzi, S. Santucci, *Appl. Phys. Lett.* 82 (2003) 961.
- [50] A. Thess, R. Lee, P. Nikolaev, H. Dai, P. Petit, J. Robert, C. Xu, Y.H. Lee, S.G. Kim, A.G. Rinzler, D.T. Colbert, G.E. Scuseria, D. Tomanek, J.E. Fischer, R.E. Smalley, *Science* 273 (1996) 483.
- [51] C.K.W. Adu, G.U. Sumanasekera, B.K. Pradhan, H.E. Romero, P.C. Eklund, *Chem. Phys. Lett.* 337 (2001) 31.
- [52] J. Liu, A.G. Rinzler, H. Dai, J.H. Hafner, R.K. Bradley, P.J. Boul, A. Lu, T. Iverson, K. Shelimov, C.B. Huffman, F. Rodriguez-Macias, Y.-S. Shon, T.R. Lee, D.T. Colbert, R.E. Smalley, *Science* 280 (1998) 1253.
- [53] M. Cinke, J. Li, B. Chen, *Chem. Phys. Lett.* 365 (2002) 69.
- [54] P. Chen, X. Wu, J. Lin, K.L. Tan, *Science* 285 (1999) 91.
- [55] C. Liu, Y.Y. Fan, M. Liu, H.T. Cong, H.M. Cheng, M.S. Dresselhaus, *Science* 286 (1999) 1127.
- [56] R.T. Yang, *Carbon* 38 (2000) 623.
- [57] A. Giuseppi-Elie, C. Lei, R.H. Baughman, *Nanotechnology* 13 (2002) 559.
- [58] B.R. Azamian, J.J. Davis, K.S. Coleman, C.B. Bagshaw, M.L.H. Green, *J. Am. Chem. Soc.* 124 (2002) 12664.
- [59] M. Musameh, J. Wang, A. Merkoci, Y.H. Lin, *Electrochem. Commun.* 4 (2002) 743.
- [60] T.J. Webster, M.C. Waid, J.L. McKenzie, R.L. Price, J.U. Ejiofor, *Nanotechnology* 15 (2004) 48.

- [61] T.D.B. Nguyen-Vu, H. Chen, A.M. Cassell, R. Andrews, M. Meyyappan, J. Li, *Small* 2 (2006) 89.
- [62] T.D.B. Nguyen-Vu, H. Chen, A.M. Cassell, R. Andrews, M. Meyyappan, J. Li, *IEEE Trans. Biomed. Eng.* 54 (2007) 1121.
- [63] P.G. Collins, K. Bradley, M. Ishigami, A. Zettl, *Science* 287 (2000) 1801.
- [64] G.U. Sumannasekera, C.K.W. Adu, S. Fang, P.C. Eklund, *Phys. Rev. Lett.* 85 (2000) 1096.
- [65] E.S. Snow, J.P. Novak, P.M. Campbell, D. Park, *Appl. Phys. Lett.* 82 (2003) 2145.
- [66] K. Bradley, J.C.P. Gabriel, G. Gruner, *Nano Lett.* 3 (2003) 1353.
- [67] R.J. Chen, S. Bangsaruntip, K.A. Drouvalakis, N.W.S. Kam, M. Shim, Y. Li, W. Kim, P.J. Utz, H. Dai, *Proc. Natl. Acad. Sci. U.S.A.* 100 (2003) 4984.
- [68] K. Bradley, M. Briman, A. Star, G. Gruner, *Nano Lett.* 4 (2004) 253.
- [69] A. Star, J.C.P. Gabriel, K. Bradley, G. Gruner, *Nano Lett.* 3 (2003) 459.
- [70] R.J. Chen, H.C. Choi, S. Bangsaruntip, E. Yenilmez, X. Tang, Q. Wang, Y.L. Chang, H. Dai, *J. Am. Chem. Soc.* 126 (2004) 1563.
- [71] A. Star, E. Tu, J. Niemann, J.C.P. Gabriel, C.S. Joiner, C. Valcke, *Proc. Natl. Acad. Sci. U.S.A.* 103 (2006) 921.
- [72] S. Rosenblatt, Y. Yaish, J. Park, J. Gore, V. Sazonova, P.L. McEuen, *Nano Lett.* 2 (2002) 869.
- [73] X. Tang, S. Bansaruntip, N. Nakayama, E. Yenilmez, Y.L. Chang, Q. Wang, *Nano Lett.* 6 (2006) 1632.
- [74] S. Heinze, J. Tersoff, R. Martel, V. Derycke, J. Appenzeller, P. Avouris, *Phys. Rev. Lett.* 89 (2002).
- [75] K.-S. Song, G.-J. Zhang, Y. Nakamura, K. Furukawa, T. Hiraki, J.-H. Yang, T. Funatsu, I. Ohdomari, H. Kawarada, *Phys. Rev. E* 74 (2006) 041919.
- [76] A.J. Bard, L.R. Faulkner, *Electrochemical Methods: Fundamental and Applications*, Wiley, New York, 2001.
- [77] R.M. Wightman, *Anal. Chem.* 53 (1981) 1125A.
- [78] S. Fletcher, M.D. Horne, *Electrochem. Commun.* 1 (1999) 502.
- [79] J. Koehne, H. Chen, J. Li, A.M. Cassell, Q. Ye, H.T. Ng, J. Han, M. Meyyappan, *Nanotechnology* 14 (2003) 1239.
- [80] J.E. Koehne, H. Chen, A.M. Cassell, Q. Yi, J. Han, M. Meyyappan, J. Li, *Clin. Chem.* 50 (2004) 1886.
- [81] Y. Tu, Y.H. Lin, Z.F. Ren, *Nano Lett.* 3 (2003) 107.
- [82] Y.H. Lin, F. Lu, Y. Tu, Z.F. Ren, *Nano Lett.* 4 (2004) 191.
- [83] Y. Tu, Y.H. Lin, W. Yantasee, Z.F. Ren, *Electroanalysis* 17 (2005) 79.
- [84] G.D. Liu, Y.H. Lin, Y. Tu, Z.F. Ren, *Analyst* 130 (2005) 1098.
- [85] J.J. Gooding, R. Wibowo, J.Q. Liu, W.R. Yang, D. Losic, S. Orbons, F.J. Mearns, J.G. Shapter, D.B. Hibbert, *J. Am. Chem. Soc.* 125 (2003) 9006.
- [86] J.Q. Liu, A. Chou, W. Rahmat, M.N. Paddon-Row, J.J. Gooding, *Electroanalysis* 17 (2005) 38.
- [87] F. Patolsky, Y. Weizmann, I. Willner, *Angew. Chem. Int. Ed.* 43 (2004) 2113.
- [88] E.J. Severin, B.J. Doleman, N.S. Lewis, *Anal. Chem.* 72 (2000) 658.
- [89] C. Wei, L.M. Dai, A. Roy, T.B. Tolle, *J. Am. Chem. Soc.* 128 (2006) 1412.

15 Carbon-Supported Catalysts for the Chemical Industry

VENU ARUNAJATESAN, BAOSHU CHEN, KONRAD MÖBUS,
DANIEL J. OSTGARD, THOMAS TACKE, and DORIT WOLF

15.1 INTRODUCTION

The use of catalysts in the chemical industry is one of the major contributors to the economy of a chemical process. Most of today's chemical production processes utilize a catalytic step. In most cases the catalyst plays the most important role, as it controls the activity and the selectivity of the process and as such has a direct impact on the economics. Especially supported catalysts are of high interest. The typically high-surface-area supports provide a good utilization of the catalytically active metal by means of high dispersion and stabilization of small metallic particles. This is especially true for precious metals, where sometimes up to 100% of the precious metal is accessible for the catalytic reaction.

In the fine chemical and pharmaceutical industry a relatively large amount of carbon-supported catalysts are used. The advantage of carbon as a support is the stability under acidic and basic conditions, which does not apply for alumina or silica. Alumina and silica are dissolved under basic conditions; alumina is also sensitive to acids [1,2]. Another important topic for the overall economy of a process is the recovery, refining, and recycling of the metal. This is especially easy for precious metals supported on carbon catalysts, because the support material can simply be burned to receive highly loaded precious metal containing ashes from where the precious metal can be recovered in high yields [3,4].

Two processes that are discussed in more detail later are selective hydrogenation and selective oxidation. Here the catalyst is essential to minimize the formation of undesired by-products that otherwise would end up as waste. For those processes it is our goal to achieve high selectivity of close to 100% by complete conversion of the starting materials. In other applications the catalyst is used for cleaving protective groups or for waste treatment and recycling of side products.

Most processes in the fine chemical industry are typically carried out in batch mode, where the powdered catalyst is suspended in the reaction medium. For the production of bulk chemicals extruded or granulated carbon-supported catalysts are used in fixed-bed reactors. To date, the most important carbon supports from an industrial point of view is activated carbon and carbon black. The main reason for the success of those materials is their commercial availability and variety of different grades, so that the final catalyst can be tailored to the end user's requirements. On a worldwide basis, 908,000 metric tons of activated carbon was produced in 2005 [5]. Only a small fraction of that is used as catalyst support. Other carbon supports, such as carbon aerogels and carbon nanotubes, are in the focus of modern catalytic research but so far have not been used in commercial processes. Since there are various scientific publications in the field of carbon and its use as catalyst support, the focus of this contribution is on the industrial importance of carbon supports for precious metal powder catalysts, their requirements, properties, manufacturing, and industrial applications.

15.2 REQUIREMENTS FOR CARBON MATERIALS AS CATALYST SUPPORTS IN INDUSTRIAL APPLICATIONS

15.2.1 Activated Carbon

The properties and requirements of activated carbon supports are closely related to the requirements of the catalyst. There are a series of parameters that are important for the selectivity and activity of a catalyst: for example, the surface area of the support, the distribution of the pores, and the pore volume, the purity of the activated carbon, and the number and functionality of the surface groups. In regard to engineering aspects, particle size distribution plays an important role for the filtration of the catalyst, and the mechanical stability needs to be considered for the recyclability of the catalyst.

These parameters are discussed in the following paragraphs. Besides those parameters the availability of the activated carbon and the reproducibility of the manufacturing process are crucial.

Surface Area Compared to bulk catalysts the supported catalysts have the advantage that they utilize the catalytically active metal much more efficiently. In bulk catalysts most of the metal is used to actually support the active metal and thus is lost for the catalytic process. Therefore, the support offers a high surface area for maximum dispersion of the metal crystallites. This is very important for precious metal catalysts, where the value of the precious metal (Pd, Pt, Rh, Ru) is very high. For example 100 kg of a commercial 5 wt% platinum catalyst contains 5 kg of platinum metal with a very high value. Current state-of-the-art precious metal powder catalysts have crystallite sizes in the range 2 to 20 nm. The crystallite size can be adjusted by the preparation method (e.g., it is possible to achieve 2.5-nm crystallites with a very tight size distribution on a commercial

scale). Therefore, they have to be considered as nanomaterials (e.g., a platinum catalyst with an average crystallite size of 2 to 3 nm typically shows an activity 50 to 200 times higher than that of micrometer-sized platinum crystallites) [6]. The surface area of activated carbon varies between 500 and 2000 m²/g and depends on several factors, such as the nature of the raw material and the degree and mode of activation. Most of the activated carbons used for precious metal powder catalyst have a surface areas in the range of 1000 m²/g for steam-activated carbons, and 1500 m²/g for chemically activated carbons (Figure 15.1).

Pore Size and Pore Volume Distribution Another very important factor for the performance of the catalyst in the catalytic reaction is the pore size distribution of the activated carbon support. One needs to differentiate between micro, meso, and macro pores. According to the IUPAC, micro pores are smaller than 2 nm, meso pores are in the range between 2 and 50 nm, and macropores are larger than 50 nm. These pores originate from the raw material source as shown in Figure 15.1 and the activation method. Steam-activated carbons from wood raw material have fewer micropores than coconut-based activated carbons. Even fewer micropores can be achieved for activated carbons based on wood raw material if the activation is carried out in the presence of phosphoric acid. The different pores have different meanings for the catalytic reaction. Micropores are responsible for the strong adsorption of small molecules and therefore play an important role in the adsorption of small molecules for water purification. As they are smaller than 2 nm, they are sometimes not accessible for larger molecules. The mesopores are typically considered as the part of the catalyst where the actual catalytic reaction

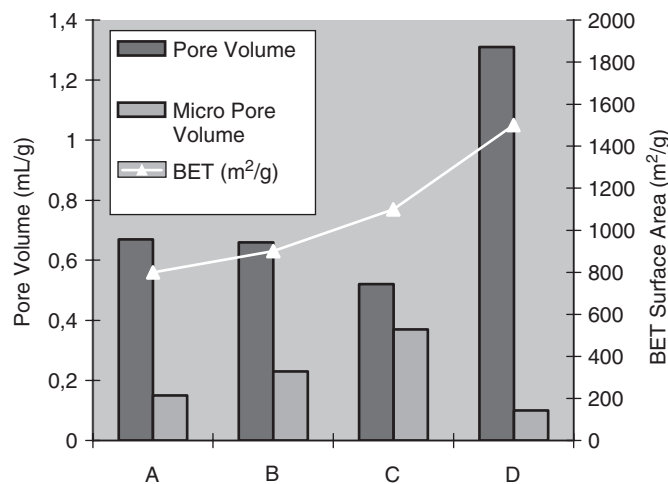


Figure 15.1 Pore volume, micro pore volume, and BET surface area of various carbons from different raw materials and different modes of activation. A, wood, steam activated; B, peat, steam activated; C, coconut, steam activated; D, wood, phosphoric acid activated.

takes place. The macropores are useful for the transport of molecules between the liquid phase and the mesopores. The porosity needs to be adjusted toward catalyst performance. As a catalyst manufacturer, Evonik Degussa has a highly diversified portfolio of commercially available activated carbon supports that can be used for catalyst manufacturing. Detailed knowledge regarding the pore size and pore volume distribution of the various supports helps to adjust these parameters to the requirements of the final catalyst for optimum performance.

Purity The purity of activated carbon is essential for the performance of the final catalyst. Impurities of activated carbon originate from the raw material and the process conditions. Ash contents of up to 20% can be possible. Wood-based activated carbons have ash contents as low as 1 wt% [7]. The ash content can be lowered further by acid treatment of the activated carbon [8]. Typically, the ash consists of alkaline and alkaline earth metal oxides, silicates, and smaller amounts of other compounds (e.g., iron). The presence of the alkaline and alkaline earth metal oxides makes those carbons more basic in nature, so that some additional adjustments are necessary during catalyst manufacturing to meet the constant quality requirements. Since the supports are used in catalysts, the presence of catalytically active compounds that could have a potential influence on the performance of the final catalyst has to be considered as well. For the manufacture of catalysts, activated carbon based on wood, peat, nut shells, and coconut are commonly used. Due to a relatively high sulfur content in activated carbons derived from coal, those carbons are typically not used as catalyst support.

Surface Functional Groups The amount and species of surface functional groups is controlled primarily by the manufacturing process. The chemical properties of most commercial activated carbons are due to the incorporation of oxygen into the carbon surface during the activation process. For manufacturing of activated carbon catalysts, surface functional groups play a very important role and as such, influence the performance in the final application, as has been shown for several examples.

Typical functional groups on the surface of activated carbon are phenols, ethers, alcohols, esters, anhydrides, and carboxylic acids. Chinoide-like structures have also been identified. The functional groups are responsible for both the acid–base and the redox properties of the activated carbon [9]. The presence of oxygen during the activation typically leads to the generation of acidic sites. Oxygen-containing surface functional groups can easily be detected and identified by temperature-programmed desorption [10]. Incorporation of nitrogen into the carbon structure leads to nitrogen modification and generation of basic sites [11].

Lately it has been found that hydrogen also plays an important role with regard to the surface chemistry of activated carbons. Experiments have shown that the surface hydrogen seems to enhance redox processes in the precious metal impregnation step of catalyst preparation. Therefore, surface hydrogen is important for controlling catalyst properties such as dispersion of the crystallites and activity, and therefore need to be monitored carefully [12].

It is generally accepted that the surface groups act as nucleation centers for the generation of highly dispersed metal crystallites. It can be easily imagined that the amount of surface functional groups influences the hydrophobic and hydrophilic character of the carbon support as well. Furthermore, the surface functionalities are assumed to stabilize the metal crystallites to minimize metal sintering.

Particle Size Distribution The intrinsic filtration behavior of activated carbon is correlated directly with the morphology of the activated carbon, which is determined largely by the nature of the raw material, and the particle size distribution. This has already been shown by Auer et al. [13]. One can think of two extremes when explaining the differences: stick- or needlelike structures, as can be found for wood-based activated carbons, and ball-like structures, as can be found in peat or coconut-based activated carbons. Generally speaking, if one has to deal with sticks, they tend to pack over each other during formation of the filtration cake. The fluid can easily pass through the relative open structure. In contrast, ball-like structures tend to pack very tight, and this leads to higher back pressure and therefore to slower filtration times.

For water purification, typically 20×50 mesh (840 to 300 μm) is already considered a fine grade. In catalytic applications, median size typically ranges from 10 to 50 μm . The shape of the particle size distribution curve has a great influence on the filtration. In general, a tighter particle size distribution curve shows improved filtration behavior (Figure 15.2).

Another aspect that needs to be considered is the attrition resistance of the support. To maintain a constant particle size distribution during the use of the catalyst, it has to be as high as possible. Especially when the catalyst is recycled and used several times, a large fraction of extremely fine particles can be

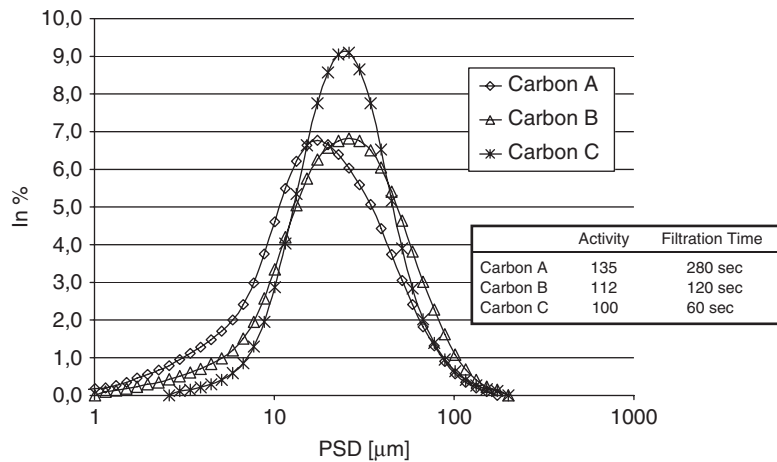


Figure 15.2 Influence of particle size distribution on activity and filtration behavior for three different types of wood-based activated carbons.

generated, and filtration could suffer. Bus loop reactors, especially, require highly attrition-resistant supports. The particle size distribution also plays an important role with respect to the catalytic performance. An increase in the geometric surface area of the solid with decreasing particle size leads to higher catalytic activity (Figure 15.2).

The aim of catalyst development is to adjust the catalyst characteristics to the requirements set by the reaction conditions, reactor equipment, and available filtration units. Thus, a close collaboration between catalyst supplier and customer is required to assure optimum catalytic performance.

The characteristics mentioned above also apply for fixed-bed catalysts. However, the requirements for granulated and extruded activated carbons in regard to the mechanical strength and attrition resistance are even higher. To meet the demand of high attrition resistance, preferably activated carbons from coconut shells are used.

15.2.2 Carbon Black

Carbon black is elemental carbon in a very fine particulate form that is more amorphous than graphite. It consists of planes of carbon atoms fused together randomly to form spherical particles that adhere to each other to create chainlike aggregates (see Figure 15.3), which in turn form agglomerates [14]. The spherical particles range from about 10 to 500 nm [14], and the average aggregate diameters range from 100 to 800 nm [15]. The typical classes of carbon black

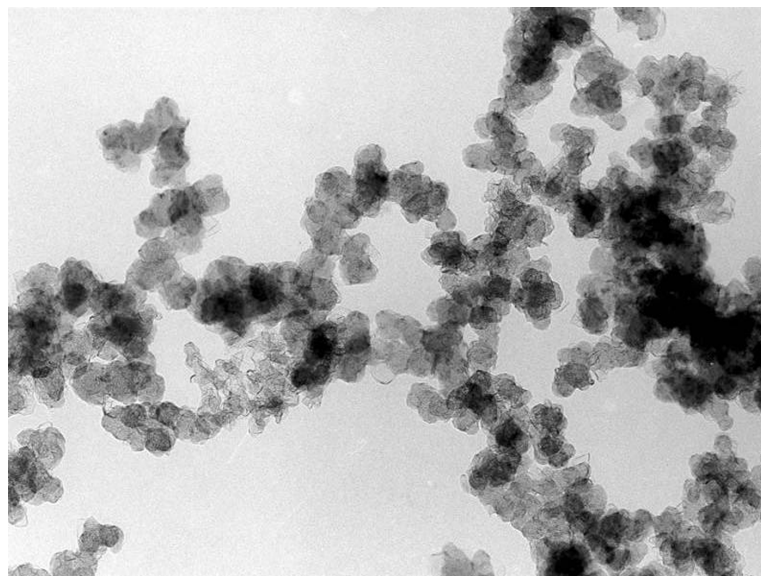


Figure 15.3 Transmission electron micrograph of carbon black, where the spherical primary particles are about 30 nm in diameter.

are characterized by the size distribution of the spherical particles, degree of aggregation, degree of agglomeration, types of surface moieties, and method of production. The two main types of carbon black are produced by either the incomplete combustion method, where the carbon source is oxidized in a limited amount of oxygen, or the thermal decomposition method in the absence of oxygen (see below). The furnace blacks are made via the incomplete combustion method, and they may contain up to 15 wt% oxygen [13]; acetylene black is made by the thermal decomposition method and is relatively oxygen free. Approximately 95% of the carbon blacks produced are furnace blacks. Carbon blacks are used for the production of tires (ca. 70%), automotive parts (ca. 10%), industrially molded and extruded rubber products (ca. 10%), and nonrubber uses (ca. 10%). The nonrubber uses include inks, paints, plastics (especially for UV stable and conductive plastics), paper, batteries, and ceramics [16]. The application of carbon black as a catalyst support is a very small part of the nonrubber category.

The surface area and pore structure of a material are important properties that determine its suitability as a catalyst support. Furnace blacks have surface areas ranging from 100 to 1500 m²/g, and the surface areas of acetylene blacks range from 60 to 300 m²/g [13]. These macro porous materials are generally believed to have “flat surfaces” with no meso or micro pores [17,18]; however, it has since been determined that they contain small amounts of pores, similar to those found on activated carbons [17–19]. The standard nitrogen BET techniques do not seem to be adequate for determining the surface area and porosity of carbon blacks. Some researchers recommend the use of carbon dioxide as an adsorbate and the comparison of its isotherms to those of nitrogen and argon seem to give the best overall description of carbon black surfaces [20–22]. Others still use only nitrogen and argon isotherms and apply more elaborate mathematical treatments to the data, such as lattice density functional theory (LDFT) [17] and grand canonical Monte Carlo (GCMC) simulation [23] to obtain satisfactory results. The fitting of these models to the adsorption data also provides insight into the properties of the measured carbon black, such as the density of surface defects, which can play an important role in catalytic applications. Schröder and colleagues [24] used the adsorption of ethylene to determine not only the surface area, but also the concentration of four types of surface sites, corresponding to graphitic planes, amorphous carbon, crystallite edges, and slit-shaped cavities. While all of these sophisticated methods provide valuable information that can help in the selection of a carbon black as a support, the most important characteristics are its high macro porosity for the free flow of materials in and out of this catalytic system, and the relatively low meso and micro porosity, leading to a high percentage of accessible surface area.

Carbon blacks are conductive, and this also influences their performance as a catalyst support, due to the shifting of electron density between them and the catalytic metal crystals on them. This not only allows for a more intimate interaction between the support and the catalytic metal, but it also provides another method to optimally adjust the reactant’s adsorption strength for the best activity and selectivity. The level of carbon black conductivity was found to be a

function of the structure of its particles, where highly entangled particles have shorter average interparticle distances and improved tunneling conductivity [25]. High-resolution transmission electron microscopy (HRTEM) has also shown that the aggregates are comprised of inseparable particles that are continuous on the lattice scale with graphene layers instead of crystallites [26], indicating that the ratio of pi-to-sigma bond character is very important for approximating the conductivity behavior of these materials. Electron energy loss spectroscopy (EELS) has been used by some researchers [27,28] to determine the ratio of pi-to-sigma bond character and the curvature of the graphene sheets of these materials. They have also used EELS to determine hydrogen's influence as a reactive agent on structure during carbon black formation. One can see that both the type of aggregates and the distances between the aggregates play an important role in the conductivity of carbon blacks. Hence it should not be surprising that the compression level of carbon blacks influences their conductivity, due to the shorter distances between the aggregates [29,30], and this provides yet another tool for the further optimization of carbon blacks as catalyst supports.

Carbon blacks can be pretreated prior to use with materials such as HCl [31], amines [32], and surfactants [33] to improve their catalytic performance, and they can also be functionalized with aryl radicals, esters, dienophiles (e.g., maleic acid), and other materials to additionally enhance their performance [34]. One can functionalize carbon blacks by oxidization with hydrogen peroxide [35], ozone [36], and nitric acid [37] to produce oxygen-containing anchoring groups for the adsorption of precious metal compounds, and this has produced highly active catalysts. It is interesting to note that it is more difficult to oxidize acetylene blacks with nitric acid than it is furnace blacks. Hence, acetylene blacks may be the support of choice when the catalyst needs to survive a reaction medium containing nitric acid [37]. However, acetylene black can be electrochemically oxidized [38] with ozone if this type of surface functionalization is needed. Carbon blacks can also be defunctionalized via high-temperature treatments in inert gases to give a graphitized carbon black with a more hydrophobic character [13] that is ideal for producing the cathodes of fuel cells.

One can use practically the same catalyst preparation methods with carbon blacks as with activated carbon supports to give comparable results. In fact, some precious metal compounds reduce upon contact with furnace black, resulting in a change of the furnace black structure around the metal particle [39]. It has been observed [40] that carbon blacks can be oxidized by the metal crystals supported on them at rather low temperatures (from 398 to 468 K). In fact, some metals may form carbides [41], and this type of metal–support interaction will clearly affect the performance of the catalyst.

Table 15.1 describes the properties of three different carbon blacks and the catalysts made on them via a simple chloroplatinic acid impregnation in an excess aqueous solution followed by their treatment in an undisclosed reducing gas at 573 K for 2 hours [42]. The percentage of accessible surface area for both the Vulcan XC-72R and the Black Pearls was around 66%, and this did not change after they were impregnated with from 5 to 20 wt% Pt. The percentage of

Table 15.1 Characterization of Various Carbon Blacks and Their Respective Catalysts

Carbon Black Type	Pt (wt%)	BET SA (m ² /g)	Microspore Area (m ² /g)	External Area (m ² /g)	Accessible Area (%)	Average Pore Size (nm)	Pt Particle Size ^a (nm)	H ₂ Generation, ^b (mL/min)
Vulcan XC-72R	0	235	82	153	65	9.4		
Acetylene black	0	1304	184	1120	86	3.1		
Black Pearls	0	1487	486	1001	67	8.6		
Vulcan XC-72R	5	215	80	136	63	10		405
Vulcan XC-72R	10	192	72	120	63	9.4	4.5	1689
Vulcan XC-72R	20	170	57	113	67	12	4.1	2301
Acetylene black	20	823	127	695	84	3.4	34.7	2309
Black Pearls	20	1196	406	787	66	6.8	31.3	1916

Source: Ref. 42.

^aMeasured by x-ray diffraction.

^bH₂ generation via NaBH₄ decomposition from a 10-mL/min stream of a 10% NaBH₄/5% NaOH solution under an N₂ atmosphere with 100 mg of catalyst over 20 minutes.

accessible surface area for the acetylene black with and without 20 wt% Pt was rather constant and ranged from 84 to 86%. The acetylene black appears to be the preferred support on the basis of its more open structure, and the consistency of the percentages of accessible area between the supports and the catalysts with different metal loadings suggests that there was no pore blocking during preparation. The pore sizes of the Vulcan XC-72R material ranged between about 9 and 12 nm, that of the Black Pearls dropped from 8.6 nm for the support to 6.8 nm for the catalyst, and the pore sizes of the acetylene black remained around 3 nm after loading it with 20 wt% Pt. It is difficult to determine how accurate the pore size measurements are; however, they do suggest that pore blocking may have occurred during preparation of the catalyst on the Black Pearls but not for those on the Vulcan XC-72R or the acetylene black. The average Pt crystal sizes of the Vulcan XC-72R-supported catalysts were the smallest of the three supports (ca. 4.5 nm), and it was independent of the metal loading. The acetylene black-supported Pt crystals were considerably larger (34.7 nm on the average), as were those on the Black Pearls (with an average of 31.2 nm). Actually the average Pt crystal size is very close to the size of the primary acetylene black spheres for this catalyst. Interestingly, the average Pt particle sizes on these supports did not greatly influence their activity for the generation of hydrogen. Other factors, such as surface accessibility and support conductivity, may have played a more important role for these catalysts. Hence, the influence of the type of carbon black allows one to work outside the typical metal crystal surface area-to-activity relationship. Although there are many advantages to the use of carbon blacks as catalyst supports, their major caveat is that they can be difficult to handle. One problem in particular is that their filtration from the reaction medium can be difficult and one needs to use either a filter press, a centrifugal discharge filter (e.g., the ZHF from Pall GmbH), or any other adequate system for the removal of this very fine agglomerating material from the reaction medium.

15.3 INDUSTRIAL MANUFACTURE OF CARBON SUPPORTS

15.3.1 Activated Carbon

There are already comprehensive reviews and books that deal with the manufacture of activated carbon supports [43–45]. Since only a small fraction of the nearly 1 million metric ton worldwide production of activated carbon is used as catalyst support, intensive quality control of a given carbon support is necessary to make sure that the final catalyst meets all the requirements of the customer and can be manufactured in a reproducible and constant quality over years. This also requires that the raw materials needs to be chosen very well.

The industrial processes start typically from raw materials that are available in rather high quantities (peat, wood, coconut shells, nut shells, fruit pits). These raw materials (e.g., wood chops or sawdust) are transformed into activated carbon by two main processes. The first is the precarbonization of the wood under oxygen-deficient conditions to give charcoal. The charcoal is than activated by steam or carbon dioxide at 1073 to 1373 K to yield activated carbon. During activation the carbon structure is built up by controlled burn-off. The reaction conditions, but also the production equipment, has a strong influence on the porosity of the final activated carbon products [46]. The activated carbons are milled and sieved afterward to achieve the particle size distribution desired and eventually are washed to decrease the ash content. These steam-activated carbons can then be used directly or with some additional modifications for the manufacture of catalysts. The second main process is the chemical activation process of mostly lignocellulosic raw materials (e.g., wood, sawdust, and peat). The raw material is mixed with a chemical reagent that dehydrates the organic moieties in the raw material. Phosphoric acid, zinc chloride, sulfuric acid, and sodium or potassium hydroxide are commonly used as chemical reagents. It is then treated at comparably low temperatures of 673 to 1073 K. For environmental reasons, zinc chloride activation is currently not done in Europe [47]. The internal porosity of activated carbon created by chemical activation is due primarily to the action of the chemical dehydration agent. These activated carbons are also processed further to yield the desired particle size distribution. For fixed-bed processes the activated carbon bodies are produced by extrusion of precarbonized material with binders followed by further carbonization and finally, activation.

15.3.2 Carbon Black

As mentioned previously, carbon blacks can be produced with a carbon source by either its incomplete combustion with a limited amount of oxygen or its thermal decomposition in the absence of oxygen [14]. Furnace blacks are typically produced by burning natural gas and liquid aromatics in a furnace with a limited and controlled amount of oxygen at about 1673 K. The ensuing cracking and polymerization of hydrocarbons followed by their dehydrogenation lead to the formation of turbostratic carbon particles. Immediately after the reaction zone, the carbon black is quenched to 473 to 523 K with a water spray to impede

Table 15.2 Types of Carbon Blacks and Their Sources

Carbon Black Type	Chemical Process	Particle Diameter (nm)	Feedstock
Lamp black	Incomplete combustion	50–100	Coal tar hydrocarbons
Channel black	Incomplete combustion	10–30	Natural gas
Furnace black	Incomplete combustion	10–80	Natural gas/liquid aromatic
Thermal black	Thermal decomposition	150–500	Natural gas
Acetylene black	Thermal decomposition	35–70	Acetylene

Source: Ref. 14.

its further reaction with oxidizing gases such as steam and CO₂. Nonetheless, some oxidation does occur during the quenching step, and this creates additional surface oxide groups [13]. Acetylene black is produced in the absence of oxygen via thermal decomposition at very high temperatures (>2773 K [13]) and its surface is rather devoid of surface oxide groups. Thus, the adsorptive properties of acetylene black is determined by its olefinic character (i.e., the ratio of pi-to-sigma bonds; see above). Table 15.2 covers the preparation of many different types of carbon blacks according to their carbon source, the preparation process, and their resulting particle diameter. These methods provide a wide variety of materials to choose from, so that one can select the right type of carbon black for the intended application.

15.4 MANUFACTURE OF CARBON-SUPPORTED CATALYSTS

15.4.1 Powder Catalysts

The performance of a catalyst for a certain application depends on a number of important parameters. As noted earlier, the characteristics of the catalyst support chosen has a strong influence. Additionally, some other key factors coming from the preparation process determine the final performance, especially selectivity and activity. Those factors are the precious metal loading, the metal distribution of the precious metal crystallites, the size of the crystallites and their spatial distribution, the oxidation state of the metal, and the addition of modifiers. The metal loading of a catalyst is typically in the range 1 to 20% for precious metal powder catalysts. A fuel cell catalyst can have metal loadings of up to 60%. This parameter can easily be adjusted by the amount of precious metal used during catalyst preparation.

In regard to the metal distribution of the metal crystallites, one can differentiate between uniform and eggshell distribution as shown in Figure 15.4. Between those extreme types, other distribution patterns are possible, such as broad eggshell distribution. Which metal location is required depends on the specific catalytic reaction and needs to be determined in detail during the process

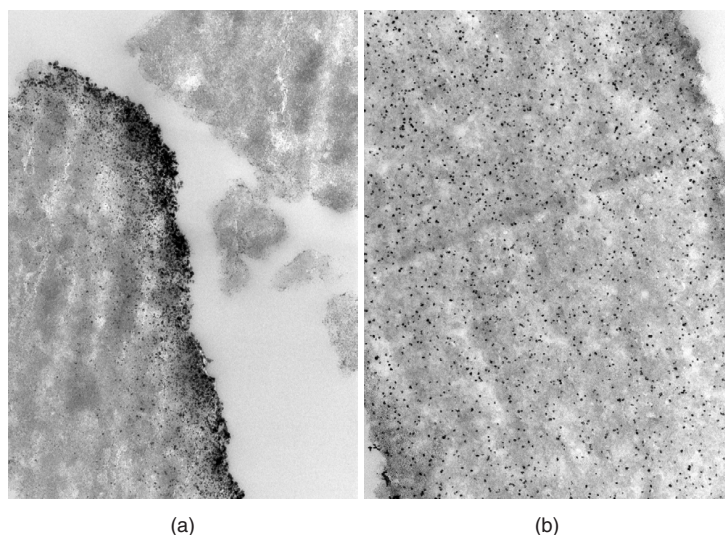


Figure 15.4 Transmission electron micrograph of palladium on activated carbon catalyst: (a) the metal crystallites are located on the edge of the carbon support; (b) uniform distribution of the crystallites. In both cases the crystallites are 2 to 3 nm in size.

of catalyst evaluation. Another factor that needs to be considered is that of the pressure conditions of the technical process (e.g., if a hydrogenation must be carried out). Under low-pressure conditions (1 to 5 bar of hydrogen), typically eggshell catalysts are preferred because they are more active at this pressure. At higher pressure, the preference shifts toward a more uniform distribution, for activity reasons. The activity is also strongly influenced by the size of the metal crystallites. For most applications the metal crystallites should be as small as possible to achieve a high metal surface area. However, if it comes to selectivity for certain reactions, larger crystallites might show improved product yields. Control over the crystallite size distribution is achieved by the treatment of the carbon support and how the precious metal is deposited on the support [48,49]. The influence of metal dispersion on activity and selectivity needs to be evaluated during the catalyst selection process. The oxidation state of the metal crystallites is important for the performance of a catalyst. Sometimes oxidic catalysts that are reduced *in situ* exhibit better performance than reduced catalysts.

Finally, the addition of modifiers can improve the performance of a catalyst. These modifiers depend largely on the reaction. Since there are currently many commercial catalysts that include modifiers, it is not possible to give a comprehensive overview in this chapter. The authors would just like to mention one example where copper is used as a modifier for the selective hydrogenation of halonitrobenzenes to the corresponding anilines without dechlorination [50]. A few examples are given in detail in Section 15.6.

15.4.2 Preparation Technology

A lot of work has been done to achieve an understanding of catalyst preparation and how different parameters influence performance. Several reviews have been published [39,51]. Some authors express the idea that our knowledge is still not sufficient, others state that catalyst preparation has lost all empirical aspects. The fact is that there are a huge number of patents on catalyst preparation, and every patent claims to be the most active and selective catalyst. New methods for making improved catalysts show up almost every day. Most of those use high-cost raw materials and use conditions that are prohibitive for the commercial manufacturing process. The recipes used commercially are considered to be proprietary secrets, depending strongly on the equipment used, and small details play a crucial role for each catalyst. It is the know-how of the catalyst manufacturer which ensures that the catalyst can be produced reproducibly over a long period.

Typical methods that are applicable for manufacture on a large scale include ionic adsorption, colloid deposition, and electroless plating. As an example, uniformly impregnated catalysts are available through the adsorption of ionic species such as $[Pt(NH_3)_4]^{2+}$, $[PtCl_6]^{2-}$, and $[Pd(OH)_4]^{2-}$ onto the carbon support. On the other hand, eggshell catalysts can be made by the deposition of precious metal colloids. The metal colloids adsorb on the external surface of the support. Electroless plating is typically used for the deposition of a second metal on an already existing metal crystallite. In this way, well-defined bimetallic and modified catalysts are available [52].

If a reduced catalyst is required, a final reduction step is carried out at the end of the preparation. Possible reducing agents, such as hydrogen, formaldehyde, hydrazine, sodium formate, or sodium boron hydride, can be used. Care has to be taken since these reducing agents are potentially hazardous materials, and safe handling is required.

In contrast to powder catalysts, which are typically manufactured in batch processes, the production of fixed-bed catalysts on carbon supports rely primarily on impregnation methods (e.g., incipient wetness impregnation). The manufacturing process has to be separated into different steps using multiple pieces of equipment.

15.5 REACTION TECHNOLOGY

The reactor in which chemical reactions take place is the most important piece of equipment in each chemical plant. A variety of reactors are used in industry, but all of them can be assigned to certain basic types or a combination of these “ideal” reactors [53]: (1) batch stirred-tank reactor, (2) continuous stirred-tank reactor, and (3) tubular reactor. The ideal stirred-tank batch reactor is characterized by complete mixing, while in the ideal tubular reactor, plug flow is assumed. In contrast to the stirred-tank batch reactor with well-defined residence time, the continuous stirred-tank reactor has a very broad residence-time distribution. In

the next two sections we describe catalytic stirred-tank and loop reactors briefly for batch operation, and catalytic fixed-bed reactors for continuous operation, as examples of industrial reactors.

15.5.1 Batch Stirred-Tank and Loop Reactors

Stirred-tank batch reactors in multipurpose plants remain the “workhorse” in fine chemicals processing due to their high flexibility and short turnaround times between the production of different chemicals. Most often, a large number of different chemical reactions can be carried out in a single reactor with a large window for the selection of proper reaction conditions, such as solvent, temperature, pressure, catalyst, and residence time. Due to longer downtimes and higher labor requirements, operating costs are higher than with continuous stirred and tubular reactors. Production in multipurpose plants is carried out in relatively small (0.5 to 10.0 m³) stirred-tank batch reactors with annual throughput in the range 1 to 1000 metric tons (MT) for pharmaceuticals and 500 to 10.000 MT for agrochemicals, respectively.

Whenever possible, stirred-tank reactors are equipped with wall baffles inside the vessel (Figure 15.5). These baffles prevent the rotation (“swirl”) of the reaction mixture with the stirrer, and provide good overall mixing, particle suspension, and distribution of hydrogen bubbles in the case of hydrogenation reactions [54].

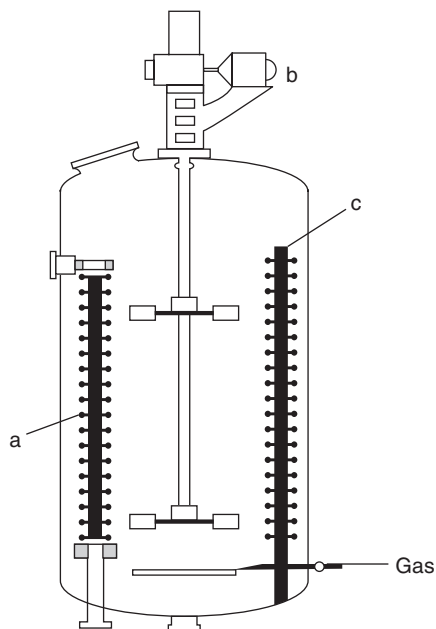


Figure 15.5 Baffled batch stirred-tank reactor: a, heating or cooling coil; b, motor drive; c, baffle. (From ref. 54.)

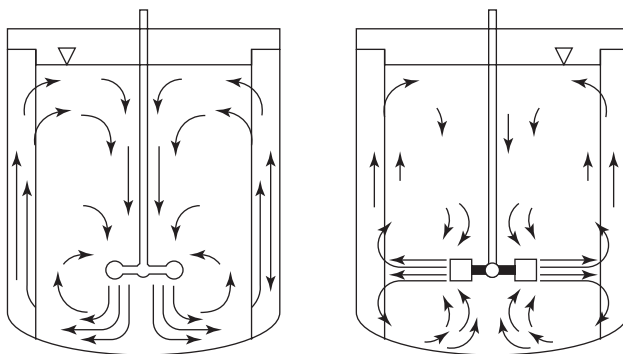


Figure 15.6 Flow patterns in a baffled tank reactor with axial-flow propeller and radial-flow turbine. (From ref. 55.)

In Figure 15.6 the flow patterns in a baffled tank, generated by an axial-flow propeller and a radial-flow turbine stirrer, are shown. A large variety of stirrers is available (Figure 15.7). The selection is made initially based on the viscosity of the reaction mixture [54].

Stirred-tank reactors and loop reactors are very often used in selective hydrogenation reactions in batch or continuous configuration. Companies such as Biazzì, Davy Process Technology, DeDietrich, Lurgi, Pfaudler, and others offer these reactors typically in combination with charge and discharge vessels, feeding pumps, heat exchanger, catalyst separation equipment, and so on. In all hydrogenation reactors, hydrogen, catalyst, and substrate are brought together in the absence of oxygen. Liquid substrates may be hydrogenated directly or in the presence of a suitable solvent. Solvents help to moderate reaction selectivity and reaction heat and aid in catalyst handling and recovery [55]. Preferably, hydrogenation is done at elevated pressure. In consequence, commercial reactors are offered for operating pressure typically up to 6.0 MPa.

Stirred-tank reactors in combination with hollow-shaft turbines for high internal hydrogen recirculation and improved hydrogen dispersion into the liquid are very efficient. Loop reactors, in particular venturi loop reactors, are also very efficient. In this reactor type the reaction mixture, including the powdered catalyst, is circulated back at high flow in a loop connected to a venturi, where hydrogen is sucked in due to a local under pressure. The intense turbulence achieves a very large interfacial area between tiny bubbles and the liquid catalyst suspension (“slurry”). An external heat exchanger on the loop enables very efficient heat removal, convenient for highly exothermic reactions in order to reach an almost isothermal operation. Due to the intense turbulence, venturi loop reactors are restricted to attrition-resistant catalysts. Figure 15.8 shows a typical loop reactor.

After the reaction, the most expensive solid catalyst is separated from the reaction mixture for recycling back into the process or refining to the catalyst vendor.

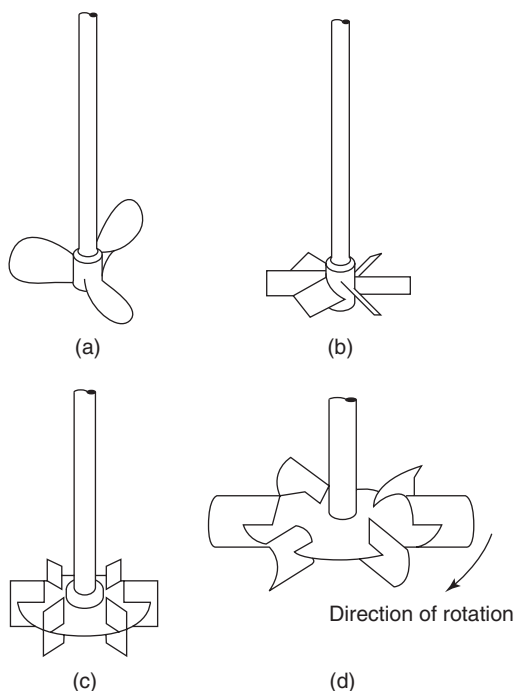


Figure 15.7 Agitators for low-viscosity liquids ($<0.5 \text{ Pa}\cdot\text{s}$): (a) propeller; (b) pitched-blade turbine; (c) turbine; (d) curved blade turbine. (From ref. 54.)

Filtration is the preferred separation method and is typically done using vacuum, pressure, or centrifugal force. Pressure filters are, in fact, most suited when the catalyst must be kept in a closed system for safety reasons [56]. A typical case is the separation of reduced precious metal catalysts such as palladium or platinum on activated carbon in hydrogenation reactions in the presence of solvents with high vapor pressure where the presence of oxygen traces must be prevented in any case in order to prevent fire or explosion. State-of-the-art closed pressure filters such as Fundabac filter systems (Dr. Müller AG, Switzerland) allow fully automated filtration, backwashing of filter candles, and cake discharge under completely tight conditions. In Figure 15.9 the scheme of a typical hydrogenation plant for fine chemical production is outlined.

15.5.2 Fixed-Bed Reactors

Catalytic fixed-bed reactors are the most important type of reactor for the synthesis of large-scale industrial chemicals and intermediates. Fixed-bed reactors for industrial synthesis are operated under constant (stationary) operating conditions over longer periods of time, ranging from months to years. Various reactor

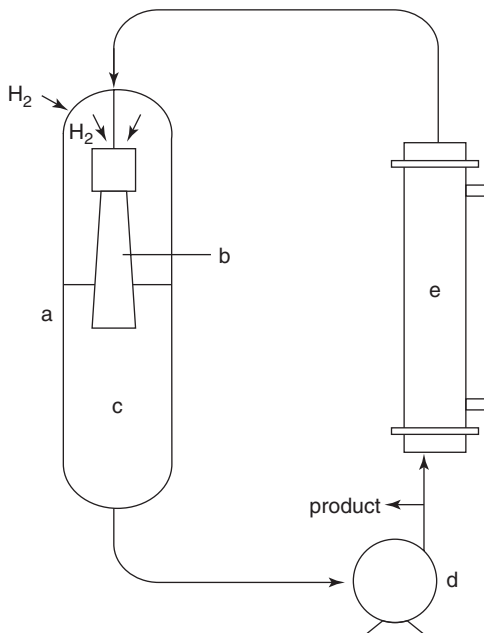


Figure 15.8 Buss loop reactor: a, tank; b, ejector nozzle; c, reacting liquid; d, pump; e, heat exchanger. (From ref. 53.)

designs, such as fixed-bed reactors with an integrated heat supply or removal or multitubular fixed-bed reactors with the heat carrier circulating around the tubes, offer reasonable temperature control in order to influence the chemical reaction in the desired way. Two fixed-bed reactor examples are shown in Figure 15.10.

To achieve a low-pressure drop along the catalyst bed, suitable catalyst forms and arrangements, including spheres, extrudates, and hollow cylinders, as well as structured catalyst packings in the form of monoliths with parallel channels or parallel stacked plates, may be used. Typical continuous fixed-bed catalyst reactions are described in Section 15.6 (in particular, in Section 15.6.1).

15.6 INDUSTRIAL APPLICATIONS

15.6.1 Fatty Acid Hydrogenation

Fatty acids are used in various industrial applications in the form of the free acid or as derivatives such as soaps, esters, alcohols, or amides. End uses of fatty acid-derived products are mainly in the detergent, personal care, soap, cosmetics, and plastics sector. In 2000 the world production capacity of fatty acids was more than 5 million metric tons, with renewable fats and oils being the most important

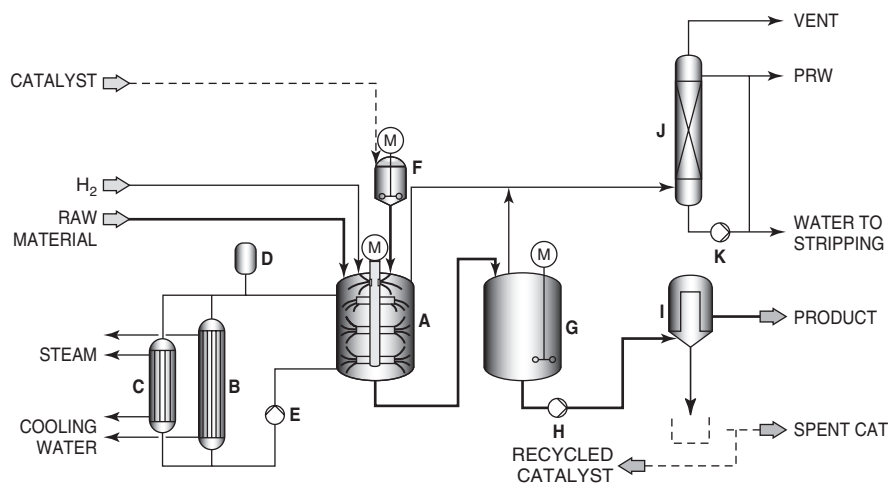


Figure 15.9 Biazzini hydrogenation process design.

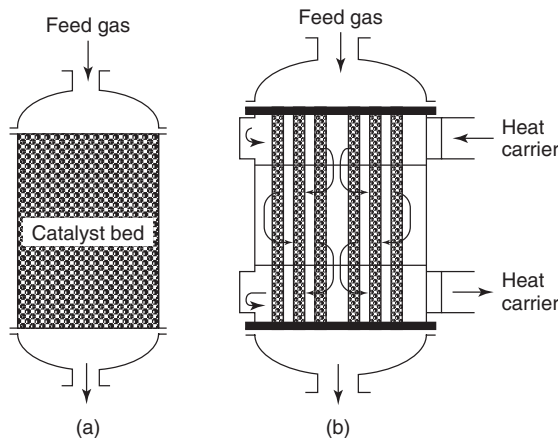


Figure 15.10 Basic types of catalytic fixed-bed reactors: (a) adiabatic fixed-bed reactor; (b) multitubular fixed-bed reactor. (From ref. 57.)

source [58]. In total more than 1 million MT of free fatty acids are hydrogenated on an annual basis for various oleochemical applications. Since the melting point of the hydrogenated products increases, the hydrogenation is also expressed as hardening [59].

The state-of-the-art technology in free fatty acid hydrogenation is characterized by discontinuous operation and the use of powdered nickel on silica catalysts. Known disadvantages of this process are discontinuous operation, low

space–time yields, and high variable costs (e.g., labor, energy, catalyst filtration). The nickel catalyst also causes some problems in that the catalyst is deactivated through formation of nickel soaps. In consequence, free fatty acids must be separated by distillation after the hydrogenation step, which causes high purification costs. Finally, nickel residues must be disposed of, which is getting more and more difficult. Due to the limitations of batch processing and the disadvantages of the nickel catalyst, various attempts have been made in the past to overcome these problems. Over the last three decades various companies (Ruhrchemie [59], Henkel/Degussa [60], Henkel [61,62], J. Brown/Davy Process Technology, and Lurgi/Degussa [63]) were involved in the development of continuous processes operating with palladium-based fixed-bed catalysts. In the mid-1990s Henkel's continuous fixed-bed process came on stream in Düsseldorf-Holthausen, Germany. Activated carbon or titania-based palladium catalysts are highly active for the hydrogenation of free fatty acids and are stable under reaction conditions, even in the presence of water impurities.

Lurgi and Degussa investigated various reaction conditions (liquid space velocity, temperature, hydrogen pressure, and hydrogen to feedstock ratio) and catalyst formulations in order to develop the concept of a commercial plant as described in Figure 15.11. A slight excess of hydrogen was found to be sufficient to achieve good hydrogenation results. Despite a sulfur content of up to 26 ppm in the free fatty acid feedstock, a 2 wt% palladium on activated carbon catalyst was able to retain high activity even after more than 4300 hours onstream. Suitable reaction conditions are temperatures up to 473 K, liquid space velocities on the order

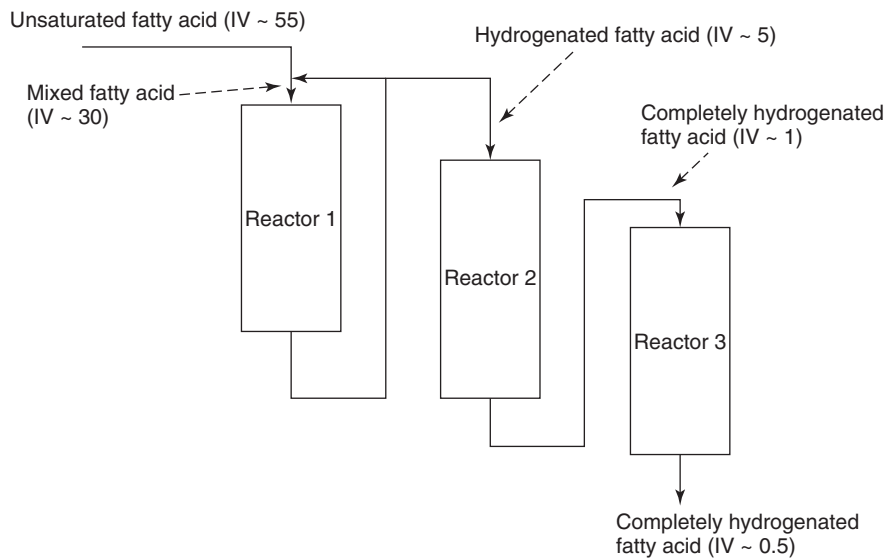


Figure 15.11 Three-step catalytic trickle-bed hardening of free fatty acids. (From ref. 64.)

of 1/h, a total pressure of <2.5 MPa, and a hydrogen excess of approximately 10% mole hydrogen per mole feedstock. Compared to a commercially applied supported nickel catalyst operated in a discontinuous stirred-tank reactor, catalyst consumption at least 23 times lower for the fixed-bed process (0.126 kg of 2 wt% palladium on activated carbon (2.52 g palladium) per metric ton of fatty acid was determined. The new fixed-bed process described offers advantages over the discontinuous stirred-tank reactor process with supported nickel catalysts used currently, including (1) high throughput of raw materials, (2) low catalyst consumption, (3) stable fixed-bed catalyst, (4) no nickel contamination of product, (5) significantly reduced catalyst poisoning by sulfur, (6) no need for the separation of catalyst powders, and (7) no catalyst sensitivity against water [64].

15.6.2 Selective Nitrobenzene Hydrogenations

The hydrogenation of nitrobenzenes can be achieved successfully with various heterogeneous catalyst systems [13]. A new catalyst system introduced on a commercial scale uses a vanadium-doped platinum catalyst with an additional modifier for the reduction of nitroaromatic compounds bearing other reducible functional groups (Figure 15.12) [65]. This system tolerates groups such as CC double and triple bonds, halogens, and carbonyl groups, which are easily reduced if the catalyst is not modified with vanadium.

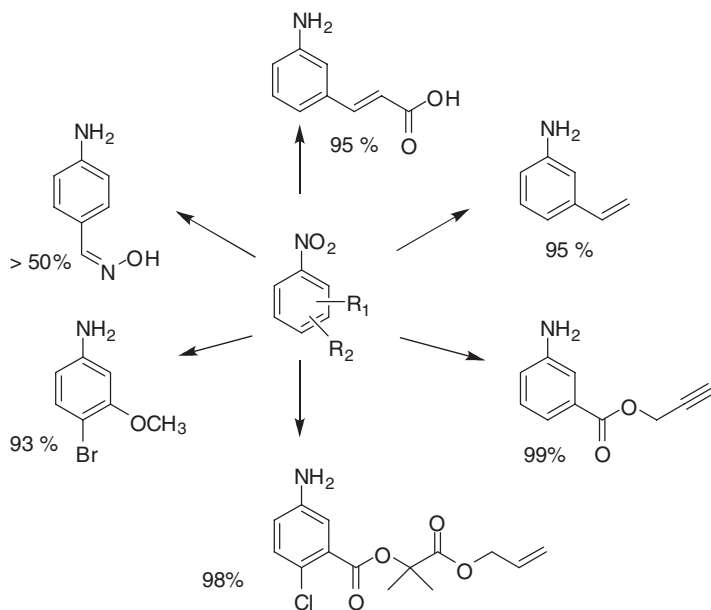


Figure 15.12 Platinum vanadium on activated carbon catalyst for the selective hydrogenation of nitroaromatic groups. The percentages present the yield of the desired product.

15.6.3 Reductive Alkylation

Reductive alkylation is an effective method to synthesize secondary and tertiary amines from primary amines and hence is practiced commercially for the synthesis of a variety of fine and specialty chemicals. These include corrosion inhibitors such as the derivatives of cyclohexylamine, rubber chemicals such as *N*-(1,3-dimethylbutyl)-*N'*-phenyl-*p*-phenylenediamine (6-PPD; see Figure 15.13), pharmaceutical intermediates, dye intermediates, and pesticides [66–70]. The reaction starts out as the condensation of an amine with a carbonyl compound followed by reduction of the intermediate imine (a Schiff base) to the desired amine. If the carbonyl compound has an α -proton that can be abstracted, this secondary amine can be further reduced to tertiary amine [65]. Due to the relatively small volume of such chemicals, the production is usually achieved in a batch process over a heterogeneous catalyst at pressures of 5 to 35 bar and temperatures of 323 to 423 K. Nishimura [71] provides an excellent overview of the literature for the synthesis of primary, secondary, and tertiary amines via reductive alkylation.

Platinum group metals are capable of facilitating reductive alkylation of alkyl and aryl amines with ketones or aldehydes. Carbon-supported palladium and platinum are commonly used as commercial catalysts for reductive alkylation [72]. Platinum is more effective than palladium in alkylating amines and carbonyls of higher molecular weight. The typical by-products of reductive alkylation are the loss of the carbonyl compound via its reduction to an alcohol, hydrogenation of the aromatic ring (if present), and hydrolysis of the C–N bond. Additionally, these catalysts are susceptible to poisoning by sulfur, which may be present as an impurity in the industrial feedstock.

Greenfield and co-workers have shown that the use of transition metal sulfides can overcome the disadvantages of Pt or Pd catalysts. Both base-metal and precious-metal sulfides were effective in catalyzing reductive alkylation of aromatic amine and nitro compounds with aliphatic ketones [73,74]. A variety of base-metal sulfides, including those of Re, Fe, Co, Ni, Mo, W, and Ni-W, catalyzed the reductive alkylation of alkyl- and arylamines with ketones. Rhenium sulfide, the most active of the base-metal sulfides was also capable of hydrogenating any excess ketone to alcohol. Among the sulfides of the platinum group, the Rh was most active while Pd was least active; Ru and Pt seem to possess similar activity at an intermediate level. However, the sulfides of the platinum group

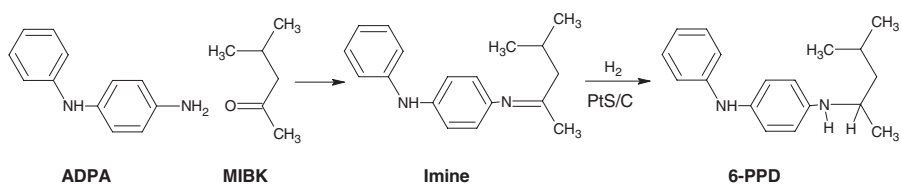


Figure 15.13 Manufacture of 6-PPD via reductive alkylation over Pt/C.

metals were found to be more active and selective than the base-metal sulfides and hence are used more widely in industry. The high cost of precious metals has pushed both the catalyst manufacturer and the user to optimize the process and the amount of Pt or Pd required to achieve certain productivity.

Mylroie et al. [75] showed that experimental design could be used to optimize the process conditions and thereby achieve a higher productivity. Thakur et. al. [76] showed that increasing the sulfur loading of the sulfided Pt catalyst led to an increase in activity. Extending this work, Arunajatesan et. al. [67] used experimental design to optimize the variables in catalyst preparation and improve the catalyst activity for the synthesis of 6-PPD. They found that among the three catalyst preparation parameters examined—Pt loading, S loading, and pH—the ratio of Pt/S was the key parameter. If the sulfur on the catalyst is either under loaded ($S/Pt \sim 0.1$ mol/mol) or overloaded ($S/Pt \sim 3$ mol/mol), the activity of the catalyst was low. An intermediate level of 0.6 mol S/mol Pt yielded the highest reaction rate, immaterial of the Pt loading. In general, the sulfides of platinum group metals appear to be more active than the PGM itself for the reductive alkylation of bulky and sterically hindered molecules.

15.6.4 Toluenediamine

One of the largest industrial applications of carbon black–supported catalysts is the hydrogenation of dinitrotoluene (DNT) to toluediamine (TDA). The resulting TDA is then processed further with phosgene to form toluediisocyanate (TDI), which can be reacted with various diols and other cross-linking agents to produce polyurethane foams and films. The hydrogenation of DNT is a very exothermic and hydrogen-demanding reaction that is further complicated by this reactant's strong adsorption onto the catalyst. Hence, it is easy to have a hydrogen-deficient surface during this reaction, and this usually leads to enhanced metal leaching and rapid catalyst deactivation due to coke formation. Figure 15.14 displays the DNT hydrogenation scheme. The DNT hydrogenation data over a Pd/C catalyst from Neri et al. [78] have shown that this reaction can take three or more parallel routes. The 2,4-DNT can be hydrogenated through an intermediate 4-hydroxyamino-2-nitrotoluene (4HA2NT) before it is converted to 4-amino-2-nitrotoluene (4A2NT) and eventually, TDA. It is possible that 4HA2NT goes directly to TDA without forming 4A2NT. The 2,4-DNT can also form 4A2NT and then TDA directly without generating 4HA2NT at all. The last route forms the 2-amino-4-nitrotoluene (2A4NT) intermediate that proceeds to TDA. Interestingly, 2-hydroxyamino-4-nitrotoluene (2HA4NT) has not been found in any of the reaction mixtures [78], and due to the explosive nature of hydroxyl amines, the 4HA2NT should always be avoided. Regardless of the route, all of the intermediates mentioned above are very active and adsorb strongly. Thus, these intermediates and DNT can all readily yield undesired side products such as tars (e.g., dimers), light boilers (e.g., ring hydrogenated products and toluidines), products with water (e.g., methylaminocyclohexenones), and others (e.g., *N*-allyldiaminotoluenes) if the catalytic surface is hydrogen deficient.

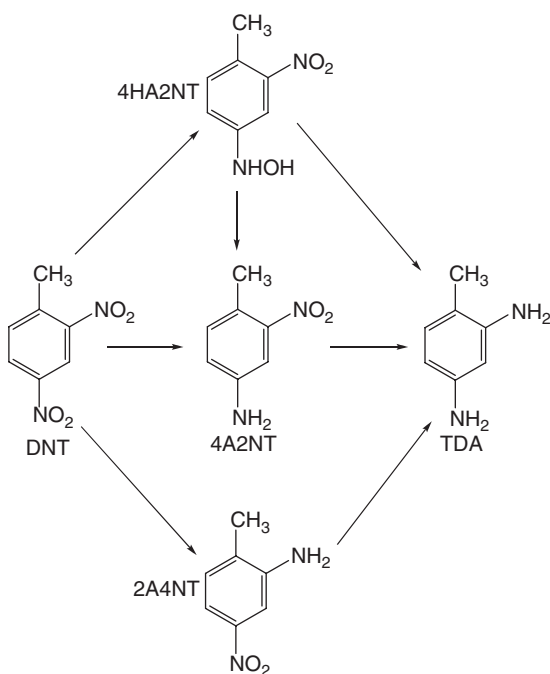


Figure 15.14 Hydrogenation of dinitrotoluene (DNT). (From ref. 77.)

This can be avoided by suspending the catalyst in a hydrogen-rich TDA–water mixture with the same ratio as the stoichiometric product mixture and pumping in only enough DNT so that it is immediately hydrogenated to completion [79]. This is typically how this reaction is performed on a commercial scale; however, this may not be the best testing method on a lab scale since the activity of the catalyst depends on the pump speed, and the lifetime of the catalyst could last for days. Another laboratory testing method would be to pulse the DNT into the hydrogen-rich stoichiometric TDA–water mixture so that there would be a slight access over a very limited period of time. In this way, one could measure the activity of the catalyst as a function of how much TDA per kilogram of precious metal was already formed to give a catalyst deactivation profile.

This catalyst has been optimized over the years [80–82], and the best support was found to be acetylene black due to its highly olefinic nature. Palladium was initially chosen as the main catalytic metal, due to its high activity and low cost. This was improved by promoting it with a small amount of platinum; however, this catalyst was too active and yielded unwanted side products via reactions such as ring hydrogenation. The selectivity of this catalyst was then corrected by the addition of iron oxide, which impeded the undesired reactions. Iron has also been proven to be a promoter for the hydrogenation of aliphatic nitro compounds [83]

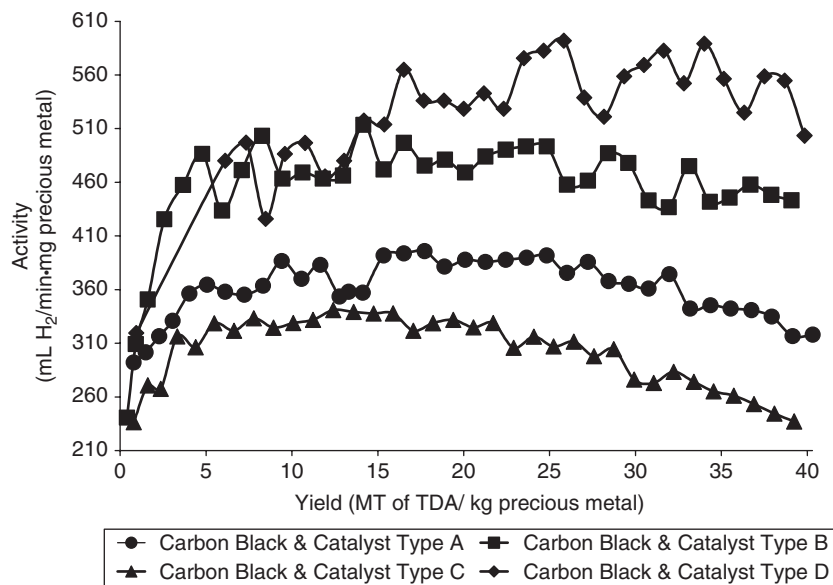


Figure 15.15 DNT pulse hydrogenation data of four different catalyst preparation methods on four different carbon blacks with the same metal combination. (From ref. 84.)

as well as for nitro-aromatics, where it was additionally useful for avoiding ring hydrogenation [82]. One of the catalysts from this optimization work was a 0.77% Pd + 0.09% Pt + 0.85% Fe metal combination supported on acetylene black that exhibited not only high activity but also high selectivity. Further improvements to this system, such as the preparation method and the further screening of other carbon blacks, have made this catalyst one of the best for the production of TDA. Figure 15.15 displays the DNT pulse hydrogenation data for four different catalysts on four different carbon blacks with the same trimetallic combination. Clearly, the type of carbon black and the preparation method are both very critical for the performance of this catalyst, and further optimizations are planned for its continued enhancement [84].

15.6.5 Butanediol

The worldwide market for butanediol (BDO) in 2003 was about 800,000 MT, of which more than half of the production used the Reppe process, which uses acetylene and formaldehyde as the raw materials. However, the industry is moving toward the cheaper technology of using maleic anhydride obtained from butane as the raw material [85]. Although other commercial processes are used to synthesize BDO starting from butadiene, dichlorobutene, or propylene oxide, we limit ourselves to processes where carbon-supported catalysts are used: the

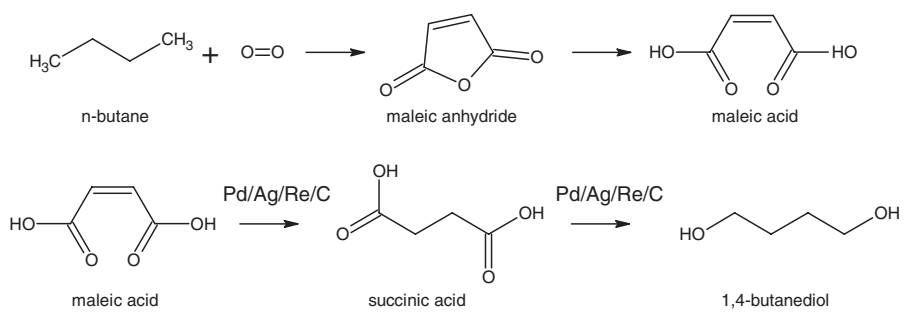


Figure 15.16 BP-Lurgi process for the manufacture of BDO from *n*-butane.

BP/Lurgi (butane; Figure 15.16) and the Mitsubishi (butadiene; Figure 15.17) processes [86–88].

The Geminox process oxidizes *n*-butane in air over a vanadium–phosphorous oxide catalyst in a fluid-bed reactor to maleic anhydride, which is then quenched to maleic acid by absorbing it into water. This highly acidic stream is then pumped to two high-pressure fixed-bed hydrogenation reactors containing carbon-supported catalysts to convert maleic acid to BDO. The major product of reaction, a mixture of 1,4-butanediol, tetrahydrofuran (THF), and γ -butyrolactone, is then separated by fractional distillation. The yield of

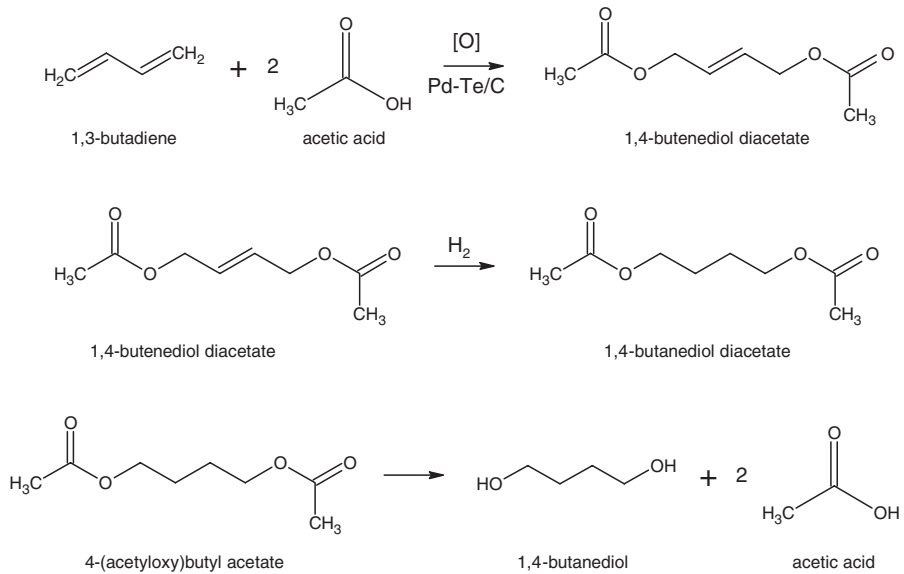


Figure 15.17 Mitsubishi process for the manufacture of BDO from butadiene.

BDO and THF is typically over 90 mol% based on maleic acid. The number of nonutilizable by-products, such as *n*-butanol, *n*-butyric acid, methane, and propane, is small.

The formation of BDO occurs through the successive hydrogenation of maleic acid and succinic acid over a multimetallic Pd–Ag–Re/C catalyst in a trickle-bed reactor [89]. The catalyst uses a nitric acid–treated 30 × 70 mesh activated carbon (ACL40 from CECA S.A., France) as the support. After the acid treatment, the support is washed, dried, and impregnated with a solution of nitrates of Pd and Ag, and perrhenic acid, along with some acetonitrile. The catalyst is then dried and activated in the reactor using hydrogen at 280°C for 5 hours. The resulting catalyst (3% Pd/3% Ag/6% Re/C) was highly selective to BDO (93%) with *n*-butanol (ca. 5%), THF (ca. 2%), and some GBL as by-products. A similar catalyst, 4% Pd/4% Ag/8% Re/C (containing same volumetric density of metals) when prepared without the oxidation of the carbon, yielded significantly lower selectivity toward BDO (50%) and higher amounts of THF (ca. 22%) and *n*-butanol (ca. 23%) with trace amounts of GBL.

Butanediol is also manufactured by oxidizing butadiene with acetic acid to form 1,4-butanediol diacetate over a Pd–Te/C catalyst. This may be hydrogenated further to 1,4-butanediol diacetate (1,4-DBA) over a Ni or Pd catalyst. 1,4-DBA is then hydrolyzed over an ion-exchange resin to obtain BDO and acetic acid. The carbon support used for manufacture of the Pd–Te catalyst requires a special pore size distribution so as to attain high activity and stability of the catalyst. The inventors describe the support as preferably having a pore volume greater than 0.55 cm³/g, of which at least 55% is contributed by pores larger than 300 nm. The catalyst is prepared by first oxidizing the carbon support with nitric acid at 363 K for 3 hours, filtered and impregnated with nitrates of Pd and Te. A typical catalyst containing 3.6% Pd and 0.65% Te supported on such a special structural carbon yielded acceptable acetoxylation activity at about 60 bar and 353 K for over 4000 hours. However, a carbon support of lower pore volume and smaller pores deactivated after about 500 hours.

15.6.6 Purified Terephthalic Acid

Purified terephthalic acid (PTA) is one of the largest-scale chemicals produced worldwide. Main fields of application for PTA include PET chips, PET films, PET fibers, and bottle resins. Two principal processes are used for the purification of raw terephthalic acid: esterification distillation and ester cleavage of dialkyl terephthalates, and direct hydrogenation and crystallization [90]. The latter process was discovered by the Standard Oil Co. and later licensed worldwide, becoming the dominant process for PTA. The general process is to hydrogenate 4-carboxybenzaldehyde, which is an impurity of terephthalic acid in the presence of an extruded Pd/C catalyst. Process conditions are typically 373 to 573 K and 200 to 1500 psi [91].

Although PTA catalysts have been commercialized for more than 30 years, research activities are still ongoing [92–94]. The main focus of the research has

been on improvement of the Pd/C catalyst. In general, porous coconut carbon in extruded form is used as the support. Palladium metal is impregnated on the carbon support as chloride solution or another type of compound. After all necessary production steps, including washing and drying, the final catalyst typically has 0.5% Pd loading. The Pd metal crystallites are preferably distributed on the outer layer of the carbon support. Due to the acidic environment for purifying terephthalic acid, Pd could be dissolved and thus the catalytic activity reduced. Another major cause of catalyst deactivation is Pd sintering.

15.7 TESTING AND EVALUATION OF CARBON CATALYSTS

15.7.1 Current Methods for Catalyst Evaluation

The setup for testing of catalysts has to be as close as possible to the technical conditions of catalyst application. Therefore, powder catalysts for liquid and gas–liquid reactions are usually tested in slurry reactors, which can be operated continuously, under semibatch conditions (constant pressure of the reaction gas, compensation of gas uptake) or in the complete batch mode (no compensation of gas uptake, record of pressure drop of the gas phase). In contrast, catalysts for continuous fixed-bed applications have to be tested in continuous lab-scale fixed-bed reactors. The latter can be operated under either steady-state or non-steady-state (transient) conditions.

Slurry Reactors for Testing Powder Catalysts Reactions with powder catalysts are usually three-phase reactions: solid, liquid, and gas. Thus, testing of powder catalysts is usually performed in stirred-tank reactors (size 100 to 1000 mL) which have to guarantee efficient mass transfer and isothermicity by both constructional means and optimization of reaction conditions. A large gas/liquid-phase surface area improves the gas transfer and is realised on a labscale by the use of an agitator for gas injection, a high stirrer speed, and baffles. Alternatively or in parallel if possible, the gaseous pressure can be increased.

In case of very exothermic reactions, a good heat exchange must be provided. This is usually realized by cooling coils, cooling jackets, or in case of the loop reactor, by an external heat exchanger [95]. If the slurry reactors are operated continuously or in the semibatch mode, the catalyst activity can be derived conveniently by the quotient $p(\dot{V}_{\text{gas,inlet}} - \dot{V}_{\text{gas,outlet}})/RTV_{\text{gasphase}}$. If the reactor is operated in the batch mode, activity data must be derived from the formation of the derivative dp/RTd (reaction time), for a defined reference point in time. Complementary catalytic performance data can be derived based on selectivity values at a certain degree of conversion.

Steady-State Reactors for Testing Fixed-Bed Catalysts Lab-scale fixed-bed reactors for catalyst testing usually reveal diameters between 5 and 15 mm. Steady-state reactors are operated in either an integral or a differential mode.

The advantage of the differential mode of reactor operation is the direct derivation of the molar rate of changes of reactants. However, differential conditions can be ascertained only in a narrow range of conversion of reactants. For the plug-flow reactor type, the criterion for the differential range of conversion is the appearance of a linear relationship between concentration and contact time. Then the molar rate of change can be derived simply by the quotient $\Delta c/\tau$, where Δc is the difference of inlet and exit concentration of a reaction component, and τ is the contact time in the reactor. A possibility for establishing experimental conditions allowing the direct derivation of the molar rate of changes based on simple $\Delta c/\tau$ quotients even for larger ranges of conversion is the use of gradient-free reactors corresponding to fluid-dynamic conditions of continuous stirred-tank reactors.

While for slurry reactors this operation can be realized simply by stirring, for heterogeneous catalytic reactions, special construction for complete gas mixing within the catalyst bed is required. Typical constructions for this purpose are the Berty reactor with its different modifications [96,97] and the Carberry reactor [98,99]. In the Berty reactor, the catalyst is fixed in a basket through which gas is flown in a fast internal recycle forced by a turbine. The gas stirring in the Carberry reactor is realized by a rotating basket.

Gradient-free reactor types do reveal neither concentration nor temperature gradients (difference between reactor entrance exit below 2 K) and hence can be operated isothermally even if reactions with significant heat generation or consumption have to be studied. If isothermal conditions cannot be warranted, the heat balance of the reactor system must be solved in addition to the mass balance. Unfortunately, this situation is related to several disadvantages:

1. Except for adiabatic reactor operation, precise control of heat exchange is difficult. The local rate of heat exchange between the reactor and the surrounding and the local temperature are interrelated and depend on the fluid-dynamic conditions inside the reactor.
2. Catalyst testing under nonisothermal conditions suffers from the fact that activity will change with location inside the reactor corresponding to differences in temperature. These circumstances indicate that as far as it is possible to establish isothermal conditions, such a mode of reactor operation should be realized for the determination of intrinsic activity and selectivity of catalysts.

An advanced tool for providing isothermicity along a catalytic reaction zone might be provided by micro-structured reactors [100,101]. This reactor concept is based on a multichannel unit with channel dimensions in the range 50 to 200 mm width and depth. Meanwhile, there are a large variety of technologies to produce these structures for different materials (i.e., metals, ceramics, glass, etc.). Besides the small channel dimension, another characteristic of such micro-reactor structures is the high wall/channel volume ratio. This leads to the fact that the heat transport of these structures is determined primarily by axial heat conductivity

through the reactor wall, which allows isothermal reactor operation even for highly exothermic reactions [102].

Non-Steady-State Reactors for Testing Fixed-Bed Catalysts In non-steady-state reactors, reaction conditions such as temperature or reactant concentrations are changed temporarily [103–105]. Temperature-programmed surface reaction (TPSR) experiments, temperature-programmed desorption (TPD), and temperature-programmed reduction and oxidation (TPR, TPO) [106,107] are established methods dealing with non-steady-state reactor operation. Among these methods, TPSR is a technique that can be applied directly under reaction conditions relevant for catalytic processes.

Starting from a defined initial state of the catalyst surface (certain coverage and temperature) the temperature is raised and the response of reactant concentration or pressure at the reactor outlet is recorded by analytical methods with high time resolution. The variation of heating rates allows to draw conclusions with respect to mechanisms of desorption and reaction as well as the calculation of the activation energies of these processes.

The other group of methods is based on sudden jumplike disturbances of the concentration of reactants after establishing a defined steady state of the reactor system. From the different shapes of responses at the reactor outlet, conclusions can be drawn concerning reaction mechanisms such as rate-determining steps and catalyst reconstruction phenomena.

Pulse methods are based on the principle that a sequence of concentration pulses passes the catalyst bed until no change in the shape of the pulse response is observed. Depending on the pulse frequency, one can attain nearly steady-state conditions [108].

Reverse chromatography is a method by which small amounts of reactants are pulsed into a carrier gas. The state of the catalyst surface is not changed significantly, and the pulse shape at the reactor exit indicates interaction of the reactant molecules with the catalytic surface.

15.7.2 High-Throughput Testing of Carbon Powder Catalysts

Selection of optimal precious metal powder catalysts based on activated carbon with respect to their activity and selectivity is essential in the synthesis of fine and intermediate chemicals. Due to the tremendous number of substrates and the diversity of catalyst types (different degrees of reduction, dispersion of metal, and morphology of activated carbon supports), the process of finding the optimal combination of catalyst and application is very time consuming. Therefore, high-throughput tools might accelerate the selection process. However, the degree of reactor parallelization and miniaturization is limited, due to the heterogeneity of the activated carbon material and the possible appearance of mass transport effects. To guarantee the reproducibility of catalyst behavior and process scalability, appropriate test conditions and reactor setups have to be chosen. The following aspects have to be considered: (1) A minimum mass of catalyst is

required to obtain statistically representative activity data; (2) a maximum mass of catalyst, in turn, must not be exceeded to avoid mass transfer limitation; and (3) the mass of catalyst used for testing determines the volume and construction of the reactor.

In Figure 15.18, results of a statistical analysis for predicting the minimum amount of catalysts (5 wt% Pt) are shown, from which it can be concluded that the sampling error becomes unacceptable if the catalyst mass becomes lower than 5 mg. Related to this minimum mass of catalyst, a minimum reactor volume of 20 mL can be derived. This can be considered as a reasonable reactor size for high-throughput testing of carbon catalysts. The usual degree of parallelization related to 20-mL reaction vessels is between 8 and 32. A variety of suitable high-throughput units for testing powder catalysts is commercially available.

The extent of mass-transfer limitation in a high-throughput reactor setup is illustrated exemplarily in Figure 15.19 for the hydrogenation of cinnamic acid over different Pd and Pt catalysts. The activities of these catalysts were determined both in a lab-scale reactor of 300 mL with an impeller (values plotted on the y-axes) and in a 20-mL reactor with a magnetic stirrer (values plotted on the x-axes). For good agreement between test results in both reactors, the points should follow the diagonal in Figure 15.19. However, a systematic deviation becomes obvious: Activity values in the 300-mL reactor converge against a value of $1200 \text{ mL} (\text{H}_2)/\text{g}\cdot\text{min}$. In the 20-mL reactor, much higher activity values are measured, and the highly active catalysts can still be distinguished. This indicates that the mass-transport process in the miniaturized reactors is significantly faster than in the 300-mL reactors despite the slower agitation rate in the 20-mL reactors (1500 min^{-1}) than the 2000 min^{-1} in the 300-mL reactor. Obviously, agitation is more efficient in the 20-mL reactors due to the small liquid

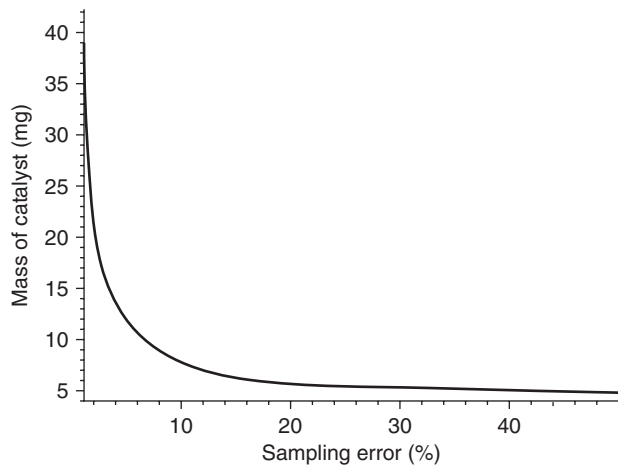


Figure 15.18 Calculated relationship between mass of catalyst and catalyst sampling error for a commercial Pt/activated carbon catalyst.

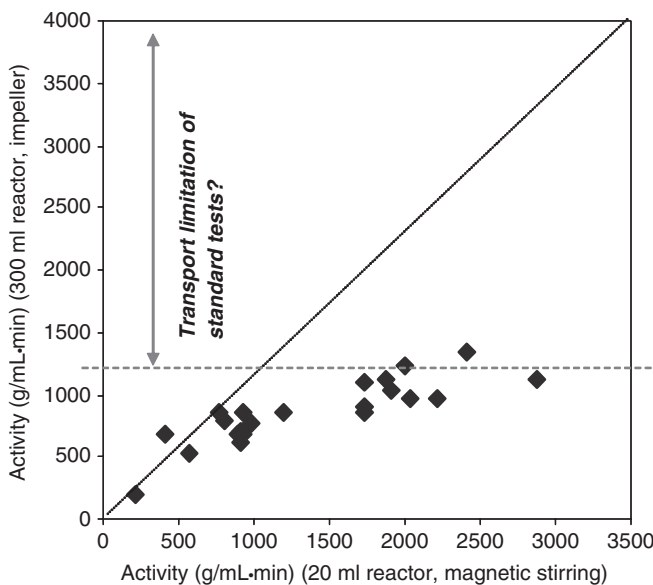


Figure 15.19 Parity plot of activity in cinnamic acid hydrogenation at 1 bar determined in a 300-mL reactor (y-axes) and in a 20-mL reactor (x-axes) using different Pt/C and Pd/C catalysts.

volume. The effect becomes even more pronounced for faster reactions such as hydrogenation of (chlorinated) nitro-aromatics.

Accordingly, selection and optimization of catalysts for various gas–liquid reactions can be accelerated for conditions close to the technical process since miniaturized high-throughput reactors with optimal size reveal improved mixing efficiency. Moreover, the critical scale-up parameters can also be derived from this methodology.

15.7.3 Catalyst Profiling

The development of catalysts based on carbon supports is related to the challenge that solid properties determining the catalytic properties are not easily accessible. Regardless of the fact that catalysts do not show obvious differences with respect to solid properties (e.g., morphological and surface properties of the carbon support, metal particle size, particle dispersion or solid phase and oxidation state of the active metal), they often reveal differences in their catalytic behavior. For industrial application of catalysts in fine chemistry, these circumstances are serious obstacles for a straightforward rational development and the identification of suitable catalysts for conversion of certain substrates.

Against this background, *catalytic performance profiling* can help to determine specific characteristics of heterogeneous catalysts for fine-chemical applications

[109]. Catalytic performance profiling is a heuristic method that takes into account the complexity of the relationship between the catalyst preparation method and catalytic performance in a large diversity of classes of reactions of (multifunctional) substrates.

In Figure 15.20 the principles of catalytic profiling analysis are explained. Catalytic profiling analysis includes a set of test reactions that are very sensitive with respect to catalyst properties and/or the recipes of preparation. From

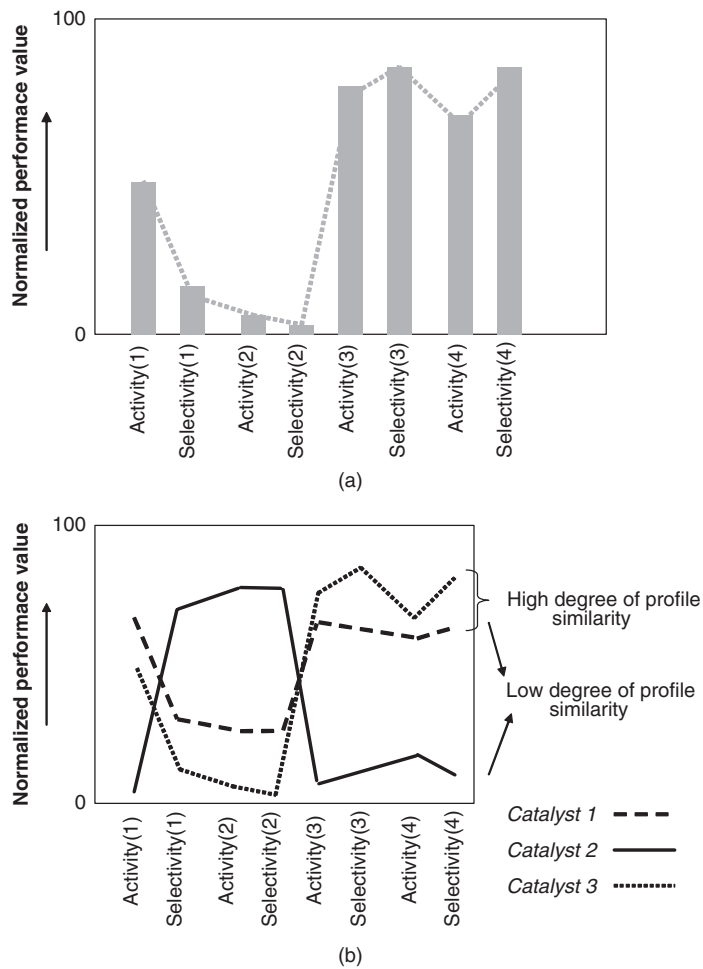


Figure 15.20 Concept for catalyst profiling based on a set of sensitive test reactions: (a) determination of particular performance data for an individual catalyst (activity and selectivity values in different test reactions); (b) visualization of performance profiles from the particular performance values as fingerprints for individual catalysts as a basis of similarity analysis.

activity and selectivity values measured for a set of test reactions [Figure 15.20(a)], corresponding performance profiles [Figure 15.20(b)] can be derived which can be understood as unique catalytic fingerprints for individual catalysts. The profiling method allows a fast identification of strength and weaknesses of a catalyst. Based on this approach, libraries of heterogeneous catalysts can be built up which cover a wide diversity of catalytic properties and hence a wide range of fine-chemical applications. Moreover, catalytic performance profiling is a useful tool for quality indication to control the transfer of lab-scale recipes of catalyst preparation to the technical scale of catalyst production as well as to identify fluctuation in raw material quality (e.g., the quality of carbon supports).

15.8 CONCLUSIONS

Carbon materials are used extensively as cost-effective supports for heterogeneous precious metal catalysts in chemical industry. Their stability under acidic and basic conditions as well as the facile recovery of the active precious metal simply by burning off the carbon from the spent catalyst make these supports ideal for many catalyst applications. Activated carbons are the most commonly used carbon supports, and they are usually produced by one of two different methods. Wood can be precarbonized under oxygen-deficient conditions to form charcoal that is activated with either steam or carbon dioxide followed by milling, sieving, and washing to give the desired particle size distribution and residual ash level. Another method uses lignocellulosic raw materials such as wood, sawdust, and peat, and these may be processed into activated carbons by mixing them with a chemical activation reagent (e.g., phosphoric acid, zinc chloride, sulfuric acid, potassium hydroxide), treating them at 673 to 1073 K followed by milling, sieving, and washing as described previously. Carbon blacks can also be used as catalyst supports and they are produced by either the incomplete combustion of coal tar, natural gas, or liquid aromatics; or the thermal decomposition of acetylene or natural gas. In the case of fixed-bed supports, the precarbonized material is usually extruded with binders followed by further carbonization, activation, and washing. Both the method of production and the raw material being used will determine the properties of the activated carbon and its suitability as a catalyst support. Some of the most critical properties of carbon supports are their particle size distribution, surface area, pore volume distribution, pore volume, purity, types of surface groups, concentration of the surface groups, particle morphology, and hydrogen content. These carbons are produced in very large volumes with only a considerably small amount of them being used as catalyst supports. The advantage of this situation is that there will always be a consistent long-term supply of these materials, and the disadvantage is that these vendors have very little economic incentive to design an application-specific carbon support for the catalyst industry. Even though there is a suitable level of consistency in the long-term quality of these supports, they are still processed natural materials that may have occasional batch-to-batch variations that one needs to take into

consideration. It is the know-how of catalyst producers that allows them to develop robust catalyst recipes that deliver the same performance each and every time regardless of the batch-to-batch variations of the carbon supports. Hence, it is very important to replicate newly developed catalyst formulations on many more than just one batch of the chosen carbon support before they are introduced into the marketplace. A short, albeit not exhaustive list of critical recipe controlled catalyst properties that one can use to develop optimized formulations include the choice of precious-metal(s), precious-metal loading, metal distribution on the support (e.g., eggshell or uniform), metal crystallite size, spatial distribution of the metal crystals, oxidation state of the metal, addition of modifiers, and choice of carbon support. The choice and application of the appropriate catalyst recipe needs take into consideration the reaction type, reactor type, reaction conditions, and the properties of the best overall carbon support for this application listed above. Large-volume chemical products are usually produced with fixed-bed reactors that are excellent for providing hydrogen to the reaction site (especially in the trickle phase) and the rapid separation of the product from the catalyst. Examples of this include the production of BDO and the purification of PTA. Smaller-scale fine and specialty chemicals (e.g., 6-PPD) are more economical to produce with stirred-tank reactors, where heat exchange is optimal and recent developments have improved the distribution of hydrogen. Loop reactors may utilize the positive aspects of both fixed-bed and stirred-tank reactors, and their use in the chemical industry is increasing steadily. The production of some high-volume products may involve challenging reactions, such as the hydrogen-demanding exothermic reduction of DNT to TDA, and this is typically carried out in a continuous stirred-tank or loop reactor, where the addition of DNT is limited to the rate at which it can immediately be hydrogenated to completion.

These examples demonstrate that the economics of commercial chemical transformations on catalytic surfaces are determined by the reaction conditions as well as both reactor and catalyst design. Thus, it is always prudent to involve catalyst experts when designing new processes and reactors, and due to ever-improving catalyst technology, it is also possible to enhance the economics of an existing process by the further optimization of the catalyst. In this respect, carbon supports provide catalytic chemists with a very flexible and economic platform on which to ply their craft.

REFERENCES

- [1] P. Roisson, J.-P. Brunelle, P. Nortier, in A.B. Stiles, Ed., *Catalyst Supports and Supported Catalysts*, Butterworth, Boston, 1987, p. 11.
- [2] A.B. Stiles, Ed., *Catalyst Supports and Supported Catalysts*, Butterworth, Boston, 1987, p. 57.
- [3] C. Hagelucken, *Erzmetall* 49 (1996) 122.
- [4] Degussa AG, *Precious Metal Cycle and Precious Metal Recovery*.

- [5] <http://www.freedomiagroup.com>.
- [6] N. Tian, Z. Zhou, S.-G. Sun, Y. Ding, Z.L. Wang, *Science* 316 (2007) 732.
- [7] F. Derbyshire, M. Jagtoyen, M. Thwaites, in J.W. Patrick, Ed., *Porosity in Carbons: Characterization and Applications*, 1995, p. 227.
- [8] P. Albers, K. Deller, B.M. Despeyroux, G. Prescher, A. Schaefer, K. Seibold, *J. Catal.* 150 (1994) 368.
- [9] D.S. Cameron, S.J. Cooper, I.L. Dodgson, B. Harrison, J.W. Jenkins, *Catal. Today* 7 (1990) 113.
- [10] J.L. Figueiredo, M.F.R. Pereira, M.M.A. Freitas, J.J.M. Orfão, *Carbon* 37 (1999) 1379.
- [11] C. Pinel, E. Landrivon, H. Lini, P. Gallezot, *J. Catal.* 182 (1999) 515.
- [12] P.W. Albers, J. Pietsch, J. Krauter, S.F. Parker, *Phys. Chem. Chem. Phys.* 5 (2003) 1941.
- [13] E. Auer, A. Freund, J. Pietsch, T. Tacke, *Appl. Catal. A* 173 (1998) 259.
- [14] <http://www.cancarb.com/thermax1.html>.
- [15] IARC, Carbon black, *International Agency for Research on Cancer—Summaries and Evaluations*, Vol. 65, 1996. <http://www.inchem.org/documents/iarc/vol65/carbon.html>.
- [16] E.L. Crump, EPA-452/D-00-003, May 2000, pp. 1–16.
- [17] P. Kowalczyk, K. Kaneko, A.P. Terzyk, H. Tanaka, H. Kanoh, P.A. Gauden, *Carbon* 42 (2004) 1813.
- [18] M. Kruk, M. Jaroniec, J. Choma, *Carbon* 36 (1998) 1447.
- [19] P. Kowalczyk, E.A. Ustinov, A.P. Terzyk, P.A. Gauden, K. Kaneko, G. Rychlicki, *Carbon* 42 (2004) 843.
- [20] F. Stoeckle, T.A. Centeno, *Carbon* 43 (2005) 1184.
- [21] F. Stoeckle, A. Guillot, A.M. Slasli, D. Hugi-Cleary, *Carbon* 40 (2002) 211.
- [22] F. Ehrburger-Dolle, M. Holz, J. Lahaye, *Pure Appl. Chem.* 65(10) (1993) 2223.
- [23] A. Wongkoblap, D.D. Do, *Carbon* 45 (2007) 1527.
- [24] A. Schröder, M. Klüppel, R.H. Schuster, J. Heidberg, *Carbon* 40 (2002) 207.
- [25] I. Balberg, *Carbon* 40 (2002) 139.
- [26] W. Zhu, D.E. Miser, W.G. Chan, M.R. Hajaligol, *Carbon* 42 (2004) 1841.
- [27] A. Braun, F.E. Huggins, N. Shah, Y. Chen, S. Wirick, S.B. Mun, C. Jacobsen, G.P. Huffman, *Carbon* 43 (2005) 117.
- [28] C. Jaeger, T. Henning, R. Schlögl, O. Spillecke, *J. Non-Cryst Solids* 258 (1999) 161.
- [29] J. Sánchez-González, A. Macías-García, M.F. Alexander-Franco, V. Gómez-Serrano, *Carbon* 43 (2005) 741.
- [30] N. Probst, E. Grivei, *Carbon* 40 (2002) 201.
- [31] A. Albers, R. Burmeister, K. Seibold, G. Prescher, S.F. Parker, D.K. Ross, *J. Catal.* 181 (1999) 145.
- [32] H.G. Yoon, K.W. Kwon, K. Nagata, K. Takahashi, *Carbon* 42 (2004) 1877.
- [33] X. Dang, Y. Wei, S. Hu, *Anal. Sci.* 20 (2004) 307.
- [34] K. Bergemann, E. Fanghänel, B. Knackfuß, T. Lüthge, G. Schukat, *Carbon* 42 (2004) 2338.

- [35] J.L. Gómez de la Fuente, M.V. Martínez-Huerta, S. Rojas, P. Terreros, J.L.G. Fierro, M.A. Pena, *Carbon* 43 (2005) 3002.
- [36] Z.B. Wang, G.P. Yin, P.F. Shi, *Carbon* 44 (2006) 133.
- [37] K. Kamegawa, K. Nisikubo, M. Kodama, Y. Adachi, H. Yoshida, *Carbon* 40 (2002) 1447.
- [38] D. Wei, S. Kato, R. Ichino, M. Okido, *Metall. Mater. Trans. B* 31 (2000) 235.
- [39] P.A. Simonov, V.A. Likhobov, in A. Wieckowski, E.R. Savinova, C.G. Vayenas, Eds., *Catalysis and Electrocatalysis at Nanoparticle Surfaces*, Marcel Dekker, New York, 2003, pp. 409–454.
- [40] D.A. Stevens, J.R. Dahn, *Carbon* 43 (2005) 179.
- [41] L. Tröger, A. Freund, P. Albers, K. Seibold, G. Prescher, *Ber. Bunsenges. Phys. Chem.* 101 (1997) 851.
- [42] C. Wu, H. Zhang, B. Yi, *Catal. Today* 93–95 (2004) 477.
- [43] O. Wohler, F. von Sturm, E. Wege, H. von Kienle, M. Voll, P. Kleinschmit, in W. Gerhartz, Ed., *Ullmann's Encyclopaedia of Industrial Chemistry*, Vol. A5, VCH, Weinheim, Germany, 1986, p. 95.
- [44] R.C. Bansal, J.-B. Donnet, F. Stoeckli, *Active Carbon*, Marcel Dekker, New York, 1988.
- [45] F. Rodríguez-Reinoso, M. Molina-Sabio, *Carbon* 30 (1992) 1111.
- [46] F. Derbyshire, M. Jagtoyen, M. Thwaites, in J.W. Patrick, Ed., *Porosity of Activated Carbons: Characterization and Applications*, 1995, p. 227 ff.
- [47] H. Kienle, E. Baeder, in *Activated Carbon*, Ferdinand Enke Verlag, Stuttgart, Germany, 1980.
- [48] R. Burmeister, B. Despeyroux, K. Deller, K. Seibold, P. Albers, *Stud. Surf. Sci. Catal.* 78 (1993) 361.
- [49] P. Albers, R. Burmeister, K. Deller, B. Despeyroux, German patent DE 4308101, 1994, to Degussa.
- [50] K. Deller, B. Despeyroux, E. Peldszus, B. Kleinwaechter, U.S. patent 5,512,529, to Degussa.
- [51] M. Campanati, G. Fornasari, A. Vaccari, *Catalysis Today* 77 (2003) 299.
- [52] J.R. Ebner, T.S. Franczyk, Int. patent WO 96/01146 (1996), to Monsanto Company.
- [53] K.D. Henkel, in *Ullmann's Encyclopedia of Industrial Chemistry*, 7th ed., electronic encyclopedia, Wiley-VCH, Weinheim, Germany, 2007.
- [54] J.C. Middleton, K.J. Carpenter, in *Ullmann's Encyclopedia of Industrial Chemistry*, 7th ed., electronic encyclopedia, Wiley-VCH, Weinheim, Germany, 2007.
- [55] P.N. Rylander, in *Ullmann's Encyclopedia of Industrial Chemistry*, 7th ed., electronic encyclopedia, Wiley-VCH, Weinheim, Germany 2007.
- [56] W. Gösele, C. Alt, in *Ullmann's Encyclopedia of Industrial Chemistry*, 7th ed., electronic encyclopedia, Wiley-VCH, Weinheim, Germany, 2007.
- [57] G. Eigenberger, in *Ullmann's Encyclopedia of Industrial Chemistry*, 7th ed., electronic encyclopedia, Wiley-VCH, Weinheim, Germany, 2007.
- [58] D.J. Anneken, S. Both, R. Christoph, G. Fieg, U. Steinberner, A. Westfechtel, in *Ullmann's Encyclopedia of Industrial Chemistry*, 7th ed., electronic encyclopedia, Wiley-VCH, Weinheim, Germany, 2007.
- [59] Canadian patent 1,157,844, 1981, to Ruhrchemie.

- [60] Patents DE 41 09 502C2, to Degussa; EP 0 505 863 B1, 1991, to Henkel.
- [61] Patents DE 42 09 832 A1, EP 0 632 747 B1, 1992, to Henkel.
- [62] E. Gritz, in G. Ertl, H. Knözinger, Eds., *Handbook of Heterogeneous Catalysis*, VCH Weinheim, Germany, 1997, p. 2221.
- [63] H. Buchold, T. Tacke, I. Beul, C. Rehren, P. Panster, poster presentation, Annual AOCS Meeting, Orlando, FL, 1999.
- [64] T. Tacke, I. Beul, C. Rehren, P. Panster, H. Buchold, in M.E. Ford, Ed., *Catalysis of Organic Reactions*, Marcel Dekker, New York, 2001, p. 91.
- [65] B. Chen, U. Dingerdissen, J.G.E. Krauter, H.G.J. Lansink-Rotgerink, K. Moebus, D.J. Ostgard, P. Panster, T.H. Riermeier, S. Seebald, T. Tacke, H. Trauthwein, *Appl. Catal. A* 280 (2005) 17.
- [66] K.S. Hayes, *Appl. Catal. A* 221 (2001) 187.
- [67] V. Arunajatesan, M. Cruz, K. Moebus, B. Chen, in S.R. Schmidt, Ed., *Chemical Industries (Catalysis of Organic Reactions)*, Vol. 115, CRC Press, Boca Raton, FL, 2007, p. 481.
- [68] J.C. Saukaitis, U.S. patent 5,644,056, 1997, to Hoechst Celanese Corporation.
- [69] V.L. Mylroie, U.S. patent 5,861,535, 1999, to Eastman Kodak Company.
- [70] H.E. Petree, J.B. Nabors, U.S. patent 4,272,238, 1980, to Ciba-Geigy Corporation.
- [71] S. Nishimura, *Handbook of Heterogeneous Catalytic Hydrogenation for Organic Synthesis*, Wiley, New York, 2001, p. 226.
- [72] F.S. Dovell, H. Greenfield, U.S. patent 3,336,386, 1967, to Uniroyal Inc.
- [73] F.S. Dovell, H. Greenfield, *J. Org. Chem.* 29 (1964) 1265.
- [74] H. Greenfield, *Ann. N.Y. Acad. Sci.* 145 (1967) 108.
- [75] V. Mylroie, L. Valente, L. Fiorella, M.A. Osypian, in R.E. Malz, Jr., Ed., *Chemical Industries (Catalysis of Organic Reactions)*, Vol. 68, Marcel Dekker, New York, 1996, p. 301.
- [76] D.S. Thakur, B.D. Roberts, T.J. Sullivan, G.T. White, N. Brungard, E. Waterman, M. Lobur, in J.R. Kosak, T.A. Johnson, Eds., *Catalysis of Organic Reactions*, Vol. 53, Marcel Dekker, New York, 1994, p. 561.
- [77] <http://www.evonik.com/catalysts>.
- [78] G. Neri, M.G. Musolino, S. Galvagno, *Ind. Eng. Chem. Res.* 34 (1995) 2226.
- [79] R.G. Benner, A.C. Stevenson, U.S. patent 2,619,503, 1952, to DuPont.
- [80] D.P. Graham, L. Spiegler, U.S. patent 2,823,235, 1958, to DuPont.
- [81] J.M. Hamilton, L. Spiegler, U.S. patent 3,127,356, 1964, to DuPont.
- [82] J.R. Kosak, in R.E. Malz, Jr., Ed., *Catalysis of Organic Reactions*, 68 (1968) 31.
- [83] E. Auer, M. Berweiler, M. Gross, J. Pietsch, D.J. Ostgard, P. Panster, in M.E. Ford, Ed., *Catalysis of Organic Reactions*, 82 (2001) 293.
- [84] D.J. Ostgard, U. Packruhn, M. Göttlinger, unpublished results.
- [85] *Chemical Week*, May 12, 2004, p. 35.
- [86] K.L. Ring, T. Kalin, M. Yoneyama, in *1,4 Butanediol*, CEH Marketing Research Report, 2001.
- [87] J. Haji, I. Yokotake, T. Yamaguchi, S. Masato, M. Nobuyuki, U.S. patent 5,177,254, 1993, to Mitsubishi Chemical Industries.

- [88] S.E. Pedersen, J.G. Frye, T.G. Attig, J.R. Budge, U.S. patent 5,698,749, 1997, to Standard Oil Company.
- [89] T.R. Felthouse, J.C. Burnett, B. Horrell, M.J. Mummey, Y.K. Kuo, in *Kirk-Ohmer Encyclopedia of Chemical Technology*, Vol. 15, Wiley, New York, 2001, p. 481.
- [90] D.H. Meyer et al., U.S. patent 3,584,039 1971, to Standard Oil Company.
- [91] I. Puskas, D.E. James, U.S. patent application 4421676 A, 1983, to Standard Oil Company.
- [92] N. Pernicone, *Catal. Today* 44 (1998) 129.
- [93] M. Malentacchi, L. Cavalli, C. Rubini, European patent application 879641 A1, 1998, to Süd-Chemie.
- [94] J.F. White, U.S. patent application 0119665 A1, 2003, to Engelhard.
- [95] A.K.S. Murthy, *Chem. Eng.* (1999) 94.
- [96] J.M. Berty, *Chem. Eng. Prog.* 70 (1974) 121.
- [97] J. Nelles, *Chem. Technol.* 39 (1987) 328.
- [98] P.C. Borman, A.N.R. Bos, *AIChE J.* 40 (1994) 862.
- [99] J.J. Carberry, in R. Anderson, M. Boudart, Eds., *Cataysis: Science and Technology*, Springer, Heidelberg, Germany, 1980.
- [100] W. Ehrfeld, H. Löwe, V. Hessel, T. Richter, *Chem. Ing. Technol.* 69 (1997) 931.
- [101] W. Ehrfeld, V. Hessel, H. Löwe, *Microreactors: New Technology for Modern Chemistry*, Wiley, Chichester, UK, 2000.
- [102] N. Steinfeldt, O. Buyevskaya, D. Wolf, M. Baerns, *Stud. Surf. Sci. Catal.* 136 (2001) 185.
- [103] C.O. Bennett, *Catal. Rev. Sci. Eng.* 13 (1976) 121.
- [104] P. Biloen, *J. Mol. Catal.* 21 (1983) 17.
- [105] H. Kobayashi, M. Kobayashi, *Catal. Rev. Sci. Eng.* 10 (1974) 139.
- [106] D.P. Woodruff, T.A. Delchar, *Modern Techniques in Surface Science*, Cambridge University Press, Cambridge, UK, 1994.
- [107] J.W. Niemandsverdriet, *Spectroscopy in Catalysis*, VCH, Weinheim, Germany, 1995.
- [108] A.R. Garayhi, F.J. Keil, *Chem. Eng. Sci.* 4 (2001) 56.
- [109] D. Wolf, S. Seebald, T. Tacke, in S.R. Schmidt, Ed., *Catalysis in Organic Reactions*, CRC Press, Boca Raton, FL, 2007, p. 487.

Index

- ab initio, 95
Absorption, 497
Acetylene black, 545
 structure, 434
 surface area, 440
Acid-base catalysis, 179
Acidic groups, 61, 179, 188, 235
Acidity, 204
ACM monoliths, 422
Acridine-type nitrogen, 228
Activated carbon, 177, 482, 536
 ash contents, 538
 as supports for PEMFC electrocatalysts, 434
 formation, 4, 434
 industrial manufacture, 544
 particle size distribution, 539
 point of zero charge, 63
 pore size distribution, 537
 pore volume distribution, 537
 properties, 6
 surface area, *see* BET surface area
Activated carbon fibers, *see* Carbon fibers
Active carbon, *see* Activated carbon
Active sites, 178, 179
Acylation, 415
Adsorbent, 47, 177
Adsorption, 413, 447
Advanced oxidation processes (AOPs), 198
Aging of carbons, 250
Alkyl aromatics, 181
Alkylation, 555
Alkyl chlorides, dehydrochlorination of, 254
AM1 (Austin model 1), 95
Ammonia, 191
 decomposition, 133, 349
 synthesis, 141, 349
 treatment with, 189, 223
Ammoxidation, 224
Amorphous carbon, 9, 541
Aniline, 200, 546
Anthralur®, 219
Aqueous suspensions, 492
Armchair sites, 22, 101
Aromatics hydrogenation, *see* Hydrogenation
Atomic force microscopy (AFM), 487
Atom-transfer radical polymerization (ATRP), 346
Autoxidation of carbons, 254
Basal planes, 16, 47, 98, 178, 441, 515
Basic groups, 48, 59, 201, 234
Basicity, 199
Batch-stirred tank reactor, 548
BDO, *see* Butanediol
Benzyl alcohol oxidation, 139
BET surface area
 of activated carbons, 9, 63, 435, 536
 of carbon aerogels, 377, 436
 of carbon blacks, 9, 63, 434, 541
 of carbon nanotubes, 326, 437, 518
 of graphite, 9
 of Sibunit, 435
Biazzi hydrogenation process, 552
Bimetallic catalysts, 136, 140, 149, 169, 171, 343, 446, 451, 547
Biocatalysis, biocatalyst, 405
Biosensing, 520
Boehm titration, 58
Bond energies, 103
BP-Lurgi process, 559. *See also* Butanediol
Brønsted acidity, 80
Butanediol, 558
Calorimetry, 72
Carbenes, 22, 101, 275
Carbides, 318, 542
Carbon
 acido-basic properties, 21, 49, 201, 234, 251

- Carbon (*continued*)
 allotropic forms, 10, 507
 bulk properties, 16
 chlorination, 52, 242
 corrosion, 466
 diffusion, 313
 electrical conductivity, 16, 237, 327, 510
 fluorination, 54, 275
 gasification, 30, 110, 120, 232
 inertness, 136
 interaction with proton-conducting polymers, 432
 macrostructure, 5
 magnetic properties, 17
 mechanical properties, 17, 330
 microstructure, 5
 nanostructure, 8
 nucleation, 320
 nucleus, 319
 oxidation, 273
 precipitation, 314
 thermal conductivity, 16, 330
- Carbon aerogels, 178, 373
 as support for PEMFC electrocatalysts, 460
 density, 376
 mechanical properties, 376
 preparation, 374
 structure, 436
 surface area, *see* BET surface area
- Carbon black, 483, 540
 conductivity, 541
 corrosion, 466
 electrochemical oxidation, 466
 functionalized, 542
 preparation, 541
 structure, 433
 supported platinum, 443, 542
 surface area, *see* BET surface area
- Carbon-ceramic composite, 407, 530
- Carbon dioxide, conductometric determination, 244
- Carbon fibers, 4, 45, 131, 188, 195, 220, 443
- Carbon gels, 373. *See also* Carbon aerogels
- Carbonization, 222, 374, 484
- Carbon molecular sieve, 181
- Carbon nanofibers, 149, 157, 185, 309, 408, 510
 as supports for PEMFC electrocatalysts, 462
 structure, 325
 surface area, *see* BET surface area
- Carbon nanotubes, 148, 185, 309, 482
 as supports for PEMFC electrocatalysts, 462
- BET surface area, *see* BET surface area
 electronic properties, 324, 512
 growth mechanism, 12, 313
- hybridization, 327
 macroscopic shaping, 331
 properties, 326
 SEM, 332, 333
 structure, 324, 437, 508
 TEM, 310
- Carbon-oxygen reaction, 25, 54, 106, 121
- Carbon-TiO₂ composite, 486
- Carbon xerogels, 205, 375
- Catalyst profiling, 565
- Catalyst utilization factor, *see* Utilization factor
- Catalytic carbon deposition, 318
- Catalytic layer (CL), 430
- Catalytic wet air oxidation (CWAO), 203, 350, 386
- Cell density, 402, 408
- Centaur®, 225
- Chainlike aggregates, 540
- Channel black, 433
- Charge transfer, 328
- Chemical vapor deposition (CVD), 139, 172, 222, 311, 331, 338, 403
- Chlorination of surface, effect on catalytic activity, 242
- Cinnamaldehyde hydrogenation, 343, 390, 404
- Citronellal hydrogenation, 136
- CNDO (complete neglect of differential overlap), 94
- CO hydrogenation, *see* Fischer-Tropsch synthesis
- Coating, 403
- Coke, 3, 182, 254
- Colloids, 336
- Commercial catalysts, 546
- Conduction band, 497
- Conductometric analysis, *see* Carbon dioxide, conductometric determination
- Confinement effect, 267, 325
- Contact angle, 442
- Contact resistance, 431
- Continuous stirred tank reactor, 547
- Coprecipitation, 139, 345
- Cordierite, 408
- Corrosion
 of carbon materials, 464
 of MEAs, 467
- Crotonaldehyde hydrogenation, 135, 343
- Crystallite parameters
 crystallite height (L_c), 27, 435
 crystallite width (L_a), 27, 435
- CVD coating, 403
- Cyanosilylation, 353
- Cyclic voltammetry, 443, 524
- Cyclohexene hydrogenation, 341

- Dechlorination, 546
 D-glucose, 405
 Dehydration of alcohols, 186
 Dehydrochlorination, 254
 Dehydrogenation, 180, 352
 De-NO_x, 190, 356
 Deposition precipitation, 139, 165, 337
 Desulfurization, 52, 188
 DFT (density functional theory), 96, 319
 Dibenzothiophene, 143
 Diffusion limitations, 414
 Dipcoating, 403
 Dipole-dipole interactions, dispersive interactions, 46
 Double layer capacitance, 441
 Dry-mixing, 56
 D-sorbitol, 416
 Dusting, *see* Metal dusting
- Edge planes, *see* Graphene edges
 EHT (extended Hückel theory), 94
 Electrical conductivity, *see* Carbon; Carbon black; Carbon nanotubes
 Electrocatalysts, 429
 characterization, 446
 preparation, 443
 Electrocatalytic activity
 catalyst utilization, 452
 intrinsic catalytic activity, 452
 Electrochemically active surface area (EASA), 452
 Electronic structure methods, 94
 Electron paramagnetic resonance (EPR), 487
 Electron spin resonance (ESR), 18, 68
 Electron transfer, 26, 342, 350, 497, 509
 Electrostatic interactions, 26, 62, 138, 445
 Elemental analysis, 58
 Eley-Rideal (ER) mechanism, 100
 Encapsulation, 268, 277
 Energy dispersive x-ray analysis (EDX), 72
 Environmental catalysis, 45, 81, 350, 384
 Enzyme, 355, 413, 518
 EPMA (electron probe microanalysis), 410
 Epoxidation, 290, 294
 Esterification, 206, 351, 405
 Ethylbenzene, *see* Oxidative dehydrogenation of ethylbenzene (ODE)
 Extended x-ray absorption fine structure spectroscopy (EXAFS), 450
 External mass transfer limitations, 415
- Filamentous carbon, 309
 Fischer-Tropsch synthesis, 149, 344
 Fixed-bed reactor, 550
- Flue gas, 194
 Fluidized bed, 311
 Fuel-cell catalysts, 354, 387
 Fullerenes, 340, 349, 509
 Furnace black, 433, 440, 542
- Gallic acid, 200
 Gas diffusion layer, 461
 Gasification, 5, 56, 182, 232
 inhibiting effect on, 236
 Geminox® process, 559
 Graphene edges, 13, 17, 47, 101, 115, 271, 323, 465, 511
 Graphite
 electrochemical properties, 516
 electronic properties, 512
 Graphitization, 27, 68, 349, 465
 structure, 509
 Graphitized carbon black, 143
- Halogenation, 206
 Halogenization, 56
 Halonitrobenzene, 546
 HDS, *see* Hydrodesulphurization
 Heat treatment, 3, 50, 51, 56, 188, 245, 380
 Heterogenised transition metal complexes, 267
 Heteropolyacids, 351, 392
 Hexachloroplatinic acid, 138, 158, 389, 542
 HF (Hartree-Fock), 96
 High surface area graphite (HSAG), 141
 High-throughput testing, 563
 HMO (Hückel molecular orbital theory), 94
 Hybrid QM/MM, 97
 Hydrochloric acid, adsorption of, 234
 Hydrocracking, 206
 Hydrodechlorination, 354, 392
 Hydrodehalogenation, 206
 Hydrodenitrogenation (HDN), 143
 Hydrodesulphurization, 143, 351
 Hydroformylation, 297, 345
 Hydrogel, 374
 Hydrogenation, 147, 340, 389, 405, 551, 554
 asymmetric, 298
 of alkenes, 296, 340
 of aromatics, 342
 of CO and CO₂, 147, 344
 of ethylene, 341
 of α,β unsaturated aldehydes, 134, 341, 389, 404
 selective, 135, 342, 405
 Hydrogen bond, 46, 95, 269
 Hydrogen bromide, carbon-catalyzed synthesis, 250
 Hydrogen chloride, adsorption of, 234

- Hydrogen cyanide, treatment with, 224
 Hydrogen peroxide, 196, 468
 Hydrogen storage, 104
 Hydrogen sulphide, 194, 356
 Hydrotreating reactions, 143
 Hydroxyl radicals, *see* Radicals
- Immobilization, 268, 405
 Impregnation method, 382, 444
 Incipient wetness impregnation (IWI), 137, 157, 336
 INDO (intermediate neglect of differential overlap), 107
 Inductive coupled plasma (ICP), 58
 Infrared spectroscopy, 63, 335, 467, 487
 Inhibiting effect
 of aging on gasification reactions, 252
 of boron, on carbon oxidation, 18
 of surface chlorination on catalytic activity, 242
 of surface oxides on catalytic activity, 252
 Integral type, 403
 Internal diffusion limitations, 414
 Interphase interaction, 498
 Inverse gas chromatography, 75
 Ion adsorption, 158
 Ionic liquids, 342
 Iridium catalysts, 284, 354
 Iron catalysts, 133, 336, 348, 557
 Isoelectric point, 26, 61, 138
 Isomerization reactions, 136
- Jacobsen catalyst, 280, 285, 292
- Kapton®, 220
 Kevlar®, 220
 Kjeldahl analysis, 227
 Knovenagel condensation, 206, 356, 393
- Lactone, 49, 467. *See also* Oxygen containing functional groups
 Lamp black, 433
 Langmuir-Hinshelwood (LH) mechanism, 100, 490
 Langmuir-type isotherms, 240
 LCAO (linear combination of atomic orbitals), 101
 LCBO (linear combination of atomic bond orbitals), 101
 Leaching, 269, 280, 345, 349, 356, 418
 Lennard-Jones potential, 104
 Lewis acidity, 80, 186
 Lewis base, 233
- Lipase, 413
 Loop reactor, 548
- Many-body Tersoff potential, 123
 Mass transfer, 415, 489, 561
 Mass transport in PEMFC, 460
 Melamine-formaldehyde resins, 220
 Membrane electrode assembly (MEA), 430
 Mesopores, *see* Pore
 Metal
 carbides, 314, 318, 380
 distribution, 545
 dispersion, 132, 164, 268, 322, 338, 389, 453, 546
 dusting, 317
 oxides, 449, 491, 538
 phosphides, 334
 sulfides, 143, 334
 Metal-doped carbon aerogels, 379, 383
 Metalloporphyrins, carbon supported, 283
 Metal-support interaction, 123, 145, 322, 454, 483
 Methanation, 142, 349
 Methanol
 dehydration, 187
 oxidation, 140, 219, 249, 350, 430
 synthesis, 345
 Mesoporous carbon, 146, 390. *See also* Ordered mesoporous carbon
 MIBK (methyl isobutyl ketone), 353
 Microemulsion, 140
 Micropores, 20, 132, 166, 180, 393, 537. *See also* Pore
 Microreactors, 357
 Micro-structured reactors, 562
 MNDO (modified intermediate neglect of differential overlap), 95
 Mitsubishi process, 559. *See also* Butanediol
 Mizoroki-Heck reaction, 393
 MNDO (modified neglect of diatomic overlap), 95
 Modifier, 545
 Molecular dynamics (MD) simulations, 97
 Molecular mechanics (MM), 97
 Molecular simulations (MS), 93
 Molecule immobilization, 268
 Møller/Plesset perturbation (MP) theory, 96
 Molybdenum catalysts, 139, 380
 Monolithic carbon gel, 376
 Monolithic stirred reactor (MSR), 413
 Monoliths, 373, 402
 Monte Carlo (MC) methods, 98
 Mullite, 422
 Multi-walled carbon nanotubes, 309

- Nanoelectrode, 524
- Nanoparticles, 313
- Naphthalenetrisulphonic acid, 200
- NDDO (neglect of diatomic differential overlap), 95
- Nickel catalysts, 162, 168, 314, 343, 348, 382
- NiMo catalysts, 133
- Nitrobenzene, 202, 342, 554
- Nitrogen-doped carbon nanotubes, 325
- Nitrogen species in carbons, 50, 179, 228, 272, 538
- Nitrogen, quantitative determination, *see* Kjeldahl analysis
- Nomex®, 220
- Noncovalent interactions, 268
- NO_x reduction, 190. *See also* De- NO_x
- NO_x removal, 177, 350, 491
- Nuclear magnetic resonance (NMR), 69
- NVE ensemble, 97
- NVT ensemble, 97
- Ohmic losses, 452
- Ordered mesoporous carbon, 436
- Organic pollutants, 200
- Organometallic complexes, carbon supported, 267
- Oxalic acid, 200
- Oxamic acid, 200
- Oxidation, 54
 - of alkanes, 294
 - of arsenite ions, 249
 - of benzyl alcohol, 139
 - of cyanide ions, 249
 - of cyclohexanol, 404
 - of Fe(II) ions, 205, 246
 - of hydrogen, 429
 - of hydrogen sulphide, 194, 247
 - of methanol, *see* Methanol oxidation
 - of methyl mercaptan, 248
 - of NO_x , 190, 491
 - of oxalic acid, 244
 - of Sn(II) chloride, 249
 - of sulfur dioxide, 188, 244
 - of sulfurous acid, 238
- Oxidative dehydrogenation, 181
- Oxidative dehydrogenation of ethylbenzene (ODE), 181, 356
- Oxidative treatments, 140
- Oxidizing agents, 48, 334
- Oxygen containing functional groups, 21, 49, 201, 234, 251, 440, 538
- Oxygen reduction reaction (ORR), 387, 431
- Ozone, 198, 275
- π -complexation, 80
- $\pi - \pi$ interactions, 269, 274
- Palladium
 - complexes on carbon, 296, 297
 - effect on aging, 252
 - interaction with carbon nanotubes, 328, 339
 - on activated carbon, 139
 - on activated carbon fibers, 169
 - on carbon aerogels, 382
 - on carbon nanotubes, 334
 - reduction, 169
 - sintering, 161
- Palladium catalysts
 - dispersion, 160
 - for fuel cells, 355
 - for hydrodechlorination, 354, 392
 - for hydrogenation, 147, 341, 390, 404, 561
 - for Mizoroki-Heck reaction, 393
 - preparation, 139, 164, 166, 337
 - TEM, 165
- PAN-based carbon fibers, 220
- Pelletization, 331
- pH, 61
- Phenolic compounds, 200
- Phenols, 202, 342, 350
- Phenol-formaldehyde resins, 220
- Phenolic surface groups, 138, 252. *See also* Oxygen containing functional groups
- Phosgene, 177, 250, 556
- Photodecomposition, *see* Photodegradation
- Photodegradation, 492
- Photosensitization, 492
- Physical adsorption, 26, 75, 121
- pK_a distribution, 60
- Platinum
 - adsorption energy on graphite, 455
 - colloids, 445
 - electrochemical deposition, 446
 - interaction with carbon nanotubes, 328, 339
 - on activated carbon, 564
 - on carbon aerogels, 379
 - on carbon black, 132, 542
 - on carbon nanotubes, 333, 462
 - nanoclusters, 123
 - sputtering, 443
- Platinum catalyst
 - cyclic voltammetry, 450
 - for carbon gasification, 379
 - for catalytic wet air oxidation, 350, 386
 - for fuel cells, 355, 387, 432
 - for hydrogenation, 134, 342, 389, 565
 - for hydrogen oxidation reaction, 446
 - for reductive alkylation, 555
 - for selective oxidation, 404

- Platinum catalyst (*continued*)
 for xylene combustion
 particle size effect in, 453
 poisoning, 455
 preparation, 138, 168, 333, 337
 reduction, 449
 TEM, 339
 utilization factor, *see* Utilization factor in
 PEMFC
 vanadium doped, 554
 PM3 (parametric method 3), 95
 Point of zero charge (PZC), 21, 61, 158
 Polarization curve, 431
 Polarography, 78
 Polyacrylonitrile, *see* Pyrolyzed polyacrylonitrile
 Polymer wrapping, 274
 Polymerization of olefins, 136, 300, 345
 Polyol method, 171
 Pore, 537
 connectivity, 19
 diffusion, 179
 filling, 461
 shape, 133
 size and volume distribution, 537
 structure, 158, 164
 Pore size distribution, 19, 196, 537
 Potentiometric titration, 60
 PPP (Pariser-Parr-Pople), 94
 Precipitation, 139, 165
 Proton exchange membrane fuel cells (PEMFC),
 429
 PtRu catalysts, 355
 for fuel cells, 355
 for hydrogenation, 343
 on carbon nanotubes, 462
 preparation, 172
 TEM, 339, 448
 XRD, 449
 PtSn catalysts, 136, 355
 Pyridine, 143, 222
 Pyridine-N-oxides, 229
 Pyridine-type groups, 50, 189, 220
 Pyrolytic carbon, 3, 313
 Pyrolyzed polyacrylonitrile, 180
 Pyrone-like structures, 22, 234
 Pyrrole-type nitrogen, 228
 Pyruvic acid, 200
 QCISD, 96
 QCISDT, 96
 QM (quantum mechanics), 97
 Quaternary nitrogen, 229
 Quinone-type groups, 22, 441. *See also* Oxygen
 containing functional groups
 Radicals, 15, 68, 197, 220, 224, 248, 386, 497
 Raman spectroscopy, 18, 325
 Raney catalysts, 406
 Reductive alkylation, 555
 Reppe process, 558
 Rideal-Eley mechanism, 188
 Ring-opening metathesis polymerization
 (ROMP), 346
 Rhenium catalysts, 145, 555
 Rhodium
 catalyst for hydroformylation, 345
 chiral complexes on carbon, 282
 complexes on carbon, 296, 297, 342, 345
 interaction with carbon nanotubes, 339
 Ruthenium
 complexes on carbon, 287, 338
 interaction with carbon nanotubes, 339
 on activated carbon, 160
 on carbon aerogels, 382
 on carbon nanotubes, 333
 SEM, 410
 TEM, 409, 448
 Ruthenium catalysts
 for ammonia decomposition, 133, 349
 for ammonia synthesis, 134, 141, 349
 for catalytic wet air oxidation, 350
 for Fischer-Tropsch synthesis, 149
 for hydrogenation, 135, 343, 404, 421
 for reductive alkylation, 555
 preparation, 164, 168, 337
 stability, 418
 SCF (self consistent field), 94
 Selective catalytic reduction (SCR), 191
 Selective hydrogenation, *see* Hydrogenation
 Selective oxidations, 206, 535
 Semiconductor, 237, 433, 439, 498, 509, 512
 Semi-empirical methods, 94
 Sibunit, 177, 435, 450
 Silvera-Goldman potential, 104
 Single-walled carbon nanotubes, 104, 309, 483
 Sintering, 134
 Skeletal isomerization catalysts, 351, 391
 Slurry catalyst, 331, 418
 Sol-gel process, 350, 373, 485
 Solubility
 of C in metals, 316
 of N in carbons, 220
 SO_x oxidation, 188, 244
 Spectroscopic methods, 63, 227
 Spill-over, 22, 342
 Sputtering, 382
 Stability, 418
 Steady state reactors, 561

- Steam activation
 of activated carbon, 537
 of carbon gel, 376
- Stone-Wales defects, 329
- Styrene, 136, 181, 346, 393
- Succinic acid, 200
- Sucrose, carbons prepared from, 220
- Sulfur halides, 177
- Sulfurization, 143
- Sulfurous acid, oxidation of, 238
- Sulfur species in carbon, 51, 55
- Supercritical deposition, 382
- Superoxide radical anions, 257
- Supersaturation, 319
- Support covalent bonding, 268
- Surface area, *see* BET surface area
- Surface chemical properties, 134
- Surface chemistry, 45, 58, 75, 180, 219
- Surface diffusion, 492
- Surface functionalization, 336
- Surfactants, 200
- Sutton-Chen potential, 123
- Synergy factor, 492
- Temperature programmed desorption (TPD), 76, 162, 179
- Terephthalic acid, 560
- Textile dyes, 200, 488
- Textural properties, 144, 181
- Thermal blacks, 433
- Thermogravimetric and differential thermal analysis (TGA-DTA), 487
- Thiophene, 144, 351
- TiO₂, photocatalysis by, 350, 481
- Toluenediamine, 556
- Total organic carbon (TOC), 201, 487
- Transesterification, 356, 405
- Transmission electron microscopy (TEM), 433, 487
- Trickle-bed reactors, 401, 560
- Tubular reactor, 547
- Turbostratic carbon, 544
- Ultramicro electrode (UME), 525
- Ultrasonic treatment, 491
- Unsaturated aldehydes,
 see Hydrogenation
- Urea, 225
- Utilization factor in PEMFC, 457
- UV-vis, 486
- Valence band, 497, 512
- Vinyl chloride, synthesis of, 254
- Volatile organic compounds combustion,
 384
- Voltammetry, 78
- Vulcan, 388, 542
 as support for PEMFC electrocatalysts,
 433
- Washcoat, 410
- Water-gas shift reaction, 351
- Water-in-oil emulsion, 446
- Water management, 460
- Water splitting, 356, 495
- Wettability
 carbon blacks, 442
 contact angle of water, 442
- Wheeler-Weisz modulus, 414
- Wilkinson catalyst, 282, 284
- X-ray absorption spectroscopy, 449
- X-ray diffraction (XRD), 18, 449, 486
 carbon blacks, 434
 d_{002} spacing, 434
- L_a , *see* Crystallite parameters
- L_c , *see* Crystallite parameters
- X-ray near-edge spectroscopy (XANES), 230, 450
- X-ray fluorescence, 72
- X-ray photoelectron spectroscopy (XPS), 66, 227, 487
- Young-Laplace equation, 461
- Zero point of charge, *see* Point of zero charge (PZC)
- Zigzag sites, 17, 22, 101, 513, 520